Alexis Le Pichon · Elisabeth Blanc
Alain Hauchecorne *Editors*

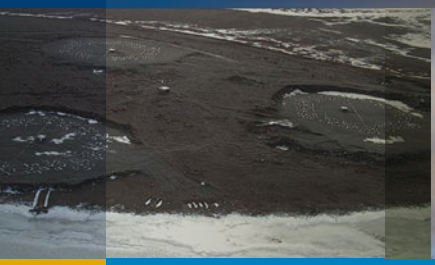

Infrasound Monitoring for Atmospheric Studies

Challenges in Middle Atmosphere Dynamics and Societal Benefits

Second Edition

Springer

Infrasound Monitoring for Atmospheric Studies

Alexis Le Pichon · Elisabeth Blanc
Alain Hauchecorne
Editors

Infrasound Monitoring for Atmospheric Studies

Challenges in Middle Atmosphere Dynamics and Societal Benefits

Second Edition

Springer

Editors
Alexis Le Pichon
CEA, DAM, DIF
F-91297 Arpajon
France

Elisabeth Blanc
CEA, DAM, DIF
F-91297 Arpajon
France

Alain Hauchecorne
SHTI
LATMOS/IPSL
Guyancourt
France

ISBN 978-3-319-75138-2 ISBN 978-3-319-75140-5 (eBook)
https://doi.org/10.1007/978-3-319-75140-5

Library of Congress Control Number: 2018935869

Cover illustration: Sarychev Peak, Kurile Islands—Earth Science and Remote Sensing Unit, NASA Johnson Space Center. *Source* https://earthobservatory.nasa.gov/IOTD/view.php?id=38985—Three array elements of station I23FR. Courtesy of the Comprehensive Nuclear-Test-Ban Treaty Organization —ALOMAR. Leibniz-Institute of Atmospheric Physics. Courtesy of the Dr. Gerd Baumgarten —Noctilucent clouds (NLC) in polar regions. Leibniz-Institute of Atmospheric Physics. Courtesy of the Dr. Gerd Baumgarten

This Springer imprint is published by the registered company Springer Nature Switzerland AG
The registered company address is: Gewerbestrasse 11, 6330 Cham, Switzerland

Foreword

Infrasound, sound at frequencies lower than the limit of human hearing, is generated by human activities that include nuclear-weapon testing and the use of explosives in mining, and by natural events and processes such as volcanic eruptions, thunderstorms and the interactions of ocean waves. Infrasound propagates through the atmosphere and can be refracted down to the surface far from its source. The refraction takes place primarily in the relatively warm regions that occur in the upper stratosphere and lower mesosphere, at heights close to 50 km, and in the thermosphere, above 100 km. The path taken by the infrasound depends also on the wind field, and is sensitive not only to the climatological average state but also to the presence of variations associated with planetary and gravity waves, and atmospheric tides.

Measurement of infrasound at the ground enables explosive events to be detected and longer lived sources to be monitored. Estimates may be made of the location and nature of the source if atmospheric conditions are sufficiently well known, usually from the analysis of observations employed routinely for numerical weather prediction and climate monitoring. This led to the establishment of a global network of infrasound measurement stations by the Preparatory Commission for the Comprehensive Nuclear-Test-Ban Treaty Organization (CTBTO) as one component of its system for detecting nuclear explosions. The routine monitoring provided by the 50 or so CTBTO infrasound stations that are now fully operational is supplemented for general purposes by regional and national networks of receivers. Prototype operational systems for remotely detecting and subsequently monitoring volcanic eruptions are also now being implemented, in support of civil aviation.

Conversely, if the location and nature of the source of detected infrasound are well known, inferences may be drawn as to the prevailing atmospheric conditions and how well they are known from other types of observation. Numerical weather predictions systems increasingly include representations of the upper stratosphere and mesosphere, but the operational global observing system at these heights comprises only satellite-based radiance measurements that have limited vertical resolution and are subject to biases that have to be estimated once instruments are in orbit. Moreover, the modelling on which data analysis and forecasting depend is

subject to errors that are larger in the upper stratosphere and above than they are lower in the atmosphere. Addressing these issues is important because of the potential for improving weather forecasts that arises at certain times from the influence of middle and upper atmospheric conditions on the evolution of the lower atmosphere.

Complementary measurement techniques are vital for interpreting infrasound signals to gain insight into the dynamics of the upper stratosphere and mesosphere, and for supporting the improvement of modelling and routine observational analysis of the region. The latter could include bias correction of the operational radiance data from the higher sounding channels. These improvements should lead in turn to better characterization of infrasound sources. Both ground-based remote sensing using instruments such as lidars of different types, meteor radars, microwave wind radiometers and airglow spectrometers, and specialized satellite missions have roles to play. Related needs are for ready access to current and past data from these types of observation, with wide geographical coverage.

This book contains a comprehensive set of articles covering many aspects of infrasound detection and the uses to which measurements are put. It provides accounts of some of the important complementary types of observation and what has been learnt from them. It describes the substantial scientific and technological advances, developments in understanding the dynamics of the upper stratosphere and mesosphere, and progress towards wider societal benefit made since the first volume was published in 2010. This includes important contributions made within the ARISE and ARISE2 projects funded under successive European-Union programmes for research and technological development.

Reading, UK

Dr. Adrian Simmons
European Centre for Medium-Range
Weather Forecasts, Member of the Advisory
Boards for ARISE and ARISE2

Preface

The publication of this book comes shortly after the Comprehensive Nuclear-Test-Ban Treaty (CTBT) marked its twentieth anniversary in 2016. This important milestone offered an opportunity for the global community to take stock of achievements in banning nuclear tests thus far, and to encourage new momentum in strengthening the global commitment to the Treaty and to further develop its verification regime. The Comprehensive Nuclear-Test-Ban Treaty Organization (CTBTO) which is mandated to establish this verification regime in anticipation of the entry into force of the CTBT is constantly improving and upgrading its capacity in this regard. As the network of monitoring stations has grown over the past few decades, the technology has also improved to the effect that the system is now far more sensitive and accurate than was originally envisaged by its designers. Simultaneously, as we enhance the awareness of the benefits offered by the Treaty, we have also expanded the civil and scientific applications of the International Monitoring System (IMS) data to provide ever greater value for the international community. The scientific community and Member States have been reaping the benefits of this increased capacity and the development and prospects of the infrasound technology are an excellent example to illustrate this dynamic.

In many ways, the current state of infrasound technology as a science owes its existence to the CTBT, having been a marginal—and top secret—endeavour by a few states to keep an eye on atmospheric nuclear tests during the Cold War. When I joined CTBTO as Director of the International Data Centre (IDC) a decade ago, I realized the full potential of infrasound technology for explosion monitoring, but also for civil and scientific applications. I have witnessed the fast evolution of infrasound technology towards maturity, especially in terms of measurement systems, calibration capability, data processing and impact across numerous applications. In order to make it a more effective tool for explosion monitoring, CTBTO has pushed the technology forward by supporting the complete redesign of the IDC

infrasound automatic and interactive review system between 2004 and 2010. These efforts 'paid off' not least with the contribution of the technology to the detection of the underground nuclear test announced by DPRK on 12 February 2013.

Beyond nuclear test detection, infrasound technology has also contributed to the detection of a number of significant events with global impact such as the 2011 Tohoku earthquake that triggered the Fukushima accident, large volcanic eruptions such as Calbuco in Chile in 2015 or Mount Kelud in Indonesia in 2014, as well as the largest ever infrasound recorded event: the meteor that broke up over Chelyabinsk, Russia in 2013 which was a 500 kT airburst.

Specificities of the technology have been integrated into the IDC software re-engineering efforts and remain a priority today in order to strengthen the technical and scientific credibility of the organization.

CTBTO also actively participates in international collaboration projects on infrasound technology, such as the European infrastructure project ARISE (Atmospheric dynamics Research InfraStructure in Europe) and with the International Civil Aviation Organization (ICAO) in investigating the usefulness of IMS data and IDC products for the international civil aviation community in identifying and characterizing volcanic eruptions. We have also strengthened our collaboration with the international metrology community to provide measurement traceability in the IMS frequency range and to ensure that the IMS needs were the main driver for the definition of primary standards for infrasound technology.

As of June 2017, 82% of the IMS infrasound network is certified and our objective is to reach 90% completion level by 2019. There is a good momentum as illustrated by the recent installation of the station I16CN in Kunming, China in January 2017 and I20EC in Galapagos Islands, Ecuador in June 2017. While sustainability of the IMS network is a day-to-day challenge, innovative engineering solutions are being developed to optimize our systems and make them more robust.

Over the 20 years of its existence, the CTBT has resulted in an almost complete stop to nuclear testing. At the same time, our detection—and deterrence—capabilities continue to improve. The infrasound community has played an important role in this and as a result we have seen the renaissance of infrasound technology as a science that has been brought to maturity to support credible operations. We need to continue our endeavour to further optimize its implementation, to maintain the level of excellence and to make it accessible to a larger base of users in the service of the international community.

Vienna, Austria

Dr. Lassina Zerbo
CTBTO Executive Secretary
Vienna International Centre

Contents

Contributors

John-Paul Abbott Agriculture Research Services, Applied Technology Research Unit, US Department of Agriculture, Wooster, OH, USA

Kirkpatrick Alberts II Army Research Laboratory, Adelphi, MD, USA

Guillaume Angot Laboratoire atmosphères, milieux et observations spatiales (LATMOS), UVSQ Université Paris-Saclay, Sorbonne Université, CNRS, Guyancourt, France

Thibault Arnal CEA, DAM, DIF, F-91297 Arpajon, France

Nimar Arora Bayesian Logic, Cambridge, USA

Stephen Arrowsmith Sandia National Laboratories, Albuquerque, NM, USA

Jelle Assink R&D Department of Seismology and Acoustics, Royal Netherlands Meteorological Institute (KNMI), De Bilt, The Netherlands

Gerd Baumgarten Leibniz-Institute of Atmospheric Physics, Rostock University, Kühlungsborn, Germany

Elisabeth Blanc CEA, DAM, DIF, F-91297 Arpajon, France

Mark Boslough Sandia National Laboratories, Albuquerque, NM, USA

Daniel Bowman Sandia National Laboratories, Albuquerque, NM, USA

Nicolas Brachet CEA, DAM, DIF, F-91297 Arpajon, France

David Brown Geoscience Australia, Canberra, Australia

Peter Brown Department of Physics and Astronomy, University of Western Ontario, London, ON, Canada

Paola Campus Department of Earth Sciences, University of Firenze, Florence, Italy

Joshua Carmichael Los Alamos National Laboratory, Los Alamos, USA

Corentin Caudron Laboratoire de Volcanologie, G-Time, Département de Géosciences, Environnement et Société, Université Libre de Bruxelles, Brussels, Belgium

Lars Ceranna Federal Institute for Geosciences and Natural Resources (BGR), Hannover, Germany

Maurice Charbit Telecom Paris, Paris, France

Andrew Charlton-Perez Department of Meteorology, University of Reading, Reading, UK

Il-Young Che Earthquake Research Center, Korea Institute of Geoscience and Mineral Resources, Daejeon, Korea

Igor Chunchuzov Obukhov Institute of Atmospheric Physics, Moscow, Russia

Chantal Claud Laboratoire de Météorologie Dynamique (LMD) CNRS, Ecole Polytechnique, Palaiseau, France

Sandra Collier Army Research Laboratory, Adelphi, MD, USA

François Coulouvrat Sorbonne Universités, UPMC Univ Paris, CNRS, UMR 7190, Institut Jean Le Rond d'Alembert, Paris, France

David Cugnet LMD, PSL Research University, Ecole Normale Supérieure, Paris, France

James Cutts Jet Propulsion Laboratory, California Institute of Technology, Pasadena, CA, USA

Alvaro de la Camara Dpto. Fisica de la Tierra y Astrofisica, Univ. Complutense de Madrid, Madrid, Spain

Catherine de Groot-Hedlin Laboratory for Atmospheric Acoustics, Institute of Geophysics and Planetary Physics, Scripps Institution of Oceanography, University of California, San Diego, La Jolla, CA, USA

Rosmarie de Wit Space Weather Laboratory, NASA Goddard Space Flight Center, Greenbelt, MD, USA; Zentralanstalt für Meteorologie und Geodynamik (ZAMG), Vienna, Austria

Douglas Drob Naval Research Laboratory, Washington, DC, USA

Patrick Espy Department of Physics, Norwegian University of Science and Technology (NTNU), Trondheim, Norway

Läslo Evers R&D Department of Seismology and Acoustics, Royal Netherlands Meteorological Institute (KNMI), De Bilt, The Netherlands; Faculty of Civil Engineering and Geosciences, Department of Geoscience and Engineering, Delft University of Technology, Delft, The Netherlands

Thomas Farges CEA, DAM, DIF, F-91297 Arpajon, France

David Fee Wilson Alaska Technical Center and Alaska Volcano Observatory, Geophysical Institute, University of Alaska Fairbanks, Fairbanks, AK, USA

Beatriz Funatsu CNRS, Université de Nantes, UMR 6554 LETG, Nantes, France

Thomas Gabrielson Pennsylvania State University, State Colleg, PA, USA

Pierre Gaillard CEA, DAM, DIF, F-91297 Arpajon, France

Louis-Jonardan Gallin CEA, DAM, DIF, F-91297 Arpajon, France

Milton Garces Infrasound Laboratory, HIGP, SOEST, University of Hawaii at Manoa, Kailua-Kona, HI, USA

Steven Gibbons NORSAR, Kjeller, Norway

Jason Goad Florida Atlantic University, Boca Raton, USA

David Green AWE Blacknest, Brimpton, UK

Doug Grimmett SPAWAR Systems Center Pacific, San Diego, USA

Jonas Hagen Institute of Applied Physics, University of Bern, Bern, Switzerland

Giles Harrison Department of Meteorology, University of Reading, Reading, UK

Alain Hauchecorne Laboratoire Atmosphères Milieux et Observations Spatiales/IPSL, CNRS, UMR 8190, UVSQ, UPMC, Guyancourt, France; Laboratoire atmosphères, milieux et observations spatiales (LATMOS), UVSQ Université Paris-Saclay, Sorbonne Université, CNRS, Guyancourt, France

Chris Hayward Roy M. Huffington Department of Earth Sciences, Southern Methodist University, Dallas, USA

Michael Hedlin Laboratory for Atmospheric Acoustics, Institute of Geophysics and Planetary Physics, Scripps Institution of Oceanography, University of California, San Diego, La Jolla, CA, USA

Robert Hibbins Department of Physics, Norwegian University of Science and Technology, Trondheim, Norway

Jens Hildebrand Leibniz-Institute of Atmospheric Physics, Rostock University, Kühlungsborn, Germany

Josef Höffner Leibniz-Institute of Atmospheric Physics, Rostock University, Kühlungsborn, Germany

Patrick Hupe Federal Institute for Geosciences and Natural Resources, Hannover, Germany

Philippe Husson Meteo France, VAAC Toulouse, Toulouse, France

Jeffrey Johnson Department of Geosciences, Boise State University, Boise, ID, USA

Bernd Kaifler DLR, German Aerospace Center, Oberpfaffenhofen, Germany

Niklaus Kämpfer Institute of Applied Physics, University of Bern, Bern, Switzerland

Philippe Keckhut Laboratoire Atmosphères Milieux et Observations Spatiales/IPSL, CNRS, UMR 8190, UVSQ, UPMC, Guyancourt, France; Laboratoire atmosphères, milieux et observations spatiales (LATMOS), UVSQ Université Paris-Saclay, Sorbonne Université, CNRS, Guyancourt, France

Sergey Khaykin Laboratoire Atmosphères Milieux et Observations Spatiales/IPSL, CNRS, UMR 8190, UVSQ, UPMC, Guyancourt, France; Laboratoire atmosphères, milieux et observations spatiales (LATMOS), UVSQ Université Paris-Saclay, Sorbonne Université, CNRS, Guyancourt, France

Tae Sung Kim Earthquake Research Center, Korea Institute of Geoscience and Mineral Resources, Daejeon, Korea

Attila Komjathy Southwest Research Institute, San Antonio, TX, USA

Sergey Kulichkov Obukhov Institute of Atmospheric Physics, Moscow, Russia

Tormod Kværna NORSAR, Kjeller, Norway

Jean-Marie Lalande IMS (Univ. Bordeaux – CNRS – BINP), Talence Cedex, France

Matthieu Landès European-Mediterranean Seismological Centre C/O CEA, DAM, DIF, F-91297 Arpajon, France

Jan Laštovička Institute of Atmospheric Physics ASCR, Bocni II, Prague, Czech Republic

Christopher Lee Department of Meteorology, University of Reading, Reading, UK

Jonathan Lees Department of Geological Sciences, University of North Carolina, Chapel Hill, NC, USA

Alexis Le Pichon CEA, DAM, DIF, 91297 Arpajon, France

François Lott LMD, PSL Research University, Ecole Normale Supérieure, Paris, France

Emanuele Marchetti Department of Earth Sciences, University of Firenze, Florence, Italy

Régis Marchiano Sorbonne Universités, UPMC Univ Paris, CNRS, UMR 7190, Institut Jean Le Rond d'Alembert, Paris, France

Omar Marcillo EES-17, Geophysics Group Los Alamos National Laboratory, Los Alamos, NM, USA

Graeme Marlton Department of Meteorology, University of Reading, Reading, UK

Julien Marty CTBTO, Vienna International Centre, Vienna, Austria

Robin Matoza Department of Earth Science and Earth Research Institute, University of California, Santa Barbara, CA, USA

Pauline Maury Laboratoire Atmosphères Milieux et Observations Spatiales/IPSL, CNRS, UMR 8190, UVSQ, UPMC, Guyancourt, France

Pierrick Mialle CTBTO, IDC, Vienna International Center, Vienna, Austria; CTBTO PTS/IDC, Vienna, Austria

Christophe Millet CEA, DAM, DIF, F-91297 Arpajon, France

Nahoudha Mzé Laboratoire atmosphères, milieux et observations spatiales (LATMOS), UVSQ Université Paris-Saclay, Sorbonne Université, CNRS, Guyancourt, France

Peter Näsholm NORSAR, Kjeller, Norway

Guillaume Nief CEA, DAM, DIF, F-91297 Arpajon, France

John Noble Army Research Laboratory, Adelphi, MD, USA

Junghyun Park Roy M. Huffington Department of Earth Sciences, Southern Methodist University, Dallas, USA

Anna Perttu Earth Observatory of Singapore, Singapore, Singapore

Christoph Pilger Federal Institute for Geosciences and Natural Resources (BGR), Hannover, Germany

Randall Plate SPAWAR Systems Center Pacific, San Diego, USA

Katy Pol CEA, DAM, DIF, F-91297 Arpajon, France

Markus Rapp DLR, German Aerospace Center, Oberpfaffenhofen, Germany

Richard Raspet National Center for Physical Acoustics, University of Mississippi, University, MS, USA

Bruno Ribstein CEA, DAM, DIF, F-91297 Arpajon, France; CMLA, ENS Cachan, CNRS, Université Paris-Saclay, 94235 Cachan, France

Maurizio Ripepe Department of Earth Sciences, University of Firenze, Florence, Italy

Jeff Rothman Geophysical Institute, University of Alaska Fairbanks, Fairbanks, AK, USA

Rolf Rüfenacht Leibniz Institute of Atmospheric Physics, Kühlungsborn, Germany; Institute of Applied Physics, University of Bern, Bern, Switzerland

Kayla Seiffert Department of Geological Sciences, University of North Carolina, Chapel Hill, NC, USA

Elizabeth Silber Department of Earth, Environmental and Planetary Sciences, Brown University, Providence, RI, USA

Luca Simonini Thales Alenia Space, Cannes, France; Thales Solution Asia, Thales Research and Technology, Singapore, Singapore

Tereza Šindelářová Institute of Atmospheric Physics ASCR, Bocni II, Prague, Czech Republic

Pieter Smets R&D Department of Seismology and Acoustics, Royal Netherlands Meteorological Institute (KNMI), De Bilt, The Netherlands; Faculty of Civil Engineering and Geosciences, Department of Geoscience and Engineering, Delft University of Technology, Delft, The Netherlands

Wolfgang Steinbrecht Meteorologisches Observatorium, Deutscher Wetterdienst, Hohenpeißenberg, Germany

Gunter Stober Leibniz-Institute of Atmospheric Physics, Rostock University, Kühlungsborn, Germany

Brian Stump Roy M. Huffington Department of Earth Sciences, Southern Methodist University, Dallas, USA

Dorianne Tailpied Nanyang Technological University, Singapore, Singapore; Earth Observatory of Singapore, Singapore, Singapore

Benoit Taisne Earth Observatory of Singapore, Singapore, Singapore; Asian School of the Environment, Nanyang Technological University, Singapore, Singapore

Carrick Talmadge National Center for Physical Acoustics, University of Mississippi, Oxford, MS, USA

Julien Vergoz CEA, DAM, DIF, F-91297 Arpajon, France

Roger Waxler National Center for Physical Acoustics, University of Mississippi University, Oxford, MS, USA

Jeremy Webster Earth and Environmental Sciences, Los Alamos National Laboratory, Los Alamos, NM, USA

Cornelis Weemstra Faculty of Civil Engineering and Geosciences, Department of Geoscience and Engineering, Delft University of Technology, Delft, The Netherlands

Eliot Young Southwest Research Institute, San Antonio, TX, USA

Jiao Yu Department of Physics, Liaoning Shihua University, Fushun, Liaoning Province, People's Republic of China

Introduction

The establishment of the global infrasound network of the International Monitoring System (IMS), one of the four technologies supporting the Verification Regime of the Comprehensive Nuclear-Test-Ban Treaty (CTBT) contributed to the renaissance of infrasound research. Since then, infrasound, the science of low-frequency acoustic waves, has developed into a broad interdisciplinary field, encompassing academic disciplines, such as geophysics and meteorology. We are now approaching an era where time windows of several decades will benefit from continuous data acquisition. The increased number of operating IMS infrasound stations and the establishment of regional infrasonic arrays have evidenced an unprecedented potential of such enhanced network in terms of detection capability, in particular for the monitoring of extreme atmospheric events at global scale. Recent thorough analyses of infrasound records from natural events, such as the 500 kT meteor which exploded over Chelyabinsk (Russian Federation) on 15 February 2013, have also confirmed the potential of this technology to detect, locate and characterize natural hazards with high societal benefits.

Infrasonic waves propagate over broad spatial scales, sampling on their paths the lower, middle and upper atmosphere along the source-to-receiver path. In recent years, systematic investigations of low-frequency acoustic signals have evidenced quantitative relationships between infrasound observations and atmospheric dynamical parameters over a range of altitudes where measurements are sparse and rare. Since atmospheric specifications are routinely used in a large variety of atmospheric sciences and applications, the validation of their values and main features is relevant to a broad scientific community, which by now uses infrasound as a consolidated verification technique.

The volume *Infrasound Monitoring for Atmospheric Studies* published in 2010 by Springer (IBSN 978-1-4020-9507-8) reviewed the most important areas of theory and application of infrasound, offering also a state of the art of infrasound studies applied to atmospheric measurements. Since 2010, a number of worldwide institutions have engaged in active research programmes based on infrasound technology. Significant technical and scientific advances have thus been achieved in various fields, spanning through engineering, signal processing and propagation

modelling. Going beyond the mandate of verification of compliance with the CTBT, these studies promote the potential benefits of infrasound monitoring techniques for civil and scientific applications. The global character of the observed phenomena and the level of knowledge reached today in this science encourage the broadening of our current areas of research which, in turn, require a closer cooperation with upper atmosphere physicists and meteorologists.

The Middle Atmosphere (MA, including the stratosphere and mesosphere) is a dynamical region: the vertical and meridional structure of its temperature and its zonal wind are sensitive to atmospheric waves, which carry energy and momentum flux between different atmospheric layers. In the stratosphere, the propagation and the breaking of large-scale planetary waves are the cause of very spectacular stratospheric warming events that can destroy the polar vortex and reverse the zonal wind in mid-winter, leading to summer-like conditions with prevailing easterly winds. In the mesosphere, the amplitude of gravity waves originating from solar thermal tides increases with altitude due to the exponential decrease of the atmospheric density, until reaching a critical level where the gravity waves break. The MA mean state and variability is, as of today, poorly constrained in Numerical Weather Prediction (NWP) models due to lack of satellite observations to be incorporated in such models. In the stratosphere, the temperature is measured by thermal infrared and microwave sounders, but with a very poor vertical resolution (about 10 km). In the mesosphere, neither temperature nor wind data are assimilated above the top altitude of radiosonde (around 30 km). Validation of atmospheric analysis and forecast products, in particular in regions above 30 km altitude, are important for NWP applications, since the interaction between stratosphere and troposphere cannot be neglected. Several studies have indeed demonstrated that the quality of medium-range weather forecasts depends on the quality of the representation of the MA. In order to better capture the stratospheric–tropospheric interactions, weather and climate forecasters are thus moving towards a more comprehensive representation of the atmosphere. There is, therefore, a strong need for high-quality temperature and wind data in this region.

In recent years, the development of complementary ground-based observational platforms in several observation sites, including infrasound and innovative atmospheric remote sensing methods, have provided new scientific insight into the understanding of geophysical source phenomenology and related atmospheric processes. These platforms include Rayleigh lidars and airglow spectrometers for the measurements of the vertical temperature profile, Doppler lidars, radars and microwave radiometers for wind measurements. Such instruments provide additional integrated information on the structure of the stratosphere where data coverage is sparse. Until now, the instruments were operated independently from each other: one of the main achievements of the European Commission (EC)-funded ARISE Project has been to coordinate the observations from these technologies in three main sites around the ALOMAR Observatory in Northern Scandinavia, the Haute-Provence Observatory in Southern France and the Maïdo Observatory in Reunion Island. At these sites, each instrument maintains its independent level of accuracy, altitude range, vertical and time resolution. The synergy between the

respective measurements provides a higher degree of information on the atmospheric state and evolution than what would be obtained through independent measurements. The vertical profiles derived from the measurements of these instruments are now used to simulate the propagation of infrasound waves and to compare such simulations with the observations recorded by co-located microbarometers. In reverse, the observed characteristics of infrasound detections can be used to better constrain atmospheric wind and temperature profiles. In addition, new studies using lidar and mesospheric airglow observations complemented by satellite measurements help to determine with a higher degree of precision the interaction between atmospheric layers and the influence of large-scale waves on the atmospheric dynamics: this constitutes a first step towards their assimilation in NWP models. The new infrastructure reinforces collaborations among scientists while developing and integrating a large set of complementary networks: through the integration of different independent MA measurement techniques currently not assimilated in NWP models, it provides a quantitative understanding of the stratosphere–troposphere dynamical coupling, which will contribute significantly to several NWP applications.

The first impact of these technical developments and researches concerns the development of innovative and robust methods, capable of generating high societal benefits, to remotely monitor extreme events, such as volcanoes or severe weather. A second impact concerns the development of refined weather forecasting and climate models through the quantification of uncertainties and biases in the MA wind and temperature. It is expected that a better representation of gravity waves in stratosphere-resolving climate models and forcing on the troposphere will improve the accuracy in short- and medium-range weather forecasts. It can be expected that such investigations will be of considerable value for NWP applications, since climate science including monthly and seasonal predictability requires an improved quantitative understanding of the dynamical coupling between the MA and the troposphere. Besides the atmospheric science community, the evaluation of NWP models is essential for the future verification of the CTBT, since improved atmospheric models are extremely helpful to assess the IMS network performance at higher resolution, reducing source location errors and improving characterization methods. Capitalizing on such scientific and technical advances should reinforce the potential benefit of a routine and global use of infrasound for civil applications and enlarge the scientific community interested in the operational aspects of infrasound monitoring.

This comprehensive volume reviews the latest researches, developments and applications performed by experts in instrumentation, propagation, sources and observations, putting an emphasis on relevant contributions for middle-upper atmospheric dynamics. It offers both a state-of-the-art assessment of infrasound technology and relevant complementary observations and associated models, addressing new perspectives on key issues and challenges for climate related studies and civil applications.

The first part of this volume presents an overview on strategies that have been developed and implemented to increase data availability and network detection

capability of the IMS network, opening new perspectives for a growing number of civil and scientific applications. This part reviews the latest advances in the design and optimization of sensitive infrasound sensors and wind-noise reduction techniques. Non-traditional infrasound sensors such as maritime and free-flying infrasound sensors hosted by balloons are now being under study: the challenges and potential of such technologies to improve the existing network detection capability are discussed. A framework for evaluating the detection algorithms and the hypotheses developed for their operation is proposed. The standardization of both signal and noise models motivates the elaboration of alternative approaches to advance in the performance of detection and feature extraction algorithms. In the context of the future verification of the CTBT, the development and implementation of improved detection and location procedures now offer efficient tools to provide a realistic measure of the network performance and better characterize, at local, regional and global distances, the source at the origin of the detected signals.

The second part illustrates the potentiality of dense regional networks to detect local and regional small-magnitude surface explosions and to discriminate between natural and anthropogenic phenomena. The global IMS network has been designed to detect atmospheric explosions with an equivalent yield of 1 kiloton (1 kT) or more worldwide. Since the yield of anthropogenic sources generally remains much below 1 kT, most of events associated to such sources are only reported in single-station detection lists. Combining dense regional seismic and infrasound networks like the ones operated by the Institute of Geoscience and Mineral Resources (KIGAM) in South Korea or by the Norwegian Seismic Array (NORSAR), allows the development of more detailed source and propagation studies. Another example is the deployment of the USArray Transportable Array (TA), with an average interstation spacing of 70 km, which has demonstrated its capability to detecting and identifying sources of smaller energy than the ones which would have been observed by using a more sparse station distribution. In this new era of massive datasets, there is a unique opportunity to examine geophysical phenomena in more detail than before: the analyses of long-term collected signals from well identified sources, covering a wide range of distances and directions, highlight the existence of strong spatio-temporal variations in the waveform characteristics. Systematic assessments of the variability of the recorded infrasonic wave field at regional and global scales, on a broad range of timescales thus provide essential input data for studies of the middle-upper atmosphere.

Over the last decade, there have been significant improvements in global data assimilation capabilities of the lower, middle and upper atmosphere: the third part reviews operational and scientific research on atmospheric models that are available for the calculation of infrasound propagation. Full-wave numerical modelling techniques are now capable of describing the combined effects of the source and the atmosphere that influence propagation predictions in realistic conditions, by accounting for diffraction and scattering effects by atmospheric inhomogeneities. Conducting consistent analyses on a routine-basis provides an extensive database for help quantifying the relationship between infrasonic observables and atmospheric specifications, thus opening new areas of investigations in inverse

problems. Inversion procedures are proposed to delineate the vertical structure of the wind field, in a range of altitude inaccessible to operational ground-based weather stations and meteorology satellites. Such studies benefit from an infrastructure that integrates various MA measurement techniques and provide independent measurements.

The fourth part explores the utilization of infrasound, large-scale gravity and planetary waves to improve the spatio-temporal resolution of the middle-upper atmosphere dynamics and to better understand the physical processes controlling the interaction between atmospheric layers. With the increasing number of ground-based atmospheric observation networks deployed around the globe, the validation of analysis products in NWP models is relevant for a wide variety of applications. Characterizing large-scale atmospheric disturbances and simulating the variability of the atmosphere from ground to the ionosphere remain a challenge for all climate models. In particular, the lack of stratospheric variability in the low-top models has an impact on the stratosphere–troposphere coupling: these models do not produce long-lasting tropospheric impacts which are observed. Thus, correctly predicting the evolution of large-scale atmospheric perturbations like sudden stratospheric warming events (SSWs) can provide useful information on the longer term influences of the MA dynamics on the troposphere and lead to improved medium-range weather forecasts.

The infrasound monitoring system also offers a unique opportunity to provide in near-real time continuous relevant information about natural hazards, like severe thunderstorms, tornadoes or large volcanic eruptions. These phenomena produce large-scale waves over a broad range of time and spatial scales. The chapters in the fifth part discuss the potential benefits of infrasound measurements for detecting, locating and providing reliable source information and chronology of such events. In particular, these investigations are of considerable value for monitoring eruptive processes of active volcanoes. With the advent of civil aviation and the exponential growth in the air traffic, the problem of a volcanic ash encounter has become an issue, which needs to be addressed in real time. Infrasound observations can complete satellite detection of hazardous volcanic clouds, which is limited in time and can suffer from the cloud cover over large areas, leading to a more efficient mitigation of the risk of volcanic ash encounters and of ash cloud impact on aviation. This part of the volume provides a detailed status of the art in volcano monitoring at local, regional and global scales using infrasound technology and highlights the need for an integration of the IMS infrasound network with local and regional infrasound arrays capable of providing a timely early warning to the Volcanic Ash Advisory Centers (VAACs).

Editors thank all authors for their motivation in this project and their very valuable contributions. They are also grateful to Drs. J. Assink, G. Baumgarten, D. Bowman, P. Campus, A. Charlton-Perez, I. Y. Che, C. Claud, C. De Groot Hedlin, P. Espy, T. Farges, P. Gaillard, S. Gibbons, D. Green, M. Haney, G. Haralabus, M. Hedlin, J. Johnson, J. Lastovicka, F. Lott, J. F. Mahfouf, J. Marty, R. Matoza, P. Mialle, C. Pilger, K. Pol, R. Rufenacht, A. Simmons, C. Szuberla and B. Taisne

for their insightful reviews and comments on the initial drafts and supports during the completion of this book.

This book is dedicated to the memory of Dr. Jocelyn Guilbert, scientific expert and head of Laboratoire de Détection et de Géophysique at CEA, who died on 21 August 2016 after a courageous battle with cancer. Eminent seismologist, interested in source rupture process and propagation, and the development of high-resolution array techniques applied to dense networks, Jocelyn has earned an international recognition for his contribution in volcano seismology and innovative seismoacoustic approaches to model earthquake-generated infrasound. He inspired and shared his passion for fundamental and applied research in geophysics through stimulating discussions, encouraging explorative studies on emerging scientific problems.

Alexis Le Pichon
Elisabeth Blanc
Alain Hauchecorne

Part I
Instrumentation, Network and Processing: Instrumentation

Chapter 1
The IMS Infrasound Network: Current Status and Technological Developments

Julien Marty

Abstract The International Monitoring System (IMS) comprises 337 globally distributed facilities for seismic, hydroacoustic, infrasound, and radionuclide monitoring. This chapter focuses on the infrasound component of the IMS, often referred to as the IMS infrasound network. The chapter begins with an overview of the network and of the main challenges associated with its establishment, sustainability, and detection capability. It follows with a general description of IMS stations as well as with a review of the latest advances in array geometry, wind-noise reduction systems, infrasound sensors, calibration, meteorological data, data acquisition systems, and station infrastructure. This chapter is intended for researchers and engineers who are interested in the specifications, design, status, and overall capabilities of the IMS infrasound network or in the construction of state-of-the-art infrasound stations.

1.1 Introduction

The Comprehensive Nuclear-Test-Ban Treaty (CTBT) prohibits States Parties from carrying out, encouraging, or in any way participating in the execution of a nuclear explosion. The Treaty was adopted by the United Nations General Assembly on September 10, 1996 and opened for signature in New York on September 24, 1996. Twenty years later, it enjoys near-universality with 183 States Signatories and 166 ratifying States. Even with this high level of adherence, the CTBT has not yet entered into force. It still awaits ratification from 8 States out of the 44 specific nuclear technology holder States listed in Annex 2 to the Treaty. In the meantime, the Preparatory Commission (PrepCom) for the Comprehensive Nuclear-Test-Ban Treaty Organization (CTBTO) is responsible for promoting the CTBT and establishing a verification regime. The objective of the verification regime is to ensure compliance with the Treaty. It is composed of four elements, one of them being the International Monitoring System (IMS). The IMS comprises 337 globally distributed facilities for seismic, hydroacoustic, infrasound, and radionuclide monitoring as well as

J. Marty (✉)
CTBTO, Vienna International Centre, P.O. Box 1200, 1400, Vienna, Austria
e-mail: julien.marty@ctbto.org

A. Le Pichon et al. (eds.), *Infrasound Monitoring for Atmospheric Studies*,
https://doi.org/10.1007/978-3-319-75140-5_1

respective means of communication between these facilities and the International Data Centre (IDC) located in Vienna, Austria. This chapter focuses on the infrasound component of the IMS, often referred to as the IMS infrasound network. The main objective of the IMS infrasound network is the monitoring of atmospheric nuclear explosions although this network can also contribute to the monitoring of near-surface underwater explosions and shallow underground explosions. The most recent examples of such a contribution are the detection by two IMS infrasound stations of clear infrasound signals generated by the subsurface nuclear tests announced by the Democratic People's Republic of Korea (DPRK) on February 12, 2013 and September 3, 2017 (CTBTO 2013d, 2017b).

The development of the infrasound monitoring technology began soon after the first atmospheric nuclear explosions were carried out in 1945. The technology evolved rapidly over the following decades with advancements in measurement systems as well as in propagation and source models (Thomas et al. 1971). These advancements began to slow after the Partial Test Ban Treaty, prohibiting the testing of nuclear weapons in the atmosphere, underwater, and in the outer space, was signed in 1963. The last atmospheric nuclear explosion was conducted in 1980 and it is estimated that, between 1945 and 1980, 520 nuclear tests were carried out in the atmosphere for a total yield of 545 Mt (Pavlovski 1998). When CTBT negotiations started in 1994, research in the field of infrasound had made little progress over the preceding decades (Evers and Haak 2010). The urgent need to define requirements for the IMS infrasound network revitalized research on this technology (Dahlman et al. 2011). Whereas global seismological networks were already operational as the Treaty opened for signature, the IMS infrasound network was a first attempt at establishing a global infrasound network. Most specifications for this new network were, therefore, defined based on studies carried out during the Treaty negotiations and shared similarities with the seismic technology. In 2001, continuous and high-quality data started flowing in near real time from the first IMS infrasound stations to the IDC. The processing of this unique set of data quickly led to studies on station performance and brought about optimizations in infrasound station design and specifications (Christie and Campus 2010). Research also focused on global network detection capability, demonstrating through modeling that any atmospheric explosion with a yield greater than 1 kT TNT equivalent would be detected by the IMS infrasound network anywhere on Earth at any time (Le Pichon et al. 2009; Green and Bowers 2010). These theoretical results were confirmed through ground truth calibration experiments (Fee et al. 2013) and by the detection of explosion-like events, such as the breaking up of meteors in the atmosphere (Le Pichon et al. 2013).

Beyond explosion monitoring, data from the IMS infrasound network was rapidly found beneficial in the study of a number of natural (volcanoes, tornadoes, meteorites, lightning, calving of icebergs and glaciers, large earthquakes, auroras, etc.) and man-made (industrial activities, quarry blasts, rocket launches, supersonic aircraft, etc.) sources (Campus and Christie 2010). It has been known since the 1883 explosion of the Krakatoa volcano that natural sources can produce low-frequency sounds capable of propagating several times around the globe (Symons 1888). However, the continuous recording of global infrasound data has allowed civil

and scientific applications such as volcano information systems (Marchetti et al. 2019), the detection of near-Earth objects impacting the atmosphere or the better modeling of the middle atmosphere dynamics (Le Pichon et al. 2015). Furthermore, it was recently demonstrated that IMS infrasound data were not only accurate in the IMS frequency band (0.02–4 Hz) but also as down to 1-day period, paving the way to the global monitoring of atmospheric acoustic-gravity and gravity waves (Marty et al. 2010). Since the last atmospheric nuclear test occurred well before the establishment of the first IMS infrasound station, these growing civil and scientific applications based on IMS infrasound data are essential for supporting the sustainability of the IMS infrasound network and ensuring that the infrasound technology remains at the state of the art for Treaty verification purposes.

This chapter begins with an overview of the IMS infrasound network (Sect. 1.2) and of IMS infrasound stations (Sect. 1.3). The latest advances in array geometry (Sect. 1.4), wind-noise reduction systems (Sect. 1.5), sensors (Sect. 1.6), calibration (Sect. 1.7), meteorological data (Sect. 1.8), data acquisition systems (Sect. 1.9), and station infrastructure (Sect. 1.10) are then reviewed in the framework of the IMS specifications for infrasound stations.

1.2 The IMS Infrasound Network

1.2.1 Overview

The IMS infrasound network is composed of 60 globally distributed stations, whose locations are defined in Annex 1 to the Protocol to the Treaty (Fig. 1.1). Each of these stations is composed of an array of infrasound measurement systems capable of recording the micro-pressure changes produced at ground by the propagation of infrasonic waves. IMS infrasound stations continuously transmit these pressure fluctuation data together with state-of-health information to the IDC through the Global Communication Infrastructure (GCI). The data are then processed in near real time, with IDC automatic detection algorithms extracting infrasonic wave parameters from pressure fluctuation measurements for each station independently (Mialle et al. 2019). These wave parameters, together with station processing information from the seismic and hydroacoustic monitoring technologies, are used as inputs to IDC automatic source localization algorithms. The output of the IDC automatic processing of seismo-acoustic data includes event parameters, which are collected in Standard Event Lists (SELs). SELs are reviewed by IDC seismo-acoustic analysts within 2 days and the resulting events recorded in Reviewed Event Bulletins (REBs) (CTBTO 2011b). Natural events are automatically screened out from REBs within a few hours and the final results are published in Standard Screened Event Bulletins (SSEBs). The automatic and interactive processing of infrasound data has been operational since 2010 in the IDC. States Signatories have the right of full access to all IMS data and IDC products.

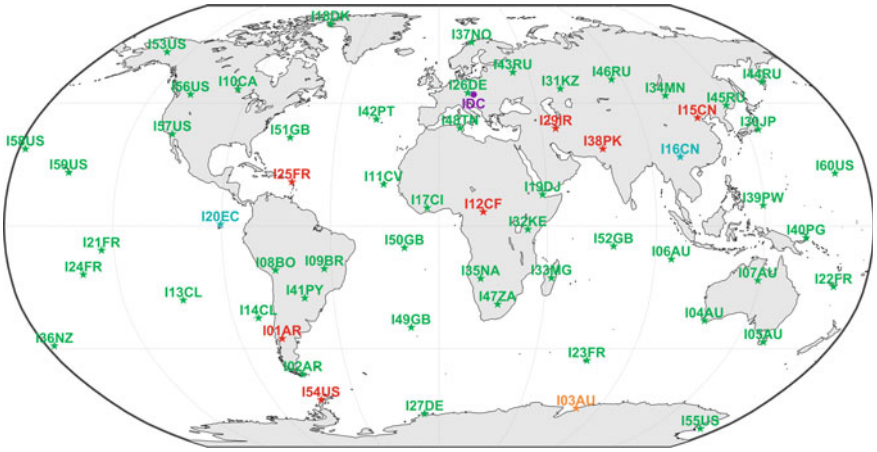

Fig. 1.1 Overview of the IMS infrasound network as of June 2017 with certified stations (green), installed stations (turquoise), stations under construction (orange), planned stations (red), and the IDC (purple)

When the CTBT opened for signature in 1996, only a few research infrasound stations were operating across the globe (Campus and Christie 2010). The establishment of 60 new infrasound stations was, therefore, a huge engineering challenge, especially since the international community was initially targeting an early Entry into Force (EiF) of the Treaty. From 1997 to 2006, the PrepCom focused its efforts on station constructions and certifications. The first IMS infrasound station was certified in 2001, and till 2006 between five and eight new infrasound stations were certified every year (Fig. 1.2). At this point, the total number of certified stations reached 37. Following this intense station construction period, the number of new certifications decreased to one or two stations per year for two main reasons. First, the remaining stations proved to be the most difficult to build primarily because of land availability, engineering, and political factors. Second, ensuring continuous operation of the existing stations became a competing priority. Stations that had failed since certification or had low data availability were repaired or upgraded. By 2012, 45 stations, representing 75% of the network, were certified with network data availability approaching 92% (Fig. 1.2). By this time, because of further reduced opportunities to build new stations, the progressive degradation of older stations and the PrepCom mandate to protect the investment already made by States Signatories, resources were progressively shifted from station construction to station upgrade. Nevertheless, efforts to establish the remaining stations continued with one new certification per year on average.

As of June 2017, the IMS infrasound network includes 49 certified stations, representing 82% of the network (Fig. 1.1). The installations of stations I16CN and I20EC were completed in January and June 2017, respectively. Stations I03AU is currently under construction. These three stations are planned to be certified over

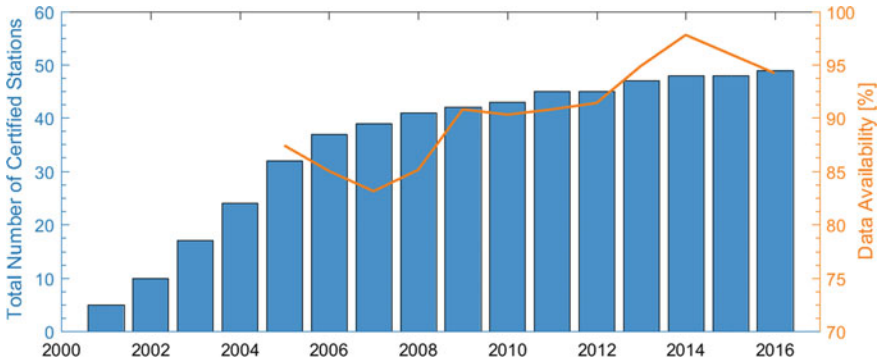

Fig. 1.2 Total number of certified stations (blue bars) and data availability for the overall IMS infrasound network (orange curve) as a function of time

the 2017–2018 time period. The minimum requirement for the infrasound network completeness to support the commissioning of the IMS specifies that 85% of the IMS infrasound stations shall be sending data to the IDC (CTBTO 2011c). This important milestone in the commissioning of the IMS is, therefore, expected to be met by 2018. The construction of the eight remaining stations has yet to be started. Site surveys were recently carried out for stations I01AR and I25FR. With land permits currently under negotiation with relevant authorities, it is expected that both these stations will be certified by 2020. This would bring the network to a 90% completion level and allow for the fulfillment of the minimum requirement for network completeness even in the case of outage of three stations. Negotiations for establishing stations I12CF, I15CN, I29IR, I38PK, and I54US are currently on hold because of pending resolution of land availability, security, or political issues. Finally, the last station with code 28 does not appear in Fig. 1.1 because its location is currently under the status "To be determined". During Treaty negotiations, this station was intended to be located in India. However, in June 1996, because of disagreement of the terms in the Treaty, India requested that this station be removed from the protocol to the Treaty (Dahlman et al. 2011). It is worth noting that Fig. 1.1 displays stations at their current locations, which do not always correspond to initial Treaty locations. For the majority of stations, the difference between the two locations does not exceed a few tenths of a degree and resulted from identifying a suitable piece of land in the area of the Treaty coordinates. However, for 11 stations the change exceeds 100 km, including 2 stations where the distance was about 1500 km. These more significant changes of coordinates were often due to the absence of a sustainable or high-performance solution in the vicinity of the Treaty coordinates. The impact of these coordinate changes on station performance and global network detection capability was carefully assessed before being officially approved by the PrepCom.

1.2.2 Data Availability

The IMS infrasound network is designed to detect an atmospheric nuclear explosion conducted at any given time and any point on the Earth. For this reason, the network must be continuously operational and strict specifications for Data Availability (DA) are defined in the draft Operational Manual for Infrasound Monitoring and the International Exchange of Infrasound Data further referred to as the IMS Operational Manual (CTBTO 2009, 2016d). Minimum requirements for DA are defined at the station level with each IMS infrasound station required to exceed the DA threshold of 98% over a 1-year period. It is worth noting that the DA definition has evolved since the first version of the IMS Operational Manual (CTBTO 1999) and currently includes data quality criteria. In order to be accounted for, data must be geophysical (segments with zeros, constant values, or absence of input from the sensor are discarded) and secure (authenticated, absence of site tampering). DA is also now computed on the minimum number of channels for an IMS infrasound station to be mission capable. Requirements for mission capability are defined in the IMS Operational Manual and will be discussed in Sect. 1.4.

Although all IMS infrasound stations currently include digital signing capability, the definition of the relevant data surety procedures is still underway. Since DA, as defined in the IMS Operational Manual, discards non-authenticated data, it is currently not very representative of the network status. For this reason, a Data Availability Unauthenticated (DAU) metric is also computed in the IDC. It is this metric which is represented in Figs. 1.2 and 1.3. Figure 1.2 shows that DAU at the network level increased from about 83% in 2007 to almost 98% in 2014. Since then, a slight decrease to 95% has been observed. As for all IMS Operational Manual requirements, the threshold of 98% will strictly apply after EiF. In the meantime, the network is in provisional operation with a DA midterm objective of 90% over the 2014–2017 time period (CTBTO 2013c) and a requirement of 96% for the commissioning of the IMS (CTBTO 2011c). Figure 1.3 shows the percentage of stations fulfilling DA requirements for these different thresholds. Since 2013, about two- thirds of the IMS infrasound stations are fulfilling the 98% threshold on a yearly basis, with a peak of nearly three quarters in 2014. Over the past 4 years, about 80% of the stations have been meeting the midterm objective of 90% with an increase of nearly 95% in 2014.

With the majority of IMS infrasound stations being installed in remote and harsh environments, fulfilling DA requirements for each of them is a real challenge. The CTBT assigns to the Technical Secretariat the responsibility of supervising, coordinating, and ensuring the operation of the IMS network in accordance with the IMS Operational Manuals. Since the Treaty has not yet entered into force, this responsibility currently falls upon the Provisional Technical Secretariat (PTS) located in Vienna, Austria (CTBTO 1996). The IMS Operational Manual defines the Station Operator (SO) as the entity responsible for the operation and maintenance of a specific station. SOs are typically designated by the States hosting the stations. They must ensure that their stations are operating properly, especially in meeting the data availability, data quality, and data surety requirements (CTBTO 2009). The duties

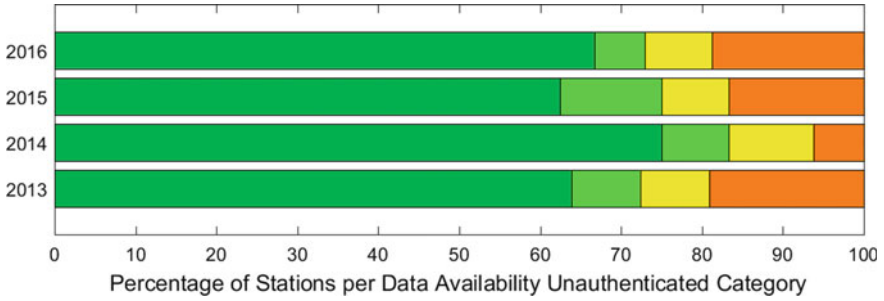

Fig. 1.3 Number of certified IMS infrasound stations with DAU above 98% (green), between 96 and 98% (light green), between 90 and 96% (yellow) and below 90% (orange) in percentage of the total number of stations

of the SOs include performing preventive maintenance and providing timely troubleshooting and repair in case of unexpected data outages. Proactivity, responsiveness, and technical skills of SOs are, therefore, by far the main drivers for achieving high data availability. For this reason, it is essential that capacity building efforts continue, including regular training and follow-up activities with the objective of encouraging SOs to define their own station monitoring routines and strengthening collaboration within the SO community. In parallel, SOs' performance should be evaluated against the IMS Operational Manual to ensure that all SOs comprehensively fulfill their duties (Nikolova et al. 2015).

Beyond the crucial role of SOs, IMS infrasound stations must be designed to be as reliable and resilient as possible within the available resources. To do so, data storage and retransmission capabilities are included at different levels, with these capabilities being verified at the time of certification or revalidation (Sect. 1.3). Except in the case of a complete station outage, data should be retransmitted to the IDC at the end of the outage and most stations should fulfill DA requirements. In reality, this is not always the case for three main reasons. First, the older stations have limited capabilities and will need to be upgraded in the future (Sect. 1.3.3). Second, minor equipment upgrades or configuration changes are from time to time performed without testing all station capabilities again. Third, data losses sometimes result in a combination of issues which are often hard to anticipate or simulate at the time of station testing. IMS infrasound stations shall also include redundancy at the array geometry level to ensure that mission capability and thus data availability are preserved even in case of the loss of array elements (Sect. 1.4). Stations shall also be designed to avoid single points of failure through the deployment of automatic or semiautomatic back-up systems. The adequate level of spare equipment shall be continuously available at the stations, especially for equipment necessary to maintain station mission capability. While equipment diversity is limited through the network because of the specificity of IMS requirements, attention shall be given to rely on different equipment models to avoid catastrophic network failure (Sect. 1.9). Finally, beyond standard manufacturer testing, station equipment shall undergo extensive testing in

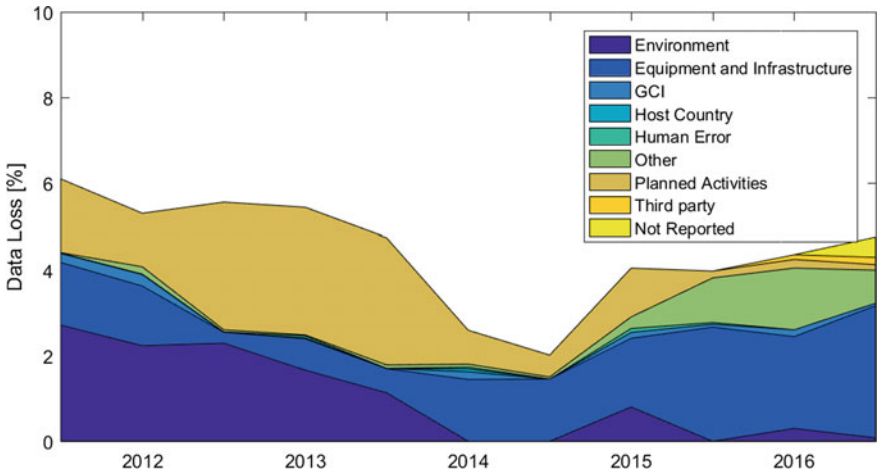

Fig. 1.4 Causes of station failure in percentage of data loss computed for the IMS infrasound network on a biannual basis over the 2011–2016 time period

operational conditions before being approved for deployment in the IMS network (Sects. 1.6 and 1.9).

In parallel with these station design measures, statistics on station failures are computed by the PTS with the objective of verifying whether the implemented engineering solutions and processes lead to reliability improvements. Figure 1.4 shows the causes of station failure in percentage of data loss for the IMS infrasound network from 2011 to 2016. A significant decrease of failures because of "Environment" (dark blue) and "Planned Activities" (brown) can be observed since 2011. The first is primarily due to the repair of stations that failed under harsh environmental conditions and to the development and implementation of earthing and lightning protection standards throughout the network (CTBTO 2010). The second relates to the development of strategies for preserving data availability during preventive maintenance and upgrade activities (Sect. 1.3.3). "Equipment and Infrastructure" is currently the main source of station downtime with power issues accounting for 50% of the total downtime. This has already triggered changes in station power system designs to ensure that noncritical equipment be installed on independent power sources from that of critical equipment. It has also led to the launch of a series of engineering projects such as (a) the development of a standard software solution to provide SOs with state-of-health information on the power systems installed at their stations (Sect. 1.9), (b) the review of state-of-the-art power solutions with the objective of defining and testing a set standard power systems for IMS stations (Sect. 1.10) and (c) the definition of standard procedures for the regular testing of station back-up power systems.

While providing a useful overview of failures at a network level, the current failure analysis approach has shown several limitations. First, it rarely allows identifying issues that are not already known by the PTS through the daily operation of the network. Second, it is often difficult to determine if equipment failures occurred because

of the equipment itself or because of external factors such as environment or misuse. Third, information on failure causes is retrieved from the IMS Reporting System which has not been designed to meet the requirements of failure analysis (CTBTO 2017a). These factors combined decrease the level of confidence in the reported results. The current approach, therefore, needs to be complemented by additional engineering activities. As discussed above, these activities could include (a) the definition of processes to ensure that the adequate level of spare equipment is available at the stations, (b) the storage in a common database of station-specific information such as fine-tuning configuration parameters, frequent operational issues, identified risks, and mitigation plans, (c) the regular monitoring of station data retransmission patterns after station outages in order to detect malfunctions, and (d) the implementation of state-of-health monitoring and alert systems at the stations to help SOs anticipating station failures and ease station troubleshooting when necessary. To conclude this section, the fulfillment of DA requirements by all IMS infrasound stations is a real challenge. It can only be achieved with the commitment of all stakeholders (SOs, PTS, States Signatories) and the implementation of specific engineering activities dedicated to this objective.

1.2.3 Detection Capability

Infrasonic waves are elastic waves with frequencies ranging from the acoustic cut-off frequency (about 3 mHz for standard atmospheric conditions) to the low-frequency limit of human hearing (20 Hz). In the atmosphere, the propagation of infrasonic waves is mainly driven by wind and temperature (De Groot-Hedlin et al. 2010). As the temperature typically decreases with altitude in the lower atmosphere, infrasonic waves produced close to the ground propagate upwards. They can then be refracted back to the ground if the effective sound velocity becomes larger than its surface value (Evers and Haak 2010). This always happens in the thermosphere because of the strong temperature gradient but also commonly occurs at lower altitudes. In the troposphere, temperature inversion or jet streams near the tropopause can lead to highly effective sound velocities. Infrasound waveguides are also commonly formed between the stratosphere and the ground because of the solar radiative heating of stratospheric ozone combined with strong seasonal stratospheric winds. Except when the measurement systems are located at a few kilometers from the source, infrasonic waves are, therefore, observed at the ground after one or several bounces in the atmosphere. Because of their relatively small attenuation, infrasonic waves can be detected at great distances from the source through the pressure fluctuations they produce. To illustrate the complexity of infrasonic wave propagation in the atmosphere, Fig. 1.5 displays the simulated infrasound propagation paths for the meteor explosion observed offshore Portugal on March 9, 2017 (CNEOS 2017).

The capability to detect and locate an atmospheric explosion is the ultimate goal of the IMS infrasound network. For practical purposes, the IMS Operational Manual specifications were defined for a yield greater than 1 kT TNT equivalent (Christie

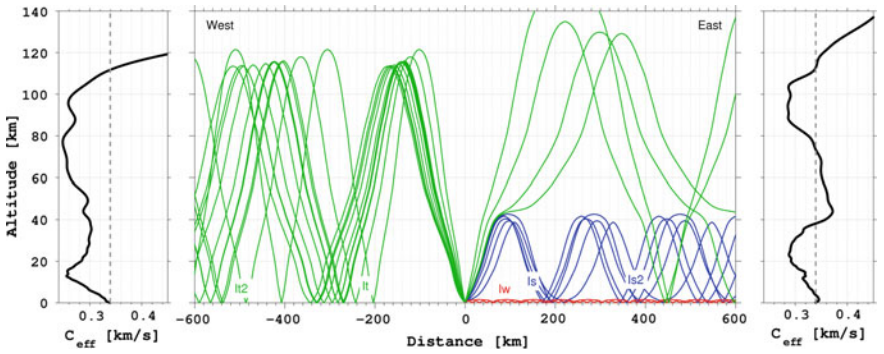

Fig. 1.5 Simulation of infrasonic wave propagation for the meteor explosion observed offshore Portugal (40.5N, 18.0W) on March 9, 2017 (CNEOS 2017) using 1-D ray-tracing (with eikonal equation) and ECMWF weather model (courtesy J. Vergoz). The red, blue, and green paths represent the tropospheric, stratospheric, and thermospheric paths respectively. The effective sound velocity models toward the West and the East are displayed in black on the left and right side of the figure, respectively, with the gray-dashed line representing the effective velocity at the ground

and Campus 2010). The capability to detect such small yield is tightly linked to the local, regional, and global dynamics of the atmosphere. Changes in atmospheric temperature or wind occurring on a seasonal, daily, or even hourly basis can completely modify parameters such as the noise level at the ground or wave propagation paths. The IMS network and stations must, therefore, be designed to minimize as much as possible the impact of these changes on global network detection capability and ensure that the 1 kT yield detection threshold is met anywhere at any time.

As IMS infrasound stations are relatively sparse around the globe, signals of interest generally travel for thousands of kilometers through the Earth's atmosphere before they reach the first stations. The amplitude of these signals is significantly attenuated before it is measured and usually relatively small compared to background pressure fluctuations produced at the ground by wind turbulence (Walker and Hedlin 2010). One of the main challenges of the infrasound technology is, therefore, the detection of signals with low signal-to-noise ratios (SNRs) as soon as the wind velocity at the ground exceeds a few tenths of meters per second. To mitigate this effect, it is absolutely crucial that infrasound stations are installed in areas with as little wind as possible and protected from local wind turbulence (Sect. 1.3). Those are key requirements when selecting the station location during the site survey process (CTBTO 1997a). Dense forests are usually the best locations for infrasound stations but even small bushes can help in reducing the noise when it is not possible to find forested areas around Treaty coordinates. To further reduce wind-generated noise, the IMS Operational Manual also requires that acoustic filtering systems are installed at all IMS infrasound measurement systems (Sect. 1.5). These systems, commonly referred to as Wind-Noise-Reduction Systems (WNRS), can reduce the amplitude of background pressure fluctuations by tens of decibels in high wind conditions while preserving the integrity of infrasound signals. Finally, the IMS Operational

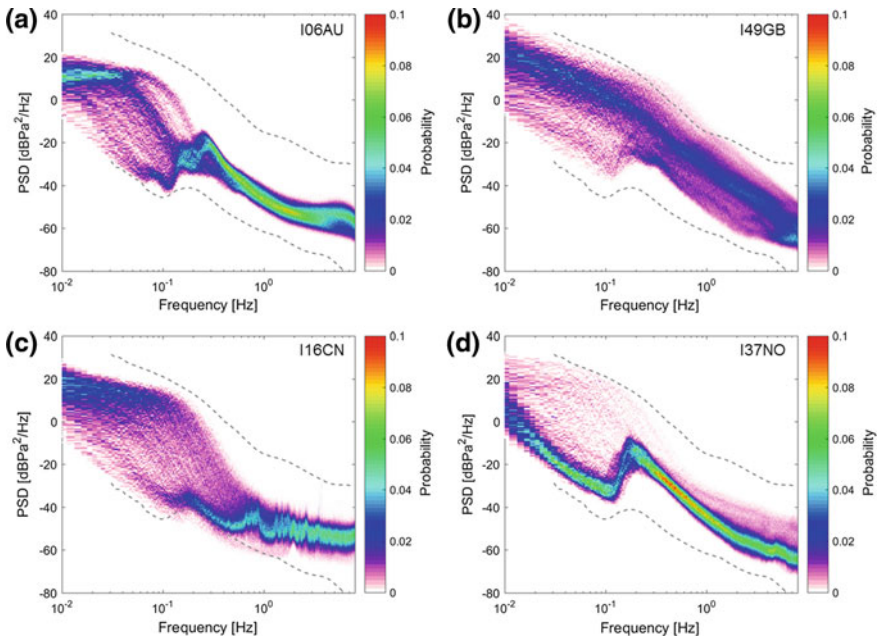

Fig. 1.6 Probability density functions as a function of noise power for each frequency band in February 2017 for stations **a** I06AU (H6), **b** I49 GB (H2), **c** I16CN (H3), and **d** I37NO (H7). The Power Spectral Densities (PSDs) are computed over 1-h time period using Welch's method (Welch 1967; McNamara and Buland 2004) and are corrected from the system response including WNRS, sensor, and data acquisition system. The gray-dashed lines represent a high- and low-noise model (Bowman et al. 2005)

Manual recommends installing additional array elements when the station is located in a noisy environment with the objective of improving the SNR at the data processing stage (Sect. 1.4). As an illustration, Fig. 1.6 displays, for four IMS stations, the Probability Density Functions (PDF) as a function of noise power for each frequency band. It shows, for example, that the spectral levels observed at station I49 GB are in average well above that of station I06AU. Both stations are located on remote oceanic islands but station I49 GB is located at a much windier location with no vegetation around and its WNRSs have a slightly reduced efficiency (because of land constraints). In comparison, station I06AU is installed within a dense forest and include standard WNRSs. The high level of background noise recorded at station I49 GB explains for the most part the very limited contribution of the station to the global IMS network detection capability (Fig. 1.7).

Apart from wind-generated background noise, the other main challenge of the infrasound technology is the complexity and the dynamics of the wave propagation medium. Unlike seismic waves which travel in the relatively stable medium of the Earth's interior, infrasonic waves propagate through the complex and continuously changing medium of the atmosphere (Fig. 1.5). Depending of the atmospheric

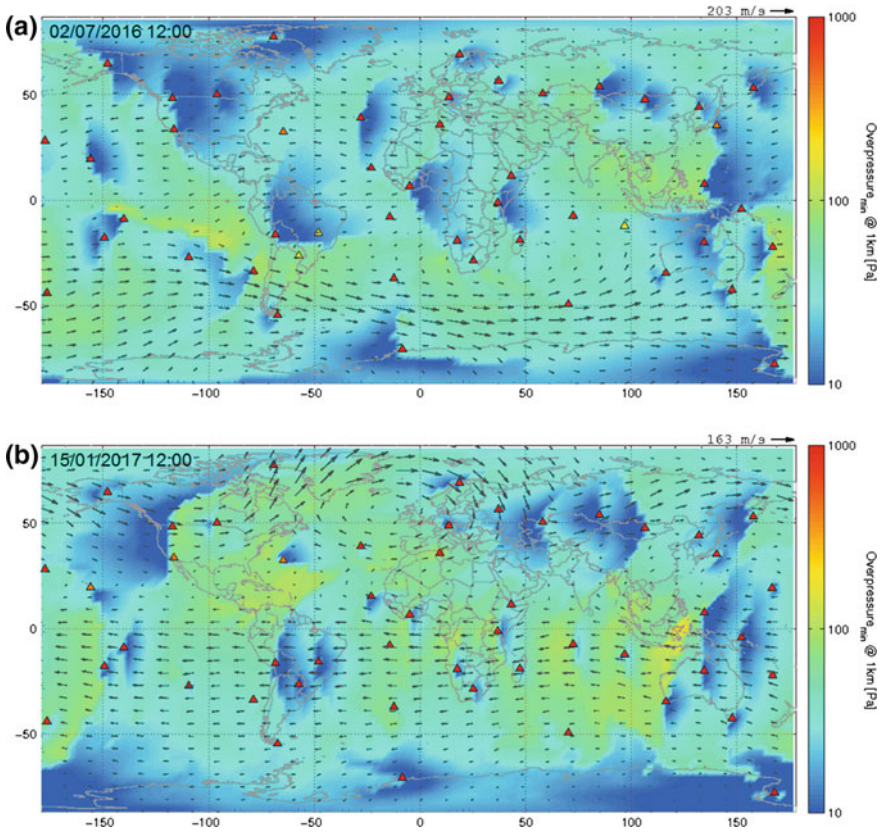

Fig. 1.7 Detectability maps computed for the IMS infrasound network with DTK-NetPerf, the PTS infrasound threshold monitoring software using frequency-dependent attenuation relation (Le Pichon et al. 2012), real-time atmospheric specifications from ECMWF and real-time station noise computed in the IDC. The computations are made for single-station coverage, frequencies of 1 Hz, source on the ground, and background noise levels estimated in the 0.2–2 Hz frequency band. The color codes the minimum detectable source amplitude at a reference distance of 1 km from the source (in Pa peak-to-peak). The arrows represent the wind direction and maximum speed (arrow length) between 40 and 50 km altitude. IMS infrasound stations are indicated by triangles, with the following color codes: red for mission capable stations, orange for non-mission capable stations but partially sending data, and yellow for stations sending no data at the time of the simulation

conditions, the same source can generate multiple arrivals, one arrival or no arrival at all at the same station. The network must, therefore, include a sufficient number of stations to ensure a continuous level of detection capability. At the time of the Treaty negotiations, intense expert discussions occurred on this topic with estimations ranging from 20 to 120 for the minimum number of infrasound stations required to continuously detect a 1 kT-TNT-equivalent atmospheric explosion all over the globe (Conference on Disarmament 1995). Experts finally agreed on a 60-station network as defined in the Treaty. Since then, network detection capability models have

confirmed that any yield greater than 1 kT TNT equivalent would be detected at any time by at least two IMS infrasound stations (Green and Bowers 2010; Le Pichon et al. 2009, 2012, 2019). As an illustration, Fig. 1.7 shows network detection capability maps for the IMS infrasound network at two points in time in Summer 2016 and Winter 2017. It can be seen that the seasonal oscillation of the zonal (East–West) component of stratospheric winds in both hemispheres significantly modify the area covered by each station. Even though the detection capability of the IMS infrasound network is generally well below the 1 kT threshold, modeling results have shown that it can move closer to this threshold at certain time periods when stratospheric wind velocity vanishes in certain areas of the globe (Le Pichon et al. 2019). The computation of network detection capability maps in near real time is, therefore, seen a valuable tool for decision-making. Such maps can be used for prioritizing maintenance actions when stations are down or impacted by unusual high-noise levels and for focusing reliability efforts on stations without which the network would go above the required detection threshold.

Recurrent sources of infrasound can also increase the noise level in the IMS frequency range and reduce station detection capability. The most well-known example of such sources are the microbaroms which commonly produce one or several bumps in the pressure fluctuation spectra around the 0.1–0.5 Hz frequency band (Fig. 1.6). Microbaroms are detected all over the globe and are produced by the nonlinear interaction of ocean surface waves traveling in different directions (Waxler and Gilbert 2006). Although microbaroms energy reduces station detection capability, the continuous monitoring of such infrasound source can be used as a means to assess station performance (Sect. 1.3.3). Other recurrent infrasound sources are generally local and produce signals above 1 Hz. They include surf noise, dams, gas flares, ice cracks, airports, industrial activities, etc. IMS infrasound stations shall obviously be installed far enough from such sources so these sources do not reduce the station detection capability. In reality, it is not always the case for two main reasons. First, it is sometimes not possible to find an available piece of land far enough from local sources (on small islands for example). Second, array processing techniques that could have allowed characterizing such sources at the time of site selection (and discarding noisy locations) have only started being used over the past years during the site survey process (Sect. 1.3.2). Figure 1.8 shows, for example, the large number of high-frequency detections continuously observed at stations I10CA (surrounded by two dams, North (red) and South (green) azimuths) and I06AU (surf noise, East (blue) azimuths) potentially limiting the detection capability of these two stations in the high- frequency part of the IMS frequency band. Another example is the high-frequency spikes continuously recorded at station I16CN and linked to industrial activities surrounding the station location (Fig. 1.6).

Finally, station detection capability is also linked to data quality. As per the IMS Operational Manual, both the SO and the PTS have the responsibility to monitor data quality and to inform each other when unusual signals such as bursts, spikes, and constant values are detected. It is then the responsibility of the SO to seek a solution to the problem. Both the SO and the PTS also need to monitor station noise levels in order to track long-term changes and help identifying instrumental

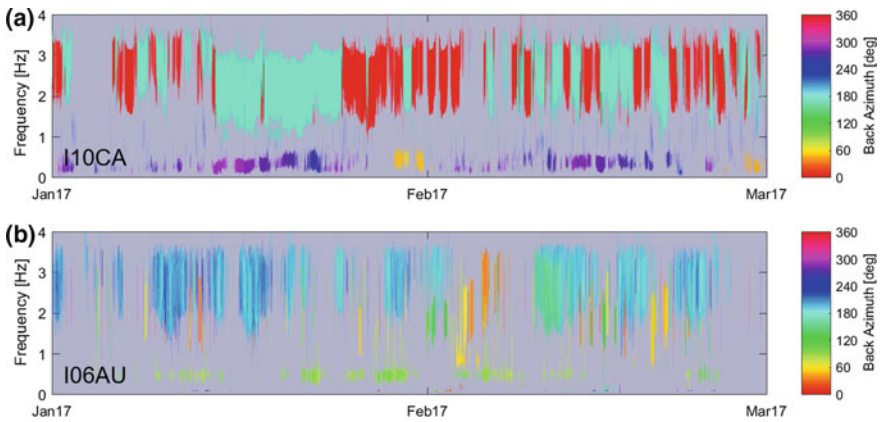

Fig. 1.8 IDC SEL3 detections in function of time, frequency, and back azimuth (color) for stations **a** I10CA and **b** I06AU

malfunction or problems with WNRS. When due to external factors, increased noise levels can lead to station or array element relocation. In reality, SOs are currently more often contacted by the PTS for data availability issues rather than data quality issues unless the data quality issues significantly affect IDC processing results. On the other hand, not all SOs regularly assess data quality as required in the IMS Operational Manual. Stations with highest data quality are often those for which SOs work in close cooperation with National Data Centres (NDCs) or associated research institutions. In that case, because data is also of interest for national applications, data quality issues are reported by national institutions. For this reason, capacity building efforts shall also target NDCs with the objective of improving data quality and station detection capability.

1.3 IMS Infrasound Stations

1.3.1 General Description

Each IMS infrasound station is composed of an array of distant measurement sites located in a 1–4 km-diameter area and commonly called array elements. The spatial distribution of these elements will be discussed in Sect. 1.4. Each of these array elements includes an infrasound measurement system composed of a WNRS, an infrasound sensor, and a data acquisition system. These three components will be discussed in Sects. 1.5, 1.6, and 1.9 respectively. The main function of infrasound measurement systems is to measure atmospheric pressure fluctuations and convert them into digital, time-stamped and digitally signed data packets. Apart from the infrasound measurement system, each array element also includes systems for power

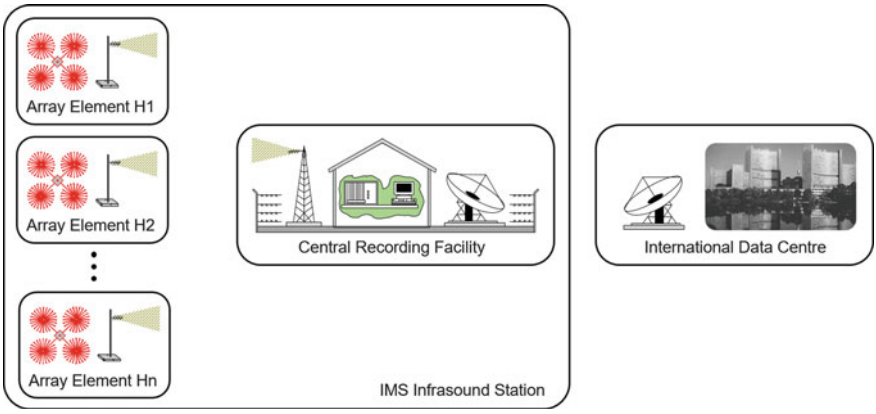

Fig. 1.9 Schematic illustration of an IMS infrasound station

and data communication with the Central Recording Facility (CRF). All equipment at the array elements are usually installed inside a single equipment vault, whose purpose is to protect the equipment from the environment and vandalism. Equipment vaults are secure, generally fire resistant, thermally insulated, and waterproof when necessary.

Equipment vaults are typically powered through standalone photovoltaic systems or power cables coming from the CRF. Since without power no data can be recorded, a lot of attention is given to the reliability and resilience of the power solutions implemented at IMS infrasound stations (Sect. 1.10). Communication systems between the array elements and the CRF are usually based on radio (UHF historically and now more frequently SHF) or fiber optic communication systems. CRF equipment includes hardware and software for data acquisition, buffering, formatting, digital signature, and transmission to the IDC. The GCI is commonly implemented through satellite communication and GCI equipment at the CRF consists of an integrated services router, satellite router, and VSAT antenna. CRF equipment is usually less ruggedized than that installed at the array elements and requires more stable and clean operating environment. Apart from critical equipment, CRFs typically include a small workbench, a data analysis computer, and an adequate storage environment for spare equipment. For this reason, CRFs require more power than array elements and are usually powered through a combination of diesel generators, photovoltaic systems, or mains power when available. Host Countries can decide to collect data at a central communication node before forwarding the data to the IDC. Communication between the station and the central communication node is in that case done through an Independent Sub-Network (ISN) which is the responsibility of the Host Country. The link between the central communication node and the IDC remains through the GCI. Figure 1.9 displays a schematic illustration of an IMS infrasound station and Fig. 1.10 pictures IMS infrasound stations in various environments.

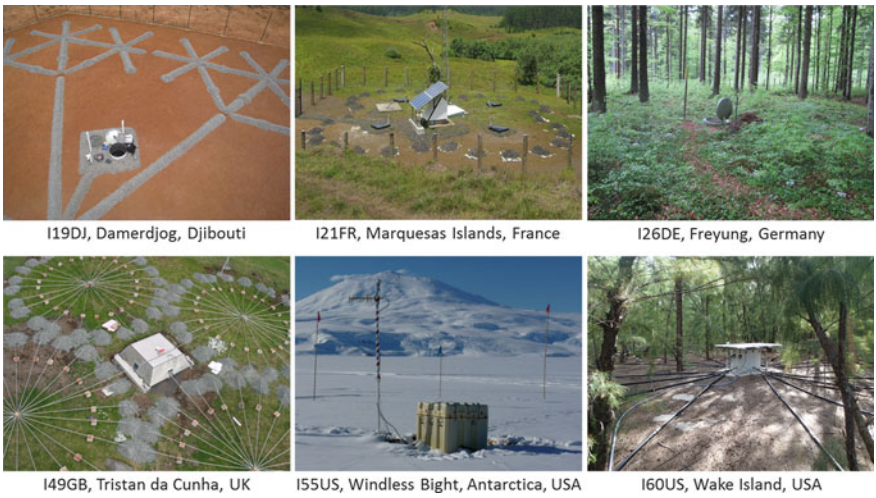

Fig. 1.10 Pictures of IMS infrasound stations in different environments and with distinct WNRS and vault designs: I19DJ (hexagonal closed pack pipe array, underground vault), I21FR (star pipe array, surface vault), I26DE (T-rosette pipe array, underground vaults), I49 GB (rosette pipe array, surface vault), I55US (radial pipe array, above ground box), and I60US (radial pipe array, above ground box)

1.3.2 Establishment

The standard process for establishing a new IMS infrasound station starts with the negotiation of a Facility Agreement between the Host Country and the PrepCom. This agreement constitutes the legal framework for the establishment and operation of the stations to be hosted by the Country. To enter into force, the Facility Agreement must be ratified by the Host Country. As this can take some time, it is not rare that the Host Country initiates the station establishment process prior to the ratification of such agreement. Facility Agreements are recently more often a prerequisite for starting a new station establishment process because of the political or legal nature of the issues delaying the construction of the remaining stations. The next step is the identification of an appropriate location for the station. The Host Country must propose several suitable locations that are assessed by the PTS during the Site Survey process (CTBTO 1997a). Site Survey requirements include that IMS infrasound stations should be located in areas with as little wind as possible, preferably inside dense forests, and as far as possible from local and continuous sources of infrasonic waves. The station location shall also be secure with the possibility to install a robust power and data communication infrastructure. At the end of the Site Survey process, the location of all array elements and the CRF is approved by the PTS. If the identified station location is not located within Treaty coordinates, a change of coordinates is officially requested to the PrepCom (Sect. 1.2.1). Once the station infrastructure is built and the equipment installed, a period of testing and evaluation starts to verify

that the station functions reliably and in agreement with IMS specifications (CTBTO 2009). After this period which usually lasts from 6 months to a year, the PTS determines or is notified by the Host Country that the station is ready for certification. Once the PTS is assured that the site, the station equipment, and the infrastructure meet, or in some specific cases substantially meet, the technical specifications for IMS stations, the station is certified and promoted into IDC operation.

1.3.3 Sustainability

Maintaining and operating a sparsely distributed global network such as the IMS infrasound network presents multiple complexities of a technological, logistical, environmental, and administrative nature (CTBTO 2017c). Station operation and maintenance activities, therefore, require a high level of coordination between SOs, Host Countries, and the PTS. With the first IMS infrasound stations built more than 15 years ago, many stations are now due for major upgrades to address equipment obsolescence, deteriorating infrastructure, or necessary engineering enhancements. Station major upgrades are often much more challenging than station establishment because of the necessity to preserve station DA during the upgrade process, to integrate new and legacy components together, and to fulfill the latest IMS requirements (calibration, authentication, command and control, etc.). Major upgrades are, therefore, often multiyear projects requiring extensive planning, detailed design, and mock-up testing of the equipment. Upgrading a station also provides a good opportunity to review and improve the station performance in terms of detectability and contribution to the network. This can lead to relocation of some array elements (Sect. 1.4), modification of the WNRS design (Sect. 1.5), use of infrasound sensors with self-noise more adapted to the station noise conditions (Sect. 1.6), or significant changes in power and data communication systems to improve DA or noise reduction through the preservation of vegetation (Sect. 1.10). As an example, Fig. 1.11 shows the significant increase in the number of infrasound arrivals detected by station I56US after 2010. About I07AU, although the number of detections remained stable after the 2013 upgrade, the contribution of the station to the network was enhanced because of reduction of the uncertainties associated with the computation of wave parameters. It can be seen, for example, that the azimuth (in dark blue in Fig. 1.11) and trace velocity (Fig. 1.12) distribution of the microbaroms detections is much more narrow after than before the upgrade. This is mainly due to the installation of WNRSs with much more stable responses and to the relocation of one of the array elements (Marty et al. 2013).

When stations are first established, they undergo a long period of testing and evaluation before being certified and promoted into operations. However, during a station upgrade, even in case of quasi-complete reconstruction, the station must continue fulfilling IMS DA requirements. This is probably the main challenge when upgrading a station, since the total downtime cannot exceed a few days (Sect. 1.2.2). To achieve this result, the PTS has developed different strategies based on lessons learned from

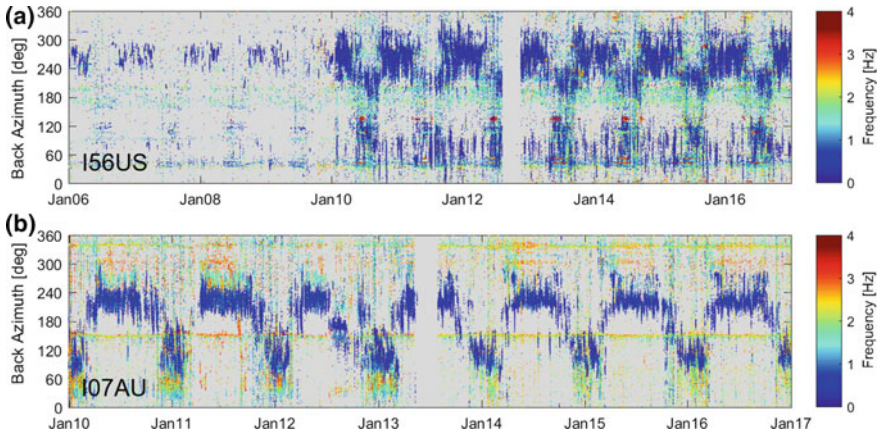

Fig. 1.11 IDC SEL3 detections in function of time, back azimuth, and frequency (color) for stations **a** I56US and **b** I07AU

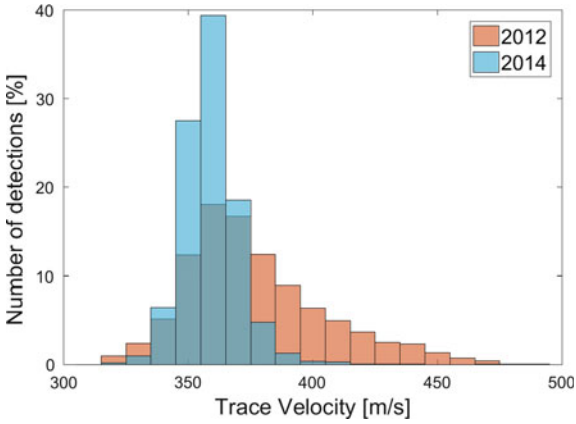

Fig. 1.12 Trace velocity distribution of IDC SEL3 microbaroms detections for station I07AU in 2012 (red) and 2014 (blue)

past upgrades. These include (a) the replacement of devices that do not include data storage and retransmission capability with equipment having such capabilities, (b) the progressive upgrade of the array elements to ensure that the minimum number of channels for the station to be mission capable is always available, (c) the installation of a new station in parallel to the existing with the old station only decommissioned after the new station is fully tested and promoted into operations, or (d) the installation of a temporary station in parallel to the IMS station to cover the gap during the station upgrade process. Finally, when the major upgrade is completed, the station is revalidated by the PTS to ensure that it continues fulfilling all technical specifications for IMS stations (CTBTO 2008). Revalidation uses similar procedures as for station certification.

1.4 Array Geometry

1.4.1 General Requirements

In 1996, the Infrasound Expert Group to the Ad Hoc Committee on a Nuclear Test Ban Working Group on Verification made several recommendations on infrasound array geometry (Conference on Disarmament 1995). These recommendations were included as minimum requirements for infrasound station specifications in the Report of Working Group B to the Second Session of the Preparatory Commission for the Comprehensive Nuclear-Test-Ban Treaty Organization (CTBTO 1997b). These minimum requirements were later on integrated into the IMS Operational Manual (CTBTO 2009). They include that the minimum number of array elements shall be four, the array geometry shall be a triangle with a component at the center and the array aperture shall range from 1 to 3 km with 3 km as recommended spacing. These minimum requirements also specify that the number of array elements can be increased in case of noisy station locations or whenever an increased capability for the station is required. This latter specification provides a high degree of freedom in the design of infrasound arrays with no stringent requirement for element positioning for stations with more than four elements. This specification together with land constraints and the different views of Host Countries on the infrasound technology can explain for the most part the wide range array geometries that were implemented across the IMS infrasound network. Figure 1.13 displays the array geometry of the 49 certified IMS infrasound stations as of June 2017.

The IMS Operational Manual also defines mission capability requirements. These requirements are used to prioritize corrective maintenance actions through the network with non-mission capable stations getting categorized as the highest priority for repair (CTBTO 2009). Mission capability requirements have a significant impact on DA because the DA metric is computed on the minimum number of channels for the station to be mission capable (Sect. 1.2.2). This means that it is possible for a station to have 100% DA even with nonoperational array elements. A four- element infrasound station is considered mission capable if at least three of the elements are operational. For stations with more than four elements, the array geometry determine the combinations of element failures that may occur before mission capability is lost (CTBTO 2009; Carter 2011). Mission capability rules for such arrays are, therefore, station specific but they shall ensure in any case that at least 70% of the elements of the same station are operational for the station to be considered mission capable.

1.4.2 Number of Elements

Shortly after the installation of the first IMS infrasound stations, concerns were raised regarding the potentially limited capability of stations with four elements only (CTBTO 2001). At the time, the main reasoning for increasing the number of array

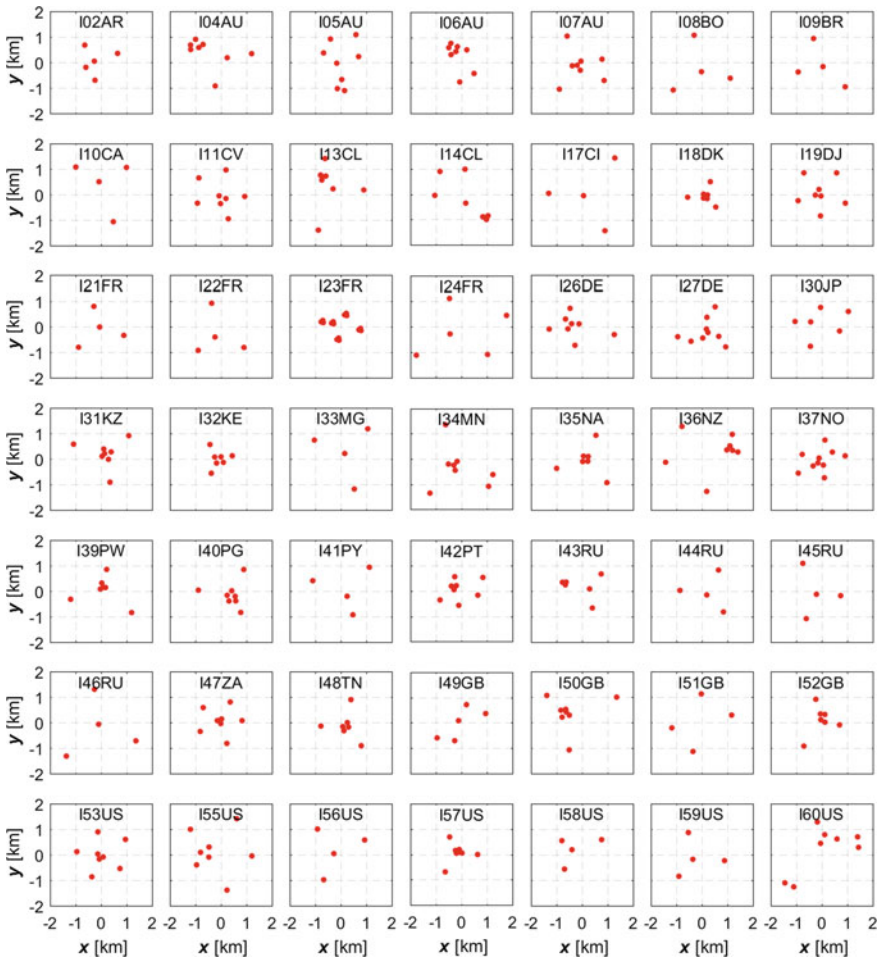

Fig. 1.13 Array geometry of the 49 certified IMS infrasound stations

elements was the risk of array aliasing. It , however, probably relates more to the need of finding an acceptable compromise between signal detection and wave parameter estimation and of minimizing the impact of element loss on the overall station detection capability (Sect. 1.4.3). Based on the fact that it was less costly to correct this potential problem by installing stations with additional elements at the beginning rather than to retrofit already installed stations, the WGB to the Fifteenth Session of the Preparatory Commission for the CTBTO recommended in its report that IMS infrasound stations be installed with up to 8 elements (CTBTO 2001). A few years later, the benefits of adding array elements were summarized by the 2003 Expert Group Meeting on array geometry (CTBTO 2003). It was shown, for example, that four element stations had a very limited detection capability when one element was

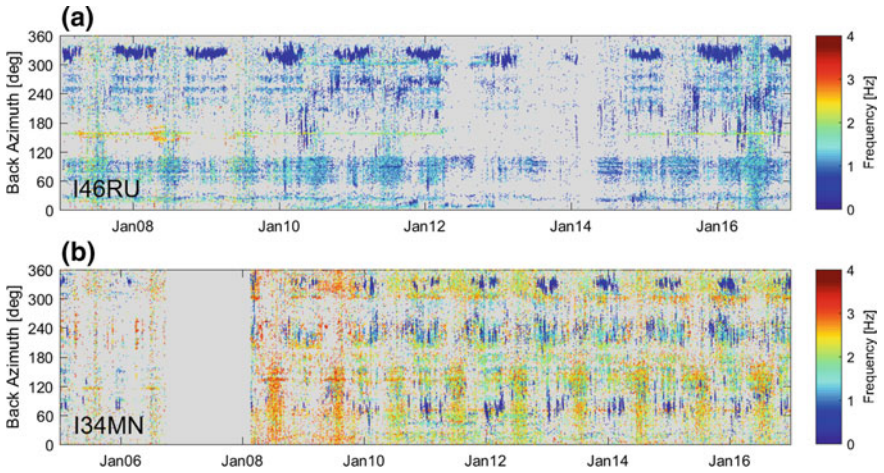

Fig. 1.14 IDC SEL3 detections in function of time, back azimuth, and frequency (color) for stations **a** I46RU and **b** I34MN

not sending data or was subject to high noise (Firbas and Brachet 2003; Le Pichon 2003). As an illustration, Fig. 1.14 shows the significant drop in detection capability of the four-element station I46RU over the 2012–2014 time period because of the loss of an element.

As a result, the Expert Group recommended building stations with more than four elements, with eight elements being seen as a good comprise between detection capability, and construction and operational costs (CTBTO 2003). Based on these WGBs and Expert Group's recommendations, the majority of IMS infrasound stations constructed since then have been built with a minimum of eight elements except when this was not possible because of land restrictions or prohibitive costs. When possible, existing four array element stations have also been upgraded with additional elements, usually at the time of a major equipment or infrastructure upgrade (Sect. 1.3.3). Figure 1.14 shows the significant increase in detection capability of station I34MN after the upgrade from four to eight elements in 2007. As of 2016, the number of array elements at IMS infrasound stations varies from 4 to 15 with most stations including either 4 or 8 array elements (Table 1.1). Only two stations include more than 8 array elements: I23FR which was installed with 15 elements with the objective of improving the SNR at an extremely noisy location and I37NO which includes 10 array elements because of the interest of the Host Country in the monitoring of sources with frequency above the IMS frequency band (requiring shorter inter-distances between elements).

Table 1.1 Number of IMS infrasound stations with a defined number of array elements

Number of array elements	Number of stations
4	15
5	3
6	2
7	5
8	21
9	1
10	1
15	1

1.4.3 Aperture and Element Distribution

The aperture of IMS infrasound arrays ranges from 1 to 3.9 km. Only two stations (I24FR, I60US) exceed the 3 km aperture IMS Operational Manual requirement because of land constraints but both these stations include elements that allow forming triangles with an aperture smaller than 3 km. As discussed in Sect. 1.4.1, since the IMS Operational Manual does not specify any requirements for element positioning for stations with more than four elements, a wide range of array geometries can be found in the IMS infrasound network (Fig. 1.13). These geometries can be roughly grouped as follows:

(a) Triangle with an element at the center—14 stations;
(b) Small aperture array (4–5 elements) embedded in the center of a larger aperture triangle—10 stations;
(c) Small aperture triangle embedded inside a larger aperture pentagon—6 stations;
(d) Small aperture array (3–5 elements) outside a larger aperture array (3–5 elements)—7 stations;
(e) Other distributions—12 stations.

Based on experience gained from the processing of data from the first IMS infrasound stations, the 2003 Expert Group Meeting drew several conclusions on the array element distribution (CTBTO 2003). The Expert Group first recommended that the array geometry be adapted to local meteorological conditions and second that the array elements be positioned in an irregular manner in order to have a better distribution of inter-element spacing than a completely symmetric configuration. These two general recommendations were not always followed in the design of the next generation of IMS infrasound stations with some stations still built with symmetrical geometries and apertures not optimized for local noise conditions (Christie and Campus 2010). In 2012, after the certification of 43 stations, a second Expert Group Meeting on array geometry was organized in Korea (Marty et al. 2012b). The Expert Group started by reviewing the existing models for the design of IMS infrasound array geometries. It concluded that although some of these models could

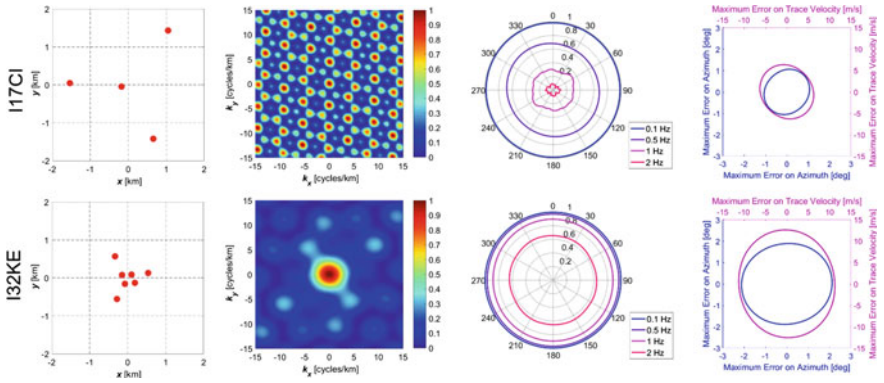

Fig. 1.15 Array layout, frequency–wavenumber power spectral density, array correlation coefficient (Christie and Campus 2010), and estimation of wave parameter uncertainties (Szuberla and Olson 2004) for station I17CI and I32KE

provide qualitative information, none of them could really be used to determine an optimal aperture and element distribution for IMS infrasound stations.

The frequency–wavenumber power spectral density (Capon 1969) frequently referred to as "array response" has often been mentioned in the literature as a meaningful tool for designing infrasound array geometries and especially to characterize array aliasing (e.g., Evers and Haak 2001; Christie and Campus 2010). However, the objective of the IDC detection algorithms is the estimation of wave parameters based on the computation of time delays between signal arrivals at the different elements of the same array. This does not relate to the concept of spatial aliasing and the frequency–wavenumber power spectral density does not really provide relevant information for designing of IMS infrasound arrays. If spatial aliasing was to be a criteria, the minimum requirements from the IMS Operational Manual would be completely inadequate because avoiding spatial aliasing at 4 Hz would require four-element arrays to have an aperture smaller than 100 m and not around 1–3 km as per IMS requirements. Figure 1.15 shows the frequency–wavenumber power spectral density for two IMS infrasound stations. If array aliasing would be relevant for IDC processing, data from four- element IMS stations such as I17CI would be unusable.

A second modeling technique consists in estimating the averaged degree of signal coherence expected between all array elements in function of the wave azimuth (Christie and Campus 2010). This technique is derived from the coherence loss model proposed by Mack and Flinn (1971). Although this technique integrates the concept of coherence loss, which is a central issue for infrasound signal detection, it does not take into account the concept of wave parameter estimation which is the final output of IDC detection algorithms. With this technique, the closer the array elements are, the better the results, with the best results obtained when all array

elements co-located. In addition, the technique does not take into account wind-generated background noise at the station, which is one of the main factors driving coherence loss in the IMS frequency band. Figure 1.15 shows that the best results are obtained for station I32KE, which is the station with the smallest aperture. However, such a small aperture design does not always allow for the precise estimation of wave parameters especially in low frequency. Poor parameter estimation affects the output of IDC localization algorithms which primarily use signal arrival time, back azimuth, and velocity at multiple stations to locate events (Mialle et al. 2019). A third type of model consists in using the Cramér–Rao Bound (CRB) to estimate the uncertainties on wave parameters due to potential errors on intercorrelation-based delay measurements (Kay 1993; Szuberla and Olson 2004). Although this model covers the concept of wave parameter estimation, it does not take into account the loss of coherence. With this model, the larger the distances between the array elements are, the better the results, with the best results obtained for infinite distances. The best performance is, therefore, obtained for larger aperture arrays (Fig. 1.15). This leads to opposite results from those obtained with the array correlation coefficient method described above.

Because of the absence of models providing quantitative results, the 2012 Expert Group Meeting decided to define general recommendations for the design of IMS infrasound arrays instead of proposing a standard configuration. As in 2013, the Expert Group emphasized the importance of avoiding symmetrical designs and adapting the design to station environmental conditions. It also listed the following recommendations:

(a) The overall IMS infrasound network detection capability shall be considered when designing or upgrading infrasound array geometries;
(b) The station detectability, resolution, and robustness to the loss of elements shall be optimized to the station location;
(c) Since the computation of wave azimuth and velocity are of same importance for the data processing, infrasound arrays shall remain omnidirectional and not directive;
(d) IMS infrasound array geometries shall be optimized to the 0.1–1 Hz frequency band.

In parallel, the Expert Group identified the need to develop a new model that would take into account the two main concepts of the IDC automatic processing, i.e., the detection of spatially coherent signal and the estimation of wave parameters. This includes the development of a coherence loss model for the IMS frequency band as the model proposed by Mack and Flinn (1971) is based on acoustic-gravity wave observations across a 45 km aperture array. Following the Expert Group's recommendation, several coherence loss models were proposed based on the analysis of explosive events with high SNR (Nouvellet et al. 2013; Rakotoarisoa et al. 2013; Green 2015) or of microbaroms (Charbit 2015). This is a complex task because

coherence loss is due to a combination of factors such as slightly different propagation paths within the atmosphere between the source and the different array elements or the background noise level at the array elements. Coherence loss, therefore, depends on parameters such as the frequency content of the source, distance between the source and the receiver, state of the atmosphere, and background noise levels at the station. It, therefore, seems difficult to define a general model that would be valid for any event, any station location, and any time. Assuming that an averaged coherence loss model is defined for a specific station location, it is then possible to use the CRB to estimate an optimized array geometry and aperture (Charbit 2015). Mission capability criteria should also be considered and the model should be run for any sub-combination of array geometries to ensure that the station performance is not significantly affected by the loss of one or two specific array elements. As an example, with the exception of the most southern element, the I04AU elements are almost all aligned along the same axis (Fig. 1.13). The loss of the southern element would, therefore, make difficult the accurate estimation of wave parameters for most azimuths.

1.4.4 Conclusion

The design of IMS infrasound arrays is a trade-off between detection and accurate estimation of the wave parameters. This trade-off is primarily driven by the coherence loss of infrasound signals with distance and the background noise levels at the station location. Background noise levels mainly relate to wind-generated turbulence, whose intensity can significantly and rapidly vary through time. The lower the noise conditions, the larger the array aperture can be and the better wave parameters can be estimated. For this reason, installing array elements at locations with background noise as low as possible is of much higher importance than designing the "perfect" theoretical array geometry. This usually means identifying locations in forests as dense as possible. Noise levels recorded during station site surveys should play a crucial role in the design of infrasound array geometries (Sect. 1.3.2). It is important that the geometry is optimized to the station location during the design phase because it can be difficult and costly to move array elements once the station has been constructed. As discussed in Sect. 1.4.2, IMS infrasound stations should also, whenever possible, include at least eight array elements in order to be resilient to the loss of array elements. To conclude, because of the absence of quantitative models, the main criteria to be considered for the design of IMS infrasound arrays are land constraints, noise levels, homogeneous inter-distance and azimuth distributions, aperture adapted to averaged wind conditions, resilience to loss of elements, and costs.

1.5 Wind-Noise Reduction Systems

1.5.1 General Requirements

Atmospheric turbulence, which is often the main source of pressure fluctuations in the IMS infrasound frequency band, can be divided into two categories: convective and mechanical (Walker and Hedlin 2010). In the atmospheric boundary layer, mechanical turbulence is usually due to the interaction between the wind and the Earth's surface (topography, buildings, forests, etc.) whereas convective turbulence is primarily produced by the diurnal heating of the Earth's surface by solar radiation. The influence of wind velocity on the background noise of pressure fluctuations is significant with pressure fluctuation spectra increasing with a steep averaged rate of 5–7 dB per m/s in the IMS frequency band (Hedlin and Alcoverro 2005). For this reason, the IMS Operational Manual requires that an acoustic filtering system consisting of "noise reduction pipes" be installed at all IMS infrasound array elements with the objective of attenuating the pressure fluctuations produced by wind turbulence (CTBTO 2009). This type of acoustic filtering system is often referred to as a "pipe array". The IMS Operational Manual requires that the acoustic response of each infrasound measurement system, including the acoustic filtering system, be flat and stable within ±5% over the 0.02–4 Hz passband (Sects. 1.6 and 1.7). It also states that the response of the acoustic filtering systems installed at all of the array elements of the same station shall be identical. This latter requirement is essential to ensure proper computation of wave parameters as IDC detection algorithms are based on array processing (Brachet et al. 2010).

1.5.2 Pipe Arrays

A pipe array consists of a number of low-impedance air inlets distributed over a spatial area and linked to the infrasound sensor through a network of pipes and manifolds. Pipe arrays are the most common type of wind-noise reduction system (WNRS) and they are currently installed at all IMS infrasound stations. The noise reduction comes from the fact that, at similar frequencies, infrasound signals remain coherent over much larger areas than wind turbulence (Mack and Flinn 1971; McDonald and Herrin 1975). By averaging pressure fluctuations over an area small in comparison with infrasound wavelengths but large with regards to the turbulence scale, it is possible to attenuate the pressure fluctuations produced by wind turbulence while preserving the integrity of infrasound signals (McDonald and Douze 1971). The maximum theoretical noise reduction to be expected with pipe arrays is equal to the square root of the number of air inlets. This corresponds to about 20 dB for the standard PTS 18-m diameter pipe array composed of 96 air inlets (Hedlin and Alcoverro 2005). This maximum theoretical threshold is usually reached in the

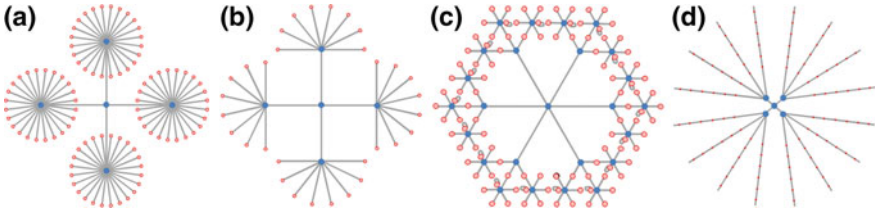

Fig. 1.16 Four most common types of pipe array configurations installed at IMS infrasound stations with **a** rosette, **b** star, **c** hexagonal closed pack, and **d** radial

higher part of the IMS frequency band because of the small scale of wind turbulence eddies in comparison with the inter-distance between two air inlets.

A wide range of pipe array designs have been studied over the past 60 years (e.g., Daniels 1959; Grover 1971; Hedlin et al. 2003; Alcoverro 2008). In the course of the establishment of the IMS infrasound network, different pipe array designs have also been implemented at IMS infrasound stations (Marty et al. 2012a). IMS pipe arrays can be grouped into four categories: rosette, star, hexagonal closed pack (HCP), and radial (Figs. 1.10 and 1.16). For each category, different pipe array diameters ranging from 10 to 70 m can be found in the IMS infrasound network. The acoustic responses for the most common types of IMS pipe arrays are shown in Fig. 1.17. It can be seen that the acoustic response of all pipe arrays display a flat amplitude response (±3 dB) over the IMS frequency band with the exception of the 70-m rosette configuration. It should be noted that the acoustic response of the 70-m rosette and 36-m HCP include significant phase variations over the IMS frequency band. These phase variations are not only due to the larger diameter of the systems but also to the use of resonance suppressors (Hedlin et al. 2003; Marty et al. 2017). Resonance suppressors are capillaries with a diameter of about 1 mm that are installed within manifolds or along pipes. Without these capillaries, the acoustic response of pipe arrays with larger diameter would exhibit large resonances within the IMS frequency band (Fig. 1.18). These resonances relate to the length of pipes terminated by low impedance outputs.

The installation of resonance suppressors at IMS infrasound stations has been a controversial topic (Christie and Campus 2010; Walker and Hedlin 2010). Although such devices can allow for pipe arrays with large diameter to comply with the flat amplitude response requirement of the IMS Operational Manual, they also introduce significant instabilities in the system response (Marty et al. 2017). By introducing a device with such a small diameter, any minor partial obstruction of the device can significantly distort the response of the measurement system and lead to an increased error in the computation of wave parameters, including a possible nondetection (Alcoverro 2008; Marty et al. 2011a). Figure 1.18 displays the acoustic response of a 70-m rosette pipe array with slightly different resonance suppressor diameters around the adapted diameter (1.2 mm). It can be seen that a simple particle (moisture, dirt, humidity) with a diameter of a few tenths of a millimeter and lodged within the resonance suppressor would significantly alter the system response. Such particles were found within some operational IMS pipe arrays, and the impact on

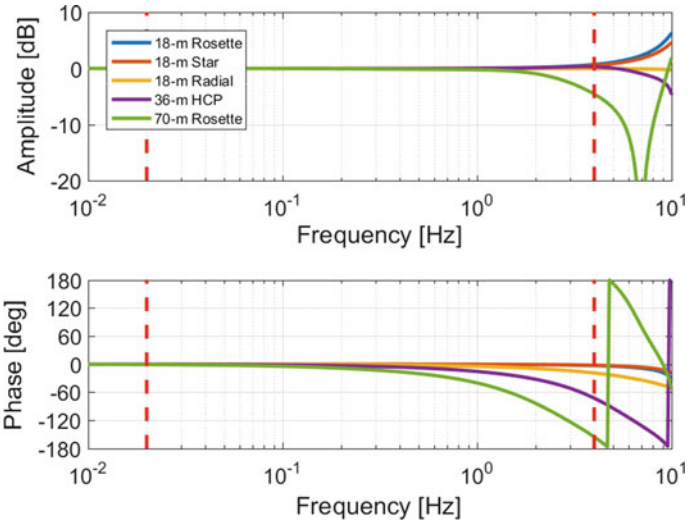

Fig. 1.17 Acoustic responses of five main types of pipe arrays installed at IMS infrasound stations to the arrival of an infrasound signal with a 30° angle from the horizontal using model developed by Gabrielson (2013). The vertical dashed red lines delimit the IMS frequency band. The phase response of the 18-m rosette pipe array does not appear in most of the frequency band because it almost perfectly overlaps with phase response of the 18-m star pipe array

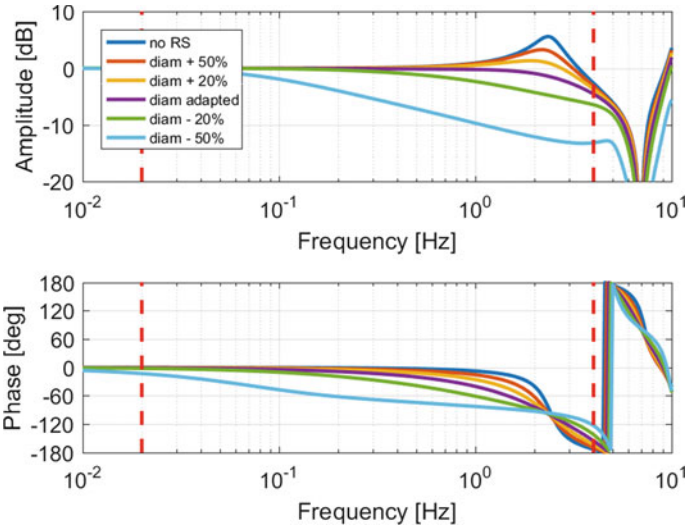

Fig. 1.18 Acoustic responses of the 70-m rosette pipe array to the arrival of an infrasound signal with a 30° angle from the horizontal using model developed by Gabrielson (2013) without Resonance Suppressors (RS) and with RS with different diameters around the adapted value. The vertical dashed red lines delimit the IMS frequency band

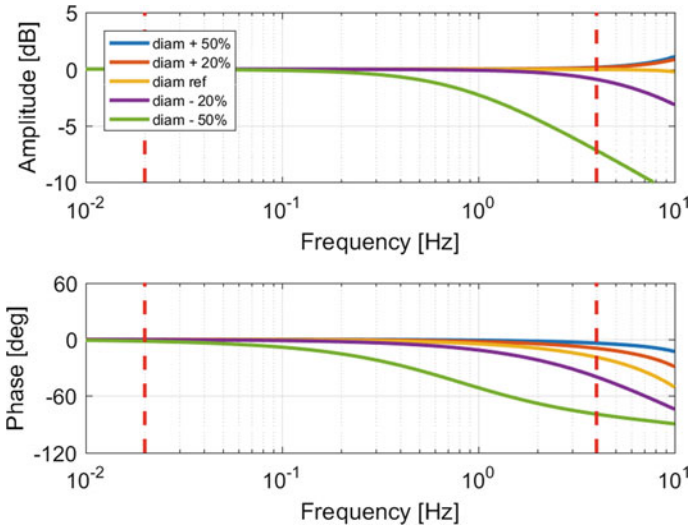

Fig. 1.19 Acoustic responses of the 18-m radial pipe array to the arrival of an infrasound signal with a 30° angle from the horizontal using model developed by Gabrielson (2013) with different hole diameters. The vertical dashed red lines delimits the IMS frequency band

the overall system response and on the results of the IDC automatic processing was demonstrated (Marty et al. 2011a, 2013). In addition, since the induced phase shifts are not constant over the IMS frequency band, the different frequency components of the same signal are shifted with different time delays (Fig. 1.18). The form of the wave packet is, therefore, altered, leading to potential misestimation of event magnitudes. For these reasons, the Infrasound Expert Group Meeting on WNRS organized in Jordan in 2011 recommended that resonance suppressors be removed from IMS pipe arrays (Marty et al. 2011b). This recommendation has been progressively applied across the IMS infrasound network since 2012 as stations undergo major upgrade (Sect. 1.3.3).

The IMS infrasound network still includes a few radial systems which exhibit similar issues as pipe arrays with resonance suppressors. The diameter of the holes drilled into the pipes is usually of the order of 1 mm which makes the system response very sensitive to any minor obstruction or inaccurate drilling. It can be seen in Fig. 1.19 that variations in hole diameter of a few tenth of millimeters have a significant impact on the overall system response. Such variations of responses were observed during PTS station revalidation visits (CTBTO 2013a). As with resonance suppressors, the response of the system is, therefore, highly sensitive to the environment (dust, ice, etc.) making it difficult to ensure stable and identical responses between all of the array elements of the same station. Additionally, radial pipe array layouts at IMS infrasound stations were found to differ from the theoretical layout primarily because of the thermal dilation of the hose material. Under direct solar radiation, the hoses tend to curve and move away from their original position.

Whereas radial pipe arrays are currently not recommended by the PTS, it seems that their performance in term of noise reduction could slightly exceed that of the standard PTS pipe arrays in the highest part of the IMS frequency band (Fee et al. 2016). This could be due to the holes of radial pipe arrays being located closer to the ground than the air inlets of standard PTS pipe arrays.

It must also be noted that the acoustic response of pipe arrays with diameters larger than 18 m can significantly depend on the wave elevation angle (Hedlin et al. 2003). This is an issue for the IDC automatic processing because an elevation angle would have to be assumed and the phase response corrected prior to running IDC detection algorithms. A compromise should be found between SNR improvement and flat and stable acoustic response as required by the IMS Operational Manual. The 2011 Expert Group recommended that the PTS is provided with acoustic response models for pipe arrays (Marty et al. 2011b). At the time, three acoustic models for pipe arrays were identified (Alcoverro and Le Pichon 2005; Gabrielson 2013; Brown et al. 2014b). A benchmark study was organized between three models and an experiment carried out with the objective of experimentally validating the models (Marty et al. 2017). The experiment validated two of the models including that developed by Gabrielson (2013), which was made available to the PTS. Using this model, it was determined that the PTS standard 18-m rosette pipe array was one of the best compromises in terms of stability of the response over the IMS frequency band, noise reduction (Denis and Le Floch 2015), and cost. Although the system does not perform much noise reduction below 0.04 Hz, it is compliant with IMS requirements. IMS stations are, therefore, being progressively upgraded with the standard PTS 18-m pipe array configuration in the framework of station major upgrade (Sect. 1.3.3).

Apart from modeling, the PTS has also made significant efforts since 2012 to improve the robustness of the standard PTS pipe array. Pipe array components which were originally made of plastic, galvanized steel, copper, or aluminum are now all made of stainless steel. These changes have allowed increasing the system lifetime and prevent issues such as rusting or destruction from wildfires. In addition, the number of connections between the different pipe array components was reduced and the connection seals reinforced to reduce chances of pressure leakage. This has significantly reduced SO maintenance activities with the standard PTS pipe array now considered nearly maintenance free. In parallel, the PTS is testing flexible high-pressure hydraulic hoses including two metallic mesh hoses (Tecalemit T214). The objective is to replace stainless steel pipes when dense vegetation does not allow for the installation of rigid pipes or ease transportation in extremely remote locations. In the past, vegetation was systematically cut in order to install the pipe array and protect it from falling trees and fruits. Since no pipe array can be more efficient than a dense forest, the PTS strategy now consists of adapting the pipe array design to the environment. The development of solutions with flexible hoses has shown to be extremely useful in that framework though they cannot be deployed in places subject to wildfire. It was also demonstrated that the addition of gravel over air inlets can help further increasing the SNR (Denis and Le Floch 2015). Gravel is, therefore, added over the air inlets of IMS pipe arrays wherever it is logistically possible and does not

significantly increase SO maintenance activities. Finally, as wind velocity increases with height, installing air inlets as close as possible to the ground is an important factor to consider for an efficient noise reduction.

Standard procedures are currently being developed for type approval and acceptance testing of IMS pipe arrays in accordance with the IMS Operational Manual. To support these efforts, a standard pipe array system has been installed at the manufacturer's facilities in order to thoroughly test any minor design change before implementation throughout the IMS network. Pressure valves have also been added on the top of each air inlet of operational pipe arrays in order to have to the capability to pressure test pipe arrays at the time of certification, revalidation or whenever it is suspected that there is an issue with the performance of the system. In parallel, data quality metrics based on the regular computation of PSDs are being tested at the PTS to track potential increases in station noise and trigger pipe array maintenance actions. Finally, the progressive implementation of IMS calibration requirements allows for the regular monitoring of pipe array acoustic responses and performance at IMS stations (Sect. 1.7).

In conclusion, the PTS has made significant efforts since the 2011 Expert Group Meeting to develop a standard pipe array system with well-characterized and stable acoustic response, extended lifetime, reduced maintenance, and fully compliant with IMS Operational Manual requirements. Since the frequency responses of IMS pipe arrays are now well characterized, it has become possible to integrate them into the IDC response files. IDC response files currently only the response of the sensor and data acquisition system for infrasound channels. Although the acoustic response of the standard PTS pipe array is close to one across the entire IMS frequency band, it departs from unity at higher frequencies. For this reason, pipe array responses are planned to be progressively integrated into IDC responses files over the next years.

1.5.3 Other Methodologies

Apart from pipe arrays, most other WNRSs consist of either wind protection structures, digital filtering with dense sensor network or sensors measuring spatially integrated pressure. The objective of wind protection structures is to try to isolate the measurement system from wind turbulence (Walker and Hedlin 2010). A number of wind protection structures of different sizes, shapes, and porosity have been designed over the past 40 years (e.g., Shams et al. 2005; Liszka 2008; Christie and Campus 2010; Raspet et al. 2019). Depending on the structure porosity, spatial averaging can also occur over the surface of the structure leading to further attenuation of wind-generated noise (Hedlin and Raspet 2003). The advantage of wind protection structures is that large systems can be designed without having to worry about resonances as with pipe arrays. The drawback is that these systems can "catch" more wind than pipe arrays because of their three-dimensional structure and the increase of wind velocity with height. The structures necessary to achieve a similar noise reduction as with pipe arrays could also not be adapted to installation within dense

forests, which are the primary location for IMS infrasound stations. Wind protection structures could, however, be considered for open field locations on the top of existing pipe arrays (Hedlin et al. 2003; Christie and Campus 2010). Prior to considering deployment at IMS infrasound stations, the acoustic response of such systems should be well characterized and it should be demonstrated that it remains stable through time. The system lifetime should also be evaluated in operational conditions.

Dense sensor networks could also be used to improve the SNR. The basic averaging of data from n sensors obviously leads to similar performance as with a pipe array with n air inlets located at the same location as the sensors (Dillion et al. 2007). However, advanced signal processing techniques could be used to better separate pressure fluctuations produced by wind turbulence and infrasound waves (Walker and Hedlin 2010; Frazier 2012, 2014). Similar noise reduction as with standard pipe arrays could, therefore, be achieved with a reduced number of sensors. Sensors could also be distributed over an area larger than standard pipe array dimension due to the absence of concern with resonances. The costs of such systems is currently prohibitive as the price of a single IMS-compliant sensor is similar to that of complete standard PTS pipe array. Operation and maintenance costs would also significantly increase and further development would be required for testing and validating the associated data processing technique. However, as technology evolves such solutions could become progressively less expensive and should be reviewed in the future.

The main example of a sensor measuring spatially integrated pressure is the optical fiber infrasound sensor (OFIS). This sensor is composed of two optical fibers that are helically wrapped around a sealed silicone tube. This creates a Mach–Zender interferometer that measures diameter change of the tubular diaphragm due to a pressure change (Zumberge et al. 2003; De Wolf et al. 2013). The fiber-wrapped tube is encased in insulation and installed inside a perforated drainage tube. An advantage of such systems is that they can be deployed over larger areas than pipe arrays due to the absence of resonance. The defined layout should ensure that the acoustic response of the system does significantly depend on wave azimuth and is identical at all array elements. More work may be required to characterize the susceptibility of the system to temperature and develop calibration methods in agreement with IMS requirements (Sect. 1.7). More importantly, as the system includes the sensing device, it should be thoroughly tested against all IMS Operational Manual requirements for infrasound sensors (Sect. 1.6).

In conclusion, it is likely that other wind-noise reduction methodologies could provide in the future better performance in terms of noise reduction than standard PTS pipe arrays. In order to comply with IMS Operational Manual requirements, the acoustic response of the new systems should be accurately modeled and it should be demonstrated that the system response remains flat and stable through time over the entire IMS frequency band including in harsh environments. The new systems should also ensure that the same response can be achieved at all array elements of the same station. In addition, the lifetime of the structure should be similar as that of the PTS standard pipe array (at least 15 years) and the cost not to be prohibitive. If such a new system would demonstrate to outperform the standard PTS pipe arrays and to meet all IMS requirements, the IMS Operational Manual would need to be updated

as it currently only allows for the installation of pipe arrays as acoustic filtering systems (CTBTO 2009). Finally, the progress made over the past 10 years to model the four main types of wind-generated noises, namely turbulence–sensor interactions, turbulence–turbulence interactions, turbulence–mean shear interactions, and acoustic noise generated by the wind, should be highlighted (Shields 2005; Raspet et al. 2006, 2019). The better understanding of these different types of noises could lead to the design of a new generation of WNRSs better adapted to local wind-noise conditions.

1.6 Infrasound Sensors

1.6.1 General Requirements

The IMS Operational Manual lists eight minimum requirements for infrasound sensor specifications, further referred to as the IMS requirements in this Section (Table 1.2). Infrasound sensors must be microbarometers with response flat and stable within ±5% in amplitude over the 0.02–4 Hz passband. They must be able to operate between −10 and +45 °C and sometimes even beyond for stations located in extreme locations. Since calibration requirements will be extensively discussed in Sect. 1.7, this section will mainly focus on self-noise, dynamic range, and response requirements.

The IMS requirement for sensor noise was defined in 1996 based on knowledge on the minimum infrasound background noise and on the performance of the most advanced sensors at the time (CTBTO 1997b). More recent studies have shown that the minimum infrasound noise level recorded in the IMS network at 1 Hz is in fact about 16 dB lower than the reference value specified in the IMS Operational Manual (Bowman et al. 2005). This means that sensors with a self-noise equal to the

Table 1.2 IMS minimum requirements for infrasound sensor specifications (CTBTO 2009)

Characteristics	Minimum Requirements
Sensor type	Microbarometer
Measured parameter	Differential pressure
Passband	0.02–4 Hz
Sensor response	Flat-to-pressure over the passband
Sensor noise	⩽18 dB below minimum acoustic noise[a]
Calibration[b]	⩽5% in absolute amplitude
Dynamic range	⩾108 dB
Standard temperature range[c]	−10 °C–+45 °C

[a] Minimum acoustic noise level at 1 Hz: ∼5 mPa/$\sqrt{\text{Hz}}$
[b] Periodicity: once per year (minimum)
[c] To be adapted for some specific sites

IMS requirement would have in reality a self-noise only 2 dB below the minimum measured infrasound noise at 1 Hz. It is generally assumed that in order to obtain a reliable measurement, the sensor self-noise needs to be at least 10 dB below the minimum acoustic noise (Ponceau and Bosca 2010). The IMS requirement for sensor self-noise is also defined at a single frequency only whereas the intent is for the sensor self-noise to be below the minimum infrasound noise over the entire IMS passband. The IMS requirement for sensor self-noise could be updated by specifying a minimum ratio between the minimum noise level expected at the station and the sensor self-noise over the IMS passband. This is what is done for the IMS seismic technology for which the sensor self-noise is required to at least 10 dB below minimum earth noise at the site. Such a requirement obviously implies knowing the minimum noise level at the station location or using a standard worldwide low noise model as a reference. The development of a accurate global low-noise model in the IMS frequency range should be a priority task in the near future. This model would be used not only for refining IMS specifications but also as a reference for equipment testing and data quality control. The development of such model is not an easy task as the input data need to be of the uppermost quality and must be corrected from the responses of the measurement systems. As seen in Sect. 1.5, a few IMS stations include, for example, nonstandard WNRS designs whose responses are not well characterized or fluctuate throughout time. Data from these stations should be discarded when computing a global low-noise model. For this reason, the model proposed by Bowman et al. (2005) is still used as a reference in this chapter as it is less affected by low quality data as the model proposed by Brown et al. (2014a). It is suspected that this latter model underestimates the minimum noise level in high frequency by up to a factor of 10 because of issues with the WNRS response of station I55US (Fee and Szuberla 2012).

Dynamic range corresponds to the ratio between the largest and the smallest amplitudes that can be recorded by a sensor. It is commonly derived from the ratio between the maximum level before signal clipping and the self-noise level. The objective of the dynamic range requirement is to ensure that the infrasound measurement system and the sensor specifically are able to accurately record both small and large amplitude infrasound signals. As seen in Sect. 1.5, the infrasound background noise level is highly frequency- and wind-dependent. The analysis of IMS worldwide measurements has shown that the infrasound background noise decreases with a slope of about −20 dB/decade in the IMS frequency band and can vary by as much as 60 dB at a single frequency depending of the wind conditions. This leads to a ratio of about 110 dB between the largest and smallest signal amplitudes commonly observed in the IMS frequency band (excluding close source measurements) (Bowman et al. 2005). With the addition of 10 dB for ensuring that the sensor self-noise is sufficiently below the minimum acoustic noise, the minimum requirement for infrasound sensor dynamic range should in reality be at least 120 dB. This value is slightly larger than the IMS requirement, which was defined as 108 dB in 1996 (CTBTO 1997b). A high dynamic range does not imply that the sensor is able to cover the entire infrasound amplitude range. A sensor with an extremely low self-noise could, for example, exceed the requirement for dynamic range while not being

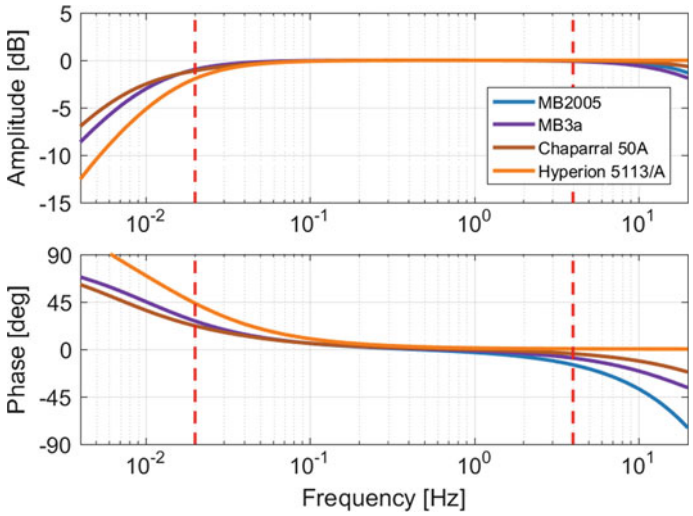

Fig. 1.20 Responses of MB2005, MB3a, Chaparral Physics 50 A and Hyperion 5113/A sensor models as per manufacturer data (CEA/Martec 2005; CEA/Seismowave 2014a; ChaparralPhysics 2010; Merchant 2015). The MB2005 response does not appear in low frequency because it perfectly overlaps with the MB3a response. The amplitude response of all sensors is flat ±3 dB in the IMS frequency band (vertical red dashed lines)

able to record high-amplitude infrasound signals. The IMS requirement for dynamic range could be updated with defining threshold values for the smallest and highest amplitudes to be recorded. Since there is already a defined specification for sensor self-noise, the specification for dynamic range could, in fact, be replaced by a specification on "signal clipping level". The maximum threshold before signal clipping should obviously be greater than the maximum background infrasound noise level observed in the IMS frequency band but could also be defined in relation with a maximum amplitude of explosion-generated infrasound signals to be expected to be recorded by IMS infrasound stations.

Finally, the flat-to-pressure requirement for the sensor response seems rather strict and probably not adapted to the shape of the infrasound background noise. The use of sensors with flat-to-pressure-derivative response could, for example, allow better matching of typical infrasound background noise levels in the IMS frequency band. The requirement for sensor response could, therefore, be updated similarly as for the IMS seismic technology for which different shapes of sensor responses are allowed. In addition, the term "flat" is not defined and could lead to different interpretations. It is commonly interpreted as flat in amplitude within 3 dB with no specific requirement for the phase. Figure 1.20 displays the responses (as per manufacturer data) of the main infrasound sensor models to be discussed in the next section.

1.6.2 Description

Infrasound sensors are commonly composed of a mechanical device sensitive to pressure fluctuations and of a transducer. Pressure fluctuations induce a distortion on the mechanical device that is then converted into a dynamic voltage by the transducer (Ponceau and Bosca 2010). In the first years of the network construction, two infrasound sensor models were successfully tested against IMS requirements: MB2000 and Chaparral 5 (CEA/DASE 1998; Kromer and McDonald 2000). Shortly after, the MB2005 model with slightly improved operational characteristics compared to the MB2000 was also approved for deployment in the IMS infrasound network (CEA/Martec 2005; Hart 2009). Over the past two decades, the MB2000/MB2005 sensors have been demonstrated to perform well in operating conditions with excellent response stability through time and very low sensitivity to temperature and absolute pressure fluctuations (Ponceau and Bosca 2010; Hart et al. 2013). For this reason, by 2012, MB2000/MB2005 sensors were deployed at over more than 90% of the network. Because of the high stability of their response, MB2000/MB2005 sensors are also used by expert infrasound laboratories such as the Commissariat à l'énergie atomique et aux énergies alternatives (CEA) and Sandia National Laboratories (SNL) as reference sensors for laboratory calibration (Sect. 1.6.3). The two drawbacks of this sensor model are (a) the level of the self-noise in high frequency, which can exceed the minimum acoustic background noise above 1 Hz at the quietest IMS stations (Fig. 1.21) and (b) the susceptibility to ground motion (Alcoverro et al. 2005). The sensitivity to ground motion is flat to acceleration and small enough that it rarely impacts measurements in the IMS frequency band. Although using data from mixed modality sensors can generate complications, IMS infrasound stations equipped with MB2000/MB2005 sensors currently contribute to the detection of high-amplitude seismic events for which regional IMS seismic stations sometimes clip due to the tuning of these stations to the detection of extremely low-amplitude events (Mialle et al. 2019). Seismic and infrasound arrivals are differentiated by IDC categorization algorithms due to different wave velocities.

The case of the Chaparral Physics 5 model is almost opposite. The sensor self-noise as measured in laboratory is very low compared to the minimum acoustic noise in the IMS frequency band and the sensor susceptibility to ground motion is negligible. However, the sensor response and self-noise are highly sensitive to environmental conditions. It was demonstrated that even when installed in a thermally insulated vaults at IMS stations, the sensor response could vary well outside IMS requirements (Szuberla et al. 2013) and the noise due to the sensor susceptibility to temperature could be higher than the minimum infrasound background noise (CTBTO 2011a). For this reason, starting from 2013, Chaparral Physics 5 sensors were progressively replaced by Chaparral Physics 50 A sensors across the IMS network (Chaparral-Physics 2010; Hart and Rembold 2010). This new generation of sensors was shown to be less sensitive to the environment while keeping some issues such as amplitude distortion and sensitivity stability (Hart and Jones 2011; CTBTO 2013b).

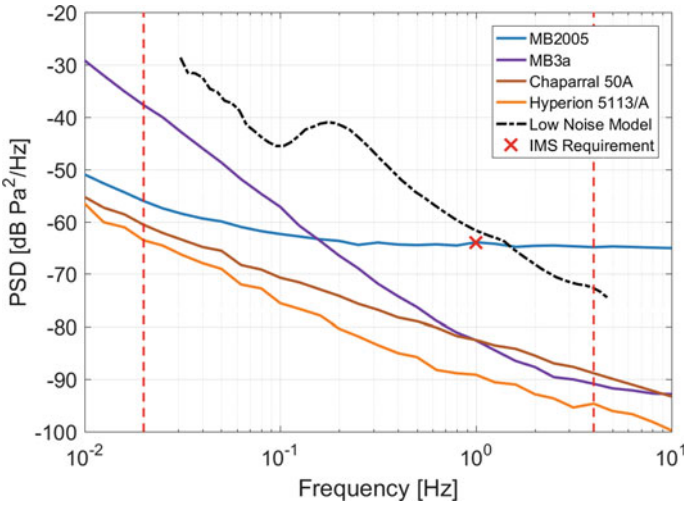

Fig. 1.21 Independent laboratory self-noise measurements for MB2005, MB3, Chaparral 50 A, and Hyperion 5113/A sensors (Merchant 2015; Merchant and Slad 2015). The red cross and the black-dotted line represent the IMS minimum requirement for sensor noise and the infrasound low-noise model (Bowman et al. 2005) respectively. The vertical dashed red lines delimits the IMS frequency band

Over the past years, two new sensor models were successfully tested against IMS requirements: MB3a (CEA/Seismowave 2014a; Merchant 2014) and Hyperion 5113/A (Merchant 2015; Nief et al. 2019). Unlike the MB2005 sensor, the MB3a sensor self-noise is at least 10 dB below the minimum acoustic noise in the entire IMS frequency band (Fig. 1.21). The MB3 power consumption is much smaller thanks to the use of a passive transducer. The sensor also includes a calibration coil that allows verifying the stability of the sensor in the field. In addition to the successful laboratory testing of the sensor against IMS requirements, the MB3 sensor was installed in operational conditions for 3 months in parallel with an existing IMS station before it was accepted for deployment in the network (Marty 2014b). The objective of this extensive testing was to ensure that the sensor would fulfill IMS requirements not only in laboratory but also in operational conditions. The self-noise of the Hyperion 5113/A sensor is at least 25 dB below the minimum acoustic noise in the IMS frequency band. The sensor measures both pressure and acceleration and the sensitivity of its pressure channel to acceleration is very low (Nief et al. 2019). The sensor has not yet been deployed at an IMS station. As of June 2017, MB2000/MB2005, Chaparral Physics 50 A and MB3 sensors were, respectively, installed at about 80, 15 and 5% of the network.

1.6.3 Type Approval

Since infrasound sensors are the key piece of equipment at an infrasound station, much attention is given to their design and testing (Nief et al. 2019). This section will focus on the testing of new sensor models against IMS requirements before approval for deployment into the IMS network. Acceptance testing of each individual sensor after manufacturing will be discussed in Sect. 1.7. The PTS has to date relied on two infrasound expert laboratories, SNL and CEA, for type approval of a new infrasound sensor. Testing results provided by these two laboratories have formed the baseline for the PTS to approve a sensor for deployment in the IMS network. With the increasing number of infrasound sensors in the market, the need to define standard definitions for IMS specifications as well as standard testing procedures has become more and more important. This task is challenging because there are no internationally recognized measurement standards available for the IMS infrasound frequency range. The current state of the art has a lower limiting frequency of 2 Hz and suitable primary calibration methods are still under development by the National Measurement Institute (NMI) community (Avison and Barham 2014). For this reason, the PTS organized two expert group meetings on infrasound sensors in 2013 and 2014 (Marty 2013, 2014a). As an outcome of these meetings, it was proposed that the PTS coordinates a pilot interlaboratory comparison study over the 2015–2016 time period. Three expert laboratories welcomed the initiative and agreed to participate: CEA, SNL, and the University of Mississippi. The outcome of this first study was far beyond initial expectations with a very high level of collaboration and information sharing between the three expert laboratories on topics that had been seen as quite sensitive (Doury et al. 2015). The three laboratories agreed on definitions for infrasound sensor specifications and provided a full description of their testing equipment and methodologies (CTBTO 2015). The same set of infrasound sensors was sent to the three expert laboratories for testing and results compared between the laboratories (Fig. 1.22).

Based on this success, all three laboratories agreed to repeat the study over the 2017–2018 time period. The PTS reached out the expert community with the objective of increasing the number of participants to the study. As a result, Los Alamos National Laboratories (LANL) agreed to join the study as a fourth expert laboratory. For this second pilot interlaboratory comparison study, the objectives were (a) further refinement of definitions for IMS sensor specifications based on lessons learned from the first pilot study, (b) homogenization of methods for the computation of measurement uncertainties, (c) inclusion of a reference microphone calibrated by a NMI, (d) contracting of NMIs for supervising the study and analyzing the results, and (e) focus on two main specifications encompassing most IMS requirements: self-noise and frequency response (CTBTO 2016d). Different midterm objectives were defined for these two specifications. Since results provided by the three laboratories during the first study were in good agreement for the frequency response, working with the International Metrology Community to provide measurement traceability was defined as a midterm goal. As results were significantly different for sensor

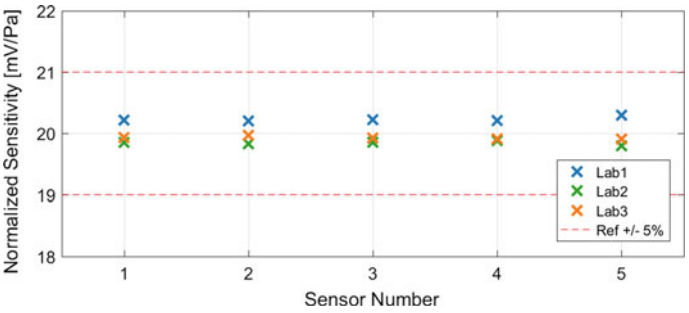

Fig. 1.22 Example of results obtained during the Pilot Interlaboratory Comparison Study 1 for the sensitivity at 1 Hz measured by the three laboratories for the same set of five sensors. Measurement uncertainties are not displayed since they were computed differently by the laboratories. Since no reference values were defined for the sensor sensitivities, the values were normalized by the mean of the values obtained by the three laboratories. All values are within the ±5% IMS minimum requirement for calibration (red dashed lines)

self-noise, the laboratories decided to focus on converging toward a standard and state-of-the-art measurement methodology. While the main objective of these pilot studies remains to fine-tune IMS infrasound sensor specifications and testing methodologies, it is also expected that these efforts lead in the long term to the definition of international standards for the infrasound technology and support the development of the next generation of infrasound sensors.

The successful laboratory testing of a new infrasound sensor model against current IMS requirements is, however, not enough to ensure that the sensor model will properly perform once deployed in the operational conditions. This is primarily due to the fact that (a) IMS requirements were defined at a time when knowledge of infrasound technology was much more limited and (b) laboratory testing is performed in stable and controlled environments masking potential susceptibility of a sensor model to environmental conditions or power source quality. For these reasons, in parallel of the pilot studies, the four expert laboratories agreed to support the PTS on the definition of more detailed sensor specifications for optimal operation (Marty 2013). The four laboratories have started defining sensor requirements for susceptibility to temperature, absolute pressure, and ground motion (Marty 2017). It is expected that the measurement of such specifications in a laboratory environment will help to anticipate undesirable sensor behavior in operational conditions. Since these additional specifications are still under development, the PTS currently requests that a new infrasound sensor model be deployed in operational conditions for a least 3 months in parallel to an IMS station as part of the type approval process for a new sensor (Marty 2014b). The objective of such a test is to compare the performance of the new sensor model in operational conditions against the well- characterized performance of an existing station through regular calibrations and array processing.

1.7 Calibration

1.7.1 General Requirements

Calibration is an essential process to ensure data quality and trustworthiness. As defined in the IMS Operational Manual, it encompasses three distinct processes: "acceptance testing", "initial calibration", and "on-site calibration". When an infrasound measurement system is to be deployed at an IMS station, specification data provided by the manufacturers for each individual piece of equipment are first reviewed to ensure that the delivered equipment meets sensor model specifications. This initial phase is called acceptance testing. The initial calibration is then performed with two objectives: (a) verifying that the system response remains within tolerances of the manufacturer-supplied data once the equipment is installed in operational conditions at the station (b) establishing a baseline for future calibrations (CTBTO 2009). The on-site calibration consists of measuring the system response and comparing it against the baseline response established at the time of the initial calibration. It shall be performed at least once a year or whenever it is suspected that the baseline calibration is affected (after equipment replacement for example). If the results of the on-site calibration are not within tolerances of the baseline, the SO must inform the PTS and initiate the necessary maintenance actions.

Both initial and on-site calibration must be full frequency response calibration. This means that a broad range of frequencies covering the entire 0.02–4 Hz passband shall be excited. The IMS Operational Manual also specifies that both sensor and WNRS shall be calibrated. The result of the on-site calibration shall be within 5% in amplitude of the baseline results over the IMS passband (Table 1.2). Unlike for the IMS seismic technology, there is currently no requirement on the phase response. This is probably due to the fact that estimating the phase response was seen as difficult at the time of the requirement definition. However, the IMS Operational Manual states that phase measurements are necessary to establish the full system response that is required for data processing at the IDC. In the case of the IMS seismic technology, the minimum calibration requirement of 5° accuracy is defined for the phase response. The same threshold is currently used as a reference for the IMS infrasound technology although defining a frequency-dependent requirement would probably be advisable. Finally, the IMS Operational Manual states that in order to perform on-site calibration activities, each infrasound array element shall be equipped with an internal or external calibration unit. It also specifies that initial calibration shall include a self-noise measurement at each array element.

1.7.2 Calibration Technique

Over the past decade, different techniques were investigated for the calibration of infrasound measurement systems. These include the use of active sources such as

pistonphones (Starovoit et al. 2006) or infrasound generators (Park et al. 2009), or the development of self-calibrated microbarometers (Nief et al. 2019). However, none of these techniques have solved the two main challenges for calibration of IMS infrasound measurement systems: the inclusion of the WNRS and the coverage of the entire IMS frequency band. The calibration of infrasound measurement systems started taking a new turn when Gabrielson (2011) observed that coherent signals at a scale much larger than the size of wind turbulence structures could be generally observed in the entire IMS frequency band for extremely low-wind conditions. This meant that for such wind conditions, the background noise of pressure fluctuations in the IMS frequency band was most likely formed by a superposition of pressure fluctuations produced by the propagation of infrasonic waves. It was, therefore, possible to use this ambient background noise of pressure fluctuations as a broadband source of infrasound waves.

An in-situ response estimation technique based on the comparison between the background measurement recorded by an IMS measurement system and a reference system was developed by Gabrielson (2011). The same year the PTS organized an expert group meeting to review infrasound sensor calibration methodologies (Marty et al. 2011c) and the decision was made to test the newly developed in-situ response estimation technique at three IMS infrasound stations (Gabrielson 2013). While the results were very positive two main issues remained: (a) the difficulty to obtain results within 5% in amplitude of the nominal response over the entire IMS frequency band and (b) the estimation of the uncertainties associated with the reference measurement systems. The first issue was solved through the enhancement of the data processing technique (Charbit et al. 2015; Marty et al. 2017) and the second one mitigated through the use of independent, stable and, whenever possible, regularly calibrated reference measurement systems (Marty 2014b). Two additional expert group meetings were organized in 2013 and 2014 to refine the calibration methodology (Marty 2013, 2014a) and in 2014, following a PTS recommendation (Marty 2014b), the PrepCom encouraged the PTS to integrate this new calibration technique into the IMS infrasound network (CTBTO 2014b). The PrepCom reiterated this statement in 2016 after the long-term testing and validation of the calibration technique at the first IMS infrasound station (Marty 2016; CTBTO 2016b). Calibration equipment and results will be further described in the next two sections dedicated to initial and on-site calibration.

1.7.3 Initial Calibration

Since no technique fulfilling IMS requirements was available for initial calibration before 2012, only basic functionality checks were performed at the time of station certification or revalidation. The objective of these checks was to ensure that both the sensor and Data Acquisition System (DAS) were performing in general agreement with manufacturer specifications. The WNRS response was not measured, no full frequency calibration was performed, and no response sensitivity was computed.

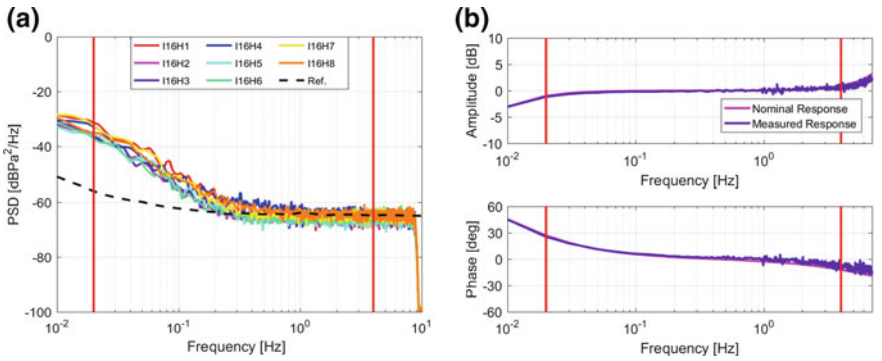

Fig. 1.23 **a** Self-Noise of all I16CN array elements with sealed sensors. The self-noises overlap very well above 0.3 Hz with the reference self-noise (black-dashed line) measured in the laboratory. Discrepancies in low frequency are a known bias from the method (with sealed sensors, any minor change of temperature leads to significant change in pressure) **b** Full frequency response of I16H3 infrasound measurement system (WNRS, sensor and DAS). Both measured and modelled responses overlap very well and the measured sensitivity at 1 Hz is within 0.8% of the nominal value (IMS requirement $\leqslant$5%). The vertical dashed red lines delimits the IMS frequency band in both figures

Therefore, there was no reference system response established at the time of certification and manufacturer specifications were always used as a baseline. Starting in 2012, the development of a full frequency calibration technique (Sect. 1.7.2) has allowed the PTS to progressively go through the entire initial calibration process at the time of station certification or revalidation. To accomplish this, the PTS uses an external and portable calibration unit composed of a reference MB2005 sensor and Taurus 24-bit DAS. Since 2015, the calibration units are complemented with MB3d sensors, which correspond to the 24-bit digital version of the MB3a sensors discussed in Sect. 1.6 (CEA/Seismowave 2014b). The calibration unit is deployed next to the operational measurement system as close as possible to the center of the WNRS. The sensor is connected to a short pipe terminated by a static pressure head (Vaisala 2005; Lanzinger and Schubotz 2012). When possible the static pressure head is covered by gravel to improve noise reduction. The full frequency response of the infrasound measurement system (WNRS, sensor, and DAS) is then computed from the comparison between the operational and reference data streams. As an illustration, initial calibration results measured at station I16CN are presented in Fig. 1.23.

The comparison of initial calibration results with manufacturer supplied data and the definition of a baseline for future calibration as required by the IMS Operational Manual mainly depends on the sensor model used at the station. Deviations from manufacturer values for DASs and from modeling results for WNRSs are usually negligible in the IMS frequency band. If they are not, the DAS is replaced or the WNRS characteristics measured again. In the case of MB2000/MB2005 sensors, initial calibration results are almost always within a few percent of manufacturer-supplied data with the difference smaller than the uncertainties of the initial calibration technique. In the rare cases when the difference in sensitivity exceeds the

5% IMS requirement, the sensor is replaced with a spare and the non-compliant sensor sent back to the manufacturer. Due to the very close values between sensor model response, manufacturer-supplied data for a specific sensor, and initial calibration results, it is the sensor model response that is used as a baseline for future calibration. This significantly simplifies the on-site calibration process and equipment replacement procedures because the same baseline response is used for all the array elements of all IMS stations using MB2000/MB2005 sensors. The process for Chaparral 50 A sensors is more complex because the response of these sensors (a) depends on the altitude at which the sensor is deployed and (b) varies from sensor to sensor (Sect. 1.6). Initial calibration results cannot be compared with manufacturer-supplied data and distinct baseline values are defined for each array element.

The PTS together with the infrasound expert laboratories and NMIs is currently working on the definition of standard procedures for the calibration of the PTS reference equipment (Marty 2017). Currently, the process mainly focusses on sensors since it is here again assumed that deviations from manufacturer values are negligible for the reference DAS. The response of the PTS reference sensor is regularly (before and after shipment to a station for example) compared at the PTS against the response of a group of reference sensors based in Vienna. From this group of sensors, there are some that always remain in Vienna while others are sent on a regular basis for calibration to expert laboratory such as CEA or SNL. This process allows the establishment of a chain of calibration between the reference sensor deployed at the station during initial calibration and a laboratory standard (Kramer et al. 2015).

1.7.4 On-site Calibration

The on-site calibration implemented in operations for the IMS seismic technology is a quite complex and resource-demanding process (CTBTO 2016a). Since the calibration process requires a series of actions from the SO and the IMS seismic stations can be non-mission capable during calibration, a precise worldwide schedule is necessary to ensure that the SO is available and that not two stations in the same region are calibrated at the same time. The SO has to then perform a series of actions which can take up to several days for the larger IMS seismic arrays. The SO is also responsible for processing calibration data and reporting results to the PTS. SO training dedicated to calibration activities are, therefore, organized on a regular basis. In addition, the calibration process highly depends on the type of equipment installed at the station. This means that station-specific procedures are required and that new procedures and training are needed when equipment at the station is upgraded or when a new SO is appointed. Lessons learned from the rolling-out of on-site calibration activities across the IMS seismic network were taken into account when defining the on-site calibration process for the IMS infrasound technology.

The on-site calibration technique for the IMS infrasound technology is based on the installation of a reference infrasound measurement system within the existing equipment vault (Fig. 1.24). The reference system is connected to a short pipe terminated by an air inlet. Both operational and reference infrasound data are sent to the IDC and the system response is derived from the comparison of these two data streams (Sect. 1.7.2). The advantages of this calibration technique are numerous. First, the operational data stream is never affected by the calibration process and the calibration does not need to be scheduled. Second, the technique does not require any action from the SO. Third, the technique is independent from the operational measurement system and no extra costs are involved for updating calibration equipment, procedures, or training when operational equipment is upgraded. Fourth, the same technique is used at all IMS infrasound stations and the computation of the results is automatically performed in a standard way in the IDC. Fifth, the system response can be computed retroactively allowing the verification of the proper functioning of the measurement system before or after an event of interest, for example. For all the above reasons, the on-site calibration process for the IMS infrasound technology is seen as reliable and cost-effective (Marty 2014b). In addition, the technique allows for computation of the system response at any time and allows closely monitoring the stability of the system response through the year. Whereas the calibration method for the IMS seismic technology is currently not traceable to standards, it is expected that the setup used for the calibration of IMS infrasound stations will allow linking the reference sensor installed in the vault with laboratory standards (Kramer et al. 2015). Such process as well as standard procedures for the on-site calibration of IMS infrasound stations are currently being defined with the support of the infrasound expert laboratories and NMIs (Marty 2017).

On-site calibration equipment was deployed for the first time at station I26DE in May 2015. Before this, the response of IMS infrasound measurement systems had never been measured at IMS stations. It was previously assumed that the responses were in agreement with the theoretical responses and stable through time with no means to verify it. This is still the case at most IMS infrasound stations. Since the MB2005 sensors were already in use at station I26DE and the response of these sensor models is known to be very stable in operational conditions (Sect. 1.6), it was decided to use the MB2005 sensors as reference sensors and to install MB3a sensors as operational sensors. This provided the added advantage of reusing existing sensors and improving the station detection capability thanks to the use of sensors with lower self-noise in high-frequency. In order to validate the on-site calibration technique, full system responses were computed every 2 days for more than a year. The stability of the method was found to exceed initial expectations and the responses of I26DE eight array elements were measured in agreement with IMS specifications (Fig. 1.25). Following this long-term testing phase, the PrepCom encouraged the PTS to continue the deployment of the infrasound station calibration capabilities through the IMS infrasound network (CTBTO 2016b). On-site calibration equipment was installed at station I37NO in 2016. At this station as well, the decision was made to use the existing MB2005 sensors as reference sensors and to install MB3a sensors as operational sensors. Full frequency system responses were measured at all array

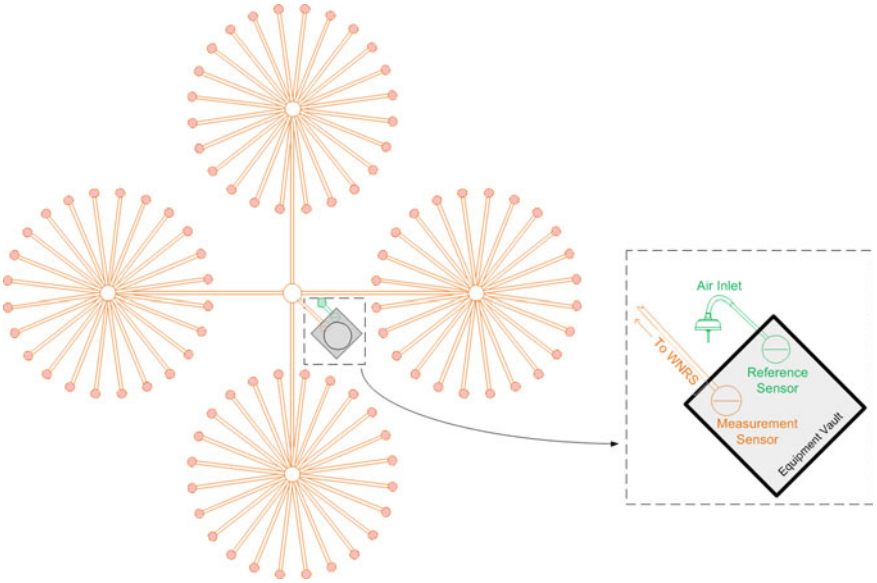

Fig. 1.24 Drawing of operational measurement system (orange) and reference system (green) used for on-site calibration at a standard IMS infrasound array element

elements in agreement with IMS specifications and the method demonstrated again to be very stable through time (Fig. 1.25). In addition to validating this method, the calibration results at these two stations provided a unique feedback on the stability of IMS infrasound measurement systems. These results also validated all the efforts described in Sect. 1.5 to model and improve the stability of the WNRS responses.

1.8 Meteorological Data

In addition to differential pressure measurements recorded at all array elements, the IMS Operational Manual requires that meteorological measurements including wind speed, wind direction, and temperature, be made at one or more of the array elements. These measurements will be further referred to as IMS meteorological measurements. The goal of IMS meteorological measurements is to provide information on station environmental conditions to support the interactive analysis of infrasound data. IMS Operational Manual minimum requirements for meteorological sensor specifications are listed in Table 1.3.

Although required, meteorological measurements were never made a priority in comparison with differential pressure measurements. This probably relates to the fact that these auxiliary measurements are not used by IDC automatic processing algorithms, nor taken into account in data availability statistics. As a consequence, the

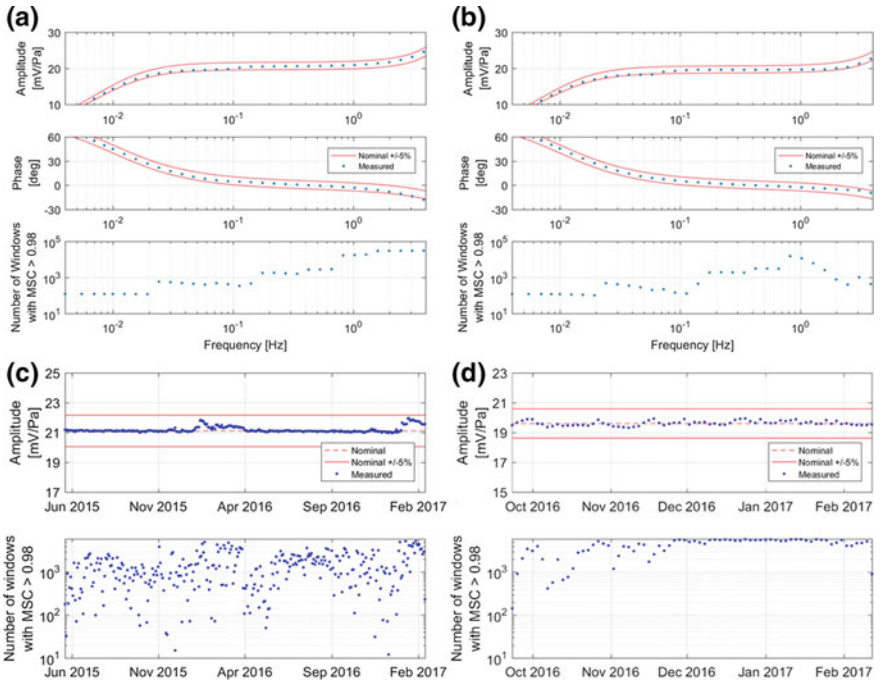

Fig. 1.25 On-site calibration results for station I26DE and I37NO. Figures **a** and **b** display the measured full frequency response (amplitude, phase, and number of time windows with magnitude squared coherence >0.98 between the measurement and reference signals) for stations I26DE (H7) and I37NO (H3) respectively. Figures **c** and **d** display the measured sensitivity at 1 Hz through time (including number of time windows with magnitude squared coherence >0.98 between the measurement and reference signals) for stations I26DE (H7) and I37NO (H3) respectively. All results in the four figures are within IMS requirements (red lines)

availability and quality of meteorological measurements have been generally much lower than that of differential pressure measurements and a significant number of IMS meteorological channels do not currently fulfill all IMS minimum requirements. An infrasound expert group was organized in the Republic of Korea in 2012 with the main objectives of reviewing the status of IMS meteorological measurements, discussing state-of-the-art developments in the area, and providing recommendations to the PTS (Marty et al. 2012c). The expert group reinforced the fact that meteorological measurements were useful for operational (information on station detection capability, estimation of trace velocities, and incidence angles) and engineering purposes (information for adapting WNRSs and array geometry to station-specific environmental conditions). However, the expert group highlighted that it was currently difficult to use IMS meteorological data due to their low quality. It was, therefore, recommended that more attention be given to the installation, maintenance, and documentation of meteorological channels and measurement systems.

Table 1.3 IMS minimum requirements for meteorological sensor specifications (CTBTO 2009)

Sensor	Characteristics	Minimum requirements
Wind speed[a]	Range[b]	0–50 ms^{-1}
	Threshold	$\leqslant$0.2 ms^{-1}
	Accuracy	$\pm$0.2 ms^{-1}
	Resolution	$\leqslant$0.2 ms^{-1}
	Sampling rate	$\geqslant$1 sample per minute
Wind direction[a]	Range	0–360°
	Threshold	$\leqslant$0.2 ms^{-1}
	Accuracy	$\pm$2.5°
	Resolution	1.0°
	Sampling rate	$\geqslant$1 sample per minute
Temperature[c]	Range[b]	−40 °C–+50 °C
	Accuracy	$\pm$0.3 °C
	Sampling rate	$\geqslant$1 sample per minute

[a] includes heater for anemometer where required
[b] to be adapted for some specific sites
[c] includes appropriate radiation shield

Part of the issue with meteorological measurements is related to data acquisition at the array elements. The same DASs used for differential pressure recording have often been used to acquire meteorological data in order to benefit from developments already made on DASs for IMS-specific requirements such as data formatting or authentication (Sect. 1.9). However, the acquisition of meteorological data is different in many ways from that of differential pressure. Meteorological measurements correspond to absolute and not differential values and meteorological sensors are usually not designed for sampling rates as high as those required for differential pressure. Integration of meteorological sensors with DASs was not always thoroughly tested resulting in a number of issues such as overshooting (due to high sampling rate), variable offset (change of electronic channel offset through time), or scaling (wrong sensitivities). For this reason, the 2012 expert group recommended (a) standardizing meteorological equipment across the network, (b) performing advanced integration testing with DASs, (c) developing on-site calibration procedure at the time of station certification and revalidations, and (d) providing SOs with spares (Marty et al. 2012c). While these recommendations are progressively implemented through the network, the PTS is also investigating the use of off-the-shelf digital meteorological packs, which can now be integrated with the new generation of DASs or with microcomputer devices (Sect. 1.9). These types of solutions are expected to solve most of the above-mentioned integration issues and are seen as the way forward for reliable IMS meteorological measurements.

At the time of the expert group meeting in 2012, IMS meteorological data were sampled with frequencies ranging from 0.05 to 20 Hz (Marty 2012). These sampling frequencies are significantly greater than the IMS minimum requirement of

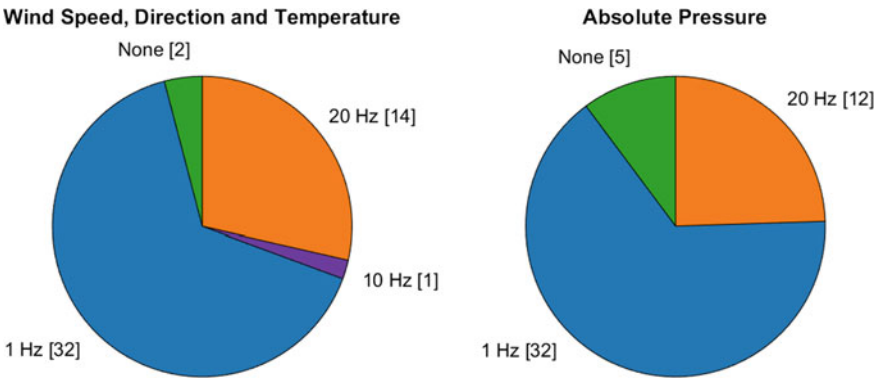

Fig. 1.26 Sampling frequencies distribution for wind speed, direction, and temperature (same distribution) and absolute pressure data recorded at IMS infrasound stations as of 2016 (with number of stations within bracket)

1 sample per minute (Table 1.3). The expert group, therefore, proposed to standardize the sampling frequency to 1 Hz across the network as this appeared to be a reasonable compromise for scientific, engineering, and operational purposes. This recommendation has progressively been implemented through the network and is still a work in progress (Fig. 1.26). Although IMS requirements specify that meteorological measurements be made at one or more of the array elements, currently all of the IMS infrasound stations only include one meteorological station which typically is located in the center of the array. The 2012 Expert Group reiterated that there could be value added by installing several meteorological sensors at the same infrasound station in case of environmental conditions significantly different from one array element to another. This could help adapting WNRSs and array geometry to station-specific locations. With the same objective in mind, the expert group also proposed the use of 3D wind sensors to better characterize local wind turbulence (Sect. 1.5).

Although there is no IMS requirement for absolute pressure measurements, most IMS stations send absolute pressure data. Unlike the required IMS meteorological data, absolute pressure information is commonly sent from all array elements of the same station. This is because MB2000/MB2005 sensors are installed in most of the networks (Sect. 1.6) and that these sensors measure both differential and absolute pressure. As for the required IMS meteorological measurements, little attention was given to the quality of absolute pressure data leading to significantly inaccurate values across the network (wrong sensitivities, sensor output not properly adjusted). It was also demonstrated that there was very little value added by recording the data since the differential pressure output from the MB2000/MB2005 sensors could be deconvolved up to several-day period (Marty et al. 2010). Whereas the 2012 Expert Group recognized that absolute pressure can provide useful state-of-health information, it recommended measuring this variable at one array element of each station only and using a dedicated external absolute pressure sensor instead of the absolute pressure output of MB2000/MB2005 sensors. As for the required IMS

meteorological channels, the expert group recommended homogenizing sampling frequencies of absolute pressure data to 1 Hz across the network (Fig. 1.26).

Finally, the 2012 Expert Group proposed to investigate possible standardization of meteorological equipment at IMS infrasound stations with meteorological equipment deployed at IMS radionuclide stations and with World Meteorological Organization (WMO) specifications. It was later determined that IMS meteorological data could have limited value for the WMO because of differences between IMS and WMO requirements (mainly in terms of equipment and sitting) (Martysevich et al. 2015). Since IMS infrasound stations are often located in remote areas with no WMO weather station close by, the WMO nevertheless expressed its interest in the IMS meteorological measurements (Krysta 2015). These data could be integrated into meteorological data assimilation models, which are of high importance for the modeling of infrasound propagation, network detection capability, and atmospheric transport. The PTS recently contacted the Zentralanstalt für Meteorologie und Geodynamik (ZAMG) as the representative institute in Austria for WMO activities in order to discuss the sharing of IMS meteorological data with the WMO community.

1.9 Data Acquisition Systems

1.9.1 General Requirements

Data acquisition is usually done in two steps at IMS infrasound stations. First a data acquisition system (DAS) installed within the equipment vault converts the analog output of the infrasound sensor into a digital, time-stamped, digitally signed and formatted data packet known as a subframe, which is transmitted to the CRF. This type of DAS is often called digitizer because its main function is analog-to-digital conversion. A second type of DAS located at the CRF receives subframes from all the array elements and groups them into a larger data packet known as a frame. Frames are also time-stamped and digitally signed before they are sent to the IDC. All these actions at the CRF are performed by software running on industrial class or rugged computers. The IMS Operational Manual lists minimum requirements for DAS specifications (Table 1.4). IMS Infrasound data must be sampled at a rate higher than 10 samples per second and each data frame must be shorter than 30 s. All IMS infrasound stations use a standard sampling rate of 20 samples per second and a frame length of 20 s. IMS data must be formatted to Group of Scientific Experts (GSE) format. The GSE defined the CD-1.0 and later on the CD-1.1 data format for continuous data transmission to the IDC (IDC 2001). Data from all IMS infrasound stations are currently received in one of the two CD formats at the IDC with stations progressively upgraded to CD-1.1.

DAS resolution is required to be higher than 1 count per 1 mPa. This requirement is rather loose since the infrasound background noise level can reach 0.2 mPa in the IMS passband. The minimum requirement on resolution could, therefore, be

Table 1.4 IMS Operational Manual requirements for infrasound DAS specifications (CTBTO 2009)

Characteristics	Minimum requirements
State-of-health	Status data transmitted to the IDC
Sampling rate	⩾10 samples per second
Resolution	⩾1 count per 1 mPa
Timing accuracy	⩽1 ms
Standard temperature range[a]	−10 °C–+45 °C
Buffer at station or NDC	⩾7 days
Data format	Group of scientific experts format
Data frame length	⩽30 s
Data transmission	Continuous

[a] To be adapted for some specific sites

updated by specifying a minimum ratio between the lowest infrasound noise at the station and the DAS self-noise. A requirement for sensor noise is already defined in such a way (Sect. 1.6). Therefore, the specifications for sensor and resolution could be unified into a single "system noise" specification that would be required to be at least 10 dB below the minimum local infrasound noise. The minimum requirement of 7 days for data buffer at the station or NDC is easily fulfilled with existing data storage devices. In addition, typical DASs installed at the array elements also include extended data storage capacity. Therefore, the minimum requirement for data buffering at the CRF could be raised and extended to the array elements. This would increase the amount of data that could be retransmitted after a communication outage with the CRF or the IDC and support the effort to fulfill IMS DA requirements (Sect. 1.2.2). Although the CTBT only requires uninterrupted data transmission for IMS primary seismic stations, the IMS Operational Manual specifies that data transmission from IMS infrasound stations shall be continuous (CTBTO 2009) and the IDC Operational Manual specifies that data should be received in the IDC with a maximum delay in transmission of 5 min (CTBTO 2011b).

In addition to the minimum requirements for DAS specifications, the IMS Operational Manual also describes data surety requirements for IMS stations. Each array element and the CRF must include digital signature and anti-tampering devices. These devices are used by DASs to digitally sign data and trigger state-of-health security bits. Commands sent to IMS stations from remote locations are also required to be authenticated and this process is handled by DASs as well on the station side (CTBTO 2000). The need to integrate DASs with IMS infrasound and meteorological sensors has led to the definition of additional operational requirements. Examples include the capability to acquire both analog and digital meteorological data, power sensors, handle central timing solutions, or send integrated broadband calibration signals. It has also led to the definition of advanced requirements for specifications such as cross-talk, common mode rejection, harmonic distortion, or anti-aliasing filtering. Limiting DAS power consumption is another critical requirement as it

ensures that no upgrade of the power system is required when installing a new DAS at the station. The list of current operational requirements for IMS DASs, therefore, goes much beyond the list of the minimum requirements listed in Table 1.4 (CTBTO 2016c).

1.9.2 Description

In order to differentiate the two types of DASs described in the previous section, the DAS located inside the equipment vault will be further referred to as the digitizer and the DAS located at the CRF as the Data Acquisition and Forwarding Software (DAFS). There are currently five different digitizer models used across the IMS infrasound network (Fig. 1.27). Digitizer lifetime is estimated to be within 10–25 years depending on the models and the environment in which the digitizers are deployed. Since the first IMS infrasound stations were installed more than 15 years ago approximately 25% of the digitizers have already been upgraded. It is the intent of the PTS to keep at least four different models of digitizers across the IMS infrasound network. The objective is to prevent a major network outage in case of malfunctioning of one of the models. As an example, in 2016, due to a bug in GPS receiver firmware, the timing system of two digitizer models started drifting with time. Because of the diversity of the digitizer models used across the network, this issue only affected a part of the network. All digitizer models used in the IMS network have been successfully tested against IMS specifications by independent expert laboratories before they were approved for deployment. As discussed in Sect. 1.9.1, the lists of type approval tests was progressively extended with additional specifications in order to ensure the proper integration of digitizers with infrasound and meteorological sensors. More recently the PTS also started defining additional functionality and field tests for type approval of new digitizers with the support of expert laboratories. Functionality tests allow covering areas such as data formatting, calibration, authentication or command and control. Field tests allow stressing digitizers in operational conditions similarly as what is done for infrasound sensors (Sect. 1.6). The objective of all these tests is to ensure that digitizers will fulfill IMS requirements once deployed at IMS stations.

At the beginning of the network construction, all DAFS were proprietary software associated with the digitizer model used at the array elements. Such a solution was difficult to sustain due to the uniqueness of IMS requirements and their evolution with time. The PTS, therefore, decided in 2000 to start developing a standard software solution to interface with all types of digitizer models installed at IMS array elements. This solution, called Standard Station Interface (SSI), was deployed at the first IMS station in 2001 and is now deployed on more than 80% of the IMS infrasound network. The development of this solution resulted in reduced development costs, improved data availability, and flexibility to quickly incorporate new requirements. Apart from data acquisition, buffering, formatting, and digital signature, the SSI software also handles tasks such as calibration and command and control. After more than a decade of steady development, the SSI is now able to interact with all

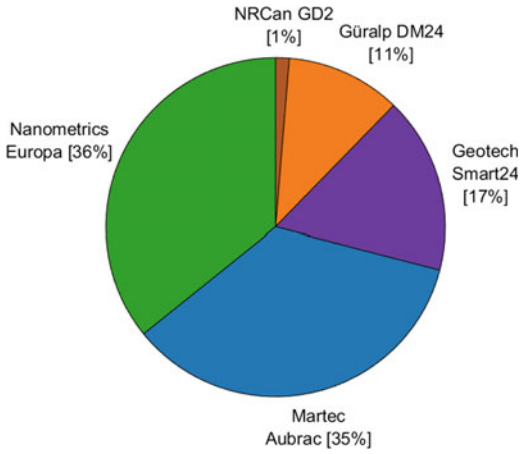

Fig. 1.27 Distribution of DAS models (digitizers) through the IMS infrasound network as of 2016

digitizer models deployed across the IMS network. The PTS is currently focusing on consolidating the last software release through the completion of the documentation, integration of the software into a standard testing environment, and improvement of the release process. The objective is to have a well-tested, documented, and robust version of the software by beginning of 2018. In parallel, a state-of-health component of the software is being developed for monitoring the status of the different SSI processes as well as of most station components (digitizers, communication and power systems). It is expected that this new module will ease SO monitoring activities. The storage of station state-of-health information at the CRF will also support station troubleshooting activities when required. Finally, it must be noted that the SSI software is currently being tested by Host Countries and the PTS on ruggedized microcomputer devices. It is expected that such devices could handle tasks such as data formatting and digital signature at the few stations for which digitizers currently do not have this capability.

1.10 Station Infrastructure

A robust infrastructure has been and will remain the basis for a high-performance station. No infrasound equipment can properly perform without a reliable power supply and protection against the environment. The analysis of station failures over the past 5 years have confirmed that power and environment are two of the main sources of data loss (Sect. 1.2.2). A lot of attention should, therefore, be given to station infrastructure design and station-specific environmental conditions should be taken into account. The IMS Operational Manual requires that a reliable primary power source capable of meeting DA requirements be installed at all IMS infrasound stations. Secondary sources of power are also required at the CRF and the array elements. The

IMS Operational Manual also recommends that stations consume as little power as possible in order to limit power back-up capacity, reduce maintenance costs, and increase DA. At the array elements, the replacement of obsolete DASs and sensors during station upgrade contributes to the reduction of power consumption. The PTS is also testing ultralow power consumption (below 5 W) computers to replace the current standard CRF SSI computers which consume about 400 W. This would significantly reduce power needs at the CRF and would allow for the installation of smaller, more robust, and maintenance-free power solutions. A few DC-powered CRFs were also recently upgraded with DC equipment in order to discard inverters and further reduce power consumption. In parallel, the PTS is reviewing state-of-the-art power solutions with the objective of defining and testing a set standard power systems for IMS stations. Particular attention is being given to solutions deployed in polar regions. Damage done to stations due to direct or indirect lightning has led to the definition of strict IMS standards for earthing and lightning protection (CTBTO 2010). Low-power consumption and redundancy are criteria that have also been made mandatory in the framework of the third GCI contract. GCI equipment will be replaced at all IMS stations over the 2017–2018 time period, and for the first time, all stations will include a back-up GCI link.

As discussed in Sect. 1.2.3, IMS infrasound measurement systems should be installed wherever possible inside dense forests in order to reduce the influence of wind on infrasound measurements. However, in the past vegetation has often been cleared around infrasound array elements to allow open sky access for solar panels and GPS antennas as well as direct line of sight for radio communication. The PTS has, therefore, decided to change its approach for building IMS infrasound array elements in recent years. The preferred solution for power and data communication is now through cables coming from the CRF (CTBTO 2014a). This type of solution allows using central timing and does not require the use of a GPS unit at array elements. It also allows installing one single-power source for the entire station. This reduces maintenance activities and simplifies the installation of back-up power systems. In addition, radio communication systems are more likely to fail under harsh environment than fiber optic systems. The use of fiber optic systems also reduces power consumption and generally eliminates the need for masts, which can increase the probability of lightning strike. When it is not possible to bring power and communication at the array elements through cables, a second vault is now installed in an open area at a reasonable distance from the equipment vault, which remains within dense vegetation. In the past, very large and deep underground vaults were often installed as it was assumed that temperature fluctuations could affect infrasound measurements. This led to a number of flooded vaults through the network due to high-water tables, snow melts, or heavy rains. The PTS now installs small surface vaults with high ingress protection levels, long life time, and thermal protection adapted to equipment operating ranges. Finally, the station infrastructure needs to be properly and regularly maintained by the SOs in order to ensure high data availability. This includes the planning and execution of well-defined preventive maintenance activities, such as the regular maintenance of diesel generators, timely replacement

of batteries, cleaning of solar panels, clearing of access roads, or measurement of grounding system resistivity.

1.11 Conclusion and Perspectives

The IMS infrasound network is a unique network. It is the only global infrasound network and its very strict operational requirements makes IMS infrasound data relevant not only for nuclear explosion monitoring, but also for a growing number of civil and scientific applications. As of June 2017, 82% of the IMS infrasound network is certified and it is anticipated that this number will reach 90% by 2020. Since the publication of the first version of this book in 2010, significant advances have been made in the characterization and optimization of IMS infrasound measurement systems. Development in array geometry, WNRSs, and calibration have allowed enhancing data quality and, therefore, network detection capability. Engineering processes have also been put in place to increase data availability at all IMS infrasound stations. The two main engineering challenges across the network are currently the fulfillment of IMS requirements for data availability and quality assurance. Sustaining high data availability requires robust and station-specific design, skilled and proactive SOs, continuous performance monitoring, and timely equipment and infrastructure upgrades. Although significant progress has been made over the past years with the development of a quality assurance infrastructure for the IMS infrasound technology, additional engineering efforts are required to define standard procedures, reach measurement traceability and roll out on-site calibration equipment through the network. Due to the uniqueness of the IMS infrasound network and of the IMS requirements, the PTS plays a key role in the development the infrasound technology. As highlighted in this chapter, it is expected that over the next 5 years engineering and development activities around the IMS infrasound network focus on the following:

(a) Deployment of robust, well-characterized and IMS-compliant WNRSs across the network;
(b) Refinement of standard procedures for type approval, acceptance testing, and calibration of IMS infrasound measurement systems;
(c) Integration of WNRS frequency responses into IDC responses files to enhance amplitude and phase corrections of IMS infrasound data;
(d) Strengthening of collaboration with the international metrology community to provide measurement traceability in the IMS frequency range;
(e) Update to the reference infrasound low-noise model;
(f) Development of advanced models for the design of infrasound array geometries;
(g) Enhancement of station state-of-health monitoring capabilities;
(h) Definition of standard and state-of-the-art power solutions for IMS stations;
(i) Standardization of meteorological equipment installed at IMS infrasound stations and sharing of data with the international meteorological community;

(j) Implementation of network detection capability models in operations for prioritizing maintenance actions.

The objective of these development activities is to reach compliance with IMS Operational Manual specifications at all IMS infrasound stations. These activities will also contribute in reinforcing the credibility of the IMS infrasound technology and support preparation for the Entry into Force of the CTBT. In parallel, the PTS will continue technology watch activities to stay at the forefront of scientific and technical innovation and ensure that the IMS infrasound technology stands at the state of the art for Treaty verification purposes. All these activities will lead to the provision of infrasound data with enhanced quality to States Signatories and open new possibilities to the scientific community for the monitoring of the atmosphere and of infrasound sources.

Acknowledgements The author would like to thank all the PTS/IMS/ED Seismo-Acoustic Unit in alphabetical order V. Bereza, B. Doury, M. Jusko, A. Kramer, M. Lefeldt, P. Martysevich, V. Miljanovic, G. Perez, J. Robertson, Y. Sid Ahmed, and Y. Starovoit for their continuous efforts building, sustaining, and enhancing the IMS seismo-acoustic network. The author would also like to thank in alphabetical order R. Barham, P. Campus, M. Charbit, T. Gabrielson, P. Grenard, T. Héritier, A. Le Pichon, J. Merchant, J. Mattila, P. Mialle, S. Nikolova, R. Rembold, and J. Vergoz for their valuable comments to this chapter.

Disclaimer The views expressed herein are those of the author and do not necessarily reflect the views of the CTBTO Preparatory Commission.

References

Alcoverro B (2008) The design and performance of infrasound noise-reducing pipe arrays. In: Havelock D, Kuwano S, Vorländer M (eds) Handbook of signal processing in acoustics. Springer, New York, pp 1473–1486

Alcoverro B, Le Pichon A (2005) Design and optimization of a noise reduction system for infrasonic measurements using elements with low acoustic impedance. J Acoust Soc Am 117:1717–1727

Alcoverro B, Martysevich P, Starovoit Y (2005) Mechanical sensitivity of microbarometers MB2000 (DASE, France) and Chaparral 5 (USA) to vertical and horizontal ground motion. InfraMatics 9:1–10

Avison J, Barham R (2014) Report on key comparison CCAUV.A-K5: pressure calibration of laboratory standard microphones in the frequency range 2 hz to 10 kHz. Technical report, National Physical Laboratory

Bowman JR, Baker GE, Bahavar M (2005) Ambient infrasound noise. Geophys Res Lett 32:L09803

Brachet N, Brown D, Le Bras R, Mialle P, Coynr J (2010) Monitoring the Earth's atmosphere with the global IMS infrasound network. In: Le Pichon A, Blanc E, Hauchecorne A (eds) Infrasound monitoring for atmospheric studies. Springer, Berlin, pp 29–75

Brown D, Ceranna L, Prior M, Mialle P, Le Bras R (2014a) The IDC seismic, hydroacoustic and infrasound global low and high noise models. Pure Appl Geophys 171:361–375

Brown D, Szuberla C, McComarck D, Mialle P (2014b) The influence of spatial filters on infrasound array responses. Pure Appl Geophys 171:575–585

Campus P, Christie D (2010) Worldwide observations of infrasonic waves. In: Le Pichon A, Blanc E, Hauchecorne A (eds) Infrasound monitoring for atmospheric studies. Springer, Berlin, pp 29–75

Capon J (1969) High-resolution frequency-wavenumber spectrum analysis. Proc IEEE 57(8):1408–1418
Carter J (2011) Waveform data availability and pts performance monitoring: updates and progress. WGB 37 – Waveform Expert Group
CEA/DASE (1998) Microbarometer MB2000 – Technical Manual
CEA/Martec (2005) Microbarometer MB2005 – User Manual
CEA/Seismowave (2014a) Microbarometer MB3a – User Manual
CEA/Seismowave (2014b) Microbarometer MB3d – User Manual
ChaparralPhysics (2010) Operation manual for the model 50A infrasound sensor
Charbit M (2015) Loss of coherence model. Technical report, CTBTO
Charbit M, Doury B, Marty J (2015) Evaluation of infrasound in-situ calibration method on a 3-month measurement campaign. Infrasound technology workshop 2015, Vienna, Austria
Che I-Y, Park J, Kim I, Kim TS, Lee H-L (2014) Infrasound signals from the underground nuclear explosions of North Korea. Geophys J Int 198:495–503
Christie D, Campus P (2010) The IMS infrasound network: design and establishment of infrasound stations. In: Le Pichon A, Blanc E, Hauchecorne A (eds) Infrasound monitoring for atmospheric studies. Springer, pp 29–75
CNEOS (2017). https://cneos.jpl.nasa.gov/fireballs/
Conference on Disarmament (1995) Report of the infrasound expert group to the Ad Hoc committee on a nuclear test ban working group on verification (CD/NTB/WP.283). Geneva
CTBTO (1996) Resolution establishing the preparatory commission for the Comprehensive Nuclear-Test-Ban Treaty Organization (CTBT/MSS/RES/1)
CTBTO (1997a) Report of working group B to the fourth session of the preparatory commission for the Comprehensive Nuclear-Test-Ban Treaty Organization – Annex VI (CTBT/PC/IV/1/Add.2)
CTBTO (1997b) Report of working group B to the second session of the preparatory commission for the Comprehensive Nuclear-Test-Ban Treaty Organization (CTBT/PC/II/1/Add.2)
CTBTO (1999) Operational manual for seismological monitoring and the international exchange of seismological data – draft (CTBT/WGB/TL-11/2/Rev.2)
CTBTO (2000) Command structure for IMS stations (CTBT/PTS/INF.280)
CTBTO (2001) Report of working group B to the fifthteen session of the preparatory commission (CTBT/PC-37/WGB/1)
CTBTO (2003) Minutes of infrasound experts meeting. UCSD, La Jolla
CTBTO (2008) Revalidation of performance of international monitoring system facilities (CTBT/PTS/INF.934)
CTBTO (2009) Operational manual for infrasound monitoring and the international exchange of infrasound data – draft (CTBT/WGB/TL-11,17/17/Rev.5)
CTBTO (2010) IMS earthing and lightning protection minimum standard
CTBTO (2011a) I59US. Hawaii, USA - Revalidation Report
CTBTO (2011b) Operational manual for the international data centre – draft (CTBT/WGB/TL-11,17/19/Rev.5)
CTBTO (2011c) Report of working group B to the thirty-seventh session of the preparatory commission (CTBT/PC-37/WGB/1)
CTBTO (2013a) I55US. Windless Bight, Antarctica - Revalidation Report
CTBTO (2013b) I58US. Midway Islands, USA - Certification Report
CTBTO (2013c) Midterm strategy: 2014–2017 (CTBT/PTS/INF.1249)
CTBTO (2013d) https://www.ctbto.org/press-centre/press-releases/2013/ctbto-detects-radioactivity-consistent-with-12-february-announced-north-korean-nuclear-test/
CTBTO (2014a) CTBTO preparatory commission IMS communication and maintenance guidelines
CTBTO (2014b) Report of working group B to the forty-third session of the preparatory commission (CTBT/PC-43/WGB/1)
CTBTO (2015) Technical protocol for pilot study PTSAVH.A-PS1

CTBTO (2016a) Annual report on the calibration of IMS seismic and hydroacoustic T-phase stations and sensor orientation (ECS/DIS/WGB-47/PTS-MATERIAL/11)
CTBTO (2016b) Report of working group B to the forty-sixth session of the preparatory commission (CTBT/PC-46/WGB/1)
CTBTO (2016c) Terms of reference for the the supply of high resolution digitizers and engineering services for IMS stations
CTBTO (2016d) Updated sections of the draft operational manual for infrasound monitoring and the international exchange of infrasound data incorporating changes agreed after the issuance of revision 5 (CTBT/WGB/TL-11,17/58/Rev.1)
CTBTO (2017a) Failure analysis of IMS stations (ECS/WGB-48/PTS/10)
CTBTO (2017b). https://www.ctbto.org/the-treaty/developments-after-1996/2017-sept-dprk/technical-findings/
CTBTO (2017c) Medium term strategy: 2018–2021 (CTBT/PTS/INF.1395)
Dahlman O, Mackby J, Mykkeltveit S, Haak H (2011) Detect and deter: can countries verify the nuclear test ban?. Springer, Berlin
Daniels F (1959) Noise-reducing line microphone for frequencies below 1 cps. J Acoust Soc Am 31(4):529–531
De Groot-Hedlin C, Hedlin M, Drob D (2010) Atmospheric variability and infrasound monitoring. In: Le Pichon A, Blanc E, Hauchecorne A (eds) Infrasound monitoring for atmospheric studies. Springer, pp. 475–507
De Wolf S, Walker K, Zumberge M, Denis S (2013) Efficacy of spatial averaging of infrasonic pressure in varying wind speeds. J Acoust Soc Am 133(5):3739
Denis S, Le Floch C (2015) Wind noise reduction systems: complementary results. Infrasound technology workshop 2015, Vienna, Austria
Dillion K, Howard W, Shields FD (2007) Advances in distributed arrays for detection of infrasonic events. J Acoust Soc Am 122:2960
Doury B, Denis S, Jusko M, Larsonnier F, Marty J, Merchant J, Nief G, Rembold R, Slad G, Symons NCT, Waxler R (2015) Interlaboratory comparison pilot study. In: Infrasound technology workshop 2015, Vienna, Austria
Evers L, Haak H (2001) An optimal infrasound array at Apatity (Russian Federation). KNMI. ISBN: 90-369-2193-7 publication 195
Evers LG, Haak HW (2010) The characteristics of infrasound, its propagation and some early history. In: Infrasound monitoring for atmospheric studies. Springer, pp 3–27
Fee D, Szuberla C (2012) Proposed re-drilling of wind-noise reducing ppipe at I55US. Technical report, UAF
Fee D, Szuberla C, Helmericks J, Tytgat G, Blom L, Winkleman A, Rembold R, Knox J, Gabrielson T, Talmadge C, Waxler R (2016) Preliminary results from the US NACT R&D testbed infrasound array. Infrasound technology workshop 2016, Quito, Ecuador
Fee D, Waxler R, Assink J, Gitterman Y, Given J, Coyne J, Mialle P, Garcés M, Drob D, Kleinert D, Hofstetter R, Grenard P (2013) Overview of the 2009 and 2011 sayarim infrasound calibration experiments. J Geophys Res 118(12):6122–6143
Firbas P, Brachet N (2003) Processing data from incomplete infrasound arrays. IMS workshop 2003, Vienna, Austria
Frazier G (2012) Using parametric models for wind noise for improved detection of transient acoustic signals. Infrasound technology workshop 2012, Daejon, Republic of Korea
Frazier G (2014) Application of parametric empirical Bayes estimation to enhance detection of infrasound transients. Infrasound technology workshop 2014, Vienna, Austria
Gabrielson T (2011) In situ calibration of atmospheric-infrasound sensors including the effects of wind-noise-reduction pipe systems. J Acoust Soc Am 130(3):1154–63
Gabrielson T (2013) In-situ calibration of infrasound elements: summary report (2009–2013). Technical report, Nuclear Arms Control Treaty
Green DN (2015) The spatial coherence structure of infrasonic waves: analysis of data from international monitoring system arrays. Geophys J Int 201:377–389

Green DN, Bowers D (2010) Estimating the detection capability of the international monitoring system infrasound network. J Geophys Res 115(D18):D18116

Grover F (1971) Experimental noise reducers for an active microbarograph array. Geophys J R Astron Soc 26(1–4):41–52

Hart D (2009) Evaluation of the microbarometer 2005 infrasound sensor. Technical report, Sandia National Laboratories

Hart D, Jones K (2011) Infrasound sensor evaluation performed at the Facility for Acceptance, Calibration and Testing (FACT) site. Infrasound technology workshop 2011, Dead Sea, Jordan

Hart D, Rembold R (2010) Evaluation of two Chaparral physics model 50A infrasound sensors. Technical report, Sandia National Laboratories

Hart D, Rembold R, Hedlin M, Coon C, Szuberla C, Fee D, Helmericks J, Marty J (2013) I56US Newport, WA component upgrade: evaluation of the replaced digitizers and infrasound sensors. In: Science and technology conference 2013

Hedlin M, Alcoverro B (2005) The use of impedance matching capillaries for reducing resonance in rosette infrasonic spatial filters. J Acoust Soc Am 117(4):1880–1888

Hedlin M, Alcoverro B, D'Spain G (2003) Evaluation of rosette infrasonic noise-reducing spatial filters. J Acoust Soc Am 114:1807–1820

Hedlin M, Raspet R (2003) Infrasonic wind-noise reduction by barriers and spatial filters. J Acoust Soc Am 114(3):1379–1386

IDC (2001). IDC Documentation - Continuous Data Subsystem CD-1.1

Kay SM (1993) Fundamentals of statistical signal processing: estimation theory. Prentice Hall, Upper Saddle River

Kramer A, Doury B, Grasse T, Jusko M, Marty J, Charbit M, Nikolova S (2015) Progress in the integration of on-site calibration capability at IMS infrasound stations: towards measurement quality assurance. Infrasound technology workshop 2015, Vienna, Austria

Kromer R, McDonald T (2000) Infrasound sensor models and evaluation. Technical report, Sandia National Laboratories

Krysta M (2015) Meeting of the WMO/CBS (World Meteorological Organization/Commission for Basic Systems) expert team on emergency response activities (ET-ERA). Technical report, CTBTO

Lanzinger E, Schubotz K (2012) A laboratory intercomparison of static pressure heads. Technical report, WMO CIMO TECO, Brussels, Belgium

Le Pichon A (2003) Infrasound network evaluation – identified sources of instabilities. IMS workshop 2003, Vienna, Austria

Le Pichon A, Assink JD, Heinrich P, Blanc E, Charlton-Perez A, Lee CF, Keckhut P, Hauchecorne A, Rfenacht R, Kmpfer N, Drob DP, Smets PSM, Evers LG, Ceranna L, Pilger C, Ross OCC (2015) Comparison of co-located independent ground-based middle atmospheric wind and temperature measurements with numerical weather prediction models. J Geophys Res Atmos 120:8318–8331

Le Pichon A, Ceranna L, Pilger C, Mialle P, Brown D, Herry P, Brachet N (2013) The 2013 Russian fireball largest ever detected by CTBTO infrasound sensors. Geophys Res Lett 40(14):3732–3737

Le Pichon A, Ceranna L, Vergoz J (2012) Incorporating numerical modeling into estimates of the detection capability of the IMS infrasound network. J Geophys Res 117:D05121

Le Pichon A, Ceranna L, Vergoz J, Tailpied D (2019) Modeling the detection capability of the global IMS infrasound network. In: Le Pichon A, Blanc E, Hauchecorne A (eds) Infrasound monitoring for atmospheric studies, 2nd edn. Springer, Dordrecht, pp 593–604

Le Pichon A, Vergoz J, Blanc E, Guilbert J, Ceranna L, Evers L, Brachet N (2009) Assessing the performance of the International monitoring system's infrasound network: geographical coverage and temporal variabilities. J Geophys Res 114:D08112

Liszka L (2008) Infrasound: a summary of 35 years of infrasound research. IRF scientific report 291, Institutet for rymdfysik. ISBN 978-91-977255-0-7

Mack H, Flinn E (1971) Analysis of the spatial coherence of short-period acoustic-gravity waves in the atmosphere. Geophys J R Astron Soc 26(1–4):255–269
Marchetti E, Ripepe M, Campus P, Le Pichon A, Brachet N, Blanc E, Gaillard P, Mialle P, Husson P (2019) Infrasound monitoring of volcanic eruptions and contribution of ARISE to the volcanic ash advisory centers. In: Le Pichon A, Blanc E, Hauchecorne A (eds) Infrasound monitoring for atmospheric studies, 2nd edn. Springer, Dordrecht, pp 1141–1162
Marty J (2012) Meteorological data recorded at IMS infrasound stations. Infrasound technology workshop 2012, Daejon, Republic of Korea
Marty J (2013) IMS infrasound sensors: specifications, tests, calibration. Technical report, Infrasound Expert Group Meeting 2013, Vienna, Austria
Marty J (2014a) Infrasound sensor specifications and interlaboratory comparison. Technical report, Infrasound Expert Group Meeting 2014, Vienna, Austria
Marty J (2014b) Work and progress on the infrasound station calibration programme, including work on self-calibrating sensor. In: WGB 43 – technology refreshment
Marty J (2016) Progress on infrasound sensor calibration. In: WGB 46 – technology refreshment
Marty J (2017) Quality assurance for IMS infrasound data. Technical report, Infrasound Expert Group Meeting 2017
Marty J, Denis S, Gabrielson T, Garcés M, Brown D (2017) Comparison and validation of acoustic response models for wind noise reduction pipe arrays. J Atmos Ocean Technol 34:401–414
Marty J, Denis S, Garcés M (2011a) Performance assessment of infrasound station IS07. Infrasound technology workshop 2011, Dead Sea, Jordan
Marty J, Kramer A, Mialle P (2013) IS07 major upgrade. Infrasound technology workshop 2013, Vienna, Austria
Marty J, Kramer, A, Polzer P (2012a) IMS acoustic filtering systems. Infrasound technology workshop 2012, Daejon, Republic of Korea
Marty J, Le Pichon A, Evers L (2011b) IMS wind noise reduction systems. Technical report, Infrasound Expert Group Meeting 2011, Dead Sea, Jordan
Marty J, Le Pichon A, Evers L (2011c) On-site calibration techniques. Technical report, Infrasound Expert Group Meeting 2011, Dead Sea, Jordan
Marty J, Le Pichon A, Evers L (2012b) Array geometry of IMS infrasound stations. Technical report, Infrasound Expert Group Meeting 2012, Daejeon, Republic of Korea
Marty J, Le Pichon A, Evers L (2012c) Meteorological data recorded at IMS infrasound stations. Technical report, Infrasound Expert Group Meeting 2012, Daejeon, Republic of Korea
Marty J, Ponceau D, Dalaudier F (2010) Using the international monitoring system infrasound network to study gravity waves. Geophys Res Lett 37:L19802
Martysevich P, Marty J, Polzer P (2015) Status of meteorological measurements at IMS infrasound stations. Infrasound technology workshop 2015, Vienna, Austria
McDonald J, Douze EJ, Herrin E (1971) The structure of atmospheric turbulence and its application to the design of pipe arrays. Geophys J R Astron Soc 26(1–4):99–109
McDonald J, Herrin E (1975) Properties of pressure fluctuations in an atmospheric boundary layer. Bound -Layer Meteorol 8(3–4):419–436
McNamara DE, Buland RP (2004) Ambient noise levels in the continental united states. Bull Seismol Soc Am 94(4):1517–1527
Merchant J (2014) MB3a infrasound sensor evaluation. Technical report, Sandia National Laboratories
Merchant J (2015) Hyperion 5113/A infrasound sensor evaluation. Technical report, Sandia National Laboratories
Merchant J, Slad G (2015) Chaparral 50A and MB2005 infrasound sensor international evaluation comparison. Technical report, Sandia National Laboratories
Mialle P, Brown D, Arora N, colleagues from IDC (2019) Advances in operational processing at the international data centre. In: Le Pichon A, Blanc E, Hauchecorne A (eds) Infrasound monitoring for atmospheric studies, 2nd edn. Springer, Dordrecht, pp 209–248

Nief G, Talmadge C, Rothman J, Gabrielson T (2019) New generations of infrasound sensors: technological developments and calibration. In: Le Pichon A, Blanc E, Hauchecorne A (eds) Infrasound monitoring for atmospheric studies, 2nd edn. Springer, Dordrecht, pp 63–89

Nikolova S, Araujo F, Aktas K, Malakhova M, Otsuka R, Han D, Assef T, Nava E, Mickevicius S, Agrebi A. (2015). Operation of international monitoring system network. In: EGU. (number 2015-14269 in 17)

Nouvellet A, Charbit M, Roueff F, Le Pichon A (2013) Coherence parameters estimation from noisy observations. Infrasound technology workshop 2013, Vienna, Austria

Park J, Garcés M, Thigpen B (2009) The rotary subwoofer: a controllable infrasound source. J Acoust Soc Am 125(4):2006–2012

Pavlovski OA (1998) Radiological consequences of nuclear testing for the population of the former USSR (Input information, models, dose, and risk estimates). Springer, Berlin, pp 219–260

Ponceau D, Bosca L (2010) Specifications of low-noise broadband microbarometers. In: Infrasound monitoring for atmospheric studies. Springer, Berlin, pp 119–140

Rakotoarisoa T, Rambolamanana G, Randrianarinosy F, Ramanantsoa A, Andrianaivoarisoa J (2013) Infrasound station performance assessment using correlation. Infrasound technology workshop 2013, Vienna, Austria

Raspet R, Abbott J-P, Webster J, Yu J, Talmadge C, Alberts II K, Collier S, Noble J (2019) New systems for wind noise reduction for infrasonic measurements. In: Le Pichon A, Blanc E, Hauchecorne A (eds) Infrasound monitoring for atmospheric studies, 2nd edn. Springer, Dordrecht, pp 91–124

Raspet RJW, Dillon K (2006) Framework for wind noise studies. J Acoust Soc Am 199:834–843

Shams Q, Zuckerwar ABS (2005) Compact nonporous windscreen for infrasonic measurements. J Acoust Soc Am 118(3):1335–1340

Shields FD (2005) Low-frequency wind noise correlation in microphone arrays. J Acoust Soc Am 117:3489–3496

Starovoit Y, Kunakov V, Martysevich P (2006) About dynamical calibration of microbarometers. InfraMatics 14:1–12

Symons GJ (1888) The eruption of Krakatoa and subsequent phenomena. Trübner, London

Szuberla C, Fee D, Waxler R, Gabrielson T (2013) Long-term in-situ calibration of the I53US IMS array elements. Infrasound technology workshop 2013, Vienna, Austria

Szuberla C, Olson J (2004) Uncertainties associated with parameter estimation in atmospheric infrasound arrays. J Acoust Soc Am 115(1):253–258

Thomas J, Pierce A, Flinn E, Craine L (1971) Bibliography on infrasonic waves. Geophys J R Astron Soc 26:399–426

Vaisala (2005). *SPH10 Static Pressure Head – Installation and Maintenance Guide*

Walker K, Hedlin M (2010) A review of wind-noise reduction methodologies. In: Le Pichon A, Blanc E, Hauchecorne A (eds) Infrasound monitoring for atmospheric studies. Springer, Berlin, pp 141–182

Waxler R, Gilbert KE (2006) The radiation of atmospheric microbaroms by ocean waves. J Acoust Soc Am 119:5

Welch PD (1967) The use of fast fourier transform for the estimation of power spectra: a method based on time-averaging over short, modified periodograms. IEEE Trans Audio Electroacoust AU-15:70–73

Zumberge M, Berger J, Hedlin MAH, Husmann E, Nooner S, Hilt R, Widmer-Schnidrig R (2003) An optical fiber infrasound sensor: a new lower limit on atmospheric pressure noise between 1 and 10 Hz. J Acoust Soc Am 113(5):2379

Chapter 2
New Generations of Infrasound Sensors: Technological Developments and Calibration

Guillaume Nief, Carrick Talmadge, Jeff Rothman and Thomas Gabrielson

Abstract This chapter explains the principles of functioning of sensors dedicated to record infrasound data. For various sensor models, the types of infrasound pressure transducers are described, and the performances are given, in terms of self-noise, sensitivity, and passband. The way to calibrate these infrasound sensors and infrasound stations on field is also reported. An in situ calibration method using additional reference sensors to an infrasound station has been developed to recover the overall response of the station element including the wind noise reducing system.

2.1 Background

An infrasound sensor can be defined as an equipment sensitive to infrasonic pressure fluctuations and delivering an electric signal accordingly. It is associated with a digitizer (acquisition unit), and most of the time to a wind noise reducer (Marty 2019; Raspet et al. 2019), to complete the measuring chain. Recently, some infrasound sensors can be found in digital versions. This means that the analog-to-digital conversion is realized inside the sensor itself. The digitizer is then embedded and not externally connected to the sensor using cables. This chapter is dedicated to infrasound sensors themselves, excluding digitizers (even if embedded inside the sensor) and wind noise reducing systems (Raspet et al. 2019).

G. Nief (✉)
CEA, DAM, DIF, F-91297 Arpajon, France
e-mail: guillaume.nief@cea.fr

C. Talmadge
National Center for Physical Acoustics, University of Mississippi, Oxford, MS, USA

J. Rothman
Geophysical Institute, University of Alaska Fairbanks, Fairbanks, AK, USA

T. Gabrielson
Pennsylvania State University, State Colleg, PA, USA

A. Le Pichon et al. (eds.), *Infrasound Monitoring for Atmospheric Studies*,
https://doi.org/10.1007/978-3-319-75140-5_2

More precisely, the sensor is composed of a mechanical device which is sensitive to pressure changes. This device is associated with a transducer. Pressure fluctuations induce motions and constraints on the sensitive mechanics, and the transducer converts them into a dynamic voltage. Various transducers and mechanics have been used in the past decades, and the following sections describe some of them which are, to our knowledge, field operational.

The design of infrasound sensors is of course driven by the characteristics of the infrasound atmospheric pressure changes that geophysicists want to record and analyze. A good sensor should have a negligible influence on the recorded signal; this can be achieved by choosing the right transducer, sensitive mechanics, and signal conditioning association. Hereafter, major constraints on sensor designing are examined.

2.1.1 Infrasonic Background Noise and Implication on Sensor's Self-noise

The ideal infrasound sensor should be able to measure any infrasonic pressure variations, even at low amplitudes. The knowledge of the lowest infrasound background noise in the Earth's atmosphere is thus an important input to sensor design in terms of sensor self-noise. Because of the signal-to-noise ratio influence, it is generally considered that for geophysics applications, the self-noise of sensors has to be 10–30 dB lower than the infrasonic minimum noise.

Taking advantage of data from the International Monitoring Network (IMS) Marty (2019), Bowman et al. (2007) have proposed a model for infrasonic minimum background noise. Median and high noise models have also been derived from the dataset. This low noise model, expressed in PSD in the 0.02–8 Hz frequency band, is a good reference for sensor designing and testing (Fig. 2.1).

Even though the LNM is barely reached in a realistic field environment, comparison of a generic sensor self-noise PSD to the LNM gives a good idea of its resolution capabilities. As the LNM has roughly a −20 dB/decade slope, the resolution needed is frequency dependent. It will have to be less than 0.1 mPa rms for the higher frequency part. This means that the sensor has to be very quiet, to a level that is not easy to achieve.

The transducer self-noise is often constraining the overall self-noise of the sensor. It has to be chosen carefully or specially designed. Signal conditioning analog electronics also have to be chosen as noiseless as possible. In particular, one must pay attention to resistor thermal noise, amplifier voltage and current low-frequency noises, and input impedances. Finally, increasing sensitivity of the pressure-sensitive mechanics in some way helps to minimize the overall self-noise of the sensor.

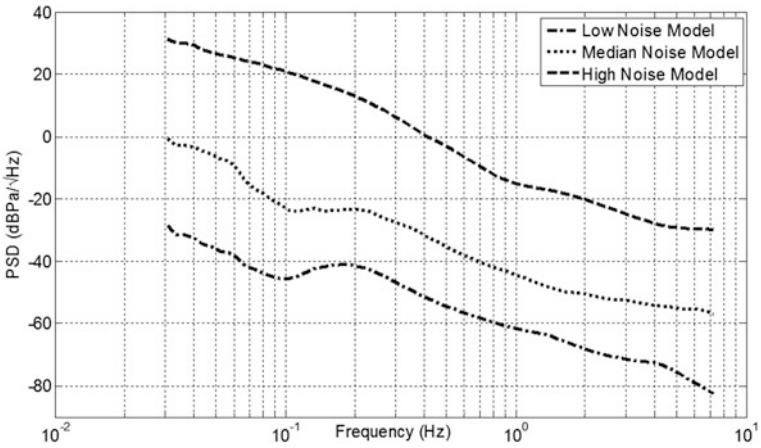

Fig. 2.1 Infrasound low, median, and high noise model from (Bowman et al. 2007)

2.1.2 *Pressure Variation Range and Implication on Sensor's Dynamic Range*

The ideal infrasound sensor should also be able to measure any infrasonic pressure variations at high amplitude. Excluding measuring pressure variations close to the sources of infrasound, which can involve very strong pressure signals, and different types of pressure sensors, the peak-to-peak amplitude will generally not exceed 1000 Pa for typical infrasound events. At a fixed location, atmospheric pressure changes very barely reach 100 hPa peak-to-peak.

This means that the ratio of minimum to maximum pressure variations on the full infrasound frequency band is of order 10^8. The dynamic range of the sensor is thus ideally also of that order. This is of course very hard to achieve when designing the various parts of the sensor (electronics, mechanics, and transducer), regardless of the dynamic range of the digitizer by itself.

2.1.3 *Environmental Constraints*

Infrasound stations are currently installed all over the earth, and the network comprising the IMS of the Comprehensive Nuclear-Test-Ban Treaty is a good example. Various altitudes of the stations imply static atmospheric pressures ranging from 1 atmosphere at sea level to 0.6 atmosphere at about 4000 m. The ideal infrasound sensor, which is a pressure sensor, has to behave similarly at these two extremes. In practice, on site, during installation most sensors would need some adjustments to the static pressure level. For example, a mechanical adjustment can

be needed for adapting the mechanics to a new equilibrium position, or a vent has to be opened to equalize outside pressure and inner volume pressure.

The temperature can also vary a lot, between various locations of stations and at a particular location with the seasons. These variations can range from −40 to 60 °C. The sensors have to be designed to minimize the effects of the temperature variations on its behavior. For example, the material of the mechanics can be chosen to have minimal thermal dilatation coefficient, and the sensors can be buried in surface vaults with a good thermal inertia. At the minimum, the variations of the sensitivity of sensors with static pressure and temperature would have to be known by the manufacturers. Those variations would also have to be homogeneous within the series of the same types of sensors. Nevertheless, the effects of temperature and static pressure are difficult to measure and require lab hardware like pressure chambers and thermal enclosures.

Sensors can be installed in places with very different climates: dry and hot desert, polar region, or tropical area. They are also installed for very long periods of time, up to 20 years or even more. Compared to seismic sensors, the infrasound sensor-sensitive mechanics/transducer is in direct contact with outside air. This means that it has to be as robust as possible to corrosion, dust, and condensation.

Finally, infrasound station sites are often very remote. A reliable electrical power source can be difficult to install in such locations. This means that the powering electronics of the sensor may need robustness and dedicated filtering.

2.2 Field-Tested Sensors Descriptions

The next paragraphs explain the principles of operation of some infrasound sensors which are field operational.

2.2.1 Absolute Sensors Using Sealed Bellows as Pressure-Sensitive Element

To measure absolute pressure variations, a pressure reference is needed. This can be achieved by sealing a bellows under a relative vacuum (Fig. 2.2). The vacuum inside the bellows provides the reference (Haak and De Wilde 1996). Once sealed, the atmospheric pressure variations deflect the bellows. Its upper surface height changes according to these pressure variations. The inner vacuum allows a minimal pressure reference change with varying temperature. The bellows are positioned inside a measurement cavity which is connected to external pressure through inlets.

Fig. 2.2 Picture of two types of vacuum-sealed bellows

2.2.1.1 Bellows Mechanical Behavior

As the upper surface of the bellows behaves as a piston, a one degree of freedom movement is assumed. Equation (1) governing the movement of the bellows under a pressure change can be written as a classical mass/spring/dashpot system (Fig. 2.3).

$$M(\Delta\ddot{z}) + R(\Delta\dot{z}) + K\Delta z = S\Delta P_c, \tag{1}$$

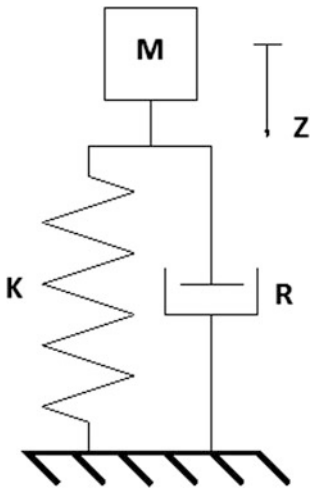

Fig. 2.3 Classical mass/spring/dashpot model of bellows

where M is the mobile mass mostly due to the upper part of the bellows, K its overall stiffness, S its effective area on which the pressure is acting, R is the fluid friction coefficient, ΔP_c is the pressure variation in the measurement cavity, and Δz the upper surface position (relative to the equilibrium position).

In practice, the transducer (or at least a part of the transducer, see Sect. 2.1.3) is fixed on the upper surface of the bellows, its mass is included in M, the total moving mass.

In the frequency domain, the transfer function between the input ΔP and the output Δz can be written as a first-order resonant system

$$\frac{\Delta z}{\Delta P_c} = \frac{S}{K}\left(\frac{1}{1+2\varepsilon\frac{j\omega}{\omega_0}+\left(\frac{j\omega}{\omega_0}\right)^2}\right), \tag{2}$$

where $\omega_0 = \sqrt{\frac{K}{M}}$, $\varepsilon = \frac{R}{2\sqrt{KM}}$ and ω is the angular frequency.

This equation is interesting in terms of sensor design. In order to have a stronger movement of the bellows with a fixed pressure variation, the ratio $\frac{S}{K}$ is the driving parameter. This can be achieved by choosing a more compliant bellow (decreasing K) or increasing its diameter (increasing S).

The frequency response of the bellows is driven by the natural frequency ω_0. This response is flat in frequency and phase from static pressure to the upper of the infrasound range only if ω_0 is out of this frequency range. This can be achieved by increasing the ratio $\sqrt{\frac{K}{M}}$ using a stiffer bellow (increasing K) or a lighter bellow (decreasing M). Moreover, the decreasing of the mobile mass decreases the ground motion sensitivity of the bellows. A compromise must be found between a compliant and large bellow for increasing the sensitivity and a stiff and light bellows for increasing the natural frequency.

Considering that the infrasound frequencies are below the resonant frequencies, the sensitivity of the bellows in $\frac{m}{Pa}$ can be reduced to the $\frac{S}{K}$ parameter. In other words, this means that the bellows can be modeled as a pressure-driven spring.

2.2.1.2 Measurement Cavity and Inlets Acoustical Behavior

The bellows are placed in an air cavity, which is connected to the atmosphere through inlets. The characteristics of these acoustic elements have an influence on the overall response of the sensor.

In practice, the dimensions of the measurement cavity and inlets are very small compared to the wavelength of the infrasound waves. This means that they can be modeled as discrete acoustical elements using lumped parameters. The cavity is equivalent to an acoustic compliance with losses and the inlet to an acoustic loss

and acoustic mass. The compliance C_c of the measurement cavity can be expressed as

$$C_c = \frac{V_c}{\gamma P_c}, \tag{3}$$

where V_c is the cavity volume, γ is the specific heat ratio of air, and P_c is the absolute pressure inside the cavity. The value of γ depends on the thermal regime of the heat exchange inside the cavity. The adiabatic regime corresponds to higher frequency behavior, where $\gamma = 1.4$ for air. This case corresponds to classical acoustic wave propagation. For lower frequencies, the regime is isothermal, and $\gamma = 1$. In the intermediate frequency domain, the thermal regime is neither adiabatic nor isothermal and γ is a complex, value varying with frequency between 1.4 and 1 in amplitude.

The variations of amplitude and phase of γ depend on the ratio $\frac{V_c}{S_c}$ of the volume V_c to the inner surface S_c of the cavity (see Mentink and Evers 2011). This ratio defines a characteristic length L_c to be compared to the thermal penetration depth $\delta = \sqrt{\frac{2a}{\omega}}$, where a is the thermal diffusivity of air. If $L_c \gg \delta$ regime is adiabatic and $L_c \ll \delta$ corresponds to the isothermal regime.

For the complex shapes of practical cavities, the thermal conduction regime transition is very difficult to compute. Setting up experiments to measure this effect is not easy either. The transition between the two regimes often occurs in the infrasound frequency band and can span over decades. Nevertheless, the effects are often weak and the objective is to minimize them in order to keep the response as flat as possible over the infrasound band.

The inlets can be modeled by a cylinder with an acoustic loss R_i and acoustic mass M_i

$$R_i = \frac{8\mu l_i}{2\pi r_i^4} \tag{4a}$$

and

$$M_i = \frac{\rho l_i}{2\pi r_i^2}, \tag{4b}$$

where μ is the viscosity coefficient of air, ρ its density, l_i the length of the inlet and r_i its radius. R_i is the classical description for a cylindrical capillary.

It is convenient to describe acoustic and mechanics systems using an electrical circuit analogy. The analogy is based on the similarity of pressure to voltage and volume flow to current. An acoustic impedance, the ratio of pressure to volume flow (in $Pa\,s/m^3$), is equivalent to an electrical impedance, the ratio of voltage to current (in Ω). The following table shows the various parameters of the infrasound sensor and their analogy in electric components (Table 2.1).

Table 2.1 Electroacoustic model of the various part of an infrasound sensor

Bellows			Cavity		Inlet	
Compliance	Mass	Dashpot	Acoustic compliance	Acoustic losses	Acoustic mass	Acoustic losses
$\frac{1}{K}$	M	R	C_c	R_c	M_i	R_i
Electric analog						
Capacitor	Coil	Resistor	Capacitor	Resistor	Coil	Resistor
$C_b = \frac{S^2}{K}$	$L_b = \frac{M}{S^2}$	$R_b = \frac{R}{S^2}$	C_c	R_c	$L_i = M_i$	R_i

The equivalent acoustic impedances Z_b, Z_c, and Z_i of the bellows, cavity and inlet, respectively, can be written as (see Alcoverro and Le Pichon 2005)

$$Z_b = R_b + j\omega L_b + \frac{1}{j\omega C_b}, \tag{5a}$$

$$Z_c = R_c + \frac{1}{j\omega C_c} \tag{5b}$$

and

$$Z_i = R_i + j\omega L_i. \tag{5c}$$

The acoustic model of the sensor is shown in Fig. 2.4.

According to the above model, the transfer function between the external pressure P_e and the measurement cavity pressure P_c

$$\frac{P_c}{P_e} = \frac{\left(Z_b^{-1} + Z_c^{-1}\right)^{-1}}{Z_i + \left(Z_b^{-1} + Z_c^{-1}\right)^{-1}}. \tag{6}$$

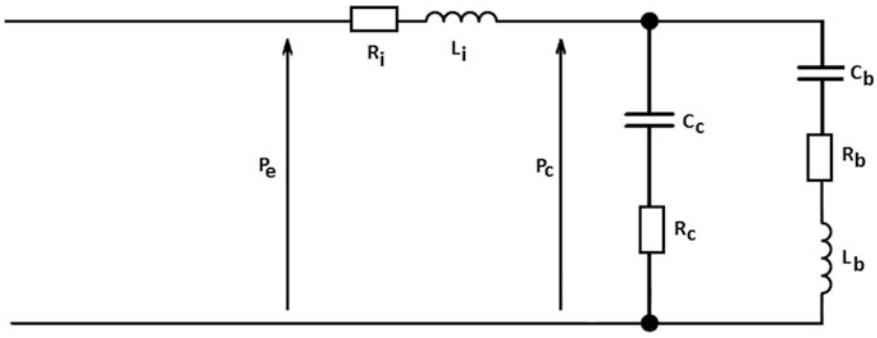

Fig. 2.4 Acoustic model of the sensor

Considering the low frequencies (infrasound frequency band), the transfer function can be simplified by taking into account the compliance of the bellow, the acoustic compliance of the measurement cavity and the resistive part of the inlet as

$$\frac{P_c}{P_e} = \frac{1}{1 + j\omega(C_b + C_c)R_i}. \tag{7}$$

This represents a low-pass filter. The cutoff frequency can be increased by decreasing the measurement cavity volume, or increasing the inlet radius.

The inlets are typically connected to a wind noise reducing system in the field environment. This wind noise reduction device can be composed of pipes with varying lengths: from a few meters to a few tens of meters (see Sect. 2.3.3). Of course, the pipes have an acoustic response which can influence the overall response of an infrasound element. The pipes can be modeled using classical acoustic transmission lines with losses. The acoustic impedances of the wind noise reducing system are described in Alcoverro and Le Pichon (2005).

2.2.1.3 Transducers

The displacement of the upper surface of the bellows, proportional to the pressure variation as presented above, has to be converted into an analog voltage by a motion transducer. Depending on the desired performance, various types of transducers can be used. Two types of transducers are examined here, as they are the ones chosen for two field operational sensors:

- An active displacement transducer: the linear variable differential transformer (LVDT);
- A passive velocity transducer: the magnet and coil transducer.

LVDT

This type of device is a well-known device for measuring displacement. A ferritic core moves in an electrical transformer system composed of three coils (Fig. 2.5).

The central, or primary, coil is driven by an alternating current. A voltage is induced in the two lateral coils through the mutual inductances. Whenever the ferritic core moves inside this transformer, the mutual inductances change between the primary and the secondary coils, and the voltage in the secondary coils changes accordingly. The amplitude of the output voltage is proportional to the displacement of the ferritic core (Fig. 2.6).

In the case of infrasound sensors, the ferritic core is attached to the upper part of the bellows. The voltage measurement of the bellows displacement is, thus, directly proportional to the pressure variations.

The main advantage of this type of transducer is its robustness to the environment, because the coils can be completely sealed. There is also no contact between

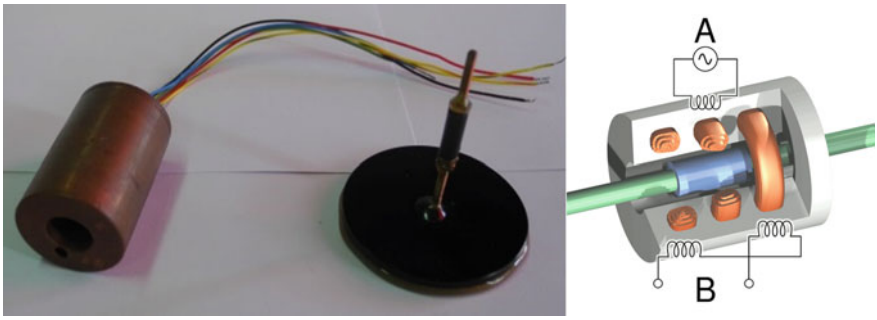

Fig. 2.5 Picture and schematic view of a LVDT transducer

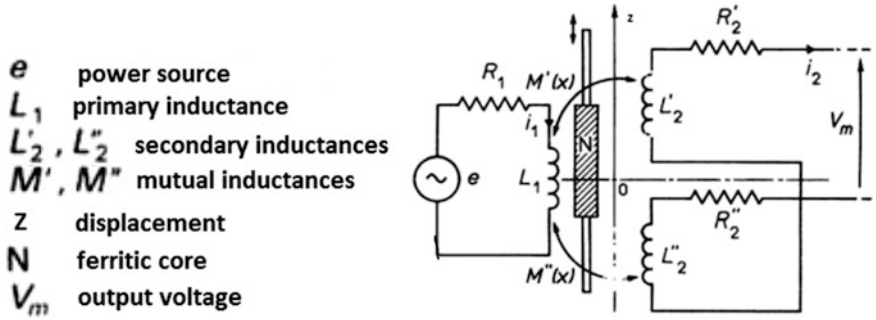

Fig. 2.6 Principle of operation of the LVDT transducer (adapted from Parmantier and Kratz 2009)

the core and the coils. The transducer is flat for frequencies down to static displacement and has a wide dynamic range. Its main drawback is a slightly higher self-noise level at high frequencies in the infrasound band. This device is used in MB2000/MB2005 sensors, designed by CEA (Fig. 2.7).

The output of the sensor is flat down to static pressure, but it is electronically high pass filtered (100 s of cutoff period) in order to avoid saturation of the output in low frequency. A low-pass filter is applied to the analog signal with adjustable cutoff frequency. The sensor may also provide outputs with no high-pass filter, with a decreased sensitivity, in order to monitor static pressure. The nominal sensitivity of the MB2005 is 20 mV/Pa for the filtered output and 1 mV/Pa for the static pressure output.

The following figures give the frequency response in V/Pa of the filtered output and the intrinsic noise of this type of sensor (Figs 2.8 and 2.9).

This type of sensor has been widely used since 2000, especially in the infrasound stations of the IMS.

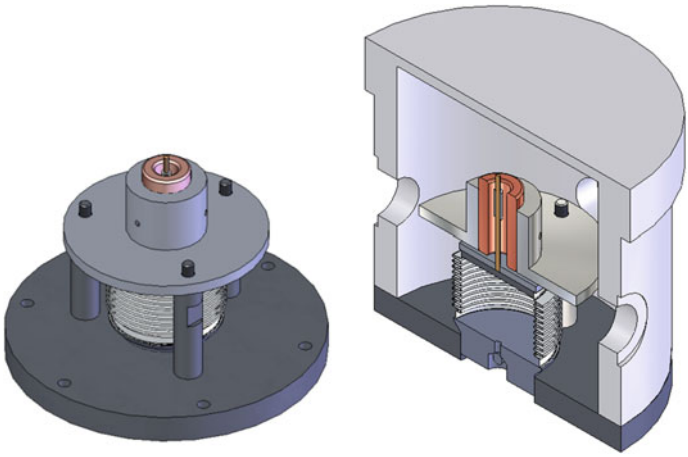

Fig. 2.7 Schematic view of MB2005 sensor

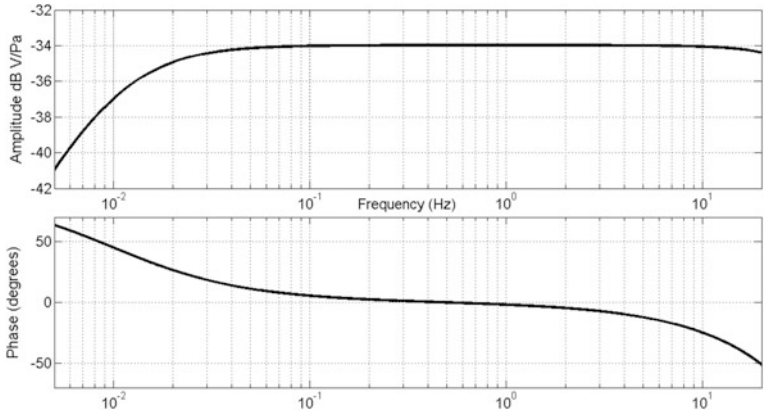

Fig. 2.8 Frequency response of MB2005 sensor

Magnet and coil transducer

This type of velocity transducer is widely used in seismometers, and geophones. It is composed of a coil moving in permanent magnetic field created by a magnet (Fig. 2.10).

This movement creates an induced voltage in the coil proportional to its velocity, according to the following equation:

$$\Delta u = Bl(\Delta \dot{z}), \tag{8}$$

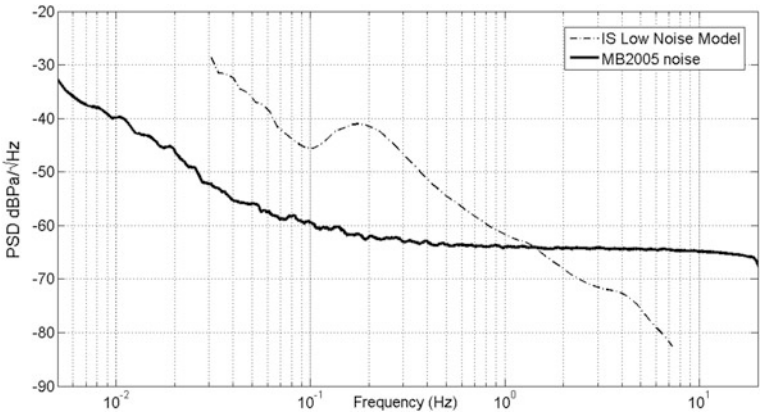

Fig. 2.9 Self-noise of MB2005 sensor

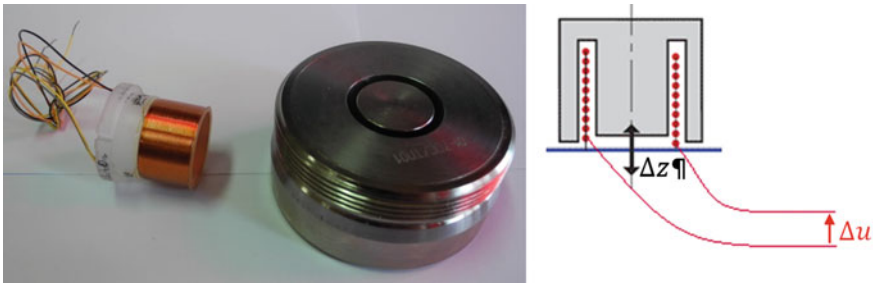

Fig. 2.10 Picture and schematic view of a magnet and coil transducer

where Δu is the induced voltage, B the magnetic field intensity (in Tesla), l the total length of the coil wire, and $(\Delta \dot{z})$ the velocity of the coil in the axis of the system.

When used in an infrasound sensor, the coil is attached to the upper surface of the bellows and the magnet has a fixed position. Combining Eqs. (2) and (8), gives the following transfer function

$$\frac{\Delta u}{j\omega \Delta P_c} = \frac{SBl}{K}\left(\frac{1}{1+2\varepsilon_1 \frac{j\omega}{\omega_0}+\left(\frac{j\omega}{\omega_0}\right)^2}\right). \tag{9}$$

Equation (9) shows that the output analog voltage is proportional to $(j\omega \Delta P_c)$, which corresponds to pressure derivative. For frequencies sufficiently lower than the resonant frequency, the sensitivity before signal conditioning is $\frac{SBl}{K}$ in $\frac{V}{Pa/s}$.

This type of transducer has a very low self-noise and has a flat response down to zero frequency versus pressure derivative. It is electrically passive, so the power

consumption of the sensor is only due to the signal conditioning electronics, and can thus be very low. MB3 sensor, designed by CEA and marketed by *Seismowave* company, uses this type of transducer (Fig. 2.11).

The output of the sensor is integrated to pressure, using an electronic circuit with a cutoff period of 100 s. The high frequencies are low-pass filtered. The sensor also provides the output proportional to the pressure derivative. The nominal sensitivity of the integrated output is 20 mV/Pa in the passband. Next figures present the integrated output frequency response in V/Pa and the measured self-noise (Figs 2.12 and 2.13).

This type of sensor is planned to be installed in IMS stations for their remote calibration capability (see Sect. 2.3.2).

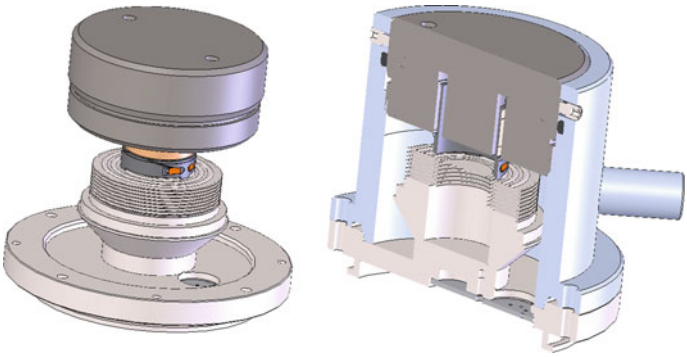

Fig. 2.11 Schematic view of MB3 sensor

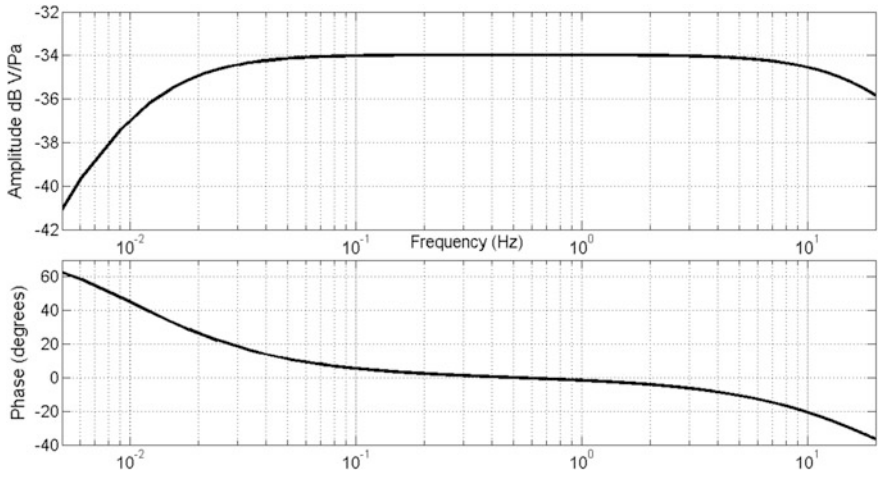

Fig. 2.12 Frequency response of MB3 sensor

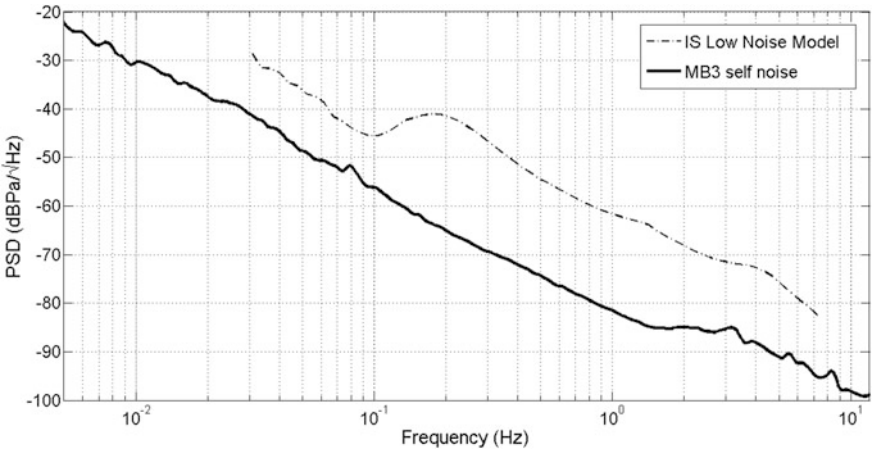

Fig. 2.13 Self-noise of MB3 sensor

2.2.2 Piezoelectric Infrasound Sensor

The National Center for Physical Acoustics (NCPA) has developed a new class of atmospheric infrasound sensor configurable for broadband outdoor measurements. This technology has been transferred to Hyperion Technology Group, Inc., who produce commercially available versions of these sensors.

The standard version of the sensor is flat within 3 dB from 0.03 to 150 Hz, with a nominal maximum transducible pressure of 200 Pa peak-to-peak. Other versions include an ultra-broadband measurement for calibration systems (flat within 3 dB from 0.001 to 150 Hz), a blast-wave version for very high level sounds (up to at least 110 kPa peak-to-peak) for blast-wave characterizations, and a compact low-power ("USArray") version suitable for installing in vaults.

A seismically decoupled sensor has been developed. Two versions of this have been deployed, the NCPA SD sensor, which cancels the seismic signal passively, and the Hyperion Model 5000, which uses a custom summing/differencing preamplifier developed at the NCPA, and provides separate pressure and acceleration. In addition to a more exact cancelation of the seismic signal, this has about a 3 dB lower electronic noise floor. The nominal pressure sensitivity of this sensor is 140 mV/Pa, and the nominal sensitivity (in the seismic channel) to acceleration is 1460 mV/(m/s^2). The sensitivity to acceleration in the pressure channel is less than 10 mV/(m/s^2).

The sensor can be configured with a "high-frequency cap" or to accept porous hoses, both of which are to mitigate wind noise effects. Both of these versions are ruggedized and water resistant, allowing the sensor to be placed directly in an external environment. The high-frequency 3 dB "knee-point" is associated with the Helmholtz resonance of the sensor. A non-water-resistant version of the sensor top has been developed that offers a flat frequency response to ~1000 Hz.

The physical mechanism for infrasound transduction is provided by commercially available piezoelectric-ceramic ("piezoceramic") transducers. Current NCPA designs utilize a 35 mm diameter sensing element with a 47 nF capacitance. In lump-sum models, these sensors can be considered as purely capacitive with a charge source that is connected to a high input-impedance instrumentation amplifier.

The configuration of sensing elements used on an NCPA sensor plate is shown in Fig. 2.14. Here, two elements are oriented upwards (positive polarity) and two elements oriented downwards (negative polarity). Both elements in each orientation are electrically in parallel. And all four elements share a common ground. Note that the sensing elements are mounted over a sealed back volume. This configuration reduces direct sensitivity to temperature (pyroelectric effect) as well as the effects of temperature gradients across the sensing plate.

This configuration results electrically in a differential signal. This signal is conditioned and amplitude by a high-impedance preamplifier. This preamp consists of an electrical network (which controls the band-start properties of the amplifier) in series with an INA 116 instrumentation amplifier, which has ±15 V rail voltages.

The overall sensitivity of the infrasound sensor is determined by the pressure sensitivity of the individual sensing elements (typically 2.8–3.0 mV/Pa) and the net gain of the instrumentation amplifier. Capacitors can be placed in parallel to the sensing elements, to provide a voltage divider network, when a lower pressure

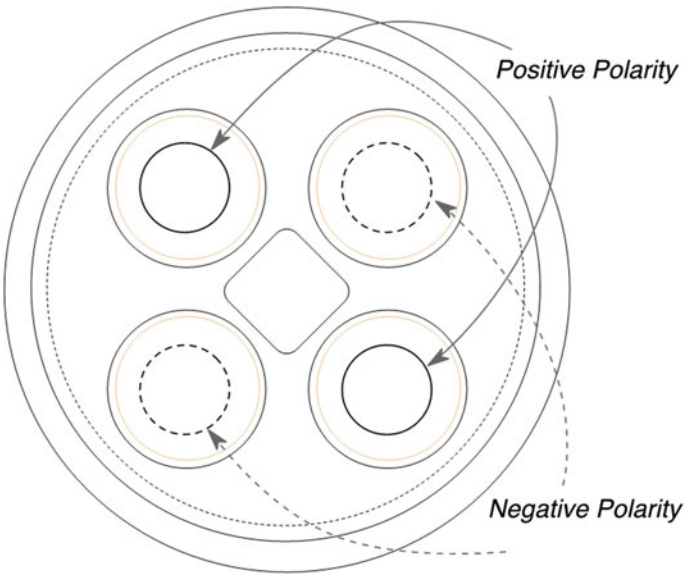

Fig. 2.14 Illustration of the NCPA sensor plate configuration showing the arrangement of the four sensing elements

sensitivity than 2.8–3.0 mV/Pa is needed. The nominal gain of the instrumentation amplifier is 50, giving a nominal gain for the NCPA sensors of 0.150 V/Pa.

It should be noted that there is a voltage drop from the internal diodes on the INA 116 that provide input overvoltage protection, so the actual range of output voltages from the instrumentation amplifier is only ±14.2 V for a ±15 V power supply. For the NCPA sensors, with a gain of 50, the actual transducible pressure range is about ±14.2 V/(0.150 V/Pa) ≈±95 Pa. Note that the Hyperion version of these sensors "tweak" the gain resistors on the instrumentation amplifier to recover so that the sensitivity is about 140 mV/Pa, yielding a maximum transducible pressure range of ~±100 Pa.

A simple version of the network would be resistors in parallel to the sensing elements. This network results in a single zero at $f = 0$ and a pole at $if_0 = 1/(2\pi RC)$. For this circuit, the sensitivity function is

$$S(f) = \frac{S_0 f}{f - if_0}, \quad |S(f)| = \frac{S_0 f}{\sqrt{f^2 + f_0^2}}, \quad \arg(S(f)) = \text{atan2}(f_0, f). \tag{10}$$

The USArray sensor has this electronic configuration, with R = 500 MΩ and S_0 = 20 mV/Pa. Using C = 47 nF, this gives $f_0 = 6.77$ mHz.

All of the other NCPA sensors use an electronic circuit that produces a 3-pole/3-zero sensitivity function, which we represent as

$$S(f) = S_0 \frac{f}{f - if_0} \bullet \frac{f}{f - if_1} \bullet \frac{f}{f - if_2}. \tag{11}$$

The transfer functions for these various sensors are shown in Fig. 2.15. The corresponding pole values and nominal sensitivities are shown in Table 2.2. Note the poles are given in frequency space and that the relationship between the frequency-space parameters in Table 2.2 and the corresponding Laplacian-space poles $s_n = -2\pi f_n$.

The typical sensor self-noise for the various NCPA and Hyperion sensors is shown in Fig. 2.16, below.

2.2.3 Chaparral MEMs-Based Sensors

The Chaparral M60 (see Fig. 2.17) is a new high performance, miniaturized, infrasound sensor based on the MEMs technology developed by Chaparral Physics to enable mobile infrasound measurements that would otherwise be impractical. The new device is slightly larger than an ice hockey puck, weighs 200 g, and consumes less than 150 mW. The sensitivity is 0.4 V/Pa and self-noise at 1 Hz is less than 0.63 μPa^2/Hz. The characteristics were verified using a calibrator traceable to the Sandia National Laboratories calibration chamber. Applications for this

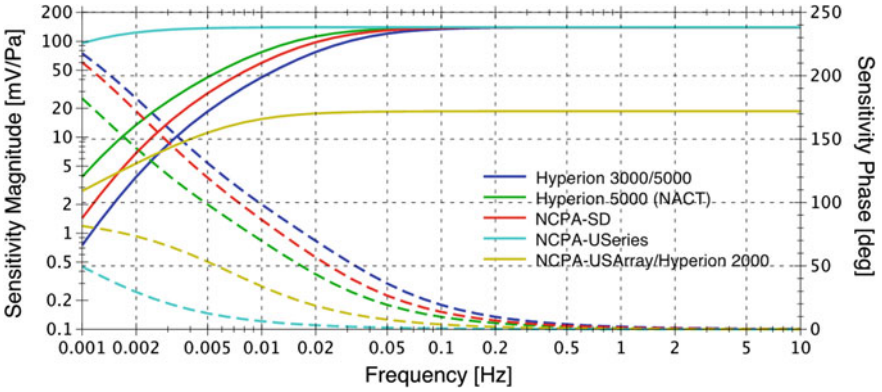

Fig. 2.15 Transfer functions for the various NCPA/Hyperion sensors. (Dashed lines show the phase responses.)

Table 2.2 Nominal sensitivities and poles for the various NCPA/Hyperion sensor configurations. Note that each pole has a matching zero at $f = 0$

Sensor	S0 (mV/Pa)	F_0 (mHz)	f_1 (mHz)	f_2 (mHz)
NCPA SD	150	1.38	2.67	20.0
Hyperion	140	1.49	3.39	29.5
Hyperion NACT	140	0.743	1.69	14.8
NCPA USeries	150	0.0108	0.0310	1.07
USArray	20	0.677	NA	NA

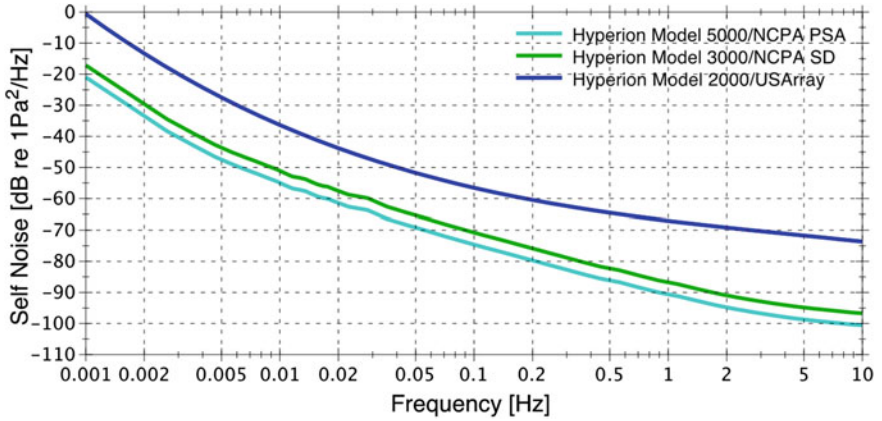

Fig. 2.16 Typical sensor self-noises for various NCPA and Hyperion sensors. Note that the actual noise floor depends on the front-end gain of the preamplifier, which can be adjusted from 1 to 200 (corresponding to sensitivities of approximately 3–600 mV/Pa). Higher front-end gains correspond to lower effective self-noises, when expressed in Pa^2/Hz

Fig. 2.17 Chaparral Model M60 infrasound sensor

sensor include man-portable arrays, mobile installations, and unmanned aerial system-based measurements.

The characteristics of this sensor are similar to the Chaparral Model 25 and this performance has been confirmed in field testing. The sensor consumes less than 150 mW of power and has a flat frequency response (< 3 dB) from 0.03 to 245 Hz (Fig. 2.18, left). Sensor self-noise PSD is about −68 dB re 1 Pa^2/Hz at 1 Hz (Fig. 2.18, right). Between 0.05 and 2 Hz, the dynamic range of the standard sensor is about 91 dB. A higher performance model has just entered production; featuring a 112 dB dynamic range at 1 Hz and a 6 dB reduction in self noise at frequencies above 1 Hz.

The microphone sensitivity is 400 mV/Pa, with the full-scale peak-to-peak pressure being 55 Pa. Lower sensitivity models, the M60 VX (30 mV/Pa) and

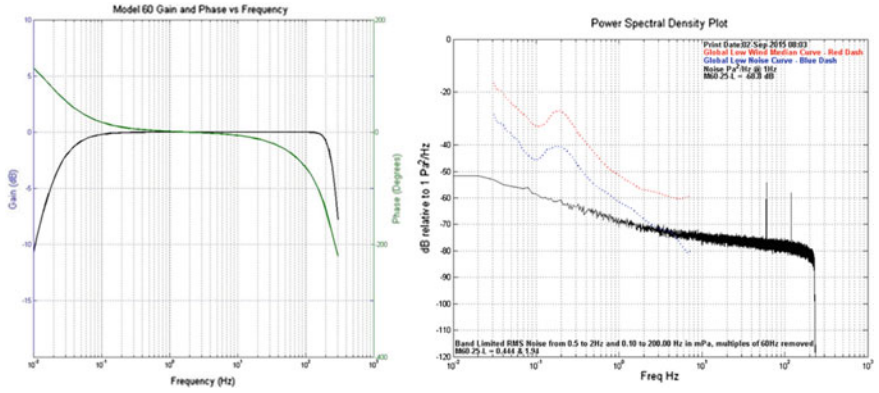

Fig. 2.18 (Left) Transfer function for the M60 sensor. (Right) Measured self-noise for the standard gain M60 sensor

M60 UAHP (9 mV/Pa) are also available, which, respectively, have full-scale peak-to-peak pressures of 720 Pa and 2000 Pa. The sensitivity of individual sensors is within 5% of the nominal value, with the variation in temperature less than 5% from −40 to ±60°C, and less than 0.5% from 10 to 60°C. The sensitivity to acceleration of the standard sensor is about 0.04 Pa/(m/s^2).

Environmental Testing

Sensitivity to vibration was measured by placing the test sensor on an ETS L315 M shaker. The acceleration amplitude was set to 4.9 m/s^2, and measurements were obtained between 10 and 50 Hz. The results of these measurements are shown in Fig. 2.19. A digital filter was applied to eliminate interference generated by the power amplifier that drives the table. The measured sensitivity to acceleration was found to be 0.0408 Pa/(m/s^2). Little variability in the sensitivity to acceleration was observed over the 10–50 Hz range.

Temperature stability was measured for 25 sensors using a Test Equity 1000 series temperature chamber (Fig. 2.20). A speaker, mounted inside a sealed enclosure, was driven by a Wavetek Model 29 DDS function generator at 10 Hz to serve as a common infrasound source for both microphones. Temperatures were allowed to stabilize for 1 h between steps. The temperature chamber was turned off for a short time while measurements were being made to eliminate noise caused by air circulating in the chamber. The measured gain stability is outstanding between −40 and 20 °C. The sensitivity varied by less than 4% over the temperature range −40 to 60 °C.

2.3 On Site Calibration of Infrasound Sensors and Stations

2.3.1 Introduction

Calibration of infrasound sensors and stations is of major importance for accurately estimating the parameters of infrasound events. The accurate absolute amplitude of

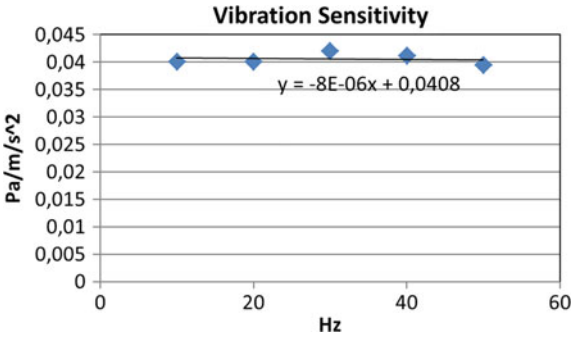

Fig. 2.19 Measured sensitivity to acceleration of the M60 sensor

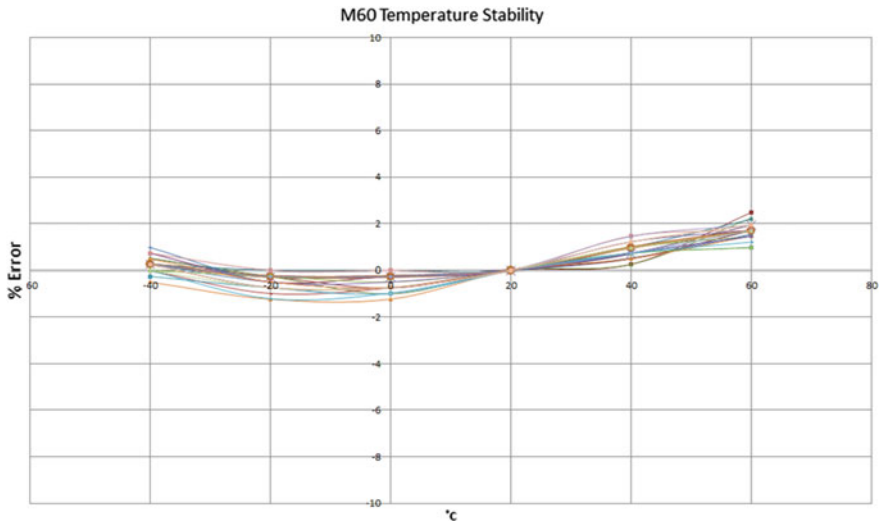

Fig. 2.20 Variability of the pressure sensitivity of the M60 sensor from −40 to 60°C

the pressure signal is needed to make quantitative measurements. The complex frequency response shape (amplitude and phase) must be known for infrasound signal processing. A single infrasound station is generally composed of a few elements (from 4 to 10). Each of them is composed of a sensor connected to a wind noise reducing system. Possible discrepancies in the responses of the different elements of the station can lead to bias in the estimations of the parameters of a coherent infrasound wavefront propagating over the station.

The generation of calibration infrasound signals with controlled amplitude is not an easy task. In laboratories, various devices have been developed to produce calibrated pressure changes, generated by volume changes of sealed cavity to which the sensor under test is connected. But these devices cannot easily be transported to the field. Once installed, the sensor would need to be removed from the measuring chain, taken to the lab, tested, and installed again at the station.

Thereafter, we describe techniques that can be applied on field to calibrate the infrasound sensor itself or a full station element (sensor and wind noise reducing system) without dismantling the sensor from the measuring chain.

2.3.2 Remote Calibration of Sensors Using a Magnet and Coil Transducer

Magnet and coil devices are already widely used to perform calibration of seismometers. The principle is that a magnet and coil can be used as an actuator, as in loudspeakers for example. The coil, attached to the moving part of the sensor, is

immersed in a permanent magnetic field created by the magnet. Whenever a calibrated electrical current flows through the coil, a calibrated force (the Laplace force) is created in the main axis of the system. This force is proportional to the intensity of the current, according to the equation

$$F = Bl_c i_c, \tag{12}$$

where F is the force created, i_c the intensity of the calibrated electrical current, B the intensity of the magnetic field, and l_c the total length of the calibration coil wire. This force creates a known acceleration movement of the moving part of the sensor.

In practice, most digitizers dedicated to geophysics have a calibration output designed for seismometers that use this technique. This means that many digitizers include a precise electric voltage signal generator dedicated to sensor calibration. These signals are available to be sent to the calibration coil of the sensors connected to the digitizer.

This idea is used in the MB3 sensor for being able to be remotely calibrated. Taking advantage of the transducer of the sensor, a second coil is wrapped under the measurement coil. The magnet is the same for both transducer and calibration coils. The force created on the bellows directly simulates a calibrated pressure acting on the bellows.

The calibration circuit inside the sensor can be adjusted to a fixed calibration constant (in equivalent $\frac{Pa}{V}$) using a simple adjustable resistor R_c in series with the calibration coil. The calibration-simulated pressure P_c is expressed by

$$P_c = \frac{Bl_c i_c}{S} = \frac{Bl_c u_c}{S.(R_c + R_{coil})}, \tag{13}$$

where S is the effective area of the bellows, R_{coil} the value of electrical resistance of the calibration coil, R_c the adjustable resistor value, and u_c the calibration voltage from the digitizer calibration output.

The calibration circuit is left open whenever the sensor is running with no calibration process engaged. The calibration coil has thus no effect during nominal operation of the sensor. Even though the calibration coil moves together with the measurement coil inside the magnetic field, the current flowing through the calibration coil is null in an open circuit.

The transfer function between the simulated pressure and the calibration voltage is flat in the infrasound band. In higher frequencies, electrical transformer behavior between the measurement and calibration coils might occur. This has to be avoided when designing the coils.

It is then possible to simulate any type of pressure signal $P_c(t)$ in order to calibrate the sensor. An example is given on the figure below. A broadband pressure signal with a PSD of a −20 dB/decade slope can be sent to the sensor. This type of signal is interesting because it can be adjusted to overcome the high noise model. This allows having a sufficient signal-to-noise ratio over the entire infrasound band during calibration of a sensor installed at a station (Fig. 2.21).

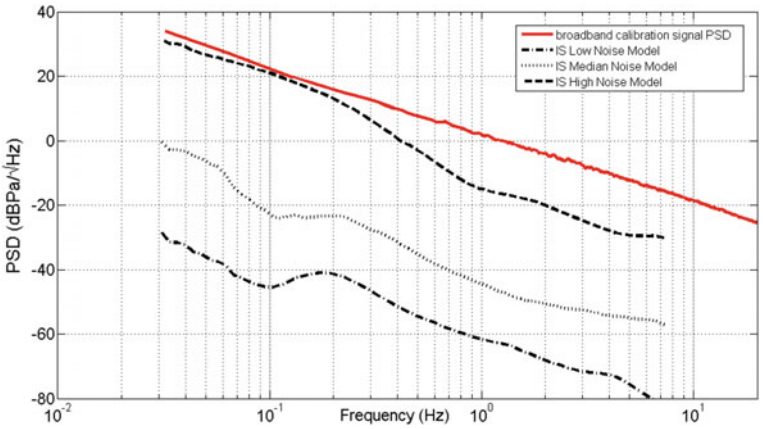

Fig. 2.21 Broadband calibration signal compared to high-noise model

The computed response curve to this known excitation is presented against the nominal response of the sensor (Fig. 2.22).

The figure shows high accuracy between measured and theoretical response of an MB3 sensor. Of course, the other type of calibration signals like sine waves with a varying frequency can also be used to check the frequency response of the sensor.

It is worth noticing here that the simulated pressure is injected inside the measurement cavity of the sensor. As a consequence, this method gives the response of the moving part of the sensor (i.e., the bellows), of the transducer and of the signal conditioning electronics (gains and filters). The acoustical part (inlets and cavity)

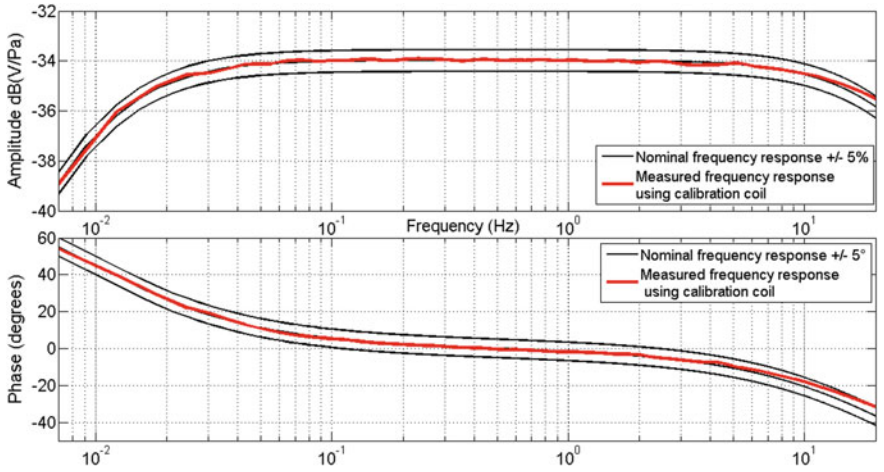

Fig. 2.22 Measured frequency response of MB3 sensor using calibration coil compared to nominal response

and wind noise reducing system cannot be tested by this technique. Next paragraph describes a method using one or more reference sensors, allowing for the computation of the overall transfer function of an infrasound sensor including the wind noise reducing system.

2.3.3 In Situ Calibration of the Whole Infrasound Station Element

Successful detection and identification of events recorded by an infrasound array depend on a complete understanding of the performance of each element of that array. Characterization of the microbarometer is important; however, all other components—the wind noise reduction system, the digitizer, and the telemetry link—also impact the recorded signals. Consequently, in situ evaluation of the performance of the entire infrasound station in its fully operational state is of critical value.

Ideally, the infrasound element should be calibrated without disturbing its operation. This goal led to the development of the ambient-noise-based reference-sensor comparison method for in situ calibration (Gabrielson 2011). In this method, the overall response of the infrasound array element is compared to the response of a co-located, laboratory-calibrated reference sensor using ambient noise as the common excitation.

By using a reference-sensor system that is completely independent of the infrasound station, the impact of all components of the operational system can be measured. The primary product of this method is the complex frequency response (magnitude and phase) of the infrasound element including the responses of the wind noise reduction system (WNRS), the microbarometer, and the digitizer. At the same time, system problems—excessive noise or signal artifacts—can be detected.

2.3.3.1 Configuration

There are a number of variations of the in situ method. The most effective version uses two reference sensors positioned near and symmetrically about the geometric center of the infrasound element's WNRS. With three channels—the two reference outputs and the element output—the response of the infrasound element can be expressed as functions of cross-spectra between various pairs of channels.

In situ calibration can be done with a single reference sensor; however, the response of the infrasound element is then a function of one cross-spectrum and one auto-spectrum. Since the auto-spectrum will have a frequency-dependent bias related to uncorrelated noise components, high-quality results can only be obtained when the coherence is very high. This complicates the analysis and requires more favorable conditions than the two reference sensors technique.

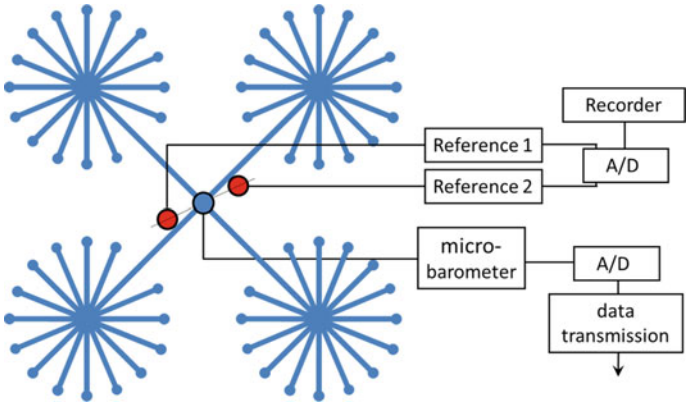

Fig. 2.23 Schematic illustration of reference-sensor deployment. The two references (red) are positioned near and symmetrically about the geometric center of the WNRS. The data from the references are recorded independently of the operational element

The recommended variant requires two reference sensors. Figure 2.23 illustrates the layout in schematic form for an infrasound element that uses a rosette-style WNRS. The two reference sensors are shown as red circles near the center of the blue WNRS. The components associated with the references (power, digitizer, data recorder) are self-contained; no connection to the infrasound system is required. The infrasound element data is recovered directly from the operational data stream.

Both the digitizer for the reference sensors and the digitizer for the infrasound element are synchronized to GPS time so all three channels are time aligned. In what follows, the subscripts 0, 1, and 2 are used to denote the infrasound element (0), and the two reference channels (1 and 2). The known (from laboratory calibration) complex frequency responses of the two references are H_1 and H_2; the unknown frequency response of the infrasound element is H_0. The averaged cross-spectrum between any two channels is G with subscripts to denote those channels. (Averaging is required to realize gain against uncorrelated noise.)

2.3.3.2 Response Estimation

With this notation, there are two expressions that give estimates of the element frequency response, H_0. The first expresses that unknown response in terms of the reference response, H_1,

$$H_0 = \left(\frac{G_{02}}{G_{12}}\right)^* \cdot H_1, \tag{14}$$

while the second expresses the element response in terms of the other reference response, H_2

$$H_0 = \left(\frac{G_{01}^*}{G_{12}}\right) \cdot H_2. \tag{15}$$

The asterisk indicates the complex-conjugate quantity. These equations give two estimates for the unknown response. In practice, these two estimates are averaged to produce a response referenced to the approximate phase center of the WNRS.

Notice that the two response estimation equations use only cross-spectra, not auto-spectra. The averaged cross-spectrum provides a reduction in the influence of incoherent-noise components; whereas, the auto-spectrum does not. Reduction of this incoherent-noise bias is one of the principal advantages of the two-reference methods.

If the reference-sensor signals are digitized separately from the infrasound element (as in the figure above), then the reference channels can be sampled at a higher sample rate. For example, if the normal operational sample rate for the infrasound element is 20 Hz and the reference channels are sampled at 50 Hz, then the resulting response estimate will include the roll-off of the infrasound element digitizer's anti-alias filter.

2.3.3.3 Coherence Screening

The two-reference method minimizes biases in the response estimate so this method can be used with lower coherence than the one-reference method; however, low coherence results in higher uncertainty in either approach. Consequently, the process can be improved by screening for high coherence periods. In the two-reference method, there are two estimates for coherence relative to the infrasound element:

$$\gamma_{01}^2 = \frac{|G_{01}|^2}{G_{00}\,G_{11}}; \quad \gamma_{02}^2 = \frac{|G_{02}|^2}{G_{00}\,G_{22}}. \tag{16a, b}$$

The cross-spectra in these equations must be averaged. Single record coherence is identically unity.

Suppose 24 h of reference-sensor data are collected and it is desired to use at least 4 h with 200 s records in the averaging process (144 averages using a record overlap of 50%). One strategy is to form a window 4 h long and slide that window through the 24 h file, then select the result with an acceptably high coherence. This works well at sites that experience a reliable drop in wind overnight; however, if the wind is irregular in speed with no continuous 4 h periods of low wind, the simple sliding window process is not effective.

A more flexible approach involves using a shorter window and shorter records to identify segments of the data file that have high coherence. As this shorter window (minutes, rather than hours long) slides through the data file, those portions that produce high coherence are saved. After completing the scan of the recorded data, the saved portions are combined into a longer averaging window (with longer

records). The overall coherence of the noncontiguous sample can be substantially higher than the coherence of any contiguous sample. This segment selection can also be performed separately for individual frequency regions to further maximize the overall coherence and minimize the uncertainty of the response estimate.

2.3.3.4 Uncertainty

The theoretical uncertainty in the response estimate is challenging to derive in the general case; however, Bendat and Piersol (Bendat and Piersol 2000, Eq. 9.90) give an approximate form for the normalized error in the limit of a large number of averages. Their expression is equivalent to one standard deviation, δ, with respect to the frequency response normalized to one

$$\delta = \pm\sqrt{\frac{(1-\gamma^2)}{2N\gamma^2}}. \tag{17}$$

Here, N is the number of records used in the cross-spectrum averaging. For $N > 50$ and $\gamma^2 > 0.5$, this approximation gives a result reasonably close to the observed uncertainty. Values from this approximation should be regarded as rough approximations; the actual variations in the calculated response estimate provide a more reliable indication of uncertainty.

Advantages of the in situ method:

1. The method can be employed without disturbing normal station operation.
2. The entire element system is measured, not just the microbarometer.
3. The use of long averaging times and coherence screening can result in response estimates with low uncertainty.
4. The method can be incorporated into an operational system as a permanent calibration method.
5. The method performs well for
    a. Sites that are sheltered or that have abundant natural windbreaks (trees, brush).
    b. Sites that experience regular periods of low wind (often at night).
    c. Frequencies in the microbarom region and in the higher frequencies characteristic of anthropogenic noise.
    d. Very low frequencies (below 0.01 Hz) where the wind-associated turbulence is the excitation signal rather than ambient acoustic noise. This occurs at any site with the elevated wind. While this frequency region is below the IMS band of interest, knowing the response in this region permits developing a low-frequency response model of the system that can connect the response measured there to the response measured in the microbarom region, thereby bridging a difficult measurement region.

Disadvantages:

1. The method depends on ambient noise for excitation.
2. Good results require periods of low wind.
3. The magnitude and phase of the reference sensors must be known and stable under the expected environmental conditions.
4. The method (unless incorporated into the permanent station hardware) requires a site visit.
5. The method can require very long monitoring periods for
   a. Sites with persistent, moderate-to-strong winds and little natural protection.
   b. Sites with very low levels of the higher frequency (above 1 Hz) anthropogenic noise.

References

Alcoverro B, Le Pichon A (2005) Design and optimization of a noise reduction system for infrasonic measurements using elements with low acoustic impedance. J Acoust Soc Am 117 (4):1717–1727

Bendat J, Piersol A (2000) Random data: analysis and measurement procedures, 3rd edn. Wiley, NY

Bowman JR, Shields G, O'Brien MS (2007) Infrasound station ambient noise estimates and models: 2003–2006. In: Infrasound technology workshop, Tokyo, Japan 13–16 Nov 2007

Dravida S (2007) Development of a self-calibrating infrasound microphone and its adaptability to lower audible frequencies, PhD Thesis, University of Mississippi, 116 p

Gabrielson TB (2011) In-situ calibration of atmospheric-infrasound sensors including the effects of wind-noise-reduction pipe systems. J Acoust Soc Am 130:1154–1163

Haak HW, De Wilde GJ (1996) Microbarograph systems for the infrasonic detection of nuclear explosions. Scientific Report WR 96–06, KNMI

Marty J (2019) The IMS infrasound network: current status and technological developments. In: Le Pichon A, Blanc E, Hauchecorne A (eds) Infrasound monitoring for atmospheric studies, 2nd edn. Springer, Dordrecht, pp 3–62

Mentink JH, Evers LG (2011) Frequency response and design parameters for differential microbarometers. J Acoust Soc Am 130(1):33–41

Parmantier Y, Kratz F (2009) Capteurs: definitions, principes de détection. Techniques de l'ingénieur R400:1–13

Ponceau D, Bosca L (2010) Low noise bradband microbarometers. In: Infrasound monitoring for atmospheric studies. Springer

Raspet R, Abbott J-P, Webster J, Yu J, Talmadge C, Alberts II K, Collier S, Noble J (2019) New systems for wind noise reduction for infrasonic measurements. In: Le Pichon A, Blanc E, Hauchecorne A (eds) Infrasound monitoring for atmospheric studies, 2nd edn. Springer, Dordrecht, pp 91–124

Chapter 3
New Systems for Wind Noise Reduction for Infrasonic Measurements

Richard Raspet, John-Paul Abbott, Jeremy Webster, Jiao Yu, Carrick Talmadge, Kirkpatrick Alberts II, Sandra Collier and John Noble

Abstract Wind noise is a significant problem for infrasound detection and localization systems. Pipe arrays are commonly used for suppressing wind noise by area averaging the relatively incoherent wind noise. The area averaging and physical construction of the pipe arrays limit the ability of the array to measure infrasound pulses with waveform fidelity. The need for waveform fidelity is motivated by the recent increase in the ability to predict waveforms theoretically from the

R. Raspet · C. Talmadge
National Center for Physical Acoustics, University of Mississippi, University, MS, USA
e-mail: raspet@olemiss.edu

C. Talmadge
e-mail: clt@olemiss.edu

J.-P. Abbott
Agriculture Research Services, Applied Technology Research Unit, US Department of Agriculture, Wooster, OH, USA
e-mail: johnpaul.abbott@ars.usda.gov

J. Webster (✉)
Earth and Environmental Sciences, Los Alamos National Laboratory, Los Alamos, NM, USA
e-mail: jwebster8@gmail.com

J. Yu
Department of Physics, Liaoning Shihua University, Fushun, Liaoning Province, People's Republic of China
e-mail: yujiaojoy@hotmail.com

K. Alberts II · S. Collier · J. Noble
Army Research Laboratory, Adelphi, MD, USA
e-mail: william.c.alberts4.civ@mail.mil

S. Collier
e-mail: sandra.l.collier4.civ@mail.mil

J. Noble
e-mail: john.m.noble.civ@mail.mil

A. Le Pichon et al. (eds.), *Infrasound Monitoring for Atmospheric Studies*,
https://doi.org/10.1007/978-3-319-75140-5_3

meteorology data. This chapter investigates large cylindrical and hemispherical porous windscreens, which employ single-point sensors with little or no waveform distortion. The theory of wind noise generation is briefly outlined to provide a basis for understanding the windscreen research. Next, four recent experiments measuring the wind noise reduction of porous cylindrical screens with respect to bare sensors mounted flush with the ground, the wind noise reduction of porous fabric domes with respect to a sensor sitting on the ground surface, the wind noise reduction of porous metal domes with respect to other sensors, and the wind noise reduction of porous cylinders and fabric domes with respect to flush-mounted sensors and each other. The second and third experiments also demonstrate the ability of the windscreens to record impulses with waveform fidelity. The largest screens provide up to 20 dB of wind noise reduction down to wavenumbers on the order of the inverse of the height of the windscreen. A theory of wind noise reduction is developed and leads to a better understanding of the relative contribution of wind noise generated at the surface of the screen and wind noise generated by flow through the screen. It is concluded that construction of domes large enough to provide signal enhancement down to 0.1 Hz is feasible and would provide high fidelity time waveforms for comparison with theoretical predictions.

3.1 Introduction

Perhaps, the greatest impediment to the detection and analysis of infrasonic signals are the intrinsic pressure fluctuations due to air turbulence, known as wind noise, always present in the atmosphere. These fluctuations are the dominant source of the noise through which infrasonic signals must be detected (Marty 2019; Mialle et al. 2019). Wind noise levels increase dramatically with decreasing frequency and mean noise levels can easily equal or exceed the levels of the signal to be detected. Walker and Hedlin (2009) provide a complete review of methodologies and research for wind noise reduction prior to 2010.

Pipe arrays, porous-hose arrays, and other wind noise-reducing filters that act by averaging over a large area are band limited. For frequencies high enough that the acoustic wavelength is comparable to the size of the filter, the signal is distorted by the filter itself. For frequencies low enough that the wind noise coherence length is comparable to the size of the filter, the filter becomes ineffective. This limits the spectral region for which the system response is flat and wind noise is suppressed to a bandwidth ratio that corresponds to the ratio of sound speed to the wind speed. For a 10 m/s wind, this ratio is around 40. The predicted system response can be used to compensate the spectrum at higher frequency, but information about the waveform in the temporal domain is lost.

Hedlin and Raspet (2003) compared the scaled reduction of a wind barrier with the wind noise reduction provided by pipe arrays and concluded that the "wind barrier holds promise for significant wind noise reduction with a smaller footprint device." In addition the acoustic signal "enters the microbarometer from free air and

therefore dispersion of broadband signals that is known to occur in narrow pipes is not a concern." This chapter reports on research on wind barriers since the 2010 review by Walker and Hedlin (2009).

Section 3.2 is a review of the fundamentals of wind noise generation as a necessary background to understand the results and interpretation of results. Section 3.3 presents four different studies of the wind noise reduction of porous wind fences and domes. Section 3.4 develops a theory of wind noise reduction by wind fences and domes that can be used to develop an understanding of how the barriers work and for design purposes, and Sect. 3.5 presents the conclusion of the chapter.

3.2 Fundamentals of Wind Noise Generation by Turbulence

One of the largest obstacles in infrasound measurements is wind noise. Pressures generated by turbulent fluctuations in the air generate noise with spectra that follows an inverse power law in the wavenumber or frequency domain. These fluctuations dominate in the infrasound and near infrasound region and can easily swamp acoustic signals in long-range sound propagation measurements.

Pressure fluctuations generated by turbulent flow are not acoustic in nature... there is no wave equation that describes their propagation. They do not travel at the speed of sound, but rather at (roughly) the mean speed of the air flow that entrains them. Turbulence is chaotic in nature, and therefore discourages active cancelation, however it does have properties that can be extracted from sufficiently long time averages; the most important of which is the power spectral density (PSD), which has the form of a von Kármán spectra.

To analyze wind noise, it is useful to divide it into two separate families, *stagnation* pressures, which occur when the turbulence interacts with a bluff body (such as a microphone), and *intrinsic* pressures, which are defined as the wind noise that would be measured if there were no measurement device in the flow. The intrinsic pressures can be further divided into turbulence–turbulence interaction pressures, which arise from turbulence in the air interacting with other turbulence, and turbulence–shear interaction pressures, which arise from turbulence interacting with the wind shear layer near the ground.

In this section, the von Kármán spectra will be introduced, and then the three components of the wind noise will be discussed along with simplified predictions that can be used to calculate the expected wind noise from the measured velocity spectra. A brief discussion of spherical windscreens is included along with a discussion of the effects of diameter on their frequency response.

The goal of this section is to give the reader a working understanding of the analysis of wind noise and the basic methods of passive reduction. A deeper understanding of the physics involved can be gained from the referenced articles.

3.2.1 The von Kármán Form of Turbulent Spectra

Atmospheric turbulence is a chaotic system which resists instantaneous prediction. Like most chaotic systems, however, some properties of turbulence can be estimated from sufficiently long time averages. An example is the one-dimensional turbulent velocity spectrum in the near infrasound region, which can usually be fit with the form as follows:

$$F_{11}^{1}(k_1) = \frac{C}{\left[1 + (k_1\lambda)^2\right]^{5/6}}. \tag{3.1}$$

In this work, k_1, k_2, and k_3 are the wavenumbers in the direction of flow, vertically, and horizontally perpendicular to the flow respectively. Equation 3.1 is of the form of the von Kármán spectra used by George et al. (1984) to model the turbulence in a free jet. C and λ serve as fit parameters to the measured spectra and will be used throughout this chapter in the predictions for the various wind noise components. The F_{11}^{1} notation was introduced by George et al. with the superscript indicating that it is the one-dimensional velocity power spectral density, and the subscripts indicating that it is formed from the spatial Fourier Transform of the correlation function of the velocity components in the direction of flow. The wavenumber along the flow, k_1, is calculated by relating the measured turbulent frequency f and the mean convection velocity using Reynold's frozen turbulence hypothesis,

$$k_1 = \frac{2\pi f}{U_c}. \tag{3.2}$$

Here, U_c is the convection velocity of the turbulence and is defined as the rate at which the turbulent structures are pulled along by the wind. This value varies with frequency, and can be measured using two anemometers aligned along the direction of the wind separated by a distance d. The time t for the turbulence to travel that distance can be found by cross-correlation of the two signals filtered into relevant frequency bands. This is impractical for many measurements. In flow measurements, the convection velocity is often estimated as

$$U_c = 0.7U \tag{3.3}$$

where U is the average free stream wind velocity (Trupea et al. 2007). Yu et al. (2011a) found good results and agreement with correlation studies using the average wind speed at 2.0 m as U in Eq. 3.3. Correlation measurements at separated microphones confirmed that this choice produces a reasonable measurement of the average convection velocity. This approximation is reasonable for most infrasonic turbulence and will be used in the calculations presented in this chapter unless otherwise noted. Figure 3.1 shows an example of a wind velocity power spectral density along with a least squares fit of Eq. 3.1. The velocity measurement represents 15 minutes of data, and was taken in unstable, unsteady conditions. Fifteen minutes was chosen as it

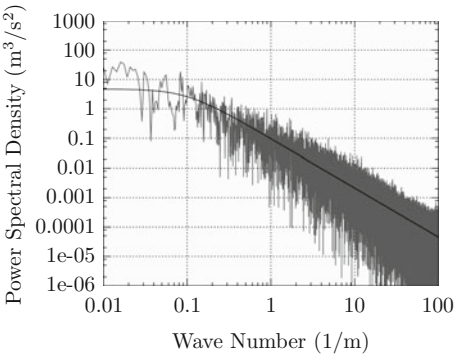

Fig. 3.1 Example power spectral density of the measured turbulent velocities with its fit to Eq. 3.1

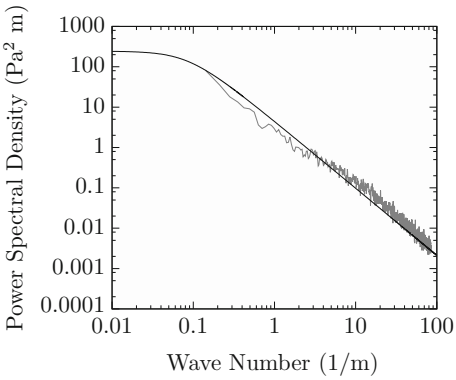

Fig. 3.2 Power spectral density of the stagnation pressures measured with a bare microphone along with the prediction calculated from Eq. 3.8

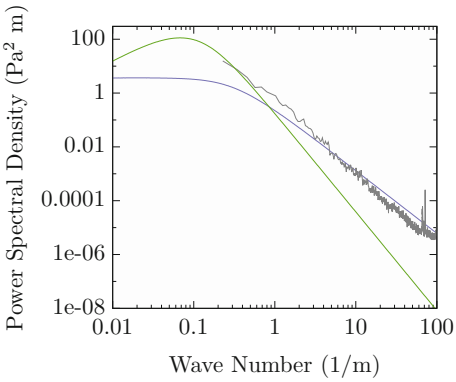

Fig. 3.3 Power spectral density of the intrinsic pressures measured with a large 1.0 m windscreen along with the predictions calculated from the turbulence–turbulence Eq. 3.12 (blue), and the turbulence–mean shear Eq. 3.13 (green)

was long enough to get a suitable statistical measure of low-frequency contributions while being short enough to not be effected significantly by changing atmospheric conditions. No averaging was done when calculating the PSD in Fig. 3.1 in order to preserve the low- frequency components necessary to achieve an accurate fit. In Figs. 3.2 and 3.3, the spectra were averaged in order to show the quality of the predictions.

Throughout this chapter, spectra will be presented in terms of the wavenumber. The wavenumber representations can be related to physical scales of the atmospheric structure and to the size of the wind noise reduction system. In addition, wind noise reduction data presented in terms of wavenumber spectra has been shown to be independent of wind speed. If the frequency representation is used, data from different wind conditions must be presented separately.

The conversion of frequency spectra to wavenumber spectra is given using Eq. 3.2 and

$$F(k) = \frac{U_c F(f)}{2\pi} \tag{3.4}$$

where $F(f)$ is the power spectral density in the frequency representation, and $F(k)$ is the power spectral density in the wavenumber representation.

3.2.2 Stagnation Pressure Interaction Spectrum

Stagnation pressure contributions to wind noise are fluctuations due to the interaction of the turbulent wind with a bluff body (such as a microphone) placed in its path. Raspet and Webster (2008) derived a prediction for this contribution for small objects in the flow using Bernoulli's equation expanded in terms of the air density ρ, the free stream velocity U, and the fluctuating components u_i,

$$P(t) = \frac{1}{2}\rho U^2 + \rho U u_1 + \frac{1}{2}\rho u_i u_i. \tag{3.5}$$

Following the procedure outlined by George et al. (1984), the pressure spectral density in terms of the fits to the measured velocity spectrum was derived by first calculating the mean pressure,

$$\overline{P(t)} = \frac{1}{2}\rho U^2 + \rho U\overline{u_1} + \frac{1}{2}\rho\overline{u_i u_i}, \tag{3.6}$$

by assuming isotropic turbulence, $\overline{u^2} = \overline{u_i^2}$, and $\overline{u_1} = 0$. This allows Eq. 3.5 to be written in terms of the fluctuation pressures p,

$$p(t) = \rho U u_1 + \frac{1}{2}\rho u_i u_i - \frac{3}{2}\rho\overline{u^2}. \tag{3.7}$$

A complete derivation of the prediction is given by Raspet et al. (2008). For ease of use, a simplified expression for the stagnation pressure interaction spectra is provided by fitting the result to curves of the form of Eq. 3.1. The result is,

$$F^1_{pps}(k_1) = \frac{1.44U^2C}{[1+(k_1\lambda)^2]^{5/6}} + \frac{1.451C^2}{\lambda[1+0.1129(k_1\lambda)^2]^{5/6}}. \tag{3.8}$$

The first term is $1.44U^2$ times Eq. 3.1 and behaves accordingly. The second term is a constant at low wavenumber and decays at a rate of $k_1^{-5/3}$ at high wavenumber, with the transition determined by

$$\lambda_S = 0.3360\lambda. \tag{3.9}$$

This indicates that the stagnation process shifts the source-to-inertial region transition to higher wavenumbers than what is measured in the incident velocity spectrum. In measurements near the earth's surface, the second term will generally be significant in the inertial range.

Figure 3.2 shows an example of wind noise measured by an unscreened microphone, along with the prediction calculated from Eq. 3.8.

3.2.3 *Intrinsic Wind Noise*

Intrinsic wind noise is defined as wind noise that would exist if there were no obstacles in the wind's path. The components of intrinsic wind noise are turbulence–turbulence interaction pressures, and turbulence–shear interaction pressures. As the name implies, turbulence–shear interaction pressures are due to the interaction of turbulent fluctuations with the ground's shear layer and become small as the height above the ground increases. The sum of the turbulence–turbulence and turbulence–shear interactions represents the lower limit of wind noise that a compact windscreen could be expected to achieve. Reduction of intrinsic wind noise in the flow above the surface can be accomplished using a spherical windscreen that is large compared to the size of the fluctuations of the frequency of interest ($d \approx U_c/f$). For frequencies less than 1 Hz, the sizes of interest are large, and construction of spherical windscreens large enough to reduce intrinsic wind noise at those frequencies becomes impractical.

3.2.4 *Turbulence–Turbulence and Mean Shear–Turbulence Interaction Pressure Spectra in the Flow*

The turbulence–turbulence interaction spectra are generated by the interaction of the turbulence with itself. Raspet and Webster (2008) derived predictions for this component by following the work of George et al. (1984), beginning with the Navier–Stokes equation for incompressible flow,

$$\frac{1}{\rho}\nabla^2 p = -\frac{\partial^2 u_i u_j}{\partial x_i \partial x_j}. \tag{3.10}$$

The derivation uses the Green function solution to write the fluctuating pressure in terms of the average velocity and the fluctuating velocity components. A constant mean shear and a unidirectional average flow are assumed. The cross-correlation of the fluctuating pressures at two points is written in terms of the correlation of the fluctuating velocities at the two points. This cross-correlation contains terms which represent the turbulence interacting with the mean shear (assumed linear) and the turbulence interacting with the turbulence. The Fourier transform of the cross-correlation of the pressures was taken and simplified by assuming isotropic turbulence. Finally the one-dimensional spectrum along the direction of flow was generated by integrating the three-dimensional spectrum over the k_2, k_3 plane, and noting that the energy spectrum for isotropic turbulence is (Batchelor 1951),

$$E(k) = \frac{55}{18}(k\lambda)^4 \frac{C}{[1 + (k\lambda)^2]^{17/6}}. \tag{3.11}$$

The complete derivation of the final forms for the turbulence–turbulence and mean shear–turbulence interaction formula is beyond the scope of this chapter. However, a simplified expression for the turbulence–turbulence interaction spectra is provided by Raspet and Webster (2008),

$$F^1_{ppt}(k_1) = 0.811 \frac{C^2}{\lambda} \frac{1}{[1 + 0.1792(k_1\lambda)^2]^{7/6}}, \tag{3.12}$$

where C and λ are calculated from the fit to the measured turbulence velocity spectrum. The turbulence–mean shear interaction spectra is approximated by

$$F^1_{ppm}(k_1) = \frac{7.380CK^2\lambda^2(k_1\lambda)^{5/3}}{[1 + 1.622(k_1\lambda)^2]^{8/3}}. \tag{3.13}$$

We note that Eq. 3.13 overestimates the pressure contribution at low wavenumbers since the assumption of linear shear does not hold over the scales of low-frequency turbulence. Yu and Raspet (2011b) investigates the effect of turbulence anisotropy and nonconstant wind shear on the turbulence–shear interaction. The results cannot be represented with a simple fit and are not required for the study of wind fences and domes.

Figure 3.3 shows an example of the intrinsic pressure spectrum measured by a microphone embedded in a large (1.0 m diameter) windscreen, compared to predictions calculated from Eq. 3.13 and a fit to Eq. 3.12.

3.2.5 Wind Noise Levels Measured at the Surface

Elliot (1972) and Fuchs (1972) hypothesized that flush-mounted microphones would measure the intrinsic pressure fluctuations in a flow. Dillion (2005) built and tested

a flush-mounted microphone in outdoor flows to test this hypothesis. He obtained consistent results if the microphone was covered by a thin sheet of porous material. His spectra could not be modeled by the turbulence–turbulence and turbulence–mean shear contributions described by Eqs. 3.12 and 3.13. Near the ground, the wind speed is small but the wind speed gradient is large and rapidly changing. The vertical turbulence is suppressed by the presence of the ground.

Yu (2009) developed a calculation for the turbulence–shear interaction pressure at the surface under a wind velocity profile and turbulence spectra modeled with the form of the von Kármán spectra given by Eq. 3.1. The calculation followed the method of Kraichnan (1956), who calculated the pressure fluctuations under a turbulent boundary layer.

Near the surface, the turbulence–shear interaction is much greater than the turbulence–turbulence interaction since the vertical gradient of the mean horizontal velocity is large. Under this assumption, the source equation becomes

$$\nabla^2 p(\vec{x}, t) = -2\rho s(x_2)\partial V_2/\partial x_1, \tag{3.14}$$

where $s(x_2)$ is the vertical gradient of the average longitudinal velocity,

$$s(x_2) = \frac{dU_1}{dx_2} \tag{3.15}$$

and V_2 is the vertical component of the turbulent velocity. This section uses Kraichnan's notation for mean and fluctuating components of velocity.

In most cases the wind velocity profile was well modeled by a logarithmic profile,

$$U_1(x_2) = \begin{cases} a\ ln\left(\frac{x_2}{x_0}\right), & x_2 \geq x_0 \\ 0 & 0 \leq x_2 < x_0, \end{cases} \tag{3.16}$$

which leads to a velocity gradient of

$$s(x_2) = \begin{cases} \frac{a}{x_2}, & x_2 \geq x_0 \\ 0 & 0 \leq x_2 < x_0. \end{cases} \tag{3.17}$$

More general gradients were considered in Yu (2009) and Yu et al. (2011a), but the logarithmic profile produced good predictions for all measurements performed in the research.

Following Kraichnan, the turbulence field is modeled by the superposition of two homogeneous and isotropic fields:

$$\widetilde{V_1}(\vec{x},t) = 2^{-\frac{1}{2}}[V_1(\vec{x},t) + V_1(\vec{x}^*,t)], \tag{3.18}$$

$$\widetilde{V_2}(\vec{x},t) = 2^{-\frac{1}{2}}[V_2(\vec{x},t) - V_2(\vec{x}^*,t)], \tag{3.19}$$

$$\widetilde{V_3}(\vec{x},t) = 2^{-\frac{1}{2}}[V_3(\vec{x},t) + V_3(\vec{x}^*,t)], \tag{3.20}$$

where $V_1(\vec{x},t)$, $V_2(\vec{x},t)$, $V_3(\vec{x},t)$ are turbulence components of the isotropic homogeneous flow and $x_1^* = x_1$, $x_2^* = -x_2$, and $x_3^* = x_3$. $V_1(\vec{x},t)$ is in the flow direction, $V_2(\vec{x},t)$ is the vertical flow, and $V_3(\vec{x},t)$ is in the horizontal direction perpendicular to the flow. This construction gives zero vertical velocity near the ground. $\widetilde{V_2}(\vec{x},t)$ is then substituted into the source equation. Next, the power spectral density is formed and evaluated using the double Fourier transform in the horizontal plane, yielding:

$$\begin{aligned}\left|p(0,\vec{\kappa},\omega)\right|^2 = {} & 4(2\pi)^{-3/2}\rho^2 k_1^2 \kappa^{-2} \int_0^\infty \int_0^\infty e^{-\kappa(x_2+x_2')} \\ & \times S(x_2')S(x_2)\left[\mathcal{R}_{22}(x_2'-x_2,\vec{\kappa},\omega) - \mathcal{R}_{22}(x_2'+x_2,\vec{\kappa},\omega)\right] dx_2 dx_2'.\end{aligned} \tag{3.21}$$

Here, $\mathcal{R}_{22}$ is the real part of the Fourier transform,

$$\mathcal{R}_{22}(x_2,\vec{\kappa},\omega) = \frac{1}{\sqrt{2\pi}} \int_{-\infty}^{\infty} cos(k_2 x_2)\mathcal{R}_{22}(\vec{k},\omega)dk_2 \tag{3.22}$$

Yu et al. (2011a) evaluates Eq. 3.21 directly in terms of integration over x_2 and x_2' for the logarithmic gradient in Eqs. 3.16 and 3.17 and shows

$$\begin{aligned}\left|p(0,k_1)\right|^2 = {} & \frac{440a^2\rho^2 k_1^2 C\lambda^4}{9\pi} \int_0^\infty \int_0^\infty \frac{dk_2 dk_3}{[1+(k\lambda)^2]^{17/6}} \\ & \times \int_{x_0}^\infty \frac{e^{-\kappa x_2} sin(k_2 x_2)dx_2}{x_2} \int_{x_0}^\infty \frac{e^{-\kappa x_2'} sin(k_2 x_2')dx_2'}{x_2'}.\end{aligned} \tag{3.23}$$

This equation gives the power spectral density of the pressure fluctuations for a logarithmic velocity profile with roughness length x_0 and horizontal velocity spectra of von Kármán form with fit parameters C and λ as in Eq. 3.1.

For practical use, the infrasound sensor is placed in a hole and covered with a layer of porous foam (see Fig. 3.4). This method provides consistent measurements independent of the sensor shape and vent distribution. Figure 3.5 displays measured and predicted wind noise levels for different foam thicknesses. The atmospheric values for each figure is presented in Table 3.1. The wind noise spectra measured by flush-mounted sensors under thin foam provides a sensor-independent standard for comparison with other wind noise reduction methods. Some of the studies presented in this chapter compare wind noise levels to soaker hose arrays or to surface-emplaced Hyperion infrasound sensors for direct comparison of the relative wind noise reduction of the different treatments.

Table 3.1 Data used to generate the plots in Fig. 3.5

Figure	Foam thickness (cm)	U (m/s)	U_c (m/s)	C	λ	a	x_0 (m)
Top left	1.27	2.01	1.40	2.83	14.76	0.55	0.006
Top right	2.54	2.44	1.71	6.67	20.75	0.40	0.007
Bottom left	5.08	3.00	2.10	1.64	8.59	0.57	0.011
Bottom right	1.27 + 3.81 cm gap	3.11	2.17	1.73	7.81	0.54	0.007

Yu (2009) also investigated the extent of the source region as a function of k by truncating the integration at different heights. A rough criteria was that the source region in space for wavenumber k is approximately $1/k$ high. The source region is distributed but limited to distances on the order of a few wavelengths from the sensor.

3.3 Reduction of Infrasonic Wind Noise by Windscreening Devices

Early work on windscreening established the importance of the wind screen porosity on wind noise reduction. If the windscreen is too porous, the flow past the microphone is unabated. If it is not porous enough, turbulence is generated by the screen and more wind noise is generated (Schomer et al. 1990; Ballard and Izquierdo 1965).

Morgan (1993) later developed a model for wind noise reduction of spherical windscreens based on the hypothesis of Phelps (1938). Phelps assumed that the low-

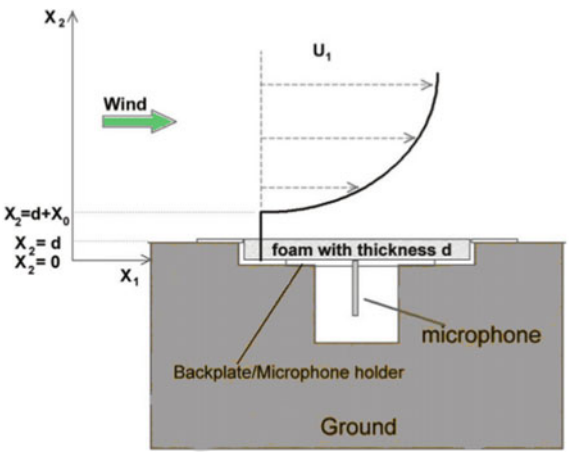

Fig. 3.4 Drawing of the experimental setup for studying the effect of foam thickness on measured pressures

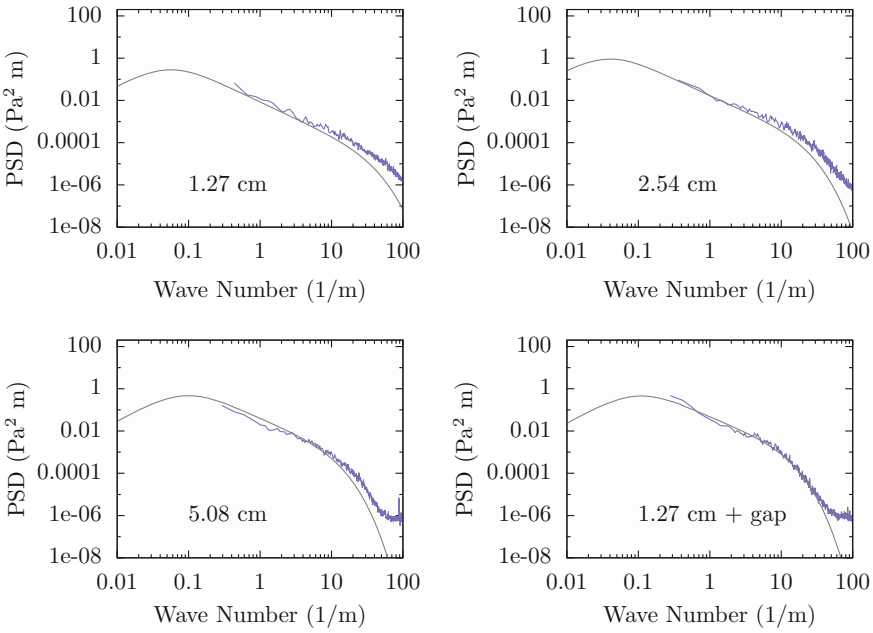

Fig. 3.5 Measured pressure spectra with predictions for microphones under four different thicknesses of foam. 1.27 cm (top left), 2.54 cm (top right), 5.08 cm (bottom left), and 1.27 cm thickness with a 3.81 cm air gap (bottom right)

frequency pressure distribution had the same angular dependence as steady flow past a smooth sphere. Later measurements by Raspet et al. (2007) showed that in outdoor turbulent flows, velocity, and pressure correlation lengths were much smaller near the spherical windscreen than they were in the free stream flow, and that the pressure distribution has no resemblance to the steady flow distribution. The reduction in the correlation lengths leads to efficient area averaging of the pressure fluctuations at the surface of the sphere, and leads to better wind reduction at lower frequencies than would be expected. This section describes the testing and application of these ideas to large structures for the reduction of infrasonic wind noise.

Section 3.3.1 describes wind noise measurements performed with large cylindrical windscreens versus wind noise measured by flush-mounted sensors (FMS) as the porosity and size are varied. Section 1.3.2 evaluates portable 2.0 m diameter fabric domes of different porosity versus a bare HFS Hyperion sensor on the ground. This research also measured the acoustic transfer function using an impulse source. Section 3.3.3 reports on a comparison of the wind noise reduction of the fabric domes and wind fences versus flush-mounted sensors. By employing a common standard, the wind noise reductions of the two methods can be compared. Section 3.3.4 presents comparisons of porous metal domes of different sizes with bare sensors on the ground and porous hose arrays.

3.3.1 Wind Fence Enclosures

Abbott (2014) and Abbott et al. (2015) report on an extensive experimental investigation of the wind noise abatement of 10- and 20-sided circular shaped wind fences, initially 2.9 m tall and 5.0 m in diameter, constructed from chain-link fence panels. The study examined the effect on the noise abatement for a wide variety of porosities, sizes, and the addition of secondary windscreen layers. Noise abatement was measured by comparing the measured wind noise of two infrasonic pressure sensors, one at the center of a wind fence enclosure and the second (the reference) upwind of the enclosure. Both sensors were covered by a 2.54 cm thick sheet of foam, and mounted flush to the ground. Data is plotted on a decibel scale as $10\,log(PSD_{out}/PSD_{in})$, with the x-axis in wavenumber to account for differing convection velocities on different days.

Hedlin and Raspet (2003) employ the principle of wavenumber scaling in their analysis. Morgan (1993) demonstrated that wind noise reductions plotted versus the wavenumber times the characteristic dimension are independent of wind speed and windscreen size. This principle implies that long-term statistical samples are not needed if the wind noise reductions are calculated from a size-independent baseline.

The scaling is only valid if the reference signal is independent of sensor design. Currently, only a flush-mounted sensor provides this independence. The reduction plots in this section use this method and can be used to predict wind noise levels for different turbulence conditions and wind velocity profiles (Sec. 3.2.5).

The porosity, ϕ, of the wind fence enclosure was varied by using different arrangements of privacy slats inserted vertically into the chain-link fencing. Porosity is defined as the percent ratio of open area versus total surface area for an individual chain-link fence panel. The study demonstrated that reductions are largest for porosities between 40 and 55%, with maximum reduction values between 13 and 15 dB;

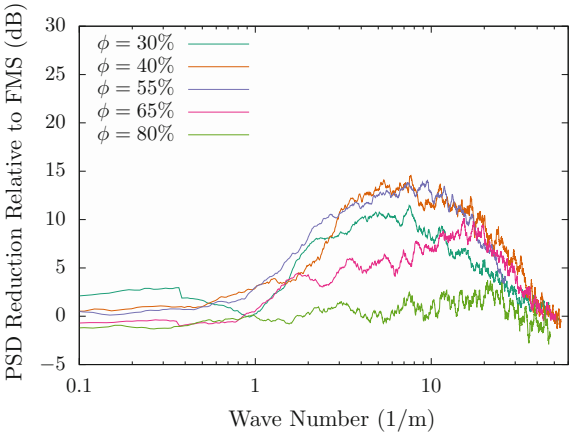

Fig. 3.6 Measured wind noise spectra reductions, in decibels, at different wall porosities across a wind fence enclosure 2.9 m high, 5.0 m in diameter, with an open bottom gap and open top

see Fig. 3.6. Mid-range porosities minimize the combined effect of the turbulence interactions inside and at the surface of the wind fence enclosure.

We note two facts about the wind noise reduction plot in Fig. 3.6 and all following plots which display the wind noise reduction versus the flush-mounted sensor in wavenumber space.

1. The wind noise spectrum measured by a particular windscreen for a given wind velocity profile and turbulence spectrum can be calculated from Eq. 3.23 by subtracting the reduction plot.
2. The wind noise reduction becomes small or negligible at higher wavenumbers. This is not a limitation of the windscreen, but rather the wind noise itself becomes negligible in this limit. The wind noise itself is small from the lowest effective wavenumber up to the limits on the microphone itself.

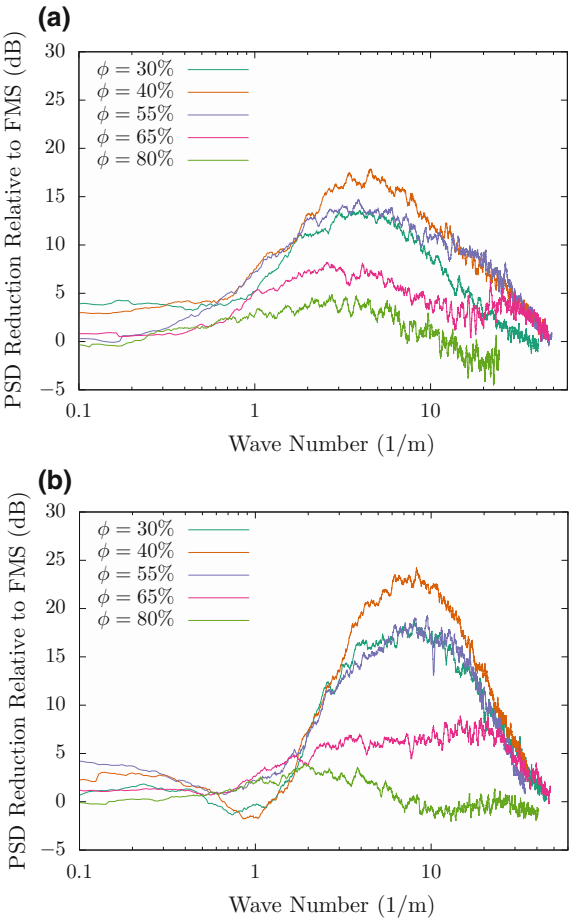

Fig. 3.7 Measured wind noise spectra reductions, in decibels, at different wall porosities across a set of wind fence enclosures that are **a** 5.8 m high and 5.0 m in diameter and **b** 2.9 m high and 10.0 m in diameter

The size of the fence was varied by independently increasing the height from 2.9 to 5.8 m, and then enlarging the diameter from 5.0 to 10.0 m. The 5.8 m tall fence achieved maximum reductions of 13–17 dB, similar to the 2.9 m tall fence but for a lower frequency band; see Fig. 3.7a. The shift is due to the taller wind fence effecting more of the low- frequency source region at higher elevations. The 10.0 m diameter fence achieved maximum reduction values of about 17–25 dB, but did not shift to a different frequency band. For both larger screens, the 40% porosity produced larger reductions than the 55% porosity. A constant 3–5 dB reduction for frequencies below 0.5 Hz was observed for both the 5.8 m high fence and the 10.0 m diameter fence with $\phi = 40\%$; see Fig. 3.7b. The narrow frequency band of the reduction curves that approaches 0 dB is due to microbarom detection. The results demonstrate that the height of the structure principally affects the frequency range where the noise abatement occurs and to a lesser extent the magnitude of the reductions. The magnitude of the reductions is principally affected by the diameter of the wind fence enclosure. The improved reductions for both cases are due to more effective area averaging due to a larger surface area and increased separation distance between the microphone and surface interactions at the surface of the enclosures.

Secondary windscreen layers were added concentrically by nestling a small foam-covered dome or a smaller wind fence structure inside a larger structure. Of the secondary windscreens tested, the small foam-covered dome was the most effective, and only its results will be shown here. In the data it is referred to as a shroud. When the foam dome was combined with the wind fence enclosures, the maximum noise reductions improved to approximately 20 dB for all porosities from the 2.9 m tall and 5.0 m diameter fence, to 23 dB for the 5.8 m tall fence, and to 22–27 dB for the 10.0 m diameter wind fence; see Fig. 3.8. The secondary windscreen enhances the reductions by suppressing the wind noise generated by the residual turbulence that passes inside the wind fence enclosure. Best reductions are achieved when the noise generated by the residual turbulence can be reduced to levels that are negligible when compared to the noise generated by the incident turbulence.

The results of this study show that the best reductions were achieved for a 10.0 m diameter wind fence at 40–55% porosity range, combined with the foam dome; with maximum reduction values of 27 dB at 3–7 Hz, reductions of 10 dB and higher in the 1–30 Hz frequency spectrum, and a constant reduction of 3–6 dB below 0.5 Hz to the lower limit of the measurement.

3.3.2 Fabric Wind Domes

Noble et al. (2014a) from the U.S. Army Research Laboratory investigated the use of fabric domes to reduce wind noise in the near infrasound range. This study was an engineering study and used a Hyperion sensor in the flow as the reference. For this reason, the results cannot be scaled and are presented as average levels in different wind speed ranges. The detailed results have been reported in Noble et al. (2014a) and in a series of talks (Collier et al. 2014; Noble et al. 2014b; Collier et al.

2014). This section reports on the comparison of the domes to a Hyperion sensor on the ground and to a porous-hose rosette for wind noise reduction and for acoustic transmission.[1]

Experiment

Based on previous wind noise reduction studies, it was anticipated that a commercially available hemispherical tent frame would provide a geometry appropriate for spatial averaging; and by using different fabrics, different porosities could be tested. The tent frame selected was 2 m in diameter by North Face. The first porous fabric was approximately 7% open (acrylic and PVC blend) by Sunbrella Sling; the second porous fabric was approximately 35% open (coated polyester mesh) by Phifertex.

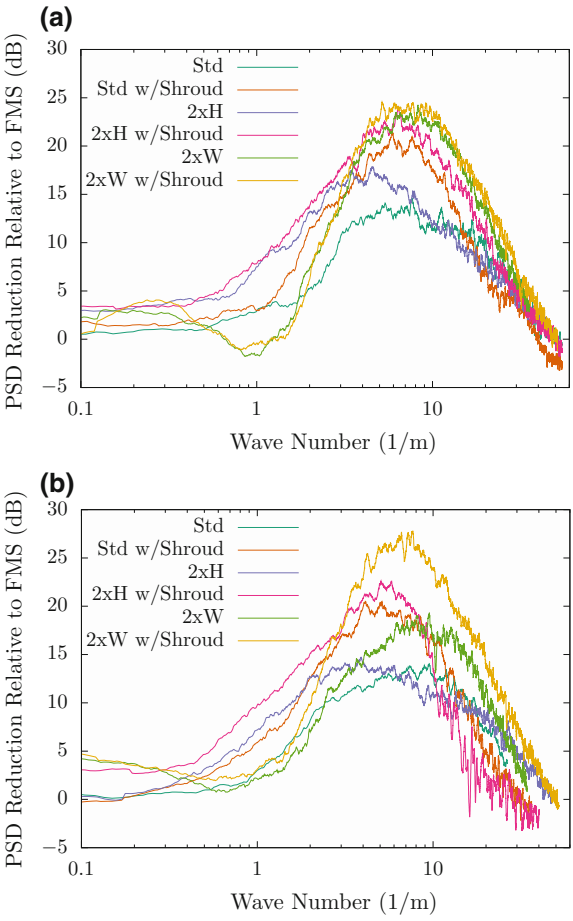

Fig. 3.8 Measured wind noise spectra reductions, in decibels, for the standard (2.9 m high and 5.0 m width), double height (5.8 m high and 5.0 m diameter), and double width (2.9 m high and 10.0 m width) wind fence enclosures combined with and without the foam shroud at **a** 40% and **b** 55% wall porosities

[1]The research in Sects. 3.3.2, 3.3.3, and 3.4 was sponsored in part by the Army Research Laboratory and was accomplished under Cooperative Agreement Number W911NF-13-2-0021.

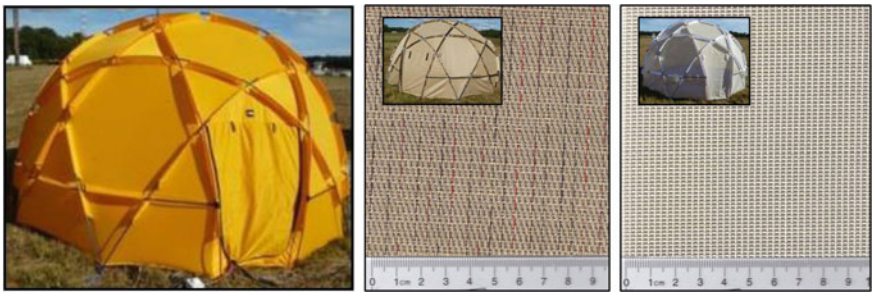

Fig. 3.9 Fabric wind domes: (left) nonporous nylon, (center) porous Sunbrella Sling, approximately 7% open, and (right) porous Phifertex, approximately 35% open

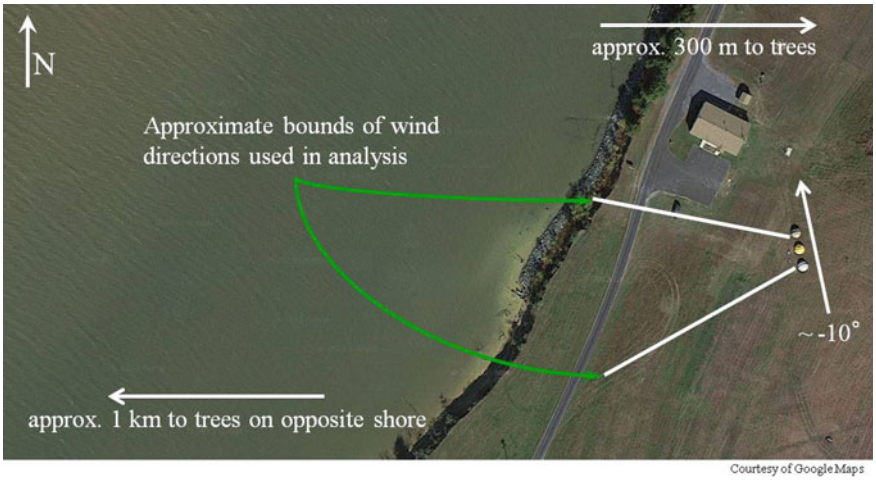

Fig. 3.10 Aerial view of the experimental test site in Southern Maryland

The final fabric was nonporous nylon (210 denier nylon with 1500 mm waterproof rated polyurethane coating) by North Face. These domes are pictured in Fig. 3.9.

In order to examine the performance under differing atmospheric conditions, experiments were conducted over a 6-week period in southern Maryland, as shown in Figs. 3.10 and 3.11. The layout of the domes was designed to avoid introducing artificial wind noise downstream, based on the prevailing wind direction. Infrasonic and atmospheric data was collected interior to each dome, as well as exterior. Each dome housed a Hyperion IFS-3000 infrasound sensor, a Chaparral Model 2 infrasound sensor, and a R. M. Young Model 2000 ultrasonic anemometer. Outside were a Chaparral Model 2 with a 20-ft radius porous-hose rosette, a Hyperion IFS-3000 with a 20-ft porous-hose rosette, a Hyperion IFS-3000 with a high-frequency shroud (HFS), four R. M. Young Model 2000 ultrasonic anemometers, and an Airmar 150WX. Complete details of the experiment can be found in Noble et al. (2014a).

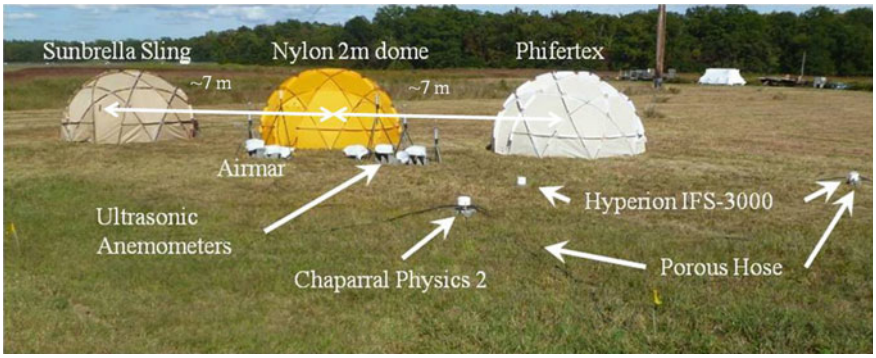

Fig. 3.11 Experimental arrangement: the placement of the domes is based on the prevailing wind direction

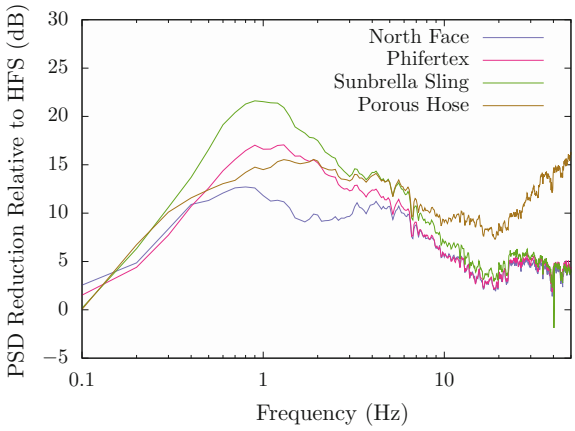

Fig. 3.12 Low winds (<3 m/s) for Hyperion sensors with wind noise suppression relative to outside sensor with HFS

The performance of the fabric domes is benchmarked to the porous-hose rosette and the HFS under three different wind conditions: low, defined by winds less than 3 m/s, medium, winds between 3 and 6 m/s, and high, winds greater than 6 m/s.

Wind Noise Reduction Relative to HFS Sensor

The ratio of the PSDs of the Hyperion sensors with fabric domes (blue, red, green) and porous-hose rosette (brown) to the PSD of the Hyperion sensor with the HFS are presented in Figs. 3.12, 3.13, and 3.14. For low wind conditions, Fig. 3.12, we observe that all of the fabric wind domes and the porous-hose rosette reduce the wind noise by a similar amount below 0.4 Hz. Increasing in frequency, in the range 0.4 to 4 Hz, the Phifertex dome and porous-hose rosette perform similarly and the Sunbrella Sling dome further reduces the wind noise by ∼5 dB, whereas the nonporous North Face nylon dome's performance is less than the porous-hose rosette's. Increasing further in frequency, 4–10 Hz, the domes' and porous-hose rosette's reductions are within 5 dB of each other.

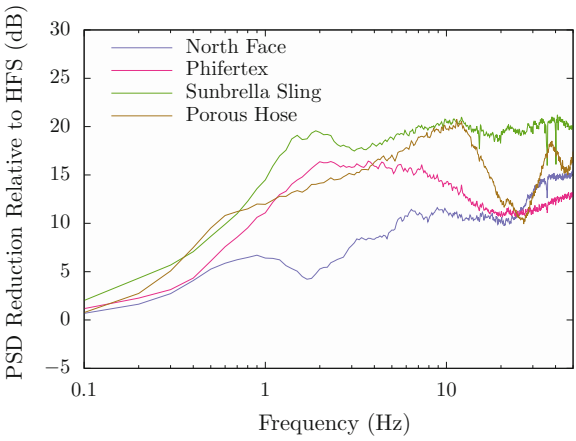

Fig. 3.13 Medium winds (3–6 m/s) for Hyperion sensors with wind noise suppression relative to outside sensor with HFS

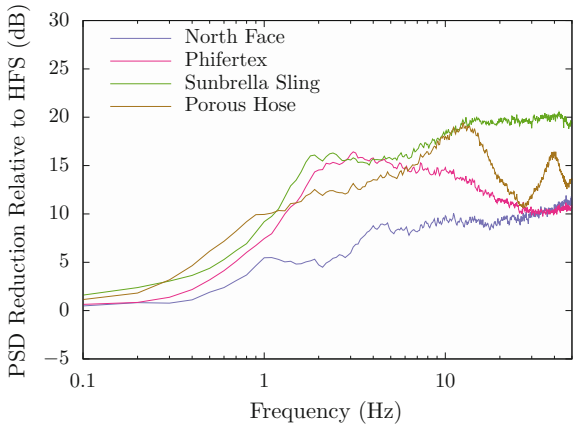

Fig. 3.14 High winds (>6 m/s) for Hyperion sensors with wind noise suppression relative to outside sensor with HFS

For medium winds, Fig. 3.13, the reductions for all the wind noise suppression devices have increased in magnitude, and some of the features observed for low wind conditions are more apparent. Most significantly, the noise reduction of the Sunbrella Sling dome is maintained at frequencies above 10 Hz; whereas, the noise reduction of the nylon dome, Phifertex dome, and the porous-hose rosette decrease. The performance of the Phifertex dome begins to significantly deviate from that of the Sunbrella Sling dome at roughly 6 Hz.

Typical results for high-wind conditions are shown in Fig. 3.14. In the low-frequency ranges between 0.1 and 1 Hz, all of the noise suppression schemes are within 5 dB. Above 1 Hz, the results for the HFS-only sensor and the nylon dome significantly deviate from those of the porous-hose rosette and two porous domes. The Phifertex dome, until 8 Hz, stays within 3 dB of the Sunbrella Sling dome. For the porous-hose rosette, this frequency range extends to roughly 10.5 Hz.

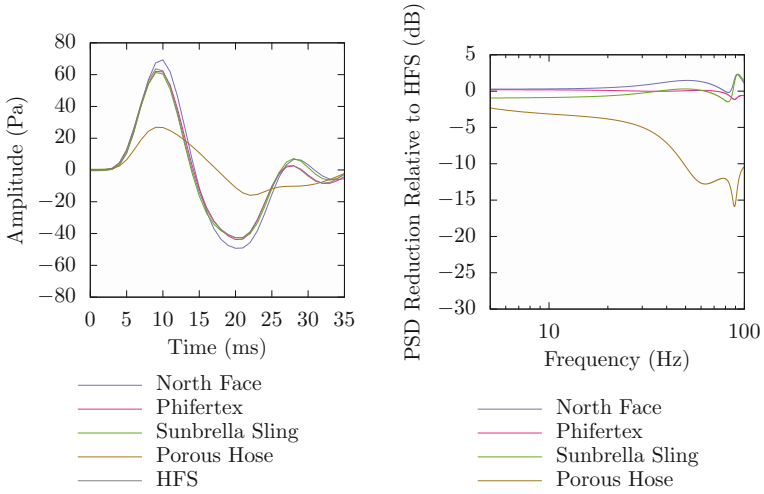

Fig. 3.15 Acoustic responses for different fabric domes. Data is for an explosive impulse measured simultaneously at all sensors. Left plot shows the time series, right plot shows the spectra comparison

Transfer Function

Figure 3.15 (left) shows the time series of an explosive impulse measured simultaneously by all of the Hyperion infrasound microphones. The waveforms measured in the Phifertex and the Sunbrella Sling domes compare extremely well with those measured outside with the HFS. This figure also shows that there is a marked improvement of the Phifertex and Sunbrella Sling windscreens over the typical porous-hose rosette currently used for infrasound arrays —the amplitude of the signal measured with the porous-hose wind screen is roughly half of that measured in the porous domes. The 6 dB loss in amplitude leads to a significant reduction in detection range. Looking at the difference spectra, Fig. 3.15 (right), the porous domes have a relatively flat frequency response from 5 to 60 Hz, while the porous-hose rosette significantly attenuates the signal above 30 Hz. This figure also shows the distortion of the signal by the nylon dome due to a slight amplification of the pressure between roughly 20–80 Hz and the introduction of a time delay in the waveform of the impulse. It is clear that the acoustic response of the Hyperion sensor inside the domes are identical to the acoustic responses of the Hyperion sensor outside of the domes, in contrast to the acoustic response of the porous-hose array.

3.3.3 Wind Noise Reduction of Fabric Domes and Wind Fences Relative to the Flush-Mounted Sensor

Section 3.3.2 compared the wind noise reduction and acoustic transmission of fabric domes, porous hoses and a HFS sensor placed on the ground in an engineering study. The long- term results were binned into wind noise classes and the spectra presented in the frequency domain.

In this section, the wind noise reduction of the domes is compared to the flush-mounted sensor and the reductions are plotted versus wavenumber. Wind fences prepared for the investigation of Sect. 3.3.1 are also evaluated in this section so that a clear comparison can be made between the reductions produced by the domes and wind fences.

The ARL domes and UM wind fences, previously described, were also tested concurrently in order to make a direct comparison of their performances. This test was conducted at the UM test site. The wind noise reduction relative to the flush-mounted sensor are plotted versus wavenumber in Fig. 3.16. All of the wind noise reducing devices provide significant reduction of the wind noise between 0.8 and 30 Hz except for the nonporous dome. The larger wind fences provide slightly more reduction than the smaller porous domes. Scaling arguments cannot be applied for a definitive comparison since the shape of the enclosure is different (hemispherical vs cylindrical). None the less, Fig. 3.16 provides a useful compilation of reductions versus the sensor independent flush-mounted sensor.

3.3.4 Wind Noise Reduction with Porous Metal Domes

The National Center for Physical Acoustics has engaged in a multiyear study to determine the efficacy of porous metal domes in reducing wind noise and transmitting an acoustic infrasound signal with fidelity. The measurement compares the wind noise levels measured under a metal dome with bare NCPA infrasonic sensors on the ground surface, and to NCPA sensors coupled to porous hoses.

The preliminary study presented here used a NCPA infrasound sensor on the ground and in the flow as a reference. In addition, the site was surrounded by trees. The comparisons are certainly a valid indication of the relative effectiveness of the various domes and sensor arrays, however the absolute reductions cannot be extrapolated to other locations and conditions. The results are presented in the frequency domain for different wind speed ranges.

Experimental Design

Wind noise observations were collected near a seven element array (See Fig. 3.17). Pressure fluctuations were transduced using seismically decoupled NCPA infrasound sensors and recorded using either a GEOTECH SMART 24 or a REFTEK 130/S digitizer, where the data were digitized at 24 bits at a 100-Hz sampling rate. In both cases, the digitizers were connected to GPS antennas. In some cases, both digitizers

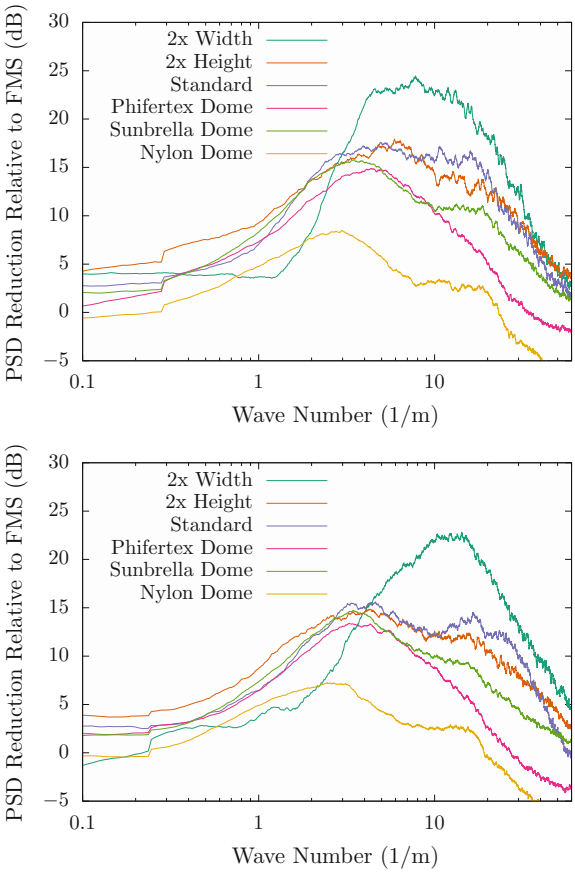

Fig. 3.16 Average of the measured wind noise PSD reductions relative to flush-mounted sensor for the ARL fabric porous domes and the standard (2.9 m high and 5.0 m width), double height (5.8 m high and 5.0 m diameter), and double width (2.9 m high and 10.0 m width) wind fence enclosures for (top) 40% and (bottom) 55% fence porosities

were operated together with as many as 12 analog sensors. Most of the data shown here were collected at the UMBFS array.

Most NCPA sensors were equipped with a "high- frequency shroud" (HFS) shown in Fig. 3.18, left. The HFS has 24 ports connecting the sensor manifold to the external atmosphere. This design is intended to pass-through high-frequency acoustic signals, but integrates over turbulent signals (which typically have much shorter scale lengths) in order to filter wind noise. This design is effective mainly for frequencies above 20 Hz. Above 150 Hz, the Helmholtz resonance of the HFS becomes important and leads to about a maximum 6 dB amplification at approximately 300 Hz.

Porous-hose measurements were obtained by attaching four porous hoses to the "porous-hose cap" (PHC) version of the NCPA sensor shown in Fig. 3.18 right. Typically 50-foot length ACE brand 3/8 in. diameter closed-pore soaker hoses were used. These hoses are the most commonly commercially available type of hose sold in the United States, and require a minimum of at least 5 PSI pressure differential between interior and external atmosphere in order for water interior to the hose to leak out

of the hose (hoses which have this properly have an "Element" emblem attached to their front cover).

For use as an infrasound filter, when properly installed, they are effectively both air and watertight. A second style, 50-foot length, 1/2 inch diameter, open-pored porous hoses sold by Colorite Waterworks were also used. Unlike the ACE-brand hoses, both air and water can freely interchange between the interior and exterior environment.

The first dome design deployed for large-scale infrasound measurements at the NCPA was a 45 in. (1.1 m) hemispherical dome. The frame for this dome was a "papasan" chair frame covered with 1 inch foam enclosed in protective fabric. The cost per dome was typically under 200 USD. This configuration was used in a quarry experiment for an experiment near the Littleton, MA area (Waxler et al. 2012). These domes have since been used in ground-truth explosion measurements performed in New Mexico as well a numerous other deployments.

It was found that this system was effective for wind noise treatment above 2 Hz, and also did not significantly modify the acoustic waveform. The main disadvantage of these domes was the foam material could be damaged by animals and the papasan frame deteriorated over time in wet environments.

A long-duration study comparing the relative efficacy of domes of different diameters to porous hoses was performed between December 2013 and June 2014. One interest of this study was to assess whether domes made with more durable materials had as good of wind noise reduction characteristics as the original foam cover. For these tests, metal frames were constructed and clad with perforated aluminum sheet metal. Our tests suggested that about 30% effective open area was optimal for the cover of the metal frames. For most of our domes, aluminum sheets perforated with

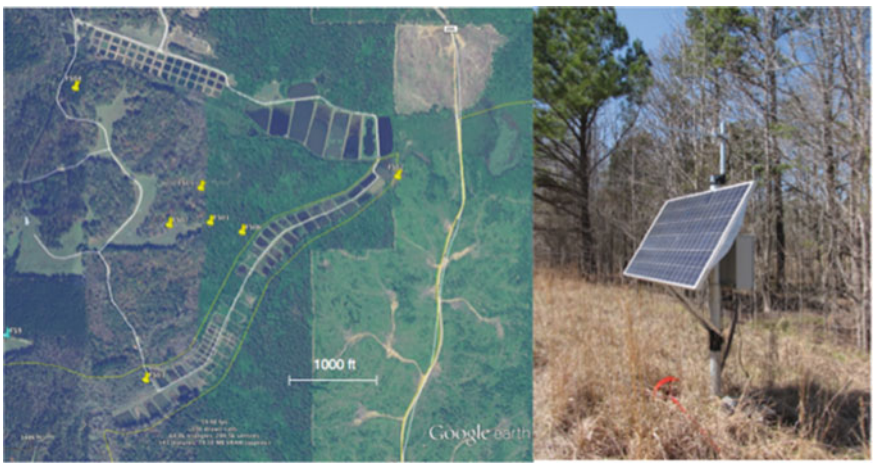

Fig. 3.17 Layout of the seven element array used in conjunction with the porous metal dome measurements

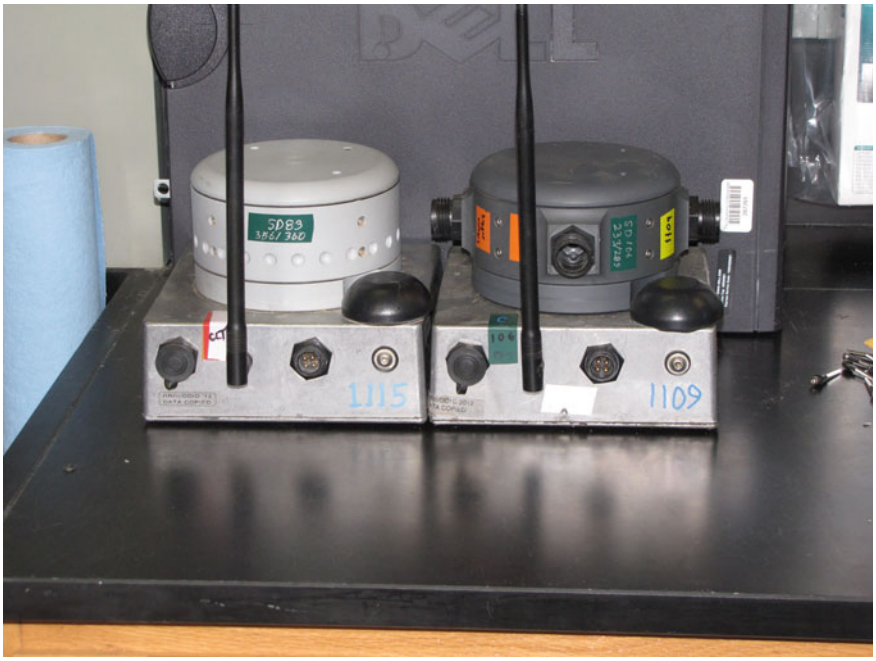

Fig. 3.18 NCPA digital sensors. At left is the digital sensor with a "high frequency shroud." At right is as four-port porous-hose cap

3/16 in. diameter holes on a 5/16 in. spacing (32% effective open area) were used. For this study, diameters of 45 in. (1.1 m), 60 in. (1.5 m), and 96 in. (2.4 m) were used.

Analysis of the data from these was used to select a dome with a diameter of 240 in. (6.1 m) for testing. The dome frame (Fig. 3.19, left) was manufactured by Pacific Domes, Inc. The final dimensions were 6.1 m diameter and 3.7 m high.

Fig. 3.19 (Left) The frame for the 6 m dome. (Right) The completed 6 m dome is at right. The 2.4 m dome is seen in front

Including materials and labor, the approximate installation cost for one dome was approximately 8000 USD. This dome was completed in June of 2015. The completed dome is shown in Fig. 3.19, right.

The array measurements were collected in a field near the "UM7" element, as shown in Fig. 3.20. In many respects, the UMBFS site is not ideal from the perspective of turbulence measurements (e.g., the presence of nearby trees, lack of horizontal fetch). This site was selected based on physical security and based on representing a realistic scenario for a "real-world" deployment of a wind dome.

Wind Noise Reduction Referenced to a Bare High-Frequency Sensor

In these measurements, the reference sensor was a bare sensor sitting on the ground with a High-Frequency Shroud (HFS) attached. The reductions are calculated by taking the ratio of the PSDs between the test and reference sensors and converting that to dB. Thus, the larger the factor, the better a particular sensor treatment performed in filtering wind noise. The results of one example measurement comparing

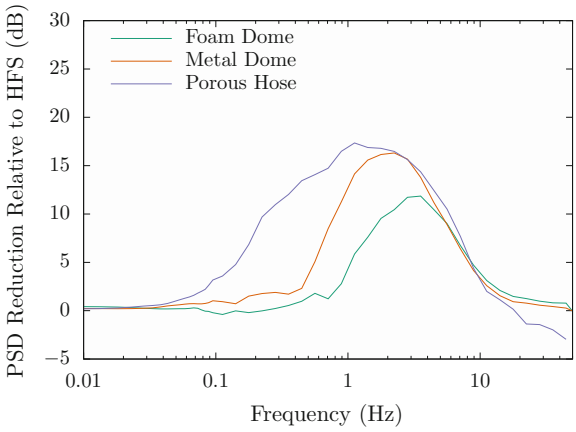

Fig. 3.20 An example noise reduction factor comparison for a 1.1 m Foam Dome, a 2.4 m Metal Dome, and a Porous Hose. Mean wind speed during this measurement was 4.5 m/s

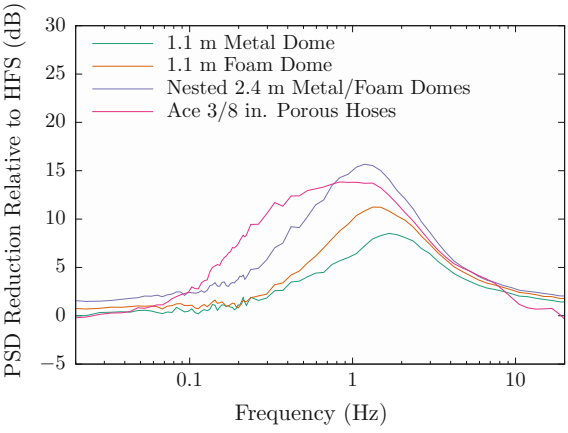

Fig. 3.21 An example noise reduction factor comparison for a 1.1 m foam dome nested within a 2.4 m Metal Dome and an ACE 3/8 in. porous hose. Mean wind speed during this measurement was 6.0 m/s

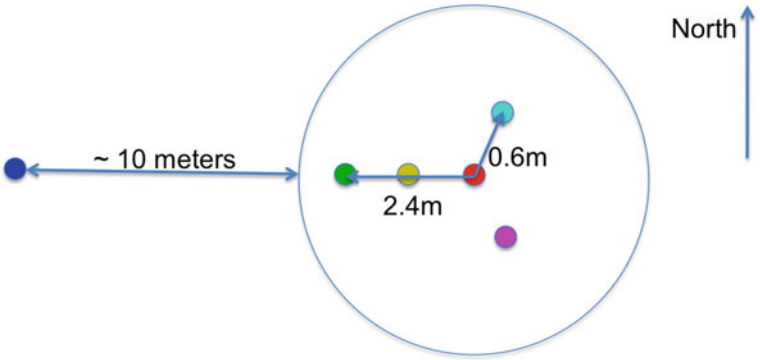

Fig. 3.22 Diagram showing the position of the sensor elements in the 6 m metal dome measurement

a 1.1 m foam dome, a 2.4 m metal dome, and a porous hose are shown in Fig. 3.20. As anticipated, the larger dome performs better than the smaller with the porous hose being the best. At higher frequencies (typically above 10 Hz), the attenuation of the acoustic signal as well as noise led to a net poorer performance for the porous hoses. This pattern was repeated throughout these measurements. The wind noise reduction factor for a second measurement period is shown in Fig. 3.21. As with the earlier case, the porous hose performs better at low frequencies (typically below 1 Hz), and its performance rolls off above approximately 10 Hz. For these high-wind noise conditions, it also performed less well than the 2.4 m dome in the region of best performance for that dome.

Finally, we show results for the 6 m dome. For this particular measurement period, five elements were placed interior to the 6 m dome and one "bare" element was placed on the ground 10 m upwind to the front of the dome (see Fig. 3.22). Unfortunately for this measurement period, light winds (less than 3 m/s) were typically present. Because the wind speeds were low compared to previous testing, the amount of attenuation was lower than shown above. However, the relative pattern between domes (larger domes producing more attenuation) was still observed.

The PSD and wind noise reduction factors for the interior sensors and exterior sensor are shown in Fig. 3.23.

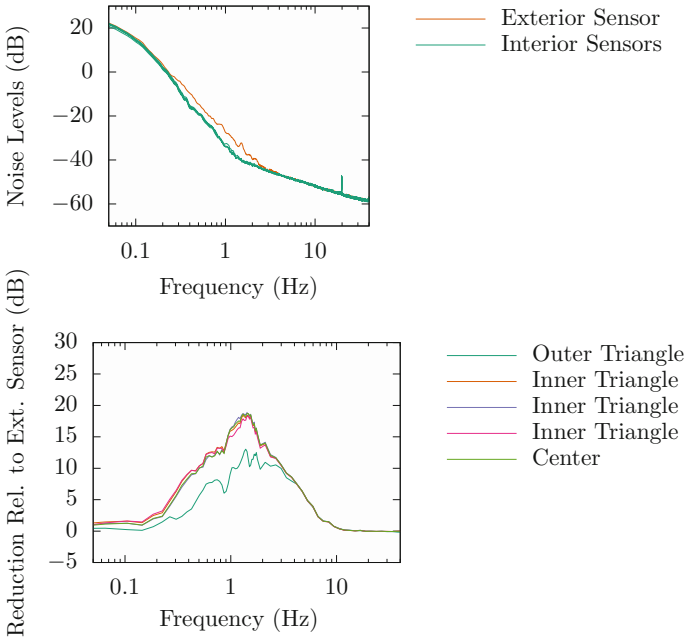

Fig. 3.23 (top) PSDs for 6 m metal dome array. (bottom) Wind noise reduction factors compared to external element.

Acoustical Transmission of the Wind Domes and Porous Hoses

By looking at periods with very low wind speeds, the influence of the windscreen on long-range propagating sound can be evaluated. The spectra for a quiet period (wind speed < 0.5 m/s) are shown in Fig. 3.24 below. As can be seen in this figure, all of the sensors' spectra essentially overlap, except for the porous hose sensor with Colorite porous hoses connected to it. For this sensor, the roll-off at high frequency is interpreted as acoustic signal attenuation, rather than a reduction in wind noise.

The inferred signal attenuation for each sensor can be computed by taking the ratio of spectra between the test sensor and the "bare" reference sensor, as shown in Fig. 3.24. From this figure, we conclude that the effect of the windscreen is less than 1 dB from 0.2–50 Hz for all configurations except the sensor with Colorite porous hoses attached.

Dome Summary

The metal domes covered with perforated sheet metal (30% open area) are as effective as foam-covered domes. Because of their greater durability, these are preferred for long-duration deployments. Fifty-foot porous hoses performed better than any of the domes at low frequencies (typically below 0.5 Hz). However, the 2.4 and 6 m domes often produced more wind noise attenuation near their best frequency. Domes produced no measurable attenuation or distortion of the acoustic waveform, while porous hoses consistently attenuated the acoustic signal at higher frequencies.

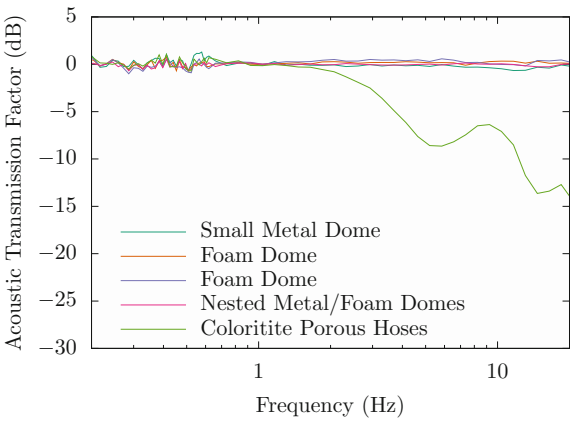

Fig. 3.24 Plot showing the acoustic responses for various domes and a porous hose referenced to a "bare" reference sensor

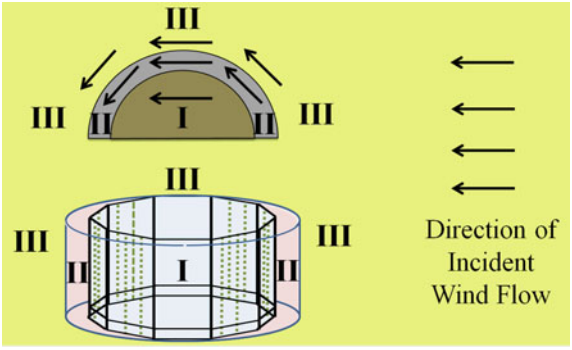

Fig. 3.25 Sketch depicting the location of the three source regions relative to the ARL domes and wind fence enclosures. Wind flow direction is from right to left. The sketch is not drawn to scale

3.4 Reduction Theory

This section develops a reduction theory for windscreen enclosures in general, and will analyze both wind fence enclosures and the ARL porous fabric domes (Sects. 3.3.1 and 3.3.2). The hypothesis is that the wind noise measured at the center of a wind fence enclosure or similar enclosed windscreening device is due to a combination of the different wind noise source interactions from the various flow regions around the enclosure (Noble et al. 2014a; Abbott and Raspet 2015). These interactions can be divided into (I) the flow inside of the enclosure, (II) the flow at the surface of the enclosure, and (III) the unperturbed flow away from the enclosure; see Fig. 3.25. Criteria are established for which regions contribute for a given wavenumber. It is assumed the contributions can be summed incoherently.

The flow inside of the enclosure can be treated using the calculations of the turbulence–shear interaction pressures and the turbulence–turbulence interaction pressures as discussed in Sect. 3.2.4 of this chapter. Similarly, the flow outside of the enclosure, or the undisturbed region, can be modeled as the turbulence–shear interaction pressure. The flow interaction pressure at the surface of the enclosure is

more complicated. Determining the contribution from this interaction is analogous to calculating the electric potential at the interior of a shell with a given surface potential where the calculated pressure at the center of the enclosure is equal to the solid angle average of the pressure fluctuations at the surface,

$$p(0,t) = \frac{1}{4\pi} \int p(\vec{r},t) \frac{\vec{r} \cdot d\vec{s}}{r^3} \tag{3.24}$$

For the wind fence, $\vec{r} = b\hat{r} + z\hat{z}$, $d\vec{s} = \hat{r}bdzd\theta$, $r = \sqrt{b^2 + z^2}$, where b is the radius of the wind fence. For a hemispherical enclosure like the ARL domes, $\vec{r} = b\hat{r}$, $d\vec{s} = \hat{r}b^2 sin\theta d\theta d\phi$, where b is the radius of the ARL dome, θ is the polar angle, and ϕ the azimuthal angle. From theory and measurements (Noble et al. 2014a; Abbott and Raspet 2015) it is assumed that the pressure fluctuation source, $p(\vec{r},t)$, at a position on the surface of the enclosure is proportional to the stagnation pressure due to the change in wind velocity far away from the surface of the enclosure, U_∞, to the velocity inside the screen, U_{in}, or

$$p = -\rho_0 v(U_\infty - U_{in}) \tag{3.25}$$

where ρ_0 is the density of air and v is the measured turbulence at the surface of the enclosure. The spectrum of the measured turbulence is modeled by the von Kármán form.

The power spectral density of the pressure is calculated from the product of Eq. 3.24 with its complex conjugate using Eq. 3.25. The double integration over the surface areas and long time average result in the correlation of the turbulent velocities

$$\langle v^*(s',k)v(s,k)\rangle = \frac{Ce^{-\alpha(k)D}}{\left[1 + (k\lambda)^2\right]^{5/6}} \tag{3.26}$$

where k is the wavenumber, λ and C are fit parameters, and $\alpha(k)$ is the measured inverse correlation length assuming an exponential form, and D is the shortest arc length between the two integration points. The integration is over the actual surface of the fence or dome. A factor of two is introduced to account for pressure doubling at the ground. For the cylindrical wind fences, the shortest arc can be selected by letting

$$\triangle\theta = \cos^{-1}(\cos(\theta - \theta')). \tag{3.27}$$

Measurements show that the correlation lengths are drastically shortened by the flow distribution in the vicinity of the screen. The flow may still have the same large spatial correlation as in free space, but the layers and regions of the flow are traveling past the sensor at different rates; see Fig. 3.26.

The solution for this is the contribution at the surface of a cylindrical enclosure:

$$\left|P_{cyl}(0,k)\right|^2 = \frac{\rho_0^2 b^4 C}{(2\pi)^2}\int_0^h\int_0^{2\pi}\int_0^h\int_0^{2\pi}\frac{(U_\infty - U_{in})^2 e^{-\mu k^q\sqrt{(b\triangle\theta)^2+(z'-z)^2}}dz'd\theta'dzd\theta}{(b^2+z'^2)^{3/2}(b^2+z^2)^{3/2}[1+(k\lambda)^2]^{5/6}}. \tag{3.28}$$

The shortest arc length for the dome is the great circle arc given by

$$D = b\,\cos^{-1}\left[\sin\theta\sin\theta'\cos(\phi'-\phi)+\cos\theta\cos\theta'\right], \tag{3.29}$$

where θ, θ' are the polar coordinates, and ϕ, ϕ' are the azimuthal angles on the hemisphere. The integral to predict the wind noise generated at the surface of the dome is

$$\left|P_{dome}(0,k)\right|^2 = \frac{\rho_0^2 C}{(2\pi)^2}\int_0^{2\pi}\int_0^{\pi/2}\int_0^{2\pi}\int_0^{\pi/2}\frac{(U_\infty - U_{in})^2\, e^{-\mu k^q D}\sin\theta\,\sin\theta'\,d\phi'\,d\theta'\,d\phi\,d\theta}{[1+(k\lambda)^2]^{5/6}}. \tag{3.30}$$

Predictions are calculated from the measured mean wind velocity and turbulence. It is assumed that the turbulent flow in the undisturbed region dominates the low-frequency contribution since turbulence wavelengths significantly larger than the wind barrier will not be modified by the barrier. Likewise, it is also assumed that the wind noise at the surface of the barrier mostly influences contributions at higher frequencies, since these frequencies correspond to turbulence scales on the order of the screen size and smaller.

$$\left|P_c(0,f)\right|^2 = \begin{cases}\left|P_{TS-Out}(0,f)\right|^2, & 0 < f \le f_{trans}\\ \left|P_{TS-In}(0,f)\right|^2 + \left|P_{TT-In}(0,f)\right|^2 + \left|P_{Surf}(0,f)\right|^2, & f \ge f_{trans}.\end{cases} \tag{3.31}$$

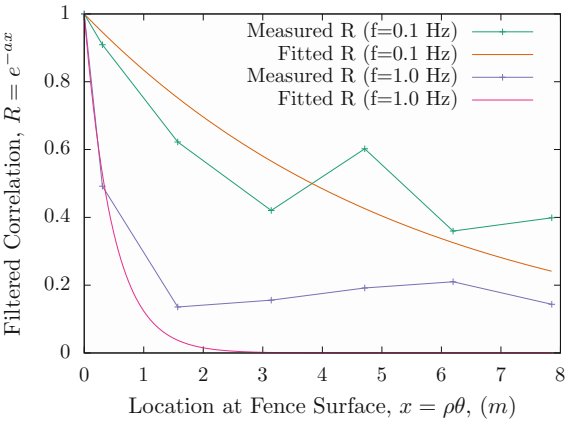

Fig. 3.26 Measured correlations around the surface of the 30% porous fence that have been filtered into octave band frequencies, and their respective fits to the form $R_i = e^{-ax}$

A reasonable hypothesis for the transition frequency is determined by considering when a volume enclosed by a wavelength, V_λ, is equal to 100 times the volume enclosed by the windscreen device, V_{ws}, or

$$V_\lambda = 100 V_{ws} \tag{3.32}$$

where the volumes of a wavelength, cylindrical and hemispherical windscreens of radius, r, and height, h, are respectively,

$$V_\lambda = \frac{2}{3}\pi\lambda^3 \tag{3.33}$$

$$V_{cylindrical} = \pi r^2 h \tag{3.34}$$

$$V_{hemisphere} = \frac{2}{3}\pi r^3. \tag{3.35}$$

Substituting Eqs. 3.33, 3.34, and 3.35 into Eq. 3.32 and solving for the wavelength, λ, gives the transition points for the wind fence (cylindrical) and fabric dome (hemispherical) as,

$$\lambda_{cylindrical} = \sqrt[3]{150 r^2 h} \tag{3.36}$$

$$\lambda_{hemisphere} = \sqrt[3]{100 r^3}. \tag{3.37}$$

For the predictions for the 2.9 m tall and 5.0 m diameter wind fence enclosures and the Sunbrella Sling ARL fabric dome shown in Fig. 3.27 this gives wavelengths of approximately 12.0 and 9.4 m, respectively, or about four times the height of the devices.

The predictions for the individual contributions of the three regions (a, c, and e plots) and the sum of the predictions (b, d, and f plots) are shown in Fig. 3.27; where plots (a–b) and (c–d) show the predictions for a 2.9 m tall and 5.0 m diameter wind fence at 30 and 40% porosities respectively and plots (e–f) show the predictions for the Sunbrella Sling ARL Dome. The individual contributions are shown in frequency space to show their relative sizes in the space in which they are summed, and the summed predictions are shown in wavenumber space to allow for easier comparison to other plots in this chapter.

As demonstrated by the data, the unperturbed flow contributes only at very low frequencies where the enclosures —wind fence or ARL dome—are not very effective. The turbulence due to the surface and interior flows for the enclosures contribute primarily at the middle frequencies with the relative magnitude of the contributions depending on the porosity of the wind fence. This is especially true for the ARL domes, where the interior contribution is completely negligible, and the surface contribution dominates for nearly the entire measured spectrum. The agreement between the calculated levels and the measured wind noise levels is rea-

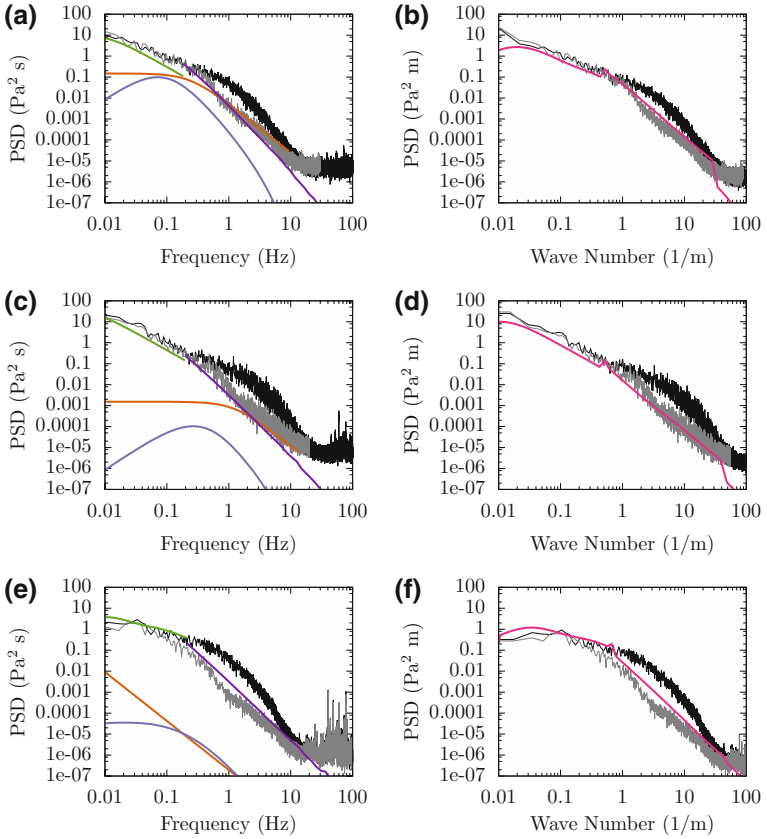

Fig. 3.27 Measurements and predictions for the three regions shown in Fig. 3.25. Plots **a**, **c**, and **e** show the individual components along with the measured data from inside (gray) and outside (black). In the left side plots, the components are interior turb–turb (orange), interior turb–shear (blue), Surface (purple), and Undisturbed (green). Plots **b**, **d**, and **f** show the same measured data with the sum of the three components (magenta)

sonable considering the approximate source description and limited measurement of the correlation lengths. The description certainly provides a good understanding of the contributing mechanisms for wind noise generation and reductions.

3.5 Conclusions

The results of the four studies presented in this study show that large porous wind fences and porous domes are effective in reducing wind noise at infrasonic frequencies while not affecting the coherence and wave shape of infrasonic waves. The

results of Sects. 3.3.1, 3.3.4, and 3.4 can be used to design wind fences or domes to achieve given wind noise reduction levels for differing meteorological conditions. The cylindrical fences produce slightly higher reductions than the domes, but the domes completely enclose the sensor and offer better environmental isolation and security. Achieving the reduction at lower frequencies requires reasonably large structures since the source region for the shear turbulence interaction pressure is large. The theory and results of Abbott and Raspet indicate that a stringent requirement for the lowest frequency of interest be that the height h be approximately equal to the inverse wavenumber. Pipe arrays are effective for low-frequency measurements but are severely band limited and require regular maintenance. Porous domes offer good waveform fidelity across a very large band. Construction of domes large enough to provide signal enhancement down to 0.1 or 0.2 Hz is feasible and can potentially provide more robust wind noise reduction than systems currently being used.

References

Abbott J (2014) Optimization of wind fence enclosures for infrasonic wind noise reduction. PhD thesis, University of Mississippi

Abbott J, Raspet R (2015) Calculated wind noise for an infrasonic wind noise enclosure. J Acoust Soc Am 138(1):332–343

Abbott J, Raspet R, Webster J (2015) Wind fence enclosures for infrasonic wind noise reduction. J Acoust Soc Am 137(3):1265–1273

Ballard HN, Izquierdo M (1965) Reduction of microphone wind noise by generation of proper turbulent flow. U.S. Army Electronics and Development AR262, DDC No. AD455966

Batchelor GK (1951) Pressure fluctuations in isotropic turbulence. Proc Camb Philos Soc 47:359–374

Collier SL, Raspet R, Noble JM, Alberts WCK, Webster J (2014) Analysis of wind noise reduction by semi-porous fabric domes. J Acoust Soc Am 136:2139

Collier SL, Noble JM, Alberts WCK, Raspet R, Coleman MA, Webster J (2014) Wind noise reduction for infrasound sensing. In: Proceedings of 2014 meeting of the Military Sensing Symposia (MSS) specialty group on battlefield acoustic and seismic sensing, magnetic and electric field sensors, Springfield, VA, 28–31 October 2014

Dillion K (2005) An investigation of wind noise over a flat plate. Master's thesis, University of Mississippi

Elliot JA (1972) Instrumentation for measuring static pressure fluctuations within the atmospheric boundary layer. Bound -Layer Meteorol 2:476–495

Fuchs HV (1972) Measurement of pressure fluctuations within subsonic turbulent jets. J Sound Vib 22(3):361–378

George WK, Beuther PD, Arndt REA (1984) Pressure spectra in turbulent free shear flows. J Fluid Mech 148:155–191

Hedlin M, Raspet R (2003) Infrasonic wind-noise reduction by barriers and spatial filters. J Acoust Soc Am 114(3):1379–1386

Kraichnan RH (1956) Pressure fluctuations in turbulent flow over a flat plate. J Acoust Soc Am 28:378–390

Marty J (2019) The IMS infrasound network: current status and technological developments. In: Le Pichon A, Blanc E, Hauchecorne A (eds) Infrasound monitoring for atmospheric studies, 2nd edn. Springer, Dordrecht, pp 3–62

Mialle P, Brown D, Arora N and colleagues from IDC (2019) Advances in operational processing at the international data centre. In: Le Pichon A, Blanc E, Hauchecorne A (eds) Infrasound monitoring for atmospheric studies, 2nd edn. Springer, Dordrecht, pp 209–248

Morgan S (1993) An investigation of the sources and attenuation of wind noise in measurement microphones. PhD thesis, University of Mississippi

Noble JM, Alberts II WCK, Collier SL, Raspet R, Coleman MA (2014a) Wind noise suppression for infrasound sensors. Army Research Laboratory Technical Report, ARL-TR-6873

Noble JM, Alberts WCK, Raspet R, Collier SL, Coleman MA (2014b) Infrasound wind noise reduction via porous fabric domes. J Acoust Soc Am 135:2409

Phelps WD (1938) Microphone wind screening. RCA Rev 3:203–212

Raspet R, Webster J, Yu J (2007) Spherical windscreen research. BAE Systems/US Army Research Labs Award Number RP6887 Final Report

Raspet R, Yu J, Webster J (2008) Low frequency wind noise contributions in measurement microphones. J Acoust Soc Am 123:1260–1269

Schomer PD, Raspet R, Brunner J, Marshall D, Wagner M, Walker D (1990) Reduction of wind noise for unattended blast noise monitoring. Noise Control Eng J 34:77–88

Trupea C, Yarin AL, Foss JF (2007) Springer handbook of experimental fluid mechanics. Springer, New York

Walker KT, Hedlin MAH (2009) A review of wind noise reduction methodologies. In: Pichon AL, Blanc E, Hauchecome A (eds) Infrasound monitoring for atmospheric studies. Springer, Dordrecht, pp 141–182

Waxler R, Di X, Talmadge C, Hetzer C, Kleinert D, Buchanan H, Bonner J, Reinke R (2012) Report on the results of an experiment in a quarry in the western suburbs of Boston. In: Inter-noise and noise-con congress and conference proceedings, Institute of Noise Control Engineering

Yu J (2009) Calculation of wind noise measured at the surface under turbulent wind fields. PhD thesis, University of Mississippi

Yu J, Raspet R, Webster J, Abbott J (2011a) Wind noise measured at the ground surface. J Acoust Soc Am 129:622–631

Yu J, Raspet R, Webster J, Abbott J (2011b) Improved prediction of the turbulence-shear contribution to wind noise pressure spectra. J Acoust Soc Am 130:3590–3594

Chapter 4
Geoacoustic Observations on Drifting Balloon-Borne Sensors

Daniel Bowman, Jonathan Lees, James Cutts, Attila Komjathy, Eliot Young, Kayla Seiffert, Mark Boslough and Stephen Arrowsmith

Abstract Infrasound microphones on free flying balloons experience very little wind noise, can cross regions that lack ground station coverage, and may capture signals that seldom reach the Earth's surface. Despite the promise of this technique, until recently very few studies had been performed on balloon-borne acoustic sensors. We summarize the history of free flying infrasound stations from the late 1940s to 2014 and report on results from a series of studies spanning 2014–2016. These include the first efforts to record infrasound in the stratosphere in half a century, the presence of a persistent ocean microbarom peak that is not always visible on the ground, and the detection of distant ground explosions. We discuss the unique operational aspects of deploying infrasound sensors on free flying balloons, the types of signals detected at altitude, and the changes to sensor response with height. Finally, we outline the applications of free flying infrasound sensing systems, including treaty verification, bolide detection, upper atmosphere monitoring, and seismoacoustic exploration of the planet Venus.

D. Bowman (✉) · M. Boslough · S. Arrowsmith
Sandia National Laboratories, Albuquerque, NM, USA
e-mail: dbowma@sandia.gov

J. Lees
Department of Geological Sciences, University of North Carolina, Chapel Hill, NC, USA

J. Cutts · A. Komjathy
Jet Propulsion Laboratory, California Institute of Technology, Pasadena, CA, USA

E. Young
Southwest Research Institute, San Antonio, TX, USA

K. Seiffert
Department of Geological Sciences, University of North Carolina, Chapel Hill, NC, USA

A. Le Pichon et al. (eds.), *Infrasound Monitoring for Atmospheric Studies*,
https://doi.org/10.1007/978-3-319-75140-5_4

4.1 Introduction

Geoacoustic sensor networks are almost always located on the Earth's surface (Marty 2019). There are compelling reasons, on the other hand, for fielding such networks in the free atmosphere. For example, motivations for free floating airborne acoustic stations include

- Dramatically reduced wind noise (Raspet et al. 2019)
- Placement in elevated ducts containing signals that do not reach the ground
- Greater range for direct acoustic arrivals
- Three-dimensional acoustic wave field above the ground is virtually unexplored
- The acoustic energy flux from the lower to the upper atmosphere has never been measured directly

Naturally, there are many technological and conceptual challenges to fielding sensors in the atmosphere. Constant atmospheric motion makes station keeping difficult, whereas powered flight systems, on the other hand, may introduce unacceptable noise levels. The temperature, solar radiation, and pressure environments as elevation rises can become increasingly hostile to delicate instrumentation. Most seismo-acoustic signal processing techniques assume a stationary receiver, virtually unattainable above the surface of the Earth. Deploying fixed aperture sensor arrays is very difficult because a rigid structure of the necessary size is prohibitively difficult to launch. Multiple separate units will continuously change their orientation with respect to each other and eventually drift apart.

These possibilities and challenges motivated a return to balloon-borne stations after a hiatus of over half a century. The series of experiments began as a proof of concept and evolved into the first operationally robust-free flying geoacoustic sensor networks since the advent of the digital era. This chapter describes the history, operational aspects, experimental results, and recent applications of free flying balloon-borne geoacoustic stations.

4.2 History

The first attempt to record acoustic waves above the Earth's surface began in the aftermath of World War II. After the discovery of the Sound Fixing and Ranging channel (SOFAR; Officer 1958) in the ocean, investigations commenced into a possible atmospheric analogue. The project, called MOGUL, began in 1946. Its objective was to detect the acoustic signature of Soviet nuclear blasts and ballistic missile flights at extreme range using balloon-borne microphones. Although the project only lasted about 4 years, it led to significant improvements in balloon technology. However, there is no information on the acoustic signals detected during the flights. Project MOGUL's enduring legacy is the Roswell Incident, in which one of the balloons landed in eastern New Mexico and was mistaken for a UFO (Weaver and McAndrew 1995; Peebles 1997).

Another series of balloon flights in the early 1960 s investigated acoustic waves between 0.2 and 150 Hz at altitudes up to 22 km. Over 30 flights were conducted. Some of these deployments consisted of one microphone hanging tens of meters beneath another one, allowing for direction of arrival estimation (Wescott 1964a; Coffman 1965).

The main finding of this experiment was that background noise in the 17–22 km altitude range consists of acoustic radiation from atmospheric turbulence (Wescott 1961, 1964a, b; Meecham and Wescott 1965). Time delays between channels on double sensor flights indicated that the waves originated from a planar region of randomly distributed acoustic sources below the balloons. Wescott (1964a) further observed a 30 dB background noise variation between day and night.

Spectrograms revealed signatures of piston engine aircraft above about 30 Hz (see Fig. 4.1). Doppler shifts and ground-reflected modes were both observed. Pulses of broadband signal were related to jet aircraft. Other, unknown events were recorded as well. These events were below 5 Hz and had amplitudes in the 1 Pa range. They occurred several times per hour in the summer and once every 1–2 h in the winter. They lasted from one minute to several minutes.

The next half century saw very few attempts to record geoacoustic signals above the surface of the Earth. Microphones on dropsondes were used to capture blast waves from underground and surface explosions (Banister and Hereford 1991) and sensors on tethered aerostats were employed to quantify sonic booms from experimental aircraft (Veggeberg 2012; Naka et al. 2013). Research into free flying geoacoustic arrays began again in 2014 and is presently ongoing; results from this work comprise the remainder of the chapter.

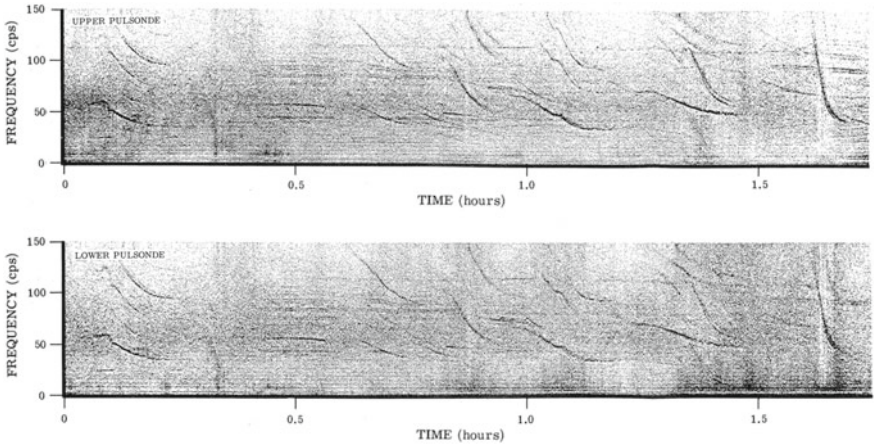

Fig. 4.1 Spectrograms from a double-sensor balloon flight on February 28, 1961 presented in Wescott (1964a)

4.2.1 Recent Progress

4.2.1.1 The HASP 2014 and 2015

Geoacoustic research in the stratosphere recommenced in 2014 as part of the High Altitude Student Platform (HASP). The HASP is an annual zero pressure balloon flight from Ft. Sumner, New Mexico, that carries up to 12 student payloads into the stratosphere for 5–29 h depending on atmospheric conditions (Guzik et al. 2008). Geoacoustic payloads were deployed on the 2014, 2015, and 2016 flights (Fig. 4.2). Instrumentation on the HASP 2014 consisted of a single Omnirecs Datacube digitizer, located on the gondola, with three InfraBSU microphones strung out on the "flight ladder" connecting the gondola to the parachute. The successful operation of the sensors and digitizer during the flight provided strong indication that geoacoustic data acquisition was possible at high altitudes. Initial results indicated that the stratosphere contained a highly unusual infrasound wave field (Bowman and Lees 2015a), but evidence from later experiments suggested that these signals were most likely from non-acoustic sources.

The HASP 2015 flight lasted much longer (about 29 h) due to low- wind speeds in the stratosphere. Two Omnirecs Datacube digitizers and six InfraBSU microphones

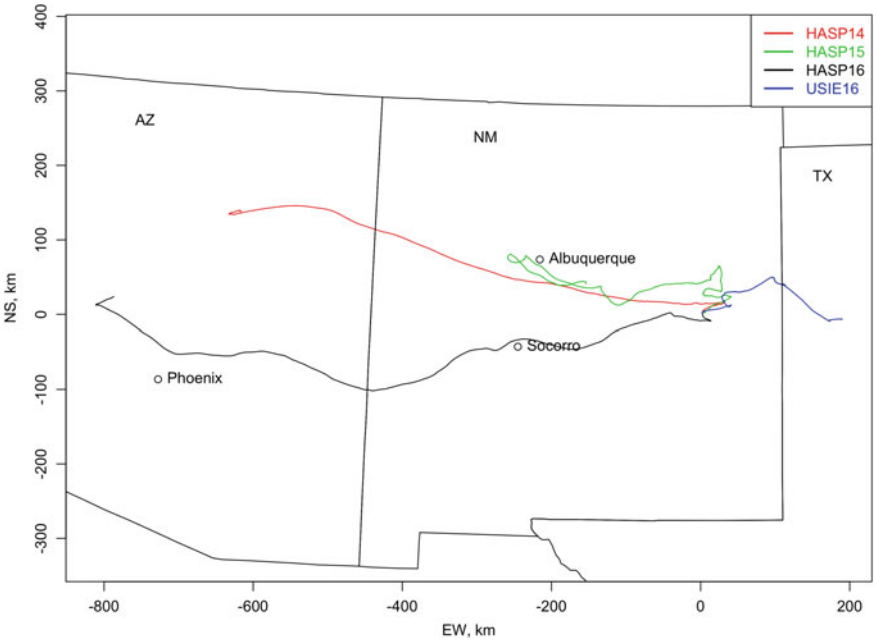

Fig. 4.2 Flight paths of the HASP and SISE/USIE balloon flights

were deployed, five on the flight ladder and one on the gondola. Two Gem infrasound sensor/loggers developed by Boise State University (see Anderson et al. 2018) were also on board. A spectral peak in the ocean microbarom range was identified during the quietest period of the flight (Bowman and Lees 2016). However, results from the HASP 2015 showed, again, severe interference from non-acoustic sources, which led to identification of this interference on the HASP 2014 as well (Bowman 2016).

4.2.1.2 The 2015 Weather Balloon Flight

Concerns about electronic interference experienced by the HASP 2014 and 2015 experiments prompted a new sensor/digitizer design that eschewed long analog signal cables, introduced a mechanically disabled "control" microphone, and implemented a microphone pair with reversed pressure polarities. This sensor trio was designed to rigorously distinguish between true pressure fluctuations and spurious signals. They were flown to an altitude of 28 km on a continuously ascending latex weather balloon over central North Carolina in Fall 2015. The design worked as expected. It also recorded the burst of the weather balloon at the top of its trajectory and confirmed a drop in wind noise amplitude at certain elevations as had been seen on the first two HASP flights. The three-component microphone configuration pioneered during this flight directly led to the successes of three flights in 2016.

4.2.1.3 The HASP 2016

The HASP 2016 was designed to distinguish between pressure signals and those induced by other phenomena. Two independent payloads were flown, each configured using the design tested on the weather balloon as described above. One consisted of an Omnirecs Datacube with three InfraBSU infrasound microphones contained in a small box on the gondola, and the other consisted of a Trimble Ref Tek 130 digitizer with three InfraBSU microphones and a triple-axis accelerometer located in a box attached to the flight ladder. The suspicious signals recorded on the first two HASP flights were absent, and a prominent ocean microbarom peak was present through most of the flight. Thus, the HASP 2016 successfully demonstrated the operation of a reliable geoacoustic sensor network in the stratosphere.

4.2.1.4 SISE/USIE

Previous experiments lacked "ground truth" acoustic sources with which to evaluate the detection thresholds of balloon-borne geoacoustic sensors. Thus, an active source experiment was fielded during Fall 2016. The Stratospheric Infrasound Sensitivity Experiment (SISE) (Young et al. 2016) and the UNC-Sandia Infrasound Experiment (USIE) were included as secondary payloads aboard a Columbia Scientific Ballooning Facility zero- pressure flight out of Ft. Sumner, New Mexico (Fig. 4.2). The SISE

payload was mounted on a boom extending from the gondola. It consisted of ten differential pressure transducers, five of which contained mechanical filters similar to those used in InfraBSU microphones. Data were digitized using a custom board. The USIE payload was located beneath the flight deck of the gondola. It consisted of two Omnirecs Datacube digitizers, five InfraBSU microphones (one control, two with normal polarity, two with reversed polarity), and a Chaparral 60 microphone. See Sect. 4.5.1 for an explanation of "control" microphones and the polarity reversal method. In addition, a prototype solar hot air balloon carrying a lightweight Gem infrasound acquisition system (Anderson et al. 2018) was launched about an hour after the zero pressure balloon. An extensive network of ground geoacoustic stations was deployed in the expected flight path of the zero pressure balloon and near the blast site.

On the day of the flight, three 3000 lb ANFO detonations (2400 lb TNT equivalent) were carried out at the Energetic Materials Research and Testing Center (EMRTC) in Socorro, New Mexico. One shot was performed at 1800 UTC, the second at 2000 UTC, and the third at 2230 UTC. All three shots were detected by instrumentation on the zero pressure balloon, and the second was detected by the Gem on the solar hot air balloon. The solar hot air balloon was over 250 km from the blast site when it detected the second shot, and the zero pressure balloon was 395 km from the blast site when it recorded the third shot. No ground station further than 6 km from the blast site recorded the first shot, but the second two explosions were detected on a single ground station 180 km from the blast site. None of the ground stations near the zero pressure balloon's trajectory recorded any of the blasts.

4.2.1.5 ULDB 2016

A geoacoustics sensor package was included as a secondary payload on the NASA Ultra Long Duration Balloon (ULDB) flight launched from Wanaka, New Zealand on May 16, 2016. The package contained an Omnirecs Datacube digitizer with three infraBSU microphones: one control and reversed polarity pair. The ULDB landed in Peru on July 2, 2016 for a total flight duration of 46 days, including one circumnavigation of the South Pole (Fig. 4.3). The sensor package recorded data for 17 days, starting at about 5 min prior to launch. This time period included one circumnavigation of Antarctica. The data set returned by this experiment is the longest continuous acoustic recording in the stratosphere thus far. The ocean microbarom was present continuously, and other signals of unknown provenance were detected from time to time. The constant microbarom peak suggests that free flying microphones may be more consistently sensitive to far-field infrasound in this frequency range than stations on the Earth's surface. This is because local noise often obscures the ocean microbarom peak, particularly during the day (Bowman et al. 2005).

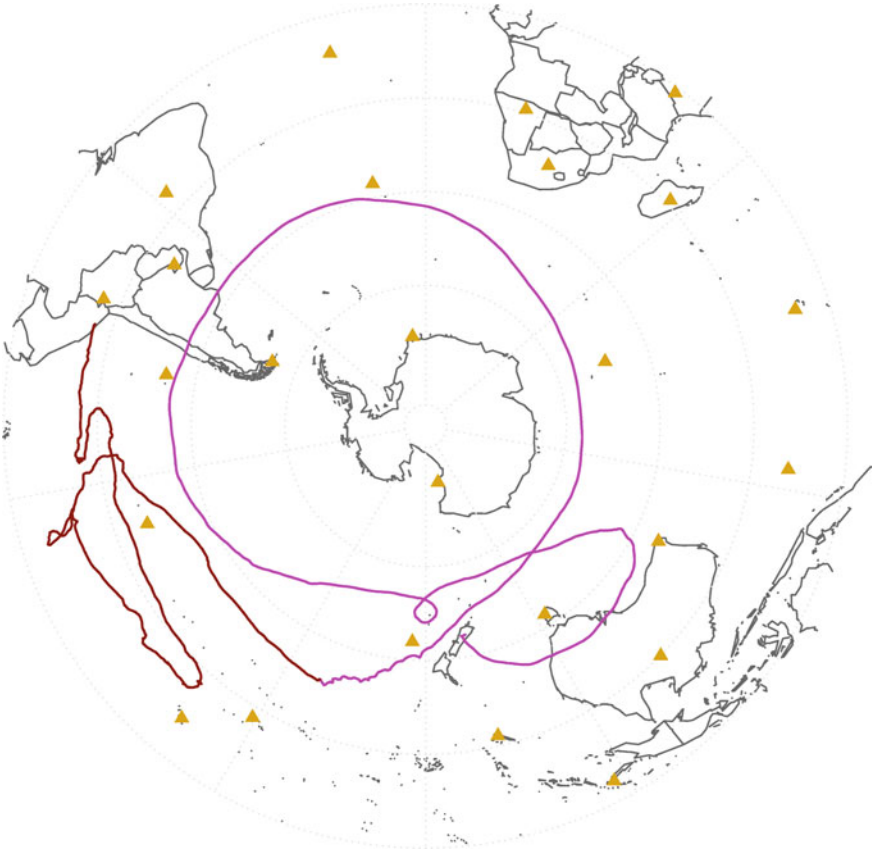

Fig. 4.3 Flight path of the 2016 ULDB experiment. The magenta line shows when the sensor package was operational. The red line shows the path of the balloon after the sensor ran out of battery power. The triangles denote International Monitoring System infrasound stations

4.3 Operational Aspects of Free Flying Sensors

4.3.1 Flight Systems

Balloons can drift at altitudes ranging from <1 km (Doerenbecher et al. 2016) to over 53 km (Saito 2014). Flight durations can range from a few hours to 744 days (Lally 1991). Balloon designs vary depending on altitude, flight duration, launch facilities, and cost. Since 2014, infrasound sensors have been launched on continuously ascending weather balloons, zero pressure balloons, superpressure balloons, and solar hot air balloons (see Figs. 4.4 and 4.5).

Fig. 4.4 A zero pressure balloon (left) and a solar hot air balloon (right) launched during the SISE/USIE infrasound experiment

- Weather balloons consist of an elastic envelope that expands as the balloon rises. Eventually, the balloon bursts, and the payload parachutes back down to Earth. These flights are seldom more than 3 h long and reach altitudes of 28–40 km.
- Zero pressure balloons consist of rigid envelopes with vents. When the balloon reaches its neutral buoyancy, or "float" point, excess gas is vented to prevent pressurization of the envelope. These balloons can fly for several days, but must drop ballast during the night to maintain flight. Therefore, time aloft is limited by the amount of ballast on board.
- Superpressure balloons are unvented, retaining their lift gas through the day/night cycle and eliminating the need for ballast. They can fly for over 2 years (Lally 1991). For additional details on the performance and dynamics of zero-pressure and superpressure balloons, see Yajima et al. (2009) and Morris (1975).
- Solar-powered hot air balloons utilize a dark-colored envelope to absorb sunlight, heating the air inside the envelope enough to gain positive lift (Bowman et al. 2015). They fly as long as the sun shines and land after sunset.

See Fig. 4.6 for time/altitude plots of infrasound payloads on the balloon types described above.

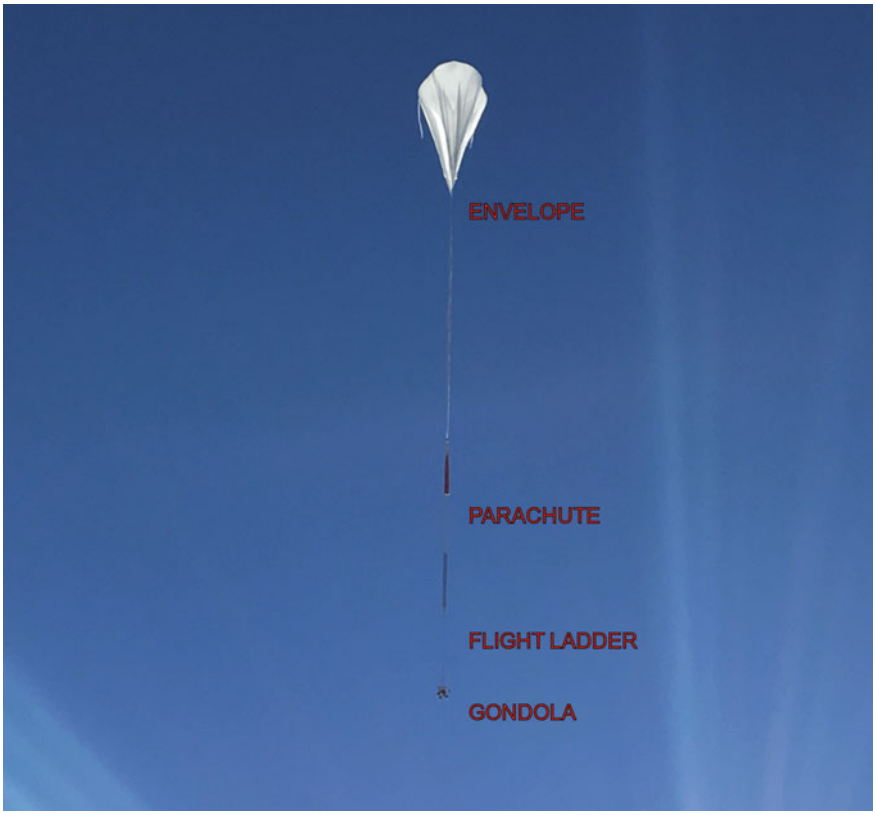

Fig. 4.5 The SISE/USIE zero pressure balloon several minutes after launch. Instrumentation on the HASP flights was located on the gondola and attached to the flight ladder, whereas microphones on SISE/USIE and the ULDB were located on or in the gondola. The distance from the gondola to the top of the balloon is approximately 150 m

4.3.2 Environmental Considerations

Geoacoustic sensors on balloons experience very different pressure and temperature conditions than those on the surface. They can experience high levels of interference from other instrumentation on the balloon (tracking and telemetry systems, other payloads) and possibly the ambient environment as well (cosmic rays). This can affect survivability of instrumentation at altitude, maintenance of appropriate signal-to-noise ratios, and the ability to distinguish between acoustic waves and spurious phenomena.

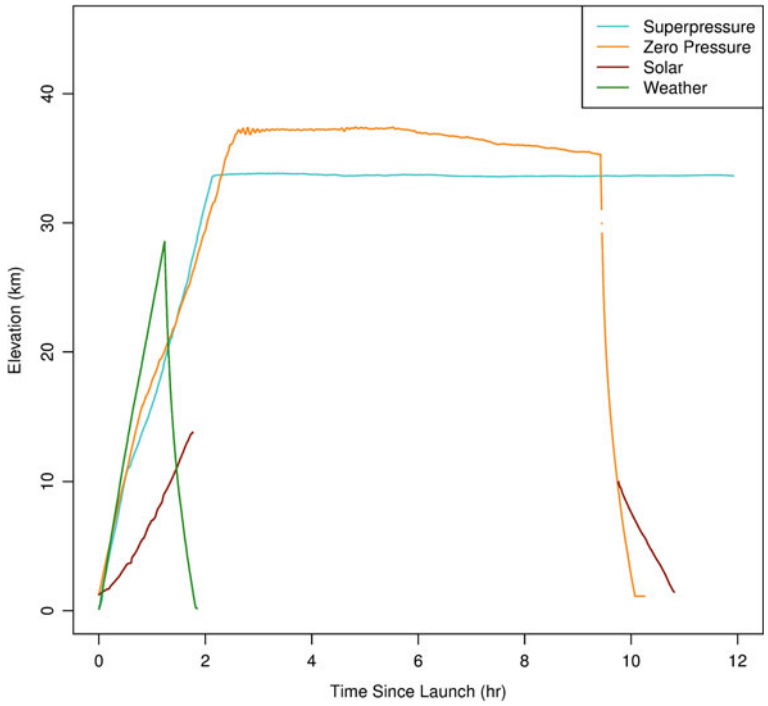

Fig. 4.6 Elevation profiles for four different types of balloons recently used in geoacoustic studies. The superpressure balloon example is from the first few hours of the 2016 ULDB flight. The zero pressure and solar hot air balloons are from the 2016 SISE/USIE experiment. Note that the solar hot air balloon lost GPS tracking above 13.8 km. The weather balloon trajectory is from the test flight in 2015

4.3.2.1 Pressure and Temperature

Ambient pressure decreases by over two orders of magnitude from sea level to the middle stratosphere. This changes the thermal resilience of instrumentation, affects the frequency response of infrasound sensors, and impacts the absolute pressure amplitude of acoustic waves. As air density decreases, thermal transfer changes from convection dominated to radiation dominated. As a consequence, the actual air temperature is much less significant than objects' albedo and exposure to sunlight. Dark-colored objects heat up dramatically during the day, whereas temperatures after sunset plummet to levels seldom achieved on the Earth's surface. For example, a black square exposed to sunlight reached over 84 °C during the HASP 2014 flight. At night on the HASP 2015, flight ladder instrumentation dropped to −55 °C. Furthermore, instrumentation that relies on air flow for cooling may become dangerously warm. Thus, it is important to perform pre-flight thermal/vacuum testing to ensure instrumentation can survive extreme temperatures and low pressures. For example, all HASP payloads must operate nominally during a 6–8 h test in which temperature is

varied from −40 to +40 Celsius at surface and stratospheric pressures before being allowed to fly.

Microphones are extremely sensitive to minute pressure fluctuations by design. Their calibrations may be invalid in the low-pressure environment at altitude. Also, they can be damaged by the rapid pressure drop during ascent or the even more rapid pressure rise during descent. All recent experiments have utilized vented backing volume microphones for this reason. This allows the sensors to equilibrate once they reach the float portion of the flight, although they are often saturated during ascent and descent.

A vented backing volume microphone has one chamber open to ambient pressure and another chamber connected to the atmosphere by a capillary tube. The chamber/capillary tube combination creates the acoustic equivalent of a resistor–capacitor circuit, allowing long period pressure fluctuations through but blocking high-frequency ones. A diaphragm between the open and partially blocked chamber deflects in response to unequal pressures between the two, creating a voltage that is then digitized. The result is a mechanical high- pass filter (Marcillo et al. 2012; Mutschlecner and Whitaker 1997). The corner period of this filter is

$$T = 2\pi RC \tag{4.1}$$

where R is the acoustic resistance of the capillary tube and C is the acoustic capacitance of the backing chamber.

Assuming Poiseuille flow, the acoustic resistance is

$$R = \frac{8\eta}{\pi r^4} l \tag{4.2}$$

where η is the shear viscosity of the fluid, r is the radius of the capillary tube, and l is the length of the capillary tube (Mutschlecner and Whitaker 1997).

The acoustic capacitance of the backing chamber is

$$C = \frac{V}{\gamma \bar{P}} \tag{4.3}$$

where V is the backing volume, γ is the adiabatic gas constant, and $\bar{P}$ is ambient pressure. Since acoustic capacitance is inversely proportional to ambient pressure, microphones on high-altitude balloon flights often have orders of magnitude greater corner periods than the same microphone design at sea level (see Fig. 4.7). Acoustic resistance is somewhat sensitive to temperature due to variations in shear viscosity, but is relatively insensitive to pressure changes (Ames Research Staff 1953). Thus, the capacitance term dominates corner frequency variations with altitude. Sensor frequency response may vary with decreasing air density due to the upward shift in the isothermal/adiabatic transition, but the effect is likely small and will not affect the corner period (see Mentik and Evers 2011, Sect. 4). However, a sensor characterization study in a pressure chamber capable of reproducing stratospheric conditions

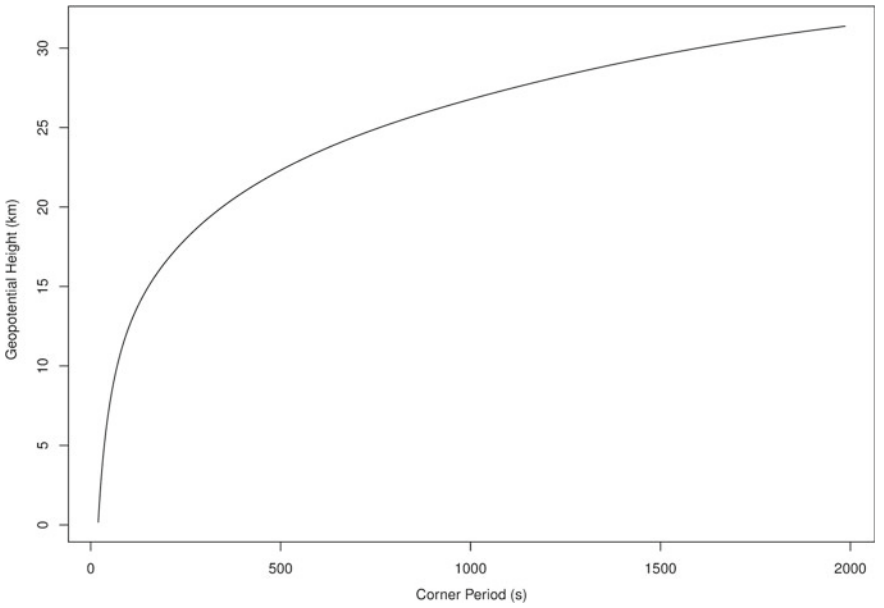

Fig. 4.7 Model of the frequency response of a vented infrasound microphone with altitude. The microphone has a 20 s corner period at 1000 mb. The pressure/height profile is from the August 9, 2014 18Z analysis Global Forecast System model run over Chapel Hill, North Carolina. This figure originally appeared in Bowman (2016)

would be valuable. An initial attempt is reported in Bowman (2016), but the experiment would have benefited from a better controlled acoustic source.

4.3.2.2 Signals from Non-Pressure Sources

Infrasound sensors on high-altitude balloons may acquire signals that are not related to pressure fluctuations. These include amplitude spikes and narrow band, constant frequency signals. Spikes tend to occur during the latter part of the ascent and throughout the float period. They vary with instrument position on the flight system. For example, during the SISE/USIE flight, they were present on the SISE payload, which was hanging from a boom projecting from the gondola. They were not seen on the USIE payload, which was beneath the flight deck and behind metal solar shields. They were observed on the HASP 2014 and 2015 flights, in which microphones and digitizers were relatively unshielded, but not during the HASP 2016, when all equipment was in thicker containers. The cause of these spikes is unclear, but they are probably not related to mechanical jostling or temperature variations. This is because the SISE and USIE payloads were on the same gondola, and SISE was very well insulated; yet SISE-detected spikes and USIE did not. We speculate that they may be due to cosmic rays, which increase with altitude (see Dawton and

Elliot 1953), static electric discharge, or lightning-induced electromagnetic interference (Anderson et al. 2014) in some cases.

Narrow band, constant frequency signals were observed during the latter part of the HASP 2015 flight. They were polarity reversed between a pair of consistent pressure polarity microphones, indicating that they might be related to electromagnetic interference. A sporadic 10 Hz signal was seen on the ULDB 2016 flight as well. This is in the frequency range of vibrational modes observed on other balloon missions (Barthol et al. 2011), although it could be related to electromagnetic interference like that on HASP 2015 as well.

Another, more enigmatic signal class was observed on the HASP 2014 and 2015 flights (see Fig. 4.8). They do not occur during thermal/vacuum tests or full system checkouts at ground conditions prior to launch. They are quite complex and hard to explain; indeed they led Bowman and Lees (2015a, 2016) to speculate that they were a new class of acoustic waves not seen on the Earth's surface. However, reasons for attributing them to non-pressure signals include

- No phase shift across a pair of microphones vertically separated by almost 15 m
- Only present on deployments with long analog cables between sensors and digitizers (HASP 2014 and 2015)
- Not observed in over 2 weeks of flight data in 2016 (including HASP 2016)
- Presence of other interference such as spikes and polarity reversed narrow band signals
- Installation of high-power transmitting equipment on the balloon gondola
- No known Earth surface analogue

Difficulties with this explanation include

- The narrow band signals are all below 30 Hz
- Signals have the correct pressure polarity
- Similar gliding frequency bands may be present in spectrograms shown in Wescott (1964a)
- Generation mechanism of electromagnetic interference in this frequency band is unclear
- Acoustic wave field at this altitude is poorly known

The origin of these complex, narrow band signals is difficult to determine. The HASP scientific payload contained a variety of student experiments, including electric motors and radio transmission equipment, that could have generated electromagnetic radiation. The HASP gondola telemetry system utilizes high-power transmitters as well. Interference from ground-based anthropogenic electromagnetic signals is possible, but the diagnostic 60 Hz AC power peak is not present in balloon spectra. Natural radio sources such as Schumann resonance are in the appropriate frequency range (Barr et al. 2000), but do not have the gliding characteristics shown in Fig. 4.8. The only meteorological differences between the HASP 2014 and 2015 and other New Mexico flights (the HASP 2016, SISE/USIE) was the presence of thunderstorms in the former case. This may be a clue about the cause of these signals, acoustic or otherwise. Regardless, they make detection of lower amplitude acoustic

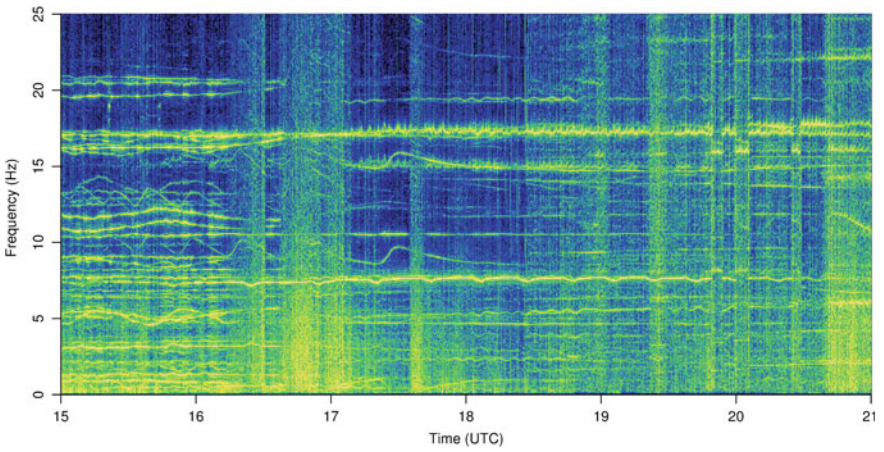

Fig. 4.8 Narrow band signals recorded during the HASP 2014 flight on August 9, 2014. Their cause is unknown

signals very difficult. Until the cause of these signals is known for certain, investigators should avoid using long analog cables during balloon infrasound deployments. If cabling is required, it should only convey digital signals and be well shielded. Alternatively, fiber optic or wireless systems could be used instead. It is also possible, albeit unlikely, that these unusual signals represent true acoustic waves that were not present on later flights.

4.3.3 Payload Design

Sensor packages designed for free flight operate under very different environmental conditions and operational restrictions than those on the ground. The need for thermal insulation must be balanced with the requirement for at least part of the package to be in direct contact with the atmosphere. The insulation material and outer covering of all equipment must be light colored or kept completely out of sunlight to prevent overheating. It is also important to prevent direct exposure to the night sky to reduce radiation loss. Despite these measures, equipment may experience extreme temperatures from time to time, and it is important that all components are able to survive such variations.

Objects on balloons can experience sudden accelerations during launch, flight termination, and landing. Thus, onboard equipment should be able to remain in place and functioning through brief periods of up to 10 g acceleration. Equipment should be protected from being crushed or shattered in case of impact on a hard surface, particularly if data are stored locally rather than telemetered. It can take days to

weeks to recover equipment if it has landed in a remote area, and water landings are possible as well.

The height ceiling of GPS chips used for timing, vibrational, and rotational modes of the flight system, and proximity to high-energy systems such as radio transmitters used for telemetry are all considerations for balloon-borne systems. Electronics on high-altitude balloons are susceptible to interference, although the source of these signals is presently unclear (recall Fig. 4.8). Thus, it is imperative to take a conservative approach. Cable length should be as short as possible, and the use of long signal wires carrying analog outputs should be strictly avoided. Shielding of the entire sensor/digitizer package using metal plates and aluminum foil appears to be an effective means of reducing spurious signals. Including a control and an opposite pressure polarity pair of microphones as described in Sect. 4.2.1.2 serves as a final sanity check.

For payloads included on large zero pressure or superpressure balloons, the entire sensor/digitizer package can be included in a hard-shelled box. Metal sides provide electronic shielding; alternatively plastic boxes can be lined with aluminum foil or plates. The exterior of the box should be painted white or covered in white tape to avoid excessive solar heating. The interior of the box should be padded with dense Styrofoam or other thermal insulation that will not off-gas at low pressures. All equipment should be securely attached to anchor points on the box. Tubes leading from microphone ports to the outside of the box can provide atmospheric coupling without sacrificing thermal control. However, it is important to make sure no object is airtight (including the box itself) to allow pressure to equalize during ascent and descent. Ideally, the instrument enclosure should be placed inside the gondola chassis to provide additional thermal control and protection against violent landings. See the left panel in Fig. 4.9 for an example.

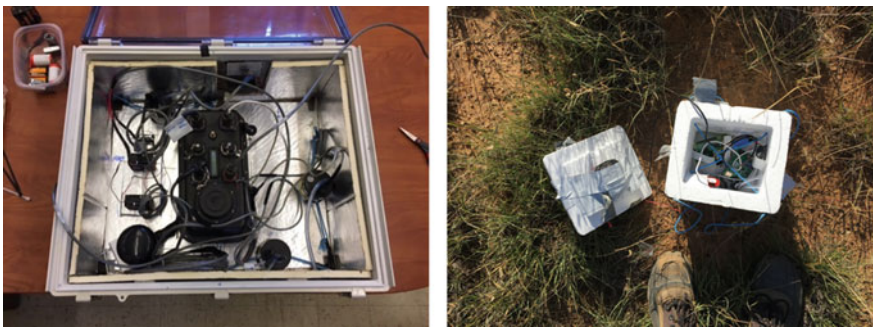

Fig. 4.9 An infrasound payload for the HASP 2016 flight (left). Note the hard-shelled box, inner layer of insulation, and secure equipment mounting. The entire enclosure was covered in white tape before flight. The SISE/USIE solar balloon payload box (right) was constructed from the inner lining of a medical-grade foam shipper. This photo was taken during recovery of the payload and envelope several weeks after landing. The box was opened prior to taking the photo

The weight of the sensor/digitizer package is an extreme constraint when using low-lift flight systems like solar hot air balloons. In this case, reasonably robust instrumentation boxes can be constructed from medical-grade foam shipping boxes (see Fig. 4.9, right panel). These boxes are made from high-density Styrofoam that have survived 46 days in the stratosphere without noticeable off-gassing. They can be damaged upon landing, however, and thus equipment inside them should be water resistant to the extent possible.

4.4 Pressure Signals Recorded During Flight

4.4.1 Wind Noise

Wind noise is virtually nonexistent during the float phase of a high altitude balloon flight. This is because the flight system is a quasi-Lagrangian particle that is advected along at the mean wind velocity, resulting in exceptionally low air flow across the microphone ports (Raspet et al. 2019). Transient wind-related signals are possible even at float due to layers of turbulence (Haack et al. 2014) and the passage of gravity waves (Zhang et al. 2012), although their pressure amplitude will be several orders of magnitude lower than equivalent wind at the ground due to decreased air density at altitude. These effects may be present on existing flights although they have not been identified yet. Calculations by Bowman and Lees (2015a) indicate that vortex shedding could occur depending on the level of wind shear across the flight train, although this has not yet been seen in the data either.

Although wind noise dominates the ascent and descent, it drops rapidly with altitude. Figure 4.10 shows RMS amplitudes and a spectrogram of pressure signals recorded on infrasound microphones on a weather balloon. Wind noise is very high immediately after launch, but decreases with altitude due to progressively lower air density. A decrease in both the magnitude and variance in wind noise is observed at about 22 km altitude (just after 1 h in the spectrogram). This occurs at approximately this altitude on much larger balloons as well (the HASP, for example). The reason for this decrease may have to do with lower turbulence in the stratosphere, lower levels of wind shear, or a change in the properties of the balloon wake with decreasing Reynolds number. Results from this flight suggest that it may be possible to detect far-field acoustic signals even on an ascending balloon provided the detectors are above about 22 km. Wind mitigation strategies, such as soaker hoses like those used on ground stations, might further improve an ascending balloon's detecting capability. Methods designed to avoid the balloon's turbulent wake could be employed as well (see Barat et al. 1984).

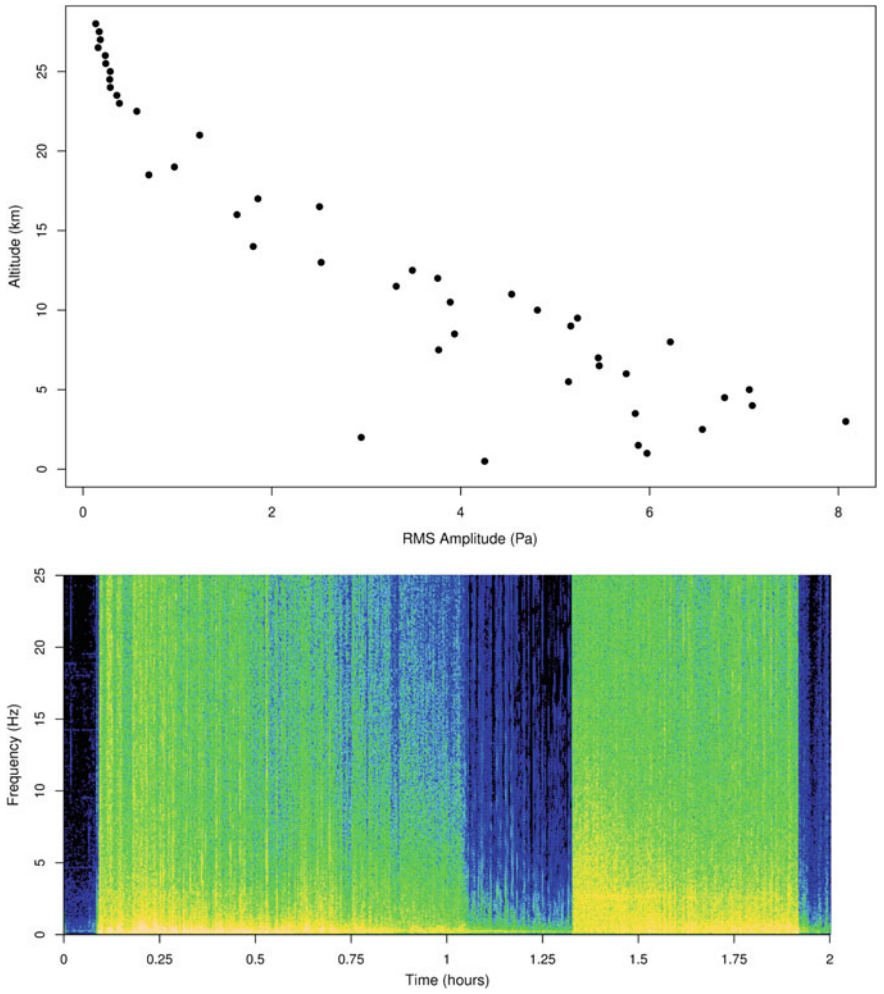

Fig. 4.10 RMS amplitude in the 0.1–20 Hz band versus elevation during ascent (top) and flight Fourier spectrogram (bottom) of pressure signals recorded on a balloon. Launch occurs at about 0.1 h after the start of the spectrogram. The balloon reaches 22 km just after the 1 h mark; this corresponds with the change in trend on the RMS amplitude plot. The balloon bursts at about 1.3 h and the payload lands just before the 2 h mark

4.4.2 Long Period Oscillations

Vertical motion of the flight system will result in pressure fluctuations. Assuming the motion is small, the signal will equal the altitude change multiplied by the local pressure gradient. Since the gradient is negative, a rise in altitude results in a drop in pressure, and vice versa. Therefore, long period pressure signals that are 180° out of phase with elevation are a diagnostic of vertical balloon motion.

The presence of a resonant peak in balloon motion spectra has been observed in several previous studies. Anderson and Taback (1991) described sinusoidal motion of an ascending zero pressure balloon, Morris (1975) discussed "overshoot" motion of zero pressure balloons upon reaching float, and Quinn and Holzworth (1987) illustrate the spectral peak of neutral buoyancy oscillations of superpressure balloons. In theory, this peak should lie just below the Brunt–Vaisälä frequency of the local atmosphere (Anderson and Taback 1991).

Pressure data from the three HASP flights as well as the USIE experiment confirm that the dominant oscillatory mode has a period of about 5 min, consistent with Brunt–Vaisälä frequencies for the middle stratosphere (Zhang et al. 2012). The highest amplitude oscillations occur just after attaining float, where they can have amplitudes of tens of Pa. The motion decays over time, but may last up to 45 min. Similar oscillations were excited during a series of ballast drops during the HASP 2015 flight, where amplitudes were under 10 Pa. Unlike the sporadic motion of the zero pressure flights described above, the superpressure and solar hot air balloons oscillated virtually continuously (Fig. 4.11). While the pressure amplitude on the superpressure balloon was below 10 Pa, the solar hot air balloon experienced up to 30 Pa excursions during the time period examined. Examination of the long period pressure power spectrum of the superpressure balloon indicated a resonant peak near the typical mid-stratosphere Brunt–Vaisälä period, as expected.

Since an object floating at neutral buoyancy behaves as a damped harmonic oscillator, energy in the resonant frequency range must be added to sustain its motion. This indicates that forcing functions, such as gravity waves, may have acted to

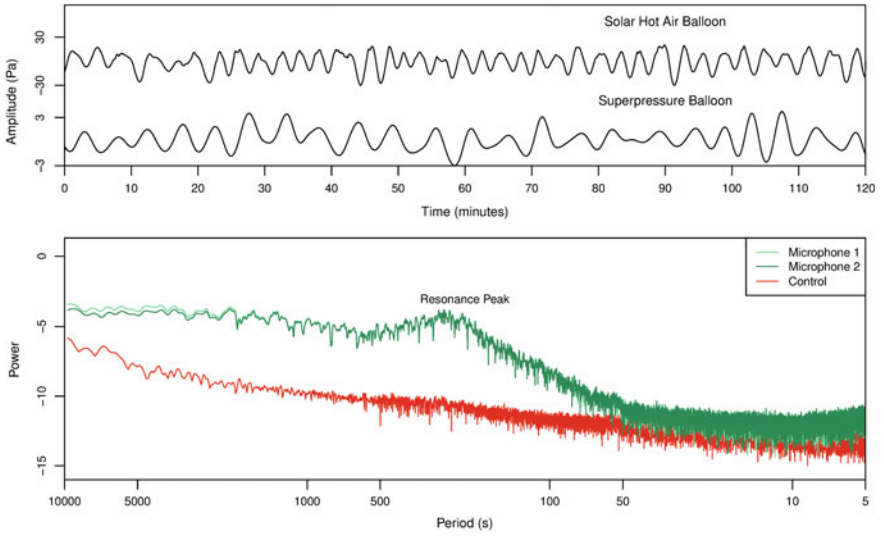

Fig. 4.11 Waveforms of long period pressure oscillations on the SISE/USIE solar hot air balloon at 15 km elevation and the 2016 ULDB superpressure balloon at 34 km. The spectra shows a 14 day Welch spectrum of long period motion on the 2016 ULDB superpressure flight

continuously excite the superpressure balloon. Since the solar hot air balloon was in a lower and more turbulent region, it may have received input from wind buffeting or even uneven heating due to envelope rotation. In this light, it is curious to note the comparatively undisturbed motion of zero pressure balloons; perhaps they are more efficiently damped or were simply not exposed to the same amount of forcing energy as the other two flights.

Pressure time series from these balloon flights have not been rigorously investigated for the presence of gravity waves, although such analysis may be promising and should be pursued in the future. However, the balloon resonant peak will obscure gravity wave characteristics in certain frequency ranges. Large pressure fluctuations have an impact on geoacoustic measurements as well: they may cause sensitive microphones to clip if their dynamic range is not sufficient. Sensors flying at stratospheric altitudes must either have a corner frequency sufficiently high enough to attenuate signals in the 100–300 second band or a dynamic range of >10 Pa.

4.4.3 Ocean Microbarom

The ocean microbarom is an ubiquitous infrasound signal generated by colliding surface waves in certain maritime regions (Landès et al. 2012; Waxler and Gilbert 2006; Ceranna et al. 2019). It has a frequency of 0.13–0.35 Hz and often travels great distances with minimal attenuation (Campus and Christie 2010). Microbarom detections on ground stations are strongly diurnal, with most occurring during the night. This is thought to be from lower wind noise during nocturnal hours (Bowman et al. 2005) and changes in propagation path due to semidiurnal thermospheric tides (Rind 1978). While microbaroms are often considered "noise" because they obscure signals of interest in their frequency range, they also serve as a useful reference signal to determine if infrasound sensors are operating as expected.

Spectral peaks in the microbarom range were observed on both the HASP 2014 and HASP 2015 flights (Bowman and Lees 2016), although noise in the frequency band of interest made them difficult to distinguish. However, clear ocean microbarom spectral peaks occurred on all three stratospheric flights in 2016 (ULDB 2016, HASP 2016, SISE/USIE) and on the SISE/USIE solar hot air balloon in the upper troposphere.

Figure 4.12 shows the ocean microbarom peak during the SISE/USIE experiment. The spectra were calculated over a 4.5 h period starting in early afternoon local time. The peak is entirely absent on local ground stations, consistent with the general lack of detections during the day reported in the literature. However, the ocean microbarom is evident on the solar hot air balloon (elevation approximately 15 km) and prominent on the SISE/USIE balloon (elevation 34 km). The amplitude difference between the two is likely a combination of atmospheric conditions (see Eq. 4.5) and background noise. Eight of the 14 ground sensors had high-frequency wind shrouds installed, but the lack of detection on the ground is still probably due to wind noise. Alternatively, the microbarom signal could be in an elevated acoustic duct during this time and thus not reaching the ground at all.

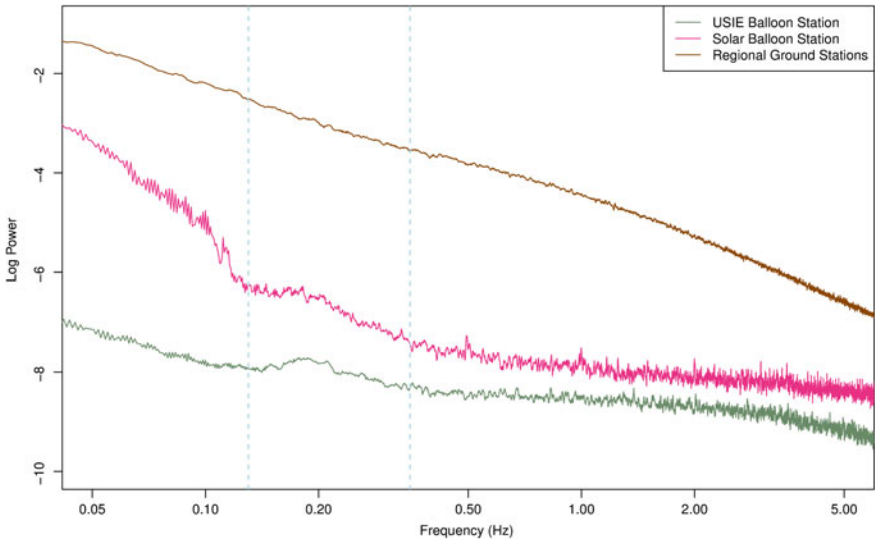

Fig. 4.12 Ocean microbarom peak recorded by airborne stations during the SISIE/USIE experiment. Each trace is a 10 min Welch spectrum from 1915 to 2345 UTC (1315 to 1745 local time), September 28, 2016. Five sensors were averaged together on the USIE balloon, one on the solar hot air balloon, and 14 channels across four locations on the ground near the balloons' flight path. Dashed blue line indicates the ocean microbarom frequency range per Campus and Christie (2010)

The microbarom is continuously recorded for the entirety of the 2016 ULDB experiment (see Fig. 4.13). The spectral power fluctuates by almost three orders of magnitude, indicating the possibility that the sensors flew very close to the source area during part of the flight. The peak is present throughout the day/night cycle, indicating that the lack of a microbarom peak during the day on ground stations is due to tropospheric rather than stratospheric phenomena. This is consistent with diurnal wind noise patterns.

4.4.4 Explosions

The SISE/USIE experiment was designed to test detection threshold of a free flying station with respect to distant sources. Three approximately 1000 kg TNT equivalent explosions were detonated while infrasound sensors were at float on a zero pressure balloon several hundred kilometers away. A prototype solar hot air balloon carrying a lightweight infrasound station was in flight near the zero pressure balloon as well. The zero pressure balloon was at an altitude of about 35 km, and the solar hot air balloon was at an altitude of about 15 km. Ground stations were deployed at distances of 5.8, 180, 260, 300, and 350 km, although the latter station was only active for the second two shots.

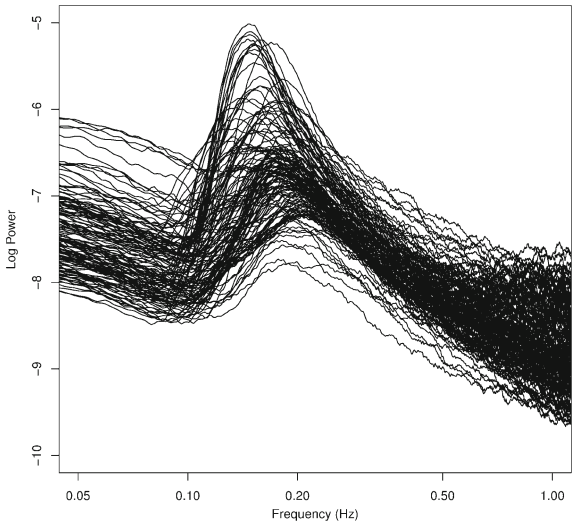

Fig. 4.13 Ocean microbarom peak recorded by the ULDB superpressure flight from Wanaka, New Zealand from May 18 to June 4, 2016. Each trace is a 10 min window Welch spectrum stacked over 3 h

The first blast was detected on the zero pressure balloon when it was 330 km away, however none of the ground stations farther than 6 km away captured the signal. This includes three stations lying between the blast site and the balloon. The station on the solar hot air balloon did not detect it either due to wind noise during ascent.

The signal recorded on the zero pressure balloon consisted of three arrivals. The first arrival traveled with a celerity of 290 m/s and the last at 280 m/s, both consistent with stratospherically refracted signals (Negraru et al. 2010).

The second blast was detected on the zero pressure balloon when it was 360 km away, and on the solar hot air balloon when it was approximately 300 km away from the source (Fig. 4.14). Ground stations 5.8 and 180 km away also detected the acoustic signal. Arrivals on the zero pressure balloon, the solar hot air balloon, and the ground station traveled at stratospheric celerities. The signal consisted of a single arrival on all four stations.

The third blast was detected on the zero pressure balloon when it was 395 km away from the source, but was not detected on the solar balloon. It was also observed on ground stations at 5.8 and 180 km away.

The SISE/USIE experiment was unique in that it detected signals from a known source. These signals resemble some waveforms detected on the superpressure balloon during its circuit of the southern hemisphere. Figure 4.15 compares the first shot in the SISE/USIE series with an event detected on the ULDB 2016 when it was about 1700 km east/southeast of New Zealand. The signal on the superpressure balloon is lower amplitude and lower frequency than that on SISE/USIE, but the time gap between the first and second arrivals is similar (15 s vs. 20 s). The rarefaction (negative) phase of the first arrival is higher amplitude than the compressional (positive phase) on both balloons. The second arrival appears shorter and more impulsive than the first arrival. The presence of multiple phases and large rarefactions

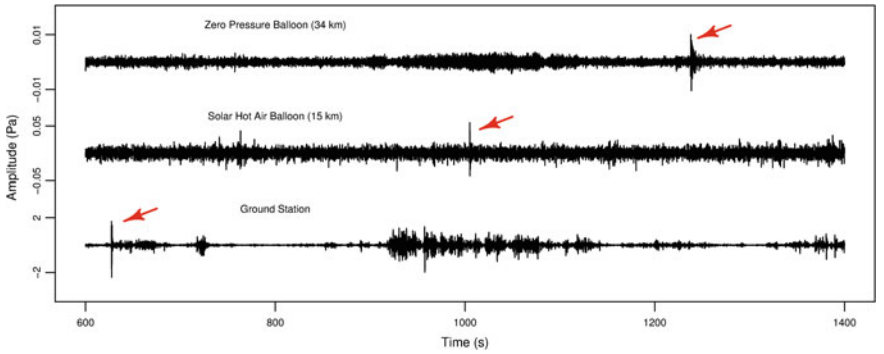

Fig. 4.14 A distant explosion captured by a solar hot air balloon in the upper troposphere and a zero pressure balloon in the middle stratosphere during the SISE/USIE experiment

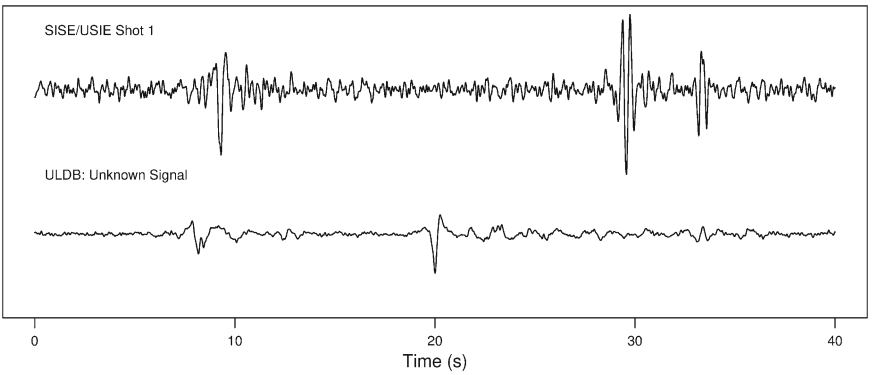

Fig. 4.15 The first shot in the SISE/USIE series recorded on a zero pressure balloon at 35 km elevation compared to a signal detected on the ULDB superpressure balloon. Peak-to- peak amplitude for the top and bottom signals were about 0.066 and 0.035 Pa, respectively

suggest that these signals are traveling along multiple paths through the atmosphere, some of which involve postcritical reflection. The lower frequency of the superpressure balloon signal indicates that the source was larger and/or further away than the SISE/USIE shot. However, the provenance of this waveform is highly speculative at present.

4.4.5 Other

The HASP 2016, SISE/USIE, and ULDB flights recorded many pressure fluctuations of unknown origin. Since data from these experiments were retrieved shortly before the time of writing, a detailed analysis of these events has not yet been performed.

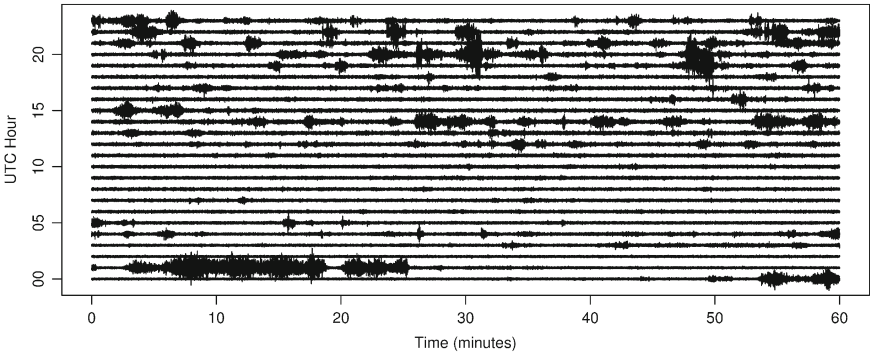

Fig. 4.16 A day of waveforms recorded on the ULDB. The trace starts at 00 UTC on May 29, 2016. Data were band passed between 0.1 and 5 Hz

In general, the events have frequencies below 10 Hz and occur anywhere from less than one to several per hour on the HASP 2016 and USIE/SISE flights.

Figure 4.16 shows pressure fluctuations recorded during 1 day of the ULDB flight. Although activity is quite variable on a tens of minutes timescale, pressure amplitudes seldom exceed 0.1 Pa peak to peak. Analysis of spectrograms indicates that there are several types of event occur during the flight. Several low-frequency (<5 Hz) broadband events occur per hour, typically lasting around 10 s or less. Discrete bursts that span the infrasound range can occur up to around 10 times per hour, though several hours can pass without a single one. There are a few episodes of sustained broadband events lasting up to 45 min as well, with most energy below 10 Hz. The occurrence of sporadic events below 5 Hz several times per hour is consistent with observations made by Wescott (1964a), but the other types were not mentioned. A definitive explanation for these pressure fluctuations awaits detailed analysis and perhaps future flights with anemometers and accelerometers on board. Cameras could also identify local disruptions to the flight system that generate pressure signals or even image a distant event responsible for an infrasound arrival.

4.5 Noise Sources, Detection Thresholds, and Other Considerations

4.5.1 Noise

Wind is the biggest contributor to noise levels on ground geoacoustic sensors in most locations (Walker and Hedlin 2010). However, a free floating balloon at neutral buoyancy in a stratified atmosphere is advected at the mean wind speed and experiences minimal differential air flow. Sources of localized wind, such as shear across the

flight line, gravity waves, balloon oscillations, and turbulence also appear to be minimal as well. Indeed, the effect of fluid motion on free flying microphones appears to be rarely, if ever, a consideration.

The current state of understanding posits three sources of noise on geoacoustic sensors during level flight: electromagnetic interference, instrument self-noise, and unwanted pressure fluctuations. Issues with electromagnetic interference and mitigation strategies are discussed in Sect. 4.3.2.2 and will not be repeated here. Instrument self-noise denotes the level of interference generated by the sensor, digitizer, and power system in the absence of external signal sources. It can be reduced by increasing the digitizer gain and/or voltage output of the sensor. A simple way to quantify this is to include one microphone that is identical to the others, except that its ability to record pressure has been curtailed. This can be accomplished by removing the mechanical filter on an InfraBSU microphone as previously described.

Self-noise was an issue on the HASP 2016, for example. Figure 4.17 indicates that the self-noise of the digitizer on the flight ladder (Trimble Ref Tek 130, gain of 32) is much higher than that on the gondola (Omnirecs Datacube at gain of 64). Signal levels on the two active gondola microphones are similar to the mechanically disabled gondola microphone above about 1 Hz, indicating that the detection threshold above this frequency is determined by digitizer noise and electromagnetic interference. Microphone pairs on the gondola and the flight ladder were mechanically reversed to isolate outside electronic interference as described in Sect. 4.3.2.2. For a microphone pair M_+ and M_- in which pressure response polarity has been flipped, non-pressure signals common to both can be eliminated to create a denoised microphone M_d

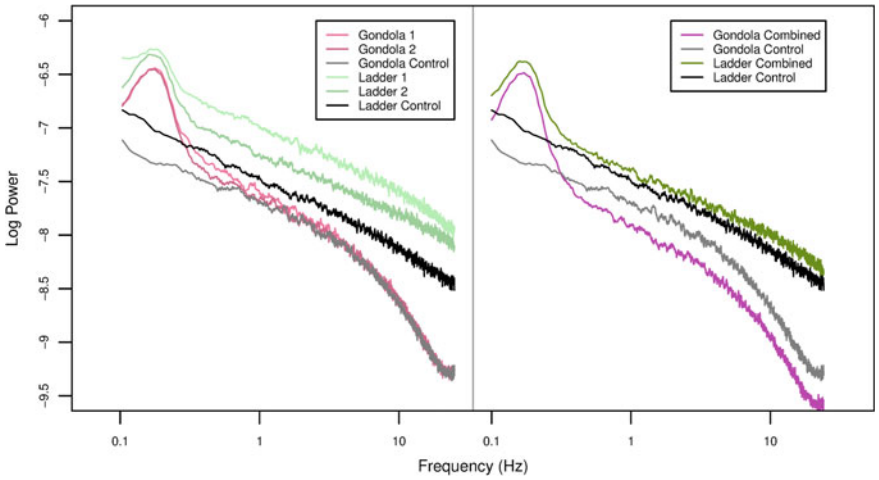

Fig. 4.17 Operational and intentionally disabled "control" microphones on the gondola and flight ladder of the HASP 2016 flight (left panel) compared to operational microphones combined into a single channel via Eq. 4.4 versus control microphones (right panel)

$$M_d = \frac{M_+ - M_-}{2}. \tag{4.4}$$

The result is to increase the sensitivity of the denoised gondola microphone above that of the control channel (Fig. 4.17). the same operation applied to the ladder microphone pair does improve the sensitivity, but not to the same extent as on the gondola microphones. This suggests a simple $\sqrt{2}$ noise reduction produced whenever two sensor channels are averaged together, indicating that the noise on the ladder is internally rather than externally generated.

Pressure fluctuations from temperature and altitude variations can produce long period signals that tend to fall in the gravity wave range. Signals near the balloon resonance frequency and in the microbarom band will be obscured as well. Beyond this, the nature of the acoustic background in the free atmosphere is poorly understood at present. Wescott (1964a) reported root mean square (RMS) acoustic amplitudes of between 0.003 and 0.1 Pa just below 1 Hz with diurnal variations. The acoustic source was believed to be turbulence in the troposphere. The noise floor from electromagnetic interference and digitizer self-noise appears to be higher than background acoustic noise during recent flights (recall Fig. 4.17).

4.5.2 Detection Thresholds

The difference in amplitude of an acoustic wave measured at two different elevations depends on the density, pressure, and speed of sound at each location. The pressure amplitude ratio θ of an acoustic wave traveling from point 1 to point 2 is proportional to the square root of the inverse ratio of their acoustic impedances:

$$\theta = \sqrt{\frac{c_2\rho_2}{c_1\rho_1}} \tag{4.5}$$

where ρ is density and c is the speed of sound (Rayleigh 1894; Banister and Hereford 1991). When comparing pressure amplitude of acoustic waves measured on ground stations to those measured at least one wavelength above the Earth's surface, amplitude doubling due to reflection must be taken into account as well. Thus, the pressure amplitude A_1 on the ground is related to the pressure amplitude A_2 in the atmosphere by

$$A_2 = A_1\frac{\theta}{2}. \tag{4.6}$$

It is instructive to construct a reference pressure amplitude of an acoustic wave measured at the Earth's surface using ambient pressure, temperature, and density values at sea level set forth in the U. S. Standard Atmosphere (NOAA 1976). Then Eq. 4.6 becomes

$$A_2 = A_1 \frac{\sqrt{c_2 \rho_2}}{41} \tag{4.7}$$

where sound speed is in meters per second, and density is in kilograms per cubic meter. Note that this includes the ground reflection adjustment described above. Accordingly, an acoustic wave measured on a ground station at sea level and again at an altitude of 35 km will suffer a 26-fold pressure amplitude reduction from this effect alone. However, this model is simplistic and probably too conservative. It does not take into account atmospheric waveguides and focusing, which can greatly enhance signal amplitudes in certain regions. The true attenuation factor is likely quite variable depending on the atmospheric profile and propagation path of the acoustic wave.

Figure 4.18 suggests that the actual signal-to-noise ratio on the HASP 2016 balloon is comparable to that of ground stations in the area when the adjustment factor θ is applied. However, the presence of the microbarom peak on the balloon but not on the ground suggests that the free flying station actually performs better in the 2-second period range. Indeed, the balloon outperforms the low-noise ground station below 1 Hz and the higher noise (less protected) station below about 8 Hz. The microphones and data acquisition system on the balloon were relatively cheap, low-end models; replacing them with lower noise floor instruments could have further improved signal quality on the HASP 2016.

Noise sources on free flying stations are composed of

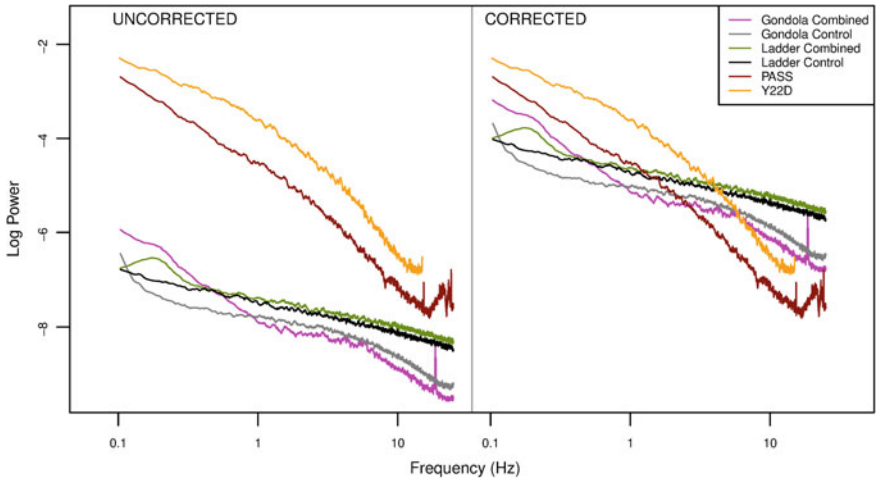

Fig. 4.18 Denoised and reference microphones on the HASP 2016 flight compared with ground stations in the area. The left panel shows the balloon microphone spectrum uncorrected for atmospheric conditions, and the right panel shows the spectrum adjusted for pressure, density, and temperature effects per Eq. 4.5. Spectra were generated using data recorded as the HASP 2016 passed almost directly over co-located ground stations PASS and Y22D. PASS had a wind mitigation system consisting of four 15 m long soaker hoses, and Y22D had no wind protection. Balloon data were scaled to the altitude of the ground stations using the 1976 Standard Atmosphere (NOAA 1976)

$$\epsilon = \epsilon_w + \epsilon_p + \epsilon_e + \epsilon_s + \epsilon_v + \epsilon_a \tag{4.8}$$

where ϵ_w is from wind noise, ϵ_p is from non-hydrodynamic pressure fluctuations (barometric, temperature, and elevation changes), ϵ_e is outside electromagnetic interference, ϵ_s is internal sensor/digitizer noise, ϵ_v is sensor motion (i.e., vibration) and ϵ_a is undesired acoustic waves. On the ground,

$$\epsilon_w \gg \epsilon_p + \epsilon_e + \epsilon_s + \epsilon_v + \epsilon_a \tag{4.9}$$

at frequencies above several tens of seconds. On balloons, $\epsilon_w \approx 0$. The contribution ϵ_p is typically a very long period on ground and free flying stations, although balloons suffer high levels just below the Brunt–Vaisälä frequency due to resonance. Noise on balloon-borne stations appears to consist of contributions from ϵ_e and ϵ_s as noted above, particularly at higher frequencies. Bowman and Lees (2015a) did not find evidence of vibration noise ϵ_v during the first HASP flight, and later results are consistent with this conclusion. This is probably due to the stability of balloon systems at float combined with very low motion sensitivity of the InfraBSU microphones included in each experiment (Marcillo et al. 2012). The ocean microbarom is a near constant source of ϵ_a in the 5 s period vicinity during balloon flights and sometimes on the ground as well.

The signal-to-noise ratio (SNR) of a single geoacoustic sensor with respect to unity amplitude can be expressed as

$$\text{SNR} = \left(\frac{1}{\epsilon_n + \epsilon_a}\right)^2 \tag{4.10}$$

where

$$\epsilon_n = \sum \epsilon_w + \epsilon_p + \epsilon_e + \epsilon_s + \epsilon_v \tag{4.11}$$

is the total contribution of non-acoustic noise. Since acoustic noise ϵ_a and signals of interest suffer the same attenuation factor θ with changes in atmospheric conditions, Eq. 4.10 can be rewritten as follows:

$$\text{SNR} = \left(\frac{1}{\theta\epsilon_n + \epsilon_a}\right)^2. \tag{4.12}$$

Thus, θ is more properly thought of as an enhancement of non-acoustic noise rather than an attenuator of acoustic signals as far as detection thresholds are concerned.

For an ideal geoacoustic sensor, $\epsilon_n \to 0$, and thus the value of θ is nugatory. Such an ideal sensor cannot exist at the Earth's surface due to the unavoidable influence of ϵ_w. The task of reducing ϵ_e and ϵ_s is much more tractable, however, which suggests that a free flying station could approach the theoretical upper limit of acoustic sensitivity described above. The region in which ϵ_a is lowest is likely the stratosphere because it is far from localized acoustic sources at the Earth's surface and is generally less turbulent than the troposphere.

4.5.3 Other Considerations

4.5.3.1 Station Keeping

The atmosphere is in constant motion, and anything embedded in it will not remain in the same location for long. This can be an advantage, since free flying stations can sample large regions in a matter of days. For example, the 2016 ULDB flight circumnavigated the Earth in 2 weeks. However, attempts to target specific phenomena can be difficult because the trajectory of the geoacoustic station depends on wind velocities at all elevations between launch and float altitudes. For example, the SISE/USIE balloon was supposed to fly westward from the launch facility and pass within 100 km of the blast site. Since the launch was delayed for several weeks, the biannual reversal of stratospheric winds actually carried the balloon east, resulting in a much greater range (over 300 km).

Flight paths can be planned with reasonable accuracy by utilizing variations in wind fields at various altitudes. Figure 4.19 shows wind profiles in the mid-latitudes over 1 year. Strong winds between 5 and 15 km above sea level permit rapid eastward motion most of the time. Winds between 15 and 22 km tend to be light and variable, allowing a station at this altitude to drift only a few kilometers per hour. Above about 22 km, the stratospheric winds carry stations east during the summer and west during the winter. A flight system with the ability to change altitude can remain relatively stationary by utilizing the opposing summer stratospheric and tropospheric winds to shift back and forth.

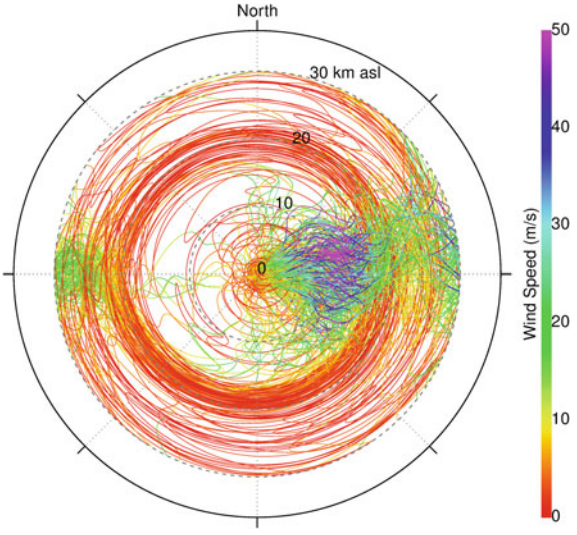

Fig. 4.19 Wind profiles above Chapel Hill, North Carolina, USA generated from Global Forecast System analysis model runs (Bowman and Lees 2015b)

4.5.3.2 Doppler Shift

Since free flying stations are almost always moving with respect to stationary acoustic sources, the resulting signal experiences a Doppler shift. The frequency f_r of the Doppler-shifted signal is related to the original frequency f, the speed c_b of the balloon, the local sound speed c_s at the balloon, the signal-receiver back azimuth θ_b, the balloon motion azimuth θ_m and the source- balloon elevation angle ϕ via

$$f_r = \frac{f}{1 + (c_b/c_s)\cos(\theta_b - \theta_m)\cos\phi} \tag{4.13}$$

This expression was adapted from Lighthill (1978). Thus, a 10 Hz ground source recorded by a balloon moving at 20 m/s could be shifted up to 10.7 Hz (approaching) or down to 9.4 Hz (receding) assuming a sound speed of 304 m/s in the stratosphere.

While the Doppler shift can obscure the true frequency content of signals recorded on balloons, it also can be useful in certain situations. For example, a Doppler-shifted transient signal recorded on two balloons some distance apart will provide the necessary constraint to define a unique source location, provided the sensors are moving in different directions. Also, a single free flying station can localize the source of a persistent signal if it lasts a sufficient amount of time.

4.5.3.3 Direction of Arrival

Acoustic arrays are a powerful tool in ground-based geoacoustic monitoring, but deploying them in the free atmosphere is difficult. Vertically oriented linear arrays are the simplest to construct and were used to good effect by Wescott (1964a). Smaller vertical arrays were deployed on the HASP flights as well. This sensor distribution can measure the angle of incidence of up and down going waves, but they cannot distinguish azimuth. A horizontal array with the necessary aperture for azimuth discrimination would need to be several tens of meters across. Such a contraption could not be launched, but perhaps could be unfolded once float is attained. In any case, the engineering challenges are formidable.

Another possibility is to utilize multiple flight platforms. The SISE/USIE experiment demonstrated this by recording a far-field explosion on two stations at different locations and altitudes (recall Fig. 4.14). In another case, two identical superpressure balloons launched minutes apart stayed within 200 km of each other for 14 days (Lally 1967). Thus, it is possible to have the floating equivalent of a regional geoacoustic array for several weeks at a time, although the network will eventually drift apart. Since the sensor spacing would almost certainly be greater than the acoustic wavelength, array processing methods such as the grouping technique of de Groot-Hedlin and Hedlin (2015) would be required.

Finally, a sensor that could detect air motion associated with a passing acoustic wave would permit direction of arrival determination. This is conceptually equivalent to a P-wave arrival on a seismometer. Proposed designs have included measuring

the motion of the flight system as a result of an impinging wave, acoustic gradiometry, and precise sampling of the wind field. However, none of these have advanced beyond the conceptual stage.

4.6 Applications

4.6.1 Treaty Verification and Natural Hazards Monitoring

The International Monitoring System (IMS) was developed to enforce the Comprehensive Nuclear-Test-Ban Treaty (CTBTO). The IMS consists of a global network of seismic, hydroacoustic, radiological, and infrasound stations tasked with detecting and characterizing clandestine nuclear blasts. When the network is complete, the infrasound component will comprise 60 stations. As of this writing, 49 are certified, 3 are under construction, and 8 are in the planning stages. Simulations indicate that explosions with yields greater than 420 tons nuclear equivalent will be detected over 95% of the Earth with a probability of 90% or greater (Green and Bowers 2010) once the IMS is complete. This fulfills the design goals of the network (Christie and Campus 2010).

In addition, infrasound has recently become a useful means of determining if a volcanic eruption has occurred (Matoza et al. 2017). This is because infrasound is produced only when an eruption is in progress, unlike seismic activity that is not necessarily associated with material ejection (Fee and Matoza 2013). Recently, Tailpied et al. (2016) demonstrated the efficacy of the IMS for monitoring Yasur volcano in the south Pacific and Etna volcano in the Mediterranean, and Fee et al. (2016) utilized infrasound recorded on seismometers to characterize eruptions on remote volcanoes in the Aleutians. Tsunamis also generate powerful infrasound signals (Le Pichon et al. 2005), which could provide amplitude estimates and early warning if captured before they make landfall.

Despite the robust nature of the IMS network, there are logistical and environmental issues that can affect its detection capability. For example, there are regions of the southern ocean that are 3500 km from the nearest land, creating a 7000 km gap in ground network aperture. Stations on remote islands suffer from high levels of wind noise, further degrading detection capabilities in large maritime regions. Sensors located in desert areas often suffer severe wind noise during the day, whereas those at high latitudes may experience high wind noise at any time (Christie and Campus 2010). Variability in stratospheric winds can have a large impact on detection capability, particularly in the tropics (Le Pichon et al. 2012). Local sources of coherent infrasound increase clutter on some stations also (Matoza et al. 2013).

Balloon-borne stations are unaffected by wind noise, removing one of the major impediments to far-field acoustic signal detection. They are able to travel over the open ocean, providing coverage where land stations cannot (recall Fig. 4.3). Balloons can be placed in elevated acoustic ducts, where they can detect signals that

never reach the ground. Finally, they are far from local infrasound sources at the Earth's surface. They would be particularly effective in the tropics and over the southern oceans, where atmospheric conditions and lack of ground station coverage can degrade IMS detection capability (see Fig. 5 in Le Pichon et al. 2012 and Fig. 5 in Green and Bowers 2010). Stations drifting near remote volcanoes can provide eruption detection capability, which is critical for those that lie near aircraft flight paths. Balloons over ocean basins might provide a detection system for tsunamigenic infrasound also.

Small superpressure balloons can remain in the stratosphere for over 2 years (Lally 1991). Geoacoustic sensor platforms on such balloons could be launched from southern regions such as New Zealand, where they would circle the Earth every couple of weeks. A succession of launches could ensure sensor spacing of several thousand kilometers, improving the 7000 km gap described above. Balloon motion also would provide a constraint on acoustic velocity in these poorly instrumented regions. A similar network could be deployed near the equator. Furthermore, stations could be deployed in response to specific operational or atmospheric conditions (e.g., loss of an IMS station, decreased detection capability during the biannual stratospheric wind reversal).

The development of a permanent balloon-borne geoacoustic network would require investments in launch facilities, data telemetry, and new analysis techniques. Their tendency to drift off course would result in inevitable network degradation over time. Indeed, the constantly changing position implies that the network configuration would only be known a week or two in advance. Despite these challenges, the motivation and technology required to realize a free flying network already exist.

4.6.2 Bolide Detection

Stratospheric infrasound sensors can monitor the flux of space-borne objects that burn up in the Earth's atmosphere. The Chelyabinsk bolide was a prime example: 20 IMS infrasound stations sensed the 460 kt TNT equivalent explosion, and some of them even recorded the waves on their second circuit around the globe (Le Pichon et al. 2013). Smaller bolides are regularly detected by satellites that monitor the flashes resulting from their burn-up in the atmosphere since about 10 % of the energy of a bolide's explosion is emitted as optical or infrared light (Brown et al. 2002a). The Jet Propulsion Laboratory's Fireball and Bolide web page (Jet Propulsion Laboratory 2016) currently reports a few events per month with energies down to 0.1 kt TNT equivalent (see Fig. 4.20).

Balloon-borne geoacoustic stations may improve sensitivity to bolides at the small end of the Near-Earth Object (NEO) distribution of impactors. While the amplitude of a pressure wave does decrease as the ambient pressure itself decreases (recall Eq. 4.5), the lack of wind noise greatly improves the signal-to-noise ratio. Furthermore, bolide explosions typically take place between 20 and 30 km altitude (Edwards et al. 2006), where the energy of the explosions may be efficiently trapped

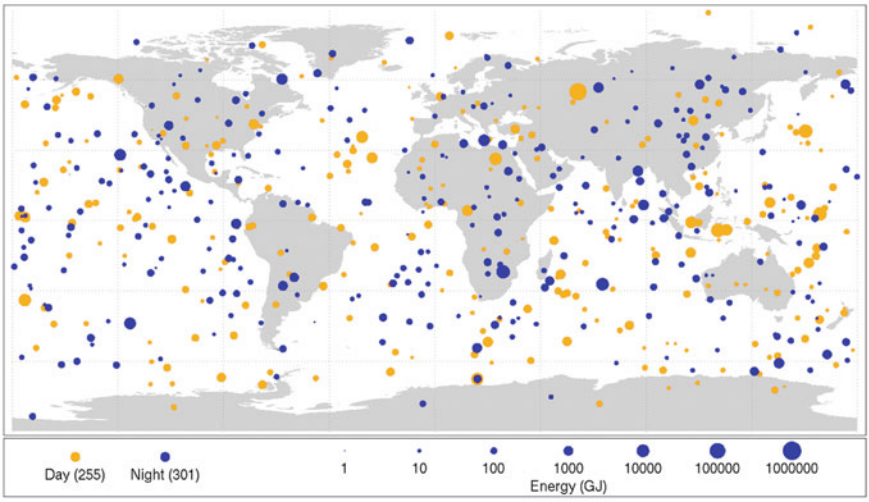

Fig. 4.20 A map of 556 bolide detections between 1994 and 2013 with associated optical energies. Note that the population below 1 kt TNT equivalent is likely very underrepresented. About 30% of the 0.1 kt TNT equivalent bolides were seen on the IMS infrasound network as well. Image credit: NASA

in a stratospheric duct. Finally, the strength and density of the bolide may translate into acoustic signatures that can distinguish between distinct NEO impactor populations.

Period-yield relations originally developed for infrasound signals from nuclear blasts also provide a robust measure of the total energy of bolide events (Brown et al. 2002b). A NEO traveling at 3 km/s has kinetic energy approximately equal to twice its mass in TNT. The minimum impact velocity is 11 km/s (the Earth's escape velocity), and some NEOs have velocities that are significantly higher. As an example, a 0.1 kt event (total impact energy) results from a 4500 kg object traveling at 14 km/s. If this object had a density of 2.7 g/cm^3 (like granite), then its size would be equivalent to a 165 cm cube. In fact, balloon-borne infrasound sensors could detect much smaller energies. For example, the SISE/USIE experiment (see Sect. 4.2.1.4) successfully detected two explosions with the kinetic energy equivalent of a 50-kg NEO impacting the Earth's atmosphere at 14 km/s.

The prospects for bolide infrasound detection using a network of long-duration balloon-borne platforms bear further study. There are some basic questions at present: what is the optimum range in altitude for best sensitivity to bolides? How are bolide-generated infrasound waves likely to propagate in the stratosphere? What distribution of balloons is necessary to provide sufficient sensitivities around the globe? Nevertheless, it seems that a network of infrasound sensors on small, long-duration superpressure balloons may improve our sensitivities to small NEO impactors by an order of magnitude or more.

4.6.3 Upper Atmosphere Energetics and Ionospheric Disturbances

Up going acoustic waves carry energy into the upper atmosphere, where they dissipate as heat. Calculations by Rind (1977) indicate that the ocean microbarom can heat the 100–140 km region by over 30 K per day Analysis by Hickey et al. (2001) also predicts thermospheric heating on the order of tens of Kelvin, although acoustic waves do not appear to heat the mesopause region (Pilger and Bittner 2009). The elevation at which acoustic heating occurs is dramatically lower for narrow band acoustic waves due to nonlinear effects (Krasnov et al. 2007).

Acoustic and acoustic-gravity waves of sufficient amplitude can perturb the ionosphere, producing fluctuations that can be detected using ground-based GPS (Cahyadi and Heki 2015) and continuous Doppler sounders (Krasnov et al. 2015). These disturbances have been generated by rockets (Mabie et al. 2016), earthquakes (Krasnov et al. 2015), tsunamis (Wu et al. 2016), explosions (Drobzheva and Krasnov 2003), and thunderstorms (Davies and Jones 1973), among others. While the detection and characterization of ionospheric disturbances have obvious implications for the remote monitoring of natural hazards, open questions remain about the relationship between the acoustic source and resulting high-altitude fluctuation. For example, Chum et al. (2012) found that predicted values for air motion in the ionosphere were two times higher than those measured from infrasound during the Tohoku earthquake.

Free flying sensors in the troposphere and stratosphere are able to intercept up going acoustic waves as they travel from their source to the upper atmosphere, providing a critical constraint that cannot be measured on the Earth's surface. Indeed, measurements of the acoustic background noise as well as a possible direct overflight of the ocean microbarom during the 2016 ULDB experiment may provide the first glimpse of the energy flux from the stratosphere into the mesosphere and beyond. However, it is likely that the acoustic background varies by location and time of year. Also, the ULDB sensor package cannot determine the direction of arrival of the signals. Experiments designed to measure up going acoustic flux should include a vertically oriented linear array and take place in several locations over different seasons.

4.6.4 Signals Inaccessible to Ground Sensors

In general, the acoustic velocity profile of the troposphere causes infrasound signals to refract away from the Earth's surface. The prevalence of wind noise also limits infrasound detection thresholds, particularly during the day (Bowman et al. 2005). This suggests that balloon-borne platforms might be a better venue for long-term studies of phenomena such as the ocean microbarom. For example, Rind (1977) investigated the thermospheric tide's effect on ocean microbarom propagation but

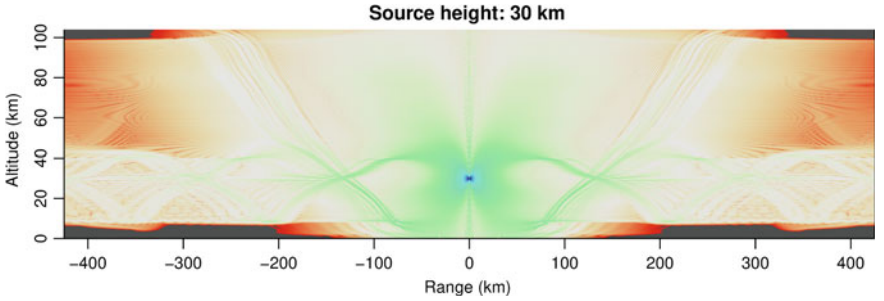

Fig. 4.21 Simulation of transmission loss from a 1 Hz acoustic source at an elevation of 30 km using atmospheric data from September 28, 2016 over central New Mexico. The cross section is oriented East–West

noted that surface winds prevented observations 10 to 30% of the time. In contrast, the ocean microbarom is nearly constant on high-altitude balloon deployments.

Infrasound signals generated by wind flow over mountains (Walterscheid and Hickey 2005) or during thunderstorms (Farges and Blanc 2010) may be difficult to observe due to adverse ground conditions. Furthermore, they may be directional in nature; the "charge contraction" signal during lightning discharge is one example (Balachandran 1983). Sensors in the stratosphere may provide unique insights into the acoustic wave field from these phenomena.

Propagation models suggest that acoustic sources near the tropopause may generate signals that travel in an elevated, bidirectional duct (see Fig. 4.21). Waves trapped in this duct may propagate to much greater distances than those elsewhere, making this a possible analog for the SOFAR channel in the ocean. Phenomena that could generate infrasound in this region include thunderstorms, bolides, and rockets. The presence of thunderstorms during flights in 2014 and 2015 but not 2016 offers a tentative acoustic explanation for the unusual signals described in Bowman and Lees 2015a (recall Fig. 4.8), although it is difficult to understand how they could have been generated.

4.6.5 The Exploration of Venus

Recently, researchers have begun to explore the possibility of conducting infrasound measurements from balloons floating in the atmosphere of Venus. This section is concerned with what motivates this interest, the acoustic properties of Venus, and progress in addressing the key technical questions that must be solved before a Venus balloon infrasound mission is conducted.

4.6.5.1 Why Explore Venus with Balloon Infrasound?

During the 50 years of planetary exploration, researchers have exploited the electromagnetic spectrum very thoroughly making observations from gamma rays to very low frequency radio waves. However, there has been no attempts to use infrasound for planetary exploration.

The primary driver for considering infrasound is the dense atmosphere of Venus that precludes orbital remote sensing observations of the surface with electromagnetic radiation except for very limited spectral bands. This thick atmosphere also ensures that the surface is extremely hot (approaching 465 °C over broad areas) such that our twin planet also presents a formidable challenge for in situ investigations with landers and rovers.

Seismology is a powerful technique that is responsible for much of what we know about the Earth's interior, has played a key role in characterizing the lunar interior, is about to be applied at Mars with the InSight mission and can play a key role in answering fundamental questions about Venus. However, seismic instruments used at the Moon and Mars will not work under Venus surface conditions (465 °C and 90 bars).

A study sponsored by the Keck Institute for Space Studies (KISS) entitled "Venus Seismology" conducted in 2014 and published in March 2015 (Stevenson et al. 2015) explored alternative techniques that can be implemented from balloons floating high in the Venus atmosphere, where temperatures are comparatively benign or from Venus orbit. A workshop was held in June 2014 in which three coauthors participated unaware that at virtually the same time other coauthors were initiating an effort to revive geoacoustic investigations using balloons on Earth. The report on the KISS study published in March 2015 concluded that infrasound generated by quakes on Venus can be observed either directly from balloons floating high in the atmosphere or indirectly by monitoring infrared radiation from a spacecraft orbiting Venus. Moreover, because of the dense atmosphere of Venus, the signals from an event of a given size were almost two orders of magnitude larger than they would have been for a terrestrial balloon. Explosive volcanic events on Venus could also be observed with infrasound signals although this possibility was not explored in any detail. The next section focuses on the balloon infrasound observations and includes a discussion of how to determine if Venus is seismically active and if so to explore the interior structure of Venus using infrasound measurements.

4.6.5.2 Venus Atmosphere Characteristics and Balloon Flight

The atmospheric temperature and density profiles of Fig. 4.22 indicate that the average surface temperature is about 465 °C and the pressure is 90 bars—the equivalent of a depth of about 1 km of seawater. With increasing elevation, the temperature and pressure both decrease steadily and an altitude of 55 km, the pressure is about 500 mb and the temperature is about 40 °C. In 1985, two Soviet VEGA balloons were deployed in the Venus atmosphere and floated near 55 km. Each was tracked from

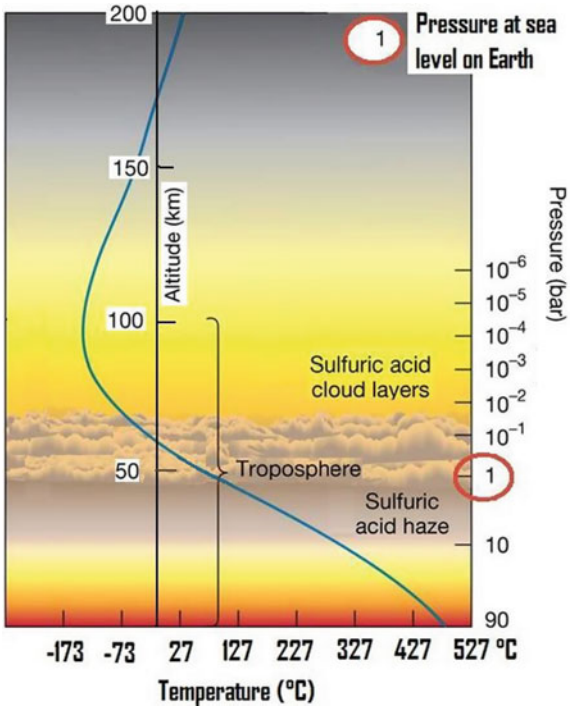

Fig. 4.22 Density and temperature profile of the Venusian atmosphere

Earth for 2 days before their batteries were exhausted (Blamont 1985; Sagdeev et al. 1986).

Venus also differs profoundly from Earth in other ways. Unlike the Earth and Mars which spin on their axes with very similar periods (Mars is 24 h and 40 min) and with their spin axes tilted to their orbital planes, Venus rotates very slowly in a direction that is opposite to its orbital motion and the Venus day (243 earth days) is longer than its year (225 days). Moreover, the spin axis is essentially orthogonal to its orbit and so there are no seasons. These differences have consequences for the atmospheric circulation on Venus.

In contrast with the very slow rotation of the surface of Venus, the atmosphere at balloon altitudes is in very rapid motion (super-rotation) with a zonal flow of approaching 100 m/s relative to the surface. Based on the VEGA balloon tracking there is also a modest motion in a meridional direction that is most likely due to a result of Hadley cell circulation. Based on what currently is known about Venus, a balloon deployed near the equator would circumnavigate the planet every 5 days and gradually drift irregularly toward the nearest pole in a time period of a month or perhaps more. As a result, infrasound observations would be conducted over the better part of hemisphere in the course of a 1-month mission, which would be terminated by loss of solar power at high latitudes.

Fig. 4.23 Venus balloon prototype (5.5 m diameter, 4.5 kg payload capacity). The balloon includes an exterior Teflon film for protection from sulfuric acid in the Venus clouds

During the past two decades, the Jet Propulsion Laboratory (JPL) has been investigating a number of different approaches to the design of Venus balloons. At this time, the most mature of these is a superpressure balloon similar in concept to the Soviet VEGA balloon and the terrestrial superpressure balloons discussed in Sect. 4.3.1. A prototype of a 5.5 m balloon designed to carry a 4.5 kg payload at Venus appears in Fig. 4.23.

Tests have demonstrated that this balloon can tolerate extended exposure to the sulfuric acid mist on Venus and multiple day–night temperature cycles as the balloon repeatedly circumnavigates the planet. Several proposals have been made to NASA's Discovery program for atmospheric investigations with this balloon without success so far. However, a flagship mission called Venus Climate Mission incorporating a superpressure balloon was included in the recommendations of the National Research Council's Planetary Science Decadal Survey (Squyres 2011).

Other balloon concepts have also been considered for Venus, which would permit controlled excursions in altitude. Reversible fluid balloons take advantage of unique properties of the Venus atmosphere including its high temperature and molecular weight (Jones 1995). This permits the use of water and ammonia as both a buoyancy fluid and a means of controlling altitude. These fluids are more easily stored than

helium or hydrogen while in transit to Venus. More recently, the Adaptable Multi-Segment Altitude Control (AM-SAC) balloon has been devised with the capability for large-altitude excursions and periods of stable flight over widely different altitudes (de Jong 2015). As promising as these new ideas are, the baseline mission for exploring the potential of infrasound remains a helium-filled superpressure balloon deployed on entry into the Venus atmosphere.

4.6.5.3 Acoustic Sources on Venus

Potential natural sources of infrasound on Venus include seismic events, explosive volcanism, meteors, and atmospheric disturbances. Evidence for occurrences and likely magnitudes of these sources at Venus can be culled from the observations that have been collected by past missions such as Magellan and Venus Express and the currently operating Akatsuki mission. On Venus, there are no anthropogenic acoustic signatures except on the rare occasion a spacecraft enters the atmosphere. It is important to understand these levels and the characteristic signatures of the natural sources so that they can be confidently discriminated from one another.

The Magellan mission mapped Venus with a synthetic aperture radar to a resolution of about 75 m/pixel. As shown in Fig. 4.24, these maps reveal a rich variety of tectonic features and widespread evidence of volcanism. The timescale for this activity remains controversial but the Venus surface appears to be much younger than Mars and the Moon. Some scientists hold the opinion that Venus was dramatically resurfaced in a single event. Others contend that these events have occurred continually through its history up to the present day (Frankel 1996).

The morphology of the structural features seen in radar images as well as the youthfulness of the planet surface testify to the potential for seismic activity. There seems to be plenty of evidence that the crust of Venus has experienced stress. However, the contemporary rate of stress release is unknown and it is possible that, as on Earth, much of it is aseismic.

Two competing conditions on Venus will influence the likelihood of stress release. On the one hand, the lack of water would result in a larger fraction of seismic energy release; on the other hand, the higher temperatures would limit the magnitude of stress release events. Quakes resulting from mineral phase changes may be also be important on Venus although they have no physical expression at the surface. The KISS study team considered that Venus was likely to be significantly less active than Earth but more active than Mars. For planning purposes, a conservative level of 25x less active than Earth was assumed. Because of the unique characteristics of the Venus atmosphere, even this low level may be readily detectable with infrasound techniques.

Venus has over 1600 major volcanoes or volcanic features, and there are many more volcanoes smaller in size. No one has yet counted them all, but the total number may be over 100,000, meaning that Venus may have more volcanic landforms than any other planet in the Solar System (Volcano World 2017). A key question is how

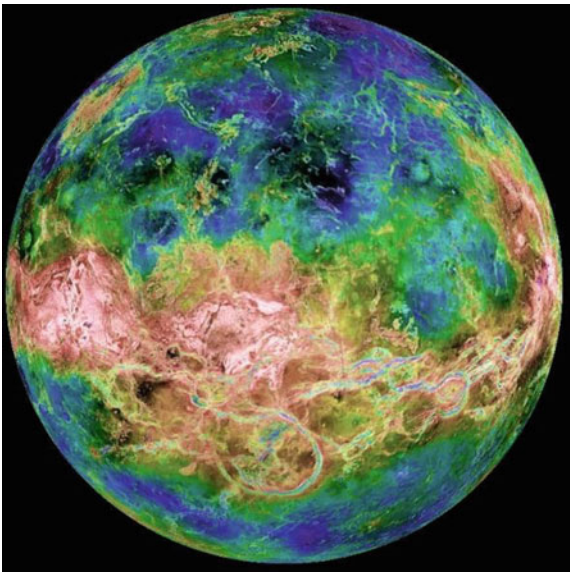

Fig. 4.24 Radar map of Venus based on images from NASA's Magellan spacecraft. Venus exhibits a variety of volcanic and tectonic features

many of these volcanoes are active and how active. There are currently two lines of evidence indicating continuing activity.

The first line of evidence is the occurrence of large episodic changes in the concentration of sulfur dioxide in the atmosphere. On at least two occasions since the advent of space observations, the global concentration of sulfur dioxide above the clouds has risen abruptly and has been followed by a slow decline of a factor of 10 in concentration extending over about 10 years (Marcq et al. 2013). This is believed to be consistent with a large volcanic eruption punching through the cloud layer into the Venus stratosphere followed by the gradual return to a stable condition with low SO_2 at these altitudes. However, it is not possible to rule out atmospheric instabilities as a cause.

Another line of evidence relates to the characteristics and behavior of some volcanoes as viewed in narrow infrared windows in the atmosphere (Smrekar et al. 2010). Some of these volcanoes exhibit an enhanced emissivity suggesting that they result from relatively recent flows. However, there is no way to say how recent. Other scientists have even reported actual temporal changes in the character of the flows during the Venus Express mission (Shalygin et al. 2015). Admittedly, these results are not widely accepted. With no definitive results yet on the occurrence of volcanism using conventional methods and questions about whether improvements in conventional infrared instrumentation can ever answer them (the dense atmosphere sets the fundamental limit to detecting these effects) interest is now turning to where infrasound techniques from balloon altitudes or orbit could provide an answer.

Meteors can be expected to be a source of acoustic energy just as they are on the Earth. A number of meteoroid streams impacting Earth also intersect the orbit of

Venus (Beech 1998), but there are no predictions of the rate of impacts at Venus. Actual observations of the rate using infrasound techniques would be of significant scientific interest. Meteors are believed to be important in the nucleation of the Venus clouds and so any information on the rate of meteor infall and the composition of the infalling material would be significant.

Observations from both the Venus Express and Akatsuki spacecraft have indicated the formation of gravity waves on Venus, which appear to result from atmospheric flow over topographic features (Fukuhara et al. 2017; Ando et al. 2015). These propagate into the cloud layer and would be observable at balloon altitudes. There is also indirect evidence for lightning on Venus (e.g., Russell et al. 2007) but confirmatory optical signatures are yet to be verified. If lightning does occur, it would be a potential source of infrasound (Farges and Blanc 2010).

4.6.5.4 Propagation of Seismo-Acoustic Waves on Venus

The primary motivation for infrasound investigations of Venus has been the possibility of seismic acoustic observations with the goal of understanding the level and distribution of seismicity on Venus and the possibility of probing the interior structure by exploiting the signatures from large quakes. Accordingly, more analysis has gone into understanding propagation from seismic sources than volcanoes, meteors or atmospheric disturbances.

Acoustic waves from a seismic event on Venus are coupled much more efficiently into the atmosphere than on Earth. The coupling efficiency is intermediate between that for the Earth's atmosphere and the Earth's ocean. Signals propagating from directly above the epicenter or from surface waves propagating out from the quake epicenter both travel vertically upward into the atmosphere.

Because the atmosphere is primarily carbon dioxide, attenuation is higher than it would be in an atmosphere with nonpolar molecules. As illustrated in Fig. 4.25, the attenuation is frequency dependent and only affects frequencies well above 10 Hz at the altitude of a floating platform (54 km). For observations of infrasound from an orbiting platform it may be important at much lower frequencies.

Acoustic signals originating from a Venusquake and reaching a balloon can be characterized as one of two types. The epicentral wave originating from directly above the epicenter propagates directly through the atmosphere to the site of observation. The Rayleigh wave propagates as a surface wave in the solid body of the planet. Vertical surface displacements caused by the Rayleigh wave directly beneath the balloon then propagate up to balloon altitudes. In Fig. 4.26, the analysis by Garcia et al. (2016) indicates that the surface displacements of the Rayleigh waveform are faithfully recorded in pressure variations at balloon altitudes.

Accordingly, there are several possible avenues to using balloon-borne infrasound measurements to investigate the seismicity and interior structure of Venus. Measurements of epicentral waves could make it possible to detect very small quakes on Venus (<Me=3) and produce a first map of global seismicity. Detection of large quakes could enable propagation times of Rayleigh waves to be measured and hence

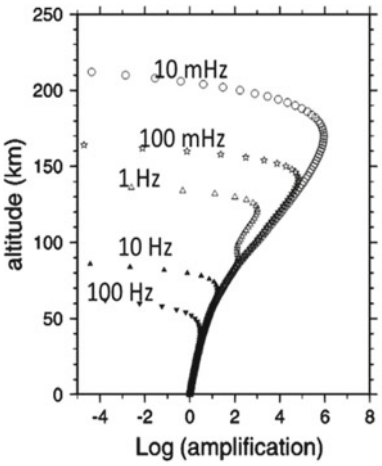

Fig. 4.25 Acoustic wave amplification as a function of altitude on Venus from Garcia et al. (2016). Frequency-dependent attenuation is insignificant at balloon altitudes

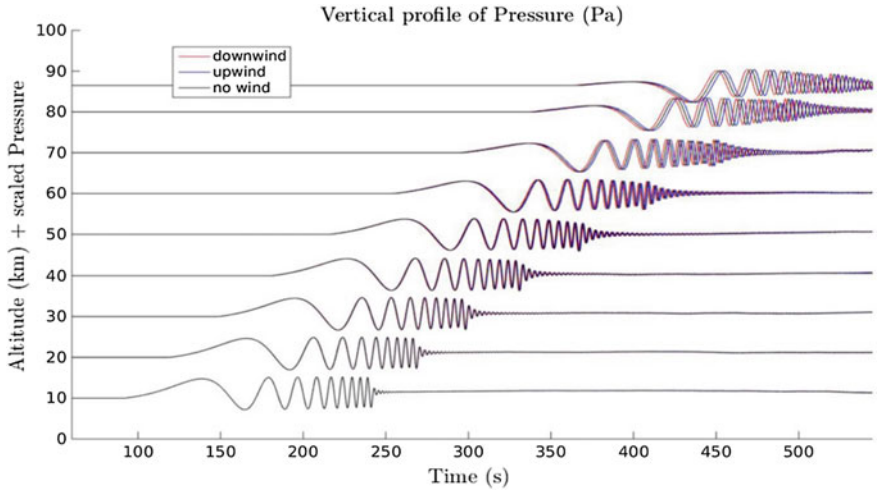

Fig. 4.26 Infrasound waveforms as a function of altitude form a faithful replica of the Rayleigh wave that drives them up to balloon altitudes (Garcia et al. 2016)

information about the planet's interior to be gathered. The preferred approach for this would be a network of balloons that could observe the seismo-acoustic signatures of the same event at several locations around the planet. However, there is a more remote possibility of using the single seismic station approach that is being pioneered by the Mars Insight mission (Lognonné et al. 2012).

4.6.5.5 Venus Quake Detection

Infrasonic pressure signals emanating either directly above the epicenter of a seismic event or from the Rayleigh waves would be detected by sensors located on a balloon floating in the favorable environment of the middle atmosphere of Venus near 55 km altitude. Discrimination of epicentral signals originating from quakes from other sources and background will be a challenge. The baseline approach is to deploy two or more microbarometers on a tether beneath the balloon. Comparisons of the signals between the sensors would be used to discriminate pressure variations resulting from an upwardly propagating wave from the surface from the effects of altitude changes due to updrafts and downdrafts and changes in buoyancy of the balloon. On the other hand, an acoustic arrival with frequency dispersion will represent strong evidence of Rayleigh wave excitation. That is because dispersive acoustic waves are relatively rare and tend to form within low elevation waveguides (Herrin et al. 2006; Negraru and Herrin 2009); such a wave train would be invisible to a high altitude balloon. Lamb waves also exhibit dispersion, but are confined to low altitudes as well (Bretherton 1969). Other sensing approaches being explored include the use of sensitive accelerometers on the pole pieces of the balloon to measure the response of the balloon to the passage of an acoustic wave, which may make it possible to detect the azimuthal direction of the wave. The platform would circumnavigate Venus every five days enabling a survey of Venus seismicity.

Infrasound originating from quakes may also be detected as a modulation of airglow signals at 1.27 and 4.3 μm. These signatures could be detected from a Venus orbiter, but likely not from ground or space based platforms near Earth. Complementary observations of the same event at the much higher frequencies that are possible from in situ platforms on the surface and in the middle atmosphere would greatly enhance the ability to survey seismicity and probe the Venus interior.

4.6.5.6 Earth as a Testbed for a Venus Balloon Infrasound Experiment

Venus is not the place to begin experimenting with different techniques for measuring infrasound. Accordingly, JPL in collaboration with the Institut Supérieur de l'Aéronautique et de l'Espace (ISAE) of Toulouse, France has begun a program of test flights intended to validate techniques for detecting Venus quakes using Earth as an analog environment. The initial tests will involve sensors on tethered balloons and hot air balloons followed by flights on both the troposphere and the stratosphere to explore different dimensions on the measurement challenge. There is now tremendous potential for information exchange and collaboration between the JPL/ISAE group, whose primary interest is planetary research, with other groups who are embarking on balloon infrasound work from a terrestrial perspective.

4.7 Conclusions

Geoacoustic investigations of the free atmosphere have begun again after a 50-year pause. Preliminary results suggest that these free flying systems have lower noise and a greater detection range. In addition, they may record elements of an acoustic wave field that seldom reaches Earth's surface. Since the stations constantly move and signal direction of arrival is difficult to ascertain, these free flying systems are not a substitute for ground arrays except in regions such as the open ocean. Rather, they compliment the existing ground infrasound network by providing a new window into geoacoustic phenomena. Continued refinement of flight systems, sensors, and experiment design will bring new discoveries and opportunities in the emerging science of high altitude geoacoustics.

Acknowledgements Sandia National Laboratories is a multi-mission laboratory managed and operated by National Technology and Engineering Solutions of Sandia, LLC., a wholly owned subsidiary of Honeywell International, Inc., for the U.S. Department of Energy's National Nuclear Security Administration under contract DE-NA0003525. The views expressed here do not necessarily reflect the views of the United States Government, the United States Department of Energy, or Sandia National Laboratories.

References

Ames Research Staff (1953) Equations, tables, and charts for compressible flow. Technical report, National advisory committee for aeronautics. Report 1135

Anderson JF, Johnson JB, Arechiga R, Thomas R (2014) Mapping thunder sources by inverting acoustic and electromagnetic observations. J Geophys Res Atmos 119:13287–13304

Anderson JF., Johnson JB, Bowman DC, Ronan TJ (2018) The Gem infrasound logger and custom-built instrumentation. Seismol Res Lett 89(1):153–164

Anderson WJ, Taback I (1991) Oscillation of high altitude balloons. J Aircr 28(9):606–608

Ando H, Imamura T, Tsuda T, Tellman S, Pätzold M, Häusler B (2015) Vertical wavenumber specra of gravity waves in the Venus atmospher obtained from Venus express radio occultation data: evidence for saturation. J Atmos Sci 72:2318–2329

Balachandran NK (1983) Acoustic and electric signals from lightning. J Geophys Res 88(C6):3879–3884

Banister JR, Hereford WV (1991) Observed high-altitude pressure waves from an underground and a surface explosion. J Geophys Res 96(D3):5185–5193

Barat C, Cot C, Sidi C (1984) On the measurement of the turbulence dissipation rate from rising balloons. J Atmos Ocean Technol 1:270–275

Barr R, Llanwyn Jones D, Rodger CJ (2000) ELF and VLF radio waves. J Atmos Solar-Terr Phys 62:1689–1718

Barthol P, Gandorfer A, Solanki SK, Schüssler M, Chares B, Curdt W, Deutsch W, Feller A, Germerott D, Grauf B, Heerlein K, Hirzberger J, Kolleck M, Meller R, Muller R, Riethmüller TL, Tomasch G, Knölker M, Lites BW, Card G, Elmore D, Fox J, Lecinski, A, Nelson P, Summers R, Watt A, Martıinez Pillet V, Bonet JA, Schmidt W, Berfkefeld T, Title AM, Domingo V, Gasent Blesa JL, del Toro Iniesta JC, López Jiménez A, Álvarez Herrero A, Sabau-Graziati L, Widani C, Haberler P, Härtel K, Kampf D, Levin T, P'erez Grande I, Sanz-Andrés A, Schmidt E (2011) The sunrise mission. Solar Phys 268:1–34

Beech M (1998) Venus-intercepting meteoroid streams. Mon Not R Astron Soc 294:259–264

Blamont J (1985) The exploration of the atmosphere of Venus by balloons. Adv Space Res 5(9):99–106
Bowman DC (2016) Infrasound from ground to space. PhD thesis, The University of North Carolina at Chapel Hill
Bowman DC, Lees JM (2015a) Infrasound in the middle stratosphere measured with a free flying acoustic array. Geophys Res Lett 42(22):10010–10017
Bowman DC, Lees JM (2015b) Near real time weather and ocean model data access with rNOMADS. Comput Geosci 78:88–95
Bowman DC, Lees JM (2016) Direct measurement of the acoustic wave field in the stratosphere. In: Proceedings of the 2016 IEEE aerospace conference
Bowman DC, Norman PE, Yang X (2015) Solar balloons: a low cost, multi-hour flight system for the lower stratosphere
Bowman JR, Baker GE, Bahavar M (2005) Ambient infrasound noise. Geophys Res Lett 32:L09803
Bretherton FP (1969) Lamb waves in a nearly isothermal atmosphere. Q J R Meteorol Soc 95:754–757
Brown P, Spalding RE, ReVelle DO, Tagliaferri E, Worden SP (2002a) The flux of small near-Earth objects colliding with the Earth. Nature 420:294–296
Brown PG, Whitaker RW, ReVelle DO, Tagliaferri E (2002b) Multi-station infrasonic observations of two large bolides: signal interpretation and implications for monitoring of atmospheric explosions. Geophys Res Lett 29(13):1636
Cahyadi, M. N. and Heki, K. (2015). Coseismic ionospheric disturbance of the large strike-slip earthquakes in North Sumatra in 2012: m_w dependence of the disturbance amplitudes. Geophys J Int 200:116–129
Campus P, Christie DR (2010) Worldwide observations of infrasonic waves. In Le Pichon A, Blanc E, Hauchecorne A (eds) Infrasound monitoring for atmospheric studies. Springer Science and Business Media, pp 185–234
Ceranna L, Matoza R, Hupe P, Le Pichon A, Landés M (2019) Systematic array processing of a decade of global IMS infrasound data. In: Le Pichon A, Blanc E, Hauchecorne A (eds) Infrasound monitoring for atmospheric studies, 2nd edn. Springer, Dordrecht, pp 471–482
Christie DR, Campus P (2010) The IMS infrasound network: Design and establishment of infrasound stations. In Le Pichon A, Blanc E, Hauchecorne A (eds) Infrasound monitoring for atmospheric studies, Springer Science and Business Media, pp 29–75
Chum J, Hruska F, Zednik J, Lastovicka J (2012) Ionospheric disturbances (infrasound waves) over the Czech Republic excited by the 2011 Tohoku earthquake. J Geophys Res 117:A08319
Coffman JW (1965) A balloon-borne microphone system. In: Korn AO (ed) Proceedings of the 1964 Air Force Cambridge research laboratories scientific balloon symposium, L. G. Hanscom Field, Bedford, Massachusetts
Davies K, Jones JE (1973) Acoustic waves in the ionospheric F2 region produced by severe thunderstorms. J Atmos Terr Phys 35:1744–1787
Dawton DI, Elliot H (1953) Day and night measurements of the total cosmic ray intensity at balloon altitudes. J Atmos Terr Phys 3:217–222
de Groot-Hedlin C, Hedlin MA (2015) A method for detecting and locating geophysical events using groups of arrays. Geophys J Int 203:960–971
de Jong M (2015) Venus altitude cycling balloon. In: Venus lab and technology workshop
Doerenbecher A, Basdevant C, Drobinski P, Durand P, Fesquet C, Bernard F, Cocquerez P, Verdier N, Vargas A (2016) Low atmosphere drifting balloons: platforms for environmental monitoring and forecast improvement. Bull Am Meteorol Soc
Drobzheva YV, Krasnov VM (2003) The acoustic field in the atmosphere and ionosphere caused by a point explosion on the ground. J Atmos Solar-Terr Phys 65:369–377
Edwards WN, Brown PG, ReVelle DO (2006) Estimates of meteoroid kinetic energies from observations of infrasonic airwaves. J Atmos Solar-Terr Phys 68:1136–1160
Farges T, Blanc E (2010) Characteristics of infrasound from lightning and sprites near thunderstorm areas. J Geophys Res Space Phys 115:A00E31

Fee D, Haney M, Matoza R, Szuberla C, Lyons J, Waythomas C (2016) Seismic envelope-based detection and location of ground-coupled airwaves from volcanoes in Alaska. Bulletin of the Seismol Soc Am 106(3):1024–1035

Fee D, Matoza RS (2013) An overview of volcano infrasound: from hawaiian to plinian, local to global. J Volcanol Geoth Res 249:123–139

Frankel C (1996) Volcanoes of the solar system. Cambridge University Press

Fukuhara T, Futaguchi M, Hashimoto GL, Horinouchi T, Imamura T, Iwagaimi N, Koyama T, Murakami S, Nakamura M, Ogohara K, Sato M, Suzuki M, Taguchi M, Takagi S, Ueno M, Watanabe S, Yamada M, Yamazaki A (2017) Large stationary gravity wave in the atmosphere of Venus. Nat Geosci

Garcia RF, Mimoun D, Brissaud Q, Poler G, Lebonnois S (2016). Infrasound from Venus quakes: numerical modeling and balloon observation project. In: International Venus conference

Green DN, Bowers D (2010) Estimating the detection capability of the international monitoring system infrasound network. J Geophys Res 115:D18116

Guzik TG, Besse S, Calongne A, Dominique A, Ellison SB, Gould R, Granger D, Olano D, Smith D, Stewart M, Wefel JP (2008) Development of the High Altitude Student Platform. Adv Sp Res 42:1704–1714

Haack A, Gerding M, Lübken F-J (2014) Characteristics of stratospheric turbulent layers measured by LITOS and their relation to the Richardson number. J Geophys Res Atmos 119:10605–10618

Herrin ET, Kim TS, Stump B (2006) Evidence for an infrasound waveguide. Geophys Res Lett 33:L07815

Hickey MP, Schubert G, Walterscheid RL (2001) Acoustic wave heating of the thermosphere. J Geophys Res Sp Phys 106(A10):21543–21548

Jet propulsion laboratory (2016) Fireball and bolide reports

Jones JS (1995) Reversible fluid balloon altitude control concepts. In: Proceedings of the 11th lighter-than-air systems technology conference

Krasnov VM, Drobzheva YV, Chum J (2015) Far-field coseismic ionospheric disturbances of Tohoku earthquake. J Atmos Solar-Terr Phys 135:12–21

Krasnov VM, Drobzheva YV, Lastovicka J (2007) Acoustic energy transfer to the upper atmosphere from sinusoidal sources and a role of nonlinear processes. J Atmos Solar-Terr Phys 69:1357–1365

Lally VE (1967) Superpressure balloons for horizontal soundings of the atmosphere. Technical report, National Center for Atmospheric Research

Lally VE (1991) Manned orbital balloon flight—available techniques. In:International balloon technology conference

Landès M, Ceranna L, Le Pichon A, Matoza RS (2012) Localization of microbarom sources using the IMS infrasound network. J Geophys Res 117:D06102

Le Pichon A, Ceranna L, Pilger C, Mialle P, Brown D, Herry P, Brachet N (2013) The 2013 Russian fireball largest ever detected by CTBTO infrasound sensors. Geophys Res Lett 40:3732–3737

Le Pichon A, Ceranna L, Vergoz J (2012) Incorporating numerical modeling into estimates of the detection capability of the IMS infrasound network. J Geophys Res 117:D05121

Le Pichon A, Herry P, Mialle P, Vergoz J, Brachet N, Garcés M, Drob D, Ceranna L (2005) Infrasound associated with the 2004–2005 large Sumatra earthquake and tsunami. Geophys Res Lett 32:L19802

Lighthill J (1978) Waves in fluids. Cambridge University Press, Cambridge, England

Lognonné P, Banerdt WB, Hurst K, Mimoun D, Garcia R, Lefeuvre M, Gagnepain-Beyneix J, Wieczorek M, Mocquet A, Panning M, Beucler E, Deraucourt S, Giardini D, Boschi L, Christensen U, Goetz W, Pike T, Johnson C, Weber R, Larmat K, Kobayashi N, Tromp J (2012). InSight and single-station broadband seismology: From signal and noise to interior structure determination. In: 43rd lunar and planetary conference

Mabie J, Bullett T, Moore P, Vieira G (2016) Identification of rocket-induced acoustic waves in the ionosphere. Geophys Res Lett

Marcillo O, Johnson JB, Hart D (2012) Implementation, characterization, and evaluation of an inexpensive low-power low-noise infrasound sensor based on a micromachined differential pressure transducer and a mechanical filter. J Atmos Ocean Technol 29:1275–1284
Marcq E, Bertaux J-L, Montmessin F, Belyaev D (2013) Variations of sulphur dioxide at the cloud top of Venus's dynamic atmosphere. Nat Geosci 6:25–28
Marty J (2019) The IMS infrasound network: current status and technological developments. In: Le Pichon A, Blanc E, Hauchecorne A (eds) Infrasound monitoring for atmospheric studies, 2nd edn. Springer, Dordrecht, pp 3–62
Matoza RS, Green DN, Le Pichon A, Shearer PM, Fee D, Mialle P, Ceranna L (2017) Automated detection and cataloging of global explosive volcanism using the International Monitoring System infrasound network. J Geophys Res Sol Earth 122:2946–2971
Matoza RS, Landés M, Le Pichon A, Ceranna L, Brown D (2013) Coherent ambient infrasound recorded by the International Monitoring System. Geophys Res Lett 40:429–433
Meecham WC, and Wescott, J. W. (1965). High-altitude noise background. In: Proceedings of the 5th international congress on acoustics
Mentik JH, Evers LG (2011) Frequency response and design parameters for differential microbarometers. J Acoust Soc Am 130(1):33–41
Morris AL (ed) (1975) Scientific ballooning handbook. National Center for Atmospheric Research. NCAR-TN/1A-99
Mutschlecner JP, Whitaker RW (1997) The design and operation of infrasonic microphones. Technical report, Los Alamos National Laboratories
Naka Y, Shindo S, Makino Y, Kawakami H (2013) Systems and methods for aerial and ground-based sonic boom measurement. Technical report, Japan Aerospace Exploration Agency
Negraru PT, Golden P, Herrin ET (2010) Infrasound propagation in the "Zone of Silence". Seismo Res Lett 81(4):615–625
Negraru PT, Herrin ET (2009) On infrasound waveguides and dispersion. Seismo Res Lett 80(4):565–571
NOAA (1976) U.S. standard atmosphere 1976. Technical report, National Oceanic and Atmospheric Administration, National Aeronautics and Space Administration, and the United States Air Force
Officer CB (1958) Introduction to the theory of sound transmission. McGraw Hill Book Company
Peebles C (1997) High frontier: The U. government printing office, S. Air Force and the Military Space Program. The U. S. Government Printing Office, U. S
Pilger C, Bittner M (2009) Infrasound from tropospheric sources: impact on mesopause temperature? J Atmos Solar-Terr Phys 71:816–822
Quinn EP, Holzworth RH (1987) Quasi-lagrangian measurements of density surface fluctuations and power spectra in the stratosphere. J Geophys Res 92(D9):10926–10932
Raspet R, Abbott J-P, Webster J, Yu J, Talmadge C, Alberts II K, Collier S, Noble J (2019) New systems for wind noise reduction for infrasonic measurements. In: Le Pichon A, Blanc E, Hauchecorne A (eds) Infrasound monitoring for atmospheric studies, 2nd edn. Springer, Dordrecht, pp 91–124
Rayleigh (1894) The theory of sound, vol 2. Macmillan and Co
Rind D (1977) Heating of the lower thermosphere by the dissipation of acoustic waves. J Atmos Terr Phys 39:445–456
Rind D (1978) Investigation of the lower thermosphere results of ten years of continuous observations with natural infrasound. J Atmos Terr Phys 40:1199–1209
Russell CT, Zhang TL, Delva M, Magnes W, Strangeway RJ, Wei HY (2007) Lightning on Venus inferred from whistler-mode waves in the ionosphere. Nature 450:661–662
Sagdeev RS, Linkin VM, Blamont JT, Preston RA (1986) The VEGA Venus balloon experiment. Science 231(4744):1407–1408
Saito, Y. (2014). Quest for altitude. Accessed 2 Dec 2016
Shalygin EV, Markiewicz WJ, Basilevsky AT, Titov DV, Ignatiev NI, Head JW (2015) Active volcanism on Venus in the Ganiki Chasma rift zone. Geophys Res Lett 42:4762–4769

Smrekar SE, Stofan ER, Mueller N, Treiman A, Elkins-Tanton L, Helbert J, Piccioni G, Drossart P (2010) Recent hot-spot volcanism on Venus from VIRTIS emissivity data. Science 328:605–608
Squyres S (2011) Vision and voyages for planetary science in the decade 2013–2022
Stevenson D, Cutts J, Mimoun D (2015) Probing the interior structure of Venus. Technical report, Keck Institute for Space Studies
Tailpied D, Le Pichon A, Marchetti E, Assink J, Vergniolle S (2016) Assessing and optimizing the performance of infrasound networks to monitor volcanic eruptions. Geophys J Int
Veggeberg K (2012) Development of a sonic boom measurement system at JAXA. In: Proceedings of the acoustics 2012 Nantes conference
Volcano World (2017) Volcano world: Venus. Accessed 4 Jan 2017
Walker KT, Hedlin MA (2010) A review of wind-noise reduction technologies. In: Infrasound monitoring for atmospheric studies, chapter 5, pp 141–182. Springer Science and Business Media
Walterscheid RL, Hickey MP (2005) Acoustic waves generated by gusty flow over hilly terrain. J Geophys Res Sp Phys 110:A10307
Waxler R, Gilbert KE (2006) The radiation of atmospheric microbaroms by ocean waves. J Acoust Soc Am 119(5):2651–2664
Weaver RL, McAndrew J (1995) The Roswell report: fact versus fiction in the New Mexico desert. Government Printing Office, U.S
Wescott JW (1961) Atmospheric background at high altitudes. In: Proceedings of the symposium on atmospheric acoustic propagation
Wescott JW (1964a) Acoustic detection of high-altitude turbulence. Technical report, The University of Michigan
Wescott JW (1964b) Acoustic detection of high altitude turbulence. In: Korn AO (ed) Proceedings of the 1964 Air Force Cambridge Research Laboratories scientific ballooning symposium, L. G. Hanscom Field, Bedford, Massachusetts
Wu Y, Llewellyn Smith SG, Rottman JW, Broutman D, Minister J-BH (2016) The propagation of tsunami-generated acoustic-gravity waves in the atmosphere. J Atmos Sci 73:3025–3036
Yajima N, Izutsu N, Imamura T, Abe T (2009) Scientific Ballooning: Technology and applications of exploration balloons floating in the stratosphere and the atmospheres of other planets. Springer Science and Business Media
Young EF, Brown P, Boslough M, Ballard C, Dougherty E, Dullea C, Garner K, Heaney M, Thom I., Von Hendy, M., Wahl, K., and Young, E. (2016). Detection of infrasound disturbances from the Earth's stratosphere. In: Proceedings of the 2016 IEEE aerospace conference
Zhang SD, Yi F, Huang CM, Huang KM (2012) High vertical resolution analyses of gravity waves and turbulence at a midlatitude station. J Geophys Res Atmos 117:D02103

Chapter 5
Measuring Infrasound from the Maritime Environment

Doug Grimmett, Randall Plate and Jason Goad

Abstract Worldwide infrasound coverage is obtained using fixed, land-based sensing networks. However, two-thirds of the earth's surface is composed of oceans, and while islands in the ocean already host sensing stations, no capability yet exists to monitor infrasound from sensors fielded directly in the maritime environment. Deployment in the maritime would greatly enhance the ability to monitor natural and anthropogenic sources of infrasound around the world through improved event detection, localization, and classification. The additional sensing may also facilitate improved knowledge of global atmospheric environmental conditions. The advantages and challenges of infrasound sensing in the maritime environment are described, as are potential host platforms for fielding them. Some technical challenges for this concept include sensor motion, wind noise, composing arrays of sensors and survivability in the ocean environment. An in-depth analysis of one of these, the negative impact of ocean heave on performance, is described along with a potential solution for its mitigation.

5.1 Introduction

A variety of natural and anthropogenic sources produce very-low-frequency acoustic waves that can be received hundreds to thousands of kilometers away. These acoustic waves are typically in the infrasound band, between 0.033 and 20 Hz, and below human hearing range. Land-based microbarometer sensors and networks have shown the capability of detecting infrasound signals originating from natural and anthropogenic sources. Natural sources of infrasound include earthquakes, meteors, volcanoes, tsunamis, auroras, and ocean swells (Christie and Campus 2010). Among anthropogenic sources are atmospheric and underground nuclear explosions.

D. Grimmett (✉) · R. Plate
SPAWAR Systems Center Pacific, San Diego, USA
e-mail: grimmett@spawar.navy.mil

J. Goad
Florida Atlantic University, Boca Raton, USA

A. Le Pichon et al. (eds.), *Infrasound Monitoring for Atmospheric Studies*,
https://doi.org/10.1007/978-3-319-75140-5_5

Because of their low frequency, infrasound waves experience little attenuation, and can, therefore, propagate to, and be detectable from, very long distances. Although the signals are inaudible, they may be detected using advanced infrasound sensing technology at ranges of 100s–1000s of kilometers (Marty 2019; Mialle et al. 2019).

The Comprehensive Nuclear Test Ban Treaty Organization (CTBTO) operates a worldwide network of 60 infrasound monitoring stations (Christie and Campus 2010), as shown in Fig. 5.1. The primary purpose is to detect nuclear test explosions, and approximately 85% of the network is currently operational (Marty 2019). The USArray Transportable Array (TA) is a wide area network of 400 seismic sensors with about 70 km spacing, deployed and redeployed over various regions of the United States since 2007 (the current deployment region is in Alaska). Most of these stations also include a single infrasound sensor, in addition to the primary seismic sensor, to monitor atmospheric signals (Meltzer 1999). These, and other national and international land-based infrasound sensors, sensor arrays, and networks, are located across the globe and are capable of detecting natural and anthropogenic sources of infrasound occurring at great distances (Nief et al. 2019).

Wide infrasound coverage is obtained using such fixed, land-based sensing networks. However, two-thirds of the earth's surface is composed of oceans, and while islands in the ocean host sensing stations, no capability yet exists to monitor infrasound from sensors fielded directly in the maritime environment. In this chapter, we investigate the potential of such maritime fielding of microbarometer sensors on boats, buoys, or unmanned surface vehicles (USVs). The potential advantages of such a maritime infrasound capability, and the technical challenges to be overcome, are discussed. One particular problem to be overcome is the effect of ocean heave on sensor performance. Vertical motion, such as that produced by ocean heave, induces interfering pressure fluctuations on the sensor which may obscure the infrasound signals-of-interest. An approach to overcome this interference is described using an external heave measurement and an adaptive noise cancellation algorithm (Grimmett et al. 2016).

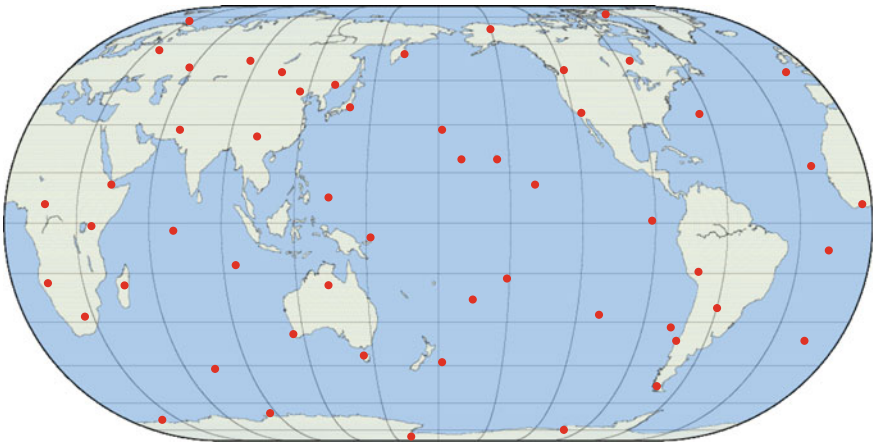

Fig. 5.1 The locations of CTBTO infrasound monitoring stations worldwide

In addition to maritime infrasound, other nontraditional, non-land-based infrasound collection environments are being explored, such as sensors being hosted by balloons in the atmosphere (Bowman et al. 2019).

5.2 Advantages of Infrasound Measurements from the Maritime Environment

The challenges of developing a working maritime infrasound sensing capability may be significant; however, if overcome, it offers great potential for improvements in infrasound signal detection, localization, classification, and environmental assessment.

5.2.1 Detection

To achieve global worldwide coverage, about 15 of the currently operating CTBTO infrasound monitoring stations are located on remote islands, amidst vast ocean expanse, thousands of miles from the earth's continental land masses. For example, CTBTO stations at Midway (IS58) and Tahiti (IS24) are located in the middle of the vast Pacific Ocean, Kerguelen (IS23) is in a remote area of the South Indian Ocean, and Tristan da Cunha (IS49) is in the middle of the South Atlantic Ocean. Even though these remotely located island stations may be thousands of kilometers from neighboring stations, they are a key adjunct to the CTBTO continental-based stations; without them, the network would be unable to provide adequate global infrasound detection coverage (Green and Bowers 2010; Le Pichon et al. 2019).

Outside the CTBTO network, national or other infrasound networks may be very limited in their coverage, being constrained by available land locations and perhaps national borders. The placement of infrasound sensors in the oceans has the potential to provide an expansive, new, remote environment from which infrasound signal detection can be made to supplement the coverage obtained with land-based networks. Placement of sensors in ocean locations may offer coverage where it does not exist, or when current land-based monitoring coverage is less reliable due to fluctuating environmental conditions. Gaps in detection coverage may be filled with appropriate placement and operations from the technology deployed directly in the oceans.

Performance of infrasound sensor detection coverage is a function of many variables, but foremost is the location of the sensor(s) and the prevailing environmental conditions. The atmospheric conditions between the infrasound signal-of-interest and the sensor will largely determine whether there will be a viable propagation path connecting them. The propagation is a function of the sound velocity profile, which is mainly dependent on temperature gradients and wind, and can either result in connected stratospheric, thermospheric, or surface-ducted paths,

or in shadow zones where significant energy does not arrive (de Groot-Hedlin et al. 2010; Waxler and Assink 2019). The infrasound signal frequency will determine how much attenuation it is subjected to before arriving at a sensor. The presence of gravity waves can further complicate and modify the expected propagation conditions (de Groot-Hedlin et al. 2010). Further, these environmental factors vary over time, which, in turn, affects the performance at the infrasound sensor. Perhaps the most obvious example of this is the seasonal effect of the stratospheric winds (de Groot-Hedlin et al. 2010; Le Pichon et al. 2012; Ceranna et al. 2019). Zonal winds shift from easterly in summer, to westerly in winter; noting that the Northern hemisphere summer occurs during the Southern hemisphere winter. (de Groot-Hedlin et al. 2010). Good infrasound propagation is achieved when traveling downwind; therefore, a station's best zonal coverage performance area will switch east to west and west to east with the seasons, twice a year. Maritime infrasound sensors may be situated to augment existing land-based coverage in desired directions during the "difficult" season. For example, a source of infrasound originating on a continent's east coast in the northern hemisphere may be detected by a further inland, land-based monitoring station to the west during summer. However, during winter the favorable propagation direction will be to the east, where only ocean, not land, is available to optimally position a receiving infrasound station. Further, it is well known that infrasound background noise levels are diurnal: higher levels are seen during daytime than nighttime (de Groot-Hedlin et al. 2010). A greater spatial distribution of sensors may yield better performance by having nodes favorably positioned such that they are in a time of lower diurnal-induced background noise level at the time of signal reception. Additionally, some sources of infrasound have very directional propagation properties, like the shock waves associated with meteors and bolides traveling at supersonic/hypersonic speeds. In such cases, the direction of acoustic propagation is nearly perpendicular to the line-of-flight, so only sensors situated properly relative to the trajectory and with a good propagation path are likely to receive the infrasound signal (Pilger et al. 2015). The more sensors that are available to be distributed geographically, the more diverse detection opportunities are presented; robustness to infrasound signal detection and coverage of infrasound source locations is therefore improved.

5.2.2 Event Localization and Classification

Infrasound event detection is merely a starting point. Data and information fusion between multiple infrasound stations provide valuable additional information. When multiple stations detect an event, the joint information may be used to provide a localization estimate of the detected signals' common source. Processing of a single infrasound array can provide an estimate of the arriving signal's back azimuth, but it does not provide the range to the event (Cansi 1995). When multiple arrays observe the same infrasound event, their respective back-azimuth estimates may be combined through a cross-fixing process to provide a localization estimate

(Bratt and Bache 1988; Mialle et al. 2019). The more arrays that are combined, and the more that these arrays are located in geometrically advantageous (diverse) ways (i.e., with orthogonal look directions to the event), the better the localization estimate's accuracy. Even if the infrasound stations are only composed of a single sensor (as in the USArray's Transportable Array) rather than an array, and are unable on their own to determine a back azimuth, correlation methods have shown that events can be localized with a sparse network of nondirectional sensors (De Groot-Hedlin and Hedlin 2015; Vergoz et al. 2019; de Groot-Hedlin and Hedlin 2019). Further, if the infrasound source is moving, as in the case of a meteor/bolide, a network of sensors is better able to track its trajectory through time. In addition to localization and tracking benefits, being able to correlate events among multiple sensors provides increased detection confidence and additional data to better classify the type of infrasound event, as well as derive quantities of interest about the source event which produced it. In some cases, reduction in false alarm rate can be achieved by requiring a minimum number of correlated detections from different stations. Better infrasound coverage in the oceans could provide a more regular grid, and would avoid network configuration asymmetries that are constrained by land-only installations. It is clear then that adding additional sensors to a sensing network is advantageous, and, therefore, introducing sensors into the maritime environment offers to improve infrasound event localization, tracking, and classification. This is done by providing greater geographic distribution and geometric diversity that would not be possible when limited to land-based sites.

5.2.3 Environmental Assessment

Infrasound propagation is subject to a variety of atmospheric conditions. It is essential to understand the effects of the environment in order to understand infrasound monitoring performance. Signal detection will depend on propagation paths and their losses, and the environment may also significantly modify the source signal along its propagation path to a sensor (e.g., it may spread the signal in time, etc.). Modeling infrasound depends on environmental descriptions, which are not always known well enough to produce accurate results (Drob 2019; Waxler and Assink 2019; Chunchuzov and Kulichkov 2019). Often the environmental descriptions are averages over large areas, or they are historical instead of for the current time. With infrasound sensors operating in different locations (including vast oceanic areas), inversion techniques (Drob et al. 2010; Assink et al. 2019) can be used to obtain better estimates and understanding of the atmospheric effects and conditions worldwide which impact infrasound performance. Having sensors in the maritime environment will provide richer data collection opportunities to support scientific studies of the atmosphere and provide environmental assessments for operational systems.

5.3 Challenges of Infrasound Measurements from the Maritime Environment

The sensor most often employed to measure infrasound is the microbarometer, which provides very accurate measurements of acoustic signals with very low frequency. Microbarometers are typically designed for outdoor use on land, where they can maintain performance during exposure to the elements. Land-based monitoring sites are normally composed of multiple (up to 10) sensors spaced from a few hundred meters to a few kilometers apart, each with a wind filtering system, forming an array. The stations include data acquisition and communication technology and the required electrical power for operations. The systems are calibrated appropriately for their installed locations. There will be significant challenges to fielding microbarometers in a maritime environment, compared to a land-based site.

5.3.1 Survivability

The maritime environment is a much harsher operating environment than most land sites. Exposure to extremes in weather and the effects of water, salt, wind, and humidity require significant efforts in ocean engineering to ensure system survivability, proper sensor operations, and to ensure a persistent operational capability. Waterproofing and weatherproofing of the system components will be essential. The sensor must be open to the atmosphere, but at the same time prevent water ingress, requiring some form of water shielding.

5.3.2 Sensor Motion

Maritime deployment will expose the sensor(s) to motion effects, since the hosting platform is likely to move with ocean swell/waves of a rough ocean surface. The sensor may experience motion along six degrees of freedom: surge, sway, yaw, pitch, roll, and heave. The most significantly impacting of these will be the heave motion, as even small changes in altitude will induce a change in the ambient atmospheric pressure. Microbarometer sensors will measure the pressure changes due to altitude changes, which look like an infrasound signal; in fact, it acts as an interference signal against which infrasound signals must be detected. Of all the technical challenges discussed here, this particular challenge has been addressed and will be discussed in more detail later.

In addition, some microbarometers are more sensitive to accelerations that are not necessarily accompanied by appreciable displacement than others. At this stage of investigation, it is unclear how different the acceleration effects on the sensor will be between land and maritime deployment. Should acceleration effects prove a significant degrading interference effect or performance-limiting factor, seismically decoupled or insensitive microbarometers may be preferred for maritime deployments.

5.3.3 Wind

Wind is the main contributor to the infrasound sensor's noise background level. Maritime environments are characteristically windy, and maritime deployment schemes will, therefore, require additional mitigation or compensation methods to reduce the negative impact of the resulting noise. Some oceanic locations and seasons will be exposed to lower winds than others and may be better suited for infrasound sensor deployment. During times of high seas and high winds, sensor performance may be compromised until calmer weather develops. Possible mitigation approaches are to develop suitable wind shrouds/filters/screens, or adaptive wind noise cancellation algorithms (Frazier 2014), tailored for use in a maritime environment.

5.3.4 Multi-element Arrays

To validate infrasound detections and determine their direction, arrays of infrasound sensors are usually employed. Since the sensor spacing for infrasound array elements is on the order of several hundreds of meters, maritime deployment will require multiple platforms. In some cases, they may be moving relative to one another, and sensor element positions must be tracked over time. Another implication is that this will require some telemetry to send the sensors' data to a fusion center for array processing.

Considering these challenges, the detection performance of a maritime infrasound monitoring system may be characterized as

$$SE = SL_{SOI} - TL + AG - [(N_{heave} - PG_{heave}) \oplus (N_{wind} - PG_{wind} - F_{wind}) \oplus N_{other}] - DT, \tag{5.1}$$

which is an equation for signal excess (SE) expressed in dB units, re 20 μPa. Signal excess is the amount of excess signal energy above the minimum required for the system to detect the infrasound signal-of-interest (SOI). Positive values indicate detectability, with higher values indicating stronger detections. SL_{SOI} is the sound pressure level of the SOI at its originating location, *TL* is the transmission loss (including the effects of spreading and absorption) along the propagation path from source to receiver, and *DT* is the detection threshold, i.e., how much signal-to-noise ratio is required before detections can be confidently called by the operator or automatic detection algorithm. For a given SOI, detection capability can be improved by locating the monitoring system such that a favorable propagation path connects the source and receiver, minimizing *TL*. *AG* is the processing or array gain achieved by combining multiple sensors of an array, either by correlation processes or beam forming. The background noise above which detection must be made is indicated by the power sum ($\oplus$) of the terms in brackets. The ocean heave interference, N_{heave}, may be reduced by implementation of an adaptive interference cancellation algorithm (described in detail later) providing a processing gain of PG_{heave}. The wind noise, N_{wind}, may be reduced/filtered by a physical screen or other system which provides a gain against the wind of F_{wind}. It may also be possible to reduce wind noise through adaptive processing approaches, providing a gain of PG_{wind}.

A processing approach for cancellation of the heave interference has been developed and will be described in more detail later. With a solution for heave interference available, wind mitigation remains a significant concern and challenge. Maritime wind noise in the infrasound band has yet to be studied in detail, and the amount of such noise that is mitigable is unknown. It is likely that infrasound wind noise is prevalent in the maritime environment and will thus be the detection-limiting term in the signal excess equation. Therefore, future efforts will investigate maritime wind noise and its mitigation.

5.4 Infrasound Sensor Hosts in the Maritime Environment

Infrasound sensors to be deployed in the maritime environment may be hosted on ships, ocean buoys, and unmanned surface vehicles (USVs). Figure 5.2 shows examples of various types of maritime infrasound sensor hosts. These are now discussed in more detail.

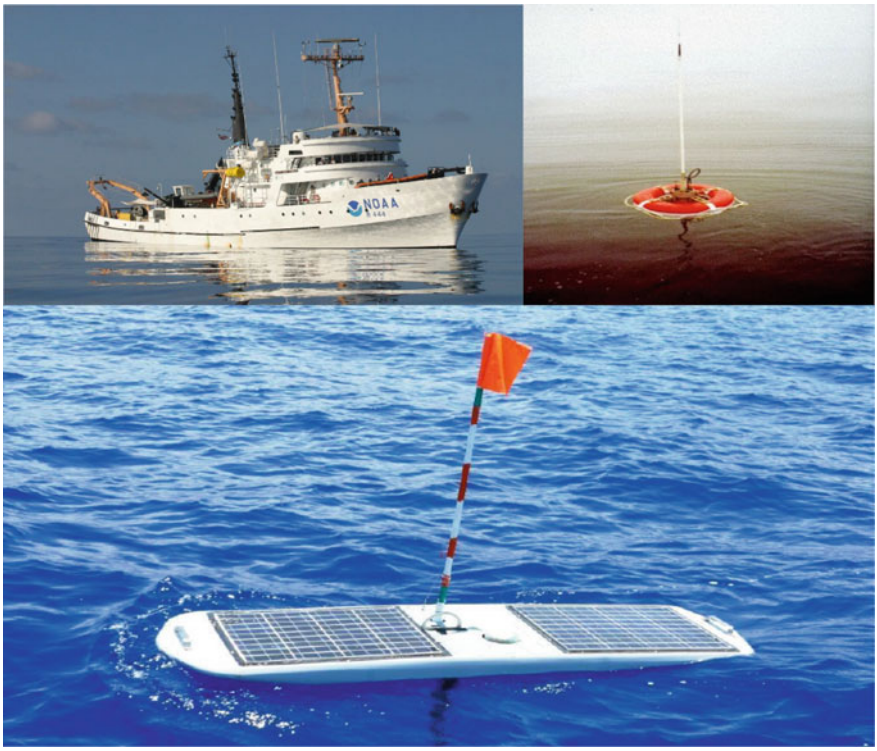

Fig. 5.2 Potential maritime hosts for infrasound sensing: ships (top left), ocean buoys (top right), and unmanned surfaces vehicles (bottom)

5.4.1 Ships

Of the possible maritime host platforms, ships have the highest mobility, allowing for relocation of the sensor to different areas of the ocean in the least amount of time. The sensor will be subject to heave, pitch, roll, ship vibration, and engine noise—all potential negative impacts on sensor performance. Onboard ships, there may be more options available to mitigate the effect of wind with ample deck space available, such as through intelligent sensor placement and the design of larger shrouds or distributed inlets such as can be obtained using long, perforated hoses. The practicality of using a set of ships to form an infrasound array is dubious because they must operate in close proximity, they are hugely expensive to operate, and will surely have higher priority tasking, making them unsuitable for affordable, persistent infrasound sensing missions. This leads us to consider unmanned host platforms, like ocean buoys and USVs.

5.4.2 Ocean Buoys

Normally, ocean buoys are moored to the ocean bottom and could potentially provide a persistent, autonomous, but nonmobile infrasound monitoring option. They would be subject to heave, pitch, and roll, and some lateral drift, constrained by the mooring's watch circle, but would likely experience less vibration and seismic interference than ships. Wind mitigation efforts may be more challenging due to the limited buoy real estate and the continuous exposure to the environment. Multiple moorings in the close proximity suitable for an infrasound array (hundreds of meters) may be prohibitive due to the risk of tangling and the array shape will dynamically change due to ocean current drift and winds. Normally, buoys will be subject to ocean surface waves and swell, resulting in sensor heave, pitch, and roll. A Spar buoy is a type of buoy with a tall, thin shape and which is very stable in the ocean, and much less sensitive to heave, pitch, and roll, creating a better potential platform for an infrasound sensor. A complication with any buoy is that deeper water greatly increases the difficulty of establishing and maintaining a buoy mooring, reducing the amount of available deployment area in the oceans. Drifting buoys, on the other hand, would be easier to deploy, but difficult to control location and to maintain the proximity needed for a multi-sensor array configuration.

5.4.3 Unmanned Surface Vehicles

Since around the early 1990s, there has been a large amount of development and innovation in the area of unmanned surface vehicles (Motwani 2012; Manley 2008). Development of USVs began with existing ships being outfitted with remote controls. Over time, smaller USVs have been developed, ranging from small ships to rigid-hulled inflatable boats (RHIBs) to platforms less than 10 feet long. The initial uses for USVs were military in nature, but now that the technology has matured, and smaller, cost-effective platforms can be secured, missions for civilian purposes, by industry and academia, are on the increase. The advantages of such systems are that the platforms can remain unmanned, are low cost (relative to manned ships), require no moorings, are mobile, and can perform various useful missions, including environmental surveys and remote sensing missions.

USV technology has moved from being remotely operated vehicles (ROV) to autonomous systems that perform tasking with a minimum of human interaction. Some USVs are now capable of harvesting wave, wind, and solar energy to provide their propulsion and power their systems and payloads. This is a significant development because it enables persistent operations without recovery, refueling, or maintenance. Such systems have the potential to operate in an unmanned state, conducting missions, for up to a year in duration. This emerging technology offers the opportunity to develop USV host platforms for infrasound sensing in the

maritime environment. Figure 5.3 shows example USV platforms which have been developed.

Table 5.1 compares ships, buoys, and USVs as potential maritime host platforms for the infrasound sensing application. Ship solutions are not deemed feasible for dedicated infrasound data collection because of the prohibitive expense and the improbability of being available during times of particular interest. Conventional

Fig. 5.3 Examples of Unmanned Surfaces Vehicles: DARPA's Sea Hunter, (top left), Ocean Aero's Submaran (top right, Copyright Ocean Aero Inc. Used with permission.), AutoNaut (bottom left, Copyright AutoNaut Ltd, with permission), ASV Global C-Enduro (bottom right, Copyright ASV Global, used with permission)

Table 5.1 Potential performance indicators for different maritime platforms

Parameter	Ships	Conventional buoys	Small USVs
Motion	Significant	Significant (unless Spar buoy)	Significant
Vibration problem	Significant	Minimal	Minimal
Wind problem	Low	High	High
Forming an array	Costly	Difficult	Possible
Platform autonomy	No	Yes	Yes
Platform mobility	High	None	Medium
Sensor survivability	High	Challenging	Challenging
Persistence	Low	High	Medium

ocean buoys are an option; they can be made persistent but it would be difficult to configure multiple buoys to form an array. Small USVs offer good persistence and the possibility of forming arrays due to control over their position. Ocean heave and wind noise will be challenging technical problems to solve for all three types of host platforms.

5.5 The Impact of Ocean Heave on Infrasound Data Collection in the Maritime Environment

Infrasound waves are longitudinal acoustic pressure waves. Infrasound pressure fluctuations for sources of interest are small compared to the ambient pressure. The ambient pressure at sea level is referred to as the atmospheric pressure (or hydrostatic pressure), which is due to the accumulated weight of the air in all of the atmospheric layers above; its nominal value is 101,325 Pa (or 1 atm). The received pressure wave signals for various infrasound sources range from about 5,000 to 1,000,000 times smaller than the ambient pressure. Ambient pressure decreases with altitude according to

$$P = P_0 \left(1 - \frac{Lh}{T_0}\right)^{\frac{gM}{RL}}, \tag{5.2}$$

where P_0 is sea level atmospheric pressure in Pa, h is the altitude in m, L is the temperature lapse rate for dry air in K/m, T_0 is sea level temperature in degrees Kelvin, g is gravitation acceleration in m/s^2, M is the mass of dry air in kg/mol, and R is the universal gas constant (8.31447 J/(mol K)) (Standard Atmosphere 1976).

Near sea level, where the infrasound sensor is to be located, changes in pressure due to slight changes in ocean heave can simply be approximated by the change in the force of gravity per area of air with given density as the volume of air above the sensor changes due to changing height, yielding

$$\Delta P = -\rho g \Delta h, \tag{5.3}$$

where ρ is the air density in kg/m^3. For a standard atmosphere (1 atm and 0 °C), $\rho = 1.2754$ kg/m^3, and

$$\frac{\Delta P}{\Delta h} \approx -12.5 \frac{\text{Pa}}{\text{m}} \tag{5.4}$$

That is, at sea level the pressure gradient with altitude is approximately −12.5 Pa/m. The implication is that an infrasound sensor, deployed in the maritime environment and moving vertically up and down (heaving) with ocean swell, will also be subject to pressure fluctuations due to changes in ambient atmospheric pressure. This heave-induced pressure change may be of significant strength given

typical sea surface swell of 1–2 m, with greater swells possible. It appears as an infrasound signal even though it is not, and it has the potential to obscure and interfere with the detection of actual infrasound signals-of-interest. If the heave-induced signal and the infrasound signal-of-interest occupy different and disjoint frequency bands, applying standard filtering methods will be successful in separating them. However, if the heave frequency spectrum and the infrasound signal spectrum overlap in frequency, then a more sophisticated heave compensation method must be applied, as described later. In addition, there is the possibility of additional pressure fluctuations due to non-propagating evanescent wave effects very near the ocean surface. However, the magnitude and impact of this potential effect for our sensor in the ocean environment require further study.

5.5.1 Sea Surface Characteristics

Tides produce cyclical changes in ocean water levels due to the gravitational forces of the moon and sun, the earth's rotation, and other factors. A common tidal effect is a semi-diurnal or diurnal period of fluctuation of several feet of water level, and it depends largely on geographic location and the moon's orbit. However, the frequency of a semi-diurnal tide is about once every 12 h, or 2.3e−5 Hz, which is well below the infrasound band propagation lower limit of around 0.003 Hz. Therefore, although an infrasound sensor exposed to tidal effects will experience ambient pressure fluctuations due to tidal heave; these can easily be ignored or filtered out since there are no infrasound signals-of-interest that low in frequency. Additionally, many infrasound sensors are AC-coupled to remove slowly varying pressure fluctuations below the infrasound measurement band.

Ocean surface roughness is driven by wind. When winds of certain speed and direction are sustained over enough time, the ocean surface becomes what is termed a "fully developed" sea. Wave size increases with increasing wind speed and increased the duration of the wind. The Beaufort scale (www.metoffice.gov.uk/corporate/library/catalogue.html; Petersen 1927) is an empirical table of sea conditions ("sea state") versus wind speed which is commonly used by seafarers. Beaufort numbers range from 0 (calm conditions) to 12 (hurricane conditions), increasing through breezes to strong wind to gales in between, with wave heights correspondingly increasing (over a range from 0 to 15 m). For the maritime infrasound application, it is important not only to understand the magnitude of ocean wave heave that the sensor will be subject to, but also the ocean wave frequencies (swell periods) associated with them.

The sea surface roughness can be characterized as a superposition of many waves with different periods (frequencies), heights, and directions. There may be more than a single source contributing to the generation of waves at any given location. Oceanographers typically use sea surface spectra to characterize the wave energy in the ocean as a function of frequency (and sometimes direction). The frequencies of the sea surface roughness (waves) are inversely related to the period

of the swell (i.e., $T_p = 1/f$). "Seas" often refer to localized, chaotic waves with many periods (broad frequency spectra), and can be distinguished from "swell", which is a well-behaved undulation (narrow spectral peak) that has propagated from longer distances. Oceanographic wave buoy instruments are commercially available which produce sea surface spectra by direct measurement of ocean heave (http://www.datawell.nl/Home.aspx; http://axystechnologies.com/). Predictions of sea surface spectra can be made using models, for assumed wind speeds. The Pierson–Moskowitz model is a simple, effective model which provides insight into the effects of sea surface roughness as a function of wind speed (Pierson and Moskowitz 1964), though more complicated models also exist (Hassellmann et al. 1980). Pierson–Moskowitz models a fully developed sea with a sea surface spectrum of the form:

$$S(\omega) = \frac{\alpha g^2}{\omega^5} e^{-\beta(\omega_0/\omega)^4}, \tag{5.5}$$

where α and β are dimensionless constants given by 7.79×10^{-3} and 0.74, respectively; g is gravitational acceleration. The reference frequency is given by $\omega_0 = g/U$, where U is the wind speed at a reference height of 19.5 m (often a reference of 10 m is also used).

Figure 5.4 shows examples of Pierson–Moskowitz spectra, which are observed to increase in peak energy level, become more peaked, and shift to lower frequencies at higher sustained wind speeds. Other useful parameters can be derived from the spectra, such as the predominant wave period (corresponding to the spectral peak) and the "significant wave height" (referred to as $H_{1/3}$ or H_s), which is the mean trough-to-crest wave height of the highest third of waves. This is a commonly used oceanographic parameter, which is consistent with what human observers estimate while at sea. Most wave heights will be less than $H_{1/3}$, but occasionally waves may be much higher. The mean wave height is approximately 0.7 times $H_{1/3}$ (Holthuijsen 2007). These parameters are shown in Fig. 5.5 for various wind speeds.

The ocean will cause the sensor to heave up and down by the magnitude of the wave heights and over a frequency band corresponding to the sea surface spectrum. Most sea surface spectra show that wave energy is contained within a frequency band of 0.03–0.3 Hz (which corresponds to wave periods of approximately 3–30 s). Networks of coastal and open-ocean oceanographic buoys provide web access to real time and historical data, including wind speed/direction, sea surface spectra, etc. (http://cdip.ucsd.edu/; http://www.ndbc.noaa.gov/); Fig. 5.6 shows various historical sea surface spectra, as measured from the Scripps Institute of Oceanography Coastal Data Information Program (CDIP) ocean buoy #067 (http://cdip.ucsd.edu/). Four different measurements are shown for different seasons, with different weather conditions. The 2013 spectra (blue and red) show low total energy and a broad spectrum of wave frequencies. The Jan 2014 spectrum shows a mix of two distinct swells. The April 2014 spectrum shows a single, very strong, long

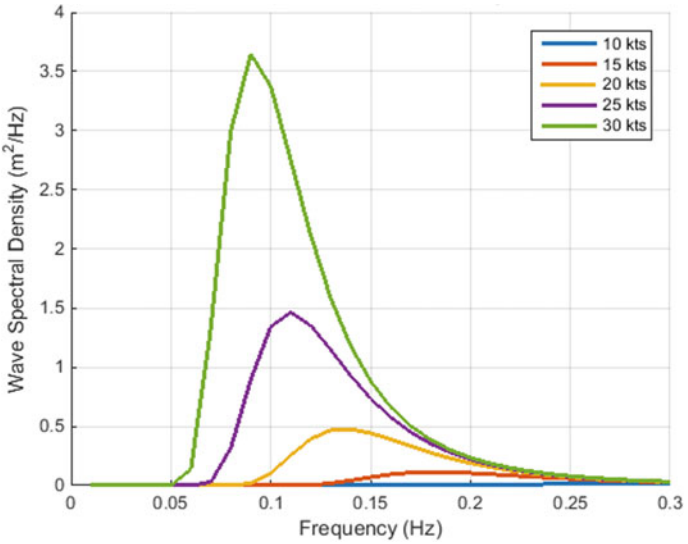

Fig. 5.4 Pierson–Moskowitz sea surface spectra for various wind speeds

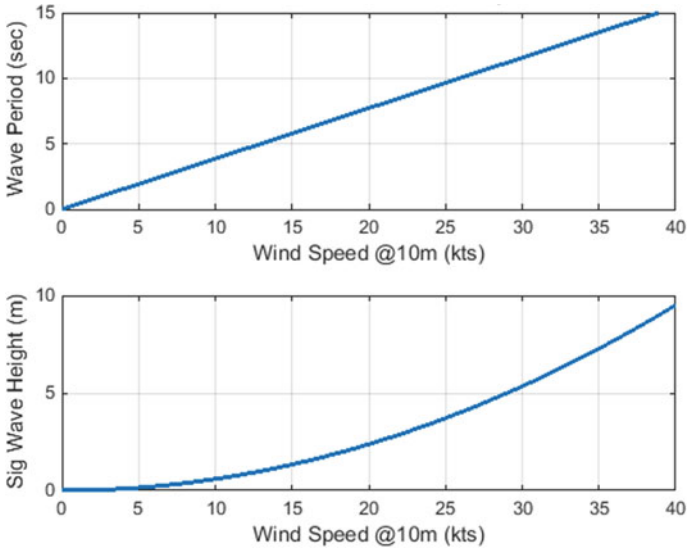

Fig. 5.5 Pierson–Moskowitz-predicted wave period and significant wave height as a function of wind speed

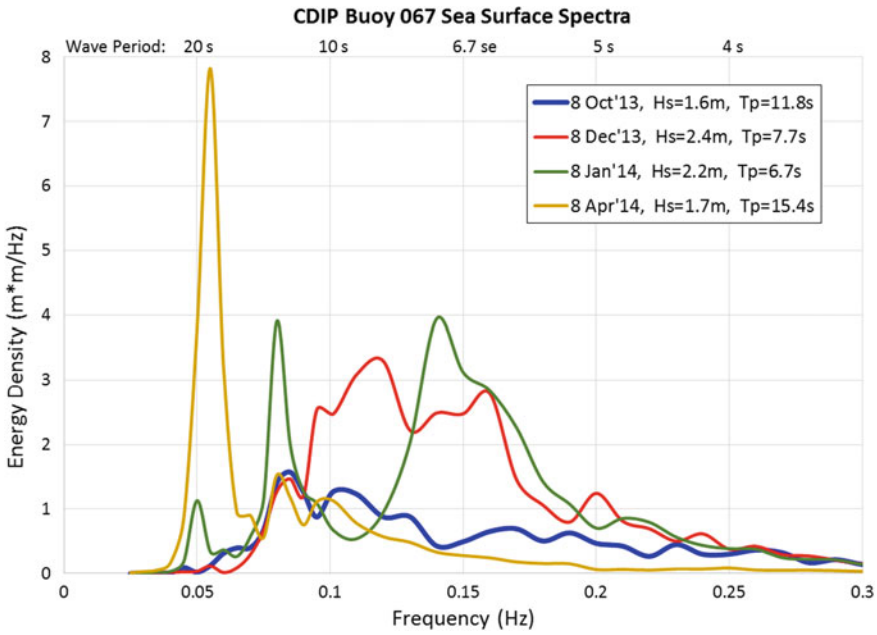

Fig. 5.6 CDIP Buoy 067 Sea Surface Spectra measurements

wave period swell. The significant wave height and wave period of the spectrum peak is also indicated.

As shown, both predictions and measurements indicate the ocean heave frequencies will be predominately within the 0.03–0.3 Hz frequency band. This wave energy band is directly within the infrasound band, and, therefore, the potential exists that ocean heave-induced pressure fluctuations sensed by a maritime infrasound sensor will interfere with the monitoring of infrasound signals-of-interest that are within this band, as depicted in Fig. 5.7. In fact, not surprisingly, the ocean heave frequency band overlaps with the microbarom band, as they are both driven by the same oceanographic effect. This also overlaps with the band used to monitor for nuclear explosions, potentially obscuring them from being detected. If the frequency content of the infrasound signal-of-interest and the sea surface spectrum band do not overlap in frequency, signal processing with conventional filtering techniques (low- or high-pass filtering) will adequately be able to separate the infrasound signals from the interfering heave-induced signals. However, if their spectra overlap, there will be interference unless the sensor heave is mitigated or compensated for in some manner.

This discussion is focused on the infrasound interference signal due to heave (N_{heave} in Eq. 5.1). As is clearly understood from the previous discussion, sea surface roughness is correlated to winds. Independent of heave interference, wind noise (N_{wind} in Eq. 5.1) will be another significant limiter to detection performance. However, the wind noise at the sensor location will be determined by the strength of

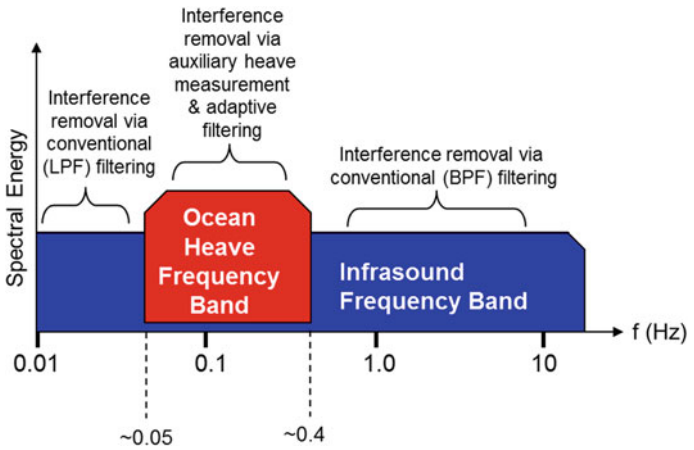

Fig. 5.7 Ocean heave contamination of the infrasound band

local winds, not necessarily the winds which produced the swell, which may have been generated by winds at great distances away. For example, the swell of April 2014 in Fig. 5.6 is a single, clean, long-period swell which was presumably generated far away and propagated a long distance to the sensor, where local winds may be calm. Also, there is a latency effect: swell is generated only after sustained winds exist for an adequate amount of time, and it dies away some time after the generating winds have died off. Thus, it is entirely possible for a sensor to experience large wave motion, yet not be overcome by wind noise.

5.5.2 *Ocean Heave Mitigation*

A proposed solution to the heave interference problem is to obtain an independent measurement of the infrasound sensor's heave as a reference signal to cancel the heave-induced pressure fluctuation from the infrasound sensor's signal. This is done by using a collocated inertial measurement unit (IMU), which tracks sensor motion, usually with 3-axis accelerometers and 3-axis gyros, and can independently compute accurate measurements of heave motion while being insensitive to other infrasound signals. This measurement should be highly correlated to the heave-induced interference pressure, and therefore can be used in an adaptive noise cancellation algorithm (Widrow and Stearns 1985); Fig. 5.8 shows a block diagram of such a process. The microbarometer senses the pressure signals originating from an infrasound signal-of-interest ($SL_{SOI} - TL$, in Eq. 5.1), if present, the infrasound background noise level ($(N_{wind} - PG_{wind} - F_{wind}) \oplus N_{other}$, in Eq. 5.1), and the interfering pressure fluctuations resulting from ocean heave (N_{heave}, in Eq. 5.1). A noisy estimate of the heave is obtained via the external IMU and serves as a

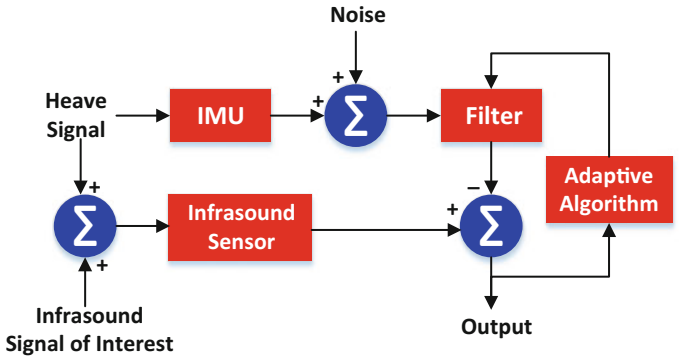

Fig. 5.8 Diagram of the interference cancellation filter algorithm

reference signal. The filter operates as a finite impulse response (FIR) filter with adjustable weights, and thus includes a tapped delay line of N samples (taps) of the IMU signal, which are each multiplied by an adjustable weighting coefficient. The sum of the weighted IMU samples is subtracted from the infrasound sensor sample to produce the system output. Successful subtraction, $N_{heave} - PG_{heave}$, depends on good correlation between the reference and heave pressure signals. The output is also supplied as an error signal to an adaptive algorithm through a feedback loop, which adjusts the weights of the adaptive filter to minimize the error for the next iteration of the filter's operation. There are a number of adaptive algorithms that can be used, including least mean squares (LMS) and recursive least squares (RLS) as two of the simplest and most common (Widrow and Stearns 1985). Proper tuning of the algorithm parameters is required to obtain optimal performance for a specific signal characterization. As the filter adapts using this feedback loop, it drives the output to be as small as possible, which corresponds to maximum removal of the correlated heave signal and the output more closely representing just the infrasound SOI ($SL_{SOI} - TL$) and/or the natural infrasonic background and wind noise ($([N_{wind} - PG_{wind} - F_{wind}) \oplus N_{other}]$, in Eq. 5.1).

5.6 Infrasound Data Collection and Heave Cancellation from Ship-Hosted Infrasound Sensor

Initial testing of the heave compensation method was performed with data collected during February, 2016, off the coast of Southern California, during an at-sea experiment. A Hyperion Inc. IFS-5000 microbarometer (com/wp-content/uploads/2013) originally developed by the National Center for Physical Acoustics (NCPA) was fielded onboard the R.V. Acoustic Explorer (AX) research vessel, shown in Figs. 5.9 and 5.10. The microbarometer was installed on the upper afterdeck of the AX, nearly above the ship's center of rotation (COR) to reduce any negative effects

Fig. 5.9 Acoustic Explorer research vessel

Fig. 5.10 The Hyperion IFS-5000 microbarometer sensor (left) and the SBG inertial measurement unit (right)

of pitch and roll. In addition, an SBG Ekinox-A AHRS (attitude, heading, reference system) IMU (https://www.sbg-systems.com/products/ekinox-high-performance-mems-ahrs), shown in Fig. 5.10, was installed in close proximity to the microbarometer, within about 1–2 feet. Any residual distance offset between the IMU and COR was measured and programmed into the IMU firmware to be accounted for in its heave calculation algorithm. The ship deployed and these sensors recorded for about a 1 week period. Sea conditions during the period were low, with swell causing heave fluctuations of usually less than 0.5 m.

A representative 5-min segment of microbarometer pressure and IMU heave data was selected for a heave cancellation analysis. The raw microbarometer pressure and IMU heave timeseries data were low-pass filtered below 0.5 Hz in order to isolate the effect of heave from other higher frequency acoustic energy which may have been present in the data (and which can be recovered via normal band pass filter methods because they are out of the heave band). The pressure and heave (IMU) time series were resampled to have a common sample rate of 25 Hz, which is oversampled by a factor of about 10. The heave data were converted from distance units (meters) to pressure units (Pa) using the relationship in Eq. 5.4. Figure 5.11 shows a comparison between a 120-s segment of the pressure and heave signal time series. The performance of the adaptive cancellation filter is dependent upon the degree to which the two signals are correlated (Grimmett and Zabal 1993). The normalized correlation function was computed between these signals and the peak correlation coefficient was found to be 0.97; this high degree of correlation is also visually evident in the time series. There is a small difference in amplitude due to the fact that the conversion of the IMU heave from meters to pressure is based on an average approximation (Eq. (5.4)), not a location/time-specific value, in addition to measurement inaccuracies of both the microbarometer and IMU, the latter of which has a maximum accuracy of 2.5 cm of heave. However, this is easily compensated for by the filter taps of the adaptive filter. Their spectra, computed over the entire 300-s time window, are shown overlaid in Fig. 5.12, and are also seen to be very similar within the ocean heave band. It is clear for this data segment that the heave is sufficiently strong to be a dominant effect, potentially obscuring other quieter infrasound signals that may be present.

In order to assess and quantify the performance of the algorithm, we choose to inject an artificial signal to represent our infrasound signal-of-interest (SOI). Doing this also facilitates being able to quantitatively assess the algorithm's performance under different SOI sound pressure levels. For the artificial signal, we chose one that occupies a similar frequency band as the actual heave which was present during the experiment. Although, in general, the SOI would be generated from an event other than ocean heave, for this analysis we have obtained a separate, uncorrelated ocean heave measurement obtained from an ocean monitoring buoy which is a part of the CDIP network (http://cdip.ucsd.edu/) to use as our SOI due to ease of availability and guarantee of the desired frequency content within the heave band. Figure 5.13 shows a portion of the artificial SOI compared to the microbarometer-received signal. Note that we choose to inject the signal only after 60 s, with no signal injected during the first minute of the data used in this analysis. This will enable us to understand the performance of the algorithm when there is no SOI present. In this figure, the SOI has been amplitude scaled so that it has equivalent power as the heave-dominated microbarometer pressure signal, i.e., a SOI-to-Heave ratio (SHR) of 0 dB. The normalized correlation coefficient between the nonzero portion of the injected SOI and the sensor pressure signal was 0.27, and is clearly observed to be uncorrelated. Figure 5.14 shows a comparison of the two signals' spectra, which shows that although they occupy the same frequency band,

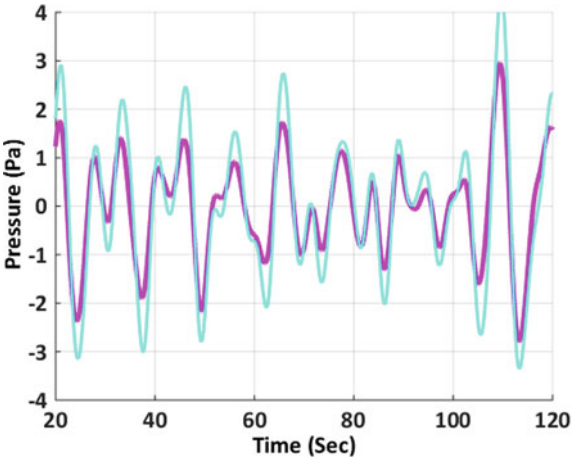

Fig. 5.11 Microbarometer pressure signal time series (magenta) and IMU heave signal time series (cyan) selected for analysis

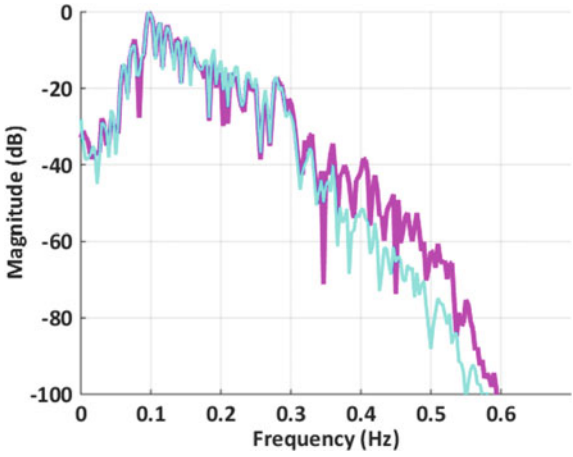

Fig. 5.12 Microbarometer pressure signal spectra (magenta) and IMU heave signal spectra (cyan) corresponding to the signals in Fig. 5.11

they do not share a similar, detailed spectral structure, even within the ocean heave band.

The artificial SOI is injected into the data set by summing with the received microbarometer pressure signal, as shown in Fig. 5.15 (green curve). This composite signal is composed of: the as-yet unobservable infrasound background noise, the heave-induced pressure signal, and the injected artificial SOI with a signal-to-heave ratio of 0 dB (shown over the interval from 60 to 120 s). Before 60 s we see that the composite is just the microbarometer signal, which is dominated by the heave effect. This composite signal serves as the input to the adaptive noise cancellation system. The IMU heave measurement is fed to the system as the reference signal (the cyan curve from Fig. 5.11). The RLS algorithm was used to update an adaptive filter with a length of 11 taps. The RLS algorithm has an exponential weighting, or forgetting factor, $0 < \lambda < 1$, which defines how much to

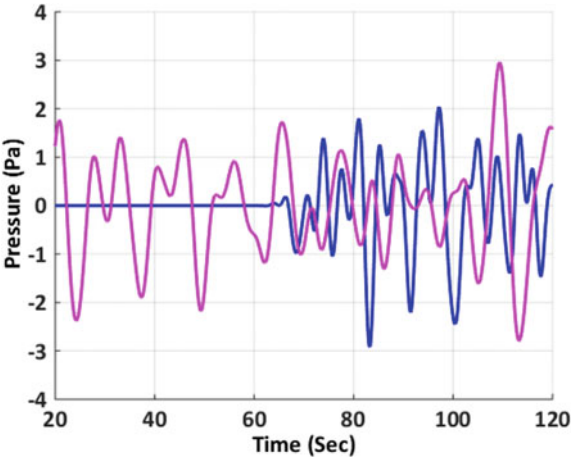

Fig. 5.13 Time series of the artificial infrasound signal-of-interest (SOI) (blue), SHR = 0 dB, injected after 60 s, compared to the microbarometer pressure signal time series (magenta)

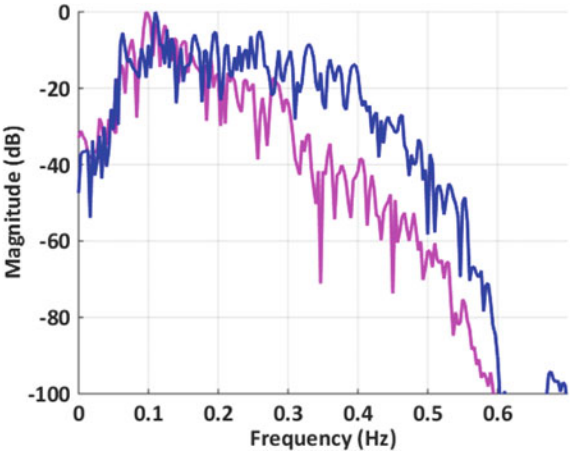

Fig. 5.14 A comparison of the spectra of the artificial infrasound SOI (blue) and the microbarometer pressure signal (magenta), corresponding to the time series signals in Fig. 5.13

weight past samples versus the current sample. It is approximately equivalent to a sliding window of length $\frac{\lambda}{1-\lambda}$ samples. In this case, a value of 0.9999 has been used, corresponding to approximately 10,000 samples, or 400 s at the 25 Hz sample rate.

The output of the adaptive filter is compared with the input signal in Fig. 5.16. The result shows effective cancellation of the heave-induced pressure component, while the injected SOI has been recovered. The residual output signal seen before 60 s is likely the actual infrasound noise background without the interference of ocean heave. Figure 5.16 compares the injected SOI and the adaptive filter's output. In this example, the cancellation algorithm has effectively recovered the SOI (shown over the interval from 60 to 120 s) and revealed its estimate of the true (heave less) infrasonic natural and wind noise background (before 60 s).

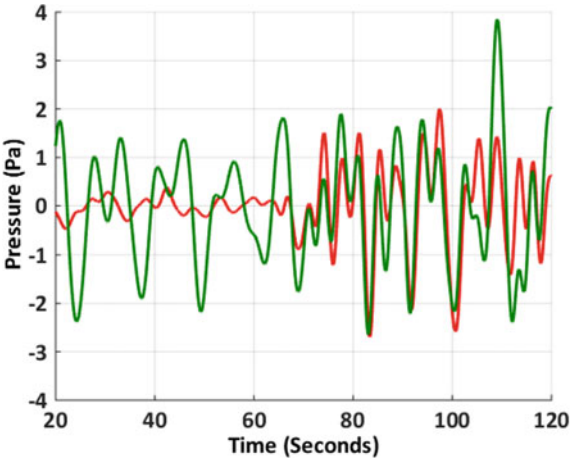

Fig. 5.15 Comparison of the composite signal (with injected artificial infrasound SOI of equal power to heave, SHR = 0 dB) input to the adaptive cancellation filter (green) and the filter's output (red)

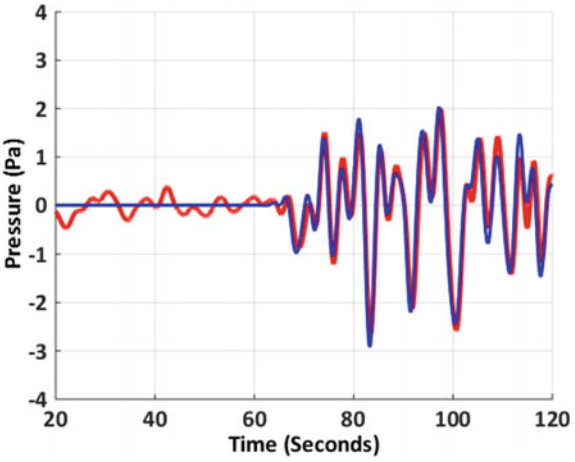

Fig. 5.16 A comparison of the injected infrasound SOI, SHR = 0 dB (blue) and the adaptive cancellation filter's output (red)

Figure 5.17 shows the filter input and output when the SOI has been reduced in power by 9 dB relative to the previous example. Here the filter's input looks very nearly identical to the heave-dominated sensor pressure signal, since the SOI is small. The output shows that the SOI has been recovered and that it is still detectable above the infrasound noise floor. Figure 5.18 shows the similarity of the injected SOI and the recovered SOI. Finally, we run the adaptive cancellation filter without injecting any SOI; Fig. 5.19 shows the heave-dominated pressure signal input and the estimated, heave-less infrasound noise background. The algorithm's heave power reduction is found to be about 14 dB, for the conditions of this experiment, with the given infrasound noise floor level, and the heave fluctuations that were limited to less than 0.5 m.

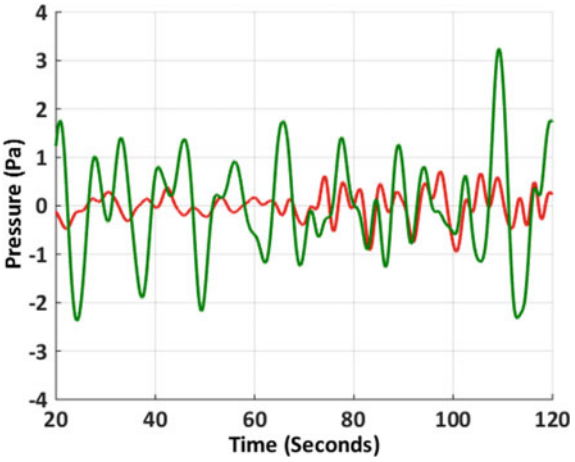

Fig. 5.17 Comparison of the composite signal (with injected artificial infrasound SOI of 1/8 the power of the heave, SHR = −9 dB) input to the adaptive cancellation filter (green) and the filter's output (red)

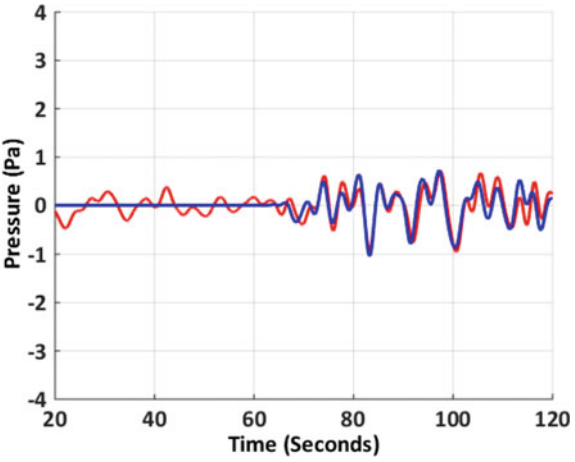

Fig. 5.18 A comparison of the injected infrasound SOI (blue) and the adaptive cancellation filter's output (red), for the data in Fig. 5.17

In order to fully characterize the performance of the heave cancellation algorithm, we now scale the injected SOI over a range of SOI-to-Heave ratios to characterize the effectiveness of SOI recovery and heave cancellation. The input signal SHR is varied by doubling the SOI mean power (via 3 dB steps) from −24 dB to +12 dB relative to the heave-dominated pressure signal (SHR = 0 dB implies the equal power case presented in Figs. 5.8, 5.9, 5.10 and 5.11). For each of these cases, we evaluate the cancellation performance.

Figure 5.20 shows the acoustic power levels of the various signals in the processing, in dB relative to the power of the heave. Three regimes are indicated: power of the SOI less than the power of the noise background ($P_N > P_{SOI}$), power of the SOI greater than the power of the heave interference ($P_{SOI} > P_H$), and power of the SOI greater than noise power but less than the heave interference ($P_N <$

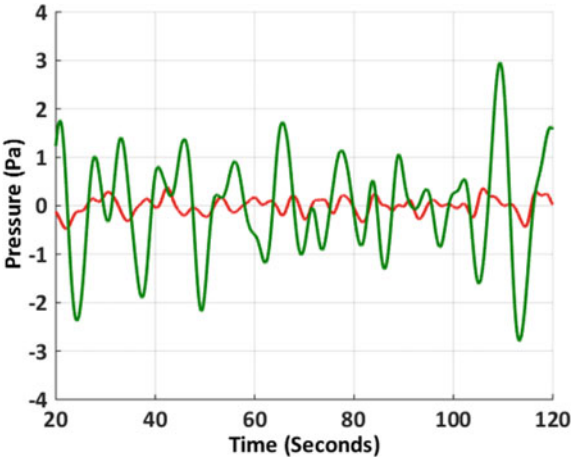

Fig. 5.19 Comparison of the composite signal (without any injected artificial infrasound SOI, SHR = −Inf dB) input to the adaptive cancellation filter (green) and the filter's output (red)

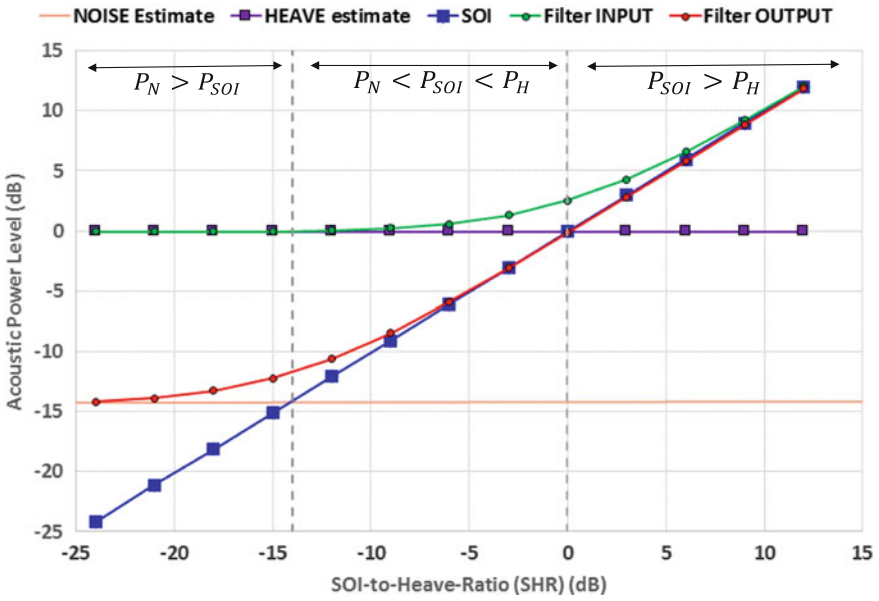

Fig. 5.20 Mean acoustic power levels as a function of the SHR. The filter input (green) is the composite (power sum) of the noise floor (orange), the heave (purple), and the SOI (blue). The output (red) is shown for three regimes: SOI power below the noise, SOI power above the heave, and SOI between the noise and the heave

$P_{SOI} < P_H$). The heave interference power is shown to be constant at 0 dB and the filter output noise background was determined to be −14 dB. This was estimated by measuring the amount of suppression achieved by the filter when no SOI was injected.

The filter input signal is the composite (power sum) of the acoustic noise background, the heave-induced interference, and the SOI. We see that the filter input power is dominated by the heave, until the SOI power becomes equal to the heave. As the SOI power increases further in the regime $P_{SOI} > P_H$, the filter input signal becomes dominated by the SOI. Here, the SOI may already be strong enough to be detectable above the heave interference, however, the heave reduction algorithm will further increase its detectability. When dominated by the SOI, the filter's output signal has the heave removed while retaining the SOI, so its power is close to the power of the SOI. As the input SOI power drops in the regime $P_N < P_{SOI} < P_H$, we see that the filter is able to reduce the output power to the point that the SOI becomes dominant. In this regime, the SOI is not detectable at the input, but after applying the algorithm, it becomes detectable. When the input SOI power drops below the infrasound noise floor ($P_N > P_{SOI}$), the SOI is obscured by the infrasound noise floor and therefore will not be recoverable using this method, even when the heave has been reduced by its maximum amount. Other noise cancellation processes (e.g., beam forming, etc.) could be considered to improve detectability in this case, if multiple, appropriately spaced sensors are available.

The estimated noise level in Fig. 5.20 is actually a combination of three residual signals: unsuppressed heave, heave measurement noise, and infrasound background. The first consists of any remaining pressure fluctuations due to heave that were not removed by the adaptive filter. This is presumed to be small due to the lack of correlation between the input and output signals. The heave measurement noise is an artifact due to inaccuracies in both the microbarometer and IMU in capturing the vertical displacement of the platform. The infrasound background consists of actual sources of low-frequency pressure waves that exist in the environment. Because these are unknown, it is impossible for us to identify how much of the output signal power is due to each of these three components. Thus, it is important to understand that the 14 dB reduction in output power shown here is only a lower bound on the amount of heave suppression that has been achieved; the actual heave remaining in the output signal may, in fact, be much lower than, and dominated by, the measurement noise and/or the natural infrasound background. The SOI detectability (the difference between SOI and combined obscuring signals) is always improved by the same amount (14 dB in our case) regardless of injected SOI level, despite the fact that the output power is affected less and less as SOI level increases due to its detectability being higher to begin with. The amount of detectability improvement possible with this algorithm will depend on the difference between the power levels of the data's heave interference (due to ocean swell) and the infrasound noise background, as well as how correlated the filter reference signal is with the heave content in the data and how well the algorithm is tuned. The detectability improvement observed will depend on the SOI level with respect to the amount of combined background noise of the three aforementioned sources.

5.7 Infrasound Data Collection and Heave Cancellation from USV-Hosted Infrasound Sensor

Another experiment was conducted to collect infrasound data from a USV platform, rather than from a ship. The Hyperion microbarometer and SBG IMU (described previously) were installed on a Liquid Robotics Wave Glider SV-2 USV (http://liquidr.com/). The Wave Glider is composed of a surfboard-sized surface float and a subsurface glider unit, as shown in Fig. 5.21. The surface float provides GPS and navigation, communications gear, space for payload electronics, and solar panels for electrical power. The unit harvests wave energy for propulsion; as the ocean heave draws the float up and down, the tension with the glider unit provides forward propulsion. The unit can be navigated remotely through a server connected to the internet. It is persistent and can remain on a mission for up to one year, traveling at speeds of 0–1.5 knots.

Figure 5.22 shows the Wave Glider with the microbarometer installed on a slightly raised platform. A colander is put over the top of the Wave Glider to act as a shroud and provide some wind noise reduction for the sensor. The sensor was also

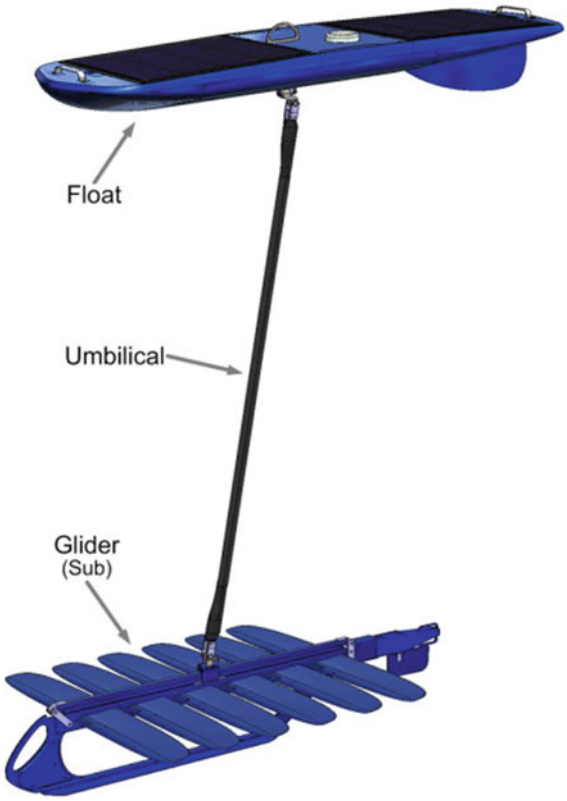

Fig. 5.21 The Wave Glider® SV2—designed and manufactured by Liquid Robotics, Inc. Image used with permission

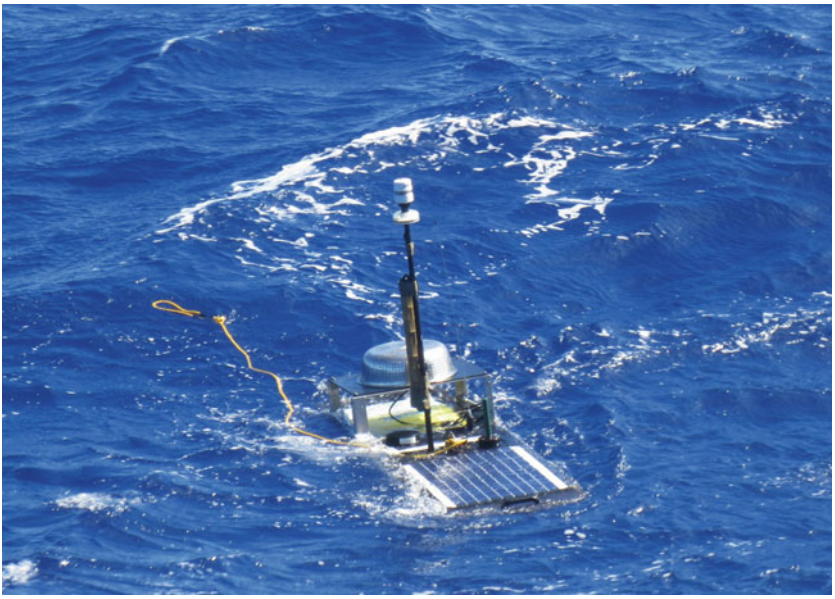

Fig. 5.22 The USV-hosted infrasound sensor configuration

wrapped in open cell, nearly acoustically transparent foam to further reduce wind noise and to provide some resistance to water penetration. The IMU and data collection electronics were housed inside the float in a payload bay. The mast hosts GPS and Iridium satellite communications antennas. The system was deployed for operations for 1 day in the Pacific Ocean off the coast of Hawaii and was piloted remotely. Data was collected and the instrument performance was evaluated. The sea conditions produced swell of about 0.5–1.5 m over the data collection period.

An analysis similar to that done with the ship-hosted experiment was performed to demonstrate the heave cancellation. Here the injected SOI was chosen to be an infrasound detection of the Chelyabinsk meteor event, which occurred in February 2013. This event was detected by many infrasound stations around the world. Time series data of this event, detected by a single microbarometer in the USArray TA (Station G42A, LDF channel located in Wisconsin, U.S.A.), was obtained from the Incorporated Research Institutions for Seismology (IRIS) (http://www.iris.edu/hq/). Figure 5.23 shows a spectrogram of the Chelyabinsk infrasound event, from which a SOI was extracted, amplitude-scaled, and injected into the Wave Glider-hosted microbarometer data.

Figure 5.24 shows the microbarometer data (magenta) before SOI injection compared to the IMU signal (cyan) for a 200-s data segment. The extracted Chelyabinsk meteor signal was scaled into Pascals (from A/D counts, because sensor calibration information was not available) such that it would have equal power as the received microbarometer data, which are both shown overlaid in Fig. 5.25. These were then summed and the composite signal (SOI, heave, and infrasound

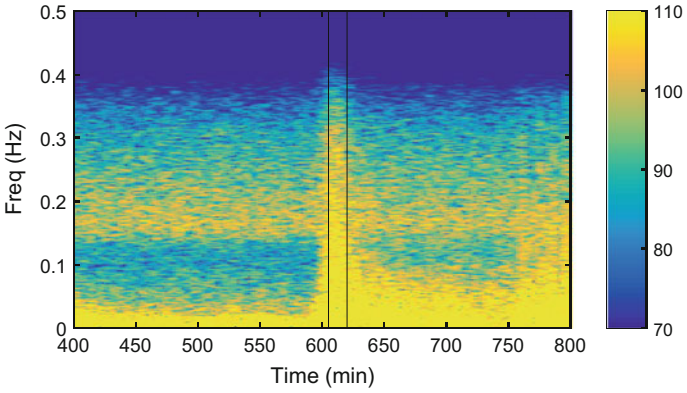

Fig. 5.23 Spectrogram of the Chelyabinsk meteor detection data (in dB), with a highlighted section from which a signal-of-interest was extracted, scaled, and used for algorithm demonstration

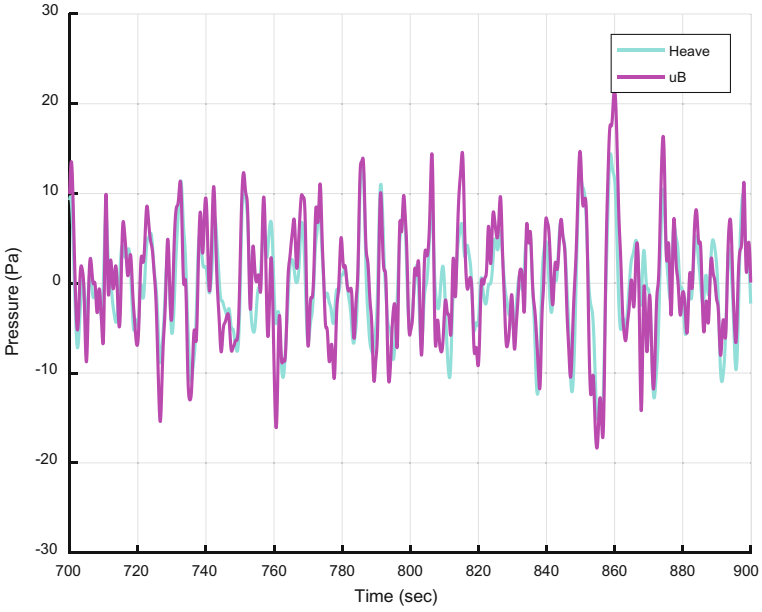

Fig. 5.24 The Wave Glider-hosted microbarometer data (magenta) compared to the heave signal (cyan)

background) was input to the adaptive heave cancellation filter. The results are shown in Fig. 5.26, where reductions in the heave are evident. Figure 5.27 compares the injected SOI with its recovered version after adaptive filtering and reasonable results are obtained.

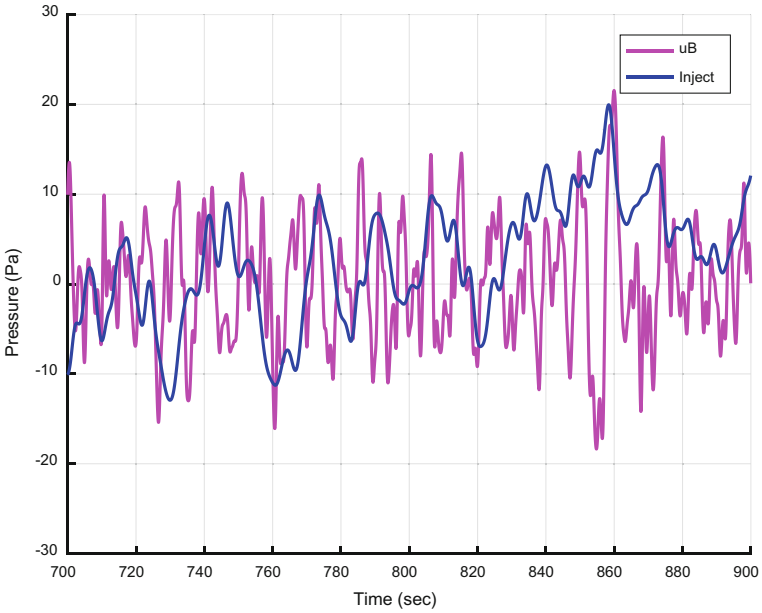

Fig. 5.25 The microbarometer data (magenta) and the injected, scaled Chelyabinsk signal (blue)

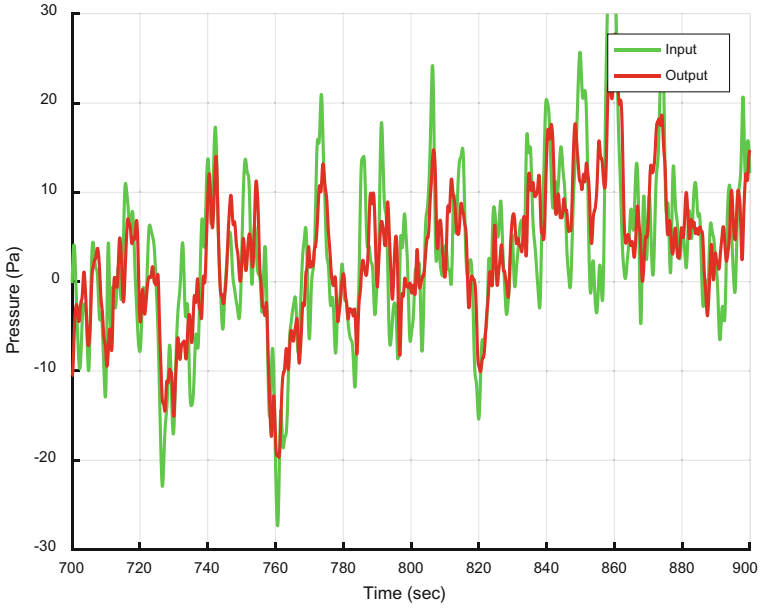

Fig. 5.26 The adaptive heave cancellation input (sum of scaled Chelyabinsk signal and microbarometer signal, in green), and algorithm output (red)

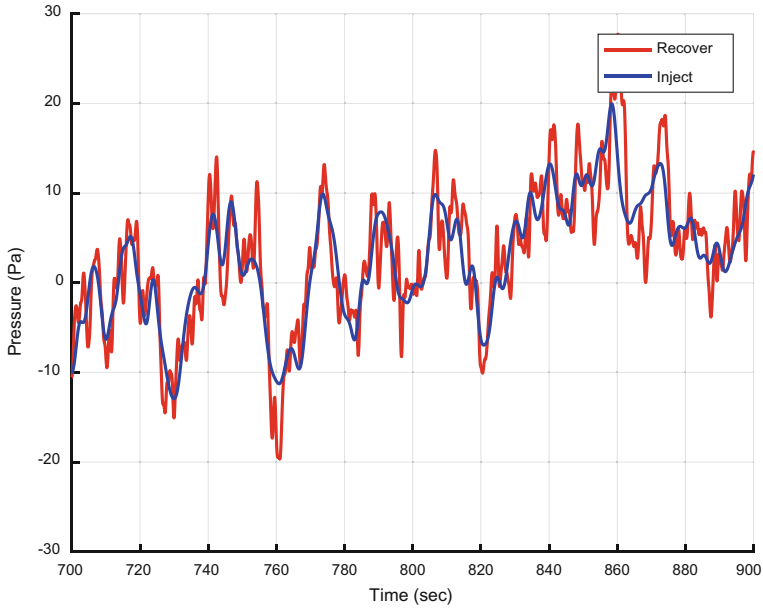

Fig. 5.27 The injected, scaled Chelyabinsk signal (blue) and algorithm output signal (red) showing the good recovery of the Chelyabinsk signal

5.8 Summary

Infrasound monitoring stations are normally land-based systems. The successful development of infrasound data measurement systems fielded in the maritime environment offers the potential to collect valuable infrasound data over the expansive oceanic areas of the globe. This can potentially augment land-based stations by providing improvements in detection and infrasound event coverage. In addition, it offers improvement in infrasound event localization, tracking, and classification/verification. The oceans offer the possibility of a denser worldwide network of infrasound sensing that would provide an increased understanding of the atmospheric effects and impacts on infrasound propagation.

To make maritime infrasound stations viable, various challenges must be overcome. The main foreseen challenges are: protecting and making the sensor survivable in the maritime environment, overcoming the negative effects of sensor motion due to ocean heave, ocean wind noise mitigation, and forming multi-element arrays of sensor while in the maritime. Work so far has focused on sensor survivability and sensor motion mitigation.

Actual deployments on the ocean have been accomplished onboard ship and USV host platforms. The USV deployments have been made over only short durations and in a limited set of ocean/environmental conditions. Better protection of the sensor will be required, such that it is open to the atmosphere but closed to

water. Improvements are being developed to provide a more robust weatherproofing to the system. While the sensors deployed on a ship were better protected from water and wind, they did suffer from significant ship noise and vibration. The USV implementation showed promise by providing a lower background noise floor than the ship. The heave interference signal has been prominent in data sets from both ship and USV, even though the ocean swell they were subject to was small. A potential solution to the ocean heave problem has been demonstrated on these data with an adaptive noise cancellation algorithm and the use of an external heave reference signal obtained from an IMU.

Further efforts are needed to validate this preliminary work undertaken so far, and to investigate solutions to remaining problems and answers to open questions. First, a characterization of the wind noise levels in the ocean environment is needed. Mitigation methods, including windscreens or multi-sensor cancellation methods are to be explored. Also, once performance on a single sensing node is determined to be adequate, we aim to demonstrate the capability of forming arrays of sensors in the ocean environment by configuring and sailing a small group of USVs.

Deployments over longer durations and in different ocean conditions are needed to assess reliability. Such a long-term deployment will provide opportunities for a demonstration of actual, attributable infrasound signal to be detected. Such efforts will continue to explore the feasibility and potential that a maritime infrasound sensing technology may offer.

Acknowledgements We acknowledge the SPAWAR Systems Center Pacific NISE program, which provided the required funding to perform this work. We acknowledge the managers, captain, and crew of the R.V. Acoustic Explorer ship for their experimental support in collecting the infrasound measurements used herein. We acknowledge Talmadge Carrick (National Center for Physical Acoustics) and Chad Williams (Hyperion Technology Group) for useful discussions and advice on sensor configurations during experimentation.

References

Assink J, Smets P, Marcillo O, Weemstra C, Lalande J-M, Waxler R, Evers L (2019) Advances in infrasonic remote sensing methods. In: Le Pichon A, Blanc E, Hauchecorne A (eds) Infrasound monitoring for atmospheric studies, 2nd edn. Springer, Dordrecht, pp 605–632

Axys Technologies. http://axystechnologies.com/

Bowman C, Lees J, Cutts J, Komjathy A, Young E, Seiffert K, Boslough M, Arrowsmith S (2019) Geoacoustic observations on drifting balloon-borne sensors. In: Le Pichon A, Blanc E, Hauchecorne A (eds) Infrasound monitoring for atmospheric studies, 2nd edn. Springer, Dordrecht, pp 125–171

Bratt SR, Bache TC (1988) Locating events with a sparse network of regional arrays. Bull Seismol Soc Am 78:780–798

Cansi Y (1995) An automatic seismic event processing for detection and location: the P.M.C.C. method. Geophys Res Lett 22(9):1021–1024

Ceranna L, Matoza R, Hupe P, Le Pichon A, Landès M (2019) Systematic array processing of a decade of global IMS infrasound data. In: Le Pichon A, Blanc E, Hauchecorne A (eds) Infrasound monitoring for atmospheric studies, 2nd edn. Springer, Dordrecht, pp 471–482

Christie DR, Campus P (2010) The IMS infrasound network: design and establishment of infrasound stations. In: Le Pichon A, Blanc E, Hauchercorne A (eds) Infrasound monitoring for atmospheric studies. Springer

Chunchuzov I, Kulichkov S (2019) Internal gravity wave perturbations and their impacts on infrasound propagation in the atmosphere. In: Le Pichon A, Blanc E, Hauchecorne A (eds) Infrasound monitoring for atmospheric studies, 2nd edn. Springer, Dordrecht, pp 551–590

Datawell BV. http://www.datawell.nl/Home.aspx

De Groot-Hedlin CD, Hedlin M (2015) A method for detecting and locating geophysical events using groups of arrays. Geophys J Int 203:960–971

de Groot-Hedlin C, Hedlin M, Drob D (2010) Atmospheric variability and infrasound monitoring. In: Le Pichon A, Blanc E, Hauchercorne A (eds) Infrasound monitoring for atmospheric studies. Springer

de Groot-Hedlin C, Hedlin M (2019) Detection of infrasound signals and sources using a dense seismic network. In: Le Pichon A, Blanc E, Hauchecorne A (eds) Infrasound monitoring for atmospheric studies, 2nd edn. Springer, Dordrecht, pp 669–699

Drob D (2019) Meteorology, climatology, and upper atmospheric composition for infrasound propagation modeling. In: Le Pichon A, Blanc E, Hauchecorne A (eds) Infrasound monitoring for atmospheric studies, 2nd edn. Springer, Dordrecht, pp 485–508

Drob DP, Meier RR, Picone JM, Garces MM (2010) The IMS infrasound network: design and establishment of infrasound stations. In: Le Pichon A, Blanc E, Hauchercorne A (eds) Infrasound monitoring for atmospheric studies. Springer

Frazier G (2014) Application of parametric empirical Bayes estimation to enhance detection of infrasound transients. Presentation of infrasound technology workshop 2014, comprehensive test ban treaty organization, Oct 2014

Green DN, Bowers D (2010) Estimating the detection capability of the International Monitoring System infrasound network. J Geophys Res 115:D18116. https://doi.org/10.1029/2010JD014017

Grimmett D, Zabal X (1993) Performance criteria for coherent interping reverberation suppression, Naval Command Control and Ocean Surveillance Center, RDT&E Division (NRAD), TD 2591, Dec 1993

Grimmett D, Plate R, Goad J (2016) Ocean Heave cancellation for a maritime infrasound sensor. In: Proceedings of the MTS/IEEE oceans'16 conference, Sept 2016, Monterey, California

Hassellmann DE, Dunckel M, Ewing JA (1980) Directional wave spectra observed during JONSWAP 1973. J Phys Oceanogr 10:1264

Holthuijsen LH (2007) Waves in oceanic and coastal waters. Cambridge University Press, p 70

Hyperion Technology Group. http://hyperiontg.com/wp-content/uploads/2013/08/IFS5000SpecSheet.pdf

Incorporated Research Institutions for Seismology. http://www.iris.edu/hq/

Le Pichon A, Ceranna L, Vergoz J (2012) Incorporating numerical modeling into estimates of the detection capability of the IMS infrasound network. J Geophys Res 117:D05121. https://doi.org/10.1029/2011JD016670

Le Pichon A, Ceranna L, Vergoz J, Tailpied D (2019) Modeling the detection capability of the global IMS infrasound network. In: Le Pichon A, Blanc E, Hauchecorne A (eds) Infrasound monitoring for atmospheric studies, 2nd edn. Springer, Dordrecht, pp 593–604

Liquid Robotics. http://liquidr.com/

Manley JE (2008) Unmanned surface vehicles, 15 years of development. In: Proceedings of the MTS/IEEE oceans 2008 conference, Sept 2008, Quebec City, Canada

Marty J (2019) The IMS infrasound network: current status and technological developments. In: Le Pichon A, Blanc E, Hauchecorne A (eds) Infrasound monitoring for atmospheric studies, 2nd edn. Springer, Dordrecht, pp 3–62

Meltzer A (1999) The USArray initiative. Geol Soc Am Today 9:8–10

Met Office, The Beaufort Scale, Fact sheet 6 (version 01), National Meteorological Library and Archive, Devon, United Kingdom. www.metoffice.gov.uk/corporate/library/catalogue.html
Mialle P, Brown D, Arora N, colleagues from IDC (2019) Advances in operational processing at the international data centre. In: Le Pichon A, Blanc E, Hauchecorne A (eds) Infrasound monitoring for atmospheric studies, 2nd edn. Springer, Dordrecht, pp 209–248
Motwani A (2012) A survey of uninhabited surface vehicles, Technical Report MIDAS. SMSE.2012.TR.001, Marine and Industrial Dynamic Analysis, School of Marine Science and Engineering, Plymouth University, PL4 8AA, United Kingdom
National Oceanic and Atmospheric Administration (NOAA), National Data Buoy Center. http://www.ndbc.noaa.gov/
Nief G, Talmadge C, Rothman J, Gabrielson T (2019) New generations of infrasound sensors: technological developments and calibration. In: Le Pichon A, Blanc E, Hauchecorne A (eds) Infrasound monitoring for atmospheric studies, 2nd edn. Springer, Dordrecht, pp 63–89
Petersen P (1927) Zur Bestimmung der Windstärke auf See. Annalen der Hydrographie und Maritimen Meteorologie 55:69–72
Pierson WJ, Moskowitz L (1964) A proposed spectral form for fully developed wind seas based on the similarity theory of A. A. Kitaigorodskii. J Geophys Res 69:5181–5190
Pilger C, Ceranna L, Ross JO, Le Pichon A, Mialle P, Garces MA (2015) CTBT infrasound network performance to detect the 2013 Russian fireball event. Geophys Res Lett 42:2523–2531. https://doi.org/10.1002/201sgl063482
SBG systems. https://www.sbg-systems.com/products/ekinox-high-performance-mems-ahrs
Scripps Institution of Oceanography, Coastal Data Information Program (CDIP). http://cdip.ucsd.edu/
U.S. Standard Atmosphere (1976) National Oceanic and Atmospheric Administration, National Aeronautics and Space Administration, United States Air Force, NOAA-S/T 76-1562, Oct 1976
Vergoz J, Le Pichon A, Millet C (2019) The antares explosion observed by the USArray: an unprecedented collection of infrasound phases recorded from the same event. In: Le Pichon A, Blanc E, Hauchecorne A (eds) Infrasound monitoring for atmospheric studies, 2nd edn. Springer, Dordrecht, pp 349–386
Waxler R, Assink J (2019) Propagation modeling through realistic atmosphere and benchmarking. In: Le Pichon A, Blanc E, Hauchecorne A (eds) Infrasound monitoring for atmospheric studies, 2nd edn. Springer, Dordrecht, pp 509–549
Widrow B, Stearns SD (1985) Adaptive signal processing. Prentice-Hall, Englewood Cliffs, NJ

Part II
Instrumentation, Network and Processing: Processing

Chapter 6
Advances in Operational Processing at the International Data Centre

Pierrick Mialle, David Brown, Nimar Arora and colleagues from IDC

Abstract The International Data Centre (IDC) of the Comprehensive Nuclear-Test-Ban Treaty Organization (CTBTO) Preparatory Commission receives and processes in near-real-time data from the International Monitoring System (IMS), a globally distributed network of seismic, hydroacoustic, infrasound and radionuclide stations. Once completed, the IMS network will comprise 60 infrasound stations of which 49 have been installed and certified as of beginning of 2017 (Fig. 6.1). The infrasound stations are arrays of measurement systems that are sensitive to acoustic pressure variations in the atmosphere in the IMS frequency band between 0.02 and 4 Hz. The array configurations include 4–15 elements, with typical designs of 4–8 elements, and with apertures between 1 and 3 km following IMS requirements (Marty 2018; Christie and Campus 2010). After a design and development phase of more than 10 years, the IDC automatic processing system and interactive analysis are fully operational for infrasound technology since February 2010. After reception, storage and referencing in the IDC database, the station data are automatically processed individually (e.g. the station processing stage) (Brachet et al. 2010). Based on the results of the station processing the network processing is initiated to form events with all three waveform technologies. The event information is then reported in IDC products (or bulletins) referred to as Standard Event Lists (SELs). Since 2010, the bulletin production deadlines have been revised and accommodate late arriving data and the signal propagation times for all waveform technologies (Coyne et al. 2012). The final automatic bulletin containing infrasound signals associated to waveform events is the SEL3, which is reviewed by IDC analysts. The result of the interactive review process is the Late Event Bulletin (LEB) on which event definition criteria are applied to produce the Reviewed Event Bulletin (REB). The REB is the final waveform product of the IDC and currently, during provisional operations, the target timeline for publishing the REB is within 10 days of real time. After Entry Into Force (EIF) of the

P. Mialle (✉)
CTBTO PTS/IDC, Vienna, Austria
e-mail: pierrick.mialle@ctbto.org

D. Brown
Geoscience Australia, Canberra, Australia

N. Arora
Bayesian Logic, Cambridge, USA

A. Le Pichon et al. (eds.), *Infrasound Monitoring for Atmospheric Studies*,
https://doi.org/10.1007/978-3-319-75140-5_6

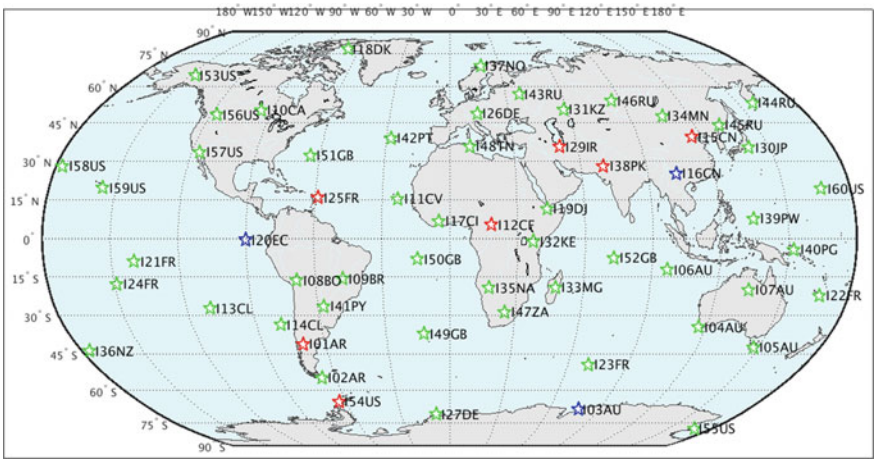

Fig. 6.1 IMS infrasound component with the location of the 60 planned arrays. The green stars denote the certified stations, the blue star for stations installed or under construction and the red stars for planned station where construction has not yet started (Status as of March 2017)

Treaty, the target timeline is reduced to 48 h. Specialized software has been developed for every processing stage at the IDC in order to improve signal-to-noise ratio, detect infrasound signals, categorize and identify relevant detections, form automatic events and perform interactive review analysis. For the period 2010–2017, thousands of waveform events containing infrasound associations appear in the IDC bulletins, and in particular in the REB and the LEB (Late Event Bulletin). This demonstrates the sensitivity of the IMS infrasound component and the IDC ability to globally monitor the infrasound activity. The unique information gathered by the IMS systems have been widely used for civil and scientific studies and have resulted in numerous publications on meteor impacts such as the largest ever infrasound recorded event that is the Chelyabinsk meteor in February 2013 (Brown 2013; Pilger et al. 2015; Le Pichon et al. 2013; Pilger et al. 2019) as well as other observed fireballs and meteors (Marcos et al. 2016; Caudron et al. 2016; Silber and Brown 2019), on powerful volcanic eruptions (Matoza et al. 2017, 2019), on controlled explosions (Fee et al. 2013), on announced underground nuclear test by the Democratic People's Republic of Korea (DPRK) (CTBTO 2013b, 2017b; Che et al. 2009, 2014) or on atmospheric dynamic research (Le Pichon et al. 2015; Blanc et al. 2019), on characterizing the infrasound global wavefield (Matoza et al. 2013; Ceranna et al. 2019), or on gravity waves study (Marty et al. 2010; Chunchuzov and Kulichkov 2019; Marlton et al. 2019) that could lead to deriving a space and time-varying gravity wave climatology (Drob 2019).

6.1 IDC Operations Review 2010–2017

6.1.1 IDC Processing System

The design and development process of the IDC infrasound system was carried out during the first years of establishment of the IDC (2000–2010) (Brachet et al. 2010). The stations in the IMS network send data to the IDC according to the Formats and Protocols specified in the corresponding IMS Operational Manual (Marty 2018). Stations in the primary seismic, hydroacoustic and infrasound networks send data continuously to the IDC and are processed automatically, while stations in the auxiliary seismic network are processed in response to a data request received from the IDC based on IDC data processing results from stations in the primary seismic, hydroacoustic, and infrasound networks. IMS data, also referred to as raw data, received at the IDC are parsed and are accessible through the IDC relational database management system. The data are then stored in the IDC database and are available for imdexAutomatic processingautomatic processing. The communication between IMS stations and the IDC, and between the IDC and users is done over the Global Communications Infrastructure (GCI).

Waveform data are automatically processed once they arrive at the IDC. Waveform station processing for continuous data stations is done in fixed time intervals with duration according to technologies, 10 min for primary seismic and hydroacoustic stations, and 30 min intervals for infrasound stations accounting for the slower propagating medium. Once a time interval has elapsed, each interval is processed as soon as 95% of data used for station processing from that station has arrived in the IDC database. This threshold is setup in order to optimize availability of results for further processing and not delay processing due to the arrival of very late data. Data from auxiliary seismic stations are processed once the requested data segments have been parsed into the IDC database.

Common to all waveform technologies is the preprocessing to perform quality control checks with DFX-QC, that is being upgraded by libwaveformqc that allows for more transparency of the quality control checks implemented. While the quality control and masking logic remain unchanged, libwaveformqc brings a number of improvements for quality control of seismic data that is out of the scope of this chapter and fixes a number of issues from DFX-QC, in particular with the spike detector (described in Brachet et al. 2010). The waveform station processing performed after the quality control checks is then technology dependent with DFX-PMCC (Data Feature eXtraction—Progressive Multi-Channel Correlation) in use for infrasound technology, while DFX runs for seismic data and DFX-HASE (Hydroacoustic Azimuth and Slowness Estimator) for hydroacoustic technology. The PMCC algorithm (Cansi 1995) implemented in DFX-PMCC described in details in Brachet et al. (2010) and is based on the 2004 version of PMCC algorithm. PMCC is an array processing method originally designed for processing data from seismic arrays and it proved to be efficient for extracting coherent signals with low

signal-to-noise ratio among noncoherent noise that characterize infrasound signals propagating at regional or global range.

PMCC performs number of computation from band-pass filtering, cross-correlating data from station channels to aggregating time-frequency signal features to improve the signal-to-noise ratio and detect signals in the processed data interval. The objective of the feature extraction is to compute wave attributes, which result among others in detection time, amplitude, azimuth, trace velocity and are written to the IDC database. For infrasound technology, the final stages of station processing are performed by the StaPro algorithm and include signal grouping and initial phase identification. This software combines criteria for all waveform technologies and signal types.

The arrivals resulting from station processing are the input in network processing, which is performed currently with the Global Association (GA) software. At the network processing stage, the arrivals are combined to form events which are published in the automatic bulletins, named SEL1, SEL2, and SEL3. After the final automatic bulletin is produced, the data are ready for review by the IDC waveform analysts using specialized software for interactive review analysis. The analysts correct mistakes in the automatic bulletin, refine the results, and scan IDC results and raw data to try to add events, which were missed by the network processing algorithm. To illustrate this stage, the infrasound processing pipeline currently operational at the IDC is summarized in Fig. 6.2.

The result of the review process by the analysts is the Late Event Bulletin (LEB) on which event definition criteria are applied to produce the Reviewed Event Bulletin (REB). The REB is the final waveform product of the IDC available to Member States. Currently, during provisional operations, the target timeline for publishing the REB (Fig. 6.3) is within 10 days of real time. After Entry Into Force (EIF) of the Treaty, the target timeline is reduced to 48 h.

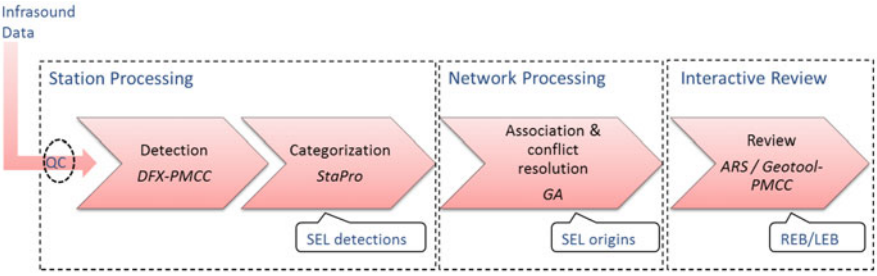

Fig. 6.2 Infrasound processing pipeline in IDC operations since February 2010

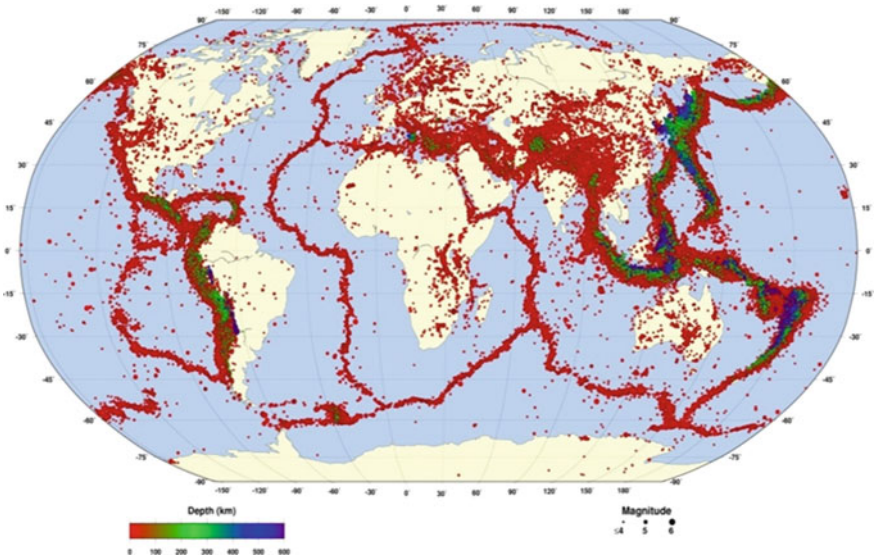

Fig. 6.3 Reviewed Event Bulletin (REB) for the period 2000–2016. The REB contains over 500,000 events formed with all three waveform technologies in agreement with event definition criteria

6.1.2 Overview of the Results of IDC Automatic and Interactive Analysis

Since February 2010, the IDC compiles the first global infrasound catalogue of events (Fig. 6.4) continuously enriched at the IDC by interactive analysis performed by IDC analysts. In over seven years, the IDC has reviewed over 445,000 waveform events of which over 50,000 contained infrasound phase associated, i.e. infrasound detections are being used to enrich the event solution (origin time and localization). After review, the IDC analysts have saved over 11,000 events with associated infrasound arrivals in the REB (Table 6.1) and nearly twice as much (over 21,000) in the raw reviewed bulletin, the LEB.

The full inclusion of infrasound technology in IDC operational activities was made possible by a multi-year effort that lead to the complete redesign of the IDC infrasound automatic and interactive software, the rewriting of interactive review procedures and the thorough redefinition of IDC analyst activities. Furthermore, since the IDC infrasound catalogue was the first global near-real-time bulletin produced for infrasound technology, the internal IDC criteria for the LEB production were relaxed in order to save and archive pure infrasound technology events made of only two infrasound associated arrivals. It should be noted that the events not matching event definition criteria for the REB are part of the LEB, but are not published into the REB. While the concept of the event definition criteria was introduced, considering the mission of the CTBTO, to look for evidence of potential Treaty

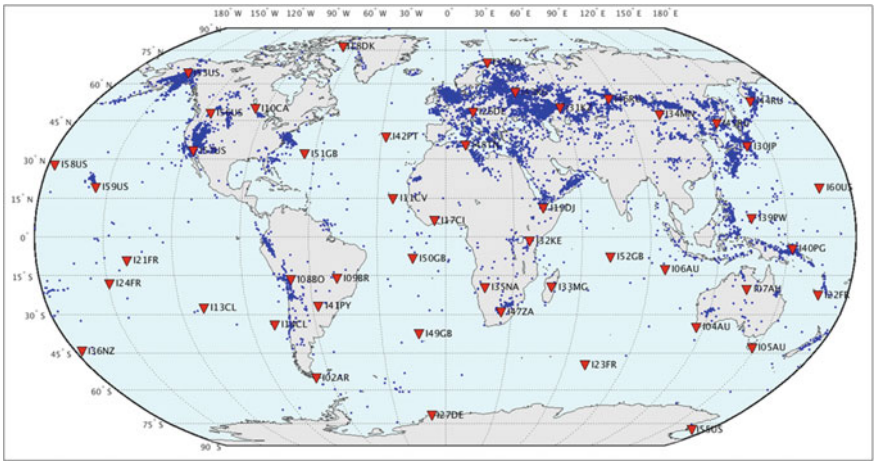

Fig. 6.4 Map of a subset of the Late Event Bulletin (LEB) for the period 10 February 2010 to 9 June 2017. All events containing at least one detection at an infrasound IMS station appear in blue circle and alongside IMS infrasound certified stations

Table 6.1 IDC processing results for the period 10 February 2010 until 4 June 2017

Bulletins	All waveforms	Mixed with Infrasound	Pure Infrasound
SEL3	445.700 (166.8/day)	50.227 (18.80/day)	36.418 (13.6/day)
LEB	349.469 (130.8/day)	21.384 (8.00/day)	11.588 (4.34/day)
REB	273.315 (102.3/day)	11.416 (4.27/day)	2.754 (1.03/day)

[a]Mixed with infrasound

violations (Coyne et al. 2012), there are multiple reasons for relaxed criteria for infrasound bulletins in order to:

1. build, as complete as possible, an infragenic picture during the CTBTO provisional status to ensure optimum global coverage,
2. compensate for the sparsity of the network as there were 42 certified IMS stations in 2010 (out of the 60 planned) covering the Earth,
3. allow a fast-tracked learning process at the IDC,
4. obtain in a limited time span a statistically significant infragenic picture for the next generation of network association algorithm that was in the proof-of-concept phase,
5. increase the understanding of the technology and its capacity as compared to design period of the network in 1996.

As the IMS infrasound component continues to expand, up to 49 certified stations by mid-2017, the relaxed LEB criteria remain in place at the IDC in 2017 under provisional operations. This deliberate choice is justified by the continuity in the learning phase of the IDC about global infrasound sources while the IMS infrasound

network remains in its installation phase. The IMS infrasound component is now reaching over 80% completion rate (Marty 2018) with the objective of 90% in 2019.

6.1.3 IDC Bulletin Highlights

Since the establishment of the first infrasound IMS stations, a large number of infrasound sources have been identified and with the advent of the IDC infrasound processing system in 2010 the number of infrasound events continued to grow at an even faster pace. While the review of infrasound sources and their characteristic is outside the scope of this chapter, it is worth noting that the IMS network and products contribute to a number of studies on anthropogenic and natural sources, such as atmospheric airbursts over Sulawesi in 2009 (Silber et al. 2011), widely covered and largest ever infrasound recorded event (to this date) over the Ural mountains in 2013 (Pilger et al. 2015; Le Pichon et al. 2013; Pilger et al. 2019) to the point that the atmospheric impacts registered by CTBTO are mentioned by non profit organization specialized on planetary defense against asteroids (CTBTO 2014).

A test case: the impact of the *2014 AA* meteor

As an illustration, on 2 January 2014, the small asteroid *2014 AA* became the only second meteor impact ever to be predicted before entering the Earth's atmosphere (Marcos et al. 2016). Just like the first occurrence, the 2008 TC3 asteroid, the infrasound signals from the impact of *2014 AA* were registered by the IMS infrasound network and was automatically detected and associated by the IDC automatic system. The reviewed analysis provided a refined list of infrasound signals associated with the meteor as well as an improved source location based on infrasound recordings. Signals recorded at three IMS infrasound stations were associated to build an event in the Atlantic, 1,450 km to the northeast of French Guyana, at coordinates (14.63N, 43.42W) with an error ellipse of semimajor 390.4 km by semiminor axis 154.8 km and a major axis azimuth of 76.4°. The source origin time of the main blast was estimated at 03:05:25 UTC with an origin time error of about 630 s. The three IMS infrasound stations that recorded the airburst are located at relatively large propagation distances, ranging from 2,900 to 4,400 km from the estimated source location.

The detection of *2014 AA* by the IMS not only demonstrate the capability of the network but also provide valuable information for cross-disciplinary studies (Marcos et al. 2016). Currently, the back azimuths and travel-times for each individual station are not corrected to account for atmospheric effects during the propagation of the waves. The acoustic source altitude and its extension are not considered for the REB solution in space as the infrasound system has been built to monitor a close-to-the-ground, explosion-like source.

The value of the time uncertainty illustrates the large variability of the infrasound event origin in time due to the heterogeneity of the atmosphere in space and time, the source altitude, and the source displacement, which are currently not fully captured

by the IDC system. The location and origin time of the airburst could be refined using atmospheric propagation modelling with real-time accurate atmospheric datasets. While more accurate, the solution would still largely depend on the limited number of observations and the numerous hypotheses made on the propagation ranges, the uncertainty of the ological models in the stratosphere, and the source altitude and dimensions in space and time. Knowing these limitations, the IDC continues to further improve its processing system and review mechanism to obtain precise event parameters for both automatic and reviewed bulletins or special event analysis.

In order to provide a quality dataset for training purposes of its analysts or National Data Centre (NDC) staff and of its newest algorithms, the IDC developed the Infrasound Reference Event Database (IRED). The IRED is a catalogue of ground truth events reviewed by IDC specialists using infrasound detections at IMS stations. It contains infrasound events of special interest with the intent to have a representative sample of different source types, different regions and different propagation paths, while the source information is derived from independent sources (such as peer-reviewed publication, press articles or other means). The IRED prove to be useful for the redesign of IDC system (Brachet et al. 2010), and has since then been sparsely updated with notable infrasound events such as the Chelyabinsk airburst or the Mount Kelud volcanic eruption (Caudron et al. 2015). This database continues to be of interest to the CTBT community and the infrasound researchers, which motivates the IDC to revisit it. To this end, the recent software development for interactive analysis mentioned in Sect. 6.2 will integrate dedicated reference event modules. This will allow the IDC to improve and update the IRED prior to its distribution to the CTBT user community (Fig. 6.5).

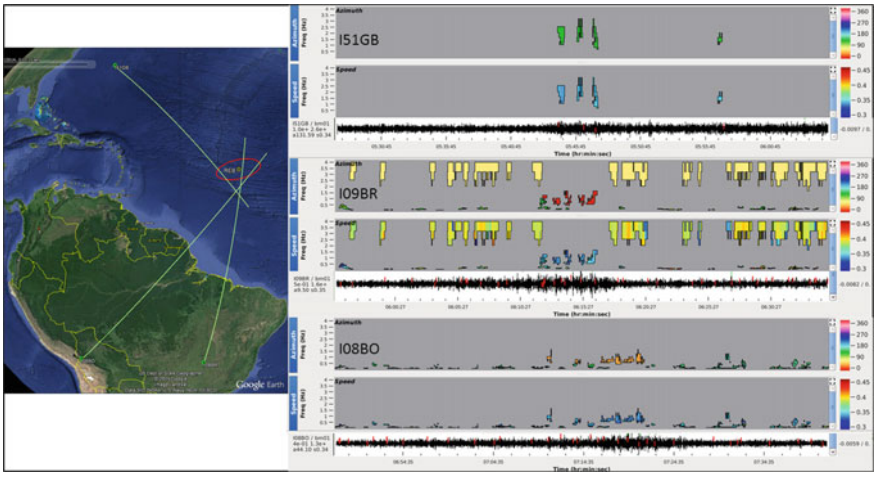

Fig. 6.5 Summarized information of the 2014 AA airburst detected by (right) 3 IMS infrasound stations in (from top to bottom) Bermuda, I51GB, in Brazil, I09BR, and in Bolivia, I08BO, and (left) the corresponding location by the IDC

While the IDC infrasound products offer a global and rapid picture of infrasound source activity, it requires sustained and constant efforts by IDC analysts to review and correct the results of the automatic system. Since its establishment, the IDC has been committed to continually improving its algorithms, software and procedures for all verification technologies and while the infrasound system was fully redesigned prior to 2010, the IDC re-engineering that started in 2012 focused on areas where enhancements could be made such as station processing and event association.

6.2 IDC Operational System with Infrasound Technology

In 2010, the IDC completed the introduction of infrasound technology in every aspect of its operation activities. Afterwards, efforts rapidly shifted to ensure a smooth transition of IDC activities to include infrasound technology. These efforts focused on the assessment of the performance of the infrasound data processing and the reporting to CTBTO Member States, the training and preparation of IDC analysts for routine operations and the update of procedures and guidelines for analysis at the IDC, the support for requests from National Data Centres on newly available infrasound related information, and the preparation of procedures for testing newly installed and certified IMS infrasound stations or upgraded facilities. In 2012, the IDC identified areas for improvement of its infrasound system, in particular, to address software limitation in the legacy system from the Prototype International Data Centre (PIDC). And in 2013, the Provisional Technical Secretariat (PTS) Midterm Strategy (CTBTO 2013a) was published stating that "*As part of its re-engineering effort, the IDC Division will deploy new signal processing, event association and analyst tool to increase valid events detected and reduce the analyst workload*".

This provided a mandate for IDC to continue its work on the review of its station and network processing algorithms and on the redesign of the interactive software, and also to keep abreast of new developments from the research community and pursue enhanced collaboration with IMS for introducing (or re-introducing) stations in IDC operations.

6.2.1 Performance Review and Updating IDC Procedures

The IDC processes seismo-acoustic data from the global network of the IMS for the three waveform technologies. The IDC automatic system is introduced in Sect. 6.1 and illustrated in Fig. 6.2. Automatic data analysis is done in near-real-time. The detection framework, composed of DFX-PMCC followed by StaPro, produces high-quality detection list for IMS infrasound data and the network association algorithm, GA, aggregates event bulletins containing infrasound events and seismo-acoustic

events enriched with infrasound detections. The outcome of this fully automated process is then methodically examined during interactive review by expert analysts.

IDC analysts perform their review activities using the Analyst Review Station (ARS) following predetermined sets of IDC procedures (Horner 2009). ARS provide access to a number of display panels and functionalities such as raw data from IMS waveform stations, the results of the automatic station processing (phase attributes and time picking in particular) and tools to visualize or compute waveform attributes, modify or add event hypothesis and save the results of analyst review in the LEB.

Specifically for infrasound technology, the review of infrasound signals detected by station processing is made available in ARS through a specific graphical module integrated within the IDCs Geotool software (Geotool-PMCC). Currently, Geotool-PMCC may only be used to visualize existing results, and does not allow the user to interactively process or re-process infrasound data using a different set of detection parameters.

At the time of the introduction of infrasound technology in IDC operations, resources were dedicated to ease the infrasound related activities. The efforts concentrated on:

- continuously assessing the performance of the automatic system to ensure that results were in alignment with those of the IDC test environment (also known as IDC testbed),
- updating the IDC procedures for interactive analysis of infrasound only events and seismic-acoustic events. This task included the training of IDC analysts to prepare them for the review of infrasound detections and infrasound events, but also the support of the infrasound analysis group for routine analysis and the inclusion of high-quality events in IDC products,
- creating procedures for the inclusion in IDC operational environment of newly installed IMS infrasound stations or IMS stations going through upgrade activities. In order to facilitate this activity, the infrasound station configuration and processing is installed or updated in the IDC testbed for testing, and after a period of a few weeks an assessment is made by the IDC to support the decision to promote the station to IDC operational environment,
- updating station parameters and processing configuration to account for station performance changes (such as loss of sensor data or change in station behaviour), to optimize the quality of the detection bulletin and ease routine analysis
- preparing system enhancements based on the performance assessment and with the goals to reduce analyst workload and raise the quality of IDC products. This motivated the IDC to conduct several projects such as the infrasound only pipeline project to upgrade the network processing stage (Mialle 2012, 2013), which ended in the development of an infrasound model for NET-VISA that is presented in Sect. 6.2.2, and a project to develop a new detection and interactive display package, presented in this Section.

IDC analysts recognize the value of the infrasound legacy system, from the results of the automatic system (station and network processing) to the set of specialized software used for interactive review, and have developed working habits to efficiently

review event hypothesis from the SEL3, modify them and possibly scan for missed events by the network processing software in order to produce the final IDC products. The infrasound system of the IDC allowed to produce high-quality products over several years, which constitutes today a unique and unmatched dataset of infrasound events (Mialle 2015).

6.2.1.1 Towards a Re-engineered Detection and Interactive Display System

In its re-engineering review effort, the IDC identified the need for continuity of service offered to the analysts while enhancing the results and tools. Other areas of improvement for the IDC are turned towards the use of modern software practice including modularity, flexibility, open-source software and state-of-the-art algorithms.

Since 2004, numerous updates and improvements have been implemented in the PMCC software developed at CEA/DASE (Cansi and Pichon 2008; Matoza et al. 2013), which is widely used by CTBTO member states. In term of performances, the PMCC algorithm has proven to be satisfactory and it fulfills the need of the IDC for its automatic system and routine analysis (Marcillo et al. 2019). However, given the significant advancements in infrasound technology since the design and the installation of the first IMS station and the objective of the PTS to keep abreast of new developments, the IDC worked on a program to upgrade its methods for infrasound processing from the control of data quality to the automatic association of infrasound phases for bulletin production and in particular on a framework for station processing with integration of the interactive review modules. Since the PMCC algorithm and graphical interface have proven to have satisfactory performance and fulfils all need of the IDC for its automatic system and routine analysis and it is widely used in the infrasound user community, the DTK-PMCC and DTK-GPMCC (respectively the station processing algorithm and the related graphical user interface) were developed based on research community needs and IDC operational requirements (Fig. 6.6). DTK-PMCC produces PMCC results consisting of detections (that are based on PMCC pixels, described in Brachet et al. 2010 and giving, in particular, the time of arrival of detected signals) and detections attributes such as back azimuth, trace velocity, amplitude estimation, the number of array elements that detected the pixel and more (an exhaustive list of attribute is provided in the DTK-GPMCC user manual).

This software library providing a detection framework for waveform arrays is specifically designed for multipurpose usage:

- The package fully satisfies the needs of the IDC to be integrated in its operational system for both automatic and interactive analysis, where DTK-PMCC and DTK-GPMCC usage is decoupled. The automatic results produced by DTK-PMCC are stored in the IDC database and are made accessible for interactive review through DTK-GPMCC.

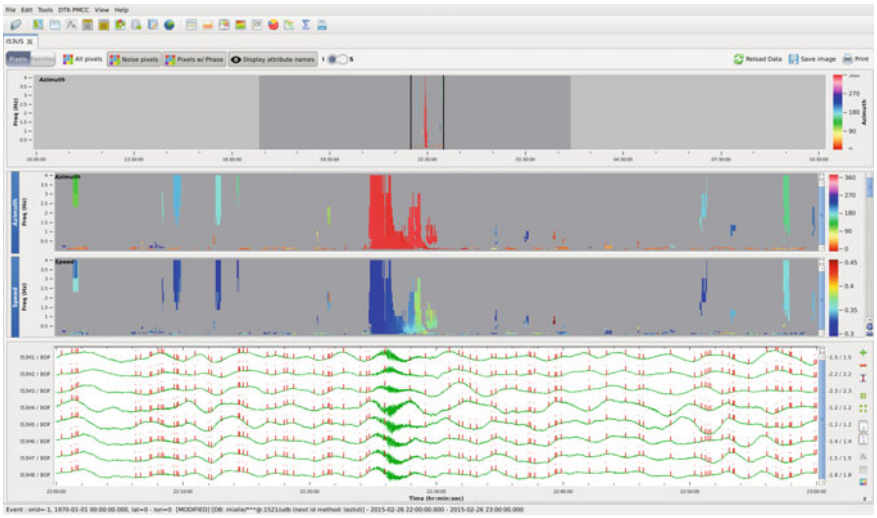

Fig. 6.6 DTK-GPMCC interface for infrasound station I53US, Fairbanks, Alaska, USA, and a fireball signal detected on 26 February 2015. The user interface retains a familiar feeling for IDC operational activity while including additional functionalities and ergonomic enhancements

- For the IMS engineering and maintenance team during site survey activities and for station installation or upgrade, where waveform analysis and station capability activities are performed in the field.
- The software package also addresses a request from NDCs to be provided with specialized software allowing to analyse IMS infrasound data.

In its standalone version, the software gives the ability to the user to recompute the PMCC results, which in addition to in-the-field usage is valuable for NDC activities. Special event analysis is also facilitated with the package thanks to the combination of PMCC algorithm and interface with additional functionalities, such as computation of power spectral density, spectrogram or projection on topographic map of PMCC detection pixels.

In addition to the specific use of DTK-PMCC and DTK-GPMCC, the main high-level requirements for the package were to optimize user friendliness for an improved user experience, computation performance for fast and accurate computation and modularity for allowing the evolution of the algorithm and the implementation of additional functionalities. Some of the notable improvements and design choices for the DTK-PMCC platform are given as follows:

- the complete redesign of the software to include recent programming techniques for graphic engines, processing algorithms and software ergonomics,
- the development of a multi-platform and standalone tool including the ability to communicate with IDC databases (but not exclusively) or to operate in a disconnected mode (with input and output files), and to process multiple data formats widely used by the user community (either *CSS* or *miniSEED*),

- the incorporation of a flexible parametrization of detection attributes and pixel family aggregation (which is the process of combining PMCC pixels into families of pixels that correspond to detections, as explained in Brachet et al. 2010), including the capability to implement proposed standard configurations from the research community (Le Pichon et al. 2010; Garces 2013),
- the evolution of the algorithm to improve computation of wave parameters for nonplanar arrays. Edwards and Green (2012) demonstrated neglecting the elevation for nonplanar arrays can lead to significant biases when estimating the two-dimensional horizontal components of the slowness vector, even for small altitude differences between sensors compared to the horizontal array aperture, Nouvellet et al. (2014) developed a theoretical formulation of the bias/variance of the two-dimensional and three-dimensional estimators, which was integrated into the DTK-PMCC algorithm.

The introduction of DTK-PMCC software in the IDC environment enables new capabilities for the IDC thanks to multi-threading implementation and automatic processing system improvements. In particular, the IDC aims at better characterizing all received signals in their wave parameter space by implementing in its operational system a PMCC configuration with logarithmically-spaced frequency bands and window lengths that vary linearly with the period as implemented by Matoza et al. (2017, 2013), Ceranna and Le Pichon (2015), Ceranna et al. (2019). Such modification has a strong impact on subsequent processing stages, such as phase characterization and network processing phases and. These effects are being evaluated by the IDC in order to ensure the implementation of solutions with improved detection capabilities while reducing analyst workload.

The DTK-PMCC software is currently implemented in the IDC development environment and being used for special event analysis. It is progressively being integrated into the operational environment of the IDC to replace the legacy system while also being used for field deployments and IDC training activities.

6.2.1.2 Infrasound Technology in NDC-in-a-Box

After a two year development and integration effort, infrasound station processing, quality control and interactive review tools are available in the NDC-in-a-Box software package. This software package gives the NDCs the capability to receive and analyse seismic, hydroacoustic, infrasound and radionuclide data and it supports treaty verification and civil and scientific applications at NDCs. For waveform technologies, this development has been made possible thanks to European Union (EU) Council Decision V (for the period 2014–2015) and continued under EU Council Decision VI (2015–2016) in allowing NDCs to process the data available from the IMS for both treaty monitoring and for national purposes.

Since 2016, NDC-in-a-Box enables NDCs to more easily combine IMS waveform data and IDC processing results with data from local and national stations and from other global networks. It significantly expands NDCs processing capabilities,

in particular with real-time automatic processing, as well as in the area of infrasound data processing. These efforts have created a strong NDC user base and the project results help to gain NDC trust in the credibility of the verification system as it gives all NDCs the chance to become active contributors to the CTBT verification process either by inter NDC interaction, through communication with the IDC, or to help assess and enhance IDC software and products.

The IDC remains dedicated to further development of the NDC-in-a-Box capabilities for the verification technologies. Upgrade of the packages will be rolled out towards NDCs as they become available. In 2017, the IDC prepared dedicated training session to ensure the continuous support of the user base and its expansion.

6.2.2 Global Network Association Algorithm

In its effort to sustain the IDC capacities and continuously improve its methods, the IDC has been working on the replacement of its network association software, i.e. GA, and decided to evaluate possible improvement by developing NET-VISA, a Bayesian inference system that computes the most likely global event history given the record of local sensor data (Arora et al. 2010).

6.2.2.1 Background

The IDC interest lies in enhancing the automatic system for the identification of valid signals and the optimization of the network detection threshold by identifying ways to refine signal characterization methodology and association criteria for all waveform technologies.

Due to the recent implementation of infrasound technology in IDC operations in 2010 and given the objective to improve network processing during period of high seismicity, possibly including aftershock sequences, the original NET-VISA developments concentrated on seismic technology alone. Indeed NET-VISA stands for NETwork processing—Vertically Integrated Seismic Analysis and it was originally composed of a physics-based, probabilistic model and a heuristic inference algorithm designed to find the most probable set of seismic events which can explain a series of arrivals detected by a seismic array (Arora et al. 2010). It was demonstrated that under normal circumstances, NET-VISA produces a bulletin that is more complete and accurate than the IDC's final automatically produced bulletin, the SEL3 (Arora et al. 2013).

In 2014, NET-VISA probabilistic generative model was extended to incorporate hydroacoustic data from the IMS network. The updated model included the coupling of seismic waves into the ocean's SOFAR (SOund Fixing And Ranging) channel, as well as the propagation of hydroacoustic waves from underwater explosions. The inference algorithm has also been updated to hypothesize both the seismic and underwater events in order to associates arrivals from seismic and hydroacoustic

stations, to the appropriate event, and labels the signals. NET-VISA performances remain high for both technologies, which paved the path for both implementation of NET-VISA in IDC operational environment and developments towards infrasound technology (Arora and Prior 2014).

In 2015, NET-VISA was extended to incorporate infrasound data from the IMS. However, infrasound technology presents additional challenges as a large number of signals are produced by nuisance sources, often detected by single stations and that are not of interest for the verification regime. Despite effort to identify and categorize detections from such sources (Brachet et al. 2010), the repetitive nature of this clutter and its variability in wave attributes leads to a significant number of false event hypotheses due to the true or random matching of clutter at multiple stations. A probabilistic model of clutter was built and used as part of NET-VISA (Arora and Mialle 2015).

6.2.2.2 The Association Problem

All of the events in the SEL3 generated by GA software need to be closely examined by highly trained human analysts before the final data products of the IDC are released. These final bulletins are the carefully curated LEB and its subproduct of high-quality REB. The REB is the same as the LEB except that a number of events have been filtered out as they do not meet event definition criteria, such as having a minimum number of defining arrivals from primary IDC stations associated with them. In order to produce these lists, a majority of SEL3 events must be manually altered and corrected. Overall for seismic, hydroacoustic and infrasound technologies close to half of the events are thrown out or completely rebuilt using detections that had been erroneously assigned to other events. This proportion is reaching over 80% for pure infrasound events.

The pipeline processing of the IDC system implies that the association of signals finds its origins in the station processing stage, building on both signal detection and phase categorization, and strongly depends on event location. Continuously the automatic signal processing system of the IDC identify features of interest in the raw waveform data. Once a signal has been detected for any of the three waveform technologies, the IDC system computes a number of wave attributes, including its arrival time, amplitude, azimuth, slowness or trace velocity. These are all features of the arrival of energy from a true event. Nevertheless, they might not actually have been caused by a physical source. The detection (also referred as arrival) might just reflect station noise, in which case its attributes are random numbers. Alternatively, the arrival might originate from a weak event or anthropogenic activity that occurred near the station and that was not picked up at any other station of the IMS network. It could also either be a nuisance source like distant gas flares or microbaroms or a false detection immediately following a true arrival and being split up by the detection system as it often occurs for infrasound and seismic technologies. In the latter case, the arrival attributes are closely correlated to those of the arrival that preceded it.

False arrivals such as this are called coda arrivals (of which split detections are a subcategory).

The fundamental challenge of creating a fused seismic—hydroacoustic—infrasound bulletin is to work backwards from a list of arrivals to come up with a set of events that can explain them without missing real events. A balanced compromise needs to be found between avoiding missed events while minimizing spurious events formed by association of unrelated arrivals, where the latter has a lower cost for the IDC (Prior et al. 2013). This is a complex task with the objective to find time, location and magnitude of an event, based on associating arrivals together. However, in order to associate arrivals with events, it is necessary to know when and where the events took place.

During the development phase of NET-VISA, an iterative approach was followed to implements models for each waveform technology separately. The creation of the final bulletin lies on the separation of technologies on the first order to avoid cross-pollution of events, with a consolidation phase to obtain a fused bulletin of technologies.

In the IDC processing pipeline, detected signals from a single station are examined first to determine an initial phase label (e.g. *Pn*, *P*, *Lg*, *H*, *I*). Next, the detections from the entire network are clustered together to form events based on their arrival time, azimuth, slowness or trace velocity, amplitude, and phase label. During this stage, seismic and hydroacoustic phase labels may be modified according to a limited set of transformation rules. This, however, does not apply to infrasound technology in the current implementation of GA and NET-VISA respects the phase labelling provided by the phase identification process, performed by StaPro software, of infrasound (*I*) or noise (*N*) phases, where the latter are not considered.

Locations of the events are then computed using their associated arrivals. Further attributes of the event like seismic magnitude are then computed from the amplitude measurements when seismic signals are associated to an origin. Finally, other global measures, as well as other detection attributes like signal-to-noise ratio (*SNR*) or signal duration, are examined using simple heuristics to determine event quality, and then a decision is made to either keep the event or discard it.

In this context, a large number of possible events gets created, and false detections almost always are associated with an event. In addition, once an event has several associated arrivals it does not get discarded, which ends up in reporting false events in the bulletins. When spurious detections get associated with true events, they impact negatively the solution for the event's position and time. Such events generate an acceptable solution location but are often not plausible. An example would be for event built from arrivals from distant stations while regional stations do not have matching detections. In that case, an analyst would quickly discard this event on the basis of negative evidence. But because event parameters are physically possible and the negative evidence is not captured, it remains on the automated list. However, since NET-VISA considers the negative information of missed detection this issue leaves it unaffected.

The ultimate goal of NET-VISA is then to produce an automatic bulletin that is an improvement over SEL3 in several ways:

1. it produces a fused bulletin for the three waveform technologies,
2. it produces fewer false events without missing events,
3. it finds more events which will pass analyst scrutiny,
4. it associates more arrivals correctly with events,
5. it finds lower magnitude events,
6. it locates events more accurately,
7. it takes into account negative information from missed detections.

In order to achieve these goals, NET-VISA needs to solve the following problems (not necessarily in this order):

- generate a list of likely events,
- determine which arrivals can be associated with events (even if their phase label has to be changed),
- classify unassociated arrivals as false or coda (in the case of split detections, they are handled by marking detections as coda and removing the events),
- work out the time, magnitude and location for the events.

Furthermore, NET-VISA needs to solve these problems using methods which are, as much as possible, physically and experimentally realistic, and the results need to be transparent and reproducible.

6.2.2.3 Methodology

NET-VISA uses probabilistic inference to work out the waveform bulletin, which best explains a set of arrivals at IMS stations, where the bulletin is the conclusion of the process and detections provide the evidence. The word inference means the process of reaching a conclusion based on evidence and reasoning. NET-VISA associates arrivals with events, finding the correct phase label for the arrivals. Arrivals which are not associated with events are classified as either false or coda.

A full set of proposed events, associations, phase labels and classification to explain a set of arrivals is called a world. Reasoning, in the context of NET-VISA, means assigning a probability to various hypothesized worlds and searching for the one that has the highest probability and is consistent with the evidence. High probability worlds tend to contain events which happen often in nature (such as earthquakes along tectonic plate boundaries or mining events). But they can also have unusual events if those events are either supported by high-quality evidence or it is difficult to find a better explanation for the data. Once the highest probability world has been found, the output bulletin is assembled from the events and associations in it. It should be noted that for the final processing step, standard IDC software is used to compute event location and magnitude estimation for each event.

NET-VISA is composed of two main parts, a Generative Model (*GM*), which gives instructions for evaluating the probability of a world, and an Inference Algorithm (*IA*), which performs the search. The *GM* is essentially a template, which formalizes the relationships between factors in seismic, hydroacoustic and infrasound

network analysis. The relationships are described in terms of physical laws and Probability Distribution Functions (PDFs). For example, the relationship between the time of an event and the detection of a phase at a given station is predicted using a deterministic function, the *IASPEI* earth model or the derived equivalent for other waveform technologies (Coyne et al. 2012; Brachet et al. 2010). Once this prediction has been made, the difference between predicted and observed arrival times is modelled as a Laplace distribution. This is, in particular, the case for the computation of infrasound celerities for each event hypothesis. The parameters of this distribution along with many others in the GM must be found empirically. This is done by training the GM using historic arrivals and LEB bulletins. Different parameters are found for each station and each phase.

Because the details of the IMS network and the nature of detected signals may change with time, The IDC NET-VISA needs to be periodically retrained so that the parameters of the PDFs accurately reflect the current network. During training, a parameter file (sometimes called the model file) is generated containing the model parameters which can then be used in subsequent runs of the *IA*.

6.2.2.4 NET-VISA at the IDC for All Waveform Technologies

The IDC implemented NET-VISA in its processing environment and it is currently working on its full integration, while continuously evaluating its performance against other IDC bulletins (SEL3 and LEB/REB) or against other available sources of information such as the ground truth bulletin from the International Seismological Centre (ISC) (Bondar et al. 2017). The IDC NET-VISA is specifically designed to run at IDC and is integrated with the IDC database. NET-VISA is divided into two modules to perform learning and inference actions.

The IDC NET-VISA is currently installed on the development platform of the IDC and rolling progressively towards integration in the test and operational environments of the IDC. NET-VISA can be run in parallel to the GA program, which currently produces SEL3. It is foreseen that GA will continue operating in all three environments for continuous cross-evaluation of the performance of the programs. The waveform bulletin that is the output of NET-VISA is structurally equivalent to SEL3 and it can be reviewed by IDC analysts using the same Analyst Review Software (ARS) used for routine operation. For evaluation purposes, a bulletin can, therefore, be produced from NET-VISA output and directly compared to the standard LEB. And for implementation at the IDC, analysts are involved to review datasets of SEL3 and of Net-VISA output. These efforts are anticipated to lead to the inclusion of NET-VISA for IDC operational activities.

NET-VISA is designed to handle all three waveform technologies and as such its event hypothesis specifies whether it is an underground, underwater, or atmospheric event.

6.2.2.5 Application to Infrasound Technology

The IDC collects waveforms from IMS infrasound measurement systems and automatically detects signal onsets and associates them to form event hypotheses. However, a large number of signal onsets are due to local, regional or global clutter sources such as microbaroms (from standing waves in the oceans), waterfalls, dams, gas flares, surf (ocean breaking waves) and others. These sources are either too diffuse or too local to form events. Worse still, the repetitive nature of this clutter leads to a large number of false event hypotheses due to the random matching of clutter at multiple stations.

Previous studies, for example, Vergoz et al. (2011), have worked on categorization of clutter using long-term trends on detection azimuth, frequency, and amplitude at each station. Continuing the reasoning, the objective is to build a probabilistic model of clutter that is used as part of NET-VISA.

The resulting model is a fusion of seismic, hydroacoustic and infrasound processing built on a unified probabilistic framework.

Infrasound specificities

NET-VISA incorporate several infrasound specific features due to the particular nature of infrasound signals and infrasound processing. Those are:

- Static prior using a whole year's worth of data:
  An infrasound model is built for NET-VISA with an appropriate event location and detection rate prior. The priors are learned once over a time interval and they are not learned again, hence the concept of static prior rather than continuously learning on recent data and product, which would be dynamic. The comparison of static and dynamic priors lead to select the static prior as it offers an optimum compromise between computation efforts and bulletin quality. As a baseline, the static prior is built using the year 2012 as learning period. However, once implemented in IDC operational environment the static prior will be trained at regular intervals on recent data and products in order to accommodate for the evolutions of the IMS network and of the seismo-acoustic activity.
  It is foreseen that once NET-VISA will be fully integrated into the IDC operational process, the infrasound static prior will be retrained on more recent data once a year.
- Clutter model to avoid building events from nuisances sources, such as gas flares:
  The infrasound clutter model is designed on the analysis of the IDC processing results for the year 2012. A large number of detections is related to clutter sources that can be local to the array or from distant continuous sources. Infrasound stations are affected in various ways (Fig. 6.7), where the detection rate of unassociated arrivals indicate the impact on results and the complexity of the problem. Features of interest are extracted for nuisance sources such as microbaroms or local and regional anthropogenic and natural sources, such as gas flares or large waterfalls (Figs. 6.8 and 6.9: The figures display the bandwidth of the kernel density estimate along the azimuth and frequency dimensions). A diverse clutterfield

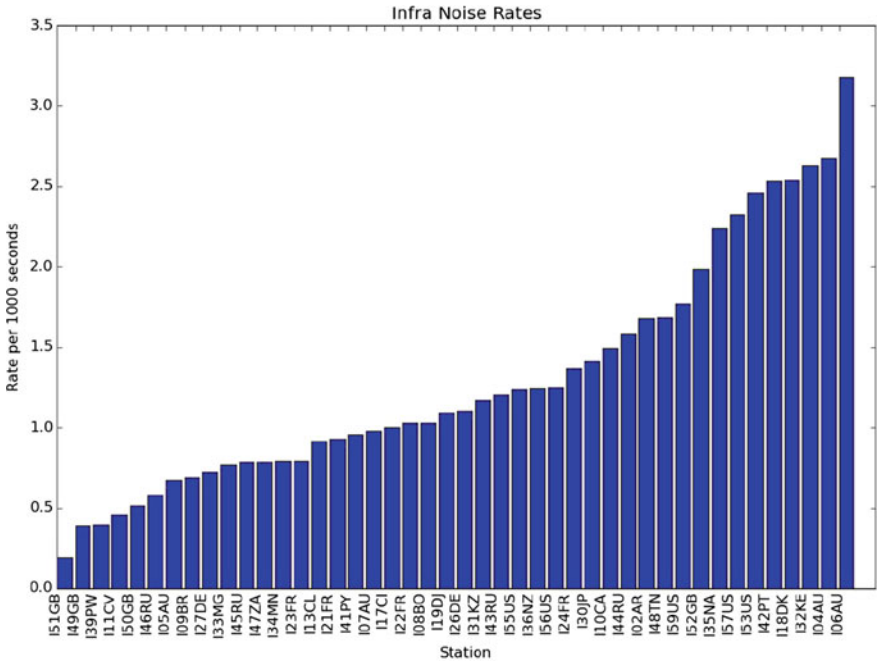

Fig. 6.7 Noise rate at each station is inferred to be the number of unassociated arrivals. Example for the year 2012 and for all IMS certified infrasound arrays at the time

such as the one for stations I06AU and I31KZ is quite common for most IMS infrasound stations, and it highlights the complexity of forming events without due consideration of the source of noise.
To this end, a clutter model is incorporated into NET-VISA and it is being used for building events. Two clutter priors are used:

– a static prior, that is a station-dependent long-term prior, of infrasound detections that will use all unassociated detections at each station over a period of time.
– a short-term 3 h prior using data preceding the inference interval to incorporate short-term clutter sources.

Taking the clutter model into account, an event is then considered real if the probability of the event occurring and generating its associated detections and misdetections is higher than the probability of those same detections being generated by noise sources including repetitive clutter.

- Disentangling seismo-acoustic versus pure infrasound associations:
  The primary objective is to ensure that high-quality infrasound events (i.e. atmospheric event) and seismic events (i.e. underground event) remain unaffected by the fusion process, while allowing seismic-acoustic event to be created (i.e. close

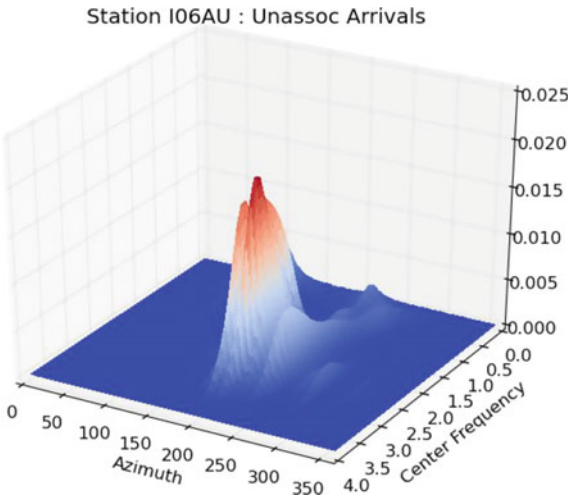

Fig. 6.8 Infrasound clutter model showing all the unassociated arrivals detected at IMS station I06AU (Cocos Island, Australia) for 2012 distributed by azimuth and centre frequency. I06AU is a typical island station "polluted" by local ocean breaking waves signals. The larger peaks from the south and southeast direction and for frequencies above 2 Hz corresponds to signals from the nearby shores, while the lower amplitude peaks to the southeast and east corresponds to microbarom detections

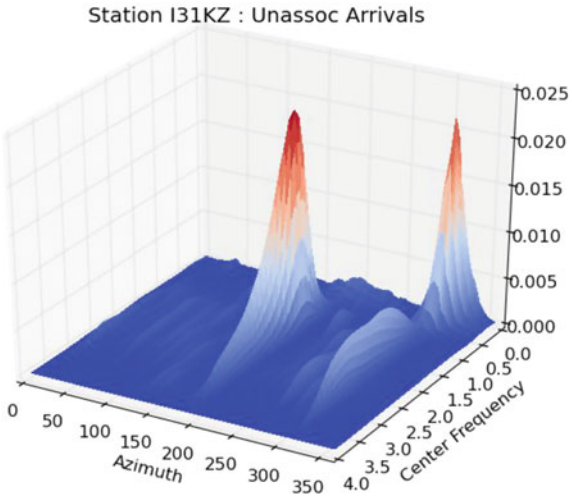

Fig. 6.9 Infrasound clutter model showing all the unassociated arrivals detected at IMS station I31KZ (Kazakhstan) for 2012 distributed by azimuth and centre frequency. I31KZ is a station with a number of regional anthropogenic sources. In particular, the 1–2 Hz peak with an azimuth close to 180° corresponds to gas flare from the extraction field located about 200 km away. The low-frequency peak from the northeast is due to microbarom detections from North Atlantic

to the ground event). In practice in NET-VISA, a seismic event is not allowed to steal an infrasound detection if an existing viable infrasound event can explain the detection. The second action is the separation of the detection probability and azimuth residuals between detections from seismo-acoustic and pure infrasound events (Figs. 6.10 and 6.11) based on the LEB results.
Those criteria help to obtain better inconsistency and overlap for infrasound events created by NET-VISA.

- Identification of useful infrasound detection features:
For each infrasound detection, a number of features are obtained either from the IDC processing system that corresponds to the various attributes stored in the IDC database or from a combination of such results. Likelihood models are then created for each feature using the phases associated to events in the LEB bulletin. The objective here is to extract the most meaningful features for the association stage using automatic detections and the human review results. A large number of features is obtained by the IDC station processing stage, however, they do not all have the same weight for deciding on phase association. Here is the resulting feature selection for the current implementation of NET-VISA using the 2012 information from the IDC:

  1. Features kept—backazimuth (Fig. 6.12), celerity, trace velocity, energy (which depends on amplitude and duration), and frequency (Fig. 6.13)
  2. Features dropped—consistency, family size, and duration (however duration appears in the kept features as part of the energy feature)

With the evolution of the IDC station processing system, it is foreseen that features used for association will be revisited in order to search for an optimum combination that will further reduce the false alarm rate of the network processing system. In particular, it is well known that given the design of the IDC system into consecutive time intervals infrasound detections are often split across those which results in suboptimal estimation of the parameter and most specifically of the duration of the detection (or family size of the PMCC pixel family). Further effects due to the processing limitation in 2010 are also impacting detections in proximity of direction of arrivals of neighbouring nuisance sources, such as microbaroms, which could inflate the duration of the detection (or its family size). This behaviour further motivated the IDC to limit the influence of these features for the association stage or to drop them entirely. However, ongoing development efforts will allow to revisit the criterion once implemented in IDC operational environment.

NET-VISA Event Formation Criteria

In NET-VISA an event, composed of seismic, hydroacoustic and/or infrasound data, is considered real if the probability of the event occurring and generating its associated detections and misdetections is higher than the probability of those same detections being generated by noise sources, including repetitive clutter.

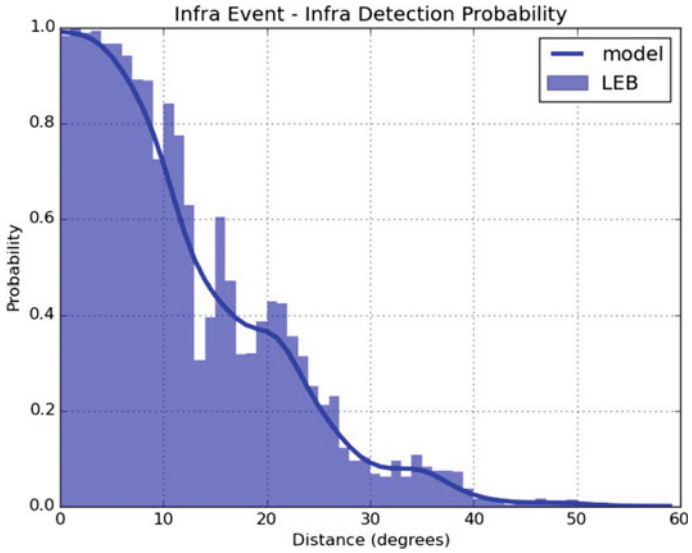

Fig. 6.10 Distribution of detection probability of infrasound associations for infrasound only events with respect to the distance between source and station, learned empirically on LEB for the year 2012

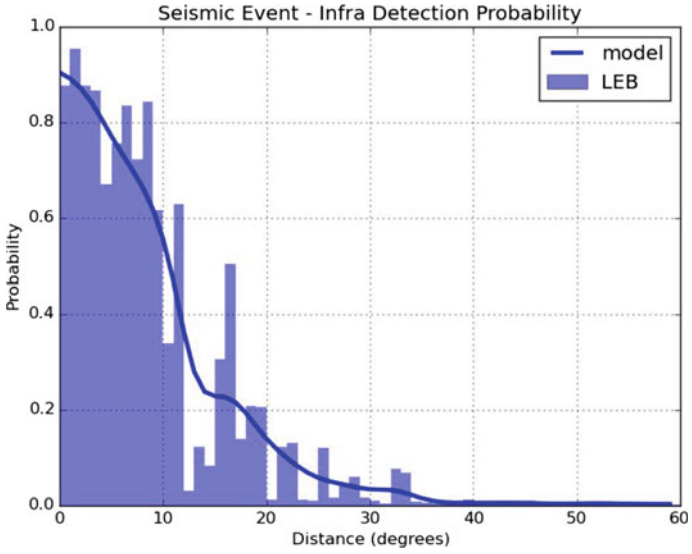

Fig. 6.11 Distribution of detection probability of infrasound associations for seismic-acoustic events with respect to the distance between source and station, learned empirically on LEB for the year 2012

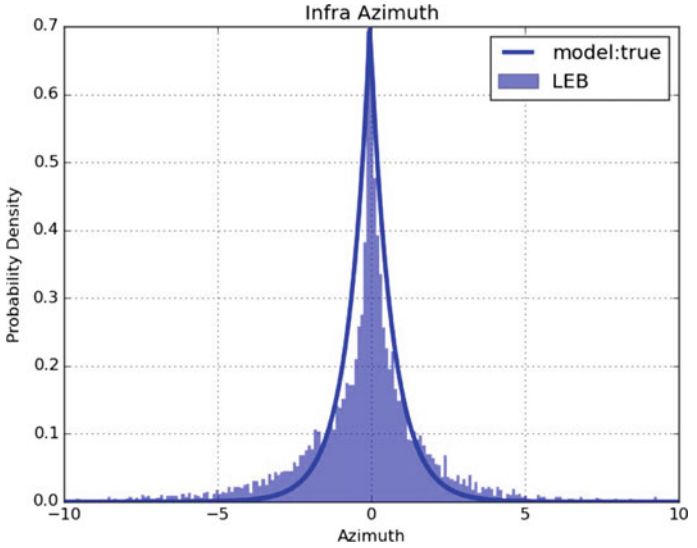

Fig. 6.12 Infrasound back azimuth for detections from year 2012 obtained by IDC processing system for all IMS infrasound arrays

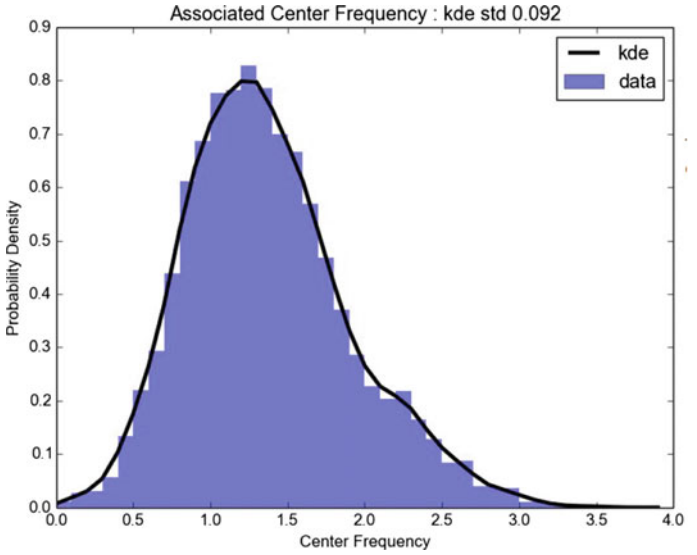

Fig. 6.13 Infrasound central frequency for detections from year 2012 obtained by IDC processing system for all IMS infrasound arrays.eps

Although the seismic, hydroacoustic, infrasound or mixed events are treated in the same way by NET-VISA, there, however, exist differences between infrasound and seismic technologies:

- For infrasound technology, the prior on number of events is artificially inflated, while it is learned from data in seismic. The starting point for this choice is that the evidence for phase association from infrasound detections is weaker compared to the seismic case since the arrival time uncertainty is a lot higher and the trace velocity gives little information unlike slowness for seismic technology. Inflating the prior then allows NET-VISA to hypothesize an event with just two detections. Another reason is the relatively low number of infrasound events in comparison to seismic events, as there are over 10–20 times more seismic events than infrasound events in the reviewed bulletins. In addition, the coverage of infrasound events while being global is far from being uniform as it is dominated by the human activity in the northern hemisphere.
- The infrasound event time is relatively uncertain up to 100 s, while it is just a second in the seismic case. This is due to the high heterogeneity of the medium that the IDC system does not currently account for. This remains an area where effort is needed for the automatic processing system.
- The noise phases (*N*) at infrasound stations are not considered for the association stage, which is not the case for seismic where all phases are considered. In the case of infrasound station processing, the high number of anthropogenic and natural nuisance sources surrounding a station are prefiltered by the categorization algorithm, StaPro. However, StaPro performance rate to accurately categorize phases is about 80–90% depending on stations and station environments. Indeed island stations are subjected to a high volume of detections from wave crashing on the shore in various directions and from variable distances to the station, which can affect categorization performances (Brachet et al. 2010). Another justification for dropping the *N* phases comes from the inflation of the infrasound prior. On the contrary, in the seismic case since the prior is not inflated the *N* phases that are not appropriate for event formation are automatically dropped while the more reasonable ones are kept.
  NET-VISA is then only considering infrasound phases (*I*) for event formation criteria and for its clutter model.

Regarding the inference concept, the rationale behind it is to start by proposing events along the back azimuth of detection for distances up to 60° away from the origin and at 0.5° intervals. Additional events, following this approach are also considered within a 2° perturbation of the back azimuth.

The existing algorithm, developed for seismic technology (Arora et al. 2013), is used for associating detections to the proposed events and a reassociation mechanism allows to find the best event for a detection, where "best" corresponds to the overall probability of the world.

The association and reassociation step then trigger a relocation and recomputation of the origin time of the event to best explain the associated detections. These updated events are then checked against the model criteria and those not justified by

it are deleted. In the case of pure infrasound events (i.e. events that are hypothesized to occur in the atmosphere), the association of infrasound detections at infrasound station (i.e. infrasound detections at seismic stations are not currently considered) is preferred.

Infrasound results with NET-VISA

The infrasound model has been implemented for multiple revisions of NET-VISA based on learning period of processing results for the whole year of 2012 and tested on the whole of 2013 against the results of the IDC automatic system, the SEL3 produced by GA (Fig. 6.14, that contains 54,327 events), and of the reviewed bulletins, the LEB (Fig. 6.15, that contains 42,782 events).

The evaluation of the infrasound considers that two events in two different bulletins are identical if they share two similar arrivals where the arrivals are detected at the same station and if they are:

- within 500 s in time of each other and
- point to a back azimuth within 5° of each other

In its mid-2017 evaluation in the IDC development environment, NET-VISA is running for all waveform technologies for the year 2013 and produces 60,904 events (Fig. 6.16) of which 3,383 events contain infrasound phases associated (Fig. 6.17). NET-VISA is implemented and continuously run in real-time in the IDC environment for further testing, evaluation and integration in routine operation of the method.

One of the main motivations for the IDC to work on the integration of an infrasound model into NET-VISA is related to the high proportion of spurious seismic-acoustic associations from the current operational system. The objective was to reduce spurious associations, while retaining a similar level of overlap compared

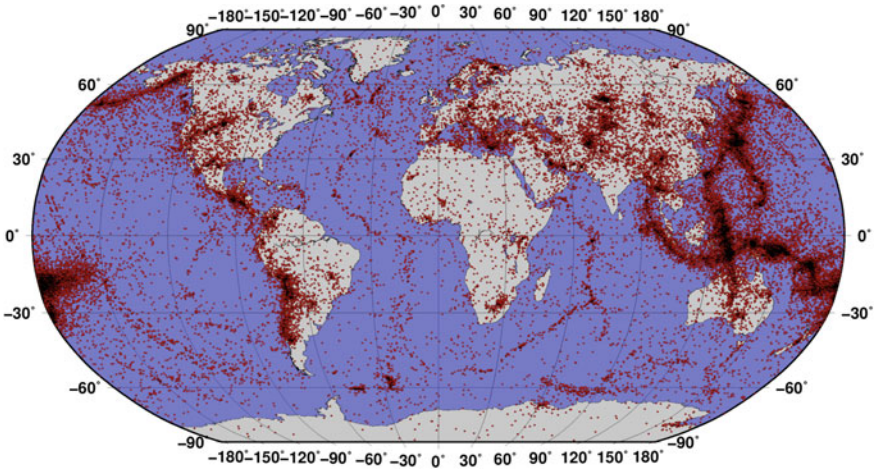

Fig. 6.14 SEL3 events (produced by GA) for all three waveform technologies for 2013

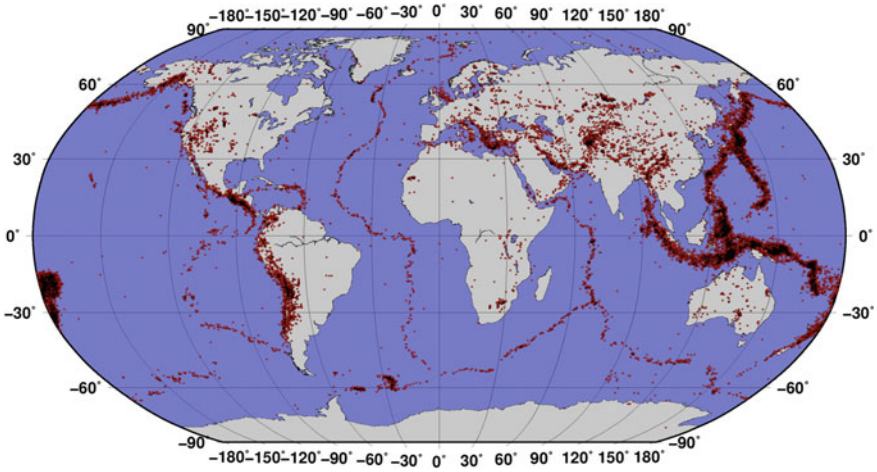

Fig. 6.15 LEB events for all three waveform technologies for 2013

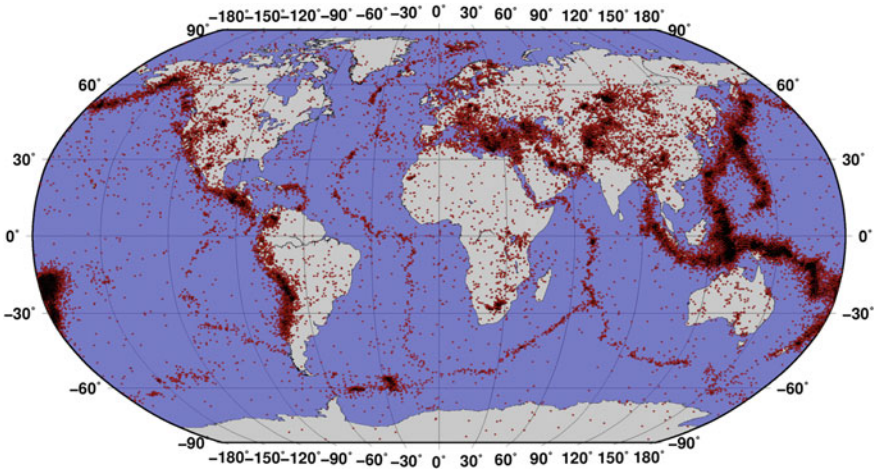

Fig. 6.16 NET-VISA results for all three waveform technologies for 2013

to the review bulletins. For the year 2013, the NET-VISA performances are positive as:

- the overlap, which is the proportion of the reference dataset (i.e. LEB) that is included in the test dataset (i.e. produced by NET-VISA), with the LEB climbs from 24.7% with the GA generated SEL3 to 42% with NET-VISA,
- the reduction in spurious seismic-acoustic associations compared to the SEL3 reaches 90%,
- and the inconsistency, which is the proportion of the test dataset that is not included in the reference dataset, reaches 85.3%.

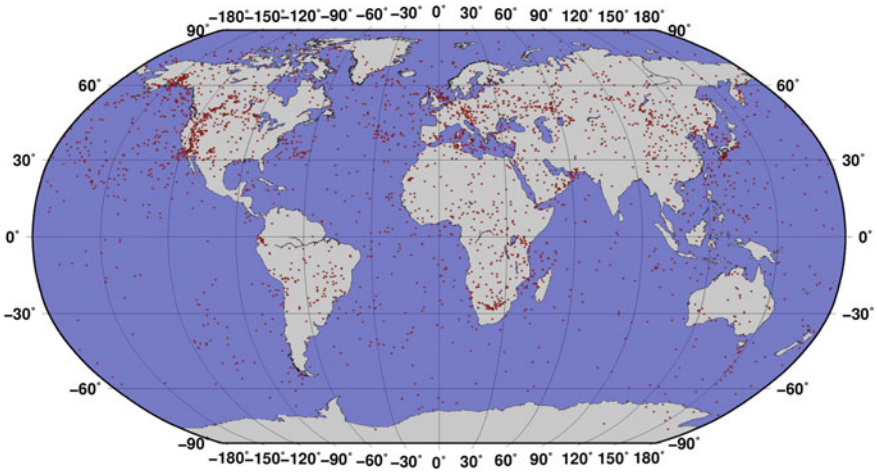

Fig. 6.17 NET-VISA results for 2013 for events containing infrasound arrivals

By comparison with the overall seismic-acoustic results of over 80% overlap and under 55% inconsistency, the infrasound results remain modest largely due to the difficulty to constrain events in a heterogeneous atmosphere and the lack of baseline datasets to build the Bayesian inference on. However, the progress is significant when compared with the current operational system of the IDC, that is the only global operating network processing system for infrasound technology. The results are in line with the objectives set by the PTS (CTBTO 2013a) and efforts will be pursued to continuously enhance the performance of the association algorithm (CTBTO 2017a).

While the IDC remains focused on optimizing the performance of the detection and association algorithms, it also remains committed on sustaining and updating existing operational capabilities with respect to its evolving station network.

6.3 Network Performance and Evolution of the Infrasound Processing

For effective Treaty monitoring, the networks need to be well maintained and effectively operated in order to optimize network performance. Network performance for the different technologies of the IMS is a function of both technical and environmental influences. Operation and maintenance of the stations contribute to the availability and technical quality of the data, while noise from various natural and man-made sources and atmospheric conditions influence the detection thresholds. High network performance provides confidence in the effectiveness of the monitoring system and such performance measures are key element for operation and maintenance of the network. As a means to protect its assets, the PTS is inter-

ested in estimating its network performance capabilities. The objective is here to understand the effectiveness of the network, which requires an assessment of the detection capabilities.

The IMS infrasound network was designed to reliably detect and localize relatively small atmospheric nuclear explosion at any point on the globe (Brachet et al. 2010; Christie and Campus 2010; Marty 2019; Mialle et al. 2019). Even in its partially implemented state, the IMS infrasound network already demonstrates its ability to detect and locate low energy infrasound events around the Earth at any given period of time (Green and Bowers 2010; Le Pichon et al. 2008, 2019). A prerequisite to estimate the monitoring capability of the IMS infrasound network is the ability to predict the signal amplitude at any location and assess whether the signal of interest is detectable above background noise of the stations (Pilger et al. 2015). Network performance simulations also need to take into account source and propagation effects, such as source frequency content and accurate atmospheric specifications (Le Pichon et al. 2012).

6.3.1 Network Performance

Background on network performance integration at the CTBTO

In 2009, the PTS acquired the NetSim software to enhance its network performance capabilities for waveform technologies. This network simulation software provided a sufficient level of expertise for seismic and hydroacoustic technologies (Prior and Brown 2011). However, the infrasound implementation and accuracy was not satisfactory and a change of approach. The NetSim Infrasound approach was based on seismic attenuation laws with a corrective wind term obtained from empirical atmospheric specifications for a set of fixed dates and using a uniform station noise model. The network performance results compared to calibration explosion (such as the Sayarim Infrasound Calibration Experiments (Fee et al. 2013)) demonstrated that a redesign of the software was required for infrasound technology in order to account for atmospheric propagation effects and to implement updated attenuation relations.

A collaborative effort was then initiated with the international scientific community on the vDEC (virtual Data Exploitation Centre) platform, that led to the development of DTK-NetPerf, which is a modular tool with user-defined frequency-dependent semiempirical attenuation relations (Le Pichon et al. 2012, 2019), using real-time realistic atmospheric specifications (provided by the European Centre for Medium-range Weather Forecast, ECMWF) and individual time-varying station noise level computed by the IDC (Brown et al. 2014). After implementation, testing and evaluation on the vDEC platform, the software was introduced into the IDC environment. It was used on multiple Ground Truth case studies from the IDC Infrasound Reference Event Database (IRED). This validation tests helped to identify improvement requirements for the software.

Modelling technique

To model the detection capability of an arbitrary infrasound network, it is necessary to predict the signal amplitude at any required time and location, and further evaluate whether the signal can be detected at the receivers. Unlike seismic waves that propagate through the Earth where propagation conditions do not significantly change with time, infrasonic waves propagate through the ever-changing atmosphere.

Various approaches considering empirical yield-scaling relationships derived from remote observations have been proposed (in particular by Whitaker 1995; Green and Bowers 2010; Le Pichon et al. 2012). However, the conclusions of these studies may be misleading because they do not include an accurate description of the time-varying atmosphere (Fee et al. 2013). Infrasound waves can propagate over regional to global distances without significant attenuation through atmospheric waveguides thanks to specific temperature and wind gradients. This propagation is characterized by the properties of refraction, reflection, diffraction, advection, attenuation and dispersion (Waxler and Assink 2019). High-frequency signals and high atmospheric absorption at high altitudes (Bass 1995), strongly attenuate thermospheric phases, which are rarely detected beyond regional distances (less than 20° distance as confirmed by the IDC Reference Event Database, IRED Brachet et al. 2010). Under favourable temperature and wind conditions, the acoustic energy is ducted by the stratospheric waveguides where wave refraction towards the ground occurs. Atmospheric specification provided by meteorological models such as ECMWF capture this behaviour and allow to simulate with accuracy the region of probable detections of infrasound signals propagating in the atmosphere (as demonstrated by Kulichkov et al. 2010; Millet 2015; Le Pichon et al. 2019).

Various effective techniques exist to realistically propagate the acoustic energy over various distances in a stratified atmosphere, such as the parabolic equation (PE) method. The PE method takes into account diffraction and scattering effects created by the atmospheric small-scale structure and massive range-independent PE simulations are examined by Le Pichon et al. (2012, 2019) to quantify the infrasound network performance in high spatio-temporal resolution. These results help to better understand factors affecting propagation predictions. The frequency-dependent semiempirical attenuation relations are then considered for infrasound detection capability at the IDC.

Implementation at the IDC

Compared with NetSim, improved performance of the IMS network is observed due in particular to the modelling of efficient stratospheric ducting in under low wind conditions. This prediction is consistent with recent observations of calibration experiments showing multiple stations recording relatively low yield explosions at distance of several thousands of kilometres (Fee et al. 2013).

DTK-NetPerf produces global detection capability maps with the requested spatio-temporal variation, which is currently 1° and every 3 h given the atmospheric datasets provided by ECMWF. The maps are produced in near-real-time at the IDC and provide support for routine analysis and for network performance assessment in normal operation or for maintenance activities.

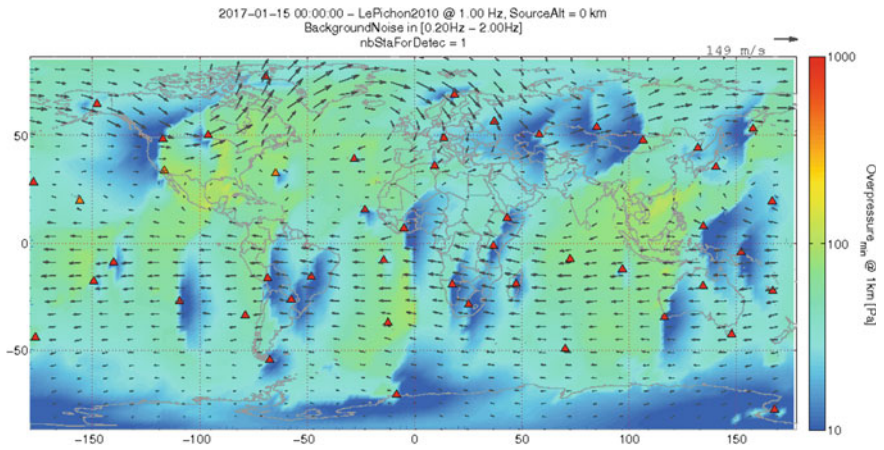

Fig. 6.18 Detectability map computed with DTK-NetPerf, using frequency-dependent attenuation relation (Le Pichon et al. 2012), ECMWF atmospheric specifications and real-time station noise computed by the IDC (Brown et al. 2014) for the operational IMS infrasound network on 01 January 2017 at 00:00 UTC. The computations are made for single station coverage, frequencies of 1 Hz, ground-based source and background noise level estimated in [0.2–2] Hz. IMS infrasound stations are indicated by triangles (red for fully operational, orange for station sending data but non-mission capable and yellow when no data is available). The colour codes the minimum detectable source amplitude at a reference distance of 1 km from the source (in Pascal (Pa) peak-to-peak amplitude)

Network performance variations are mainly expected due to maintenance operations, data outage (that can be related to communication or power issues), variation of the local environmental conditions and the atmospheric heterogeneity. Such variations can be observed at short and long time scale and at regional or global distances:

- monthly to seasonal variations typically exhibit important changes in the middle atmosphere as reported by Tailpied et al. (2016). At the global scale, this can be observed for various periods, for example between May and June with the Figs. 6.20 and 6.21 demonstrating high variability in detection patterns.
- diurnal variations: as illustrated in Figs. 6.18 and 6.19. Network capabilities are highly dependent on the local background noise variations and impact drastically station to station detection capabilities (Brown et al. 2014).
- daily variations, which helps, in particular, routine analysis for recurrent seismic-acoustic sources that may or may not be detected by the infrasound network.
- year to year variation, which is crucial as the IMS infrasound component is still under installation and historical stations start to go through revalidation and upgrade (Marty 2018).

The network detection capability maps demonstrate the variability in the network performance in space and time, which illustrates the complexity to operate a global infrasound network to ensure continuous detection capability leading to the production of accurate automatic and reviewed detection lists and event bulletins. Understanding the effectiveness of the network at any given time and location, however, helps to better fulfill the CTBTO mission and build trust in the verification regime.

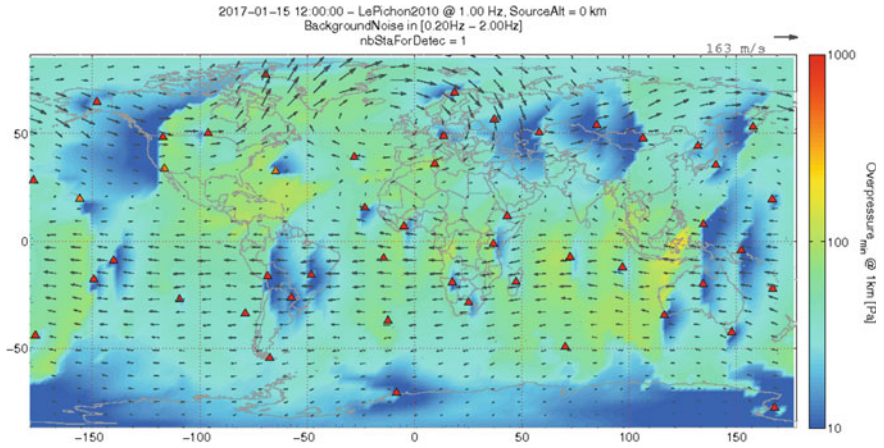

Fig. 6.19 Detectability map computed with DTK-NetPerf, with similar configuration as Fig. 6.18 for the 01 January 2017 at 12:00 UTC

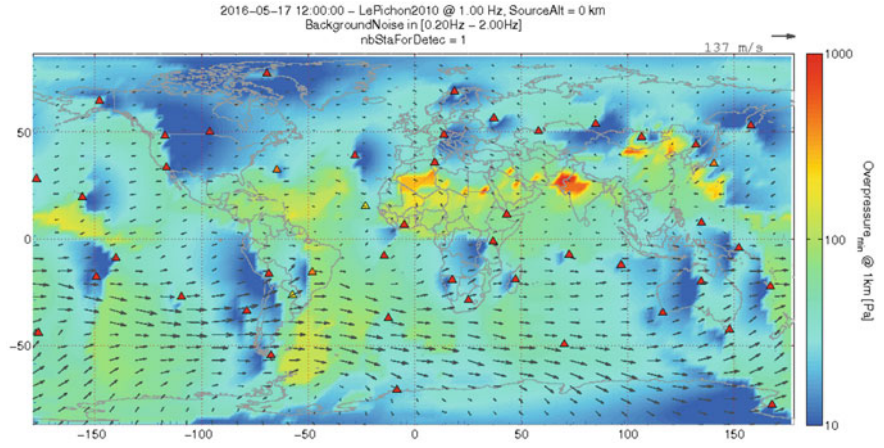

Fig. 6.20 Detectability map computed with DTK-NetPerf, with similar configuration as Fig. 6.18 for the 17 May 2016 at 12:00 UTC

6.3.1.1 Infrasound Magnitude Estimation Efforts

An aspect of IDC processing that remains to be completed is an order of magnitude estimate of the source size for infrasound events. The IDC worked on incorporating an infrasound magnitude estimate into IDC development processing pipeline, which is being made possible by the establishment of amplitude attenuation relations introduced at the beginning of Sect. 6.3. Three magnitude estimates are being determined, where the first two are based on amplitude attenuation with distance, and assume either the high-energy amplitude-range attenuation (Whitaker et al. 2003), or

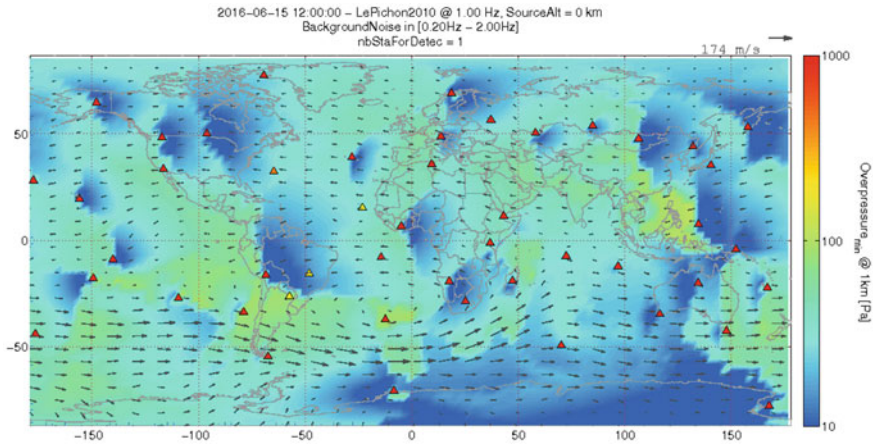

Fig. 6.21 Detectability map computed with DTK-NetPerf, with similar configuration as Fig. 6.18 for the 15 June 2016 at 12:00 UTC

the refinements frequency-dependent semiempirical attenuation relations (Le Pichon et al. 2012) that include stratospheric ducting and the effects of absorption and geometric spreading. The third magnitude estimate is based on the period of the dominant acoustic return at maximum amplitude that was derived from measurements of atmospheric nuclear explosions as developed by the U.S Air Force Technical Applications Centre (AFTAC) (Edwards et al. 2006).

While the work on infrasound magnitude is an initial attempt at defining event size, it is a crucial aspect for the IDC processing system as it moves towards full specification of infrasound event origins. As one may expect, the seismic magnitude estimates remain unaffected by this implementation, where the objective is to provide an order of magnitude estimate for infrasound source size independent of source to station distance. As a baseline, the infrasound magnitude uses a logarithmic scale in analogy to seismic magnitudes while assuming that a magnitude 3 event corresponds to a one-kiloton high explosive yield.

The magnitude estimates are tested for automatic events from IDC processing system and for well-defined explosive volcanic events to demonstrate the practical implementation and in order to provide a first assessment for this method (Brown et al. 2015). This results from both routine processing and for selected significant events are presented to the analyst for the three magnitude types and open a path towards further development of the method including stratospheric wind specification and towards further evaluation prior to its possible implementation in IDC routine operations.

6.3.1.2 Towards Using of Atmospheric Specification in an Operational Environment

In its current re-engineering efforts, the IDC identified requirements, whose implementation in a re-engineered system would introduce significant changes to its waveform data processing. Some of the requirements are dependent upon scientific and technical advances. However, the IDC re-engineered software architecture is being designed, in terms of data structures and component interfaces, with the intent to accommodate integration of such changes into future version of the software. One requirement identified is related to the use of atmospheric datasets in infrasound network processing for association of phases and location of infrasound sources.

As described in Sect. 6.2, the latest enhancements to infrasound network processing, consist in the inclusion of infrasound capabilities in the NET-VISA software. NET-VISA provides improved performance of the IDC infrasound bulletin compared to the historical automatic association software. However, the IDC is seeking continuous improvement of its automatic products and remains interested in the infrasound scientific research efforts, which demonstrated that event characterization can be further improved taking into account state-of-the-art atmospheric specification (such as those provided by ECMWF) together with propagation modelling capabilities (Millet 2015; Waxler et al. 2015; Waxler and Assink 2019; Chunchuzov and Kulichkov 2019).

One approach under consideration is extending the infrasound model in NET-VISA using real-time atmospheric specifications or derived products produced by an infrasound propagation algorithm. However, while long-range infrasound propagation modelling is a useful tool for special event analysis, the inherent unpredictability of the atmosphere results in a poorly constrained propagation medium and a large number of propagation paths. The resolution of this problem often requests long computation times, while the IDC processing system is operating in near-real-time (as described in Sect. 6.1). This issue can be addressed with a probabilistic framework seeking a numerical approach that describes long-range propagation at the lowest numerical cost and complexity. Given that each plausible atmospheric state produces large deviations from the state-of-the-art atmospheric specification, the task is complex.

An alternative approach considers propagation modelling based on reduced-order models provided by the numerical platform FLOWS (Fast Low-Order Wave Simulation (Bertin et al. 2014; Cugnet et al. 2019). The method is based on a fast low-order stochastic algorithm that makes it possible to predict signals and uncertainties in complex and poorly constrained media. The uncertainties associated with a hypothesized event and atmospheric dynamics are represented in terms of confidence intervals, which are an important indicator for measuring the relevance of numerical results. The reduced models are obtained by retaining a few propagating modes, with the aim of simplifying the acoustic model to the point that the predicted statistics and sensitivities of signals are correct. In the atmosphere, these modes are confined within waveguides causing the sound to propagate through multiple paths to the receiver.

FLOWS performance are under consideration using several ground truth events recorded by IMS infrasound stations and documented in the IRED. By statistically examining the manifestation of the uncertainty within the waveforms, it is possible to determine how to update the numerically obtained signals from a sequence of reduced models and how to decide whether a recorded signal is plausible or not, which would be invaluable information for the NET-VISA or any association algorithm of infrasound phases.

The question remains whether the use of atmospheric data together with computationally efficient infrasound propagation methods help significantly improving the performance of the association algorithms. The IDC is considering several options from the full integration of propagation modelling techniques to the use of derived characteristics from the atmospheric specifications with the objective to further improve its infrasound processing system. However, for such implementation, the current availability of high accuracy atmospheric specifications from external provider (such as ECMWF) is not in agreement with IDC automatic bulletin production timeline.

6.4 Concluding Remarks and Potential Future Improvements

After completely designing the infrasound processing system and implementing the procedure for the daily analysis of seismic-acoustic event, infrasound technology has now been fully integrated for over seven years into IDC operational environment. The uniqueness of the IMS infrasound network and the IDC operational processing system place the PrepCom as a cornerstone of infrasound technology research and development for nuclear test verification and for civil and scientific applications (CTBTO 2017a).

Because the IDC is committed to continuously improve its methods and it is dedicated to build a trustworthy verification system, it entered into a re-engineering period. This large endeavour currently focuses on the upgrade and enhancement of the IDC system for the three waveform technologies. A number of re-engineered system have already gone through system engineering requirement to development phase, while a few systems are currently ready to be rolled into the IDC operational environment following strict testing and evaluation stages. This is, in particular, the case for the network association method, NET-VISA and the station processing and interactive review platform, DTK-PMCC and DTK-GPMCC. The latest being also made available to the Member States to further enhance the verification regime and advance NDC capabilities. These efforts have created a strong NDC user base and the resulting NDC-in-a-Box project help gaining NDC trust in the credibility of the verification system.

Beyond the current active projects to enhance its system, the IDC pursue efforts for the infrasound technology with a technology readiness level (Graettinger et al. 2002) with a multi-year horizon in particular on (in no specific order):

- the use of atmospheric specifications in infrasound network processing, with several approaches being considered for the extension of the infrasound model in NET-VISA to either use real-time atmospheric specifications or derived products produced by an infrasound propagation algorithm. However, the inherent unpredictability of the atmosphere makes it a complex task, in particular in the context of a fully automated real-time system,
- the need to revisit the phase categorization problem building on the experience from the current IDC station processing system and the newly developed clutter model for NET-VISA,
- pursuing efforts to develop and implement a framework for detector evaluation for the IDC (Charbit et al. 2014; Marcillo et al. 2019),
- the development and implementation of a state-of-the-art platform for special event analysis.

In alignment with PTS objectives, the commitment the IDC to improve its system ensures the sustainment and enhancement of its existing capabilities in order to continue building a trustworthy and credible verification system, and support the preparation for Entry into Force of the CTBT.

Acknowledgements The authors thank the IDC waveform analysts, in particular, the infrasound team, for their sustained efforts to produce high-quality IDC products. The authors would also like to thank staff from the Software Application and Automatic Processing System Sections of the IDC for their dedication for
technology development and implementation. The authors are thankful to the Acoustic Group from the Engineering and Development Section of the IMS for the successful installation and station upgrade and their collaboration.
Enhancing NDC-in-a-Box with infrasound data processing capabilities and with real-time automatic processing of seismic-acoustic data was supported by the European Union (EU) Council Decision V during 2014–2015 and by EU Council Decision VI during 2016–2017.

Disclaimer The views expressed herein are those of the author and do not necessarily reflect the view of the CTBTO Preparatory Commission.

References

Arora N, Russell S, Kidwell P, Sudderth E (2010) Global seismic monitoring as probabilistic inference. In: Lafferty J, Williams CKI, Shawe-Taylor J, Zemel RS (eds) Advances in neural information processing systems, vol 23, pp 73–81

Arora N, Russell S, Sudderth E (2013) NET-VISA: network processing vertically integrated seismic analysis. Bull Seismol Soc Am (BSSA) 103(2A):709–729

Arora N, Prior M (2014) A Fusion model of seismic and hydro-acoustic propagation for treaty monitoring. In: Oral presentation at European geophysical union, EGU2014-15796

Arora, N, Mialle P (2015) Global infrasound association based on probabilistic clutter categorization. In: Oral presentation at American geophysical union, fall meeting 2015, abstract S51F-04

Bass H (1995) Atmospheric absorption of sound: further developments. J Acoust Soc Am 97(1):680–683

Bertin M, Millet C, Bouche D (2014) A low-order reduced model for the long range propagation of infrasounds in the atmosphere. J Acoust Soc Am 136(1):37–52. https://doi.org/10.1121/1.4883388

Blanc E, Pol K, Le Pichon A, Hauchecorne A, Keckhut P, Baumgarten G, Hildebrand J, Höffner, Stober G, Hibbins R, Espy P, Rapp M, Kaifler B, Ceranna L, Hupe P, Hagen J, Rüfenacht R, Kämpfer, Smets P (2019) Middle atmosphere variability and model uncertainties as investigated in the framework of the ARISE project. In: Le Pichon A, Blanc E, Hauchecorne A (eds) Infrasound monitoring for atmospheric studies, 2nd edn. Springer, Dordrecht, pp 845–887

Bondar I, Le Bras R, Arora N, Tomuta E (2017) Evaluation of NetVisa association and location performance using ground truth events and RSTT model based SSSCs. Presented at the science and technology conference, Vienna, Austria

Brachet N, Brown D, Bras RL, Cansi Y, Mialle P, Coyne J (2010) Monitoring the Earth's atmosphere with the global IMS infrasound network. In: Le Pichon A, Blanc E, Hauchecorne A (eds) Infrasound monitoring for atmospheric studies. Springer, New York, pp 77–118

Brown PG et al (2013) A 500-kiloton airburst over Chelyabinsk and an enhanced hazard from small impactors. Nature 503:238–241

Brown D, Ceranna L, Prior M, Mialle P, Le Bras RJ (2014) The IDC seismic, hydroacoustic and infrasound global low and high noise models. Pure Appl Geophys 171:361–375

Brown D, Mialle P, Le Bras R (2015) Infrasound magnitude estimation. In: Science and technology conference, Vienna, Austria. T1.1-P12

Cansi Y (1995) An automatic seismic event processing for detection and location: the P.M.C.C. method. Geophys Res Lett 22:1021–1024

Cansi Y, Le Pichon A (2008) Infrasound event detection using the progressive multi-channel correlation algorithm. In: Havelock D, Kuwano S, Vorlander M (eds) Handbook of signal processing in acoustics. Springer, New York

Caudron C, Taisne B, Garcs M, Alexis LP, Mialle P (2015) On the use of remote infrasound and seismic stations to constrain the eruptive sequence and intensity for the 2014 Kelud eruption. Geophys Res Lett. 42:6614–6621. https://doi.org/10.1002/2015GL064885

Caudron C, Taisne B, Perttu A, Garcs M, Silber EA, Mialle P (2016) Infrasound and seismic detections associated with the 7 September 2015 Bangkok fireball. Geosci Lett 3(1):26

Ceranna L, Le Pichon A (2015) The coherent field of infrasound—a global view with the IMS, General Assembly 2016, held 17–22 Apr 2016 in Vienna, Austria, p 5580

Ceranna L, Matoza R, Hupe P, Le Pichon A, Landès M (2019) Systematic array processing of a decade of global IMS infrasound data. In: Le Pichon A, Blanc E, Hauchecorne A (eds) Infrasound monitoring for atmospheric studies, 2nd edn. Springer, Dordrecht, pp 471–482

Charbit M, Mialle P, Brown D, Given J (2014) A framework for detection software evaluation. In: Oral presentation at the infrasound technology workshop, Vienna, Austria

Chunchuzov I, Kulichkov S (2019) Internal gravity wave perturbations and their impacts on infrasound propagation in the atmosphere. In: Le Pichon A, Blanc E, Hauchecorne A (eds) Infrasound monitoring for atmospheric studies, 2nd edn. Springer, Dordrecht, pp 551–590

CTBTO (2013a) CTBTO Midterm strategy for the period 2014–2017, CTBT/PTS/INF.1249

CTBTO (2013b), Overview of the 2013 North Korea announced nuclear test, https://www.ctbto.org/press-centre/press-releases/2013/ctbto-detects-radioactivity-consistent-with-12-february-announced-north-korean-nuclear-test/

CTBTO (2017a) CTBTO Medium term strategy for the period 2018–2021, CTBT/PTS/INF.1395

CTBTO (2017b), Technical findings of the 2017 North Korea announced nuclear test, https://www.ctbto.org/the-treaty/developments-after-1996/2017-sept-dprk/technical-findings/

CTBTO newsroom (2014). https://newsroom.ctbto.org/2014/04/24/ctbto-detected-26-major-asteroid-impacts-in-earths-atmosphere-since-2000/

Che I-Y, Kim TS, Jeon J-S, Lee H-I (2009) Infrasound observation of the apparent North Korean nuclear test of 25 May 2009. Geophys Res Lett 36:L22802. https://doi.org/10.1029/2009GL041017

Che I-Y, Park J, Kim I, Kim TS, Lee H-L (2014) Infrasound signals from the underground nuclear explosions of North Korea. Geophys J Int 198(1):495–503. https://doi.org/10.1093/gji/ggu150

Christie R, Campus P (2010) The IMS infrasound network: design and establishment of infrasound stations. In: Le Pichon A, Blanc E, Hauchecorne A (eds) Infrasound monitoring for atmospheric studies. Springer, New York, pp 29–75

Coyne J, Bobrov D, Bormann P, Duran E, Grenard P, Haralabus G, Kitov I, Starovoit Y (2012) CTBTO: goals, networks, data analysis and data availability. In: Bormann P (ed) New manual of seismological observatory practice 2 (NMSOP-2). Deutsches GeoForschungsZentrum GFZ, Potsdam, pp 1–41

Cugnet D, de la Camara A, Lott F, Millet C, Ribstein B (2019) Non-orographic gravity waves: representation in climate models and effects on infrasound. In: Le Pichon A, Blanc E, Hauchecorne A (eds) Infrasound monitoring for atmospheric studies, 2nd edn. Springer, Dordrecht, pp 827–844

Drob D (2019) Meteorology, climatology, and upper atmospheric composition for infrasound propagation modelling. In: Le Pichon A, Blanc E, Hauchecorne A (eds) Infrasound monitoring for atmospheric studies, 2nd edn. Springer, Dordrecht, pp 485–508

Edwards WN, Brown PG, ReVelle DO (2006) Estimates of meteoroid kinetic energies from observations of infrasonic airwaves. J Atmos Solar-Terr Phys 68:1136–1160

Edwards WN, Green DN (2012) Effect of interarray elevation differences on infrasound beamforming. Geophys J Int 190(1):335–346

Fee D, Waxler R, Assink J, Gitterman Y, Given J, Coyne J, Mialle P, Garces M, Drob D, Kleinert D, Hofstetter R, Grenard P (2013) Overview of the 2009 and 2011 Sayarim infrasound calibration experiments. J Geophys Res Atmos 118: https://doi.org/10.1002/jgrd.50398

de la Fuente Marcos C, de la Fuente Marcos R, Mialle P (2016) Homing in for New Year: impact parameters and pre-impact orbital evolution of meteoroid 2014 AA. Astrophys Space Sci 361(11):358 (33 pp)

Garces MA (2013) On infrasound standards, part 1 time, frequency, and energy scaling. InfraMatics 2(2):13–35. https://doi.org/10.4236/inframatics.2013.22002

Graettinger CP, Garcia-Miller S, Siviy J, Van Syckle PJ, Schenk RJ (2002) Using the technology readiness levels scale to support technology management in the DOD's ATD/STO environments: a findings and recommendations report conducted for army CECOM (CMU/SEI-2002-SR-027), Carnegie Mellon Software Engineering Institute

Green DN, Bowers D (2010) Estimating the detection capability of the international monitoring system infrasound network. J Geophys Res 115:D18116. https://doi.org/10.1029/2010JD014017

Horner B (2009) Rules, guidelines and procedures for analysis of waveform data at the international data centre, version 1.0, prepared under contract no. 744 for the CTBTO preparatory commission—international data centre—monitoring and data analysis section, Vienna, Austria

Kulichkov SN, Chunchuzov IP, Pupov OI (2010) Simulating the influence of an atmospheric fine inhomogeneous structure on long-range propagation of pulsed acoustic signals. Izv Atmos Ocean Phys 46(1):60–68

Le Pichon A, Vergoz J, Herry P, Ceranna L (2008) Analyzing the detection capability of infrasound arrays in Central Europe. J Geophys Res 113: https://doi.org/10.1029/2007JD009509

Le Pichon A, Matoza R, Brachet N (2010) Cansi Y (2010) Recent enhancements of the PMCC infrasound signal detector. Inframatics 26:5–8

Le Pichon A, Ceranna L, Vergoz J (2012) Incorporating numerical modeling into estimates of the detection capability of the IMS infrasound network. J Geophys Res 117(D5): https://doi.org/10.1029/2011JD016670

Le Pichon A, Ceranna L, Pilger C, Mialle P, Brown D, Herry P, Brachet N (2013) The 2013 Russian fireball largest ever detected by CTBTO infrasound sensors. Geophys Res Lett 40(14):3732–3737

Le Pichon A, Assink JD, Heinrich P, Blanc E, Charlton-Perez A, Lee CF, Keckhut P, Hauchecorne A, Rüfenacht R, Kämpfer N, Drob DP, Smets PSM, Evers LG, Ceranna L, Pilger C, Ross O, Claud C (2015) Comparison of co-located independent ground-based middle atmospheric wind and temperature measurements with numerical weather prediction models. J Geophys Res Atmos 120:8318–8331. https://doi.org/10.1002/2015JD023273

Le Pichon A, Ceranna L, Vergoz J, Tailpied D (2019) Modeling the detection capability of the global IMS infrasound network. In: Le Pichon A, Blanc E, Hauchecorne A (eds) Infrasound monitoring for atmospheric studies, 2nd edn. Springer, Dordrecht, pp 593–604

Marcillo O, Arrowsmith S, Charbit M, Carmichael J (2019) Infrasound signal detection: re-examining the component parts that makeup detection algorithms. In: Le Pichon A, Blanc E, Hauchecorne A (eds) Infrasound monitoring for atmospheric studies, 2nd edn. Springer, Dordrecht, pp 249–271

Marlton G, Charlton-Perez A, Giles Harrison R, Lee C (2019) Calculating atmospheric gravity wave parameters from infrasound measurements. In: Le Pichon A, Blanc E, Hauchecorne A (eds) Infrasound monitoring for atmospheric studies, 2nd edn. Springer, Dordrecht, pp 701–719

Marty J (2019) The IMS infrasound network: current status and technological developments. In: Le Pichon A, Blanc E, Hauchecorne A (eds) Infrasound monitoring for atmospheric studies, 2nd edn. Springer, Dordrecht, pp 3–62

Matoza R, Fee D, Green D, Mialle P (2019), Volcano infrasound and the international monitoring system. In: Le Pichon A, Blanc E, Hauchecorne A (eds) Infrasound monitoring for atmospheric studies, 2nd edn. Springer, Dordrecht, pp 1023–1077

Mialle P, Brown D, Arora N and colleagues from IDC (2019) Advances in operational processing at the international data centre. In: Le Pichon A, Blanc E, Hauchecorne A (eds) Infrasound monitoring for atmospheric studies, 2nd edn. Springer, Dordrecht, pp 209–248

Marty J, Ponceau D, Dalaudier F (2010) Using the international monitoring system infrasound network to study gravity waves. Geophys Res Lett 37:L19802. https://doi.org/10.1029/2010GL044181

Marty J (2018) The IMS infrasound network: status and state-of-the-art design. In: Le Pichon A, Blanc E, Hauchecorne A (eds) Infrasound monitoring for atmospheric studies, vol 2. Springer, New York

Matoza RS, Landes M, Le Pichon A, Ceranna L, Brown D (2013) Coherent ambient infrasound recorded by the International Monitoring System. Geophys Res Lett 40(2):429–433. https://doi.org/10.1029/2012GL054329

Matoza RS, Green DN, Le Pichon A, Shearer PM, Fee D, Mialle P, Ceranna L (2017) Automated detection and cataloging of global explosive volcanism using the International Monitoring System infrasound network. Solid Earth, J Geophys Res

Matoza RS, Fee D, Green DN, Mialle P (2018) Volcano infrasound and the International Monitoring System. In: Le Pichon A, Blanc E, Hauchecorne A (eds) Infrasound monitoring for atmospheric studies, vol 2. Springer, New York

Mialle P (2012) Developments with the Infrasound only pipeline on vDEC and more. In: Infrasound technology workshop, Daejeon, South Korea, 8 Oct 2012

Mialle P (2013) Infrasound developments at the IDC. In: Infrasound technology workshop, Vienna, Austria, 7 Oct 2013

Mialle P (2015) IDC infrasound technology developments. In: Infrasound technology workshop, Vienna, Austria, Oct 2015

Millet C (2015) Infrasound propagation and model reduction in randomly layered media. J Acoust Soc Am 137:2372. https://doi.org/10.1121/1.4920620

Nouvellet A, Charbit M, Rouet F, Le Pichon A (2014) Slowness estimation from noisy time delays observed on non-planar arrays. Geophys J Int 198(2):1199–1207

Pilger C, Ceranna L, Ross JO, Le Pichon A, Mialle P, Garces MA (2015) CTBT infrasound network performance to detect the 2013 Russian fireball event. Geophys Res Lett 42(7):2523–2531. https://doi.org/10.1002/2015GL063482

Pilger C, Ceranna L, Le Pichon A, Brown P (2019) Large meteoroids as global infrasound reference events. In: Le Pichon A, Blanc E, Hauchecorne A (eds) Infrasound monitoring for atmospheric studies, 2nd edn. Springer, Dordrecht, pp 451–470

Prior M, Brown D (2011) Modelling global seismic network detection threshold. Science and technology conference. Austria, Vienna, pp T3–P12

Prior MK, Tomuta E, Poplavskiy A (2013) Quantitative assessment of the detection performance of global association algorithms. Science and technology conference. Austria, Vienna, pp T3–P99

Silber EA, Le Pichon A, Brown PG (2011) Infrasonic detection of a near-Earth object impact over Indonesia on 8 October 2009. Geophys Res Lett 38(12):

Silber E, Brown PG (2019) Infrasound monitoring as a tool to characterize impacting near-earth objects (NEOs). In: Le Pichon A, Blanc E, Hauchecorne A (eds) Infrasound monitoring for atmospheric studies, 2nd edn. Springer, Dordrecht, pp 939–986

Tailpied D, Le Pichon A, Marchetti E, Assink J, Vergniolle S (2016) Assessing and optimizing the performance of infrasound networks to monitor volcanic eruptions. Geophys J Int 208(1):437–448. https://doi.org/10.1093/gji/ggw400

Vergoz J, Gaillard P, Le Pichon A, Brachet N, Ceranna L (2011) Infrasound categorization towards a statistics based approach. In: Oral presentation at the infrasound technology workshop, Dead Sea, Jordan

Waxler R, Evers LG, Assink J, Blom P (2015) The stratospheric arrival pair in infrasound propagation. J Acoust Soc Am 137(4):1846–1856

Waxler R, Assink J (2019) Propagation modeling through realistic atmosphere and benchmarking. In: Le Pichon A, Blanc E, Hauchecorne A (eds) Infrasound monitoring for atmospheric studies, 2nd edn. Springer, Dordrecht, pp 509–549

Whitaker RW (1995) Infrasonic monitoring. Paper presented at the 17th annual seismic research symposium, on monitoring a comprehensive test-ban treaty (CTBT), LA-UR 95-2775, Los Alamos National Laboratory, 11–15 Sept, Scottsdale, Arizona, USA

Whitaker RW, Sandoval TD, Mutschlecner JP (2003) Recent infrasound analysis. Paper presented at 25th annual seismic research symposium, LANL, Tucson, Arizona, USA

Chapter 7
Infrasound Signal Detection: Re-examining the Component Parts that Makeup Detection Algorithms

Omar Marcillo, Stephen Arrowsmith, Maurice Charbit and Joshua Carmichael

Abstract Detecting a Signal Of Interest (SOI) is the first step in many applications of infrasound monitoring. This intuitively simple task is defined as separating out signals from background noise on the basis of the characteristics of observed data; it is, however, deceptively complex. The problem of detecting signals requires multiple processes that are divisible at their highest level into several fundamental tasks. These tasks include (1) defining models for SOIs and noise that properly fit the observations, (2) finding SOIs amongst noise, and (3) estimating parameters of the SOI (e.g., Direction Of Arrival (DOA), Signal-to-Noise Ratio (SNR) and confidence intervals) that can be used for signal characterization. Each of these components involves multiple subcomponents. Here, we explore these three components by examining current infrasound detection algorithms and the assumptions that are made for their operation and exploring and discussing alternative approaches to advance the performance and efficiency of detection operations. This chapter does not address new statistical methods but does offer some insights into the detection problem that may motivate further research.

7.1 Introduction

The intuitively simple task of separating out signals from background noise on the basis of the characteristics of observed data or mathematical models is deceptively complex. Most infrasound applications exploits signal detection using array data and will be the focus of this chapter. The foundational theory on which array-based signal detectors have been built was constructed for radar and other applications

O. Marcillo (✉) · J. Carmichael
Los Alamos National Laboratory, Los Alamos, USA
e-mail: omarcillo@lanl.gov

S. Arrowsmith
Sandia National Laboratories, Albuquerque, USA

M. Charbit
Telecom Paris, Paris, France

A. Le Pichon et al. (eds.), *Infrasound Monitoring for Atmospheric Studies*,
https://doi.org/10.1007/978-3-319-75140-5_7

(see Krim and Viberg 1996 for a review). However, as most experts in the field are aware, the practice of applying the theory to infrasound data is often very challenging, particularly because the narrowband assumption fails. The wavelengths of infrasonic signals in the bandwidth required to monitor for large atmospheric explosion are large—between 3.5 and 0.35 km. At these distances, the conditions of the local atmosphere (temperature, wind speed, and direction) are variable, as are the characteristics of noise at each array element (Mack and Flinn 1971).

Most infrasound research in the area of signal detection has been driven by the inclusion of an infrasound network as part of the International Monitoring System (IMS) that is used to verify compliance with the Comprehensive Nuclear Test Ban Treaty (CTBT) Marty (2019). Arrays are an integral part of the design of the IMS infrasound network and early work provided constraints for array designs (Christie and Campus 2009; Marty 2019). Digital detector method developed for radar, seismology (Cansi 1995) and from image processing domains (Brown et al. 2008) were deployed to exploit the data from these arrays (Mialle et al. 2019). Most of these detectors operated under the assumption that the received signals associated a single SOI appear, the sensor level, as filtered versions of a same signal. This assumption is called perfect coherence. A particular case of interest for infrasound source is the case where the received signals are delayed/attenuated versions of a same signal. The other most commonly used assumption is that the noise is Gaussian, temporally and spatially white. All these assumptions lead to simple algorithms whose trade-off between false alarms and missed detections can be clearly quantified.

However, there are many other coherent sources of infrasound routinely detected by the IMS, such as microbaroms (Stopa et al. 2011; Landès et al. 2012; Walker 2012; Ceranna et al. 2019) and some volcanic activity (Dabrowa et al. 2011; Matoza et al. 2019). Such infrasound sources are often of no interest to verifying compliance with the CTBT. Rather, they are often considered nuisance sources. Compounding this problem, the perfect coherence of infrasound signals is often lost by propagation (Mack and Flinn 1971; Nouvellet et al. 2013; Green 2015). As detectors are included in pipeline processing, more sophisticated algorithms are needed to identify the signals of interest amongst permanent sources of coherent noise (e.g., microbaroms). Practical approaches that have been proposed included detection categorization algorithms (Brachet et al. 2010; Mialle et al. 2019) and adaptive thresholds (Arrowsmith et al. 2009). However, while these approaches have enabled the construction of event catalogs (Arrowsmith et al. 2015), they leave significant limitations. In particular, there remains a disconnect between the simplistic assumptions exploited by detection theory and practice for infrasound data processing. This chapter does not address new statistical methods but does offer some insights into the detection problem that may motivate further research.

This chapter is organized to show the different components involved in infrasound signal processing for detection purposes. We will examine these components in the following subsections of this chapter: (1) defining signal and noise models, (2) detecting signals in noise, and (3) parameter estimation/extraction.

7.2 Examining the Component Parts of Detectors

The term "detection" implies the process of finding something that is hidden. For our specific purposes, we extend the action of finding within detection to extracting features (parameters) that are used to characterize signals. Infrasound monitoring processes a stream of infrasound array data and performs detection by (1) defining noise and signal characteristics, (2) identifying signals of interest (SOI) that are distinct from noise, and (3) extracting parameters that characterize the SOI (Fig. 7.1). In most cases, the noise and SOI are quantitatively similar, therefore, signal separation, and parameter extraction prove challenging.

7.3 Defining Signal and Noise

Noise can be defined as attending to one or a combination of various criteria, such as coherence, power, origin, frequency content, or duration. We define two types of noise, namely, (1) physical and (2) operational noise. For array data, physical noise is any signal that is incoherent across the elements of the arrays. This definition includes very local pressure fluctuations generated by wind (Morgan and Raspet 1992) and intrinsic sensor self-noise. Infrasonic arrays typically have sensors separated at distances much larger than the mean size of turbulence, and thus turbulence is incoherent. These disturbances can propagate across elements (for the ones separated short distances) at lower speeds (Fehr 1967) than the speed of sound that we can distinguish and filter them out. Infrasonic signals that are coherent across the array might be considered noise depending on monitoring objectives, and we refer to these coherent signals as operational-type noise. Microbaroms (Donn and Naini 1973), for example, are a type of signal that are coherent but are considered noise for most

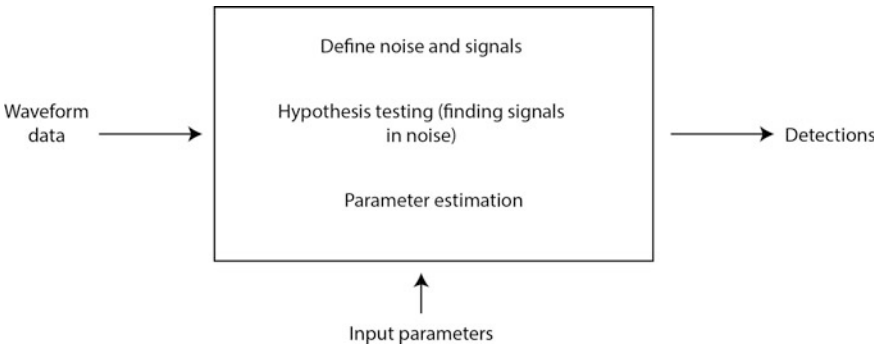

Fig. 7.1 The high-level components of infrasound signal detection algorithms. Differentiating signals from noise requires us to define parameters (dimensions) that can distinguish between the two

studies (Bowman et al. 2005). Figure 7.2 shows 24 h of data from one array element of a station of the IMS network (IS57, US) along with wind measurements from a collocated weather station to illustrate the variability of the infrasonic background noise and its relation to changing atmospheric conditions. The first 15 h of the day are characterized by a low-amplitude signal with amplitude below a tenth of a Pascal and wind speeds averaging between 2–3 m/s and a wide range of directions between −20° and 70°. The Power Spectral Density (PSD) of the overpressure waveform of a representative section of this period (cyan region) shows the very distinctive microbarom peak center at 0.2 Hz (Bowman et al. 2005) and multiple sharp peaks

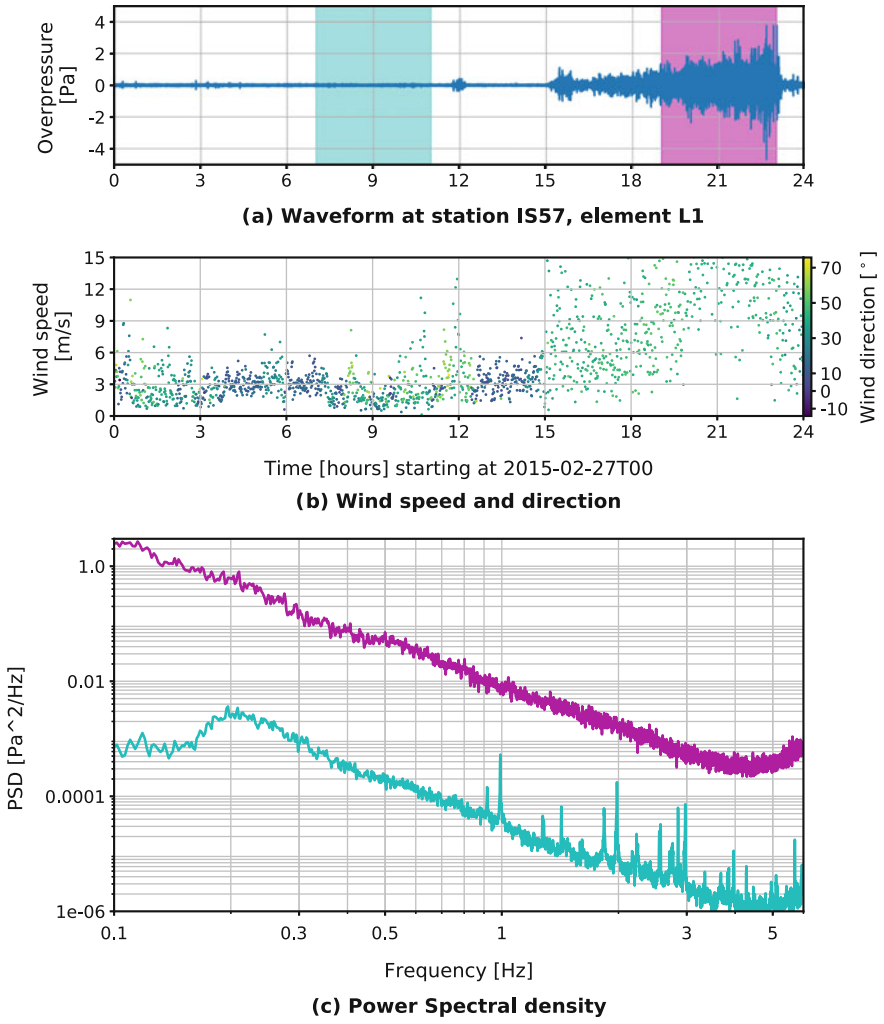

Fig. 7.2 Waveform and weather conditions for station IS57, element I57L1

above 0.9 Hz. Most of these peaks repeat at integer multiples of the first four peaks and may be related to sound from wind turbines (Marcillo et al. 2015; Pilger and Ceranna 2017). After hour 15 the amplitude of the overpressure increases with increasing wind speeds. Note also that wind direction after hour 15 is more stable between 40° and 50°. The PSD for a representative section of this period (magenta region) shows the typical characteristics of wind-induced noise that completely masks the other elements of the background noise.

Figure 7.3 shows array processing results (back-azimuth estimation) of the 24-h period described above. Two regions, before and after hour 15, are clearly separated in the coherence and the back-azimuth estimation maps. The microbarom and wind-turbine regions (around 0.2 Hz and above 0.9 Hz, respectively) show the highest values for coherence and stable back-azimuth estimations. The region after hour 15, where the signal is dominated by wind-induced noise, displays (as expected) very low coherence and a wide distribution for the estimation of back azimuths. This example shows two intervals with background noise with very different characteristics that resemble our definitions of operational- and physical-type noises.

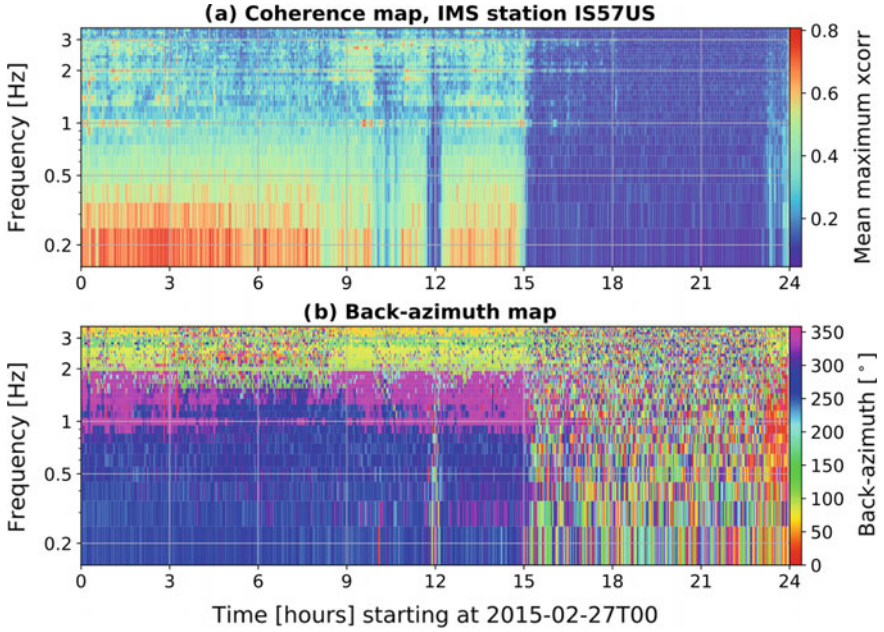

Fig. 7.3 Physical and Operational noise. 24 h of data from IMS station IS57 (Pinon Flats, California, US) that were processed using the Bartlett beamformer. The frequency bands were between 0.1 and 4 Hz with 0.1 Hz steps, a 200-s window, and 50% overlap. Panel **a** shows a map of the average maximum cross-correlation. Back azimuths are determined for each subwindow in each frequency using the maximum F-value criteria (Panel **b**)

In order to detect nuclear explosions (e.g., IMS network) exceeding a certain yield, definitions of signal have to be clarified. Given the sparsity of the 60-array network within the IMS network, SOIs triggered by nuclear explosions have generally propagated great distances (typically 100's–1000's to 10,000's of kilometers) through atmospheric waveguides (typically the stratospheric waveguide) (Drob et al. 2003). Infrasound SOIs, per our current definition, originate from atmospheric nuclear tests (Don and Ewing 1962; Donn and Ewing 1962; Dahlman et al. 1971), large chemical explosions (Ceranna et al. 2009; Green et al. 2011; Fee et al. 2013), large vulcanian eruptions (Fee and Matoza 2013; Matoza et al. 2019), and bolides that explode as terminal bursts (Le Pichon et al. 2013; Silber and Brown 2019). Acoustically, these signals are indistinguishable from nuclear detonations. Our definition of SOI excludes real infrasound waves from a wide-variety of natural and man-made sources including local events that are not detected at 100's to 1000's of kilometers (e.g., small charge explosions (Arrowsmith and Taylor 2013; Taylor et al. 2013), thunder (Anderson et al. 2014), moving vehicles) and continuous wave sources (e.g., wind farm (Marcillo et al. 2015; Pilger and Ceranna 2017) and anthropogenic noise). All of these excluded signals are now part of a refined concept of operational-type noise, which includes interference for unwanted coherent signals and random pressure fluctuations. To detect nuclear events, we must screen out the cacophony of infrasound from local and continuous wave sources, which are not applicable to the International Data Center (IDC) monitoring mission, and can be falsely associated at the network level to form spurious events (Arrowsmith et al. 2015). While they may be of general scientific interest, to consider such infrasound as signals results in too many false alarms when processing data on the sparse IMS network.

To formalize the discussed ideas about signals and noise we formulate the concept as a mathematical model. This modeling starts with array observations (multichannel data) that consist of M waveforms associated to the M elements of an array that are described by $x(t) = [x_1(t), x_2(t), \ldots, x_M(t)]^T$, where $x_m(t)$ $(1 \leq m \leq M)$ denotes an infrasound record measured on sensor m. In the presence of a SOI located far from the sensor array, a planar wave propagates across the array with a slowness vector $\boldsymbol{\theta} = (\theta_x, \theta_y, \theta_z)$ and an associated signal $s(t)$. Signal $s(t - \tau_m(\boldsymbol{\theta}))$ defines the waveform observation at the mth element of this array with a propagation delay τ_m:

$$\tau_m(\boldsymbol{\theta}) = r_m^T \boldsymbol{\theta}, \tag{7.1}$$

where $\boldsymbol{r}_m$ is the 3D location of the mth element.

In the presence of additive noise $w_m(t)$, we have:

$$x_m(t) = s(t - \tau_m(\boldsymbol{\theta})) + w_m(t) \tag{7.2}$$

The noise vector $w(t) = [w_1(t), w_2(t), \ldots, w_M(t)]$ is assumed to be a stationary spatially and temporally white random process, i.e., for any m, m', t, and t':

$$E\left(w_m(t), w_{m'}\left(t'\right)\right) = \sigma^2 \delta\left(t - t'\right)\delta_{mm'}, \tag{7.3}$$

where $\boldsymbol{E}$ is the expected-value operator, σ the standard deviation, δ_m the Kronecker's symbol, and $\delta(t)$ the Dirac's function. $w(t)$ is the realization of our definition of physical-type noise. This signal model with a coherent signal of interest and an incoherent noise can be expanded for a more realistic case if an interfering coherent (it can also be continuous) signal $v(t)$ (which is not of interest) is superimposed with the noisy SOI. The signal at the m-th element can be written as follows:

$$x_m(t) = s(t - \tau_m(\boldsymbol{\theta})) + v(t - \xi_m) + w_m(t), \tag{7.4}$$

where the term $v(t - \xi_m) + w_m(t)$ is now a realization of an operational-type noise. As our observations are based on discrete measurements of the wavefield, the sampling theorem can be applied to these continuous-time models to construct discrete-time versions. To apply this theorem, we assume that the continuous signals are band limited with the maximum frequency components f_m and that the recording system sampling rate (f_s) of the signals is $f_s \geq 2f_m$. With these assumptions, discrete version of Eq. 7.2 can be written as follows:

$$x_{n,m} = s_{n,m}(\boldsymbol{\theta}) + w_{n,m} \tag{7.5}$$

where $s_{n,m}(\boldsymbol{\theta}) = s(nT_s - \tau_m(\boldsymbol{\theta}))$, the integer $n = 0, \ldots, N-1$, and $T_s = 1/f_s$. In the rest of this manuscript, we will use the notation $x_n = [x_{n,1}, x_{n,2}, \ldots, x_{n,M}]^T$, $\boldsymbol{s}$ the sequence $s(0)$, $s(T_s)$, …, $s((N-1)T_s)$, and $s_n(\boldsymbol{\theta}) = [s_{n,1}(\boldsymbol{\theta}), s_{n,2}(\boldsymbol{\theta}), \ldots, s_{n,M}(\boldsymbol{\theta})]^T$. It is worth to notice that $s_n(\boldsymbol{\theta})$ depends only on $\boldsymbol{s}$ and $\boldsymbol{\theta}$ and can be denoted $s_n(s, \boldsymbol{\theta})$.

7.4 Detecting Signals Embedded in Noise

The main task in this step of processing infrasound records involves a binary test between the presence or absence of a noisy SOI in the data. Statistical inference analysis can be used to test the hypothesis of the absence of a SOI. The M-length vectors x_n are assumed to be independent and identically distributed (i.i.d.) with probability density function $f(x_n|\mu)$, where the parameter vector μ includes $\boldsymbol{\theta}$, σ^2, and $\boldsymbol{s}$ and belongs to the full parameter set $\chi = (R \times R \times R), R^+, R^N$. The "noise only" hypothesis H_0 is the subset χ_0 of χ such that $s = 0$. The counter-hypothesis is $H_1 = \chi - H_0$ and refers to the noise plus SOI hypothesis in the subset χ_1. To test H_0, a common approach consists of comparing a real-valued function (test statistic) based on the full observation $X = (x_1, x_2, \ldots, x_N)$ to a given threshold. The two competing hypotheses are expressible in general form as follows:

$$\begin{cases} H_0: X \sim f(x|\mu), \mu \in \chi_0 \\ H_1: X \sim f(x|\mu), \mu \in \chi_1 \end{cases} \tag{7.6}$$

Binary hypothesis testing will make the correct decision or incur an error by rejecting H_0 when it is true (type I error) or accepting H_0 when it is false (type II error). The next sections present a few test statistics that are commonly used in infrasound detection research. Section 7.6, in particular, quantifies performance comparisons between test statistics using Receiver Operating Characteristics (ROC) curves.

7.4.1 Tests Based on Construction of a Likelihood Function

A common test statistic for hypothesis testing based on the construction of likelihood functions is the Generalized Likelihood Ratio Test (GRLT). We construct these signal detectors from log-likelihood functions, whereby we replace the unknown source and noise parameters $\mu \in \chi_i$ in each PDF with their maximum likelihood estimates $\hat{\mu}_i = \arg\max_{\mu \in \chi_i} f(x|\mu)$. The ratio of logarithmic ratio of the resultant PDFs defines a scalar screening statistic $S_{GLRT}(x)$ (Kay 2013; Charbit 2017):

$$S_{GLRT}(x) = \frac{\max\limits_{\mu \in \chi} \sum_{n=1}^{N} \log(f(x_n|\mu))}{\max\limits_{\mu \in \chi_0} \sum_{n=1}^{N} \log(f(x_n|\mu))}, \tag{7.7}$$

where the log function is the natural (base e) logarithm. We explicitly decide if an SOI is present by comparing the size of $S_{GLRT}(x)$ to a threshold for event declaration γ. This comparison forms the log generalized likelihood ratio test, or log GLRT

$$S_{GLRT}(\boldsymbol{X}) \underset{H_0}{\overset{H_1}{\gtrless}} \gamma \tag{7.8}$$

To objectively select γ, we apply the Neyman–Pearson criteria, which estimates a value for γ that is consistent with a prescribed false alarm probability, $Pr_{FA} = \alpha$. This probability Pr_{FA} measures the rate at which Eq. 7.8 would choose H_1 when H_0 is true

$$\max_{\mu \in \chi_0} Pr_{FA}[S_{GLRT}(X) > \gamma|\mu] = \alpha \tag{7.9}$$

The scalar α measures the probability of identifying a non-existing signal event and is conventionally called the false alarm on noise, or just the false alarm probability. The explicit form of $S_{GLRT}(X)$ that includes maximum likelihood estimates of the competing PDFs was derived by Blandford (1974) and is expressed as follows:

$$F(X,\boldsymbol{\theta}) = \frac{\frac{1}{M}\sum_{n=1}^{N}\left(\sum_{m=1}^{M} x_{n,m}(\boldsymbol{\theta})\right)^2}{\frac{1}{M-1}\sum_{n=1}^{N}\sum_{m=1}^{M}\left(x_{n,m}(\boldsymbol{\theta}) - \frac{1}{M}\sum_{m=1}^{M} x_{n,m}(\boldsymbol{\theta})\right)^2} \tag{7.10}$$

To form this ratio, we first beamform waveform data using time delays that are defined in $\boldsymbol{\theta}$ space, then maximize the coherence of the resultant sum. We then compute the energy of this resultant waveform stack, as well as the residual beam energy. When waveform sample data are Gaussian distributed, this ratio has a noncentral F-distribution at every sample and is, therefore $F(X,\boldsymbol{\theta})$ is called the F-detector statistic. This detection statistic and the decision rule (Eq. 7.8) often give higher than predicted false alarm rates (when applied to real data) because the assumption of the Gaussian distribution of the noise is not realistic. Microbaroms can spectrally overlap with SOIs leading to inflation of the F-detector statistic and an increased type I errors (false alarms).

7.4.2 Tests Based on the Time Difference of Arrival (TDOA)

We can derive test statistics from the times of arrival of a SOI to the array elements. Tests using TDOA are based on estimating the time difference of arrival $\Delta t_{k,l}$ of a signal to a sensor pair (k, l). $\Delta t_{k,l}$ can be estimated using cross-correlation as follows:

$$\widehat{\Delta t}_{k,m} = \underset{\varrho}{\operatorname{argmax}}\left(\sum_{i} x_{i,k}x_{i+\varrho,m}\right)T_s \tag{7.11}$$

Examples of tests using TDOA are the Progressive Multichannel Correlation (PMCC) detector (Cansi 1995) and the Maximum Cross-Correlation Method (MCCM) (Lee et al. 2013).

The PMCC algorithm (Cansi and Pichon 2008) is a detector widely used in infrasound research (Brachet et al. 2010) which tests the consistency of arrival times of signals across the array. The relationship $r_{kmp} = \Delta t_{k,m} + \Delta t_{m,p} + \Delta t_{p,k}$ defined for a sensor triad (k,m,p) is the main component of the PMCC algorithm. $r_{kmp} = 0$ if a signal is present (closure relationship) and $r_{kmp} \neq 0$ in the presence of physical-type noise. r_{kmp} is estimated for all possible triads in the array. The consistency (C_κ) for a subnetwork with κ elements ($\kappa \leq M$) is defined as follows:

$$C_\kappa = \sqrt{\frac{6}{(\kappa-1)(\kappa-2)} \sum_{1 \le k < m < p < \kappa} \hat{r}_{kmp}^2} \tag{7.12}$$

PMCC defines a threshold to trigger detection for this subnetwork. If a detection is triggered, additional elements of the array are progressively added to the initial subnetwork and a test is run to assert that the new element can be added to the detection. This detection schema generates independent elementary detections (or PMCC pixels) at different frequency bands and time windows (Brachet et al. 2010; Mialle et al. 2019). These pixels are linked based on similarity into a frequency–time detection or PMCC family. Note that the distribution of C_κ is not known and also that its magnitude does not depend on the noise levels. The MCCM (Lee et al. 2013) tests the average of the maximum value of the normalized cross-correlation (Neidell et al. 1969) between all sensor pairs against a threshold.

7.4.3 Enhancements to the Classical Approach

Several enhancements to the classical approach described above can be identified. First, the signal and noise models along with the detectors, are formulated only in terms of some measure of the coherence of waves across an array. Second, while the detectors account for physical-type noise, they do not properly account for operational-type noise because they assume gaussianity and stationarity. To mitigate these limitations, different strategies have been adopted to operationalize coherence-based signal detectors in order to account for operational-type noise. One strategy is to implement a post-detection categorization algorithm to screen signals of interest from operational-type noise on the basis of additional properties of the waveforms (e.g., frequency) or the detection itself (e.g., detection duration) (e.g., Brachet et al. 2010). Another approach is the use of adaptive strategies to adjust detector thresholds on the basis of the characterization of elements of the operational-type noise (e.g., Arrowsmith et al. 2009). For example, in the presence of correlated noise, such as microbaroms, the F-statistic is distributed as $cF_{2BT,2BT(M-1)}$, where B is the bandwidth, T is the time window, M the number of sensors, $c = 1 - MP_c/P_u$, and P_c/P_u is the ratio of correlated to uncorrelated noise power (Shumway et al. 1999). Arrowsmith et al. (2009) implemented an algorithm to scale the distribution $cF_{2BT,2BT(M-1)}$ with a $1/c$ value so the new distributions follow traditional $F_{2BT,2BT(M-1)}$. This procedure allows the estimation of a detector threshold to find detections with a specified statistical significance in the presence of coherent noise. Updating the c value regularly allows the detector to adapt to temporal changes in noise. Figure 7.4 shows an example of detections based on the dynamic F-Statistics (magenta area) for the case of infrasound signals from a bolide. The F-values average a number between 3.5 and 4. These high F-values are most likely related to microbaroms and would trigger events continuously with high

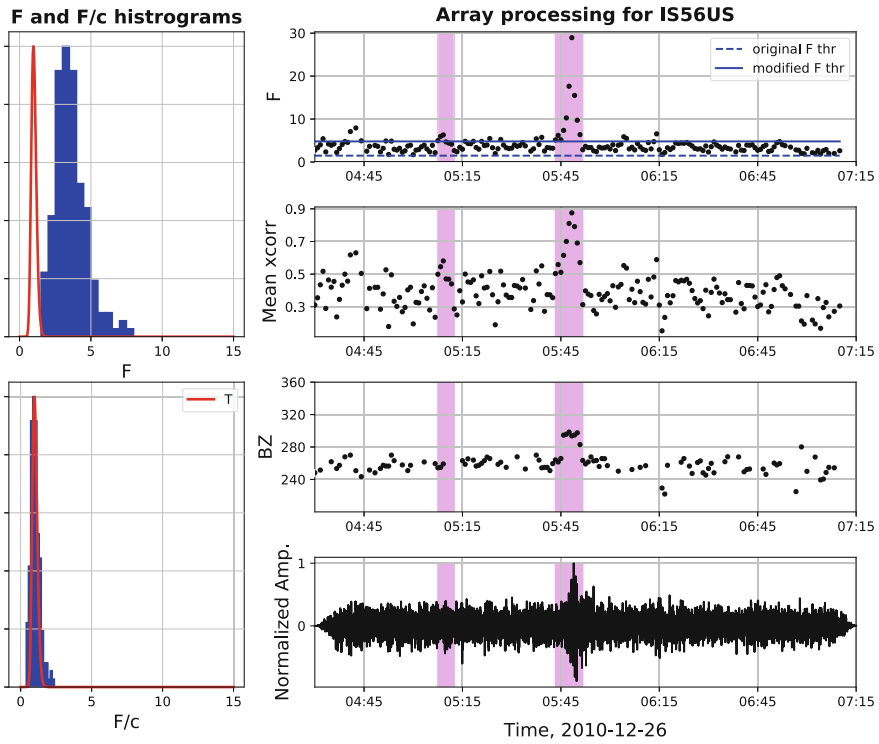

Fig. 7.4 Event detection based on Dynamic *F*-Statistics. The infrasound is from a bolide detected on December 26th, 2010 by IMS station I56US. On the left, the distribution of the theoretical F-statistics (red) and a histogram of the F-values for the array in blue (original, top, and modified, bottom). On the right, array processing results, F-values, mean cross-correlation, back azimuth, and detections (red horizontal lines)

confidence under the assumption of Gaussian noise only (the dashed blue line is the threshold for detections with false alarm probability lower than 0.01). The adaptive F-detector is used here to scale the distribution and allows for adapting to the background noise (operational-type noise) so only the transient event is detected (the solid blue line is the new threshold for detections with the same false alarm probability, 0.01). This schema has been applied to regional networks and shown to be successful at detecting transient events in the presence of interfering signals (Park et al. 2014, 2016).

An even more general approach, which is currently being explored (Arrowsmith et al. 2017), is to use a Kernel Density Estimator (KDE) (Scott 2008) to estimate the distribution of a given test statistic from a set of empirical observations of that statistic over a long-time window. Because the distribution of the test statistic is based on empirical data, it includes noise and possibly also signal, and is really a distribution of the ambient background of that test statistic. We test for $H_0 =$ ambient background signal, plus noise by taking some transform of the observed

data in a moving time window of duration T_S, which we shall denote as $S(\underline{x})$. The function, $S(\cdot)$, can be any transform that can be applied to data, resulting in a single numerical value (e.g., the semblance, correlation, etc.). If we denote a set of realizations of a specific transform in a time interval of duration T_{kde} as $(S_1, S_2, \ldots, S_n)$, then the KDE is

$$\hat{f}_h(S) = \frac{1}{Nh} \sum_{i=1}^{N} K\left(\frac{S - S_i}{h}\right), \tag{7.13}$$

where $K(\cdot)$ is the kernel (typically a Gaussian kernel) and $h > 0$ is a smoothing operator.

Figure 7.5 illustrates the concept behind a multivariate adaptive detector. Multiple test statistics are evaluated in different transform windows, denoted as T_S^i for the window corresponding to the i'th transform. A single KDE window, T_{kde}, is used to estimate the distribution of each test statistic, $\hat{f}_h(S)$.

We convert each KDE estimate to a p-value, where the p-value is defined as follows:

$$p = \int_{S_{\text{obs}}}^{\infty} \hat{f}_h(S) dS, \tag{7.14}$$

where S_{obs} is an observed, individual value of the transform.

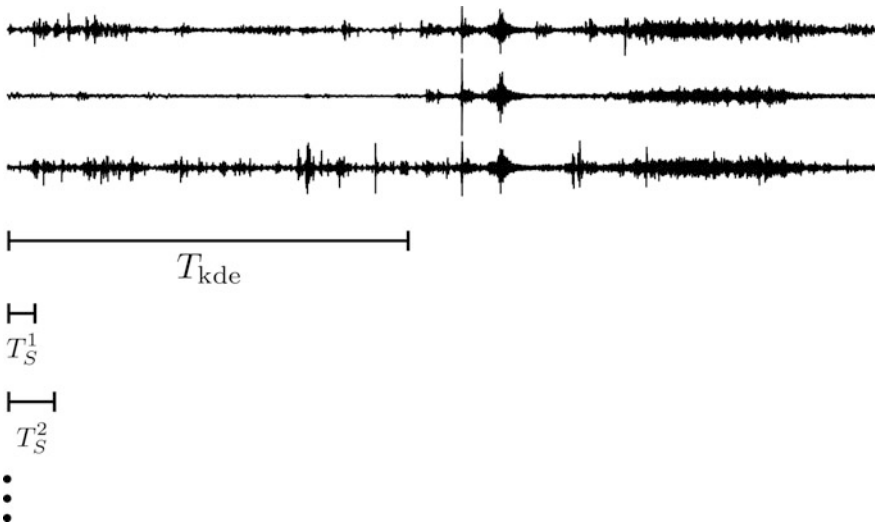

Fig. 7.5 A multivariate detector is based on the computation of multiple test statistics estimated in short time windows, with the distribution of each test statistic evaluated in a large time window of duration $\mathbf{T_{kde}}$

Given multiple transforms, which exploit different signal properties, we can combine the p-values associated with all k transforms using the Fisher's method

$$\chi^2 = -2 \sum_{i=1}^{k} \ln p_i \tag{7.15}$$

Geometrically, if different transforms are orthogonal, the use of this multivariate approach serves to increase the separation between signal and noise distributions (Fig. 7.6).

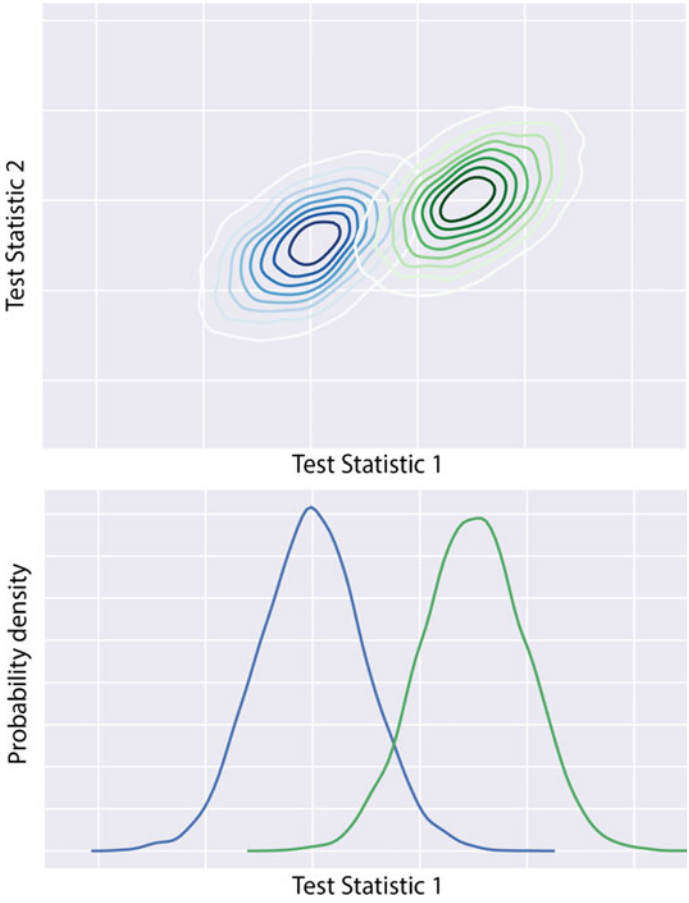

Fig. 7.6 Hypothesis testing is about defining a threshold to distinguish between signal and noise models. The threshold can be determined by considering models for both signal and noise, or by considering only the noise model. In practice, the noise model can be more easily determined from background data empirically, but having both signal and noise models is optimum. These techniques are commonly applied in one dimension (e.g., using coherence or an equivalent measure such as correlation, F-statistic, or semblance) but multivariate approach serves to increase the separation between signal and noise distributions

In our implementation, only the "ambient" distribution is defined in practice, and therefore each detection statistic is weighted by its ambient distribution in calculating a multivariate p-value. Because the ambient distribution is defined in a window of time T_{kde}, and we are not strictly required to consider the noise as physical or operational, there will always be p-values below some detection threshold and the use of at least one additional constraint is needed to prevent false alarms. Figure 7.7 illustrates the result of applying this method using two transforms, one based on the coherence of waves across a network, and a second based on the consistency of back azimuth. More details on this specific bivariate detector are provided in (Arrowsmith 2018).

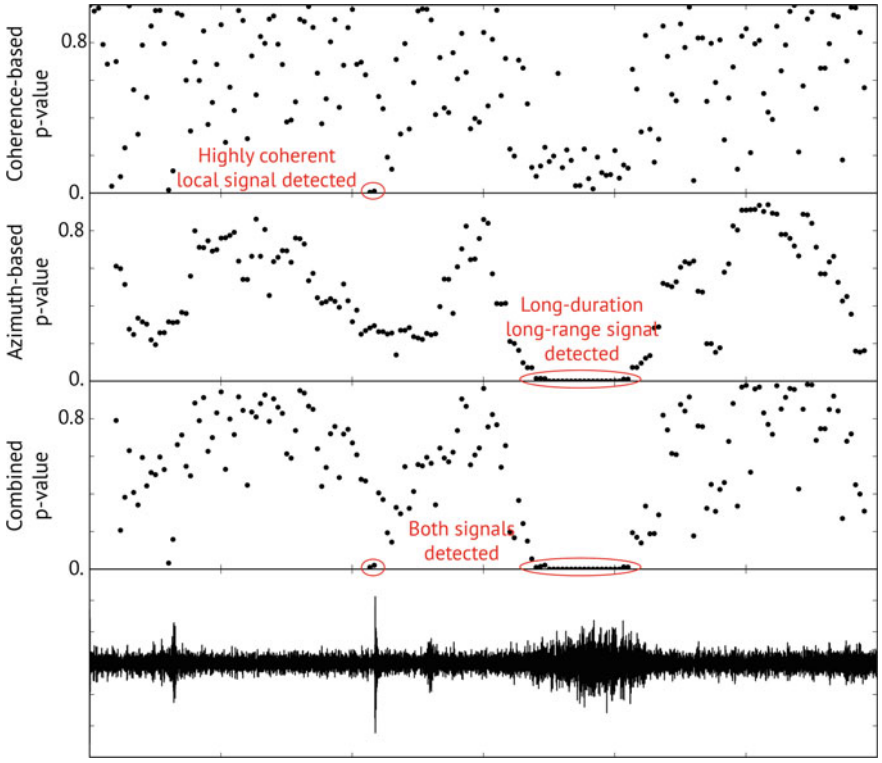

Fig. 7.7 Illustration of a multivariate detector based on coherence of waves across an array and the stability of the DOA applied to data from I56US on 02/24/2014. Each property is quantified in the form of p-values, enabling their combination via Fisher's method. While the individual detectors detect different signals, the combined approach detects both local and long-range (decorrelated) signals and provides additional information on these signal types

7.5 Parameter Estimation

After a SOI is detected the next step is to extract parameter information that can be used for characterizing the signal. In this section, we review some of most common techniques utilized for the extraction of waveform parameters. We are most interested in the extraction of the direction and speed of propagation of the SOI (estimated usually using the slowness vector) as the shape of the SOI can suffer significant changes (especially for signals propagating at global distances) and the estimation of the precise time of arrival can be difficult to estimate for very emergent signals. As we noted in the previous section, some detection test statistics can detect and extract parameter information simultaneously while others defer the parameter extraction for a second stage. For example, the F-detector will simultaneously detect and extract the slowness vector as part of its detection schema. PMCC (Cansi and Pichon 2008) calculates the TDOA to apply the consistency criteria for detection, afterwards, the already calculated TDOA are used for parameter estimation in a substage of the detection. MCCM, on the other hand, only uses the maximum cross-correlation and does not to need to compute the TDOA for its operation. Post-processing based on array geometry and estimation of the TDOA estimate the slowness vector in a subsequent processing stage. Note that for infrasound analysis, detection and parameter estimation can be performed simultaneously without much of computationally burden even for real-time applications (compare to processing for radar applications with high number of array elements and sampling rates) as the sampling rate of most system is not higher than a few 100 s of samples per second (sps), e.g., the sampling rate for the IMS stations is 20 sps, and infrasound arrays have only 4 and 15 elements. In this section, we will review the concepts behind common array processing techniques used for parameter estimation. See Olson and Szuberla (2009) for a review of the most common methods as they are applied to infrasound analysis.

The standard techniques to process array (multichannel) data can be divided into spectral-based and parametric methods (Krim and Viberg 1996). Parametric methods, such as Maximum Likelihood technique are considered to attain high-resolution but require initial information of the statistical characteristics of the data (noise and signal) and a search in a multidimensional parameter space that can be computationally complex. Spectral-based techniques such as the conventional beamforming (Bartlett), Capon (1969), or the Multiple Signal Classification, MUSIC (Schmidt 1986), require less initial information and are less complex to implement. These spectral techniques are based on constructing a spectrum-like function of a characteristic of the waveforms (e.g., beam power, coherence, and consistency), evaluating/mapping the function in the parameter space ($\boldsymbol{\theta}$), and finding the values of the parameters that maximize the spectrum.

The conventional beamforming (Bartlett) steers the covariance matrix of the observations (R) into the different elements of the 2D slowness space and looks for the values that maximize the beam power. The spectrum for the classical beamformer (Bartlett) is defined as follows:

$$\Lambda_B(\boldsymbol{\theta}) = a_{\boldsymbol{\theta}}^H R a_{\boldsymbol{\theta}}, \tag{7.16}$$

where $a_{\boldsymbol{\theta}} = a(\boldsymbol{\theta})$ is the steering vector and H is the complex conjugate operator. The Capon and MUSIC algorithms, usually called super-resolution methods, are subspace methods that rely on the decomposition of the covariance matrix R into eigenvalues (λ) and eigenvectors (v). Capon is also known as the Minimum Variance Distorsionless filter and calls for minimizing the power contributed for signals that are not in the steered direction. Capon usually shows higher performance than the classical beamformer. MUSIC can provide asymptotically unbiased estimates of the number and direction of arrival of signals, polarization, and waveforms and noise/interference strengths (Schmidt 1986). MUSIC uses a signal-noise model that is an extension of the model described by Eq. 7.2

$$x_m(t) = \sum_{j=1}^{K} s_m^j\left(t - \tau_m^j\right) + w_m(t), \tag{7.17}$$

where K is the total number of signals present in the waveform. This general signal-noise model has the advantage of potentially removing the unwanted coherent signals from operational-type noise. MUSIC relies on determining and separating eigenvalue populations for noise and signal, and thus determining the number of sources present in the observations. A spatial spectrum function is defined as follows:

$$\Lambda_{CM}(\boldsymbol{\theta}) = \left[\sum_{j=K+1}^{r} \frac{\left|a_{\boldsymbol{\theta}}^H v_j\right|^2}{\beta_j}\right]^{-1}, \tag{7.18}$$

where β_j is a coefficient, for all values of $j = 1, 2, \ldots, r$. For $K = 0$ and $\beta_j = \lambda_i$ (organized from the largest to the smallest) this expression is the Capon spectrum function (Shumway et al. 2008). If K is the number of signals and $\beta_j = 1$ this expression is the MUSIC spectrum function. MUSIC is sensitive to over-estimation of the number of sources). Other algorithms such as the Akaike Information Criteria (Akaike 1974), cumulative percentage of total variation (Jolliffe 2002) criteria, or the Bayesian Information Criterion (Wit et al. 2012) could be used for estimating the number of sources present in the data.

7.6 Evaluating Detectors

An ideal detector, i.e., the one that always identifies events without producing false detections, cannot be implemented in practice. Such an ideal detector requires an infinitely large threshold for declaration. Therefore, there is a trade-off between reducing missed event detections and reducing false ones. Too many false

detections can overwhelm the subsequent processing, i.e., association and location. However, depending on the objectives of the detection system, missing events of interest could have serious implications (e.g., the objective of the IMS is to monitor compliance for the CTBT). Thus, measuring the performance of a detector is important as that can help us tune the different parameters of the detector to reach specific requirements (Brown et al. 2000). A common methodology for assessing the performance of event detectors is the use of Receiver Operating Characteristics (ROC) curves (Arrowsmith et al. 2009; Runco Jr et al. 2014; Park et al. 2017).

A ROC curve of a detector is defined in two related ways. The first, conventional ROC curve is defined by the probability of accepting H_1 when H_1 is true (detection rate) as a function of the probability of rejecting H_0 when H_0 is true (false alarm). For the generation of a ROC for a specific detector, two large databases with available ground truth information are required. The first database consists of N_0 examples under H_0 and the other of N_1 examples under H_1. Let us consider a detection algorithm with a function test Λ. Working with the two databases we obtain two sequences of values. Figure 7.8 shows typical histograms of the two sequences. The more distant the two histograms, the easier it is to discriminate between two hypotheses. To further explore this, we compute the ROC curve as it follows: we compute the area of H_0 to the right of a given threshold value η, that gives the false alarm rate α_0. The area to the right to η of H1 gives the detection rate β_0. We report the point of coordinates (α_0, β_0) as a function of η to provide the ROC

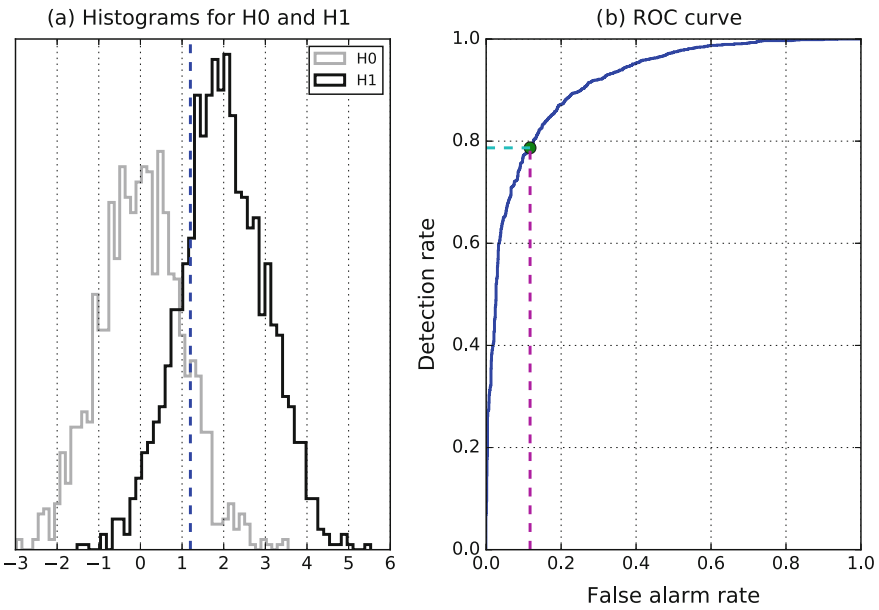

Fig. 7.8 Histograms for H_0 and H_1 and corresponding ROC curve

curve. A typical ROC curve shape is reported on panel b. The closer the curve is to the point of coordinates (0, 1), the more efficient the detector is.

The datasets required to construct a ROC can have multiple forms and it is important that the characteristics of the H_0 and H_1 resemble the type of noise and signals that the detector will operate on. A common approach for the construction of datasets for detector testing is the implantation of events (real or synthetic SOI-type waveforms) in real or synthetic background noise (Brown et al. 2000; Kohl et al. 2005; Charbit and Mialle 2015). The amplitudes of the embedded signals can be scaled to mimic the arrival of signals under different signals-to-noise ratios. To detect such scaled, embedded signals, it is practical to construct the second type of ROC curve that compares detection rates against some measure of the embedded signal SNR (Richards 2005). More explicitly, these ROC curves are defined by the probability of accepting H_1 when H_1 is true (detection rate) as a function of signal/waveform SNR, for a fixed probability of rejecting H_0 when H_0 is true (false alarm). The predictive capability of a detector is then evaluated by comparing these semi-empirical ROC curves against semi-theoretical ROC curves. The semi-empirical ROC curves are constructed in four stages by (1) scaling the amplitude of a reference infrasound waveform that records a known source, (2) embedding these data into records of real noise, (3) processing these data with a digital detector, and (4) counting true detections. In this case, the signal's original amplitude is scaled to a prescribed value selected from a scaled, "relative" SNR grid ΔSNR defined as

$$\Delta SNR = 20\log_{10}\left(\frac{A_S}{A_N}\right) - 20\log_{10}\left(\frac{A_{S,0}}{A_{N,0}}\right) \tag{7.19}$$

Equation 7.19 compares the root-mean-square amplitude A_S of the scaled waveform to root-mean-square amplitude A_N of the background noise, relative to the signal amplitude $A_{S,0}$ and noise amplitude $A_{N,0}$ of the original data. Scalar ΔSNR has units of decibels. The scaled waveform is then superimposed with recorded noise sampled from a selected time period and processed with the detector. Each processing window includes a detection threshold η that is consistent with a constant false alarm rate α_0, as computed from the F-distribution that is best parameterized for the data (see Eq. 7.8). Data statistics that exceed η, at the prescribed waveform embedding time, are counted as true detections. Similarly, missed detections are counted where the detector fails to register an event at a known waveform infusion time. This process is repeated over many noise records for each SNR value. Therefore, the detector processes waveforms over a grid of ΔSNR values, for each noise field record. Naturally, these records of the noise field also include significant signal clutter. Therefore, the scaled, embedded waveforms occasionally superimposed with other infrasound signals that not attributable to a known source (in contrast to H_0). This signal interference creates variability in the observed detector performance. Such events elevate false detection counts whenever waveforms localize outside the detector window.

Theoretical ROC curves are generated in parallel with the semi-empirical detection process. In this case, the statistical parameters of the *F*-distributed detection statistic (Eq. 7.10) that were estimated from the data are used to construct PDFs under the signal-present hypothesis. This PDF is further parameterized by a noncentrality parameter that depends on the effective degrees of freedom within the data and the signal amplitude, which is prescribed by the ΔSNR grid value. This parameter estimates that shape these *F*-distributions are updated in each processing window, as the noise is likely to be nonstationary over sufficiently long-time durations. The theoretical waveform detection probability β_0 is then the right-tail integral of these PDFs, taken from the concurrent threshold η to infinity. Last, this probability is scaled by the number of waveform counts to compare against semi-empirical counts.

Figure 7.9 compares empirical ROC curves against predicted ROC curves using this method. The infrasound source, in this case, is a 1.7 kg solid charge detonated at 1 m above the ground. The separated gray stair plots illustrate five days of detection counts using infused and scaled waveforms. The solid black curves show five days of predicted cumulative probability counts. In each case, predictions are made from PDFs that employ shaping parameters like $\hat{c}$, that were estimated directly from the data and updated hourly (see the discussion following Sect. 7.4.3

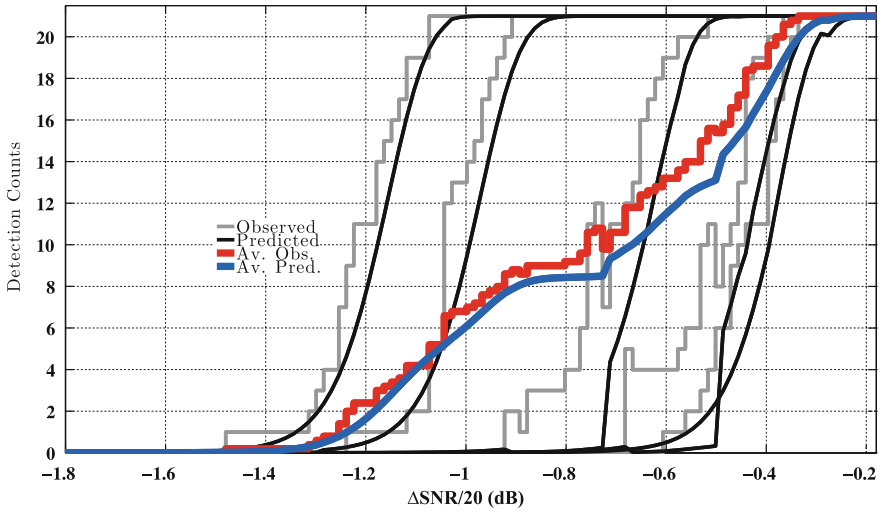

Fig. 7.9 Semi-empirical ROC curves computed over five distinct days of noise records (stair plots) shown with associated, theoretical ROC curves (smooth curves). Data include 4–20 Hz acoustic waveforms beamformed on a small aperture, four element array that records a 1.7 kg Composition-B solid charge detonated 1 m over dry ground. Detection counts are computed from an *F*-detector operating at a 10^{-3} constant false alarm rate and plotted against scaled ΔSNR (Eq. 7.19) to improve readability. Thickest curves show empirical (red stair plot) and theoretical (blue plot) averages over the five-day collection period. Each processing window includes 21 infused waveforms

for parametric definitions). The blue solid curves show the average of these predicted ROC curves; the red stair plot shows the average empirical ROC curves. The time-averaged predictions agree well with the observed detections. The slight outperformance by the observed ROC likely results from the multiple detection opportunities afforded the detector over each waveform segment that is not quantified by the predicted, noncentral *F*-distribution. Despite such slight performance discrepancies, such ROC curve comparisons do provide a quantitative comparison between the predicted versus observed performance of infrasound detectors in real noise environments. This second type of ROC curve is additionally useful for estimating threshold SNR values at which a detector provides a desired probability of detecting an infrasound waveform. In summary, there is a clear need for future research in this area to explore the performance of detectors under both physical- and operational-type noise and the construction of infrasound specific datasets that can be used for assessing the performance of different detection methodologies.

7.7 Conclusions

The detection of infrasonic signals generated by atmospheric explosions is very challenging given the wide range of characteristics of the signals and complexity of the acoustic wavefield (acoustic backgrounds). We have defined physical- and operational-type noise and show how this separation can improve signal and noise models, as well as detector evaluation efforts. We show that the classical mathematical description of signals and noise for detection is based only on physical-type noise and its characteristics, mainly de-correlation, but in practice, we have to use operational-type noise instead. We discussed strategies to compensate for the use of operational-type noise when the physical-type noise is assumed and described a methodology to combine different detectors based on different aspects of the waveform to improve detection. Combining different estimates of the waveform can significantly help in the detection process and more research in this direction may be required especially as we hope to reduce thresholds in order to detect smaller events. Last, direct comparison between semi-empirical and semi-theoretical Receiver Operating Characteristic (ROC) curves provide a quantitative method to assess the predictive capability of infrasound detectors.

References

Akaike H (1974) A new look at the statistical model identification. IEEE Trans Autom Control 19 (6):716–723

Anderson JF, Johnson JB, Arechiga RO, Thomas RJ (2014) Mapping thunder sources by inverting acoustic and electromagnetic observations. J Geophys Res: Atmos 119(23):13,287–213,304

Arrowsmith S (2018) False alarms and the IMS infrasound network: Towards a quantitative understanding of the factors influencing the creation of false events. Geophys J Int (Submitted)

Arrowsmith S, Euler G, Marcillo O, Blom P, Whitaker R, Randall G (2015) Development of a robust and automated infrasound event catalogue using the International Monitoring System. Geophys J Int 200(3):1411–1422

Arrowsmith S, Nippress A, Green D (2017) False alarms and the IMS infrasound network: towards a quantitative understanding of the factors influencing the creation of false events. Geophys J Int (In Prep)

Arrowsmith SJ, Taylor SR (2013) Multivariate acoustic detection of small explosions using Fisher's combined probability test. J Acoust Soc Am 133(3):El168–El173

Arrowsmith SJ, Whitaker R, Katz C, Hayward C (2009) The F-detector revisited: an improved strategy for signal detection at seismic and infrasound arrays. Bull Seismol Soc Am 99(1):449–453

Blandford RR (1974) Automatic event detector at Tonto-Forest seismic observatory. Geophysics 39(5):633–643

Bowman JR, Baker GE, Bahavar M (2005) Ambient infrasound noise. Geophys Res Lett 32(9):1–5

Brachet N, Brown D, Le Bras R, Cansi Y, Mialle P, Coyne J (2010) Monitoring the earth's atmosphere with the global IMS infrasound network. In: Infrasound monitoring for atmospheric studies, Springer, pp 77–118

Brown DJ, Katz CN, Wang J, Whitaker RW (2000) Tuning of automatic signal detection algorithms for IMS style infrasound arrays. In: 22nd Annual DoD/DoE seismic research symposium, New Orleans, LA, DTIC Document

Brown DJ, Whitaker R, Kennett BLN, Tarlowski C (2008) Automatic infrasonic signal detection using the Hough transform. J Geophys Res: Atmos 113(D17):D17105

Cansi Y (1995) An automatic seismic event processing for detection and location: the P.M.C.C. Method. Geophys Res Lett 22(9):1021–1024

Cansi Y, Pichon AL (2008) Infrasound event detection using the progressive multi-channel correlation algorithm. In: Havelock D, Kuwano S, Vorländer, M (eds) Handbook of signal processing in acoustics. Springer, New York, NY, pp 1425–1435

Capon J (1969) High-resolution frequency-wavenumber spectrum analysis. Proc IEEE 57 (8):1408–1418

Ceranna L, Le Pichon A, Green DN, Mialle P (2009) The Buncefield explosion: a benchmark for infrasound analysis across Central Europe. Geophys J Int 177(2):491–508

Ceranna L, Matoza R, Hupe P, Le Pichon A, Landès M (2019) Systematic array processing of a decade of global IMS infrasound data. In: Le Pichon A, Blanc E, Hauchecorne A (eds) Infrasound monitoring for atmospheric studies, 2nd edn. Springer, Dordrecht, pp 471–482

Charbit M (2017) Digital Signal Processing (DSP) with python programming. Wiley

Charbit MJ, Mialle P (2015) Application of the framework for detection software evaluation. In: CTBT: science and technology 2015 conference. Vienna, Austria, T3.3-P5

Christie DR, Campus P (2009) The IMS infrasound network: design and establishment of infrasound stations. In: Le Pichon A, Blanc E, Hauchecorne A (eds) Infrasound monitoring for atmospheric studies. Springer Netherlands, Dordrecht, pp 29–75

Dabrowa AL, Green DN, Rust AC, Phillips JC (2011) A global study of volcanic infrasound characteristics and the potential for long-range monitoring. Earth Planet Sci Lett 310(3–4):369–379

Dahlman O, Israelson H, Wagner H (1971) Ground motion and atmospheric pressure waves from nuclear explosions. Nat-Phys Sci 232(30):79–+

Don WL, Ewing M (1962) Atmospheric waves from nuclear explosions. J Geophys Res 67(5):1855–&

Donn WL, Ewing M (1962) Atmospheric waves from nuclear explosions. 2. The soviet test of 30 October 1961. J Atmos Sci 19(3):264–273

Donn WL, Naini B (1973) Sea wave origin of microbaroms and microseisms. J Geophys Res 78 (21):4482–4488

Drob DP, Picone JM, Garcés M (2003) Global morphology of infrasound propagation. J Geophys Res 108(D21):1–12

Fee D, Matoza RS (2013) An overview of volcano infrasound: from Hawaiian to Plinian, local to global. J Volcanol Geoth Res 249:123–139

Fee D, Waxler R, Assink J, Gitterman Y, Given J, Coyne J, Mialle P, Garces M, Drob D, Kleinert D, Hofstetter R, Grenard P (2013) Overview of the 2009 and 2011 Sayarim infrasound calibration experiments. J Geophys Res-Atmos 118(12):6122–6143

Fehr U (1967) Measurements of infrasound from artificial and natural sources. J Geophys Res 72(9):2403–2417

Green DN (2015) The spatial coherence structure of infrasonic waves: analysis of data from international monitoring system arrays. Geophys J Int 201(1):377–389

Green DN, Vergoz J, Gibson R, Le Pichon A, Ceranna L (2011) Infrasound radiated by the Gerdec and Chelopechene explosions: propagation along unexpected paths. Geophys J Int 185(2):890–910

Jolliffe IT (2002) Principal component analysis. Springer, New York

Kay SM (2013) Fundamentals of statistical signal processing: practical algorithm development. Pearson Education

Kohl B, Bennett TJ, Bondár I, Barker B, Nagy W, Reasoner C (2005) Development of a network data set for evaluating detection and network processing performance. In: 27th seismic research review: ground-based nuclear explosion monitoring technologies, Rancho Mirage, CA

Krim H, Viberg M (1996) Two decades of array signal processing research—the parametric approach. IEEE Signal Process Mag 13(4):67–94

Landès M, Ceranna L, Le Pichon A, Matoza RS (2012) Localization of microbarom sources using the IMS infrasound network. J Geophys Res 117(D6):D06102

Le Pichon A, Ceranna L, Pilger C, Mialle P, Brown D, Herry P, Brachet N (2013) The 2013 Russian fireball largest ever detected by CTBTO infrasound sensors. Geophys Res Lett 40(14):3732–3737

Lee DC, Olson JV, Szuberla CAL (2013) Computationally robust and noise resistant numerical detector for the detection of atmospheric infrasound. J Acoust Soc Am 134(1):862–868

Mack H, Flinn EA (1971) Analysis of the spatial coherence of short-period acoustic-gravity waves in the atmosphere. Geophys J Int 26(1–4):255–269

Marcillo O, Arrowsmith S, Blom P, Jones K (2015) On infrasound generated by wind farms and its propagation in low-altitude tropospheric waveguides. J Geophys Res: Atmos 120(19):9855–9868

Marty J (2019) The IMS infrasound network: current status and technological developments. In: Le Pichon A, Blanc E, Hauchecorne A (eds) Infrasound monitoring for atmospheric studies, 2nd edn. Springer, Dordrecht, pp 3–62

Matoza R, Fee D, Green D, Mialle P (2019) Volcano infrasound and the international monitoring system. In: Le Pichon A, Blanc E, Hauchecorne A (eds) Infrasound monitoring for atmospheric studies, 2nd edn. Springer, Dordrecht, pp 1023–1077

Mialle P, Brown D, Arora N, colleagues from IDC (2019) Advances in operational processing at the international data centre. In: Le Pichon A, Blanc E, Hauchecorne A (eds) Infrasound monitoring for atmospheric studies, 2nd edn. Springer, Dordrecht, pp 209–248

Morgan S, Raspet R (1992) Investigation of the mechanisms of low-frequency wind noise generation outdoors. J Acoust Soc Am 92(2):1180–1183

Neidell NS, Taner MT, Koehler F (1969) Semblance and other coherency measures for multichannel data. Geophysics 34(6):1012–&

Nouvellet A, Charbit M, Le Pichon A, Roueff F, Che IY (2013) Coherence parameters estimation from noisy observations. In: Infrasound technology workshop, Vienna

Olson JV, Szuberla CAL (2009) Processing infrasonic array data. In: Handbook of signal processing in acoustics, pp 1487–1496

Park J, Arrowsmith SJ, Hayward C, Stump BW, Blom P (2014) Automatic infrasound detection and location of sources in the western United States. J Geophys Res: Atmos 119(13):7773–7798

Park J, Hayward CT, Zeiler CP, Arrowsmith SJ, Stump BW (2017) Assessment of infrasound detectors based on analyst review, environmental effects, and detection characteristics. Bull Seismol Soc Am 107(2):674–690

Park J, Stump BW, Hayward C, Arrowsmith SJ, Che IY, Drob DP (2016) Detection of regional infrasound signals using array data: testing, tuning, and physical interpretation. J Acoust Soc Am 140(1):239–259

Pilger C, Ceranna L (2017) The influence of periodic wind turbine noise on infrasound array measurements. J Sound Vib 388:188–200

Richards MA (2005) Fundamentals of radar signal processing. McGraw-Hill

Runco AM Jr, Louthain JA, Clauter DA (2014) Optimizing the PMCC algorithm for infrasound and seismic nuclear treaty monitoring. Open J Acoust 4(04):204

Schmidt RO (1986) Multiple emitter location and signal parameter-estimation. IEEE Trans Antennas Propag 34(3):276–280

Scott, DW (2008) Kernel density estimators. In: Multivariate density estimation. Wiley, pp 125–193

Silber E, Brown P (2019) Infrasound monitoring as a tool to characterize impacting near-earth objects (NEOs). In: Le Pichon A, Blanc E, Hauchecorne A (eds) Infrasound monitoring for atmospheric studies, 2nd edn. Springer, Dordrecht, pp 939–986

Shumway RH, Kim S-E, Blandfor R (1999) Nonlinear estimation for time series observed on arrays. In: Ghosh S (ed) Asymptotics, nonparametrics, and time series. CRC Press, p 227

Shumway RH, Smart E, Clauter DA (2008) Mixed signal processing for regional and teleseismic arrays. Bull Seismol Soc Am 98(1):36–51

Stopa JE, Cheung KF, GarcÈs MA, Fee D (2011) Source of microbaroms from tropical cyclone waves. Geophys Res Lett 38(5):L05602

Taylor SR, Arrowsmith SJ, Anderson DN (2013) Development of a matched filter detector for acoustic signals at local distances from small explosions. J Acoust Soc Am 134(1):El84–El90

Walker KT (2012) Evaluating the opposing wave interaction hypothesis for the generation of microbaroms in the eastern North Pacific. J Geophys Res-Ocean 117

Wit E, van den Heuvel E, Romeijn JW (2012) All models are wrong…': an introduction to model uncertainty. Stat Neerl 66(3):217–236

Chapter 8
Explosion Source Models

Milton Garces

Abstract Explosive detonations produce shocked transients with highly nonlinear pressure signatures in the near field. This chapter presents the properties and defining characteristics of a suite of theoretical source pressure functions representative of detonations and deflagrations, and constructs criteria for defining reference blast pulses. Both the primary positive overpressure and the negative underpressure phases contribute to the temporal and spectral features of a blast pulse.

8.1 "All Models Are Wrong, but Some Are Useful". G. Box

This chapter compares explosion models in the context of traditional scaling laws and provides relations for validating propagation models and signal processing algorithms. Although the explosion pulses in this chapter are defined by very specific blasts pulse features and parameters available in the open literature, the principles and methods should be transportable to the characterization of other types of transients.

Pressure records near controlled explosive detonations have shocked onsets and predictable waveforms. Yet, the same blast signature recorded at far distances can have emergent amplitude onsets and complicated codas induced by interactions with boundaries and propagation through the atmosphere. This work concentrates on characterizing explosion waveform parameters before far-field distortion sets in. Prior studies have concentrated on the destructive initial phase of a shocked blast pulse, which is roughly defined by its time duration and peak overpressure. An explosive's peak overpressure is a measure of its brisance or shattering ability (e.g., Smith and Hetherington 1994), and the product of the overpressure and duration is

M. Garces (✉)
Infrasound Laboratory, HIGP, SOEST, University of Hawaii at Manoa,
73-4460 Queen Kaahumanu Hwy. #119, Kailua-Kona, HI 96740, USA
e-mail: milton@isla.hawaii.edu

A. Le Pichon et al. (eds.), *Infrasound Monitoring for Atmospheric Studies*,
https://doi.org/10.1007/978-3-319-75140-5_8

proportional to its momentum. However, the often neglected negative phase of the pressure signature contains useful information for explosion characterization and identification beyond the blast zone.

The literature on blast parameters spans over half a century and is riddled with inconsistencies in units and measurement standards. Baker (1973, Chap. 1) reviews some of the blast pulse representations used during the Cold War of the late twentieth century. He recommends that "one should only use the simplest form commensurate with the accuracy desired for any given analysis" in the selection of a source pressure function, and functional representations and metrics were adequately matched to the analog field measurements of the time. The turn of the twenty-first century brought a resurgence of interest in source physics (e.g., Koper et al. 2002; Bonner et al. 2013). Modern field equipment and computing methods (e.g., Kim and Rodgers 2017), coupled with the rapidly growing ubiquity of sensor systems (e.g., Stone 2016), will permit improvements in the characterization of blast parameters and an assessment of their accuracy. This chapter reframes and extends traditional blast models and scaling relations in the context of recent and ongoing source physics studies. Selected data are presented in this work to illustrate the established approach to blast scaling and how it could be further standardized.

Observed blast signatures for the June 1993 Minor Uncle (MU) and June 1991 Distant Image (DI) surface detonations of ~2 long (imperial) tons of high explosive are shown in Figs. 8.1 and 8.2, respectively. The pulses are scaled in amplitude by their peak overpressure and in time by the duration of the positive pulse. Figure 8.1 corresponds to actual measurement ranges less than 10 km, and Fig. 8.2 to ranges greater than 30 km. Recording station distances are generally scaled by the cube root of site-corrected explosion yields for comparison amongst different data sets. Equivalent site-corrected yield-scaled ranges relative to 1 kg TNT in free air are shown in the figure legends. The positive pressure phase is traditionally characterized by its peak overpressure p_p and its duration t_p, defined as the time from the shock onset to the first zero crossing of the gauge pressure. The integral of the pressure over the positive phase duration, referred to as the positive impulse, is also often reported in the literature. In order to draw attention to the pulse shape, Figs. 8.1 and 8.2 scale the gauge pressure and time by the peak overpressure and positive pulse duration, respectively. Although the negative pressure phase is not as well documented as the positive phase (e.g., Teich and Gebbeken 2010), it may also be roughly characterized by its minimum pressure, or peak underpressure p_n, and the duration t_n from the first to the second zero crossing of the pressure. Please refer to Appendices 4 and 5 for more details on the conversion from long tons at the surface to metric tonnes (10^3 kg) in free air.

As the distance from the origin increases, blast pulses generally transition from clear shocked overpressures to emergent onsets and complicated codas. A predictable nonlinear shocked front generally persists up to scaled distances of ~100 m/kg$^{1/3}$, beyond which atmospheric effects can prevail and distort the waveform (e.g., Kim and Rodgers 2016, 2017). This signal distortion and

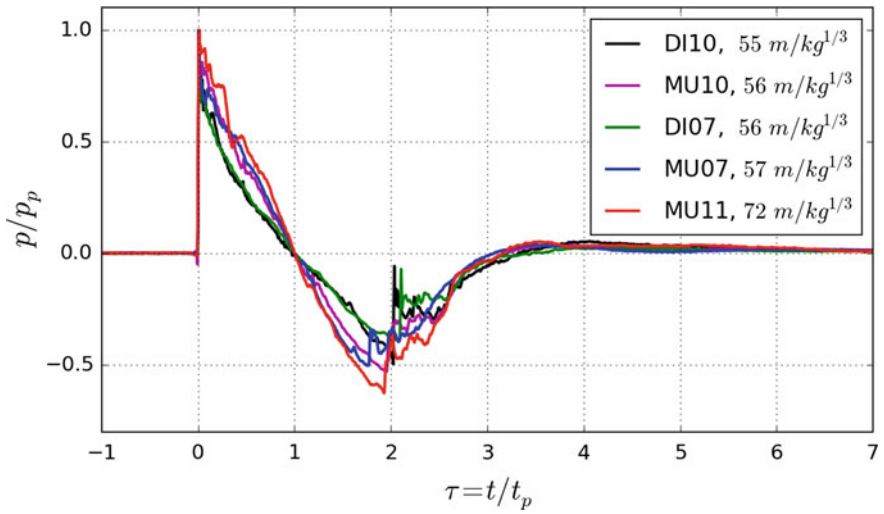

Fig. 8.1 Representative Minor Uncle (MU) and Distant Image (DI) stations with scaled shocked blast pulses for yield-scaled ranges less than 100 m/kg$^{1/3}$. The station identification is after the event code. Note: secondary pulses in the negative pressure phase

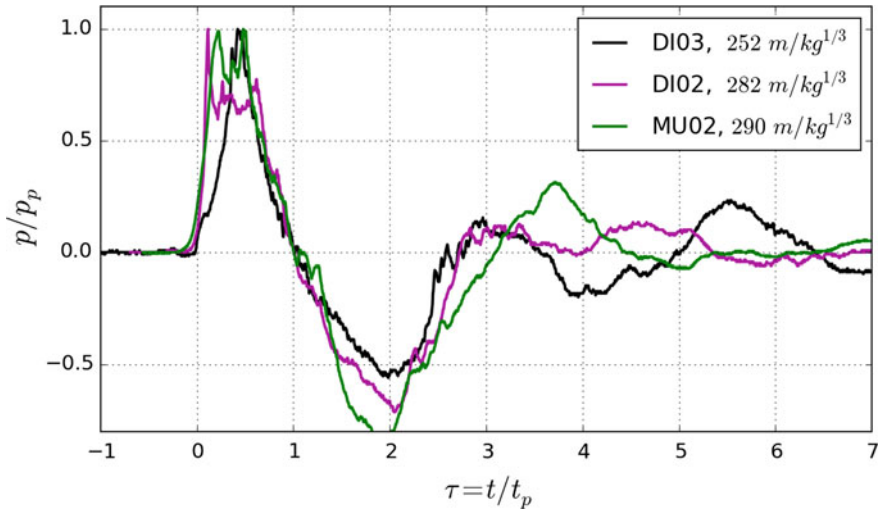

Fig. 8.2 Representative Minor Uncle (MU) and Distant Image (DI) stations with more emergent scaled blast pulses for yield-scaled ranges greater than 200 m/kg$^{1/3}$. The station identification is after the event code

degradation with increasing range can diminish the ability to recognize high explosive (HE) detonations from low explosive (LE) deflagrations.

The negative pulse duration can be lengthened by noncompressible effects (Cole 1948), ground hydrodynamics, as well as by merging secondary gas bubble oscillations (e.g., Rigby et al. 2014). Baker (1973) discussed further complications that may be induced by nuclear radiation (pp. 8–9). It is likely that observed positive and negative pulse durations differ from theoretical predictions that assume no boundary or atmospheric effects and only model the primary gas bubble oscillation. The secondary and tertiary pulses seen in the negative phase of Fig. 8.1 (referred to as pete and repete in Chap. 1 of Baker 1973) are common for HE (e.g., Gitterman and Hofstetter 2012) and possible for NE (Needham 2010, Sect. 4.4), although they are not well observed or documented for near-surface nuclear explosions. Gitterman (2013) proposes using the presence or absence of secondary shocks as a discriminant for single-charge nuclear versus HE *surface* blasts and to help identify HE type and yield.

Single-charge low explosives (LE) deflagrations are expected to have a slower rise time at the same scaled ranges where HE's would have shocked onsets, so they can be easier to identify in the near field. Unfortunately, pressure–time histories from low explosives and internal blasts can vary substantially, as they are generally less regulated, more diverse, and do not explode as fast (and cleanly) as high explosives (e.g., Smith and Hetherington 1994). Dispersion, attenuation, and acoustic propagation effects can make it difficult to discriminate between nuclear explosive (NE), HE, and LE blasts at distances much greater than 200 m/kg$^{1/3}$ (Fig. 8.2).

This chapter develops a suite of scalable transient functions that may be representative of detonations and deflagrations beyond the highly nonlinear finite amplitude range in the near field (<20 m/kg$^{1/3}$) but before the multiply reflected and refracted far-field range ($\gg$200 m/kg$^{1/3}$). It is assumed that the explosion occurs in a perfectly isotropic and isothermal unbounded medium. Boundary effects and secondary gas bubble oscillations observed on real high explosive detonations (e.g., Brode 1959; Barker 1973; Gitterman and Hofstetter 2012) are not included in the functional representations.

The primary criteria for the selection of representative source time functions are a reasonable similarity with observed blast waveforms that have a characteristic positive phase overpressure p_p and timescale t_p, as well as the ability to support a balanced impulse. Section 2.2 of Cole (1948) and Sect. 5.6 of Bethe et al. (1958) discuss how conservation of mass and momentum require that the total impulse per unit area I of a blast pulse $p(t)$ integrated over its lifetime should vanish,

$$I = \int_0^\infty p(t)dt = 0. \tag{8.1}$$

The balanced impulse condition asserts that that atmosphere returns to its ambient pressure and the air parcel velocity returns to rest after the passing of the pulse. This constraint may be of particular importance in fluid dynamic propagation codes that require momentum balance. In practice, the afterflow induced by

noncompressible flow induced by the shock may take a long time to converge near the source due to boundary effects and the influence of secondary pulses (e.g., Baker 1973).

To frame the fearful symmetry of a blast is no small feat, and the idealized functional representations of explosion pulses presented in this chapter are works of fiction. In the spirit of Box (1976), this chapter seeks an economical description of blast pulses in terms of a concise set of standardized scaled parameters. As mentioned in the opening paragraph, it is hoped that these simple pulses may be useful as reference signatures or synthetics for propagation model initialization, the design of detection and feature extraction algorithms, uncertainty quantification, and transfer function evaluations. At the very least, they can provide exact test functions for scientific computing (Wilson et al. 2014).

8.2 Explosion Source Time Functions

Canonical source time functions for explosions can be expressed by a combination of polynomials and exponentials. Four candidate exponentially decaying functional forms are proposed in order of increasing complexity,

$$f_{\mathrm{F46HE}} = (1-\tau)e^{-\alpha\tau}, \tag{8.2}$$

$$f_{B55LE} = \tau(1-\tau)e^{-2\alpha\tau}, \tag{8.3}$$

$$f_{G95HE} = (1-\tau)(\tau_0-\tau)e^{-\alpha\left[\frac{\tau_0+1}{2\tau_0}\right]\tau}, \tag{8.4}$$

$$f_{G95LE} = \tau(1-\tau)(\tau_0-\tau)e^{-\alpha\left[\frac{\tau_0+1}{\tau_0}\right]\tau}, \tag{8.5}$$

where all functions are to be evaluated at a scaled time $\tau \geq 0$ and are zero for $\tau < 0$. The pulses have a clearly defined start time with a discontinuous derivative at the onset scaled time $\tau = 0$, but are smooth and have continuous derivatives and integrals for $\tau > 0$. Since all models vanish at the first zero crossing $\tau = 1$, it is possible to mix and match the functions at the first crossing to construct hybrid waveforms. This can introduce a discontinuity in the derivatives at the splice point, resulting in unsightly yet insightful synthetic pulses. Although it is possible to increase the degree of the polynomial (Garcés 1995), the functions under consideration will provide sufficient diversity and complexity for this exposition.

These four functional forms are mathematically concise and convenient but not practical. Additional criteria need to be adopted to match the metrics that are used for geophysical pulse modeling and interpretation. Constraints specific to blast physics are applied to provide more familiar but less concise variations of the canonical expressions for practical infrasound applications.

A blast pressure record p_i may be expressed in terms of an amplitude-scaled canonical f_i at a scaled reference time τ_{ref},

$$p_i(\tau) = \frac{p(\tau_{ref})}{f_i(\tau_{ref})} f_i(\tau) \tag{8.6}$$

with scaled time τ,

$$\tau = \frac{t}{t_p} \tag{8.7}$$

where t is time and t_p is the positive pulse duration. The impulse balance requirement of Eq. 8.1 is satisfied by setting the exponential decay parameter α to unity (Appendix 1). The exponential decay is also referred to as the waveform parameter in Kinney and Graham (1985). Although α is mathematically unconstrained, impractical overdampened and underdampened pulses result when α deviates substantially from its balanced value of unity. Defining the maximum peak pressure as p_p, and setting $\alpha = 1$, the amplitude-corrected impulse-balanced exponentially decaying canonical source pressure functions can be expressed as

$$p_{\text{F46HE}}(t) = p_p \left(1 - \frac{t}{t_p}\right) e^{-\frac{t}{t_p}}, \quad \tau_{ref} = 0 \tag{8.8}$$

$$p_{\text{B55LE}}(t) = p_p \left(\frac{2e^{2-\sqrt{2}}}{\sqrt{2}-1}\right) \frac{t}{t_p} \left(1 - \frac{t}{t_p}\right) e^{-2\frac{t}{t_p}}, \quad \tau_{ref} = 1 - \frac{\sqrt{2}}{2} \tag{8.9}$$

$$p_{\text{G95HE}}(t) = p_p \left(\frac{2-\sqrt{2}}{2+\sqrt{2}}\right) \left(1 - \frac{t}{t_p}\right) \left(\frac{2+\sqrt{2}}{2-\sqrt{2}} - \frac{t}{t_p}\right) e^{-\left(2-\sqrt{2}\right)\frac{t}{t_p}}, \quad \tau_{ref} = 0 \tag{8.10}$$

$$p_{\text{G95LE}}(t) \simeq p_p \, 2 \frac{t}{t_p} \left(1 - \frac{t}{t_p}\right) \left(\frac{3+\sqrt{3}}{3-\sqrt{3}} - \frac{t}{t_p}\right) e^{-\left(3-\sqrt{3}\right)\frac{t}{t_p}}, \quad \tau_{ref} \simeq 0.328. \tag{8.11}$$

In these forms, F46HE in Eq. 8.8 can be recognized as the Friedlander (1946) detonation pulse associated with high explosive (HE) detonations. The B55LE pulse may be representative of low explosive (LE) deflagrations, and can be recognized as a variation of the Brode (1955, 1956, Eq. 76) pulse also used by Bonner et al. (2013) and others to fit the negative pulse duration. The representative detonation G95HE and deflagration G95LE pulses were developed by Garcés (1995), and have been modified from that work so as to match the positive pulse duration as the reference time metric.

Two source pressure functions consisting only of polynomials are introduced. These two expressions introduce a different family of solutions, are representative

of HE blasts, have a clear shocked onset time, and are impulse-balanced. The first is a balanced version of the Reed (1977) pulse

$$p_{\mathrm{R77HE}}(t) = p_p\left(1-\frac{t}{t_p}\right)\left[1-\frac{7}{25}\frac{t}{t_p}\right]\left[1-\left(\frac{7}{25}\frac{t}{t_p}\right)^2\right], \quad 0\le\tau\le\frac{25}{7} \tag{8.12}$$

and the second is a hybrid combination of the Granström (1956) negative pulse with a triangular positive impulse, where

$$p_{\mathrm{G17HE}}(t) = p_p\left(1-\frac{t}{t_p}\right), \quad 0\le\tau\le 1,$$

$$p_{\mathrm{G17HE}}(t) = p_p\frac{1}{6}\left(1-\frac{t}{t_p}\right)\left(1+\sqrt{6}-\frac{t}{t_p}\right)^2, \quad 1<\tau\le 1+\sqrt{6}. \tag{8.13}$$

The functions are zero outside of the specified domains and have continuous first derivatives for $\tau > 0$. By definition, the total impulse vanishes for all the balanced pulses.

Figure 8.3 shows the normalized impulse-balanced shocked detonation pulses at scaled ranges between 25 and 100 m/kg$^{1/3}$. A characteristic Minor Uncle shocked blast pulse with the same pressure and time scaling is shown for comparison. It is worth noting that the peak overpressure may be challenging to capture in the field, and the underpressure may be modified by secondary and tertiary pulses, resulting

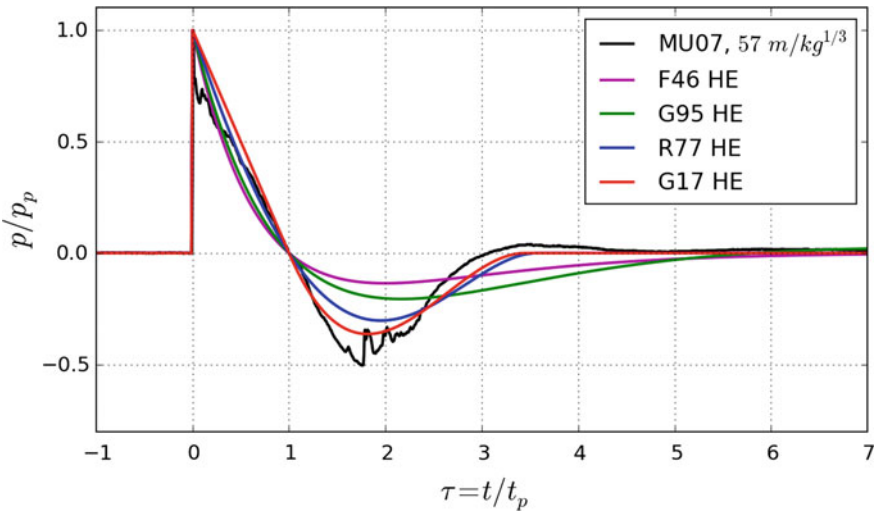

Fig. 8.3 Amplitude-normalized impulse-balanced canonical functions for the F46HE Freidlander (1946), G95HE Garcés (1995), R71HE Reed (1977), and the hybrid G17HE detonation pulses. A representative Minor Uncle shocked waveform is shown for comparison

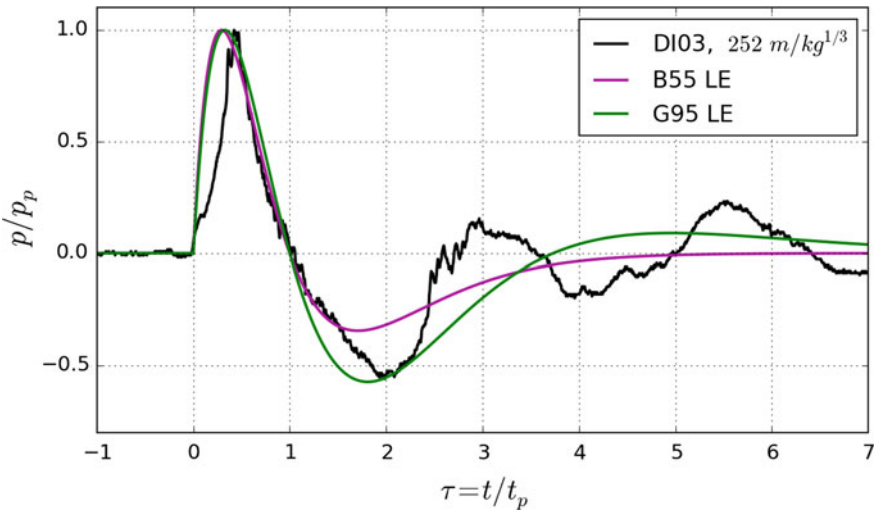

Fig. 8.4 Amplitude-normalized impulse-balanced canonical functions for the B55 and G95 deflagration pulses. A representative far-field Distant Image waveform is shown for comparison

in variability in the measured positive and negative phase ratios. Figure 8.4 shows the normalized impulse-balanced unshocked canonicals that may be associated with deflagrations or other types of slower internal blasts (e.g., Kinney and Graham 1985). The far-field signature for a dispersed emergent blast from Distant Image observed at a range beyond 200 m/kg$^{1/3}$ is also shown to illustrate how the deflagration canonicals may not match the details of observed far-field explosion signatures. Similarly, the shocked blast waveform templates that will be dissected in the next sections are not expected to consistently work well beyond yield-scaled ranges much greater than 200 m/kg$^{1/3}$, although under favorable atmospheric and topographic conditions they may be applicable in the far field.

Each candidate explosion pulse is presented separately in Sect. 8.3, which also introduces triangular and hybrid pulses. A reader pressed for time may wish to jump to the summary in Sect. 8.4.

8.3 Explosion Pulses

This work aims to construct a self-consistent mathematical and computational framework with a tolerable level of congruence with selected scaling relationships that have endured the test of time. The tabulated blast parameters of Kinney and Graham (1985), hereafter referred to as KG85, are used as primary references as they consistently use metric units and are routinely used in blast studies (e.g., Koper et al. 2002; Kim and Rodgers 2016). The KG85 tables provide a scaled gauge pressure,

$$\bar{p}(t) = \frac{p_a(t) - \langle p_a \rangle}{P}, \tag{8.14}$$

where $p_a(t)$ is the instantaneous pressure, $\langle p_a \rangle$ is the averaged ambient pressure within a sensing system's passband, and P is the ambient barometric pressure. Please refer to Appendix 4 for more details. The upcoming discussions refer to $p(t)$ as the gauge pressure

$$p(t) = p_a(t) - \langle p_a \rangle \tag{8.15}$$

and would correspond to a demeaned, detrended waveform recorded with a differential pressure sensor. The positive phase gauge overpressure p_p and duration t_p are the traditional defining blast pulse parameters.

The KG85 equations predict a peak gauge overpressure of 840 Pa for a 1 kg spherical TNT charge of HE detonated in free air and observed at a range of 100 m. Using a nominal sea level pressure of 101.325 kPa, the scaled gauge pressure $\bar{p}_p$ is 0.00829, which is rounded to 0.008 in Table XI Part A of KG85. The gauge pressure is ~0.8% of the ambient barometric pressure. The tabulated Mach number is 1.003, or 0.3% away from unity. At a scaled range of 100 m/kg$^{1/3}$, the blast pulse can be characterized as a weak shock moving at near acoustic speeds. The corresponding tabulated positive phase pulse duration t_p is 0.0042 s, and is shown as a stable near-constant value until the end of the KG85 tables for HE. Actual times and ranges must be rescaled by the cubed root of the yield. In principle, the 1 kg HE at 100 m specification is equivalent to 1 tonne of TNT at 1 km, or 1 ktonne TNT at 10 km (Table 8.1). However, blast parameters for large kt-yield ANFO explosions may follow the NE tables closer than the HE (Appendix 5). A 1 ktonne of HE blast should be equivalent to 2 ktonnes of NE (Appendix 4), with an equivalent scaled distance of 8 km NE. Although 2 ktonnes NE at 8000 m is just outside of the KG85 tables, the equations permit extrapolation (Appendix 4). As shown in Table 8.1, the extrapolated KG85 NE positive phase has a longer duration than for HE, although the predicted overpressures match well. The equivalent KG85 ranges, scaled pressures, and durations are summarized in Table 8.1 for 1 kg TNT at 100 m. As discussed in Appendix 5, care should be taken when using the tables for different high explosives with different burn rates (R. Reinke, personal communication).

Table 8.1 KG85 equivalent ranges for 1 kg HE (TNT) and 2 kg NE (~1 kg HE)

Yield HE (TNT)	HE Scaled Distance	KG85HE $\bar{p}_p$	KG85HE t_p (s)	Yield NE	NE Scaled Distance	KG85NE $\bar{p}_p$	KG85NE t_p (s)
1 kg	100 m	0.008	0.0042	2 kg	80 m	0.008	0.0067
1 tonne	1 km	0.008	0.042	2 tonne	800 m	0.008	0.067
1 ktonne	10 km	0.008	0.42	2 ktonne	8 km	0.008	0.67
1 Mtonne	100 km	0.008	4.2	2 Mtonne	80 km	0.008	6.7

Ongoing studies should provide improvements over the KG85 predictions (e.g., Kim and Rodgers 2016, 2017).

This section discusses each pulse in detail. The Friedlander pulse description should be read with care as it introduces key definitions and concepts that will be used repeatedly throughout this chapter. In the Friedlander exposition, I rescale the negative phase pulse parameters to express the underpressure, the underpressure drop time, the pulse lifetime, the positive impulse, the impulse symmetry, the spectral pseudo period, and the pulse energy in terms of the positive phase overpressure p_p and time duration t_p. These pulse parameters conveniently inherit the correct cubed root yield scaling when they are expressed relative to t_p.

8.3.1 Friedlander Pulse

Friedlander (1946) represented a shocked pressure pulse a short distance from a blast as

$$p_F(t) = p_p\left(1 - \frac{t}{t_p}\right)e^{-\frac{t}{t_p}}, \quad t \geq 0, \tag{8.16}$$

where t_p is the first zero crossing, or positive pulse duration, and p_p is the peak overpressure, and p_F is used as shorthand for p_{F46HE}. The total impulse of the Friedlander pulse is zero. This is the simplest and most mathematically tractable explosion pulse, and to first order it fits the observed blast positive pulse shape (e.g., KG85).

Although real detonation pulses have a finite rise time t_{rise} (the time to reach to peak overpressure p_p), it is very small relative to the positive pulse duration and it is treated as zero. In contrast to the rise time, the time to reach the minimum pressure (referred to as the peak underpressure p_n) is more substantial. The pressure minimum p_n occurs at a time t_{min}

$$\frac{t_{min}}{t_p} = 2, \tag{8.17}$$

where

$$p_n = -p_p e^{-2} \tag{8.18}$$

or

$$\left|\frac{p_p}{p_n}\right|_F = e^2 \approx 7.4 \tag{8.19}$$

The ratio of the peak positive to the peak negative gauge pressure is a key quantity to track for all blast pulses. The scaled drop time τ_d is here defined relative to the positive pulse duration as

$$\tau_{drop} \equiv \frac{t_{min} - t_p}{t_p} = \frac{t_{min}}{t_p} - 1 \tag{8.20}$$

and is a measure of the rate of descent of the negative phase. For the Friedlander pulse,

$$\tau_{drop\,F} = 1 \tag{8.21}$$

so the Friedlander drop time is as long as the positive phase duration. The negative phase duration t_n for gradually decaying pulses can be estimated from its approach to the second zero crossing

$$p\left(\frac{t_p + t_n}{t_p}\right)/p_n \cong e^{-1}. \tag{8.22}$$

Thus, the pulse lifetime τ_e can be defined as the e-folding depth of the peak underpressure p_n,

$$\tau_e \equiv \frac{t_e}{t_p} = \frac{t_p + t_n}{t_p} = 1 + \frac{t_n}{t_p} \tag{8.23}$$

where

$$p(\tau_e)/p_n \cong e^{-1}, \tag{8.24}$$

and it is assumed that the solution is found before and near the second zero crossing of the blast pulse. For the special case of the Friedlander pulse, the scaled pulse lifetime and negative phase durations are

$$\tau_{e\,F} \equiv \frac{t_e}{t_p} = 1 + 2\pi \approx 7.3, \tag{8.25}$$

$$\tau_{n\,F} \equiv \frac{t_n}{t_p} = 2\pi \approx 6.3. \tag{8.26}$$

The drop time τ_d, or the time from the first zero crossing to the peak underpressure, is sometimes reported in relation to the negative phase duration, where

$$\tau_{drop/t_n\,\mathrm{F}} \equiv \tau_{d\,F}/\tau_n = 1/2\pi \approx 0.16. \tag{8.27}$$

Due to instrumental difficulties in accurately capturing the peak overpressure, the integral over time of the positive part of the pulse has been traditionally used as a robust metric for explosions. Direct integration of the Friedlander pulse yields

$$I_{p\,F} = \int_0^{t_p} p(t)dt = \left[\frac{t_p p_\mathrm{p}}{2}\right] M_{1\,F} = \left[\frac{t_p p_\mathrm{p}}{2}\right] 2e^{-1} \approx \left[\frac{t_p p_\mathrm{p}}{2}\right] 0.74. \tag{8.28}$$

where the scaled first moment M_1 is defined as

$$M_1 \equiv 2\int_0^1 \left[\frac{p(\tau)}{p_p}\right] d\tau. \tag{8.29}$$

and evaluated in Appendix 1 for all the pulses. Using the impulse balance condition along with the pressure and pulse duration ratios we can rewrite the negative impulse as,

$$|I_{n\,F}| = \frac{t_p p_\mathrm{p}}{e^1} = \frac{e^1 t_n |p_\mathrm{n}|}{2\pi} \tag{8.30}$$

and assert

$$\frac{I_{1\mathrm{p}}}{|I_{1\mathrm{n}}|} = \frac{p_\mathrm{p} t_p}{|p_\mathrm{n}| t_n} \frac{2\pi}{e^2} \equiv 1. \tag{8.31}$$

The product of the positive and negative phase peak pressure and duration ratios can provide a prompt measure of the impulse symmetry between the positive and negative phases. The symmetry parameter is hereby defined as

$$\mathcal{g} \equiv \frac{p_p}{|p_n|} \frac{t_p}{t_n}. \tag{8.32}$$

For the Friedlander pulse,

$$\mathcal{g}_F = \frac{e^2}{2\pi} \approx 1.2\,. \tag{8.33}$$

It is known that the Fourier spectrum of the Friedlander pulse peaks at a frequency f_p (in Hz) that can be expressed in terms of the positive pulse duration

$$f_p = \frac{1}{2\pi t_p}. \tag{8.34}$$

The Friedlander pulse can be expressed in terms of its angular frequency $\omega_p = 2\pi f_p$ as

$$p_F(t) = p_p\left(1 - \omega_p t\right)e^{-\omega_p t} \tag{8.35}$$

with Fourier transform (Appendix 1)

$$\frac{P_F(j\omega)}{t_p p_p} = \left[\frac{1}{t_p p_p}\right]\frac{j\omega p_p}{\left(\omega_p + j\omega\right)^2} = \frac{j\left(\omega\, t_p\right)}{\left[1 + j\left(\omega t_p\right)\right]^2} \tag{8.36}$$

and unilateral energy spectral density

$$S_F = 2|P_F|^2 = \left(\frac{2\omega_p\omega}{\omega_p^2 + \omega^2}\right)^2 S_{\max F} = \left(\frac{2\left(\omega\, t_p\right)}{1 + \left(\omega\, t_p\right)^2}\right)^2 S_{\max F}, \tag{8.37}$$

where the peak in the spectrum occurs at $\omega_p t_p = 1$

$$S_{\max F} = \frac{p_p^2}{2\omega_p^2} = \frac{\left(t_p p_p\right)^2}{2}. \tag{8.38}$$

The pulse spectrum is symmetric about its peak frequency, with −6 dB/octave drop away from its peak level $S_{\max F}$. Since the peak spectrum is at a frequency $f_s = f_p$,

$$f_{sF} = \frac{\omega_p}{2\pi} = \frac{1}{2\pi t_p} = \frac{1}{6.28\, t_p} = \frac{1}{t_n}, \tag{8.39}$$

the *negative* pulse duration of a balanced Friedlander pulse defines the peak spectral frequency. This is admittedly a circular argument, and its purpose is to point out that the peak spectral frequency can be regarded as representative of the central frequency of the blast wavelet, which will depend on the total shape of the pulse. I define the apparent spectral period, or pseudo period t_s, of the pulse as

$$\tau_{sF} \equiv \frac{t_s}{t_p} \equiv \frac{2\pi}{\omega_p t_p} = \frac{1}{f_s t_p}. \tag{8.40}$$

For the special case of the Friedlander pulse, where $\omega_p t_p = 1$

$$\tau_{sF} = \tau_{nF} = 2\pi \approx 6.28. \tag{8.41}$$

The influence of the negative phase on the spectrum is significant. For example, a 1 tonne HE nominal positive pulse duration of 0.042 s at 1 km would yield a negative pulse duration of 0.26 s. If the blast pulse resembled the balanced Friedlander, it would have a spectral peak at 3.8 Hz.

From Parseval's theorem (Appendix 1), the exposure per frequency band, with units of Pa^2 s, can be obtained through direct integration of the pressure or the spectral density in the band of interest

$$xE = \int_{-\infty}^{\infty} |p(t)|^2 dt = \int_{-\infty}^{\infty} |P(f)|^2 df. \tag{8.42}$$

The Friedlander exposure can be expressed as

$$xE_{\mathrm{F}} = t_p p_p^2 \int_0^{\infty} \left[\frac{p(\tau)}{p_p}\right]^2 d\tau = \left[\frac{t_p p_p^2}{2}\right] M_{2F} = \left[\frac{t_p p_p^2}{2}\right] 0.5. \tag{8.43}$$

where the scaled second moment M_2 is defined as

$$M_2 \equiv 2 \int_0^{\infty} \left[\frac{p(\tau)}{p_p}\right]^2 d\tau. \tag{8.44}$$

and evaluated in Appendix 1 for all the pulses. Due to its high overpressure to underpressure ratio, the majority of the blast energy for the Friedlander pulse is contained in the positive phase, with

$$xE_{\mathrm{pF}} = \int_0^{t_p} p_1^2 dt = \left[\frac{t_p p_p^2}{2}\right] \frac{(1 - e^{-2})}{2}. \tag{8.45}$$

Thus, the positive pulse exposure is representative of the blast energy for the Friedlander-type pulse. The scaled second moment M_2 is selected to represent the relative efficiency of the pulse energy relative to the reference value of

$$xE_{\mathrm{ref}} = \frac{t_p p_p^2}{2} \tag{8.46}$$

$$M_2 = \frac{xE}{xE_{\mathrm{ref}}} \approx \textit{relative efficiency}. \tag{8.47}$$

The Friedlander relative efficiency of $M_{2F} = 0.5$ means that this pulse delivers half the energy as the reference.

The balanced Friedlander is beloved for its ease of implementation as well as its mathematical conciseness and elegance, and is a good first-order representation of the positive phase of a blast pulse. It has some limitations: its rise time is instantaneous, there is no flexibility in the curvature of the positive phase, and the negative phase amplitude, duration, and curvature do not match observations. However, the Friedlander is an adequate representation of a shocked positive phase and is likely to remain in the canon as a venerable benchmark for an impulse-balanced blast pulse.

This section rescaled the negative phase pulse parameters in terms of the positive phase overpressure p_p and time duration t_p, as well as defined the pressure drop time t_{drop}, the pulse lifetime t_e, the scaled positive impulse (or first moment) M_1, the symmetry parameter $\mathcal{G}$, the pseudo period t_s, and finally the scaled exposure (or second moment) M_2, which also serves as a measure of the relative effectiveness of a source function. These representative parameters will be evaluated and compared for each pulse in the next sections.

8.3.2 Hybrid Modified Friedlander Pulse

It is well known that the Friedlander pulse does not match observations to a high level of accuracy (e.g., Reed 1977). It is often replaced by the modified Friedlander (MF) equation (e.g., Ford et al. 2014), which includes the waveform parameter α in the exponential term, as in the expression for f_{F46HE} in Eq. 8.2. However, the modified Friedlander is only impulse-balanced at $\alpha = 1$, so beyond the hydrodynamic range, it is not representative of a stable pulse. Substantial effort has gone into deriving exact equations for the hybrid Friedlander, with additional details in Appendix 2, and much insight could be drawn from the discussion in this section. The conclusion of this hybrid MF study is that it introduces awkward discontinuities at the first zero crossing and produces unrealistic pulses that have little resemblance to observed blast pulses. Such deficiencies may not dissuade a determined signature designer, and this section should help expedite the construction of hybrid functions.

Rigby et al. (2014) and Bonner et al. (2013) follow the approach of Teich and Gebbken (2010) to construct hybrid pulses to match observed blast waveform parameters by using the pulse fitting functions

$$p_{\mathrm{MF}} = p_p(1-\tau)e^{-\alpha_p \tau}, \quad 0 \le \tau \le 1 \tag{8.48}$$

$$p_{\mathrm{MF}} = |p_n|\alpha_n e^{(1+\alpha_n)}(1-\tau)e^{-\alpha_n \tau}, \quad \tau \ge 1 \tag{8.49}$$

where p represents the gauge pressure, p_p is the maximum blast pressure (peak overpressure), p_n is the minimum blast pressure (peak underpressure), τ represents the scaled time, and waveform parameters α_p and α_n are implemented for the

positive and negative phases of the hybrid Modified Friedlander (MF) pulse, respectively. As presented in Appendix 2, the pressure minimum p_n occurs at a time t_{min}

$$\frac{t_{min}}{t_p} = 1 + \frac{1}{\alpha_n}. \tag{8.50}$$

As with the Friedlander pulse, we define the negative phase duration from the pulse lifetime

$$p(\tau_e)/p_n \cong e^{-1}, \tag{8.51}$$

with solution

$$\tau_{e\,MF} = \frac{t_e}{t_p} = 1 + \frac{t_n}{t_p} = 1 + \frac{2\pi}{\alpha_n} \tag{8.52}$$

where the negative pulse duration t_n is

$$\tau_{n\,MF} = \frac{t_n}{t_p} = \frac{2\pi}{\alpha_n} \tag{8.53}$$

As noted in Appendix 2, the total impulse is the zero frequency (DC offset) of the Fourier transform,

$$I_{p\,MF} = P_{1p}(0) = p_p t_p \frac{\left(\alpha_p - 1 + e^{-\alpha_p}\right)}{\alpha_p^2} = \left[\frac{p_p t_p}{2}\right] M_1 \tag{8.54}$$

$$I_{n\,MF} = P_{1n}(0) = -\frac{|p_n| t_p}{\alpha_n} e^1 = -\frac{|p_n| t_p}{2}\left(\frac{2e^1}{\alpha_n}\right) \tag{8.55}$$

where in this section M_1 is shorthand for the scaled first moment $M_{1\,MF}$ in Appendix 1,

$$M_1 = 2\left[\frac{\alpha_p + 1 + e^{-\alpha_p}}{\alpha_p^2}\right]. \tag{8.56}$$

An impulse-balanced solution must satisfy $I_{1p} + I_{1p} = 0$, or

$$\left|\frac{p_p}{p_n}\right|_{HMF} = \frac{1}{M_1}\left(\frac{2e^1}{\alpha_n}\right), \tag{8.57}$$

which can be rewritten as,

$$\alpha_n = \frac{|p_n|}{p_p}\left(\frac{2e^1}{M_1}\right), \tag{8.58}$$

or

$$|p_n| = p_p\left[\frac{1}{2e^1}\alpha_n M_1\right]. \tag{8.59}$$

The impulse-balanced Hybrid Modified Friedlander (HMF) is expressed as

$$p_{\mathrm{HMF}} = p_p(1-\tau)e^{-\alpha_p\tau}, \quad 0 \le \tau \le 1 \tag{8.60}$$

$$p_{\mathrm{HMF}} = p_p\left[\frac{1}{2}M_1\alpha_n^2 e^{\alpha_n}\right](1-\tau)e^{-\alpha_n\tau}, \quad \tau \ge 1 \tag{8.61}$$

and has pulse lifetime

$$\tau_{e\,HMF} = 1 + M_1\frac{\pi}{e^1}\frac{p_p}{|p_n|} \approx 1 + 1.16M_1\frac{p_p}{|p_n|}. \tag{8.62}$$

The scaled first moment M_1 substantially simplifies the interpretation of the impulse balance condition and provides insight on the properties of the positive phase of the modified Friedlander. M_1 can be considered a very simple measure of concavity for exponentially pulses: when less than unity, the positive phase is concave upwards, when it exceeds unity it is concave downwards, and when unity the positive impulse is a right triangle. In the latter two cases it is incorrect to use the Friedlander equation for the positive pulse shape. For Friedlander-type pulses, this places the limit

$$M_1 \le 1. \tag{8.63}$$

In the special case of a small positive waveform parameter, a Taylor expansion yields

$$\lim_{\alpha_p \to 0} M_1 \approx 1 - \frac{\alpha_p}{3}. \tag{8.64}$$

For small α_p, the decay rate of the positive pulse is approximately linear and the positive impulse can be estimated by integrating over a triangular area. The impulse symmetry parameter $\mathcal{G}_{MF}$ for the hybrid modified Friedlander pulse is

$$\mathcal{G}_{MF} = \frac{p_p}{|p_n|}\frac{t_p}{t_n} = \frac{1}{M_1}\left(\frac{e^1}{\pi}\right) \approx \frac{0.865}{M_1} \geq 0.865\,. \tag{8.65}$$

As shown in Appendix 4, both the HE and NE KG85 tables for the positive impulse have M_1 values that exceed unity. This is not acceptable for the KG85 use cases. Alternate expressions for the impulse are developed from the tabulated values of the positive decay coefficients and presented in Appendix 4. The Fourier transform is also provided in Appendix 2 for the general unbalanced case. The exposure for the positive phase (Appendix 2) can be expressed as

$$xE_{p\,MF} = \int_0^1 p_{mF}^2(\tau)d\tau = \lfloor\frac{t_p p_p^2}{2}\rfloor \frac{2\alpha_p^2 - 2\alpha_p + 1 - e^{-2\alpha_p}}{2\alpha_p^3}, \tag{8.66}$$

where the maximum exposure for the hybrid Friedlander positive pulse occurs with vanishing α_p,

$$\lim_{\alpha_p \to 0} xE_{p\,MF} = t_p p_p^2 \int_0^1 (1-\tau)^2 d\tau = \left[\frac{t_p p_p^2}{2}\right]\frac{2}{3}, \tag{8.67}$$

which is the exposure of a triangular positive phase. On the other hand, for a large wavenumber parameter

$$\lim_{\alpha_p \to \infty} M_1 \approx \frac{2}{\alpha_p}, \tag{8.68}$$

$$\lim_{\alpha_p \to \infty} I_p \approx \frac{p_p t_p}{\alpha_p}. \tag{8.69}$$

Large α_p values in the KG85 tables would correspond to pulses with sharp high-amplitude positive phases and a negligible negative phase. Although the waveform parameter itself is unbound, in practice only a narrow range of values centered around unity produce reasonably dampened pulses for all the candidate functions. From Appendix 2, the exposure of a balanced negative phase is

$$xE_{n\,HMF} = \int_1^\infty p_{mF}^2(\tau)d\tau = t_p p_p^2\left[\frac{1}{2e^1}\alpha_n M_1\right]^2 \frac{e^{-2\alpha_n}}{4\alpha_n^3} = \left[\frac{t_p p_p^2}{2}\right] M_1^2\left(\frac{e^{-2\alpha_n - 2}}{8\alpha_n}\right) \tag{8.70}$$

with total exposure for the balanced HMF

$$xE_{HMF} = \left[\frac{t_p p_p^2}{2}\right]\left\{\frac{2\alpha_p^2 - 2\alpha_p + 1 - e^{-2\alpha_p}}{2\alpha_p^3} + M_1^2\left(\frac{e^{-2\alpha_n - 2}}{8\alpha_n}\right)\right\}. \tag{8.71}$$

The rest of this section concentrates on the special HMF solution to the pressure ratio

$$\left.\frac{p_p}{p_n}\right|_{ref} = 2 \tag{8.72}$$

that is used for the reference triangular impulse and energy, which is close to the mean values for the pulses shown in Fig. 8.1 as well as the HE and NE ratios in Appendix 4. In the reference case

$$\alpha_{n\,ref} = \frac{e^1}{M_1} \tag{8.73}$$

Consider $M_1 = 1$ for a triangular positive phase,

$$\alpha_{n\,ref}(M_1 = 1) = e^1 \approx 2.72 \tag{8.74}$$

the exposure provides a quick metric on the energy distribution,

$$xE_{HMF} = \left[\frac{t_p p_p^2}{2}\right]\left\{\frac{2}{3} + \left(\frac{e^{-2\alpha_n - 2}}{8}\right)\right\} = \left[\frac{t_p p_p^2}{2}\right]\left\{\frac{2}{3} + \mathcal{O}\left(10^{-3}\right)\right\}. \tag{8.75}$$

The negative phase is so severely attenuated that the exposure is essentially that of the triangular pulse. Decreasing the scaled moment only exacerbates the problem as it increases the negative waveform parameter. Specifying waveform parameters and pressures in the positive and negative phases also introduces an artificial and unsightly discontinuity in the time derivative at the first zero crossing (Appendix 2), where

$$\left.\frac{p_{p\,MF}{}'}{p_{n\,MF}{}'}\right|_{\tau = 1} = \frac{p_p}{|p_n|}\left(\frac{e^{-\alpha_p} - 1}{\alpha_n}\right). \tag{8.76}$$

Attempts to construct hybrid Friedlander pulses with the B55 pulse did not lead to substantially improved waveforms. A case study is shown in Appendix 3 for the special reference case of a triangular positive phase with

$$\left.\frac{p_p}{p_n}\right|_{ref} = 2, \quad \alpha_p = 0, \tag{8.77}$$

the slope discontinuity is

$$\left.\frac{p_{pMF}{}'}{p_{nMF}{}'}\right|_{\tau=1} = 2\left(\frac{e^{-1}}{e^{1}}\right) = 2e^{-2} \approx 0.27. \tag{8.78}$$

Teich and Gebbken (2010) seek to reduce this discontinuity by keeping the wavenumber parameter constant. However, the discontinuity remains except for the pressure ratios specified by the balanced Friedlander pulse,

$$\alpha_p = \alpha_n = 1, \quad M_{1F} = 2e^{-1}, \quad \frac{p_p}{|p_n|} = e^2. \tag{8.79}$$

It is not possible to impulse balance the modified Friedlander functional forms without introducing a derivative discontinuity, in particular, for the KG85 NE specifications which prescribe a large waveform parameter with high curvature and reduced area (small first moment). Due to irreconcilable issues with the tabulated KG85 NE values for impulse and wave parameters, in the discussions that follow I will be treating the NE wavenumber parameter as an unknown.

For the sake of completeness, I consider the KG85 tabulated value of the positive waveform parameter for 1 kg HE at 100 m/kg$^{1/3}$

$$\alpha_p = 0.15. \tag{8.80}$$

Since it is small, one may use Taylor expansion approximation

$$M_1 \approx 1 - \frac{\alpha_p}{3} = 0.95 \tag{8.81}$$

which yields the relation

$$\alpha_n = \frac{|p_n|}{p_p} 5.72. \tag{8.82}$$

The pulse lifetime is

$$\tau_e = 1 + \frac{2\pi}{\alpha_n} = 1 + 1.1\frac{p_p}{|p_n|}. \tag{8.83}$$

and it is possible to balance the pulse duration with the pressure ratios. The 2 kt case study data in Fig. 8.1 shows pulse lifetimes of $\tau_e \sim 3$, but we already surmised the negative phase durations are overdamped for a reference pressure ratio of ~2. One can compromise by using

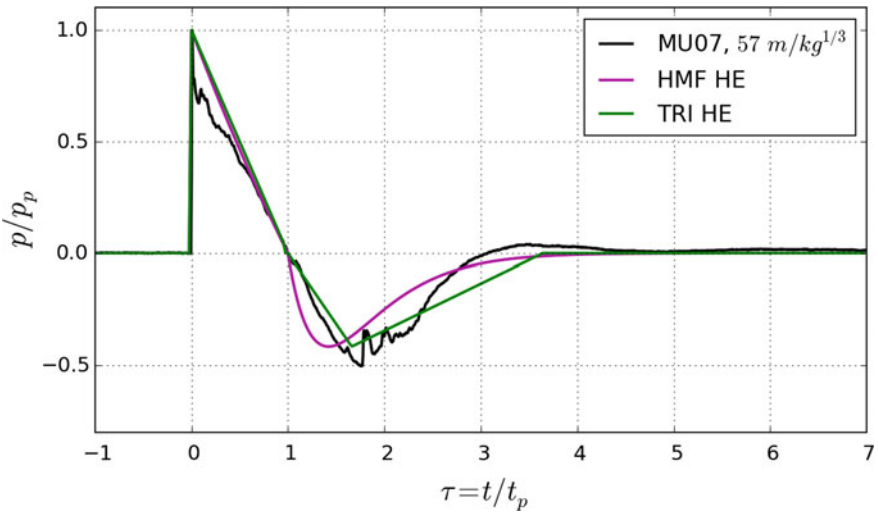

Fig. 8.5 Balanced Hybrid Modified Friedlander (HMF) using KG85 tables. The slope discontinuity is abrupt, the drop time is too short, and the negative phase is overdampened. Triangular approximation shown in green

$$\frac{p_p}{|p_n|} = 3 \Rightarrow \alpha_n = 1.9, \tau_e = 1 + \frac{2\pi}{\alpha_n} = 4.3 \tag{8.84}$$

to provide a HMF pressure pulse with a reasonable pressure ratio and duration. Appendix 3 shows hybrid Friedlander and Friedlander-Brode pulses for $\alpha_n = 2$. Alternatively, one may select to match the drop time instead of the pulse lifetime. This flexibility in the HMF parameter selection comes at the expense of an inevitable discontinuity at the first zero crossing. I use the KG85 tabulated values and the expressions in Appendix 4 for the peak underpressure (also shown in Table 8.4) evaluated at 1 tonne and 1 km,

$$\frac{p_p}{|p_n|} = 2.4, \alpha_p = 1.5, \alpha_n = 2.38, \tau_n = 2.6$$

to produce the balanced HMF pulse shown in Fig. 8.5.

The discontinuity in slope and unrealistic waveforms produced by the hybrid modified Friedlander equations may be less than optimal for many studies, and other possible methods and criteria for constructing hybrid pulses are considered.

8.3.3 Triangular Approximation

This section retreats to a simpler, skeletal pulse representation that can provide very accessible reference metrics. The far-field positive waveform parameter α_p tabulated by KG85 for HE is small, and the positive impulse may be approximated by a right triangle. Rigby et al. (2014) provide an expression for a triangular (linear) pulse where the negative pulse rise time is ¼ of the total negative pulse duration, as recommended by UFC 3-340-02 (see Fig. 2-190 of that reference). The triangular pulse is an excellent example of an extreme but useful simplification of a shocked positive phase and elucidates some of the compromises of blast pulse matching.

Let $t_{\Delta p}$ be a fictional positive pulse duration evaluated so as to preserve the impulse,

$$t_{\Delta p} = \frac{2I_p}{p_p} \leq t_p \tag{8.85}$$

$$\tau_p = \frac{t_{\Delta p}}{t_p} \tag{8.86}$$

where the fictional positive pulse duration approaches the observed value as the positive phase approaches a triangular shape. Let $t_{\Delta n}$ be the estimated negative pulse duration estimated from the negative impulse

$$t_{\Delta n} = \frac{2I_n}{p_n} \tag{8.87}$$

$$\tau_{\Delta n} = \frac{t_{\Delta n}}{t_p}. \tag{8.88}$$

The negative rise time, or the time from the first zero crossing to the peak underpressure relative to $t_{\Delta n}$, is explicitly specified as

$$\tau_{\Delta drop/tn} = \frac{t_{\Delta drop}}{t_{\Delta n}} = 0.25. \tag{8.89}$$

For $\tau = \frac{t}{t_p}$, the gauge pressure for the triangular pulse can be represented as

$$p_\Delta = p_p(1-\tau), \quad 0 \leq \tau \leq \tau_p \tag{8.90}$$

$$p_\Delta = 0, \quad \tau_p \leq \tau \leq 1 \tag{8.91}$$

$$p_\Delta = -|p_n|\frac{4}{\tau_{\Delta n}}(\tau - 1), \quad 1 < \tau \leq 1 + \frac{\tau_{\Delta n}}{4} \tag{8.92}$$

$$p_{\Delta} = -|p_n|\frac{4}{3\tau_{\Delta n}}(\tau_{\Delta n} + 1 - \tau), \quad 1 + \frac{\tau_{\Delta n}}{4} < \tau \le 1 + \tau_{\Delta n} \tag{8.93}$$

An example of the triangular pulse is shown in Fig. 8.5 using the same parameters as for the HMF in the same figure. The primary strength of the triangular representation is that all parameters can be fitted from observed positive and negative pressures and durations, and readily estimated with a pencil and ruler on paper. The triangular shape function shown in Fig. 8.5 is expected to have discontinuous derivatives at all the transition points and would not respond well to digital filtering. Its impulse is, by definition, the area under the triangles

$$I_{\Delta p} \equiv \frac{t_{\Delta p} p_p}{2}, \quad I_{\Delta n} \equiv -\frac{t_{\Delta n}|p_n|}{2}, \quad M_{\Delta 1} \equiv 1. \tag{8.94}$$

The triangular pulse sets a baseline for the simplest impulse balance condition and is used as the reference impulse in the scaled first moments of Appendix 1. The condition of impulse balance for the triangular pulse constrains the peak underpressure and the negative pulse duration, which are relevant parameters for engineering glass panels to better withstand blasts (Rigby et al. 2014). An impulse-balanced triangular pulse must satisfy

$$\frac{t_{\Delta n}}{t_{\Delta p}} = \frac{p_p}{|p_n|}, \tag{8.95}$$

and has unity symmetry parameter

$$\mathcal{g}_{\Delta} = 1\,. \tag{8.96}$$

At least one of the positive and negative phase parameters must have some flexibility to balance the impulse. Blast pulse fitting criteria generally involves the ratios of the positive and negative pressures and durations, and at least one of the parameters must be adjusted to match impulse, slope, or energy specifications. The total exposure is substantially simplified by the impulse balance requirement, as

$$xE_{\Delta} = \frac{t_{\Delta p} p_p^2}{3} + \frac{t_{\Delta n} p_n^2}{3} = \frac{t_{\Delta p} p_p^2}{3}\left[1 + \left(\frac{t_{\Delta n}}{t_{\Delta p}}\right)\left(\frac{p_n}{p_p}\right)^2\right], \tag{8.97}$$

$$xE_{\Delta} = \frac{t_{\Delta p} p_p^2}{3} + \frac{t_{\Delta n} p_n^2}{3} = \frac{t_{\Delta p} p_p^2}{3}\left[1 + \left(\frac{|p_n|}{p_p}\right)\right]. \tag{8.98}$$

If $\frac{p_p}{|p_n|} = 2$, then $\tau_n = \frac{t_n}{t_p} = 2$ and the pulse lifetime is

$$\tau_e = 1 + \frac{t_n}{t_p} = 3 \tag{8.99}$$

with total exposure

$$xE_{\Delta 2} = \left(\frac{2}{3} + \frac{1}{3}\right)\frac{t_{\Delta p} p_p^2}{2} = \frac{t_{\Delta p} p_p^2}{2} \tag{8.100}$$

which is used as the reference scale for the second moment, or

$$M_{2\Delta} \equiv 1, \text{for } \frac{p_p}{|p_n|} = 2. \tag{8.101}$$

For this choice of peak overpressure to underpressure ratio, the positive phase contributes two-thirds of the energy, whereas the negative phase brings in the remaining one-third. Note that the reference balanced triangular pulse can deliver twice the energy of the Friedlander pulse.

As illustrated by the simple triangular pulse expressions, it is not generally possible to balance the impulse and fit the negative pressure and pulse duration. One may fit the pressure and duration but abandon impulse balance, or insist on impulse balance and fit only the underpressure under the assumption that it may be a more robust quantity than the negative duration. The topic of parameter selection will reemerge in the construction of hybrid pulses.

8.3.4 G95HE Detonation Pulse with Secondary Oscillation

From the previous discussion it is clear that exponential impulse-balanced canonicals generally only have three degrees of freedom—the overpressure, the positive pulse duration, and the waveform parameter—and they generally set the negative phase properties. Various blast pulses were considered by Garcés (1995) in the context of volcanic explosions, although the functional forms in that work did not use positive pulse duration as the time baseline. The G95HE detonation pulse is representative of a shocked onset with an extended coda and a precisely specified negative pulse duration, and reinforces the effect of the negative phase on the pulse parameters. The balanced expression is

$$p_{\text{G95HE}}(t) = p_p \left(\frac{2-\sqrt{2}}{2+\sqrt{2}}\right)(1-\tau)\left(\frac{2+\sqrt{2}}{2-\sqrt{2}} - \tau\right) e^{-\left(2-\sqrt{2}\right)\tau}, \tau_{p3ref} = 0 \tag{8.102}$$

The peak overpressure is p_p at the onset, and the peak negative overpressure occurs at $\tau_{nMin} \approx 2.16452$,

$$p_{\mathrm{n}} = p_{\mathrm{G95HE}}\,(2.16452) = -p_p\left(\frac{2-\sqrt{2}}{2+\sqrt{2}}\right)\frac{6}{5} \approx -0.206\,p_p \tag{8.103}$$

$$\left|\frac{p_p}{p_n}\right|_{G95HE} = \left(\frac{2+\sqrt{2}}{2-\sqrt{2}}\right)\frac{5}{6} \approx 4.9 \tag{8.104}$$

with negative pulse duration

$$\tau_{n\,G95HE} = \frac{t_n}{t_p} = \left(\frac{2+\sqrt{2}}{2-\sqrt{2}}\right) \approx 5.8 \tag{8.105}$$

and pulse lifetime

$$\tau_{e\,G95HE} = \frac{t_e}{t_p} = 1 + \left(\frac{2+\sqrt{2}}{2-\sqrt{2}}\right) \approx 6.8 \tag{8.106}$$

The negative rise time, or drop time, can be expressed in terms of the negative phase duration as

$$\tau_{drop/t_n\,G95HE} \equiv \left(\frac{t_{min}}{t_p} - 1\right)/\tau_n = (2.2-1)/5.8 \approx 0.2 \sim \frac{1}{5}. \tag{8.107}$$

The balanced G95 detonation pulse has a shorter underpressure duration than the balanced Friedlander, which has a negative pulse duration of $2\pi t_p$, and its rise time is closer to that of the reference triangular pulse.

The positive impulse is

$$I_{p\,G95HE} = \left[\frac{p_p t_p}{2}\right] M_{1\,G95HE} \approx \left[\frac{p_p t_p}{2}\right] 0.79, \tag{8.108}$$

and the impulse symmetry parameter for the hybrid G85HE pulse is

$$\mathscr{G}_{G95} = \frac{p_p}{|p_n|}\frac{t_p}{t_n} = \frac{5}{6} \approx 0.83, \tag{8.109}$$

which is lower than the minimum value for the impulse-balanced hybrid Friedlander pulse.

The Fourier transform can be expressed as

$$\frac{P_{G95HE}(j\omega)}{t_p p_p} = \frac{\left(\omega t_p\right)^2}{\left(\sqrt{2}-2-j\omega t_p\right)^3} \tag{8.110}$$

with spectrum

$$S_{G95HE} = 2|P_{G95HE}|^2 = \frac{2\left(t_p p_p\right)^2\left(\omega\, t_p\right)^4}{\left[\left(2-\sqrt{2}\right)^2+\left(\omega t_p\right)^2\right]^3}. \tag{8.111}$$

and peak at angular frequency

$$\omega\, t_p = 2\sqrt{3-2\sqrt{2}} \approx 0.83 \tag{8.112}$$

corresponding to a peak scaled frequency

$$t_p f_{s\,G95HE} = \frac{\omega\, t_p}{2\pi} \approx 0.13. \tag{8.113}$$

The secondary oscillation increases the effective duration of the pulse and it leaves a mark in the spectrum, which peaks at a characteristic pseudo period of

$$\tau_{s\,G95HE} = \frac{t_s}{t_p} = 7.6. \tag{8.114}$$

which is longer than the estimated pulse lifetime. The total exposure is computed from

$$xE_{\mathrm{G95HE}} = \left[\frac{t_p p_p^2}{2}\right] M_{2\,\mathrm{G95HE}} \approx \left[\frac{t_p p_p^2}{2}\right] 0.64. \tag{8.115}$$

The sustained oscillation in the extended coda introduces additional energy to the G95HE pulse, making its total contribution ~4/3 greater than the balanced Friedlander pulse.

The next two detonation pulses belong a different family of source pressure functions, as they consist of polynomials with no exponential terms. These last two pulses are included because their prior use in the literature and their better match to observed detonation pulses.

8.3.5 R77HE Reed Pulse

The Reed (1977) pulse has a well-defined shocked onset as well as clear first and second zero crossings.

$$p_{\mathrm{R77}}(t) = p_p(1-\tau)\left[1-\frac{7}{25}\tau\right]\left[1-\left(\frac{7}{25}\tau\right)^2\right], \quad 0 \le \tau \le \frac{25}{7}, \tag{8.116}$$

The peak overpressure is p_p at the onset, and the peak negative overpressure occurs at

$$\tau_{min} = \frac{1}{14}\left(3\sqrt{89}-1\right) \approx 1.95, \tag{8.117}$$

$$p_{\mathrm{n}} = p_{\mathrm{R77}}(\tau_{min}) = -p_p 27\left(\frac{1513\sqrt{89}-11821}{218750}\right) \tag{8.118}$$

$$\left|\frac{p_p}{p_n}\right|_{R77} = \frac{218750}{27\left(1513\sqrt{89}-11821\right)} \approx 3.3$$

and has an unambiguous negative pulse duration

$$\tau_{n\,R77} = \frac{t_n}{t_p} = \left(\frac{18}{7}\right) \approx 2.6, \tag{8.119}$$

and pulse lifetime

$$\tau_{e\,R77} = \frac{t_e}{t_p} = \left(\frac{25}{7}\right) \approx 3.6, \tag{8.120}$$

The drop time relative to the negative phase duration is

$$\tau_{drop/t_n\,R77} = \left(\frac{t_{min}}{t_p}-1\right)/\tau_n = (1.95-1)/2.57 \approx 0.37. \tag{8.121}$$

so it drops relatively slow compared to the reference of 0.25. The impulse is

$$I_{p\,R77} = \left[\frac{p_p t_p}{2}\right] M_{1\,R77HE} \approx \left[\frac{p_p t_p}{2}\right] 0.9, \tag{8.122}$$

with impulse symmetry

$$\mathcal{G}_{R77} = \frac{p_p}{|p_n|}\frac{t_p}{t_n} = \approx \frac{3.30}{2.57} = 1.3. \tag{8.123}$$

The R77 has the nice property that its derivative vanishes at the pulse lifetime τ_e. Unlike the previous pulses (except for the triangular pulse), it has no exponential decay terms and consists solely of polynomials.

Unlike the Friedlander pulse, the Fourier transform of the R77 pulse is complicated,

$$\begin{aligned}\frac{P_{\mathrm{R77}}(j\omega t_p)}{t_p p_p}\left[15625(\omega t_p)^5\right] = &-j(\omega t_p)^4 15,625 + (\omega t_p)^3 20,000 \\ &+ j(\omega t_p)^2 6,300 + (\omega t_p) 9,408 + j8,232 \\ &+ e^{-j(\omega t_p)\left(\frac{25}{7}\right)} 168\left[j(\omega t_p)^2 75 + (\omega t_p) 119 - j49\right],\end{aligned} \tag{8.124}$$

and is best handled numerically. The peak spectrum occurs near

$$\omega t_p \approx 1.4 \tag{8.125}$$

for a peak scaled frequency of

$$t_p f_{peak\,R77} \approx \frac{1.4}{2\pi} = 0.22 \tag{8.126}$$

corresponding to a pseudo period of

$$\tau_{s\,R77} = \frac{2\pi}{\omega t_p} \approx 4.5. \tag{8.127}$$

The total exposure over the pulse lifetime is

$$xE_{\mathrm{R77}} = \left[\frac{t_p p_p^2}{2}\right] M_{2\,R77HE} \approx \left[\frac{t_p p_p^2}{2}\right] 0.78 \tag{8.128}$$

and is close to the reference value.

8.3.6 Hybrid Granström, Friedlander, and Triangular Pulses

Rigby et al. (2014) uses a special case of the G95 Low Explosive (G95LE) deflagration pulse for curve fitting of the negative pulse duration. He attributes its origin to Granström (1956), and its use is recommended by the US Naval Facilities Engineering Command Design Manual (1986) and the US Army Blast Effects Design Spreadsheet (2005). It is referred to as the cubic negative phase expression by Rigby et al. (2014), and used to construct a hybrid pulse with the modified Friedlander for the positive phase.

The negative phase of the Granström (1956) pulse is rewritten as

$$p_{\ddot{\mathrm{G}}}(\tau_n) = -\frac{|p_{\mathrm{n}}|}{\tau_n^3}\left(\frac{3^3}{2^2}\right)(\tau-1)(1+\tau_n-\tau)^2, \quad 1 \le \tau \le 1+\tau_n \tag{8.129}$$

With extrema at $\tau_{min} = 1 + \frac{\tau_n}{3}$ and well-defined zero crossings at $\tau = 1$ and $\tau = 1 + \tau_n$. Its negative impulse is,

$$I_{\ddot{\mathrm{G}}} = -t_n|p_{\mathrm{n}}|\left(\frac{9}{16}\right). \tag{8.130}$$

As with the R77 pulse, the negative Granström phase has the nice property that both the pressure and its derivative vanish at the end of the pulse lifetime $\tau_e = 1 + \tau_n$. As with the other hybrid pulses, a discontinuity may be introduced at the first $\tau = 1$ zero crossing. The slope of the Granström pulse at the first zero crossing, approaching from the right, is

$$\left.\frac{dp_{\ddot{\mathrm{G}}}}{dt}\right|_{t \to t_p^+} = -\frac{|p_n|}{t_n}\frac{27}{4}. \tag{8.131}$$

It is possible to balance the slope for a hybrid Granström–Friedlander (GF) pulse by matching the Friedlander positive phase slope

$$\left.\frac{dp_{HF}}{dt}\right|_{t \to t_p^-} = -\frac{p_p}{t_p}e^{-\alpha_p}. \tag{8.132}$$

A slope-matched solution would satisfy

$$\alpha_{p\,Slope} = ln\left[\frac{p_p}{|p_n|}\frac{t_n}{t_p}\frac{4}{27}\right]. \tag{8.133}$$

Matching the impulse is also possible for certain parameter sets, although it may come at the expense of introducing a discontinuous derivative at the zero crossing. For small α_p, I use the approximation

$$I_{\mathrm{MF}} = \frac{t_p p_p}{2}\left(1 - \frac{\alpha_{p\,Bal}}{3}\right) = t_n |p_{\mathrm{n}}|\left(\frac{9}{16}\right) = \left|I_{\ddot{\mathrm{G}}}\right| \tag{8.134}$$

$$\alpha_{p\,Bal} = 3\left[1 - \frac{9}{8}\frac{|p_n|}{p_p}\frac{t_n}{t_p}\right] \geq 0. \tag{8.135}$$

However, a Friedlander pulse with a small waveform parameter is essentially a triangular positive phase, which is substantially easier to evaluate and balance. The triangular approximation provides the maximum positive moment for a shocked pulse as well as the steepest slope to the zero crossing going into the negative phase, allowing the pulse to complete a fuller negative excursion to rapidly deliver more power. For the case of a triangular positive phase, the impulse and slope can be set to

$$I_{\Delta \mathrm{p}} = \frac{t_p p_p}{2} = t_n |p_{\mathrm{n}}|\left(\frac{9}{16}\right) = \left|I_{\ddot{\mathrm{G}}}\right| \tag{8.136}$$

$$\left.\frac{dp_{\Delta p}}{dt}\right|_{t=t_p} = -\left.\frac{p_p}{t_p}\right|_{\Delta} = -\frac{|p_n|}{t_n}\frac{27}{4} \tag{8.137}$$

which eliminates the waveform parameter and has an interesting solution. The slope-matched and impulse-balanced hybrid combination of a the Granström negative phase and a triangular positive phase defines the canonical G17HE (or GT for short) pulse, which is expressed as

$$p_{\mathrm{GT}}(t) = p_p\left(1 - \frac{t}{t_p}\right), \quad 0 \leq \tau \leq 1 \tag{8.138}$$

$$p_{\mathrm{GT}}(t) = p_p \frac{1}{6}\left(1 - \frac{t}{t_p}\right)\left(1 + \sqrt{6} - \frac{t}{t_p}\right)^2, \quad 1 < \tau \leq 1 + \sqrt{6}, \tag{8.139}$$

where the functions are zero outside of the specified domains. The peak overpressure occurs at time zero, and the peak underpressure is at

$$\tau_{min} = 1 + \frac{\sqrt{6}}{3} \approx 1.82 \tag{8.140}$$

with

$$\left|\frac{p_p}{p_n}\right|_{GT} = \left(\frac{3}{2}\right)^{\frac{5}{2}} \approx 2.76 \tag{8.141}$$

$$\tau_{n\,GT} = \frac{t_n}{t_p} = \sqrt{6} \approx 2.45 \tag{8.142}$$

$$\tau_{e\,GT} = 1 + \frac{t_n}{t_p} = 1 + \sqrt{6} \approx 3.45. \tag{8.143}$$

The drop time in terms of the negative phase duration is

$$\tau_{drop/t_n\,GT} = \left(\frac{t_{min}}{t_p} - 1\right)/\tau_n = (1.81 - 1)/2.45 \approx 0.33 \sim \frac{1}{3}. \tag{8.144}$$

Since the positive phase is a right triangle, the impulse matches the reference exactly,

$$I_{p\,GT} = \frac{t_p p_p}{2}, M_{1\,GT} = 1. \tag{8.145}$$

The symmetry parameter is

$$\mathcal{G}_{GT} = \frac{p_p}{|p_n|}\frac{t_p}{t_n} = \approx \frac{2.75}{2.45} = 1.1\ , \tag{8.146}$$

which approaches the triangular pulse approximation. The impulse-balanced GT pulse yields the largest exposure of all the pulses considered in this chapter, and has continuous first derivatives everywhere except at time zero.

As with the R77 pulse, the Fourier transform of the GT pulse is complicated and its power spectrum is not amenable to a closed form solution, although it can be readily computed numerically from

$$\begin{aligned}\frac{P_{\mathrm{G17}}(j\omega t_p)}{t_p p_p} = &\frac{1 - j(\omega t_p) - e^{-j\omega t_p}}{(\omega t_p)^2} + \frac{e^{-j(\omega t_p)(1+\sqrt{6})}}{3(\omega t_p)^4} \\ &\left\{j(\omega t_p)\sqrt{6} + 3 + e^{j(\omega t_p)\sqrt{6}}\left[3(\omega t_p)^2 + j(\omega t_p)2\sqrt{6} - 3\right]\right\}.\end{aligned} \tag{8.147}$$

The peak spectrum occurs near

$$\omega t_p \approx 1.58 \sim \frac{\pi}{2} \tag{8.148}$$

for a peak frequency of

$$t_p f_{peak\,GT} \approx \frac{1}{4} = 0.25 \tag{8.149}$$

which would correspond to a pseudo period of

$$\tau_{s\,GT} = \frac{t_s}{t_p} = \frac{2\pi}{\omega t_p} \approx 4, \tag{8.150}$$

which approaches the pulse lifetime of 3.45. The total exposure over the pulse lifetime is

$$xE_{\mathrm{GT}} \approx \left[\frac{t_p p_p^2}{2}\right] 0.95 \tag{8.151}$$

which is commensurate with the triangular pulse effectiveness and delivers twice as much acoustic power as the balanced Friedlander pulse.

The next two pulses are presented primarily to offer a contrast to weak shocked pulses from detonations. The B55LE and G95LE may be representative of some types of internal blasts (e.g., KG95; Smith and Hetherington 1994).

8.3.7 B55 Deflagration Pulse

The B55LE (B55 for short) pulse has a slower onset, with a less abrupt derivative discontinuity at the origin (Fig. 8.1). Exact expressions for the B55 pulse are cumbersome but tractable. This pulse has been historically used for fitting the negative phase (Brode 1955, 1956; Bonner et al. 2013), and its properties in this context are described in some detail in Appendix 3. However, this emergent pulse shape could be representative of a deflagration, and has a balanced canonical form

$$p_{\mathrm{B55}}(t) = p_p \left(\frac{2e^{2-\sqrt{2}}}{\sqrt{2}-1}\right) \frac{t}{t_p} \left(1 - \frac{t}{t_p}\right) e^{-2\frac{t}{t_p}}, \tau_{p2ref} = 1 - \frac{\sqrt{2}}{2}, \tag{8.152}$$

with rise time to the peak overpressure of

$$\tau_{rise} = 1 - \frac{\sqrt{2}}{2} \approx 0.29, \tag{8.153}$$

time to the peak underpressure of

$$\tau_{min} = 1 + \frac{\sqrt{2}}{2} \approx 1.71, \tag{8.154}$$

and positive to negative pressure ratio

$$\left|\frac{p_p}{p_n}\right|_{B55} = \frac{\left(\sqrt{2}-1\right)\exp\left[-2+\sqrt{2}\right]}{\left(\sqrt{2}+1\right)\exp\left[-2-\sqrt{2}\right]} \approx 2.9. \tag{8.155}$$

The pulse lifetime can be estimated numerically from its e-folding time as

$$\tau_{e\,B55} = \frac{t_e}{t_p} = 3.01518 \approx 3 \tag{8.156}$$

with corresponding negative phase duration

$$\tau_{n\,B55} = \frac{t_n}{t_p} \approx 2. \tag{8.157}$$

The drop time in terms of the negative phase duration is

$$\tau_{drop/t_n\,B55} = \left(\frac{t_{min}}{t_p} - 1\right)/\tau_n \approx 0.35. \tag{8.158}$$

The positive impulse for the balanced B55 canonical is

$$I_{p\,B55} = \left[\frac{t_p p_p}{2}\right] M_{1\,B55} = \left[\frac{t_p p_p}{2}\right] 1.2 \tag{8.159}$$

with symmetry parameter

$$\mathcal{G}_{B55} = \frac{p_p}{|p_n|}\frac{t_p}{t_n} \approx 1.5\,. \tag{8.160}$$

As anticipated, for the concave-downwards B55 pulse the positive impulse exceeds the impulse from the triangular pulse.

The balanced canonical pulses have very few degrees of freedom available. As with the Friedlander pulse, it is possible to construct hybrid B55 pulses at the expense of introducing an additional discontinuity in the slope at the intercept time. A hybrid comparison is presented in Appendix 3 using the positive phase modified Friedlander and a negative phase modified Brode expressions. The negative Friedlander and Brode phases are sufficiently similar that it may be preferable to use the more tractable Friedlander hybrids.

The Fourier transform $P_{\mathrm{B55}}(j\omega)$ of the balanced B55 pulse can be expressed as

$$\frac{P_{\mathrm{B55}}(j\omega)}{t_p p_p} = \left(\frac{2e^{2-\sqrt{2}}}{\sqrt{2}-1}\right)\frac{-\omega t_p}{\left(\omega t_p - 2j\right)^3} \tag{8.161}$$

with peak at

$$\omega t_p = \sqrt{2} \approx 1.41 \tag{8.162}$$

or

$$t_p f_{peak\,B55}(Hz) = \frac{\omega t_p}{2\pi} = \frac{1}{\sqrt{2}\pi} \approx 0.23. \tag{8.163}$$

In the case of a secondary oscillation, the pulse lifetime only captures the first two zero crossings and underestimates the time duration that shapes the peak spectrum, which has a pseudo period of

$$\tau_{s\,B55} = \frac{2\pi}{\omega t_p} = \sqrt{2}\pi \approx 4.4. \tag{8.164}$$

The total exposure is

$$xE_{B55} \approx \left[\frac{t_p p_p^2}{2}\right] 1.18. \tag{8.165}$$

The slower rise time of the Brode pulse makes it useful for testing energy estimators and constructing blast synthetics that will not become too unstable due to Gibbs ringing at the onset.

8.3.8 G95LE Deflagration Pulse with Secondary Oscillation

A candidate reference source function for deflagrations or low-passed filtered detonations would have more gradual onset as well as an extended coda oscillation. The deflagration model developed by Garcés (1995) has been modified to keep the positive pulse time as the reference time standard. Its balanced amplitude-corrected form is

$$p_{\mathrm{G95LE}}(t) \simeq p_p 2\frac{t}{t_p}\left(1-\frac{t}{t_p}\right)\left(\frac{3+\sqrt{3}}{3-\sqrt{3}}-\frac{t}{t_p}\right)e^{-\left(3-\sqrt{3}\right)\frac{t}{t_p}}, \quad \tau_{ref} \simeq 0.328 \tag{8.166}$$

The numerically computed rise time to the peak underpressure is

$$\tau_{rise} \approx 0.328, \tag{8.167}$$

with estimated peak underpressue at

$$\tau_{min} \approx 1.809. \tag{8.168}$$

The peak underpressure is

$$p_n = p_{\mathrm{G95LE}}\left(\frac{t}{t_p} = 1.809\right) = -p_p 2 \times 0.284 \approx -0.568 p_p \tag{8.169}$$

with corresponding pressure ratio

$$\left|\frac{p_p}{p_n}\right|_{G95LE} \approx 1.8. \tag{8.170}$$

The zero crossings are explicit in the pulse definition, with a second zero crossing at

$$\tau_{e\,G95LE} = \frac{t_e}{t_p} = \left(\frac{3+\sqrt{3}}{3-\sqrt{3}}\right) \approx 3.7 \tag{8.171}$$

corresponding to a negative pulse duration of

$$\tau_{n\,G95LE} = \frac{t_n}{t_p} = 2.7. \tag{8.172}$$

Its positive impulse is

$$I_{p\,G95LE} \approx \left[\frac{t_p p_p}{2}\right] 1.2 \tag{8.173}$$

which is very similar to the B55 pulse. The symmetry parameter is

$$\mathcal{G}_{G95LE} = \frac{p_p}{|p_n|}\frac{t_p}{t_n} = \approx \frac{1.76}{2.73} = 0.6\,, \tag{8.174}$$

and quite different from the Brode pulse due to the continued oscillation in the coda. The drop time in terms of the negative phase duration is

$$\tau_{drop/t_n\,G95LE} = \left(\frac{t_{min}}{t_p} - 1\right)/\tau_n = (1.81-1)/2.73 \approx 0.3. \tag{8.175}$$

The G95LE Fourier transform is

$$\frac{P_{\mathrm{G95LE}}(j\omega)}{t_p p_p} = -2\left(2+\sqrt{3}\right)\left\{\frac{(\omega t_p)^2}{\left[\left(3-\sqrt{3}\right)+j\omega t_p\right]^4}\right\}. \tag{8.176}$$

with peak spectrum at the angular frequency

$$\omega_p t_p = \sqrt{12-6\sqrt{3}} \approx 1.27 \tag{8.177}$$

where

$$t_p f_{peak\,G95LE}(Hz) = \frac{\sqrt{12-6\sqrt{3}}}{2\pi} \approx 0.2 \tag{8.178}$$

As in B55 deflagration, the effective pulse period is greater than the lifetime, with

$$\tau_{s\,G95LE} = \frac{2\pi}{\omega_p t_p} \approx 5. \tag{8.179}$$

The total exposure is

$$xE_{G95LE} \approx \left[\frac{t_p p_p^2}{2}\right] 1.7. \tag{8.180}$$

As with the G95HE pulse, the secondary oscillation permits a higher amplitude negative phase excursion and yields a substantially larger exposure than the previous pulses. It is possible that secondary oscillations may help shape the amplitude and duration of the asymptotic blast pulses, and can balance the impulse over the longer lifetime of the pulse.

8.4 Synthesis

This section distills the detonation and deflagration pulses into a set of readily computable parameters that can be used for automatic signature feature extraction and blast identification. In the near and intermediate fields, a fast rise time and high overpressure may be a sufficient trigger for the initialization of blast pulse parameterization and scaling. In the far field, the observed signals will be distorted by propagation paths and only some of the defining source parameters may survive.

Table 8.2 Primary parameters for the impulse-balanced blast pulses with continuous derivatives past the onset

	p_p/p_n	τ_n	M_1	M_2	$\mathcal{G}$
Detonation					
TRI	2.000	2.000	1.00	1.00	1.00
GT	2.756	2.449	1.00	0.95	1.13
R77	3.303	2.571	0.90	0.78	1.28
G95	4.857	5.828	0.79	0.64	0.83
F46	7.389	6.283	0.74	0.50	1.18
Deflagration					
G95	1.760	2.732	1.21	1.71	0.64
B55	2.903	2.000	1.17	1.18	1.45

Table 8.3 Blast parameters for scaled time

	τ_e	τ_s	τ_{rise}	τ_{min}	$\tau_{d\ re\ tn}$
Detonation					
TRI	3.00		0	1.500	0.25
GT	3.45	4.0	0	1.816	0.33
R77	3.57	4.5	0	1.950	0.37
G95	6.83	7.6	0	2.165	0.20
F46	7.28	6.3	0	2.000	0.16
Deflagration					
G95	3.73	5.0	0.328	1.809	0.30
B55	3.00	4.4	0.293	1.707	0.35

The blast parameters for the continuous impulse-balanced pulses are summarized in Tables 8.2 and 8.3, where the pulses are ordered relative to the reference overpressure to underpressure ratio of 2. These balanced pulses have at most two free parameters. The traditional input parameters are the peak overpressure and the positive phase duration. However, for a specified blast wave template, the positive (or negative) impulse or exposure could be readily used as a replacement for either of them. The triangular and hybrid modified Friedlander pulses may also accept a third parameter, which could be the waveform parameter (positive or negative) or the impulse, to define the pulse shape at the expense of introducing slope discontinuities at the splice point. The physics-based requirement of impulse balance, coupled with the specification of a continuous slope, reduces the free variables back to two.

The parameters in Tables 8.2 and 8.3 use the skeletal triangular approximation to the blast pulse as a template for defining the reference scales. The slope balanced G17HE pulse, referred to as the GT pulse, has the closest cumulative parameter match to the reference template, with the R77 coming in as a close contender. The G95HE pulse provides insight on the effects of an oscillating coda, which could reduce the spectral peak frequency by nearly an octave. This could overestimate the yield by a factor of ~8. The F46 Friedlander pulse is an elegant benchmark for testing other reference pulses, but should not be expected to match the negative phase properties of real blasts.

The canonical Brode and G95LE pulses, which may be considered as representative of low explosive (LE) deflagrations rather than HE detonations, introduce the least slope discontinuities and have a less abrupt onset. Although historically only used for matching the negative pulse duration, their gentler onsets can make them useful for reducing Gibbs ringing in digital systems as well as for modeling other types of transients. The deflagration pulses are presented as detonation counterexamples (*not* detonations), with slow rise times and scaled first moments exceeding unity. As mentioned in earlier sections, it may be difficult to recognize HE detonations from LE deflagrations in the far field due to propagation-induced signal distortion.

Table 8.4 evaluates the temporal blast parameters predicted for 1 tonne of TNT at a range of 1 km (and its equivalent, as shown in Table 8.1), which is recommended as a reference scaled range for infrasound applications.

The triangular template is only intended for illustration: any signature template can be used to scale the first, second, or higher moments, as well as any other parameters that may facilitate signal identification. In this study, the GT pulse could replace the triangular template without dramatically altering the scaled first and second-moment reference metrics. First and second moments can be promptly estimated from data through the numerical integration of the absolute pressure and squared pressure within a specified window. A statistical specification of salient signature features, attached to standardized, transportable, and scalable metrics, should facilitate rapid and robust automatic signal classification. The representative 2 kt Minor Uncle shocked blast pulse, the Friedlander (1946) canonical, and the G17HE (GT) pulses are shown in Fig. 8.6 to illustrate potential improvements in signature feature similarity.

Table 8.4 Blast parameters for a positive pulse duration of 0.04 s = 40 ms for 1 tonne of TNT

	t_p (ms)	t_n (ms)	t_e (ms)	t_s (ms)	f_s (Hz)
Detonation					
TRI	40	80	120		
GT	40	98	138	160	6.3
R77	40	103	143	180	5.6
G95	40	233	273	303	3.3
F46	40	251	291	251	4.0
Deflagration					
G95	40	109	149	198	5.0
B55	40	80	120	178	5.6

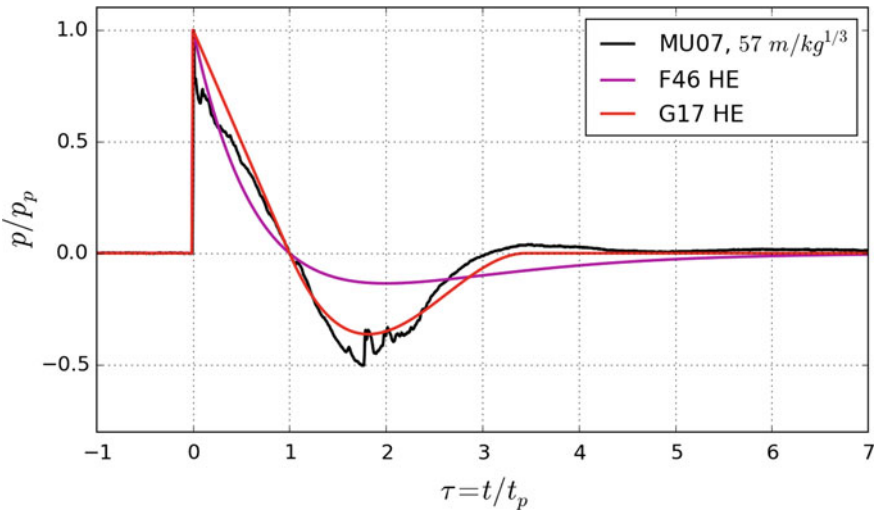

Fig. 8.6 Comparison between a representative 2 ktonne blast waveform, the Friedlander (1946) blast pulse, and the G17HE (GT) detonation pulse. The GT pulse does not capture the curvature of the positive phase duration, but it has a closer similarity to the total pulse. The theoretical pseudo period of the GT pulse is $4t_p$

8.4.1 Some Practical Considerations

A recurrent challenge in recording shocked blast signatures is capturing the rapid rise time from the ambient levels to the peak overpressure. This abrupt, discontinuous pressure jump is not captured well with most sensors and data acquisition systems unless they are specifically designed to do so. The rise time can be on the order of milliseconds to microseconds, depending on the mass and type of explosive. In digital data acquisition systems and computer models, it is very easy to undersample the rise time and miss the peak pressure value. For any given digital system, the minimum rise time that can be observed is the sample interval (the inverse of the sample rate), and the observed peak shock pressure will depend on how the analog and digital recording systems handle steep nonlinear inputs. The sample rate also defines the passband of the analysis. The spectral peak for the GT pulse, with pseudo period $\tau_{sGT} = 4$ (Table 8.3), will be at

$$f_{sGT} = \frac{1}{4t_p} \tag{8.181}$$

and the sample rate should be substantially higher than the peak frequency. However, in the far field, the dominant period is likely to be longer due to linear and nonlinear propagation effects. Proper data acquisition systems and signal processing algorithms will apply an anti-aliasing filter before the Nyquist frequency, so the

effective bandwidth will be less than one half of the sample rate. The duration of the analysis record sets the spectral resolution, and should also be selected carefully relative to the target yield.

Some signals will be recorded with sensors and data acquisition systems that may not have a flat frequency response in the signal bandpass (e.g., Garcés 2014). The effects of a recording systems frequency response on blast metrics can be investigated numerically by applying the sampling rates and filters present in field recordings to representative theoretical functions embedded in noise models. The reader is strongly encouraged to compute the discrete Fourier transform or wavelet transform of the exact source pressure functions provided herein, as well as invert the exact Fourier transforms to the time domain, to perform sensitivity studies and quantify measurement uncertainties prior to the collection, analysis, and interpretation of digital data.

8.4.2 Standard Blast

As the blast shock moves away from its origin, it transitions to a weakened state where its overpressure is a small fraction of the ambient barometric pressure, its amplitude decays as the inverse of distance, and it propagates at acoustic velocities. Although clearly shocked and obviously nonlinear, the blast pulse is sometimes treated as approximately linear and used as input for propagation models (e.g., Vergoz et al. 2013). Theoretical predictions (e.g., Miles 1967; Bethe et al. 1958) and the KG85 tables suggest that stable expressions may be estimated for HE and NE blasts in a scaled range when the weakly shocked pulse can almost be treated as linear. Although such an idyllic state does not exist, this useful fiction can be helpful in understanding and modeling blasts at large ranges.

Kim and Rodgers (2016, 2017) observed a reasonable fit to the KG85 tables for scaled ranges <50 m/kg$^{1/3}$, with substantial deviations above 100 m/kg$^{1/3}$. Selected blast pulse parameters and scaling relations for explosives are presented in Appendix 4. The variability of the KG85 scaled impulse for HE shown in Fig. 8.8 increases substantially past 100 m/kg$^{1/3}$. Both the HE and NE pressure and time ratios shown in Fig. 8.13 approach stable, near-constant values closer to 100 m/kg$^{1/3}$. Based on the asymptotic behavior of the KG85 solutions and the observations of Kim and Rodgers (2016), this work proposes a reference distance of 100 m/kg$^{1/3}$ for HE and NE. This scaled distance is also recommended because of the relative ease of applying power scaling relations to factors of ten (Table 8.1).

In principle, a 1 tonne blast observed at 1 km would propagate somewhat like an acoustic pulse that could be reasonably represented by the intermediate-range parameters in the KG85 tables. The equivalent scaled range would be Z = 100 m/kg$^{1/3}$, and the scaled positive pulse duration would be 0.042 s. The scaling relations are evaluated at 1 km for a reference yield of 1 tonne (1000 kg) of TNT, and are shown in Table 8.4 referenced to the standard atmosphere at sea level. The peak GT frequency for 1 ton at 1 km is ~6.3 Hz, which places it at the upper limit of the

0.02–8 Hz detection passband of the International Monitoring System. A ½ tonne blast would yield the same pressure at a range drop of 1/3 octave (800 m) with a corresponding pulse duration drop equivalent to a one-third octave rise to 8 Hz. The standardized 1/3 octave band scaling proposed by Garcés (2013) is a natural fit to the Sach's scaling laws for blast pulses.

The relations in Appendix 4 show that the asymptotic ratio of the overpressure to the underpressure for HE and NE is approximately 2 for both cases (HE ~ 2.4, NE ~ 1.8). The published ratio of the asymptotic negative to positive pulse durations for HE is ~3, whereas for NE it is ~2. In contrast to the KG85 tables, the ANSI standard does not show a stabilization of the positive and negative durations at large ranges, although they agree in the overpressure estimates. This work adheres to KG85 and uses the ANSI time duration ratios to estimate the asymptotic underpressure duration. Recent work by Schnurr et al. (2017) suggests that the observed ratio between the negative and positive phase duration is close to 2.

The aim of this chapter is to demonstrate how the various canonical shape functions can be used to fit blast pulses, and nominal values of the pressure and phase duration ratios will suffice to meet that aim. Tables 8.5, 8.6, and 8.7 summarize the nominal blast pulse values derived from the various scaling relations developed in Appendix 4.

Table 8.5 Predicted blast pressures for 1 tonne HE and NE at 1 km (Appendix 4)

	KG85 p_p, Pa	p_n, Pa	p_p/p_n	Rounded p_p/p_n
HE	840.0	349.8	2.4	2
NE	503.2	263.3	1.9	2

Table 8.6 Predicted phase durations for 1 tonne HE and NE at 1 km (Appendix 4)

	KG85 t_p, s	Published t_n/t_p	Rounded t_n/t_p	Averaged NE and HE
HE	0.04203	3.31	3	2.58
NE	0.0568	1.85	2	2.58

Table 8.7 Nominal Blast Pulse Specifications for 1 tonne HE at 1 km, rounded to 1/3 octave bands. Note the peak pressure has the same precision as KG85 Table XI

p_p, Pa	p_p/p_n	t_p (s)	t_s (s)	f_s (Hz)
800	2	0.04	0.16	6.3

8.4.3 Blast Magnitudes

There are various classic metrics used for characterizing transients. In the presence of noise or complex waveforms, many of these metrics can be challenging to implement. The simplest metric is the peak pressure, which is usually large and dominant near the source. The peak pressure may not be robust at large measurement ranges where the peak signal amplitude is commensurate with the noise. It is easy to miss the peak overpressure when digitizing sharp transients, or to remove analog and digital recording system artifacts. Where the pulse shape can be clearly separated into positive and negative phases, the impulse can be a more stable measure as it takes into account the total area under the positive portion of the pulse. The next useful metric is the exposure of a pulse, defined as the integral of the pressure squared over a window. This metric is often represented as a sound pressure level in decibels. Both the impulse and the exposure can be rapidly estimated from integration of the pressure or its variance over a window.

The far-field energy flux of finite amplitude shock across a unit area of a fixed surface normal to the direction of propagation is estimated by Eq. 7.4 of Cole (1948)

$$\frac{E}{4\pi R^2} = \frac{1}{\rho c}\int_0^t p^2(t')dt' + \frac{1}{\rho R}\int_0^t p(t)\left[\int_0^{t'} p(t)dt\right]dt'. \tag{8.182}$$

The first term is a measure of the work performed by the shock. The second term is a measure of noncompressive effects and is expected to be negligible over the duration of the pulse with increased time and distance. The two terms decay differently in range and time and are indicative of the rates of work performed by the shock wave and the slower mass-dominated noncompressive flow. Although both integrals can be evaluated exactly for all the pulses presented in this chapter, this is beyond the scope of this work. In the far field, the blast energy, in Joules, or yield in tonnes, could be estimated from the second moment over the pulse lifetime

$$\frac{E}{E_0} = \frac{R^2}{R_0^2}\frac{xE}{xE_{ref}} = \frac{R^2}{R_0^2}M_2 = \frac{2R^2\int_0^{t_e}|p(t)|^2dt}{t_{p0}\left(p_{p0}R_0\right)^2}. \tag{8.183}$$

The concept of a distance-independent infrasonic magnitude is useful. Stevens et al. (2002) review various logarithmic yield relations in the context of estimating global infrasound network detection thresholds at large distances. They address 6 kiloton to 58 megaton nuclear yields from Soviet tests and introduce infrasound magnitudes for acoustic and Lamb waves. Ens et al. (2012) also provide an overview of yield relations useful for meteor studies. Here, I address the relatively early stages of the weak shock when the overpressure and positive phase duration are predictable, the yield-scaled positive pulse duration is nearly constant, and the pressure decays as the inverse of range. In this very specific situation, a logarithmic acoustic magnitude scale referenced to 1 kg at 100 m, with $t_{p0} = 0.004$, $p_{p0} = 800\,\text{Pa}$, could be readily estimated from

$$M_A \approx log_{10}\left[\frac{t_p\left(p_pR\right)^2 M_2}{(0.004\,\mathrm{s})(800\,\mathrm{Pa}\times 10^2\,\mathrm{m})^2}\right] \tag{8.184}$$

where the magnitude is zero at the reference yield and increments by one for each order of magnitude increase in yield. The influence of geometric spreading is included in the $\left(p_pR\right)$ term, which works only when $p_p \sim 1/R$. However, as long as the pressure can be traced back to the reference range so that it remains nearly constant when it is range-corrected, then energy would remain proportional to the squared amplitude and can be represented by a magnitude relation of a similar form. Note there is a hidden $W^{2/3}$ term in this expression. From Table 8.1, a 1 tonne blast at a range of 1 km would yield $M_A = 3$. Similarly, a 1 ktonne atmospheric blast observed at a range of 10 km would return $M_A = 6$. The second moment M_2 is a measure of the relative efficiency of the pulse, and could also be used as correction factor for different types of explosives.

If the positive phase duration is well-defined and the impulse is better constrained than the peak pressure, it is also possible to use the impulse with

$$t_p\left(p_pR\right)^2 = \frac{4}{t_p}\left(\left[\frac{t_pp_p}{2}\right]R\right)^2 \approx \frac{4}{t_p}\left(\frac{I_pR}{M_1}\right)^2. \tag{8.185}$$

When the pulse parameters of an observed blast match those of the reference blast template, the first and second moments should be close to unity.

The possibility of using the pseudo time or spectral peak for magnitude estimates is practical as these quantities may be more readily accessible for distal observations. Ens et al. (2012) discuss the AFTAC period-yield relations developed from observations of surface nuclear shots at ranges of 1,300–8,500 km. The far-field dominant period $t_{s\,far}$ in seconds is used to estimate the nuclear yield from

$$log_{10}\left(\frac{W_{NE}}{1\,kt\,NE}\right) = 3.34\,log_{10}\left(t_{s\,far}\right) - 2.58,\; W_{NE} < 100\,kt. \tag{8.186}$$

This can be rewritten as

$$\frac{W_{NE}}{1\,kt\,NE} = \left(\frac{t_{s\,far}}{5.92\,\mathrm{s}}\right)^{3.34} \tag{8.187}$$

which is very close to Sach's yield scaling for time. Explicit in this expression is an asymptotic pseudo period of 5.92 s for 1 kt NE (~0.17 Hz spectral peak). Using the GT relation for the pseudo period t_s and the predicted positive phase duration $t_{p\,NE}$ in Table 8.6 for 1 kt NE at 10 km (scaled from 1 tonne NE at 1 km),

$$t_{s\,GT\,re\,1\,kt\,NE} = 4\,t_{p\,NE} = 4 \times 0.57\ \text{s} = 2.3\ \text{s} \tag{8.188}$$

which would correspond to a spectral peak of 0.44 Hz. The yield in the far field can also be estimated from the dominant period with

$$\frac{W_{NE}}{1\,kt\,NE} = \left(\frac{t_{s\,far}}{2.6\,t_{s\,GT\,re\,1\,kt\,NE}}\right)^{3.34} \tag{8.189a}$$

which would correspond to a lengthening by a factor of ~2.6 of the effective pseudo period from 2.3 to 5.92 s (or a reduction of the spectral peak f_s from 0.44 to 0.17 Hz) with increasing range. This could be generalized as

$$\frac{W}{W_{ref}} = \left(\frac{t_{s\,far}}{2.6\,t_{s\,GT\,ref}}\right)^{3.34}. \tag{8.189b}$$

As an example, for 1 kg HE at 100 m (Table 8.7) one can use nominal values of $t_p = 0.004$ s, $t_{s\,GT} = 0.016$ s $(f_{s\,GT} = 63\ \text{Hz})$ to express the far-field relation as

$$\frac{W}{1\ \text{kg HE}} = \left(\frac{t_{s\,far}}{0.0416}\right)^{3.34}. \tag{8.189c}$$

A far-field blast signature with a spectral peak at 16 Hz and a corresponding pseudo period of 0.0625 s would have an estimated yield of ~4 kg HE.

Different pulses would scale according to the $\tau_s = \frac{t_s}{t_p}$ ratio shown in Table 8.3. The G95HE pulse with $\frac{t_s}{t_p} = 7.6$ has the longest pseudo period due to its extended coda, with

$$\frac{W}{W_{ref}} = \left(\frac{t_{far}}{1.4\,t_{s\,G95HE\,ref}}\right)^{3.34}. \tag{8.190}$$

The Friedlander pulse demonstrated that the negative phase of a blast pulse can define its spectral peak. The rescaling of the AFTAC relation in this section suggests that the whole blast pulse—not only its positive phase—influences the dominant period at long ranges, and quantifying its evolution could improve yield estimates.

Acknowledgements I am thankful to D. R. Russell for his generous assistance in sorting through the blast literature and for sharing code and papers. D. Green contributed a careful and constructive review, with key corrections, and R. Reinke kindly shared the Distant Image and Minor Uncle data and origin information, as well as his expertise in blast measurements. I am also grateful to A. Rodgers and K. Kim for mission context. Many thanks to J. Schnurr for assisting in the digitization and interpolation of legacy published curves, and B. Williams for his helpful comments. This work was supported by the Consortium for Verification Technology under Department of Energy National Nuclear Security Administration Award DE-NA0002534.

Appendix 1. A Moment or Two

Practical explosion source pressure functions often take the form

$$p(\tau) = \frac{p(\tau_{ref})}{f_i(\tau_{ref})} f_i(\tau) \tag{8.191}$$

where τ_{ref} is generally the scaled time of the peak overpressure or underpressure and τ is the scaled time referenced to the positive pulse duration t_p,

$$\tau = \frac{t}{t_p}. \tag{8.192}$$

The magnitude of the derivative at the onset time and first zero crossing can be readily evaluated from

$$\frac{dp_i(t)}{dt} = \frac{1}{t_p}\frac{dp_i(\tau)}{d\tau}. \tag{8.193}$$

Likewise, integration over time may be represented as

$$\int_0^{t_p} p\left(\frac{t}{t_p}\right) dt = \left(t_p p_p\right) \int_0^1 \frac{p(\tau)}{p_p} d\tau \tag{8.194}$$

$$\int_0^{t_p} \left[p\left(\frac{t}{t_p}\right)\right]^2 dt = \left(t_p p_p^2\right) \int_0^1 \left[\frac{p(\tau)}{p_p}\right]^2 d\tau. \tag{8.195}$$

The Fourier Transform pair used in this work is

$$P(j\omega) = \int_{-\infty}^{\infty} p(t) e^{-j\omega t} dt = t_p p_p \int_{-\infty}^{\infty} \left[\frac{p(\tau)}{p_p}\right] e^{-j(\omega t_p)\tau} d\tau \tag{8.196}$$

$$p(t) = \frac{1}{2\pi} \int_{-\infty}^{\infty} P(j\omega) e^{j\omega t} d\omega. \tag{8.197}$$

Note that all the pulses in this chapter vanish for negative time, so only the positive time interval contributes to the Fourier transform. It is very easy to add an unnecessary factor of two if this is not taken into account.

The total impulse I of a balanced pulse must satisfy,

$$I_1 = \int_0^{\infty} p_1(t) dt = P_1(j\omega = 0) = 0. \tag{8.198}$$

This is equivalent to a vanishing fist moment. Due to difficulties in capturing the peak pressure and rise time, the positive impulse—the integral over time of the positive phase of a recorded waveform—has been traditionally used as a fairly robust metric for explosions. The scaled first moment M_{1p} of the positive phase can be expressed in terms of a reference positive impulse, the overpressure p_p, and the positive phase duration t_p as

$$I_{\mathrm{p}} = \int_0^{t_p} p(t)dt = \left(t_p p_p\right) \int_0^1 \left[\frac{p(\tau)}{p_p}\right] d\tau \tag{8.199}$$

$$M_1 \equiv \frac{2I_{\mathrm{p}}}{t_p p_p} = 2\int_0^1 \left[\frac{p(\tau)}{p_p}\right] d\tau. \tag{8.200}$$

Parseval's Theorem provides a measure of the signal exposure xE

$$xE = \int_{-\infty}^{\infty} |p(t)|^2 dt = \int_{-\infty}^{\infty} |P(f)|^2 df = \frac{1}{2\pi}\int_0^{\infty} S(\omega)d\omega \tag{8.201}$$

where S is the unilateral energy spectral density in $\mathrm{Pa}^2/\mathrm{Hz}^2$. The expression for the total signal exposure has units of Pa^2 s and is a measure of the total energy in the signal. The exposure can be readily converted to decibels with the selection of an appropriate reference value (e.g., Garcés 2013). For finite pulses with a clear onset at zero time, the scaled second moment M_2 can be expressed as

$$xE = \int_0^{\infty} |p(t)|^2 dt = \left(t_p p_p^2\right) \int_0^{\infty} \left[\frac{p(\tau)}{p_p}\right]^2 d\tau \tag{8.202}$$

$$M_2 \equiv \frac{2xE}{t_p p_p^2} = 2\int_0^{\infty} \left[\frac{p(\tau)}{p_p}\right]^2 d\tau \tag{8.203}$$

These definitions are a factor of two larger than the formal mathematical expressions for the first and second moments of normalized functions so that they can be scaled relative to the impulse and exposure of a reference triangular pulse approximation. Normalization by the second moment is generally required for the construction of wavelets. Scaled first moments for the positive phase and total second moments for the balanced canonicals are provided below.

The impulse-balanced triangular approximation for $\frac{p_p}{|p_n|} = 2$ is used as the reference impulse and exposure, where

$$M_{1\,\Delta} = 2\frac{1}{2} = 1, \tag{8.204}$$

$$M_{2\,\Delta 2} = 2\frac{1}{2} = \frac{2}{3} + \frac{1}{3} = 1, \tag{8.205}$$

with ~67% of the energy in the positive phase and a non-negligible 33% in the negative phase. The G17 pulse has a close match to the selected blast reference, with

$$M_{1\,G17HE} = 2\frac{1}{2} = 1 \tag{8.206}$$

$$M_{2\,G17HE} = 2\left(\frac{1}{3} + \frac{2\sqrt{6}}{35}\right) \approx \frac{2}{3} + 0.140 \approx 0.95. \tag{8.207}$$

and a similar distribution in power, as is expected since the G17 pulse uses the triangular approximation for the positive phase. The balanced Friedlander delivers about half of the power as the G17, with

$$M_{1\,F46HE} = 2e^{-1} \approx 0.74 \tag{8.208}$$

$$M_{2\,F46HE} = 2\frac{1}{4} = 0.5. \tag{8.209}$$

The modified Friedlander positive moment is provided for completeness

$$M_{1\,MF} = 2\left[\frac{\alpha_p + 1 + e^{-\alpha_p}}{\alpha_p^2}\right]. \tag{8.210}$$

The G95HE pulse slightly improves over the F46 in terms of power, and begins to show the contributions from the negative phase,

$$M_{1\,G95HE} = 2\frac{1}{\sqrt{2}}e^{\sqrt{2}-2} \approx 0.79 \tag{8.211}$$

$$M_{2\,G95HE} = 2\frac{3\left(2+\sqrt{2}\right)}{32} \approx 0.64. \tag{8.212}$$

The Reed (1977) pulse begins to resemble the positive triangular pulse and takes another step up in power delivery

$$M_{1\,R77HE} = 2\frac{34,992}{78,125} \approx 0.9 \tag{8.213}$$

$$M_{2\,R77HE} = 2\frac{8,440}{21,609} \approx 0.78, \tag{8.214}$$

although it is not as efficient as the G17 pulse. The deflagration pulses are not expected to match the detonation criteria, and the differences can be immediately observed in the scaled first and second moments.

$$M_{1\,B55LE} = 2\left(1+\sqrt{2}\right)e^{-\sqrt{2}} \approx 1.17 \tag{8.215}$$

$$M_{2\,B55LE} = 2\frac{\left(3+2\sqrt{2}\right)}{32}e^{4-2\sqrt{2}} \approx 1.18. \tag{8.216}$$

The area under the curve is larger, and thus these pulses have a greater scaled positive impulse as well as a larger exposure. deflagration pulses are generally not as destructive as detonations because of their slower rise times. Finally, the large negative phase of the G95LE, coupled with the broad concave-downwards first phase, yields

$$M_{1\,G95LE} = 2\frac{3+2\sqrt{3}}{3}e^{\sqrt{3}-3} \approx 1.21 \tag{8.217}$$

$$M_{2\,G95LE} = 2\frac{123+71\sqrt{3}}{288} \approx 1.71, \tag{8.218}$$

with almost double the exposure as the reference blast.

Appendix 2. Modified Friedlander Pulse Properties

The Hybrid Modified Friedlander equation implements different exponential decay parameters for the positive and negative phases of the blast pulse,

$$p_{1p} = p_p f\left(\tau, \tau_0, \alpha_p\right)/max(f) \quad for \quad 0 < \tau \leq 1 \tag{8.219}$$

$$p_{1n} = |p_n| f(\tau, \tau_0, \alpha_n)/|min(f)| \quad for \quad \tau \geq 1 \tag{8.220}$$

$$\tau = t/t_p \tag{8.221}$$

where p represents overpressure, p_p is the maximum blast pressure (peak overpressure), p_n is the minimum blast pressure (peak underpressure), t represents time, t_p is the positive pulse duration, with $\tau = 1$ at $t = t_p$, and waveform parameters α_p and α_n are implemented for the positive and negative phases of the pulse, respectively.

The peak overpressure is as specified with p_p, but the peak underpressure must be corrected by

$$\tau_{min} = 1 + \frac{1}{\alpha_n}, \quad f_1(\tau_{min}) = \frac{e^{-(1+\alpha_n)}}{\alpha_n}. \tag{8.222}$$

The negative Friedlander pulse e-folding time, or lifetime is *defined* as the time where the *negative* pressure reduces to 1/e of its (minimum) value. By defining the negative pulse duration as

$$\frac{t_n}{t_p} = \frac{2\pi}{\alpha_n} \tag{8.223}$$

the pulse lifetime is

$$t_e = t_p + t_n = t_p + \frac{2\pi t_p}{\alpha_n} \tag{8.224}$$

$$\tau_e = \frac{t_e}{t_p} = 1 + \frac{2\pi}{\alpha_n} = \tau_{min} + \frac{2\pi - 1}{\alpha_n}, \tag{8.225}$$

where

$$\frac{|p_{1n}(\tau_e)|}{|p_n|} \approx \frac{2e^{-3}}{\pi} \approx 0.032 \sim e^{-1}. \tag{8.226}$$

As can be readily verified, a Friedlander pulse with $\alpha_n \geq 2\pi$ has a rapidly decaying negative pulse with a negative duration that is shorter than the positive pulse duration t_p.

For the special case of the balanced Friedlander, where $\alpha_n = 1$

$$t_n(\alpha = 1) = 2\pi\, t_p. \tag{8.227}$$

Applying different waveform parameters and pressures in the positive and negative phases introduces an artificial and unsightly discontinuity in the derivative at the first zero crossing

$$\left.\frac{dp_{1p}}{dt}\right|_{t=t_p} = -\frac{p_p}{t_p} e^{-\alpha_p} \tag{8.228}$$

$$\left.\frac{dp_{1n}}{dt}\right|_{t=t_p} = -\frac{|p_n|\alpha_n}{t_p} e^{1}. \tag{8.229}$$

Exact (unscaled) first and second moment expressions for the positive and negative components of the Friedlander pulse, where $f_{1p,n} = f_{F46HE}(\alpha_p, \alpha_n)$, are

$$\int_0^1 f_{1p}(\tau) d\tau = \frac{e^{-\alpha_p} + \alpha_p - 1}{\alpha_p^2} \tag{8.230}$$

$$\int_1^{\infty} f_{1n}(\tau)d\tau = \frac{-e^{-\alpha_n}}{\alpha_n^2} \tag{8.231}$$

$$\int_0^1 f_{1p}^2(\tau)d\tau = \frac{2\alpha_p^2 - 2\alpha_p + 1 - e^{-2\alpha_p}}{4\alpha_p^3} \tag{8.232}$$

$$\int_1^{\infty} f_{1n}^2(\tau)d\tau = \frac{e^{-2\alpha_n}}{4\alpha_n^3} \tag{8.233}$$

and the Fourier transforms for the positive and negative phases are

$$P_{1p} = \int_0^{t_p} p_{1p}(t)e^{-j\omega t}dt = \frac{p_p t_p}{\alpha_p^2 h_p^2}\left(\alpha_p h_p - 1 + e^{-\alpha_p h_p}\right) \tag{8.234}$$

$$P_{1n} = \int_{t_p}^{\infty} p_{1n}(t)e^{-j\omega t}dt = -\frac{|p_n|t_p}{\alpha_n h_n^2}e^{(1+\alpha_n)}e^{-\alpha_n h_n} \tag{8.235}$$

where

$$h_{p,n} = 1 + \frac{j\omega t_p}{\alpha_{p,n}}. \tag{8.236}$$

Note that the impulse is the Fourier transform evaluated at the zero (DC) frequency.

Appendix 3. Modified Brode Pulse

The canonical B55 pulse can be expressed as

$$f_2 = \tau(1-\tau)e^{-2\alpha\tau}, \tag{8.237}$$

with slope at its zero crossing of

$$\left.\frac{df_2}{d\tau}\right|_{\tau=1} = -e^{-2\alpha}. \tag{8.238}$$

Its extrema are at

$$\tau_{max} = \frac{(\alpha+1) - \sqrt{\alpha^2+1}}{2\alpha}, \tag{8.239}$$

$$\max(f_2) = f_2(\tau_{max}) = \frac{\left(\sqrt{(\alpha^2+1)}-1\right)\exp\left[-(\alpha+1)+\sqrt{\alpha^2+1}\right]}{2\alpha^2}, \tag{8.240}$$

$$\tau_{min} = \frac{(\alpha+1)+\sqrt{\alpha^2+1}}{2\alpha}, \tag{8.241}$$

$$\min(f_2) = f_2(\tau_{min}) = -\frac{\left(\sqrt{(\alpha^2+1)}+1\right)\exp\left[-(\alpha+1)-\sqrt{\alpha^2+1}\right]}{2\alpha^2}. \tag{8.242}$$

The impulse is obtained from

$$I_{2p} = \int_0^{t_p} p_2(t)dt = \frac{t_p p_p}{max(f_2)} \int_0^1 f_2(\tau)d\tau, \tag{8.243}$$

$$I_{2n} = \int_{t_p}^{\infty} p_2(t)dt = \frac{-t_p|p_n|}{|min(f_2)|} \int_1^{\infty} f_2(\tau)d\tau. \tag{8.244}$$

The explicit solutions for the impulse are

$$I_{2p} = t_p p_p \frac{(\alpha\cosh\alpha - \sinh\alpha)exp\left[\left[1-\sqrt{\alpha_p^2+1}\right]\right]}{\alpha_p\left(\sqrt{\left(\alpha_p^2+1\right)}-1\right)}, \tag{8.245}$$

$$I_{2n} = -t_p|p_n|\frac{(\alpha_n+1)exp\left[1-\alpha_n+\sqrt{\alpha_n^2+1}\right]}{2\alpha_n\left(\sqrt{(\alpha_n^2+1)}+1\right)}. \tag{8.246}$$

One possible hybrid pulse can use the *negative* Brode pulse for the underpressure to balance the modified Friedlander overpressure, requiring the numerical solution of

$$\frac{\bar{p}_p}{\bar{p}_n}M_1 = \frac{(\alpha_n+1)exp\left[1-\alpha_n+\sqrt{\alpha_n^2+1}\right]}{\alpha_n\left(\sqrt{(\alpha_n^2+1)}+1\right)} \tag{8.247}$$

I follow Brode (1955) and Bonner et al. (2013) in using the B55 pulse as a fitting function for the negative phase of the pulse with duration t_n, where

$$\tau_B = \frac{t-t_p}{t_n} \tag{8.248}$$

$$p_{Bn} = -\frac{|p_n|}{\max(f_2)}\tau_B(1-\tau_B)e^{-2\alpha_n\tau_B}, \quad 0 \le \tau_n \le 1. \tag{8.249}$$

To facilitate evaluation relative to the same standardized time scale t_p, let

$$\tau_n = \frac{t_n}{t_p} \tag{8.250}$$

$$\tau_B = \frac{\tau - 1}{\tau_n} \tag{8.251}$$

$$p_{Bn} = -\frac{|p_n|}{\max(f_2)}\left(\frac{\tau-1}{\tau_n}\right)\left(\frac{\tau_n+1-\tau}{\tau_n}\right)e^{-2\alpha_n\frac{\tau-1}{\tau_n}}, \quad 1 \le \tau \le 1+\tau_n \tag{8.252}$$

Brode (1955) and Bonner et al. (2013) use a value of $\alpha_n = 2$ to fit the negative phase of explosion blasts, with solution

$$p_{Bn} = -|p_n|\frac{13.894}{\tau_n^2}(\tau-1)(1+\tau_n-\tau)e^{-4\frac{\tau-1}{\tau_n}}, \quad 1 \le \tau \le 1+\tau_n \tag{8.253}$$

$$I_{Bn} \approx \frac{-t_n|p_n|}{2.2} \tag{8.254}$$

The hybrid curve fits shown in Fig. 8.7 introduce another discontinuity at the zero crossing, where the canonical Brode function would have otherwise smoothly continued its oscillation. The solutions for the Friedlander-Brode hybrids are rather similar to the Friedlander hybrids, and may not warrant the extra effort in most situations.

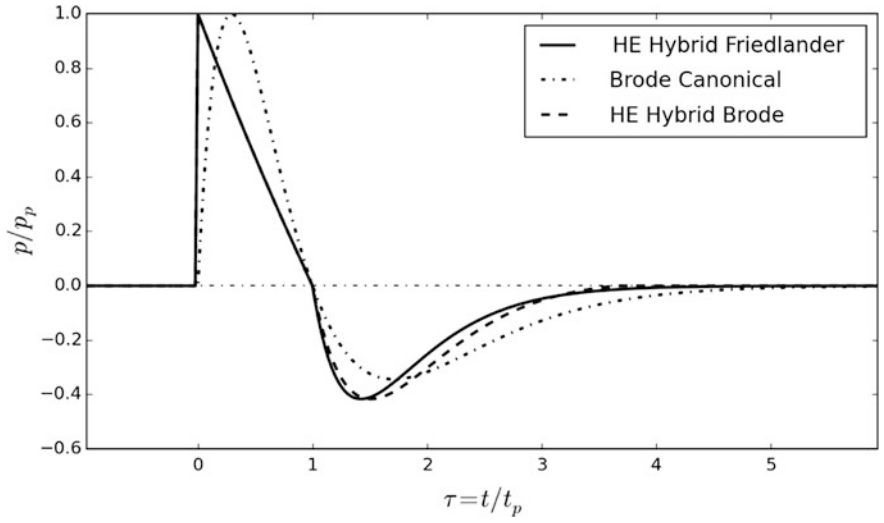

Fig. 8.7 Comparison of Friedland (solid line) and Friedland–Brode (dashed line) hybrid, with similar slope discontinuities. The canonical balanced B55 pulse is shown for comparison

Appendix 4. Selected Positive and Negative Pulse Properties for Detonations

This section uses the Kinney and Graham (1985) tables and formulas as a starting point, as they are a time-tested and often quoted standardized set of metrics that are available in the open literature. The aim of this chapter is to provide a family of fitting function with methods that are transparent, reproducible, and transportable to blast data sets that can provide two key parameter pairs: the peak overpressure and underpressures, and the positive and negative phase durations (or their ratios). Since it can be challenging to accurately capture the peak pressures when the rise times are fast, the impulse—the pressure integrated through time—can be a more robust metric and could substitute the peak overpressure. It is generally possible to estimate the overpressure from the impulse of Friedlander-type positive phases. As suggested in the main chapter, it may also be useful to consider secondary pulses when estimating pulse lifetimes as they can elongate the negative phase. Secondary pulses may help recognize single-charge high explosive (HE) from nuclear (NE) surface blasts (e.g., Gitterman 2013). Another useful parameter that could be better documented is the observed rise time (referenced to the data collection system's sample interval and passband) from ambient to peak pressure. The rise time could be a useful discriminant for detonations and deflagrations at short ranges, as well as assist in identifying propagation effects at longer ranges.

Kinney and Graham (1985) and ANSI S2.20 (1983) Relations for Detonations

Kinney and Graham (1985), hereafter referred to as KG85, build their equations on Hopkinson scaling from World War I and Sachs scaling from World War II, which encapsulate the hydrodynamics of explosions near the source. It is important to recognize that KG85 assumes a modified Friedlander blast pulse shape for the positive phase. They tabulate key blast parameters for both HE and NE using consistent metric units and provide useful expressions that behave almost linearly at large ranges with acoustic propagation velocities and finite amplitudes with inverse range pressure scaling. Table 8.8 summarizes the reference values used in this chapter.

Some tabulated parameters and functional relations for blast waves are also provided by ANSI S2.2 for 1 ktonne NE. The pertinent values extending beyond the KG85 tables are also rescaled to 1 kg NE and presented in Table 8.9.

The peak overpressure at 10 km from 1 ktonne NE is predicted to be the same as would be measured at 1 km from 1 tonne NE, or at 100 m from 1 kg NE.

There are issues with most published tabulated blast values and equations, and KG85 is no exception. Amongst the issues in the KG85 tabulated values are formulas, which are given as follows:

Table 8.8 Reference values for blasts

US standard atmosphere (1976) sea level (0.0 m)		
Description	*Units*	*Value*
Static pressure	Pa	1.01325E+05
Temperature	K	288.15
Sound speed	m/s	340.294
Density	kg/m^3	1.225
Scaling standards		
Distance	m	1.0
Time	s	1.0
Mass	kg	1.0
Energy, 1 kg TNT	J	4.184E+06

Table 8.9 ANSI S2.2 standard for a yield of 1 kilotonne (10^6 kg) NE as a function of actual range R scaled to a 1 kg yield at an equivalent scaled range Z

R, m (10^6 kg)	Z, m (1 kg)	p_p (Pa)	t_p, s (10^6 kg)	t_p, s (1 kg)
1.00E+03	1.00E+01	8.92E+03	0.34	0.0034
1.00E+04	1.00E+02	518.3	0.52	0.0052
1.00E+05	1.00E+03	38.78	0.93	0.0093

1. Typo in the 30 m HE propagation time t_a. It has been replaced by 80.3 ms.
2. Inconsistent tabulated and equations units. Some times are in milliseconds, impulses are provided in bars, and some of the equations state incorrect units. Here they have all been converted to meters, kilogram, seconds (MKS), with pressures in Pa.
3. The tabulated reference pressures are incompatible with the equations unless the reference pressure P is 1 bar, or alternatively, that the pressures are given in bars. This can be confirmed by comparing the tabulated values and equations as well as by comparing Table X and Table XI, Part A and B (D. Russel, personal communication).
4. Tabulated values for the positive impulse are not consistent with positive pressure, duration, and waveform parameter values (Guzas and Earls 2010). Specifically, the condition

$$\frac{2I_p}{p_p t_p} \equiv M_1 = \frac{2\left(\alpha_p - 1 + e^{-\alpha_p}\right)}{\alpha_p^2} = \leq 1 \tag{8.255}$$

   is not satisfied with either HE or NE tabulated values for the impulse (Fig. 8.8).

5. The HE and NE tables do not overlap in scaled range.

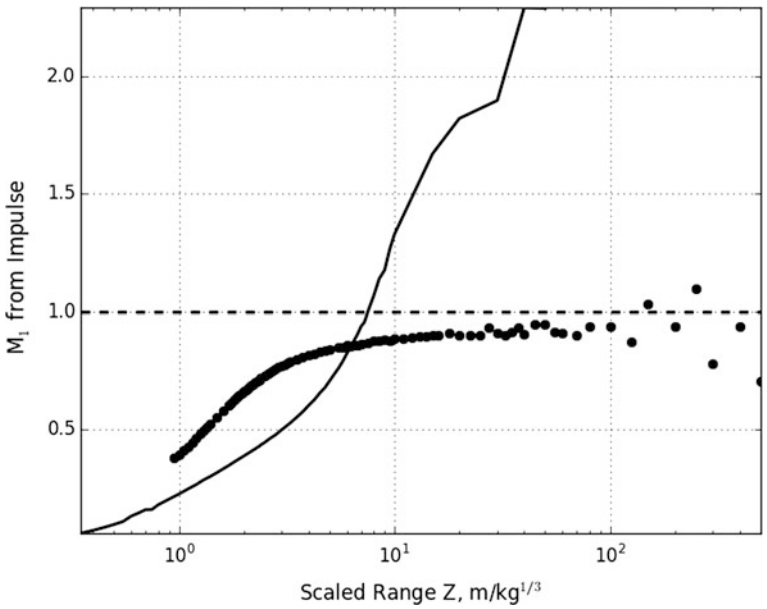

Fig. 8.8 Scaled positive impulse M_1 inferred from the KG85 tables for HE (dots) and NE (line). The positive impulse can only exceed the triangular area (unit scaled moment) if the positive phase has substantial downwards concavity, in which case it would no longer resemble the classic concave-upwards positive Friedlander pulse. This suggests the tabulated impulse and waveform parameters should be treated with caution, in particular for NE. Note the substantial increase in HE variability past 100 m/kg$^{1/3}$

6. The HE tables extend to the quasi-linear acoustics range (unit Mach number, small overpressure relative to ambient), whereas the NE tables stop short.
7. The NE tables extend deeper into the near-field hydrodynamic range, the HE tables do not get as close.
8. The reference yield for HE is 1 kg, and the reference for NE is 1 ktonne.
9. The positive period values for NE do not match the ANSIS2.20 standard.
10. There is no information on the negative phase of the blast pulse.

Despite these inconveniences, KG85 is one of the most consistently used standards and is a primary reference in this chapter. Although most of the material in this appendix is derivative, some corrections to published expressions are presented and new simplifying expressions are introduced.

In the detonation literature in general, and KG85 in particular, distance is scaled by atmospheric density and energy release, and may be expressed as

$$Z = f_d R_m / W^{1/3} \tag{8.256}$$

where R is distance in units of meters, f_d is a transmission factor for distance, and W is the equivalent explosive mass or energy. Although this is the traditional way of expressing the scaling relations, mathematical purist would rightfully recoil at the dimensional mayhem it creates. A more dimensionally correct formulation of the scaled distance would be,

$$\bar{Z} = f_d \frac{R}{R_0} \left(\frac{W}{W_0} \right)^{-\frac{1}{3}} \tag{8.257}$$

where R is distance in units of R_0, f_d is a transmission factor for distance, and W is the equivalent explosive mass or energy in units of W_0. This dimensionless scaled distance introduces the problem of not tracking the reference yield, which can lead to ambiguity and confusion. For the sake of continuity and ease of use, I refer to the traditional KG85 scaled distance to track the units, while the formulas use the more correct nondimensional form.

The reference yield is traditionally mass in kg of TNT for high explosives (HE) and kilotonnes of TNT for nuclear blasts (NE). In this work, *kt* is used as the abbreviation for 10^3 metric tons (10^6 kg) where space is limited. Equivalent explosive yields are referenced to the nominal energy produced by the detonation of TNT, where 1 kg of TNT yields 4.184×10^6 J = 4.2 MJ, and one kilotonne yields = 4.184×10^{12} J ~ 4.2 TJ (Table 8.8).

$$Z_{HE} = f_d R_m / W_{kg}^{1/3} \tag{8.258}$$

$$Z_{NE} = f_d R_m / W_{ktonnes}^{1/3} \tag{8.259}$$

Scaled distances can be converted from HE to NE values (and vice versa) from

$$Z_{NE} = f_d R_m / \left(W_{\mathrm{kg}} \frac{1\, kt}{10^6\, \mathrm{kg}} \right)^{1/3} = 10^2\, Z_{HE}. \tag{8.260}$$

The dimensionless distance transmission factor accounts for changes in atmospheric density ρ at the source location, and can be expressed in terms of static ambient pressure P and temperature T in Kelvins as

$$f_d = \left(\frac{\rho}{\rho_0} \right)^{\frac{1}{3}} = \left(\frac{P}{P_0} \right)^{\frac{1}{3}} \left(\frac{T_0}{T} \right)^{\frac{1}{3}}. \tag{8.261}$$

At the reference yield, pressure, and temperature, the scaled distance is the actual distance. Time may also be scaled relative to the reference conditions by accounting for the change in density and sound speed, c, and has a transmission factor

$$f_\tau = \left(\frac{\rho}{\rho_0}\right)^{\frac{1}{3}} \frac{c}{c_0} = \left(\frac{P}{P_0}\right)^{\frac{1}{3}} \left(\frac{T_0}{T}\right)^{\frac{1}{3}} \left(\frac{T_0}{T}\right)^{-\frac{1}{2}} = \left(\frac{P}{P_0}\right)^{\frac{1}{3}} \left(\frac{T}{T_0}\right)^{\frac{1}{6}}. \tag{8.262}$$

KG85 expresses the scaled time as

$$t_Z = t f_\tau / W^{1/3}. \tag{8.263}$$

As with the scaled distance, a more correct dimensional representation would be

$$\bar{t}_Z = f_\tau \frac{t}{t_0} \left(\frac{W}{W_0}\right)^{-\frac{1}{3}} \tag{8.264}$$

with t_0 a reference time scale, such as MKS seconds. Since it is possible to track the scaled time reference through the KG85 scaled distance, this work uses the nondimensional scaling in the time formulas.

As an example, the duration of the positive phase of a blast pulse may be expressed as

$$t_p = \frac{t_{Zp}}{f_\tau} W^{\frac{1}{3}} = t_{Zp} W^{\frac{1}{3}} \left(\frac{P}{P_0}\right)^{-\frac{1}{3}} \left(\frac{T}{T_0}\right)^{-\frac{1}{6}}. \tag{8.265}$$

Its equivalent dimensionally correct (but more cumbersome) form for HE would be,

$$\begin{aligned} t_p &= (1\,s)\bar{t}_{Zp} \left(\frac{W_{\mathrm{kg}}}{1\mathrm{kg}}\right)^{\frac{1}{3}} \left(\frac{P}{P_0}\right)^{-\frac{1}{3}} \left(\frac{T}{T_0}\right)^{-\frac{1}{6}} \\ &= (s)\bar{t}_{Zp} \frac{W_{\mathrm{kg}}^{1/3}}{\mathrm{kg}^{1/3}} \left(\frac{P}{P_0}\right)^{-\frac{1}{3}} \left(\frac{T}{T_0}\right)^{-\frac{1}{6}}, \end{aligned} \tag{8.266}$$

where the reference units are explicitly expressed. The nondimensional forms are seldom used in the literature, and it is usually left up to the reader to interpret and reconcile the various units and standards. The site corrections for time and range may be small (on the order of a few percent) for near-surface shots, but can be significant for the case of high-altitude blasts.

As discussed in Sect. 8.2, a gauge pressure $p(t)$ can be readily obtained from a differential pressure sensor from

$$p(t) = p_a(t) - \langle p_a \rangle \tag{8.267}$$

where $p_a(t)$ is the instantaneous blast pressure and $\langle p_a \rangle$ the mean atmospheric pressure within the instrument passband. This process would be equivalent to demeaning and detrending a pressure record. The peak gauge overpressure p_p is one of the primary metrics of blast waves, and it is defined as the difference in the peak

dynamic pressure relative to the averaged ambient pressure $\langle p_a \rangle$. The KG85 tables provide a scaled peak positive pressure from the gauge pressure over the reference barometric pressure P, not to be confused with the averaged long-period pressure over an instrument's passband $\langle p_a \rangle$,

$$\bar{p}(t) = \frac{p_a(t) - \langle p_a \rangle}{P} = \frac{p(t)}{P}, \quad \bar{p}_p = \frac{p_p}{P}, \tag{8.268}$$

As noted earlier in this section, the reference pressure $P = P_0$ at sea level in Table XI of KG85 is 1 bar = 1.0132510^5 Pa.

Since the peak gauge overpressure is scaled by the ambient pressure,

$$p_p = \bar{p}_p P = \bar{p}_p P_0 \left[\frac{P}{P_0}\right] \tag{8.269}$$

where there may be a substantial overpressure correction for shots above sea level due to the exponential decay rate of pressure with elevation.

There are various corrections that should be considered. If a blast is detonated near the surface, the blast energy is distributed over a half-space and a hemispherical magnification factor to the yield should be applied. The nominal magnification correction is a maximum factor of two for a perfectly reflecting surface but would be unity for a perfectly absorbing surface (Baker 1973, p. 121). Thus, the equivalent yield of a surface shot is at most twice that of a free-air blast for a perfectly reflecting surface (KG85, Chap. 8; Kim and Rodgers 2016), and is bounded by,

$$W_{spherical} \leq W_{hemisphere} \leq 2\, W_{spherical}. \tag{8.270}$$

Guzas and Earls (2010) recommend a magnification factor of 1.8 due to ground absorption, whereas Baker (1973, p.128) reports a factor of 1.7 along with a thorough historical perspective with abundant primary references.

A second factor of two arises in the rough conversion of NE to HE. Since only ~50% of a nuclear explosion is converted to mechanical energy, the general practice (ANSI S2.20-1983) is to divide the NE yield by a factor of two, or multiply the equivalent chemical yield by a factor of two,

$$W_{NEkt} \approx 2\, W_{HE\,kt}. \tag{8.271}$$

Thus, the 2013 Chelyabinsk meteor, with an estimated yield of ~500 kt of TNT (HE), would have an equivalent yield of 1 megatonne of NE. Without some knowledge of the source conditions it is possible to be off by a factor of 4 in yield estimates, for a cubed root scaling factor of ~1.6 in blast parameter variability.

Surface reflections can also add uncertainty in pressure measurements, in particular for ground observations from sources aloft. Guzas and Earls (2010) provide an excellent summary of this topic. The classical linear acoustic correction for

normal incidence onto a perfectly reflecting surface is a factor of two in the incident pressure. Other possible sources of uncertainty include the amount of detonated explosive and its relative effectiveness at the time of detonation. ANSI S2-20 specifies a minimum variation of 10–20% in airblast characteristics due to uncertainties in effective detonation mass, even for nuclear explosions. More telling is a footnote in the same standard, where it states that the type of "ton" used is well within this error margin, as the difference between short, long and metric tons is at most 12%, and cubed root scaling would reduce the variability of blast parameters to 4%. It is not unusual for researchers and organizations to develop scaling relations specific to their environments and data sets (e.g., Gitterman and Hoffstetter 2012) to reduce some of this variability. A review of the manifold scaling relations in the literature is beyond the scope of this work.

The next section of this appendix evaluates (and sometimes modifies) some of the tabulated KG85 blast parameters for the positive phase as well as includes some expressions for the negative phase parameters. Only scaled distances with tabulated values for the positive wave parameter are considered.

KG85 Positive Pulse Properties

For high explosives (HE) the KG85 reference yield is 1 kg TNT. For a scaled distance Z_{HE} of

$$0.952\,\mathrm{m/kg}^{1/3} \le Z_{HE} \le 500\,\mathrm{m/kg}^{1/3}, \tag{8.272}$$

the dimensionless scaled peak overpressure is

$$\bar{p}_{p\,HE} = \frac{808\left[1+\left(\frac{\bar{Z}_{HE}}{4.5}\right)^2\right]}{\sqrt{1+\left(\frac{\bar{Z}_{HE}}{0.048}\right)^2}\sqrt{1+\left(\frac{\bar{Z}_{HE}}{0.32}\right)^2}\sqrt{1+\left(\frac{\bar{Z}_{HE}}{1.35}\right)^2}}. \tag{8.273}$$

For nuclear explosives (NE), the reference yield is 1 ktonne = 1 Mkg TNT. For a scaled distance Z_{NE} of

$$35\,\mathrm{m/ktonne}^{1/3} \le Z_{NE} \le 5000\,\mathrm{m/ktonne}^{1/3},$$

the dimensionless scaled peak overpressure is

$$\bar{p}_{p\,NE} = 3.2\times 10^6 (\bar{Z}_{NE})^{-3}\sqrt{1+\left(\frac{\bar{Z}_{NE}}{87}\right)^2}\left[1+\frac{\bar{Z}_{NE}}{800}\right]. \tag{8.274}$$

The duration of the blast wave is defined by KG85 as the time between the passing of the shock front and the end of the positive pressure phase. The scaled duration of the positive pressure phase, in seconds (s), can be expressed as

$$t_{p\,HE} = (s)\frac{W_{\mathrm{kg}^{1/3}}}{\mathrm{kg}^{1/3}}\frac{0.98\left[1+\left(\frac{\bar{Z}_{HE}}{0.54}\right)^{10}\right]}{\left[1+\left(\frac{\bar{Z}_{HE}}{0.02}\right)^{3}\right]\left[1+\left(\frac{\bar{Z}_{HE}}{0.74}\right)^{6}\right]\sqrt{1+\left(\frac{\bar{Z}_{HE}}{6.9}\right)^{2}}} \tag{8.275}$$

for $0.952\ \mathrm{m/kg}^{1/3} \le Z_{HE} \le\ 500\ \mathrm{m/kg}^{1/3}$,

$$t_{p\,NE} = (s)\frac{W_{kt}^{1/3}}{kt^{1/3}}\frac{0.18\sqrt{1+\left(\frac{\bar{Z}_{NE}}{100}\right)^{3}}}{\sqrt{1+\left(\frac{\bar{Z}_{NE}}{40}\right)}\left[1+\left(\frac{\bar{Z}_{NE}}{285}\right)^{5}\right]^{\frac{1}{6}}\left[1+\left(\frac{\bar{Z}_{NE}}{50000}\right)\right]^{\frac{1}{6}}} \tag{8.276}$$

for $35\ \mathrm{m/ktonne}^{1/3} \le Z_{NE} \le\ 5000\ \mathrm{m/ktonne}^{1/3}$.

As mentioned earlier, nondimensional scaling with units of seconds are implemented as minor KG85 modifications. The positive pulse duration reaches a stable constant value at relatively short ranges, which makes the pulse duration (and its related quantity, the peak period) a relatively stable parameter for yield estimations.

An empirical equation for the positive impulse per area was obtained independent of the KG85 data for chemical explosives. As discussed earlier in this section, the KG85 impulse equation does not work well with the other parameters, and exceeds the maximum gamma value expected from a triangular pulse. Higher self-consistency can be obtained from the waveform parameter α

$$I_p = \int_0^{\tau_p} p_1(t)dt = \frac{p_p t_p}{2}\frac{2(\alpha - 1 + e^{-\alpha})}{\alpha^2} = \frac{p_p t_p}{2} M_1 \tag{8.277}$$

where the positive α for HE is estimated after Guzas and Earls (2010) using

$$\alpha_{HE} = \sum_{i=1}^{N} c_i Z_{HE}^{i-1}. \tag{8.278a}$$

The interpolation coefficients for HE are given in Table 8.10, where the range is extrapolated beyond the KG85 tables assuming the wavenumber parameter remains constant. This is not expected to be the case for much greater ranges, although the tabulated values trend this way.

The waveform parameter coefficients for NE are can be represented by

Table 8.10 Polynomial coefficients for the HE decay coefficient, after Guzas and Earls (2010)

Scaled distance	c1	c2	c3	c4	c5
$m/kg^{1/3}$					
$0.95 \leq Z < 2.4$	1.76074E+01	−2.67855E+01	1.78607E+01	−5.65557E+00	6.94164E−01
$2.4 \leq Z < 6.5$	4.43216E+00	−2.71877E+00	7.41973E−01	−9.34132E−02	4.46971E−03
$6.5 \leq Z < 40$	7.11610E−01	−6.26846E+02	3.32532E−03	−8.24049E−05	7.61887E−07
$40 \leq Z \leq 500$	2.51614E−01	−1.76758E−03	9.51638E−06	−2.19712E−08	1.79135E−11
$500 < Z$	1.20000E−01				

Table 8.11 Coefficients for the NE decay coefficient. Same scaled range as the KG85 NE table

c1	c2	c3	c4
114.420775188	0.0599916445386	628.976460729	0.784945951096

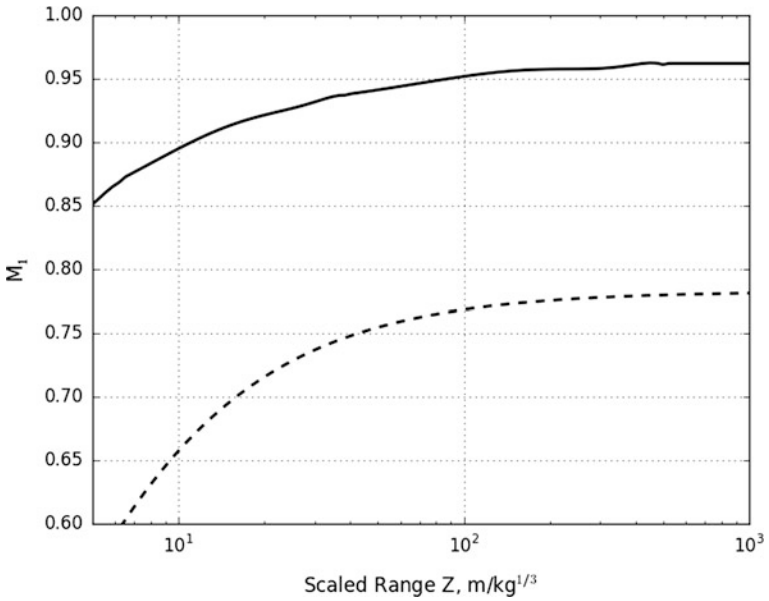

Fig. 8.9 Scaled positive impulse M_1 for HE (solid) and NE (dashed) derived from the interpolated waveform parameters

$$\alpha_{NE} = c_1 e^{-c_2 Z_{NE}} + c_3 \frac{1}{Z_{NE}} + c_4 \tag{8.278b}$$

with coefficient provided in Table 8.11 for the same scaled range as the KG85 NE pressure and pulse duration. Both the HE and NE positive impulse are computed for interpolation and their resulting well-behaved M_1 is shown in Fig. 8.9. This work does not use the tabulated KG85 impulse values as they are inconsistent with the other parameters.

The accuracy and utility of the tabulated waveform parameter are not clear, as it is not readily obtained from field measurements and seems to have a very narrow range of applicability. The corrected waveform parameter tables are presented here for the sake of completeness.

A curve fit was performed for the acoustic travel time accounting for the propagation speed to transition to the acoustic limit at a range where the Mach number is close to unity. The expression for HE is

$$t_{a\,HE} = (s)\frac{W_{kg}^{1/3}}{kg^{1/3}} \frac{0.2}{\left[1 + \left(\frac{\bar{Z}_{HE}}{10}\right)^{-0.75795}\right]^{3.14415}}, Z_{HE} \le 10\,\mathrm{m/kg^{1/3}} \tag{8.279}$$

$$t_{a\,HE} = (s)\frac{W_{kg}^{1/3}}{kg^{1/3}} \left\{ \frac{0.2}{[2]^{3.14415}} + \frac{[\bar{Z}_{HE} - 10]}{340.294} \right\}, Z_{HE} > 10\,\mathrm{m/kg^{1/3}}. \tag{8.280}$$

For the NE case

$$t_{a\,NE} = (s)\frac{W_{kt}^{1/3}}{kt^{1/3}} \frac{50}{\left[1 + \left(\frac{\bar{Z}_{NE}}{100}\right)^{-0.43385}\right]^{9.76}}, Z_{NE} \le 1\,\mathrm{km/ktonne^{1/3}} \tag{8.281}$$

$$t_{a\,NE} = (s)\frac{W_{kt}^{1/3}}{kt^{1/3}} \left\{ \frac{50}{\left[1 + (10)^{-0.43385}\right]^{9.76}} + \frac{[\bar{Z}_{NE} - 1000]}{340.294} \right\}, Z_{NE} > 1\,\mathrm{km/ktonne^{1/3}} \tag{8.282}$$

For 1 tonne at a range of 1 km the predicted time difference between the shock and acoustic propagation times is small and may require high sample rates, accurate origin information, and reliable environmental data to validate. A comparison of the tables and formulas are presented in Figs. 8.10, 8.11 and 8.12.

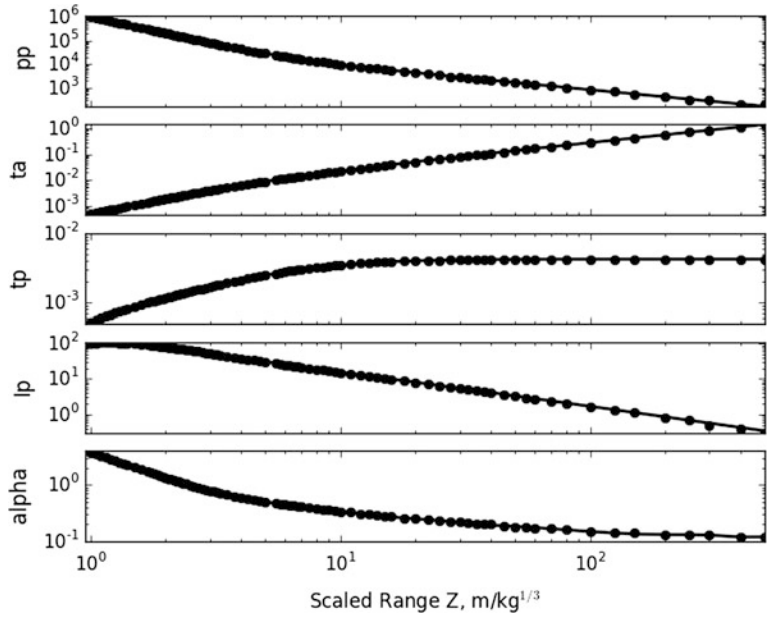

Fig. 8.10 KG85 tabulated data (dots) and equations (solid) for HE

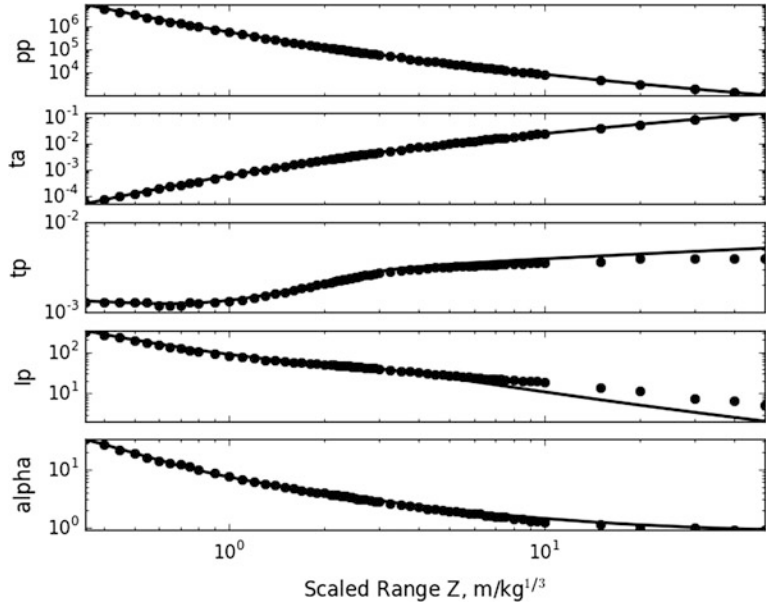

Fig. 8.11 KG85 tabulated data (dots) and equations (solid) for NE, converted to a scaled distance of m/kg$^{1/3}$. The divergence in the positive impulse is due to the incompatibility of this parameter with all other tabulated data

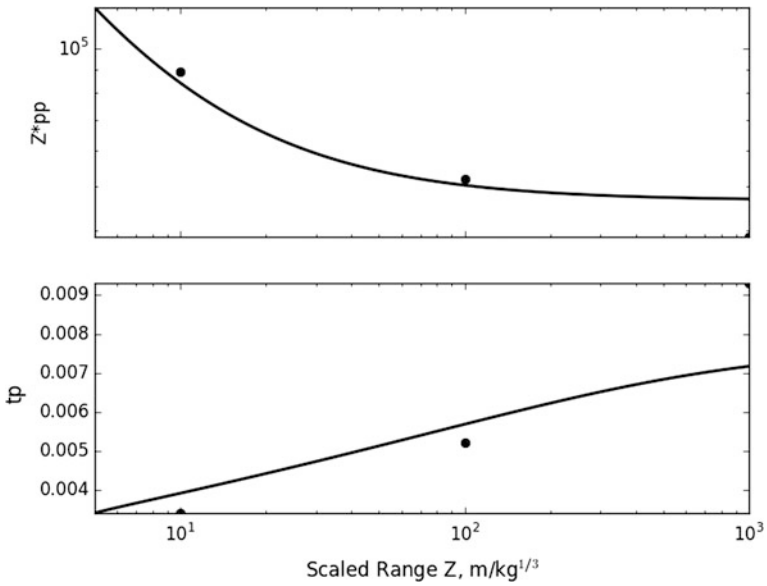

Fig. 8.12 ANSI tabulated data (dots) and extrapolated equations (solid) for NE, converted to a scaled distance of m/kg$^{1/3}$

Overpressure to Underpressure Ratios

Although addressed in the early literature (e.g., Sect. 5.9 of Bethe et al. 1958), the properties of negative phase of a blast have been largely ignored not only because it is considered secondary to the main positive blast phase, but also because it can be difficult to measure (Baker 1973). Recent interest in the effects of the negative phase (e.g., Rigby et al. 2014) have helped in evaluating and consolidating the literature on the topic. The negative pressure at sea level was estimated by Larcher (2008) relative to 1 kg HE by two linear approximations, and is consistent with the curves presented in Smith and Hetherington (1994). A lowpass filter functional form is implemented here to match the constant value at short scaled distances and the asymptotic linear slope at large scaled distances,

$$|\bar{p}_{n\,HE}| = \frac{10^4\,\text{Pa}}{P}\left[1+\left(\frac{\bar{Z}_{HE}}{3.5}\right)^2\right]^{-\frac{1}{2}} \rightarrow \frac{1}{\bar{Z}_{HE}}\frac{3.5\times 10^4\,\text{Pa}}{P}. \tag{8.283}$$

The negative pressure for NE can also be estimated from the 1 kton DNA reference (Needham and Crepeau 1981) using a similarly coarse approximation at large scaled distances,

$$|\bar{p}_{n\,NE}| = \frac{3.35425 \times 10^4\ \text{Pa}}{P_0}\left[1 + \left(\frac{\bar{Z}_{NE}}{80}\right)^2\right]^{-\frac{1}{2}}. \tag{8.284}$$

The ratios of peak overpressure to underpressure for 1 kg of HE and NE at a reference range of $100\,\text{m/kg}^{1/3}$ are

$$\frac{p_{p\,HE}}{|p_{n\,HE}|} \approx \frac{840}{350} \approx 2.4, Z_{HE} = 100\,\text{m/kg}^{1/3}, \tag{8.285}$$

$$\frac{p_{p\,NE}}{|p_{n\,NE}|} \approx \frac{503}{268} \approx 1.9, Z_{NE} = 100\,\text{m/kg}^{1/3}. \tag{8.286}$$

The negative pulse durations present some challenges because of their vulnerability to secondary shocks and ground effects. I concentrate on estimating the ratio of the negative and positive pulse duration. For impulse-balanced blast pulses, this ratio is set by the waveform shape and the overpressure to underpressure ratio. The simplest example is for the triangular pulse. As discussed in the main text, an impulse-balanced triangular pulse must satisfy

$$\frac{t_{\Delta n}}{t_{\Delta p}} = \frac{p_p}{|p_n|} \tag{8.287}$$

where the pressure ratio and the positive phase duration sets the negative phase duration. In other words, for simple impulse-balanced pulses of a prescribed shape, at most three blast parameters can be specified.

Similarly, the theoretical pulse duration ratio for the impulse-balanced hybrid modified Friedlander (HMF) pulse can be estimated from

$$\frac{t_n}{t_p} = M_1 \frac{\pi}{e^1}\frac{p_p}{|p_n|} \le \frac{\pi}{e^1}\frac{p_p}{|p_n|} \approx 1.16\frac{p_p}{|p_n|}, \tag{8.288}$$

which is consistent with the triangular pulse approximation. Computed pressure and time duration ratios are shown in Fig. 8.13 as a function of scaled range using the KG84 values for the waveform parameter, which determine the first moment M_1 (Fig. 8.9) in Eq. 8.288. It should be noted that the KG85 values lead to overdampened negative phases (Figs. 8.5 and 8.7) for both HE and NE, and the negative phase duration shown in Fig. 8.13 is almost surely underestimated. The HE ratios reach a near-constant value after $20\,\text{m/kg}^{1/3}$, whereas the NE ratios appear to stabilize closer to $100\,\text{m/kg}^{1/3}$. This suggests that a reference range of $100\,\text{m/kg}^{1/3}$ would be reasonable for both HE and NE blasts.

In the literature, Fig. 8.5 of ANSI 2.20 shows the positive and negative pulse durations. It is possible to estimate from the upper limit of the ANSI curve as $t_{p\,NE} \sim 0.52$ s, $t_{n\,NE} \sim 0.96$ s at a yield of 1 ktonne and a range of 10 km, which is equivalent to 1 tonne at 1 km, or 1 kg at 100 m,

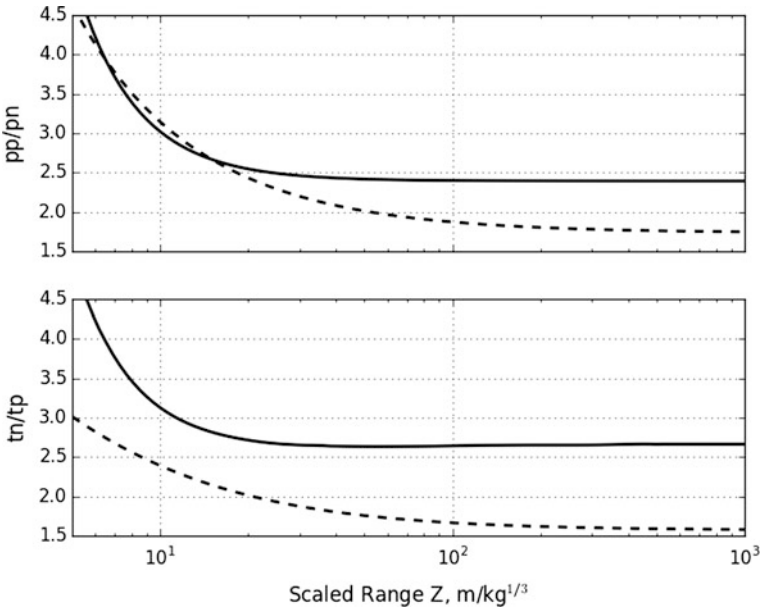

Fig. 8.13 overpressure to underpressure ratio (upper panel) and negative to positive phase duration (lower panel) for HE (solid) and NE (dashed) using the lowpass filter approximation for the underpresure and the impulse balance for the negative phase duration

$$\frac{t_{n\,NE}}{t_{p\,NE}} = \frac{0.96}{0.52} \approx 1.85, Z_{NE} = 100\,\mathrm{m/kg^{1/3}}, \tag{8.289}$$

corresponding to an overpressure to underpressure ratio of approximately two. The HE negative pulse duration at sea level is reported by Larcher (2008) as

$$t_{n\,HE} = (s)\frac{W_{kg}^{1/3}}{kg^{1/3}} 1.39 \times 10^{-2}, 1.9\,\mathrm{m/kg^{1/3}} < Z_{HE}. \tag{8.290}$$

Using the positive pulse duration at the reference range,

$$\tau_{n\,HE} = \frac{t_{n\,HE}}{t_{p\,HE}} \approx \frac{0.0139}{0.0042} \approx 3.31, Z_{HE} = 100\,\mathrm{m/kg^{1/3}}, \tag{8.291}$$

which would correspond to a pressure ratio of approximately three, and is likely to be affected by ground effects and secondary pulse oscillations. On the other hand, $\tau_n = 3$ corresponds to a pulse lifetime $\tau_e = 4$, which is the effective spectral pseudo period of the balanced G77 (GT) pulse.

Synopsis

Substantial effort was placed in revisiting the KG85 and ANSI standards as starting points for the next iteration of blast parameter estimation. This work proposes a reference range and yield of 1 km for 1 tonne (100 m for 1 kg, 10 km for 1 ktonne) for HE and NE blasts. At this scaled range, shocked blast pulses propagate near acoustic speeds, and the overpressure is a fraction of atmospheric pressure at sea level, and decays roughly as the inverse distance.

The aim of this chapter is to illustrate different approaches to blast pulse characterization. The duration ratios appear to be less stable than the pressure ratios, and in the interest of simplicity and clarity a single-digit-precision reference peak overpressure to underpressure ratio of 2 is used consistently as a representation of HE and NE blasts, and is expressed as

$$\left.\frac{p_p}{p_n}\right|_{ref} \equiv 2. \tag{8.292}$$

It is also possible to make some useful simplifying reductions of the KG85 relations near the scaled distance $Z_{HE} \sim 100\,\mathrm{m/kg}^{1/3}$, where geometrical spreading is near spherical. Near the yield-scaled reference range, but before the far field, we can express the overpressure and positive phase duration (or pseudo period) as

$$\frac{p_p}{p_{ref}} = \frac{R_{ref}}{R}\left(\frac{W}{W_{ref}}\right)^{\frac{1}{3}}, \tag{8.293}$$

$$\frac{t_p}{t_{ref}} = \left(\frac{W}{W_{ref}}\right)^{\frac{1}{3}}, \tag{8.294}$$

where the reference values could be provided by Table 8.1 or Table 8.6. These simplifications should provide reasonable values near the reference range ± a factor of two, and may be practical for rapid first-order estimates when losses due to spherical spreading are dominant.

Appendix 5. Minor Uncle and Distant Image 2 kt Case Studies

The Distant Image and Minor Uncle tests were performed at White Sands Missile Range (WSMR), New Mexico, approximately 6.5 km south from the ground zero of Trinity. Trinity had an equivalent yield of ~20 kt TNT, and the Distant Image (DI) and Minor Uncle (MU) events were approximately one order of magnitude smaller. The MU had the same ground zero as DI after the previous crater was filled

Table 8.12 Origin times and locations for Distant Image and Minor Uncle, courtesy of R. Reinke

	Yield	Date (Local)	Time (Local)	Ground Zero GZ	GZ height asl
Distant Image (DI)	2650 long tons ANFO. Surface hemisphere	6/20/91	10:05 MDT	33.619953°N, 106.477619°W	1500 m
Minor Uncle (MU)	2431 long tons ANFO. Surface hemisphere	6/10/93	09:10 MDT	33.619953°N, 106.477619°W	1500 m

in. The apparent MU crater radius was 42 m with an apparent depth of 22 m below surface (R. Reinke, personal communication). The center of the crater can be estimated from Google Maps at 33.619953°N and 106.477619°W at an elevation ~1500 m above sea level. The origin times and location for the DI for MU tests are presented in Table 8.12.

There may be some uncertainty in the actual weight of detonated explosives. For the purposes of this discussion, it is assumed the ammonium nitrate, fuel oil (ANFO) is completely and simultaneously detonated. The next step is to convert the yield of the surface hemispherical charges in long (imperial) tons to the equivalent weight of a spherical charge in free air for comparison with the KG85 tables. The conversion from imperial tons to metric tonnes is straightforward, but there is some uncertainty on the relative effectiveness (RE) factor of ANFO with respect to TNT. At the time of the tests, an ANFO RE of 0.8 was recommended, whereas the current recommended ANFO RE is closer to 0.83 (R. Reinke, personal communication). An additional source of variability is the magnification factor from the reflected energy off the ground. In a perfectly reflecting boundary, the magnification factor doubles the yield. However, the resulting crater is evidence of energy losses to the ground, and in practice, a magnification factor of 1.8 is recommended (e.g., Guzas and Earls 2010). Table 8.13 below presents some upper and lower estimates for yield conversion of a surface hemispherical charge to an equivalent spherical charge in free air. The exact values are not as important as the range of values and their effect on the scaling of the blast pulse parameters.

Table 8.13 Estimated upper and lower bounds for the equivalent spherical DI and MU yields in ktonnes

	DI yield, imperial ktons	MU yield, imperial ktons	Imperial ton to metric tonne	ANFO RE factor	Magnification factor	DI spherical yield, ktonnes	MU spherical yield, ktonnes
Lower bound	2.65	2.431	0.454	0.8	1.8	1.73	1.59
Upper bound	2.65	2.431	0.454	0.83	2	2.00	1.83

In addition to the yield scaling, the temperature and pressure at ground zero will affect the range scaling, peak pressure, positive pulse duration, and pulse propagation time (KG85). The KG85 tables are provided relative to a reference pressure of 1013.25 mbar (1013.25 × 102 Pa) and a temperature of 288.15 K. The standard atmosphere pressure and temperature at a height 1500 m above sea level are 845.6 mbars and 278.4 K. However, the measured pressure and temperature for Minor Uncle were 853 mbar and ~293 K (20 C), respectively, which was unseasonably cool due to a frontal passage (R. Reinke, personal communication). The average temperature at White Sands in June at ~10 AM local time is expected to be closer to 303 K (~86 F) as the ground warms up in early summer. For the purposes of illustration, the measured ambient pressure and temperature are used for Minor Uncle, and the standard atmosphere pressure and average temperature are used for Distant Image to compare the effects local weather variability on the blast parameter estimates. Table 8.14 summarizes estimated site and yield corrections from MU and DI, as well as percent errors that may be introduced by rounding up in yield or not implementing the corrections. The last column of Table 8.14 only keeps two significant figures. The peak overpressure correction seems to be most vulnerable due to its linear dependence on the ambient pressure, in contrast to the cubed root dependence of the temporal and spatial correction factors. The distance correction is the next most vulnerable, with the time transmission factor being the least sensitive. The differences between the MU and DI site-dependent correction factors are small, which is reassuring as it is not always possible to have access to the local meteorology during unscheduled detonations.

Conservative predicted pulse parameters from KG85 could be evaluated by using a magnification factor of 1.8 and an ANFO RE factor of 0.8. However, it would be reasonable to represent both the MU and DI tests as detonations with an equivalent TNT yield of 1.8 ktonnes of TNT (with a ~4% error) at a 1500 m asl elevation with a standard atmospheric pressure of 845.6 mbar and an average temperature of 303 K at White Sands between the hours of 9–10 AM local time in June. As shown in Table 8.14, this would correspond to a peak overpressure correction of 0.84, a distance transfer function fd = 0.93, and a time transfer function ft = 0.95. Thus, at the end of this analysis, the 2 kt surface shot scales to ~2 ktonnes of TNT in free air (11% error). This variability is well within the ANSI expectations. In the main text, I refer to the combination of these two shots as the 2 kt case study.

Representative waveforms for 2 kt case study are shown in Figs. 8.1 and 8.2 in the main text. They are scaled by the peak pressure and the positive pulse duration. To construct this scaling, it is necessary to estimate the blast arrival time ta, the peak overpressure pp, and the positive pulse duration tp. The observed parameters can be yield-corrected and compared directly with standard blast parameter tables and formulas to assess their predictive accuracy and design refinements. The rise time to reach the overpressure, coupled with the data collection sample rate, would also be of interest, and could use the pulse onset threshold needed to estimate the arrival time. The negative pulse parameters can also be computed and expressed in terms of the peak overpressure and the positive pulse duration. Pertinent negative pulse

Table 8.14 Uncertainty estimates for yield scaling and site corrections

	DI	MU	Average DI and MU
Min yield, ktonnes	1.73	1.59	1.7
Max yield, ktonnes	2.00	1.83	1.9
Mean yield, ktonnes	1.86	1.71	1.8
Lower Sach's yield correction, $W^{1/3}$	12.01	11.67	12
Upper Sach's yield correction, $W^{1/3}$	12.59	12.23	12
Variability in Sach's yield correction using 1.8 kt (%)	3.5	5.0	4
Variability in Sach's yield correction using 2 kt (%)	7	15	11
GZ pressure, mb	845.6	853	849
GZ temperature, K	303	293	298
GZ/Reference, Pressure ratio	0.835	0.842	0.84
GZ pressure correction, percent (%)	17	16	16
GZ/Reference, Temperature ratio	1.052	1.017	1.0
Distance correction, KG85 f_d	0.926	0.939	0.93
Distance correction, percent (%)	7.4	6.1	6.8
Time correction, KG85 f_t	0.949	0.947	0.95
Time correction, percent (%)	5.1	5.3	5.2

parameters include the scaled pressure and time of the peak underpressure, tmin, the underpressure duration tn, the total pulse lifetime te, and the scaled pressure threshold used to evaluate the pulse lifetime. With these parameters in place, it is possible to numerically compute positive and negative impulses, evaluate pulse shape parameters, as well as refine equivalent energy estimates for individual blast signatures.

The 2 kt case study also brings up another important issue of cubed root scaling and the differences between the 1 kg and 1 ktonne tables. Table 8.15 shows a comparison between the observed and predicted site-corrected KG85 overpressure and peak period for 2 ktonnes HE, and Table 8.16 shows the same comparison for

Table 8.15 KG85, 2 ktonne HE

R (km)	pp (Pa)	tp (s)	Z HE ($m/kg^{1/3}$)	pp HE/pp obs	tp HE /tp obs
7.2	1460	0.83	42	1.15	0.84
7.2	1670	0.84	42	1.01	0.83
7.3	1145	0.90	43	1.45	0.77
7.3	1933	0.80	43	0.86	0.87
9.2	865	0.86	54	1.51	0.81
33.0	195	1.01	194	1.86	0.70
37.0	83	1.21	217	3.88	0.58
37.0	200	1.00	217	1.62	0.71
Average		0.93	107	1.67	0.76

Table 8.16 KG85, 4 ktonne NE (2 ktonne HE equivalent)

R (km)	pp (Pa)	tp (s)	Z NE (m/kg$^{1/3}$)	pp NE/pp obs	tp NE/tp obs
7.2	1460	0.83	33	1.18	1.16
7.2	1670	0.84	33	1.03	1.15
7.3	1145	0.90	34	1.48	1.07
7.3	1933	0.80	34	0.88	1.20
9.2	865	0.86	43	1.49	1.16
33.0	195	1.01	154	1.63	1.20
37.0	83	1.21	172	3.39	1.01
37.0	200	1.00	172	1.41	1.23
Average		0.93	84.6	1.56	1.15

Table 8.17 Negative phase properties

Z HE (m/kg$^{1/3}$)	pp/pn obs	pp/pn HE	pp/pn NE	tn/tp obs	te/tp obs
42	1.90	2.04	2.15	1.64	2.64
42	2.24	2.04	2.15	1.68	2.68
43	1.99	2.03	2.15	1.51	2.51
43	2.54	2.03	2.15	1.72	2.72
54	1.66	2.02	2.06	1.62	2.62
194	1.83	2.01	1.83	1.45	2.45
217	1.20	2.01	1.82	1.66	2.66
217	1.43	2.01	1.82	1.57	2.57
Average					
107	1.85	2.02	2.01	1.61	2.61

4 ktonnes NE, which should be equivalent to 2 ktonnes NE. For the large DI and MU yields, the NE tables provide closer agreement to the measured 2 ktonne yield, in particular for the positive phase duration. Variability in the positive pulse duration is to be expected due to the different burn times of NE and ANFO HE (e.g., Petes et al. 1983), as well as between TNT and ANFO (Reinke, personal communication). Table 8.17 shows that the predicted ratios between the peak overpressure and underpressure are consistent for the HE and NE predictions in Appendix 4 for the scale ranges pertinent to this case study, as was the case for ANFO (Petes et al. 1983).

References

ANSI S2.20-1983 (ASA 20-1983) (1983) Estimating air blast characteristics for single point explosions in air, with a guide to evaluation of atmospheric propagation effects, American National Standard

Baker WE (1973) Explosions in air. University of Texas Press, Austin, Texas

Bethe HA, Fuchs K, Hirschfelder JO, Magee JL, von Neumann R (1958) Blast wave. Technical Report LA-2000, DTIC Document

Bonner JL, Russell DR, Reinke RE (2013) Modeling surface waves from aboveground and underground explosions in alluvium and limestone. Bull Seismol Soc Am 103(6):2953–2970

Box GEP (1976) Science and statistics. J Am Stat Assoc 71:791–799. https://doi.org/10.1080/01621459.1976.10480949

Brode HL (1955) Numerical solutions of spherical blast waves. J Appl Phys 26(6):766–775. https://doi.org/10.1063/1.1722085

Brode HL (1956) Point source explosions in air, The Rand Corporation, Research Memo RM-1824-AEC

Brode HL (1959) Blast wave from a spherical charge. Phys Fluids 2:217. https://doi.org/10.1063/1.1705911

Cole RH (1948) Underwater explosions. Princeton University Press, New Jersey

Ens TA, Brown PG, Edwards WN, Silber EA (2012) Infrasound production by bolides: a statistical study. J Atmos Sol-Terr Phys 80:208–229

Freidlander FG (1946) The diffraction of sound pulses. I. Diffraction by a semi-infinite plate. Proc R Soc Lond A 186:322–344

Ford SR, Rodgers AJ, Xu H, Templeton DC, Harben P, Foxall W, Reinke RE (2014) Partitioning of seismoacoustic energy and estimation of yield and height-of-burst/depth-of-burial for near-surface explosions. Bull Seismol Soc Am 104:608–623. https://doi.org/10.1785/0120130

Garcés MA (2014) Ubiquitous waveform sensing: infrasound, NNSA review of monitoring research (RMR) for ground-based nuclear explosion monitoring technologies, Albuquerque, New Mexico, 17–19 June

Garcés MA (2013) On infrasound standards, Part 1. Time, frequency, and energy scaling. Inframatics 2:13–35. https://doi.org/10.4236/inframatics.2013.22002

Garcés MA (1995) The acoustics of volcanic explosions. PhD Thesis, University of California, San Diego

Gitterman Y, Hofstetter R (2012) GT0 explosion sources for IMS infrasound calibration: charge design and yield estimation from near-source observations. Pure Appl Geophys. https://doi.org/10.1007/s00024-012-0575-4

Gitterman Y (2013) Secondary shock features for large surface explosions: results from the Sayarim military range, Israel and other experiments. Shock waves. https://doi.org/10.1007/s00193-013-0487-y

Granström SA (1956) Loading characteristics of air blasts from detonating charges, Technical Report 100, Transactions of the Royal Institute of Technology, Stockholm

Guzas E, Earls C (2010) Air blast load generation for simulating structural response. Steel Compos Struct 10(5):429–455

Kim K, Rodgers A (2016) Waveform inversion of acoustic waves for explosion yield estimation. Geophys Res Lett 43. https://doi.org/10.1002/2016gl069624

Kim K, Rodgers A (2017) Influence of low-altitude meteorological conditions on local infrasound propagation investigated by 3-D full waveform modeling. Geophys J Int 210:1252–1263. https://doi.org/10.1093/gji/ggx218

Kinney GF, Graham KJ (1985) Explosive shocks in air, 2nd edn. Springer, New York, p 269

Koper KD, Wallace TC, Reinke R, Leverette J (2002) Empirical scaling laws for truck bomb explosions based on seismic and acoustic data. Bull Seismol Soc Am 92:527–542

Larcher M (2008) Pressure-time functions for the description of air blast waves, JRC Technical Note, No. 46829, Joint Research Centre, European Commission

Miles JW (1967) Decay of spherical blast waves. Phys Fluids 10(12):2706–2708. https://doi.org/10.1063/1.1762097

Needham CE, Crepeau JE (1981) The DNA nuclear blast standard (1kt), DNA 5648T report prepared by Systems, Science, and Sofware, Inc. for the Defense Nuclear Energy (DNA)

Needham CE (2010) Blast waves. Springer. ISBN-13: 978-3642052873

Petes J, Miller R, McMullan F (1983) User's guide and history of ANFO as a nuclear weapons effect simulation explosive, Defense Nuclear Energy Report Number DNA-TR-82-156

Reed JW (1977) Atmospheric attenuation of explosion waves. J Acoust Soc Am 61(1):39–47
Rigby SE, Tyas A, Bennet T, Clarke SD, Fay SD (2014) The negative phase of the blast load. Int J Prot Struct 5(1):1–20. ISSN 2014-4196
Schnurr J, Garces MA, Rodgers A, Kim K (2017) Improved recording and modeling for near-surface explosion forensics. Fall Meeting of the American Geophysical Union, pp S51B–0592
Smith PD, Hetherington JG (1994) Blast and ballistic loading of structures. Butterworth-Heinemann, Oxford, England
Stevens JL, Divnov II, Adams DA, Murphy JR, Bourchik VN (2002) Constraints on infrasound scaling and attenuation relations from Soviet explosion data. Pure Appl Geopys 159:1045–1062
Stone R (2016) Who dropped the bomb? Science 351:1138–1140
Teich M, Gebbeken N (2010) The influence of the underpressure phase on the dynamic response of structures subjected to blast loads. Int J Prot Struct 1(2):219–234
Unified Facilities Criteria (2014) Structures to resist the effects of accidental explosions, 2014. US DoD, Washington DC, USA, UFC-3-340-02, 2008, Change 2, 1 Sept 2014
US Naval Facilities Engineering Command (1986) Blast resistant structures. Alexandria, VA, DM 2.08
US Army Corps of Engineers (2005) Methodology manual for the single-degree-of-freedom blast effects design spreadsheets (SBEDS). ACE Protective Design Center, Omaha, NE, USA, PDC-TR-06-01
Vergoz J, Le Pichon A, Ceranna L, Mialle P, Gaillard P, Brachet N (2013) Incorporating numerical modeling into estimates of the detection capability of the IMS infrasound network. In: 2013 infrasound technology workshop, Vienna, Austria
Wilson G, Aruliah DA, Brown CT, Chue Hong NP, Davis M, Guy RT et al (2014) Best practices for scientific computing. PLoS Biol 12(1):e1001745. https://doi.org/10.1371/journal.pbio.1001745

Part III
Observations – From Local to Global: Regional Monitoring

Chapter 9
The Antares Explosion Observed by the USArray: An Unprecedented Collection of Infrasound Phases Recorded from the Same Event

Julien Vergoz, Alexis Le Pichon and Christophe Millet

Abstract On October 28, 2014, the launch of the Antares 130 rocket failed just after liftoff from Wallops Flight Facility, Virginia. In addition to one infrasound station of the International Monitoring Network (IMS), the explosion was largely recorded by the Transportable USArray (TA) up to distances of 1000 km. Overall, 180 infrasound arrivals were identified as tropospheric, stratospheric or thermospheric phases on 74 low-frequency sensors of the TA. The range of celerity for those phases is exceptionally broad, from 360 m/s for some tropospheric arrivals, down to 160 m/s for some thermospheric arrivals. Ray tracing simulations provide a consistent description of infrasound propagation. Using phase-dependent propagation tables, the source location is found 2 km east of ground truth information with a difference in origin time of 2 s. The detection capability of the TA at the time of the event is quantified using a frequency-dependent semiempirical attenuation. By accounting for geometrical spreading and dissipation, an accurate picture of the ground return footprint of stratospheric arrivals as well as the wave attenuation are recovered. The high-quality data and unprecedented amount and variety of observed infrasound phases represents a unique dataset for statistically evaluating atmospheric models, numerical propagation modeling, and localization methods which are used as effective verification tools for the nuclear explosion monitoring regime.

9.1 Introduction

On October 28, 2014 at 22:22:42 UTC, the launch of an Antares 130 rocket failed just after liftoff from Wallops Flight Facility, Virginia, at location 37.83 N, 75.49 W. A small explosion occurred at the bottom of the rocket 7 s after the vehicle cleared the

J. Vergoz (✉) · A. Le Pichon · C. Millet
CEA, DAM, DIF, F-91297 Arpajon, France
e-mail: julien.vergoz@cea.fr

A. Le Pichon et al. (eds.), *Infrasound Monitoring for Atmospheric Studies*,
https://doi.org/10.1007/978-3-319-75140-5_9

tower, and it fell back down onto the pad. The Range Safety officer sent the destruct command just before ground impact, creating a huge explosion 21 s after liftoff at 22:23:03 UTC (Pulli and Kofford 2015). The cause of the incident is still officially unknown and would be due to a failure of the first stage engine (NASA 2015).

Three different types of acoustic sources successively emitted infrasound signals (Pulli and Kofford 2015): (1) first stage ignition and rocket liftoff during the first 7 s of ascendant flight at subsonic velocity (Lighthill 1963; Varnier 2001), (2) the small explosion occurring at the bottom of the rocket associated to the incident, and (3) the rocket explosion caused by the destruct command. The latter source is massive and unquestionably the most energetic. It is the only one that has been captured by remote stations, at distances larger than 100 km. These three sources have been observed at 57 km, where the measured amplitudes and frequency content provide detailed information about their energy (Pulli and Kofford 2015).

With an average inter-station spacing of ~2000 km, the sparse spatial sampling of the acoustic wave field by the International Monitoring System (IMS) (Marty 2019) infrasound network does not allow precise propagation studies, especially at regional distances. The benefits of augmenting the spatial coverage of the IMS network to provide a detailed picture of acoustic wave propagation has been demonstrated by number of studies (Green et al. 2009; Edwards et al. 2014; Gibbons et al. 2015; Che et al. 2017; de Groot-Hedlin and Hedlin 2019). For the large-scale Sayarim calibration experiments (on August 26, 2009 and January 26, 2011), the temporary deployed array stations at regional and telesonic distances measured a unique collection of high amplitude infrasound phases (tropospheric, stratospheric and thermospheric) and allowed specific propagation effects to be highlighted that IMS stations could not capture (Fee et al. 2013; Waxler and Assink 2019). For the Antares explosion, only one infrasound station of the IMS network (I51GB, in Bermuda) recorded multiple arrivals from the event at about 1100 km.

With an inter-station spacing of about 70 km, the Transportable USArray (TA) provides a unique set of high temporal frequency surface atmospheric pressure observations at a continental scale. It consists of approximately 400 seismo-acoustic stations primarily deployed for seismic measurements. This dense measurement platform offers opportunities for detecting and locating geophysical events (Walker et al. 2011; De Groot-Hedlin and Hedlin 2015; de Groot-Hedlin and Hedlin 2019) and reveals large acoustic events that may provide useful insight into the nature of long-range infrasound propagation in the atmosphere (De Groot-Hedlin and Hedlin 2014; Assink et al. 2019). At the time of the event, the TA was located close to the east coast of the United States and surrounded the explosion. 226 operating stations were located at less than 2000 km from the event and all were equipped with single infrasound microphones.

In this chapter, we present a detailed analysis of infrasound recordings generated by the explosion of the Antares rocket associated to its destruction. This event is

among the most interesting, recent explosive sources representing a unique dataset for statistically evaluating atmospheric models, numerical propagation modeling and localization methods. Section 9.2 presents the observation network, the recording conditions influenced both by the surface background noise level and the general circulation of the atmosphere from the ground to the lower thermosphere, and an overview of near and far-field infrasound recordings. Section 9.3 presents both ray tracing simulations and source location results. It is shown that phase identification is made without ambiguity so that location results obtained with and without phase-dependent travel time curves can be compared. The frequency-dependent attenuation of stratospheric phases is studied as a function of the effective sound speed in Sect. 9.4. Observations and simulation results are discussed in the last Section.

9.2 Observations Network and Recordings Conditions

9.2.1 Observation Network

The TA consists of 400 high-quality broadband seismographs and atmospheric sensors that have been operated at temporary sites across the United States from West to East in a regular grid pattern. In August 2007, the first footprint was established from North to South along the westernmost quarter of the United States. The TA finished its eastward migration in fall 2013, just before the Antares accident, and is still deployed in Alaska in June 2017. The inter-station distance is about 70 km; such a dense network is very useful for studying regional infrasound propagation and studying middle atmospheric dynamics (de Groot-Hedlin and Hedlin 2019). Data from each station are continuously transmitted to the Array Network Facility at the University of California, San Diego, where initial operational and quality checks are performed, and then sent to the Incorporated Research Institutions for Seismology (IRIS) Data Management Center (https://www.iris.edu), where all data and associated metadata are archived.

Infrasound sensors are single Hyperion microphones with a flat response between 0.01 and 20 Hz (Merchant 2015). They are not connected to a wind noise reducing system (Raspet et al. 2019). No standard array processing method, as used at the International Data Center (IDC) to process IMS infrasound network data (Mialle et al. 2019), can be applied to identify the arrivals recorded by the TA. As a consequence, the exploitation of such a network for infrasound propagation and atmospheric studies requires quiet meteorological conditions for an unambiguous discrimination between infrasound arrivals and wind bursts.

Among the 400 stations, 226 were operational and located at less than 2000 km from the launch pad at the time of the Antares event. A large high-pressure system was centered off the Eastern USA shore and at liftoff time (22:22:42 UTC),

the night has just fallen so that atmospheric turbulence reduced and night breezes have not yet risen on the coast. Thanks to those stable atmospheric conditions in the boundary layer, most of the stations of the TA exhibited low acoustic background noise before the accident, as shown in Fig. 9.1. Background noise levels are Root Mean Squared (RMS) values calculated in the 0.05–0.5 Hz frequency band for 20 min time windows, just before the fastest arrivals (set to 360 m/s at all stations, see Sect. 2.4). In this frequency band, the RMS amplitude calculated at all station is a good proxy to assess local wind noise conditions (Alcoverro and Le Pichon 2005; Walker and Hedlin 2009). This measure provides an estimate of the capability of the station to detect a broadband or low-frequency signal, such as thermospheric waves. Background colors are absolute wind speeds derived from zonal and meridional wind speeds of the first level of the ECMWF operational products (https://www.ecmwf.int/) at 21:00 UTC. At most stations, the synoptic wind speed does not exceed 3 m/s. 60% of the stations exhibit RMS amplitudes lower than 0. 1 Pa RMS, with lowest values reached in the northeast and southwest quadrants. Following this procedure, 180 identified phases at 74 stations (shown in Fig. 9.1) have been picked at the quietest stations (blue), except for the closest stations, where amplitudes are large enough to be picked whatever wind noise. In particular,

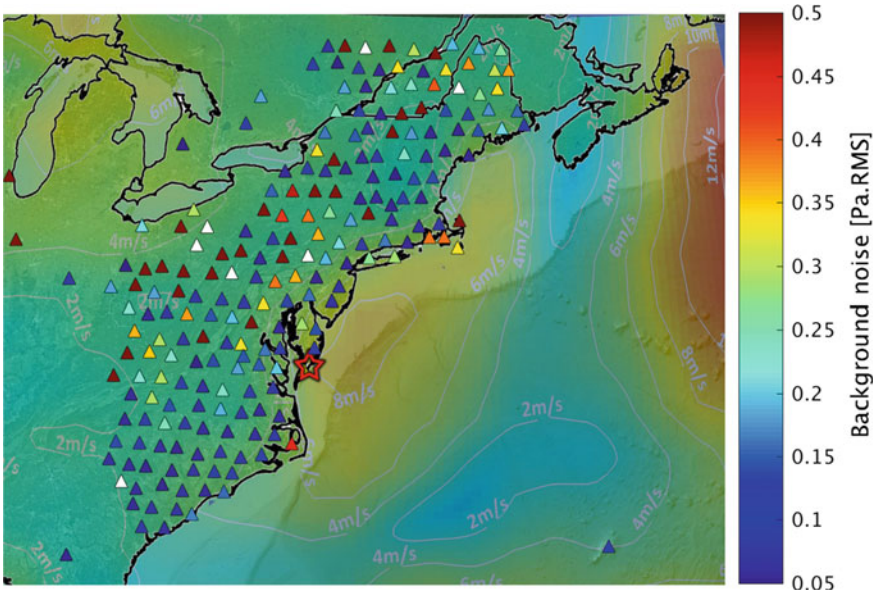

Fig. 9.1 Status of the transportable USArray at the time of Antares accident. Red star is the rocket launch pad location, triangles are stations with colors referring to acoustic background noise just before liftoff. White triangles are stations without data. Background colors code wind speed values extracted from the first level of ECWMF operational analyses, at 21:00 UTC. The steady boundary layer in addition to favorable propagation conditions has allowed picking 180 infrasound arrivals that propagated in the tropospheric, stratospheric and thermospheric waveguides

all thermospheric phases (see Sect. 2.4.3) have only been recorded on dark blue stations in the southwest quadrant. This procedure allows the probability of misidentification of arrivals on single sensors to be reduced.

9.2.2 Atmospheric Specifications

Regarding propagation modeling, the temperature and wind specifications are extracted from the ECMWF operational analyses part of the Integrated Forecast System (IFS) (91 vertical levels up to 0.01 hPa with a horizontal resolution of half a degree and a temporal resolution of 3 h) from the ground to about 80 km altitude. Above 90 km, the empirical MSIS-00 (Picone et al. 2002) and HWM-07 (Drob et al. 2008) models are used for temperature and wind speed, respectively. A cubic spline curve fitting approach is applied between 80 and 90 km to connect ECMWF wind and temperature profiles with empirical models.

In Fig. 9.2, snapshots of maximum horizontal winds are plotted for three different slices of altitude, ranging from the lower troposphere to the lower mesosphere. In addition, range-dependent vertical profiles of down- and crossed winds, temperature and effective sound speed are shown for two stations located at approximately 1000 km from the event, in opposite directions: TIGA (South-West, green station) and H65A (North-East, red station). The effective sound speed represents the combined effects of refraction due to sound speed gradients and advection due to along-path wind on infrasound propagation. Color gradient shows the variability of the different parameters along the great circle paths, between the source (in black) and the two selected stations (in color).

Above the TA stations, the propagation conditions are exceptional because winds blow northeastwards from the ground level to ~80 km altitude. Such a feature is very clear in Fig. 9.2d, e showing positive down and crossed winds until 80 km for northeastwards propagation. Two main geometric ducts exist. First, a stable stratospheric duct for which the effective sound speed between 40 and 80 km is much larger than the effective sound speed at the ground level. In this range of altitude, crossed winds reach 80 m/s, which significantly deflect the wavefront from its original launch direction (Garcés et al. 1998). Second, a thin duct in the boundary layer, between the ground level and around 1 km altitude (Fig. 9.2h) was generated by a temperature inversion (more pronounced in the vicinity of the source) coupled with moderate jets (around 20 m/s). As opposed to the stratospheric duct, the tropospheric duct varies significantly in strength, so that range-dependent features are expected to be of importance for propagation simulations. The altitudes of refraction of the waves propagating in this duct are comparable to typical infrasound wavelengths (between tens of meters to more than one kilometer) so that dispersion signatures are expected to be observed for such paths (De Groot-Hedlin 2017).

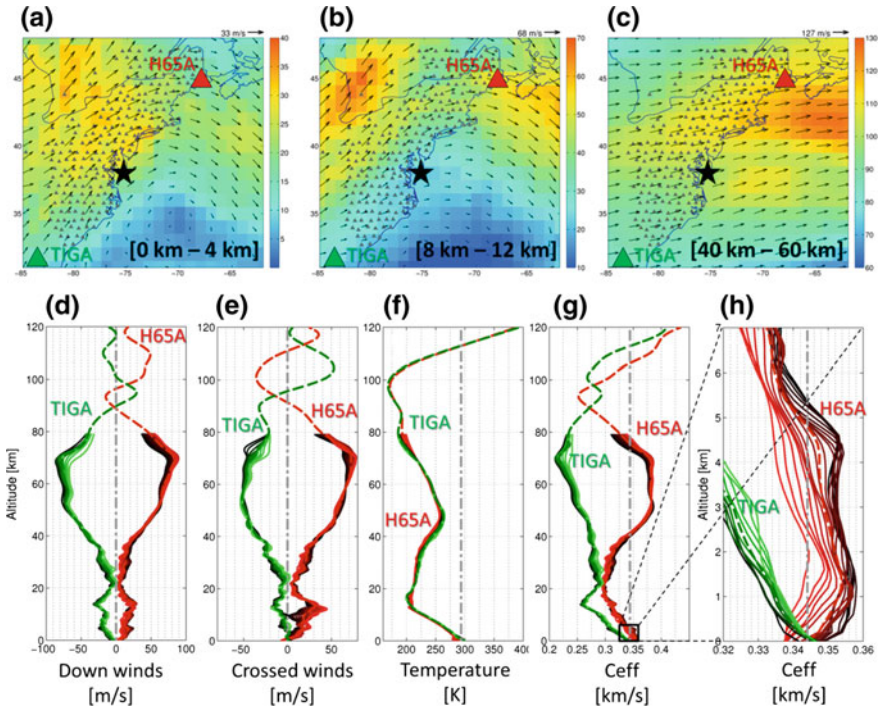

Fig. 9.2 Maps of maximum horizontal winds derived from ECMWF operational analyses in the lower troposphere (**a**), tropopause (**b**) and stratopause (**c**). At all altitudes, winds blow northeastwards. Range-dependent vertical profiles of down winds (**d**), crossed winds (**e**), temperature (**f**), effective sound speed (**g**) until 120 km and zoom of the effective sound speed until 7 km (**h**), are plotted for two stations located about 1000 km from the event, in opposite directions (H65A northeast and TIGA southwest). Color gradients show the vertical variability of the different parameters along the great circle paths, between the source (black star on the maps corresponding to the black profiles below) and the two stations (colored triangles on the maps corresponding to the colored profiles below)

9.2.3 Near-Field Measurements

When searching for infrasound arrivals generated by an event of interest, it is the routine for the analysts to focus first on the closest stations, regardless of propagation conditions. Such an approach is well suited when the spatial distribution of the stations is sparse and the number of stations is limited (e.g., the IMS infrasound network). Array processing helps to discriminate between wind gusts and coherent arrivals (Mialle et al. 2019) and to check whether arrival times and direction of arrivals are consistent with the event. Analyzing waveforms from a dense network of single sensors can also provide a detailed picture of propagation paths at a regional scale.

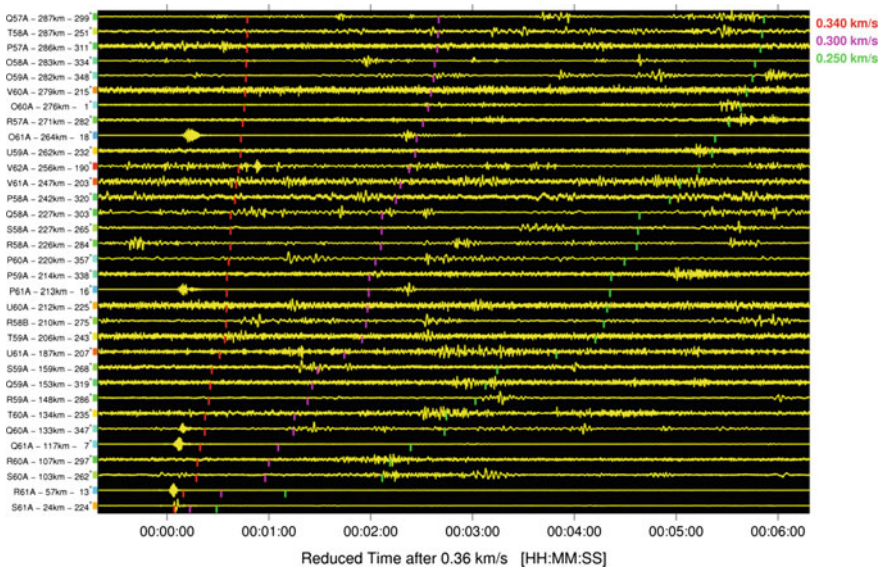

Fig. 9.3 Waveforms of the 34 closest infrasound stations located at less than 300 km from the source, sorted by distance from bottom to top. Station names, distances, and azimuths are specified to the left. A 0.5–4 Hz passband filter is applied and amplitudes are normalized. X-scale is reduced time relative to 360 m/s. Vertical red, magenta, and green vertical bars indicate, respectively 340 m/s, 300 m/s, and 250 m/s celerities so that arrivals associated to the event are typically expected to be visible between the red and green bars (Brown et al. 2012). For these stations, time windows, and filter parameters, only a few arrivals with celerities larger than 340 m/s and around 300 m/s are identified, especially to the northern part of the network

Figure 9.3 shows the waveforms from the 34 closest stations of the USArray located at distances less than 300 km from the Wallops Flight Facility. Waveforms are filtered in the 0.5–4 Hz frequency band and plotted in a time window adjusted to travel times controlled by celerities ranging from 250 to 340 m/s, typical of thermospheric and tropospheric propagation (Brown et al. 2002; Fee et al. 2013). Under strong stratospheric jets conditions, fast stratospheric arrivals (Waxler et al. 2015) can propagate with celerity as high as 360 m/s. Thermospheric waves can propagate at celerity as low as 210 m/s (Assink et al. 2012) and even significantly lower as shown in this study. For that reasons, time windows have been extended accordingly in Fig. 9.3. The vertical red, magenta, and green vertical bars indicate celerities of 340, 300, and 250 m/s, respectively. Surprisingly, no clear arrivals are identified between these bars excepted at two stations (O61A, P61A) with arrivals at around 300 m/s. Only the two closest stations S61A (24 km) and R61A (57 km) exhibit high amplitude single arrivals with different signatures (see details on Fig. 9.4). At other stations, only a few arrivals with a celerity around 360 m/s can be identified unambiguously to the North, with azimuths ranging between 347° and 16°. It is worth noting that due to the event location and the coast orientation, most

of the 34 closest stations are located West of the event, which in this situation is upwind (see Sect. 2.2).

Only two stations are located at distances less than 100 km from the event, while 32 are between 100 and 300 km. These two stations captured well the main explosion caused by rocket destruction, but also exhibit signals from the ignition and liftoff (R61A), as well as the small explosion at the bottom of the rocket (S61A, R61A). The analysis of these signals provides information about the chronology and the energy ratios of the event (Pulli and Kofford 2015).

The rocket destruction labeled as "explosion" on Fig. 9.4 is captured by the two stations with different signatures. The corresponding arrivals are manually picked as "Iw". The closest station, S61A, located 24 km southwest of the event, exhibits a symmetrical "N shape" wave with a dominant frequency of 0.4 Hz, a maximum overpressure peak of 7.6 Pa and a celerity of 342 m/s. The other station, in the opposite direction and 2.4 times farther, exhibits a clear dispersive wave train of 6 s duration with maximum energy between 0.5 and 4 Hz, a maximum amplitude of 24 Pa (more than three times larger than the one observed at the closest station) and a high celerity value of 360 m/s. As shown in Fig. 9.2h, the temperature inversion coupled with the shallow northeastwards jets cause very different propagation in opposite directions, even at short distances. The dominant frequencies observed at R61A are consistent with the duct thickness of about 1 km and the downwind advection of about 20 m/s explains the high celerity for that arrival.

This analysis illustrates how the propagation medium significantly affects waveforms even at short distances, suggesting that particular caution has to be paid when processing waveforms, especially when estimating the acoustic source energy. Existing empirical models such as those proposed by Kinney and Graham (1985) or Pierce et al. (1973) do not take into account the variability of the atmosphere (Garces 2019). Fitting the N shape wave observed at S61A with theoretical blast waves (Reed 1977) would lead to large errors: the measured positive phase duration is inconsistent with the maximum overpressure peak. To get around this problem associated to atmospheric conditions, Kim and Rodgers (2016) propose a full 3-D finite difference method that can reasonably be applied when considering propagation ranges of a few tens of kilometers.

The small explosion which occurs at the bottom of the rocket (NASA 2015; Pulli and Kofford 2015) is labelled here as "incident" and is visible at both S61A and R61A stations. Due to the favorable North Eastwards tropospheric jet, the frequency content is very different at the two stations. While most of the energy is trapped in the shallow tropospheric duct for R61A with maximum amplitudes between 0.5 Hz and 4 Hz, the signal at S61A exhibits much higher frequencies, between 8 and 20 Hz. The most energetic arrival is associated with the rocket destruction and is the only one detected at larger distances. In the following, we focus only on signals generated by this event.

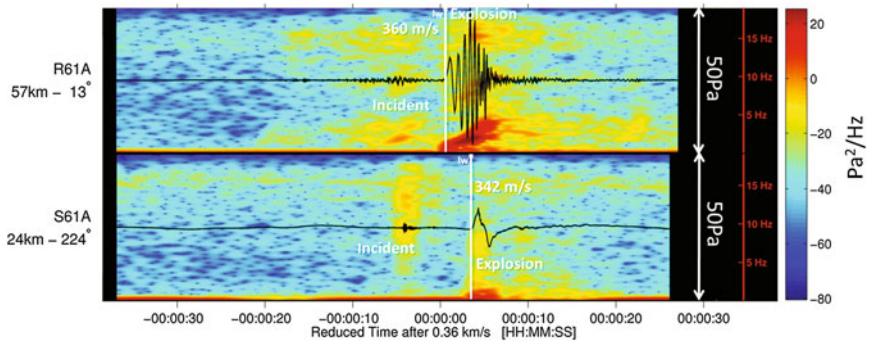

Fig. 9.4 Details on raw waveforms recorded by the two stations located at distance less than 100 km from the event (S61A, 24 km, South-West and R61A, 57 km, North-East). Spectrograms between 0.1 and 20 Hz are plotted in the background. The same amplitude and frequency vertical scales have been applied for both stations. The manually picked vertical white bars are associated to the rocket destruction event. For that latter event, the frequency content and waveform signatures are different at the two stations, with maximum amplitude more than 3 times larger at R61A, although 2.4 times farther than S61A

9.2.4 Far-Field Measurements

Signals with the largest signal-to-noise ratio (SNR) are expected in regions where the background noise is the lowest (blue stations on Fig. 9.1) along North/North-East paths (favorable tropospheric and stratospheric propagation, see Fig. 9.2). This identification strategy is more efficient than the one adopted in Sect. 2.3, where signals of interest can be drowned within incoherent noise, as shown in Fig. 9.3, on which signals are difficult to identify.

9.2.4.1 Tropospheric Phases

Overall, 27 tropospheric arrivals have been identified. 26 arrivals have been manually picked at 26 stations North-East of the event up to 1051 km, plus one at the closest station S61A located 24 km South-West of the event. Picks are represented by vertical white bars labeled as "Iw" in Fig. 9.5. All tropospheric arrivals recorded North-East have common features, which are given as follows:

(1) The celerity values are abnormally high for tropospheric arrivals (between 360 m/s for the closest stations and 350 m/s for the farthest stations) while typical values are expected around the speed of sound at the ground level (i.e., 340 m/s). This feature is explained by the moderate northeastwards advection

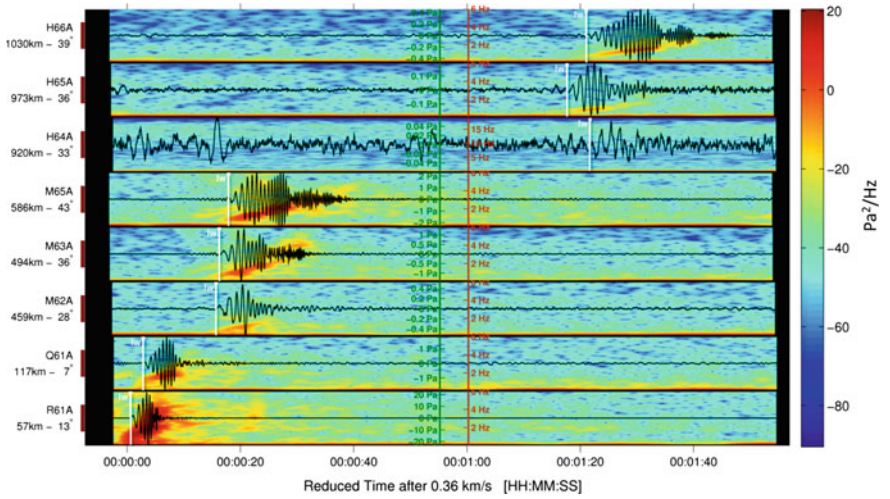

Fig. 9.5 Example of tropospheric dispersive waves at distances ranging from 57 to 1030 km in the North-East direction. Station names, distances, and azimuths are specified to the left. A 0.5–4 Hz passband filter is applied and amplitudes are normalized by station. X-scale is reduced time relative to 360 m/s. Spectrograms between 0.1 and 6 Hz are plotted in the background. While waveforms are different in shapes, amplitudes, and durations, they exhibit similar dispersion patterns

in lower troposphere (around 20 m/s) which persists along the North-East coastline.

(2) The frequency contents are comparable, between 0.5 and 4 Hz, with pronounced dispersion patterns increasing with distance. The most striking dispersion curves are shown in Fig. 9.5. This feature is explained by the shallowness of the tropospheric duct. When the thickness of the waveguide is comparable to the signal wavelength (maximum refracting height of ~1 km altitude), dispersion occurs (Waxler 2003; Talmadge et al. 2008). It is worth noting that waveforms vary significantly in shape, amplitude, and duration from one station to another depending on the structure of the waveguide.

(3) The amplitudes of the tropospheric waves strongly depend on the direction of propagation, as it can be observed when comparing signals at M62A, M63A, and M65A to signals at H64A, H65A, and H66A. These differences are explained by two effects: (1) the shallow tropospheric duct slightly weakens with more northernly propagation; (2) the propagation to the easternmost stations occurs above the ocean. For example, the propagation path to H66A, located 1030 km North-East (39°) of the event is almost purely oceanic and the maximum amplitude is 0.5 Pa. For H65A (973 km, 36°) and H64A (920 km, 33°), the amplitude drops down to 0.15 and 0.05 Pa, respectively. Within these

ducts, the atmospheric attenuation is comparable, only ground/topography interactions change. The same behavior is observed at M62A, M63A, and M65A. Full waveform modeling accounting for ground impedance and topography could explain this effect (e.g., Waxler and Assink 2019; de Groot-Hedlin and Hedlin 2019).

9.2.4.2 Stratospheric Phases

Following the same methodology, a large amount of stratospheric phases have been manually identified and picked at distances between 197 km (P61A) and 1154 km (I51 GB). Stations, where stratospheric arrivals are picked, are located in a narrow range of azimuths (except for the I51 GB IMS station), revealing the footprint of stratospheric branches thanks to the high density of stations. 107 stratospheric arrivals are labeled from Is1 to Is7, with celerities ranging from 270 to 340 m/s.

Figure 9.6 shows the waveforms of the 14 quietest stations located North-East of the event (most stations are located in directions between 26° and 36°), from 57 km (R61A) to 973 km (H65A). Unlike Fig. 9.3, phase picking and labeling is straight-forward: the fastest arrivals are tropospheric waves and are recognized from their pronounced dispersive patterns (see previous section). Then, the first visible stratospheric bounce occurs at 213 km (Q61A), second bounce at 386 km (N62A), third bounce at 636 km (K63A), fourth bounce at 804 km (I63A), and fifth bounce at 920 km (H64A). Phase labeling is made without any ambiguity at stations with high SNR values (like those of Fig. 9.6) and are compared to other nearby stations for which the identification is trickier.

Is1 is still observed at more than 1000 km with a celerity of 340 m/s, which is typical for tropospheric arrivals. Fast stratospheric arrivals have already been observed in the literature (Evers and Haak 2007), however, they do not belong to the fast branch as identified by Waxler et al. (2015). For this event, all picked stratospheric arrivals have arrival times consistent with propagation at shallow incidence angles, as confirmed by ray tracing simulations (see Sect. 9.3). Such observation is original and occurs because of the uncommon atmospheric state where moderate to strong winds blow in a North-East direction at all altitudes from ground to lower mesosphere (Fig. 9.2d, red curves). North-East advection here plays a major role in controlling the propagation times of both tropospheric and stratospheric phases.

However, a few stratospheric arrivals have much smaller celerity values, between 270 and 290 m/s. Such arrivals are only observed at quiet northern stations with azimuth ranging from 356° to 15° (J57A, J58A, J59A). The frequency content and waveform amplitudes at those stations are lower than at other stations and correspond to effective sound speed ratios (dimensionless parameter defined by the

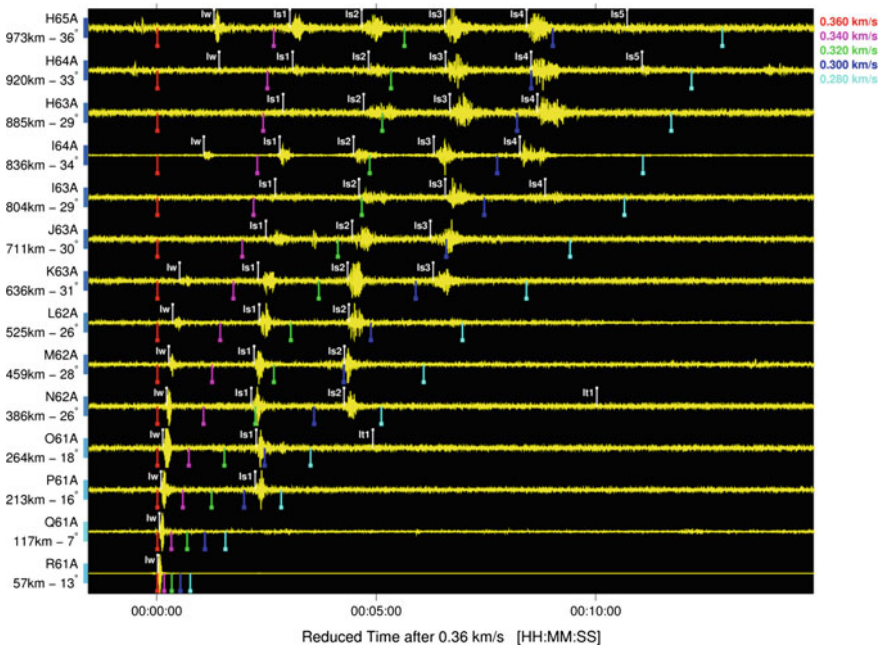

Fig. 9.6 Example of tropospheric and stratospheric returns at North-East stations from 57 to 973 km, sorted by distance from bottom to top. Station names, distances, and azimuths are specified to the left. A 0.5–4 Hz passband filter is applied and amplitudes are normalized by station. X-scale is reduced time relative to 360 m/s. The vertical white bars, manually picked as Iw and Is phases, are associated to the rocket destruction. Such a representation allows identifying unambiguously stratospheric branches from Is1 (which persists from 213 to 1000 km) to Is5 (which appears at 920 km). These branches are consistent with the so-called "slow stratospheric branches" (see Sect. 9.3) and are unusually fast for such typical stratospheric branches (Is1 celerity is 340 m/s at 973 km). The vertical colored bars indicate celerities from 360 m/s (red) to 280 m/s (cyan)

ratio between the effective sound speed at 50 km altitude and the sound speed at the ground level) slightly lower than 1. Arrival shapes are more emergent and last longer compared with stations, where the effective sound speed is larger than 1. These diffracted arrivals (depicted as "Is diff" on Fig. 9.9) observed upwind were reported by Green et al. (2011).

9.2.4.3 Thermospheric Phases

In the downwind direction, the increase of the effective sound speed with altitude refracts infrasound back to the ground surface. In contrast, when acoustic propagation occurs upwind, the decrease of the effective sound speed refracts infrasound upwards. The ground-to-stratosphere acoustic waveguide is less likely to exist, increasing the likelihood that the sound will propagate toward the thermosphere.

The decrease of density in the mesosphere and lower thermosphere controls the wave attenuation, the effects of which are especially pronounced at high frequencies. While vibrational losses are the main process of absorption in the middle atmosphere (up to 60 km at 0.5 Hz), classical and rotational relaxation losses dominate above ~80 km altitude (Sutherland and Bass 2004). Moreover, at such altitudes, signal amplitude increases due to the reduction in density. The high amplitude compressional phases are 'hot' and therefore travel faster, while the high amplitude rarefaction phases are 'cold' and therefore travel slower. Hence the signal lengthens as the compressional and rarefaction phases move at different speeds (e.g. Pierce et al. 1973, Gainville et al. 2009; Sabatini et al. 2016). The signal duration and dominant frequency are essentially controlled by the source energy and the turning height of the waves (Waxler and Assink 2019). Consequently, the dominant frequency of the thermospheric returns is expected to be lower than other tropospheric and stratospheric phases.

By lowering the frequency band, the SNR decreases as the background noise is more sensitive to atmospheric turbulences and wind bursts (Walker and Hedlin 2009). Because thermospheric returns are predicted in all directions due to the strong increase of the temperature in the lower thermosphere, focus is given to the stations which exhibit the lowest background noise (i.e., dark blue stations in Fig. 9.1), without preferred directions.

46 thermospheric phases have been picked and identified mostly on stations located South-West from 187 km (U61A) to 1026 km (TIGA). Following the same strategy applied for stratospheric arrivals, It1 to It4 phases have been identified. Figure 9.7 presents the waveforms at 30 stations, where 46 arrivals have been picked. Due to the strong attenuation of these phases, their observations are often limited to the first thermospheric bounce for energetic events (e.g., Ceranna et al. 2009). As was done for stratospheric arrivals, visualizing waveforms in a reduced time plot (Fig. 9.7) allows consecutive branches to be identified, and phases are labelled without ambiguity. The number of picked thermospheric phases is unprecedented. Ray tracing simulations (Fig. 9.13) and arrival alignments in range-celerity plots (Fig. 9.9) provide results consistent with these observations. A brute force identification of low SNR phases, trace by trace, without selecting station considering their background noise levels would have been probably impossible.

The following thermospheric returns exhibit unusual features:

(1) Celerities of most arrivals are exceptionally low. Among the 44 picked arrivals, 35 have celerities between 160 and 220 m/s. The first It2 pick at V59A (at 336 km) and It3 pick at W57A (at 501 km) have celerities of 160 m/s, which is significantly low compared with values found in the literature. So far, only Assink et al. (2012) reported celerities of 220 m/s at the first thermospheric bounce from volcano eruptions. Due to the northeastwards tropospheric flow, tropospheric phases propagate as high as 360 m/s (Sect. 2.4.1) and a few stratospheric phases propagate at 340 m/s (Sect. 2.4.2). In the opposite direction, the propagation is upwind (Fig. 9.2d, green curves) at all altitudes so that advection reduces wave celerities.

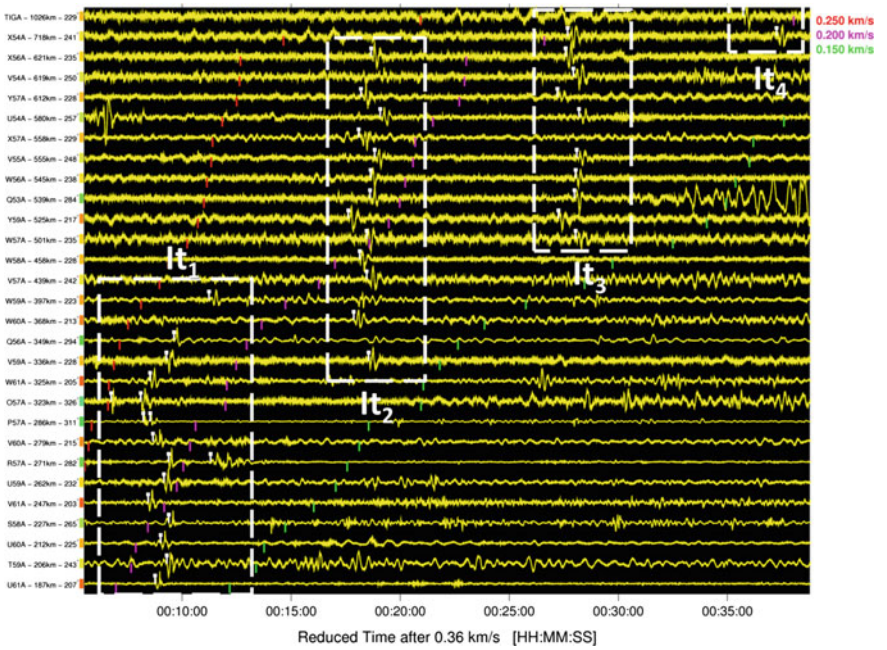

Fig. 9.7 Waveforms at the 29 quietest stations of the South-West quadrant, from 187 km (U61A) to 1026 km (TIGA), sorted by distance from bottom to top. X-scale is reduced time relative to 360 m/s. Station names, distances, and azimuths are specified to the left. A broad 0.05–10 Hz passband filter is applied to capture low frequencies and shocks. Amplitudes are normalized by station. 44 thermospheric returns are manually picked. The vertical white bars are manual It picks associated to rocket destruction. Such a representation allows the identification of unambiguously thermospheric branches from It1 (beyond 187 km) to It4 (beyond 718 km). Exceptionally low celerities are associated to the first It2 and It3 arrivals, which are as low as 160 m/s. The vertical colored bars indicate celerities from 250 m/s (red) down to 150 m/s (green)

(2) Bounces occur at short distances from the source. For example, the first thermospheric bounce is observed at 187 km. This is unusual for the thermospheric return which generally occurs between 200 and 300 km.
(3) While It3 and It4 arrivals are stable in shape and duration, the arrivals at the first thermospheric bounce exhibit very different signatures (see Fig. 9.8). Depending on the distance and the direction, the results of nonlinear effects and absorption in the mesosphere and lower mesosphere combined with additional caustic effects cause, some It1 phases to exhibit typical "N" shape shocks while others exhibit smoothed "U" shapes, or a simple sine arch. This collection of shapes provides useful information on both propagation medium (turning height) and source energy (from arrival duration).

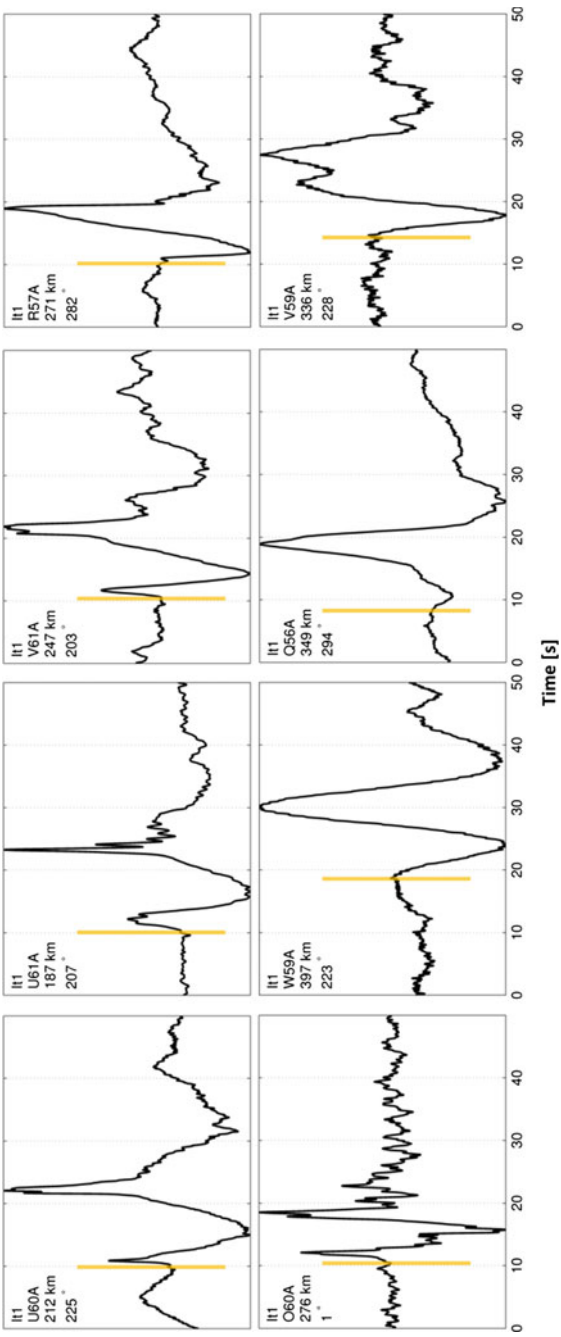

Fig. 9.8 Representative signatures of thermospheric phases at the first bounce. Station names, distances, and azimuths are specified in the top left corner of each panel. Depending on the distance and the direction, some It1 phases exhibits typical "N" wave (Q56A, R57A), shocked "U" (U60A, U61A, O60A) and smoothed "U" waves (W59A) or a simple sine arch wave (It2 → It4, not plotted here). The vertical orange bars are manual It1 picks

9.2.4.4 Observations Summary

Such a dense measurement platform offers good opportunities to provide detailed insight into propagation features at regional and continental scales (Walker et al. 2011; De Groot-Hedlin and Hedlin 2015), even when conventional array processing methods such as PMCC (Progressive Multi-Channel Correlation, Cansi 1995) or F-detector (Smart and Flinn 1971) cannot be applied. The amount and variety of infrasound arrivals observed for this event are uncommon with 180 manual picks identified as tropospheric, stratospheric or thermospheric arrivals at 74 stations of the TA. The dense spatial coverage of the TA and high SNRs allow clear and unambiguous phase identification. The exceptional range of arrival celerities, ranging from 360 m/s for tropospheric phases down to 160 m/s for thermospheric phases is the most striking result.

Figure 9.9a shows the spatial distribution of the different phases detected. Figure 9.9b shows all picks in a classical celerity-range diagram, useful for identify propagation branches. A blind identification and phase labeling have been done without simulation (e.g., ray tracing, see Sect. 9.3). The different tropospheric, stratospheric, and thermospheric branches are identified in waveform plots, considering the quietest stations, appropriate filter parameters, and time windows.

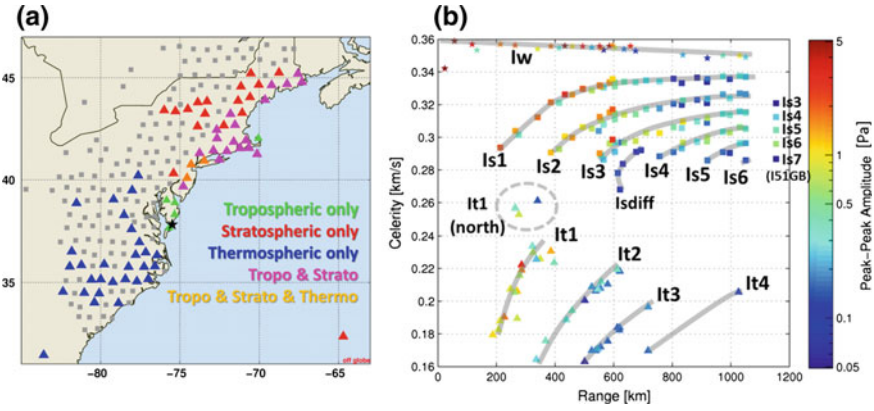

Fig. 9.9 **a** Spatial distribution of detecting stations. Colors indicate phase types. Green stations detect only tropospheric arrivals, red stations detect only stratospheric arrivals, blue stations detect only thermospheric arrivals, magenta stations detect both tropospheric and stratospheric arrivals, and orange stations detect tropospheric, stratospheric and thermospheric arrivals. The atmospheric state at the time of the event together with event location, coast orientation, and station distribution explain the South-West/North-East separation of thermospheric/tropospheric–stratospheric phases. **b** Celerity-range diagram. Colored squares and triangles represent stratospheric and thermospheric arrivals, respectively. Color codes the peak-to-peak amplitude in Pa. Iw, Is1 to Is6 and It1 to It4 branches are identified (gray lines) and show the unexpected broad range of celerities, from 360 m/s for tropospheric arrivals detected at the closest stations down to 160 m/s for some It2 and It3 thermospheric phases. The celerity of Is1 branch reaches 340 m/s at 1000 km, which is also an unusual observation

Branches of different phases are highlighted in gray in Fig. 9.9b. Iw, Is1 to Is6 and It1 to It4 branches are identified. Three main groups of arrivals do not align properly with these branches, which are given as follows:

- Five stratospheric arrivals at the IMS station I51 GB at 1154 km (Is3 to Is7) cannot be labeled without simulation (see Fig. 9.10 in the next section). Unlike other stratospheric arrivals which are picked North-East of the event, no stations is located to the South-East.
- Four It1 arrivals denoted as "It1 (north)" in Fig. 9.9b. These thermospheric arrivals are the only ones that have been picked to the North (N61A, N62A, O60A, and O61A), under stratospheric downwind conditions. Unlike all other picked thermospheric arrivals to the South-West, associated celerities to the North range between 245 and 260 m/s (Fig. 9.9a, orange stations).
- Five stratospheric arrivals along "Isdiff" branch. These stratospheric arrivals are the only ones which have been picked for paths where the effective sound speeds are slightly lower than 1, at the western most red stations I59A, I60A, J57A, J58A, and J59A (Fig. 9.9a). Arrivals at those stations are more diffused and exhibit lower celerities and smaller amplitudes compared to those of geometric arrivals. These arrivals are also studied in Sect. 9.4.

9.3 Phase Identification and Location

180 phases associated to the Antares event have been identified at 74 stations. From these phases, 185 measures were derived: 180 arrival times (175 at TA stations, 5 at I51 GB) and 5 back azimuths (at I51 GB). We have seen in Sect. 9.2 that extreme celerity values of most of those phases are unusual while other are more typical especially for stratospheric returns, as shown by Nippress et al. (2014) under typical summer conditions. The impact of the broad range of celerities derived from ray tracing simulations on the source location is here evaluated and compared with the location result using empirical propagation tables.

9.3.1 Construction of Propagation Tables

The first step in the location procedure is to build propagation tables in celerity and azimuthal deviation from a pre-location, by station and by phase, and to assign them to each measure. Such tables depend on the atmospheric state between the source and the stations, at the time of the event. This step requires the construction of propagation tables per phase and bounce order, and the labeling of the detected infrasound phases. Considering the various types of phases, the possibly large number of bounces and the likely rough pre-location, the probability of wrong phase identification is high and can degrade the location result when done automatically.

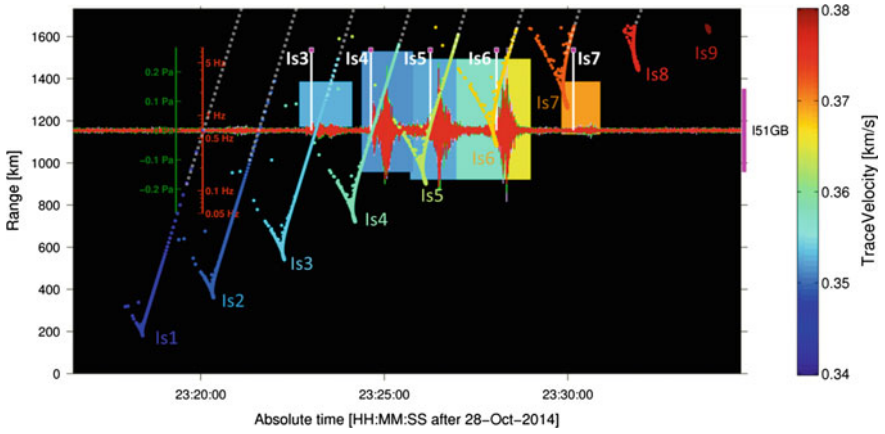

Fig. 9.10 Recorded waveforms at I51 GB, 1154 km South-East of the event. Ray bounces superimposed in the range-time space allow the identification of stratospheric arrivals, from Is3 to Is7. Colored rectangles in the background are PMCC detections in the time-frequency space with trace velocity color coded. Dashed gray lines are linear extrapolation of slow celerity stratospheric branches, referred to as "branch extension" in the next Section

In the automatic processing pipeline, phase-dependent empirical tables are generally preferred. Brown et al. (2002), Brachet et al. (2009) and Fee et al. (2013) showed that the different phases have distinct celerity ranges. Celerities have typical values of 340, 300, and 250 m/s for tropospheric, stratospheric, and thermospheric arrivals, respectively. In the case of the Antares event, celerities exhibit deviations beyond wide ranges already highlighted in several studies (Ceranna et al. 2009; Assink et al. 2012; Waxler et al. 2015). In order to quantify the location errors, location results derived from empirical tables and ray tracing simulations with phases interactively labeled are compared.

Classical ray tracing methods (e.g., Candel 1977) are often used to compute arrival time and geometrical wave characteristics needed to build propagation tables (e.g., Ceranna et al. 2009). The main reasons are given as follows:

- low computational cost, well adapted to operational constraints;
- the azimuthal deviations can be estimated from the set of three-dimensional ray paths which compose each table;
- a time and range-dependent atmosphere are handled without significant increase of computation time;
- propagation tables can be built automatically per phase and per bounce order and associated to distinct ray trajectories, unlike fast full waveform modeling techniques such as normal modes or parabolic equation methods (Waxler and Assink 2019).

However, the ray tracing method models the propagation of acoustic waves in the geometrical acoustic limit and exhibits limitations which restrict its utilization in operation, as follows:

- The high-frequency hypothesis is based on the assumption that space and time scales of atmospheric properties (temperature, wind, and density) are much larger than acoustic wave scales. All phases cannot be modeled by ray tracing as the high-frequency approximation made in the Eikonal equation does not account for diffraction (Gainville et al. 2009) which can explain the leakage of acoustic energy out of geometric acoustic ducts. The normal mode technique efficiently overcomes this limitation (Assink et al. 2019) thanks to its capability to calculate separately frequency-dependent modes for phase velocities which are sensitive to borderline cases (i.e., for which $C_{\text{eff-ratio}}$ is close to 1).
- Ray tracing is not sensitive to fine-scale atmospheric structures such as turbulence and gravity waves, as diffraction is the mechanism responsible for partial wave refractions on such small structures (e.g., Kulichkov 2009; Kulichkov et al. 2010; Kulichkov et al. 2019).
- To improve the location result, normal mode techniques can incorporate a probabilistic description of propagation models by applying a perturbative approach (e.g., Millet et al. 2007; Cugnet et al. 2019).

The long-range propagation is simulated here using the Windy Atmospheric Sonic Propagation ray theory-based method (WASP-3D) which accounts for the spatiotemporal variations of the horizontal wind terms along the raypaths in spherical coordinates (Virieux et al. 2004). This method provides all the required kinematic parameters of each ray (travel time, incidence angle, and azimuth deviation) for comparisons with measurements. It is worth highlighting that so far, despite its identified limitations, ray tracing is the only propagation code which allows azimuthal deviations at telesonic ranges to be estimated with reasonable computation times and propagation tables to be built automatically.

For each source to station propagation path, 11 equally spaced azimuths within an interval of $\pm 10°$ centered on the true bearing are considered. In each direction, 200 rays are launched, with elevation angles ranging between 0 and 40° from the horizontal and a step of 0.2°. Among the 2200 (200×11) simulated trajectories, only rays intersecting a volume of 20 km radius, 2 km thickness, centered on the station are selected. These rays are automatically classified and labeled depending on their turning heights and number of ground reflections before reaching the station. Rays refracting below 15 km are labeled as Iw (tropospheric), between 15 and 70 km as Is (stratospheric), and above 70 km as It (thermospheric). A suffix indicating the bounce order is appended to the label. By applying this procedure, which is preferred to costly eigenray techniques, statistics on set of rays which compose each table are calculated. Extracted celerity models and azimuthal deviations are median values of rays of each table.

The celerity model is associated to each arrival which has been labeled following the methodology presented in Sect. 9.2. At I51 GB, in addition to the celerity models, azimuthal corrections are also considered.

Because no closer station exists between the source and I51 GB (the path is purely oceanic), branches cannot be identified and the five recorded arrivals cannot be labeled without simulations. In Fig. 9.10, a comparison of ray simulations with

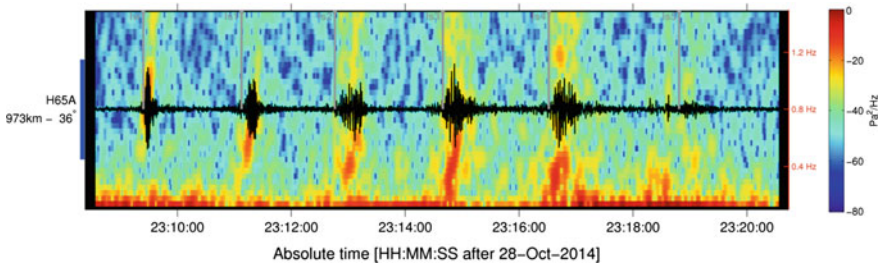

Fig. 9.11 Evidence of a dispersive tropospheric signature on the stratospheric arrivals at station H65A, located 973 km North-East of the Antares event. A fraction of the energy ducted in the narrow tropospheric duct leaks upwards by diffraction and is refracted back to the ground in the stratopause region. The dispersive pattern is conserved during the stratospheric propagation and is less pronounced for higher incidence angles: Is4 and Is5 exhibit less dispersion than Is1 and Is2

the signals suggest that the first recorded phase is Is3 and the last one is Is7. I51 GB is the only array of the IMS network that detected the event. This station consists of four elements with an aperture of 2.4 km. PMCC detections have been calculated with the DTK-PMCC software by applying a 1/3rd log-scaled frequency band configuration (Garcés 2013). The detection results are displayed by rectangles in the time-frequency space on Fig. 9.10, superimposed upon the waveforms. Element I51H1, which was significantly noisier than the 3 other elements, was not used for the calculation. Colored rectangles represent trace velocity values increasing with time (from 350 m/s for Is3–370 m/s for Is7) as the elevation angle of the waves increases with the bounce order. Such an observation is typical for ground to ground propagation (e.g., Ceranna et al. 2009). Ray simulations coupled with array processing confirm that stratospheric phases are associated with slow celerity branches for waves propagating at shallow elevation angles. Fast arrivals exhibit significantly higher trace velocities. At I51 GB, 10 measures are used for the source location: five arrival times and five back azimuths together with celerity models and azimuthal deviations derived from ray tracing simulations.

9.3.2 Extension of Propagation Branches

For TA stations, stratospheric ray branches North-East of the event are not as clear as the ones at I51 GB. In Fig. 9.12, ray simulations are compared to the waveforms at 14 stations, with azimuths ranging from 26° to 36°. Unlike at station I51 GB, the first two stratospheric bounces (in blue) are range limited and do not extend beyond 1000 km, as observed on the waveforms. Thus, remote observations cannot be used for location as no Is1 rays reach stations above 350 km. This is explained by the strong tropospheric duct which traps all rays with the lowest incidence angles. By considering refraction effects only, waves propagating at shallow angles cannot escape into the stratosphere. However, a fraction of this energy leaks in the

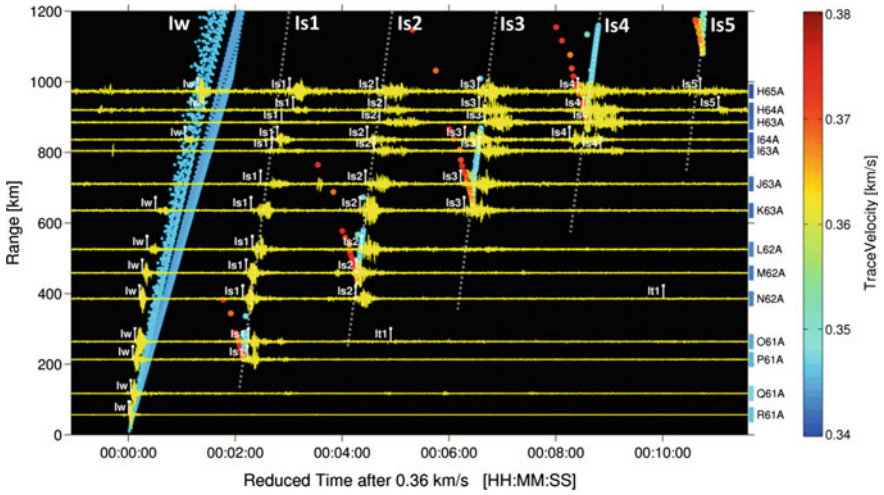

Fig. 9.12 Ray tracing results for 14 stations located North-East of the event, in the 26–36° azimuth range. Ray bounces superimposed in the range/time space allow identifying tropospheric (Iw) and stratospheric (Is) arrivals, from Is1 to Is5. The colorbar codes the ray trace velocity (and associated wave incidence angle). Due to the strong interaction between the tropospheric and the stratospheric ducts, ray tracing cannot explain all recorded arrivals. The manual extension of the stratospheric branches represented by dashed gray lines allows here capturing diffraction effects

stratospheric duct and can be observed at stratospheric distances. Evidence of that phenomenon is the dispersive pattern of some stratospheric arrivals observed in Fig. 9.11.

Due to the high-frequency approximation intrinsic to ray tracing techniques, this diffractive effect cannot be modeled. Rays with higher incidence angles escape from the tropospheric duct which explains the increase in ray bounce density with increasing bounce order: Is3 and Is4 tables can correctly be built with the methodology described above, without being perturbed by the tropospheric duct.

In order to work around those limitations, stratospheric branches are extended manually to build all stratospheric tables for stations that have an effective sound speed ratio larger than 1. This extension is represented by gray lines on Fig. 9.12. In a range-independent atmosphere, slow celerity branches are parallel when moving away from the caustic (shown by gray dashed lines on Fig. 9.10). For the sake of simplicity, the extension is done in parallel to the well-defined Is4 branch (see Fig. 9.12). Such branch extensions are also justified by classical interaction between the acoustic wave field and small-scale atmospheric structures such as gravity waves, which tend to lengthen the location extent of each bounce area. Finally, celerity models for which no rays are intercepted in the vicinity of the stations are built manually and associated with the corresponding measures. All measures and associated models are summarized in the Appendix (Table 9.1).

This method is valid for stratospheric arrivals only if a geometric duct is predicted. For the “Isdiff” branch, as identified on Fig. 9.9b, the effective sound speed

at the stratopause is lower than the sound speed at the ground level. In such conditions, no stratospheric extension is possible because all rays escape into the thermosphere. As a consequence, such arrivals cannot be used for location (represented as orange lines in Table 9.1).

The methodology for building propagation tables is also valid for thermospheric arrivals. The interaction with the tropospheric duct is not an issue like for stratospheric arrivals because thermospheric arrivals are recorded South-West of the event, in directions where the tropospheric duct does not exist. In Fig. 9.13, ray bounces are overlaid to the waveforms at 11 stations located South-West of the event, with azimuths ranging from 222 to 232°. Above 90 km altitude, the effective sound speed is derived from the MSIS-00 empirical model (Picone et al. 2002) for the temperature and HWM-07 (Drob et al. 2008) for the wind speed. Between 80 and 90 km, these empirical models are connected to ECMWF wind and temperature profiles by applying a cubic spline curve fitting approach. Even if dynamical processes in the mesosphere and lower thermosphere are not well resolved by Numerical Weather Prediction (NWP) products (e.g., Le Pichon et al. 2005, 2015), the predicted arrival times are generally consistent with the observations (Fig. 9.13) even if all arrivals cannot be explained.

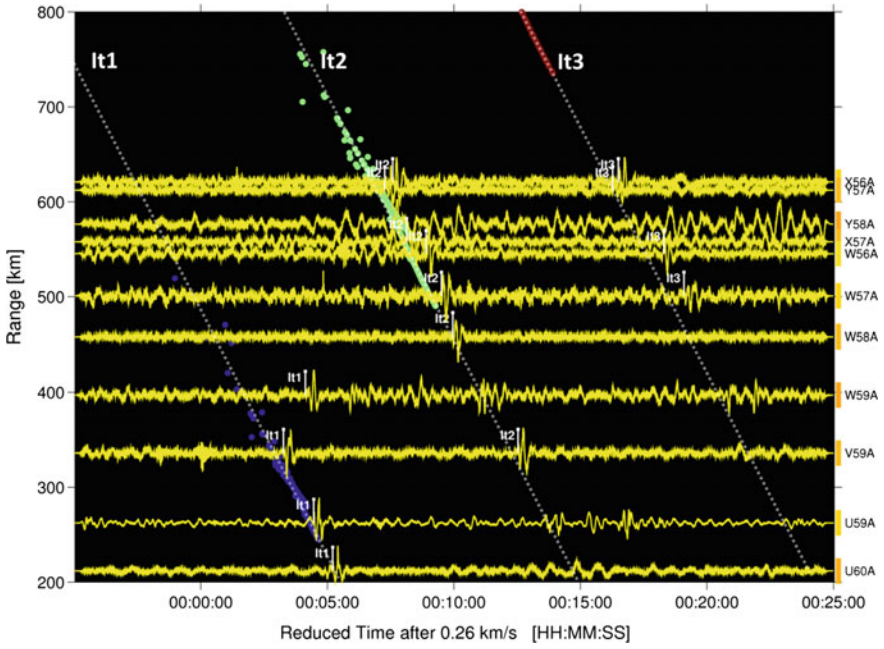

Fig. 9.13 Ray tracing results for 11 stations located southwest of the event, in the 222–232° azimuth range. Ray bounces superimposed in the range/time space allow identifying thermospheric arrivals, from It1 to It3. Colors represent the bounce order. Compared with modeling, thermospheric bounces occur at shorter distances from the source

Of specific interest are bounces occurring at short distances from the source, which is uncommon for thermospheric returns. For example, the first thermospheric bounce in the direction of U60A is observed at 212 km, the second thermospheric bounce at 336 km (V59A) and the third thermospheric bounce at 500 km. Such short distances are not explained by ray tracing and would deserve to be studied. They are probably the results of poorly constrained models, combined with unpredicted diffraction effects.

The branch extension process has to be done again but this time for shorter distances, unlike stratospheric phases for which the extensions had to be done for larger distances. It1, It2, and It3 tables can thus be built even when no thermospheric rays are intercepted. All measures and associated models are summarized in Table 9.1. The only two arrivals not used for the location are It4 (orange lines in Table 9.1).

9.3.3 Source Localization

The localization procedure used in operations at the French National Data Center (NDC) is a grid search algorithm, in which both arrival times and back azimuths are taken into account and weighted. The weights associated with the arrival times and back azimuths are referred as Tweight and Bweight, respectively. Since the origin time is not known, differential travel times are considered for all possible pairs of stations. The localization procedure is described as follows:

- For each two-station combination, the differential travel times are computed for each point of the grid and linearly weighted (if the difference is equal to zero, the corresponding weight is one; if the difference is larger than Tweight, the corresponding weight is null).
- For each back azimuth measure, the differential is computed at each point of the grid and linearly weighted (if the difference is equal to zero, the corresponding weight is one; if the difference is larger than Bweight, the corresponding weight is null).
- All obtained weighted functions are added up in order to provide a two-dimensional probabilistic density function, where its minimum provides the best location.
- The origin time is the median value estimated from the resulting spatial location and celerity models.

Tweight and Bweight are typically taken equal to 300 s and 10°, respectively. The grid size, centered on the Antares event, is 1000 km × 1000 km with a resolution of 500 m. In order to provide a realistic picture of the location, propagation models are randomly perturbed with a uniform distribution centered on the ray tracing results. A maximum perturbation of 10 m/s is taken for the celerity and 3° for the azimuth (Ceranna et al. 2009). The localization procedure is performed 500

times. The 95% confidence ellipse is finally calculated from the location distributions. Two types of locations are computed: one using empirical propagation tables and one using propagation tables derived from ray tracing simulations. The ground truth location is 2014/10/28 22:23:03-37.834 N, 75.488 W.

- *Tables derived from ray tracing*. 176 of the 185 measures are used. Only phases that belong "Isdiff" branch and It4 are not used for the reasons provided above. The obtained location is 2014/10/28 22:23:01-37.83 N, 75.76 W. The location and 95% confidence ellipse are plotted in Fig. 9.14a. The exhaustive list of measured arrival times, measured back azimuths, celerity models, azimuthal deviations, and residuals for both time and back azimuth are summarized in Table 9.1. Peak-to-peak amplitudes are also provided for information. The location is found 2 km East of ground truth information with a difference in origin time of 2 s. The ellipse major axis is 10 km long. Despite significant time residuals, which reach one minute for some thermospheric phases and several tens of seconds for stratospheric phases, the obtained location result is consistent given the large number of measures. Without the TA network, considering only the sparse IMS network, the location could not be obtained.
- *Empirical tables*. Only one type of phase per station is used. When several stratospheric arrivals are measured at a station, only the first one is considered with a celerity model set to 300 m/s. When several thermospheric arrivals are measured on a station, only the first one is considered with a celerity model set to 250 m/s. The celerity model for tropospheric phases is 340 m/s. Finally, 99 of the 185 measures are used in that configuration. The obtained location is 2014/10/28 22:23:47-38.11 N, 74.74 W. The location and 95% confidence ellipse are plotted in Fig. 9.14b. Compared with the location obtained with propagation

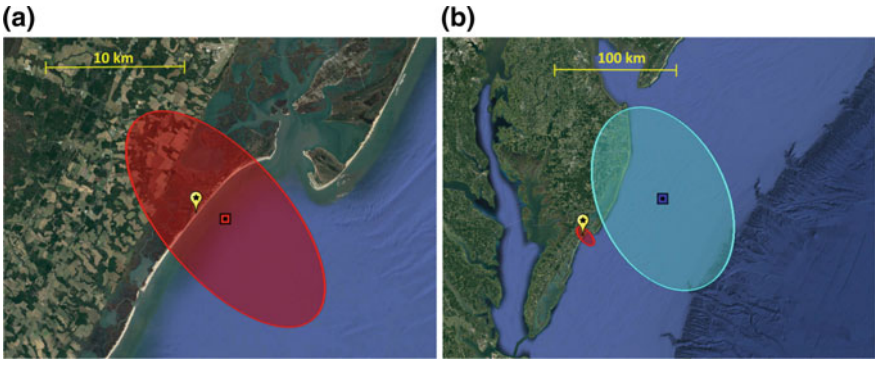

Fig. 9.14 Location results and associated 95% confidence ellipses. **a** In red from propagation tables obtained with ray tracing (176 measures), **b** in blue with phase-dependent empirical Tables (99 measures). While the first configuration provides accurate location (2 km error in space and 2 s error in origin time), the second configuration yields poor result (73 km error in space and 44 s error in time). With the uncommon celerity ranges associated to the different types of phases, the Antares location using empirical tables is not that accurate, with a confidence ellipse which does not include the true location (yellow pin)

tables derived from ray tracing, the location using empirical tables is worse. The spatial location is 73 km North-East of ground truth and the difference in origin time is 44 s. The ellipse major axis length is 80 km. Despite the density of the recording network and the amount of measures used, the final location remains far from the ground truth. One explanation is the uncommon atmospheric features at the time of the Antares event which are the cause of the unexpected celerity ranges when compared to those already reported in the literature (e.g., fast tropospheric and stratospheric phases and thermospheric phases with celerity much lower than typical values). It is worth noting that the large 95% confidence ellipse does not include the ground truth location, suggesting that model errors have been underestimated.

9.4 Attenuation of Stratospheric Phases

Depending on the atmospheric wind structure, infrasonic waves may propagate in acoustic waveguides between the ground and troposphere, stratosphere and lower thermosphere. One dominant factor influencing infrasound detection is the seasonal oscillation of the dominant East-West (zonal) component of the stratospheric wind flow. This oscillation, clearly captured in climatological wind models, controls to first order the ground locations where infrasound signals are expected to be detected since detection capability is enhanced downwind (Drob et al. 2003). Thus, in order to better interpret the recorded signals, it is important to model the detection capability of the monitoring infrasound network by predicting the signal amplitude at any source location of interest, and further evaluate whether the signal is detectable above the noise level at the receivers. A frequency-dependent semiempirical attenuation relationship derived from massive range-independent parabolic equation (PE) simulations has been developed (Le Pichon et al. 2012). This relation accounts for realistic down- and counter-wind scenarios in the stratosphere, and horizontal wind perturbations induced by gravity waves which play an important role in returning acoustic energy to the ground (Gardner et al. 1993). Beyond the first stratospheric bounce, this relation describes the attenuation by accounting for the geometrical spreading and dissipation of both stratospheric and thermospheric waves. In the far-field, the attenuation essentially varies in R^{β}, where R is the propagation range (in km) and β a dimensionless parameter which depends on the frequency and effective sound speed ratio at 50 km.

This frequency-dependent semiempirical attenuation relationship has been used to construct attenuation maps at three different frequencies: 0.3, 1, and 2 Hz (Fig. 9.15). According to the modeling, the stratospheric duct starts refracting acoustic energy back to the ground for $C_{\text{eff-ratio}}$ larger than one, hence decreasing the transmission loss. In case of downwind propagation ($C_{\text{eff-ratio}} > 1$, i.e., the case for the most easterly stations), the attenuation parameter β is roughly constant in the studied frequency range ($\beta = -0.92 \pm 0.05$). This behavior is in contrast to

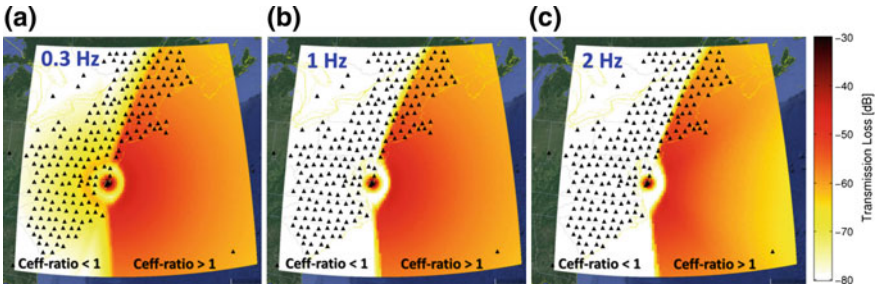

Fig. 9.15 Geographical distribution of the pressure wave attenuation at three frequencies: **a** 0.3 Hz, **b** 1 Hz and **c** 2 Hz. The color scale codes the attenuation (in dB) calculated from the source at a reference distance of 1 km to the receiver. Geographical and frequency-dependent effects are depicted: according to the station location relative to Ceff-ratio = 1 border, a strong frequency dependence of the transmission loss is observed

propagation occurring in upwind direction. In such situation ($C_{\text{eff-ratio}} < 1$; i.e., the case for the most westerly stations), sound propagating upwards is more attenuated due to the low particle density and nonlinear dissipation in the thermosphere (Sutherland and Bass 2004). Between 0.3 and 2 Hz, a much stronger attenuation is predicted for $C_{\text{eff-ratio}} = 0.9$, with $\beta = -1.25 \pm 0.11$ at 0.3 Hz and $\beta = -1.78 \pm 0.12$ at 2 Hz, respectively. The delimitation between these two regions ($C_{\text{eff-ratio}} = 1$) is clearer at higher frequencies (Fig. 9.15c).

In the $C_{\text{eff-Ratio}} < 1$ region, the transmission loss is strongly frequency-dependent. At 0.3 Hz (Fig. 9.15a), the first thermospheric bounce is visible with a predicted attenuation as high as 70 dB at 600 km. At 1 and 2 Hz, the attenuation is larger than 80 dB and the shadow zone is deeper.

In the $C_{\text{eff-Ratio}} > 1$ region, the differences occur at ranges larger than 500 km and at higher frequencies. For example, at I51 GB station, the predicted transmission loss is comparable at 0.3 and 1 Hz while it is 10 dB larger at 2 Hz.

9.4.1 *Attenuation of Stratospheric Phases as a Function of Frequency and $C_{\text{eff-ratio}}$*

To compare the predicted and measured transmission losses (extracted from amplitudes of picked phases summarized in Table 9.1) as a function of range, frequency, and $C_{\text{eff-ratio}}$, two different subsets of stations have been considered.

A first set of eight stations has been selected at a range of about 600 km (±50 km) (Fig. 9.16a). This configuration allows focusing on the attenuation of the stratospheric phases as of function a frequency and $C_{\text{eff-ratio}}$. The background noise level along this 500 km long line is low enough to identify stratospheric arrivals at a constant range from the event, with $C_{\text{eff-ratio}}$ values ranging evenly from 1.15 (red colors indicating downwind situation for eastern stations) down to 0.9 (blue colors

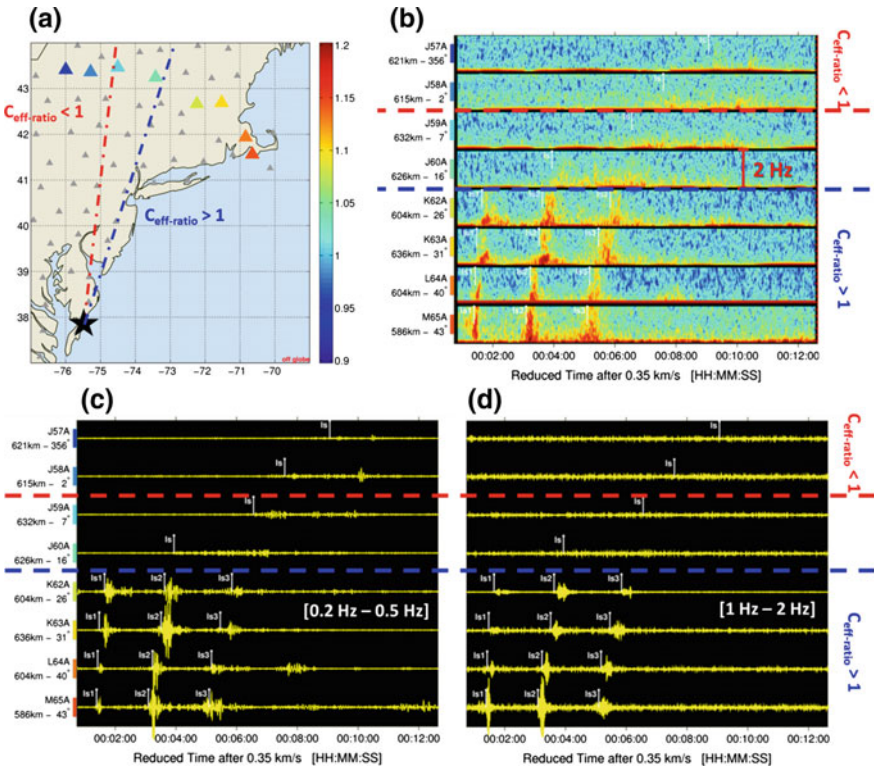

Fig. 9.16 Attenuation of stratospheric phases as a function $C_{eff\text{-}ratio}$ and signal frequency. Eight stations have been thoroughly chosen at a fixed distance from the Antares explosion (about 600 km) with continuous decreasing values of $C_{eff\text{-}ratio}$, from 1.15 down to 0.9. Stations are highlighted in color in panel (**a**) according to $C_{eff\text{-}ratio}$ values. The corresponding spectrograms between 0 and 2 Hz are plotted in panel (**b**), waveforms filtered between 0.2 and 0.5 Hz are plotted in panel (**c**), and waveforms filtered between 1 and 2 Hz are plotted in panel (**d**). Waveforms and spectrograms are sorted by $C_{eff\text{-}ratio}$ from top to bottom. The same amplitude scales are applied to all stations. $C_{eff\text{-}ratio} = 1$ borders are plotted as thick dashed lines on all subpanels, in red without taking into account crossed winds, in blue taking into account crossed winds. In the $C_{eff\text{-}ratio} > 1$ region, east of the blue line, broadband well-separated arrivals are observed. Beyond $C_{eff\text{-}ratio} = 1$ border, west of the red line, high frequencies are strongly attenuated, as shown in the spectrograms and waveforms, and stratospheric arrivals become narrow low-frequency band diffuse signals ("Isdiff" branch discussed in Sect. 2.4.4). The transition occurs when $C_{eff\text{-}ratio} = 1$ blue border is crossed, i.e., when crossed winds are taken into account

indicating upwind situation for western stations). This single line is clearly visible in Fig. 9.1 with the alignment of dark blue stations with low background noise. The corresponding spectrograms (Fig. 9.16b) and waveforms filtered in two different frequency bands (Fig. 9.16c: low-frequency band between 0.2 and 0.5 Hz, Fig. 9.16d: high-frequency band between 1 and 2 Hz) are represented. The same amplitude scales have been applied to the waveforms. The $C_{eff\text{-}ratio} = 1$ border

without taking crossed winds into account is shown by a red dashed line on all subpanels, and a dashed blue line that takes into account crossed winds.

- As predicted, in the geometrical ducting region ($C_{eff\text{-}ratio} > 1$, East of blue dashed line), low and high-frequency signals are efficiently ducted and the broadband feature is conserved whatever the value of $C_{eff\text{-}Ratio}$ above 1. It is noteworthy that when downwind propagation occurs, any significant wind component in the stratosphere, such that $C_{eff\text{-}Ratio} > 1$, comparable signal attenuation is predicted. This feature contradicts the Los Alamos National Laboratory (LANL) relation (Whitaker 2003), which predicts an exponential variation in signal amplitude with changing wind speed. Our model attenuation follows an approximately binary variation with the effective sound speed ratio.
- Crossing westwards the $C_{eff\text{-}Ratio} = 1$ border, high frequencies are strongly attenuated, as shown in Fig. 9.15. This effect is clearly visible on both spectrograms and waveforms: when the $C_{eff\text{-}ratio} < 1$ region is reached (dashed blue line), only low frequencies remain. Broadband well-separated arrivals change into narrow low-frequency band emergent signals. These low-frequency stratospheric arrivals labeled as "Isdiff" branch (Sect. 2.4.4) are not used for the location because they are not modeled by ray tracing (Sect. 9.3). As opposed to the $C_{eff\text{-}Ratio} > 1$ region, low-frequency signal amplitudes depend on $C_{eff\text{-}Ratio}$ values (e.g., J59A has stronger amplitude than J57A while M65A has comparable amplitude to K63A).
- Unlike the prediction, it is clear in Fig. 9.16c that such low-frequency diffuse signals already start being observed at $C_{eff\text{-}ratio}$ values larger than one (i.e., below the red dashed line, Fig. 9.16c). At any location, $C_{eff\text{-}ratio}$ is derived from the averaged stratospheric winds projected in the direction of propagation, without taking into account the crossed wind component. In strong stratospheric jet conditions (reaching 80 m/s at the turning heights, see Fig. 9.2d, e), the strong advection shifts the $C_{eff\text{-}ratio} = 1$ border eastwards. With azimuthal deviations simulated by ray tracing (Sect. 9.3), the border is shifted by 9.2° (dashed blue line on Fig. 9.16). By applying this correction, the frequency contents of the detected signals are consistent with the predicted frequency-dependent attenuations. Such a three-dimensional effect should be taken into account when $C_{eff\text{-}ratio}$ is close to 1 and strong crossed winds occur. Full waveform modeling techniques in which propagations is simulated in a vertical plane, such as normal modes or parabolic equation method, would fail in predicting waveform shapes and amplitudes in such directions if crossed winds are not considered. In addition, when $C_{eff\text{-}ratio}$ is close to 1, the predicted arrival time, amplitude and duration of the signals become more sensitive to wind perturbations induced by unresolved small-scale structures (e.g., Kulichkov et al. 2010; Green et al. 2011).

9.4.2 *Attenuation of Stratospheric Phases as a Function of Range and Frequency*

A second set of eight stations has been selected with constant $C_{eff\text{-}ratio}$ value of 1.05 with distances ranging from 386 to 918 km, as shown in Fig. 9.17a. This configuration allows focusing on the attenuation of the stratospheric phases as a function

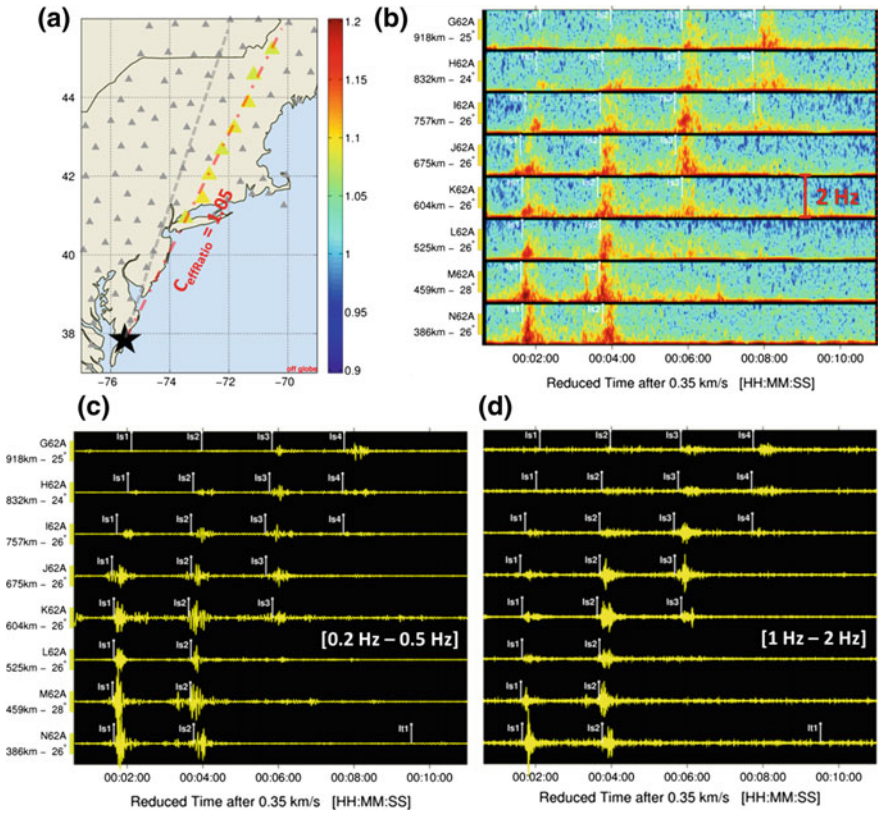

Fig. 9.17 Attenuation of stratospheric phases as a function of range and signal frequency, inside geometrical ducting regions. Eight stations have been thoroughly chosen with a fixed $C_{eff\text{-}ratio}$ value of 1.05 with continuous increasing ranges, from 386 to 918 km. Stations are highlighted in color in panel (**a**) according to their $C_{eff\text{-}ratio}$ values. Corresponding spectrograms between 0 and 2 Hz are plotted in panel (**b**), waveforms filtered between 0.2 and 0.5 Hz are plotted in panel (**c**), and waveforms filtered between 1 and 2 Hz are plotted in panel (**d**). Waveforms and spectrograms are sorted by distance from bottom to top, and the same amplitude dynamics is applied to all stations. Cross winds-corrected $C_{eff\text{-}ratio} = 1$ border is plotted as a gray dashed line on the map and $C_{eff\text{-}ratio} = 1.05$ is plotted as a red dashed line. As predicted, the attenuation of most energetic arrivals varies in $R^{-0.92}$ and is frequency independent, at first order. Broadband frequency signals are efficiently ducted especially at times when ray tracing predicts a large density of rays reaching the stations (Fig. 9.12). Diffracted arrivals associated to the branch extensions presented in Sect. 3.2 have lower frequency contents, as shown in the spectrograms and waveforms

of range and frequency inside geometrical ducting regions. In particular, the attenuation can be studied along a line of about 500 km with a regular inter-station spacing, where values of $C_{\text{eff-Ratio}}$ are comparable. The corresponding spectrograms (Fig. 9.17b) and waveforms filtered in two different frequency bands (Fig. 9.17c: between 0.2 and 0.5 Hz; Fig. 9.17d: between 1 and 2 Hz) are represented. The same amplitude dynamics is applied to the waveforms. The cross wind-corrected $C_{\text{eff-ratio}} = 1$ border is plotted as a gray dashed line on the map and the $C_{\text{eff--ratio}} = 1.05$ line is plotted in red.

- As predicted, at large distances, the attenuation of the most energetic arrivals varies in R_β, where $\beta = -0.92$ is almost frequency independent (higher frequencies are slightly more attenuated). While the energy varies in R_β, the amplitude of most energetic arrivals remains a good proxy for such a qualitative study.
- Broadband frequency signals are efficiently ducted in geometrical ducting regions, especially at times when ray tracing predicts a large density of rays reaching the stations (see Fig. 9.12). Diffracted arrivals associated to the branch extensions presented in Sect. 3.2 have lower frequency contents, as shown on the spectrograms and waveforms. On the farthest stations G62A and H62A, Is1 and Is2 arrivals have much narrower and lower frequency contents than Is3 and Is4 which are broadband.

9.5 Discussions and Concluding Remarks

The results presented in this study provide a good overview of the operational capabilities of dense regional infrasound networks to study events of interest for the Comprehensive Nuclear-Test-Ban verification regime. They also highlight the limitations of routinely used codes, especially concerning effects of unresolved gravity waves which play a significant role in infrasound propagation.

The amount and variety of infrasound arrivals associated with the Antares explosion make this event unique. Due to a large high-pressure system centered offshore in the western Atlantic and steady night conditions, most of the stations exhibited low acoustic background noise levels. In addition to these favorable observation conditions, several wind jets at altitudes ranging from ground to the lower mesosphere were all blowing North-Eastwards. Consequently, stations located North-East of the explosion along the coastline recorded tens of stratospheric and tropospheric infrasound arrivals up to 1100 km. In the opposite direction, in the South-West quadrant, stations recorded several tens of

thermospheric arrivals at ranges up to 1000 km. 175 phases were identified as tropospheric, stratospheric or thermospheric arrivals on 73 stations of the TA. The SNR is often larger than 1 and the phase identification is not ambiguous due to the density of the recording stations, even if standard array processing methods cannot be applied. The IMS station I51 GB located in Bermuda, 1154 km South-Eastwards, also recorded five stratospheric phases predicted by ray tracing simulations. Overall, 74 stations detected the event and 180 phases were manually identified, picked, and labeled. The celerity range of the recorded phases is exceptionally broad, from 360 m/s for some tropospheric phases, down to 160 m/s for some thermospheric phases. Using phase-dependent propagation tables derived from ray tracing simulations, the source was accurately located 2 km East of ground truth information with a difference in origin time of 2 s.

For comparison, the most energetic event ever recorded so far by the IMS network is the Chelyabinsk meteor of the February 15, 2013, from which the acoustic energy was estimated to be equivalent to around 500 kt of TNT (Le Pichon et al 2013). 18 TA infrasound sensors recorded this event up to 15,000 km and 56 infrasound phases were associated with the analysts at the IDC (Mialle et al. 2019). More generally, most of the acoustic events built by the IDC from the sparse global IMS infrasound network (the mean inter-station distance is about 2000 km) associate only a few infrasound stations and arrivals. In favorable observation conditions, a limited number of measures allow in-depth studies considering both source localization and characterization (Ceranna et al. 2009; Green et al. 2009). However, for events of smaller energy, the use of dense regional seismo-acoustic networks clearly improves the detection and location capability of the infrasound IMS network (e.g., Gibbons et al. 2015; Che et al. 2017).

Further studies shall be pursued to model a more realistic picture of infrasound propagation for the Antares event. The high-quality data and the unprecedented amount and variety of observed infrasound phases on a dense network would provide a statistical approach for evaluating atmospheric models, numerical propagation modeling and localization methods. Studies of specific interest for the nuclear explosion monitoring regime are to:

- Assess localization procedures and quantify associated uncertainties in space and time considering an unusual amount of measures.
- Study the dispersion and ground/ocean interaction of tropospheric phases propagating within a thin and unstable advected waveguide at ranges up to 1000 km (27 tropospheric phases were recorded with celerities ranging from 340 to 360 m/s).
- Study the attenuation of stratospheric phases. Different numerical propagation modeling methods could be tested and compared (e.g., Le Pichon et al. 2012; Waxler and Assink 2019).

- Study thermospheric propagation up to 1000 km (It1 to It4 branches have clearly been identified). 46 thermospheric arrivals were recorded from this single event, which is unprecedented. Corresponding celerities extend from very low values (160 m/s for It3 at 500 km) to typical values (250 m/s). A unique collection of shapes such as "U", "N", and shock waves, generated by nonlinear propagation in the thermosphere and caustics, are of great interest to improve our knowledge of the thermosphere (e.g., Assink et al. 2012). Numerical explorations with fully time- and range-dependent wave propagation techniques accounting for nonlinear propagation effects would provide more realistic results while still maintaining computational efficiency (Waxler and Assink, this volume).
- Assess the impact of unresolved small-scale structures in middle atmospheric models induced by naturally occurring gravity waves (e.g., Le Pichon et al. 2015) on the propagation of stratospheric waves could be addressed by considering deterministic (e.g., Green et al. 2011) or stochastic approaches (e.g., Drob et al. 2013). Moreover, due to strong stratospheric cross winds for North/North-East propagation, errors due to three-dimensional effects can be assessed.

Continuing such studies would help to further enhance network performance simulations and optimize future network design in order to monitor infrasonic sources of interest. This is an important step toward a successful monitoring regime for atmospheric or surface events and to act as an effective verification tool in the near future.

Appendix

See Table 9.1.

Table 9.1 Exhaustive list of measured phases and information relative to the location obtained from ray tracing propagation tables. From left to right: station name, phase name, range, arrival time, back azimuth (only for I51 GB), peak-to-peak amplitude in relevant frequency band, celerity model, and azimuthal deviation obtained from ray tracing (only for I51 GB), time residual, back azimuth residual, and final celerity obtained after location. The color of each line represents arrival type: red is tropospheric, green is stratospheric, blue is thermospheric, and orange indicates that the phase has not been used for location because it was not modeled

Station	Phase	Range [km]	Arrival Time [DD/MM/YYYY HH :MM :SS]	Measured θ [°]	Peak-to-Peak Amplitude [Pa]	Celerity Model [km/s]	Δθ [°]	Time Residual [s]	θ Residual [°]	Celerity [km/s]
S61A	Iw	25	28/10/2014 22:24:11	-	15.2	0.351	-	0.0	-	0.351
R61A	Iw	57	28/10/2014 22:25:41	-	48	0.350	-	1.6	-	0.353
Q61A	Iw	117	28/10/2014 22:28:31	-	3.3	0.350	-	4.3	-	0.355
Q60A	Iw	134	28/10/2014 22:29:20	-	0.39	0.350	-	4.1	-	0.353
U61A	It1	188	28/10/2014 22:40:27	-	1.00	0.178	-	7.7	-	0.180
T59A	It1	208	28/10/2014 22:41:51	-	0.76	0.179	-	29.9	-	0.184
P61A	Is1	213	28/10/2014 22:35:09	-	2.0	0.292	-	0.2	-	0.292
U60A	It1	213	28/10/2014 22:41:50	-	0.82	0.186	-	13.8	-	0.189
P61A	Iw	213	28/10/2014 22:33:00	-	1.6	0.352	-	4.8	-	0.355
S58A	It1	229	28/10/2014 22:42:54	-	1.7	0.192	-	2.1	-	0.192
V61A	It1	247	28/10/2014 22:42:53	-	0.78	0.205	-	15.4	-	0.207
O61A	Is1	263	28/10/2014 22:37:31	-	1.3	0.302	-	1.9	-	0.303
O61A	It1	263	28/10/2014 22:40:10	-	0.34	0.253	-	10.5	-	0.256
O61A	Iw	263	28/10/2014 22:35:23	-	1.9	0.349	-	11.3	-	0.355
U59A	It1	264	28/10/2014 22:44:20	-	0.56	0.206	-	0.3	-	0.206
R57A	It1a	273	28/10/2014 22:44:55	-	1.1	0.211	-	-19.7	-	0.208
R57A	It1b	273	28/10/2014 22:46:51	-	0.72	0.191	-	-2.5	-	0.191
O60A	Is1	276	28/10/2014 22:38:19	-	0.14	0.298	-	8.1	-	0.301
O60A	It1	276	28/10/2014 22:41:14	-	0.70	0.251	-	7.6	-	0.252
V60A	It1	280	28/10/2014 22:44:36	-	0.59	0.218	-	-14.2	-	0.216
P57A	It1a	288	28/10/2014 22:44:28	-	2.9	0.221	-	16.3	-	0.224
P57A	It1b	288	28/10/2014 22:44:47	-	1.6	0.219	-	10.4	-	0.220
O57A	It1a	324	28/10/2014 22:44:43	-	0.36	0.251	-	-12.4	-	0.249
O57A	It1b	324	28/10/2014 22:46:04	-	0.30	0.229	-	30.7	-	0.234
W61A	It1	325	28/10/2014 22:46:34	-	0.62	0.225	-	25.9	-	0.230
V59A	It1	337	28/10/2014 22:47:51	-	0.21	0.228	-	-9.7	-	0.226
V59A	It2	337	28/10/2014 22:57:07	-	0.24	0.169	-	-49.5	-	0.165
N61A	Is1	339	28/10/2014 22:41:12	-	1.7	0.309	-	8.0	-	0.311
N61A	It1	339	28/10/2014 22:44:45	-	0.13	0.264	-	-17.1	-	0.260
N61A	Iw	339	28/10/2014 22:39:03	-	0.82	0.348	-	13.6	-	0.353
Q56A	It1	352	28/10/2014 22:48:48	-	0.77	0.229	-	-14.3	-	0.227
W60A	It2	368	28/10/2014 22:57:54	-	0.36	0.177	-	-19.1	-	0.176
N62A	Is1	385	28/10/2014 22:43:02	-	1.8	0.321	-	-3.2	-	0.320
N62A	Is2	385	28/10/2014 22:45:09	-	1.2	0.295	-	-23.6	-	0.290
N62A	It1	385	28/10/2014 22:50:54	-	1.3	0.233	-	-25.5	-	0.230
N62A	Iw	385	28/10/2014 22:41:06	-	1.7	0.349	-	15.5	-	0.354
W59A	It1	398	28/10/2014 22:52:38	-	0.38	0.226	-	-16.4	-	0.224
M61A	Is1	413	28/10/2014 22:44:31	-	0.35	0.323	-	-13.1	-	0.320
M61A	Is2	413	28/10/2014 22:46:36	-	0.61	0.292	-	-2.4	-	0.292
M61A	Iw	413	28/10/2014 22:42:29	-	0.32	0.348	-	18.2	-	0.353
N63A	Is1	432	28/10/2014 22:45:11	-	2.9	0.327	-	-8.5	-	0.325
N63A	Is2	432	28/10/2014 22:47:05	-	1.0	0.304	-	-23.9	-	0.299
N63A	Iw	432	28/10/2014 22:43:20	-	5.7	0.351	-	10.5	-	0.354
V57A	It2	441	28/10/2014 23:01:46	-	0.31	0.193	-	-44.6	-	0.189
M62A	Is1	457	28/10/2014 22:46:28	-	1.4	0.323	-	9.6	-	0.325
M62A	Is2	457	28/10/2014 22:48:32	-	1.4	0.298	-	2.1	-	0.299
M62A	Iw	457	28/10/2014 22:44:32	-	0.99	0.351	-	11.5	-	0.354
W58A	It2	460	28/10/2014 23:02:23	-	0.36	0.189	-	67.2	-	0.195
M63A	Is1	493	28/10/2014 22:48:02	-	1.9	0.333	-	-20.8	-	0.329
M63A	Is2	493	28/10/2014 22:49:57	-	0.87	0.303	-	10.6	-	0.305
M63A	Iw	493	28/10/2014 22:46:12	-	2.7	0.351	-	15.0	-	0.354
W57A	It2	503	28/10/2014 23:04:40	-	0.061	0.202	-	-8.0	-	0.201
W57A	It3	503	28/10/2014 23:14:15	-	0.043	0.164	-	-13.0	-	0.164
L62A	Is1	524	28/10/2014 22:49:41	-	0.61	0.327	-	2.0	-	0.328
L62A	Is2	524	28/10/2014 22:51:44	-	0.66	0.309	-	-23.9	-	0.304
L62A	Iw	524	28/10/2014 22:47:43	-	0.20	0.352	-	6.5	-	0.354
Y59A	It2	525	28/10/2014 23:04:56	-	0.18	0.207	-	26.4	-	0.209
Y59A	It3	525	28/10/2014 23:14:34	-	0.16	0.171	-	-14.3	-	0.170
Q53A	It2	542	28/10/2014 23:06:34	-	0.14	0.204	-	44.3	-	0.207
Q53A	It3	542	28/10/2014 23:15:56	-	0.14	0.171	-	-8.7	-	0.171

(continued)

Table 9.1 (continued)

W56A	It2	547	28/10/2014 23:06:54	-	0.27	0.210	-	-23.2	-	0.208
W56A	It3	547	28/10/2014 23:16:18	-	0.20	0.169	-	37.5	-	0.171
K60A	Is	548	28/10/2014 22:53:09	-	0.18	-	-	-	-	0.303
M64A	Is1	551	28/10/2014 22:50:46	-	1.7	0.335	-	-20.2	-	0.331
M64A	Is2	551	28/10/2014 22:52:29	-	1.5	0.317	-	-30.7	-	0.312
M64A	Is3	551	28/10/2014 22:54:44	-	1.4	0.286	-	24.9	-	0.289
M64A	Iw	551	28/10/2014 22:48:54	-	3.2	0.351	-	15.2	-	0.355
L63A	Is1	556	28/10/2014 22:51:04	-	1.2	0.335	-	-26.0	-	0.330
L63A	Is2	556	28/10/2014 22:52:56	-	0.69	0.308	-	7.1	-	0.310
L63A	Is3	556	28/10/2014 22:55:08	-	0.27	0.287	-	5.8	-	0.288
L63A	Iw	556	28/10/2014 22:49:13	-	1.7	0.348	-	24.6	-	0.353
V55A	It2	558	28/10/2014 23:07:32	-	0.18	0.207	-	25.3	-	0.209
V55A	It3	558	28/10/2014 23:16:48	-	0.15	0.177	-	-77.4	-	0.173
X57A	It2	559	28/10/2014 23:06:56	-	0.34	0.208	-	48.0	-	0.212
L61B	Is1	565	28/10/2014 22:51:34	-	0.25	0.329	-	5.0	-	0.330
L61B	Is2	565	28/10/2014 22:53:41	-	0.28	0.303	-	22.8	-	0.307
L61B	Is3	565	28/10/2014 22:55:59	-	0.22	0.287	-	-9.6	-	0.285
L61B	Iw	565	28/10/2014 22:49:43	-	0.052	0.347	-	24.3	-	0.352
U54A	It2	583	28/10/2014 23:08:56	-	0.15	0.210	-	21.8	-	0.211
U54A	It3	583	28/10/2014 23:18:03	-	0.14	0.178	-	-33.7	-	0.176
M65A	Is1	585	28/10/2014 22:52:18	-	1.4	0.335	-	-14.8	-	0.333
M65A	Is2	585	28/10/2014 22:54:01	-	1.3	0.319	-	-27.6	-	0.314
M65A	Is3	585	28/10/2014 22:56:01	-	0.64	0.292	-	23.3	-	0.295
M65A	Iw	585	28/10/2014 22:50:28	-	4.5	0.351	-	18.2	-	0.355
M66A	Is1	595	28/10/2014 22:52:39	-	1.1	0.334	-	1.9	-	0.335
M66A	Is2	595	28/10/2014 22:54:22	-	1.9	0.318	-	-7.4	-	0.316
M66A	Is3	595	28/10/2014 22:56:19	-	2.3	0.296	-	12.1	-	0.298
M66A	Iw	595	28/10/2014 22:50:56	-	1.6	0.348	-	32.5	-	0.355
K62A	Is1	603	28/10/2014 22:53:26	-	0.44	0.328	-	12.9	-	0.330
L64A	Is1	603	28/10/2014 22:53:13	-	0.46	0.329	-	22.1	-	0.333
K62A	Is2	603	28/10/2014 22:55:24	-	0.40	0.315	-	-27.7	-	0.310
L64A	Is2	603	28/10/2014 22:55:01	-	0.50	0.311	-	20.1	-	0.314
K62A	Is3	603	28/10/2014 22:57:37	-	0.21	0.293	-	-16.2	-	0.290
L64A	Is3	603	28/10/2014 22:56:58	-	0.30	0.302	-	-38.0	-	0.296
L64A	Iw	603	28/10/2014 22:51:25	-	0.70	0.350	-	17.8	-	0.354
Y57A	It2	613	28/10/2014 23:09:33	-	0.36	0.215	-	66.7	-	0.220
Y57A	It3	613	28/10/2014 23:18:34	-	0.12	0.189	-	-82.7	-	0.184
J58A	Is	614	28/10/2014 22:59:53	-	0.11	-	-	-	-	0.278
J57A	Is	621	28/10/2014 23:01:41	-	0.089	-	-	-	-	0.268
V54A	It3	621	28/10/2014 23:19:36	-	0.15	0.184	-	-22.1	-	0.183
X56A	It2	623	28/10/2014 23:10:26	-	0.14	0.221	-	-33.1	-	0.219
X56A	It3	623	28/10/2014 23:19:20	-	0.15	0.180	-	79.6	-	0.184
J60A	Is	625	28/10/2014 22:58:12	-	0.14	-	-	-	-	0.296
J59A	Is	631	28/10/2014 23:00:09	-	0.062	-	-	-	-	0.283
K63A	Is1	635	28/10/2014 22:54:46	-	0.38	0.333	-	-2.4	-	0.333
K63A	Is2	635	28/10/2014 22:56:48	-	0.71	0.310	-	18.2	-	0.313
K63A	Is3	635	28/10/2014 22:58:45	-	0.52	0.296	-	-0.1	-	0.296
K63A	Iw	635	28/10/2014 22:52:59	-	0.15	0.353	-	1.9	-	0.353
L65A	Iw	656	28/10/2014 22:53:50	-	2.5	0.350	-	27.8	-	0.355
J62A	Is1	674	28/10/2014 22:56:46	-	0.33	0.332	-	7.1	-	0.333
J62A	Is2	674	28/10/2014 22:58:52	-	0.45	0.312	-	7.8	-	0.313
J62A	Is3	674	28/10/2014 23:00:51	-	0.71	0.297	-	0.5	-	0.297
J62A	Iw	674	28/10/2014 22:54:55	-	0.096	0.349	-	19.3	-	0.352
I59A	Is	676	28/10/2014 23:01:47	-	0.078	-	-	-	-	0.290
I60A	Is	692	28/10/2014 23:02:36	-	0.089	-	-	-	-	0.291
J63A	Is1	710	28/10/2014 22:58:25	-	0.26	0.337	-	-20.1	-	0.334
J63A	Is2	710	28/10/2014 23:00:23	-	0.36	0.317	-	-2.0	-	0.316
J63A	Is3	710	28/10/2014 23:02:10	-	0.68	0.305	-	-23.3	-	0.302
X54A	It3	720	28/10/2014 23:23:55	-	0.18	0.195	-	36.4	-	0.197
X54A	It4	720	28/10/2014 23:33:29	-	0.14	-	-	-	-	0.170
I62A	Is1	756	28/10/2014 23:00:47	-	0.26	0.336	-	-18.2	-	0.333
I62A	Is2	756	28/10/2014 23:02:45	-	0.19	0.317	-	-1.6	-	0.317
I62A	Is3	756	28/10/2014 23:04:43	-	0.99	0.306	-	-29.6	-	0.302
I62A	Is4	756	28/10/2014 23:06:47	-	0.14	0.284	-	29.7	-	0.288
I63A	Is1	803	28/10/2014 23:02:58	-	0.070	0.333	-	17.5	-	0.335

(continued)

Table 9.1 (continued)

I63A	Is2	803	28/10/2014 23:04:53	-	0.14	0.324	-	-35.4	-	0.320
I63A	Is3	803	28/10/2014 23:06:50	-	0.42	0.302	-	34.2	-	0.305
I63A	Is4	803	28/10/2014 23:09:07	-	0.15	0.289	-	15.4	-	0.290
H62A	Is1	831	28/10/2014 23:04:40	-	0.070	0.336	-	-29.0	-	0.332
H62A	Is2	831	28/10/2014 23:06:24	-	0.098	0.317	-	16.3	-	0.319
H62A	Is3	831	28/10/2014 23:08:25	-	0.25	0.302	-	30.4	-	0.305
H62A	Is4	831	28/10/2014 23:10:21	-	0.21	0.296	-	-33.0	-	0.293
I64A	Is1	835	28/10/2014 23:04:33	-	0.52	0.338	-	-17.9	-	0.335
I64A	Is2	835	28/10/2014 23:06:13	-	0.37	0.323	-	-4.6	-	0.322
I64A	Is3	835	28/10/2014 23:08:03	-	0.98	0.309	-	4.3	-	0.309
I64A	Is4	835	28/10/2014 23:10:01	-	0.67	0.298	-	-18.6	-	0.296
I64A	Iw	835	28/10/2014 23:02:49	-	0.20	0.353	-	-20.5	-	0.350
H63A	Is1	884	28/10/2014 23:06:53	-	0.034	0.334	-	10.9	-	0.336
H63A	Is2	884	28/10/2014 23:08:43	-	0.12	0.325	-	-19.1	-	0.322
H63A	Is3	884	28/10/2014 23:10:41	-	0.31	0.306	-	25.9	-	0.309
H63A	Is4	884	28/10/2014 23:12:40	-	0.26	0.302	-	-49.1	-	0.297
G62A	Is1	917	28/10/2014 23:08:53	-	0.042	0.335	-	-10.3	-	0.333
G62A	Is2	917	28/10/2014 23:10:44	-	0.064	0.326	-	-45.9	-	0.320
G62A	Is3	917	28/10/2014 23:12:36	-	0.15	0.311	-	-27.8	-	0.308
G62A	Is4	917	28/10/2014 23:14:30	-	0.53	0.301	-	-41.4	-	0.297
H64A	Is1	919	28/10/2014 23:08:43	-	0.14	0.335	-	3.1	-	0.335
H64A	Is2	919	28/10/2014 23:10:27	-	0.20	0.321	-	18.8	-	0.323
H64A	Is3	919	28/10/2014 23:12:12	-	0.64	0.314	-	-26.1	-	0.311
H64A	Is4	919	28/10/2014 23:14:09	-	0.60	0.303	-	-36.6	-	0.300
H64A	Is5	919	28/10/2014 23:16:41	-	0.14	0.287	-	-16.9	-	0.285
H64A	Iw	919	28/10/2014 23:07:03	-	0.081	0.350	-	-19.6	-	0.348
H65A	Is1	972	28/10/2014 23:11:06	-	0.29	0.339	-	-14.2	-	0.337
H65A	Is2	972	28/10/2014 23:12:45	-	0.19	0.328	-	-22.2	-	0.326
H65A	Is3	972	28/10/2014 23:14:39	-	0.31	0.315	-	-6.9	-	0.314
H65A	Is4	972	28/10/2014 23:16:30	-	0.32	0.300	-	35.0	-	0.303
H65A	Is5	972	28/10/2014 23:18:47	-	0.13	0.287	-	40.1	-	0.290
H65A	Iw	972	28/10/2014 23:09:23	-	0.37	0.351	-	-13.1	-	0.349
G64A	Is1	995	28/10/2014 23:12:31	-	0.099	0.334	-	8.9	-	0.335
G64A	Is2	995	28/10/2014 23:14:20	-	0.27	0.327	-	-31.3	-	0.323
G64A	Is3	995	28/10/2014 23:15:59	-	0.33	0.310	-	34.5	-	0.313
G64A	Is4	995	28/10/2014 23:17:51	-	0.59	0.300	-	29.1	-	0.302
G64A	Is5	995	28/10/2014 23:20:13	-	0.088	0.288	-	30.0	-	0.290
TIGA	It4	1027	28/10/2014 23:46:16	-	0.10	-	-	-	-	0.206
H66A	Is1	1030	28/10/2014 23:13:54	-	0.30	0.341	-	-37.8	-	0.337
H66A	Is2	1030	28/10/2014 23:15:35	-	0.18	0.322	-	43.4	-	0.326
H66A	Is3	1030	28/10/2014 23:17:23	-	0.27	0.316	-	0.4	-	0.316
H66A	Is4	1030	28/10/2014 23:19:07	-	0.49	0.310	-	-50.2	-	0.306
H66A	Is5	1030	28/10/2014 23:20:58	-	0.27	0.296	-	5.7	-	0.296
H66A	Iw	1030	28/10/2014 23:12:06	-	0.90	0.347	-	20.0	-	0.350
G65A	Is1	1050	28/10/2014 23:15:00	-	0.22	0.333	-	30.0	-	0.337
G65A	Is2	1050	28/10/2014 23:16:42	-	0.17	0.329	-	-32.2	-	0.326
G65A	Is3	1050	28/10/2014 23:18:38	-	0.30	0.313	-	12.9	-	0.315
G65A	Is4	1050	28/10/2014 23:20:27	-	0.34	0.309	-	-44.4	-	0.305
G65A	Is5	1050	28/10/2014 23:22:07	-	0.20	0.295	-	17.6	-	0.296
G65A	Is6	1050	28/10/2014 23:24:17	-	0.11	0.284	-	24.9	-	0.286
G65A	Iw	1050	28/10/2014 23:13:13	-	0.24	0.352	-	-30.4	-	0.349
I51GB	Is3	1153	28/10/2014 23:23:00	308.1	0.031	0.325	-1.1	-56.4	-1.9	0.320
I51GB	Is4	1153	28/10/2014 23:24:38	307.9	0.23	0.316	-1.4	-53.7	-1.5	0.312
I51GB	Is5	1153	28/10/2014 23:26:15	308.0	0.38	0.303	-1.6	11.2	-1.4	0.304
I51GB	Is6	1153	28/10/2014 23:28:03	308.1	0.56	0.293	-1.9	35.7	-1.2	0.295
I51GB	Is7	1153	28/10/2014 23:30:09	308.9	0.048	0.288	-2.3	-25.6	-1.6	0.286

References

Alcoverro B, Le Pichon A (2005) Design and optimization of a noise reduction system for infrasonic measurements using elements with low acoustic impedance. J Acoust Soc Am 117:1717–1727. https://doi.org/10.1121/1.1804966

Assink JD, Waxler R, Drob D (2012) On the sensitivity of infrasonic traveltimes in the equatorial region to the atmospheric tides. J Geophys Res 117:D01110. https://doi.org/10.1029/2011JD016107

Assink J, Smets P, Marcillo O, Weemstra C, Lalande J-M, Waxler R, Evers L (2019) Advances in infrasonic remote sensing methods. In: Le Pichon A, Blanc E, Hauchecorne A (eds) Infrasound monitoring for atmospheric studies, 2nd edn. Springer, Dordrecht, pp 605–632

Brachet N, Brown D, Le Bras R, Cansi Y, Mialle P, Coyne J (2009) Monitoring the Earth's atmosphere with the global IMS infrasound network. In: Le Pichon A, Blanc E, Hauchecorne A (ed) Infrasound monitoring for atmospheric studies. Springer, New York, pp 77–118. ISBN 978–1-4020-9508-5

Brown DJ et al (2002) Infrasonic signal detection and source location at the prototype international data center, pure and appl. Geophys. 159:1081–1125

Candel SM (1977) Numerical solution of conservation equations arising in linear wave theory: application to aeroacoustics. J Fluid Mech 83(3):465–493

Cansi Y (1995) An automatic seismic event processing for detection and location—the PMCC method. Geophys Res Lett 22(9):1021–1024

Ceranna L, Le Pichon A, Green DN, Mialle P (2009) The Buncefield explosion: a benchmark for infrasound analysis across central Europe. Geophys J Int 177:491–508

Che IY, Le Pichon A, Kim K, Shin IC (2017) Assessing the detection capability of a dense infrasound network in the southern Korean Peninsula. Geophys J Int 210:1105–1114. https://doi.org/10.1093/gji/ggx222

Chunchuzov I, Kulichkov S (2019) Internal gravity wave perturbations and their impacts on infrasound propagation in the atmosphere. In: Le Pichon A, Blanc E, Hauchecorne A Infrasound monitoring for atmospheric studies, 2nd edn. Springer, Dordrecht, pp 551–590

Cugnet D, de la Camara A, Lott F, Millet C, Ribstein B (2019) Non-orographic gravity waves: representation in climate models and effects on infrasound. In: Le Pichon A, Blanc E, Hauchecorne A (eds) Infrasound monitoring for atmospheric studies, 2nd edn. Springer, Dordrecht, pp 827–844

De Groot-Hedlin C, Hedlin M (2014) Infrasound detection of the Chelyabinsk meteor at the USArray. Earth Planet Sci Lett 402:337–345. https://doi.org/10.1016/j.epsl.2014.01.031

De Groot-Hedlin CD, Hedlin MAH (2015) A method for detecting and locating geophysical events using groups of arrays. Geophys J Int 203:960–971. https://doi.org/10.1093/gji/ggv345

De Groot-Hedlin CD (2017) Infrasound propagation in tropospheric ducts and acoustic shadow zones. J Acoust Soc Am 142:1816. https://doi.org/10.1121/1.5005889

de Groot-Hedlin C, Hedlin M (2019) Detection of infrasound signals and sources using a dense seismic network. In: Le Pichon A, Blanc E, Hauchecorne A (eds) Infrasound monitoring for atmospheric studies, 2nd edn. Springer, Dordrecht, pp 669–699

Drob DP, Picone JM, Garcés M (2003) Global morphology of infrasound propagation. J Geophys Res 108:4680. https://doi.org/10.1029/2002JD003307

Drob DP et al (2008) An empirical model of the Earth's horizontal wind fields: HWM07. J Geophys Res 113. https://doi.org/10.1029/2008ja013668

Drob DP, Broutman D, Hedlin MA, Winslow NW, Gibson RG (2013) A method for specifying atmospheric gravity wavefields for long-range infrasound propagation calculations. J Geophys Res Atmos 118:3933–3943. https://doi.org/10.1029/2012JD018077

Edwards WN, de Groot-Hedlin CD, Hedlin MAH (2014) Forensic investigation of a probable meteor sighting using USArray acoustic data. Seism Res Lett 85:1012–1018. https://doi.org/10.1785/0220140056

Evers LG, Haak HW (2007) Infrasonic forerunners: exceptionally fast acoustic phases. Geophys Res Lett 34:L10806. https://doi.org/10.1029/2007GL029353

Fee D et al (2013) Overview of the 2009 and 2011 Sayarim Infrasound calibration experiments. J Geophys Res Atmos 118:6122–6143. https://doi.org/10.1002/jgrd.50398

Gainville O, Blanc-Benon P, Blanc E, Roche R, Millet C, Le Piver F, Despres B, and Piserchia PF (2009) Misty picture: a unique experiment for the interpretation of the infrasound propagation from large explosive sources. In: Le Pichon A, Blanc E, Hauchecorne A (ed) infrasound monitoring for atmospheric studies. Springer, New York, pp 575–598. ISBN 978-1-4020-9508-5

Garcés MA, Hansen RA, Lindquist KG (1998) Traveltimes for infrasonic waves propagating in a stratified atmosphere. Geophys J Int 135:255–263

Garcés MA (2013) On infrasound standards, part 1: time, frequency, and energy scaling. InfraMatics 2:13–35. https://doi.org/10.4236/inframatics.2013.22002, http://www.scirp.org/journal/PaperInformation.aspx?PaperID=33802

Garces M (2019) Explosion source models. In: Le Pichon A, Blanc E, Hauchecorne A (eds) Infrasound monitoring for atmospheric studies, 2nd edn. Springer, Dordrecht, pp 273–345

Gardner CS, Hostetler CA, Franke SJ (1993) Gravity wave models for the horizontal wave number spectra of atmospheric velocity and density fluctuations. J Geophys Res 98(D1):1035–1049. https://doi.org/10.1029/92JD02051

Gibbons SJ et al (2015) The European Arctic: a laboratory for seismo-acoustic studies. Seism Soc Am 86:917–928. https://doi.org/10.1785/0220140230

Green D, Le Pichon A, Ceranna L, Evers L (2009) Ground truth events: Assessing the capability of infrasound networks using high resolution data analyses. In Le Pichon A, Blanc E, Hauchecorne A (ed) Infrasound monitoring for atmospheric studies. Springer, New York, pp 599–625. ISBN 978-1-4020-9508-5

Green D, Vergoz J, Gibson R, Le Pichon A, Ceranna L (2011) Infrasound radiated by the Gerdec and Chelopechene explosions: propagation along unexpected paths. J Int, Geophys. https://doi.org/10.1111/j.1365-246X.2011.04975.x

Kim K, Rodgers A (2016) Waveform inversion of acoustic waves for explosion yield estimation. Geophys Res Lett 43:6883–6890

Kinney G, Graham K (1985) Explosive Shocks in Air, 2nd edn. Springer, New York

Kulichkov SN (2009) On the prospects for acoustic sounding of the fine structure of the middle atmosphere. In Le Pichon A, Blanc E, Hauchecorne A (ed) Infrasound Monitoring for atmospheric studies. Springer, New York, pp 511–540. ISBN 978-1-4020-9508-5

Kulichkov SN, Chunchuzov IP, Popov OI (2010) Simulating the influence of an atmospheric fine inhomogeneous structure on long-range propagation of pulsed acoustic signals. Izv Russ Acad Sci Atmos Ocean Phys Engl Trans 46(1):60–68. https://doi.org/10.1134/s0001433810010093

Le Pichon A, Blanc E, Drob D (2005) Probing high-altitude winds using infrasound. J Geophys Res 110:D20104. https://doi.org/10.1029/2005JD006020

Le Pichon A, Ceranna L, Vergoz J (2012), Incorporating numerical modelling into estimates of the detection capability of the IMS infrasound network. J Geophys Res. https://doi.org/10.1029/2011jd0166702009

Le Pichon A, Ceranna L, Pilger C, Mialle P, Brown D, Herry P, Brachet N (2013) The 2013 Russian fireball largest ever detected by CTBTO infrasound sensors. Geophys Res Lett 40:3732–3737. https://doi.org/10.1002/grl.50619

Le Pichon A et al (2015) Comparison of co-located independent ground-based middle-atmospheric wind and temperature measurements with Numerical Weather Prediction models. J Geophys Res Atmos 120. https://doi.org/10.1002/2015jd023273

Lighthill MJ (1963) Jet Noise. AIAA J 1(7):1507–1517. https://doi.org/10.2514/3.1848

Marty J (2019) The IMS infrasound network: current status and technological developments. In: Le Pichon A, Blanc E, Hauchecorne A (eds) Infrasound monitoring for atmospheric studies, 2nd edn. Springer, Dordrecht, pp 3–62

Merchant BJ (2015) Hyperion 5113/GP infrasound sensor evaluation. Sandia Report SAND2015–7075, Sandia National Laboratories

Mialle P, Brown D, Arora N, colleagues from IDC (2019) Advances in operational processing at the international data centre. In: Le Pichon A, Blanc E, Hauchecorne A (eds) Infrasound monitoring for atmospheric studies, 2nd edn. Springer, Dordrecht, pp 209–248

Millet C, Robinet J-C, Roblin C (2007) On using computational aeroacoustics for long-range propagation of infrasounds in realistic atmospheres. Geophys Res Lett 34:L14814. https://doi.org/10.1029/2007GL029449

NASA (2015) Independent Review Team. Orb–3 Accident Investigation Report Executive Summary, Oct 9. https://www.nasa.gov/sites/default/files/atoms/files/orb3_irt_execsumm_0.pdf

Nippress A, Green DN, Marcillo OE, and Arrowsmith SJ (2014) Generating regional infrasound celerity-range models using ground-truth information and the implications for event location. Geophys J Int 197(2):1154–1165. https://doi.org/10.1029/2007GL029449

Picone JM et al (2002) NRL-MSISE-00 empirical model of the atmosphere: statistical comparisons and scientific issues. J Geophys Res 107. https://doi.org/10.1093/gji/ggu049

Pierce AD, Posey JW, Moo CA (1973) Generation and propagation of infrasonic waves, Air Force Cambridge Research Laboratories, Massachusetts Institute of Technology, Report AD-766472, 131 p

Pulli JJ, Kofford A (2015) Infrasound analysis of the October 28, 2014, Antares rocket failure at Wallops Island, Virginia, using video recordings as ground truth. J Acoust Soc Am 137. https://doi.org/10.1121/1.4920619

Raspet R, Abbott J-P, Webster J, Yu J, Talmadge C, Alberts II K, Collier S, Noble J (2019) New systems for wind noise reduction for infrasonic measurements. In: Le Pichon A, Blanc E, Hauchecorne A (eds) Infrasound monitoring for atmospheric studies, 2nd edn. Springer, Dordrecht, pp 91–124

Reed JW (1977) Atmospheric attenuation of explosion waves. J Acoust Soc Am 61:39–47

Sabatini R, Marsden O, Bailly C, Bogey C (2016) A numerical study of nonlinear infrasound propagation in a windy atmosphere. J Acoust Soc Am 140. https://doi.org/10.1121/1.4958998

Smart E, Flinn EA (1971) Fast frequency-Wavenumber analysis and Fisher signal detection in real time infrasonic array data processing. Geophys J Roy Astr Soc 26:279–284

Sutherland LC, Bass HE (2004) Atmospheric absorption in the atmosphere up to 160 km. J Acoust Soc Am 115(3):1012–1032, https://doi.org/10.1121/1.1631937

Talmadge C, Waxler R, Di X, Gilbert K, Kulichkov S (2008) Observation of low-frequency acoustic surface waves in the nocturnal boundary layer. J Acoust Soc Am 124. https://doi.org/10.1121/1.2967474

Varnier J (2001) Experimental study and simulation of rocket engine free jet noise. AIAA J 39 (10):1851–1859. https://doi.org/10.2514/2.1199

Virieux J, Garnier N, Blanc E, Dessa J-X (2004) Paraxial ray tracing for atmospheric wave propagation. Geophys Res Lett 31:L20106. https://doi.org/10.1029/2004GL020514

Walker KT, Hedlin M (2009) A review of wind-noise reduction methodologies. In: Le Pichon A, Blanc E, Hauchecorne A (eds) infrasound monitoring for atmospheric studies. Springer, New York, pp 141–182. ISBN 978-1-4020-9508-5

Walker KT, Shelby R, Hedlin MAH, deGroot-Hedlin C, Vernon F (2011) Western U.S. Infrasonic Catalog: Illuminating infrasonic hot spots with the USArray. J Geophys Res 116:B12305. https://doi.org/10.1029/2011jb008579

Waxler R, Evers L, Assink J, Blom P (2015) The stratospheric arrival pair in infrasound propagation. J Acoust Soc Am 137:4. https://doi.org/10.1121/1.4916718

Waxler R (2003) Modal expansions for sound propagation in the nocturnal boundary layer. J Acoust Soc Am 115. https://doi.org/10.1121/1.1646137

Waxler R, Assink J (2019) Propagation modeling through realistic atmosphere and benchmarking. In: Le Pichon A, Blanc E, Hauchecorne A (eds) Infrasound monitoring for atmospheric studies, 2nd edn. Springer, Dordrecht, pp 509–549

Whitaker RW, Sandoval TD, Mutschlecner JP (2003) Recent infrasound analysis. In: Proceedings of the 25th annual seismic research symposium in Tucson, AZ, pp 646–654

Chapter 10
Characterization of the Infrasonic Wavefield from Repeating Seismo-Acoustic Events

Steven Gibbons, Tormod Kværna and Peter Näsholm

Abstract Infrasound can provide unique data on extreme atmospheric events such as meteor impacts, severe weather systems, man-made explosions, and volcanic eruptions. Use of infrasound for remote event detection and location requires high-quality temporal and spatial atmospheric models, and infrasound generated by so-called Ground Truth events (for which the time and location are known) are necessary to evaluate atmospheric models and assess network performance. Large industrial blasts and military explosions are tightly constrained in time and space using seismic data and can generate infrasound recorded both regionally and at great distances. The most useful seismo-acoustic sources are repeating sources at which explosions take place relatively frequently. Over time, these may provide records of up to many hundreds of events from the same location from which characteristics and variability of the infrasonic wavefield and atmospheric conditions can be assessed on a broad range of timescales. Over the past 20 years or so, numerous databases of repeating explosions have been compiled in various parts of the world. Events are associated confidently with known sources, with accurately determined origin times, usually by applying waveform correlation or similar techniques to the characteristic seismic signals generated by each explosive source. The sets of sources and stations ideally result in atmospheric propagation paths covering a wide range of distances and directions, and the databases ideally include events covering all seasons. For selected repeating sources and infrasound arrays, we have assessed the variability of infrasonic observation: including the documentation of lack of observed infrasound. These observations provide empirical celerity, back azimuth deviation, and apparent velocity probability distributions. Such empirical distributions have been demonstrated in numerous recent studies to provide infrasonic event location estimates with significantly improved uncertainty estimates. Tropospheric, stratospheric, and ther-

S. Gibbons (✉) · T. Kværna · P. Näsholm
NORSAR, Kjeller, Norway
e-mail: steven@norsar.no

T. Kværna
e-mail: tormod@norsar.no

P. Näsholm
e-mail: peter@norsar.no

A. Le Pichon et al. (eds.), *Infrasound Monitoring for Atmospheric Studies*,
https://doi.org/10.1007/978-3-319-75140-5_10

mospheric returns have been observed, even at distances below 200 km. This information is now providing essential input data for studies of the middle and upper atmosphere.

10.1 Ground Truth Events

Microbarograph arrays are deployed globally to detect and classify infrasound signals generated by both natural and anthropogenic sources. In infrasound monitoring, for a given set of detected signals, we seek to locate and, if possible, identify the source which generated the signals. In infrasonic atmospheric imaging, for a given source, we seek to understand what state of the atmosphere could have resulted in the observed set of infrasound signals. The process is circular. On the one hand, the better the location and origin time of an event is known, the stronger the constraint is for estimating the state of the atmosphere. Similarly, the higher the quality of our atmospheric specification, the better the event location estimates are likely to be. We here use the word *event* to mean a source of seismic and/or acoustic waves that takes place over a very limited geographical region and that has a very limited time duration. For example, quarry blasting sequences excavate rock over a range of many tens of meters and consist of hundreds of small explosive charges detonated in ripple-fire salvos. These are considered to be events. The interaction between ocean waves can be a continuous source of seismic waves (so-called microseisms) and infrasonic waves (microbaroms) but these are not considered to be events here, both due to the large spatial extent of the source and its continuous nature. Volcanic sources may consist of events or may be an almost continuous source.

We define a Ground Truth, or GT, event as being an event for which the location (latitude, longitude, and either depth or altitude) and origin time are known. There is a long history in seismology for GT events, almost always explosions, being used for validating and refining models of Earth structure and wave propagation and for assessing the capability for locating seismic events using a given observational network. It became clear that true GT events, for which the source parameters are known exactly, were very few and far between. It was soon recognized that other events, including earthquakes, may not qualify as GT but could be well enough constrained to be useful for calibration purposes. Bondar et al. (2004), for example, derive conditions necessary for different levels of constraint on source parameters. GT5, for example, is used to denote an event whose epicenter is known to be within 5 km. The same principles apply to infrasound and a comprehensive overview of the use of GT events for interpreting the infrasonic (or seismo-acoustic) wavefield is provided by Green et al. (2009). Many of the largest GT infrasound sources are accidental explosions such as the blast at the Buncefield Oil Depot in the UK on December 11, 2005, or the Antares rocket explosion in Virginia on October 28, 2014. The location of such events is typically known exactly and the time is constrained by, for example, eyewitness reports or video footage. The explosions can be so large that multiple infrasound phases are observed over great distances (e.g., Ceranna et al. 2009; Pulli

and Kofford 2015). Experimental explosions have enormous value given the a priori knowledge of yield and configuration of explosives (in addition to time and location). The best-recorded such events carried out for nuclear-test-ban treaty verification purposes are the Sayarim desert calibration explosions (e.g., Bonner et al. 2013). Such experiments however are carried out at great expense and can usually be performed a very limited number of times. Sayarim calibration explosions were carried out both in the summer and in the winter in order to assess propagation to both westerly and easterly stratospheric wind conditions.

In seismology, the propagation medium does not change over timescales of relevance and a single calibration explosion is essentially sufficient for a given observational network. Infrasound propagates through Earth's atmosphere, a medium in continuous motion and undergoing continuous change. Multiple events are therefore necessary to sample as many different atmospheric states as possible, ideally covering timescales ranging from hours to seasons and years. It is not realistic to use only purpose-performed calibration shots but there are fortunately many sources of repeating events, mainly for industrial and military purposes, which can be classified and used as GT or near-GT for calibrating models of infrasound propagation. Identifying existing repeating sources can be the key to accessing vast datasets for exploitation without needing to fund and carry out experiments. Most of the sources are ground-based and generate seismic signals which, due to the unchanging solid Earth, act as "fingerprints" for the specific source location. A characteristic seismic signal (or the absence of such a signal) provides a high degree of confidence that an explosion has (or has not) taken place at a given place and at an accurately determined time. Our intention is to provide a guide to identifying and exploiting repeating seismo-acoustic sources and discuss how infrasound observation can illuminate the spatiotemporal variability of the infrasonic wavefield and consequently improve atmospheric profiling and infrasound monitoring.

10.2 Studies of Repeating Seismo-Acoustic Events

The International Monitoring System (IMS) for verifying compliance with the Comprehensive Nuclear-Test-Ban Treaty (CTBT) comprises four components: seismic, infrasound, hydroacoustic, and radionuclide (Marty 2019). All technologies may be used to provide evidence of an explosion in the solid earth, the atmosphere, or the oceans, although the global infrasound network is primarily intended to detect atmospheric nuclear tests (e.g., Dahlman et al. 2011). When the CTBT was opened for signature in 1996, much of the seismic network was already in place since many of the stations were existing national infrastructure. In contrast, interest in infrasound monitoring had declined significantly since the cessation of atmospheric nuclear testing and the global infrasound network essentially had to be developed from scratch (Christie and Campus 2009). Significant studies have been carried out using historical data from atmospheric nuclear tests (e.g., Whitaker and Mutschlecner 2008) although the majority of the studies carried out have used data collected in the last 20 years.

Infrasound sensors deployed at sites of the TXAR seismic array in Texas, USA, were used by Sorrells et al. (1997) to detect atmospheric signals from mine blasts at distances up to several hundred km. This study demonstrated that infrasound was likely to be detected for larger blasts, at distances beyond 175–200 km, for which the source was "stratospherically downwind". Significantly, this paper pioneered the idea that Ground Truth Databases, constrained by seismic signals, could be used to provide a benchmark for the detection of infrasound signals in a monitoring context. Around the same time, microphones with simple wind-noise reduction systems were deployed at the Kurchatov seismic array in Kazakhstan. Hagerty et al. (2002) detected seismic signals resulting from mining blasts at the Ekibastuz quarry, 250 km to the NW of the sensors, and sought the more slowly propagating infrasound signals. Infrasound was detected for only about 10% of these events and there was a clear seasonality; all the detections were in the winter, consistent with the seasonal direction of the stratospheric waveguide.

The co-location of seismic and infrasound sensors led to the development of purpose-built small aperture seismo-acoustic arrays (Stump et al. 2004) which have been used to detect and characterize the seismic and acoustic signals from industrial blasts on the Korean Peninsula (Che et al. 2002). The arrays in this network were also able to detect both seismic and infrasonic signals generated by the underground nuclear tests carried out by the Democratic People's Republic of Korea (North Korea) in 2009 and 2013 (Che et al. 2009, 2014, 2019). Che et al. (2011) present a landmark study where the variability of infrasound observations was studied for over 1000 GT mining blasts at a single quarry in the Republic of Korea (South Korea) over a period of 2 years. Infrasound signals were examined at two stations, both within 200 km of the source but with one path mainly continental to the west with significant topography and the other to the east over the open ocean. Tropospheric signals were observed at both stations with very little seasonal variation. However, stratospheric signals observed over the oceanic path were observed with an almost constant celerity (the great circle distance divided by the traveltime) whereas stratospheric signals propagating over the continental path had an almost sinusoidal seasonal celerity variation. Failing to account for this variability when trying to invert for the source location was demonstrated to result in bias.

McKenna et al. (2007) examined infrasound recorded at the I10CA array in Canada generated by GT mining blasts at the Mesabi Iron ore mine in Minnesota and found that no reliable indication of the stated explosive yield could be determined from the infrasonic signals. A similar study by Arrowsmith et al. (2008), seeking infrasound generated by quarry blasts at the Black Thunder mine in Wyoming recorded at the PDIAR array, concluded that high noise levels at the station were the most likely cause of non-detection of infrasound from many events. One of the major catalysts for study of repeating events in the western United States was the deployment of the USArray Transportable Array (TA) of 400 seismic stations which recorded ground-coupled acoustic waves (i.e., infrasound signals converted to ground motion at the receiver). With a typical inter-site distance of 70 km, the TA provided an unprecedented high spatial coverage in recording the infrasonic wavefield. One of the most important repeating sources in this part of the world is the

Utah Test and Training Range (UTTR: 41.2°N, 113.0°W) which is the site of rocket destruction explosions generating infrasound recorded out to many hundreds of kilometers. These explosions have been used both to explore the extent and variability of infrasonic observations (e.g., Hedlin and Drob 2014; Nippress et al. 2014) and to explore methods for infrasonic event location (e.g., Modrak et al. 2010; Hedlin and Walker 2013). The Reverse Time Migration approach to event location using acoustic signals identified on the seismic network was used to find many more repeating sources (Walker et al. 2011). The network's recording of the infrasonic wavefield was so impressive that, in later years when the TA progressed to the eastern United States, an infrasound sensor was deployed at each site in addition to the seismic sensor.

Another part of the world where numerous studies have been performed on repeating explosions is the north of Fennoscandia which includes Arctic regions of Norway, Sweden, Finland, and Russia (Gibbons et al. 2015a). The interest in this region stems both from the large number of sources (with many open-cast mining operations and sites of military explosions) and the large number of receivers (with over two decades of continuous seismic and infrasound data) as displayed in Fig. 10.1. While recent studies of the infrasonic wavefield in the United States have been characterized by an unprecedented spatial resolution in the recordings, the European Arctic datasets provide an unprecedented temporal coverage. A source of enormous interest has been a military test range at Hukkakero in northern Finland. Expired ammunition is destroyed at this site in a series of explosions that takes place every year in August and September. There are usually between 10 and 30 explosions each year, most often on consecutive days, and with the yield of each explosion being approximately 20T. Each explosion generates a seismic signal on the ARCES array in Norway, at a distance of approximately 180 km, which is essentially identical from event to event (constraining the origin time, the simple source-time function, and the approximate size of the blast). Since 2008, the ARCES seismic array in addition features a set of co-located infrasound sensors. This infrasound array is named ARCI and Evers and Schweitzer (2011) provides an analysis of 1 year of acoustic and seismic data recordings collected at the station.

Gibbons et al. (2007) studied infrasound propagation using the ground-coupled airwaves recorded on the same sensors between 7 and 15 min later finding that, by contrast, the converted infrasonic (acoustic) waves varied enormously between events in amplitude, duration, and traveltime. An occasional tropospheric arrival was observed, as was an even rarer thermospheric phase. The majority of infrasound signals however are presumed stratospheric returns arriving some 600–650 s after the blast. While the events are limited in season, the regularity of explosions on consecutive days gives excellent resolution to the surprisingly smooth changes of the celerity on the day-to-week timescale. Israelsson (2013) provides an analysis of data recorded at the Swedish Institute of Space Physics (IRF) arrays JMT, LYC, KIR, and SDK associated with 19 Hukkakero events in 2009.

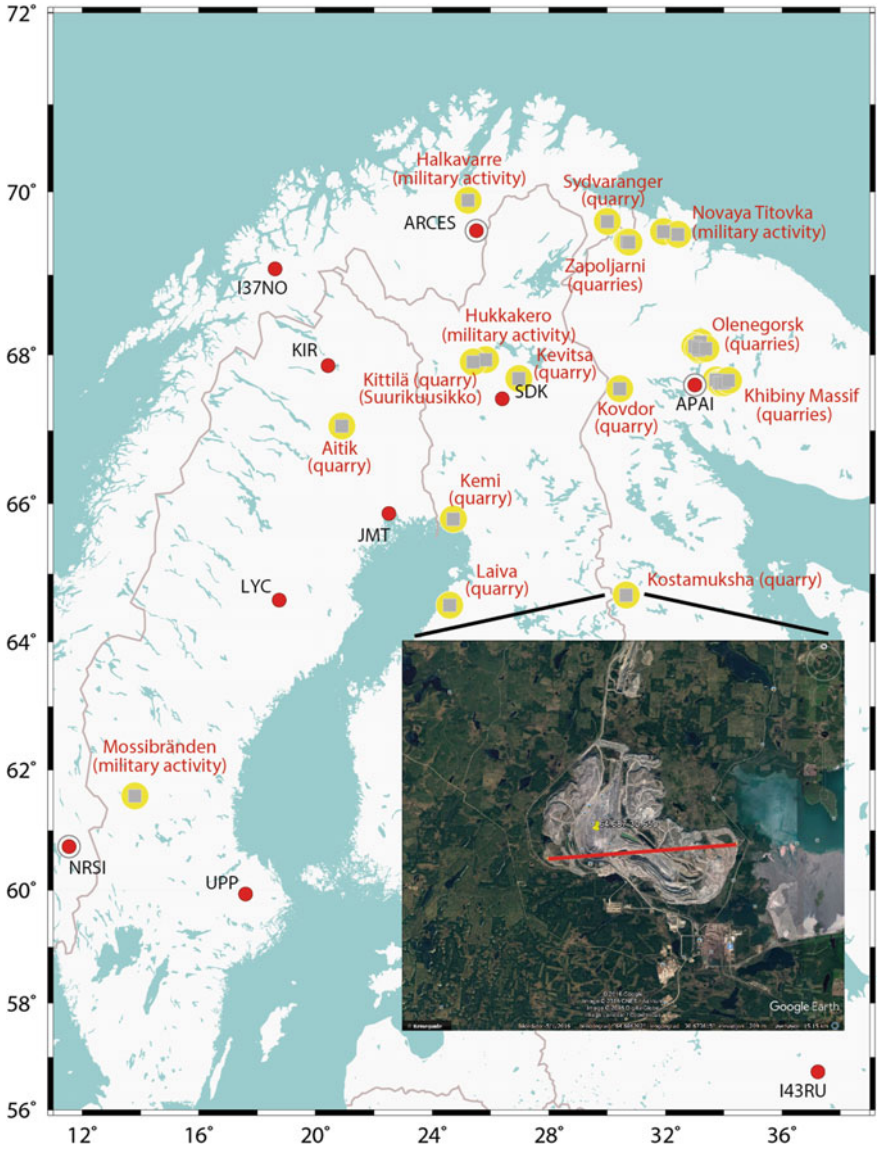

Fig. 10.1 Infrasound stations (red circles) and repeating sources of infrasound in Fennoscandia and North West Russia. The satellite image (from Google Earth) displays the Kostamuksha quarry in Russia where the length of the red line is 7.5 km. The yellow pin in the inset panel is centered on 64.687°N, 30.650°E

Gibbons et al. (2015a) provide an overview of other sources of repeating explosions in the European Arctic which have been identified from both seismic and infrasound recordings over the past 20 years or so. Like Che et al. (2011, 2019), Gibbons and Ringdal (2010) demonstrated that the seasonal variability of infrasound signals from repeating explosions in northwest Russia could differ enormously depending upon the source-to-receiver direction. More recently, Smets et al. (2015) exploited all-year-round open-cast mining blasts at Aitik in Sweden recorded at the I37NO infrasound array to assess the validity of atmospheric wind and temperature profiles. In this probabilistic approach, infrasound propagation was simulated within atmospheric ensemble temperature and wind profiles provided by the European Centre for Medium-Range Weather Forecasts (ECMWF). Such profiles are generated from realistic perturbations to the assimilated observations and initial estimate fields in the ECMWF atmospheric analysis product. The modeled and observed infrasound returns were then compared in order to approve (or refuse) the different member profiles in the ensemble set relevant to each event. Examples from this study will be presented later in this chapter.

10.3 Detecting and Classifying Seismic Events Using Seismic Data

An ideal form for Ground Truth is the reporting of an exact location and time by those carrying out the explosion. This occurs very rarely in practice since most of the explosions take place for military or industrial reasons, and not for the sake of observational geophysics. It is quite common that mine operators will be able to indicate that an explosion took place at a given mine in a certain time window (for example to within an hour) and that checking against a local seismic station will provide an accurate origin time (e.g., Harris et al. 2003; McKenna et al. 2007). If we are very fortunate, we will have an on-site seismic instrument which will provide sub-second accuracy of explosion time (c.f. Che et al. 2011). The advantages of on-site recording are so great that a considerable effort has been invested in designing specialized seismic and acoustic instruments to record both the ground motion and near-field airwave (Taylor et al. 2011).

More typically, we are restricted to remote sensing with the closest seismic stations at tens or even hundreds of kilometers from the source. However, given the longer timescales of atmospheric sound propagation, a source location error of a few kilometers (or an origin time error exceeding a second or two) will not necessarily mean that an event is not sufficiently well constrained for infrasound GT purposes. If a mine is the only source of significant seismic signals over a large region, we may be able to constrain the source location from satellite imagery and constrain the origin time to far greater accuracy than would be possible if the source location were subject to seismic network-related uncertainties. This is the case for the Kostomuksha mine in Russia; explosions at this mine are recorded well by stations at distances

exceeding 1000 km. Network location estimates from distant seismic stations (e.g., IMS seismic arrays) may have uncertainties exceeding 25 km. Google Earth reveals that 64.69°N, 30.65°E is contained within a large open-cast quarry system. A large explosion (almost always at 09:00 or 10:00 UT) near these coordinates is essentially constrained to have taken place within this complex (approximately 7.5 km across). Taking a single first seismic arrival at one of the most sensitive seismic stations (the FINES and ARCES seismic arrays) and calculating the time back to the source region is likely to constrain the origin time and location far more accurately than consulting a network bulletin.

Identical explosions that take place at a given location generate identical seismic signals (e.g., Geller and Mueller 1980). The solid earth is unchanging and the radiating seismic waves follow the same paths which results in the same ground motion at each sensor, time after time. Given truly identical sources, the only differences in the seismic signals recorded at any station will be the result of background noise and unrelated seismic energy. Very closely spaced seismic events, which generate almost identical signals, can often be located relatively with great accuracy by correlating the waveforms and measuring the very small shifts in the arrival times (e.g., Waldhauser and Ellsworth 2000). The seismic signals may be weak and correlation detectors may also provide the best way of detecting events (the sources discussed by Gibbons and Ringdal (2010) are detected seismically to 200–300 km whereas the infrasound generated is observed at far greater distances). The multichannel waveform correlation procedure, described in detail by Gibbons and Ringdal (2006), is illustrated in Fig. 10.2 for the detection of a low yield surface explosion at Hukkakero. The seismic signal at ARCES is below the background noise level but gives a clear correlation (or matched filter) detection when the signal from an earlier event is available as a waveform template. The screening criteria of Gibbons and Ringdal (2006) provide a high level of confidence that there is indeed a signal at this time from the site being monitored and, in this case, this can be confirmed by a signal at a far closer station. Infrasound from this small blast was recorded at several infrasonic arrays in Fennoscandia.

Correlators have limitations for detecting sources which result in significantly different seismic waveforms from blast to blast. This is typically the result of ripple-firing practices in which the total yield of the explosion is split between multiple small charges detonated with tiny delays. The orientation of the rock face being excavated can also be of significance and a gradual change in the nature of the seismic signal resulting from excavation of rock in the source region can frequently be observed. This need resulted in the application of subspace methods (e.g., Harris 1991; Harris and Dodge 2011) that generalize correlation detectors to consider linear combinations of signals from multiple master events (see, e.g., Chambers et al. 2015, for a recent application). Both correlation and subspace detectors are more powerful when stacking over multiple seismic sensors is possible. A mine with dimensions of many kilometers may require multiple templates to provide sufficient coverage given that the seismic signals are typically of high frequency (small wavelength) and the geographical footprint of a single signal may cover only a small fraction of the mine.

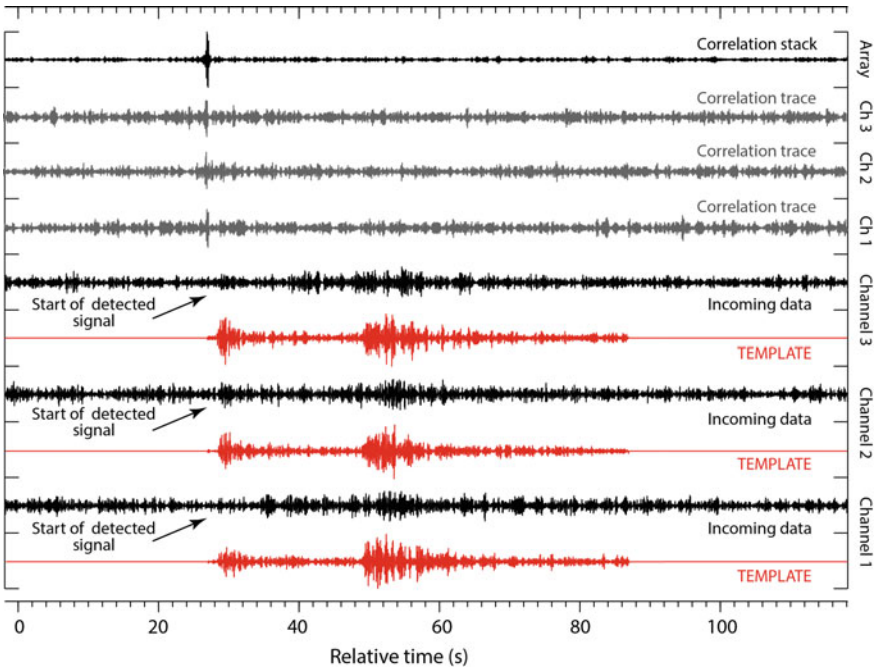

Fig. 10.2 Detection of a very low yield explosion at Hukkakero using multi-channel waveform correlation with the seismic signal from a larger explosion at the same location as a template. The master event signals from each sensor of the ARCES seismic array (red, only three channels displayed) are correlated tracewise, sample by sample, with the incoming datastreams (black). The resulting single channel correlation traces (gray) are stacked to give an array detection statistic with a greatly increased detection capability (top)

If a seismic array is available, an even more powerful method for identifying the signals with significant differences in the source-time function may be applied; empirical matched field processing (EMFP, Harris and Kværna 2010). EMFP is also a pattern detector but, rather than comparing the ground motion as a function of time, it compares narrow frequency band phase and amplitude relations between the signals recorded on different sensors in an array or network. The fact that the signal is broken down into narrow frequency bands makes EMFP robust to differences in the source-time function (e.g., when ripple-firing is used). The principle is demonstrated in Fig. 10.3. A coherent wavefront passing over two sensors an array will, for a given frequency, be observed as a sinusoid with a phase shift (represented by a color in Fig. 10.3). When we estimate the direction of an incoming wavefront using a seismic array, we are essentially testing to see which set of modeled phase shifts best matches the set of phase shifts that the incoming wavefront displays. Given the imperfect earth, with its faults and contrasts, the observed phase shifts (displayed on the right of Fig. 10.3) are often significantly different from those predicted by a simple plane wavefront model (on the left). However, the set of observed phase

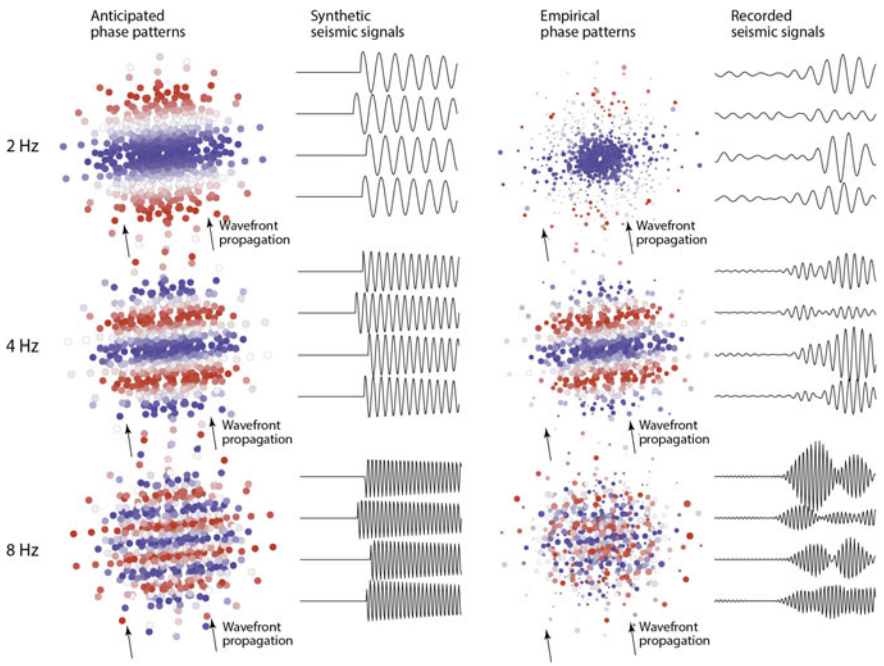

Fig. 10.3 Empirical matched field processing (EMFP) can identify the source of seismic signals even when waveform correlation fails, usually due to differences in the source-time function (as is common in ripple-fired quarry blasts). In EMFP, the signal over a seismic array is broken down into very narrow frequency bands and the pattern of phase differences between each pair of sensors is measured (see Harris and Kværna 2010). The colored symbols indicate the theoretical phase shifts (left) and the measured phase shifts (right) for a P-wave at the ARCES array from a Hukkakero explosion. The size of the symbol indicates coherence and the location of the symbol indicates the displacement vector between the two sensors. These phase-shift patterns are calculated for many very narrow frequency bands (only three are displayed) for a master event and this complex vector is stored as a signal template in the same way that a waveform is stored as a template for the correlation detector. A detection statistic measuring the similarity between this vector and the corresponding vector measured at any specified time can tell us if a new occurrence of this signal is observed

shifts for wavefronts arriving from explosions at the same site is usually very characteristic, even when the source-time function of the source is very different. Harris and Kværna (2010) demonstrate the enhanced resolution of EMFP for signals from different closely spaced mines, compared with the resolution possible using correlation detectors. This may significantly improve the source identification for infrasound modeling given many sources over a wide region, if very close seismic stations are not available.

We have reviewed several classes of seismic monitoring techniques that are applicable to different situations, in the absence of local monitoring. We suggest that a single site of large events, far from other sources of seismicity, is monitored adequately by standard network procedures (e.g., Ringdal and Kværna 1989) whereas pattern

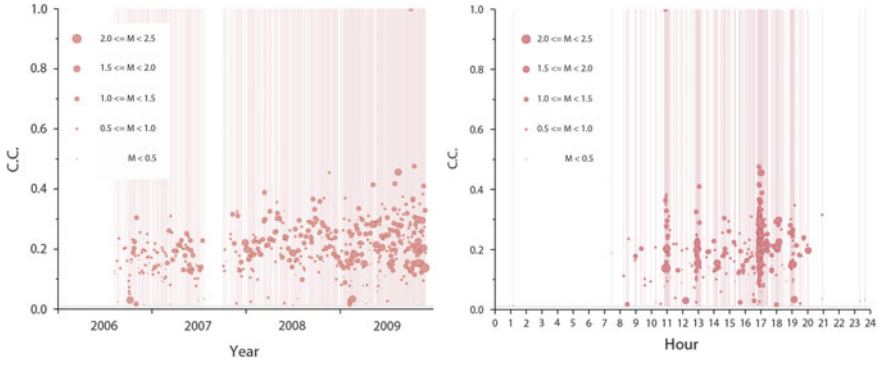

Fig. 10.4 Correlation (or matched filter) detections for a signal template at ARCES for a mining blast at Suurikuusikko (see Gibbons et al. 2015a). The detector was run on all continuous ARCES data from the start of 2006 to halfway through 2009. Each point represents a detection plotted against time (left) and time of day (right) with the symbol size representing the size of the event. No direct confirmation of events from the mine was available but analyses such as this, showing no detections at all at night, and none before the start of operations in summer 2006, indicate that there are essentially no false alarms. The screening criteria of Gibbons and Ringdal (2006) are essential for running such a detector at these low thresholds with this low false alarm rate

detectors are usually necessary for sources of weaker seismic signals or sources that are geographically close. The most sensitive form of pattern detector is the multi-channel correlation detector, but the applicability of this method decreases with differences between the seismic signals generated. In cases of signal diversity, subspace and/or matched field detectors perform better. Regardless of the method used, some form of validation check is required. The Suurikuusikko gold mine near Kittilä in northern Finland generates seismic signals recorded on the ARCES array 180 km away. Production started in the summer of 2006 and events were monitored using a single multi-channel correlation detector at ARCES. Of the 389 correlation detections displayed in Fig. 10.4, we see that none occurred prior to July 2006 and that only three occur between the times of 22h00 and 07h00 UT. Examining the plot of detections versus time of day shows a distribution which indicates industrial practice and provides confidence in the signal detector false alarm rate.

The sequence of multiple seismic events is difficult to discern from the resulting superimposed seismogram. Figure 10.5 displays the ARCES seismograms for a number of these events aligned according to the maximum correlation with the signal template. The signals, all plotted to a common vertical scale such that the relative amplitudes of the signals are real. The form of the infrasound signals recorded at Sodankylä (presumed to be tropospheric phases) appears to be quite simple and consistent from event to event, in contrast to the presumed stratospheric arrivals observed at 180 km (Gibbons et al. 2007). One of the apparent double events is indeed associated with a double acoustic signal, as indicated in the figure. Double infrasound signals can also occur from multipathing so care needs to be applied when the source-time function of the explosion is complicated.

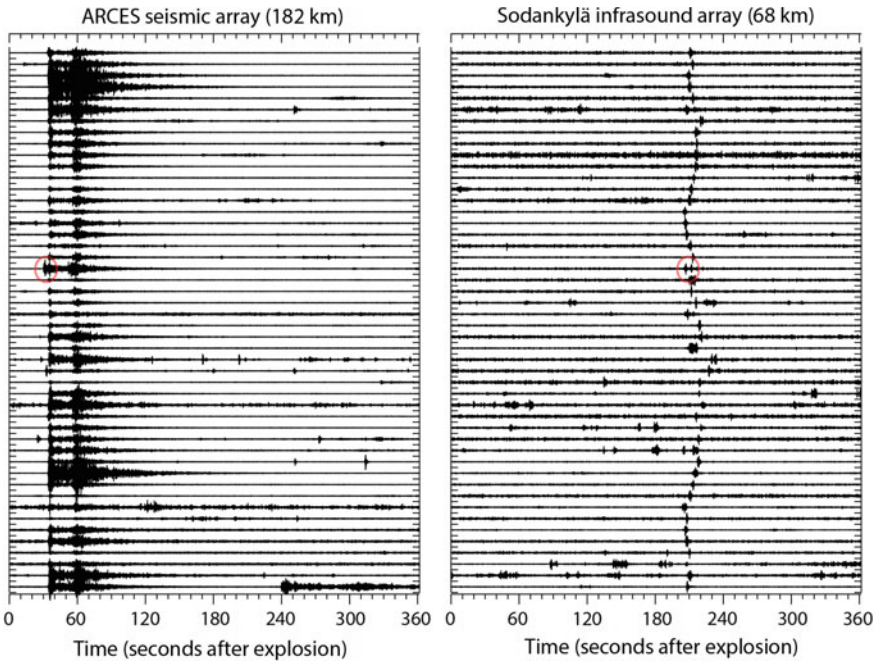

Fig. 10.5 Seismic and infrasound signals generated by different blasts at the Suurikuusikko mine in northern Finland. The seismic signals are aligned according to the maximum correlation with the master event used for the detector displayed in Fig. 10.4. Seismic signals which appear misaligned are likely due to double events. One such seismic arrival is indicated by a ring, as is the corresponding pair of infrasonic arrivals. The infrasound signals recorded at Sodankylä are of relatively short duration and arrive between 195 and 220 s after each explosion

10.4 Exploiting Infrasound Ground Truth Events for Atmospheric Modeling and Event Location Calibration

The stratosphere has a role in weather and climate predictability beyond a few days horizon (e.g., Karpencho et al. 2016). Better modeling and understanding of the stratospheric circulation and its interaction with planetary-wave generation is crucial for improving predictability in the weeks-to-months timescales. Studies have demonstrated that atmospheric infrasound data can be exploited in the evaluation of numerical weather forecasts e.g., in assessing forecast skills around an SSW (e.g., Smets et al. 2016). Smets et al. (2015) assessed ensembles of perturbed analyses provided by the ECMWF using constraints given by infrasound data combined with wave-propagation modeling. Other papers where atmospheric infrasound is used to verify, parameterize, or update atmospheric models include Chunchuzov et al. (2015), Le Pichon et al. (2015), Assink et al. (2014), Arrowsmith et al. (2016),

and Lalande et al. (2012), Chunchuzov and Kulichkov (2019), Assink et al. (2019). A more general overview of the role infrasound can play in helping us to understand the earth system is provided in Hedlin et al. (2012), de Groot-Hedlin and Hedlin (2019).

Smets et al. (2015) demonstrate that applying small-scale fluctuations to the applied wind and temperature profiles may not always be necessary to match modeled predictions with observed infrasound returns. Mining explosions at Aitik in Sweden were identified from remote seismic monitoring and, for each event, infrasound propagation simulations were carried out through ensembles of realistic atmospheric model profiles. These ensembles were provided by the European Centre for Medium-Range Weather Forecasts (ECMWF) and the profiles result from realistic perturbations both to the initial atmospheric state and to the assimilated observations. The infrasound observed at I37NO (245 km to the North West) is displayed in Fig. 10.6 and Smets et al. (2015) discuss how well these observations are matched by predictions, both with the standard and perturbed analyses. Many of the signals are predicted by the unperturbed analysis; others are predicted by particular classes of perturbations applied. A parabolic variation in celerity is observed for stratospherically downstream events (c.f. Che et al. 2011) with little observed at other times

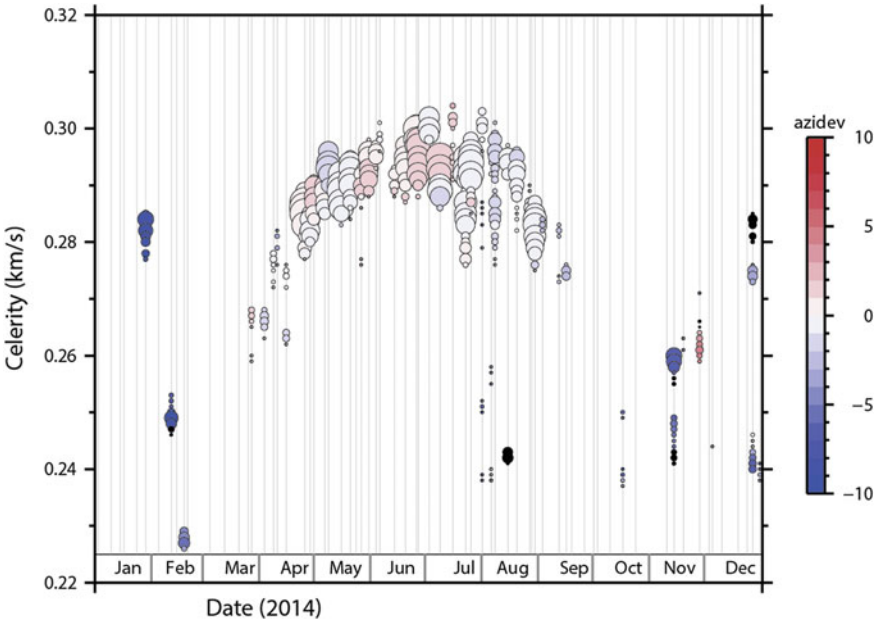

Fig. 10.6 Infrasound signal coherence at I37NO for seismically confirmed mining blasts at the Aitik quarry near Gällivare in northern Sweden (distance approximately 245 km). Each vertical line indicates an explosion at this pit and a symbol is displayed for each 10 s interval of I37NO data, bandpass filtered 1–4 Hz, for which the coherence exceeded 0.05, the apparent velocity was between 0.32 and 0.40 km/s and for which the back azimuth was between 145° and 165°. The sizes of the symbols are proportional to the coherence with the largest symbols approaching a coherence of unity

of the year. The few observations in the winter months, with significant azimuthal deviation, would be likely candidates for incorrectly associated infrasound signals. However, Smets et al. (2015) show that several of these are in fact predicted both by perturbed and unperturbed analyses.

While the Aitik explosions take place all year round, they are usually carried out once or sometimes twice per week. The Hukkakero explosions do not sample all seasons but do allow an assessment of the change in infrasound propagation over shorter timescales. Figure 10.7 displays broadband signals at I37NO (distance 320 km) for the 15 Hukkakero events from 2014. Gibbons et al. (2015a) demonstrated a relatively smooth change in the traveltime of the stratospheric phase with a moveout of up to 30 s relative to the seismically constrained origin time, but with over a minute in the variability of the arrival time of the thermospheric arrivals. In addition, the phase velocity of the stratospheric arrivals are essentially constant from day to day (indicating a consistent reflection altitude) whereas the phase velocity of the thermospheric arrivals varies significantly over the same timescales (indicating differences in the angle of descent and turning height). Figure 10.7 also indicates significant changes in the form of the signals from day to day.

Uncertainty in the anticipated celerity has consequences for the uncertainty in event location estimates (e.g., Modrak et al. 2010). The stratospheric anisotropy (which favors infrasound propagation in one direction and inhibits infrasound propagation in the other direction) means that we almost always have a large azimuthal gap

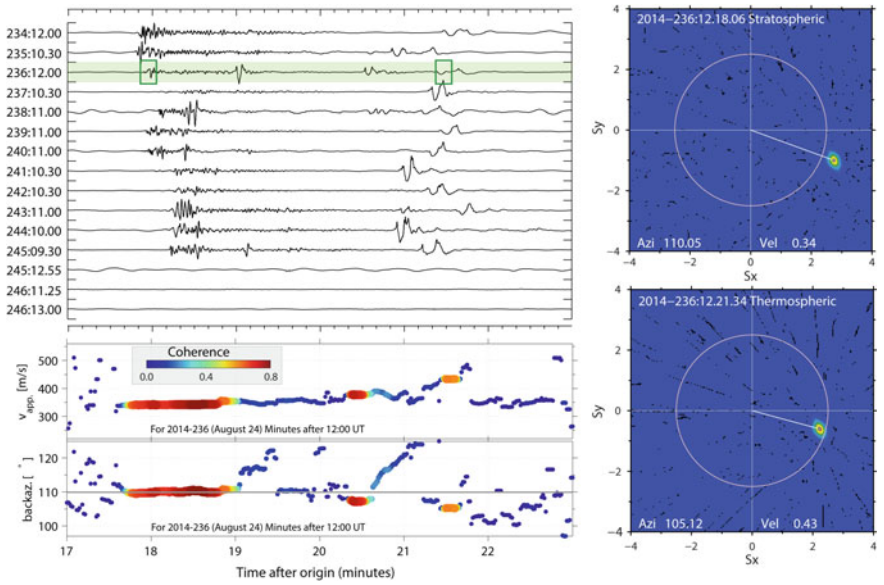

Fig. 10.7 Waveforms on I37NO for 15 explosions at Hukkakero in August and September 2014 as indicated. Waveforms in the main panel are bandpass filtered 0.03–1.50 Hz whereas the slowness analysis and processing results are performed in the 1–4 Hz band

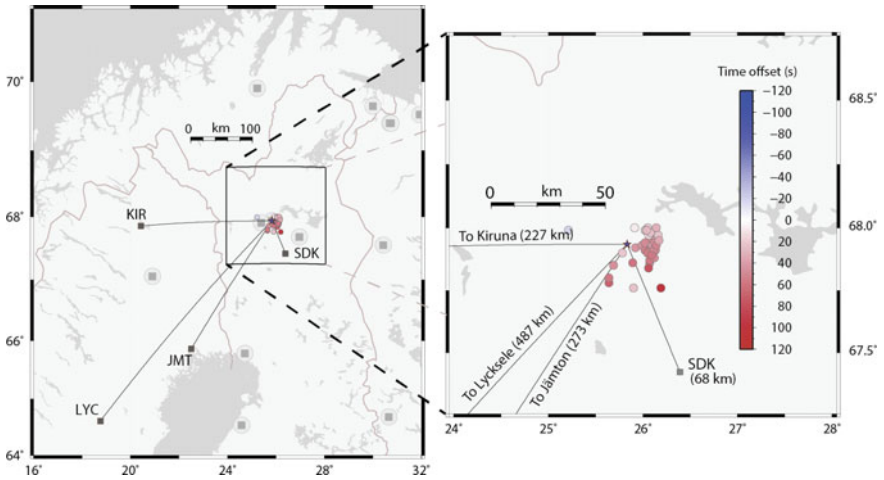

Fig. 10.8 Three-station infrasound location estimates in the CEA bulletin for 40 explosions confirmed to have taken place at the Hukkakero site (GT location 67.934°N, 25.832°E, asterisk) between 2007 and 2012. The event locations are based mostly on detections at the four Swedish Institute of Space Physics (IRF) stations shown though not all stations necessarily contribute to all events. The color of the location estimates indicates the time offset of the infrasound origin time estimate; a positive number of seconds indicated that the origin time is estimated later than the seismically confirmed GT origin time

in infrasonic event location. The back azimuth estimates of infrasound arrivals are consequently more important in the location problem than is typical in seismology. Figure 10.8 shows the location estimates made by the Commissariat à l'énergie atomique et aux énergies alternatives (CEA) for events, with contributions from at least three infrasound arrays, that were confirmed by independent seismic analysis to have taken place at Hukkakero. The detections are dominated by the Swedish Institute of Space Physics (IRF) JMT, LYC, KIR, and SDK arrays which, with apertures of only 100 m, have more limited back azimuth resolution than the considerably larger IMS infrasound arrays. However, almost all location estimates fall within 25 km of the GT location. Figure 10.8 displays the tradeoff between the location and origin time estimates and almost all events are estimated later than the seismically confirmed explosion time. The GT collection will provide empirical traveltime distributions which will allow a better calibrated location procedure and hopefully reduce significantly the spread in the location estimates.

10.5 Conclusions

Knowing the time and the location of explosive sources of atmospheric sound serves several purposes. It allows a generated infrasound signal to be used for probing the

state of the atmosphere or evaluating methods for modeling atmospheric sound propagation. If we have a location and time estimate for an event which would be expected to generate infrasound, we have a test of detection capability for a network and, in the case of an infrasonic event being formed, a calibration for the location estimate and uncertainty. At an even more fundamental level, a known source may be able to explain an infrasound signal that is detected but not necessarily associated or characterized. Figure 10.9 displays a weak, low frequency, infrasound signal detected at I18DK, Qaanaaq, Greenland. In the context of the global IMS network, this detection is one of many from which no event is constructed. Our seismic and near-regional infrasonic monitoring of northern Fennoscandia pinpoints the time of a Hukkakero explosion to 08:00 UT on August 15, 2007. This source is consistent both in direction and celerity with the signal detected almost 3 h later and 3000 km away. This signal will now contribute to our understanding of probabilistic infrasound detection at large distances.

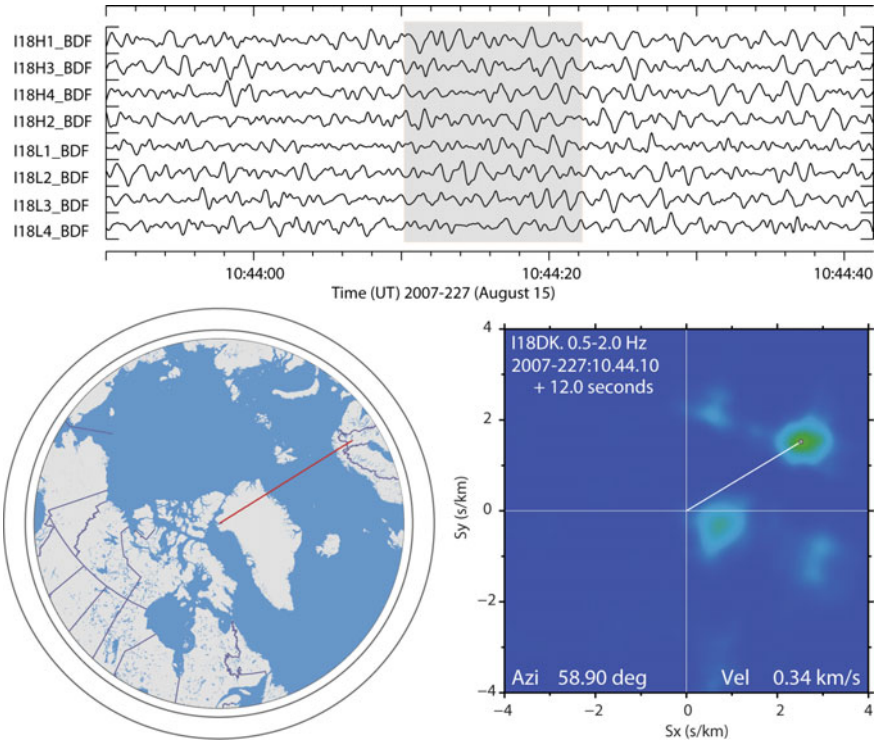

Fig. 10.9 A detection on the IMS infrasound array I18DK at Qaanaaq, Greenland, which is consistent both in time and direction with the signal from an explosion at Hukkakero (distance 2923 km). The seismic signal at ARCES indicates an origin time of 08:00 for the explosion, giving an infrasound celerity to I18DK of 0.297 km/s. The waveforms are displayed and processed in the 0.5–2.0 Hz band

Our focus has been on ground-based explosions as these typically generate seismic signals which constrain both source time and source location. While seismic monitoring is ideally performed locally, this is most often not feasible and we may be limited to remote sensing. Even at distances of several hundred kilometers, seismic recordings may constrain the source location to the order of 1 km and the source time to the order of a second: a far higher accuracy than is needed to be useful for infrasound propagation over scales of hundreds of kilometers. We have, in this paper, provided an overview of the most applicable seismic methods for constraining sources of different kinds. If a very comprehensive seismic catalog is available for a region, e.g., with completeness to below magnitude 1, we may be able to eliminate almost all ground sources for events solely constrained by infrasound signals. In a test-ban treaty monitoring context, a large number of screened events (i.e., events that can be assigned with a high level of confidence to a known source) will allow targeting of resources to signals of unknown origin.

There are numerous issues of scale, both related to the source and to the observations. For the source, the scale is mostly related to the size of the event: how much energy is released. Events that generate infrasound detected at great distances are (fortunately) few and far between. They are usually catastrophic and damaging events and, while providing unique insights into propagation modes for atmospheric sounds, sample only a single state of the atmosphere and will give little insight into the detectability of infrasound that can be expected from smaller events. Routine industrial blasts at open-cast mines generate infrasound recorded at much shorter distances but provide typically hundreds of events over timescales of years that sample many different atmospheric paths and enhance our understanding of the statistical expectation of the observed infrasound (see, e.g., Morton and Arrowsmith 2014; Smets et al. 2015; Cugnet et al. 2019). Atmospheric sound propagation at even shorter distances can be studied in detail with far smaller, nonexplosive, infrasonic sources (e.g., Jones 2014). The recent study of de Groot-Hedlin and Hedlin (2015), de Groot-Hedlin and Hedlin (2019); also includes an extensive catalog of routine industrial explosions in the USA.

Regarding the spatial scale at which the infrasonic wavefield is observed, while the global network was designed to detect large atmospheric explosions detected at multiple stations at distances of several thousand kilometers, the increasing array of civil infrasound applications has led to the deployment of many national facilities with far denser coverage than the IMS network. The lowering of the detection threshold provided by additional sites is discussed by, e.g., Le Pichon et al. (2008) and Tailpied et al. (2013). Many of the sources discussed in this paper are small with infrasound only detected out to relatively short distances. To understand the capabilities of civil infrasound monitoring, we must also understand the limitations; under which circumstances can we and can we not expect to detect infrasound from a source of interest? We have seen examples where the direction and the path over which an infrasound signal propagates has large consequences for the likelihood of detection and the expected celerity. Regarding the temporal scale, we note the value of long-term time-series data which can cover variability in the expected infrasound propagation from scales of hours and days, to seasons and years. Only now are we

approaching an era where timescales of several decades will be represented with continuous infrasound data.

We use infrasound signals to help characterize the sources of seismic signals (e.g., to provide a means of discrimination: Stump et al. 2002; Che et al. 2019) and use seismic signals, for example, to constrain the time and location of infrasound sources. An increasing interest in the seismo-acoustic wavefield (e.g., Arrowsmith et al. 2010; Hedlin et al. 2012) is likely both to increase the volume of data and enhance its exploitation. The majority of the studies discussed are made possible due to the availability of both seismic and infrasound data. The cases for augmenting seismic sensors with microbarographs (e.g., Stump et al. 2004) and infrasound arrays with seismic sensors (e.g., Gibbons et al. 2015b) are both compelling.

Acknowledgements We are grateful to Alexis Le Pichon for providing the infrasound event bulletin of the CEA (Commissariat à l'énergie atomique et aux énergies alternatives).
We thank Hans Israelsson for his lists of IMS infrasound detections associated with Ground Truth events at Hukkakero.
Data from the Sodankylä (SDK) array is obtained with thanks from the Swedish Institute of Space Physics (IRF) and data from I18DK was obtained from the International Data Center of the Preparatory Commission for the Comprehensive Nuclear-Test-Ban Treaty Organization, Vienna.
Data from ARCES and I37NO are available from NORSAR from
`http://www.norsardata.no/NDC/data/autodrm.html`
Graphics are generated using the GMT software (Wessel and Smith 1995).
The IRIS reference event infrasound database is found at
`http://ds.iris.edu/ds/products/infrasound-taired/` (last referenced January 2016).

References

Arrowsmith SJ, Hedlin MAH, Stump B, Arrowsmith MD (2008) Infrasonic signals from large mining explosions. Bull Seismol Soc Am 98:768–777. https://doi.org/10.1785/0120060241

Arrowsmith M, Arrowsmith S, Marcillo O (2016) Using sounds from the ocean to measure winds in the stratosphere. EOS 97: https://doi.org/10.1029/2016EO042563

Assink JD, Le Pichon A, Blanc E, Kallel M, Khemiri L (2014) Evaluation of wind and temperature profiles from ECMWF analysis on two hemispheres using volcanic infrasound. J Geophys Res Atmos 119(14):8659–8683. https://doi.org/10.1002/2014jd021632

Assink J, Smets P, Marcillo O, Weemstra C, Lalande J-M, Waxler R, Evers L (2019) Advances in infrasonic remote sensing methods. In: Le Pichon A, Blanc E, Hauchecorne A (eds) Infrasound monitoring for atmospheric studies, 2nd edn. Springer, Dordrecht, pp 605–632

Arrowsmith SJ, Johnson JB, Drob DP, Hedlin MAH (2010) The seismoacoustic wavefield: a new paradigm in studying geophysical phenomena. Rev Geophys 48:RG4003+. https://doi.org/10.1029/2010rg000335

Bondar I, Engdahl ER, Yang X, Ghalib HAA, Hofstetter A, Kirichenko V, Wagner R, Gupta I, Ekstrom G, Bergman E, Israelsson H, McLaughlin K (2004) Collection of a reference event set for regional and teleseismic location calibration. Bull Seismol Soc Am 94(4):1528–1545. https://doi.org/10.1785/012003128

Bonner J, Waxler R, Gitterman Y, Hofstetter R (2013) Seismo-acoustic energy partitioning at near-source and local distances from the 2011 Sayarim explosions in the Negev desert. Israel. Bull Seismol Soc Am 103(2A):741–758. https://doi.org/10.1785/0120120181

Ceranna L, Le Pichon A, Green DN, Mialle P (2009) The Buncefield explosion: a benchmark for infrasound analysis across Central Europe. Geophys J Int 177:491–508. https://doi.org/10.1111/j.1365-246x.2008.03998.x

Chambers DJA, Koper KD, Pankow KL, McCarter MK (2015) Detecting and characterizing coal mine related seismicity in the Western U.S. using subspace methods. Geophys J Int 203:1388–1399. https://doi.org/10.1093/gji/ggv383

Che IY, Jun MS, Jeon JS, Min KD (2002) Analysis of local seismo-acoustic events in the Korean Peninsula. Geophys Res Lett 29:1589+. https://doi.org/10.1029/2001gl014060

Che IY, Stump BW, Lee HI (2011) Experimental characterization of seasonal variations in infrasonic traveltimes on the Korean Peninsula with implications for infrasound event location. Geophys J Int 185:190–200. https://doi.org/10.1111/j.1365-246x.2011.04948.x

Che IY, Park J, Kim I, Kim TS, Lee HI (2014) Infrasound signals from the underground nuclear explosions of North Korea. Geophys J Int 198:495–503. https://doi.org/10.1093/gji/ggu150

Che IY, Park J, Kim TS, Hayward C, Stump B (2019) On the use of a dense network of seismo-acoustic arrays for near-regional environmental monitoring. In: Le Pichon A, Blanc E, Hauchecorne A (eds) Infrasound monitoring for atmospheric studies, 2nd edn. Springer, Dordrecht, pp 409–448

Che IY, Kim TS, Jeon JS, Lee HI (2009) Infrasound observation of the apparent North Korean nuclear test of 25 May 2009. Geophys Res Lett 36(22):L22,802+. https://doi.org/10.1029/2009gl041017

Cugnet D, de la Camara A, Lott F, Millet C, Ribstein B (2019) Non-orographic gravity waves: representation in climate models and effects on infrasound. In: Le Pichon A, Blanc E, Hauchecorne A (eds) Infrasound monitoring for atmospheric studies, 2nd edn. Springer, Dordrecht, pp 827–844

Christie DR, Campus P (2009) The IMS infrasound network: design and establishment of infrasound stations. In: Le Pichon A, Blanc E, Hauchecorne A (eds) Infrasound monitoring for atmospheric studies. Springer, Netherlands, chap 2, pp 29–75. https://doi.org/10.1007/978-1-4020-9508-5_2

Chunchuzov I, Kulichkov S (2019) Internal gravity wave perturbations and their impacts on infrasound propagation in the atmosphere. In: Le Pichon A, Blanc E, Hauchecorne A (eds) Infrasound monitoring for atmospheric studies, 2nd edn. Springer, Dordrecht, pp 551–590

Chunchuzov I, Kulichkov S, Perepelkin V, Popov O, Firstov P, Assink JD, Marchetti E (2015) Study of the wind velocity-layered structure in the stratosphere, mesosphere, and lower thermosphere by using infrasound probing of the atmosphere. J Geophys Res Atmos 120(17):8828–8840. https://doi.org/10.1002/2015jd023276

Dahlman O, Mackby J, Mykkeltveit S, Haak H (2011) Detect and deter: can countries verify the nuclear test ban? Springer Science and Business Media B, Dordrecht, The Netherlands. https://doi.org/10.1007/978-9-4007-1676-6

de Groot-Hedlin CD, Hedlin MAH (2015) A method for detecting and locating geophysical events using groups of arrays. Geophy J Int 203(2):960–971. https://doi.org/10.1093/gji/ggv345

de Groot-Hedlin C, Hedlin M (2019) Detection of infrasound signals and sources using a dense seismic network. In: Le Pichon A, Blanc E, Hauchecorne A (eds) Infrasound monitoring for atmospheric studies, 2nd edn. Springer, Dordrecht, pp 669–699

Evers L, Schweitzer J (2011) A climatology of infrasound detections in northern Norway at the experimental ARCI array. J Seismol 15:473–486. https://doi.org/10.1007/s10950-011-9237-8

Geller RJ, Mueller CS (1980) Four similar earthquakes in Central California. Geophys Res Lett 7(10):821–824

Gibbons SJ, Asming V, Eliasson L, Fedorov A, Fyen J, Kero J, Kozlovskaya E, Kværna T, Liszka L, Näsholm SP, Raita T, Roth M, Tiira T, Vinogradov Y (2015a) The European Arctic: a laboratory for seismoacoustic studies. Seismol Res Lett 86:917–928. https://doi.org/10.1785/0220140230

Gibbons SJ, Kværna T, Mykkeltveit S (2015b) Could the IMS infrasound stations support a global network of small aperture seismic arrays? Seismol Res Lett 86:1148–1159. https://doi.org/10.1785/0220150068

Gibbons SJ, Ringdal F (2006) The detection of low magnitude seismic events using array-based waveform correlation. Geophys J Int 165:149–166. https://doi.org/10.1111/j.1365-246X.2006.02865.x

Gibbons SJ, Ringdal F, Kværna T (2007) Joint seismic-infrasonic processing of recordings from a repeating source of atmospheric explosions. J Acoust Soc Am 122:EL158–EL164. https://doi.org/10.1121/1.2784533

Gibbons S, Ringdal F (2010) Detection and analysis of near-surface explosions on the Kola Peninsula. Pure Appl Geophys 167:413–436. https://doi.org/10.1007/s00024-009-0038-8

Green DN, Le Pichon A, Ceranna L, Evers L (2009) Ground truth events: assessing the capability of infrasound networks using high resolution data analyses. In: Le Pichon A, Blanc E, Hauchecorne A (eds) Infrasound monitoring for atmospheric studies. Springer, Netherlands, chap 19, pp 599–625. https://doi.org/10.1007/978-1-4020-9508-5_19

Hagerty MT, Kim WY, Martysevich P (2002) Infrasound detection of large mining blasts in Kazakstan. In: Der ZA, Shumway RH, Herrin ET (eds) Monitoring the comprehensive nuclear-test-ban treaty: data processing and infrasound, Pageoph Topical Volumes, Birkhäuser Basel, pp 1063–1079. https://doi.org/10.1007/978-3-0348-8144-9_9

Harris DB (1991) A waveform correlation method for identifying quarry explosions. Bull Seismol Soc Am 81:2395–2418

Harris DB, Dodge DA (2011) An autonomous system for grouping events in a developing aftershock sequence. Bull Seism Soc Am 101:763–774

Harris DB, Kværna T (2010) Superresolution with seismic arrays using empirical matched field processing. Geophys J Int 182:1455–1477. https://doi.org/10.1111/j.1365-246x.2010.04684.x

Harris DB, Ringdal F, Kremenetskaya EO, Mykkeltveit S, Schweitzer J, Hauk TF, Asming VE, Rock DW, Lewis JP (2003) Ground-truth collection for mining explosions in Northern Fennoscandia and Russia. In: Proceedings of the 25th seismic research review, nuclear explosion monitoring building the knowledge base, LA-UR-03-6029, Tucson, Arizona, 23–25 Sept 2003, pp 54–63

Hedlin MAH, Drob DP (2014) Statistical characterization of atmospheric gravity waves by seismoacoustic observations. J Geophys Res Atmos 119(9):2013JD021,304+. https://doi.org/10.1002/2013jd021304

Hedlin MAH, Walker KT (2013) A study of infrasonic anisotropy and multipathing in the atmosphere using seismic networks. Philos Trans R Soc A Math Phys Eng Sci 371: https://doi.org/10.1098/rsta.2011.0542

Hedlin MAH, Walker K, Drob DP, de Groot Hedlin, (2012) Infrasound: connecting the solid earth, oceans, and atmosphere. Annu Rev Earth Planet Sci 40:327–354. https://doi.org/10.1146/annurev-earth-042711-105508

Israelsson H (2013) Recordings from Hukkakero explosions in 2009 at infrasound stations of the IRF network. Technical report SIR 01-2013, SeismicInfra Research, Washington DC

Jones KR (2014) Infrasound generation from the HH seismic hammer. Technical report. SAND2014-19350, Sandia National Laboratories, Albuquerque, New Mexico. http://prod.sandia.gov/techlib/access-control.cgi/2014/1419350.pdf

Karpechko A, Tummon F, Secretariat W (2016) Climate predictability in the stratosphere. World Meteorol Organ Bull 65. https://public.wmo.int/en/resources/bulletin/climate-predictability-stratosphere

Lalande JM, Sèbe O, Landès M, Blanc-Benon P, Matoza RS, Le Pichon A, Blanc E (2012) Infrasound data inversion for atmospheric sounding. Geophys J Int 190:687–701. https://doi.org/10.1111/j.1365-246x.2012.05518.x

Le Pichon A, Assink JD, Heinrich P, Blanc E, Charlton-Perez A, Lee CF, Keckhut P, Hauchecorne A, Rüfenacht R, Kämpfer N, Drob DP, Smets PSM, Evers LG, Ceranna L, Pilger C, Ross O, Claud C (2015) Comparison of co-located independent ground-based middle atmospheric wind and temperature measurements with numerical weather prediction models. J Geophys Res Atmos 120(16):8318–8331. https://doi.org/10.1002/2015jd023273

Le Pichon A, Vergoz J, Herry P, Ceranna L (2008) Analyzing the detection capability of infrasound arrays in Central Europe. J Geophys Res Atmos 113(D12):D12,115+. https://doi.org/10.1029/2007jd009509

Marty J (2019) The IMS infrasound network: current status and technological developments. In: Le Pichon A, Blanc E, Hauchecorne A (eds) Infrasound monitoring for atmospheric studies, 2nd edn. Springer, Dordrecht, pp 3–62

Modrak RT, Arrowsmith SJ, Anderson DN (2010) A Bayesian framework for infrasound location. Geophys J Int 181:399–405. https://doi.org/10.1111/j.1365-246x.2010.04499.x

McKenna MH, Stump BW, Hayek S, McKenna JR, Stanton TR (2007) Tele-infrasonic studies of hard-rock mining explosions. J Acoust Soc Am 122:97–106. https://doi.org/10.1121/1.2741375

Morton EA, Arrowsmith SJ (2014) The development of global probabilistic propagation look-up tables for infrasound celerity and back-azimuth deviation. Seismol Res Lett 85(6):1223–1233. https://doi.org/10.1785/0220140124

Nippress A, Green DN, Marcillo OE, Arrowsmith SJ (2014) Generating regional infrasound celerity-range models using ground-truth information and the implications for event location. Geophys J Int 197:1154–1165. https://doi.org/10.1093/gji/ggu049

Pulli JJ, Kofford A (2015) Infrasonic analysis of the October 28, 2014 Antares rocket failure at Wallops Island, Virginia, using video recordings as ground truth. J Acoust Soc Am 137(4):2372. https://doi.org/10.1121/1.4920619

Ringdal F, Kværna T (1989) A multi-channel processing approach to real time network detection, phase association, and threshold monitoring. Bull Seismol Soc Am 79:1927–1940

Smets PSM, Assink JD, Le Pichon A, Evers LG (2016) ECMWF SSW forecast evaluation using infrasound. J Geophys Res Atmos 121(9):4637–4650. https://doi.org/10.1002/2015JD024251

Smets PSM, Evers LG, Näsholm SP, Gibbons SJ (2015) Probabilistic infrasound propagation using realistic atmospheric perturbations. Geophys Res Lett 42(15):6510–6517. https://doi.org/10.1002/2015gl064992

Sorrells GG, Herrin ET, Bonner JL (1997) Construction of regional ground truth databases using seismic and infrasound data. Seismol Res Lett 68:743–752. https://doi.org/10.1785/gssrl.68.5.743

Stump BW, Hedlin MAH, Pearson DC, Hsu V (2002) Characterization of mining explosions at regional distances: implications with the international monitoring system. Rev Geophys 40:1011+. https://doi.org/10.1029/1998rg000048

Stump B, Jun MS, Hayward C, Jeon JS, Che IY, Thomason K, House SM, McKenna J (2004) Small-aperture seismo-acoustic arrays: design, implementation, and utilization. Bull Seismol Soc Am 94:220–236. https://doi.org/10.1785/0120020243

Tailpied D, Le Pichon A, Marchetti E, Ripepe M, Kallel M, Ceranna L, Brachet N (2013) Remote infrasound monitoring of Mount Etna: observed and predicted network detection capability. Inframatics 2:1–11. https://doi.org/10.4236/inframatics.2013.21001

Taylor SR, Harben PE, Jarpe S, Harris DB (2011) Development of mine explosion ground truth smart sensors. In: Proceedings of the 2011 monitoring research review: ground-based nuclear explosion monitoring technologies, Tucson, Arizona, 13–15 Sept 2011. Report LA-UR-11-04823, pp 850–860

Waldhauser F, Ellsworth WL (2000) A double-difference earthquake location algorithm: method and application to the northern Hayward fault. California. Bull Seismol Soc Am 90(6):1353–1368

Walker KT, Shelby R, Hedlin MAH, de Groot-Hedlin C, Vernon F (2011) Western U.S. infrasonic catalog: illuminating infrasonic hot spots with the US array. J Geophys Res Atmos 116(B12):B12,305+. https://doi.org/10.1029/2011jb008579

Wessel P, Smith WHF (1995) New version of the generic mapping tools. EOS Trans Am Geophys Union 76:329

Whitaker RW, Mutschlecner JP (2008) A comparison of infrasound signals refracted from stratospheric and thermospheric altitudes. J Geophys Res Atmos 113(D8):D08,117+. https://doi.org/10.1029/2007jd008852

Chapter 11
On the Use of a Dense Network of Seismo-Acoustic Arrays for Near-Regional Environmental Monitoring

Il-Young Che, Junghyun Park, Tae Sung Kim, Chris Hayward and Brian Stump

Abstract A dense network of eight, seismo-acoustic arrays operates in the southern Korean Peninsula, and since the first array installation in 1999, has provided data for monitoring local and regional seismic and infrasound signals from natural and anthropogenic phenomena. The main operational purpose of the network is to discriminate man-made seismic events from natural earthquakes to produce a clean earthquake catalog, and to ensure that seismic and infrasonic data are appropriately used for analyzing and characterizing various sources using the seismo-acoustic wave fields. This chapter summarizes results of several studies that used the network dataset to; (i) Compare seasonal variations in infrasound detections with local surface weather measurements and stratospheric wind dynamics, (ii) Develop seismic and acoustic data fusion methods that enhance source discrimination synergy, (iii) Understand the characteristic of local and regional infrasound propagation using repetitive surface explosion sources, and (iv) Review infrasound observations from earthquakes and underground nuclear tests. Finally, this chapter illustrates the usefulness of dense regional networks to characterize various seismo-acoustic sources and enhance detection capability in regions of interest in the context of future verification of the Comprehensive Nuclear-Test-Ban Treaty.

I.-Y. Che (✉) · T. S. Kim
Earthquake Research Center, Korea Institute of Geoscience and Mineral Resources, Daejeon, Korea
e-mail: che10@kigam.re.kr

J. Park · C. Hayward · B. Stump
Roy M. Huffington Department of Earth Sciences, Southern Methodist University, Dallas, USA

A. Le Pichon et al. (eds.), *Infrasound Monitoring for Atmospheric Studies*,
https://doi.org/10.1007/978-3-319-75140-5_11

11.1 Introduction

Korea Institute of Geoscience and Mineral Resources (KIGAM) operates a seismo-acoustic array network (Korea Infrasound Network, KIN) in South Korea. As of 2015, this network consists of eight permanent arrays equipped with 4–12 acoustic sensors with 1–5 collocated seismometers; the sensor collocation is intended to have benefits for analyzing and characterizing seismic and infrasonic signals and the sources responsible for their generation. Development of the network began in 1999, in partial collaboration with Southern Methodist University (SMU; Dallas, TX, USA), with the primary operational purpose of detecting local and regional infrasound signals from natural and anthropogenic phenomena in and around the Korean Peninsula (Stump et al. 2004). This network has distinctive features in that the arrays record both seismic and acoustic wave fields at the same locations, which makes it possible to locate seismic events by individual arrays and discriminate surface explosions by associating the seismic events with infrasound signals. In addition, because the eight arrays of KIN comprise a spatially dense network, these data enable us to detect relatively small-amplitude infrasound signals at multiple arrays and hence produce source locations with high accuracy at local and regional distances.

Detection processing of infrasound signals is complicated by atmospheric conditions, varying in time and space. Understanding how detection algorithms are influenced by atmospheric variability is important for infrasound monitoring and can be a basis for improving the infrasound location (Marcillo et al. 2013; Blom et al. 2015). There are several studies of seasonal variations on infrasound detection (Arrowsmith and Hedlin 2005; Le Pichon et al. 2008a). Che et al. (2011) document the seasonal and path dependence of infrasound propagation using data from ground truth events across the Korean Peninsula. Park and Stump (2014) also point out that infrasound propagation and thus signal detection depends on atmospheric conditions as well as factors such as source location and array distribution as illustrated with data from the western US. Infrasound detection is also affected by station-dependent factors such as local weather, topography/vegetation, and local noise sources near the sensor sites. Local meteorological data at a station may be helpful in understanding these effects. Che et al. (2002) and McKenna et al. (2008) used local meteorological data to examine infrasound propagation characteristics around CHNAR (one of the arrays in KIN) in the Korean Peninsula. Brachet et al. (2010) used local surface wind direction, speed and temperature to analyze detection at a site. Other studies such as Marcillo and Johnson (2010) and Johnson et al. (2012) used local meteorological data to quantify the dynamic atmospheric structure near volcanoes. In this study, we compare seasonal variations in infrasound detections with local surface weather measurements and atmospheric models on the Korean Peninsula in order to quantify the contributions of these different environmental effects.

Seismic discrimination between earthquakes and explosions is a fundamental problem in the field of explosion seismology. The initial goal was to differentiate

between clandestine nuclear tests and earthquakes using various seismological methods applied to seismograms observed at local, regional, and global distances. This task supports the verification of compliance with the Comprehensive Nuclear-Test-Ban Treaty (CTBT), where the International Monitoring System (IMS) network is expected to provide data for underground explosions down to about magnitude 4. In general, conventional teleseismic discriminants, such as the ratio of body wave to surface wave magnitude (m_b:M_s), can be applied reliably to identify large events. However, this approach is limited in its ability to discriminate seismic events with a magnitude smaller than 4, due to the poor signal-to-noise ratio (SNR) at teleseismic distances (Rodgers and Walter 2002). In order to assess seismic hazards in specific regions, seismic discrimination is needed prior to characterizing natural seismic activity. In the context of seismic source discrimination, seismo-acoustic analysis that associates seismic and infrasonic signals generated from common surface explosions, comprising the bulk of man-made seismic events, is a useful method for discriminating artificial seismic events. The analysis is performed based on the differences in acoustic emission in the atmosphere between earthquakes and surface explosions, both of which are events that generate elastic waves in the solid Earth.

As a method for decontamination of seismic catalogs prior to estimation of seismicity, KIGAM has used seismo-acoustic association to identify seismic events originating from surface explosions. This review describes the seismo-acoustic method for seismic event discrimination using the infrasound data set recorded by the dense regional arrays in KIN over a long time period. To improve the detection rates, infrasound detection and association methods are systematically applied to the data set from multiple arrays to build infrasound catalogs that are sequentially linked to KIGAM seismological catalogs for seismo-acoustic association. The seismo-acoustic association further contributes to the development of pure seismic discrimination methods that rely on statistical analysis based on representative seismograms of surface explosions compared to seismograms from natural earthquakes. The data set of controlled surface explosions that generate infrasound signals acts as a source of ground truth events, to aid in understanding the time-varying characteristics of infrasound propagation, including attenuation properties over various propagation ranges. This review also addresses the detection capability of multiple arrays. To extend the understanding of infrasound propagation, infrasound signals from well-known mining activities are reviewed to characterize seasonally dependent propagation of the infrasound waves on local and near-regional scales.

At the interface between the two different media, energy transfer from one medium to the other occurs. One example is the energy transfer from the ground to the atmosphere. Ground motions caused by various sources including natural earthquakes and man-made explosions can generate local, epicentral, and diffracted infrasound signals. Local infrasound signals are recorded at the infrasound stations when the energy from seismic waves couples to the atmosphere at the receiver (Kim et al. 2004). Epicentral infrasound is generated near the source where large ground motions couples to the atmosphere. The energy coupled by ground motion around

the epicenter perturbs the air and the acoustic energy is radiated through the atmosphere as infrasound signals (Green et al. 2009; Arrowsmith et al. 2012). Diffracted infrasound is generated by secondary sources such as mountain ranges (Cook 1971; Le Pichon et al. 2002a). Diffracted infrasound has a mixed propagation path consisting of portions of the path in the ground and atmosphere (Donn and Posmentier 1964; Cook 1971). All three types of infrasound signals have been frequently recorded at KIN. The observation and application of the three types of infrasound signals from natural and man-made sources are discussed in Sect. 4 with some examples.

11.2 Korea Infrasound Network (KIN)

11.2.1 Locations and Array Configurations

In partial collaboration with SMU, KIGAM initiated an infrasound research program with the installation of the first seismo-acoustic array (CHNAR) in South Korea in 1999. The design goal of the seismo-acoustic array was to detect and locate surface explosions by observing both seismic and infrasonic signals from the surface explosions at common locations, eventually allowing discrimination of seismic events of man-made explosions from natural earthquakes (Stump et al. 2004). After the first installation, additional arrays were installed, forming the KIN array group. As of 2015, KIN consists of eight seismo-acoustic arrays (not including experimental arrays) in South Korea. All of the arrays have apertures of 0.2–1.3 km between 4 and 12 acoustic sensors/Chaparral M2 infrasound sensors (flat response: 0.1–200 Hz). Some arrays are additionally equipped with Inter-Mountain Labs (IML) sensors to both detect higher frequency signals and compare them to Chaparral sensor data. These small aperture arrays lead to increased signal correlation of infrasound signals between sensors at high frequencies. The KIN is suitable for the detection of small surface explosions at local and near-regional scales. For the arrays with relatively large aperture of ~1 km, auxiliary acoustic sensors are positioned tens of meters apart from each main sensor to record highly correlated acoustic signals. In addition, three acoustic sensors were added to one site in each array to create an acoustic sub-array with an aperture of about 100 m. All acoustic sensors are connected to porous hoses for wind noise reduction in a circular area of radius 8 m. Figure 11.1 shows the locations of the seismo-acoustic arrays in the region and relative sensor locations at each array. Individual array configurations and associated equipment (e.g., real-time data transmission and power supplies) were designed to account for site-specific conditions. The average inter-array spacing of KIN is on the order of 100 km; this dense distribution facilitates the detection of relatively small-amplitude infrasound signals from multiple arrays in order to determine the source location with high accuracy at regional distances (Che et al. 2014). As the KIN arrays have both

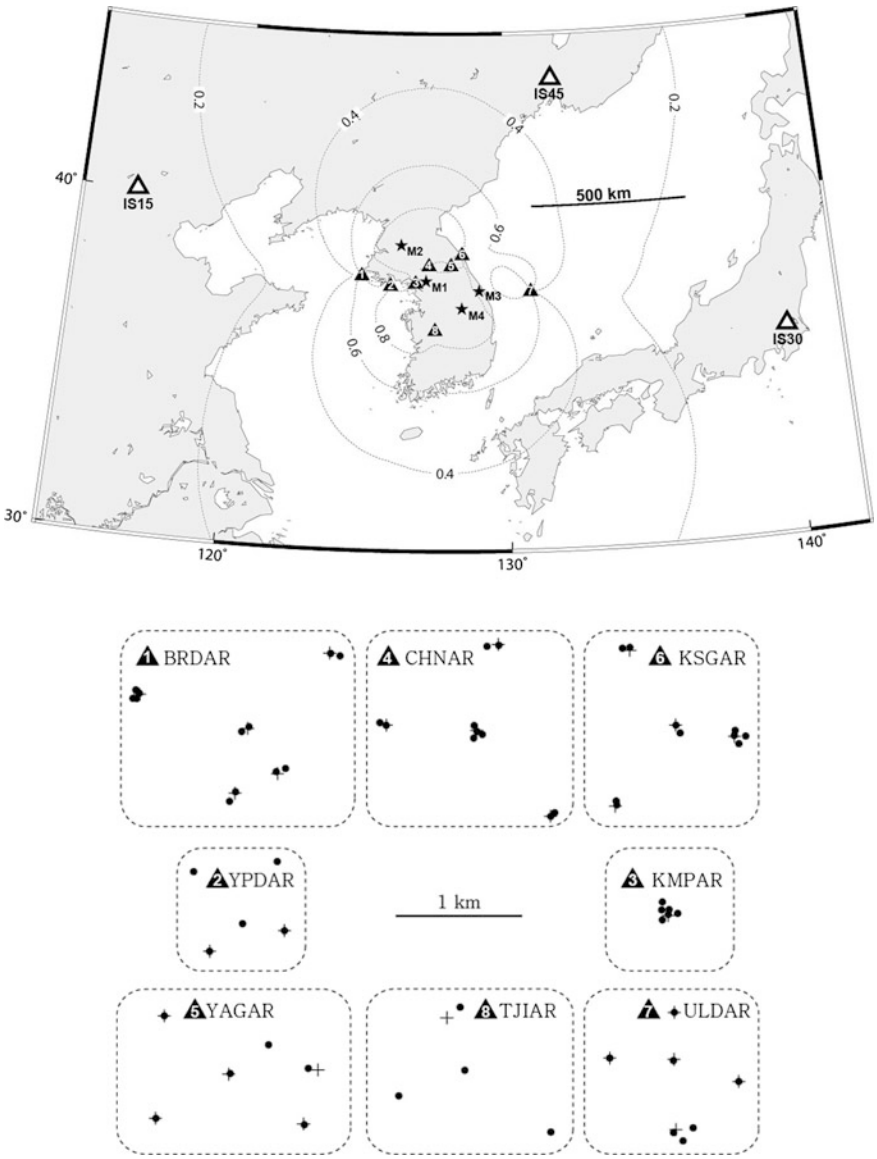

Fig. 11.1 (Top) Locations of seismo-acoustic arrays (solid triangles with number) of the Korea Infrasound Network (KIN) and nearby International Monitoring System (IMS) infrasound stations (open triangles), including currently operational or planned ones. Contours indicate applicable weights on grids for source location when azimuth intersection is applied; the weight is the normalized sum of the sine of the angle of intersection azimuth pairs (Brown et al. 2002). Four stars (M1–M4) indicate locations of known and repeatable sources that generate both seismic and infrasonic signals. (Bottom) Sensor locations in all KIN arrays; dots indicate positions of acoustic sensors (Chaparral M2) and crosses indicate seismometers

seismometers and acoustic sensors, individual arrays can locate seismic events and associate the seismic events with acoustic signals recorded at sensors collocated with seismometers. Spatially, as shown in Fig. 11.1, the KIN has an approximately collinear distribution of arrays oriented along the east–west direction and covering a distance range of about 500 km. When an azimuth intersection method is implemented on source localization, this approximate collinear distribution of arrays may result in lower location accuracy for infrasound sources outside the network, and especially at colatitudes with the east–west distributions.

Studies of detection capabilities have been carried out to assess infrasound network performance, especially for the IMS network, based on empirical yield-scaling relations (Whitaker et al. 2003) and numerical simulations (Le Pichon et al. 2009). More recently, Le Pichon et al. (2012a) developed an attenuation relation, derived from massive range-independent parabolic equation (PE) simulations, that accounts for more realistic propagation conditions and assessed the detection capability of the IMS network with improved specification of the stratospheric winds and site, time- and frequency-dependent wind noise model. These studies highlighted the importance of seasonal variations of the stratospheric zonal winds on signal detection on a global scale and predicted a detection capability of the IMS network that exceeds its design goal, with detection of atmospheric explosions equivalent to >1 kT of TNT anywhere on the globe. Following the procedure of Le Pichon et al. (2012a), the detection capability of the current KIN was assessed for the Korean Peninsula and surrounding region, and compared to assessments using only IMS stations in the region (Fig. 11.2) and with the IMS stations plus the KIN (Che et al. 2012). The minimum detectable energy for an atmospheric explosion using the KIN plus IMS network was estimated as ~10 t of TNT for three-station coverage from June to September and ~5–30 t of TNT from October to May, resulting in an improvement of the detection capability by ~20 tons of energy, compared to using only the nearby IMS stations. In addition, seasonal variation of the minimum detectable energy showed little fluctuation from

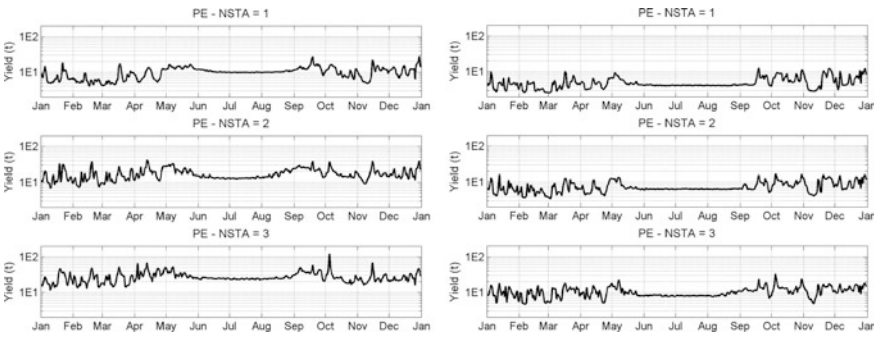

Fig. 11.2 Seasonal variation of minimum detectable energy with 1, 2, and 3 station coverage (number of station; NSTA) for the IMS network (left) and that completed by the KIN (right) for the Korean Peninsula and surrounding regions (from Che et al. 2012)

June to September, due to steady stratospheric winds during this season. On the other hand, there were large variations from October to May due to the highly variable stratospheric winds in the region during this time period (Fig. 11.2). This seasonal variation of atmospheric winds will be further discussed in Sect. 2.2. However, the simulation represents a preliminary result obtained by applying the average noise level of IMS stations to the KIN stations and conservatively setting the SNR to 1 for routine analysis. Thus, further studies are needed to estimate more realistic and precise detection capabilities for the KIN by applying station-dependent seasonal noise levels and a realistic threshold of SNR in simulations using ground truth events, which will also contribute to the validation of the calculated minimum detectable amplitude.

11.2.2 Characteristics of Seasonal Variations in Infrasound Detection

Seasonal variations in infrasound detection are compared to temporal variations in noise and signal characteristics at the arrays as well as linked to changing environmental conditions in this section. Three of the seismo-acoustic arrays (BRDAR, CHNAR, and KSGAR) in KIN were used for detection testing (as we show in the Sect. 2.1). Each of these arrays has different local environments providing the opportunity to investigate these effects; BRDAR is installed on an island in the Yellow Sea, CHNAR is in the center of the Korean Peninsula, and KSGAR is on the east side of the Korean Peninsula with an ocean influence from the East Sea although mountains surround the array. The island array has relatively higher background noise controlled by wind velocity as well as ocean waves acting as secondary sources (Stump et al. 2012). Park et al. (2011) illustrate that the optimal detection processing benefits from the careful characterization of background noise levels that are dependent on environmental measures such as wind speed and azimuth at individual arrays.

This section is composed of three parts: First, the automatic infrasound detector is introduced with detection parameter settings used in this study; Second, the effects of environmental conditions on infrasound noise levels which are crucial for signal detection at each array are discussed; and lastly, the seasonal variations in infrasound detection with atmospheric wind estimates are investigated.

There are multiple automatic infrasound detectors that use waveform correlation techniques to identify signals on array data. These detectors include the progressive multichannel correlation (PMCC) algorithm (Cansi 1995); InfraTool in MatSeis-1.7 (Hart and Young 2002); and the adaptive F-detector (AFD) (Arrowsmith et al. 2009). PMCC and InfraTool assume uncorrelated noise while calculating detection parameters based on array elements. In order to reduce false alarms, PMCC applies a progressive processing philosophy to data recorded by individual sensors in an array by first assessing cross-correlation functions of sub-arrays and then adding

additional array elements that increase the network aperture (Cansi 1995). The detailed analysis using PMCC will be shown in Sect. 3.2. InfraTool uses the Hough transform and inverse slope methods applied to multiple overlapping windows. When the null hypothesis is perfectly uncorrelated noise, the conventional F-detector is based on the F-statistic defined as the power on the beam from the array divided by the average over all channels of the power of the difference between the beam and the individual array channels defined as

$$F = \left(\frac{J-1}{J}\right) \frac{\sum_{n=n_0}^{n_0+(N-1)} \left[\sum_{j=1}^{J} x_j(n+l_j)\right]^2}{\sum_{n=n_0}^{n_0+(N-1)} \left(\sum_{j=1}^{J} \left\{x_j(n+l_j) - \left[\frac{1}{J}\sum_{m=1}^{J} x_m(n+l_m)\right]\right\}^2\right)}$$

J is the number of sensors, $x_j(n)$ is the nth sample of the waveform from sensor j, l_j is the time-lag to align the waveforms estimated by beamforming, n_0 is the starting sample index for the processing interval, and N is the number of samples in the processing window. The conventional F-distribution will produce false alarms in the presence of correlated noise. Arrowsmith et al. (2009) suggest a modification of the conventional F-detector with the inclusion of an adaptive window designed to account for time-varying, coherent noise. The theoretical F-statistic is distributed as $C \cdot F_{2BT,2BT(J-1)}$, B is the bandwidth of the filtered data, T is the processing (detection) window length used to estimate the average, and C is

$$C = \left(1 + J\frac{P_s}{P_n}\right)$$

Ps/Pn is the ratio of the correlated noise power to uncorrelated noise power (Shumway et al. 1999). The scalar C-value aligns the peak of the F-statistic distribution from the time window with the peak of the theoretical central F-distribution. Thus, the standard F-detector is modified so that it adapts in time, capturing changing noise characteristics with new estimates of C made for subsequent adaptive windows. Following this adaption, the standard p-value is utilized to declare a detection.

In order to understand the physical cause(s) of the adaptation and identify an optimum detection strategy for each array, Park et al. (2011) quantified the adaptation process in time and space using AFD and found that changes in adaptive window length at each array were related to the associated noise characteristics. Based on sensitivity tests of the C-values to the adaptive window length (1, 12, and 24 h), C-values were found to change on timescales of the order of 1 h at BRDAR and CHNAR. The optimum adaptive window was found to depend on the local site environment and background noise levels with short duration windows of

approximately 1 h recommended for infrasound detection, especially at BRDAR (Park et al. 2011). Based on analyst review, Park et al. (2017) assess automatic infrasound detectors' performance in terms of varying detection parameters and background noise conditions affected by surface weather at CHNAR.

Park et al. (2016) document seasonal environmental trends in wind velocity, direction and temperature at BRDAR, CHNAR, and KSGAR for winter (Julian days 335, 2009–059, 2010), spring (Julian days 060–151, 2010), summer (Julian days 152–243, 2010), and fall (Julian days 244–334, 2010) in order to quantify the relationship between these effects and C-value. Data from large aperture (~1 km) seismo-acoustic arrays were processed with the following parameters: time window (20 s), overlap (50%), *p*-value (0.01), and adaptive window of 1 h. Figure 11.3 compares the C-value estimates using the 1 h adaptive windows for the three arrays with 1 h-averaged wind speeds and directions. Results from CHNAR for the winter have the poorest resolution due to a lack of weather data during this time period. High C-values are observed for periods of low wind speed at all arrays, especially at CHNAR during the fall. CHNAR has a smaller range of wind speeds (<10 m/s) than BRDAR and KSGAR as a result of its inland location. Relatively high C-values of up to 5 occur during low wind conditions suggesting increased detections of local events or other source of coherent noise under these conditions at CHNAR. BRDAR has a broader range of C-values with wind speeds up to 17 m/s. This reflects the higher background noise levels at BRDAR associated with the ocean environment. The lower C-values that are correlated with high wind

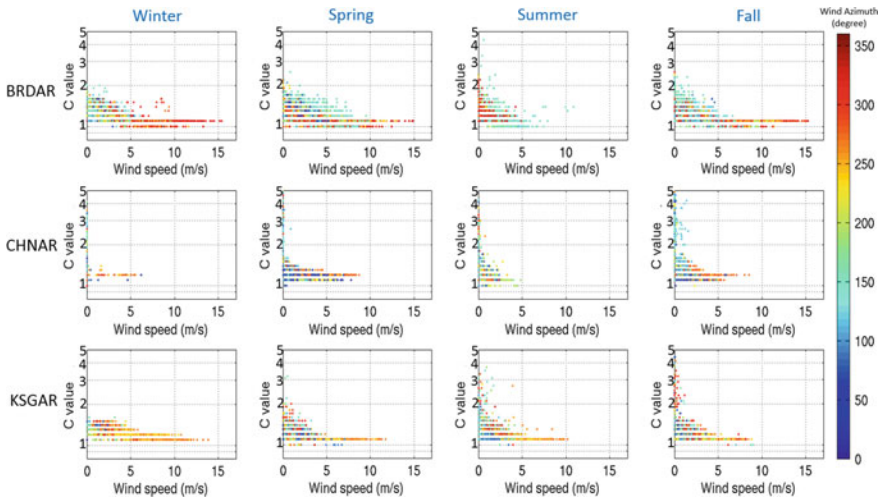

Fig. 11.3 C-value estimates from AFD as a function of wind speed and direction at BRDAR, CHNAR, and KSGAR for 1-year time period (winter: Julian days 335, 2009–059, 2010, spring: Julian days 060–151, 2010, summer: Julian days 152–243, 2010, and fall: Julian days 244–334, 2010) (from Park et al. 2016, Fig. 4b). CHNAR results are limited due to a lack of weather data during the winter

velocities are often associated with wind directions from northwest to north during the spring, fall, and winter, and from southeast to south during the summer. These trends are consistent with seasonal wind directions in Korea. KSGAR also produces somewhat higher C-values during time periods of lower wind speeds. These C-values are not as widely distributed as those at BRDAR, suggesting that the mountains that shield the site from the ocean may impact the local noise. As a whole, these observations illustrate that C-values depend on surface wind speed with secondary effects that include wind direction and local topography. These results motivate additional assessment of the infrasound detections, propagation, and quantification of background noise levels in time and space.

Figure 11.4 displays yearly variations in the correlation value and azimuth estimates for all automated detections by AFD at BRDAR, CHNAR, and KSGAR (from December 2009 to November 2010) (Park et al. 2016). The total number of detections at BRDAR and KSGAR are 15,360 and 13,859 with almost two times more at CHNAR (36,321) reflecting the lower wind speeds at this array. Based on analyses of detection time, many infrasound detections appear to be related to human activity that can include quarry and mining explosions as discussed earlier, especially near CHNAR (Stump et al. 2004; McKenna et al. 2008; Che et al. 2011). These observations are consistent with studies in the western US where similar temporal patterns were identified (Walker et al. 2011; Park et al. 2014). BRDAR has consistent detections with relatively high correlations from the northwest for the entire year with additional events from the southeast during the summer (Fig. 11.4). CHNAR and KSGAR detections produce similar patterns, consistent with seasonal wind directions across the Korean Peninsula, but with relatively lower correlation values.

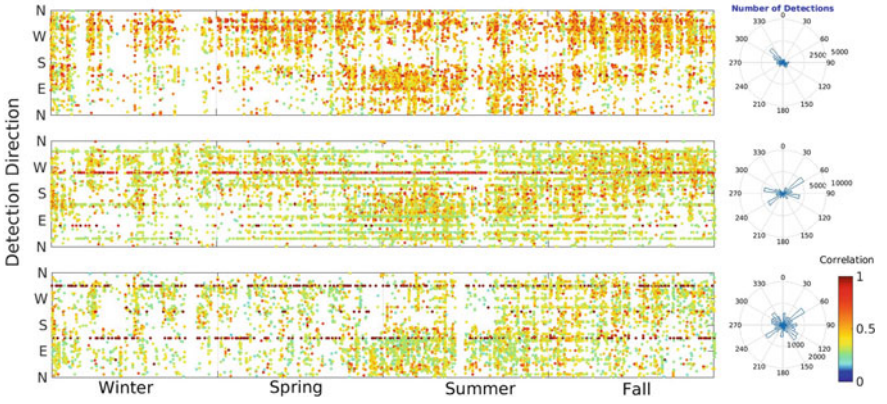

Fig. 11.4 Automated detections by AFD at BRDAR (top), CHNAR (middle), and KSGAR (bottom) using the 1-year data set (winter: Julian days 335, 2009–059, 2010, spring: Julian days 060–151, 2010, summer: Julian days 152–243, 2010, and fall: Julian days 244–334, 2010) (from Park et al. 2016, Fig. 7). The individual detection points in the plot include the correlation value (color) and are plotted as a function of back azimuth with time. The rose diagrams to the right summarize the total number of detections as a function of azimuth for the entire time period

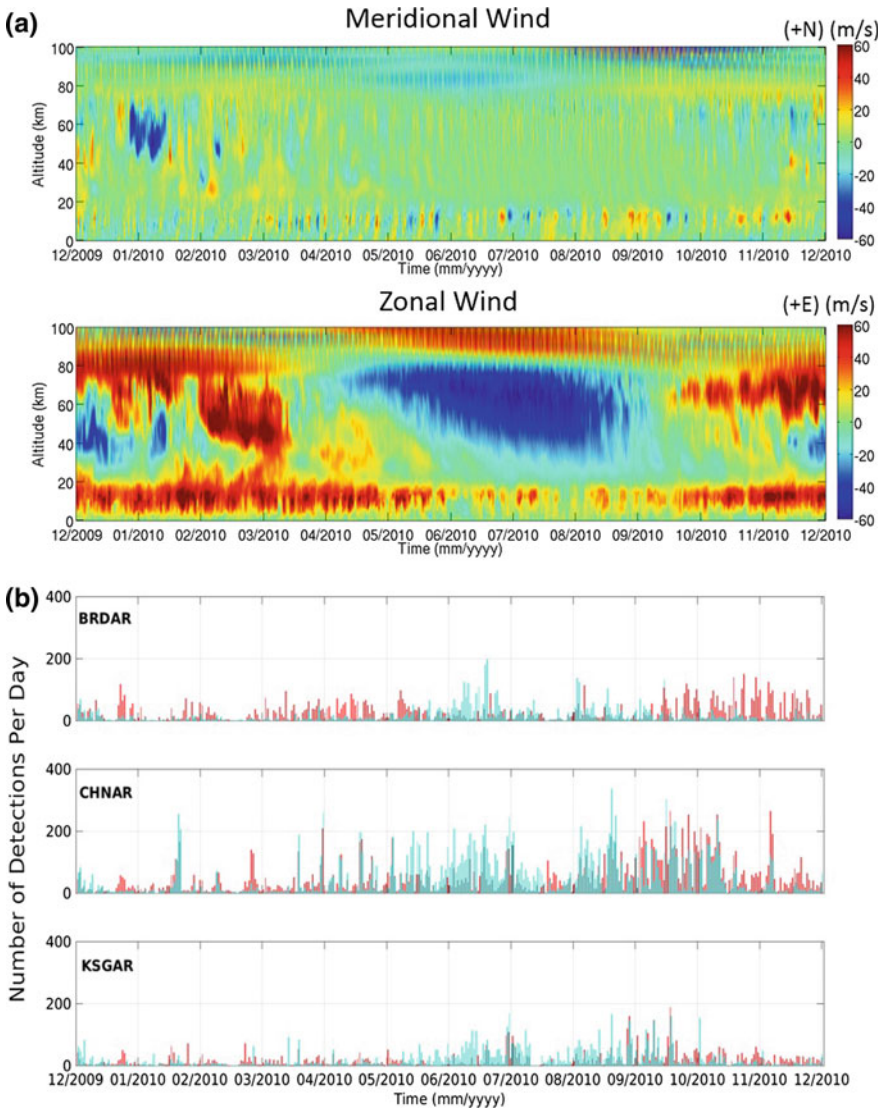

Fig. 11.5 The correlation between seasonal variations in infrasound detections and atmospheric winds estimated for 6-h intervals (0, 6, 12, and 18 h in UTC) from the Ground-to-Space (G2S) specifications by Drob et al. (2010) (from Park et al. 2016). **a** Meridional (top) and zonal (bottom) winds at CHNAR for the 1-year time period. **b** Seasonal variations in the number of infrasound detections by AFD from the west, 180° ≤ azimuth < 360° (red) and from the east, 0° ≤ azimuth < 180° (blue), at BRDAR, CHNAR and KSGAR

In order to better understand the seasonal variations in infrasound detections in Korea, the number of detections estimated by AFD from different azimuths (0° azimuth < 180° and 180° ≤ azimuth < 360°) at BRDAR, CHNAR, and KSGAR are compared to variations in atmospheric wind estimates above CHNAR (Fig. 11.5, from Park et al. 2016). Six-hour interval Ground-to-Space (G2S) model data (0, 6, 12 and 18 UT) are used with an effective horizontal resolution of 1° × 1° to make these wind estimates. Details of the G2S specification are documented in Drob et al. (2010). Figure 11.5a plots the meridional and zonal wind estimates as a function of time from the surface to a height of 100 km. Seasonal and daily variations in wind velocity and direction in the troposphere, stratosphere, and thermosphere are observed. The detection statistics from two different directions are correlated with the seasonal changes in the atmosphere as estimated for the G2S model (Fig. 11.5b). In the region, infrasound propagation is primarily controlled by stratospheric winds with most detections arriving from the east during the summer and detections from the west in the fall, consistent with other study areas (Arrowsmith and Hedlin 2005; Park and Stump 2014; Park et al. 2014). However, there are a relatively small number of detections from both directions observed during the winter that may occur during periods when stratospheric wind directions reverse associated with episodes of sudden stratospheric warming (Rind and Donn 1978; Assink et al. 2014).

As noted in the seasonal detection estimates, quantification of background noise and its relationship to seasonal variations in infrasound detections at infrasound arrays provide a basis for improving array performance estimates under changing environment conditions. These empirical estimates with time-varying atmospheric models such as G2S provide a basis for improving the assessment of the seasonal performance of arrays and networks, refining event location and possibly enhancing source characterization.

11.3 Seismo-Acoustic Analysis

11.3.1 Discrimination of Surface Explosions

Surface explosions discussed in this chapter are defined as the detonation of an amount of explosives on or near the Earth's surface. Such explosions also have sufficient energy to generate seismic waves in the Earth and acoustic waves in the atmosphere, from which signals can be observed at remote seismic and acoustic stations. Typical blasting practices used at many industrial sites to extract mineral resources or rocks from underground and open-pit mines and quarries may represent the majority of these surface explosions. Although the relative coupling of energy to the atmosphere and solid earth may be different, tools developed to characterize surface explosions may also be useful in the detection and discrimination of underground nuclear tests, the major task of the CTBT. The scale of

surface explosions ranges from small-magnitude events that are routinely monitored by regional seismic networks to larger scale nuclear tests observable at teleseismic distances. Thus, seismologically, the range of observations from surface explosions is comparable to naturally occurring earthquakes. The occurrence of surface explosions and earthquakes producing similar magnitude seismic signals in a specific region has made it necessary to discriminate surface explosions from natural earthquake activity. Man-made explosions are a potential cause of error in producing earthquake hazard assessments in regions of interest. Discrimination of explosions from earthquakes has been studied for several decades in order to identify suspected nuclear tests based on seismological methods that use differences in focal mechanisms, source–time functions, radiation patterns, and seismic waveform features between these two source types. These discrimination methods have been validated with large magnitude seismic events, such as underground nuclear tests with magnitudes equivalent to larger earthquakes; however, they are limited in their ability to identify small-magnitude seismic events, due to the low SNR and geological effects on seismic propagation at high frequency. Many studies have demonstrated that successful application of seismic discrimination methods to a given region does not guarantee its application to other regions with different geological properties.

Infrasound technology provides complementary tools for addressing event discrimination, especially for regions where seismic activity tends to be weak or moderate, such as the Korean Peninsula. Generally, small-magnitude earthquakes do not produce appreciable infrasound signals that can be detected at remote receivers, due mainly to the focal depth of the event. In contrast, a surface explosion partitions a certain amount of its energy into the atmosphere as acoustic waves, combined with a ground-shock-induced pulse and venting of explosion gases as a

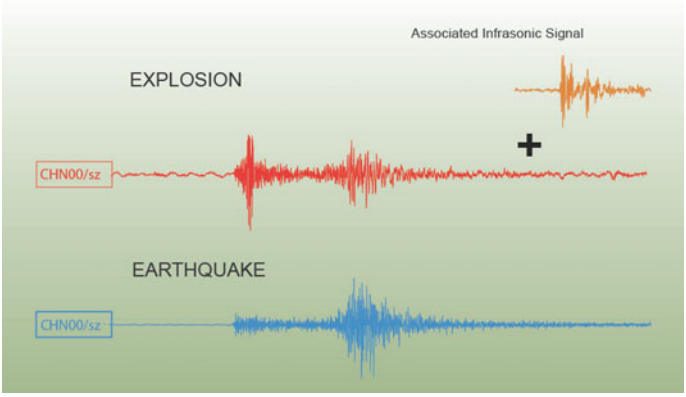

Fig. 11.6 Seismograms of a surface explosion and an earthquake that took place in a common region. In the case of the explosion, the seismic signal was followed by an infrasonic signal with consistent azimuth and propagation time for the given seismic location and origin time. These associations identify the seismogram as being generated by an explosion

function of explosive charge burial depth (Vortman 1968; Ford et al. 2014). Therefore, surface explosions with magnitude comparable to small earthquakes can be discriminated by detection of infrasound signals in association with seismic signals. Typical association of seismic and infrasonic signals is shown in Fig. 11.6.

11.3.2 Manual and Automated Association of Infrasound Signals with Seismic Events

In addition to KIN in South Korea, instrumentation deployments have resulted in the addition of separate high-quality seismic stations to the region that have further lowered the detection threshold of seismic magnitude and increased the number of detected events requiring routine seismic data processing. The operation of dense and high-quality seismic stations results in the detection of smaller sources, including seismic activities associated with industrial and mining explosions, which are included in the earthquake catalogs. Routine seismic data processing at KIGAM annually determines an average of 4000 seismic events, with magnitudes as low as zero, in and around the Korean Peninsula (32.5–43.5° N, 122.0–132.0° E). Assuming that natural earthquakes occur randomly in time and that seismic events taking place around midnight are only from natural earthquakes, roughly 80% of the total events are suspected to be of man-made origin. To assess the natural seismicity of a region, it is necessary to discriminate all seismic events in the catalog.

Seismological discrimination methods for events in the region have been studied separately (e.g., Kim et al. 1998), but KIGAM has applied infrasound technology to fulfill source identification of small-magnitude events, termed seismo-acoustic analysis, since 1999. Seismo-acoustic analysis consists of detection of infrasound signals and association with seismic events in terms of arrival time and azimuth of the detected infrasound signals; hence, it can determine whether a seismic signal is derived from a surface explosion. Searching for infrasound signals that could be associated with seismic events is implemented by comparison of infrasound wave parameters with the seismic event location and origin time. First, when a seismic event is registered in the seismic catalog, any distinct infrasonic signals following the seismic signals are searched for using band-pass-filtered acoustic data (primary monitoring passband: 0.5–5.0 Hz). Wave parameters, such as horizontal trace velocity and azimuth of infrasound signals, are determined by standard array processing based on cross-correlation between array elements (e.g., PMCC, etc.). When the calculated azimuth of the infrasound signal corresponds to a seismic epicenter, then the seismic and infrasonic signals are determined to be associated with the same surface explosion. Association between seismic and infrasonic signals is verified based on the acceptable criteria, a propagation velocity of 250–400 m/s and an azimuth difference within ±10° (Che et al. 2002), to account for the resolution of the small infrasound array geometry and azimuth deflections caused by crosswinds during propagation.

Figure 11.7 presents the results of manual seismo-acoustic analysis with more than 2000 seismic events for the time period of August 1999 to May 2008, followed by acoustic arrivals with the above acceptance criteria. The number of events is about 8% of all seismic events that occurred inland over the review period. Most of the events, with the exception of a small fraction (25 events), occurred during the day (07:00–20:00 local time). The seismic magnitude of the surface explosions ranged up to a local magnitude of 3.2, with the exception of two underground nuclear tests (UNTs) (Sect. 4.2), magnitude 4.5 and 4.9 in North Korea (discriminated as explosions based on manual analysis). The majority of seismic events were concentrated in several epicentral regions, so-called infrasonic hot spots (Walker et al. 2011). Infrasonic hot spots in South Korea correspond to well-known locations of open-pit mines, and human activity areas confirmed by field surveys. The seismic sources in North Korea are unknown, but they are inferred to be related to industrial mining activities. Seismo-acoustic analysis can be used to monitor spatial and temporal occurrences of surface explosions. For example, the events group marked "A" in Fig. 11.7, showing a linear pattern in North Korea, occurred mainly in 2000 and 2001. If the source types of the events were not identified as surface explosions, then the linear pattern of events could be interpreted as an earthquake swarm along a likely fault. Based on announcements from North Korea, these events are considered to be related to a large-scale water channel construction project that matched the linear pattern. Within the KIN arrays, CHNAR, located in the central inland region, has a higher detection rate of surface explosions than the other arrays. This is probably due to its geographical location, operation in an area of gentler topographic relief, and relatively lower noise associated with surface winds, compared to the other arrays that are located in mountainous or coastal areas; although the other arrays have similar configurations to CHNAR. TJIAR, located at the southern end of the network and outside the approximately collinear array distribution, successfully identified local explosions and extended the monitoring range to the southwestern portion of the region.

The celerity of infrasound arrivals provides information on the characteristics of infrasound propagation over a distance. Figure 11.8 shows the celerities of infrasound signals from the surface explosions indicated in Fig. 11.7. Despite the large degree of scattering, it shows a general decreasing trend of celerity versus epicentral distance. Celerity values change the most at epicentral distances beyond about 150 km, where propagation transitions from a tropospheric phase (*Iw*) to a stratospheric phase (*Is*). The trend of slower celerities continues beyond 150 km to up to 400 km from the epicenter. The scattering of celerity at specific epicentral distances from common sources results from the intrinsic uncertainty in seismic location results and seasonal variation of infrasound propagation.

In the previous section, the association of infrasound signals with seismic events was manually determined by analyses based on acceptable celerity of infrasound arrival and consistency in azimuths. Experienced analysts may use flexible acceptance criteria for manual association, although they usually follow a given set of association criteria strictly in most cases. Knowledge of existing active sources (e.g., the locations of mines) and previous association experience allow analysts to

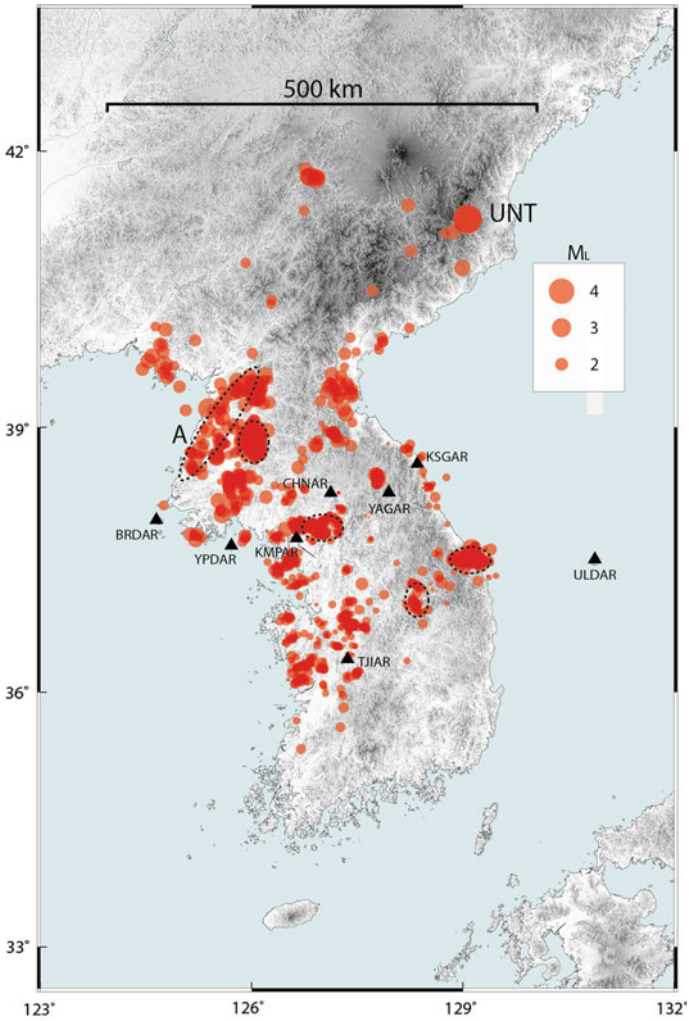

Fig. 11.7 Locations of seismic events that were not only determined by the routine seismic monitoring system but also identified as surface explosions by manual association with infrasound signals detected at one or more arrays (triangles). Manual analysis was applied to all seismic events occurring from August 1999 to May 2008 and to some other large events, including underground nuclear tests (UNTs) of North Korea, which occurred after the continuous analysis period. Dashed regions indicate some of the known infrasonic hot spots in the region. Mark "A" indicates the event group inferred to be related to civil engineering works in North Korea

confidently associate infrasound signals with seismic event pairs in which association parameters somehow deviate from the given criteria; such disagreement with the association criteria could be caused by incorrect seismic locations and/or infrasound parameter estimation based on the use of low-quality data. In addition,

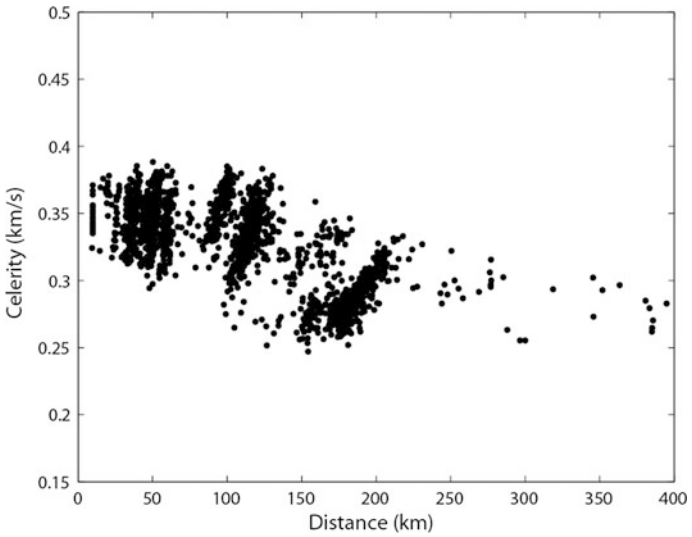

Fig. 11.8 Celerity of infrasound signals of the surface explosions shown in Fig. 11.7. Propagation distance and travel times for celerity were determined from seismic event information

analysts can successfully accomplish the association by discerning complex infrasound phases and considering other environmental factors that would weaken the association, which allows rejection of mere coincidences. Despite these benefits, however, it is difficult for the analysts to resolve larger data sets or weak signals hidden in other complicated arrivals in manual seismo-acoustic analysis.

To increase the association rate and provide support for routine data processing by analysts, it is necessary to develop a systematic procedure for automated detection and association for surface explosions. For this purpose, we implemented a basic procedure, as shown in Fig. 11.9, and applied it to a historical data set of KIN from 1999 to 2014. First, all available continuous data from the eight arrays of KIN were prepared as input for the infrasound signal detector. Coherent infrasound signals were extracted, and wave parameters were estimated using the automated infrasound detector, PMCC, as introduced in the Sect. 2.2. Using the output of the detector, a set of signals were complied that were most likely related to surface explosions before the final association step. PMCC is an array-based signal detector

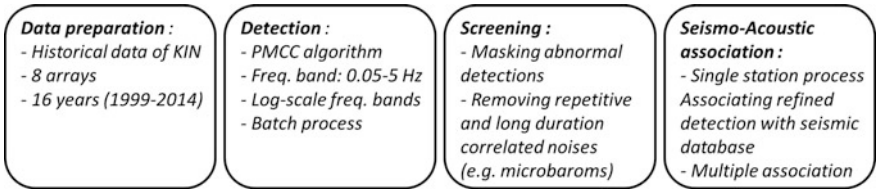

Fig. 11.9 Automated procedure applied to seismo-acoustic analysis of the historical KIN data set

using cross-correlation, which was shown to be efficient at detecting low-amplitude, coherent infrasonic signals within incoherent noise (Cansi 1995; Le Pichon et al. 2002b). Statistical studies have also demonstrated that the detection threshold of PMCC lies between a SNR of 0.15 and 0.5 (Cansi et al. 2005; Le Pichon et al. 2008a). This method estimates wave parameters, including azimuth, trace velocity, and others in a given frequency and time band (pixels). Wave parameters that obtained from processing of the starting subnetworks within the array are refined, by progressively increasing the array aperture, thus, reducing false detections. From calculation of the parameters, individual pixels that represent single detections are integrated into a pixel family (detection) when they are within the acceptable dimensionless Euclidean distance in the time–frequency–speed–azimuth domains (Le Pichon et al. 2010). In our application, all coherent infrasonic signals recorded by KIN were detected and their wave parameters estimated in the frequency range of 0.05–5 Hz by applying the PMCC to the historical recordings. In addition, log-scale frequency windows, proportional to the frequency bands, were used in the implementation to improve the detection rate and improve separation of interfering signals.

The seasonal detection of microbaroms that are well correlated with stratospheric wind directions has been shown to be useful for assessing the detection capability of infrasound waves (Landès et al. 2012; Le Pichon et al. 2012b). But, strong microbarom signals make it difficult to identify small, surface explosion-related infrasound signals and associate them with seismic events. As this study was mainly performed to discriminate surface explosions based on infrasound signals, it was necessary to remove the signals of microbaroms and any repeating arrivals caused by other local noise sources in the detection list, prior to association. Microbaroms have different characteristics than signals from surface explosions, including their continuous nature over long time intervals with similar azimuths and low-frequency band of 0.12–0.35 Hz (Donn and Rind 1972). Thus, certain criteria could be applied to separate the low-frequency, prolonged nature of microbaroms from the higher frequency, more sporadic nature of infrasound signals for surface explosions. In the overall time series, detections were grouped into a cluster, the detection of which has similar azimuth ($<10°$) and frequency differences (2 Hz), and appear consecutively again 120 s after the proceeding similar detection. If the time length of the cluster exceeded 10 min, then the cluster was assumed to be a microbarom or other repetitive source and was removed from the detection list. In addition, some basic criteria were also applied to screen out abnormal detections—small infrasound detections (PMCC family size ≤ 10 pixels), beyond the phase velocity range of 0.29–0.40 km/s, frequency <1.0 Hz. These parameters were empirically chosen based on the manual association and waveform review of the KIN data set.

Figure 11.10 shows an example of refining all detections by removing repetitive or low-frequency signals for a 1-month data set at CHNAR; the bottom panel includes refined detections that were used in the next step of association with seismic events. In this example, all detections were mixtures of large amounts of low-frequency signals (microbaroms) and some high-frequency signals, probably from human-related activities. The dominant low-frequency signals arise from the

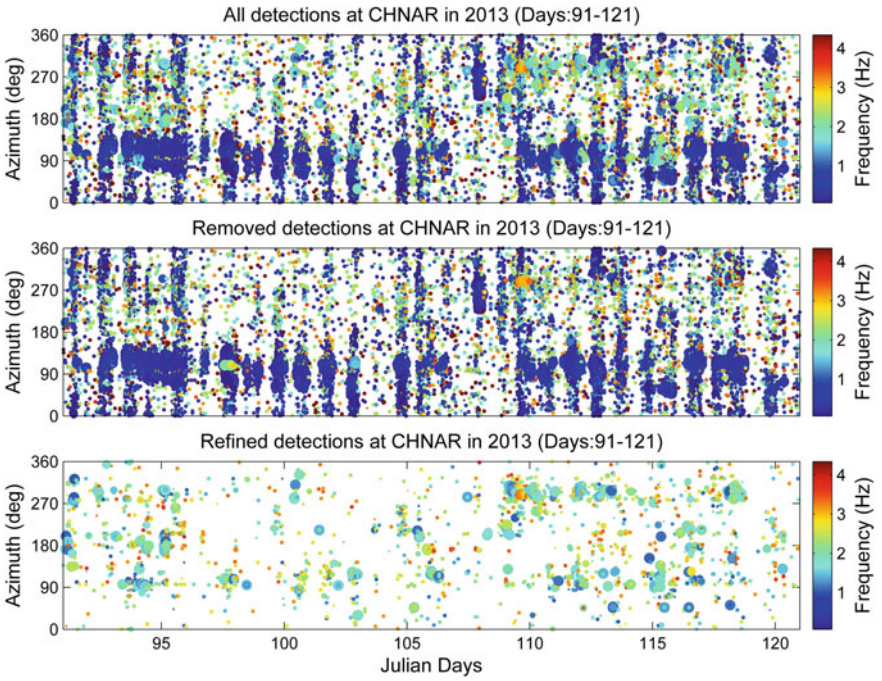

Fig. 11.10 Example illustrating the removal of repetitive or low-frequency signals from the complete detections for a 1-month data set from the CHNAR array. The upper panel shows all detection results for PMCC, middle the removed detections, and bottom panel the refined detections used as the input for the association process

NE–E–SE direction, which is the direction to the east coast of the Korean Peninsula; these detections showed diurnal variations for this example study period. The systematic detection of low-frequency signals from the continuous historical recordings provides a characteristic variation of detectability that was strongly correlated with the seasonal variations of stratospheric winds. Although it is not clearly shown in this example of refined detections, KIN arrays generally capture continuous detections of high-frequency signals from selected azimuths in plots of longer data sets that are well matched with the locations of known infrasound sources, e.g., active mines in the region. Such correlations were also observed at the daily and weekly scales, following temporal variability of the atmosphere.

Like the manual association before, the automated association procedure begins from the seismic epicenter to find likely infrasound signals in the refined detection list, based on the acceptable criteria of celerity and azimuth of detections. Automated association is commonly declared when celerity is in the range 0.26–0.36 km/s based on the empirical review of ground truth information in the region (described in the Sect. 3.3). This range is intended as more restrictive criteria for the association of infrasound signals at local and near-regional distances. A high celerity of 0.36 km/s is assigned to capture the tropospheric phase (I_w), as well as

infrasound arrivals propagating over the ocean path at lower refraction heights (Che et al. 2011). An acceptable azimuth range compared with the epicentral azimuth is first established according to the uncertainty of seismic location. Given a seismic event with error ellipse (e.g., 95% confidence level), the angle between two lines connecting the infrasound station to both tangents on the error ellipse is used as the azimuth association criterion. This seismic location uncertainty expressed as an azimuth criterion varies depending on the epicentral distance and the degree of uncertainty. In addition, an azimuth tolerance of 5° is added to the azimuth criteria consistent with the manual analysis.

All seismic events in the KIGAM catalog from 1999 to 2014 are compared with the refined detection list following the above automated association methods. The KIGAM catalog has more than 63,000 seismic events for the period in the region (~49,000 events inland), and association is implemented to all events at each array. This single-array association processing identified >24,000 seismic events with associated infrasound signals. When a seismic event is associated with multiple arrays, the event can be defined as multiple associations, described in more depth later. Single-array associated seismic events, interpreted as surface explosions, account for about 38% of the total seismic catalog of routinely identified events in and around the Korean Peninsula. The number of surface explosions per year has increased over time as a result of improved infrasound detection rates as the number of KIN arrays has increased or possibly by increased mining activities with time. This result suggests that the precision of the infrasound source location might have improved over time. Figure 11.11 (left) shows the density map of surface explosions determined from the automated result of the single-array association procedure; the results shown are comparable with manual results (Fig. 11.7). High-density regions are closely correlated with locations of domestic rock quarries and some open-pit limestone mines (dots) in South Korea.

Of the single-array source location associations, more than 2000 seismic events were associated with multiple infrasound signals that were observed at three or more arrays. Multiple infrasound observations of surface explosions provide an opportunity for independent source locations based only on the infrasound observations. The independent infrasound location provides independent evidence for the associations between seismic events and infrasound signals, and reduces the possibility of coincidental association of infrasound signals that are generated from a causal sound source on the great circle between the epicenter and receiver within the acceptable origin time. Sound source location can be simply estimated by crossing azimuths estimated at multiple arrays. The least squares method in terms of arrival time and back azimuths is also applicable for source location. In this study, we used the Bayesian infrasound source location (BISL) (Modrak et al. 2010) method for localizing the sound sources when infrasound signals were observed at multiple arrays of the KIN. BISL uses both arrival time and azimuth constraints to provide credibility bounds on event locations. Figure 11.11 (right) displays the locations of seismic events for which infrasound signals were detected at three or more arrays (NSTA ≥ 3), and distance differences between seismic epicenter and BISL location <50 km. Compared with the manual results (Fig. 11.7), the

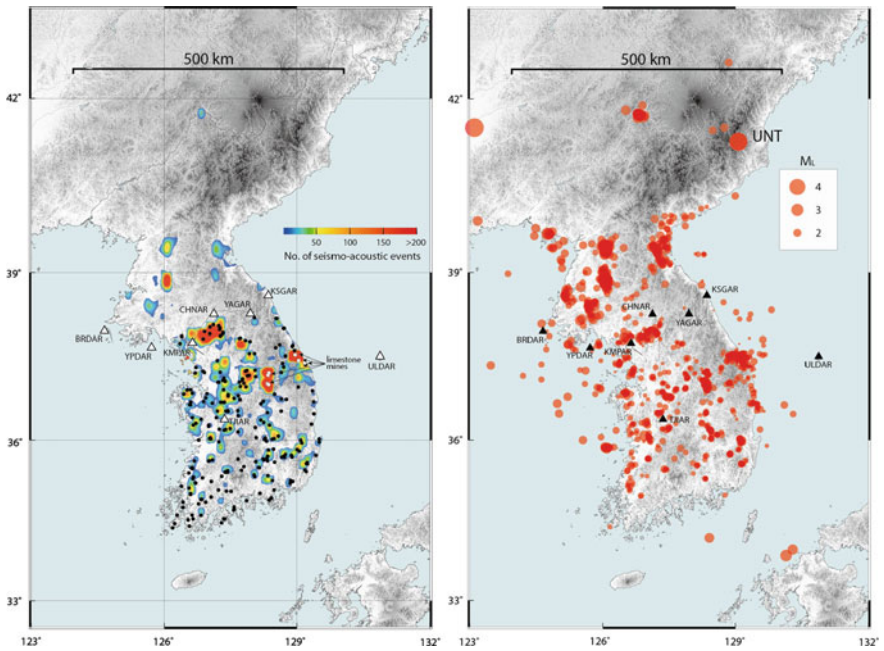

Fig. 11.11 (Left) Density map of surface explosions determined by automated single-array association for a data set of KIN from 1999 to 2014. Dots indicate quarries (black) and major limestone mines (white) in South Korea. (Right) Locations of surface explosions whose infrasound signals were associated with multiple infrasound arrays (number of stations (NSTA) ≥ 3)

automated results demonstrate the ability to expand monitoring coverage to more distant regions. Importantly, the automated process successfully detected and located two UNTs in North Korea, as confirmed by analysts. The average frequency observed from multiple infrasound signals is about 1.9 Hz and can be used as a priori information for constraining future association process. However, the association results may still produce false detections of explosions that generate both seismic and infrasonic signals. Although it may be possible for seismic events located in ocean areas to generate both signals, e.g., underwater explosions, this may not be the general case. Thus, the association results should be reviewed by analysts who make final decisions regarding surface explosions. In addition, the association criteria can be robustly adjusted by including the characteristics of infrasound arrivals and signals.

11.3.3 Infrasound Study Using Repetitive Sources

Active volcanoes, mines, and other sites that repetitively produce pressure disturbances in the atmosphere are good calibration sources or ground truth events for the

study of infrasound propagation. Repetitive infrasound signals from these sources capture transient path features and variations in the atmosphere with a time resolution controlled by the repeating intervals. The smaller the time difference between repeated sources, the finer the temporal sampling of the atmospheric structure affecting infrasound propagation. In this section, we use near-surface blasting (surface explosions) at mines as repetitive sources of infrasound. There are many active mines in South Korea, such as open-pit limestone mines and stone quarries (Lee et al. 2006). Several field surveys performed by the authors indicated that most mines commonly conduct blasting at nearly regular times on a daily basis.

As ground truth information, the exact location, origin time, and explosive charges of surface blasting are used for characterization of infrasound propagation, assessment of attenuation relations, and quantitative validation of detection capability of infrasound networks including the quantification of seasonal variations in the atmosphere. One way to acquire reliable ground truth information on surface blasting is in situ measurement of controlled repetitive sources at surface mining zones by operation of close-in instrumentation consisting of seismic and/or infrasound sensors with a global positioning system (GPS). Alternatively, seismic source parameters of repetitive surface explosions, determined remotely by seismic monitoring systems, could also be thought of as a type ground truth. Although these source parameters are less accurate than in situ direct measurements, the uncertainty in origin time is not significant compared to infrasound travel time analysis for long-distance propagations, provided the seismic source parameters are determined with adequate accuracy and precision.

Three locations, shown as star symbols M1, M2, and M3 in Fig. 11.1, indicate active surface blasting sources used in this section, in which seismic and infrasonic signals have been frequently detected by both the KIGAM routine seismic monitoring system and KIN arrays. The source area labeled M1 is the location of a rock quarry, and M3 is an open-pit limestone mine in South Korea. The source of M2 in North Korea is not known, but is inferred to be an ordinary open-air limestone mine, based on satellite images and geological formations in this region. The distances from the mines M1, M2, and M3 to CHNAR are 50 km, 113 km, and 181 km, respectively. Thus, the array is located in the geometric shadow zone for infrasound arrivals refracting at higher altitudes (possibly a thermospheric arrival, *It*).

The travel time or equivalently celerity measured from source origin time and location is a basic property of propagating waves used to identify the nature of infrasound arrivals (Kulichkov et al. 2000), or phases for multiple arrivals. Figure 11.12 shows seasonal variation of travel times of infrasound signals produced from the three mines and detected at CHNAR. The travel times for M1 and M2 were estimated based on seismic origin times; in the case of M3, the travel times were estimated from in situ measurements of source origin times (Che et al. 2011). Accordingly, the origin times in the M3 data set are more precise than those of M1 and M2, which have intrinsic uncertainty in source origin time and location. The variation in travel time, affected by the combination of seasonally dependent sound speed (ambient temperature) and wind component along the propagation direction,

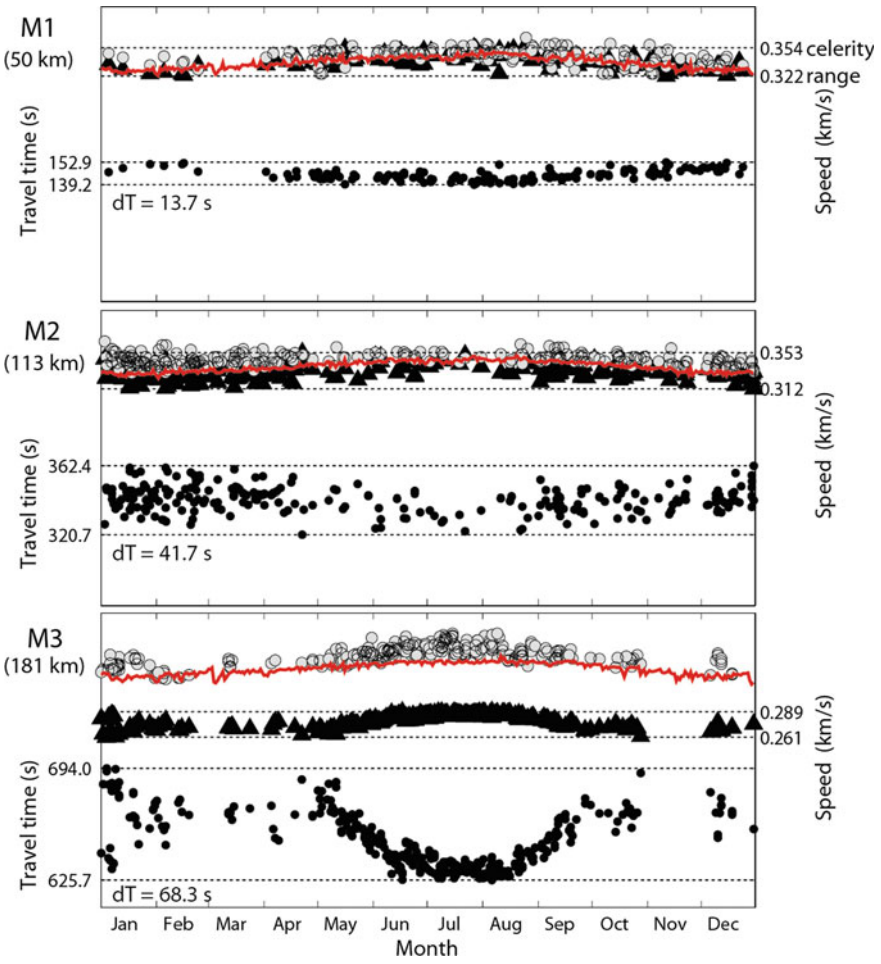

Fig. 11.12 Seasonal variations in travel time (black circles), celerity (triangles), and phase velocity (gray circles) of first arrivals from the three mines. Red lines indicate effective sound speeds on the ground at CHNAR

was more prominent in the case of M3 (propagation distance: 181 km). Systematic variations with little fluctuation from May to September were attributed to steady and favorable stratospheric winds (westerly stratospheric winds in summer as shown in Fig. 11.5a); marked variations in travel times were observed from October to April. These seasonally dependent characteristics also appear as travel times of shorter propagation distances, M1 and M2, but to a much lesser degree. M2 and M3 are in opposite directions to each other with respect to CHNAR; thus, seasonal detectability showed the reverse trends with regard to zonal wind directions, e.g., favorable zonal winds to M3 in the summer. This result is consistent with the relation between number of detections and atmospheric condition by sites,

as discussed in Sect. 2.2. As propagation distances increased from the mines to CHNAR, celerity decreased by shifting infrasound from the tropospheric to the stratospheric phase. Compared with the effective sound speeds on the ground (red lines), the celerity range of M1 shows that the infrasound arrivals were direct waves propagating through the lower troposphere with a refraction height of a few kilometers (Che et al. 2002). The celerity range of M2 is indicative of refractions at greater heights, including tropospheric and stratospheric phases. In the case of M3, all arrivals typically showed stratospheric phases, with celerity in the range of 260–289 m/s.

Phase velocity is another wave parameter that can be obtained from infrasound signals recorded at sensors arrays. Similar to celerity, it is used indirectly to infer the nature of infrasound arrivals. The relationship between fast phase velocity and slow celerity is generally valid for arrival series from a single source and suggests the presence of a layered atmospheric structure, with effective sound velocity increasing with height at the time of the ground truth (Negraru et al. 2010). By comparison with sound speed at ground level, it can also be used to infer the elevation angle of wave propagation with respect to the receiver (Le Pichon et al. 2008b). Figure 11.12 also displays the variation in phase velocity over the year; phase velocities were generally higher than sound speeds on the ground (red lines), with further widening of differences for stratospheric arrivals (M3), implying an increase in the elevation angle. Throughout the year, the phase velocity of M3 followed the seasonal variation of celerity; this implies that the ambient sound speed significantly affected the phase velocity for infrasound phases with similar turning heights.

Independent of seismic locations, the locations of mining explosions can be determined by multiple infrasound arrivals alone, e.g., using the azimuth intersection method, a least squares method with azimuths and arrival times, and BISL as mentioned previously. Location methods that incorporate infrasound arrival times generally require initial constraints on celerity for infrasound travel time calculations, which can be assigned compatible values based on observed phases with ground truth or estimated by ray tracing using an atmospheric model. Thus, a precise understanding of infrasound arrivals and atmospheric models with a sufficiently fine inhomogeneous structure in space and time provides a basis for reliable location estimates. Incorporation of seasonal variation in celerity models can also contribute to improved location accuracy. For example, an empirical celerity model, a sinusoidal curve fit to the observations in M3, was used to constrain time-dependent travel time variations for infrasound location. This approach significantly improved infrasound location accuracy, compared with the results using a constant travel time velocity (Che et al. 2011). To improve the location of mining explosions, seismic source parameters have been used as a priori information to constrain the infrasound location results (Che et al. 2009a). At a single seismo-acoustic array, a combination of seismic and infrasonic location processing demonstrated improvement in location accuracy when the infrasound azimuth was added to the seismic data (LeBras 2008). This improvement may have been due to the reliability of infrasound azimuth estimates at the array, affected by the degree of lateral deviation in medium

properties which is significantly less in the atmosphere than in the solid Earth (Modrak et al. 2010). Indeed, observations of seismic and infrasonic data from ground truth events at M3 revealed that the standard deviations of infrasound azimuth estimates were less than those of seismic arrivals: 1.4°, 4.5°, and 3.3° for infrasound *Is*, seismic *Pn*, and *Lg* arrivals, respectively. Finally, local observations of acoustic signals at mines provide constraints on acoustic source frequency. Typical surface mining activities produce an average source frequency of 1.4 Hz, corresponding to the average value of hundreds of surface explosions as measured by infrasound sensors within the other open-pit mine at M4 in Fig. 11.1. This value closely matches the average frequency of 1.9 Hz recorded at KIN arrays, obtained from automated seismo-acoustic analysis. With little or negligible dispersion in the lower atmosphere, this frequency range is useful in the search for infrasound arrivals and the complementary development of automated association techniques.

11.3.4 Seismic and Acoustic Data Fusion for Seismic Source Identification

As a concept for a data fusion process integrating multiple sensor data, operational experience has demonstrated that observations from the seismo-acoustic arrays of KIN can contribute to a reduction in the uncertainty of seismic source type identification (earthquakes and explosions), especially for small-magnitude seismic events. Although both the manual and automated processes in the seismo-acoustic analysis discussed in previous sections provide a reliable method to declare small to moderately sized surface explosions and improve the detection rate of surface explosions, a number of seismic events from explosions are not yet successfully discriminated. This low, event-dependent detectability is because infrasound propagation is significantly controlled by the effective sound velocity structure along the propagation paths as a result of different wave-ducting conditions between events and receivers. In addition, since the acoustic efficiency of surface explosions in general mining activity is reduced as a result of blast designs intended to reduce environmental disruptions, the detectability is more sensitive to the atmospheric conditions at near-regional distances.

To discriminate surface explosions that cannot be discriminated by seismo-acoustic analysis, we have developed a separate seismic discriminator using the seismic data from the KIN arrays. This seismic discriminator is a compound linear discriminant function (Che et al. 2007) and region-specific seismic discriminant that uses the seismic phase spectral and cross-spectral ratio in multiple frequency bands, incorporating a magnitude and distance amplitude correction (Walter and Taylor 2001). An optimal discriminant function requires a reliable training seismic data set (statistical populations) representing seismograms of earthquakes and explosions occurring in and around the Korean Peninsula. In addition, it is necessary for the epicenters of the training data set to be distributed as

widely and as evenly as possible over the region, in order to incorporate propagation characteristics of seismic phases along different paths and distances into the discriminant function. In the development of the seismic discriminant, the surface explosion catalogs, obtained from manual seismo-acoustic analysis (e.g., Figure 11.7), provide a reliable set of seismograms from the explosion population. Given the two representative populations of the region, the discriminator developed for the seismic array at CHNAR has a misclassification performance of 1.7% (Che et al. 2007).

Figure 11.13 shows an example of the data fusion approach for small-magnitude seismic source identification applied to a region in the peninsula where seismic signals from earthquakes and surface explosions located adjacent to each other have been frequently observed. Seismograms displayed in the figure are vertical ground motions for the two source types recorded at CHNAR with local magnitude >2 from

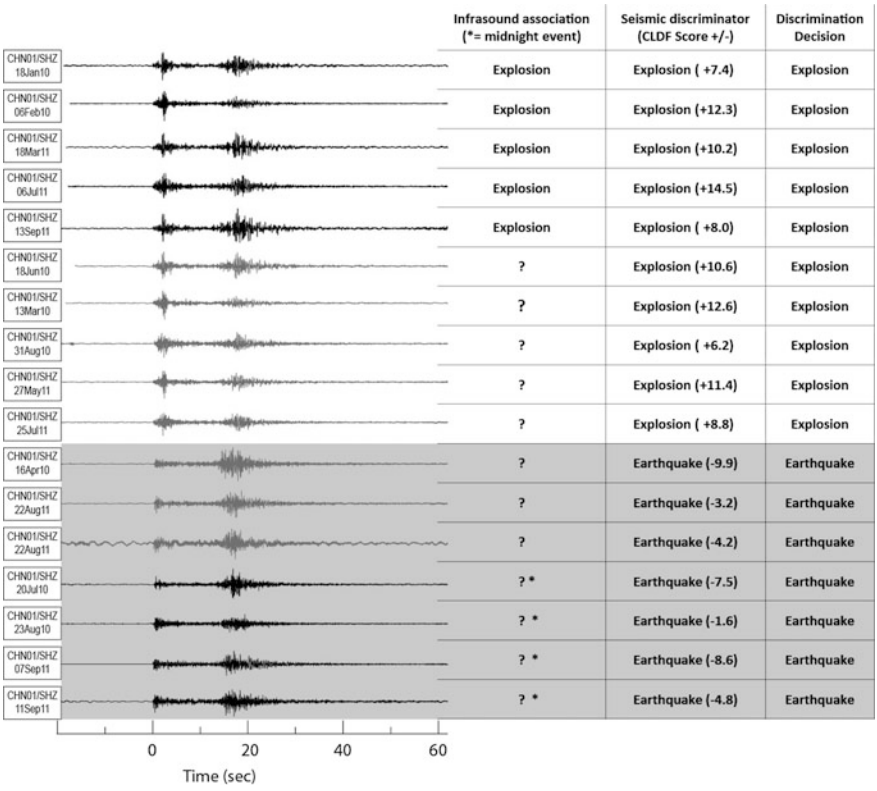

Fig. 11.13 Data fusion results for small-magnitude seismic source identification based on infrasound detection and seismic discrimination. Waveforms show vertical ground motions recorded at CHNAR from a source region where both earthquakes and explosions have occurred frequently (around M2 in Fig. 11.1). Explosion and earthquake waveforms are designated by the white and gray boxes, respectively

2010 to 2011. All five waveforms at the top are discriminated as surface explosions by seismo-acoustic analysis. The next five waveforms appear qualitatively as explosions, but no infrasound signals were associated with these events, possibly due to unfavorable propagation conditions from the epicenters to infrasound stations at the time the events occurred. The seismic discriminator was then applied to the unidentified events; these events were determined quantitatively as explosion-type. The discriminator was also used to reconfirm the source type of earthquakes by application to earthquake-like events. This example illustrates bilateral efforts to combine discriminants, developed from the wave fields associated with different elastic media, applied to the quantitative identification of surface explosions. Although each method remains as a work in progress, due to a lack of understanding of the media, the combined complementary approach provides a wealth of information on surface explosions with regard to seismic source identification.

11.4 Infrasound Observations from Ground Motions

In this section, the observation and application of local, epicentral, and diffracted infrasound signals from earthquakes and UNTs around the Korean Peninsula will be introduced with some examples. Local infrasound generated by the 2003 Tochaki-Oki earthquake was utilized to calibrate acoustic gauges in the field, in which each is composed of an acoustic gauge and wind noise reduction system (Kim et al. 2004). The local cross-coupling from seismic ground motion to infrasound signal allows the estimation of the seismic-to-infrasound transfer function which can be used to calibrate acoustic sensor attached to a noise reduction system in the field. The epicentral infrasound signals from the second (2009) and third (2013) UNTs of North Korea were used for the estimation of the released energy from the ground to atmosphere with wind correction along the path from the UNT site to a receiver (KSGAR) located at the border between North and South Korea. The ground motions from the strong seismic waves from the UNT are considered as the source of the epicentral infrasound signals. The epicentral infrasound could be also used as a source discriminant due to the signal duration differences between explosions and natural earthquakes. The diffracted infrasound signals from the second UNT were detected with a systematic back azimuth variation. The signals were used to locate the secondary sources along the northeast coast of North Korea.

11.4.1 Local Infrasound from Earthquakes and Its Application

A great earthquake, the Tokachi-Oki Earthquake (Mw = 8.3) and an aftershock (Mw = 7.4) occurred on September 25, 2003, near Hokkaido, Japan. The collision

of the Kuril arc with the northeast Japan arc in the southern part of Hokkaido triggered these events (Murai et al. 2003). Local and diffracted infrasound signals generated by these events were observed at two seismo-acoustic arrays in KIN, the prototype of CHNAR and TJIAR (Fig. 11.14). The prototype of CHNAR had a much simpler array geometry and different instruments compared to the current CHNAR. It was composed of four elements of collocated vertical GS-13 seismometers in boreholes and Validyne DP250 acoustic gauges (Stump et al. 2004). The Validyne sensor is not sensitive to ground motion (Hayward 1999). An 11-element porous hose array was connected to each infrasound sensor for background wind noise reduction. A second, 100 m aperture four-element acoustic array TJI, the prototype of TJIAR, was also different from current TJIAR in terms of array aperture and instrument type. It was installed at the existing seismic station "TJN" at KIGAM (in the center of TJI configuration in Fig. 11.14). Four Seattle Q1 infrasonic sensors, which were developed by Hayward in 2003, were installed at TJI. This sensor is also not sensitive to ground motion and thus provided the opportunity to study of local infrasound.

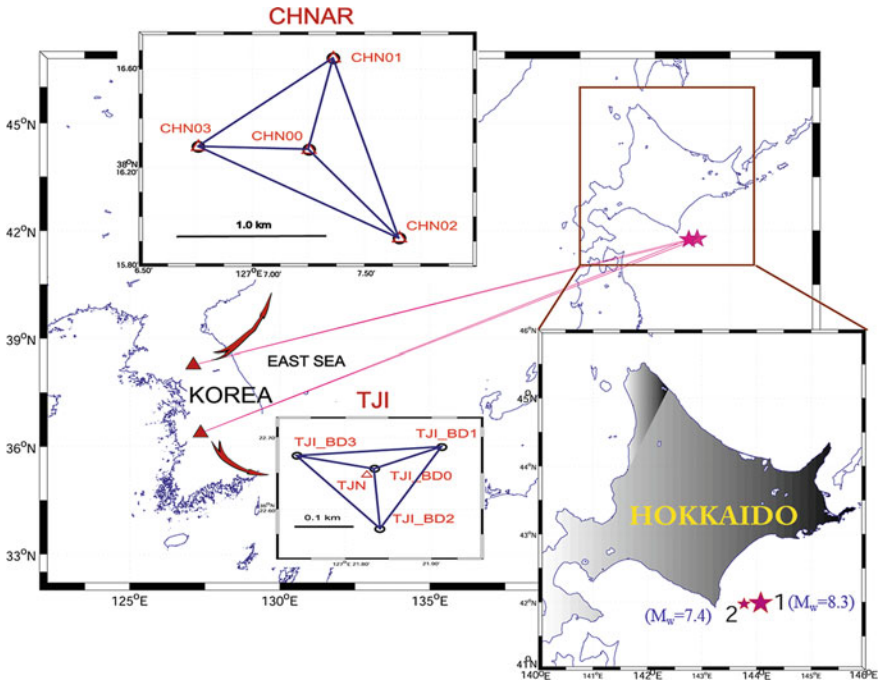

Fig. 11.14 Locations of seismo-acoustic arrays, prototypes of CHNAR and TJI (closed red triangles), and the epicenters of the Tokachi-Oki earthquake and largest aftershock (closed red stars). Open black circles represent the infrasound gauges while open red triangles represent the seismic sensors

Instrument corrections were applied to seismic signals to convert raw data to ground velocity before comparison between the seismic and coupled local infrasound signals at the two arrays. Figure 11.15 illustrates the raw seismic time series (1 and 3 in Fig. 11.15a) and band-pass-filtered infrasound time series (2 and 4 in Fig. 11.15a) at CHN00 and TJI. Diffracted infrasound signals arrive at 4482 and 4409 s after the main shock and aftershock. Comparison of the instrument corrected seismic signals with local infrasound signals shows that the waveform of the local infrasound signal is coherent with the waveform of seismic ground velocity in both amplitude and phase (Fig. 11.15b, c). The observed cross-coupling at the two seismo-acoustic arrays provides an opportunity to calculate a transfer function that quantifies the energy transfer from seismic to infrasonic signals.

The relationship between the vertical ground velocity and air pressure can be formulated as

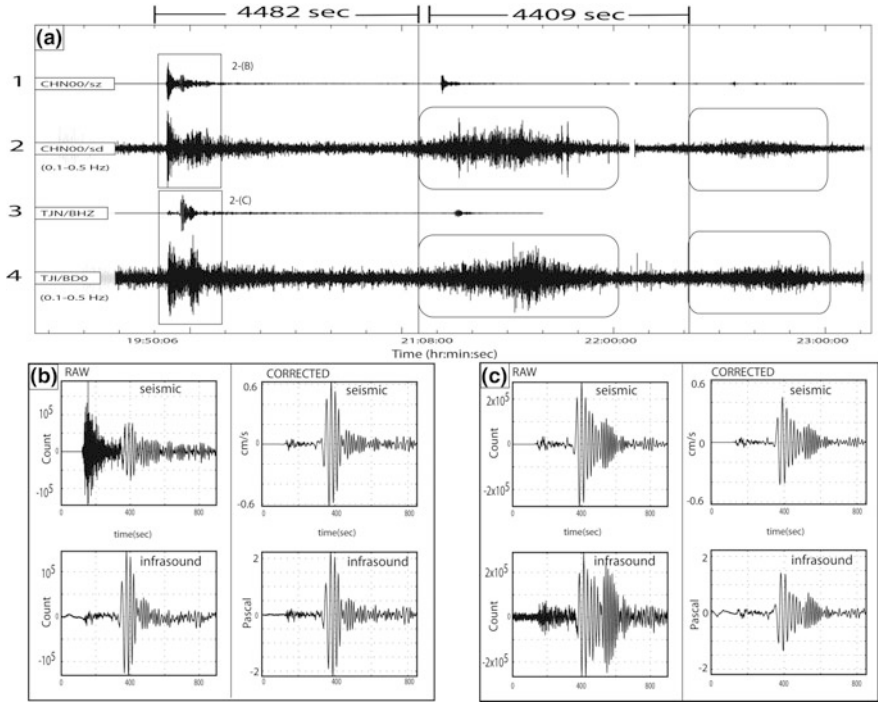

Fig. 11.15 Data Set. **a** The raw seismic traces at CHN00/sz (1) and TJN/BHZ (3) are compared with the band-pass-filtered (0.1–0.5 Hz) infrasound data at CHN00/sd (2) and TJI/BD0 (4). The data pairs in the vertical rectangular boxes are seismic data and coupled local infrasound signals. The infrasound data in the rounded rectangle window are the diffracted infrasound signals. **b** The left column is composed of raw seismic and local infrasound signals at CHN00. The right column contains the instrument corrected seismic and infrasound data set (0.01–16.0 Hz). **c** The same relationship at TJI/BD0 as demonstrated in (**b**) (Updated from Kim et al. 2004, Fig. 11.2)

$$\Delta P = \rho c v$$

where ΔP is the perturbation pressure, ρ is the density of air, c is the velocity of sound in the air and v is the vertical ground velocity (Donn and Posmentier 1964; Cook 1971). Based on this equation, the theoretical transfer function, ρc, is calculated. The results for CHNAR and TJI are 12.28 and 12.34 dB, respectively (Table 11.1). The observed transfer function, $\Delta P/v$, is estimated in the frequency domain for the comparison between the theory and observation.

The spectral ratio between local infrasound and seismic signal was estimated in the frequency domain and compared to the observed transfer function for the two arrays coincident with theory from 0.03 to 1.0 Hz (Fig. 11.16). In this frequency band, the coupling from seismic surface waves, *Rayleigh* waves, to infrasound signal dominates the transfer function (Fig. 11.16a, c). The *P* wave coupling to local infrasound signal contributes most to the transfer function at frequencies from 0.1 to 1.0 Hz with increased scatter in the transfer function observed because of the low SNR of the local infrasound signals (Fig. 11.16b, d). Lower SNR of the coupled local infrasound at higher frequencies results in greater scatter of the transfer function. The transfer function at CHN03 is lower than the predicted value by 2 dB, which was not found in the other gauges for the array. This difference was explained by water trapped in the hose array at CHN03 lowering the sensitivity of the infrasound system. The average transfer function (Table 11.1) excluding CHN03 has a difference of 0.85 dB at CHNAR and 0.96 dB at TJI compared to theory, which can be explained by the pre-deployment laboratory calibration error. The observed transfer function also reveals the corner frequency of Validyne's gauge response. The rolling off of the transfer function for CHNAR at 0.03 Hz (Fig. 11.16a) is the result of the corner frequency of the Validyne's response. However, the known Seattle Q gauge's low-frequency decay is not observed in the transfer function due to instrument self-noise (Fig. 11.16c).

The transfer function between the instrument corrected ground velocity and local infrasound shows the expected flat response and corner frequency for the two different gauge types. A change of instrument response caused by water infiltration into the noise reduction system is found from the transfer function at CHN03. For other cases, the transfer functions confirm the hose arrays do not affect the amplitude response up to 1 Hz. At frequencies above 1 Hz, small-magnitude events (Kim et al. 2010) or artificial events generated by different types of man-made sources such as vibroseis or free-falling iron pillar might be used to estimate the

Table 11.1 Comparison between mean of observed and theoretical transfer functions at two seismo-acoustic stations (After Kim et al. 2004, Table 2)

Station	Frequency (Hz)	Theory (dB)	Mean of the observed (dB)
CHNAR	0.03–0.095	12.28	11.43
TJI	0.023–0.096	12.34	11.38

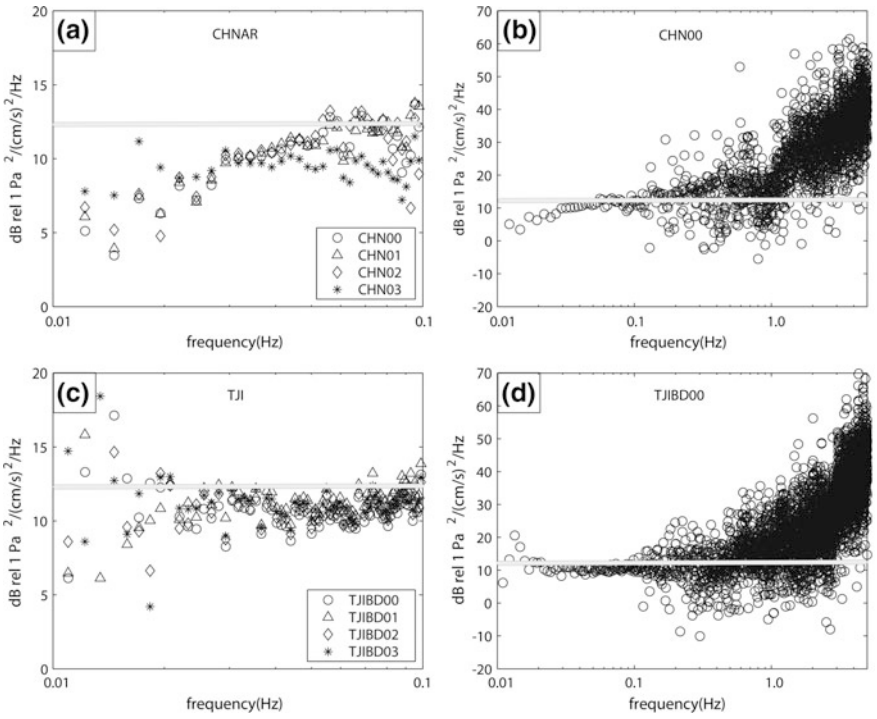

Fig. 11.16 The theoretical transfer functions estimated for the two seismo-acoustic arrays are compared with the observed transfer functions. **a** The theoretical transfer function (gray line) is compared with observed transfer functions (symbols) from 0.01 to 0.1 Hz at CHNAR. The different symbol represents the different array elements. **b** The observed transfer function at CHN00 (circle) is compared with theory (gray line) from 0.01 to 5 Hz. **c** The same relationship as demonstrated in (**a**) at TJI. **d** The same relationship as demonstrated in (**b**) at TJIBD00 (After Kim et al. 2004, Fig. 3)

seismic-to-local infrasound coupling relationship at high frequencies (Jones et al. 2015). In summary, empirically determined transfer functions suggests that local infrasound signals coupled from seismic waves can be used to calibrate infrasound gauges and wind noise reduction systems in the field.

Comprehensive Nuclear-Test-Ban Treaty Organization (CTBTO) has been installing 60 global IMS infrasound stations to monitor nuclear explosions. It also has been developing field calibration techniques for IMS infrasound stations since 2011 (Marty 2015). CTBTO proposed to use a self-calibrating sensor as a reference gauge for the calibration of IMS infrasound gauge attached to a noise reduction pipe array in the field. It is a full frequency calibration method including background noise reduction system by comparing IMS infrasound data with that of the reference gauge installed just beside the IMS stations. In relation to CTBTO's efforts to calibrate IMS infrasound station in the field, the technique presented here may be

used as another field calibration method for IMS infrasound stations, especially at sites with co-located seismometers.

11.4.2 The Utilization of Epicentral and Diffracted Infrasound from UNTs

Three UNTs were conducted by North Korea at their test site located in the vicinity of P'unggyeri in 2006, 2009, and 2013. Local, epicentral, and diffracted infrasound signals generated from UNTs have been recorded at KIN and IMS stations around the Korean Peninsula (Che et al. 2009b, 2014).

Figure 11.17 (from Che et al. 2014) displays the infrasound waveforms generated from these first three UNTs and the associated PMCC detection results for the frequency band from 0.1 to 5.0 Hz for the closest infrasound station, KSGAR. When the first UNT was executed in 2006, five arrays of the KIN were being operated and data for IS30 were available, but only KSGAR detected possible epicentral infrasound signals from the event. Although the estimated back azimuth and celerity of the signals were consistent with possible epicentral infrasound

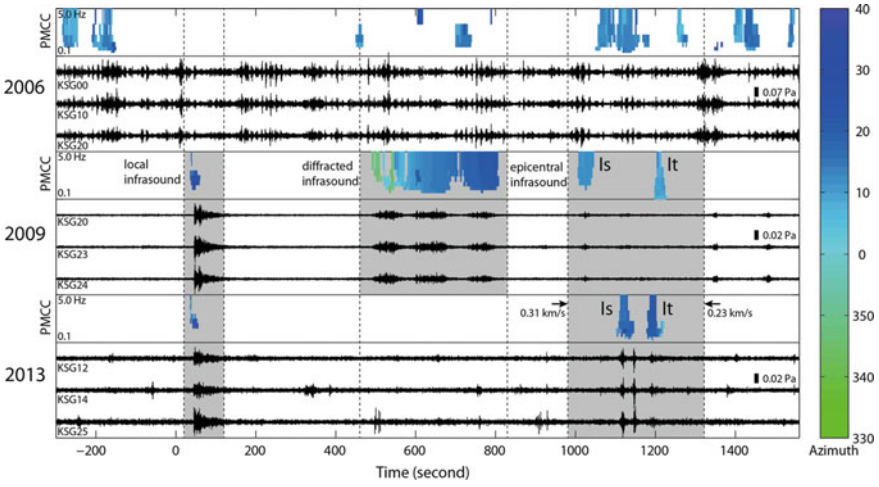

Fig. 11.17 Waveforms and PMCC detection results for infrasound data recorded at KSGAR for the three UNTs by North Korea in 2006, 2009 and 2013. In each year, three sets of waveform data from KSGAR are plotted after band-pass filtering between 2 and 7 Hz. All waveforms are aligned to seismic original time. Colors in the PMCC panels code the observed azimuth of detection at KSGAR. Only the PMCC detections from 330° to 40° are plotted. The true azimuth from KSGAR to the site is 11.3° from north. *Is* and *It* represent stratospheric and thermospheric infrasound arrivals, respectively. Local, diffracted, and epicentral infrasounds in gray boxes indicate infrasound signals generated from different source locations; around receiver location, secondary source area, and epicentral area, respectively (After Che et al. 2014, Fig. 2)

signals (Fig. 11.17, upper panel), these signals could not be uniquely associated with the event because infrasound signals with similar azimuths appeared at other times including the time period prior to the seismic arrival and extending for a long time following the event (Che et al. 2014).

Five KIN arrays to the southwest of the test site detected infrasound signals generated by the second UNT in 2009. The effective sound speed ratio ($V_{eff\text{-}ratio}$), defined as the ratio between the effective speed of sound at stratospheric altitudes and the speed of sound at ground level, showed that westward wind formed a favorable downwind condition for these stations. Local, epicentral, and diffracted infrasound signals were clearly observed at KSGAR (Fig. 11.17, middle panel). The arrival time of the diffracted infrasound signal was intermediate between the local and epicentral infrasound signals because of its mixed propagation media including components of ground and atmosphere propagation. The diffracted infrasound had a duration of 5 min with systematic variations in back-azimuth from 342.0° to 27.2°. Based on a location procedure using seismic velocity and diffracted infrasound arrival time, Che et al. (2014) localized the secondary sources which moved about 180 km from southwest to northeast along a coastal area during about 30 s. Stratospheric and thermospheric arrivals of epicentral infrasound were also detected with estimates of a celerity of 302 m/s for the stratospheric arrival and 254 m/s for the thermospheric arrival (Che et al. 2009b).

Three arrays of the KIN and two IMS stations (IS30 in Japan and IS45 in Russia) detected infrasound signals from the third UNT in 2013. These five stations were relatively located to the east of the explosion, coincident with favorable downwind condition to the east based on the atmospheric $V_{eff\text{-}ratio}$ profile (Che et al. 2014). At KSGAR, local and epicentral infrasound signals were recorded (Fig. 11.17, bottom panel). Stratospheric and thermospheric arrivals of epicentral infrasound signals were also detected from the third UNT with celerities of 273 m/s and 256 m/s, respectively, and dominant frequencies of 2.7 Hz and 0.8 Hz, respectively. There is a difference in the celerity of stratospheric arrivals from the second and third UNTs due to the seasonal variation of atmospheric conditions along the same propagation path from the site to KSGAR, consistent with the infrasound propagation path study by Che et al. (2011).

An empirical relationship between the amplitude of the epicentral infrasound turning in the stratosphere and the equivalent estimate of released energy by an explosion was developed by Los Alamos National Laboratory (LANL) (Whitaker et al. 2003; Evers et al. 2007). Based on this relationship, the relative energy released by the second and third UNTs were estimated using the epicentral infrasound signals. The amplitude of wind corrected epicentral infrasound from the 2013 UNT was estimated as 0.57 μbar at KSGAR, which is about 3.2 times larger than the 0.18 μbar from the 2009 UNT. The amplitude ratio corresponds to a 5.1 times difference in the released energy estimate based on the empirical relationship (Che et al. 2014). However, the calculated infrasound energy from an underground explosion cannot be regarded as proportional to the total yield estimates since the energy estimate is reduced due to the depth of burial, geological and atmospheric conditions at the time of the explosion (Kim et al. 2009; Stump et al. 2008;

Williams et al. 2012). The total energy release estimated in this manner is comparable to a high explosive (HE) explosion on the surface rather than the total yield of the UNT.

Another application of epicentral infrasound could be the utilization of epicentral infrasound as a source discriminant. Relatively short signal durations are expected from artificial events because of the coupling from strong *P* waves to the atmosphere while *Lg* or *Rayleigh* waves with longer duration are expected to transfer energy to atmosphere for natural earthquakes (Che et al. 2014). Whitaker (2007) has proposed a similar concept for a discriminant using infrasound amplitude versus seismic magnitude and infrasound signal duration versus seismic magnitude.

In 2016 prior to the review of this chapter, two additional presumed UNTs were detonated by North Korea on January 6 ($m_b = 4.8$) and September 9 ($m_b = 5.0$) at nearly the same location as previous three explosions. Infrasound signals generated by the fourth explosion in January were recorded at all KIN arrays (Stump et al. 2016) and one IMS station (IS45) (Assink et al. 2016). Stratospheric winds at the time of the detonation were favorable to the KIN arrays while both stratospheric and tropospheric winds were in the direction of the IMS infrasound array, IS45. The fifth explosion that occurred in September also generated infrasound signals with apparent thermospheric arrivals observed at the three closest arrays to the source (KSGAR, CHNAR, and YAGAR) (Stump et al. 2016), but not at nearby IMS stations. These detections were also consistent with atmospheric winds at the time. Ray tracing predictions using G2S atmospheric specifications are consistent with the seasonal variations of infrasound detections for all five UNTs observed at the KIN arrays and IMS infrasound stations around the Korean Peninsula (Stump et al. 2016). Comparison of infrasound arrivals from the two recent explosions illustrates that the most important factor for infrasound detection is the atmospheric model at the time of the event.

11.5 Summary

The Korea Infrasound Network (KIN) consisting of eight seismo-acoustic arrays has been in operation with partial cooperation with Southern Methodist University since the first array installation in 1999. KIN consists of dense arrays with small (~100 m) and large (~1 km) apertures that can record highly correlated signals between sensors. Therefore, the network detects infrasound signals from a variety of sources with relatively small amplitudes that are observable at smaller regional distances. The detection capability of the KIN was simulated using a numerical modeling technique that account for the effects of important parameters describing the source and the atmosphere that influence propagation. The minimum detectable energy of the KIN, along with nearby IMS infrasound stations, improves the detection capability by ~20 t of TNT compared with that provided solely by IMS stations. These observations illustrate the usefulness of dense regional networks and

combinations of the regional networks with the IMS network in the context of future CTBT verification.

We have reviewed automatic infrasound detections on the Korean Peninsula and illustrated the effects of environmental conditions such as wind speed and direction on infrasound noise levels and seasonal variation in infrasound detections. Infrasound detections are dependent on atmospheric conditions as well as local site environments, as quantified C-value variations using the adaptive F-detector (Arrowsmith et al. 2009). Knowledge of background noise as well as seasonal variations in infrasound detections at infrasound arrays provides a basis for evaluating array performance under changing environmental conditions. This information in conjunction with time-varying atmospheric models such as Ground-to-Space (G2S) offer opportunities to improve the event locations and possibly source characterization. In addition, local meteorological data may provide an opportunity to evaluate the importance of the fine scale of the atmospheric model on infrasound propagation at local distances and thus understanding time-varying noise sources close to the stations. This result may also prove useful in studies designed to resolve tropospheric atmospheric structure including the impact of local inversion layers. In all cases, the inclusion of good ground truth will complement these investigations.

The main operational purpose of the KIN is to discriminate man-made seismic events from seismic catalogs consisting of thousands of seismic events per year in and around the Korean Peninsula, and to ensure that seismic and infrasonic data from KIN are used appropriately for monitoring and discriminating low-energy seismic activity. This chapter reviewed discrimination results by first reprocessing infrasound data from over 15 years with implementation of the infrasound signal detector. The detection results showed that the sources of infrasound could be divided into microbaroms and man-made events at local/regional distances. An automated seismo-acoustic association process was developed to link seismic events and infrasound signals generated from a common source, and hence improve the detection of surface explosions using the PMCC detection algorithm, a procedure to remove coherent background noise detections, and association criteria based on analyst data reviews. When the automated process was applied to the continuous KIN data from 1999–2014, it discriminated surface explosions at a rate several times higher than manual analysis. These results were due to the adoption of a robust detection algorithm and an association process incorporating the characteristics of infrasound signals of surface explosions in the region. The locations of surface explosions determined by manual and automated analysis are nearly coincident with well-known industrial sites conducting blasts in South Korea. The seismo-acoustic analysis serves as a successful temporal and spatial monitoring technique for surface explosions. However, it needs further development to fully assess a substantial percentage of man-made explosions, due to the weak infrasound amplitude of surface explosions in the region, unfavorable propagation conditions in the atmosphere between the surface explosions and the receivers, and high levels of local noise near the array. Refined automated detections are affected by acceptable criteria parameters and therefore it is recommended that more reliable

parameters should be established based on the characteristics of infrasound signals, which can be used to discern surface explosions and microbaroms recorded at KIN arrays. In addition, further efforts to collect ground truth events are necessary to set up reliable association criteria and to validate the performance of the dense network.

The developments of discrimination methods using seismic and infrasonic analysis allow the simultaneous investigation and discrimination of small-magnitude seismic events. Acoustic and seismic wavefields occur in different media. Thus, the utility of both source identification techniques (seismo-acoustic analysis and seismic discriminator in this chapter), based on the wave fields, is dependent on propagation path effects. The detectability of infrasound that determines the success of seismo-acoustic analysis depends on the time-variant effective sound velocity structure in the atmosphere. In addition, the credibility of the seismic discriminator is partly dependent on the propagation paths on a region-by-region basis. Thus, to overcome the current incompleteness of each discriminator, it may be necessary to apply both methods simultaneously to reduce the risk of false alarms due to misclassification. Finally, to enhance the discrimination synergy, endeavors should be made in modeling robust fusion approaches, incorporating dynamic features of the atmosphere, and enlarging earthquake and explosion populations in the development of seismic discriminators.

Local, epicentral, and diffracted infrasound signals were observed and analyzed from two large magnitude earthquakes that occurred in Japan and three UNTs conducted by North Korea. Local infrasound signals observed from the Mw 8.3 Tochaki-Oki earthquake were used to calibrate infrasound sensor in the field. The cross-coupling from ground motion to the atmosphere produces a pair of coherent seismic and local infrasound signals, which provide the basis to calibrate infrasound sensor attached to a background wind noise reduction system in the field. This technique might be used as another field calibration technique for CTBTO IMS infrasound stations. Epicentral infrasound signals generated by the second and third UNTs were used to estimate the ratio of the released energy from the two explosions. The ratio produced a factor of 5.1 times difference between the two events. This ratio should be regarded as the ratio of HE on the surface rather than true yield ratio of UNTs because source depth of burial, geological and atmospheric conditions are involved in the yield estimation. In addition, the duration of epicentral infrasound signals are related to source mechanism and could be used as an additional discriminant to separate artificial events from natural earthquakes.

Acknowledgements We thank Alexis Le Pichon for supports in the assessment of detection capability of infrasound network for this chapter. This work was supported by the Basic Research Project of the Korea Institute of Geoscience and Mineral Resources (KIGAM) funded by the Ministry of Science, ICT and Future Planning of Korea.

References

Arrowsmith SJ, Hedlin MAH (2005) Observations of infrasound from surf in southern California. Geophys Res Lett 32:L09810. https://doi.org/10.1029/2005GL022761

Arrowsmith SJ, Whitaker R, Katz C, Hayward C (2009) The F-detector revisited: an improved strategy for signal detection at seismic and infrasound arrays. Bull Seismol Soc Am 99(1): 449–453

Arrowsmith SJ, Burlacu R, Pankow K, Stump B, Stead R, Whitaker R, Hayward C (2012) A seismoacoustic study of the 2011 January 3 Circleville earthquake. Geophys J Int 189:1148–1158. https://doi.org/10.1111/j.1365-246X.2012.05420.x

Assink JD, Waxler R, Smets P, Evers LG (2014) Bidirectional infrasonic ducts associated with sudden stratospheric warming events. J Geophys Res Atmos 119. https://doi.org/10.1002/2013jd021062

Assink JD, Averbuch G, Smets PSM, Evers LG (2016) On the infrasound detected from the 2013 and 2016 DPRK's underground nuclear tests. Geophys Res Lett 43(7):3526–3533. https://doi.org/10.1002/2016GL068497

Blom PS, Marcillo O, Arrowsmith SJ (2015) Improved bayesian infrasonic source localization for regional infrasound. Geophys J Int 203:1682–1693

Brachet N, Brown D, Bras RL, Cansi Y, Mialle P, Coyne J (2010) Monitoring the Earth's atmosphere with the global ims infrasound network, infrasound monitoring for atmospheric studies. In: Le Pichon A, Blanc E, Hauchecorne A (eds), pp 77–118, Springer. New York, https://doi.org/10.1007/978-1-4020-9508_1

Brown PG, Whitaker RW, ReVelle DO, Tagliaferri E (2002) Multi-station infrasonic observations of two large bolides: signal interpretation and implications for monitoring of atmospheric explosions. Geophys Res Lett 29(13):1636. https://doi.org/10.1029/2001GL013778

Cansi Y (1995) An automatic seismic event processing for detection and location: The PMCC method. Geophys Res Lett 22:1021–1024

Cansi Y, Vergoz J, Schissele E (2005) A quantitative evaluation of PMCC's detection capability. In: Proceedings of the Infrasound Technical Workshop, CTBTO and CEA/DASE, Tahiti

Che I-Y, Jun M-S, Jeon J-S, Min KD (2002) Analysis of local seismo-acoustic events in the Korean Peninsula. Geophys Res Lett 29:1589. https://doi.org/10.1029/2001GL014060

Che I-Y, Jun M-S, Jeon J-S (2007) A compound linear discriminant method for small-magnitude seismic events and its application to the North Korea seismic event of October 9, 2006. Earth Planets Sp 59:e41–e44

Che I-Y, Shin JS, Kang IK (2009a) Seismo-acoustic location method for small-magnitude surface explosions. Earth Planets Sp 61:e1–e4

Che I-Y, KimTS Jeon J-S, Lee H-I (2009b) Infrasound observation of the apparent North Korean nuclear test of 25 May 2009. Geophys Res Lett 36:L22802. https://doi.org/10.1029/2009GL041017

Che I-Y, Stump BW, Lee H-I (2011) Experimental characterization of seasonal variations in infrasonic traveltimes on the Korean Peninsula with implications for infrasound event location. Geophys J Int 185:190–200

Che I-Y, Le Pichon A, Kim IH, Lee H-I (2012) Incorporating numerical modeling into estimates of the detection capability of the KIGAM infrasound network. In: Proceedings infrasound technology workshop, Daejeon, South Korea, 8–12 Oct 2012

Che I-Y, Park J, Kim IH, Kim TS, Lee H-I (2014) Infrasound signals from the underground nuclear explosions of North Korea. Geophys J Int 198:495–503

Cook RK (1971) Infrasound radiated during the Montana earthquake of 1959 August 18. Geophys J R Astr Soc 26:191–198

Donn WL, Posmentier ES (1964) Ground-coupled air waves from the Great Alaskan earthquake. J Geophys Res 69:5357–5361

Donn WL, Rind D (1972) Microbaroms and the temperature and winds in the upper atmosphere. J Atmos Sci 29:156–172

Drob DP, Garcés M, Hedlin MAH, Brachet N (2010) The temporal morphology of infrasound propagation. Pure appl Geophys 167:437–453. https://doi.org/10.1007/s00024-010-0080-6

Evers LG, Ceranna L, Haak HW, Le Pichon A, Whitaker RW (2007) A seismoacoustic analysis of the gas-pipeline explosion near Ghislenghien in Belgium. Bull Seism Soc Am 97:417–425

Ford SR, Rodgers AJ, Xu H, Templeton DC, Harben P, Foxall W, Reinke RE (2014) Partitioning of seismoacoustic energy and estimation of yield and height-of-burst/depth-of-burial for near-surface explosions. Bull Seismol Soc Am 104:608–623. https://doi.org/10.1785/0120130130

Green DN, Guilbert J, Le Pichon A, Sebe O, Bowers D (2009) Modeling ground-to-air coupling for the shallow ML 4.3 Folkestone, United Kingdom, earthquake of 28 April 2007. Bull Seismol Soc Am 99:2541–2552. https://doi.org/10.1785/0120080236

Hart DH, Young CJ (2002) MatSeis User Manual version 1.7. https://www.nemre.nnsa.doe.gov/cgi-bin/prod/nemre/matseis.cgi

Hayward C (1999) Construction and evaluation of a simple infrasound microphone using an industrial pressure transducer, AGU poster, S11B07

Hayward C (2003) Infrasound noise reduction using inexpensive microphones, AGU poster, U31B-0017

Johnson JB, Anderson J, Marcillo O, Arrowsmith S (2012) Probing local wind and temperature structure using infrasound from Volcan Villarrica (Chile). J Geophys Res 117:D17107. https://doi.org/10.1029/2012JD017694

Jones KR, Abbott R, Hamshire J, White B, Marcillo O, Whitaker R (2015) Airborne infrasound: A new way to explore the 3D acoustic wavefield. In: Infrasound Technology Workshop 2015 Book of Abstract, 24

Kim SG, Park YC, Kim WY (1998) Discrimination of small earthquakes and artificial explosions in the Korean Peninsula using Pg/Lg ratios. Geophy J Int 134:267–276

Kim TS, Hayward C, Stump B (2004) Local infrasound signals from the Tokachi-Oki earthquake. Geophys Res Lett 31:L20605. https://doi.org/10.1029/2004GL021178

Kim TS, Kang IB, Kim GY (2009) Yield ratio estimates using regional Pn and Pg from North Korea's underground nuclear explosions. Geophys Res Lett 36:L22302. https://doi.org/10.1029/2009GL040495

Kim TS, Hayward C, Stump B (2010) Calibration of acoustic gauge in the field using seismic Lg phase and coupled high frequency local infrasound. Bull Seismol Soc Am 100(4):1806–1815

Kulichkov SN, ReVelle DO, Whitaker RW, Raspopov OM (2000) On so-called "tropospheric" arrivals at long distances from surface explosions. In: Proceedings of the ninth annual symposium on long-range propagation, Oxford, MS, 14–15 Sept, pp 229–237. National Center for Physical Acoustics

Landès M, Ceranna L, Le Pichon A, Matoza RS (2012) Localization of microbarom sources using the IMS infrasound network. J Geophys Res 117:D06102. https://doi.org/10.1029/2011JD016684

Le Pichon A, Guilbert J, Vega A, Garces M, Brachet N (2002a) Ground-coupled air waves and diffracted infrasound from the Areaquipa earthquake of June 23, 2001. Geophy Res Lett 29 (8):1886–1889

Le Pichon A, Garce´s M, Blanc E, Barthe´le´my M, Drob DP (2002b) Acoustic propagation and atmosphere characteristics derived from infrasonic waves generated by the Concorde. J Acoust Soc Am 111:629–641

Le Pichon A, Vergoz J, Herry P, Ceranna L (2008a) Analyzing the detection capability of infrasound arrays in Central Europe. J Geophys Res 113:D12115. https://doi.org/10.1029/2007JD009509

Le Pichon A, Antier K, Cansi Y, Hernandez B, Minaya E, Burgoa B, Drob D, Evers L, Vaubaillon J (2008b) Evidence for a meteoritic origin of the September 15, 2007, Carancas crater. Meteorit Planet Sci 43:1797–1809. https://doi.org/10.1111/j.1945-5100.2008.tb00644.x

Le Pichon A, Vergoz J, Blanc E, Guilbert J, Ceranna L, Evers L, Brachet N (2009) Assessing the performance of the International Monitoring System's infrasound network: geographical

coverage and temporal variabilities. J Geophys Res 114:D08112. https://doi.org/10.1029/2008JD010907
Le Pichon A, Matoza R, Brachet N, Cansi Y (2010) Recent enhancements of the PMCC infrasound signal detector. Inframatics 26 (2010)
Le Pichon A, Ceranna L, Vergoz J (2012a) Incorporating numerical modeling into estimates of the detection capability of the IMS infrasound network. J Geophys Res 117:D05121. https://doi.org/10.1029/2011JD016670
Le Pichon A, Ceranna L, Kechut P (2012b) Global scale stratospheric processes as measured by the infrasound IMS network. In: EGU general assembly conference abstracts, p 9146
LeBras RJ (2008) Multi-sensor data fusion project final report. USA: SAIC Technical report
Lee CO, Hong SS, Lee BT, Kim GS, Yun HS (2006) Spatial distribution of the dimension stone quarries in Korea. J Petrol Soc Korea 15(3):154–166
Marcillo O, Johnson JB (2010) Tracking near-surface atmospheric conditions using an infrasound network. J Acoust Soc Am Lett 128(1):EL14–EL19. https://doi.org/10.1121/1.3442725
Marcillo O, Arrowsmith SJ, Whitaker R, Anderson D, Nippress A, Green D, Drob DP (2013) Using physics-based priors in a Bayesian algorithm to enhance infrasound source location. Geophys J Int 196:375–385
Marty J (2015) Overview of IMS infrasound station and engineering projects. In: Infrasound technology workshop 2015 book of abstract, vol 6
McKenna MH, Stump BW, Hayward C (2008) Effect of time-varying tropospheric models on near-regional and regional infrasound propagation as constrained by observational data. J Geophys Res 113:D11111. https://doi.org/10.1029/2007JD009130
Modrak RT, Arrowsmith SJ, Anderson DN (2010) A Bayesian framework for infrasound location. Geophys J Int 181:399–405
Murai Y, Akiyama S, Katsumata K, Takanami T, Yamashina T, Watanabe T, Cho I, Tanaka M, Kuwano A, Wada N, Shimamura H, Furuya I, Zhao D, Sanda R (2003) Delamination structure imaged in the source area of the 1982 Urakawa-oki earthquake. Geophys Res Lett 30(9): 1490–1493
Negraru PT, Golden P, Herrin ET (2010) Infrasound propagation in the "Zone of Silence". Seismol Res Lett 81(4):614–624
Park J, Stump BW, Hayward CT, Arrowsmith SJ, Che I-Y (2011) Multiple-array detection, association, and location of infrasound and seismo-acoustic event—utilization of ground truth information. In: Proceeding of the 2011 monitoring research review: ground-based nuclear explosion monitoring technologies, vol 2, pp 798–807
Park J, Arrowsmith SJ, Hayward C, Stump BW, Blom P (2014) Automatic infrasound detection and location of sources in the western United States. J Geophys Res Atmos 119:7773–7798. https://doi.org/10.1002/2013JD021084
Park J, Stump BW (2014) Seasonal variations of infrasound detections and their characteristics in the western US. Geosci J 19(1):97–111
Park J, Stump BW, Hayward C, Arrowsmith SJ, Che I-Y, Drob D (2016) Detection of regional infrasound signals using array data—testing, tuning, and physical interpretation. J Acoust Soc Am 140(1):239–259
Park J, Hayward C, Zeiler CP, Arrowsmith SJ, Stump BW (2017) Assessment of infrasound detectors based on analyst review, environmental effects, and detection characteristics. Bull Seism Soc Am 107(2)
Rind DH, Donn WL (1978) Infrasound observations of variability during stratospheric warmings. J Atmos Sci 35:546–553
Rodgers AJ, Walter WR (2002) Seismic discrimination of the May 11, 1998 Indian nuclear test with short-period regional data from Station NIL (Nilore, Pakistan). Pure Appl Geophys. 159:679–700
Shumway RH, Kim S, Blandford RR (1999) Nonlinear estimation for time series observed on arrays, In Ghosh S (ed) Asymptotics, nonparametrics, and Time Series 227–258 Dekker, New York

Stump B, Jun MS, Hayward C, Jeon JS, Che I-Y, Thomason K, House SM, McKenna J (2004) Small-aperture seismo-acoustic arrays: design, implementation, and utilization. Bull Seism Soc Am 94(1):220–236

Stump B, Zhou R, Kim T, Chen Y, Yang Z, Herrmann R, Burlacu R, Hayward C, Pankow K (2008) Shear velocity structure in NE Chinar and characterization of infrasound wave propagation in the 1–210 kilometer range. In: Proceedings of the 29th monitoring research review: ground-based nuclear explosion monitoring technologies, Rancho Mirage, California, LA-UR-08-05261, Los Alamos National Laboratory, Los Alamos, NM, pp 287–296

Stump BW, Park J, Hayward C, Arrowsmith S, Che I-Y (2012) Performance assessment of multi-array processing with ground truth for infrasonic, seismic and seismo-acoustic events, Final report, AFRL-RV-PS-TR-2012–0123

Stump BW, Park J, Che I-Y, Hayward C (2016) Seismic and infrasound characteristics of North Korean nuclear explosions utilizing regional data, 12–16 December 2016 AGU Fall Meeting, San Francisco, CA, USA

Vortman LJ (1968) Air blast from underground explosions as a function of charge burial. Ann N Y Acad Sci 152(1):362–377. https://doi.org/10.1111/j.1749-6632.1968.tb11988.x

Walker KT, Shelby R, Hedlin MAH, de Groot-Hedlin C, Vernon F (2011) Western U.S. Infrasonic Catalog: Illuminating infrasonic hot spots with the USArray. J Geophys Res 116:B12305. https://doi.org/10.1029/2011jb008579

Walter WR, Taylor SR (2001) A revised magnitude and distance amplitude correction (MDAC2) procedure for regional seismic discriminants: theory and testing at NTS, Lawrence Livermore National Laboratory Report

Whitaker RW, Sondoval TD, Mutschlecner JP (2003) Recent infrasound analysis. In: Proceedings of the 25th seismic reserch review—nuclear explosion monitoring: building the knowledge base, 646–654, National Nuclear Security Administration, Tucson, Ariz

Whitaker RW (2007) Infrasound signals as basis for event discriminants. In: Proceedings of the 29th monitoring research review: ground-based nuclear explosion monitoring Technologies, National Nuclear Security Administration, Washington, DC., pp 905–913

Williams ED, Adams ML, Brooks L, Bowyer TW, Cobb DD, Garwin RL, Jeanloz R, Mies R, Tarter CB, Sykes LR, Hartse H, Richards RG, Vink GVD, Walter WR (2012) The comprehensive nuclear test ban treaty: technical issues for the United States. National Academy of Sciences, pp 45–52

Part IV
Observations – From Local to Global: Global Network Calibration

Chapter 12
Large Meteoroids as Global Infrasound Reference Events

Christoph Pilger, Lars Ceranna, Alexis Le Pichon and Peter Brown

Abstract The explosive fragmentation of large meteoroids entering the Earth's atmosphere is one of the strongest sources of infrasound and can be detected at distances of thousands of kilometers by arrays all over the world. Influence parameters on the detection capability are quantified for a single infrasound station and for the complete infrasound network of the International Monitoring System (IMS) operated by the Comprehensive Nuclear-Test-Ban Treaty Organization (CTBTO). They are applied to a number of strong bolides of the past 15 years including the 2013 Chelyabinsk, 2010 Sulawesi, and 2009 North Pacific events. Long-range infrasound propagation modeling and realistic atmospheric background conditions are used to identify propagation paths that connect the sources and globally distributed receivers, highlighting usual as well as unusual propagation pattern, to stations detecting and stations not detecting a meteorite event. Potential influences on infrasound detection capability are due to the directivity of the acoustic source energy emission, the long-range ducting via stratosphere and thermosphere and the diurnal change of meteorological parameters and noise conditions at the stations during the signal arrivals. Since infrasound of large bolides has probably the most similar characteristics to an atmospheric nuclear explosion, it can be utilized as reference event for studies on the global performance of the CTBTO infrasound network. Detections and non-detections of bolide infrasound at the more than 40 operational IMS infrasound stations are studied for the estimation of station and network performance and thus verification of nuclear test ban.

C. Pilger (✉) · L. Ceranna
Federal Institute for Geosciences and Natural Resources (BGR),
Hannover, Germany
e-mail: christoph.pilger@bgr.de

A. Le Pichon
CEA, DAM, DIF, F-91297 Arpajon, France

P. Brown
Department of Physics and Astronomy, University of Western Ontario,
London, ON, Canada

A. Le Pichon et al. (eds.), *Infrasound Monitoring for Atmospheric Studies*,
https://doi.org/10.1007/978-3-319-75140-5_12

12.1 Introduction

The explosive fragmentation of large meteoroids entering the Earth's atmosphere is one of the strongest existing sources of infrasonic waves and can be detected by infrasound arrays all over the world. Pressure perturbations of the strongest bolide events were detected at distances of thousands of kilometers, while for the 2013 Chelyabinsk superbolide, arrivals at long orthodrome distances (above 20,000 km) and after complete circumnavigations of the globe (up to 87,000 km) were recorded. This event was quantified having an equivalent explosive yield of up to 500 kt of TNT, being the most energetic global reference event ever recorded by the infrasound component of the International Monitoring System (IMS) network operated by the Comprehensive Nuclear-Test-Ban Treaty Organization (CTBTO) (Marty 2019).

Influence parameters on the detection capability of a single infrasound station on the one hand and of the complete global IMS infrasound network on the other hand are investigated within this study and applied to a number of strong meteoroid events of the past 15 years. Long-range infrasound propagation modeling and realistic atmospheric background conditions are used to identify propagation paths that connect the sources and globally distributed receivers. Infrasound propagation modeling calculations are performed to all IMS stations, highlighting usual as well as unusual propagation pattern, to stations detecting and stations not detecting a meteoroid event. Potential influences on infrasound detection capability are due to the directivity of the acoustic source energy emission, the long-range ducting via stratosphere and thermosphere, and the diurnal change of meteorological parameters and noise conditions at the stations during the signal arrivals.

Since the explosive fragmentation of large bolides during their atmospheric entry generates infrasound that shows probably the most similar characteristics to an atmospheric nuclear explosion, having comparable yields and generating similar pressure signatures, it can be utilized as reference event for studies on the global performance of the CTBTO infrasound network. Detections and non-detections of meteoroid infrasound at the more than 40 operational IMS infrasound stations are studied for the estimation of station and network performance and thus verification of nuclear test ban.

12.2 Infrasound from Meteoroids

Meteoroids are fragments of comets, asteroids, and planetoids entering the Earth's atmosphere. During their descent toward the surface, they heat up, disintegrate, fragment, or explode at certain altitudes typically between 10 and 100 km. Some fragments may even reach the ground and leave impact craters and remaining material, so-called meteorites. The luminous effect of heating up and exploding in the atmosphere is called meteor or fireball, while the body entering the atmosphere is often called bolide or meteoroid. The term meteoroid is further used in this chapter to

describe the material as well as the event of entry and explosion, generating shockwaves detectable as infrasound in the atmosphere (Silber and Brown 2019).

Infrasound generated by meteoroids is either a product of the trajectory of the atmospheric entry or of the final fragmentation and explosion at the end of the trajectory, while infrasound from the impact of meteorite remnants on the surface is a tertiary negligible effect for this study. Depending on the origin of the infrasound, a line source characteristic can be assumed to be due to the extended cylindrical shape of the trajectory and a point source due to a spherical explosion at the point of fragmentation (see Ens et al. 2012; Silber and Brown 2014; Henneton et al. 2015).

Infrasound from the line or point source origin propagates through the atmosphere and can be detected by infrasound arrays, as, e.g., the IMS infrasound stations distributed all over the globe. Comparable to an atmospheric nuclear or conventional explosion, the yield of the exploding meteor and generated shock wave can be quantified in kilotons of TNT equivalent (1 kt TNT = 4.185×10^{12} J). Empirical relations (e.g., Silber and Brown 2019) are used to estimate the kinetic energy of meteoroids entering the atmosphere and compare it to the explosive yields observed and quantified by remote sensing, optical observations, and pressure recordings. The frequency content of meteoroid infrasound detected at remote infrasound stations is mainly situated at frequencies below 1 Hz, since higher frequencies are attenuated after long-range propagation in the atmosphere. The stronger the yield of a meteoroid event, the lower is the dominant frequency containing most of the acoustic energy. Large bolides with tens to hundreds of kt TNT equivalents have dominant frequencies as low as 0.1–0.025 Hz (periods of 10–40 s).

One of the first meteoroid events scientifically investigated and recorded by early microbarometers (see Whipple 1930) is the Tunguska meteoroid of the 30 June 1908, where a large meteoroid exploded over Siberia at approximately 10 km altitude with a very strong yield estimated as high as 10–12.5 Mt TNT. Other strong meteorite events during the following decades were investigated by improved observation technology and their characteristics quantified by novel scientific approaches (see ReVelle 1997; Edwards 2010; Silber and Brown 2019 for an overview on the history and physics of meteor generated infrasound).

With the beginning of IMS infrasound operations and the construction of stations in a global network in the late 1990 and early 2000 years, the number of long-range and global scale detections of meteoroid events strongly increased and a number of prominent meteoroid events were detected by multiple IMS infrasound stations in the following years as well as documented in scientific literature. Table 12.1 lists a number of these events and some characteristics as reported in the corresponding literature (Brown et al. 2002; Arrowsmith et al. 2008; Silber et al. 2011; Arrowsmith et al. 2013; Le Pichon et al. 2013).

The extraordinary meteoroid of Chelyabinsk, Russia in 2013 was the strongest infrasound event recorded since the beginning of the IMS infrasound network operations and its yield was estimated with half a megaton TNT equivalent (Brown et al. 2013). Until that time, all prior detections of the IMS network were only investigated with respect to the direct, shortest line connection between the infrasonic source and the signal detecting array, the so-called short orthodrome.

Table 12.1 Large meteoroid events recorded by multiple IMS stations

Event	Region	Yield (kt TNT equivalent)	Number of detecting IMS stations	Maximum observation distance (km)
25 Aug 2000	Western Pacific	3	3	5,925
23 Apr 2001	Western Pacific	1–10	4	9,526
03 Sep 2004	Antarctica	12	6	12,918
07 Oct 2004	Indian Ocean	10–20	6	17,241
09 Dec 2006	Egypt	10–20	6	11,629
08 Oct 2009	Sulawesi	31–50	17 (23 after reanalysis)	17,509
25 Dec 2010	North Pacific	33	12 (21 after reanalysis)	14,906
15 Feb 2013	Chelyabinsk	500	20 (32 total detections)	86,663

For the Chelyabinsk meteoroid, a systematic analysis was performed (Le Pichon et al. 2013) to also identify signatures traveling long orthodrome paths between source and receivers (at distances of 20,000–40,000 km) and those, which circumnavigated the globe once or twice and were still detected at certain infrasound stations. A total of 12 more detections between 20,000 and 87,000 km were identified.

Due to the fact that strong infrasound source signals can potentially travel longer distances than 20,000 km and still be detectable, the next strongest meteoroid events of the last years (Sulawesi 2009 and North Pacific 2010) are reanalyzed within this study and compared to Chelyabinsk results to identify further station detections, focusing on long-range propagation and global detections even along the long orthodrome.

12.3 The Chelyabinsk, Sulawesi, and North Pacific Meteoroid Events

The Chelyabinsk meteoroid descended and disintegrated over the Ural Mountains with meteorite fragments up to 650 kg reaching the surface near the Russian town of Chelyabinsk and the nearby lake Cherbakul. Astronomical observations (Borovička et al. 2013) identified the object as a small asteroid with an initial diameter of about 17–20 m and a mass of 10,000 tons. The visually observed trajectory was 254 km long with a westward azimuth direction and a shallow elevation angle. The absolute brightness estimated from video records peaked with

a value of −28 mag. at approximately 30 km altitude (Brown et al. 2013), categorizing the event as a superbolide temporarily brighter than the sun. A shock wave of the atmospheric entry affected buildings, smashed windows, and was multiply eye-witnessed (Popova et al. 2013). Visual recordings, including movies, of the fireball entering the atmosphere, fragmenting and descending toward the surface were available shortly after the event. The event was recorded by various remote sensing techniques, as, e.g., optical observations by ground-based and satellite instruments, seismometers, and infrasound sensors (Heimann et al. 2013; Miller et al. 2013; Tauzin et al. 2013; Antolik et al. 2014; Krasnov et al. 2014; de Groot-Hedlin and Hedlin 2014).

In contrast to the large attention of worldwide media to this event, the Sulawesi and North Pacific meteoroid events happened with a relatively low level of media response and public interest. Thunder-like sounds and ground-shaking were reported for the Sulawesi event near the city of Bone, South Sulawesi, Indonesia and the event was also captured on amateur video (see Silber et al. 2011 and references therein), but apart from this no damage was reported; in the case of the North Pacific meteoroid, the event happened above the Pacific Ocean and far from the shore. Nevertheless, observations by remote sensing means and the infrasound detections of the IMS provided information about these two events and initiated further research with regard to these cases (Silber et al. 2011; Arrowsmith et al. 2013).

The Sulawesi meteoroid entered the atmosphere over an island region of Indonesia at a very steep elevation angle in a south-southwest to north-northeast direction. The height of maximum brightness and final fragmentation/explosion was 19.1 km, although prolonged fragmentation between 20 and 30 km altitude likely took place. The North Pacific meteoroid entered the atmosphere about 1500 km east of Japan with an initial mass of about 820 tons, diameter of 7.5–8 m, and a steep elevation angle in a northwest to southeast direction. Table 12.2 summarizes the characteristics of atmospheric entry for the three meteoroid events.

Figure 12.1 shows the global detections of the IMS infrasound network in short and long orthodrome distances from the Chelyabinsk, Sulawesi and North Pacific meteoroids for 2 days following each event. Chelyabinsk detections are shown as

Table 12.2 Characteristics of the Sulawesi, North Pacific, and Chelyabinsk meteoroid events

	Sulawesi	North Pacific	Chelyabinsk
Explosion location	4.2°S, 120.6°E	38°N, 158°E	54.8°N, 61.1°E
Explosion altitude (km)	30	19.1	26
Time of entry (UTC)	08 Oct 2009, 02:57	25 Dec 2010, 23:24	15 Feb 2013, 03:20
Azimuth angle (°)	27.5	147.2	279.5
Elevation angle (°)	67.5	61	16.5
Speed (km/s)	19	22.1	18.5
Explosive yield (kt)	31–50	33	500

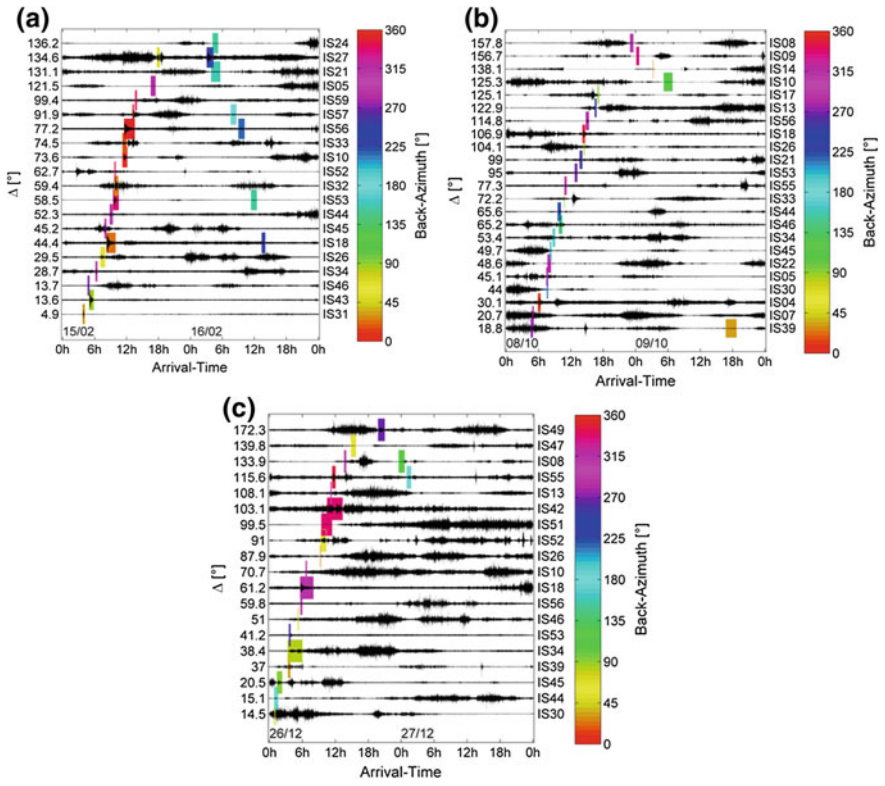

Fig. 12.1 Barograms for 2 days following **a** the Chelyabinsk 2013, **b** the Sulawesi 2009 and **c** the North Pacific 2010 meteoroid event. Averaged phase-aligned recordings of the detecting IMS infrasound stations are shown using normalized amplitude. Arrival time is given in UTC, stations are sorted by propagation distance in degrees from the source (where 360° are one circumference of the Earth, 1° ≈ 110 km). Signals are band-pass filtered between 15 and 80 s. Detections of the short (0–180°) and long (180–360°) orthodrome arrivals are indicated by colored rectangles with corresponding signal duration and color-coded back azimuth

described in Le Pichon et al. (2013), while Sulawesi and North Pacific detections result from a very broadband PMCC reanalysis performed at the German NDC.

The reanalysis was performed using PMCC (Cansi 1995) version 4 with 23 frequency bands between 0.02 and 4 Hz, having the advantage of logarithmic scaled frequency stepping and an aligned window length from 500 to 30 s accounting for multiple cycles within each band.

In comparison to the number of already identified detections for the Sulawesi and North Pacific bolides described in literature (see Table 12.1), the reanalysis defined a higher number of detecting stations and total detections from the two

events. Furthermore, some long orthodrome (>20,000 km) detections were identified for both events. One of the main goals of a complete reanalysis for these two events was to identify, if the Chelyabinsk meteoroid was a singular event generating such long-range infrasound that was also detectable on global scales or if other events were also strong enough to generate similar long-range signatures. No further signals were identified that circumnavigated the globe completely and were still detectable afterwards, but a number of detections between 20,000 and 40,000 km were identified for each event, increasing the range of interest for PMCC analyses, propagation modeling and global detection capability to the long orthodrome.

Two additional short orthodrome detections and five more long orthodrome detections were identified for the Sulawesi meteoroid using the PMCC reanalysis. Most long orthodrome detections were situated in South America, antipodal to the source region. This and a potential detection at I39PW (Palau) are indicative of a focusing effect of acoustic energy near the antipode and source regions. For the North Pacific meteoroid, six short orthodrome and three long orthodrome detection were identified complementary to the prior registered station observations. Two of the long orthodrome detections are also located near the antipodal point supportive of a focusing effect.

Since Sulawesi and North Pacific meteoroids were quite similar in source yield, region of origin, and resulting detections, only detections of the North Pacific event will be highlighted in the following.

Figure 12.2 shows PMCC analyses for North Pacific meteoroid detections at IMS infrasound stations I08BO (Bolivia), I10CA (Canada), I26DE (Germany), and I55US (United States). All four stations detected the meteoroid event along the short orthodrome (in 307°, 306°, 27° and 352° back azimuth directions, respectively), three of these detections were also reported in the CTBTO reviewed event bulletin, the I26DE detection was identified during the reanalysis in the low-frequency bands with a short but distinct signature associated to the meteoroid.

Additionally, the stations I08BO (Fig. 12.2a) and I55US (Fig. 12.2d) detected potential long orthodrome signatures from the North Pacific event, which correspond to the event in back azimuth directions (127° and 172°, respectively) and estimated arrival times and show coherent signatures of low frequency, increased amplitude, and prolonged time duration. Other stations like I10CA (Fig. 12.2b) and I26DE (Fig. 12.2c) showed no long orthodrome signatures of the event. Potential reasons for this will be discussed in the following sections.

12.4 Infrasound Propagation Modeling

The modeling of infrasound propagation in the atmosphere can be performed using ray-tracing methods (e.g., Garcés et al. 1998; Drob et al. 2003, 2010; Pilger et al. 2013), even though this method is a high-frequency approximation applied here to low-frequency infrasound from large bolides. Within this study, a two-dimensional

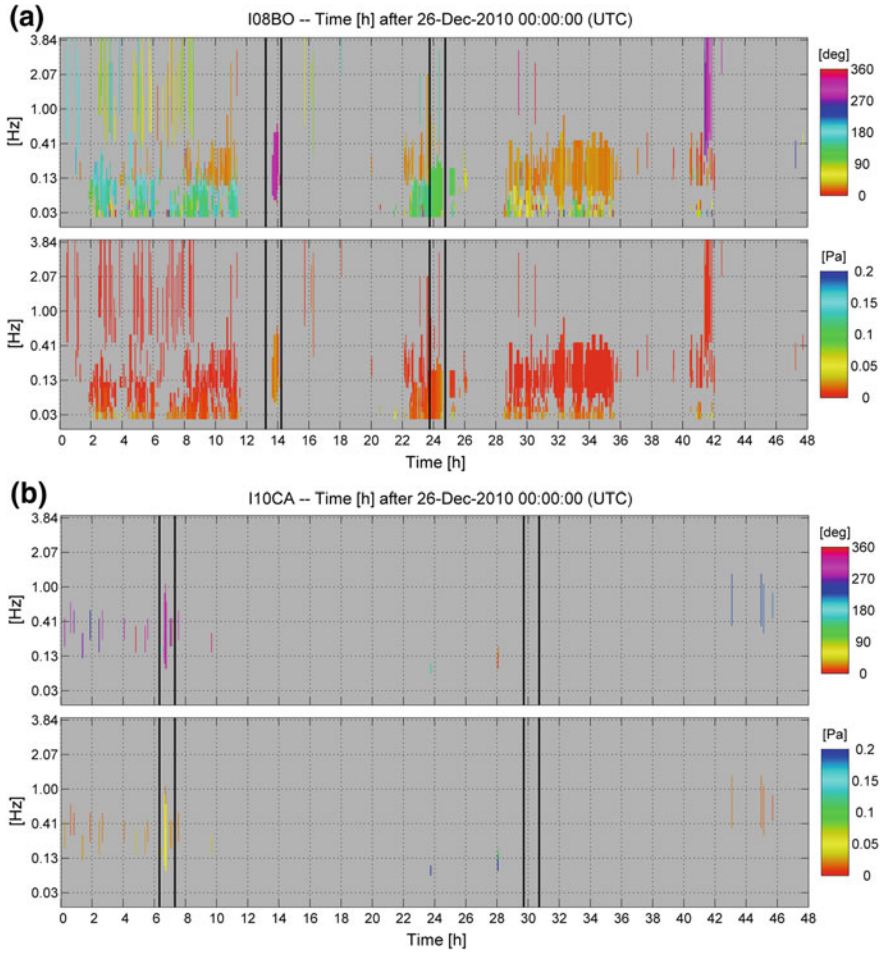

Fig. 12.2 PMCC analyses for 2 days following the North Pacific meteoroid event at **a** I08BO, **b** I10CA and **c** I26DE and **d** I55US. Color-coded information shows back azimuth directions in degree (upper frames) and amplitude in Pa (lower frames), frequencies range from 0.02 to 4 Hz (y-axes) and time ranges from 0 to 48 h following 26-Dec-2010, 00:00 UTC (x-axes). Vertical black bars frame 1 h windows of estimated signal arrival time using propagation modeling. Theoretical back azimuths expected for the meteoroid source in these frames are **a** 307° and 127°, **b** 306° and 126°, **c** 27° and 207°, **d** 352° and 172°. See text for further details

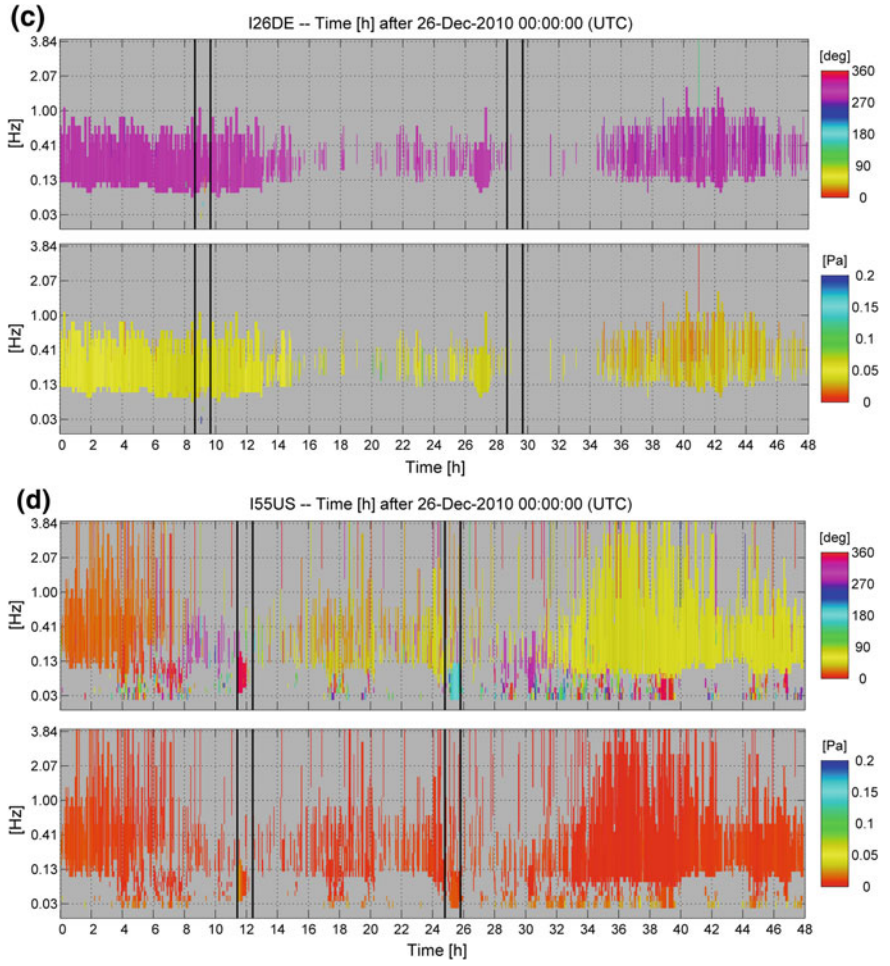

Fig. 12.2 (continued)

finite differences ray tracer is used, which is part of the Consortium for Research in Elastic Wave Exploration Seismology (CREWES) software package (see http://www.crewes.org/Reports/2000/2000-09.pdf written by Margrave).

Background atmospheric conditions within this study are modeled using temperature and wind profiles from global ECMWF-91 (www.ecmwf.int) reanalysis data with a horizontal resolution of 0.5°, merged at the top of the model (0.01 hPa) with MSISE-00 and HWM-07 climatologies (Picone et al. 2002; Drob et al. 2008) in order to extend the profiles into the thermosphere. Wind and temperature profiles are interpolated over a spatial grid of 200 m × 200 m resolution in range and altitude, respectively, as a prerequisite for ray tracing with the same resolution.

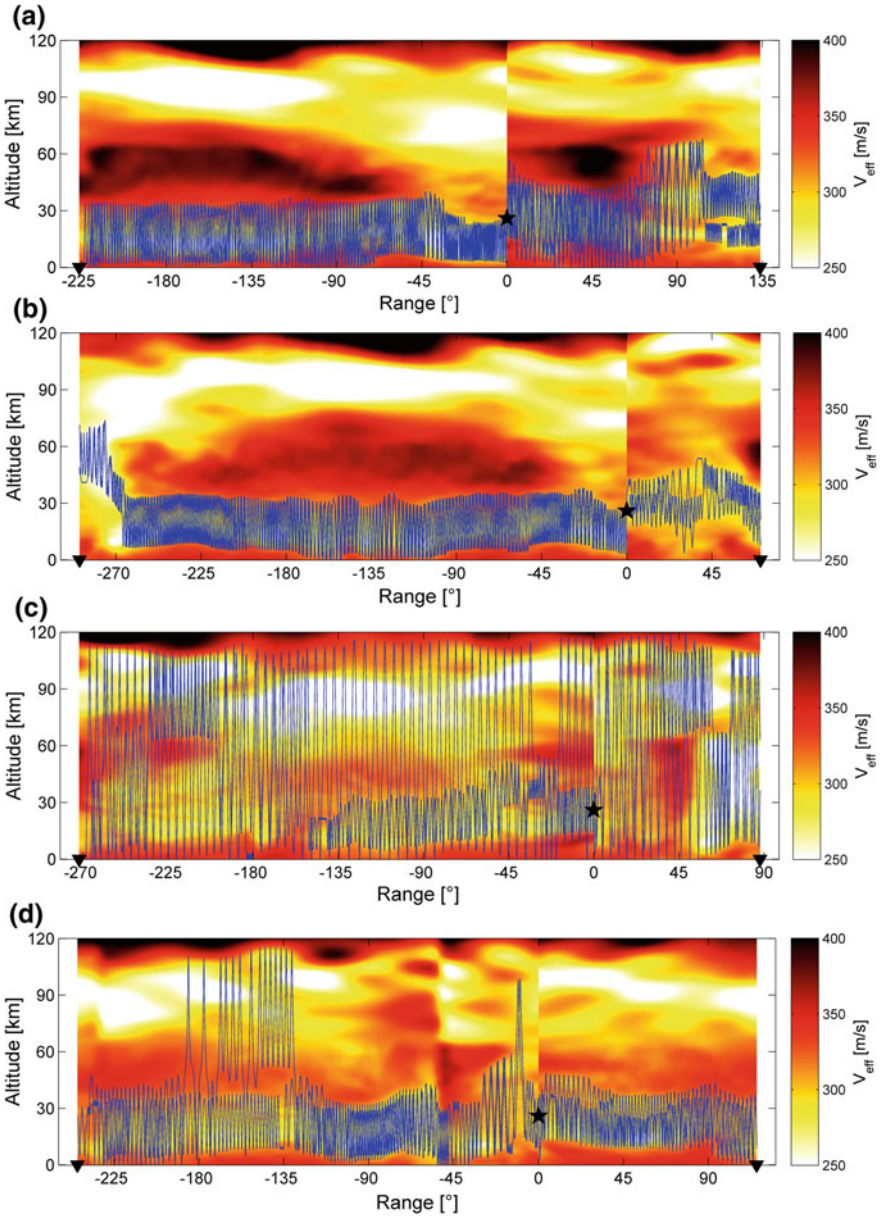

Fig. 12.3 Propagation paths from the main explosion source of the North Pacific meteoroid at 26 km altitude to stations **a** I08BO, **b** I10CA **c** I26DE and **d** I55US using a two-dimensional finite differences ray tracer. Range-dependent atmospheric specifications are given by the ECMWF-91 model on 26 December 2010 at 06:00 UTC. The effective sound speed is color-coded, where values larger than the sound speed at the ground level (darker color) indicate altitudes of minimum ray turning height. The blast source is indicated by the black star and the receiving stations by black triangles, propagation distance is given in degree from the source. Short orthodrome propagation is shown to the right, long orthodrome propagation to the left

From temperature and wind values, the effective sound speed is derived for all source-to-station propagation directions along short and long orthodromes.

Results of the modeling for the Chelyabinsk meteoroid are described and depicted in Le Pichon et al. (2013). Apart from prevalent short orthodrome modeling of source–receiver paths, also long orthodrome ray paths, and complete circumnavigations of the globe are described. The propagation from the Chelyabinsk source location to, e.g., IMS infrasound stations I21FR (Marquesas Islands, South Pacific) and I27DE (Antarctica) is modeled and displayed in short and long orthodrome stratospheric ducts, simultaneously. For both stations, the ducting conditions are more stable along the long orthodrome and these detections have a higher amplitude even though traveling a larger distance compared to short orthodrome propagation. I21FR detected the event only along the long orthodrome. The propagation to I26DE (Germany) also includes large portions of thermospheric ducting for the short orthodrome (Ig1) and a further detection after a complete circumnavigation of the globe (Ig3). Multiple circumnavigations of the globe and subsequent detections at stations as, e.g., I18DK (Greenland) and I53US (Alaska) after a maximum propagation distance of 87,000 km were also documented and reported in Le Pichon et al. (2013).

For the Sulawesi and North Pacific bolides no detections after complete circumnavigations of the globe were registered, but the reanalysis using PMCC version 4 revealed some cases of long orthodrome detections previously unnoticed. Corresponding propagation modeling defined the theoretic arrival times for these detections which were, in general, good agreement to the observations.

Figure 12.3 shows four source-to-station propagation cases for the North Pacific meteoroid event, corresponding to the stations selected in Fig. 12.2a–d, with the modeling runs along the short and long orthodrome performed simultaneously.

For I08BO (Fig. 12.3a) and I55US (Fig. 12.3d), the propagation mostly takes place in stratospheric wave ducts and corresponds well to the station detections (Fig. 12.2a, d) along both orthodromes. Segments of elevated ducting and some reflections at thermospheric altitudes seem to have no negative effects on detectability in these cases.

For I10CA (Fig. 12.3b), the short orthodrome propagation shows elevated stratospheric ducting, but the lower reflection height returns near the station to altitudes below 10 km, which in the order of the estimated infrasound wavelength and therefore low enough to permit a station detection corresponding to Fig. 12.2b. The signals following the long orthodrome path were not detected at this station, which might be due to the elevated ducting in the end of the propagation to altitudes of 40 km and above, which is a multiple of the infrasound wavelength and probably too high for any detection. Noise conditions at the station and the large distance could furthermore be a reason for this long orthodrome non-detection.

For I26DE (Fig. 12.3c), the short orthodrome propagation only allows thermospheric ray paths to connect the source with the station. Although thermospheric propagation takes place over a large distance of 90° (10,000 km), a short orthodrome detection of the North Pacific meteoroid was identified at I26DE (see the previous section) which corresponds to the modeled thermospheric propagation. No

long orthodrome detection was identified at I26DE, which is well in agreement with no clear stratospheric duct along the long orthodrome, but only thermospheric or mixed thermo/stratospheric ray paths over a total distance of 30,000 km, which might prohibit such a long-range detection.

12.5 Global Detectability

Events like the 2013 Chelyabinsk meteoroid are strong enough to generate infrasound that is in principle detectable for each IMS infrasound station around the globe, since signals from the event were detected up to (and beyond) the maximum distance of 20,000 km to any station of the global network. Nevertheless, effects like source-to-station ducting and ambient noise conditions might be favorable or unfavorable for individual stations and permit or prohibit signal detection from case to case.

Pilger et al. (2015) investigated influence parameters for the detection capability of the IMS infrasound stations with respect to the Chelyabinsk meteoroid event, taking into account short and long orthodrome propagation. Influence parameters identified within this study are the effective sound speed ratio governing stratospheric ducting, the directivity of the meteoroid source (assuming line source emission effects), and the diurnal change of ambient noise conditions.

Propagation conditions from the source to a receiving station are favorable when a stratospheric duct is established (see Fig. 12.3 and corresponding text) and the performance of this propagation can be expressed and quantified using the effective sound speed ratio between stratosphere and surface (see Le Pichon et al. 2012).

As soon as the source signal is no longer considered a point source, but the potential effects of a line source (the fireball trajectory entering the atmosphere) are also taken into account, the signal energy distribution is no longer uniform in all directions, but azimuth-dependent, favoring perpendicular directions with higher acoustic energy emission over parallel ones (e.g., see ReVelle et al. 2004; Edwards 2010).

The strongest influences on the detection capability identified and quantified in Pilger et al. (2015) were due to the noise conditions associated with diurnal changes of stability and turbulence in the surface-near atmospheric boundary layer. For a synoptic view of all worldwide locations, independent of single station locations with their individual characteristics, a global average of the station noise background differences between night and day was derived and integrated in the detection capability estimations as a simplified day-to-night change value.

A summation of the three aforementioned effects and relative quantification for a global synoptic view of the intensity effects influencing the global detection capability can be given by the following formula (Pilger et al. 2015):

$$Q_{synoptic} = 0.5 \cdot Q_{ducting} + Q_{directivity} + \mu \cdot Q_{daytime} \quad [dB]$$

To derive $Q_{synoptic}$ as dB quantified intensity ratio, effects from $Q_{ducting}$ for amplitude reduction due to propagation, $Q_{directivity}$ for the azimuth dependence and $Q_{daytime}$ for the diurnal change of noise conditions are summed. The effect of $Q_{ducting}$ is multiplied by 0.5 to convert from amplitude to energy ratio and the effect of a global all-station mean noise value $Q_{daytime}$ is multiplied by μ having values of 0 during nighttime and 1 during daytime. All Q values are negative, whereas ideal conditions are given by zero. See Pilger et al. (2015) for further details on the estimation and quantification of the different Q values.

Figure 12.4 shows a synoptic view of the influence parameters using a dB scale relative to ideal detection conditions (mean nighttime noise levels, perpendicular directions, and stratospheric ducting with high effective sound speed ratio).

It can be clearly observed from the synoptic view that the prerequisites for detection of the fireball event were favorable in Eastern Asia, North America, Greenland, Antarctica, and the Pacific Ocean while disadvantageous in Europe, Western Africa, South America, and the Atlantic Ocean. This distribution very well explains most of the short orthodrome detections and non-detections and many of the long orthodrome ones. The North America and Greenland region is especially favored by a synergy of the investigated influence conditions to also permit the observed Ig3 and Ig5 detections, while non-detections strongly cluster in the darker colored regions below the mean expectation value (contour line in Fig. 12.4).

To compare the Chelyabinsk meteoroid event with the other meteoroid test cases and investigate the general applicability of the derived influence parameters, synoptic views are also generated for the Sulawesi and North Pacific events in the same style as Fig. 12.4. Both events are similar in their nature, intensity, source region, and resulting detectability so only the North Pacific event is presented and further discussed here.

The influence of ducting and the corresponding effect of sound attenuation is quantified in the same manner as for Chelyabinsk meteoroid following Le Pichon et al. (2012). A central signal frequency of 0.1 Hz is chosen to derive the frequency-dependent decrease in signal amplitude due to long-range propagation depending on the effective sound speed ratio. Quantifying this effect results in a higher influence of ducting compared to its negligible influence in the Chelyabinsk case. This is due to the higher signal frequency chosen and the lesser total effect of the other influence parameters detailed hereafter.

Considering the influence of directivity, not only the azimuth direction of the atmospheric entry has to be taken into account for the Sulawesi and North Pacific meteoroids, but also the elevation angle. In contrast to the Chelyabinsk meteoroid case with a shallow entry angle of 16.5° and a long trajectory line within the atmosphere, Sulawesi and North Pacific have very steep entries (with 60–70° elevation angles) and correspondingly much shorter trajectories and line source effects on the acoustic energy emission. Quantifying the steepness effect with a cosine weighting function (where for Chelyabinsk the effect is already included in

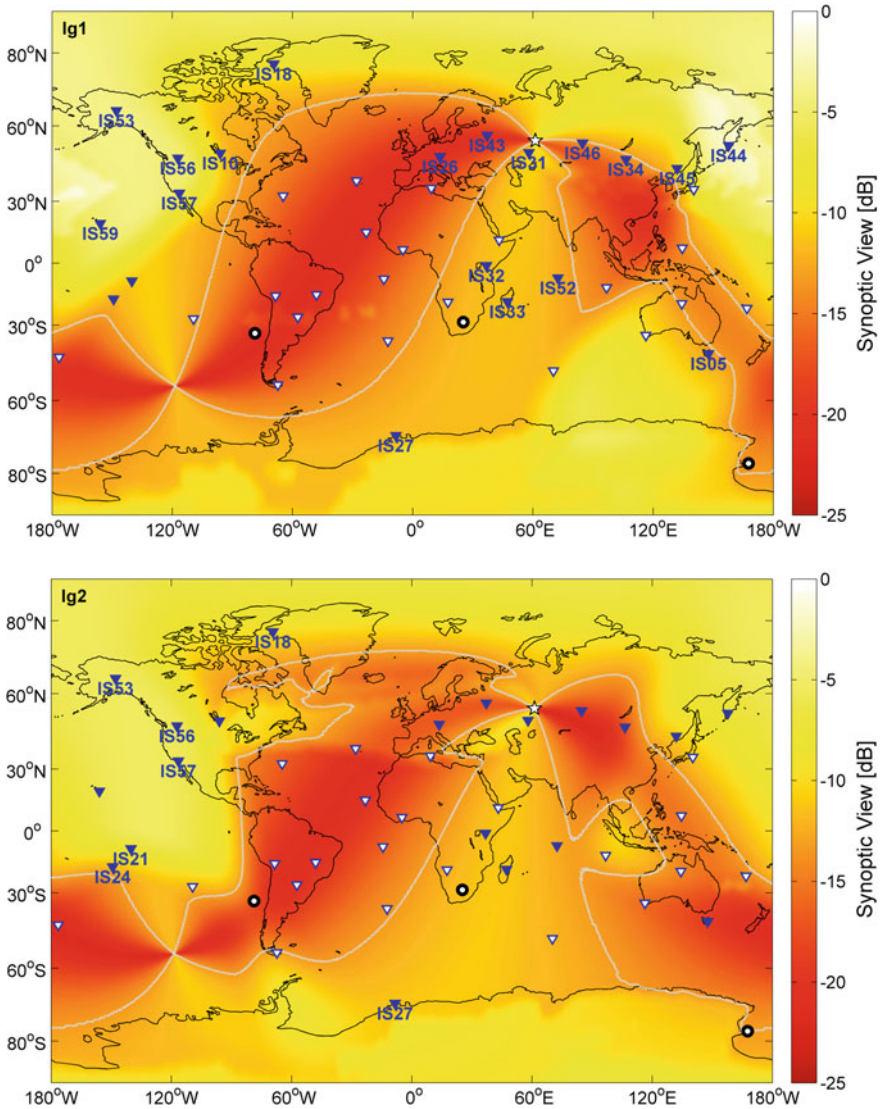

Fig. 12.4 Synoptic view of the Chelyabinsk meteoroid detection capability (including ducting, daytime, and directivity influences) along the short orthodrome (source–station distances 0–20,000 km, Ig1) and long orthodrome (source–station distances 20,000–40,000 km, Ig2) in dB (intensity reduction), respective to 0 dB for mean nighttime noise levels, perpendicular directions, and stratospheric ducting with high effective sound speed ratio. A contour line shows the all-station mean value at −13 dB, distinguishing regions above and below this average. Higher (lighter) values indicate increased detection probabilities for these conditions compared to lower (darker) values otherwise. Stations that performed Chelyabinsk detections are shown in blue and for detection along the specific orthodrome are labeled with their station number, while stations performing no detection are indicated by white triangles and temporary inoperable stations by an additional black circle. The Chelyabinsk meteoroid location is indicated by a white star

Fig. 12.4 but resulting in negligible changes since $\cos 16.5° \approx 1$), the North Pacific meteoroid steepness reduces the overall directivity effect by a factor of 2 ($\cos 61° \approx 0.5$). Favorable azimuth directions for most acoustic energy emission in this case are Southwest and Northeast (directions toward Japan and Northern America), while Southeastern and Northwestern directions are unfavorable since they are parallel to the trajectory.

The influence of the diurnal change was quantified only having two-thirds of the effect as in the Chelyabinsk case; a global all-station mean value of the noise intensity increase during daytime was derived investigating power spectra of all stations, which resulted in a 4.2 dB (intensity) noise increase during daytime for the North Pacific case compared to 6.5 dB (intensity) in the Chelyabinsk case (see Pilger et al. 2015 for the method used). For the moment, only a station derived mean value is used to distinguish day and nighttime effects on the ambient noise level and thus detection capability of a station, a more sophisticated approach using, e.g., the global distribution of a meteorological parameter like boundary layer height as a direct proxy for expected noise influences is currently under investigation.

In general, the effects of directivity and diurnal noise changes are weaker than in the Chelyabinsk case, while ducting influences are increased. Figure 12.5 summarizes the three effects of ducting, directivity and daytime for the North Pacific meteoroid event in a synoptic view of the same style as in Fig. 12.4.

Regions favorable for detection as derived from this synoptic view are along the short orthodrome (Ig1): Japan, Northern America, Greenland, most of the Arctic and Antarctic Region, Australia, Southern Africa, and the Indian Ocean. Observations agree with this for Japan, Northern America, Greenland, and Antarctica, but only 2 of 10 available stations between Southern Africa and Australia performed detections. On the other hand, 5 of 7 available stations in the Eurasian continent made detections although being in regions unfavorable for detections. Disagreements might be explained by increased ambient noise conditions for many of the Southern hemisphere island and shore locations and by relatively short distances and thus higher signal amplitudes at Northern Hemisphere stations even in thermospheric propagation directions (e.g., see Fig. 12.3c, station I26DE) and during noisier daytime conditions.

For the long orthodrome (Ig2), Southern America, the South Pacific Region, Antarctica, and Eastern Asia are in a favorable position for detections. This fairly well agrees with long orthodrome detections in IS08, Bolivia and IS55, Antarctica but is necessarily limited in completeness since only 3 of 41 stations have identified long orthodrome detections.

Another observation that can be made when comparing Figs. 12.4 and 12.5 is that the total content of intensity loss (in dB) is higher in the Chelyabinsk case than in the North Pacific case, they are about 1 dB higher in a global mean and about 1.5 dB for an all-station mean. Especially the contoured regions with high negative (red) dB values, which are unfavorable for detections, are more pronounced in the

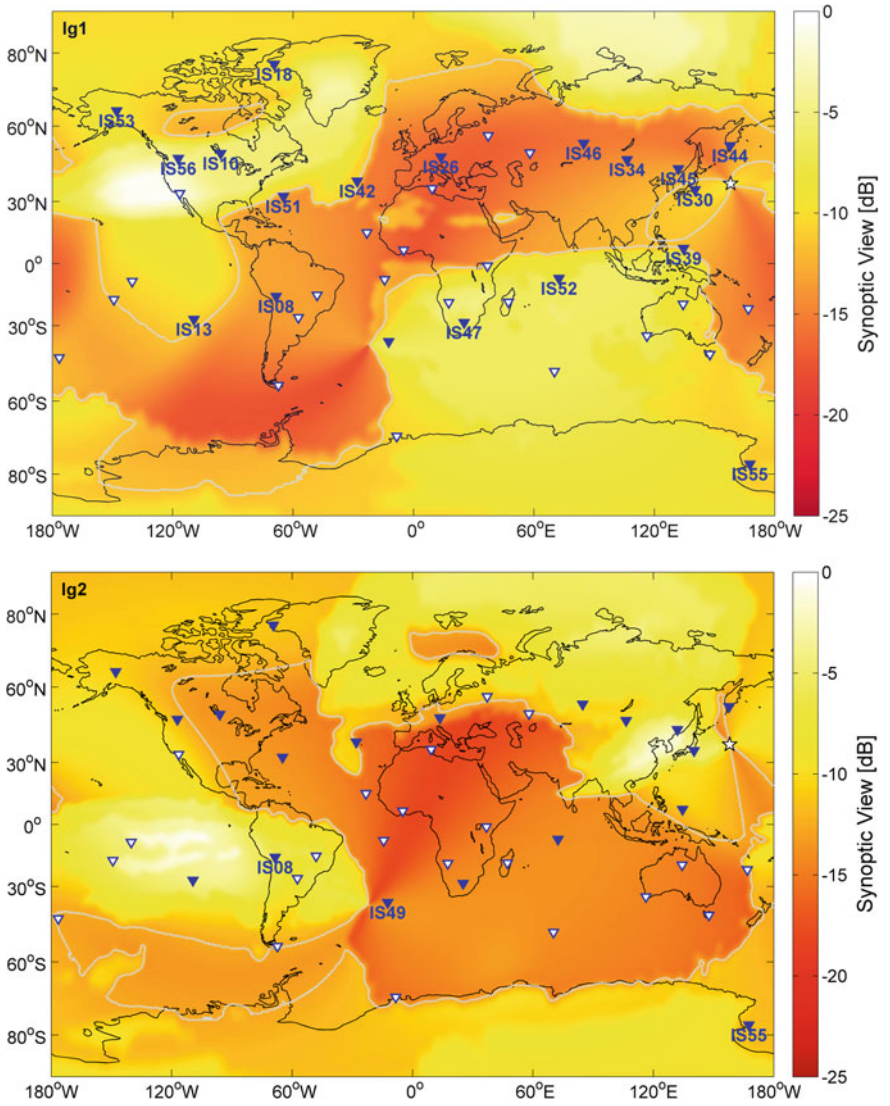

Fig. 12.5 Synoptic view for the North Pacific meteoroid event in the same style as Fig. 12.4. The contour line shows the all-station mean value at −11.5 dB

Chelyabinsk case and smoother in the North Pacific case. This well corresponds to a stronger effect of the influence parameters, especially directivity and diurnal noise changes, on detection capability in the Chelyabinsk case. Regions favorable or unfavorable for detections are strongly delimited from each other and observations very well fit this pattern, whereas for the North Pacific case, the boundary between

both regions is much smoother and many stations have observation although in unfavorable regions and vice versa. Detection capability parameters derived for the Chelyabinsk meteoroid event can thus only to a certain degree be applied to other strong meteoroid events.

12.6 Conclusions on Global Reference Events

Pilger et al. (2015) identified and quantified parameters that influence the detection capability of infrasound at global distances for the 2013 Chelyabinsk meteoroid as reference event. The parameters in the order from most to least influence were diurnal noise variation, line source directivity, and infrasound ducting.

Comparisons to other large meteoroid events of the last years in the course of this study revealed that the order and importance of the abovementioned influence parameters can change for other meteoroid events and that further specifications of these factors should be taken into account as well. These include not only the trajectories azimuth angle for directivity calculations but also the elevation angle, where a steeper entry angle into the atmosphere reduces the trajectory length and thus the influence of this parameter on detection capability.

Furthermore, the influence of diurnal changes of the ambient noise conditions could not only be estimated by a global or station-dependent mean value, but by a globally available time-dependent proxy, probably a meteorological value like the boundary layer height. To apply this parameter, further investigations on the latitude-dependent influence of the boundary layer on the ambient station noise are needed and other effects like station parameters as well as temperature and wind conditions also have to be taken into account.

In the context of ducting influences on detection capability, studies by Le Pichon et al. (2009, 2012) provide quantifications of the attenuation and signal amplitude reduction during stratospheric propagation and thus detection and location capability of the global IMS network (Ceranna et al. 2019). The propagation modeling performed for the Chelyabinsk and North Pacific meteoroid events moreover showed that also thermospheric propagation and arrivals (e.g., at I26DE) can be expected and this propagation component should be taken into account for ducting influence quantifications as well.

Investigations for the Chelyabinsk meteoroid showed that the ambient noise conditions and their diurnal changes have the strongest effect on detectability, whereas directivity had next strongest influences but was nearly independent of the elevation angle, since it was a very shallow entry into the atmosphere. Ducting effects were nearly negligible due to very low signal frequencies and thus attenuation values.

In contrast, for the North Pacific (and similarly the Sulawesi) meteoroid, directivity effects were reduced due to very steep entry angles and diurnal changes of the ambient noise conditions also had reduced global influence values, thus leaving ducting as a much stronger influence parameter.

It is concluded that the Chelyabinsk event on the one hand was a singular event with extraordinary strong yield and thus large acoustic energy emission over very long distances with very low signal frequencies, which resulted in a detection capability quite independent of propagation and attenuation, while on the other hand the classical estimation of detection capability relying on ducting and damping effects better suits for the other meteoroid events. These events also have yield estimates of more than one order of magnitude less compared to the Chelyabinsk case, which makes the 2013 Chelyabinsk meteoroid quite a unique infrasound source providing unprecedented insights in quantifying global infrasound detectability even at long orthodrome distances.

Studies provided here identifying influence parameters and generating synoptic views (Figs. 12.4 and 12.5) only take into account the comparison of relative values (day vs. night, perpendicular vs. parallel, high vs. low effective sound speed ratios) and cannot reflect absolute values as, e.g., the amplitudes observed at certain stations. To incorporate absolute values and directly compare them to observations, more sophisticated source models, improved propagation and distance effects, individual station performances including ambient noise models and technical specifications as well as global high-resolution specifications of meteorological background conditions have to be taken into account.

Studies on strong meteoroid events generally allow allocatable observations to be compared to model quantifications and thus support the investigation of potential influence parameters and estimation of new approaches to demonstrate the usefulness of meteorites as global reference events for CTBT (atmospheric) explosion monitoring and verification purposes.

The study of meteoroids as global infrasound reference events provided new insights to global infrasound detection capability and network performance, also supporting "lessons learnt from a comprehensive and global infrasound monitoring" (Le Pichon et al. 2019).

References

Antolik M, Ichinose G, Creasey J, Clauter D (2014) Seismic and infrasonic analysis of the major bolide event of 15 February 2013. Seismol Res Lett 85(2):334–343. https://doi.org/10.1785/0220130061

Arrowsmith SJ, Re Velle DO, Edwards W, Brown PG (2008) Global detection of infrasonic signals from three large bolides. Earth Moon Planet 102:357–363. https://doi.org/10.1007/s11038-007-9205-z

Arrowsmith SJ, Marcillo O, Drob DP (2013) A framework for estimating stratospheric wind speeds from unknown sources and application to the 2010 December 25 bolide. Geophys J Int 2013. https://doi.org/10.1093/gji/ggt228

Borovicka J, Spurny P, Brown PG, Wiegert P, Kalenda P, Clark D, Shrbeny L (2013) The trajectory, structure and origin of the Chelyabinsk asteroidal impactor. Nature 503:235–237. https://doi.org/10.1038/nature12671

Brown PG, Whitaker RW, ReVelle DO (2002) Multi-station infrasonic observation of two large bolides: signal interpretation and implications for monitoring of atmospheric explosions. Geophys Res Lett 29. https://doi.org/10.1029/2001gl013778

Brown PG et al (2013) A 500-kt airburst over Chelyabinsk and an enhanced hazard from small impactors. Nature 503:238–241. https://doi.org/10.1038/nature12741

Cansi Y (1995) An automatic seismic event processing for detection and location: the PMCC method. Geophys Res Lett 22:1021–1024. https://doi.org/10.1029/95GL00468

Ceranna L, Matoza R, Hupe P, Le Pichon A, Landès M (2019) Systematic array processing of a decade of global IMS infrasound data. In: Le Pichon A, Blanc E, Hauchecorne A (eds) Infrasound monitoring for atmospheric studies, 2nd edn. Springer, Dordrecht, pp 471–482

De Groot-Hedlin C, Hedlin MAH (2014) Infrasound detection of the Chelyabinsk meteor at the USArray. Earth Planet Sci Lett 402:337–345. https://doi.org/10.1016/j.epsl.2014.01.031

Drob DP, Picone JM, Garcés M (2003) Global morphology of infrasound propagation. J Geophys Res 108(D21):4680. https://doi.org/10.1029/2002JD003307

Drob DP et al (2008) An empirical model of the Earth's horizontal wind fields:HWM07. J Geophys Res 113:A12304. https://doi.org/10.1029/2008JA013668

Drob DP, Garcés M, Hedlin MAH, Brachet N (2010) The temporal morphology of infrasound propagation. Pure Appl Geophys 167:437–453. https://doi.org/10.1007/s00024-010-0080-6

Edwards WN (2010) Meteor generated infrasound: theory and observation. Infrasound monitoring for atmospheric studies. Springer, Heidelberg, Germany, pp 361–414

Ens TA, Brown PG, Edwards WN, Silber EA (2012) Infrasound production by bolides: a global statistical study. J Atmos Sol Terr Phys 80:208–229. https://doi.org/10.1016/j.jastp.2012.01.018

Garcés M, Hansen RA, Lindquist KG (1998) Traveltimes for infrasonic waves propagating in a stratified atmosphere. Geophys J Int 135:255–263. https://doi.org/10.1046/j.1365-246X.1998.00618.x

Heimann S, Gonzáles Á, Wang R, Cesca S, Dahm T (2013) Seismic characterization of the Chelyabinsk meteor's terminal explosion. Seismol Res Lett 84(6):1021–1025. https://doi.org/10.1785/0220130042

Henneton M, Gainville O, Coulouvrat F (2015) Numerical simulation of sonic boom from hypersonic meteoroids. AIAA J 53(9):2560–2570. https://doi.org/10.2514/1.J053421

Krasnov VM, Drobzheva YV, Salikhov NM, Zhumabaev BT, Lazurkina VB (2014) Estimation of the power of the Chelyabinsk meteorite blast from optical, seismic, and infrasonic observation data. Acoust Phys 60(2):155–162. https://doi.org/10.1134/S1063771014020110

Le Pichon A, Vergoz J, Blanc E, Guilbert J, Ceranna L, Evers L, Brachet N (2009) Assessing the performance of the International Monitoring System's infrasound network: geographical coverage and temporal variabilities. J Geophys Res 114:D08112. https://doi.org/10.1029/2008JD010907

Le Pichon A, Ceranna L, Vergoz J (2012) Incorporating numerical modeling into estimates of the detection capability of the IMS infrasound network. J Geophys Res 117:D05121. https://doi.org/10.1029/2011JD016670

Le Pichon A, Ceranna L, Pilger C, Mialle P, Brown D, Herry P, Brachet N (2013) The 2013 Russian fireball largest ever detected by CTBTO infrasound sensors. Geophys Res Lett 40:3732–3737. https://doi.org/10.1002/grl.50619

Le Pichon A, Ceranna L, Vergoz J, Tailpied D (2019) Modeling the detection capability of the global IMS infrasound network. In: Le Pichon A, Blanc E, Hauchecorne A (eds) Infrasound monitoring for atmospheric studies, 2nd edn. Springer, Dordrecht, pp 593–604

Marty J (2019) The IMS infrasound network: current status and technological developments. In: Le Pichon A, Blanc E, Hauchecorne A (eds) Infrasound monitoring for atmospheric studies, 2nd edn. Springer, Dordrecht, pp 3–62

Miller SD, Straka WC III, Bachmeier AS, Schmit TJ, Partain PT, Noh Y-J (2013) Earth-viewing satellite perspectives on the Chelyabinsk meteor event. Proc Natl Acad Sci USA 110:18092–18097. https://doi.org/10.1073/pnas.1307965110

Picone JM, Hedin AE, Drob DP, Aikin AC (2002) NRLMSISE-00 empirical model of the atmosphere: statistical comparisons and scientific issues. J Geophys Res 107:1468–1483. https://doi.org/10.1029/2002JA009430

Pilger C, Streicher F, Ceranna L, Koch K (2013) Application of propagation modeling to verify and discriminate ground-truth infrasound signals at regional distances. Inframatics 2013 2:39–55. https://doi.org/10.4236/inframatics.2013.24004

Pilger C, Ceranna L, Ross JO, Le Pichon A, Mialle P, Garcés M (2015) CTBT infrasound network performance to detect the 2013 Russian fireball event. Geophys Res Lett 42. https://doi.org/10.1002/2015gl063482

Popova OP et al (2013) Chelyabinsk airburst, damage assessment, meteorite recovery, and characterization. Science 342:1069–1073. https://doi.org/10.1126/science.1242642

ReVelle DO (1997) Historical detection of atmospheric impacts by large bolides suing acoustic-gravity waves. Ann N Y Acad Sci 822:284–305. https://doi.org/10.1111/j.1749-6632.1997.tb48347.x

ReVelle DO, Brown PG, Spurny P (2004) Entry dynamics and acoustic/infrasonic/seismic analysis for the Neuschwanstein meteorite fall. Meteorit Planet Sci 39(10):1605–1626. https://doi.org/10.1111/j.1945-5100.2004.tb00061.x

Silber EA, Le Pichon A, Brown PG (2011) Infrasonic detection of a near-earth object impact over Indonesia on 8 October 2009. Geophys Res Lett 38:L12201. https://doi.org/10.1029/2011GL047633

Silber EA, Brown PG (2014) Optical observations of meteors generating infrasound-I: acoustical signal identification and phenomenology. J Atmos Sol Terr Phys 119:116–128. https://doi.org/10.1016/j.jastp.2014.07.005

Silber EA, Brown PG (2017) Infrasound monitoring to identify potentially dangerous NEO. In: Le Pichon A et al (eds) Infrasound monitoring (Challenges and new perspective). Springer

Silber E, Brown P (2019) Infrasound monitoring as a tool to characterize impacting near-earth objects (NEOs). In: Le Pichon A, Blanc E, Hauchecorne A (eds) Infrasound monitoring for atmospheric studies, 2nd edn. Springer, Dordrecht, pp 939–986

Tauzin B, Debayle E, Quantin C, Coltice N (2013) Seismoacoustic coupling induced by the breakup of the 15 February 2013 Chelyabinsk meteor. Geophys Res Lett 40:3522–3526. https://doi.org/10.1002/grl.50683

Whipple FJW (1930) The great Siberian meteor and the waves, seismic and aerial, which it produced. Quart J R Meteorol Soc 56:287–304. https://doi.org/10.1002/qj.49705623601

Chapter 13
Systematic Array Processing of a Decade of Global IMS Infrasound Data

Lars Ceranna, Robin Matoza, Patrick Hupe, Alexis Le Pichon and Matthieu Landès

Abstract The ability of the International Monitoring System (IMS) global infrasound network to detect atmospheric explosions and other events of interest depends strongly on station-specific ambient incoherent noise and clutter (real but unwanted infrasound waves, coherent on an infrasound array). Characterization of coherent infrasound is important for quantifying the recording environment at each station and for assessing the detection probability of specific signals of interest. We systematically characterize coherent infrasound recorded by the IMS network over 10 years on 41 stations over a broad frequency range (0.01–5 Hz). This multiyear processing emphasizes continuous signals such as mountain associated waves and microbaroms, as well as persistent transient signals such as repetitive volcanic, surf, thunder, or anthropogenic activity. We estimate the primary source regions of continuous coherent infrasound using a global cross-bearings approach. For most IMS arrays, the detection of persistent sources is controlled by the dynamics of the stratospheric wind circulation from daily to seasonal scales. Systematic and continuous characterization of multiyear array detections helps to refine knowledge of the source of ambient ocean noise and provides additional constraints on the dynamics of the middle atmosphere where data coverage is sparse.

L. Ceranna (✉) · P. Hupe
BGR, B4.3, 30655 Hannover, Germany
e-mail: lars.ceranna@bgr.de

R. Matoza
Department of Earth Science and Earth Research Institute,
University of California, Santa Barbara, CA 93106-9630, USA

A. Le Pichon
CEA, DAM, DIF, F-91297 Arpajon, France

M. Landès
European-Mediterranean Seismological Centre C/O, CEA, DAM, DIF,
F-91297 Arpajon, France

A. Le Pichon et al. (eds.), *Infrasound Monitoring for Atmospheric Studies*,
https://doi.org/10.1007/978-3-319-75140-5_13

13.1 Introduction

The global International Monitoring System (IMS) infrasound network was designed to reliably detect a one kiloton equivalent explosion worldwide with at least two stations and thus to monitor compliance with the Comprehensive Nuclear Test-Ban Treaty (CTBT) (Christie and Campus 2010). Although the 60-station network is not yet fully established, 49 certified stations now provide global coverage of geophysical and anthropogenic events (Campus and Christie 2010; Marty et al. 2019; Mialle et al. 2019). In addition to its primary function of detecting explosions, the IMS network has demonstrated its potential application in monitoring natural hazards such as large volcanic explosions (Matoza et al. 2019) and severe weather (Waxler and Assink 2019).

The performance of the IMS network is a key concern for the CTBT as environmental noise and coherent clutter may interfere with the detection and identification of explosive events, so their understanding and characterization is important for treaty verification. The detection capability of the infrasound network exhibits significant spatiotemporal variation, which is in part controlled by the station-specific ambient recording environment, which includes incoherent wind noise and persistent unwanted real coherent infrasonic signals (clutter). Clutter can interfere with the detection or successful identification of signals of interest by effectively obscuring or overwhelming a range of look directions (at a given frequency) at a given station. Variations in clutter result from changes in both the source distribution (e.g., Landès et al. 2012) and the propagation conditions (e.g., Evers and Siegmund 2009; Assink et al. 2014), and can be characterized statistically.

IMS infrasound array data are routinely processed at the International Data Center (IDC). The wave parameters of the detected signals are estimated with the Progressive Multi-Channel Correlation method (PMCC) (Cansi 1995). This method proved to be very efficient for routine identification of low-amplitude coherent waves within incoherent noise (Mialle et al. 2019). The initial implementation of PMCC used a series of linearly spaced frequency bands, which in practice (due to computational limitation) had the disadvantage of requiring multiple independent runs to cover the broad frequency band of interest (~0.01–5 Hz). A practical benefit was subsequently gained by implementing PMCC with a variable window length and log-spaced frequency bands (Brachet et al. 2010; Le Pichon et al. 2010), which allows the full frequency range of interest to be processed efficiently in a single computational run. Using this implementation, a first global and multiyear systematic broadband (0.01–5 Hz) analysis of historical IMS records was carried out by Matoza et al. (2013). Matoza et al. (2013) made relative comparisons of the IMS stations' ambient coherent infrasound amplitudes and overall station performance characteristics from April 1, 2005 to December 31, 2010.

In this chapter, we extend our processing of the IMS continuous waveform archive to January 1, 2015, representing almost a decade of IMS waveform data considered. In Sect. 13.2, we introduce the dataset and describe the array processing scheme. In Sect. 13.3, we present the multiyear and global processing results. One dominant factor influencing infrasound detection at mid-latitudes is the spatiotemporal variability of the stratospheric waveguide structure. In particular, the seasonal reversal of the stratospheric circulation oscillation, clearly captured in climatological wind models, controls to first order where signals are expected to be detected (e.g., Drob et al. 2003; Drob 2019). Our processing results provide useful insight into the evaluation of the overall performance of the IMS network. In the last section, we apply a cross-bearing approach proposed by Landès et al. (2012) to reconstruct the main source regions of microbaroms and mountain associated waves (MAW), which dominate the background wavefield. The seasonal patterns of the microbarom source regions are compared with those predicted by nonlinear ocean wave interaction models (Longuet-Higgins 1950; Waxler and Gilbert 2006; Ardhuin and Herbers 2013). We address the implications of our results for the treaty verification which, compared to previous studies, provide progress toward an improved characterization of the space-, time-, and frequency-dependent coherent noise. Moreover, such knowledge is of importance for the development of atmospheric remote sensing methods as useful integrated information about the vertical structure of the temperature and wind are reflected in continuous signals from natural sources (e.g., Le Pichon et al. 2015; Assink et al. 2019; Chunchuzov and Kulichkov 2019; Smets et al. 2019).

13.2 Data and Methods

We perform broadband array processing with the IMS continuous waveform archive of 41 certified stations from April 1, 2005 to January 1, 2015 (Fig. 13.1, left). Each station consists of an array of at least four sensors with a flat response from 0.01 to 8 Hz. Since the IMS network is currently under construction, data availability varies throughout the time period considered. Stations recently installed are not considered in this study due to limited data availability. We restrict our analysis to stations for which there are at least 5 years of continuous recordings available. For 35 stations, data are available for more than 9 years. The spatial distribution of these sites covers a wide range of latitudes, atmospheric, and oceanic conditions (e.g., island, coastal, or interior continental stations). All infrasound stations are composed of four or more microbarometers and include spatial wind-filtering systems and communication facilities (Marty 2019).

Data are processed automatically using the Progressive Multi-Channel Correlation (PMCC) algorithm (Cansi 1995; Mialle et al. 2019). PMCC estimates the wavefront parameters (e.g., back azimuth, apparent velocity, frequency, root mean

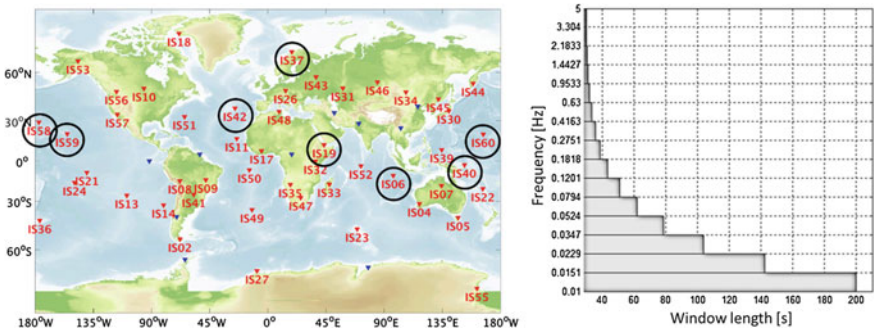

Fig. 13.1 Left: among the 48 certified IMS infrasound stations (red inverted triangles); stations with less than 5 years of archived data are not considered in this study (circled). Right: PMCC configuration using 15 log-scaled frequency bandwidths with window length linearly scaled to the period

square amplitude) of coherent plane waves in a given time window and band-pass filter from the time delays calculated between pairs of sensors. To minimize errors in the calculation of the wave parameters, distant sensors are progressively added. The progressive use of distant sensors has two main effects: the removal of false detections due to correlated noise at the scale of the starting sub-arrays, and a better estimation of the wavefront parameters by increasing the array aperture. The processing is performed over successive overlapping time windows and adjacent frequency bands covering the whole period of analysis. We implement a configuration of 15 bands spaced logarithmically between 0.01 and 5 Hz, with window lengths varying linearly with the period (Fig. 13.1, right). This configuration is a step toward practical improvement of infrasound detection algorithm to better discriminate between interfering signals by defining standard frequency bands for use in the infrasound research community (Garcés 2013).

The resulting detections can be broadly interpreted and classified into three main frequency bands:

- above 0.5 Hz, detections (~30%) are transient signals of natural or man-made origin (e.g., volcanoes, surf, industrial activity) propagating over distances of several hundred kilometers;
- between 0.1 and 0.5 Hz, detections (~60%) are dominated by microbarom signals and remote large events such as explosions, meteorites, and volcanoes (e.g., Campus and Christie 2010; Green et al. 2010; Silber et al. 2019; Matoza et al. 2019);
- below 0.1 Hz, detections (~10%) are associated with large-scale atmospheric disturbances such as MAW generated by tropospheric wind flow over high mountain ranges and, at high latitudes, geomagnetic and auroral activity (Wilson et al. 2010).

13.3 Global Infrasonic Detection and Middle Atmospheric Dynamics

Figure 13.2 summarizes results from the continuous processing for the decade 2005–2015. In the 0.1–0.5 Hz band, the dominant source is microbaroms caused by the nonlinear interaction of oceanic waves, near-continuously detected worldwide (e.g., Garcés et al. 2004; Waxler and Guilbert 2006; Landès et al. 2012). In the northern hemisphere, signals mainly originate from ocean swells in the Pacific, Atlantic, and Indian oceans. For austral IMS stations, the main sources of signals are large swell systems driven by strong continuous eastward surface winds along the Antarctic Circumpolar Current (ACC) which links the major southern oceans in the 50–60°S range (e.g., Landès et al. 2014).

The effective sound speed ratio (V_{RATIO}) defined here by the ratio between the effective sound speed at 50 km altitude and the sound speed at the ground level is

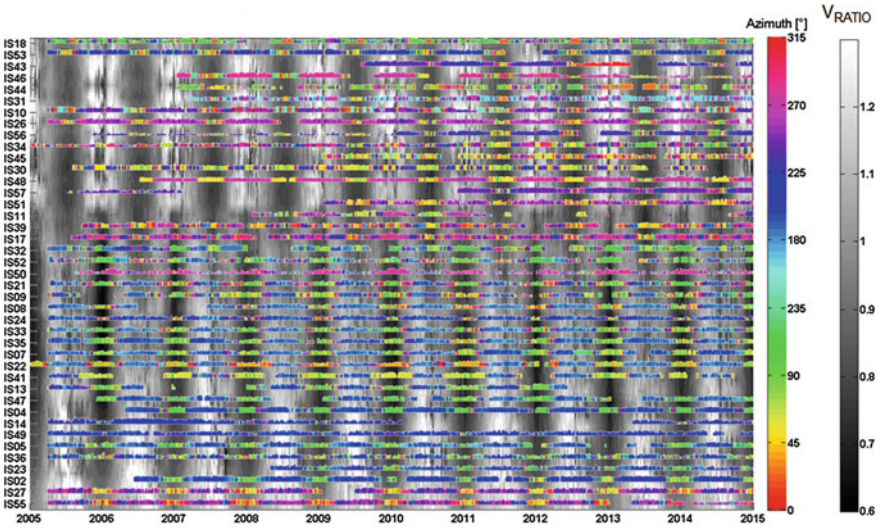

Fig. 13.2 Summary of a decade of IMS infrasound detections in the 0.01–5 Hz frequency band. The 41 IMS stations analyzed are sorted by latitude. Colored rectangles represent the number of detections (each rectangle is one week, height log-scaled with an upper limit of 2800 detections). Colors refer to the weekly averaged back azimuths. At each station, the detections (colored rectangles) are superimposed on V_{RATIO} at 50 km altitude (grayscale). The temperature and wind profiles are extracted using the ECMWF operational analyses part of the Integrated Forecast System (IFS) (91 vertical levels up to 0.01 hPa with a horizontal resolution of half a degree and a temporal resolution of 6 h). Light and dark colors indicate up- and downwind eastward propagation scenarios, respectively. As a result of the seasonal zonal wind reversals in the stratosphere, clear seasonal variations in back azimuths are observed. In the northern hemisphere summer (from June to August), signals from easterly directions dominate and vice versa during winter (from November to January). An opposite trend is noted in the southern hemisphere

superimposed on the detections. This dimensionless parameter represents the combined effects of refraction due to a sound speed gradient and advection due to along-path wind on infrasound propagation (e.g., Green et al. 2012) using the High Resolution (HRES) European Centre for Medium-Range Weather Forecasts models (ECMWF, http://www.ecmwf.int/). The observed azimuthal seasonal trend correlates well with the variation of V_{RATIO}. A clear seasonal transition in the bearings is observed correlated with changes in the stratospheric general circulation between summer and winter. Our global analysis indicates that the primary factor controlling the signal detectability is the seasonal reversal of the prevailing zonal wind at mid-latitudes, anticorrelated from the southern and northern hemispheres, since ~80% of the detections in the 0.2–2 Hz bandpass are associated with propagation downwind of the dominant stratospheric wind direction. This oscillation controls to first order where infrasound detections are predicted.

13.4 Locating the Main Source Regions of Continuous Coherent Ambient Noise

Modern seismological and infrasound networks produce large quantities of continuous waveform data that are dominated by background noise which has strong amplitudes near 0.15–0.2 Hz. The large amplitudes of background seismic and atmospheric waves, secondary microseisms and microbaroms, are generated by the interaction of ocean gravity waves with the seafloor and the atmosphere, respectively caused by the nonlinear interference of oceanic waves with the same frequency propagating in opposite directions (Longuet-Higgins 1950). Microbarom generation is directly proportional to oceanic wave interaction (e.g., Waxler and Gilbert 2006). Using the 2005–2015 broadband reprocessing results of the global IMS archive, the main source regions of continuous coherent signals can be estimated. Following the approach proposed by Landès et al. (2012), a monthly averaged spatial source distribution of microbaroms is estimated. The reconstructed regions are compared with those predicted by the theory of noise generation in the solid Earth, oceans, and atmosphere developed by Ardhuin and Herbers (2013) as an alternative to the Green's function formalism proposed by Waxler and Gilbert (2006). The microbarom source model used, valid in deep water, includes nonlinear ocean wave interaction induced by coastal reflections. Applied to acoustic waves in the atmosphere, it extends previous theories that were limited to vertical propagation only.

Figure 13.3 compares the reconstructed and modeled microbarom source regions for January, April, July, and October averaged over the 2005–2015 period. The observed and predicted source regions both exhibit a clear seasonal variability. The source amplitude and number of microbarom signals are larger in local winter than in summer. In the northern hemisphere, signals mainly originate from storms

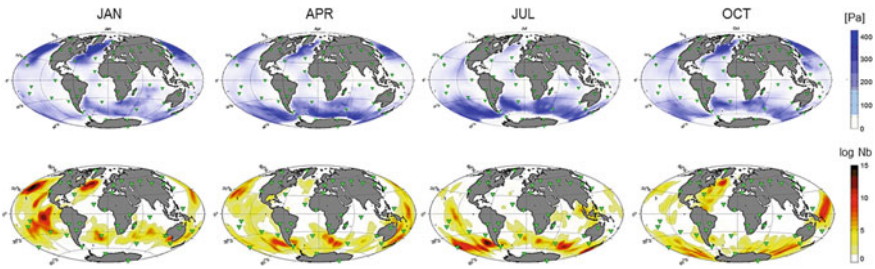

Fig. 13.3 Comparisons between the averaged reconstructed and modeled microbarom source regions for January, April, July and October over the 2005–2015 period. Top: predicted source pressure (in Pa) at the ocean–atmosphere interface highlighting regions of nonlinear interaction of oceanic waves (Ardhuin and Herbers 2013). Bottom: microbarom source regions reconstructed from the broadband reprocessing results using the cross-bearing approach developed by Landès et al. (2012); the colorbar codes the number of intersected back azimuths in a logarithm scale

traveling in opposite direction in the Pacific, Atlantic, and Indian oceans. For austral stations, signals originate from large swell systems driven by strong eastward surface winds along the ACC. Such observations are consistent with the characterization of microseismic noise recorded by worldwide distributed seismic stations (e.g., Stehly et al. 2006; Schimmel et al. 2011). In particular, Schimmel et al. (2011) showed that continental stations can record microseisms generated several thousands of kilometers away and reported similar seasonal variability and latitudinal dependence of the power of secondary microseisms.

We apply the same cross-bearing procedure to the assumed MAW signals with periods selected between 20 and 50 s. Figure 13.4 presents the averaged location results in January, April, July, and October. Hotspots of sources, inferred to be MAW, are found in local winter over the Himalayas, the Rocky and Andes Mountains in America (Le Pichon et al. 2010). Some activity is found over New Zealand where the chain of the Southern Alps culminates at 3700 m. Earlier work published by Larson et al. (1971) pointed out similar features for MAW traveling at acoustic velocities in the 10–100 s period range. Statistical analyses of long-duration atmospheric waves, lasting for several hours to several days were carried out. Using several infrasound observatories in North America, triangulation showed the principal source areas to be along the coast of British Columbia and in the inland Rocky Mountains of the British Columbia-Alberta border. Statistical analyses of MAW characteristics together with general wind circulation patterns were examined. Clear correlation between the amplitude MAW and the annual variation of both zonal and kinetic energy of tropospheric winds in the layer 850–500 hPa (altitude from about 1500–5500 m) was found. The production of infrasound by several possible aerodynamic processes has been examined (e.g., Chunchuzov 1993). The main source mechanism involved at the origin of MAW is explained by stably stratified air passing over a mountain barrier which produces an oscillatory motion of the fluid by interaction with the obstacle. Their impact on the

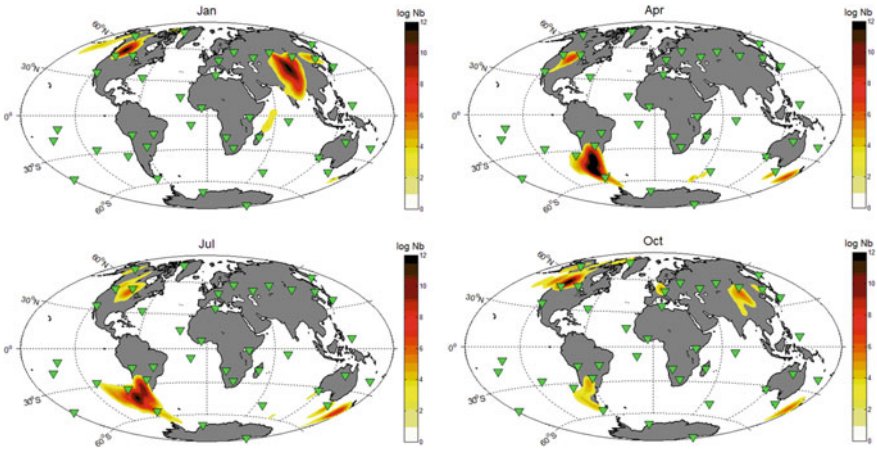

Fig. 13.4 Averaged reconstructed source regions of MAW for January, April, July, and October over the 2005–2015 period. The colorbar codes the number of intersected back azimuths of detections with periods ranging between 20 and 50 s in a logarithm scale

dynamics of the middle atmosphere has been demonstrated. Theoretical and experimental diagnostic tools to further investigate the upward propagation of the transferred energy flux of mountain waves through the lower stratosphere have been investigated (e.g., Smith et al. 2007).

13.5 Discussion and Conclusions

Reprocessing a 10-year archive of continuous waveform data from the IMS infrasound network in the 0.01–5 Hz band permits statistical characterization and analysis of the coherent ambient wavefield in the frequency band relevant to explosion monitoring. We implemented a standardized PMCC configuration between 0.01 and 5 Hz which consists of 15 log-spaced frequency bands and window lengths varying linearly with the period. This configuration allows computationally efficient broadband processing and helps with signal discrimination. It provides progress toward more accurate metrics to evaluate the detection capability of the IMS infrasound network (Marty 2019). Since the ambient noise limits the ability to detect and identify signals of interest, incorporating realistic station-, time-, and frequency-dependent coherent noise levels can improve detection capability estimates (Le Pichon et al. 2012; Green and Bowers 2010).

Comparison with the dynamical features of global atmospheric circulation highlights the strong influence of the spatiotemporal variability of the stratospheric waveguide structure on the network detection capability. Among the natural sources of infrasound dominating the coherent background noise are long lasting signals such as microbaroms and MAW observed at most middle- and high-latitude stations. The reconstructed and predicted microbarom source regions using

two-dimensional wave energy spectrum ocean wave products are in good agreement. Dominant regions are found thousands of kilometers away from the IMS stations and exhibit clear seasonal variability in amplitude and latitudinal dependence. Combining infrasound and microseism observations from long running stations would be beneficial to further assess numerical models of noise generation in the solid Earth, oceans, and atmosphere and characterize inter-decadal climate change (Schimmel et al. 2011). In the 10–100 s period range, MAW are continuously and globally detected. Triangulation using MAW observations at several stations shows prominent source energy over high mountain ranges in local winter. Climatological statistics of their characteristics can provide useful quantitative measures of orographic convective instabilities and improve the parameterization of gravity waves due to sub-grid-scale orography for Numerical Weather Prediction (NWP) applications (e.g., McFarlane 1987; Kim and Arakawa 1993).

Observations from natural sources detected worldwide are of great interest for the application of infrasound as a passive remote sensing technique of the upper atmosphere (Assink et al. 2014), for which there is renewed interest. Following the pioneering studies of Donn (1973) and Larson et al. (1971), the recent advances in measurement, processing methods, and modeling techniques provide new insights on method for continuous, passive acoustic tomography of the atmosphere using continuous broadband infrasound recordings. Today, the interpretation of these data motivates studies on passive remote sensing techniques to delineate the vertical structure of the stratospheric and mesospheric-thermospheric wind and temperature (e.g., Drob et al. 2010; Lalande et al. 2012; Assink et al. 2013; Assink et al. 2019). For example, the analysis of near-continuous infrasound detections of active volcanoes permits the evaluation of atmospheric products produced by ECMWF through the study of stratospheric propagation with a time resolution ranging from hours to multiple years (e.g., Assink et al. 2014). The global PMCC detection lists 2005–2010 produced by Matoza et al. (2013) were used for automated detection and cataloging of global explosive volcanism (Matoza et al. 2017, 2019), and the results from the present study can be used to extend these results to 2015. Comparison of regional volcano infrasound with simulations also allows the evaluation of middle atmospheric weather forecasts, providing new metrics to evaluate stratospheric skills (Smets et al. 2016).

With the increasing number of IMS stations (Marty 2019) complemented by dense regional networks at continental scales (e.g., de Groot-Hedlin and Hedlin 2019), systematic studies using historical infrasound datasets and state-of-the-art reanalysis systems provide useful integrated information about the structure of the stratosphere where data coverage is sparse (Lee et al. 2019). Of specific interest is the characterization of the four-dimensional stratopause evolution throughout the SSW life cycle and the study of the longer term influences of SSWs on the troposphere (e.g., Charlton-Perez et al. 2013; Smets and Evers 2014; Smets et al. 2019). It is expected that combining recent advances in modeling techniques, taking advantage of an infrastructure that integrates various independent middle atmospheric measurement techniques currently not assimilated in NWP models, would provide quantitative understanding of stratosphere–troposphere dynamical coupling

useful for NWP applications (Blanc et al. 2019). Beyond the atmospheric community, the evaluation of NWP models is essential in the context of the future verification of the CTBT as improved atmospheric models are extremely helpful to assess the IMS network performance in higher resolution, reduce source location errors and characterization methods.

Acknowledgements We thank the CTBTO and station operators for guaranteeing the high quality of the infrasound data. This work was performed during the course of the ARISE design study (http://arise-project.eu), funded under the H2020 Framework Programme of the European Union (grant 653980).

References

Ardhuin F, Herbers THC (2013) Noise generation in the solid Earth, oceans and atmosphere, from nonlinear interacting surface, gravity waves infinite depth. J Fluid Mech 716:316–348. https://doi.org/10.1017/jfm.2012.548

Assink JD, Waxler R, Frazier WG, Lonzaga J (2013) The estimation of upper atmospheric wind model updates from infrasound data. J Geophys Res 118. https://doi.org/10.1002/jgrd.50833

Assink JD, Le Pichon A, Blanc E, Kallel M, Khemiri L (2014) Evaluation of wind and temperature profiles from ECMWF analysis on two hemispheres using volcanic infrasound. J Geophys Res Atmos 119. https://doi.org/10.1002/2014jd021632

Assink J, Smets P, Marcillo O, Weemstra C, Lalande J-M, Waxler R, Evers L (2019) Advances in infrasonic remote sensing methods. In: Le Pichon A, Blanc E, Hauchecorne A (eds) Infrasound monitoring for atmospheric studies, 2nd edn. Springer, Dordrecht, pp 605–632

Blanc E, Pol K, Le Pichon A, Hauchecorne A, Keckhut P, Baumgarten G, Hildebrand J, Höffner J, Stober G, Hibbins R, Espy P, Rapp M, Kaifler B, Ceranna L, Hupe P, Hagen J, Rüfenacht R, Kämpfer N, Smets P (2019) Middle atmosphere variability and model uncertainties as investigated in the framework of the ARISE project. In: Le Pichon A, Blanc E, Hauchecorne A (eds) Infrasound monitoring for atmospheric studies, 2nd edn. Springer, Dordrecht, pp 845–887

Brachet N, Brown D, Le Bras R, Mialle P, Coyne J (2010) Infrasound monitoring for atmospheric studies, chapter monitoring the earth's atmosphere with the global IMS infrasound network. Springer, Dordrecht, pp 77–118. ISBN:978-1-4020-9507-8

Campus P, Christie DR (2010) Infrasound monitoring for atmospheric studies. In: (eds) Le Pichon A, Blanc E, Hauchecorne A, chapter Worldwide observations of infrasonic waves. Springer, Dordrecht, pp 195–234. ISBN:978-1-4020-9507-8

Cansi Y (1995) An automatic seismic event processing for detection and location—the PMCC method. Geophys Res Lett 22:1021–1024

Charlton-Perez AJ et al (2013) On the lack of stratospheric dynamical variability in low-top versions of the CMIP5 models. J Geophys Res 118:2494–2505. https://doi.org/10.1002/jgrd.50125

Christie DR, Campus P (2010) Infrasound monitoring for atmospheric studies. In: Le Pichon A, Blanc E, Hauchecorne A (eds) Chapter the IMS infrasound network: design and establishment of infrasound stations. Springer, Dordrecht, pp 29–76. ISBN:978-1-4020-9507-8

Chunchuzov IP (1993) On the possible generation mechanism of non-stationary mountain waves in the atmosphere. J Atmos Sci 51:2196–2206

Chunchuzov I, Kulichkov S (2019) Internal gravity wave perturbations and their impacts on infrasound propagation in the atmosphere. In: Le Pichon A, Blanc E, Hauchecorne A (eds) Infrasound monitoring for atmospheric studies, 2nd edn. Springer, Dordrecht, pp 551–590

de Groot-Hedlin C, Hedlin M (2019) Detection of infrasound signals and sources using a dense seismic network. In: Le Pichon A, Blanc E, Hauchecorne A (eds) Infrasound monitoring for atmospheric studies, 2nd edn. Springer, Dordrecht, pp 669–699

Donn WL (1973) Sea wave origin of microbaroms and microseisms. J Geophys Res 78: 4482–4488

Drob D (2019) Meteorology, climatology, and upper atmospheric composition for infrasound propagation modeling. In: Le Pichon A, Blanc E, Hauchecorne A (eds) Infrasound monitoring for atmospheric studies, 2nd edn. Springer, Dordrecht, pp 485–508

Drob DP, Picone JM, Garcés M (2003) Global morphology of infrasound propagation. J Geophys Res 108:D21. https://doi.org/10.1029/2002JD003307

Drob DP, Meier RR, Picone JM, Garcés M (2010) Infrasound monitoring for atmospheric studies. In: Le Pichon A, Blanc E, Hauchecorne A (eds) chapter inversion of infrasound signals for passive atmospheric remote sensing, pp 701–731. Springer, Dordrecht. ISBN:978-1-4020-9507-8

Evers LG, Siegmund P (2009) The infrasonic signature of the 2009 major Sudden Stratospheric Warming. Geophys Res Lett 36:L23808. https://doi.org/10.1029/2009GL041323

Garcés M, Willis M, Hetzer C, Le Pichon A, Drob D (2004) On using ocean swells for continuous infrasonic measurements of winds and temperature in the lower, middle, and upper atmosphere. Geophys Res Lett 31. https://doi.org/10.1029/2004gl020696

Garcés MA (2013) On infrasound standard, part 1: time, frequency, and energy scaling, vol 2, pp 13–35. http://dx.doi.org/10.4236/inframatics.2013.22002

Green DN, Bowers D (2010) Estimating the detection capability of the International Monitoring System infrasound network. J Geophys Res 115:D18116. https://doi.org/10.1029/2010JD014017

Green DN, Le Pichon A, Ceranna L, Evers L (2010) Infrasound monitoring for atmospheric studies. In: Le Pichon A, Blanc E, Hauchecorne A, Chapter ground truth events: assessing the capability of infrasound networks using high resolution data analyses, Springer, Dordrecht, pp 599–625. ISBN:978-1-4020-9507-8

Green DN, Matoza RS, Vergoz J, Le Pichon A (2012) Infrasonic propagation from the 2010 Eyjafjallajökull eruption: investigating the influence of stratospheric solar tides. J Geophys Res 117:D21202. https://doi.org/10.1029/2012JD017988

Kim YJ, Arakawa A (1993) Improvement of orographic gravity waves parameterization using a mesoscale gravity wave model. J Atmos Sci 52:1902–1975

Lalande JM, Sèbe O, Landès M, Blanc-Benon P, Matoza RS, Le Pichon A, Blanc E (2012) Infrasound data inversion for atmospheric sounding. Geophys J Int 190. https://doi.org/10.1111/j.1365-246x.2012.05518.x

Landès M, Ceranna L, Le Pichon A, Matoza R (2012) Localization of microbarom sources using the IMS infrasound network. J Geophys Res. https://doi.org/10.1029/2011jd016684

Landès M, Le Pichon A, Shapiro N, Hillers G, Campillo M (2014) Explaining global patterns of microbarom observations with wave action models. Geophys J Int 2014(199):1328–1337. https://doi.org/10.1093/gji/ggu324

Larson RJ, Craine LB, Thomas JE, Wilson CR (1971) Correlation of winds and geographic features with production of certain infrasonic signals in the atmosphere. Geophys J R Astron Soc 26:201–214

Le Pichon A, Matoza R, Brachet N, Cansi Y (2010) Recent enhancements of the PMCC infrasound signal detector. Inframatics Newslett 26:5–8. http://www.inframatics.org

Le Pichon A, Ceranna L, Vergoz J (2012) Incorporating numerical modeling into estimates of the detection capability of the IMS infrasound network. J Geophys Res 117:D05121. https://doi.org/10.1029/2011JD016670

Le Pichon A, Assink JD, Heinrich P, Blanc E, Charlton-Perez A, Lee CF, Keckhut P, Hauchecorne A, Rüfenacht R, Kämpfer N et al (2015) Comparison of co-located independent ground-based middle-atmospheric wind and temperature measurements with Numerical Weather Prediction models. J Geophys Res 120. https://doi.org/10.1002/2015jd023273

Lee C, Smets P, Charlton-Perez A, Evers L, Harrison G, Marlton G (2019) The potential impact of upper stratospheric measurements on sub-seasonal forecasts in the extra-tropics. In: Le Pichon A, Blanc E, Hauchecorne A (eds) Infrasound monitoring for atmospheric studies, 2nd edn. Springer, Dordrecht, pp 889–910

Longuet-Higgins MS (1950) A theory of the origin of microseisms. R Soc Lond Phil Trans A 243:1–35

Marty J (2019) The IMS Infrasound network: current status and technological developments. In: Le Pichon A, Blanc E, Hauchecorne A (eds) Infrasound monitoring for atmospheric studies, 2nd edn. Springer, Dordrecht, pp 3–62

Matoza R, Landès M, Le Pichon A, Ceranna L, Brown D (2013) Coherent ambient infrasound recorded by the International Monitoring System. Geophys Res Lett 40. https://doi.org/10.1029/2012gl054329

Matoza RS, Green DN, Le Pichon A, Shearer PM, Fee D, Mialle P, Ceranna L (2017) Automated detection and cataloging of global explosive volcanism using the International Monitoring System infrasound network. J Geophys Res Solid Earth 122:2946–2971. https://doi.org/10.1002/2016JB013356

Matoza R, Fee D, Green D, Mialle P (2019) Volcano infrasound and the international monitoring system. In: Le Pichon A, Blanc E, Hauchecorne A (eds) Infrasound monitoring for atmospheric studies, 2nd edn. Springer, Dordrecht, pp 1023–1077

McFarlane MA (1987) The effect of orographically excited gravity waves drag on the general circulation of the lower stratosphere and troposphere. J Atmos Sci 44:1775–1800

Mialle P, Brown D, Arora N (2019) Advances in operational processing at the international data centre In: Le Pichon A, Blanc E, Hauchecorne A (eds) Infrasound monitoring for atmospheric studies, 2nd edn. Springer, Dordrecht, pp 209–248

Schimmel M, Stutzmann E, Ardhuin F, Gallart J (2011) Polarized Earth's ambient microseismic noise. Geochem Geophys Geosyst 12:Q07014. https://doi.org/10.1029/2011GC003661

Silber E, Brown P (2019) Infrasound monitoring as a tool to characterize impacting near-earth objects (NEOs). In: Le Pichon A, Blanc E, Hauchecorne A (eds) Infrasound monitoring for atmospheric studies, 2nd edn. Springer, Dordrecht, pp 939–986

Smets PSM, Evers LG (2014) The life cycle of a sudden stratospheric warming from infrasonic ambient noise observations. J Geophys Res 119. https://doi.org/10.1002/2014jd021905

Smets PSM, Assink JD, Le Pichon A, Evers LG (2016) ECMWF SSW forecast evaluation using infrasound. J Geophys Res Atmos 121. https://doi.org/10.1002/2015jd024251

Smets P, Assink J, Evers L (2019) The study of sudden stratospheric warmings using infrasound. In: Le Pichon A, Blanc E, Hauchecorne A (eds) Infrasound monitoring for atmospheric studies, 2nd edn. Springer, Dordrecht, pp 723–755

Smith RB, Woods K, Jensen J, Cooper WA, Doyle JD, Jiang Q, Grubisic V (2007) Mountain waves entering the stratosphere. J Atmos Sci 65. https://doi.org/10.1175/2007JAS2598.1

Stehly L, Campillo M, Shapiro NM (2006) A study of the noise from its long-range correlation properties. J Geophys Res 111:B10306. https://doi.org/10.1029/2005JB004237

Waxler R, Gilbert KE (2006) The radiation of atmospheric microbaroms by ocean waves. J Acoust Soc Am 119:2651–2664

Waxler R, Assink J (2019) Propagation modeling through realistic atmosphere and benchmarking. In: Le Pichon A, Blanc E, Hauchecorne A (eds) Infrasound monitoring for atmospheric studies, 2nd edn. Springer, Dordrecht, pp 509–549

Wilson CR, Szuberla CA, Olson JV (2010) Infrasound monitoring for atmospheric studies. In: Le Pichon A, Blanc E, Hauchecorne A (eds) Chapter high-latitude observations of infrasound from Alaska and Antarctica: mountains associated waves and geomagnetic/auroral infrasonic signals. Springer, Dordrecht, pp 415–451. ISBN:978-1-4020-9507-8

Part V
Propagation Modelling, Network Performance and Inversion Methods: Atmospheric Models and Propagation Modelling

Chapter 14
Meteorology, Climatology, and Upper Atmospheric Composition for Infrasound Propagation Modeling

Douglas Drob

Abstract Over the last decade, there have been improvements in global data assimilation capabilities of the lower, middle, and upper atmosphere. This includes mesoscale specification capabilities for the troposphere. This chapter provides an overview of both operational and basic scientific research specifications of the atmosphere from the ground to the thermosphere that are available for the calculation of infrasound propagation characteristics. This review is intended for scientific experts, nonexperts, researchers, educators, and policy makers alike. As atmospheric specifications for the lower and middle atmosphere are now readily available, less uncertain, and also described in other chapters of this book, some additional emphasis is placed on the challenges associated with upper atmospheric specifications for modeling thermospherically ducted infrasound propagation. Otherwise, no particular emphasis is placed on any one atmospheric specification system or institutional data provider; nor anyone particular infrasound propagation application, i.e., local, regional, global, man-made, or natural.

14.1 Overview

In order to detect, locate, and discriminate energetic impulsive events via infrasound accurately, it is important to know how acoustic waveforms evolve as they propagate away from a source and are subsequently observed by seismic networks and infrasound arrays. In the case of infrasound, this requires specification of the time-dependent transfer function between the source and receivers. This time-dependent transfer function is determined by the acoustic signal characteristics, atmospheric properties, and instrument response functions of the detectors. Unlike seismic waveforms, for identical events and source to receiver configurations, the observed infrasound signal characteristics (e.g., amplitude and travel time) are highly variable due to the time dependence of the atmosphere (Rind 1978; Le Pichon et al. 2002; Drob et al. 2003). Propagation is also highly anisotropic due to the effects of winds which

D. Drob
Naval Research Laboratory, 4555 Overlook Avenue, Washington, DC 20375, USA
e-mail: douglas.drob@nrl.navy.mil

A. Le Pichon et al. (eds.), *Infrasound Monitoring for Atmospheric Studies*,
https://doi.org/10.1007/978-3-319-75140-5_14

can vary markedly with range and altitude for a given propagation path (Georges and Beasley 1977; Garcés et al. 1998).

Over the last decade, there has been considerable progress in specifying the real-time state of the atmosphere (e.g., Bauer et al. 2015), as well as in understanding the consequences for infrasound propagation. These include improvements in understanding signal travel times, amplitudes, and waveform durations, including the spatial extent of the geometric infrasound shadow zones (Evers and Haak 2007; Green et al. 2011; Evers et al. 2012; Hedlin and Drob 2014). Several recent studies show that it is now possible to explain the relevant features of recorded data tropospheric and stratospheric arrivals well by including physics-based parameterizations of subgrid-scale atmospheric internal waves in conjunction with today's standard operational meteorological data assimilation products (e.g., Chunchuzov et al. 2011; Lalande and Waxler 2016). For a number of reasons described in this chapter, corresponding success in modeling observed thermospheric infrasound propagation characteristics remains somewhat illusive (e.g., Assink et al. 2013; Lonzaga et al. 2015).

14.1.1 Atmospheric Specifications

Traditionally, the regions of the atmosphere are categorized by the vertical temperature gradients, i.e., the troposphere, stratosphere, mesosphere, and thermosphere. The local average temperature profile and altitudes of these regions are shown in Fig. 14.1. The exact altitudes vary somewhat with latitude and day of year. For this chapter, the atmospheric specifications available for infrasound propagation modeling are the easiest to describe considering three basic regions: the lower atmosphere from the earth's surface to 35 km, the middle atmosphere from 35 to 85 km, and the upper atmosphere from 85 to 450 km. The meteorology of these regions are each controlled by somewhat different physical processes, and each also has very different observational coverage. At the top of the atmosphere near ~400 km, the average distance traveled by gas particles between collisions becomes equal to the density scale height (the distance required for the density to decrease by a factor of $1/e \sim 36\%$) and thus no longer supports classically defined acoustic propagation.

For this chapter, a key distinction should be made between atmospheric data assimilation systems which produce 'analyses', and that of Numerical Weather Prediction (NWP) models which produce 'forecasts'. Analyses are the best possible estimate of the present and/or past state of the atmosphere given all available observations. A forecast is the best possible estimate of the future state of the atmosphere based on a theoretical extrapolation of analyses forward in time via a physics-based first-principles NWP model. These physics-based models integrate the four-dimensional (4D) meteorological equations of fluid motion with various parameterizations for the different subgrid-scale physical processes of the atmosphere.

One of the most important factors in providing an accurate weather forecast is producing the most accurate analysis possible. These analyses are generated

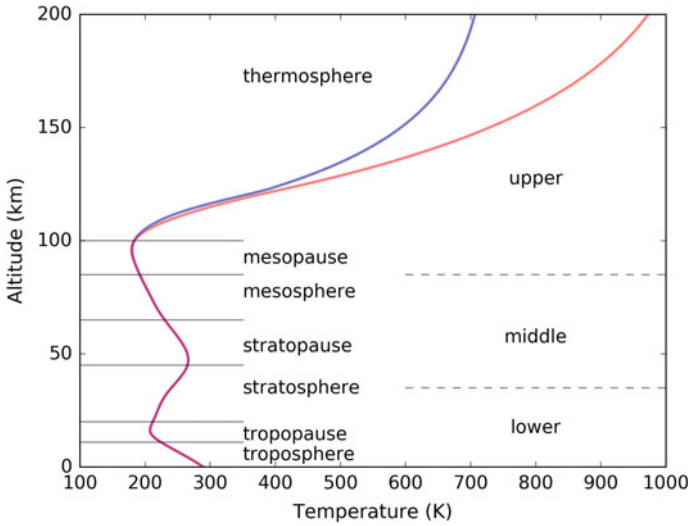

Fig. 14.1 Various regions of the atmosphere for the nomenclature in this chapter. The blue curve corresponds to low Extreme Ultraviolet (EUV) solar flux conditions (low sunspot number) and the red curve to high EUV solar flux conditions (high sunspot number)

at regular time intervals (typical every 3- to 6-h) via a data assimilation system. The system compiles the many available observations over the analysis update interval to produce an atmospheric specification which is physically self-consistent with the physics of the forecast model. These analyses are also sometimes called nowcasts or hindcasts. The self-consistency of the available noisy, disparate, and sometimes even instrument calibration biased atmospheric observations with the physical laws of the atmospheric forecast model is obtained by adding an adjoint constraint operator term to a traditional statistical field estimation cost function operator (e.g., Daley 1993). In other words, the analysis field cost function operators include both a geophysical model error covariance term to account for uncertainties in the atmospheric model, and an observational error covariance term to account for the measurement uncertainties of the available observations.

For the atmosphere below ∼35 km, given a good atmospheric model and a sufficient number of observations, today's atmospheric analysis fields are even statistically more accurate than any one single individual observation such as a radiosonde profile (e.g. Edwards 2010). This results from the fact that multiple overlapping and/or adjacent observations can work together with the geophysical constraints provided by the numerical weather prediction forecast model to mitigate measurement noise and instrument calibration biases. Furthermore, unlike an instantaneous local point measurement, operational NWP systems provide vital information about any local range dependent gradients that can be import to infrasound propagation modeling, as well as the time evolution of the atmosphere.

While the notion of ensemble numerical weather forecasting has been around for at least 25 years (e.g., Toth et al. 1997), a recent advance is the notion of ensemble

atmospheric data assimilation which provides improved knowledge about the statistical distribution of analyses based on the measurement uncertainties, as well as the statistical distribution of the forecasts to better account for uncertainties in atmospheric model physics (Zhang and Pu 2010; Houtekamer and Zhang 2016). Almost every atmospheric global data assimilation system today also utilizes a technique called four-dimensional data assimilation (4D-Var) (e.g. Courtier et al. 1994; Rabier et al. 2000). Here, the time evolution of all of the observations, typically on the order of 2×10^6 new independent measurements within a 3- to 6-h window, are reconciled with the time evolution of the atmosphere over that time interval through a simplified version of the numerical forecast model. The most advanced systems utilize hybrid techniques involving ensemble, four-dimensional data assimilation (4D-EnVar) (e.g., Lorenc 2003; Bonavita et al. 2016). Although only analyses are typically considered relevant for infrasound propagation modeling calculations, because the atmosphere is always changing utilization of archived 3-h forecasts products provide vital information between analysis update cycles (usually 6 h), and are superior to linear interpolation of 6- or 12-h analysis updates.

14.1.2 Statistical Ensembles and Internal Waves

A ubiquitous feature of the atmosphere is the internal subgrid-scale buoyancy oscillations known as gravity waves (Hines 1960; Gossard and Hooke 1975). These are not to be confused with gravitational waves (Abbott et al. 2016). These atmospheric oscillations have wave periods from ∼10 to 180 min, vertical wavelengths from 1 to 20 km, and horizontal wavelengths ranging from ∼15 to >100 km. For additional details, see Fritts and Alexander (2003). Even with the recent technological advances, owing to the spatiotemporal scales of these waves, it is impractical to deterministically measure and resolve them with any fidelity beyond a certain resolution limit in a comprehensive sense, i.e., at every possible location and time. Furthermore, these subgrid-scale phenomena must be filtered from the analysis fields during the operational data assimilation process to avoid the generation of spurious numerical artifacts when integrating the forecast model forward in time (Daley 1993).

The significance of small-scale (mid-frequency) internal atmospheric gravity waves for infrasound propagation has been clearly elucidated (e.g., Millet et al. 2007; Kulichkov et al. 2010; Lalande and Waxler 2016). It should be noted that the European Center for Medium-Range Weather Forecasting (ECMWF) ensemble analysis states presented in Smets et al. (2015) to reconcile differences between observed and modeled infrasound propagation characteristics generally represent perturbations (or random realizations) of the synoptic scale manifold of the analysis fields, i.e., the spatiotemporally resolvable but uncertain large- and medium-scale meteorological features. Here, the specifications utilized are only provided for two universal times each day (i.e., at 12-h intervals). This differs from consideration of the mid- and high-frequency atmospheric gravity wave perturbations, which have wave periods between ∼10 min and 3-h (e.g., Fritts and Alexander 2003; Drob et al. 2013; Preusse

et al. 2014). For the purposes of infrasound propagation calculations, these unresolved atmospheric perturbations can be represented as a stochastic noise field that is superimposed on the resolved background field; much in the same way that turbulence is parameterized in aerodynamic drag calculations. Unlike the large scale background atmospheric manifold, these waves influence infrasound propagation characteristics through subgrid scale refraction effects akin to weak forward scattering. These topics are described in more detail in other chapters of this book (Waxler and Assink 2019; Chunchuzov and Kulichov 2019; Cugnet et al. 2019).

Independent of infrasound propagation, these internal waves are important players in the mass, momentum, and energy budgets of the atmosphere as they transport momentum and energy into the middle and upper atmosphere through their dissipation, as well as by enhancing the eddy transport of ozone, water vapor, and heat. All operational NWP systems include gravity wave parameterizations (e.g., Ern et al. 2006; Orr et al. 2010; Geller et al. 2013). The spatial resolution of numerical forecast systems such as at the European Center for Medium-Range Weather Forecasting (ECMWF) is now even theoretically capable of deterministically resolving some of the larger scale and lower frequency internal gravity wave components. Recent detailed independent validation studies by Preusse et al. (2014) and Jewtoukoff et al. (2015) however compared the resolved gravity waves in ECMWF to observations and found that the resolved gravity waves generated in ECMWF are not yet always accurately specified and sometimes differed in their spectral characteristics from the observations. The major difficulty with the deterministic resolution of internal gravity waves in NWP analysis systems, as well as by the tuning of stochastic subgrid-scale gravity parameterizations (e.g., Warner and McIntyre 2001) is that the amplitudes, phases, and spectral characteristics of these internal oscillations vary significantly as function of time with the ambient atmospheric conditions. In particular, this is the result of time-dependent nonlinear source intermittency that is on the order of an hour or so (e.g., Hertzog et al. 2012; Costantino et al. 2015). As differences in atmospheric gravity wave parameterization schemes result in different analysis and forecast specifications in the upper stratosphere and mesosphere where observations become sparse, the measurement and characterization of the local, regional, and global evolution of these waves is an active area of scientific research.

14.2 The Challenge of Atmospheric Seismology

Although infrasound science can be considered as atmospheric seismology, there are also many important differences with traditional seismology. In seismology, the construction of solid earth models for seismic waveform synthesis is motivated by applications such as oil, gas, and mineral exploration, seismic hazard assessments, and even arms control treaty monitoring. By contrast, recent advances in atmospheric specification capabilities are motivated by applications such as commerce, agriculture, aviation, severe weather warnings, volcanic ash plume monitoring, and defense applications that are completely unrelated to infrasound propagation.

In seismology, the only viable means to obtain measurements to create and validate solid Earth models is through seismic waveform technologies. The Earth's atmosphere can however be measured through a wide variety of different in situ and remote sensing methods that are totally independent of infrasound. The in situ techniques include ground stations, ocean buoys, radiosondes, aviation-based sensors, and sounding rockets. The remote sensing techniques include ground-based vertical profilers and global satellite measurement techniques which span across the entire electromagnetic spectrum from the EUV wavelengths to Ultra high Frequency (UHF) radio waves. As the result of having multiple overlapping techniques available present atmospheric measurements are easy to intercompare and are thus well validated.

In the context of atmospheric specifications available for infrasound propagation modeling, there is an excellent understanding of the fundamental properties of the atmosphere, particularly for the lower and middle portions. The main challenge however is that unlike the solid earth, the atmosphere is time-dependent over scales from several minutes to several years. Figure 14.2 shows the approximate time and length scales for the pertinent meteorological phenomenology that determines the variability of the atmosphere that infrasound signals propagate through. A proper understanding of this time dependence is vital to understanding the limitations of present day atmospheric specifications for the calculation of infrasound propagation characteristics, and ultimately the physical limitations of infrasound waveform technologies as compared to other geophysical monitoring techniques, or in conjunction with them.

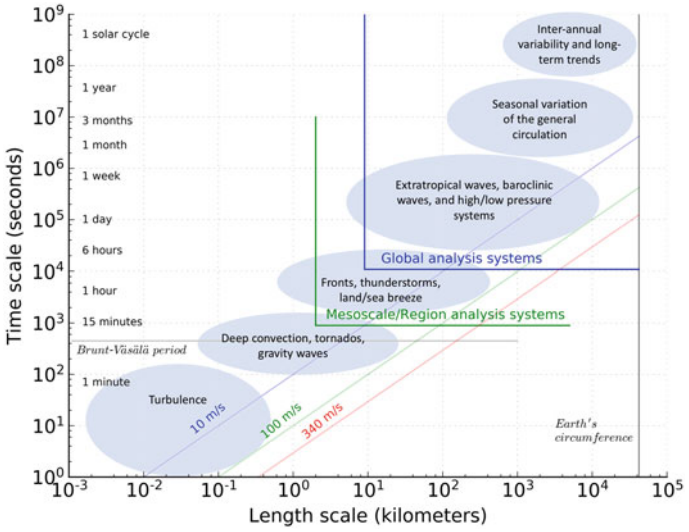

Fig. 14.2 Spatiotemporal variability of various atmospheric phenomena, including the present resolution of various regional (green) and global (blue) atmospheric data analysis and numerical weather prediction products (After Bauer et al. 2015, and others)

Table 14.1 Geophysical infrasound monitoring applications

Application	Network size[a]	Waveguide[b]	Timeliness[c]
Rayleigh wave coupling	L, R, G	R, S, T	N, H
Atmospheric remote sensing	R, G	S, T	N, H, T, C
Volcano phenomenology	L, R, G	R, S, T	N, H, T
Bolides	R, G	R, S, T	N, H
Microbarms/Microseisms	R, G	S, T	N, H, T, C
Landslides/Avalanches	L, R	R, S	N, H
Thunder and lightning	L, R	R, S	N, H
Explosion monitoring	L, R, G	R, S, T	N, H, T, C
Structural acoustics	L, R	R, S	N, H

[a]L—Local (10–100 km), R—Regional (100—750 km), G—Global (>750 km)
[b]R—Troposphere (<15 km), S—Stratosphere (15–70 km), T—Thermosphere (>70 km)
[c]N—Nowcast, H—Hindcast, T—Time series, C—Climatology

Table 14.1 shows the relevant infrasound network size, acoustic waveguides, and required temporal availability for several representative infrasound monitoring applications. The scale sizes of infrasound networks can be grouped into three general categories: local, regional, and global. While the timescales for these infrasound applications to be practical vary from several minutes to several days, the time delay and temporal resolution of the corresponding atmospheric specifications needed for infrasound propagation modeling also vary from a nowcast, hindcast, and continuous historical time series, to simple climatological averages.

The nature of the infrasound application also determines the required vertical extent of the atmospheric specifications needed to model the observed infrasound waveform characteristics (such as amplitude, frequency content, and signal duration). For near-field and regional infrasound propagation calculations over distances of no more that ∼150 km, atmospheric specifications only up to about 35 km altitude are usually needed. At these distances, consideration of topographical variations is also usually required in the vicinity of mountainous regions (Lacanna et al. 2014). For infrasound propagation calculations over distances greater than ∼150 km (and including global propagation), atmospheric specifications that include the stratosphere up to ∼70 km are usually required. Consideration of the intermediate topographic variations may or may not be required. Atmospheric specifications up to ∼140 km are required if thermospheric arrivals are to be considered in regional and global scale propagation calculations (e.g., Marcillo et al. 2013; Blom et al. 2015). Infrasound ducted in the thermosphere is however subject to significant attenuation above ∼100 km. Thus to accurately model thermospheric propagation, specification of the atmospheric composition (described later in Sect. 14.5.1) is also required in addition to winds U and temperatures T, resulting in additional challenges.

14.3 Lower Atmospheric Specifications

With respect to infrasound propagation below ~35 km, the atmosphere is the most well resolved and understood region. Highly detailed and accurate atmospheric specifications are readily available from two classes of operational numerical weather prediction systems: global scale and regional mesoscale systems. Below the tropopause, the atmosphere's meteorology is coupled to the air/land/sea interface through processes such as heat exchange, evaporation, and precipitation. Secondary effects include mountain range blocking and even surface roughness. Both aloft and near the surface, the physics of state changes between the solid, liquid, and gas phases of H_2O is one of the most important meteorological processes involved. Incoming short-wave solar radiation responsible for surface heating and outgoing long-wave radiation responsible for surface cooling are also important factors. Additional information can be found in any meteorology textbook (e.g., Fleagle and Businger 1981; Warner 2010).

The various global analysis fields are based on the observations from the integrated global observing system coordinated by the World Meteorology Organization (WMO). To generate the operational analyses $\sim 2 \times 10^6$, new independent observations are made every few hours over the globe by ground- and space-based sensors. These observations are gathered, shared, filtered, and processed by the various atmospheric data assimilation systems to produce the near-real-time analyses. A detailed list of the operational space-based sensors and ground-based stations in this network is available at the WMO website (https://www.wmo-sat.info/oscar/), as well as the many validation and product verification reports by the NWP system operators (e.g., Dee et al. 2011; Bosilovich et al. 2015). An interesting historical account of the evolution of numerical weather prediction and today's global network of weather observations is provided by Edwards (2010).

14.3.1 Global

Today, it is typical for available atmospheric analysis systems to have horizontal resolutions up to 10×10 km (~0.125°) that extend from the ground well into the middle atmosphere, and that are updated approximately every 3–6 h. Unlike a decade ago, these resolutions are now expressed in terms of kilometers rather than degrees. A partial list of the major present day operational NWP systems is provided in Table 14.2. This table also includes the acronyms and websites for these NWP centers.

Given the spatiotemporal correlations shown in Fig. 14.2, as the resolution of atmospheric specifications increases spatially, it is then equally important to simultaneously consider the temporal resolution of the specifications too. In other words, sufficient temporal resolution of the background fields is required when performing infrasound propagation calculations to properly specify the location of the resolved atmospheric structures that are resolved by the meteorological data analysis system.

Table 14.2 Representative numerical data assimilation and operational weather prediction systems

Center	System	Global resolution[1]	Vertical levels	Model top
ECMWF[a]	Integrated Forecast System (IFS)	9 × 9 km (T1279)	137	0.01 hPa (80 km)
NCEP[b]	Global Forecast System (GFS)	13 × 13 km (T1534)	64	0.27 hPa (55 km)
UKMO[c]	Unified Model (UM)	17 × 17 km (T1025)	80	0.01 hPa (80 km)
JMA[d]	Global Spectral Model (GSM)	18 × 18 km (T959)	100	0.01 hPa (80 km)

[1]T—maximum spherical harmonic spectral order
[a]European Center for Medium-Range Weather Forecasting (ECMWF), http://www.ecmwf.int
[b]National Center for Environmental Prediction (NCEP), http://www.ncep.noaa.gov
[c]United Kingdom Meteorology Office (UKMO), http://www.metoffice.gov.uk
[d]Japan Meteorology Agency (JMA), http://www.jma.go.jp/jma/indexe.html

The temporal resolution required is proportional to the spatial scale of those structures. For example, as synoptic scale waves and weather fronts can travel by as much as 200 to 300 km (~2° to 4°) over the course of 6- to 12-h, particularly in the stratosphere, it makes no sense to utilize 18 × 18 km resolution atmospheric specifications if they do not correspond to within an hour or so of the origin time of a given event.

With respect to vertical resolution, almost all of these modern systems utilize a hybrid-sigma vertical coordinate system which follows the Earth's topography near the surface, and slowly transitions to constant pressure levels in the lower stratosphere. Typical vertical resolutions are several 10 s of meters near the surface and a few kilometers near the upper boundaries. The altitudes of these vertical model levels also vary as a function of latitude, longitude, and time, so the atmospheric specifications for a given event must be interpolated to a fixed geometric coordinate system for utilization in infrasound propagation codes. A simple yet effective approach is to interpolate and extrapolate the available atmospheric fields to a fixed vertical altitude grid with respect to the Mean Sea Level (MSL), and specifically including altitudes below the Earth's surface such as near the Tibetan plateau, Greenland, or Antarctic ice shelf. The virtual atmospheric grid points that are below the Earth's surface can then be explicitly be masked out with a separate digital terrain model that better matches the resolution of the infrasound propagation calculations.

14.3.2 Regional/Mesoscale Specifications

To provide improved spatiotemporal resolution for severe storm front tracking and tracer transport monitoring of volcanic ash, remarkable advances in regional mesoscale atmospheric specifications have occurred in the past decade. Systems

with up to 2×2 km resolution are being transitioned into operations, with 13×13 km $\times$ 1-h resolutions specifications up to 35 km altitude being the legacy standard. New systems such as the NCEP High Resolution Rapid Refresh (HRRR) provide regional meteorological specifications over the Continental United States (CONUS) and Alaska with 3×3 km resolution, with outputs at 15-min cadences for some of the fields. For reasons described in Sect. 14.4, compared to the global systems, these regional system have a slightly lower upper boundary typically near a constant pressure level of ~20 hPa (~25 km). Similarly, the UKMO mesoscale system produces 2.2×2.2 km resolution fields every 3 h, as well as at 1.5×1.5 km region for local regions. The JMA operates a mesoscale regional analysis system with 5×5 km horizontal resolution that has 50 vertical levels up to 22 km, and hourly output resolution; as well as a local forecast model with 2×2 km resolution on 60 levels up to ~20 km.

To properly resolve these meteorological length and timescales, today's mesoscale systems integrate the fully compressible non-hydrostatic fluid equations (e.g., Honda et al. 2005; Saito et al. 2007). Some of the global scale systems described earlier even now include non-hydrostatic compressible terms. The highest resolution mesoscale systems are even basically capable of resolving large convective lengths scales (e.g. Prein et al. 2015). Unlike present infrasound propagation codes which compute propagation characteristics from the first- or second-order linear and/or nonlinear perturbation expansion to the fluid equations, these non-hydrostatic solutions are calculated through the first-order fully resolved Navier–Stokes equations (e.g., Giraldo and Restelli 2008). However, the spatial extent and temporal resolution of these non-hydrostatic mesoscale models are still presently much greater than is needed to directly compute synthetic infrasound waveforms for compact impulsive infrasound events.

Today's mesoscale models can also provide highly resolved assimilative specifications of soil moisture, snow depth, and other meteorological dependent groundcover information relevant to infrasound monitoring. Such information is useful for diagnosing and understanding the spatiotemporal variability of infrasound sensor array response characteristics when dedicated soil moisture and snow depth sensors are not installed (or available) at an infrasound array, or at a potential infrasound source region. Specifically historical and/or near-real-time mesoscale specification of these may provide a better understanding of the causes of site specific differences in seismo-acoustic coupling (e.g., Walker et al. 2011; Hedlin and Walker 2013). As an example, by comparing hourly averaged infrasound pressure measurements across the of USArray Transportable Array (de Groot-Hedlin and Hedlin 2015) with hourly surface pressure specifications from the NCEP CONUS Rapid Updated Cycle (RUC) system for several months in 2013, it was possible to independently locate a number of problematic infrasound sensors in the network (R. Busby, personal communication).

14.4 Middle Atmospheric Specifications

Above the tropopause, the atmospheric meteorology begins to decouple from the sea surface temperatures, land–sea contrasts, and local terrain variations, and becomes predominately coupled to the global general circulation system of the stratosphere. This is why regional mesoscale systems generally do not extend well into the stratosphere. However, solar heating driven tides and waves of all scales generated in the lower atmosphere also propagate upward into the region; so the middle atmosphere is not completely uncoupled from the regional-scale dynamics of the lower atmosphere (Andrews et al. 1987). Physical processes such as ozone photochemistry and transport (e.g., Bednarz et al. 2016), heterogeneous ice chemistry (e.g., Solomon et al. 2015), and the momentum deposition from stationary and nonstationary subgrid-scale internal waves (e.g., Ern et al. 2016) are all important factors that govern the thermal structure and dynamics of the stratosphere.

Compared to the lower atmospheric specifications, civilian consumer demand for around the clock real-time middle atmospheric specifications and forecasts is basically nonexistent. The stratosphere can however influence the upper troposphere through mass, momentum, and energy transfer processes. The occurrence and phases of large stratospheric dynamical phenomena such as the Quasi-Biennial Oscillation (QBO) and Sudden Stratospheric Warmings (SSW) can be correlated with future meteorological patterns of the troposphere (Kidston et al. 2015). Thus, the middle atmospheric component of numerical weather prediction models provides a detailed upper boundary condition to resolve the influence of upper air steering currents and self-consistently compute the incoming solar UV and outgoing atmospheric infrared radiation. Another important reason for operational NWP systems to include a fully resolved middle atmosphere is to properly account for contaminating foreground atmospheric infrared and microwave radiation contributions in satellite-based remote sensing radiance observations of the lower atmosphere. All of the numerical weather prediction and atmospheric data assimilation systems which include a fully resolved middle atmosphere have improved forecast skill.

Middle atmospheric specifications associated with NWP systems are also integral to the international climate monitoring and middle atmospheric scientific research communities. Specifically, the middle atmosphere is susceptible to subtle changes in CO_2 composition (e.g., Funatsu et al. 2016), potential climatological changes in tropospheric dynamics (e.g., Garcia et al. 2016), and O_3 to man-made byproduct such as chlorofluorocarbons (CFCs) (e.g., Douglass et al. 2014). The tracking of injections and the subsequent fallout of volcanic aerosols in the stratosphere is also vital to understanding the impact that large volcanic eruptions have on the atmosphere and climate system (LeGrande et al. 2016).

These reasons motivate governmental investments in what are also known as reanalysis systems. One such system is the Goddard Earth Observing System (Version 5) GEOS5 which is used to produce the Modern-Era Retrospective analysis for Research and Applications, version 2 (MERRA2) analysis products (Bosilovich et al. 2015; Coy et al. 2016). Similarly, other major NWP centers (see Butchart et al.

2011) such as ECMWF Dee et al. 2011, JMA Harada et al. 2016, and NCEP (Saha et al. 2014) also produce reanalysis products for independent validation, comparison, and research. These reanalysis efforts also provide benchmarks and opportunities to develop and validate improved model physics for future operational NWP systems. The various reanalysis products from these systems are made publicly accessible for scientific research purposes, but for a number reasons (e.g., production cost, data archive, and distribution requirements) most available reanalysis products lag real-time by a month to several years, and may have slightly lower resolutions than operational numerical weather prediction forecast data products. One difference between these reanalysis fields and operational system analysis fields is that the underlying model assumptions are held constant over the entire multi-decade time interval; unlike the operational analysis archives where model resolution, physics, and the number of vertical levels routinely change.

14.5 Upper Atmospheric Specifications

Presently, there are no fully operational numerical weather prediction systems that encompass the lower thermosphere. This is the result of two main issues: the first is the cost and difficulty in making routine measurements of the region, the second is the lack of operational requirements as the result of strong direct economic and societal demands. A third factor is that the fundamental physics of the region is sufficiently different from the lower and middle atmosphere such that the basic *single fluid* meteorological conservation equations for mass, momentum, and energy can no longer be utilized.

To properly model the atmosphere above ~100 km, a viable meteorological forecast system must integrate the fully coupled *multispecies* transport equations, including the first-order effects of the global scale ionospheric electrodynamics (e.g., Rees 1989; Schunk and Nagy 2009). This is a consequence of the EUV photodissociation of O_2 producing atomic oxygen (O), subsequent EUV ionization of O and O_2 which produces the ionosphere, as well as the lack of turbulent mixing above about ~105 km, all resulting in O becoming the dominant species above ~175 km. The presence of an ionosphere in the Earth's magnetic field results in electrodynamics effects such as joule heating, aurora heating, and horizontal ion-neutral momentum coupling that have first-order influences on the *meteorology* of the upper atmosphere. As a result, the existing system of governing equations utilized in lower and middle atmospheric numerical weather prediction models cannot be extended from 75 to 250 km by simply adding additional model levels and constraining those results to match operational observations of the upper atmosphere.

Despite these challenges efforts to operationalize, the NOAA Whole Atmospheric Model (WAM) (https://esgf.esrl.noaa.gov/projects/wam_ipe/) for space weather applications is an active area of both basic and applied research. First-principles models of these processes have however existed for many years. One of the first non-assimilative models that can self-consistently represent these processes on a global

scale is the National Center for Atmospheric Research (NCAR), Thermosphere-Ionosphere-Electrodynamics General Circulation Model (TIE-GCM) (Richmond et al. 1992) and the Thermosphere-Ionosphere-Mesosphere-Electrodynamics General Circulation Model (TIME-GCM) (Roble and Ridley 1994). Other coupled thermosphere-ionosphere-electrodynamic models include the Coupled Thermosphere-Ionosphere-Plasmasphere-Electrodynamics (CTIPe) model (Fuller-Rowell and Rees 1980; Fuller-Rowell et al. 2002) and the Global Ionosphere Thermosphere Model (GITM) (Ridley et al. 2006). Recently a new class of 'Whole' atmospheric models are striving to account for these processes in a self-consistent manner with the lower and middle atmosphere (see Roble 2000). Examples are the NOAA Whole Atmosphere Model (WAM) (Akmaev 2011), the Hamburg Model for the Neutral and Ionized Atmosphere (HAMMONIA) (Schmidt et al. 2006), the NCAR Whole Atmosphere Community Climate Model-Extended (WACCMX) model (Liu et al. 2010), and the Ground-to-Topside Model of Atmosphere and Ionosphere for Aeronomy (GAIA) model (Jin et al. 2011). Unlike assimilative NWP systems, these models are generally free running, i.e., they are only driven by external forcings of the system at the upper and lower boundaries, and not constrained with real-time operational data above 85 km. Where they extend to lower altitudes and overlap with existing middle atmospheric analyses, they can be 'nudged 'or constrained (e.g., Stauffer and Seaman 1990) so that the observed meteorological variations there can be extrapolated (via theoretical considerations) into the thermosphere above (Marsh 2011; Siskind and Drob 2014; Sassi and Liu 2014).

While being a promising approach for the specification of the upper atmosphere between 85 and 200 km, it may be some time before operational systems are ready for utilization by independent third parties for uses such as infrasound monitoring. The limiting factor here is the lack of an adequate and truly *operational* global satellite- and ground-based network of sensors for the atmospheric region from 85 to 250 km. Today, only basic scientific research satellite mission datasets and ground-based research measurements exist for model validation and research-to-operation purposes. Thus, near-term infrasound propagation calculations must either rely on the extrapolation of data from below 85 km to lower thermospheric altitudes via the first-principles physics-based models, serendipitously coincident basic upper atmospheric research measurement, and/or empirical climatological models.

Unfortunately, unlike lower atmospheric radiosonde profiles, no one single upper atmospheric measurement technique simultaneously measures both winds and temperatures between 65 and 140 km and, in particular, across all ground ranges from an infrasound source to an infrasound detector. While measurements from co-located ground-based sensor suites of LIDARS and MF RADARs (Liu et al. 2002; Franke et al. 2005; Suzuki et al. 2010) can be combined to approach this capability, there are only a few research facilities where such instrument suites exist. Furthermore, these combine atmospheric observations are only limited in applicability to within a few 100 km of the measurement points, as well as to within about an hour or so in time. LIDAR observations are also generally limited to altitudes below ~105 km and to cloud free nighttime only conditions, but there are some exceptions. These research facilities are however ideal for validating future operational upper atmospheric

specifications systems, as well as for developing and calibrating new measurement techniques for future space-based systems, which are all required to operate global real-time NWP systems encompassing the thermosphere.

Presently, most infrasound propagation codes that consider thermospheric propagation utilize the observationally based Naval Research Laboratory (NRL) empirical upper atmospheric climatologies, the Mass Spectrometer Incoherent Scatter Radar Model Extended (NRLMSISE-00) (Picone et al. 2002), and the Horizontal Wind Model (HWM14) (Drob et al. 2015). These are part of the International Committee on Space Research (COSPAR) International Reference Atmosphere (CIRA). These empirical models are based on 50 years of satellite- and ground-based research observations. To combine the many available disparate research measurements into a complete observational based time-dependent global specification, these models utilize the simplest form of data assimilation known as observational function fitting (Daley 1993).

The end-user FORTRAN subroutines for these empirical upper atmospheric climatologies can be obtained at https://map.nrl.navy.mil/map/pub/nrl/HWM/HWM14/ and https://map.nrl.navy.mil/map/pub/nrl/NRLMSIS/NRLMSISE-00/. The input parameters to these empirical models are the day of year, universal time, latitude, longitude, altitude, the daily, and 81-day averaged measures of $F_{10.7}$ cm^{-1} solar radio wave flux (a proxy for solar EUV radiation), and the A_p geomagnetic activity index. These indices can be obtained for dates back to 1956 and in real time from http://www.swpc.noaa.gov/products-and-data. Otherwise no inputs of external observational data sets are needed by a user to run the MSIS and HWM client subroutines. The model outputs are winds, temperature, density, pressure, and atmospheric composition as a function of the specified latitude, longitude, altitude, day of year, and universal time. By matching these empirical models to the upper boundary conditions of the near-real-time lower and middle atmospheric specifications near ~75 km, Drob et al. (2003, 2010a) developed a simple approach to generate hybrid range- and time-dependent whole atmospheric specifications from the ground to space (0 to 200 km) that can be utilized to model thermospherically ducted infrasound propagation.

For infrasound propagation calculations above ~85 km, with longitudinal wavenumbers only up to $l = 3$, and latitudinal wave numbers only up to $n = 8$, a present limitation of the NRL empirical models is their low spectral resolution. Temporally the empirical models include the annual and semiannual seasonal variations, as well as the diurnal, semidiurnal, and terdiurnal migrating tidal harmonics, with the annual and semiannual seasonal modulations thereof. While this seems surprisingly crude as compared to the lower- and middle- atmospheric specifications, the meteorology of the upper atmosphere is primarily denominated by direct cyclical in situ forcing by EUV solar radiation (e.g., Roble 1983), deep westward migrating solar heating driven tidal modes propagating upward from below (e.g., Forbes and Wu 2006), and in situ geomagnetic forcing (e.g., Fuller-Rowell et al. 1994). The predominant seasonal variations of the thermosphere are phased locked with the earth's orbit around the sun, and the tidal variations with the earth rotation, with secondary modulations by geomagnetic forcing and solar variability. On average, these

variations account for the majority of the meteorology of the upper atmosphere, about ∼75–85% depending on altitude, field, and season. Being repeatable from year to year and day to day, these can be reasonably well parameterized with 50 years of observations and an appropriate set of basis functions. See Picone et al. (2002); Drob et al. (2015) and references therein for additional details. For some infrasound calculations, this is generally sufficient.

In the upper mesosphere and lower thermosphere, there is however a significant amount of regional variability, ∼25–35% that can not be readily resolved by empirical models (e.g., Liu 2016). Such variations will have consequences for precise modeling of thermospheric infrasound propagation characteristics for specific events. Most, but not all of this variability resides in the amplitudes and phases of the migrating and non-migrating solar tides. These variations result from longitudinal variations in water vapor in the troposphere and ozone in the stratosphere where the solar heating migrating tidal variations are forced (e.g., Forbes and Wu 2006). The day-to-day tidal variability can be on the order of 30% in tidal amplitude and 1–3 h in phase, but depends on latitude, altitude, and seasons. As a consequence, the westward migrating solar semidiurnal (12-h) tidal amplitudes in HWM in the 90 to 120 km region at mid-to-high latitudes can be underestimated by as much as 30–40 m/s on any given day, however there is little disagreement when the observations are averaged over a month or so.

Although available nudged and free running first-principles thermosphere and whole atmospheric general circulation models have sufficient spatiotemporal resolution to theoretically resolve this day-to-day variability, these present *physics-based* models can also exhibit regional biases in a number of fields depending on altitude, latitude, and day of year. Integrated over longer propagation paths, these systematic biases thus have the potential to be non-negligible in the infrasound propagation modeling error budget. In summary, presently available upper atmospheric specifications for infrasound propagation calculations of thermospheric infrasound propagation are rudimentary at best as compared to the fidelity and accuracy of lower- and middle- atmospheric specifications. There are however efforts unrelated to infrasound propagation that may eventually remedy this situation in the near future.

14.5.1 Upper Atmospheric Composition

As mentioned, EUV photo-disassociation of molecular oxygen results in atomic oxygen becoming the dominant atmospheric compositional species above ∼175 km. This has important consequences for the atmospheric sound speed above ∼100 km through the ratio of specific heats (γ) and mean molecular mass ($\bar{m}$).

The global average number density profiles (n_i) of the seven major upper atmospheric species from the NRLMSISE-00 model (over the typical range solar EUV flux conditions from the minimum to the maximum of the sunspot cycle) is shown in Fig. 14.3. Much like winds and temperatures, upper atmospheric composition varies

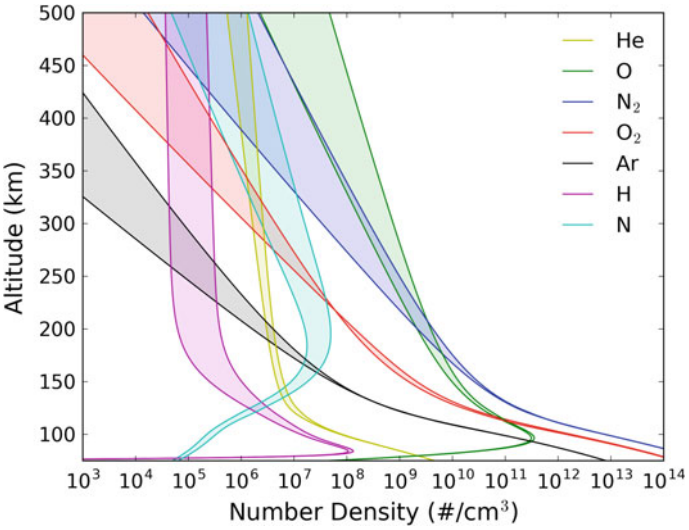

Fig. 14.3 Observed global average atmospheric number density of the seven major upper atmospheric constituents from the MSIS empirical model

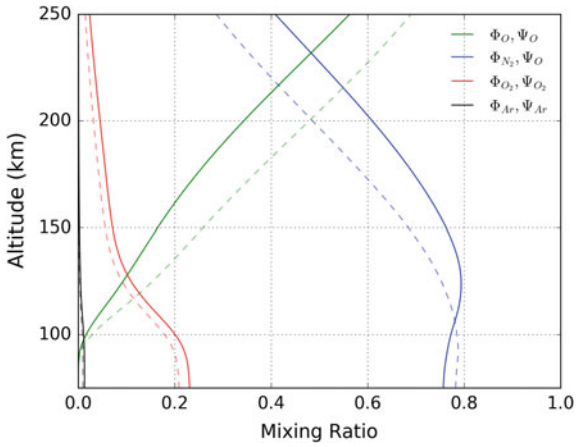

Fig. 14.4 Global average major individual species volume Φ_i (solid) and mass Ψ_i (dashed) mixing ratios (minimum solar cycle conditions) for molecular nitrogen (N_2; blue), molecular oxygen (O_2; red), and atomic oxygen (O, green)

somewhat as a function of latitude, day of year, local time, and geomagnetic activity. Such variations are reasonably well represented within the NRLMSIS-00 and theoretical first-principles models (Hedin 1987; Rishbeth and Müller-Wodarg 1999; Pedatella et al. 2016).

To highlight the significance of these compositional changes of the upper atmosphere in contrast to the lower thermosphere, the corresponding upper atmospheric volume Φ_i and mass Ψ_i mixing are shown in Fig. 14.4. The volume mixing ratio of the ith species is defined as $\Phi_i = n_i / \sum_j n_j = n_i/N = P_i/P$, where $P_i = n_i kT$ is the partial pressure, $P = nkT$ is the total atmospheric pressure, and n is the total number

density. The mass mixing ratio of the ith species is defined as $\Psi_i = n_i m_i / \sum_j m_j n_j$. The calculations shown assume that all the atmospheric constituents have the same average kinetic temperature which is reasonably below ~400 km. As seen in Fig. 14.4, departures from the constant major species composition mixing ratios of the lower and middle atmosphere; $\Phi_{N_2} = 0.7808$, $\Phi_{O_2} = 0.2093$, and $\Phi_{Ar} = 0.0009$ (see Mohr et al. 2012) begin to occur at about ~100 km.

Ignoring second-order vibrational and rotational collision effects important for high-frequency nonlinear acoustic propagation (e.g., Bass et al. 2007), the first-order expression for static sound speed is

$$c = \sqrt{\frac{\gamma RT}{\bar{M}}} = \sqrt{\frac{\gamma kT}{\bar{m}}} = \sqrt{\frac{\gamma P}{\rho}}, \tag{14.1}$$

where $\gamma = c_p / c_v$ (the ratio of specific heat at constant pressure c_p, to that at constant volume c_v), R is the universal gas constant, and $\bar{M}$ average mass, $\bar{m}$ is the average molar mass, k is the Boltzmann constant, and ρ is the mass density. While the vertical atmospheric temperature profile must clearly be taken into account for infrasound propagation calculations, it is very common to assume that $\bar{m} = 28.9645$ g/mol and $\gamma = 1.4$ are both constants. This assumption results in the approximation $c \cong 20.0464\sqrt{T}$.

Changes in the upper atmospheric composition above ~85 km influence the static sound speed through changes in both $\bar{m}$ and γ. Note that both height integrated atmospheric pressure $P(z)$ and ρ are also functions of $\bar{m}$. Given the number densities n_i, or mass mixing ratios Ψ_i, $\bar{m}$ can be calculated as

$$\bar{m} = \Big[\sum_i \frac{\Psi_i}{m_i} \Big]^{-1} = \frac{\sum_i n_i m_i}{\sum_i n_i}. \tag{14.2}$$

Figure 14.5 shows the typical vertical variations of $\bar{m}(z)$ for the composition profiles shown in Fig. 14.3. From Chapman-Enskog theory (e.g., Gombosi 1994), a reasonable first-order approximation to calculate composition dependent specific heats (c_p,c_v) in the upper atmosphere is

$$c_p = \sum_m \frac{k}{2m_m}(2 + \Gamma_m)\Phi_m + \sum_a \frac{k}{2m_a}(2 + \Gamma_a)\Phi_a \tag{14.3}$$

$$c_v = \sum_m \frac{k}{2m_m}\Gamma_m \Phi_m + \sum_a \frac{k}{2m_a}\Gamma_a \Phi_a \tag{14.4}$$

where m_m and m_a are the individual molar masses of the respective molecular and atomic species; $\Gamma_m = 5$ and $\Gamma_a = 3$ the corresponding degrees of freedom of molecular and atoms; and Φ_m and Φ_a are the individual species volume mixing ratios for molecules and atoms. The corresponding altitude-dependent profile of $\gamma(z)$ for the low solar EUV flux conditions is also shown in Fig. 14.5.

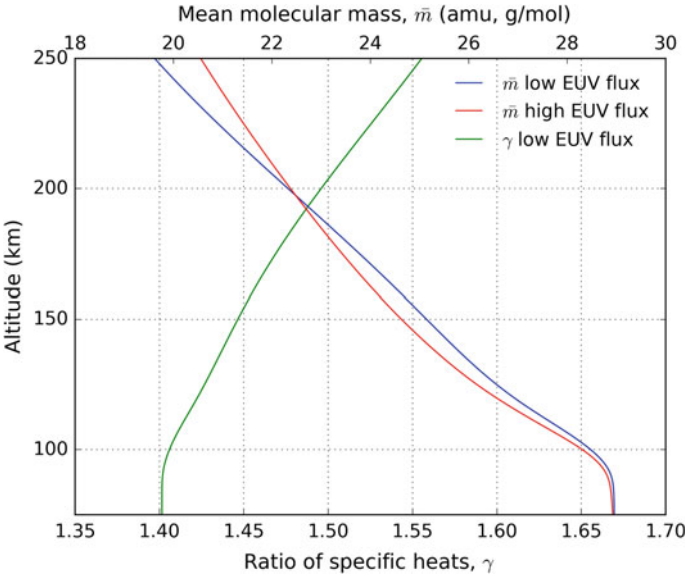

Fig. 14.5 Typical altitude variations of $\bar{m}$ for low (blue) and high (red) solar EUV flux conditions, with γ (green) shown for low EUV flux conditions

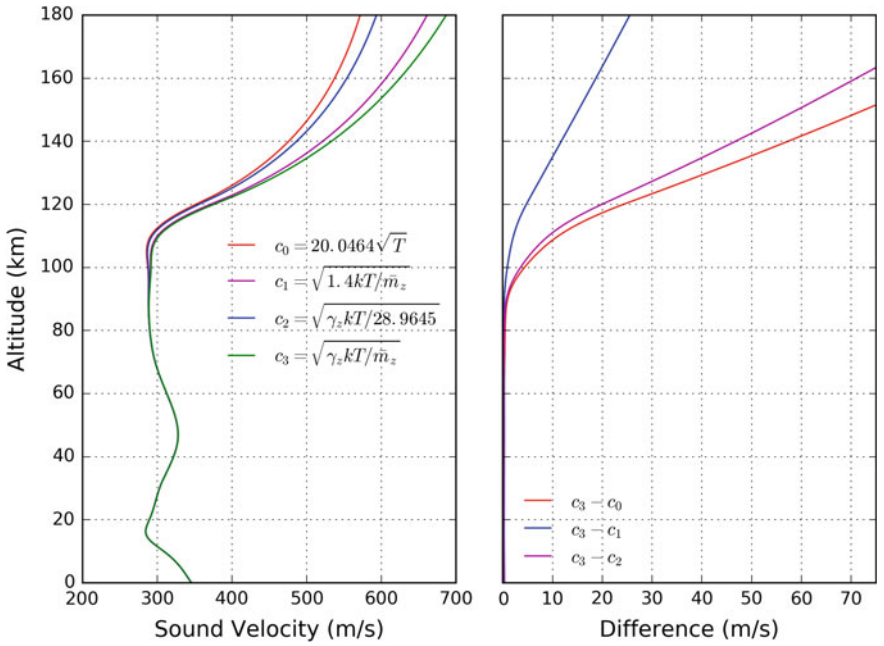

Fig. 14.6 Comparison of static sound speed calculated with various assumptions for $\bar{m}$ and γ in Eq. 14.1

The consequences of these composition variations in the calculation of the local vertical profiles of the static atmospheric sound speed is shown in Fig. 14.6. The right panel shows the difference between a temperature dependent only sound speed profile computed assuming constant $\bar{m}$ and γ, i.e., $c_0 = 20.0464\sqrt{T}$ (red), and one where $\bar{m}$ and γ vary with altitude according to composition c_3 (green). The intermediate assumptions are indicated as c_1 (magenta) and c_2 (blue). The differences $c_3 - c_0$ (right panel, red) are on the order of 25 m/s near the turning points of thermospherically ducted infrasound (∼120 km) and in excess of ∼50 m/s above 150 km. Note that these are systematic biases that will accumulate over long propagation paths. Thus when estimating upper atmospheric wind speeds from infrasound travel times (e.g., Drob et al. 2010b; Assink et al. 2013) or calculating thermospheric infrasound propagation characteristics (e.g., Lonzaga et al. 2015; Sabatini et al. 2016), it is important to account for the atmospheric composition dependent variations of $\bar{m}$ and γ.

14.6 Conclusions

Over the last decade, there has been considerable progress in global data assimilation capabilities for the lower, middle, and upper atmosphere. There is a wide array of operational and basic research specifications of the atmosphere from the ground to the thermosphere that are available for the calculation of infrasound propagation characteristics. In infrasound propagation modeling calculations, with the dramatic increase in the spatial resolution of today's lower and middle atmospheric specifications, it is also important to consider in tandem the available temporal resolution of the specifications.

As compared to available meteorological specifications of the lower and middle atmosphere, observationally based specifications of the atmosphere above ∼85 km are much lower resolution and much more uncertain. This is primarily due to the lack of routine operational observations of the region driven by direct commercial applications. On the horizon, continuing basic research efforts to support space weather modeling activities should provide improvements in the specification of density, temperature, winds, and composition of the upper atmosphere, and eventually perhaps near-real-time global assimilation capabilities like for the lower and middle atmosphere. Such efforts will provide better atmospheric specifications for infrasound propagation calculations.

Acknowledgements This work was supported by the Chief of Naval Research.

References

Abbott BP et al (2016) Observation of gravitational waves from a binary black hole merger. Phys Rev Lett 116(061):102. https://doi.org/10.1103/PhysRevLett.116.061102

Akmaev R (2011) Whole atmosphere modeling: connecting terrestrial and space weather. Rev Geophys 49(4)

Andrews DG, Holton JR, Leovy CB (1987) Middle atmosphere dynamics, vol 40. Academic press

Assink J, Waxler R, Frazier W, Lonzaga J (2013) The estimation of upper atmospheric wind model updates from infrasound data. J Geophys Res Atmos 118(19)

Bass HE, Hetzer CH, Raspet R (2007) On the speed of sound in the atmosphere as a function of altitude and frequency. J Geophys Res Atmos 112(D15)

Bauer P, Thorpe A, Brunet G (2015) The quiet revolution of numerical weather prediction. Nature 525(7567):47–55

Bednarz EM, Maycock AC, Abraham NL, Braesicke P, Dessens O, Pyle JA (2016) Future arctic ozone recovery: the importance of chemistry and dynamics. Atmos Chem Phys 16(18):12,159–12,176

Blom PS, Marcillo O, Arrowsmith SJ (2015) Improved bayesian infrasonic source localization for regional infrasound. Geophys J Int 203(3):1682–1693

Bonavita M, Hólm E, Isaksen L, Fisher M (2016) The evolution of the ECMWF hybrid data assimilation system. Q J R Meteorol Soc 142(694):287–303

Bosilovich M, Akella S, Coy L, Cullather R, Draper C, Gelaro R, Kovach R, Liu Q, Molod A, Norris P et al (2015) Merra-2: initial evaluation of the climate. NASA Technical report series on global modeling and data assimilation, NASA/TM-2015 104606

Butchart N, Charlton-Perez A, Cionni I, Hardiman S, Haynes P, Krüger K, Kushner P, Newman P, Osprey S, Perlwitz J et al (2011) Multimodel climate and variability of the stratosphere. J Geophys Res Atmos 116(D5)

Chunchuzov I, Kulichkov S (2019) Internal gravity wave perturbations and their impacts on infrasound propagation in the atmosphere. In: Le Pichon A, Blanc E, Hauchecorne A (eds) Infrasound monitoring for atmospheric studies, 2nd edn. Springer, Dordrecht, pp 551–590

Chunchuzov I, Kulichkov S, Popov O, Waxler R, Assink J (2011) Infrasound scattering from atmospheric anisotropic inhomogeneities. Izv Atmos Oceanic Phys 47(5):540–557

Costantino L, Heinrich P, Mzé N, Hauchecorne A (2015) Convective gravity wave propagation and breaking in the stratosphere: comparison between WRF model simulations and lidar data. Ann Geophys 33(9):1155–1171. https://doi.org/10.5194/angeo-33-1155-2015, http://www.ann-geophys.net/33/1155/2015/

Courtier P, Thépaut JN, Hollingsworth A (1994) A strategy for operational implementation of 4D-Var, using an incremental approach. Q J R Meteorol Soc 120(519):1367–1387

Coy L, Wargan K, Molod AM, McCarty WR, Pawson S (2016) Structure and dynamics of the quasi-biennial oscillation in MERRA-2. J Clim (2016)

Cugnet D, de la Camara A, Lott F, Millet C, Ribstein B (2019) Non-orographic gravity waves: representation in climate models and effects on infrasound. In: Le Pichon A, Blanc E, Hauchecorne A (eds) Infrasound monitoring for atmospheric studies, 2nd edn. Springer, Dordrecht, pp 827–844

Daley R (1993) Atmospheric data analysis, no 2. Cambridge university press

de Groot-Hedlin CD, Hedlin MA (2015) A method for detecting and locating geophysical events using groups of arrays. Geophys J Int 203(2):960–971

Dee D, Uppala S, Simmons A, Berrisford P, Poli P, Kobayashi S, Andrae U, Balmaseda M, Balsamo G, Bauer P et al (2011) The era-interim reanalysis: configuration and performance of the data assimilation system. Q J R Meteorol Soc 137(656):553–597

Douglass A, Strahan S, Oman L, Stolarski R (2014) Understanding differences in chemistry climate model projections of stratospheric ozone. J Geophys Res Atmos 119(8):4922–4939

Drob DP, Emmert JT, Meriwether JW, Makela JJ, Doornbos E, Conde M, Hernandez G, Noto J, Zawdie KA, McDonald SE et al (2015) An update to the horizontal wind model (HWM): the quiet time thermosphere. Earth Space Sci 2(7):301–319

Drob DP, Garcés M, Hedlin M, Brachet N (2010a) The temporal morphology of infrasound propagation. Pure Appl Geophys 167(4–5):437–453
Drob DP, Meier R, Picone JM, Garcés MM (2010b) Inversion of infrasound signals for passive atmospheric remote sensing. Infrasound monitoring for atmospheric studies. Springer, pp 701–731
Drob DP, Picone J, Garcés M (2003) Global morphology of infrasound propagation. J Geophys Res Atmos 108(D21)
Drob D, Broutman D, Hedlin M, Winslow N, Gibson R (2013) A method for specifying atmospheric gravity wavefields for long-range infrasound propagation calculations. J Geophys Res Atmos 118(10):3933–3943
Edwards PN (2010) A vast machine: computer models, climate data, and the politics of global warming. Mit Press
Ern M, Preusse P, Warner C (2006) Some experimental constraints for spectral parameters used in the Warner and Mcintyre gravity wave parameterization scheme. Atmos Chem Phys 6(12):4361–4381
Ern M, Trinh QT, Kaufmann M, Krisch I, Preusse P, Ungermann J, Zhu Y, Gille JC, Mlynczak MG, Russell III JM, Schwartz MJ, Riese M (2016) Satellite observations of middle atmosphere gravity wave absolute momentum flux and of its vertical gradient during recent stratospheric warmings. Atmos Chem Phys 16(15):9983–10,019. https://doi.org/10.5194/acp-16-9983-2016, http://www.atmos-chem-phys.net/16/9983/2016/
Evers L, Geyt A, Smets P, Fricke J (2012) Anomalous infrasound propagation in a hot stratosphere and the existence of extremely small shadow zones. J Geophys Res Atmos 117(D6)
Evers L, Haak H (2007) Infrasonic forerunners: exceptionally fast acoustic phases. Geophys Res Lett 34(10)
Fleagle RG, Businger JA (1981) An introduction to atmospheric physics, vol 25. Academic Press
Forbes JM, Wu D (2006) Solar tides as revealed by measurements of mesosphere temperature by the MLS experiment on UARS. J Atmos Sci 63(7):1776–1797
Franke S, Chu X, Liu A, Hocking W (2005) Comparison of meteor radar and Na Doppler lidar measurements of winds in the mesopause region above Maui, Hawaii. J Geophys Res Atmos 110(D9)
Fritts DC, Alexander MJ (2003) Gravity wave dynamics and effects in the middle atmosphere. Rev Geophys 41(1)
Fuller-Rowell TJ, Rees D (1980) A three-dimensional time-dependent global model of the thermosphere. J Atmos Sci 37(11):2545–2567
Fuller-Rowell T, Codrescu M, Moffett R, Quegan S (1994) Response of the thermosphere and ionosphere to geomagnetic storms. J Geophys Res Space Phys 99(A3):3893–3914
Fuller-Rowell T, Millward G, Richmond A, Codrescu M (2002) Storm-time changes in the upper atmosphere at low latitudes. J Atmos Solar Terr Phys 64(12):1383–1391
Funatsu BM, Claud C, Keckhut P, Hauchecorne A, Leblanc T (2016) Regional and seasonal stratospheric temperature trends in the last decade (2002–2014) from AMSU observations. J Geophys Res Atmos 121(14):8172–8185
Garcés MA, Hansen RA, Lindquist KG (1998) Traveltimes for infrasonic waves propagating in a stratified atmosphere. Geophys J Int 135(1):255–263
Garcia RR, López-Puertas M, Funke B, Kinnison DE, Marsh DR, Qian L (2016) On the secular trend of COx and CO2 in the lower thermosphere. J Geophys Res Atmos 121(7):3634–3644
Geller MA, Alexander MJ, Love PT, Bacmeister J, Ern M, Hertzog A, Manzini E, Preusse P, Sato K, Scaife AA et al (2013) A comparison between gravity wave momentum fluxes in observations and climate models. J Clim 26(17):6383–6405
Georges T, Beasley WH (1977) Refraction of infrasound by upper-atmospheric winds. J Acoust Soc Am 61(1):28–34
Giraldo FX, Restelli M (2008) A study of spectral element and discontinuous Galerkin methods for the Navier-Stokes equations in nonhydrostatic mesoscale atmospheric modeling: equation sets and test cases. J Comput Phys 227(8):3849–3877

Gombosi TI (1994) Gaskinetic theory, no 9. Cambridge University Press
Gossard EE, Hooke WH (1975) Waves in the atmosphere: atmospheric infrasound and gravity waves-their generation and propagation. Atmos Sci 2
Green DN, Vergoz J, Gibson R, Le Pichon A, Ceranna L (2011) Infrasound radiated by the Gerdec and Chelopechene explosions: propagation along unexpected paths. Geophys J Int 185(2):890–910
Harada Y, Kamahori H, Kobayashi C, Endo H, Kobayashi S, Ota Y, Onoda H, Onogi K, Miyaoka K, Takahashi K (2016) The JRA-55 reanalysis: representation of atmospheric circulation and climate variability. J Meteorol Soc Jpn Ser II 94(3):269–302. https://doi.org/10.2151/jmsj.2016-015
Hedin AE (1987) MSIS-86 thermospheric model. J Geophys Res Space Phys 92(A5):4649–4662
Hedlin MA, Drob DP (2014) Statistical characterization of atmospheric gravity waves by seismoacoustic observations. J Geophys Res Atmos 119(9):5345–5363
Hedlin MA, Walker KT (2013) A study of infrasonic anisotropy and multipathing in the atmosphere using seismic networks. Phil Trans R Soc A 371(1984):20110,542
Hertzog A, Alexander MJ, Plougonven R (2012) On the intermittency of gravity wave momentum flux in the stratosphere. J Atmos Sci 69(11):3433–3448
Hines CO (1960) Internal atmospheric gravity waves at ionospheric heights. Can J Phys 38(11):1441–1481
Honda Y, Nishijima M, Koizumi K, Ohta Y, Tamiya K, Kawabata T, Tsuyuki T (2005) A pre-operational variational data assimilation system for a non-hydrostatic model at the Japan meteorological agency: formulation and preliminary results. Q J R Meteorol Soc 131(613):3465–3475
Houtekamer PL, Zhang F (2016) Review of the ensemble kalman filter for atmospheric data assimilation. Monthly Weather Rev 144(12):4489–4532. https://doi.org/10.1175/MWR-D-15-0440.1
Jewtoukoff V, Hertzog A, Plougonven R, Adl Cámara, Lott F (2015) Comparison of gravity waves in the southern hemisphere derived from balloon observations and the ECMWF analyses. J Atmos Sci 72(9):3449–3468
Jin H, Miyoshi Y, Fujiwara H, Shinagawa H, Terada K, Terada N, Ishii M, Otsuka Y, Saito A (2011) Vertical connection from the tropospheric activities to the ionospheric longitudinal structure simulated by a new earth's whole atmosphere-ionosphere coupled model. J Geophys Res Space Phys 116(A1)
Kidston J, Scaife AA, Hardiman SC, Mitchell DM, Butchart N, Baldwin MP, Gray LJ (2015) Stratospheric influence on tropospheric jet streams, storm tracks and surface weather. Nature Geosci 8(6):433–440
Kulichkov S, Chunchuzov I, Popov O (2010) Simulating the influence of an atmospheric fine inhomogeneous structure on long-range propagation of pulsed acoustic signals. Izv Atmos Oceanic Phys 46(1):60–68
Lacanna G, Ichihara M, Iwakuni M, Takeo M, Iguchi M, Ripepe M (2014) Influence of atmospheric structure and topography on infrasonic wave propagation. J Geophys Res Solid Earth 119(4):2988–3005
Lalande JM, Waxler R (2016) The interaction between infrasonic waves and gravity wave perturbations: Application to observations using UTTR rocket motor fuel elimination events. J Geophys Res Atmos
Le Pichon A, Garcés M, Blanc E, Barthélémy M, Drob DP (2002) Acoustic propagation and atmosphere characteristics derived from infrasonic waves generated by the Concorde. J Acoust Soc Am 111(1):629–641
LeGrande AN, Tsigaridis K, Bauer SE (2016) Role of atmospheric chemistry in the climate impacts of stratospheric volcanic injections. Nature Geosci
Liu AZ, Hocking WK, Franke SJ, Thayaparan T (2002) Comparison of Na lidar and meteor radar wind measurements at Starfire Optical Range, NM, USA. J Atmos Solar Terr Phys 64(1):31–40

Liu HL, Foster B, Hagan M, McInerney J, Maute A, Qian L, Richmond A, Roble R, Solomon S, Garcia R et al (2010) Thermosphere extension of the whole atmosphere community climate model. J Geophys Res Space Phys 115(A12)

Liu HL (2016) Variability and predictability of the space environment as related to lower atmosphere forcing. Space Weather

Lonzaga JB, Waxler RM, Assink JD, Talmadge CL (2015) Modelling waveforms of infrasound arrivals from impulsive sources using weakly non-linear ray theory. Geophys J Int 200(3):1347–1361

Lorenc AC (2003) The potential of the ensemble Kalman filter for NWP–a comparison with 4D-Var. Q J R Meteorol Soc 129(595):3183–3203

Marcillo O, Arrowsmith S, Whitaker R, Anderson D, Nippress A, Green DN, Drob D (2013) Using physics-based priors in a Bayesian algorithm to enhance infrasound source location. Geophys J Int 353

Marsh DR (2011) Chemical–dynamical coupling in the mesosphere and lower thermosphere. Aeronomy of the earth's atmosphere and ionosphere. Springer, pp 3–17

Millet C, Robinet JC, Roblin C (2007) On using computational aeroacoustics for long-range propagation of infrasounds in realistic atmospheres. Geophys Res Lett 34(14)

Mohr PJ, Taylor BN, Newell DB (2012) CODATA recommended values of the fundamental physical constants: 2010. J Phys Chem Ref Data 41(4):043,109

Orr A, Bechtold P, Scinocca J, Ern M, Janiskova M (2010) Improved middle atmosphere climate and forecasts in the ECMWF model through a nonorographic gravity wave drag parameterization. J Clim 23(22):5905–5926

Pedatella N, Richmond A, Maute A, Liu HL (2016) Impact of semidiurnal tidal variability during SSWS on the mean state of the ionosphere and thermosphere. J Geophys Res Space Phys 121(8):8077–8088

Picone J, Hedin A, Drob DP, Aikin A (2002) NRLMSISE-00 empirical model of the atmosphere: Statistical comparisons and scientific issues. J Geophys Res Space Phys 107(A12)

Prein AF, Langhans W, Fosser G, Ferrone A, Ban N, Goergen K, Keller M, Tölle M, Gutjahr O, Feser F et al (2015) A review on regional convection-permitting climate modeling: demonstrations, prospects, and challenges. Rev Geophys 53(2):323–361

Preusse P, Ern M, Bechtold P, Eckermann SD, Kalisch S, Trinh QT, Riese M (2014) Characteristics of gravity waves resolved by ECMWF. Atmos Chem Phys 14(19):10,483–10,508. https://doi.org/10.5194/acp-14-10483-2014, http://www.atmos-chem-phys.net/14/10483/2014/

Rabier F, Järvinen H, Klinker E, Mahfouf JF, Simmons A (2000) The ECMWF operational implementation of four-dimensional variational assimilation. I: experimental results with simplified physics. Q J R Meteorol Soc 126(564):1143–1170

Rees MH (1989) Physics and chemistry of the upper atmosphere, vol 1. Cambridge University Press

Richmond A, Ridley E, Roble R (1992) A thermosphere/ionosphere general circulation model with coupled electrodynamics. Geophys Res Lett 19(6):601–604

Ridley A, Deng Y, Toth G (2006) The global ionosphere-thermosphere model. J Atmos Solar Terr Phys 68(8):839–864

Rind D (1978) Investigation of the lower thermosphere results of ten years of continuous observations with natural infrasound. J Atmos Terr Phys 40(10–11):1199–1209

Rishbeth H, Müller-Wodarg I (1999) Vertical circulation and thermospheric composition: a modelling study. Ann Geophys 17:794–805. Springer

Roble R (1983) Dynamics of the earth's thermosphere. Rev Geophys 21(2):217–233

Roble R (2000) On the feasibility of developing a global atmospheric model extending from the ground to the exosphere. Atmos Sci Across Stratopause 53–67

Roble R, Ridley E (1994) A thermosphere-ionosphere-mesosphere-electrodynamics general circulation model (time-GCM): equinox solar cycle minimum simulations (30–500 km). Geophys Res Lett 21(6):417–420

Sabatini R, Bailly C, Marsden O, Gainville O (2016) Characterization of absorption and nonlinear effects in infrasound propagation using an augmented burgers' equation. Geophys J Int 207(3):1432–1445

Saha S, Moorthi S, Wu X, Wang J, Nadiga S, Tripp P, Behringer D, Hou YT, Hy Chuang, Iredell M et al (2014) The NCEP climate forecast system version 2. J Clim 27(6):2185–2208

Saito K, Ishida JI, Aranami K, Hara T, Segawa T, Narita M, Honda Y (2007) Nonhydrostatic atmospheric models and operational development at JMA. J Meteorol Soc Jpn Ser II 85:271–304

Sassi F, Liu HL (2014) Westward traveling planetary wave events in the lower thermosphere during solar minimum conditions simulated by SD-WACCM-X. J Atmos Solar Terr Phys 119:11–26

Schmidt H, Brasseur G, Charron M, Manzini E, Giorgetta M, Diehl T, Fomichev V, Kinnison D, Marsh D, Walters S (2006) The HAMMONIA chemistry climate model: sensitivity of the mesopause region to the 11-year solar cycle and co2 doubling. J Clim 19(16):3903–3931

Schunk R, Nagy A (2009) Ionospheres: physics, plasma physics, and chemistry. Cambridge University Press

Siskind DE, Drob DP (2014) Use of NOGAPS-ALPHA as a bottom boundary for the NCAR/TIEGCM. Model Ionosphere Thermosphere Syst 171–180

Smets P, Evers L, Näsholm S, Gibbons S (2015) Probabilistic infrasound propagation using realistic atmospheric perturbations. Geophys Res Lett 42(15):6510–6517

Solomon S, Kinnison D, Bandoro J, Garcia R (2015) Simulation of polar ozone depletion: an update. J Geophys Res Atmos 120(15):7958–7974

Stauffer DR, Seaman NL (1990) Use of four-dimensional data assimilation in a limited-area mesoscale model. part I: experiments with synoptic-scale data. Monthly Weather Rev 118(6):1250–1277

Suzuki S, Nakamura T, Ejiri MK, Tsutsumi M, Shiokawa K, Kawahara TD (2010) Simultaneous airglow, lidar, and radar measurements of mesospheric gravity waves over japan. J Geophys Res Atmos 115(D24)

Toth Z, Kalnay E, Tracton SM, Wobus R, Irwin J (1997) A synoptic evaluation of the NCEP ensemble. Weather Forecast 12(1):140–153

Walker KT, Shelby R, Hedlin MA, Groot-Hedlin C, Vernon F (2011) Western us infrasonic catalog: Illuminating infrasonic hot spots with the USArray. J Geophys Res Solid Earth 116(B12)

Warner TT (2010) Numerical weather and climate prediction. Cambridge University Press

Warner C, McIntyre M (2001) An ultrasimple spectral parameterization for nonorographic gravity waves. J Atmos Sci 58(14):1837–1857

Waxler R, Assink J (2019) Propagation modeling through realistic atmosphere and benchmarking. In: Le Pichon A, Blanc E, Hauchecorne A (eds) Infrasound monitoring for atmospheric studies, 2nd edn. Springer, Dordrecht, pp 509–549

Zhang H, Pu Z (2010) Beating the uncertainties: ensemble forecasting and ensemble-based data assimilation in modern numerical weather prediction. Adv Meteorol 2010

Chapter 15
Propagation Modeling Through Realistic Atmosphere and Benchmarking

Roger Waxler and Jelle Assink

Abstract In this chapter, an overview of infrasound propagation modeling is presented. The atmosphere as a propagation medium is discussed with an emphasis on the various propagation paradigms. Some of the more commonly used propagation models are discussed and compared and repositories for open-source propagation model software are indicated.

15.1 Introduction

Infrasound produced by large, often violent, events can often be detected at great distances from the event itself. This is due to the efficient propagation of infrasound in ducts produced by temperature and wind speed gradients in the atmosphere. While there have been systems developed with which infrasound sensors are elevated on balloons or dirigibles, the primary interest is currently in ground-based detection of infrasonic signals. The atmospheric winds have a critical role in the ducting of infrasound, creating ducts where temperature gradients are insufficient to cause signals to return to the ground. Infrasound propagation is highly asymmetric and detection depends critically on the presence of wind jets aloft in the atmosphere with sufficient component from source to receiver. In addition, the atmosphere can support multiple ducts, all depending on the direction of propagation relative to wind velocity at different altitudes. Propagation in the different ducts each have their own particular characteristics, largely related to atmospheric processes at different altitudes. As a consequence, the signals received from an event can be very complicated, arriving in an extended wave train along a variety of paths and undergoing severe dispersion.

Generally speaking, the mathematics of sound propagation is well understood. In the last decade, there has been significant progress in the development and

R. Waxler (✉)
University of Mississippi, National Center for Physical Acoustics, Oxford, MS, USA
e-mail: rwax@olemiss.edu

J. Assink
R&D Seismology and Acoustics, Royal Netherlands Meteorological Institute (KNMI), De Bilt, The Netherlands

A. Le Pichon et al. (eds.), *Infrasound Monitoring for Atmospheric Studies*,
https://doi.org/10.1007/978-3-319-75140-5_15

availability of infrasound propagation models (see Norris et al. 2010 for a review published in 2010) which use specification of the atmospheric state as input. A variety of open-source infrasound propagation models are now available, and software benchmarking is beginning. A much more difficult problem is that of knowing the atmosphere well enough to characterize the propagation. A related question is that of how well the atmosphere needs to be characterized to capture the essentials of the signal propagation. In this regard, there are two philosophies that can be followed in modeling infrasound propagation: one may attempt to develop the most comprehensive model possible that covers all possible scenarios, or one may develop a suite of models of increasing complexity and make use of the simplest model that captures the relevant complexity for a given application. It is the latter approach that will be focused on here.

15.2 The Atmosphere as a Propagation Medium

Sound propagation is sensitive to the atmospheric state, in particular to the temperature and wind. Sound is refracted downwards by positive temperature gradients and upwards by negative temperature gradients. Positive wind shear refracts sound downwards and negative upwards. Thus, in order to model infrasound propagation, one must know the state of the atmosphere at the time of propagation.

The atmosphere can often be assumed to be vertically stratified in the sense that horizontal changes are on a much slower scale than vertical. In this approximation, mean temperature, pressure, density, and entropy, T_0, P_0, ρ_0, and S_0, depend only on altitude z. Let the subscript H indicate projection on the horizontal plane and let u and v be the standard atmospheric science notation for zonal and meridional wind speed, respectively. In the stratified approximation, the mean flow or wind,

$$\mathbf{v}_0 = \begin{pmatrix} \mathbf{v}_{0,H} \\ 0 \end{pmatrix} = \begin{pmatrix} u \\ v \\ 0 \end{pmatrix}, \tag{15.1}$$

has no vertical component and the horizontal components depend only on z, but are otherwise unconstrained.

In a stratified, adiabatic atmosphere with equation of state given by the ideal gas law $P_0 = \rho_0 R T_0$ the mean state can be specified by the temperature alone. Hydrostatic equilibrium implies that

$$P_0(z) = P_0(0) e^{-\frac{g}{R}\int_0^z \frac{1}{T_0(z')}\, dz'} \tag{15.2}$$

and mean density and entropy can then be inferred from the thermodynamic relations. It follows that, in stratified models of the atmosphere, a specification of the atmospheric state only requires a specification of the temperature and horizontal wind velocity components. In this approximation, which can be called the *locally*

stratified approximation, any horizontal changes in the atmosphere are accounted for by letting the temperature and wind depend on location. In practice, rather than just the temperature, atmospheric density and pressure are specified so that the gas constant R can be inferred from the ideal gas law.

In reality, the atmosphere is not vertically stratified. To a first approximation, the winds themselves are generated by horizontal pressure gradients, associated with temperature gradients, in conjunction with the Earth's rotation (Andrewes et al. 1987). These are of a sufficiently large scale that, for purposes of infrasound propagation modeling, their influence can be treated in a locally stratified approximation. On a finer scale, there are deviations from stratification induced by geographic changes such as topography and transitions from land to sea (Stull 1991; Gill 1982) as well as those induced by internal buoyancy waves (Chunchuzov 1996; Drob et al. 2013) and large-scale motions of wind jets (Fee et al. 2013).

15.2.1 The Mean Atmospheric State

Infrasound propagation typically takes place in the lower 120 km of the atmosphere. To a reasonable approximation, the temperature of the atmosphere stratifies with altitude as shown in the leftmost panel of Fig. 15.1. Near the ground, in the so-called atmospheric boundary layer which comprises the first kilometer or so, the behavior of the atmosphere can be complex undergoing diurnal variations and influenced by interaction with the ground and with the cloud cover. Above the boundary layer, the temperature of the atmosphere typically decreases with increasing altitude up to a minimum, called the tropopause, at about 15–20 km. The temperature then increases up to a maximum called the stratopause, decreases again to a minimum at the mesopause, and then increases sharply to around 200 km after which it slowly reaches a constant value of about 1000 K above 400 km (not depicted).

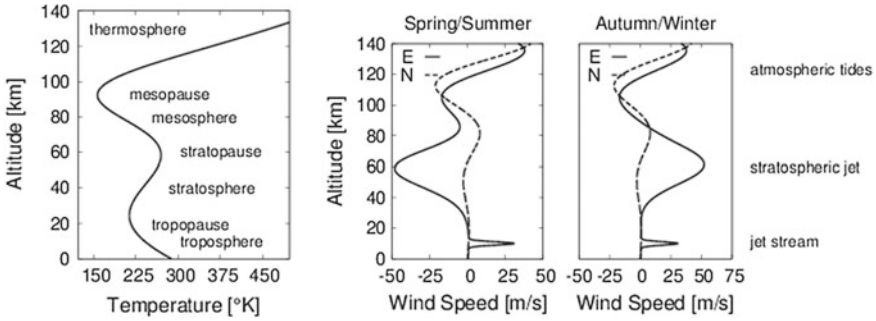

Fig. 15.1 Qualitative layers of the atmosphere and typical wind jets in the northern hemisphere; from Waxler et al. (2017)

The middle and rightmost panels of Fig. 15.1 show, qualitatively, the most common wind jets. At around 10 km altitude, one finds the jet stream and at 50–60 km, the circumpolar vortex, or stratospheric jet. The jet stream generally flows to the east, with magnitude depending on season and latitude. The stratospheric jet direction depends on the season and on the hemisphere. The stratospheric jet generally flows to the west in spring and summer and to the east in fall and winter. During the vernal and autumnal equinoxes, the circumpolar vortex breaks down and the direction of the flow reverses.

Actual atmospheric specifications are available from diverse sources in different layers of the atmosphere. The most widely used specifications are the Ground-to-Space (G2S, Drob 2019) and European Centre for Medium-Range Weather Forecasts (ECMWF) specifications. For a comparison of the two, see the discussion following Fig. 3 in Fee et al. (2013). In Fig. 15.2, temperature and wind speed specifications from the G2S model are shown for New York City at 0600 UTC on January 1, 2008. Note the temperature stratification similar to that seen in Fig. 15.1 as well as an eastward flowing jet stream and stratospheric jet, as expected.

In Fig. 15.3, taken from Fig. 2 of Fee et al. (2013), a history of the zonal (eastwardly flowing) winds over the Negev desert in the south of Israel. Around 10 km, there is an eastward flowing jet stream which becomes quite strong in the winter and dies off in the summer. Beginning at around 40 km and extending up to about 75 km, one can clearly see the circumpolar vortex. It flows steadily to the west in summer. In the winter, there is always an eastward flowing component, but the winter vortex is unstable in the northern hemisphere, occasionally breaking up and generating westward flowing components as well (Andrewes et al. 1987; Evers and Siegmund 2009; Assink et al. 2014). These instabilities are known as sudden stratospheric warming (SSW) events and are discussed at length in Smets et al. (2019).

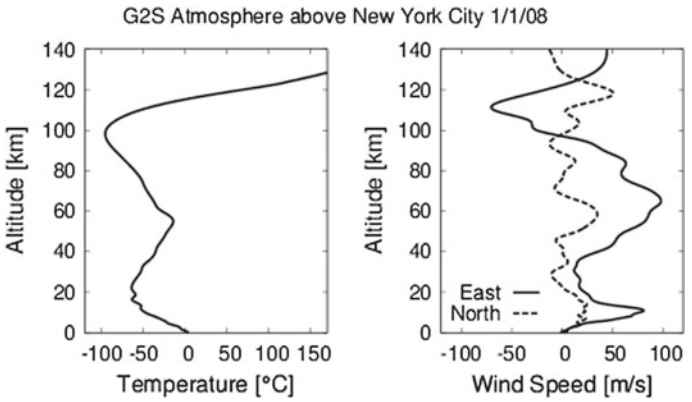

Fig. 15.2 G2S specification over NYC at 0600 UTC on January 1, 2008, from Fig. 1 of Waxler et al. (2017)

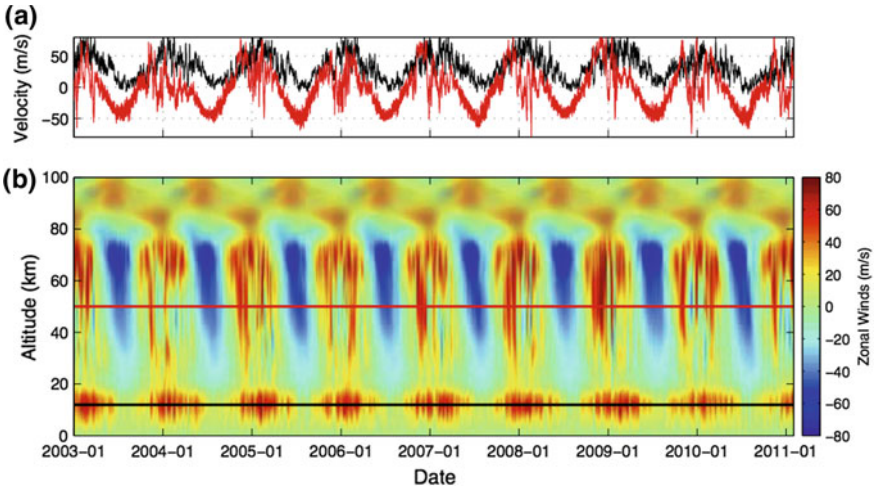

Fig. 15.3 Wind history over southern Israel from Fig. 2 in (Fee et al. 2013). Shown are the G2S specifications for the zonal (eastward flowing) winds over the Negev desert for 2003 through 2011. The upper frame shows the zonal wind magnitudes at 10 (in black) and 50 (in red) kilometers altitude

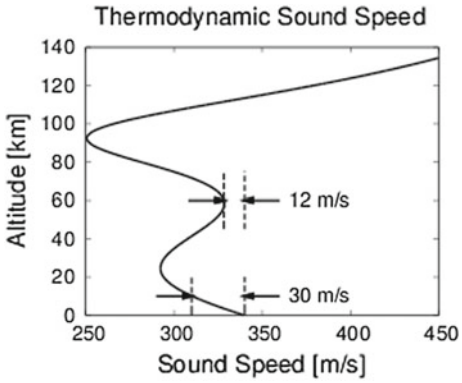

Fig. 15.4 The temperature maximum at the stratopause is typically too shallow to return signals to the ground

The influence of the winds is much greater than just influencing the details of the propagation. Wind jets can produce ducts that atmospheric temperature gradients either do not produce or cannot support. This is illustrated in Fig. 15.4 where the sound speed (temperature) at the stratopause is shown to be less than at the ground. With the exception of very cold times of the year at extreme latitudes, this is usually the case. It is a direct consequence of Snell's law that signals get refracted from regions of higher sound speed to regions of lower sound speed. In order for sound to be refracted back down to the ground, there must be regions in the atmosphere with a higher sound speed than that on the ground. In this the wind is critical. The stratospheric jet is generally required to complete the formation of a stratospheric

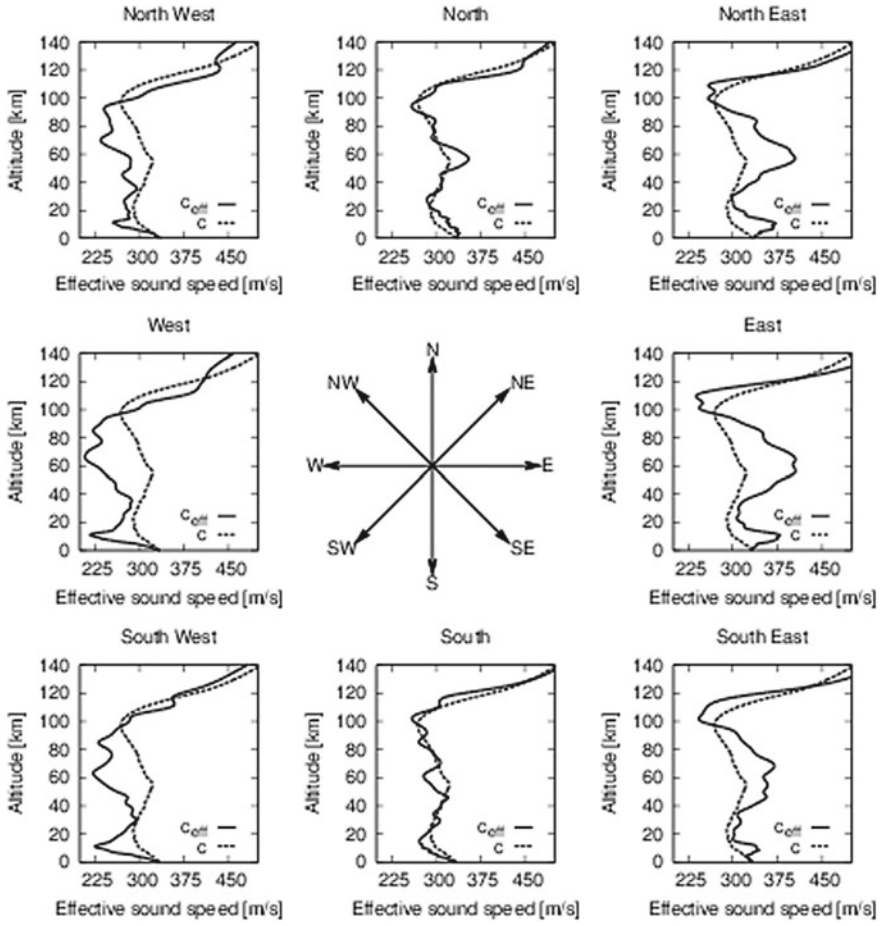

Fig. 15.5 Effective sound speed comparisons for the G2S specification over NYC at 0600 UTC January 1, 2008, from Fig. 3 of Waxler et al. (2017)

sound duct. Further, this duct is directional: sound is ducted downwind, but refracted away from the earth upwind.

For shallow angle propagation and low Mach number winds, the influence of the wind field can be well approximated using the so-called effective sound speed approximation (Pridmore-Brown 1962; Godin 2002). In this approximation, the horizontal component of the wind velocity in the direction of propagation is added to the sound speed. The resulting effective sound speed is then used in propagation models as if it were the sound speed. The effective sound speed approximation is sufficient for many applications and in all cases can be used to estimate which directions will be ducted and which will not.

In Fig. 15.5, effective sound speeds for the atmospheric specifications of Fig. 15.2 are shown for eight principle directions and compared to the actual sound speed. Note that there is no stratospheric ducting predicted to the west and south, but significant

stratospheric ducting to the north and east. In addition, in this case, the jet stream is large enough to produce a tropospheric duct to the east.

15.2.2 Fine Structure

Atmospheric specifications, such as the G2S and ECMWF specifications, are by their very nature averaged both spatially and temporally. Further, as discussed in the chapter by Douglas Drob, gravity waves in the atmosphere are filtered out of the global circulation models for a variety of reasons. In addition, the data used to constrain the specifications become increasingly sparse with increasing altitude. Acoustic propagation is sensitive to the state of the atmosphere at the time of propagation and thus to fine structure that is only partially represented in the averaged specifications. One component of the fine structure is from internal buoyancy (or gravity) waves. These are of direct interest to the atmospheric sciences community and the development of statistical models for the internal wave field is the subject of ongoing research. In recent years, significant work has been done on the adaptation of internal wave models to the augmentation of average atmospheric specifications (Chunchuzov 1996; Kulichkov et al. 2010; Lott and Millet 2010; Drob et al. 2013; Lalande and Waxler 2016).

In Fig. 15.6 is an example of the output of the internal wave model described in Lalande and Waxler (2016) given a specific G2S mean atmosphere. Several internal wave realizations are superimposed on the G2S specifications. Note that the internal wave field is zero below 20 km. This is an artifact of the linear source and propagation model used and not a representation of the actual physics.

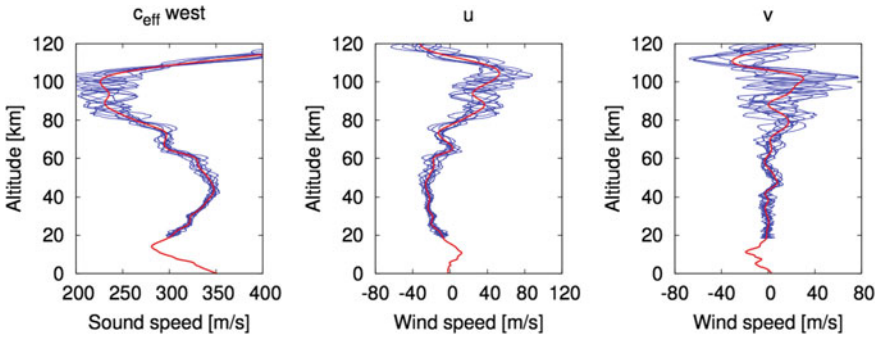

Fig. 15.6 G2S specification over Utah at 0600 UTC on August, 28 2012 with model internal wave perturbations. Effective sound speed for westward propagation in the leftmost panel, the zonal winds u in the center panel and the meridional winds w in the right panel

15.2.3 Atmospheric Attenuation

In Fig. 15.7, the density profile of the qualitative atmosphere from Fig. 15.1 is shown. The density of the atmosphere decreases dramatically with increasing altitude and this has several consequences. All stem from the fact that as the density decreases the acoustic impedance decreases proportionately. This causes acoustic pressure to decrease, proportional to the square root of the density, while particle velocity increases, proportional to the inverse square root of the density. Consequences include severely increased acoustic attenuation as well as increasing significance of the nonlinear component of the signal propagation (Rogers and Gardner 1980; Lonzaga et al. 2015; Sabatini et al. 2016; Scott et al. 2017).

The most widely used model for attenuation of acoustic signals in the atmosphere is the model developed by Sutherland and Bass (2004). The Sutherland-Bass model includes the attenuation from thermal and viscous relaxation, the so-called classical attenuation (Pierce 1989), as well as from molecular relaxation. A model for the molecular content of the atmosphere is required for the latter. The attenuation is then calculated from the linearized equations of fluid mechanics ignoring the influence of gradients of the temperature and wind. In this approximation, the acoustic field is a plane wave with parameters that depend on altitude. The imaginary part of the resulting wave number is called the attenuation coefficient, often denoted $\alpha(\omega, z)$. For more realistic models, in which the atmosphere is neither static nor isothermal, attenuation is usually included by simply adding the attenuation coefficient for a static, isothermal atmosphere to the wavenumber corresponding to the actual atmosphere,

$$\frac{\omega}{c} \rightarrow \frac{\omega}{c} + i\alpha.$$

The predicted attenuation (with humidity set to zero) is shown in the left panel of Fig. 15.8 for several values of the frequency. Attenuation increases dramatically with frequency; the classical attenuation is proportional to the frequency squared.

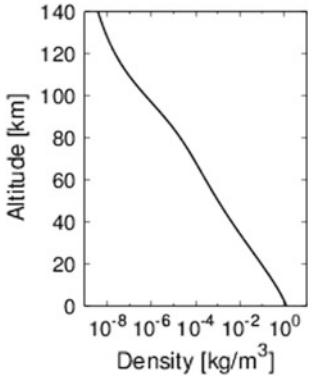

Fig. 15.7 Atmospheric density profile for the model atmosphere shown in Fig. 15.1

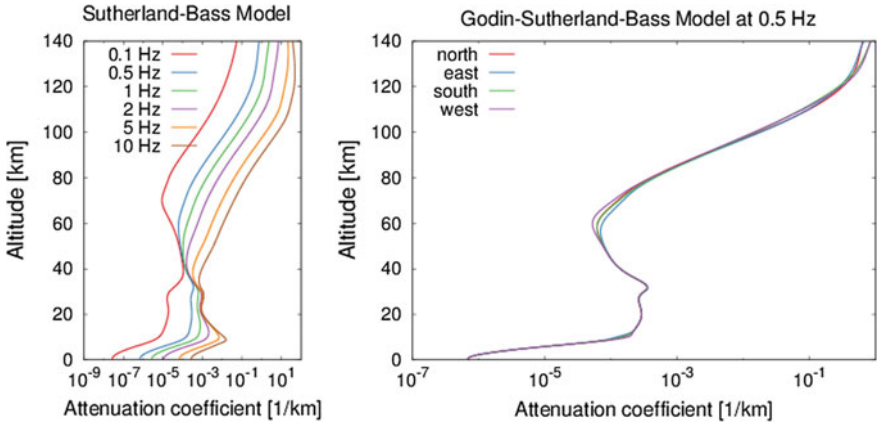

Fig. 15.8 Atmospheric attenuation models, figure from Waxler (2016). The left panel shows the Sutherland-Bass model (2004) at a range of frequencies while the right panel shows the Godin correction (2014) for the four principle propagation directions

Further, attenuation becomes severe in the thermosphere due to the dramatic decrease in atmospheric density.

More recently, Godin (2014) approached attenuation from the point of view of geometrical acoustics. Rather than ignoring gradients in the linearized equations, Godin assumes that changes in the atmosphere are small over the scale of a wavelength and applies the geometrical acoustics approximation. Godin considers acousto-gravity waves at frequencies low enough so that buoyancy waves couple with the acoustic field, but in the acoustic limit the result is simple: replace frequency ω in the attenuation model with $\omega - \mathbf{k} \cdot \mathbf{v}_0$ where $\mathbf{k}$ is the wave vector and $\mathbf{v}_0$ the wind velocity. As a result, attenuation is enhanced downwind and diminished upwind. The Sutherland-Bass attenuation at 0.5 Hz with the Godin correction is shown in the right panel of Fig. 15.8. Note that attenuation is increased slightly upwind and decreased slightly downwind.

15.3 Overview of Propagation Models

Infrasound propagation can be global. Sufficiently large signals can be detected after propagating around the globe one or more times. All layers of the atmosphere from the atmospheric boundary layer up to the lower thermosphere can be involved. On the other hand, many practical problems in infrasound propagation are local, sometimes called regional, involving ranges of less than 1000 km and often involve only the stratosphere or even just the troposphere. There are significant differences between global and regional infrasound propagation modeling. For global propagation the curvature of the Earth must be included, indeed the Earth must be considered a globe,

and deviations from atmospheric stratification become quite significant. In addition, the frequency bands relevant to global propagation tend to be lower than those relevant to regional propagation. The primary focus of this chapter will be on regional propagation in the flat Earth and locally stratified approximations in frequency bands large enough, roughly 0.1–10 Hz, that compressional (acoustic) and buoyant effects decouple.

15.3.1 The Governing Equations

To model propagation in a locally stratified atmosphere at regional ranges of no more than a few thousand kilometers, one may begin with a Cartesian model in which the Earth's surface is a horizontal plane and the atmosphere is a half-space over this plane. Let $\mathbf{x}_H$ be the projection of the displacement vector on the ground plane and let ∇_H be the corresponding horizontal gradient operator. We consider a stratified atmosphere with mean density $\rho_0(z)$, sound speed $c(z)$, and horizontal wind velocity $\mathbf{v}_{0,H}(z)$. If $p_A(\mathbf{x}_H, z, t)$ is the acoustic pressure then it is shown in Brekhovskikh and Godin (1999) (see Eq. 1.1.15 of Volume 1) that for the modeling of signals with frequency content large compared to the Brunt-Väisälä frequency (the frequency at which buoyant effects in the atmosphere become significant, nominally 0.05 Hz) in a source free region of space,

$$\left(\frac{\partial}{\partial t} + \mathbf{v}_{0,H}\cdot\nabla_H\right)\left[\frac{1}{c^2}\left(\frac{\partial}{\partial t} + \mathbf{v}_{0,H}\cdot\nabla_H\right)^2 p_A - \rho_0\nabla\cdot\left(\frac{\nabla p_A}{\rho_0}\right)\right] + 2\left(\frac{d\mathbf{v}_{0,H}}{dz}\cdot\nabla_H\right)\frac{\partial p_A}{\partial z} = 0\,. \tag{15.3}$$

For frequencies comparable to or less than the Brunt-Väisälä frequency terms involving the influence of gravity must be included and the propagating waves become acousto-gravity waves rather than simply acoustic waves (Press and Harkrider 1962; Tolstoy 1963; Pierce 1965; Godin 2012). If vertical wind shear gradients are small over a wavelength, $\frac{d|\mathbf{v}_{0,H}|}{dz} \ll \boldsymbol{\omega}$ the wave equation reduces to a much simpler form,

$$\left[\nabla_H^2 + \rho_0\frac{\partial}{\partial z}\left(\frac{1}{\rho_0}\frac{\partial}{\partial z}\right) - \frac{1}{c^2}\left(\frac{\partial}{\partial t} + \mathbf{v}_{0,H}\cdot\nabla_H\right)^2\right] p_A(\mathbf{x}_H, z, t) = 0\,. \tag{15.4}$$

Equation (15.4) is the starting point of our analysis.

Equation (15.4) must be augmented with boundary conditions. The most general local, time-invariant, linear condition is of the form (Cotté et al. 2009)

$$\frac{\partial p_A}{\partial z}\Big|_{z=0} = -\int_{-\infty}^{\infty} \mathscr{A}(\tau) p_A(\mathbf{x}_H, 0, t-\tau)\, d\tau.$$

If it is assumed that the ground surface at $z = 0$ is rigid then $\mathscr{A} = 0$ and one has the boundary condition

$$\frac{\partial p_A}{\partial z}\Big|_{z=0} = 0. \tag{15.5}$$

More generally, $\mathscr{A}(\tau)$ can be specified by its Fourier transform, $\tilde{\mathscr{A}}(\boldsymbol{\omega})$. If g is the acceleration due to gravity at the surface of the Earth and $\mathscr{Z}(\boldsymbol{\omega})$ the impedance of the ground surface (Pierce and Posey 1971) then if

$$\tilde{\mathscr{A}}(\boldsymbol{\omega}) = \frac{g}{c(0)^2} + \frac{i\boldsymbol{\omega}\rho_0(0)}{\mathscr{Z}(\boldsymbol{\omega})}$$

the leading order buoyant terms are accounted for by the first term and the influence of the ground response by the second. Here, we will restrict attention to the rigid ground approximation in which the ground impedance is infinite. This is expected to be valid for infrasound propagation that does not involve coupled acoustic and seismic modes.

Numerical methods to solve Eq. (15.4) fall into two general types. Direct time domain solvers, such as the finite-difference time domain method (Ostashev et al. 2005; de Groot-Hedlin 2008; Kim and Lees 2011), and Fourier methods in which the pressure is expressed as a Fourier superposition,

$$p_A(\mathbf{x}_H, z, t) = \frac{1}{\sqrt{2\pi}} \int_{-\infty}^{+\infty} \hat{p}_A(\mathbf{x}_H, z, \boldsymbol{\omega}) e^{-i\boldsymbol{\omega}t} d\boldsymbol{\omega}, \tag{15.6}$$

and the Fourier components $\hat{p}_A(\mathbf{x}_H, z, \boldsymbol{\omega})$ are computed. The Fourier components satisfy

$$\left[\nabla_H^2 + \rho_0 \frac{\partial}{\partial z}\left(\frac{1}{\rho_0}\frac{\partial}{\partial z}\right) + \frac{1}{c^2}(\boldsymbol{\omega} + i\mathbf{v}_{0,H} \cdot \nabla_H)^2\right] \hat{p}_A(\mathbf{x}_H, z, \boldsymbol{\omega}) = 0\,. \tag{15.7}$$

For the Fourier method, Eq. 15.7 is the fundamental equation. There are several further simplifications that are often used and will be introduced below.

Note that in the locally stratified atmosphere approximation, Eq. 15.7 is separable into horizontal and vertical differential operators. Introducing a two-dimensional wave vector $\mathbf{k}$, a solution can be built up by Fourier transform,

$$\hat{p}_A(\mathbf{x}_H, z, \boldsymbol{\omega}) = \frac{1}{2\pi} \int e^{i\mathbf{k}\cdot\mathbf{x}_H} \tilde{p}_A(\mathbf{k}, z, \boldsymbol{\omega})\, d^2k, \tag{15.8}$$

with respect to the horizontal coordinate $\mathbf{x}_H$. One finds

$$\left[\rho_0 \frac{d}{dz}\left(\frac{1}{\rho_0}\frac{d}{dz}\right) + \frac{1}{c(z)^2}\left(\boldsymbol{\omega} - \mathbf{v}_{0,H}(z) \cdot \mathbf{k}\right)^2 - |\mathbf{k}|^2\right] \tilde{p}_A(\mathbf{k}, z, \boldsymbol{\omega}) = 0\,. \tag{15.9}$$

Here, the z dependence of the atmospheric state has been made explicit. In this sense, one may identify the action of ∇_H with multiplication by the appropriate $\mathbf{k}$.

15.3.2 The Planar and Effective Sound Speed Approximations

In the planar approximation, the propagation is confined to a single vertical plane. Given a horizontal propagation direction $\hat{\mathbf{k}}$, so that the propagation plane is the one spanned by $\hat{\mathbf{k}}$ and $\hat{\mathbf{z}}$, the wind velocity vector $\mathbf{v}_{0,H}$ in Eq. 15.7 is replaced by its projection in the propagation direction,

$$\mathbf{v}_{0,H} \longmapsto (\hat{\mathbf{k}} \cdot \mathbf{v}_{0,H})\hat{\mathbf{k}} \equiv u_0 \hat{\mathbf{k}}. \tag{15.10}$$

Substituting $u_0\hat{\mathbf{k}}$ for $\mathbf{v}_H$ in Eq. 15.7, one solves as if it were spherically symmetric.

In this approximation, the influence of cross winds is ignored: predicted arrival azimuths are always the same as the geometrical azimuth from the source location and out-of-plane propagation paths are not considered. There are circumstances under which the influence of cross winds is significant, leading to deviations in travel time (Evers and Haak 2007) and even significant changes in propagation path (Blom et al. 2014); however, these are exceptional cases. The greatest limitation of the planar approximation is that deviations in the apparent signal back azimuth cannot be estimated. While these tend to be small, typically a few degrees, they can lead to large biases in estimates for signal location (Waxler et al. 2015; Blom et al. 2015; Blom and Waxler 2017) and have been used to estimate cross-wind speed and direction aloft (Pichon et al. 2002; Le Pichon et al. 2005). In addition, propagation in complex topography, in particular diffraction around hills or mountain peaks, requires out-of-plane propagation. Such phenomena have been observed and modeled in oceans (Collins et al. 1995; Smith 1999) but have not yet received serious attention in the atmosphere.

A further simplification to Eq. 15.7, called the effective sound speed approximation, is often made. In this approximation, the influence of the wind is taken into account by adding the horizontal component of the wind speed in the direction of propagation to the sound speed. One then obtains a Helmholtz-like equation

$$\left[\nabla_H^2 + \rho_0 \frac{\partial}{\partial z}\left(\frac{1}{\rho_0}\frac{\partial}{\partial z}\right) + \frac{\boldsymbol{\omega}^2}{c_{\mathit{eff}}^2}\right]\hat{p}_A(\mathbf{x}_H, z, \boldsymbol{\omega}) = 0, \tag{15.11}$$

where

$$c_{\mathit{eff}}(z) = c(z) + u_0(z).$$

If the Mach number of the wind, $\frac{u_0}{c}$, is small then

$$\frac{\omega}{c+u_0} \approx \frac{\omega}{c}\left(1-\frac{u_0}{c}+\cdots\right)$$

so that, comparing to Eq. 15.9, in the effective sound speed approximation $|\mathbf{k}|$ is replaced by $\frac{\omega}{c}$. This is equivalent to a shallow angle approximation. Thus, the effective sound speed approximation is valid if the Mach number is small and the propagation is sufficiently close to horizontal. A more rigorous treatment can be found in Godin (2002). An evaluation of the errors induced by the effective sound speed approximation in typical atmospheres can be found in Assink et al. (2017).

The value of the effective sound speed approximation is twofold. First, in this approximation the influence of the winds is clear. The effective sound speed can be plotted out at a given propagation azimuth, as in Fig. 15.5, showing qualitatively which layers of the atmosphere will provide ducts. Second, Eq. 15.11 is considerably less complex than Eq. 15.7. Much more efficient numerical solutions can be developed for the effective sound speed approximation.

Any planar model can be solved in cylindrical coordinates. Once a propagation azimuth is chosen and (15.10) is substituted in (15.7), the resulting equation is indistinguishable from the axisymmetric problem one obtains by replacing $\hat{\mathbf{k}} \cdot \nabla_H$ with the radial derivative $\frac{\partial}{\partial r}$.

15.3.3 The Geometric Acoustic Approximation

The geometric acoustic approximation is the name given to the formal high-frequency asymptotic expansion for solutions to wave equations (Pierce 1989; Brekhovskikh and Godin 1999; Ostashev and Wilson 2015). The idea behind the approximation is that, at high frequencies, solutions are characterized by rapid oscillation, modulated by a more slowly varying amplitude. This motivates seeking a solution of the form

$$\hat{p}_A(\mathbf{x},\omega) = e^{i\omega\phi(\mathbf{x})}A(\mathbf{x},\omega). \tag{15.12}$$

Substituting Eq. 15.12 into Eq. 15.7, one obtains

$$\begin{aligned} 0 = {} & \omega^2\Big(-\nabla\phi\cdot\nabla\phi+\frac{1}{c^2}(1-\mathbf{v}_0\cdot\nabla\phi)^2\Big)A \\ & + i\omega\Big(A\rho_0\nabla\frac{1}{\rho_0}\nabla\phi+2\nabla A\cdot\nabla\phi \\ & \quad + \frac{1}{c^2}\big(2A\mathbf{v}_0\cdot\nabla\phi+2\mathbf{v}_0\cdot\nabla A+2(\mathbf{v}_0\cdot\nabla\phi)(\mathbf{v}_0\cdot\nabla A)+A(\mathbf{v}_0\cdot\nabla)^2\phi\big)\Big) \\ & + \rho_0\nabla\frac{1}{\rho_0}\nabla A+(\mathbf{v}_0\cdot\nabla)^2A \end{aligned} \tag{15.13}$$

The formal procedure is to expand A as a series in $\frac{1}{\omega}$,

$$A(\mathbf{x}) = \sum_j \frac{1}{\omega^j} A_j(\mathbf{x}),$$

substitute in Eq. 15.13, and solve term by term in ω^{-j}; alternatively, one may slightly generalize by substituting into the linearized equations of fluid mechanics, without combining them into a wave equation, and then solve term by term. As such this is formally a high frequency approximation; however, it is valid when the properties of the medium change slowly over distances comparable to a wavelength and thus have application in low-frequency sound propagation through atmospheres that are not too rapidly varying.

The leading order, $\mathcal{O}(\omega^2)$, gives the so-called eikonal equation,

$$\frac{1}{c^2}(1 - \mathbf{v}_0 \cdot \nabla\phi)^2 = \nabla\phi \cdot \nabla\phi. \tag{15.14}$$

The eikonal equation leads to a geometrical form underlying the solution (Landau and Lifshitz 1987; Pierce 1989; Brekhovskikh and Godin 1999; Ostashev and Wilson 2015). Around any point $\mathbf{x}_0$, one can expand

$$\phi(\mathbf{x}) = \phi(\mathbf{x}_0) + \nabla\phi(\mathbf{x}_0) \cdot (\mathbf{x} - \mathbf{x}_0) + \ldots .$$

The term

$$\mathbf{k} = \omega \nabla\phi(\mathbf{x}_0)$$

can be interpreted as a local wavenumber, $\nabla\phi(\mathbf{x}_0)$ is known as the slowness vector. Substituting into Eq. 15.14 one finds, with $k = |\mathbf{k}|$,

$$\omega = ck + \mathbf{v}_0 \cdot \mathbf{k}$$

from which one can define a local group velocity

$$\begin{aligned} \mathbf{c}_g &= \frac{\partial\omega}{\partial\mathbf{k}} \\ &= c\frac{\mathbf{k}}{k} + \mathbf{v}_0 \\ &= c\frac{\nabla\phi}{|\nabla\phi|} + \mathbf{v}_0. \end{aligned}$$

Wavefronts are always normal to the group velocity so that the paths along which the wavefronts move, called ray paths, are always parallel to the group velocity. Let the ray paths be given by the curve $\mathbf{r}(s)$, where the parameter s can be chosen in a variety of ways, but here it is chosen to be the path length. One has the following condition for the velocity vector:

$$\frac{d\mathbf{r}}{ds} = \frac{\mathbf{c}_g}{|\mathbf{c}_g|}. \tag{15.15}$$

What's critical is the direction of the derivative, but when parameterized by path length the velocity vector has length one; hence the normalization on the right side of Eq. 15.15. Efficient algorithms for solving for the ray paths can be developed by defining $\psi = \nabla\phi$, noting that

$$\frac{d\psi}{ds} = -\frac{1}{|\mathbf{c}_g|}\Big(|\psi|\nabla c + \psi \cdot \nabla \mathbf{v}_0\Big), \tag{15.16}$$

and the solving the system given by Eqs. 15.15 and 15.16. Note that, given launch azimuth and inclination angles, φ and θ, one can parameterize points x, y, z by ray coordinates φ, θ, s.

In the case of zero wind, equivalently in the effective sound speed approximation, $\mathbf{v}_0 = 0$ and the eikonal equation reduces to

$$\frac{1}{c^2} = \nabla\phi \cdot \nabla\phi.$$

In this case, the surfaces of constant phase can be considered to be the wavefronts, and the propagation paths are always normal to the wavefronts. Introduce the ray paths, given by the curve $\mathbf{r}(s)$, where the parameter s can be chosen in a variety of ways, but is often chosen to be the path length. To determine possible ray paths, it is sufficient to enforce the condition that the ray paths be normal to the wavefront. One may choose

$$\frac{d\mathbf{r}}{ds} = c\nabla\phi$$

from which it follows that

$$\frac{d}{ds}\frac{1}{c}\frac{d\mathbf{r}}{ds} = -\frac{1}{c^2}\nabla c.$$

Higher orders in $\boldsymbol{\omega}^{-j}$ lead to the so-called transport equations. For our uses, only sub-leading order, order $\boldsymbol{\omega}$, is relevant. One finds (Brekhovskikh and Godin 1999; Ostashev and Wilson 2015)

$$\nabla \cdot (A_0^2 \mathbf{c}_g) = A_0^2(\mathbf{c}_g \cdot \nabla)\ln(\rho_0|\psi|c^3). \tag{15.17}$$

If D is the Jacobian determinant for the transformation from Cartesian to ray coordinates then one finds that, along a given ray path,

$$\frac{A_0(s_1)}{A_0(s_2)} = \Big|\frac{\rho_0(s_1)|\psi(s_1)|c(s_1)^3}{\rho_0(s_2)|\psi(s_2)|c(s_2)^3}\frac{|\mathbf{c}_g(s_2)|D(s_2)}{|\mathbf{c}_g(s_1)|D(s_1)}\Big|^{1/2} \tag{15.18}$$

so that the signal amplitude is directly related to the geometrical spreading of rays as measured by the Jacobian determinant D. A method for determining D is presented in Blom and Waxler (2017).

Finally, in modeling long-range infrasound propagation, one must account for reflections of the signal from the ground. For the ray paths themselves this is straightforward: the ray reflects upward with a launch angle equal to the angle of incidence to the ground. However, the change in the amplitude, A_0, upon reflection is nontrivial, but has been worked out in Blom and Waxler (2017). In Fig. 15.9, the results of geometrical acoustic modeling are presented for propagation in the model atmospheres shown in Fig. 15.1. The various ducts, tropospheric, stratospheric and thermospheric, and the typical propagation paths associated with them, are clearly visible.

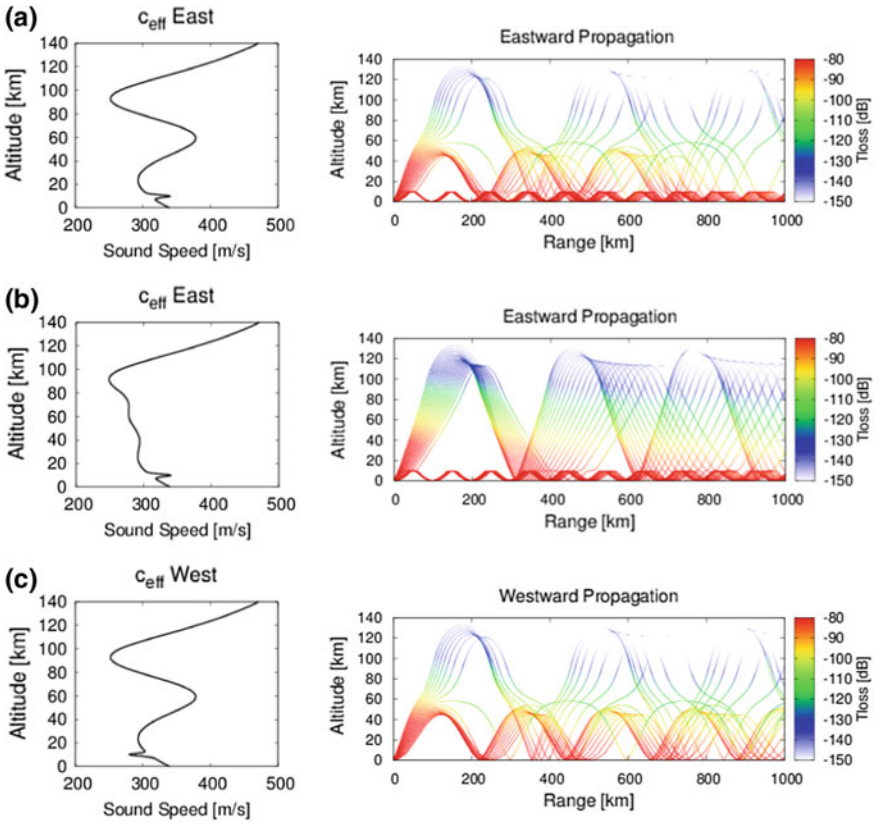

Fig. 15.9 Example ray paths and transmission loss for propagation in the ducts provided by the wind and sound speed. Effective sound speeds are shown to the left of the ray paths. The panels show eastward propagation with an eastward flowing stratospheric jet, eastward propagation with a westward flowing stratospheric jet, and westward propagation with a westward flowing stratospheric jet. From Waxler (2016)

15.3.4 Modal Expansion

Expansions in vertical modes are possible for stratified atmospheres in the planar approximation (Pierce 1965; Bertin et al. 2014; Waxler et al. 2017; Assink et al. 2017). In the effective sound speed model approximation, and adding the attenuation coefficient, one has

$$\left[\nabla_H^2 + \rho_0 \frac{\partial}{\partial z}\left(\frac{1}{\rho_0}\frac{\partial}{\partial z}\right) + \left(\frac{\omega}{c_{eff}(z)} + i\alpha(z)\right)^2\right]\hat{p}_A(\mathbf{x}_H, z, \omega) = 0\,. \tag{15.19}$$

Making the transformation

$$\hat{p}_A = \sqrt{\rho_0}\, p, \tag{15.20}$$

substituting into Eq. 15.19 and dropping terms that are small compared to $\frac{\omega^2}{c_{eff}^2}$, one obtains

$$\left[\nabla_H^2 + \frac{\partial^2}{\partial z^2} + \left(\frac{\omega}{c_{eff}(z)} + i\alpha(z)\right)^2\right]p(\mathbf{x}_H, z, \omega) = 0\,. \tag{15.21}$$

Here, p satisfies the boundary condition (Pierce 1965)

$$\frac{\partial p}{\partial z}\Big|_{z=0} = -\frac{\rho_0'(0)}{2\rho_0(0)} p|_{z=0}. \tag{15.22}$$

A solution can be obtained using separation of variables, which can be expressed in the form of an eigenfunction expansion. Consider the eigenvalue problem

$$\left[\frac{d^2}{dz^2} + \left(\frac{\omega}{c_{eff}(z)} + i\alpha(z)\right)^2 - k_H^2\right]\psi(z) = 0\,. \tag{15.23}$$

with $\psi(z) \to 0$ as $z \to \infty$ and

$$\psi'(0) = -\frac{\rho_0'(0)}{2\rho_0(0)}\psi(0). \tag{15.24}$$

The eigenvalue parameter k_H^2 can be interpreted as a horizontal wave number.

A modal expansion can be developed without the effective sound speed approximation, handling in-plane winds rigorously (Assink et al. 2017). Applying the planar approximation (15.10) to the vertical Eq. 15.9, one obtains a wide angle, high Mach number eigenfunction equation that generalizes Eq. 15.23,

$$\left[\frac{d^2}{dz^2} + \frac{1}{c(z)^2}\left(\omega - u_0(z)k_H\right)^2 - k_H^2\right]\psi(z) = 0\,. \tag{15.25}$$

This is an example of a quadratic eigenvalue problem, because the eigenvalue, k, arises quadratically in the eigenvalue equation. Methods for solving this equation and developing the resulting modal expansion for the pressure field are discussed in Assink et al. 2017.

Equation 15.23, with 15.24, is a nonself-adjoint Sturm–Liouville problem on a half-line (Waxler 2002; Waxler et al. 2017). This has several consequences. First, eigenfunctions are normalized without a complex conjugation. This is because, for operators that are not equal to their adjoints, orthonormality is between eigenfunctions and eigenfunctions of the adjoint operator. In this case, the adjoint operator is simply the complex conjugate so that the eigenfunctions of the adjoint operator are the complex conjugates of the original operator. Thus, in the orthonormality integral, the function gets complex conjugated twice, which is equivalent to having no complex conjugate at all.

Second, eigenvalues are complex valued and thus much more difficult to find. This is a serious issue. For self-adjoint eigenvalue problems, very efficient solvers can be developed. For nonself-adjoint eigenvalue problems, unless some special method can be found to find the imaginary parts of the horizontal wave numbers (as in the case of the porous ground coupled surface mode Waxler 2002) one must resort to brute force numerical solvers which can be numerically cumbersome; however, attenuation can be included as a perturbation to the wave number for modes which do not interact strongly with the thermosphere (Waxler et al. 2017).

Solutions, ψ, to Eq. 15.23 are classified by their asymptotic behavior. Generally, there are a discrete set of horizontal wave numbers, k_H, for which ψ is square integrable (normalizable). Such k_H are called the modal wave numbers and the corresponding solutions ψ are called the modes. The set of modal wave numbers is called the point spectrum. In addition, there is generally a continuum of horizontal wave numbers for which the solutions ψ are not square integrable, but remain bounded. These wave numbers are called the continuous spectrum and the corresponding solutions ψ are called the continuum eigenvectors.

To develop intuition, we begin our discussion with the lossless case, in which $\alpha = 0$. In this case, all the wave numbers are real valued and some simple criteria can be developed. In the Wentzel–Kramers–Brillouin (WKB) approximation (Landau and Lifshitz 1965), also known as the Liouville–Green method (Olver 2014), one has

$$\psi(z) \approx \frac{1}{\left((\frac{\omega}{c_{eff}(z)})^2 - k_H^2\right)^{\frac{1}{4}}} \left(A e^{i \int \sqrt{(\frac{\omega}{c_{eff}(z)})^2 - k_H^2}\, dz} + B e^{-i \int \sqrt{(\frac{\omega}{c_{eff}(z)})^2 - k_H^2}\, dz} \right). \quad (15.26)$$

The relation between the coefficients A and B is determined by connecting the solution to the boundary condition on the ground.

The temperature, and thus the sound speed, does not increase without limit as z increases, but achieves a roughly constant maximum of about 1000 K, corresponding to a sound speed of about 600 m/s (Dubin et al. 1976). Nothing definite can be said of

the wind, but it can be said that c_{eff} has a finite maximum, $c_{max} < \infty$, corresponding to a minimum wave number, $k_{min} = \frac{\omega}{c_{max}}$.

The only way for ψ to be square integrable is for $k_H > k_{min}$, or equivalently $c_{ph} < c_{max}$ where

$$c_{ph} = \frac{\omega}{k_H}$$

is the phase velocity, and for $B = 0$. The condition $B = 0$ is only satisfied by a discrete set of k_H, say k_j for $j = 1, 2, 3, \ldots$, whose phase velocities lie between the minimum and maximum values of c_{eff}. Denote the corresponding modes $\psi_j(z)$. For each $k_H < k_{min}$, there is a single solution which is oscillatory, not square integrable, but bounded, forming the continuous spectrum. Denote the corresponding continuum eigenvectors $\psi(k, z)$.

These considerations extend beyond the WKB approximation so that one has, quite generally,

$$p(\mathbf{x}_H, z, \omega) = \sum_j \tilde{p}_j(\mathbf{x}_H, \omega)\psi_j(z) + \int_{-\infty}^{k_{min}} \tilde{p}_k(\mathbf{x}_H, \omega)\psi(k, z)\, dk$$

where, away from any sources,

$$\left(\nabla_H^2 + k_H^2\right)\tilde{p}(\mathbf{x}_H, \omega) = 0$$

and $\tilde{p}$ is either $\tilde{p}_j$ or $\tilde{p}_k$ depending on whether k_H is a modal wave number or in the continuous spectrum. As discussed in Waxler et al. (2017), there is a relation between phase velocity and launch angle. Very large phase velocities, equivalently small horizontal wave numbers, correspond to steep launch angles, for which signals ascend nearly vertically into the upper atmosphere and are not relevant to long-range propagation. In particular, the contribution from the continuous spectrum can be neglected and the sum over the modes can be truncated at some large index, say N, sufficient for the expansion to converge (Waxler et al. 2017). Given a point source of unit magnitude at elevation z_s in the far field $k_{min}|\mathbf{x}_H| \gg 1$ one has, with $r = |\mathbf{x}_H|$,

$$p_j(\mathbf{x}_H, \omega) = \frac{ie^{-i\frac{\pi}{4} + ik_j r}}{\sqrt{8\pi\rho_0(z_s)k_j r}}\psi_j(z).$$

Thus, one has

$$p(\mathbf{x}_H, z, \omega) = \hat{S}(\omega)\frac{ie^{-i\frac{\pi}{4}}}{\sqrt{8\pi r\rho_0(z_s)}}\sum_j^N \frac{e^{ik_j r}}{\sqrt{k_j}}\psi_j(z_s)\psi_j(z) \tag{15.27}$$

where $\hat{S}(\boldsymbol{\omega})$ is the Fourier coefficient of the source extrapolated to some reference range; the reference range will be chosen to be one meter in this chapter. We will denote the source waveform by $S(t)$. Equation 15.27 holds true for the lossy case, $\alpha \neq 0$, as well (Waxler et al. 2017).

In Fig. 15.10, modal wave numbers and modes at $f = 0.5$ Hz are shown for an example effective sound speed profile. The effective sound speed, shown in panel (a), is the one shown in the upper panel of Fig. 15.9 and features an eastward flowing polar vortex and strong jet stream. The modal wave numbers are depicted in panel (b). They are plotted by phase speed versus attenuation coefficient, that is by $2\pi f/\mathrm{Re}\, k$ versus $\mathrm{Im}\, k$. The modal attenuation, computed perturbatively in this plot, is a measure of which altitudes the mode is supported in. Modes concentrated in the mesosphere and thermosphere have much higher attenuation coefficients that do the modes concentrated in the stratosphere, which in turn have much higher attenuation than modes concentrated in the troposphere. Accordingly, three branches are visible in Fig. 15.10b as they are separated in attenuation. The branches can also be tracked by their phase speeds: the thermospheric branch begins at about 250 m/s, the stratospheric at about 290 m/s and the tropospheric at about 320 m/s.

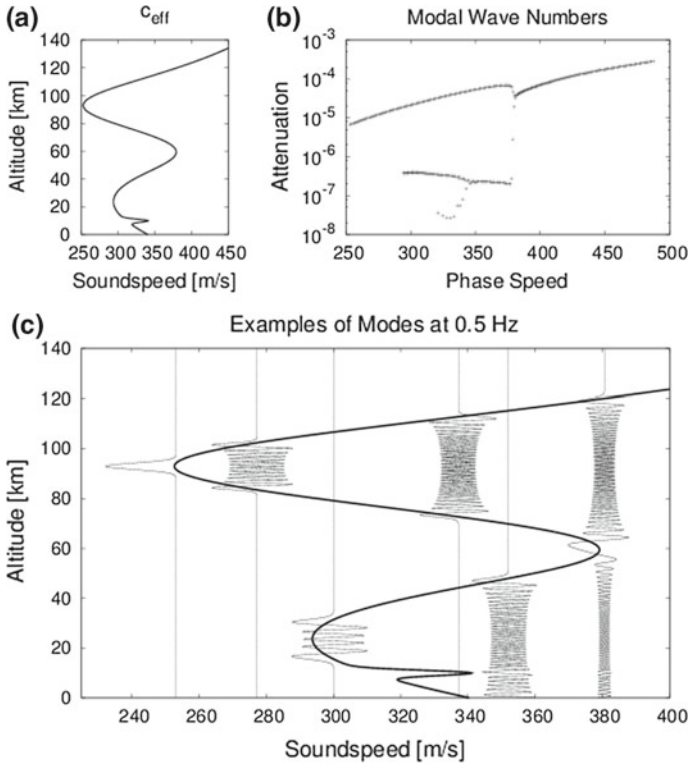

Fig. 15.10 Modal wave numbers, (**b**), and a selection of modes, (**c**), for the profile shown in (**a**)

The thermospheric branch actually continues, however we have not computed the high phase velocity modes. Note that the tropospheric and stratospheric branches do not end abruptly, but rather suddenly rise up into the next higher attenuation branch. This is a consequence of leaking between ducts captured by full wave models, but not by the geometrical acoustics models. The rate at which the attenuation rises during this transition depends on how leaky the lower duct is: the more transparent the duct, the more gradual the rise.

In Fig. 15.10c, several modes are plotted against the effective sound speed profile and shifted by their phase velocities. Note, in correspondence with the WKB approximation, that the modes fit into the regions where the effective sound speed is less than the phase speed. The regions where sound speed is greater than the phase speed are called the forbidden regions. The modes are not strictly zero in the forbidden regions, but decay exponentially with altitude in a forbidden region.

In Fig. 15.11, the transmission loss, defined to be the magnitude of the signal Eq. 15.27 produced by a unit source, in the effective sound speed profile of Fig. 15.10a at 0.5 Hz is plotted. In the upper panel, the transmission loss in a lossless atmosphere is shown and in the lower panel in a lossy atmosphere. Compare to the upper panel of Fig. 15.9 in which three clearly decoupled ducts are seen, a

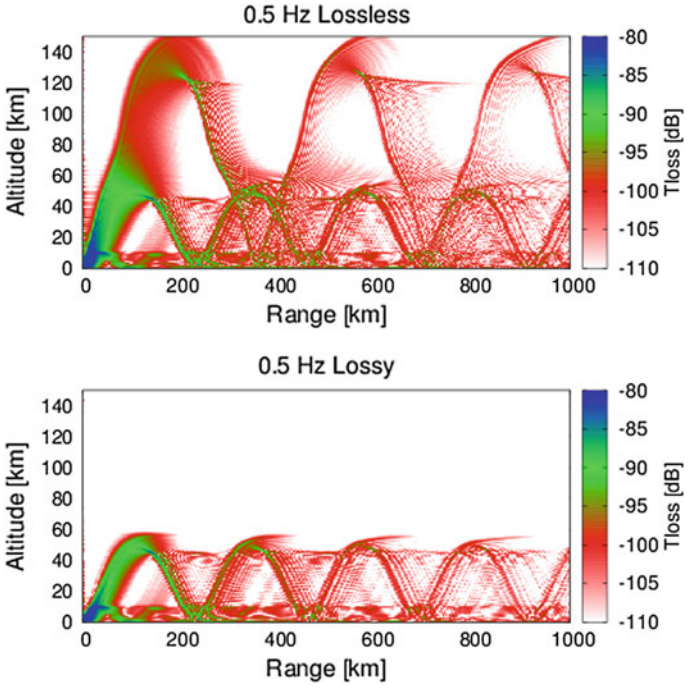

Fig. 15.11 Transmission loss as a function of altitude and range for propagation in the effective sound speed profile shown in Fig. 15.10a. Here, lossless propagation is shown in the upper panel and lossy propagation in the lower panel

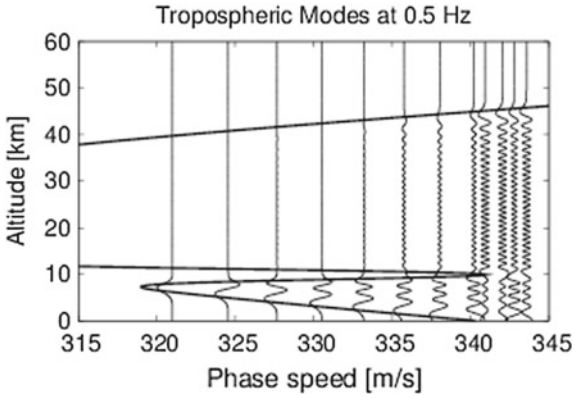

Fig. 15.12 Tropospheric modes at 0.5 Hz in the effective sound speed profile of Fig. 15.10a

tropospheric, stratospheric, and thermospheric. In Fig. 15.11, one sees the same with the exception that the tropospheric duct clearly displays energy leaking out into the stratosphere, which is then trapped in the stratospheric duct.

Energy leaks from the tropospheric duct into the stratosphere because the mode functions, and thus the acoustic pressure, are not strictly zero in the forbidden zones. The barrier to upward propagation created by the jet stream is thin enough that the tropospheric and stratospheric ducts communicate at infrasonic frequencies. To see this more clearly, in Fig. 15.12, all the tropospheric modes in the effective sound speed profile of Fig. 15.10a are shown. As the jet stream thins with increasing phase speed, the modes are able to penetrate through the forbidden zone it creates. This leads to the leaking of energy into the stratosphere.

15.3.5 Parabolic Equation (PE) Models

Although the lateral variability of the atmosphere is moderate when compared to the vertical direction, it can often not be neglected for longer range propagation. The PE method is naturally suited for range-dependent waveguides where both the atmosphere and topography may vary with range. Common to all PE methods is the solution of a so-called one-way wave equation. The one-way wave equation is typically derived by factoring the wave equation in two one-way equations and is solved by marching an acoustic starter field out in range. This implies that forward propagating energy is separated from backward propagating energy. This is only valid in the case of weak range-dependent media, for which backscatter can be neglected. PE's have been used extensively in underwater acoustics (Jensen et al. 1994). Various PE solutions have also been proposed for the simulation of infrasound in the atmosphere, ranging from solutions for effective quiescent media and near-horizontal propagation (Gilbert and Di 1993; Salomons 1998; Gilbert 2015) to more general forms that are valid for wide angle propagation in 3D inhomogeneous moving media

(Ostashev et al. 1997; Blanc-Benon et al. 2002; Godin 2002; Lingevitch et al. 2002; Lihoreau et al. 2006). The versatility of the method has contributed to its widespread use.

Here, a PE is derived from Eq. 15.11. The pressure field $\hat{p}_A(\mathbf{x}_H, z, \boldsymbol{\omega})$ can be factored as a horizontally propagating carrier wave p_H that is modulated by a slowly varying envelope function $\psi(r, z, \boldsymbol{\omega})$ by assuming that the acoustic wave propagate mainly along the principal direction. The envelope function accounts for the range-dependent effects of refraction and diffraction for the entire acoustic spectrum. The horizontally propagating field p_H satisfies the horizontal Helmholtz equation:

$$(\nabla_H^2 + k_0^2)p_H = 0 \tag{15.28}$$

In this equation, $k_0 = \frac{\boldsymbol{\omega}}{c_0}$ represents the carrier wavenumber, around which the energy $k(\boldsymbol{\omega})$ propagates with reference sound speed c_0 (typically taken as the ground sound speed). In cylindrical coordinates, solutions to this equation are Hankel functions of the first kind, $p_H = H_0^1(k_0 r)$.

Substituting the ansatz $\hat{p}_A(\mathbf{x}_H, z, \boldsymbol{\omega}) = \psi(r, z, \omega)H_0^1(k_0 r)$ in Eq. 15.11 yields

$$\psi\left[\frac{\partial^2 H_0^1}{\partial r^2} + \frac{1}{r}\frac{\partial H_0^1}{\partial r} + k_0^2 H_0^1\right] + H_0^1\left[\frac{\partial^2 \psi}{\partial r^2} + \frac{1}{r}\frac{\partial \psi}{\partial r} + \rho_0 \frac{\partial}{\partial z}\left(\frac{1}{\rho_0}\frac{\partial \psi}{\partial z}\right) + k_0^2(n^2 - 1)\psi\right] + 2\frac{\partial \psi}{\partial r}\frac{\partial H_0^1}{\partial r} = 0 \tag{15.29}$$

Here, $n(z) = \frac{k}{k_0} = \frac{c_0}{c_{eff}(z)}$. The first term is equal to the left hand side of Eq. 15.28 and equal to zero. The remaining terms can be combined and simplified, using the asymptotic or far-field form of the Hankel function:

$$H_0^1(k_0 r) \approx \sqrt{\frac{2}{\pi k_0 r}} e^{i(k_0 r - \frac{\pi}{4})} \qquad \text{for } k_0 r \gg \frac{1}{4} \tag{15.30}$$

Leading to

$$\frac{\partial^2 \psi}{\partial r^2} + 2ik_0\frac{\partial \psi}{\partial r} + \rho_0 \frac{\partial}{\partial z}\left(\frac{1}{\rho_0}\frac{\partial \psi}{\partial z}\right) + k_0^2(n^2 - 1)\psi = 0 \tag{15.31}$$

This equation can be factored out as two one-way equations, for back-propagating and forward propagating energy:

$$\left[\left(\frac{\partial}{\partial r} + ik_0\right) + i\sqrt{Q}\right]\left[\left(\frac{\partial}{\partial r} + ik_0\right) - i\sqrt{Q}\right]\psi = 0 \tag{15.32}$$

Operators $\left(\frac{\partial}{\partial r} + ik_0\right)$ and $i\sqrt{Q}$ commute for stratified media.

$$Q = \rho_0 \frac{\partial}{\partial z}\left(\frac{1}{\rho_0}\frac{\partial}{\partial z}\right) + k_0^2 n^2 \qquad \sqrt{Q} = k_0\sqrt{1+q} \tag{15.33}$$

The one-way equation for forward propagating energy is thus

$$\frac{\partial \psi}{\partial r} = ik_0\left(-1+\sqrt{1+q}\right)\psi \tag{15.34}$$

Given the field at $\psi(r,z)$, the field at $\psi(r+\Delta r,z)$ can be computed as

$$\psi(r+\Delta r,z,\omega) = e^{ik_0\Delta r(-1+\sqrt{1+q})}\psi(r,z,\omega) \tag{15.35}$$

This is the formal analytical solution for one-way propagation in the atmosphere in the limit of the effective sound speed approximation. Range dependence (deviations from vertical stratification) can be represented by a series of adjacent, range independent sections. In practice, this can be implemented by simply updating q at each range step.

Most PE methods are based on the solution of an equation of the form of Eq. 15.34 or Eq. 15.35. Various numerical methods exist that can be used to solve such equations efficiently. The critical part is with the approximation of the operator $\sqrt{Q}$. A very efficient solution is the so-called split-step Fourier (SSF) method (Hardin and Tappert 1973; Thomson 1990), in which the effects of the two terms in operator Q are split. The vertical derivative term is computed in the Fourier domain. The "Green's Function PE" (GFPE) method is an extension of the SSF method that allows for the simulation of acoustic fields over a ground surface with a certain impedance (Gilbert and Di 1993; Gilbert 2015). The validity is in principle limited to shallow angle propagation in atmospheric environments that can be approximated as effective quiescent media, such as the troposphere.

However, many infrasound applications require the simulation of propagation in the stratosphere or beyond. For such applications, Padé approximants can be used. As an example, the square root operator $\sqrt{1+q}$ can be approximated by the following rational function (Bamberger et al. 1988):

$$\sqrt{1+q} \approx 1 + \sum_{m=1}^{M} \frac{a_m q}{1+b_m q} \tag{15.36}$$

with M being the Padé order and:

$$a_m = \frac{2}{2M+1}\sin^2\frac{m\pi}{2M+1}, \quad b_m = \cos^2\frac{m\pi}{2M+1} \tag{15.37}$$

Substitution of Eq. 15.36 in Eq. 15.35 leads to a recursive form, under the assumption of small range steps, that can be solved using standard routines. The special case of $M = 1$ corresponds to the so-called Claerbout wide angle PE (Jensen et al. 1994). This PE can be used for propagation angles up to 40°, which is appropriate for the

simulation of tropospheric and stratospheric paths. Higher order Padé approximants allow for even wider propagation angles, but at the cost of computational speed. The efficient split-step Padé algorithm involves approximating the exponential operator in Eq. 15.35, which allows for much larger range steps (Collins 1992). The split-step Padé algorithm has been used in a wide angle high Mach number parabolic equation (Lingevitch et al. 2002).

In order to solve the one-way wave equation, specifications of the initial (starter) field $\psi(r_0, z)$ as well as the boundary conditions are necessary. Several choices exist for starter fields, ranging from analytical (e.g., Gaussian starter) to numerical starters (e.g., modal starters, self-starters) (Jensen et al. 1994; Salomons 2001). As the different analytic starter fields have specific beam patterns, it is important to consider a source with the appropriate aperture for the application of interest. Generally speaking, the self-starter can be considered as the optimal starter (Collins 1999).

Considering the boundary conditions, the interaction with the ground can be simulated by incorporating the impedance condition (mentioned in Sect. 15.3.1). For infrasonic frequencies, the impedance is generally assumed to be infinite, leading to rigid ground conditions. However, the topography itself may have an effect on the propagation of infrasound. In finite-difference/element implementations of the PE, topographic effects can be approximated by the consideration of a fluid with a sufficiently high sound speed below the surface. The top of the domain involves a radiation condition to simulate a continuation of the acoustic field in a homogeneous half-space. This is typically implemented using an artificial absorption layer of several wavelengths such that no energy is artificially reflected from the top of the computational domain (Gilbert and Di 1993; Jensen et al. 1994).

In Fig. 15.13, a simulation of propagation in a range-dependent atmosphere using a sixth-order Pade PE is shown. The atmospheric model is from the G2S specifications from 0600 UTC on January 26, 2011 and runs in a azimuth from the Sayarim Testing Range in Israel northeast into Jordan (Fee et al. 2013). The effective sound speed profiles at a variety of ranges are shown in (a) and in (b) one sees the result of the simulation. Note that the jet stream decreases in magnitude along the propagation path. At a little more than 300 km range, the tropospheric duct lifts off the ground as the jet stream becomes too weak to support ground returns. In addition, at about 160 km, a second stratospheric path appears with turning height at about 40 km altitude. Both of these effects are visible in the simulation.

15.3.6 Fourier Reconstruction of Impulsive Signals

Of particular interest is the propagation of impulsive signals such as those generated by large explosive events. Such signals are by their nature broadband due to the abrupt signal onset (Kinney and Graham 2013). If one uses a frequency domain propagation algorithm, such as a modal expansion, broadband signals must be built up through Fourier reconstruction, Eq. 15.6 (see, for example Waxler et al. (2017) for more a more detailed discussion). In doing so, there is a compromise between

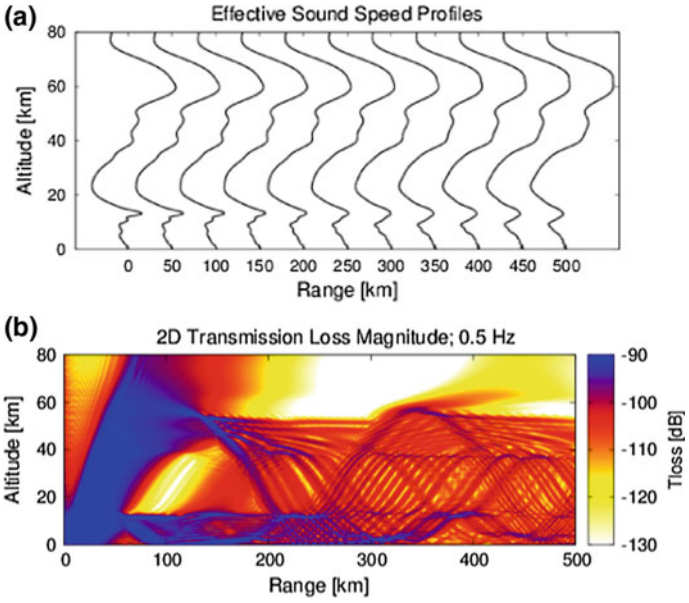

Fig. 15.13 PE simulation of propagation in a range-dependent atmosphere over Israel and Jordan on January 26, 2011 from the Sayarim testing range in the Negev desert in Israel along an azimuth 40° north of east. **a** Effective sound speed profiles at a variety of ranges. **b** PE model predictions of the Transmission loss at 0.5 Hz

bandwidth and computer run time. Higher frequency responses are typically more costly to compute. Further, infrasonic waveforms can ultimately have very long durations as a result of waveform dispersion in the ducts and multipath propagation. In order to capture the entire waveform, a sufficiently large time window must be used. In reconstructing such a signal using a discrete Fourier transform with frequency bin df, the resulting time window size is $T = 1/df$. In particular, df must be small enough so that T is greater than the duration of the wave train. This often requires quite small frequency bins which can dramatically increase the numerical cost of large bandwidth signal synthesis.

Explosive signals have very high frequency content due to their abrupt onset, with high-frequency spectral magnitudes that decrease only as an inverse power of frequency, however, the higher frequencies attenuate rapidly due to atmospheric attenuation. An example of a compromise source model is shown in Fig. 15.14 where a model source waveform is displayed. In (a), the scaled source waveform, $S(f_c t)$ is shown. Here f_c is the central frequency, corresponding to the dominant period $\tau = 1/f_c$. Its scaled spectrum, $\hat{S}(2\pi f/f_c)$, is shown in Fig. 15.14b. This source model is given explicitly by the product of a polynomial with a decreasing exponential as follows. Let

$$f(x) = x^{\beta}(1 - \frac{x}{1+\beta})e^{-x}. \tag{15.38}$$

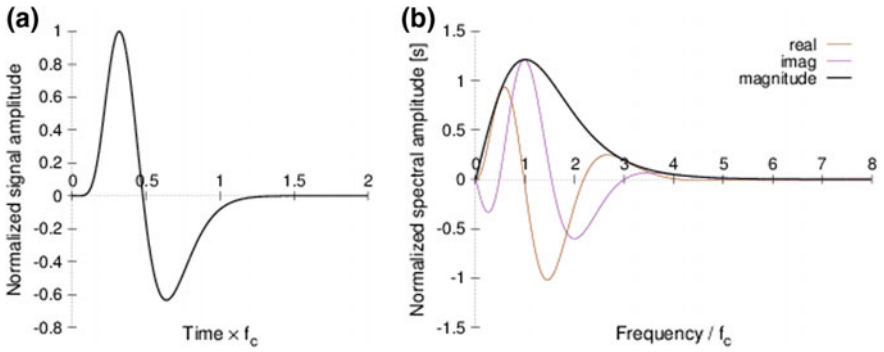

Fig. 15.14 Model initial impulse produced from Eqs. 15.38 and 15.39. **a** The scaled waveform $S(f_c t)$ is shown, where f_c is the center frequency. **b** The scaled source spectrum $\hat{S}(\boldsymbol{\omega}/f_c)$

The maximum of f is achieved at $x_0 = (1+\beta)\big(1 - \sqrt{\frac{1}{1+\beta}}\big)$ and assume that the angular frequency at which the Fourier transform of f is maximum is $\boldsymbol{\omega}_0$. Then, one obtains a source function of maximum amplitude 1 and peak frequency f_c by letting

$$S(t) = \frac{f(\frac{f_c}{\boldsymbol{\omega}_0} t)}{f(x_0)}. \tag{15.39}$$

In this model, the parameter β controls both the rise time of the impulse as well as the zero crossing. In this work, we have chosen $\beta = 8$ which gives $x_0 = 6$ and $\boldsymbol{\omega}_0 \approx 0.4776$. With this choice, the bandwidth of the impulse is approximately $5f_c$. Other initial waveforms have been proposed, for example, the form whose spectrum is given by Eq. 14 of Waxler et al. (2008). Sinusoidally modulated Gaussian pulses have also been popular, but, in our view are too narrowband to capture the impulse response reliably.

In Fig. 15.15, the results of Fourier synthesis of a broadband signal are shown. The initial waveforms of Eqs. 15.38 and 15.39 are propagated using the effective sound speed shown in Fig. 15.9c and the modal model described above. The propagation is in a stratospheric duct. The near-source diffracted signal is seen followed by a series of stratospheric pairs (Waxler et al. 2015).

15.3.7 Model Comparisons

A critical component in the development of numerical models is comparisons between model output, both as a means of validation as well as a means to identify advantages and limitation of a particular approach. Comparisons between geometrical acoustics and full wave models are particularly important because the

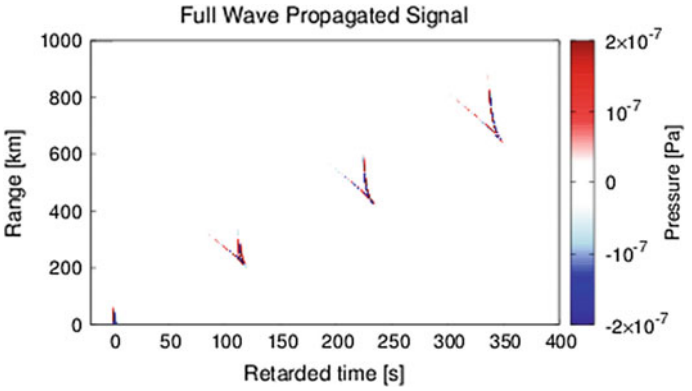

Fig. 15.15 Impulse propagation in the effective sound speed profile of Fig. 15.9c. The model waveform shown in Fig. 15.14 is propagated using the modal model described in Sect. 15.3.4. The vertical axis is the range from the source in kilometers and the horizontal axis is travel time in a 500 s window moving with speed $c_{eff}(0)$. The color bar indicates the predicted pressure for unit source amplitude at 1 m

geometrical acoustics approximation is computationally the most efficient, as well as being the model with the clearest physical interpretation. Some discrepancies between full wave and geometrical models were shown in Waxler et al. (2015). Here, we will investigate a dramatic example provided by the jet stream. The jet stream can be narrow, at points well less than a kilometer thick. Thus, at infrasonic frequencies, as mentioned above, sound can penetrate through the duct created by the jet stream. Such penetration is not captured by geometrical acoustics models.

In Fig. 15.16a, the result of propagating the initial waveform from Eq. 15.39 through the atmosphere modeled by the effective sound speed shown in Fig. 15.10 is displayed. The modal propagation algorithm was used and the broadband signal was reconstructed using Fourier synthesis. A central frequency of $f_c = 0.4$ Hz was used with a total bandwidth of 2 Hz. The vertical axis is range from the source and the horizontal axis is time in a window moving with the speed of the sound speed on the ground. Note that, due to the severe signal dispersion, to propagate out to 1000 km the time window must be at least 500 s long to capture the full wave train without suffering aliasing. This requires sampling at 500 samples per second, or with a frequency step of 0.002 Hz (Waxler et al. 2017). For comparison, in Fig. 15.16b, the ray theoretic ground strikes are plotted as a function of range and time in the same moving time window as used in (a). The corresponding propagation paths through the atmosphere for the geometrical acoustics and modal model respectively are shown in the upper panels of Figs. 15.9 and 15.11.

In Fig. 15.16a, the near-source diffracted phase is seen beginning at 0 km and 0 s and extending directly upwards (meaning that it propagates with the sound speed at the ground) until it attenuates away after about 60–70 km. Following the near-source signal, there is a string of single branch tropospheric arrivals beginning at about

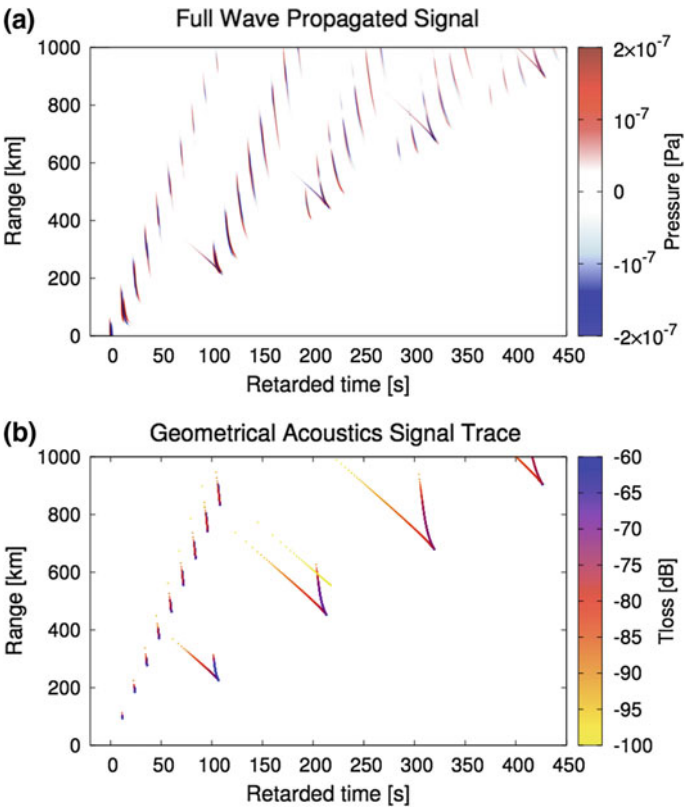

Fig. 15.16 Impulse propagation in the effective sound speed profile of Figs. 15.9a and 15.10. **a** The model waveform shown in Fig. 15.14 is propagated using the above-described modal model. The vertical axis is the range from the source in kilometers and the horizontal axis is travel time in a 500 s window moving with speed $c_{eff}(0)$. The color bar indicates the predicted pressure for unit source amplitude at 1 m. **b** The ground strikes versus time as predicted by the geometrical acoustics approximation. The vertical and horizontal axes are as in (**a**). The color bar indicates the predicted transmission loss from the spreading of the ray bundles

50 km and 10–15 s and leaving the computational domain at 1000 km and about 105 s. Then, there are four sets of strings of stratospheric arrivals beginning at about 220 km and 100 s, at 400 km and 200 s, at 600 km and 285 s, and at 800 km and 375 s. Each of the stratospheric strings of arrivals contains one double branched pair, the classical stratospheric pairs (Waxler et al. 2015), and a string of single branch arrivals which are the signals that leaked out of the tropospheric duct into the stratosphere.

In Fig. 15.16b, the signal ground strikes versus time as predicted by the geometrical acoustics approximation are plotted using the same axes and moving time window as for panel (a) and with color indicating transmission loss. The geometrical acoustics approximation fails for this example in a variety of ways. First, there's no near-source diffracted phase. This is because the atmosphere is upward

refracting near the ground so that all rays starting on the ground initially rise up into the atmosphere. Geometrical acoustics does predict the string of tropospheric phases, however, in contradistinction to the full wave model, they are each double branched, forming a sequence of tropospheric pairs (these are difficult to resolve in this plot because of the scale). In the geometric acoustics approximation, the stratospheric phases only include the classical stratospheric pair. This is because the leaked tropospheric phases are not captured since, in the geometrical approximation, energy does not penetrate into the forbidden zones. Full wave modeling shows that the tropospheric fast arrivals are transmitted through the jet stream into the stratosphere. Note that the geometrical acoustics model shows a faint thermospheric branch that is present, but not visible, in the full wave model.

To compare and test full wave models one can, in principle, obtain an exact solution by solving Eq. 15.9 and then evaluate the Fourier integral of Eq. 15.8. Such methods have been developed and are referred to as horizontal wave number transform methods (Jensen et al. 1994; Ostashev and Wilson 2015). The horizontal wave number transforms can be evaluated using the fast Fourier transform. The resulting algorithms are known as fast field programs (FFP) (West et al. 1991; Rasper et al. 1983; Talmadge and Gilbert 2000; Salomons 2001) and can be considered benchmark algorithms for stratified atmospheres against which other algorithms can be tested.

In Fig. 15.17, an example comparison of the output from various effective sound speed models is compared. The effective sound speed profiles shown in Fig. 15.9a, b, and c will be used which are denoted profile a, b, and c, respectively. The single frequency, ground-to-ground transmission loss at 0.5 Hz is investigated. In addition to the ubiquitous thermospheric duct, profile a also has a tropospheric and stratospheric duct, profile b just an additional tropospheric duct, and profile c just an additional stratospheric duct. The FFP benchmark is compared to a modal expansion with perturbative attenuation, a Pade PE with modal starter, and a modal expansion, called complex modes, with a complete treatment of attenuation.

For profiles a and c, as seen in Fig. 15.17a and c, the agreement between the three models is excellent, except in the deep first shadow zone seen in (c) between about 50 and 200 km where essentially no signal detection is predicted regardless. Note that both profile a and c feature stratospheric ducts. As discussed in detail in Waxler et al. (2017), profile b, in which there is a tropospheric, but no stratospheric duct, perturbative attenuation does not work well. This is because of the severe attenuation in the thermosphere, coupled with the fact that the tropospheric duct is leaky, connecting the tropospheric duct to the thermospheric. For profile b, the results from a modal model with complete treatment of attenuation and a model with no atmospheric attenuation at all were both included. As was shown in Waxler et al. (2017), the tropospheric phases are captured accurately by a lossless model in which the atmospheric attenuation is set to zero.

In Fig. 15.18, the predicted transmission losses from the effective sound speed models are compared to those from wide angle models that make the planar approximation, but otherwise treats the wind rigorously (Assink et al. 2017). The atmospheric profiles and azimuths that led to profiles a, b, and c from Fig. 15.9 are used

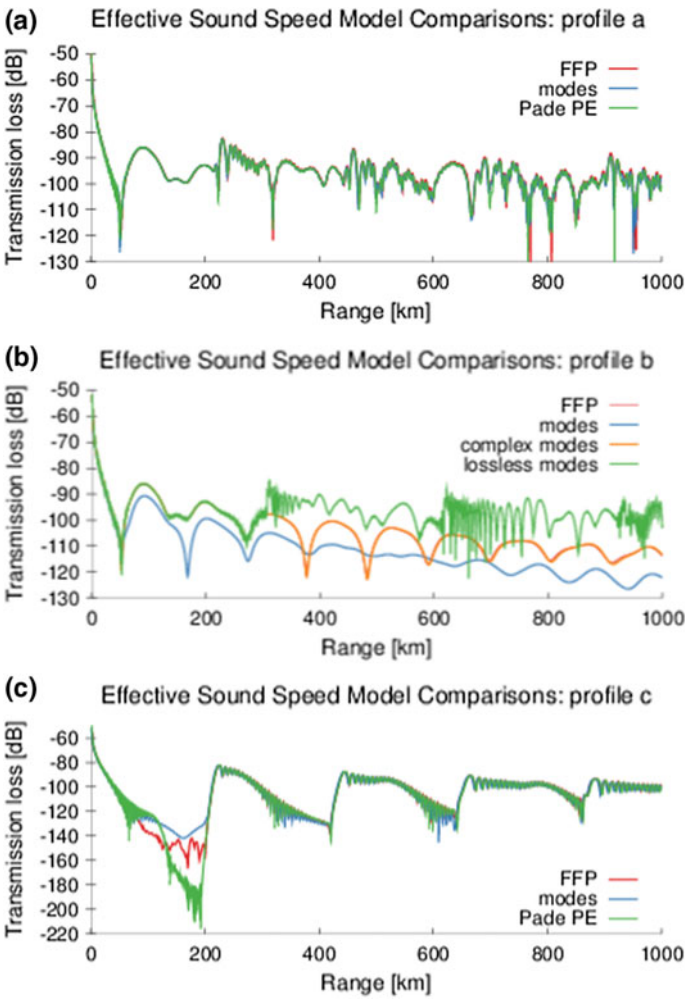

Fig. 15.17 Model comparisons for propagation in the three effective sound speeds shown in Fig. 15.9. In panel (**a**)–(**c**), the results for the profiles in the corresponding panels of Fig. 15.9 are shown

and shown in panels (a), (b), and (c) as above. For profile c, whose most predominant feature is a stratospheric duct, there is a slight mismatch between the speed of horizontal propagation as predicted by the two models. The effective sound speed approximation slightly overestimates the signal celerity, or horizontal propagation speed. This leads to the ground strike range predictions that are too short, with the mismatch increasing with increasing range; however, the effective sound speed approximation is not bad for regional ranges of a few hundred kilometers. It should be pointed out that in this case, although they have not been plotted, the FFP results,

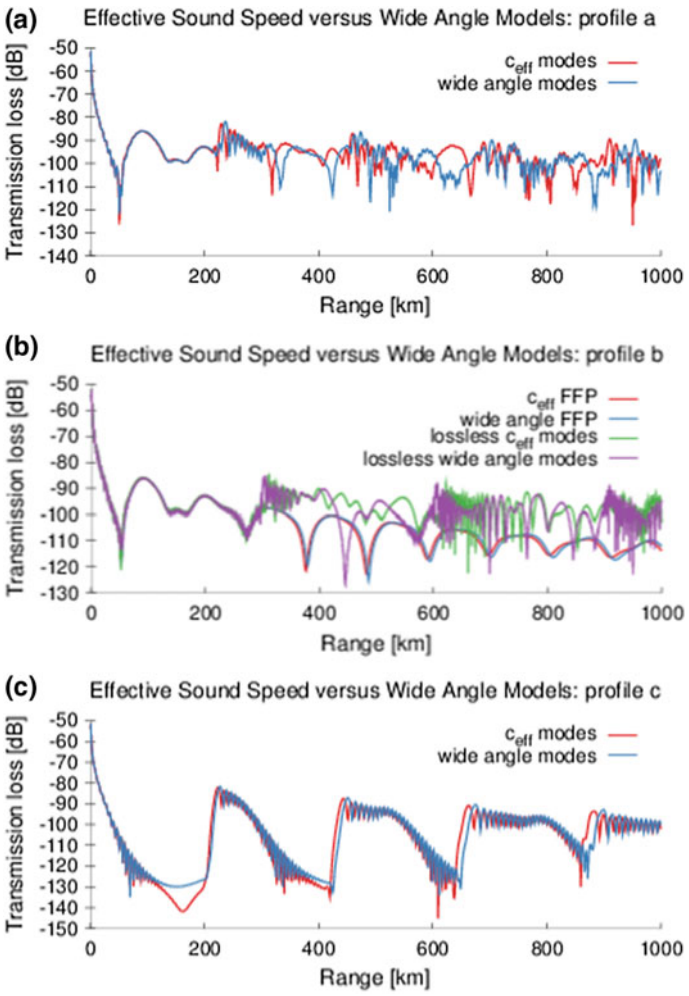

Fig. 15.18 Comparison of the effective sound speed approximation and full, though planar, treatment of wind for propagation in the atmospheres shown in Fig. 15.9. In panel (**a**)–(**c**), the results for the profiles in the corresponding panels of Fig. 15.9 are shown

with full attenuation, agree completely with the modal sums, with perturbative attenuation.

For profiles a and b, both of which feature tropospheric ducts, there are dramatic differences between the predictions of the effective sound speed and wide angle models. For profile a, the received signals are dominated by tropospheric returns until the stratospheric signals start arriving at about 220 km. Not surprisingly, since they are shallow angle, the transmission losses as predicted by the effective sound speed and wide angle models for the tropospheric duct are essentially equal. When the

stratospheric returns begin to arrive differences between the two models begin to be seen. Initially, there are small differences in striking ranges. However, as range increases more significant differences are seen. These arise because the strength of the tropospheric duct is overestimated by the effective sound speed: the troposphere is a bit more leaky than predicted. Further, the leaked energy propagates in a stratosphere whose winds are slightly less significant than predicted by the effective sound speed approximation. In the time domain, the differences between the effective sound speed and wide angle models are not significant.

For profile b, there is the added complexity that, due to the severe attenuation in the thermosphere and the coupling between the tropospheric and thermospheric ducts, the perturbative approximation to the attenuation fails (Waxler et al. 2017). Further, for the frequency considered, 0.5 Hz, thermospheric phases are highly attenuated. In Fig. 15.18b, effective sound speed and wide angle FFP's are compared as well as lossless atmosphere effective sound speed and wide angle modal sums. The lossy models show, essentially, only the tropospheric phases. For them, the effective sound speed and wide angle models are in good agreement. For the lossless models, the tropospheric parts agree well, but as soon as the thermospheric returns begin differences develop, as expected. It is shown in Waxler et al. (2017); however, that in the time domain, the thermospheric and tropospheric returns are well separated and do not interfere with each other.

The conclusion that can be drawn is as follows. For propagation in stratospheric ducts, the effective sound speed approximation with attenuation treated perturbatively is reasonable at regional ranges, unless the winds are exceptionally strong (Waxler et al. 2015). Tropospheric phases are well captured without attenuation and with the effective sound speed approximation; however, the interaction between the troposphere and the larger ducts, stratospheric and thermospheric, can be subtle, requiring either more complex numerical models, or judicious application of simpler models (Waxler et al. 2017).

15.3.8 Finite-Difference and Finite-Element Models

The techniques that have been discussed previously in this chapter have been widely used for the simulation of atmospheric infrasound because of the numerical efficiency and the ability of these models to simulate features that are observed in infrasound data. Nevertheless, these techniques remain mathematically approximate due to various assumptions, such as a (locally) stratified atmosphere or environments for which backscatter can be neglected (Jensen et al. 1994).

More recently, finite-difference and finite-element time domain techniques have become of interest for simulation of atmospheric infrasound as more complex environments (such as topography) can be incorporated more easily. The main drawback of these methods is the computational burden, but thanks to the developments in numerical methods and computing hardware (e.g., clusters), this poses less and less of a problem. The fundamental difference between finite-difference

and finite-element models is that the discretization is respectively with the governing equations and the physical domain. As a result, finite-element models are more accurate in the simulation of acoustic fields in environments with discrete boundaries such as the interface between the solid Earth and the atmosphere (Ostashev and Wilson 2015).

Finite-difference time domain solutions, in which the acoustics equations for an inhomogeneous atmosphere are solved directly, have been developed, both for linear (Ostashev et al. 2005; de Groot-Hedlin 2008) and nonlinear (Marsden et al. 2014; Sabatini et al. 2016; de Groot-Hedlin 2016) propagation problems. Among others, finite-difference methods have been used for the characterization of volcanic eruptions (Lacanna et al. 2014; Kim et al. 2015) and the estimation of explosion yield (Kim and Rodgers 2016). Currently, finite-difference models are being developed that can handle coupled seismo-acoustic problems (Sjogreen and Petersson 2016).

As time goes on, as parallel computing becomes more accessible, we expect such numerically complex models to become increasingly popular, particularly for problems with irregular boundaries and unsteady winds for which three-dimensional modeling is required.

15.3.9 Nonlinear Propagation Models

The validity of the linear approximation to fluid mechanics depends on the excursion of fluid mass being small compared to an acoustic wavelength. Consider, however, the Euler equation for the continuity of momentum flux in a fluid (Landau and Lifshitz 1987),

$$\rho\left(\frac{\partial}{\partial t} + \mathbf{v}\cdot\nabla\right) = -\nabla P.$$

This is essentially Newton's law, connecting acceleration of fluid mass to pressure gradients. For a fixed pressure gradient, as density decreases acceleration increases, as does the excursion the fluid mass undergoes during an acoustic cycle. It follows that, as density decreases, the influence of the nonlinear components of fluid motion increases, and the higher an infrasonic signal travels in the atmosphere, the more nonlinear the propagation becomes (Rogers and Gardner 1980; Gainville et al. 2010; Lonzaga et al. 2015; Scott et al. 2017; Sabatini et al. 2016).

Models for nonlinear propagation follow a sequence of approximation schemes similar to those discussed for linear propagation models. The main distinction is the significant increase in numerical and mathematical complexity over comparable linear models. As a consequence, nonlinear infrasound propagation modeling is not as well developed as linear. The most highly developed are the generalizations of geometrical acoustics to include weak nonlinearity (Rogers and Gardner 1980; Lonzaga et al. 2015; Scott et al. 2017), followed by nonlinear PE-like models having their origin in underwater acoustics (Gallin et al. 2014) and more recently by full FDTD solvers (de Groot-Hedlin 2012; Marsden et al. 2014; Sabatini et al. 2016).

We will focus our short discussion here on impulsive signals modeled using nonlinear extensions of geometrical acoustics. In these models, the linear ray paths are computed, and then a transport equation including quadratic nonlinear terms is solved along the ray path. For impulsive signals, nonlinear effects take two forms. High-frequency generation, associated with steepening of wavefronts and the formation of shock waves, and low-frequency generation, associated with period lengthening. In Fig. 15.19, the results of propagating the impulsive signal shown in Fig. 15.14 along a thermospheric path using nonlinear geometrical acoustics are shown. In (a), one sees the effective sound speed profile, in (b) the ray path and in (c) the results for a variety of signal strengths, given by the signal amplitude at one kilometer from the source. The 1 Pa source shows the linear result. As the amplitude of the source increases two effects are clearly seen: the waveform lengthens and steepens. Lengthening can become significant.

As the density of the atmosphere decreases attenuation increases as well as nonlinearity. Attenuation depends on frequency, scaling, more or less, with the square of the frequency. However, nonlinearity influences the frequency content of the signal. It follows that there is an interplay between nonlinear distortion and signal attenuation. Attenuation limits high-frequency generation and thus mitigates against shock formation. Signal lengthening lowers the frequency content of the signal (by transferring energy to lower frequencies) and thus mitigates against signal attenuation.

This is investigated in Fig. 15.20 in which the result of propagation of an impulsive signal along stratospheric and thermospheric paths is investigated. Weak and strong amplitude signals are both considered. Attenuation is insignificant in both cases for the stratospheric signals. For the thermospheric signals attenuation is visible, but is much greater for the weak signal than for the strong signal. This is consistent with the period lengthening, which is much greater for the strong signal than for the weak. We believe this is the reason that thermospheric arrivals are regularly observed, despite the fact that linear propagation at 0.5 Hz predicts that they will be of too small amplitude to be observed. In particular, to correctly model thermospheric signal returns, nonlinear propagation models must be used.

15.3.10 Software Packages

Several open-source software packages for infrasound propagation have become available in recent years, some of which have been used to perform the simulations presented in this chapter. Several of these packages are described below. It should be emphasized that all of these packages are under continued development.

A comprehensive geometrical acoustics package has been developed by, and is currently maintained by, Phil Blom at Los Alamos National Laboratories (LANL). It contains modules capable of both flat earth and round earth modeling, planar and full 3-d modeling, effective sound speed as well as rigorous wind modeling, and both stratified and arbitrary atmospheres. It also includes a 3-d eigenray solver and in all cases provides solutions to the transport equation to provide signal

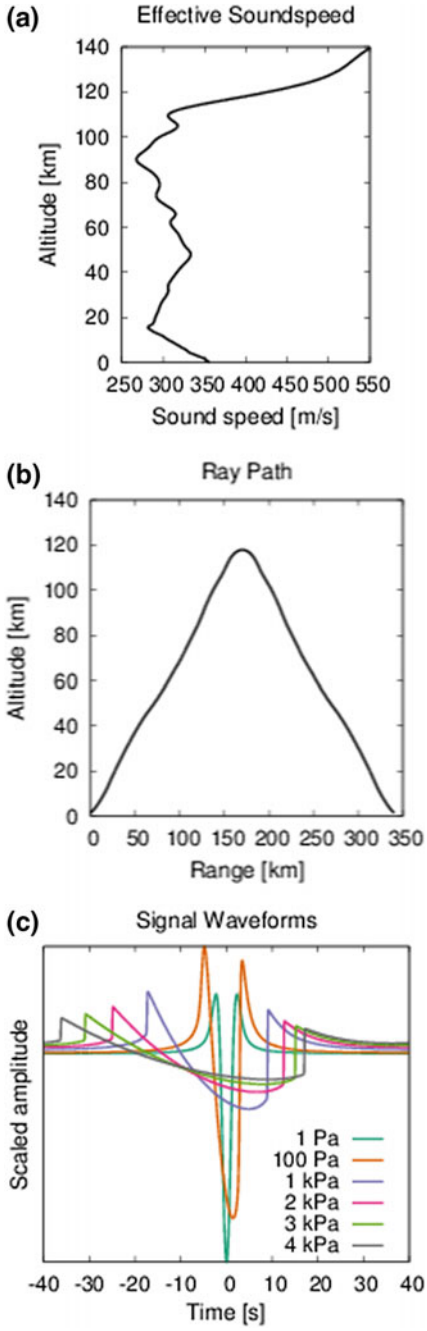

Fig. 15.19 Nonlinear propagation using nonlinear geometrical acoustics of the source waveform shown in Fig. 15.14 through the effective sound speed shown in (**a**) along the path shown in (**b**). The results for a variety of amplitudes, at one kilometer, are seen in (**c**)

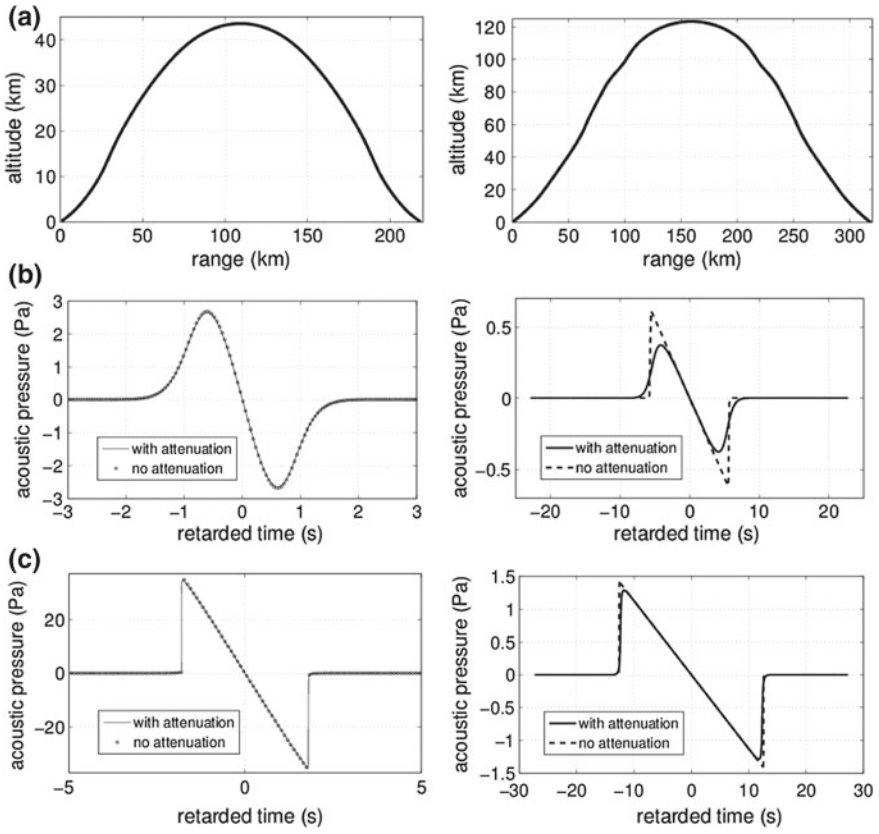

Fig. 15.20 Attenuation versus nonlinear distortion fo stratospheric and thermospheric paths. The two paths are shown in (**a**). In (**b**), propagation of a weak signal of 100 Pa at 1 Km is shown for the two paths and in (**c**) the propagation of strong signals, of 1500 Pa at 1 Km for the stratospheric path and 500 Pa at 1 Km for the thermospheric. Figures from Lonzaga et al. (2015)

amplitude estimates. The package is housed in the LANL archive at `https://github.com/LANL-Seismoacoustics`
and found in the directory `InfraGA/GeoAc`. A user's manual is included in the package.

A suite of full wave propagation models is available in the `ncpaprop` package, developed by many researchers and maintained by Roger Waxler, Claus Hetzer, and Doru Velea. It contained the full wave models presented here as well as a nonlinear ray theory module. It is available at `http://github.com/chetzer-ncpa/ncpaprop`.
An extensive user's manual, including descriptions of each algorithm, has been written and is included in the package.

Catherine De-Groot Hedlin has developed and maintains a nonlinear FDTD package available at `http://l2a.ucsd.edu/research/nlpropc`.

The code allows one to choose between linear propagation or nonlinear propagation (automatically switching over once the ratio is low enough), effective sound speed or a rigorous treatment of wind as well as atmospheric attenuation, with the ability to set attenuation to 0. The model also allows for topography in a rigid, stair step boundary approximation.

References

Andrewes DG, Holton JR, Leovy CB (1987) Middle atmosphere dynamics. Academic Press
Assink J, Waxler R, Smets P, Evers L (2014) Bidirectional infrasonic ducts associated with sudden stratospheric warming events. J Geophys Res Atmos 119
Assink J, Waxler R, Velea D (2017) A wide-angle high mach number modal expansion for infrasound propagation. J Acoust Soc Am 141(3):1781–1792
Bamberger A, Engquist B, Halpern L, Joly P (1988) Higher order paraxial wave equation approximations in heterogeneous media. SIAM J Appl Math 48(1):129–154
Bertin M, Millet C, Bouche D (2014) A low order reduced model for the long range propagation of infrasounds in the atmosphere. J Acoust Soc Am
Blanc-Benon P, Lipkens B, Dallois L, Hamilton MF, Blackstock DT (2002) Propagation of finite amplitude sound through turbulence: modeling with geometrical acoustics and the parabolic approximation. J Acoust Soc Am 111(1):487–498
Blom P, Waxler R (2017) Modeling and observations of an elevated, moving infrasonic source: eigenray methods. J Acoust Soc Am 141(4):2681–2692
Blom P, Waxler R, Frazier W, Talmadge C (2014) Observations of the refraction of microbaroms generated by large maritime storms by the wind field of the generating storm. J Geophys Res Atmos 119(12):7179–7192. https://doi.org/10.1002/2014JD021795
Blom PS, Marcillo O, Arrowsmith SJ (2015) Improved bayesian infrasonic source localization for regional infrasound. Geophys J Int 203(3):1682–1693
Brekhovskikh LM, Godin OA (1999) Acoustics of layered media I and II. Springer, New York
Chunchuzov I (1996) The spectrum of high-frequency internal waves in the atmospheric waveguide. J Atmos Sci 53(13):1798–1814
Collins MD (1992) A split-step Padé solution for the parabolic equation method. J Acoust Soc Am 93(4):1736–1742
Collins MD (1999) The stabilized self-starter. J Acoust Soc Am 106(4):1724–1726. https://doi.org/10.1121/1.427921
Collins MD, McDonald BE, Heaney KD, Kuperman WA (1995) Threedimensional effects in global acoustics. J Acoust Soc Am 97(3):1567–1575. https://doi.org/10.1121/1.413050
Cotté B, Blanc-Benon P, Bogey C, Poisson F (2009) Time-domain impedance boundary conditions for simulations of outdoor sound propagation. AIAA J 47(10):2391
Drob D (2019) Meteorology, climatology, and upper atmospheric composition for infrasound propagation modeling. In: Le Pichon A, Blanc E, Hauchecorne (eds) Infrasound monitoring for atmospheric studies, 2nd edn. Springer, Dordrecht, pp 485–508
Drob DP, Broutman D, Hedlin MA, Winslow NW, Gibson RG (2013) A method for specifying atmospheric gravity-wave fields for long-range infrasound propagation calculations. J Geophys Res Atmos 118(10):3933–3943
Dubin M, Hull AR, Champion KSW (1976) U.S. standard atmosphere, 1976. U.S. Government Printing House
Evers LG, Haak HW (2007) Infrasonic forerunners: Exceptionally fast acoustic phases. Geophys Res Lett 34(10):n/a–n/a, L10806. https://doi.org/10.1029/2007GL029353
Evers LG, Siegmund P (2009) Infrasonic signature of the 2009 major sudden stratospheric warming. Geophys Res Lett 36:L23808. https://doi.org/10.1029/2009GL041323

Fee D, Waxler R, Assink J, Gitterman Y, Given J, Coyne J, Mialle P, Garces M, Drob D, Kleinert D, Hofstetter R, Grenard P (2013) Overview of the 2009 and 2011 sayarim infrasound calibration experiments. J Geophys Res Atmos 118(12):6122–6143. https://doi.org/10.1002/jgrd.50398

Gainville O, Blanc-Benon P, Blanc E, Roche R, Millet C, Le Piver F, Despres B, Piserchia PF (2010) Misty picture: a unique experiment for the interpretation of the infrasound propagation from large explosive sources. In: Infrasound monitoring for atmospheric studies. Springer, pp 575–598

Gallin LJ, Rénier M, Gaudard É, Farges T, Marchiano R, Coulouvrat F (2014) One-way approximation for the simulation of weak shock wave propagation in atmospheric flows. J Acoust Soc Am 135(5):2559–2570

Gilbert K, Di X (1993) A fast green's function method for one-way sound propagation in the atmosphere. J Acoust Soc Am 94(4)

Gilbert KE (2015) A numerically stable formulation of the green's function parabolic equation: Subtracting the surface-wave pole. J Acoust Soc Am 137(1):EL8–EL14. https://doi.org/10.1121/1.4902423

Gill AE (1982) Atmosphere-ocean dynamics. Int Geophys Ser 30. Academic Press

Godin O (2002) An effective quiescent medium for sound propagating through an inhomogeneous, moving fluid. J Acoust Soc Am

Godin O (2014) Dissipation of acoustic gravity waves: an asymptotic approach. J Acoust Soc Am

Godin OA (2002) Wide-angle parabolic equations for sound in a 3d inhomogeneous moving medium. Dokl Phys 47(9):643–646

Godin OA (2012) Acoustic-gravity waves in atmospheric and oceanic waveguides. J Acoust Soc Am 132(2):657–669

de Groot-Hedlin C (2008) Finite-difference time-domain synthesis of infrasound propagation through an absorbing atmosphere. J Acoust Soc Am 124(3):1430–1441

de Groot-Hedlin C (2012) Nonlinear synthesis of infrasound propagation through an inhomogeneous, absorbing atmosphere. J Acoust Soc Am 132(2):646–656

de Groot-Hedlin CD (2016) Long-range propagation of nonlinear infrasound waves through an absorbing atmosphere. J Acoust Soc Am 139(4):1565–1577. https://doi.org/10.1121/1.4944759

Hardin R, Tappert F (1973) Applications of the split-step fourier method to the numerical solution of nonlinear and variable coefficient wave equations. SIAM Rev 15(423)

Jensen, F., Kuperman, W., Porter, M., Schmidt, H.: Computational ocean acoustics, 1st edn. Springer, Fifth Avenue, New York, NY, USA

Kim K, Fee D, Yokoo A, Lees JM (2015) Acoustic source inversion to estimate volume flux from volcanic explosions. Geophys Res Lett 42(13):5243–5249, 2015GL064466. https://doi.org/10.1002/2015GL064466

Kim K, Lees J (2011) Finite-difference time-domain modeling of transient infrasonic wavefields excited by volcanic explosions. Geophys Res Lett 38(6)

Kim K, Rodgers A (2016) Waveform inversion of acoustic waves for explosion yield estimation. Geophys Res Lett 43(13):6883–6890, 2016GL069624. https://doi.org/10.1002/2016GL069624

Kinney GF, Graham KJ (2013) Explosive shocks in air. Springer Science & Business Media

Kulichkov SN, Chunchuzov IP, Popov OI (2010) Simulating the influence of an atmospheric fine structure on long-range propagation of pulsed acoustic signals. Izvestiya Atmos Ocean Phys 46:60–68

Lacanna G, Ichihara M, Iwakuni M, Takeo M, Iguchi M, Ripepe M (2014) Influence of atmospheric structure and topography on infrasonic wave propagation. J Geophys Res Solid Earth 119(4):2988–3005. https://doi.org/10.1002/2013JB010827

Lalande JM, Waxler R (2016) The interaction between infrasonic waves and gravity wave perturbations: application to observations using UTTR rocket motor fuel elimination events. J Geophys Res Atmos, n/a–n/a, 2015JD024527. https://doi.org/10.1002/2015JD024527

Landau LD, Lifshitz EM (1965) Quantum mechanics. Pergamon, London

Landau LD, Lifshitz EM (1987) Fluid mechanics. Pergamon Press, Oxford

Le Pichon A, Blanc E, Drob D, Lambotte S, Dessa JX, Lardy M, Bani P, Vergniolle S (2005) Infrasound monitoring of volcanoes to probe high-altitude winds. J Geophys Res Atmos 110(D13):D13106. https://doi.org/10.1029/2004JD005587

Lihoreau B, Gauvreau B, Bérengier M, Blanc-Benon P, Calmet I (2006) Outdoor sound propagation modeling in realistic environments: application of coupled parabolic and atmospheric models. J Acoust Soc Am 120(1):110–119

Lingevitch J, Collins M, Dacol D, Drob D, Rogers J, Siegmann W (2002) A wide angle and high mach number parabolic equation. J Acoust Soc Am 111(2):729–734

Lonzaga J, Waxler R, Assink J, Talmadge C (2015) Modelling waveforms of infrasound arrivals from impulsive sources using weakly non-linear ray theory. Geophys J Int

Lott F, Millet C (2010) The representation of gravity waves in atmospheric general circulation models (gcms). In: Infrasound monitoring for atmospheric studies. Springer, pp 685–699

Marsden O, Bogey C, Bailly C (2014) A study of infrasound propagation based on high-order finite difference solutions of the navier-stokes equations. J Acoust Soc Am 135(3):1083–1095

Norris D, Gibson R, Bongiovanni K (2010) Numerical methods to model infrasonic propagation through realistic specifications of the atmosphere. In: Infrasound monitoring for atmospheric studies. Springer, pp 541–573

Olver FW (2014) Asymptotics and special functions. Academic press

Ostashev V, Juvé D, Blanc-Benon P (1997) Derivation of a wide-angle parabolic equation for sound waves in inhomogeneous moving media. Acta Acust United Acust 83(3):455–460

Ostashev VE, Wilson DK (2015) Acoustics in moving inhomogeneous media. CRC Press

Ostashev VE, Wilson DK, Liu L, Aldridge DF, Symons NP, Marlin D (2005) Equations for finite-difference, time-domain simulation of sound propagation in moving inhomogeneous media and numerical implementation. J Acoust Soc Am 117(2):503–517

Ostashev VE, Wilson DK, Liu L, Aldridge DF, Symons NP, Marlin D (2005) Equations for finite-difference, time-domain simulation of sound propagation in moving inhomogeneous media and numerical implementation. J Acoust Soc Am 117(2):503–517. https://doi.org/10.1121/1.1841531

Pichon AL, Garcs M, Blanc E, Barthlmy M, Drob DP (2002) Acoustic propagation and atmosphere characteristics derived from infrasonic waves generated by the concorde. J Acoust Soc Am 111(1):629–641. https://doi.org/10.1121/1.1404434

Pierce AD (1965) Propagation of acoustic-gravity waves in a temperature- and wind-stratified atmosphere. J Acoust Soc Am 37(2):218–227

Pierce AD (1989) Acoustics. Acoustical Society of America, Woodbury NY

Pierce AD, Posey JW (1971) Theory of the excitation and propagation of lamb's atmospheric edge mode from nuclear explosions. Geophys J Int 26(1–4):341–368

Press F, Harkrider D (1962) Propagation of acoustic-gravity waves in the atmosphere. J Geophys Res 67(10):3889–3908. https://doi.org/10.1029/JZ067i010p03889

Pridmore-Brown DC (1962) Sound propagation in a temperature- and wind-stratified medium. J Acoust Soc Am 34:438–443

Rasper R, Lee S, Gilbert R, Bong N, Richards R, Kuester E, Chang D (1983) Fast field program for a layered medium bounded by complex impedance surfaces. J Acoust Soc Am 73(S1):S94–S94

Rogers PH, Gardner J (1980) Propagation of sonic booms in the thermosphere. J Acoust Soc Am 67(1):78–91

Sabatini R, Marsden O, Bailly C, Bogey C (2016) A numerical study of nonlinear infrasound propagation in a windy atmosphere. J Acoust Soc Am 140(1):641–656

Salomons E (2001) Computational atmospheric acoustics. Kluwer, Dordrecht, The Netherlands

Salomons EM (1998) Improved green's function parabolic equation method for atmospheric sound propagation. J Acoust Soc Am 104(1):100–111. https://doi.org/10.1121/1.423260

Scott J, Blanc-Benon P, Gainville O (2017) Weakly nonlinear propagation of small-wavelength, impulsive acoustic waves in a general atmosphere. Wave Motion

Sjogreen B, Petersson NA (2016) User's guide to elac, version 1.0. Technical report LLNL-SM-704300, Lawrence Livermore National Laboratory

Smets P, Assink J, Evers L (2019) The study of sudden stratospheric warmings using infrasound. In: Le Pichon A, Blanc E, Hauchecorne (eds) Infrasound monitoring for atmospheric studies, 2nd edn. Springer, Dordrecht, pp 723–755

Smith KB (1999) A three-dimensional propagation algorithm using finite azimuthal aperture. J Acoust Soc Am 106(6):3231–3239. https://doi.org/10.1121/1.428177

Stull RB (1991) An introduction to boundary layer meteorology. Kluwer, Dordrecht

Sutherland LC, Bass HE (2004) Atmospheric absorption in the atmosphere up to 160 km. J Acoust Soc Am 99(3):1012–1032

Talmadge CL, Gilbert KE (2000) A benchmark fast-field program model for infrasound propagation. J Acoust Soc Am 108(5):2649–2649

Thomson DJ (1990) Wide-angle parabolic equation solutions to two range-dependent benchmark problems. J Acoust Soc Am 87(4):1514–1520. https://doi.org/10.1121/1.399450

Tolstoy I (1963) The theory of waves in stratified fluids including the effects of gravity and rotation. Rev Mod Phys 35:207–230. https://doi.org/10.1103/RevModPhys.35.207

Waxler R (2002) A vertical eigenfunction expansion for the propagation of sound in a downward refracting atmosphere over a complex impedance plane. J Acoust Soc Am 112(6):2540–2552

Waxler R (2016) An overview of infrasound propagation. INTER-NOISE 2016:1831–1839

Waxler R, Assink J, Velea D (2017) Modal expansions for infrasound propagation and their implications for ground-to-ground propagation. J Acoust Soc Am 141(2):1290–1307

Waxler R, Evers LG, Assink J, Blom P (2015) The stratospheric arrival pair in infrasound propagation. J Acoust Soc Am 137(4):1846–1856

Waxler R, Gilbert KE, Talmadge C (2008) A theoretical treatment of the long range propagation of impulsive signals under strongly ducted nocturnal conditions. J Acoust Soc Am 124:2742–2754

West M, Sack R, Walkden F (1991) The fast field program (ffp). a second tutorial: application to long range sound propagation in the atmosphere. Appl Acoust 33(3):199–228

Chapter 16
Internal Gravity Wave Perturbations and Their Impacts on Infrasound Propagation in the Atmosphere

Igor Chunchuzov and Sergey Kulichkov

Abstract The model of shaping of the 3-D and 1-D wavenumber spectra for the wind velocity and temperature fluctuations induced by atmospheric gravity waves is described here. Using the 3-D spectrum of gravity wave perturbations, the variances of the fluctuations of sound travel time along refracting ray paths and the azimuth of arrival of acoustic signals are estimated. These variances define the errors in localization of infrasound sources caused by gravity wave perturbations. The results of theory and numerical modeling of infrasound scattering from gravity wave perturbations are presented. With a recently developed infrasound probing method the vertical profiles of the horizontal wind velocity fluctuations in the upper stratosphere (height range is 30–52 km) and lower thermosphere (90–140 km) are retrieved. The method is based on analytic relation between scattered infrasound field in the shadow zone and the vertical profile of the layered inhomogeneities of the effective sound speed. The obtained results show a capability of the probing method in the retrieval of the detailed wind-layered structure in the stratosphere, mesosphere and lower thermosphere. The vertical wavenumber spectra of the retrieved vertical profiles of the wind velocity fluctuations in the upper stratosphere and their coherence functions are analyzed.

16.1 Introduction

Internal gravity waves (IGWs) in the atmosphere are the subject of intensive research carried out over the period of more than 50 years, beginning with the pioneering work of Hines (1960) who studied the propagation of these waves from the tropospheric gravity wave sources to the ionosphere. Such attention to the IGWs

I. Chunchuzov (✉) · S. Kulichkov
Obukhov Institute of Atmospheric Physics, 3 Pyzhevsky Per.,
119017 Moscow, Russia
e-mail: igor.chunchuzov@gmail.com

S. Kulichkov
e-mail: snk@ifaran.ru

A. Le Pichon et al. (eds.), *Infrasound Monitoring for Atmospheric Studies*,
https://doi.org/10.1007/978-3-319-75140-5_16

is associated with the numerous effects that they have on atmospheric circulation, the spatial structure and temporal variability of meteorological fields (wind velocity, temperature, density, humidity), and the turbulent regime of all atmospheric layers, starting from the atmospheric boundary layer (ABL) and up to the altitudes of mesosphere and lower thermosphere. The extensive literature, including well-known books of Gossard and Hook (1975), Lighthill (1978), Nappo (2002), Holton and Hakim (2012) and reviews (Fritts 1984; Fritts and Alexander 2003), is devoted to the results reached in studying of these effects.

Numerous observations of mesoscale variations (periods from a few minutes to a few hours) in temperature, density, wind velocity, and aerosol concentration at altitudes of the lower and middle atmosphere using radars, lidars, rocket sounding, optical sounding from space show that IGWs significantly contribute to these variations. The IGWs are also responsible for the shaping of the anisotropic wind velocity and temperature inhomogeneities with the horizontal scales exceeding their vertical scales dozens and hundreds of times (Manson 1990). The characteristic vertical scales of such inhomogeneities in the middle and upper atmosphere are in the range from tens of meters to tens of kilometers. These scales are comparable to the wavelengths of infrasonic waves with frequencies in the range 0.02–10 Hz, therefore such inhomogeneities significantly affect the propagation and scattering of infrasound.

The 3-D fluctuations in wind velocity and temperature, whose spatial scales are much larger than the wavelengths of acoustic waves, cause refraction of the acoustic ray paths in 3-D space, which leads to the fluctuations in sound propagation time and the angles of arrival of acoustic signals (Chunchuzov 2004; Kulichkov et al. 2007; Drob et al. 2013). In turn, the fluctuations in the azimuth of the arrival result in the error of localization of infrasonic sources, which should be taken into account when modeling infrasound propagation in the atmosphere (Le Pichon et al. 2019).

The effects of large-scale gravity wave perturbations on infrasound propagation can be modeled with the ray-tracing methods (Hedlin and Walker 2013). However, for the inhomogeneities, whose vertical scales are comparable with the wavelengths of acoustic waves, the effect of scattering of infrasonic field from the inhomogeneities becomes important. Some portion of the scattered field penetrates in the so-called acoustic shadow zones predicted by geometric acoustics. Such effects can be explained only by fully wave approach (Kulichkov 2004; Ostashev et al. 2005; Norris 2005; Gibson et al. 2007; Gibson and Norris 2008; Gainville et al. 2010; Chunchuzov et al. 2011, 2013, 2014). The infrasound scattering from anisotropic inhomogeneities was found to affect the observed waveforms of the signals from successive surface explosions detected in the shadow zones (Bush et al. 1997; Kulichkov and Bush 2001; Kulichkov et al. 2002; Kulichkov 2004). The finding of this effect significantly changed our concept about the distribution of both audibility and shadow zones on the ground surface, which existed since the first experiments on detecting infrasound from explosions in the atmosphere (Duckert 1931; Blokhintsev 1956).

The statistical characteristics of the fluctuations in the parameters of scattered infrasonic signals (such as travel time and angle of arrival, amplitude and duration)

over sufficiently long periods of observations apparently depend on the power spectrum of anisotropic wind velocity and temperature fluctuations, which is still poorly known. It differs significantly from the power spectrum of locally homogeneous and isotropic turbulence.

Till the present there is no single opinion about the shaping mechanism for the power spectrum of gravity wave perturbations. Recently, the nonlinear model of shaping of gravity wave spectrum for the statistical ensemble of IGWs with randomly independent amplitudes and phases has been developed (Chunchuzov 1996, 2001, 2002). This spectrum will be analyzed in Sects. 16.2–16.4. As to the individual realizations of gravity wave perturbations (instant vertical and horizontal profiles) they were obtained directly from the solutions of the nonlinear motion equations for gravity waves (Chunchuzov 2009). Such realizations vary with a horizontal coordinate in accordance with the solutions of the motion equations for gravity waves. They distinguish from the realizations obtained from the diffusive-filtering theory of gravity wave spectra (Gardner 1996) for which the range-dependence of the realizations was modeled by a Gaussian superposition over dominant horizontal wavelengths (Norris 2005; Gibson et al. 2007; Gibson and Norris 2008).

Using the obtained 3-D wavenumber spectrum for the wave-induced wind velocity and temperature fluctuations we will calculate the variances of the fluctuations of sound travel time along refracting ray paths and the azimuth of arrival of acoustic signals as functions of a range from a point acoustic source (Sects. 16.5–16.6). The results of theory and numerical modeling of infrasound propagation and scattering from gravity wave perturbations will be described in Sects. 16.7–16.8. A recently developed infrasound probing method and the vertical profiles of the wind velocity fluctuations in the middle and upper atmosphere retrieved with this method will be presented in Sects.16.9–16.11. In Sect. 16.12 the vertical wave number spectra of the retrieved fluctuations will be discussed.

16.2 Gravity Wave Perturbations in the Atmosphere

According to the observations, carried out mostly with a ground based technique, the vertical wavenumber spectrum of the horizontal wind velocity and temperature fluctuations in the middle atmosphere decays approximately as k_z^{-3} at high vertical wavenumbers k_z. Different models of formation of the internal wave spectrum in the atmosphere were proposed, especially in the 80s and 90s of the last century, to explain the observed forms of the spectra (VanZandt 1982; Dewan and Good 1986; Smith et al. 1987; Weinstock 1990; Hines 1991b; Hostetler and Gardner 1994; Gurvich 1997; Medvedev and Klaassen 1995; Chunchuzov 1996; Warner and McIntyre 1996; Dewan 1997; Eckermann 1999; Franke and Robinson 1999) and to incorporate these models into parameterization schemes for the wave drag in the atmosphere (Hamilton 1997; Alexander and Dunkerton 1999; Akmaev 2001). The

applicability of the approximations used in these models was debated, for instance, in Hines (1991a, 1993, 1996, 2001), Broutman et al. (1997), Eckermann (1999), Fritts and Alexander (2003).

It was noticed by Hines (1991a, b) that the gravity waves with the high k_z, which are within the observed k_z^{-3}—spectral tail, have very low horizontal phase speeds relative to the mean wind, comparable to the horizontal wind velocity fluctuations induced by the waves themselves. Such waves should strongly interact due to advective nonlinearity of the Eulerian fluid motion equations.

To take into account the wave-induced advection of fluid parcels it was suggested in a number of works to use a Lagrangian frame of variables for studying the dynamics of gravity waves, and then perform a variable transformation to the Eulerian frame, where the advection takes place (Chunchuzov 1996; Eckermann 1999; Chunchuzov 2001; Hines 2001; Chunchuzov 2002; Broutman et al. 2004; Pinkel 2008). As an exact transformation it strictly takes into account the advective effects associated with the nonlinear terms $(\vec{v}\nabla)\vec{v}$ in the Eulerian equations of motion without using any approximations for these terms. Using a Lagrangian approach it was found that a strong nonlinearity of the gravity wave field, when viewed in the Eulerian frame, generates a 3-D wave number spectrum with a k^{-5}-power law decay at high wave numbers k (Chunchuzov 2002). This spectrum is of highly anisotropic form as a result of a balance between the nonlinear wave energy transfer from the characteristic (vertical and horizontal) scales of internal wave sources toward smaller vertical and larger horizontal scales, and the dissipation of wave energy at small vertical scales due to wave-breaking processes. Such cascade-like energy transfer in the 3-D wave number space is caused by nonresonant wave–wave interactions, which along with wave energy dissipation play a key role in shaping of the equilibrium gravity wave spectrum. The wave-like fluid motions generated by the nonresonant interactions resemble anisotropic and vertically oriented vortices rather than the linear gravity waves, because the dispersion surfaces of these waves in the frequency wave number space are completely "smeared" by wave-induced advection.

The hypothesis about a significant role played by forward energy cascade in shaping of the spectra of the mesoscale fluctuations in the atmosphere was earlier proposed by Dewan (1997) on the basis of his saturated-cascade similitude theory. Using this theory Dewan found the forms of the horizontal and temporal gravity wave spectra, which were close to their observed forms, although he traditionally interpreted the vertical spectra as a result of the saturation of linear gravity waves caused by their convective or shear instabilities.

Lindborg (2006) also used a similitude theory added by numeric simulations of energy cascade in stratified fluid. This allowed him to derive the k_z^{-3}-form for the vertical wave number spectra (scales from 100–1000 m) and $k_h^{-5/3}$-form for the horizontal wave number spectra (scales from about 1–500 km). However, contrary to the linear wave saturation hypothesis, Lindborg (2006) assumed that both the horizontal and vertical spectra arise "… from one and the same type of nonlinear chaotic motion…" governed by the fully nonlinear Boussinesq equations. Such

highly anisotropic motions significantly differ from those induced by linear gravity waves. The conclusion made by Lindborg (2006) about the importance of a nonlinear energy cascade in shaping of highly anisotropic mesoscale fluctuations in stably stratified fluid is in agreement with that previously obtained by Chunchuzov (2002) who used a Lagrangian approach.

Earlier, the importance of the nonresonant interactions between IGWs in shaping of their energy spectrum was pointed out by Phillips (1967), who noticed that such interactions resemble cascade-like strong interactions between turbulent motions of different scales in stably stratified fluid. He found that gravity wave interactions result in the k_z^{-3}-form for their energy spectrum, which is the same as found by Lumley (1964) and Shur (1962) for the turbulence spectrum in the "buoyancy sub-range". Recently, Sukoriansky and Galperin (2013) showed that there is a buoyancy-Kolmogorov subrange transition between wave-like (anisotropic) fluctuations and the turbulence in the inertial range, through which the wave energy transfers from anisotropic wave-like fluctuations to smaller scale isotropic turbulence. Thus, the nonlinearity of hydrodynamic equations that causes cascade-like energy transfer in the 3-D wave number space seems to be the main shaping mechanism for the power spectrum of the wave-induced anisotropic fluctuations.

16.3 3-D Spectrum of Gravity Wave Perturbations

There are many random sources of gravity waves in the atmosphere such as an adaptation of meteorological fields to the state of quasi-geostrophic equilibrium, meteorological fronts, convection, jet streams, unstable wind shears, orographic disturbances of the nonstationary air flow and others. It was suggested by Chunchuzov (2001, 2002) that the nonlinearity of the motion equations for the Lagrangian parcel displacements induced by gravity waves causes wave–wave interactions so that some equilibrium wave energy distribution among Lagrangian wave modes forms due to the energetic balance between the nonlinear energy transfer from the characteristic horizontal (k_0^{-1}) and vertical (m_0^{-1}) scales of the source spectrum toward smaller scales, and the wave energy dissipation at small vertical scales. For stably stratified fluid, for which the r.m.s. vertical parcel displacements, ν_V, are much less than their r.m.s. horizontal displacements, ν_h, the ratio of the source scales, $\chi \equiv m_0/k_0$, is of the order of the ratio $\nu_h/\nu_V \gg 1$ as follows from the continuity equation under incompressible fluid approximation.

When viewed from the Eulerian frame the form of the Lagrangian spectrum is distorted due to a different advection of different fluid parcels caused by an entire gravity wave field. The characteristic scales k_0^{-1} and m_0^{-1} of the source spectrum were assumed to be much greater than the corresponding r.m.s parcel displacements ν_h and ν_v so that in the 3-D wave number space these scales are inside the characteristic surface of the ellipsoid $k_z^2\nu_v^2 + k_\perp^2\nu_h^2 = 1/2$ shown in Fig. 16.1.

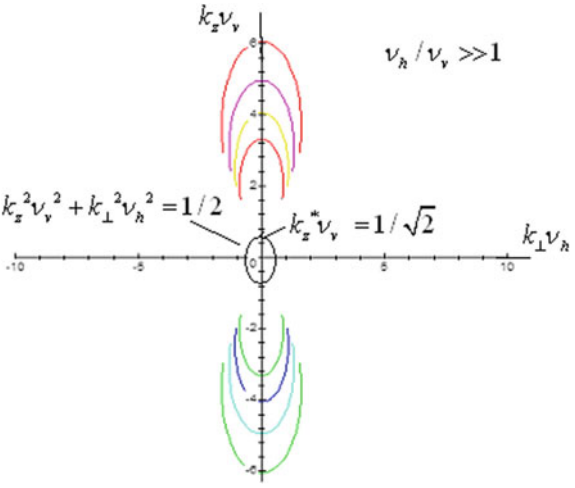

Fig. 16.1 Contours of constant amplitude of the 3-D wave number spectrum for the vertical displacements of fluid parcels induced by IGWs in the case: $\chi = 15$, $M = 3.2 \times 10^{-1}$. k_z and $k_\perp$ are vertical and horizontal wave numbers, respectively; ν_v and ν_h are the r.m.s. values of the vertical and horizontal displacements, respectively

As long as wavenumbers of wave modes obey the condition $k_z^2\nu_v^2 + k_\perp^2\nu_h^2 \ll 1$ the wave–wave interactions are weak. However, such interactions lead to the generation of the wave modes with the high wave numbers, which are outside the characteristic ellipsoidal surface: $k_z^2\nu_v^2 + k_\perp^2\nu_h^2 \gg 1/2$. For high wave numbers the amplitudes of the vertical and horizontal displacements become comparable to the corresponding vertical and horizontal scales of the wave modes, therefore the nonresonant interactions between these modes become strong. Such interactions generate a high wave number tail in the 3-D wave number spectrum of the vertical parcel displacements and velocities found by Chunchuzov (2001, 2002).

For high vertical wave numbers, $2^{1/2}|k_z|\nu_V \gg 1$, and low horizontal wave numbers $k_\perp$, such that $\frac{\chi^2 k_\perp^2}{k_z^2} \ll 1$, the 3-D spectrum $S_E(k_\perp, k_z)$ of the wave-induced vertical displacement field $S_c(\vec{r}\,, t)$ in the Eulerian frame takes the following asymptotic form:

$$\bar{S}_E(k_\perp, k_z) = \frac{\beta}{8\pi e_0}|k_z|^{-5}\exp\left\{-\frac{k_\perp^2}{4e_0 k_z^2}\right\}\left[1 + O\left(\frac{\chi^2 k_\perp^2}{k_z^2}\right)\right], \tag{16.1}$$

where the nondimensional coefficient

$$\beta = (2\pi)^{-1/2} 2^{-13} a_0^{-5/2} \exp\left\{-\frac{1}{32 a_0}\right\} \tag{16.2}$$

depends on the variance a_0 of the vertical gradient of the displacement field $S_c(\vec{r}, t)$ that characterizes the degree of nonlinearity of the gravity wave field. The coefficient e_0 characterizes the variance of the horizontal gradient of $S_c(\vec{r}, t)$. Introducing the parameter of nonlinearity of the wave field

$$M \equiv m_0 \nu_V \tag{16.3}$$

the coefficient a_0 can be expressed as follows: $a_0 = \frac{M^2}{8}$, whereas $e_0 \approx \frac{a_0}{\chi^2} \ll a_0$ and depends also on the anisotropy of the source spectrum $\chi \gg 1$. Using relation between relative temperature fluctuations $\delta T/T_0$ (here T_0 is the temperature in the undisturbed atmosphere) and vertical displacements we can also obtain the 3-D wave number spectrum for the relative temperature fluctuations: $V_T(k_\perp, k_z) = (N^2/g)^2 \underset{E}{\bar{S}}(k_\perp, k_z)$, where $\underset{E}{\bar{S}}(k_\perp, k_z)$ is given by (16.1).

The obtained 3-D spectrum (16.1)–(16.2) shows the existence of highly anisotropic spatial inhomogeneities in the displacement and temperature fields, whose anisotropy depends on the value of $e_0 \ll 1$. The contours of constant amplitude of this spectrum are significantly stretched vertically in the wave number space as seen from Fig. 16.1. This spectrum was used by Gurvich and Chunchuzov (2003, 2005, 2008) for explaining the spectra of stellar scintillations observed from space. The anisotropy of the temperature inhomogeneities was assumed to vary with their vertical scale when transferring from the wave-like fluctuations with high k_z to the low k_z, at which the gravity wave source spectrum is localized. Also, the anisotropy decreases when the vertical scales of the inhomogeneities transfer from the scale-range inherent the anisotropic wave-like fluctuations to the inertial range of locally isotropic turbulence.

The similar asymptotic form was also obtained for the 3-D spectrum of horizontal wind velocity fluctuations induced by IGWs (Chunchuzov 2002). Ostashev et al. (2005) used this spectrum for calculating the statistical characteristics of the acoustic waves scattered from anisotropic wind velocity and temperature inhomogeneities, such as a coherence function, extinction coefficient and scattering cross-section.

16.4 Model of 1-D Vertical Wave Number Spectrum of the Gravity Wave Perturbations

After integrating (16.1) over $2\pi k_\perp dk_\perp$ from 0 to ∞ we obtain a 1-D vertical wave number spectrum $S_{1E}(k_z)$ for the vertical displacements:

$$S_{1E}(k_z) = \beta k_z^{-3}, \quad m^* \ll k_z < m_c, \tag{16.4}$$

where β is given by (16.2), $m^* = \frac{1}{2^{1/2}\nu_V} = \frac{N}{2^{1/2}\sigma}$ is the characteristic vertical wave number, above which the nonresonant wave–wave interactions become strong and form a 3-D spectral tail (16.1), N is buoyancy frequency, σ is the r.m.s. value of the velocity fluctuations, and $m_c = m^* \exp\left(\frac{1}{\beta}\right)$ is the critical vertical wave number, at which the mean square vertical gradient of the vertical displacements in the

Eulerian frame, $< \left(\left| \frac{\partial S_z}{\partial z} \right| \right)^2 > = \int_0^{m_c} dk_z k_z^2 S_{1E}(k_z)$, reaches the value of the order of 1. The latter condition defines the critical vertical scale $l_c = m_c^{-1}$ of the anisotropic inhomogeneities at which wave-induced convective instability switches on and prevents an infinite increase of the displacement gradients due to wave-breaking processes.

As seen from (16.2) the amplitude β of the spectral tail (16.4) increases rapidly with increasing parameter of nonlinearity M, but starting from $M \sim 0.3$ such increase significantly slows down (Fig. 16.2), so that β reaches a broad maximum of about 0.22 at $M \sim 0.37$. Such saturation of the spectral amplitude is caused by strong nonlinearity of the gravity wave field. Similarly the vertical wave number spectrum was obtained for the wave-induced horizontal wind velocity fluctuations

$$V_E(k_z) = \alpha N^2 / k_z^3, \quad m^* \ll k_z < m_c, \tag{16.5}$$

where the coefficient $\alpha = 0.12$ at $M \sim 0.37$. The upper (critical) vertical wave number m_c limits (16.5) by the wave-induced wind shear instability condition (local Ri < 1/4).

For the lower stratosphere the typical r.m.s values of the wind velocity fluctuations are 2–3 m/s (Vincent et al. 1997). Taking $\beta \approx 0.2$ and $N = 0.02$ rad/m, which is a typical value for the buoyancy frequency in the stratosphere, we can estimate the longest (or outer) vertical scale: $L^* = 2\pi/m^* = 1.6 - 2.4$ km, and the shortest (or inner) vertical scale, $L_{\min} = 2\pi/m_c = 10 - 16$ m, that bound the k_z^{-3}-tail of the vertical wavenumber spectra.

The wave-breaking processes caused by convective and shear instabilities generate turbulent eddies with the vertical scales $2\pi k_z^{-1}$ less than $L_{\min}$. These eddies occupy the thin atmospheric layers with scales $2\pi k_z^{-1} < L_{\min}$ that intermittent with the stably stratified layers of larger scales $2\pi k_z^{-1} > L_{\min}$. Such layers of turbulence play the role of the sinks of the wave energy transferred by nonlinear cascade-like processes from the gravity wave sources through the range of scales inherent in the

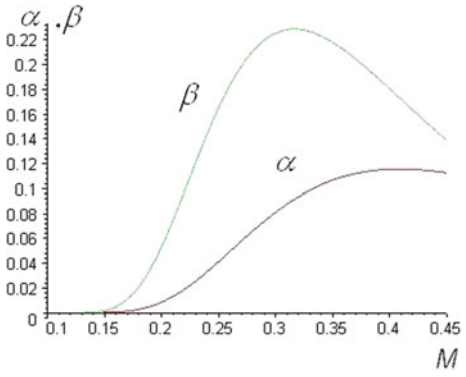

Fig. 16.2 The coefficients α and β for the vertical wave number spectra of the wave-induced horizontal wind velocity fluctuations and vertical displacements as functions of the nonlinear parameter M

k_z^{-3}-spectrum (16.4). At the same time, the turbulence being generated by the instability processes causes the dissipation of the wave modes with scales $2\pi k_z^{-1} > L_{\min}$ due turbulent viscosity (Weinstock 1985, 1990; Sukoriansky and Galperin 2013) and prevent the infinite growth of the wave-induced wind shears and spatial displacement (or potential temperature) gradients due to nonlinear generation of high wave number components of the wave spectrum. Thus, there are two competitive processes that form the equilibrium spectral tail within the scale-range (16.4): the nonlinearity of the wave system that tends to increase spatial gradients of the wave field by generating high-wavenumber spectral components, and the wave energy dissipation associated with the different wave-induced instabilities that prevent spatial gradients to grow infinitely by smoothing them.

16.5 Sound Travel Time Fluctuations Caused by Gravity Wave Perturbations

Based on the nonlinear model of the internal wave spectrum in stably stratified atmosphere the analytic expressions for the variances, vertical structure functions and frequency spectra for sound travel time fluctuations were obtained by Chunchuzov (2004). The acoustic waves were thought to have much smaller wavelengths than the scales of gravity wave perturbations, therefore a ray approximation was used up to some range x from a sound source, for which the so-called diffraction parameter $\Lambda = (R_F/x) \sim x/(6L^2 q) \ll 1$, where L is the spatial correlation scale of sound speed and wind velocity fluctuations, R_F is the radius of the first Fresnel zone, $q = \omega/c$, c is the sound speed, and ω is frequency within a spectral bandwidth of the frequency spectrum of an acoustic pulse (Flattè et al. 1979). Under the ray approximation the sound travel time $\tau(\vec{x}, t)$ along a selected ray path Γ

$$\tau(\vec{x}, t) = \int_{\Gamma} ds \left| c\vec{n} + \vec{V} \right|^{-1}, \tag{16.6}$$

where $\vec{x}$ is the radius-vector from a point source to the receiver, $\vec{V}$ is the wind velocity vector, and $\vec{n}$ is the unit normal to the acoustic wave front. The IGWs was assumed to induce small fluctuations of sound speed, $\delta c = c - c_0$, and wind velocity, $\delta\vec{V} = \vec{V} - \vec{V}_0$, with respect to their mean values c_0 and $\vec{V}_0$, whereas the mean stratification of $c_0(z)$ and $\vec{V}_0(z)$ forms an acoustic wave duct.

It was shown by Chunchuzov (2004) that the variance of the travel time fluctuations is defined by the sum $<\delta\tau^2> = <\delta\tau_{\mathrm{h}}{}^2> + <\delta\tau_{\mathrm{t}}{}^2>$ of two terms, $<\delta\tau_{\mathrm{h}}{}^2>$ and $<\delta\tau_{\mathrm{t}}^2>$, resulting from the contributions of the low-wavenumber (head) part $(k_z^2\nu_v^2 + k_\perp^2\nu_h^2 < 1/2)$ and the high-wave number (tail) part $(k_z^2\nu_v^2 + k_\perp^2\nu_h^2 \geq 1/2)$ of the 3-D wind velocity and temperature spectra (expressed through (16.1)). For

the ray paths emitted from a point source with some small elevation angle $\theta \neq 0$ and a so-called ray turning point approximation was used (Flatte et al. 1979) to obtain:

$$<\delta\tau_h^2> = (2\pi)^{1/2}[2<\mu_T^2> + <\mu_\sigma^2>]_0 R_0/m_0c_0^2, \tag{16.7}$$

$$<\delta\tau_t^2> = 2\pi R_0[(2\beta<\mu_T^2> + \alpha<\mu_\sigma^2>)/m^*]_0/3c_0^2, \tag{16.8}$$

where the expressions within the brackets $[\ldots]_0$ are taken at the turning point $(x_0, z(x_0))$ of the ray trajectory given by equation $z = z(x)$, $R_0 = \left|\frac{d^2z(x_0)}{dx^2}\right|^{-1}_{x=x_0}$ is the radius of curvature of a given ray path at the turning point, $<\mu_T^2> = <\delta T^2/4T_0^2>$ and $<\mu_\sigma^2> = <\delta V_x^2/c^2>$ are the contributions to the mean square value of sound refraction index fluctuations in the moving medium from the fluctuations of the relative temperature $\delta T/T_0$ and x-component of the wind velocity δV_x, respectively. The ray path approaching the turning point propagates almost horizontally. In this case the anisotropic inhomogeneities that are crossed by the ray path, have the longest (horizontal) correlation length (Flatte et al. 1979), therefore the main contribution to the variance of sound travel time fluctuations comes from the vicinity of the ray turning point.

As seen from (16.7)–(16.8) the variance of the travel time fluctuations $<\delta\tau_t^2>$ caused by the tail-associated part of the spectrum does not depend on the form of the source spectrum. As to the value of $<\delta\tau_h^2>$ it weakly depends on the form of the low-wavenumber part of the source spectrum and the characteristic vertical scale of the source spectrum m_0^{-1}, therefore expression (16.7) was obtained for the specific form of the source spectrum chosen by Chunchuzov (2004).

When the parameter of nonlinearity reaches the value $M \sim 0.4$, the coefficients β and α characterizing the amplitudes of the wind velocity and temperature spectra reach the maximum values of the order of 0.1 (Fig. 16.2). Since the outer vertical scale of the inhomogeneities $m^{*-1} = \sqrt{2}\nu_v = \sqrt{2}\sigma/N$, then under saturation condition $(M = m_0/(m^*\sqrt{2}) \sim 0.4)$ this scale is connected with the characteristic vertical scale of the source spectrum by relation $m_0 \approx 0.56\, m^*$.

Thus, the variance of travel time fluctuations, $<\delta\tau^2> = <\delta\tau_h^2> + <\delta\tau_t^2>$, increases with the characteristic vertical scale m^{*-1}, radius of curvature R_0, and with the variances of the sound refraction index fluctuations caused by relative temperature fluctuations, $<\mu_T^2> = <\delta T^2/4T_0^2>$, and horizontal wind velocity fluctuation $<\mu_\sigma^2> = <\delta V_x^2/c^2>$ at an altitude of turning point.

Due to proposed axial symmetry for the random gravity wave field the average potential and kinetic energies are thought to be equivalent, $N^2\nu_v^2 = \sigma^2$, therefore both $<\mu_T^2>$ and $<\mu_\sigma^2>$ are proportional to the variance ν_v^2 of the vertical parcel displacements or variance of the wind velocity fluctuations σ^2:

$$\mu_\sigma^2 = \sigma^2/(2c_0^2) = N^2\nu_v^2/(2c_0^2), \quad <\mu_T^2> = (N^2\nu_v/g)^2/4. \tag{16.9}$$

For the typical values in the stratosphere: $c_0 = 310 - 330$ m/s, $N = 0.02$ rad/s and g = 9.8 m/s^2 the ratio $\mu_T^2/\mu_\sigma^2 = (N^2c_0^2/2g^2)$ gives the value of 0.2, therefore the contribution from the wind velocity fluctuations to the variance of the acoustic refractive index fluctuations $<\mu^2>$ are five times greater than that from the temperature fluctuations.

Let us estimate the possible variances in sound travel time fluctuations for the refracting ray paths in the stratospheric wave duct after their first bounce with one turning point at some altitude of the upper stratosphere. The radius of curvature near turning point may be estimated as the rate of change of the ray elevation angle $R_0^{-1} \approx |d\theta/dx|_{x=x_0}$ for x approaching the coordinate x_0 of the turning point. For the ray trajectories calculated from the surface explosions (Kulichkov and Bush 2001) at ranges of 250–300 km from the source the estimate of R_0 gives the values in the range 57–114 km. Taking near stratopause: $\sigma = 5$m/s and $N = 0.02$ rad/s, and estimating from (16.7)–(16.8) the r.m.s travel time fluctuations under saturation condition $(m_0 \approx 0.56\, m^*)$, we obtain that $\sqrt{<\delta\tau^2>} = (0.4 - 1)$ s. The r.m.s. value $\sqrt{<\delta\tau^2>}$ increases with σ as $\sigma^{3/2}$, so if σ increases 1.5 times then $\sqrt{<\delta\tau^2>}$ increases up to 2 s.

For several bounces of the refracting ray paths in the stratospheric wave duct we should add to the variance $<\delta\tau^2>$ the contributions from each turning point, i.e., expressions (16.7) and (16.8) should be multiplied by n for n turning points. As noted earlier the range x from the source is limited by the validity of the geometric acoustic approximation: $x \ll 6L^2q$. For instance, if the frequency of the infrasound $f \sim 0.7$Hz, then for $c_0 = 330$ m/s the characteristic vertical scale of the anisotropic inhomogeneities in the upper stratosphere $L = 2.5$ km, therefore at ranges $x > 500$ km the diffractive effects become important.

For the acoustic pulses with broad frequency spectrum some of the wave lengths may be comparable to the vertical scales of the inhomogeneities. In this case, both the scattered acoustic field and the totally reflected signal in the stratospheric wave duct contribute to the stratospheric arrival and its wave form, duration, and travel time (Chunchuzov et al. 2011). The observed temporal fluctuations in the travel times of the stratospheric arrivals in the shadow zone from a series of similar surface explosions reach the values up to 10–15 s at a range of 300 km (Kulichkov et al. 2016). We assume that such fluctuations may be associated with the temporal variations in the altitude of the atmospheric layer within which the so-called Bragg condition ($2q\cos(\theta_0) = k_z$, where θ_0 is an incidence angle) for the effective scattering is satisfied (Chunchuzov et al. 2013).

16.6 Fluctuations in the Azimuth of Acoustic Wave Propagation

The 3-D wind velocity and temperature random perturbations cause a random refraction of the ray paths in the 3-D space. This results in the fluctuations of the azimuth of propagation of acoustic waves along refracting ray paths.

Let $\vec{q} = (\vec{q}_\perp, q_z)$ be the wave number vector of acoustic wave at a reception point with the azimuth φ and vertical (grazing) angle χ_v with respect to the horizontal plane containing a triangle of receivers 1, 2, and 3 whose coordinates are (*0, 0*), (x_1, *0*), and (x_2, y_2), respectively (Fig. 16.3). The angles φ and χ_v are defined by the time differences, $\Delta t_1 = t_2 - t_1$, $\Delta t_2 = t_3 - t_1$, in the arrival of the wave front to the receivers 1 and 2, 1 and 3, respectively:

$$tan(\varphi) = x_1 \Delta t_2 / (y_2 \Delta t_1) - x_2 / y_2, \qquad \cos(\chi_v) = |\vec{q}_\perp| / |\vec{q}|, \tag{16.10}$$

For $\varphi \ll 1$ the random fluctuations in the azimuth $\delta\varphi = \varphi - <\varphi>$ relative to its average value $<\varphi>$ are proportional to the fluctuations of the difference $\delta(\Delta t_2) = \delta t_3 - \delta t_1$ between the times of arrival to the receivers 1 and 3. Introducing a horizontal structure function defined by $D(\Delta x, \Delta y) \equiv <(\delta t_3 - \delta t_1)^2>$, where Δx and Δy are the differences between coordinates of the points 1 and 3, the r.m.s value of the azimuth fluctuations can be expressed as follows (Kulichkov et al. 2007):

$$(<\delta\varphi^2>)^{1/2} \approx \frac{2(<\delta(\Delta t_2)^2>)^{1/2}}{<\Delta t_1>}, \tag{16.11}$$

$$<\delta(\Delta t_2)^2> = D(0, \Delta y) \approx 6 <\delta\tau_1^2> (e_0 m^{*2} \Delta y^2), \quad (\Delta y^2 / L_h^2 << 1) \tag{16.12}$$

Here $L_h = 1/(m^* e_0^{1/2})$ is the characteristic horizontal scale of the anisotropic inhomogeneities, $<\Delta t_1>$ is the average sound travel time delay between receivers, and $<\delta\tau_1^2>$ is the variance of sound travel time fluctuations from the source to the receiver 1. The value of $e_0 \sim M^2/8\chi^2$ depends on the anisotropy $\chi^2 = m_0^2/k_0^2$ of the source spectrum and parameter of nonlinearity M that takes the value of the order of 0.4 under nonlinear saturation of the gravity wave spectrum. When the

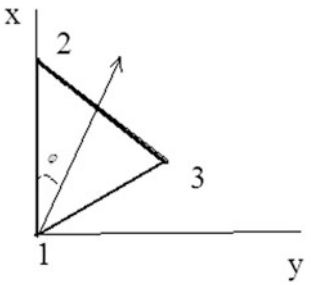

Fig. 16.3 The azimuth of propagation of an acoustic wave front with respect to a triangle array of acoustic microphones 1-2-3

characteristic frequency of the source spectrum $\omega_0 \approx N k_0 / m_0$ becomes close to the Coriolis parameter f_c, the parameter e_0 takes the lowest value

$$e_0 \approx M^2 f_c^2 / (8N^2), \tag{16.13}$$

which corresponds to the maximum anisotropy of the inhomogeneities.

For the values of e_0 in the range 0.0002–0.0026, and values of $N = 0.02\text{rad/m}$, $\sigma = 5$ m/s near ray turning point in the stratosphere, the variance $< \delta\tau_1^2 > \sim 1s^2$ at a range of 300 km (as estimated above), therefore the structure function for $\Delta y = 300$ m takes the values $D(0, \Delta y) = 0.001$–0.011. In this case the estimate from (16.11) of the r.m.s values of the azimuth fluctuations for $< \Delta t_1 > = 0.9$ s gives

$$(< \delta\varphi^2 >)^{1/2} = (4^\circ - 13^\circ) \tag{16.14}$$

The estimated values of $(< \delta\varphi^2 >)^{1/2}$ are consistent with the observed r.m.s. values of the temporal azimuth variations of the stratospheric arrivals from successive surface explosions (Kulichkov et al. 2007). They define the error in localization of infrasound sources caused by gravity wave perturbations.

16.7 Instant Realizations of Gravity Wave Perturbations

In previous sections, we analyzed the spectrum of the fluctuations caused by a high number of gravity waves with random amplitudes and phases. In the case when Lagrangian displacements are induced by two propagating gravity waves only the nonlinear shaping mechanism for the spectrum of gravity wave perturbations was studied by Chunchuzov (2009). It was shown that for the parameter of nonlinearity $M \sim 0.4$ the nonresonant wave–wave interactions generate numerous combinative harmonics of the initial two waves. The simulated instant vertical and horizontal realizations of the gravity wave field at some time are shown in Fig. 16.4. These realizations contain oscillations depending on vertical (z) and horizontal (x) coordinates. However, such oscillations are of non-sinusoidal wave form with certain steepening of their crests and troughs due to nonlinear generation of high wave number harmonics in the spatial spectra of these oscillations (shown in Fig. 16.5).

The estimates of the power spectral densities for the vertical profiles of relative temperature and horizontal wind velocity fluctuations within two atmospheric layers (24–32 km and 40–62 km) are shown in Fig. 16.5a–b. These spectra as seen show a power law decay with increasing vertical wave number close to −3 (straight line). The characteristic wave numbers m^* and m_c that bound the −3 spectral tail tend to decrease with increasing altitude.

One of the horizontal realizations of relative temperature fluctuations at some height is shown in Fig. 16.4c, and its spectral estimate is in Fig. 16.5c. This spectrum has a high-frequency tail that consists of a large number of peaks

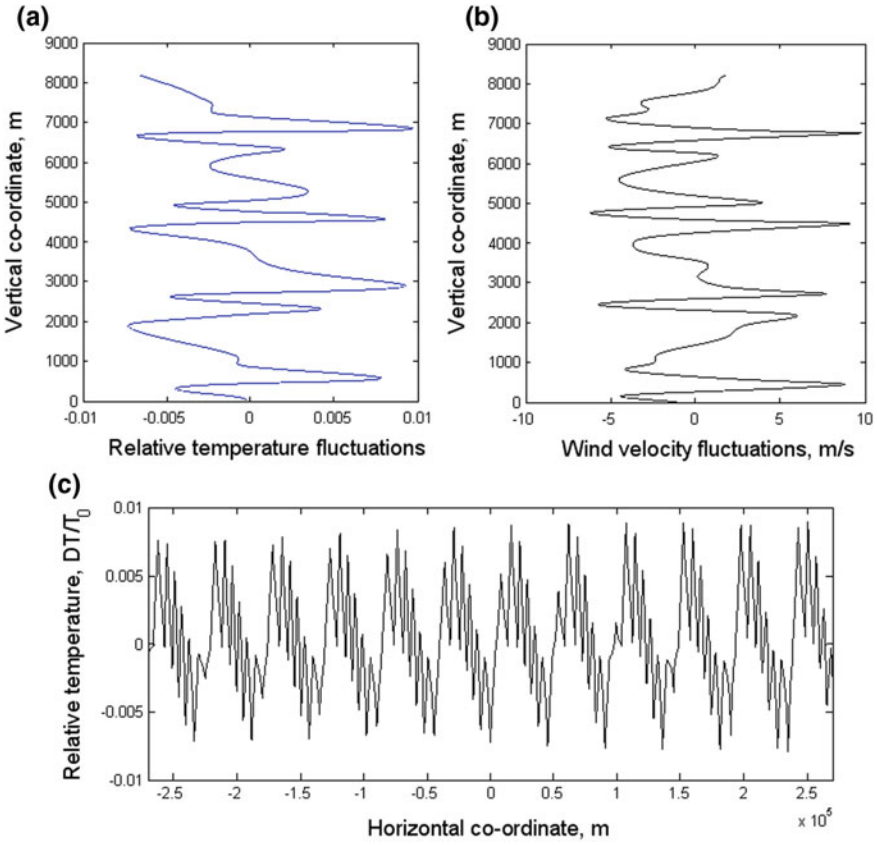

Fig. 16.4 Vertical and horizontal instant profiles of relative temperature and horizontal wind velocity fluctuations. **a** Vertical temperature profile; **b** vertical profile of the horizontal wind velocity fluctuations; **c** horizontal profile of the relative temperature fluctuations, DT/T_0

corresponding to the numerous combinative harmonics of the initial two waves. The solid line corresponds to the part of the theoretical horizontal spectrum $\frac{N^4}{g^2} e_0 \beta k_x^{-3}$ of relative temperature fluctuations obtained by integrating the 3-D spectrum (1) over high vertical wave numbers $m^* \le k_z < m_c$. This part is a contribution to the horizontal spectrum coming from the anisotropic fluctuations with the short vertical scales $l < m^{*-1} = \sqrt{2}\sigma/N$. Contrary to the vertical wave number spectrum it depends on the mean square horizontal gradient e_0 of the vertical displacements or anisotropy of the 3-D spectrum.

For the horizontal scales less than 10 km, but more than 500 м, the horizontal spectrum decreases with increasing horizontal wave number with a power close to −3, and this is consistent with the experimental horizontal spectra in the stably-stratified troposphere and stratosphere, obtained from the aircraft measurements by Vinnichenko et al. (1980) and Bacmeister et al. (1996). For larger horizontal scales,

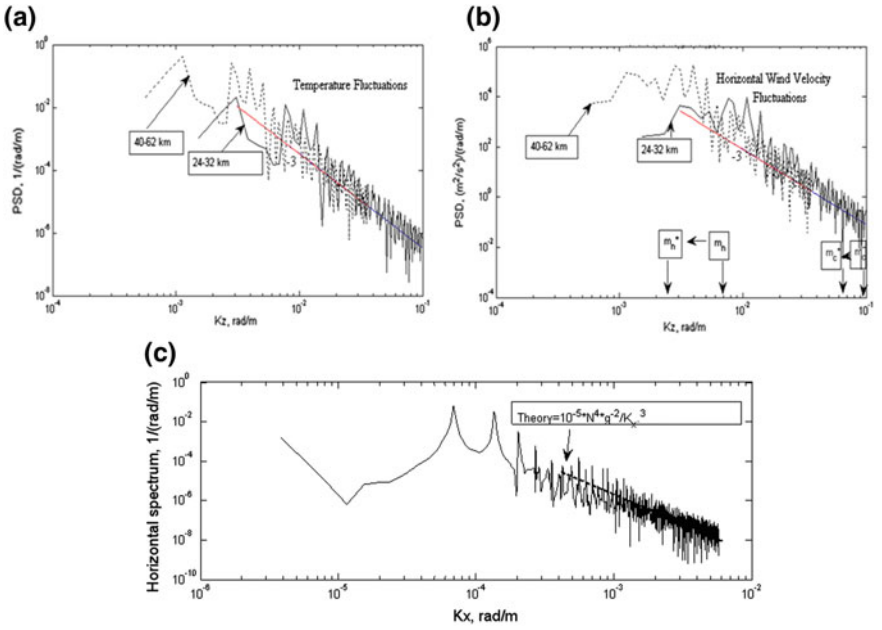

Fig. 16.5 Vertical wave number spectra of the relative temperature (**a**) and horizontal wind velocity (**b**) fluctuations corresponding to the vertical profiles shown in Fig. 16.4a–b; **c** horizontal spectrum of the horizontal wind velocity fluctuations (shown in Fig. 16.4c). Theoretical horizontal wave number spectrum is shown by straight solid line

from about 500–12 km, the experimental spectra show power law decays with the slopes from −5/3 to −2 (Bacmeister et al. 1996).

In addition to the IGWs there are almost horizontal vortices (Lindborg 2006, 2007). with the large vertical scales $l \gg 2\pi m^{*-1}$ (that are inside a characteristic ellipsoid $k_z^2\nu_v^2 + k_\perp^2\nu_h^2 \ll 1$ in 3-D wave number space) which also contribute to the horizontal spectrum. However, such vortices do not affect the vertical wave number spectrum at scales $l < 2\pi m^{*-1}$. The −5/3 range of the horizontal spectrum was previously modeled by Gurvich and Chunchuzov (2008) by assuming the dependence of the anisotropy of the 3-D spectrum on the vertical scale l as l changes from small $(l < 2\pi m^{*-1})$ to large $(l \geq 2\pi m^{*-1})$ values.

It should be noted that both the vertical and horizontal spectra of the anisotropic temperature and wind velocity inhomogeneities were obtained directly from the nonlinear motion equations for IGWs. This model of the spectra is realistic one, since it is based on a unified physical mechanism associated with the nonresonant interactions of IGWs and their dissipation at small vertical scales that form both the 3-D and 1-D (vertical and horizontal) spectra.

16.8 Effect of Atmospheric Anisotropic Inhomogeneities on the Propagation of Infrasound from Explosive Sources

The fluctuations in temperature, δT, and horizontal wind velocity component in the azimuthal direction of sound propagation, δV_x, result in the effective sound speed fluctuations

$$\frac{\delta C_{eff}}{C_{eff}} = \frac{\delta T}{2T_0} + \frac{\delta V_x}{c_0}, \tag{16.15}$$

which affect the amplitudes and phases of acoustic waves in the atmosphere, where the index 0 relates to the values of air temperature and sound speed in the undisturbed atmosphere.

When simulating a long-range infrasonic propagation from surface explosions in the atmosphere, we used the vertical wind velocity profiles in the atmosphere obtained from rocket sounding data (Kulichkov and Bush 2001; Kulichkov et al. 2002) or from self-empiric Ground-to-Space (G2S) model of the atmosphere developed by Drob et al. (2003, 2008). However, these profiles, including those obtained from routine balloon radiosounding, do not resolve fine-scale vertical structure of the wind and temperature in the atmosphere associated with the anisotropic gravity wave perturbations. To study the effect of gravity wave perturbations on infrasound signals observed from surface explosions or volcanoes we superimposed the model realizations of the effective sound speed fluctuations obtained by Chunchuzov (2009) on the self-empiric profiles of $C_{eff}(z)$ that were considered as mean profiles during period of infrasound observation.

To simulate a fine-scale structure the atmosphere was divided into layers of 8 km in depth up to an altitude of 64 and 16 km in depth at higher altitudes. When going up from one layer to the overlying layer the increase in the r.m.s displacements $\nu_V(z)$ (or r.m.s wind velocity fluctuations $\sigma(z)/N(z)$) with increasing height z and the corresponding decrease in the characteristic vertical wavenumber $m^*(z) = N(z)/\sqrt{2}\sigma(z)$ were taken into account. At altitudes z > 80 km such an increase was limited by a constant value of the r.m.s displacements ($\nu_V(z) = \text{const}$), because above turbopause ($z \geq 100$ km) a strong attenuation of gravity waves due to molecular viscosity rapidly increasing with height becomes a prevailing mechanism of the energy dissipation of IGWs and compensates the increase in their amplitudes (Gossard and Hooke 1975; Hines 1993).

Figure 16.6 shows one of the signals from volcano (v.) Tungurahua in Ecuador recorded on July 15, 2006 close to the volcano, $r = 40$ km (a), and far from it, $r = 250$ km (b) (Assink et al. 2012). The initial profile $C_{eff,0}(z)$ for the time interval covering the moment of signal recording is plotted in Fig. 16.7a (solid line) based on G2S atmospheric model. Note that for the unperturbed profile, the maximum value of $C_{eff,0}(z)$ at the stratopause height ($z = 49$ km) is smaller by 2.5 m/s than that at the source height ($z = 5$ km); therefore geometric acoustics does not predict

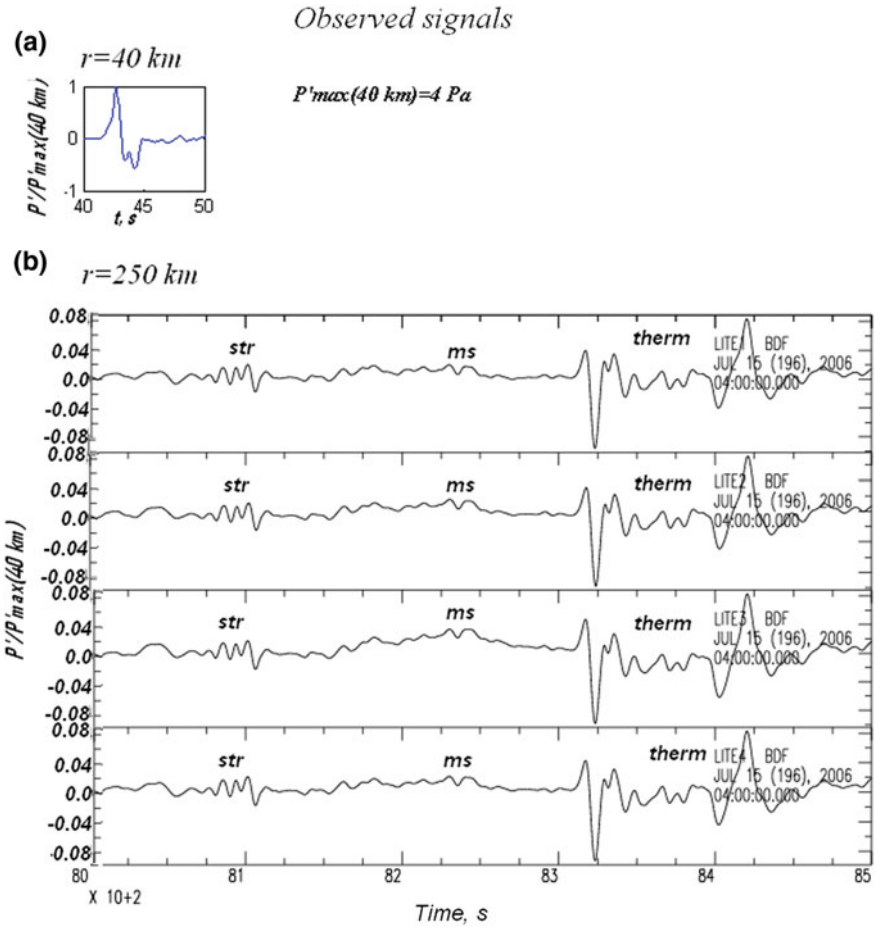

Fig. 16.6 Signals from v. Tungurahua (Equador) recorded on July 15, 2006 close to the volcano, $r = 40$ km (**a**), and far from it, $r = 250$ km (**b**). The signals are normalized by their peak amplitude (4 Pa) at a range of 40 km from a source

a total reflection of signal in the stratosphere. The same profile $C_{eff,0}(z)$, but perturbed by small range-dependent effective sound speed fluctuations $\Delta C_{eff}(z,x)$, where $\left|\Delta C_{eff}/C_{eff,0}\right| \ll 1$, is shown in Fig. 16.7c with a horizontal interval $\Delta x = 28$ km.

The acoustic field of a point source (height $z = 5$ km) calculated by pseudo-differential parabolic equation (PPE) method at a frequency $f = 0.1$ Hz for the unperturbed profile $C_{eff,0}(z)$ is shown in Fig. 16.7b. In the presence of range-dependent gravity wave perturbations in the profile $C_{eff,0}(z) + \Delta C_{eff}(z,x)$ the calculated acoustic field is shown in Fig. 16.7d. It is seen from Fig. 16.7b that the unperturbed G2S atmospheric model predicts a shadow zone at a range of 250 km

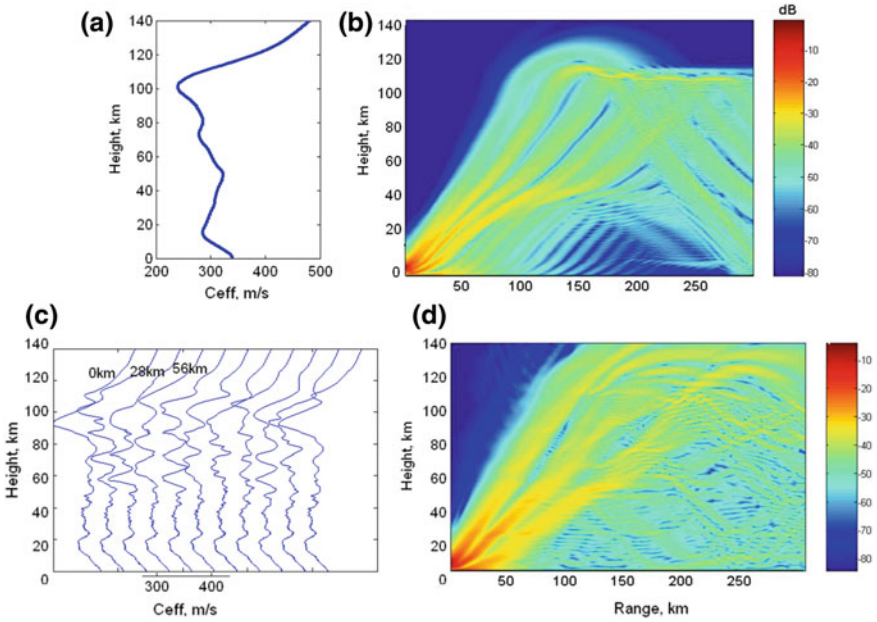

Fig. 16.7 Acoustic field of a point source (height $z = 5$ km) is shown in the right panels (**b**) and (**d**). It was calculated for $f = 0.1$ Hz by pseudo-differential parabolic equation (PPE) method: **a** for the effective sound speed profile *Ceff*(z) obtained from the G2S atmospheric model (thick line); and c) for the same G2S-model, but perturbed by range-dependent effective sound speed profiles of the *Ceff*-fluctuations shown with a horizontal interval of 28 km **c**. The difference *Ceff* (z = 50 km) − *Ceff*(z = 5 km) < 0

from a source. In the presence of the perturbations the acoustic field is scattered into a shadow zone as clearly seen from Fig. 16.7c, and this explains the appearance of stratospheric (*str*), mesospheric (*ms*) and thermospheric (*therm*) arrivals observed in the shadow zone (Fig. 16.6). Note that the values of the perturbed effective sound speed $C_{eff,0}(z) + \Delta C_{eff}(z)$ are less at a height of stratopause than near the source.

In addition to the fact that a fine-scale structure cardinally changes the horizontal distribution of the intensity of acoustic field in the geometric zones of audibility and shadow as compared to the unperturbed atmosphere, this structure also favors the occurrence of acoustic transitional waveguides. For example, one such waveguide existed within the height range 80–120 km and at ranges from 200 to 300 km from the source (Fig. 16.7b). At these ranges the vertical profile $C_{eff,0}(z) + \Delta C_{eff}(z)$ has a local minimum, which causes the propagation of wave energy in the wave duct having a horizontal size of about 100 km. Due to the range-dependence of the perturbations the local minimum existing at some range can disappear at another range, therefore the ducting wave energy can scatter outside of the transitional wave duct.

The signals calculated by PPE method at a range $r = 250$ km from a point source are shown in Fig. 16.8. In the upper panel (a) the signal corresponds to the

G2S atmospheric model (Fig. 16.7a), whereas the signal in panel (b) is obtained for the G2S-model perturbed by range-dependent *Ceff*-profiles (shown in Fig. 16.7c).

When calculating the signals reflected from both the stratospheric and thermospheric layers, we took into account the fact that the signal generated by explosion is nonlinearly distorted during its propagation to the upper atmospheric layers and takes the form of *N*-wave. Using an approximation of nonlinear geometric acoustics, we estimated an increase in its duration and the corresponding decrease in the peak amplitude of *N*-wave with an increase in the height *z* taking into account the conservation of the acoustic momentum of this wave along a chosen ray path (Kulichkov 2002, 2008; Chunchuzov et al. 2013).

Due to a decrease in atmospheric density with height, the duration of *N*-wave rapidly increases and the maximum of its Fourier spectrum shifts to the low-frequency region. Despite a strong attenuation of high-frequency components of the spectrum of *N*-wave in the lower thermosphere the nonlinear effects generate new high-frequency spectral components, so that the thickness of the shock fronts of the *N*-wave remains short as compared to its duration (Chunchuzov et al. 2013). As a result, the *N*-wave incident on the thermospheric layer has an approximate form shown in the rectangle in Fig. 16.8 (on the right). Its duration is longer than

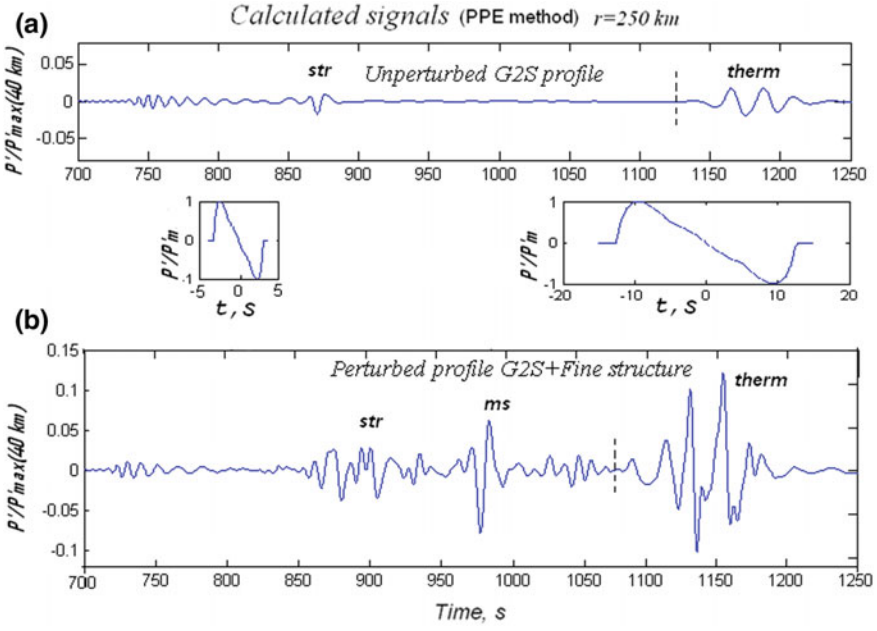

Fig. 16.8 Signals at a range $r = 250$ km from a point source calculated by PPE method **a** for G2S atmospheric model with *Ceff*(z)-profile shown in Fig. 16.7a, and **b** for G2S-model perturbed by range-dependent *Ceff*-profiles shown in Fig. 16.7c. The signals propagating from a source to the stratosphere and lower thermosphere were supposed to take the forms of *N*-waves (shown within rectangles). The signals are normalized by their peak amplitude at a range of 40 km from the source

that of the *N*-wave incident on the stratopause layer (Fig. 16.8, left rectangle). For these two *N*-waves we have taken two different frequency ranges, 0.2–1.5 Hz and 0.02–0.2 Hz, to calculate by PPE method the stratospheric and thermospheric arrivals, respectively.

In the atmosphere with fine-scale structure the amplitudes of both stratospheric and thermospheric arrivals (Fig. 16.8b) increase approximately by factors of ten and two, respectively, as compared to the case of unperturbed G2S model (Fig. 16.8a). Moreover, the entire signal (Fig. 16.8b) also contains continuous reflections from the fine-scale structure between the stratopause and the lower thermosphere, including mesospheric arrivals. With time, the characteristic frequencies of the spectra of different arrivals (stratospheric, mesospheric, and thermospheric) sequentially arriving at the receiving point are shifted to the low-frequency region (Fig. 16.8b), which is also noticeable in the observed signal in Fig. 16.6b. Such a shift is associated with both a nonlinear lengthening of the signal with increasing height and, at the same time, with an increase in the characteristic vertical scales of the atmospheric inhomogeneities that scatter acoustic field to the receiver.

Thus, both the nonlinear effects and scattering of infrasonic waves from the atmospheric anisotropic inhomogeneities explain the observed occurrence of the stratospheric, mesospheric, and thermospheric arrivals of signals in the acoustic shadow zones. These effects were recently used for developing a new method of infrasound probing of the fine-scale layered structure of the atmosphere (Chunchuzov et al. 2015a, b).

16.9 Infrasound Probing of the Atmospheric Fine-Scale Layered Structure

The method of remote sounding of the atmosphere that makes use of infrasound recordings from explosions at regional distances and the effect of total internal reflection of sound waves from the nonhomogeneous atmosphere has been used for studying the structure and dynamics of the atmosphere since the beginning of the last century (Whipple 1923, 1939; Duckert 1931). With this method, the increase of the average temperature and sound speed with height in the upper stratosphere was discovered. The reviews on studies of the atmospheric structure by infrasound from manmade and natural sources may be found, for instance, in Whipple (1939), Gutenberg (1939), Chibisov (1940), Blokhintsev (1956), Donn and Rind (1972), Le Pichon et al. (2005, 2010), Assink et al. (2012, 2013, 2019).

Among earlier studies that used acoustic remote sensing to characterize the structure of the stratosphere and MLT are the studies by Donn and Rind (1972), who used hourly averaged amplitudes of the received microbarom signal to estimate the return height and wind speed, using microbarom sources from storms over the Northern Atlantic. This method has recently been applied to analyze the life

cycle of the 2009 major Sudden Stratospheric Warming (SSW) using microbarom recordings that are located in the Arctic (Smets and Evers 2014; Smets et al. 2019).

The measurements of temporal variations of the azimuths and times of arrivals of infrasound waves propagating along refracting ray paths in the stratospheric and thermospheric acoustic wave guides are used for continuous monitoring of the wind velocity variations in the stratosphere and the MLT (Le Pichon et al. 2010; Assink et al. 2012, 2013). The long-term observations of infrasound from repetitive eruptions of v. Tungurahua in Ecuador showed the existence of the characteristic periods of tides and tidal harmonics in the temporal variations of travel times for mesospheric and thermospheric arrivals (Assink et al. 2012). The inversion method based on parameterization of wind profiles with a set of orthogonal functions obtained from *G2S* model of the atmosphere (Drob et al. 2003, 2008, 2010) enabled to retrieve vertical profiles of large-scale (as compared to the wavelengths of infrasound waves) wind velocity variations in the atmosphere (Assink et al. 2013).

It is important to note that the abovementioned inverse methods are based on ray-tracing through the atmosphere. Therefore, the wind profiles retrieved with these methods do not capture existing fine-scale wind velocity variations, whose vertical scales are comparable to the typical wavelengths of infrasound waves and less than the vertical scales of the numeric grid used in the models of the atmosphere. At the same time, such variations, due to their high vertical gradients, scatter infrasound field in the acoustic shadow zones and essentially affect waveforms and amplitudes of the observed stratospheric, mesospheric and thermospheric arrivals (Kulichkov et al. 2002; Kulichkov 2010; Chunchuzov et al. 2011, 2013, 2014, 2015a, b). In these works a full wave approach was developed to describe the scattered infrasound field in the shadow zone and find the relationship between this field and the vertical profile of the layered inhomogeneities of the effective sound speed. Based on this relationship a new probing method was recently developed (Chunchuzov et al. 2015a, b) that allows for retrieval of fine-scale vertical structure of the wind field in the upper stratosphere and the MLT (90–140 km).

The lower thermospheric layer (100–140 km) is poorly accessible for other remote sensing methods, for example, meteor radars (Merzlyakov et al. 2004; Jacobi et al. 2007) and satellites (Hays et al. 1993; Wu et al. 2008), whose long-term measurement data were combined for constructing a global empirical wind model of the MLT (Portnyagin et al. 2004). While methods are available to measure the local wind and temperature field in the middle atmosphere, these are not operationally assimilated in general circulation models (Hoppel et al. 2013). Therefore, biases in wind and temperature are to be expected at upper atmospheric levels.

The infrasound probing method described here is based on the estimation of the wind field fluctuations in the stratopause and MLT with high vertical resolution, by using volcanoes and surface explosions over the globe. Therefore, the method may significantly complement current operational and recently developed remote sensing wind measurement methods (Rüfenacht et al. 2012) in constructing an upper atmosphere wind model and parameterizing gravity wave forcing in the stratosphere and upper atmosphere (Alexander and Rosenlof 2003; Eckermann et al. 2009;

Eckermann 2011; Alexander et al. 2010). In addition, the method allows for valuable cross-validation studies of other remote sensing instruments. It is now recognized that the influence of a fine-scale wind velocity structure on the infrasound field should be taken into account in the models of long-range infrasound propagation through a realistic atmosphere (Kulichkov and Bush 2001; Liszka et al. 2009; Norris et al. 2010; Chunchuzov et al. 2011; Drob et al. 2013; Chunchuzov et al. 2014). Such models allow for better localization of numerous infrasound sources in the atmosphere and evaluation of their acoustic power (Marty 2014).

16.10 Retrieval Method for the Layered Wind Velocity Structure

The proposed sounding method retrieves vertical profiles of horizontal wind velocity fluctuations in the upper stratosphere, mesosphere, and MLT from the waveforms, amplitudes and travel times of infrasound signals recorded in the acoustic shadow zones (Chunchuzov et al. 2015a, b). To extract such information we use the relationship between the vertical profile of the effective refractive index fluctuations, $\varepsilon(z) \approx -2(\Delta c + \Delta u \sin\theta_0) c_1^{-1} \cos^{-2}\theta_0$, $|\varepsilon| \ll 1$, and the wave form of the acoustic pressure perturbations $p'(t)$ caused by a signal partially reflected from a given atmospheric layer containing vertical fluctuations of the wind velocity $\Delta\vec{V}(z)$ and sound speed $\Delta c(z)$ (or temperature $\Delta T(z)$). Here $\Delta u(z)$ is the projection of $\Delta\vec{V}(z)$ on the radius-vector directed from the source to the receiver (Chunchuzov et al. 2013)

$$p'(t) = -\frac{p'_m r_0}{4R_1} \int_{-\infty}^{\infty} dz f(t - R_1/c_1 - z/a)\varepsilon'(z), \tag{16.16}$$

where $f(t) = p'(r_0, t)/p'_m$ is an acoustic pressure normalized by its peak amplitude p'_m describing signal's waveform (Fig. 16.9a) at some distance r_0 close to a point source (placed at a height $z = z_0 < 0$), $\varepsilon'(z)$ is the derivative of $\varepsilon(z)$, θ_0 is the angle of incidence of a sound ray falling on the lower boundary $z = 0$ of the inhomogeneous atmospheric layer with the layered fluctuations $\varepsilon(z)$ between $z = 0$ and $z = H$ and undergoing a specular reflection from this boundary to the receiver at a point with $z < 0$ (see Fig. 16.9b), R_1 is the total distance from a source to the point of specular reflection and from this point to the receiver, c_1 is the average sound speed in the reflective layer, and $a \equiv c_1/(2\cos\theta_0)$ is the coefficient depending on the angle θ_0 and c_1.

From the Eq. (16.16) we have to find a function $\varepsilon(z)$ given that we know waveforms of the reflected signal, $I_0(t) = p'(\vec{r}, t)/p'_m$, and of the incident signal, $f(t) = p'(r_0, t)/p'_m$. However, it is necessary to take into account that due to the

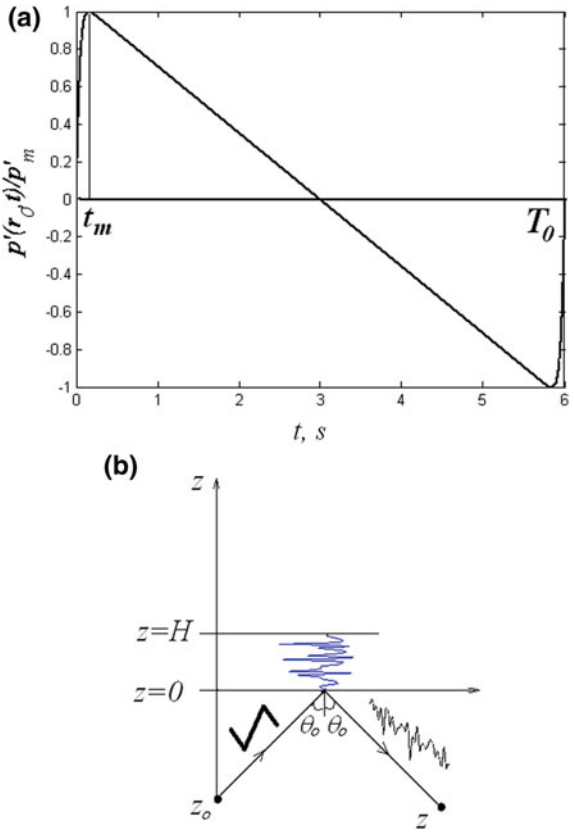

Fig. 16.9 Acoustic signal (*N*-wave) incident on the upper atmospheric layer with vertical variations in the effective refractive index $\varepsilon(z)$, and reflected signal (wave train) from this layer. **a** *N*-wave with a peak pressure amplitude $p_m^{'}$, duration T_0 and thickness t_m of a shock wave front. **b** Scheme of *N*-wave reflection from a nonhomogeneous layer $0 \le z \le H_0$ with the variations $\varepsilon(z)$; z_0 and z are the heights of an infrasound point source and receiver, respectively, θ_0 is an angle of incidence or specular reflection

nonlinear propagation of acoustic signal from impulsive source to the upper atmosphere its waveform is distorted so that the incident signal takes a form of *N*-wave at some height above ground. If the peak pressure amplitude and duration of the impulsive signal near the source are known, then the peak amplitude of the *N*-wave, its duration T_0 and the thickness of the shock wavefront as functions of increasing height above the ground can be estimated from the equations of nonlinear geometrical acoustics as in Chunchuzov et al. (2013). After estimating the peak amplitude and the duration of the *N*-wave at a height of specular reflection from the nonhomogeneous layer, the initial signal $f(t)$ near the source may be taken in the form of *N*-wave (Fig. 16.9a) with the duration T_0 corresponding to a height of reflection. In this case the inverse problem associated with Eq. (16.16) is substantially simplified, because the main contribution to the reflected wave field $I_0(t)$ comes from the short time intervals (as compared to the duration T_0) containing shock fronts of the *N*-wave, where its derivative $df(t)/dt$ reaches sharp local maxima. Therefore, after integrating Eq. (16.16) by parts the relation between the vertical profile of fluctuations $\varepsilon(z)$ and the waveform of the reflected signal $I_0(t)$ takes the following approximate form:

$$I_0(t) \approx [\varepsilon(z_1 = a \cdot (t - R_1/c_1)) + \varepsilon(z_2 = a \cdot (t - R_1/c_1 - T_0))]/2, \quad (16.17)$$

in which the second term is the result of the translation of the first term by the time interval T_0 (duration of the *N*-wave).

If the values of the recorded signal $I_0(t)$ at discrete points t_j are known then finding the fluctuations $\varepsilon(z)$ from (16.17) is reduced to solving a system of linear algebraic equations for the values of fluctuations $x_i = \varepsilon(a(t_i - R_1/c_1))/2$ at moments $t_i - R_1/c_1 > 0$. This allows us to retrieve vertical profiles of $\varepsilon(z_j)$ and fluctuations of the effective sound speed $\Delta C_{eff}(z_j) \approx \Delta c(z_j) + \Delta u(z_j) \sin\theta_0$ at heights $z_j = a(t_j - R_1/c_1)$. The technique of finding the approximate solutions for such a system by using a least square method is described in detail by Chunchuzov et al. (2015a). If the travel time of reflected signal to the receiver is known, then from the ray tracing through undisturbed atmosphere up to the midpoint of the horizontal distance between a source and receiver one can estimate the corresponding reflection height z of the incident signal and, consequently, the incidence angle $\theta_0(z)$ at this height. Knowing this angle and sound speed at the height z we can estimate the coefficient a which relates the reflection height z to the time t of the arrival of the reflected signal to the receiver. After retrieval of the fluctuations $x_i(t_i) = \varepsilon(a(t_i - R_1/c_1))/2$ the reflected signal was calculated by using (16.2) and compared to the recorded signal, from which the fluctuations $x_i(t_i)$ were obtained. As shown by Chunchuzov et al. (2015a), the r.m.s difference between the retrieved and recorded signals was within 10% of the amplitude of the recorded signal.

According to the estimates given by Chunchuzov et al. (2013), the relative temperature fluctuations caused by IGWs contribute almost five times less to the r.m.s. value of the effective sound speed fluctuations $\Delta C_{eff}(z)/c_1$ normalized by the sound speed c_1 than the relative fluctuations in the horizontal wind velocity component, $\Delta u(z)/c_1$. Due to this, the retrieved fluctuations $\Delta C_{eff}(z_j)$ are assumed to coincide with the wind velocity component fluctuations with an accuracy of 20%, i.e., within a typical accuracy of radar measurements of the wind velocity in the middle atmosphere (Murayama et al. 1992; Engler et al. 2008).

To validate the retrieved profiles of the effective sound speed fluctuations $\Delta C_{eff}(z_j)$, these fluctuations were superimposed on the corresponding *G2S* model profile, $C_{eff,0}(z_j)$ (this profile may be biased from the actual effective sound speed profile in the atmosphere). The stratospheric, mesospheric, and thermospheric arrivals were calculated using PPE method and perturbed profile $C_{eff,0}(z_j) + \Delta C_{eff}(z_j)$, and compared to the recorded arrivals. At every PPE model run, the maximum values of the retrieved fluctuations $\Delta C_{eff}(z_j)$ and their corresponding heights z_j were varied within a narrow range (the relative variations didn't exceed 20%), so that the difference in travel times and in amplitudes between calculated and measured arrivals of the signal did not exceed their measurement errors.

After reaching an agreement in the calculated and measured arrival times, we continued to vary within narrow limits the maximum values of $\Delta C_{eff}(z_j)$ in each atmospheric layer in order to reach an agreement between the calculated and

experimental ratios of the amplitudes of stratospheric and thermospheric arrivals, and the ratio between an amplitude of the stratospheric arrival and that of a signal recorded near the source.

16.11 Vertical Profiles of the Wind Velocity Fluctuations

v. Tungurahua.

The results of continuous observations of infrasound from v. Tungurahua in Ecuador were described in detail by Assink et al. (2012). The case study considered here focuses on the first three from the series of volcanic eruptions that took place on July 15, 2006 (see Fig. 3 of Assink et al. 2013). The profile $C_{eff,0}(z_j) + \Delta C_{eff}(z_j)$ retrieved from the parameters of the signals recorded at distances of about 40 and 250 km from v. Tungurahua in Ecuador is shown in Fig. 16.10. The thick line in Fig. 16.10a indicates the *G2S*-profile of $C_{eff,0}(z)$, whereas the same profile superimposed with the retrieved layered fluctuations $\Delta C_{eff}(z)$ in the stratosphere (30–52 km) and within the MLT layers, (90–102 km) and (105–140 km), is shown by a thin line. The signal propagating through the atmosphere with the perturbed profile (shown in Fig. 16.10a) and calculated by PPE method at a distance of 250 km from the volcano (its height is about 5 km) is shown in Fig. 16.10b. For comparison, the signal recorded in the experiment at a range of 250 km is also shown in Fig. 16.10b.

When calculating the signal we took into account that the nonlinear effects lead to the increase of the duration T_0 of *N*-wave with increasing height accompanied by the displacement of the maximum of its frequency spectrum toward low frequencies. As mentioned above, such an increase explains the observed displacement toward lower frequencies of the maximum of the frequency spectra of the MLT arrivals as compared to those of the stratospheric arrivals. Therefore, the stratospheric arrival was calculated by PPE method within the frequency range 0.1–1 Hz, whereas lower frequency range, 0.05–0.7 Hz, was taken for the calculating of the MLT arrivals. The calculated signal as seen in Fig. 16.10b is in a good agreement with the observed signal both in the amplitudes and travel times of the stratospheric and MLT arrivals. Some differences in the shapes of the calculated and observed arrivals are likely caused by the limited frequency band chosen for the initial signal in PPE calculations. This leads to a distortion of the calculated waveforms and vertical shifting of the frequency-dependent reflection heights for the MLT signals.

Using three successive signals from v. Tungurahua at time intervals of 15 min we retrieved the corresponding vertical profiles of the fluctuations $\Delta C_{eff}(z)$ in the lower thermosphere (105–140 km) (Fig. 16.11a). The perturbed profiles $C_{eff,0}(z_j) + \Delta C_{eff}(z_j)$ for the upper stratosphere are shown in Fig. 16.11b. Taking into consideration that the relative error in measuring of the ratio between the amplitudes of the stratospheric and thermospheric arrivals reaches 30% the estimated uncertainty of the retrieved fluctuations $\Delta C_{eff}(z_j)$ in each layer is about 2 m/s within a stratopause, and 15–20 m/s at the lower thermosphere. It is interesting to

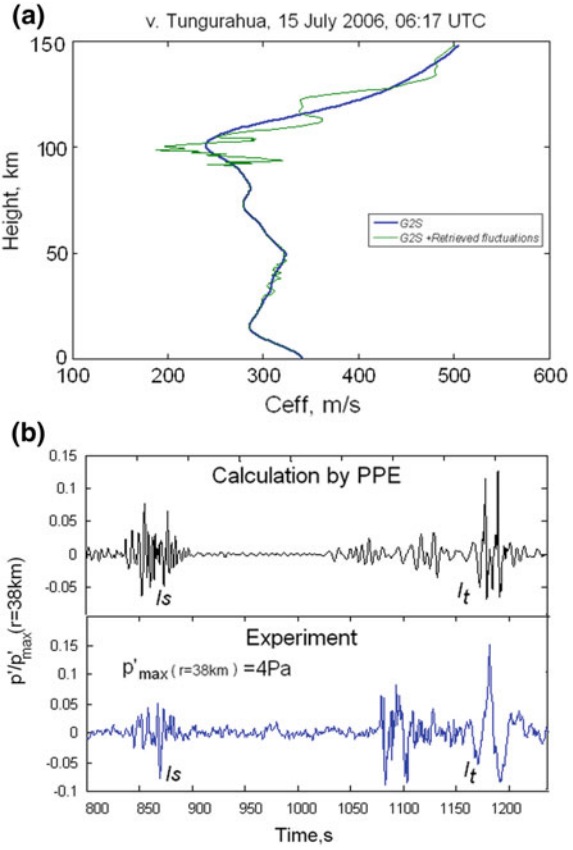

Fig. 16.10 Results of the retrieval of the vertical fluctuations $\Delta C_{eff}(z)$ near v. Tungurahua in Ecuador on July 15, 2006. **a** The G2S-profile (thick line) with superimposed fluctuations $\Delta C_{eff}(z)$ (thin line) within layers of upper stratosphere (30–52 km) and MLT: (90–102 km) and (105–130 км, **b** the signal calculated using the PPE method within the frequency range 0.07–0.7 Hz, and the signal experimentally recorded by the array at a range of 250 km from the volcano

compare the large-scale wind variations retrieved by our method in the lower thermosphere (in Fig. 16.11a, middle curve) with the most probable profiles of meridional wind in the same layer (100–130 km) obtained by the inverse method developed by Assink et al. (2013) (shown in Fig. 16.8h–i of this work). The comparison shows that the method described here retrieves the fine-scale variations $C_{eff,0}(z_j) + \Delta C_{eff}(z_j)$ in the lower thermosphere with the vertical scales shorter than 20 km (the amplitudes of such variations are in the range 30–60 m/s). When the profile $C_{eff,0}(z_j) + \Delta C_{eff}(z_j)$ is smoothed over short scales, the remaining large-scale variations with scales more than 20 km are consistent with those obtained by Assink et al. (2013).

The observed temporal variability of the profiles over the short time period of 15 min may be interpreted with the model of the nonlinear shaping of the gravity wave spectrum (Chunchuzov 2002). According to this model the interactions of atmospheric gravity waves generate a wide frequency spectrum of the wave-induced horizontal wind velocity fluctuations decaying with increasing frequency ω as $\varepsilon_0 \cdot \omega^{-2}$ for $f_c \ll \omega < N$, where N is the Brunt–Väisälä (BV) frequency,

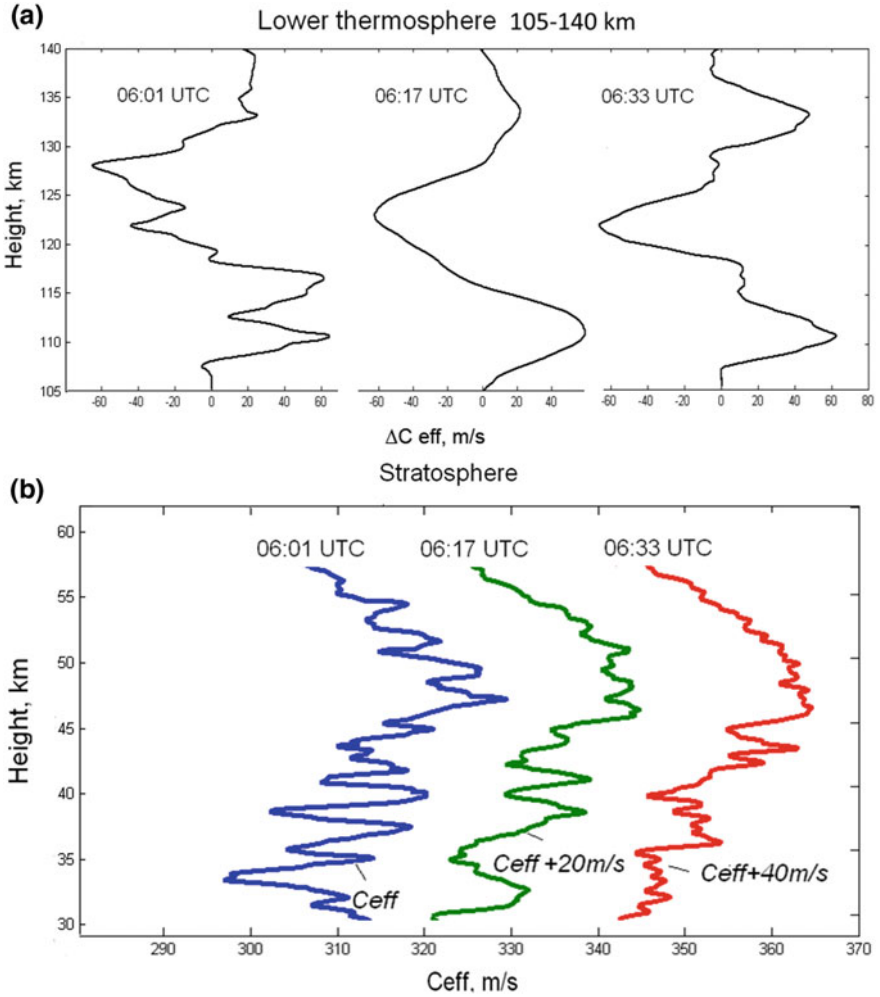

Fig. 16.11 Fluctuations $\Delta C_{eff}(z)$, retrieved from the three signals from the v. Tungurahua (July 15, 2006) following one after another with the time interval of 15 min. **a** Fluctuations $\Delta C_{eff}(z)$(horizontal axis) lower thermosphere (102–140 km). **b** Perturbed profiles within the stratosphere

f_c is a Coriolis parameter, $\varepsilon_0 = \sigma^2 \omega_0$ is the average rate of wave energy generation by random gravity wave sources, which is the product of the dispersion of the velocity fluctuations σ of fluid parcels and their acceleration $\sigma \cdot \omega_0$, and $\omega_0 \equiv Nk_0/m_0 = N/\chi$ is the characteristic frequency at which wave system pumps energy from the sources of IGWs, or maximum of the temporal spectrum of IGWs. This spectrum contains both rapidly varying wave perturbations, with the short periods of 5–10 min comparable to the Brunt–Väisälä period $2\pi/N$, and slowly varying wave perturbations with much longer periods, comparable to the inertial

period $2\pi/f_c$. The energy of these perturbations increases with their period, but all these perturbations may contribute to the temporal variability of the wind field observed in a sequence of the retrieved wind profiles in Fig. 16.11. The nonlinear dynamics of atmospheric gravity waves, planetary-scale waves, tides and their harmonics seems to affect substantially temporal variability of the wind field in the MLT as found by Assink et al. (2013) from the long-term infrasound measurements of travel times.

Surface explosion in Russia.

The profiles of $\Delta C_{eff}(z)$ have also been retrieved by using surface explosions in Russia (Udmurtia) (Chunchuzov et al. 2015a). The signals recorded by a triangle array of sensors at a range of 322 km from two consecutive surface explosions (separated by a 2-h time interval) are shown in Fig. 16.12b. Their comparison with one signal from v. Tungurahua (Fig. 16.12a) reveals common features in the waveforms of the signals. One feature is the existence of the stratospheric arrival Is

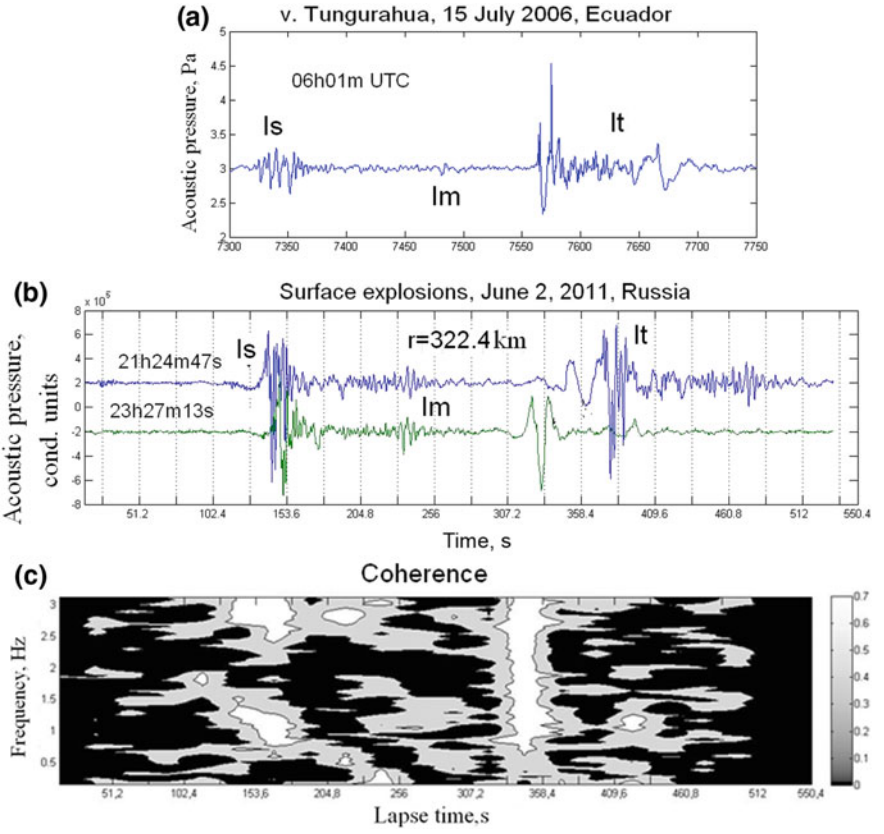

Fig. 16.12 Comparison between the signals from **a** the volcano in Ecuador (horizontal axis is a local time) and from **b** the surface explosions (Udmurtia, Russia) equivalent to 15 t of TNT, recorded at a distance of 322.4 km from the source (horizontal axis is lapse time since 04:00 UTC). The coherence of the two surface explosions (**c**)

followed by a long continuous signal of lower amplitude up to mesospheric arrival Im. The latter may be explained as a partial reflection from an isolated mesospheric layer with a high vertical gradient of wind velocity often observed within the height range 70–85 km (Kulichkov 2010). The arrival Im was previously modeled by Chunchuzov et al. (2011) (see Fig. 16.8b) using the model of gravity wave-induced perturbations. This arrival is also followed by a continuous signal of lower amplitude up to the arrival It from the lower thermosphere (90–130 km). Another common feature of the retrieved fluctuations $\Delta C_{eff}(z)$ is that their vertical wavenumber spectra show the same power law decay at high vertical wavenumbers (see next Section).

The arrivals Is, Im, and It were filtered from the background noise by calculating the cross-coherences and corresponding phase spectra of the signals recorded by the different pairs of the sensors of the array. The cross-coherence (Fig. 16.12c) calculated between the two signals from the surface explosions (shown in Fig. 16.12b) reaches local maximum of 0.7 during the time intervals, within which the stratospheric (Is) and MLT (It) arrivals were detected, although a lower cross-coherence between 0.4 and 0.6 in the frequency ranges 0.5–1.5 and 2–3 Hz holds for much longer time interval, up to 200 s. The retrieved fluctuations indicate extremely high vertical gradients, up to 10 m/s per 100 m, in the wind field within the MLT layer (90–102 km) (Chunchuzov et al. 2015a). Such gradients were previously observed near the summer mesopause below 90 km by using the wind measurements of falling spheres for during the MaCWAVE/MIDAS rocket campaign (Friitts et al. 2004) and the chemical release wind measurements (Larsen 2002).

Based on the coherence analysis of the signals in Fig. 16.12 we suggest that these signals are shaped by an interference of infrasound fields scattered from the fine-scale wind velocity and temperature anisotropic inhomogeneities that continuously fill an entire atmospheric layer (30–140) km including the stratopause and the MLT. The observed significant coherence of the signals recorded with a time delay of 2 h implies very small relative changes over a 2-h time period of the parameters describing the fine layered structure of the atmosphere such as vertical profiles of wind velocity fluctuations, their vertical wavenumber spectra, and variances.

The vertical profiles of fluctuations $\Delta C_{eff}(z)$ in the stratopause (44–54 km) and MLT (95–112 km) retrieved from the 23h27m13 s surface explosion are shown in Fig. 16.13b. The perturbed profile $C_{eff,0}(z_j) + \Delta C_{eff}(z_j)$ shown in Fig. 16.13b is a result of superimposing the fluctuations $\Delta C_{eff}(z)$ on the initially unperturbed profile $C_{eff,0}(z)$ obtained from rocket sounding data. This profile has low vertical resolution (about 1 km at stratospheric altitudes and of 5 km at higher altitudes). The dominant vertical scales of all the retrieved fluctuations tend to increase with height from a few km in the upper stratosphere to about 20 km in the MLT (90–140 km). The corresponding increase in the amplitudes of the fluctuations ranges from 6–8 to 50–60 m/s. Such an increase in both dominant scales and amplitudes of the wind velocity fluctuations is in the accordance with earlier observations of the characteristics of wind velocity fluctuations in the middle and upper atmosphere (up to 105 km) by MU radars, rockets, and falling spheres (Tsuda et al. 1992; Fritts et al.

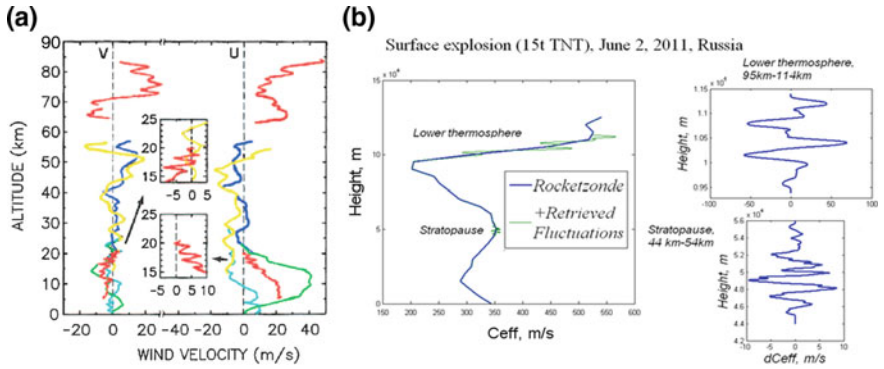

Fig. 16.13 The comparison of the vertical profiles of wind velocity fluctuations obtained by MU radar (reproduced from Tsuda 2014, Fig. 5) and infrasound sounding (Chucnhuzov et al. 2015a, b). **a** Vertical profiles of the eastward (U) and northward (V) wind velocity measured simultaneously with the MU radar (red line), a rocketsonde at Uchinoura (yellow) and Ryori (blue), and routine balloon soundings (radiosonde) at Kagoshima (light blue) and Sendai (green). Note that the MU radar observed two altitude regions: 5–20 and 65–85 km. The inset is an enlargement of the MU radar observations of the wind velocity; **b** The profile $C_{eff,0}(z_j) + \Delta C_{eff}(z_j)$ obtained from the rocket sounding data and superimposed by the fluctuations $\Delta C_{eff}(z)$ retrieved from the signal from the surface explosion detected in Udmurtia at 23h27m13 s. The enlargement of the fluctuations within stratopause and lower thermosphere is shown at the right

2004; Fritts and Alexander 2003; Tsuda 2014). This conclusion is confirmed by the comparison of the vertical profiles of wind velocity fluctuations obtained by MU radar (Tsuda 2014) and infrasound sounding. Note that the MU radar observed two altitude regions: 5–20 and 65–85 km, whereas infrasound sounding could complement these data by the wind fluctuations within stratopause (44–54 km) and lower thermosphere (90–114 km).

v. Zhupanovsky.

The signals from v. Zhupanovsky (Kamchatka) were recorded on October 11, 2013 by infrasound station IS44 at $r = 110.8$ km and array in Paratunka at $r = 91$ km. These two arrays were deep in the shadow zone and at a range of about 25 km from each other. The signals calculated by PPE ($f = 0.02$–0.5 Hz) for the unperturbed and perturbed *Ceff*-profiles are shown in Fig. 16.14a and Fig. 16.14b, respectively. They are compared to the signal recorded by one of the receivers (H1) at IS44 shown in Fig. 16.14c. The *Ceff*-profiles shown in Fig. 16.14d were retrieved from the two signals recorded at 110.8 km (IS44) and 91 km (Paratunka, PRT) from the volcano, but along different azimuthal directions.

The calculated signal for the unperturbed atmosphere (Fig. 16.14a) does not predict a long "tail" in the recorded signal (Fig. 16.14c) that lasts for a few tens of seconds. It predicts only arrival that propagated directly through troposphere from the source to the array. The difference in the arrival times (about 15 s) for calculated and recorded tropospheric arrivals is likely caused by uncertainties in tropospheric *Ceff*- profile obtained from radiosounding data.

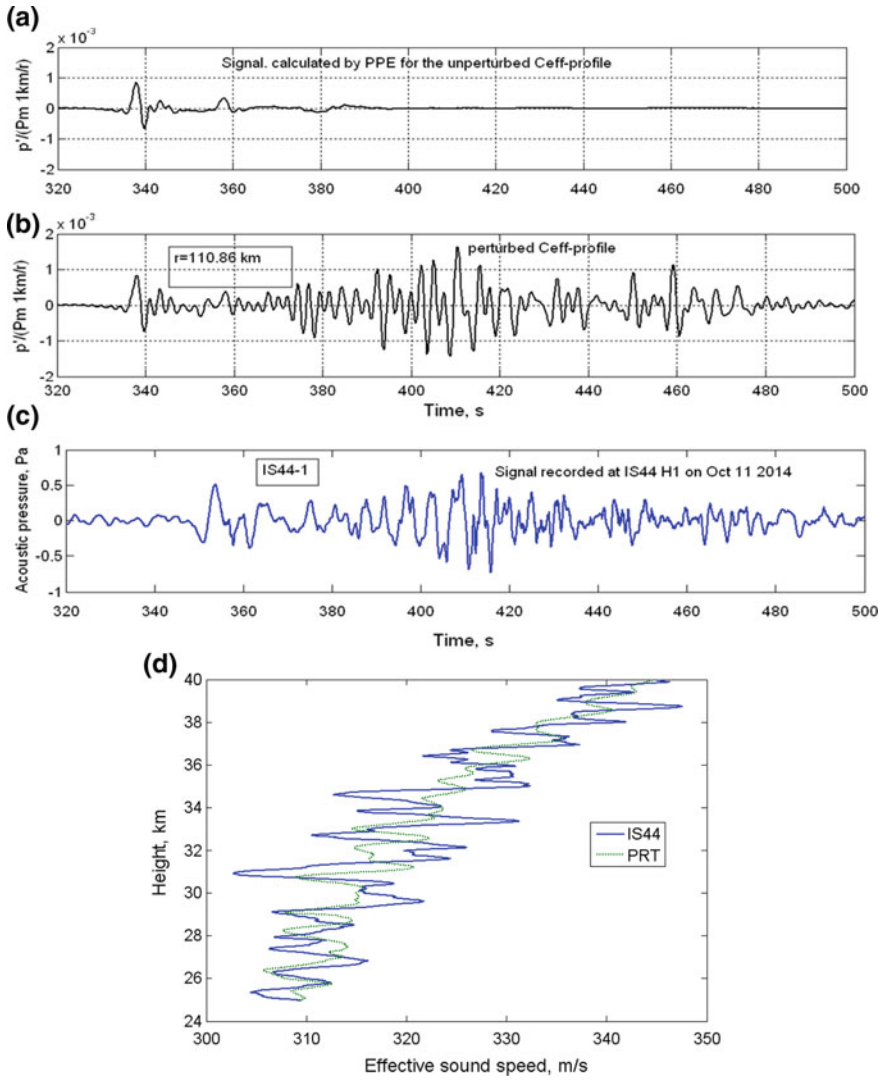

Fig. 16.14 Signals from v. Zhupanovsky recorded on Oct 11, 2013 at $r = 110.8$ km (IS44) (**c**), and calculated by PPE ($f = 0.02$-0.5 Hz) for unperturbed (**a**) and perturbed (**b**) *Ceff*-profiles. **d** The *Ceff*-profiles retrieved from two signals recorded at 110.8 km (IS44) and 91 km (Paratunka, PRT) from the volcano, but along different azimuthal directions

The appearance of the tail in the signal may be explained if the atmospheric model takes into account a fine-scale layered structure in the stratosphere (Fig. 16.14b). This structure scatters acoustic field into the acoustic shadow zone within ranges from 70 to 180 km as seen from the calculated signals versus ranges in cases of unperturbed (Fig. 16.15a) and perturbed (Fig. 16.15b) *Ceff*-profiles.

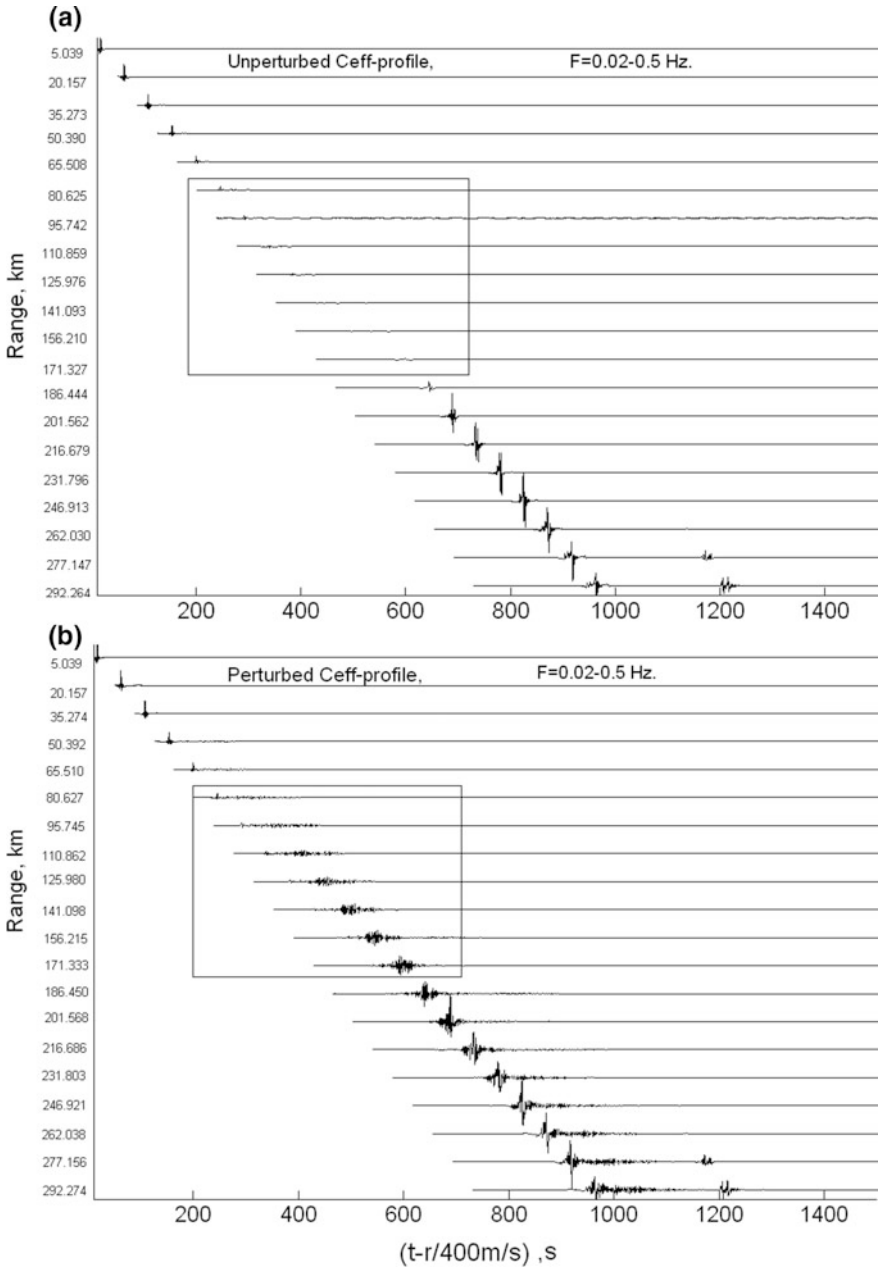

Fig. 16.15 The calculated (PPE, 0.02–0.5 Hz) signals versus ranges from 5 to 292 km from a source in cases of unperturbed (**a**) and perturbed (**b**) *Ceff*-profiles. The signals within rectangles are the stratospheric arrivals reflected from fine-scale gravity wave perturbations (**b**), which are not predicted for the unperturbed atmosphere (**a**)

Moreover, at ranges more than 180 km, i.e., in the zone of audibility, the scattering from the fine-scale structure results in the signals of much longer duration than those in the absence of this structure. These effects were found to explain the waveforms of the seismic-acoustic arrivals from the surface explosions recorded by a dense seismic array in US at ranges from 100 to 800 km from the source (Chunchuzov et al. 2014). We assume that the scattering of *N*-waves from the fine-scale structure of the stratosphere may also contribute to secondary sonic booms from supersonic aircrafts that look like wave trains with a duration of a few seconds (Rogers and Maglieri 2015).

16.12 Vertical Wavenumber Spectra of the Wind Velocity Fluctuations

The estimates of one-sided power spectral densities for the retrieved fluctuations $\Delta C_{eff}(z)$ in the stratosphere obtained from the infrasound generated by v. Karymsky, v. Tungurahua, surface explosion in Russia, v. Etna and v. Zhupanovsky are shown in Fig. 16.16a–b. At high k_z the obtained spectra may be

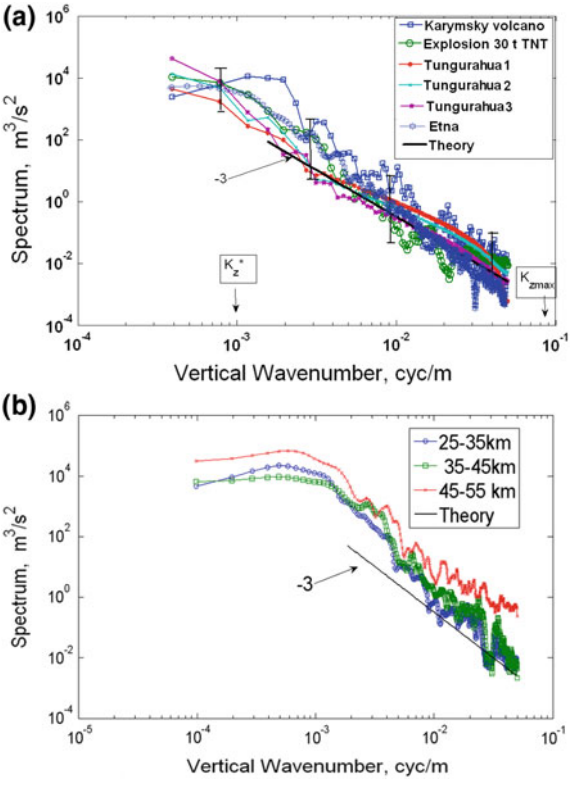

Fig. 16.16 Vertical wavenumber spectra of the horizontal wind velocity fluctuations retrieved from the stratospheric arrivals from v. Tungurahua, v. Etna, surface explosion, v. Karymsky (**a**) and v. Zhupanovsky (Kamchatka) (**b**). The horizontal axis is a cyclic vertical wavenumber $k_z/(2\pi)$. The solid line corresponds to the theoretical spectrum with a −3 power law decay. The vertical bars indicate 95% confidence intervals for the spectral estimates, and arrows show the vertical wavenumbers k_z* and $k_{z,\max}$ that confine the k_z^{-3}—spectrum

approximated by a power law k_z^{-p}, where p varies from 2.5 to 3.5, and on average close to the value $p = 3$ (Fritts and Alexander 2003), corresponding to the theoretical spectrum of atmospheric gravity wave-induced wind velocity fluctuations, $V(k_z) = \beta N^2 k_z^{-3}$ for $k_z >> k_z*$ (Chunchuzov 2002, 2009).

The r.m.s value of the wind velocity fluctuations σ may be estimated as the standard deviation of the retrieved fluctuations $\Delta C_{eff}(z)$ in the upper stratosphere, which gives σ = 2–3 m/s. Taking $\beta \approx 0.2$ and $N = 0.02$ rad/m, which is a typical value for the BV frequency in the upper stratosphere, we can estimate the longest (or outer) vertical scale: $L* = 2\pi/k_z^* = 1.6$–2.4 km, and the shortest (or inner) vertical scale, $L_{\min} = 2\pi/k_{z,\max} = 10 - 16$ m, that bound the k_z^{-3}-tail of the vertical wavenumber spectra.

Thus, all the retrieved stratospheric fluctuations $\Delta C_{eff}(z)$ show almost the same spectral power law decay in the range of vertical scales from a few kilometers to about 100 m as seen from Fig. 16.16. The same k_z^{-3}-power law for the vertical wavenumber spectra of the horizontal wind velocity fluctuations was earlier obtained from the numerous radar and lidar measurements of the temperature fluctuations in the middle atmosphere (see, for instance, Fritts and Alexander 2003; Tsuda 2014). The −3 power law decay was also found for the frequency spectra of the stratospheric and thermospheric arrivals in the shadow zone (Chunchuzov et al. 2014). The nature of such universality is associated with the nonlinearity of hydrodynamic equations that forms both the *N*-wave with a certain frequency spectrum and the anisotropic wind velocity fluctuations with a −3 slope for the vertical wave number spectrum.

The results presented here on retrieval of the detailed wind velocity structure in the upper stratosphere and MLT show the capability of the infrasound probing method in studying the statistical characteristics of the anisotropic wind fluctuations in these atmospheric layers such as variances, vertical wavenumber spectra, coherences, and characteristic scales.

16.13 Conclusions

The model of the 3-D and 1-D wavenumber spectra for the wind velocity and temperature fluctuations induced by atmospheric gravity waves was described here to calculate the statistical characteristics of infrasound waves propagating through realistic atmosphere. Using the 3-D spectrum of gravity wave perturbations, the variances of the fluctuations of sound travel time along refracting ray paths and the azimuth of arrival of acoustic signals as functions of a range from a point acoustic source have been estimated. The obtained values of the r.m.s. values of the azimuth fluctuations define the error in localization of infrasound sources caused by gravity wave perturbations, which should be taken into account when monitoring the infrasound sources in the atmosphere.

The results of theory and numerical modeling of infrasound scattering from gravity wave perturbations were presented. The vertical profiles of the horizontal wind velocity fluctuations in the upper stratosphere in the height ranges of 30–52 km and MLT (90–140 km) with a recently developed infrasound probing method have been retrieved. The method is based on analytic relation that connects the scattered infrasound field in the shadow zone with the vertical profile of the layered inhomogeneities of the effective sound speed. The obtained results show a capability of the probing method in deriving a detailed wind layered structure in the stratopause and MLT. Such information is of direct interest for the improvement of gravity wave parameterization schemes that are currently used in numerical weather prediction (NWP) models.

Despite the difference in the locations and time periods for the retrieved wind velocity profiles all of them show common features such as similar power law decays for the vertical wavenumber spectra in the upper stratosphere in the range of vertical scales from a few kilometers to about 100 m, and significant coherence of these fluctuations in the entire atmospheric layer 30–140 km over a duration of order 1 h. This implies the conservation of the statistical characteristics of the anisotropic fluctuations within the layer (30–140 km) even in quite different regions of the globe and periods of time.

Acknowledgements We thank J. Assink and R. Waxler for useful discussion of this work. This work was supported by European project ARISE and Russian grants RSF 14-27-00134 (Sects. 16.2–16.4) and RFBR 15-05-03461 (Sects. 16.5–16.7), 16-05-00438 (Sects. 16.8–16.12).

References

Akmaev RA (2001) Simulation of large-scale dynamics in the mesosphere and lower thermosphere with Doppler-spread parameterization of gravity waves. J Geophys Res 106(D1):1193–1204

Alexander MJ, Dunkerton TJ (1999) A spectral parameterization of mean-flow forcing due to breaking gravity waves. J Atmos Sci 56:4167–4182

Alexander MJ, Rosenlof KH (2003) Gravity-wave forcing in the stratosphere: observational constraints from the upper atmosphere research satellite and implications for parameterization in global models. J Geophys Res 108(D19):4597. https://doi.org/10.1029/2003JD003373

Alexander MJ et al (2010) Recent developments in gravity wave effects in climate models, and the global distribution of gravity wave momentum flux from observations and models. Q J R Meteorol Soc 136:1103–1124

Assink JD, Waxler R, Drob DP (2012) On the sensitivity of infrasonic travel times in the equatorial region to the atmospheric tides. J Geophys Res 117. https://doi.org/10.1029/2011jd016107

Assink JD, Waxler R, Frazier WG, Lonzaga J (2013) The estimation of upper atmospheric wind model updates from infrasound data. J Geophys Res 118(19):10707–10724

Assink JD, Smets P, Marcillo O, Weemstra C, Lalande J-M, Waxler R, Evers L (2019) Advances in infrasonic remote sensing methods. In: Le Pichon A, Blanc E, Hauchecorne A (eds) Infrasound monitoring for atmospheric studies, 2nd edn. Springer, Dordrecht, pp 605–632

Bacmeister et al (1996) Stratospheric horizontal wave number spectra of winds, potential temperature, and atmospheric tracers observed by high-altitude aircraft. J Geophys Res 101 (D5):9441–9470

Blokhintsev DI (1956) Acoustics of a nonhomogeneous moving medium, NACA Tech Memo 1399

Broutman D, Macaskill C, Mcintyre ME, Rottman JW (1997) On doppler-spreading models of internal waves. Geophys Res Lett 24(22):2813–2816

Broutman D, Grimshaw RHJ, Eckermann SD (2004) *On* internal waves in a Lagrangian reference frame. J Atmos Sci 61:1308–1313

Bush GA, Kulichkov SN, Svertilov AI (1997) Some results of the experiments on acoustic wave scattering from anisotropic inhomogeneities of the middle atmosphere. Izv Atmos Ocean Phys 33(4):445–452

Chibisov SV (1940) On the travel time of a sound ray in the atmosphere. Izv Akad Nauk Ser Geograf Geofiz 4:475–520

Chunchuzov IP (1996) The spectrum of high-frequency internal waves in the atmospheric waveguide. J Atmos Sci 53:1798–1814

Chunchuzov IP (2001) On the role of nonlinearity in the formation of the spectrum of atmospheric gravity waves. Izv Atmos Oceanic Phys 37(4):466–469

Chunchuzov IP (2002) On the high-wavenumber form of the Eulerian internal wave spectrum in the atmosphere. J Atmos Sci 59:1753–1772

Chunchuzov IP (2004) Influence of internal gravity waves on sound propagation in the lower atmosphere. Meteorol Atmos Phys 85:61–76

Chunchuzov IP (2009) On the nonlinear shaping mechanism for gravity wave spectrum in the atmosphere. Ann Geophys 27:4105–4124

Chunchuzov I, Kulichkov S, Popov O, Waxler R, Assink J (2011) Scattering of infrasound by anisotropic inhomogeneities of the atmosphere. Izv Atmos Ocean Phys 47(5):540–547

Chunchuzov IP, Kulichkov SN, Firstov PP (2013) On the acoustic N-wave reflections from layered nonhomogeneities of the atmosphere. Izv Atmos Ocean Phys 49(3):258–270

Chunchuzov I, Kulichkov S, Popov O, Hedlin M (2014) Modeling propagation of infrasound signals observed by a dense seismic network. J Acoust Soc Am 135(1):38–48. https://doi.org/10.1121/1.4845355

Chunchuzov IP, Kulichkov SN, Popov OE, Perepelkin VG, Vasilev AP, Glushkov AI, Firstov PP (2015a) The characteristics of a fine-scale structure of the wind velocity field in the stratosphere and lower thermosphere obtained from infrasonic signals in the acoustic shadow zones. Izv Atmos Ocean Phys 51(1):57–74

Chunchuzov I, Kulichkov S, Perepelkin V, Popov O, Firstov P, Assink JD, Marchetti E (2015b) Study of the wind velocity- layered structure in the stratosphere, mesosphere and lower thermosphere by using infrasound probing of the atmosphere. J Geophys Res 120:8828–8840. https://doi.org/10.1002/2015JD023276

Dewan EM, Good RE (1986) Saturation and the "universal" spectrum for vertical profiles of horizontal scalar winds in the atmosphere. J Geophys Res 92:2742–2748

Dewan E (1997) Saturated-cascade similitude theory of gravity wave spectra. J Geophys Res 102:29799–29817

Donn WL, Rind DH (1972) Microbaroms and the temperature and wind of the upper atmosphere. J Atmos Sci 29:156–172

Drob DP, Picone JM, Garces MA (2003) The global morphology of infrasound propagation. J Geophys Res 108(D21):4680. https://doi.org/10.1029/2002JD003307

Drob DP et al (2008) An empirical model of the earth's horizontal wind fields: HWM07. J Geophys Res 113 (A12304)

Drob DP, Meier RR, Picone JM, Garces M (2010) Inversion of infrasound signals for passive atmospheric remote sensing. In: Infrasound monitoring for atmospheric studies Le Pichon A, Blanc E, Hauchecorne A, chap 24. Springer, New York, pp 701–732

Drob DP, Broutman D, Hedlin MA, Winslow NW, Gibson RG (2013) A method for specifying atmospheric gravity wavefields for long-range infrasound propagation calculations. J Geophys Res Atmos 118. https://doi.org/10.1029/2012jd018077

Duckert P (1931) Ueber die Ausbreitung von Explosionswellen in der Erdatmosphiire. Ergeb d Kosm Physik 1:236–290

Eckermann SD (1999) Isentropic advection by gravity waves: quasi-universal M^{-3} vertical wavenumber spectra near the onset of instability. Geophys Res Lett 26:201–204
Eckermann SD, Hoppel KW, Coy L, McCormack JP, Siskind DE, Nielsen K, Kochenash A, Stevens MH, Englert CR, Hervig M (2009) High-altitude data assimilation system experiments for the northern summer mesosphere season of 2007. J Atmos Sol-Terr Phys 71:531–551
Eckermann SD (2011) Explicitly stochastic parameterization of nonorographic gravity wave drag. J Atmos Sci 68:1749–1765
Engler N, Singer W, Latteck R, Strelnikov B (2008) Comparison of wind measurements in the troposphere and mesosphere by VHF/MF radars and in-situ techniques. Ann Geophys 26:3693–3705
Flattè S, Dashen R, Munk W, Watson K, Zachariasen F (1979) Sound transmission through a fluctuating ocean. Cambridge University Press, Cambridge
Franke PM, Robinson WA (1999) Nonlinear behaviour in the propagation of atmospheric gravity waves. J Atmos Sci 56:3010–3027
Fritts DC (1984) Gravity wave saturation in the middle atmosphere: a review of theory and observations. Rev Geophys Space Phys 22:275–308
Fritts DC, Alexander MJ (2003) Gravity wave dynamics and effects in the middle atmosphere. Rev Geophys 41:1/1003. https://doi.org/10.1029/2001rg000106
Fritts DC, Williams BP, She CY, Vance JD, Rapp M, Lubken F-J, Mullemann A, Schmidlin FJ, Goldberg RA (2004) Observations of extreme temperature and wind gradients near the summer mesopause during the MaCWAVE/MIDAS rocket campaign. Geophys Res Lett 31, L24S06. https://doi.org/10.1029/2003gl019389
Gainville O, Blank-Benon Ph, Blanc E, Roche R, Millet C, Le Piver F, Despires B, Piserchia PF (2010) Misty picture: a unique experiment for the interpretation of the infrasound from large explosive sources. In: Le Pichon A, Blanc E, Hauchecorne A (eds) Infrasound monitoring for atmospheric studies. Springer, pp 575–598
Gardner CS (1996) Testing theories of atmospheric gravity wave saturation and dissipation. J Atmos Terr Phys 58:1575–1589
Gibson R, Drob D, Norris D (2007) Infrasound propagation calculation techniques using mesoscale atmospheric and terrain specifications. In: Infrasound technology workshop (ITW 2007), Tokyo, Japan
Gibson R, Norris D (2008) Recent applications of the time-domain parabolic equation (TDPE) model to ground truth events. In: Infrasound technology workshop (ITW 2005), Bermuda
Gossard EE, Hooke WH (1975) Waves in the atmosphere. Elsevier, Amsterdam, p 456
Gurvich AS (1997) A heuristic model of three-dimensional spectra of temperature inhomogeneities in the stably stratified atmosphere. Ann Geophys 15:856–869
Gurvich AS, Chunchuzov IP (2003) Parameters of the fine density structure in the stratosphere obtained from spacecraft observations of stellar scintillations. J Geophys Res 108(D5):4166. https://doi.org/10.1029/2002JD002281
Gurvich A, Chunchuzov I (2005) Estimates of characteristic scales in the spectrum of internal waves in the stratosphere obtained from space observations of stellar scintillations. J Geophys Res 110:D03114. https://doi.org/10.1029/2004JD005199
Gurvich AS, Chunchuzov IP (2008) Three-dimensional spectrum of temperature fluctuations in stably stratified atmosphere. Ann Geophys 26:2037–2042
Gutenberg B (1939) The velocity of sound waves and the temperature in the stratosphere above Southern California. Bull Am Meteorol Soc 20:192–201
Hamilton K (1997) Gravity wave processes. NATO ASI Series I, Springer, Their parameterization in Global Climate Models, p 383
Hays PB et al (1993) The high resolution Doppler imager on the upper atmosphere research satellite. J Geophys Res 98(10):713–723
Hedlin MAH, Walker KT (2013) A study of infrasonic anisotropy and multipathing in the atmosphere using seismic networks. Phil Trans R Soc A 13, 371(1984):20110542. https://doi.org/10.1098/rsta.2011.0542
Hines CO (1960) Internal atmospheric gravity waves at ionospheric heights. Can J Phys 38:1441–1481

Hines CO (1991a) The saturation of gravity waves in the middle atmosphere. Part I: critique of linear instability theory. J Atmos Sci 48:1348–1359
Hines CO (1991b) The saturation of gravity waves in the middle atmosphere. Part II: development of doppler-spread theory. J Atmos Sci 48:1360–1379
Hines CO (1993) The saturation of gravity waves in the middle atmosphere. Part IV: cutoff of the incident wave spectrum. J Atmos Sci 50:3045–3060
Hines CO (1996) Nonlinearity of gravity wave saturated spectra in the middle atmosphere. Geophys Res Lett 23:3309–3312
Hines CO (2001) Theory of the Eulerian tail in the spectra of atmospheric and oceanic internal gravity waves. J Fluid Mech 448:289–313
Holton JR, Hakim GJ (2012) An introduction to dynamic meteorology, 5th edn. Academic Press, 552 pp
Hoppel KW, Eckermann SD, Goy L, Nedoluha GE, Allen DR, Swadley SD, Baker NL (2013) Evaluation of SSMIS upper atmosphere sounding channels for high-altitude data assimilation. Mon Weather Rev 141:3314–3330
Hostetler CA, Gardner CS (1994) Observations of horizontal and vertical wave number spectra of gravity wave motions in the stratosphere and mesosphere over the mid-Pacific. J Geophys Res 99:1283–1302
Jacobi Ch, Fröhlich K, Viehweg C, Stober G, Kürschner D (2007) Midlatitude MLT meridional winds and temperatures measured with meteor radar. Adv Space Res 39(8):1278–1283
Kulichkov SN (2002) Conservation of "Acoustic Momentum" during long-range infrasonic propagation in the atmosphere. Izv Atmos Ocean Phys 38(5):582–587
Kulichkov SN (2008) Evidence for nonlinear atmospheric effects in infrasound propagation from explosions of different types and yields. In: International symposium on nonlinear acoustics (ISNA2008)
Kulichkov SN, Bush GA (2001) Rapid variations of infrasonic signals from similar explosions at long distances. Izv Atmos Ocean Phys 37(3):331–338
Kulichkov SN, Bush GA, Svertilov AI (2002) New type of infrasonic arrivals in the geometric shadow region at long distances from explosions. Izv Atmos Ocean Phys 38(4):397–402
Kulichkov SN (2004) Long-range propagation and scattering of low-frequency sound pulses in the middle atmosphere. Meteorol Atmos Phys 85(1–3):47–60
Kulichkov S (2010) On the Prospects for Acoustic Sounding of the Fine Structure of the Middle Atmosphere. In: Le Pichon A, Blanc E, Hauchecorne A (eds) Infrasound monitoring for atmospheric studies. Springer, New Yoork, pp 511–540
Kulichkov SN, Chunchuzov IP, Perepelkin VG, Svertilov AI, Baryshnikov AK (2007) On the influence of anisotropic turbulence on fluctuations in the azimuths and grazing angles of acoustic signals in the lower and middle atmosphere. InfraMatics 18(June):1–5
Kulichkov SN, Bush GA, Chunchuzov IP, Mishenin AA, Golikova EV (2016) Space-time variability of the fine structure of the upper atmosphere according to the infrasound probing data. Izv Atmos Ocean Phys 52(2):200–212
Larsen MF (2002) Winds and shears in the mesosphere and lower thermosphere: results from four decades of chemical release wind measurements. J Geophys Res: Space Phys 107(A8): SIA 28-1–SIA 28-14
Le Pichon A, Blanc E, Drob DP, Lambotte S, Dessa JX, Lardy M, Bani P, Vergniolle S (2005) Infrasound monitoring of volcanoes to probe high-altitude winds. J Geophys Res 110:D13106. https://doi.org/10.1029/2004JD005587
Le Pichon A, Vergoz J, Cansi Y, Geranna L, Drob D (2010) Contribution of infrasound monitoring for atmospheric remote sensing. In: Le Pichon A, Blanc E, Hauchecorne A (eds) Infrasound monitoring for atmospheric studies. Springer, New York, pp 629–646
Le Pichon A, Ceranna L, Vergoz J, Tailpied D (2019) Modeling the detection capability of the global IMS infrasound network. In: Le Pichon A, Blanc E, Hauchecorne A (eds) Infrasound monitoring for atmospheric studies, 2nd edn. Springer, Dordrecht, pp 593–604
Lighthill J (1978) Waves in fluids. Cambridge University Press, 504 pp
Lindborg E (2006) The energy cascade in a strongly stratified fluid. J Fluid Mech 550:207–242

Lindborg E (2007) Horizontal wavenumber spectra of vertical vorticity and horizontal divergence in the upper troposphere and lower stratosphere. J Atmos Sci 64:1017–1025. https://doi.org/10.1175/JAS3864.1

Liszka L, Enell CF, Raita T (2009) Infrasound in the atmosphere—towards a new propagation model. InfraMatics 24:1–14

Lumley JL (1964) The spectrum of nearly inertial turbulence in a stably stratified fluid. J Atmos Sci 21:99–102

Manson AH (1990) Gravity wave horizontal and vertical wavelengths: an update of measurements in the mesopause region (~80–100 km). J Atmos Sci 47:2765–2773

Murayama Y, Tsuda T, Nakamura T, Kato S, Fukao S (1992) Seasonal variation of gravity wave activity in the middle atmosphere observed with the MU RADAR. In: Proceedings of the international symposium middle atmosphere science (MAS symposium 1992), Kyoto, Japan, March 23–27, pp 24–25

Marty J (2014) Overview of the IMS infrasound network and engineering projects. In: Presentation at infrasound technology workshop (ITW 2014), Vienna, 13–16 Oct 2014

Medvedev AS, Klaassen GP (1995) Vertical evolution of gravity wave spectra and the parameterization of associated wave drag. J Geophys Res 100(D12):25841–25853. https://doi.org/10.1029/95JD02533

Merzlyakov E, Pancheva D, Mitchell N, Forbes JM, Portnyagin YuI, Palo S, Makarova N, Muller HG (2004) High- and mid-latitude quasi-2-day waves observed simultaneously by four meteor radars during summer 2000. Ann Geophys 22:773–788

Nappo CJ (2002) An introduction to atmospheric gravity waves. Academic Press

Norris D (2005) Broadband propagation modeling and scattering. In: Presentation at infrasound technology workshop (ITW 2005), Tahiti

Norris D, Gibson R, Bongiovanni K (2010) Numerical methods to model infrasonic propagation through realistic specifications of the atmosphere. In: Le Pichon A, Blanc E, Hauchecorne A (eds) Infrasound monitoring for atmospheric studies, chap. 17. Springer, New York, pp 541–573

Ostashev VE, Chunchuzov IP, Wilson DK (2005) Sound propagation through and scattering by internal gravity waves in a stably stratified atmosphere. J Acoust Soc Am 118(6):3420–3429

Pinkel R (2008) Advection, phase distortion, and the frequency spectrum of finescale fields in the sea. J Phys Oceanogr 38:291–313

Phillips OM (1967) Theoretical and experimental study of gravity wave interactions. In: Lighthill MJ (ed) Proceedings of the royal society: a discussion on nonlinear theory of wave propagation in dispersive system, London. Series A, mathematical and physical sciences, vol 299, 1456, pp 141–160

Portnyagin Yu, Solovjova T, Merzlyakov E, Forbes J, Palo S, Ortland D, Hocking W et al (2004) Mesosphere/lower thermosphere prevailing wind model. Adv Space Res 34:1755–1762

Rogers PH, Maglieri DJ (2015) Concorde booms and the mysterious east coast noises. Acoust Today 11(2):34–40

Rüfenacht R, Kämpfer N, Murk A (2012) First middle-atmospheric zonal wind profile measurements with a new ground-based microwave doppler-spectro-radiometer. Atmos Meas Tech 5:2647–2659

Shur GN (1962) Experimental investigation of the energy spectrum of atmospheric turbulence. Trudy tsent Aerol Obser, 79–90

Smets PSM, Evers LG (2014) The life cycle of a sudden stratospheric warming from infrasonic ambient noise observations. J Geophys Res 119. https://doi.org/10.1002/2014jd021905

Smets P, Assink J, Evers L (2019) The study of sudden stratospheric warmings using infrasound. In: Le Pichon A, Blanc E, Hauchecorne A (eds) Infrasound monitoring for atmospheric studies, 2nd edn. Springer, Dordrecht, pp 723–755

Smith SA, Fritts DC, VanZandt TE (1987) Evidence for a saturated spectrum of atmospheric gravity waves. J Atmos Sci 44:1404–1410

Sukoriansky S, Galperin B (2013) An analytical theory of the buoyancy–Kolmogorov subrange transition in turbulent flows with stable stratification. Phil Trans R Soc A 371:20120212. https://doi.org/10.1098/rsta.2012.0212

Tsuda T et al (1992) Characteristics of gravity waves in the middle atmosphere observed with rocketsondes at Uchinoura during DYANA campaign. In: Proceedings of the international symposium middle atmosphere science (MAS symposium), 1992, Kyoto, Japan, March 23–27, pp 141–143

Tsuda T (2014) Characteristics of atmospheric gravity waves observed using the MU (Middle and Upper atmosphere) radar and GPS (Global Positioning System) radio occultation. In: Proceedings of the Japan Academy. Series B 90, vol 90, pp 12–27

VanZandt TE (1982) A universal spectrum of buoyancy waves in the atmosphere. Geophys Res Lett 9:575–578

Vinnichenko NK, Pinus NZ, Shmeter SM, Shur GN (1980) Turbulence in the free atmosphere, 2nd edn. Plenum, New York, p 310

Vincent RA, Allen SJ, Eckermann SD (1997) Gravity -Wave Parameters in the Lower Stratosphere. In: Hamilton K, Series NATOASI (eds) Gravity wave processes, their parameterization in global climate models. Springer, Berlin, pp 7–25

Warner CD, McIntyre ME (1996) On the propagation and dissipation of gravity wave spectra through a realistic middle atmosphere. J Atmos Sci 53:3213–3235

Waxler R, Assink J (2019) Propagation modeling through realistic atmosphere and benchmarking. In: Le Pichon A, Blanc E, Hauchecorne A (eds) Infrasound monitoring for atmospheric studies, 2nd edn. Springer, Dordrecht, pp 509–549

Weinstock J (1985) Effect of gravity waves on turbulence decay in stratified fluids. J Fluid Mech 140:11–26

Weinstock J (1990) Saturated and unsaturated spectra of gravity waves and scale-dependent diffusion. J Atmos Sci 47:2211–2225

Whipple FJW (1923) The high temperature of the upper atmosphere as an explanation of zones of audibility. Nature 111:187

Whipple FJW (1939) The upper atmosphere, density and temperature, direct measurements and sound evidence. Q J R Meteorol Soc 65:319–323

Wu DL, Schwartz MJ, Waters JW, Limpasuvan V, Wu Q, Killeen TL (2008) Mesospheric Doppler wind measurements from aura microwave limb sounder (MLS). Adv Space Res 42:1246–1252. https://doi.org/10.1016/j.asr.2007.06.014

Part VI
Propagation Modelling, Network Performance and Inversion Methods: Network Performance and Inversion Methods

Chapter 17
Modeling the Detection Capability of the Global IMS Infrasound Network

Alexis Le Pichon, Lars Ceranna, Julien Vergoz and Dorianne Tailpied

Abstract The International Monitoring System (IMS) infrasound network is being deployed to ensure compliance with the Comprehensive Nuclear-Test-Ban Treaty (CTBT). Recent global scale observations recorded by this network confirm that its detection capability is highly variable in space and time. Previous studies estimated the radiated source energy from remote observations using empirical yield-scaling relations which account for the along-path stratospheric winds. Although these relations reduce the variance in the explosive energy yield estimates, large error remains. Today, numerical modeling techniques provide a basis to better predict the effects of the source and middle atmospheric dynamic parameters on propagation. In order to account for a realistic description of the dynamic structure of the atmosphere, model predictions are further enhanced by wind and temperature error distributions as measured by high-resolution middle atmospheric sounding techniques. In the context of the future verification of the CTBT, these predictions quantify uncertainties of the IMS infrasound network performance in higher resolution, and are helpful for the design and prioritizing maintenance of any arbitrary infrasound monitoring network.

17.1 Introduction

Interest in infrasound technology and research was revived after the CTBT was adopted and opened for signature in 1996. The IMS infrasound network has been designed to reliably detect and locate nuclear test explosions one kiloton down to one kiloton of TNT equivalent worldwide (Christie and Campus 2010). Even

A. Le Pichon (✉) · J. Vergoz
CEA, DAM, DIF, F-91297 Arpajon, France
e-mail: alexis.le-pichon@cea.fr

L. Ceranna
BGR, B4.3, 30655 Hannover, Germany

D. Tailpied
Nanyang Technological University, EOS, Singapore 639798, Singapore

A. Le Pichon et al. (eds.), *Infrasound Monitoring for Atmospheric Studies*,
https://doi.org/10.1007/978-3-319-75140-5_17

though the IMS network is not yet fully established, it now provides a global coverage of infrasound as infrasound signal can propagate over large distances with weak attenuation through the stratosphere and thermosphere (e.g., Drob et al. 2003; Sutherland and Bass 2004). In addition to its primary function of detecting explosions, this network has demonstrated its potential to locate and characterize geophysical and anthropogenic events (e.g., Campus and Christie 2010; Mialle et al. 2019).

To assess the monitoring capabilities of any infrasound network, it is necessary to predict the signal amplitude at any location, and further evaluate whether the signal is detectable above the noise level at the receivers. One dominant factor influencing infrasound detection at mid-latitudes is the semiannual oscillation of the dominant zonal component of the stratospheric wind flow (e.g., Drob et al. 2008; De Groot-Hedlin et al. 2010).

Different approaches incorporating various background noise models and yield-scaling relationships have been proposed (e.g., Clauter and Blandford 1997; Stevens et al. 2002). Significant advances were achieved using (i) the Los Alamos National Laboratory (LANL) yield-amplitude scaling relation derived from recordings of historical atmospheric nuclear and chemical explosions (e.g., Whitaker et al. 1995), and (ii) by considering realistic station noise models and accurate atmospheric specifications (e.g., Le Pichon et al. 2009; Green and Bowers 2010). Using state-of-the-art specifications of stratospheric winds and time-dependent station noise models, these simulations predict that explosions equivalent to ~500 t of chemical explosive would be detected over $\geq 95\%$ of the earth's surface at any time of the year (Le Pichon et al. 2009).

However, conclusions from this yield-amplitude scaling relation may be misleading as the complexities of infrasound propagation are simplified and it does not adequately describe long-range infrasound propagation. Analyses of well-calibrated reference events have revealed large spread in the yield estimates, which have been attributed to either large variability in along-path stratospheric wind speed (Green et al. 2011), or systematic overestimates of a known yield (Fee et al. 2013).

Today, numerical modeling techniques provide a basis to better understand the role of different factors describing the source and the atmosphere that affect propagation predictions. In order to quantify the infrasound network performance in higher spatiotemporal resolution, a frequency-dependent semi-empirical attenuation relation is derived from linear wide-angle range-independent parabolic equation (PE) has been proposed (Le Pichon et al. 2012). Coupled with realistic station noise and atmospheric specifications calculated along the propagation paths at 50 km altitude, network performance simulations predict the minimum detectable amplitude at a reference distance of 1 km away from the source.

Over the past decades, there have been significant advances in measuring properties of upper atmospheric regions (e.g., Killeen et al. 2006). Recently, the European Centre for Medium-Range Weather Forecasts (ECMWF) has begun to produce specifications up to 75 km altitude (http://www.ecmwf.int; ECMWF 2013). However, comprehensive observationally based specifications of wind and temperature in the Mesosphere and Lower Thermosphere (MLT, approximately 50–

110 km altitude) are limited to semi-empirical models such as the Horizontal Wind Model (HWM) (Drob et al. 2008), leading to uncertainties in infrasound propagation simulations. It has been one of the goals of the ARISE project (Atmospheric dynamics Research InfraStructure in Europe, http://arise-project.eu) measurement campaign at Haute-Provence Observatory (OHP, France, 43.93°N 5.71°E) to focus on the estimation of the error distribution in atmospheric models up to 70 km altitude (Le Pichon et al. 2015).

The main objective of this study is to evaluate the detection capability of the full IMS network while accounting for atmospheric model uncertainties. In particular, it was demonstrated that the network performance predictions are further enhanced by considering the effect of realistic atmospheric disturbances, such as gravity waves, which are excluded from the current atmospheric specifications (e.g., Hedlin and Drob 2014).

In Sect. 17.2, we introduce the methodology employed to develop a semi-empirical attenuation relation. The related effects of source frequency, stratospheric wind parameterization, and atmospheric perturbations on the propagation are shown through examples of global simulations. We address the implications of our results which, compared to previous studies, provide progress toward more realistic and more accurate space-, time-, and frequency-dependent detection levels.

In Sect. 17.3, we compare and validate the modeling results using repetitive signals from Mt. Etna (Italy) as a benchmark case study for evaluating the simulation results. Such repetitive sources open opportunities to evaluate network performance simulation methods in higher resolution and promote the potential benefits from a regional and global infrasound monitoring for civil and scientific applications (e.g., Matoza et al. 2019).

17.2 Simulating the Infrasound Network Performance: Effects of Middle Atmospheric Wind Uncertainties

To model the detection capability of an arbitrary infrasound network, it is necessary to predict the signal amplitude at any required time and location, and further evaluate whether the signal can be detected at the receivers. Infrasound can propagate over long distances without significant attenuation through atmospheric waveguides thanks to specific temperature and wind gradients (e.g., Drob et al. 2003). This propagation is characterized by the properties of refraction, reflection, diffraction, advection, attenuation, and dispersion (Waxler and Assink 2019). Due to the generally high-frequency content of the detected signals (>0.5 Hz, Mialle et al. 2019) and due to atmospheric absorption at high altitudes (Sutherland and Bass 2004), thermospheric returns are strongly attenuated and rarely detected beyond ~1000 km. Under specific temperature and wind features, most of the acoustic energy propagates through stratospheric waveguides where refraction to

the ground can be observed. Clearly captured in meteorological models, such atmospheric conditions are crucial to consider as it controls to first order where infrasound signals are expected to be detected (e.g., Ceranna et al. 2009; Green et al. 2011; Smets et al. 2015).

Infrasound propagation can usually be modeled by the classic acoustic ray-tracing method based on the laws of Snell-Descartes. However, several limits can be pointed out since the trajectories are purely geometric. This method is a high-frequency approximation and becomes less precise and even inappropriate when the size of fine atmospheric structures is comparable to the acoustic wavelength (e.g., Garcés et al. 1998). In this context, the Parabolic Equation (PE) method has been used to account for diffraction and scattering due to small-scale structure in the atmosphere such as due to gravity waves that significantly affect infrasound propagation (Lingevitch et al. 2002). The PE method is an effective technique to realistically propagate the acoustic energy over various distances in a stratified atmosphere (Gainville et al. 2010).

A frequency-dependent attenuation relation derived from massive range-independent parabolic equation simulations using a multidimensional curve-fitting approach has been proposed to predict network detection capability (Le Pichon et al. 2012). This relation combines the effect of the source-to-receiver distance, the source frequency, realistic along-path atmospheric specifications and time-varying station noise conditions (Brown et al. 2014), and a signal-to-noise ratio above which signals can reliably be detected (Evers et al. 2007). It allows calculating the pressure wave attenuation accounting for geometrical spreading and dissipation for both stratospheric and thermospheric propagation.

Figure 17.1 presents the geographical coverage of the minimum signal attenuation considering one detecting station in winter and summer. These simulations highlight the dominant effects of the seasonal oscillation of the zonal wind on the network performance. During the northern hemisphere winter, the steady eastward stratospheric currents favor long-range propagation of signals from westerly directions due to low attenuation for downwind propagating signals, as seen from the green colored regions west of the stations (Fig. 17.1a). An opposite scenario is simulated in the southern hemisphere. This global feature reverses in summer (Fig. 17.2a). This oscillation clearly captured in climatological models controls to first order the direction from where signals are expected to be detected (e.g., Drob et al. 2008).

In order to better capture stratospheric–tropospheric interactions, the weather and climate forecasting communities are moving toward a more comprehensive representation of the atmosphere (e.g., Charlton-Perez et al. 2013; Drob et al. 2013). In this context, the ARISE project aims to design a novel infrastructure by integrating new type of high-resolution and independent Middle Atmospheric (MA, 12–70 km altitude range) observation networks. Systematic comparisons between ARISE measurements techniques and output of Numerical Weather Prediction (NWP) models have shown that, on average, ECMWF temperature and wind models are in good agreement with the observations up to the stratopause. However, between 30 and 70 km, the differences are characterized by broad distributions. The largest deviations are observed in winter time hemisphere when the polar

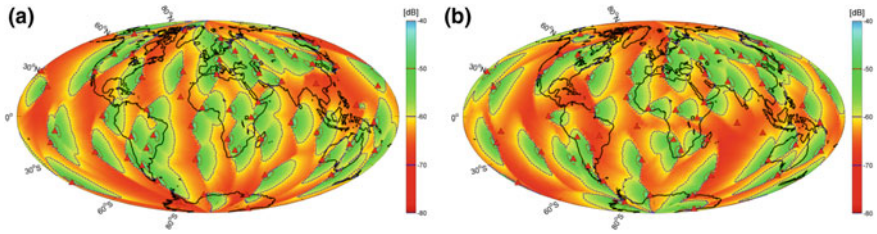

Fig. 17.1 Geographical coverage of the smallest signal attenuation with one-station coverage of the full IMS network. The red triangles indicate the location of the 59 IMS infrasound stations. Simulations are carried out at 0.8 Hz using the HWM-07 climatological stratospheric wind model (Drob et al. 2008) on the 1st of January and July, 2013 (**a** and **b**, respectively). The colormap refers to the attenuation (in dB) for sources located worldwide

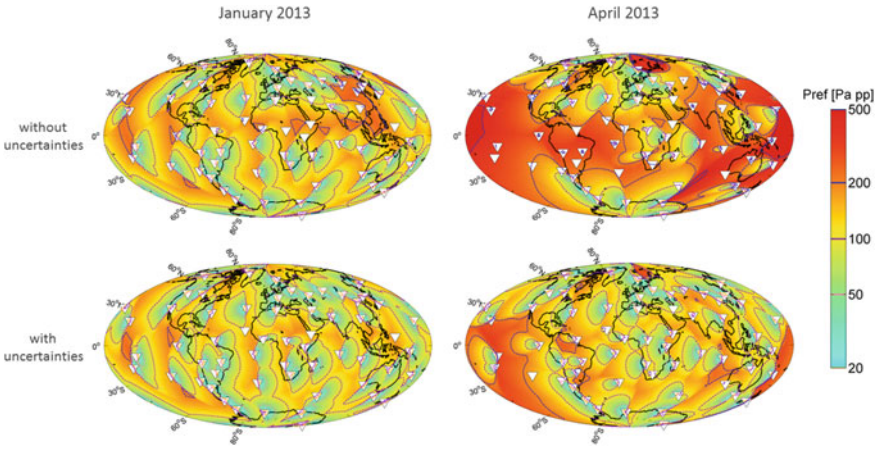

Fig. 17.2 Geographical distribution of the smallest detectable amplitude at 1 km from a source located worldwide by one-station part of the full IMS infrasound network (white triangles) on January 1, 2013 (left) and on April 1, 2013 (right). Simulations are carried out at 0.8 Hz, using ECMWF temperature and wind models with and without incorporating 10 m/s wind speed perturbations at 50 km altitude. The colormap codes the minimum detectable source amplitude in Pa (peak-to-peak)

vortex breaks down following Sudden Stratospheric Warming (SSW) events (Charlton and Polvani 2007). In particular, for the zonal wind distribution, differences between wind radiometer data and ECMWF model results reach up to 30 m/s at 50 km altitude. Furthermore, above 30 km altitude, there is a variability found in the observations on shorter timescales that NWP models do not represent (Le Pichon et al. 2015).

Following these measurement campaigns, realistic uncertainties are incorporated into ECMWF products to assess the detection capability of the IMS network. For each simulation, we compute random perturbations of the along-path wind profiles

at 50 km altitude, in a range of 10 m/s. Figure 17.2 compares the global geographical coverage of the minimum signal amplitude detectable by one IMS station during the solstice and the equinox periods, with and without adding wind uncertainties. During the equinox period, in April, the zonal winds reduce and reverse yielding higher detection thresholds (e.g., Green and Bowers 2010). When incorporating wind uncertainties, almost no change in the detection thresholds is noted during the solstices as steady stratospheric winds prevail, while during the equinox periods, small wind perturbations significantly affect the thresholds.

Figure 17.3 presents the yearly fluctuations of the smallest signal amplitude detectable by the IMS network from January 2011 to January 2014. The graphs for different frequencies show the median and 95% confidence intervals of the global detection thresholds when incorporating wind perturbations. Due to the decrease of the noise levels with increasing frequency, improved detection capability is simulated at 1.6 Hz. The lowest detection thresholds are predicted between mid-May and mid-September when the prevailing stratospheric jet currents favor westward propagation. Simulations predict large seasonal and daily fluctuations in the thresholds following the general stratospheric wind circulation. As shown in Fig. 17.1, while the detection thresholds remain unchanged when winds prevail

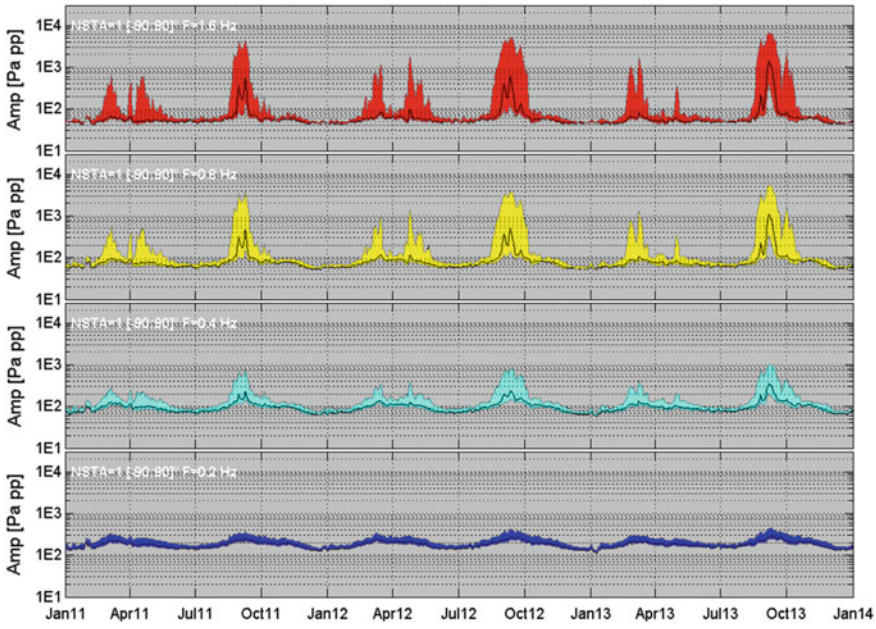

Fig. 17.3 Yearly fluctuation of predicted detection thresholds detectable by the IMS network with one-station coverage, at a 0.2, 0.4, 0.8, and 1.6 Hz (from bottom to top), from January 1, 2011 to January 1, 2014. The graphs show the median (black curve) and 95% confidence intervals (colored region) of the global detection thresholds (95% of the Earth coverage) when incorporating 10 m/s wind speed perturbations

(from June to July and from November to January), variations of one order of magnitude are noted around the equinox periods (April–September and March–October) and other intervals during which the atmosphere is in a state of transition. This step-like variation is more pronounced above 0.8 Hz whereas at lower frequencies, the attenuation is less sensitive to the strength and direction of the prevailing stratospheric winds.

17.3 Validation Using Repetitive Volcano Signals

Among the geophysical events detected by infrasound, volcanoes are unique and valuable impulsive sources to validate propagation and atmospheric remote sensing methods as they are often well instrumented in the near-field and at regional distances (e.g., Matoza et al. 2011; Dabrowa et al. 2014; Assink et al. 2014). Because of its regular activity, Mt. Etna in Italy (37.73°N, 15.00°E; 3330 m high) represents a natural repetitive source of signals to validate the simulated detection capability of the European infrasound network. Since July 2007, the University of Firenze (UNIFI, Italy) operates a small-aperture infrasound array (ETN) at a distance of approximately 5 km from the summit of Etna (e.g., Marchetti et al. 2009).

In case of major eruptions, signals from Etna can be detected at thousands of km. In particular, at a distance of about 550 km, Etna eruptions are well detected by the IMS station IS48 (Tunisia) from May to September during the downwind season due to an efficient westward stratospheric ducting (Tailpied et al. 2016). Figure 17.4 compares infrasound signals from Etna as observed at IS48 and ETN. Near-field data are useful to constrain the source activity, while far-field data provide information on atmospheric conditions along the propagation paths. From the signal amplitudes measured at IS48 and ETN, we derive the wave attenuation from January 2008 to January 2015 (Fig. 17.4a). Except from an interval lasting from 2009 and 2010, Etna has been quasi-permanently observed by IS48 from May to September. The effects of minor Sudden Stratospheric Warming (SSW) events, such as in January 2011, are clearly visible when the locally reversal of the stratospheric wind direction favored detections at IS48 also during winter. Overall, there is a first-order agreement between the observed and simulated attenuation. However, discrepancies are identified around some equinox periods and during anomalous wintertime intervals when the atmosphere is unstable (Smets et al. 2016).

Incorporating wind perturbations enlarges the detection periods by several weeks and resolves reasonably well the issue of unpredicted observations generally in September–October and March–April and during SSW events (Fig. 17.4b). While the effects of such perturbations on infrasound propagation dominate when stratospheric winds reduce and reverse, the effects are limited when stratospheric winds prevail. These deviations could be explained by misrepresented small-scale structures in ECMWF analysis (e.g., Assink et al. 2014). Alternatively, the observations could possibly be explained by partial reflections of infrasound due to

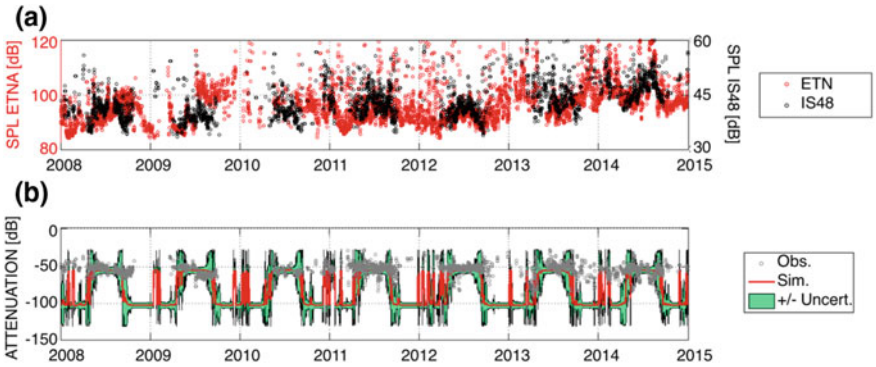

Fig. 17.4 Comparison between infrasound signals from Etna observed at IS48 and ETN, and predicted wave attenuation with and without incorporating wind uncertainties from January 2008 to January 2015. Simulations are carried out at the dominant frequency of the recorded signals (near 1.5 Hz). The upper frame **a** shows the sound pressure level (SPL) measured at Etna (in red, corrected for spreading to 1 km) and IS48 (in black). During summer, the downwind periods favor long-range propagation of signals from Mt. Etna, with a constant attenuation of about −50 dB. The lower frame **b** compares the predicted attenuation to the observed wave amplitude. Green patches delimit the 95% confidence of the predicted attenuation when incorporating 10 m/s wind perturbations at 50 km altitude. During the equinoxes, larger detection periods are noticed when incorporating these uncertainties (Tailpied et al. 2016)

steep vertical wind and temperature gradients in the upper stratosphere and the mesosphere, following the theory proposed by Kulichkov (2010).

17.4 Discussion and Conclusions

In this chapter, we evaluate the effects of small changes in the ECMWF temperature and wind profiles in the stratopause region on the IMS infrasound network detection capability. Such evaluation is useful for the verification of the CTBT, as current atmospheric specifications in the MA are essentially based on spatially and temporally averaged measurements that do not fully explain infrasound observations (e.g., Green et al. 2011).

During the course of the ARISE measurement campaigns, collocated lidar and wind radiometer profiles were used to evaluate ECMWF analyses where such models typically do not assimilate data (Blanc et al. 2019). Comparisons highlighted differences increasing with altitude. It was found that the modeled and observed temperatures and horizontal winds are in general agreement up to the stratopause, although significant small biases in both variables are noted. The largest deviations are observed above 50 km altitude and during winter months. Incorporating these uncertainties into network performance simulations allows assessing the sensitivity of the IMS network detection capability to small changes in

the stratospheric winds. The simulation results provide a good description of the global seasonal oscillation of the dominant zonal wind. In winter and summer, strong stratospheric winds are blowing in both hemispheres favoring long propagation range with a resulting improved detection capability. During the equinox periods, zonal winds reduce and reverse, yielding an increase of the source pressure amplitude. While incorporating atmospheric uncertainties yields almost no change in the detection thresholds during the solstices, significant variations are highlighted during the equinox periods when winds reduce.

Repetitive signals from Mt. Etna recorded by the station IS48 in Tunisia are used as benchmark case study for evaluating the simulation results. While a first-order agreement is found between observations and the simulation results, significant discrepancies are observed around the equinox periods and other intervals during which the atmosphere is in a state of transition. Including wind uncertainties in regions where the mean state of ECMWF products as well as its variability are subject to inaccuracies better explained unpredicted arrivals at IS48. These results indicate the potential benefit of monitoring well-identified repetitive sources to better determine the role of different factors that influence propagation predictions and more precisely infer atmospheric corrections (e.g., Smets et al. 2015). In return, improved understanding of the MA dynamics is an important step toward a successful monitoring regime for atmospheric or surface events. It is expected that continuing such studies will provide near-real-time realistic measure of the network performance and will be useful to optimize the design of future networks design to monitor regions of interest.

Beyond the context of the future verification of the CTBT, continuing such studies is helpful to promote the potential benefits of infrasound monitoring techniques for civil and scientific applications. In particular, such investigations are of considerable value for providing reliable source information and chronology of the eruptive processes on active volcanoes from local to long-range observations (Dabrowa et al. 2011; Fee and Matoza 2013; Mialle et al. 2015; Tailpied et al. 2016). The implementation of such an approach into automated eruption detection systems could lead to substantial improvements in infrasound monitoring of remote volcanic regions and provide valuable observations to prevent eruption disasters and mitigate the impact of ash clouds on aviation (Marchetti et al. 2019).

Acknowledgements All the data used in this work were collected by the University of Firenze (UNIFI), by IS48 in Tunisia and by the National Center of Cartography and Remote Sensing of Tunis in Tunisia. This work was partly performed during the course of the ARISE design study project, funded by the European Union under the H2020 Framework Programme (grant 653980).

References

Assink JD, Le Pichon A, Blanc E, Kallel M, Khemiri L (2014) Evaluation of wind and temperature profiles from ECMWF analysis on two hemispheres using volcanic infrasound. J Geophys Res Atmos 119:8659–8683. https://doi.org/10.1002/2014JD021632

Blanc E, Pol K, Le Pichon A, Hauchecorne A, Keckhut P, Baumgarten G, Hildebrand J, Höffner J, Stober G, Hibbins R, Espy P, Rapp M, Kaifler B, Ceranna L, Hupe P, Hagen J, Rüfenacht R, Kämpfer N, Smets P (2019) Middle atmosphere variability and model uncertainties as investigated in the framework of the ARISE project. In: Le Pichon A, Blanc E, Hauchecorne A (eds) Infrasound monitoring for atmospheric studies, 2nd edn. Springer, Dordrecht, pp 845–887

Brown D, Ceranna L, Prior M, Mialle P, Le Bras RJ (2014) The IDC seismic, hydroacoustic and infrasound global low and high noise models. Pure Appl Geophys 171:361–375

Campus P, Christie DR (2010) Worldwide observations of infrasonic waves. In: Le Pichon A, Blanc E, Hauchecorne A (eds) Infrasound monitoring for atmospheric studies. Springer, Berlin, pp 195–234

Ceranna L, Le Pichon A, Green DN, Mialle P (2009) The Buncefield explosion: a benchmark for infrasound analysis across Central Europe. Geophys J Int 177:491–508. https://doi.org/10.1111/j.1365-246X.2008.03998.x

Clauter DA, Blandford RR (1997) Capability modelling of the proposed international monitoring system 60-station infrasonic network. In: Proceedings of the infrasound workshop for CTBT monitoring, LA-UR-98–56, Santa Fe, New Mexico

Charlton AJ, Polvani LM (2007) A new look at stratospheric sudden warmings. Part I: climatology and modeling benchmarks. J Clim 20:449–469

Charlton-Perez AJ et al (2013) On the lack of stratospheric dynamical variability in low-top versions of the CMIP5 models. J Geophys Res Atmos 118:2494–2505. https://doi.org/10.1002/jgrd.50125

Christie D, Campus P (2010) The IMS infrasound network: design and establishment of infrasound stations. In: Le Pichon A, Blanc E, Hauchecorne A (eds) Infrasound monitoring for atmospheric studies. Springer, New York, pp 29–75

Dabrowa AL, Green DN, Rust AC, Phillips JC (2011) A global study of volcanic infrasound characteristics and the potential for long-range monitoring. Earth Planet Sci Lett 310(3):369–379. https://doi.org/10.1016/j.epsl.2011.08.027

Dabrowa AL, Green DN, Johnson JB, Rust A (2014) Comparing near-regional and local measurements of infrasound from Mount Erebus, Antarctica: implications for monitoring. J Volcanol Geotherm Res 288:46–61. https://doi.org/10.1016/j.jvolgeores.2014.10.001

De Groot-Hedlin CD, Hedlin MAH, Drob DP (2010) Atmospheric Variability and Infrasound Monitoring. In: Le Pichon A, Blanc E, Hauchecorne A (eds) Infrasound monitoring for atmospheric studies. Springer, New York, pp 475–507

Drob DP, Picone JM, Garcés MA (2003) The global morphology of infrasound propagation. J Geophys Res 108:4680. https://doi.org/10.1029/2002JD003307

Drob DP et al (2008) An empirical model of the Earth's horizontal wind fields: HWM07. J Geophys Res 113:A12304. https://doi.org/10.1029/2008JA013668

Drob DP, Broutman D, Hedlin MA, Winslow NW, Gibson RG (2013) A method for specifying atmospheric gravity-wave fields for long-range infrasound propagation calculations. J Geophys Res Atmos 118:3933–3943. https://doi.org/10.1029/2012JD018077

European Centre for Medium-Range Weather Forecasts (ECMWF) (2013) IFS documentation Cy38r1. Operational implementation 19 June 2012, Technical report, European Centre for Medium-Range Weather Forecasts, Reading, UK

Evers LG, Ceranna L, Haak HW, Le Pichon A, Whitaker RW (2007) A seismo-acoustic analysis of the gas-pipeline explosion near Ghislenghien in Belgium. Bull Seism Soc Am 97(2):417–425

Fee D, Matoza RS (2013) An overview of volcano infrasound: from Hawaiian to plinian, local to global. J Volcanol Geotherm Res 249:123–139. https://doi.org/10.1016/j.jvolgeores.2012.09.002

Fee D et al (2013) Overview of the 2009 and 2011 sayarim infrasound calibration experiments. J Geophys Res Atmos 118:6122–6143. https://doi.org/10.1002/jgrd.50398

Gainville O, Blanc-Benon Ph, Blanc E, Roche R, Millet C, Le Piver F, Despres B, Piserchia PF (2010) Misty picture: a unique experiment for the interpretation of the infrasound propagation

from large explosive sources. In: Le Pichon A, Blanc E, Hauchecorne A (eds) Infrasound monitoring for atmospheric studies. Springer, Berlin, pp 575–598

Garcés MA, Hansen RA, Lindquist KG (1998) Traveltimes for infrasonic waves propagating in a stratified atmosphere. Geophys J Int 135(1):255–263. https://doi.org/10.1046/j.1365-246X.1998.00618.x

Green DN, Bowers D (2010) Estimating the detection capability of the international monitoring system infrasound network. J Geophys Res 115:D18116. https://doi.org/10.1029/2010JD014017

Green DN, Vergoz J, Gibson R, Le Pichon A, Ceranna L (2011) Infrasound radiated by the Gerdec and Chelopechene explosions: propagation along unexpected paths. J Int, Geophys. https://doi.org/10.1111/j.1365-246X.2011.04975.x

Hedlin MAH, Drob DP (2014) Statistical characterization of atmospheric gravity waves by seismoacoustic observations. J Geophys Res Atmos 119. https://doi.org/10.1002/2013jd021304

Killeen TL, Wu Q, Solomon SC, Ortland DA, Skinner WR, Niciejewski RJ, Gell DA (2006) TIMED doppler interferometer: overview and recent results. J Geophys Res 111:A10S01. https://doi.org/10.1029/2005ja011484

Kulichkov S (2010) On the prospects for acoustic sounding of the fine structure of the middle atmosphere. In: Le Pichon A, Blanc E, Hauchecorne A (eds) Infrasound monitoring for atmospheric studies. Springer, New York, pp 511–540

Le Pichon A, Vergoz J, Blanc E, Guilbert J, Ceranna L, Evers L, Brachet N (2009) Assessing the performance of the international monitoring system infrasound network: geographical coverage and temporal variabilities. J Geophys Res 114:D08112. https://doi.org/10.1029/2008JD010907

Le Pichon A, Ceranna L, Vergoz J (2012) Incorporating numerical modeling into estimates of the detection capability of the IMS infrasound network. J Geophys Res 117:D05121. https://doi.org/10.1029/2011JD016670

Le Pichon A, Assink JD, Heinrich P, Blanc E, Charlton-Perez A, Lee CF, Keckhut P, Hauchecorne A, Rüfenacht R, Kämpfer N et al (2015) Comparison of co-located independent ground-based middle-atmospheric wind and temperature measurements with numerical weather prediction models. J Geophys Res Atmos 120. https://doi.org/10.1002/2015jd023273

Lingevitch JF, Collins MD, Dacol DK, Drob DP, Rogers JCW, Siegmann WL (2002) A wide-angle and high Mach number parabolic equation. J Acoust Soc Am 111. https://doi.org/10.1121/1.1430683

Marchetti E, Ripepe M, Ulivieri G, Caffo S, Privitera E (2009) Infrasonic evidences for branched conduit dynamics at Mt. Etna volcano, Italy. Geophys Res Lett 36:L19308. https://doi.org/10.1029/2009GL040070

Marchetti E, Ripepe M, Campus P, Le Pichon A, Brachet N, Blanc E, Gaillard P, Mialle P, Husson P (2019) Infrasound monitoring of volcanic eruptions and contribution of ARISE to the volcanic ash advisory centers. In: Le Pichon A, Blanc E, Hauchecorne (eds) Infrasound monitoring for atmospheric studies, 2nd edn. Springer, Dordrecht, pp 1141–1162

Matoza RS et al (2011) Long-range acoustic observations of the Eyjafjallajökull eruption, Iceland, April–May 2010. Geophys Res Lett 38:L06308. https://doi.org/10.1029/2011GL047019

Matoza R, Fee D, Green D, Mialle P (2019) Volcano infrasound and the international monitoring system. In: Le Pichon A, Blanc E, Hauchecorne A (eds)Infrasound monitoring for atmospheric studies, 2nd edn. Springer, Dordrecht, pp 1023–1077

Mialle P et al (2015) Towards a volcanic notification system with infrasound data, Oral T1.1-O4. In: Science and technology 2015 conference (CTBTO), 22–26 June, Vienna, Austria

Mialle P, Brown D, Arora N (2019) Advances in operational processing at the international data centre. In: Le Pichon A, Blanc E, Hauchecorne A (eds) Infrasound monitoring for atmospheric studies, 2nd edn. Springer, Dordrecht, pp 209–248

Smets PSM, Evers LG, Näsholm SP, Gibbons SJ (2015) Probabilistic infrasound propagation using realistic atmospheric perturbations. Geophys Res Lett 42. https://doi.org/10.1002/2015gl064992

Smets PSM, Assink JD, Le Pichon A, Evers LG (2016) ECMWF SSW forecast evaluation using infrasound. J Geophys Res Atmos 121. https://doi.org/10.1002/2015jd024251

Stevens JL, Divnov II, Adams DA, Murphy JR, Bourchik VN (2002) Constraints on infrasound scaling and attenuation relations from Soviet explosion data. Pure Appl Geophys 159:1045–1062

Sutherland LC, Bass HE (2004) Atmospheric absorption in the atmosphere up to 160 km. J Acoust Soc Am 115(3):1012–1032. https://doi.org/10.1121/1.1631937

Tailpied D, Le Pichon A, Marchetti E, Assink J (2016) Assessing and optimizing the performance and infrasound monitoring network. Geophys J Int 208. https://doi.org/10.1093/gji/ggw400

Waxler R, Assink J (2019) Propagation modeling through realistic atmosphere and benchmarking. In: Le Pichon A, Blanc E, Hauchecorne A (eds)Infrasound monitoring for atmospheric studies, 2nd edn. Springer, Dordrecht, pp 509–549

Whitaker RW (1995) Infrasonic monitoring. In: Paper presented at 17th annual seismic research symposium, LANL, Scottsdale, Arizona

Chapter 18
Advances in Infrasonic Remote Sensing Methods

Jelle Assink, Pieter Smets, Omar Marcillo, Cornelis Weemstra, Jean-Marie Lalande, Roger Waxler and Läslo Evers

Abstract Infrasound recordings can be used as input to inversion procedures to delineate the vertical structure of temperature and wind in a range of altitudes where ground-based or satellite measurements are rare and where fine-scale atmospheric structures are not resolved by the current atmospheric specifications. As infrasound is measured worldwide, this allows for a remote sensing technique that can be applied globally. This chapter provides an overview of recently developed infrasonic remote sensing methods. The methods range from linearized inversions to direct search methods as well as interferometric techniques for atmospheric infrasound. The evaluation of numerical weather prediction (NWP) products shows the added value of infrasound, e.g., during sudden stratospheric warming (SSW) and equinox periods. The potential transition toward assimilation of infrasound in numerical weather prediction models is discussed.

J. Assink (✉) · P. Smets · L. Evers
Seismology and Acoustics, Royal Netherlands Meteorological Institute (KNMI), P.O. Box 201, 3730 AE De Bilt, The Netherlands
e-mail: assink@knmi.nl; jelle.assink@knmi.nl

P. Smets · C. Weemstra · L. Evers
Faculty of Civil Engineering and Geosciences, Department of Geoscience and Engineering, Delft University of Technology, Stevinweg 1, 2628 CN, Delft, The Netherlands

O. Marcillo
EES-17, Geophysics Group Los Alamos National Laboratory, Los Alamos, NM 87545, United States

J.-M. Lalande
IMS (Univ. Bordeaux – CNRS – BINP), 351 Cours de la Libération, 33405 Talence Cedex, France

R. Waxler
National Center for Physical Acoustics, University of Mississippi University, Oxford, MS 38677, USA

A. Le Pichon et al. (eds.), *Infrasound Monitoring for Atmospheric Studies*,
https://doi.org/10.1007/978-3-319-75140-5_18

18.1 Introduction

Atmospheric specifications in the lower and middle atmosphere are routinely used in a wide variety of atmospheric sciences and its applications and are produced by NWP models. To initialize and constrain such models, data throughout the atmosphere is assimilated.

Various techniques exist that allow for in situ measurements of atmospheric properties. Radiosondes provide accurate wind and temperature profiles up to the lower stratosphere (near 30 km), but the information is limited to one location and the uncertainty in the measurements increases in the lower stratosphere. On a nearly global scale, satellite-based instruments allow for the indirect estimation of temperature and horizontal winds up to an altitude of about 50 km (e.g., AMSU-A). As no direct measurements are available in the region above 30 km, winds are determined through the use of the thermal wind relation, which couples the vertical gradient in wind to the horizontal gradient in temperature. Biases in satellite measurements—especially in the higher stratosphere—are of particular concern, as this may have an adverse effect on weather forecasts, even for near-term forecasts. This is further discussed by Lee et al. (2019).

While the influence of the troposphere on the stratosphere is well-known, observational, and modeling studies (Shaw and Shepherd 2008) have demonstrated that the stratosphere has an impact on the troposphere as well. Weather and climate forecasters are moving toward a more comprehensive representation of the atmosphere, in order to capture the stratospheric–tropospheric interactions, which could enhance long-term forecasts. Therefore, there is a current interest in the NWP community to validate model specifications at stratospheric altitudes using independent observations (Randel et al. 2004). This includes the analysis of potential satellite radiance measurement biases, the consideration of additional high-resolution measurements (gravity waves, momentum flux) that are currently not resolved in the model runs, and validation of currently employed gravity wave model parameterization schemes (Charlton-Perez et al. 2013).

One of the techniques that is useful for such evaluations is low-frequency acoustic sounding. As infrasound waves propagate over long distances through the troposphere, stratosphere, and mesosphere, infrasound recordings contain valuable information about the state of the atmosphere aloft (Fig. 18.1). The earliest uses of this technique date back to a century ago (Fujiwhara 1916; Whipple 1926). Today, various remote sensing techniques have surpassed acoustics in the determination of atmospheric properties at the spatiotemporal scales that are of interest for NWP.

However, the impact of the middle atmosphere on enhanced long-term weather forecasts and the relative inaccessibility of this region has lead to a renewed interest in alternative remote sensing techniques. Recently, significant advances have been made in the development of acoustic remote sensing techniques to probe inaccessible regions of the atmosphere with a very high spatiotemporal resolution. The presence of a worldwide infrasound network, including facilities from the International

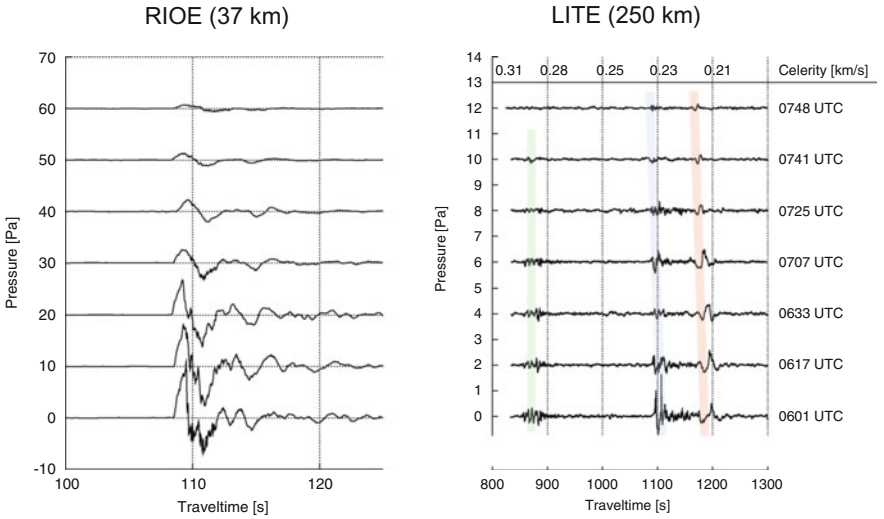

Fig. 18.1 Seven pairs of near-field (RIOE) and far-field (LITE) recordings of Mt. Tungurahua in Ecuador on 15 July 2006. Signals returning from the stratosphere, mesosphere, and lower thermosphere are marked green, blue, and red, respectively. The waveform structure and travel times (or celerity, defined as the distance between source and receiver divided by the travel time) have been used to infer properties of the wind and temperature at these altitudes, such as atmospheric tides (Assink et al. 2012, 2013) and gravity waves (Chunchuzov et al. 2015)

Monitoring System (IMS), has been useful as it provides an opportunity to monitor atmospheric wind and temperature on a regional to global scale.

Infrasonic remote sensing is not only useful for improving weather models, but can be beneficial for applications that require a precise modeling, such as the estimation of explosion location and yield. Atmospheric specifications are based on spatiotemporally averaged measurements that often do not fully explain infrasound observations. The first step comprises of the estimation of atmospheric updates to explain traveltime, trace velocity, and azimuth. Hereafter, signal duration can be used as an independent variable to estimate source yield (Kulichkov 2002; Lonzaga et al. 2015).

The remainder of this chapter is organized as follows. Section 18.2 provides a brief background of the sensitivity of infrasound to the atmosphere and discusses the relation between infrasound observables and temperature and wind. An overview of inverse methods for the estimation of temperature and wind profiles from infrasound data is discussed in Sect. 18.3. The potential of the infrasonic remote sensing method for NWP models is discussed in Sect. 18.4. Research in the field of interferometric techniques is discussed in Sect. 18.5. Finally, Sect. 18.6 summarizes the chapter.

18.2 Background

18.2.1 The Atmosphere as a Waveguide

18.2.1.1 Relevant Atmospheric Parameters

Infrasound propagation is sensitive to temperature, wind, and density (Brekhovskikh and Godin 1999). Figure 18.2 shows a conceptual model of these quantities for a stratified atmosphere. The temperature and density profiles in Fig. 18.2 are represented by polynomial fits to the US Standard Atmosphere (Lingevitch et al. 1999), the wind field is represented by a summation of sinusoids and Gaussian functions (Waxler and Assink 2019).

The division of the atmosphere into the various layers is related to the vertical temperature gradient. Significant features of the horizontal wind fields include the jet stream around the tropopause, the circumpolar vortex (or "stratospheric jet") around the stratopause and the atmospheric tides in the mesosphere and thermosphere. Generally, the zonal wind component is an order of magnitude larger than the meridional component. Vertical winds can typically be neglected for infrasound propagation, although these can be on the order of a few m/s in the mesosphere and thermosphere (Manson et al. 2002) and in deep convective regions of the troposphere. The exponential decrease in atmospheric density is due to the compressibility of air and the atmosphere's vertical extent.

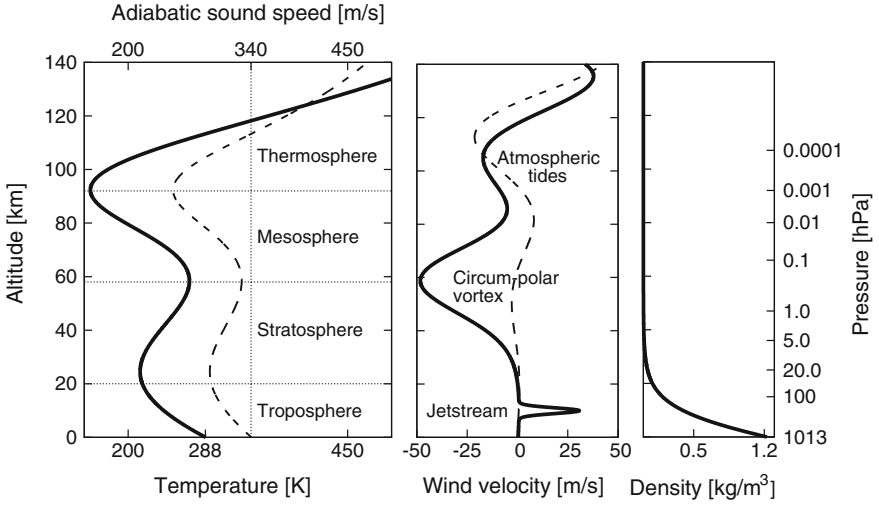

Fig. 18.2 A conceptual model of a boreal summer atmosphere's features at middle latitudes, based on the US Standard Atmosphere. Frames **a**–**c** show the absolute temperature (solid)/adiabatic sound speed (dashed), horizontal wind (zonal (W-E)—solid, meridional (S-N)—dashed), and density distribution up to 140 km altitude

In reality, the atmosphere is more variable as a function of altitude, time, and geographical location. In particular, the discussed temperature and wind features show a much finer structure. Hourly global atmospheric specifications with a high spatial resolution up to 0.1° (or ∼12 km) are currently available, e.g., through forecast systems of the European Centre for Medium-Range Weather Forecasts (ECMWF), the National Oceanic and Atmospheric Administration (NOAA) and the National Aeronautics and Space Administration (NASA). These models are mainly intended for medium-range forecasts on a global scale. An important aspect is that these models are hydrostatic, which implies that the vertical accelerations are considered to be small. Consequently, smaller scale processes for which vertical motions are critical (e.g., deep convection and higher frequency gravity waves) are parameterized. Such processes can be better resolved in non-hydrostatic mesoscale models.

Higher resolution, mesoscale models (e.g., HIRLAM, HARMONIE and WRF) are designed for the purposes of short-range weather forecasting on a more regional scale. Such models are nested and rely on global scale weather forecast models for the boundary conditions. HARMONIE and WRF are non-hydrostatic models, allowing for the computation of larger vertical velocities. These models are essential in the calculation of atmospheric gravity waves that lead to fine-scale structure, which has a significant effect on infrasound propagation (Drob et al. 2013; Chunchuzov et al. 2015). Besides gravity waves, various other phenomena contribute to fine-scale structure, including wind shear, Lee waves, and extreme weather.

The vertical extent of the global forecast systems currently reaches up to mesospheric altitudes (typically, 0.01 hPa or ∼80 km). However, the upper levels of the model, in the mesosphere, correspond to an absorptive sponge required for model stability. In addition, the models above the stratopause are currently unconstrained by data. The ground-to-space (G2S) model (Drob et al. 2003) combines the analysis products by NOAA and NASA with the mass spectrometer and incoherent scatter radar (MSIS) (Picone et al. 2002), and horizontal wind model (HWM) (Drob et al. 2008) climatologies in the upper mesosphere and thermosphere.

18.2.1.2 Atmospheric Infrasound Propagation

Infrasonic waves propagate in the atmosphere over large distances, in waveguides formed by the aforementioned temperature and wind speed variations and the Earth surface. Ground-to-ground propagation conditions are of particular interest given that most sources and receivers are ground-based, but similar concepts apply to elevated sources and receivers. Ducting is especially efficient in the tropospheric and stratospheric waveguides, because of geometrical spreading and absorption. Absorption is proportional to the acoustic frequency squared and inversely proportional to the ambient density. Hence, it is most significant in the mesosphere and lower thermosphere (Sutherland and Bass 2004). The thermospheric waveguide is therefore most efficient for the lowest infrasonic frequencies, below 0.5 Hz. Another consequence of the lower density is that nonlinear propagation effects (period lengthening and

wavefront steepening) become more significant at these altitudes. Period lengthening mitigates against signal attenuation (Lonzaga et al. 2015).

While the temperature structure forms the backbone of acoustic waveguides, (variations) in the winds are key in the determination of ducting conditions, in particular for the troposphere and stratosphere. In contrast to the lower thermosphere, the adiabatic sound speed around the tropopause and stratosphere is not sufficient to form a duct for ground-to-ground propagation, except at high latitudes where the Earth surface can be sufficiently cold. Hence, tropospheric and stratospheric propagation paths predominantly exist in the direction of the jet stream and circumpolar vortex. In exceptional cases, bidirectional stratospheric ducting conditions may exist, for example, during minor SSWs (Assink et al. 2014b).

The effective sound speed c_{eff} can be used to approximate to first order (Godin 2002) the effects of temperature T and horizontal wind $\mathbf{w}_{uv}$ in the direction of propagation ϕ:

$$\begin{aligned} c_{\text{eff}}(z) &= \sqrt{\gamma R T(z)} + \left|\mathbf{w}_{uv}(z)\right| \cos\left(\phi - \phi_{\mathbf{w}_{uv}}(z)\right) \\ &= c_T(z) + w_a(z) \end{aligned} \tag{18.1}$$

Here, $\gamma = 1.4$ and $R = 286.9\,\text{J}\,\text{kg}^{-1}\,\text{K}^{-1}$ are the ratio of specific heats and the specific gas constant for dry air, respectively. Note, that both propagation azimuth ϕ and wind direction $\phi_{\mathbf{w}_{uv}}$ are clockwise relative to the North. The orientation of the source and receiver locations determine the propagation azimuth ϕ. This angle is used to estimate the along-track wind (w_a) and cross-wind (w_c) components, by rotating the zonal (w_u) and meridional (w_v) components of the horizontal wind vector $\mathbf{w}_{uv}$.

$$\begin{pmatrix} w_a \\ w_c \end{pmatrix} = \begin{pmatrix} \sin\phi & \cos\phi \\ \cos\phi & -\sin\phi \end{pmatrix} \begin{pmatrix} w_u \\ w_v \end{pmatrix} \tag{18.2}$$

An example of infrasound propagating from a point source positioned on the ground at 0.5 Hz is shown in Fig. 18.3. The atmospheric model is somewhat typical of the boreal winter at mid-latitudes (20–60°N) and features a strong jet stream around 13 km and a circumpolar vortex around 60 km altitude. Zones of audibility are colored and represent the full-wave solution obtained by the method of normal modes (Waxler and Assink 2019; Assink et al. 2017); the dashed lines (rays) are approximately perpendicular to the wavefronts. Regions without significant acoustic energy are so-called "zones of silence". In reality, the zones of silence are filled in, for example, by scattering off small-scale structure (e.g., Chunchuzov et al. 2015).

The atmosphere is a highly dynamical medium, which leads to varying propagation characteristics around the globe (Le Pichon et al. 2005; Assink et al. 2014a). A consequence is that recorded infrasonic waveforms for repeated experiments vary drastically (Kulichkov 2010). In contrast, seismic arrivals tend to be relatively invariant over time. This suggests that the variability in the infrasonic waveforms can be

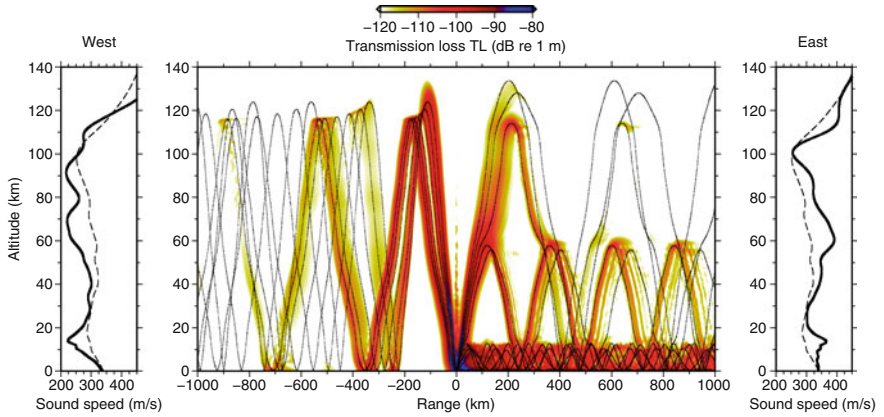

Fig. 18.3 Typical infrasound propagation conditions during the boreal winter. Effective sound speed profiles are shown on the sides with bold lines. The dashed curves in the center frame show the ray paths, dark colors indicate presence of acoustic energy at 0.5 Hz. Toward the west, infrasound propagates in the thermospheric waveguide, toward the east, infrasound propagates in the tropospheric, stratospheric, and thermospheric waveguides. Acoustic energy in the thermosphere is strongly attenuated, as indicated by the lighter colors with range

used to monitor atmospheric variability, especially in combination with seismic data from the same source. Gibbons et al. (2015) have analyzed repetitive seismo-acoustic sources in northern Scandinavia for this purpose. Donn and Rind (1972) used observations of signals from ocean wave interactions on seismic and infrasound stations (respectively microseisms and microbaroms) to monitor winds in the stratopause and lower thermosphere.

A more detailed discussion of infrasound propagation can be found by Waxler and Assink (2019).

18.2.2 Relating Wind and Temperature to Infrasound Wavefront Parameters

Consider a vertical plane through the atmosphere, intersecting source and receiver. As the atmosphere is predominantly a stratified medium, the in-plane and out-of-plane atmospheric quantities (respectively T, w_a and w_c), each have a specific influence on infrasound wavefront parameters. The former largely determine the vertical refraction along a great-circle path through vertical variations in sound speed and wind. This has an effect on the travel time (e.g., Assink et al. 2012)—as travel time and sound speed are directly related—as well as the trace velocity. The cross-winds control the out-of-plane propagation effects. This is measured as the deviation from the theoretical azimuth at a distant infrasound array.

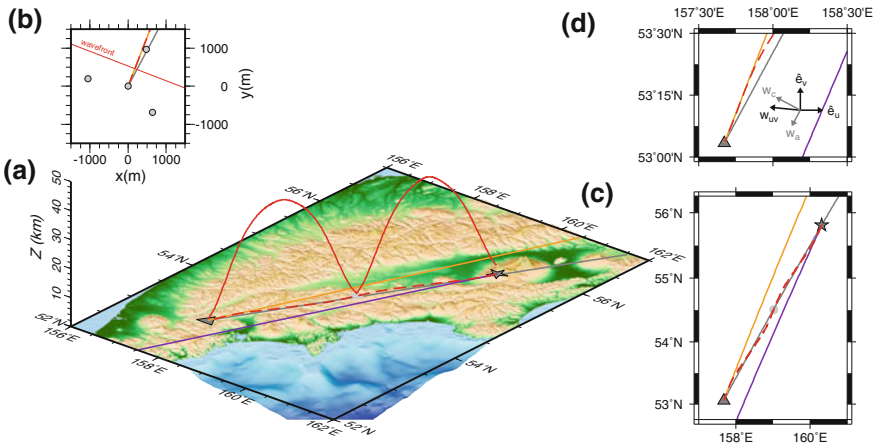

Fig. 18.4 **a** Map of the Kamchatka peninsula in Russian Federation (55.8°N, 160.3°E), **b** IMS array IS44 elements layout (triangles) with theoretical, observed and ray simulated back azimuth angles, all with respect to the array central element. The thin red line perpendicular to the observed back azimuth indicates the incoming planar wavefront. **c** Horizontal projection (top view) of (**a**) with the gray circle indicating the reflection at the ground. **d** Zoom in on (**c**), showing the receiver area with the observed and theoretical back azimuth angles. Figure adapted from Smets et al. (2016)

The azimuth deviation due to cross-wind w_c is illustrated in Fig. 18.4c, as the angle between the true azimuth (gray line) and the propagation azimuth (purple line) needed to arrive at the receiver location. Note that the propagation path is denoted by the dashed red line. At the receiver location, the observed back azimuth (orange line) does not point toward the source. Only in the hypothetical case of zero cross-wind, all four mentioned lines would align (e.g., Smets et al. 2016).

The trace velocity c_{trc} is the inverse of the horizontal projection of the slowness vector (defined as the inverse of the propagation velocity vector) and describes the horizontal propagation speed of a ray with grazing angle θ as $c_{\mathrm{trc}} = \frac{c_{\mathrm{eff}}}{\cos\theta}$. For a ray in a layered medium, trace velocity is invariant and is necessarily equal to or larger than the effective sound speed in that layer. At a ray's turning point (or return height) for which $\theta = 0°$, the trace velocity equals the effective sound speed at the return height, as illustrated in Fig. 18.5. This relationship allows for an immediate identification of return heights with associated (wide) range of trace velocities from an effective sound speed profile (Rind et al. 1973; Assink et al. 2014a; Bertin et al. 2014).

Thus, a complementary set of infrasound wavefront parameters exist that is sensitive to temperature and horizontal wind. Since these parameters can be determined using array processing techniques (e.g., Melton and Bailey 1957; Smart and Flinn 1971; Cansi 1995; Szuberla and Olson 2004), one could then invert for wind and

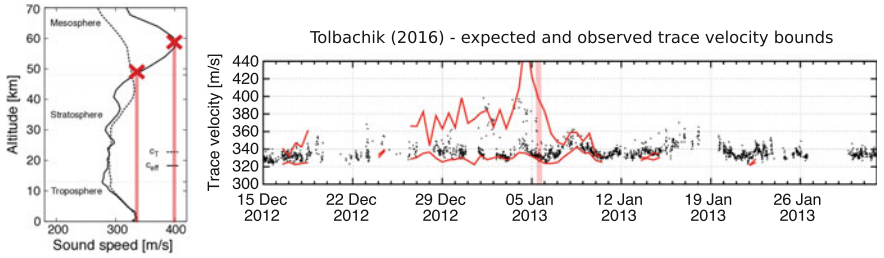

Fig. 18.5 In a layered medium, the minimum and maximum expected trace velocity can be estimated from an effective sound speed profile. This implies that trace velocity bounds can be used to estimate the return heights and corresponding sound speeds aloft

temperature in the atmosphere. In Sect. 18.3, methods are discussed that rely on ray theory. Inversion methods that use the full waveform to invert for small-scale atmospheric structure can be found by Chunchuzov and Kulichkov (2019).

18.2.2.1 The Temporal Variation of Infrasound Observations

As a consequence of the relation between atmospheric wind and temperature and infrasound wavefront parameters, temporal variations in these quantities will also be reflected in the infrasonic recordings. This illustrates the sensitivity of infrasound parameters to the upper atmosphere. Variations in upper atmospheric winds and temperatures with timescales ranging from (multi-)annual to hourly can in principle be identified by analyzing array processing results. In reality, matters can be complex due to complexities in infrasonic source characteristics, propagation paths, and adverse local wind noise conditions that may hamper detection.

Various insightful results have been obtained with the analysis of steady and impulsive infrasound sources, in particular, explosions (Kulichkov 2010) and volcanoes (Le Pichon et al. 2005; Antier et al. 2007; Assink et al. 2012), which have the advantage that the source location, timing, and frequency content are often well constrained (cf., Fig. 18.1). However, the sparsity of these sources lead to a need for a more ubiquitous and continuous source. Thanks to advances in microbarom source modeling (Waxler and Gilbert 2006), microbaroms become more and more in reach for atmospheric remote sensing (Smets and Evers 2014; Assink et al. 2014b).

The ratio of effective sound speed around the stratopause versus the ground (the effective sound speed ratio), controls to first approximation where ground-to-ground infrasound detections can be expected since ray-theoretic ground returns require a sound speed greater than or equal to that on the ground (Fig. 18.6). The circumpolar vortex determines to a large extent the effective sound speed around the stratopause.

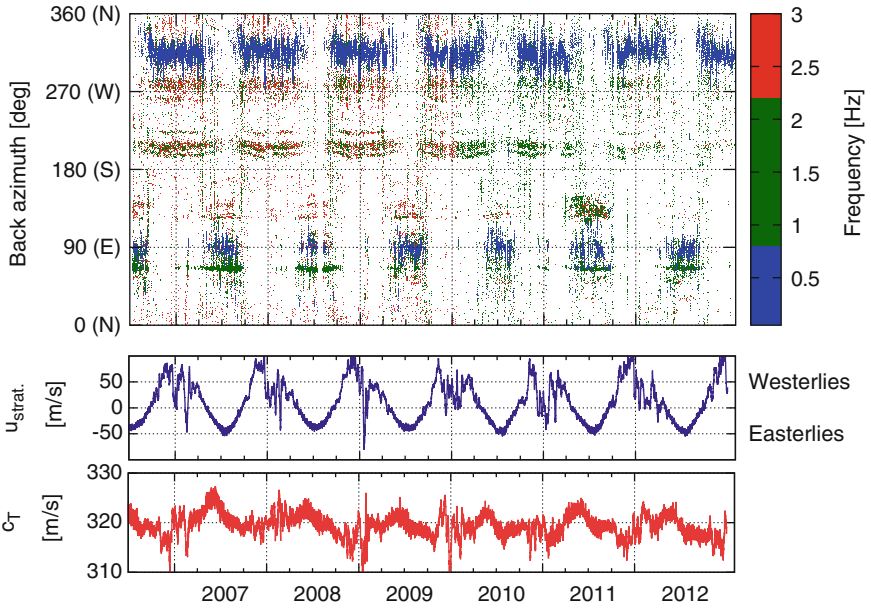

Fig. 18.6 Comparison of the stratospheric mean zonal wind and adiabatic sound speed with infrasound observations at CTBTO station IS48 in Tunisia (36°N). The zonal wind and sound speed are averaged between 5.0 and 0.2 hPa (resp. 36 and 60 km) and show the annual circulation of the circumpolar vortex including the sudden variations that are related to SSWs. The detectability of infrasound from a specific direction is related to stratospheric propagation conditions, which are largely controlled by the zonal wind

On a global scale, it was shown that the general trend in microbarom signal back azimuth recorded on the IMS network is consistent with the seasonal reversal of the circumpolar vortex (Fig. 18.7) (Garcés et al. 2004; Landès et al. 2012).

At shorter timescales, changes in the direction and intensity of the polar vortex determine the sensitivity of the arrays for sources located in specific directions. In particular, several studies have focused on the sensitivity to both minor (Assink et al. 2014b) and major (Donn and Rind 1972; Evers and Siegmund 2009; Smets and Evers 2014) SSW events. The study of SSW events, that constitute the most dramatic dynamics in the stratosphere, is of particular interest given the associated impact on the lower atmosphere (e.g., Lee et al. 2019). The study of SSWs using infrasound is further discussed by Smets et al. (2019).

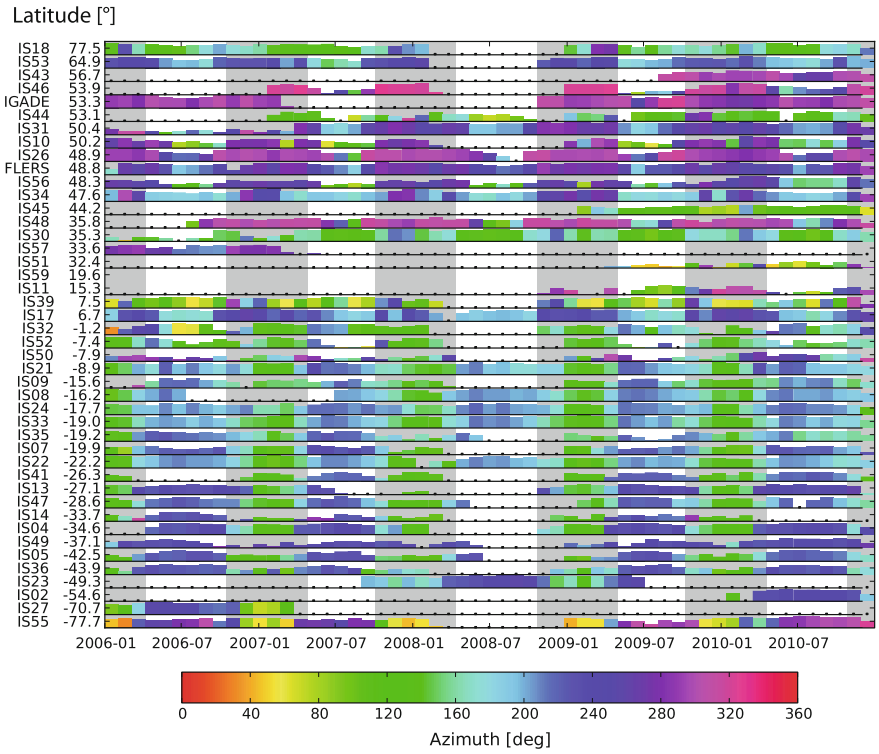

Fig. 18.7 Similar to Fig. 18.6, pointing out the trend in infrasound observations and seasons on a global scale. There is a clear relation to the effective sound speed ratio. Figure adapted from Landès et al. (2012)

18.3 Inverse Methods for Upper Atmospheric Temperature and Wind

The objective is to estimate the atmospheric wind and temperature profiles that explain ground-based infrasound observables. Infrasound wave front parameters recorded at infrasound arrays are used as input parameters. A representation of the profiles with a limited number of parameters ("model parameterization") is necessary, given the finite number of observables. This will be discussed in the following subsection. The forward problem describes how observables $\mathbf{d}$ and model parameters $\mathbf{m}$ are related through function $\mathbf{G}$:

$$\mathbf{d} = \mathbf{G}(\mathbf{m}) + \boldsymbol{\varepsilon} \tag{18.3}$$

Here, $\mathbf{G}$ and ϵ correspond to wave propagation (e.g., ray theory) and an error term, respectively. Thus, one is to solve the inverse to Eq. 18.3, thereby minimizing term ϵ.

The inverse problem is similar to the seismic tomography problem. This nonlinear inverse problem is ill-posed and therefore nonunique solutions exist. The nonuniqueness may arise due to approximations in the propagation theory (e.g., geometrical acoustics), model parameterizations, as well as the incomplete sampling of the atmosphere leading to some model parameters being better constrained by the data than others. Therefore, regularization of data and model spaces using apriori information and model appraisal are essential. A common regularization in inverse methods is Tikhonov regularization, which is a statistical regularization based on the covariance of both noise and model parameters (e.g., Snieder and Trampert 1999; Tarantola 2005).

All of the presented inversion methods throughout this section assume a stratified atmosphere. This is a reasonable approximation for propagation paths over regional distances (e.g., on the order of hundreds of kilometers). Consequently, these inversion methods can be used to invert for 1-D upper atmospheric structure in the vicinity of the infrasound array, although most of the sensitivity is confined to the refracting altitudes. Ongoing research efforts focus on the potential application of infrasound assimilation in NWP models. This requires a more global scale approach. A first step toward this is the evaluation of weather forecasts using infrasound, which is described in Sect. 18.4.

18.3.1 Parameterization of Atmospheric Profiles

In earlier studies, ad-hoc solutions have been considered as parameterizations, such as Gaussian correction factors (Le Pichon et al. 2005). Drob et al. (2010) proposed an empirical orthogonal function (EOF) analysis as parameterization method. EOF analysis allows for an efficient and appropriate description of the spatiotemporal variability of atmospheric profiles with limited degrees of freedom in the inversion. Various authors have since then adopted this method (e.g., Lalande et al. 2012; Assink et al. 2013; Arrowsmith et al. 2013; Lonzaga et al. 2015). Using EOFs, demeaned temperature and wind profiles (e.g., from ECMWF or G2S) are decomposed into a set of orthogonal functions, each scaled by a time-dependent coefficient. The original profiles can be recovered by evaluation of a sum:

$$\mathbf{m}(t,z) \approx \bar{\mathbf{m}}(z) + \sum_{n=1}^{N} \beta_n(t)\psi_n(z) \tag{18.4}$$

where $\bar{\mathbf{m}}(z)$, β_n and ψ_n represent the time-averaged profile, the model parameters and the EOFs, respectively. Wind and temperature profiles can be approximated by a limited number of terms (Drob et al. 2010). Truncation is not necessary, since the

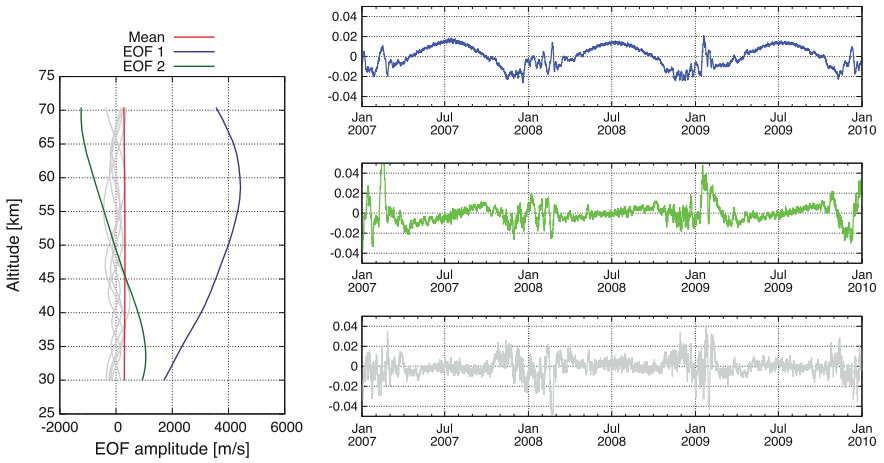

Fig. 18.8 Empirical orthogonal function (EOF) parameterization of three years of effective sound speed profiles between 30 and 70 km altitude for propagation from Mt. Etna to station IS48. The wind and temperature profiles are retrieved from ECMWF analysis. Most of the variance is described by two EOFs of the lowest order, with the higher order EOFs describing finer structure. The associated EOF coefficients are shown to the right. Figure adapted from Assink et al. (2014a)

EOFs are orthogonal and can be constructed to be sensitive to specific regions. Thus, the inverse problem is reduced to the estimation of (specific) model coefficients β_n (Assink et al. 2013; Lonzaga et al. 2015).

Infrasound propagation is sensitive to temperature and wind, which are dynamically linked through the equations of fluid dynamics. The thermal wind relation can be used to relate temperature and wind gradients in atmospheric regions where the geostrophic and hydrostatic balance applies (Andrews et al. 1987). This implies that formally temperature and wind cannot be treated independently in an inversion. In a first approach, it is assumed that the variations in wind are much larger than those in the temperature (Le Pichon et al. 2005; Drob et al. 2010; Lalande et al. 2012; Assink et al. 2013; Arrowsmith et al. 2013).

Alternatively, assuming an effective sound speed for a specific propagation azimuth, one can invert for an effective sound speed profile, taking the combined effects of wind and temperature into account. This is done by parameterizing a time series of effective sound speed profiles (Fig. 18.8) and modifying the effective sound speed EOF coefficients in the inversion procedure (Assink et al. 2014a).

Note that the imposed model parameterization imposes some form of regularization on the inversion. Using EOF analysis the inversion result will be constructed from the EOFs that are generated from the apriori models. For example, temperature and wind features with large vertical gradients are not represented as these are not present in NWP models. The retrieval of such inhomogeneities by considering partially reflected arrivals that reflect off these features, is discussed in Chunchuzov and Kulichkov (2019).

18.3.2 Solving the Inverse Problem

The solution of the inverse to Eq. 18.3 depends on the relation **G** between **d** and **m**. For linear problems, the resulting system of equations is straightforward to solve. Weakly nonlinear problems can be solved by iterative methods based on linearization, such as the Levenberg–Marquardt method. For strongly nonlinear problems in which local minima in model/data misfit are to be expected, the model space search is more involved. Various methods have been applied to solve the infrasonic inverse problem, including linearization (Lalande et al. 2012), nonlinear optimization (Le Pichon et al. 2005; Drob et al. 2010; Arrowsmith et al. 2013), and grid search methods (Assink et al. 2013). Current research focuses on the application of Monte Carlo methods that sample larger model spaces more efficiently (Sambridge and Mosegaard 2002).

18.3.2.1 Linearized Inversion

Lalande et al. (2012) have proposed an inverse method approach based on the linearization of geometrical acoustics operator **G**. This approach relies on Fermat's principle to linearly relate perturbations in travel time to perturbations in medium velocity along a reference ray. This is valid for small velocity perturbations only as the ray position is dependent on the medium velocity. The forward problem is treated in the high-frequency approximation using the Hamiltonian formulation where the complete first-order ray perturbation theory is developed in order to construct the Fréchet derivative matrix. An iterative conjugate gradient method is used to minimize the objective function. The model space is parameterized using EOFs. The choice of a starting model is a critical step since it should be located in the vicinity of the global minimum. In principle, model appraisal is feasible with iterative least-squares formalisms (Trampert and Leveque 1990).

Figure 18.9 shows example inversion results for the synthetic data set computed with NRL-G2S specifications for boreal summer conditions. For these relatively smooth wind profiles, without much fine vertical structure, the inversion works reasonably well as the original profiles are recovered successfully.

18.3.2.2 Nonlinear Optimization Methods

The study by Le Pichon et al. (2005) was the first one in the estimation upper atmospheric updates from actual infrasound data. Corrections to G2S profiles were found by correcting for unexplained observations of back azimuth values from a volcano, using a nonlinear optimization package.

This approach was further developed by Drob et al. (2010), solving Eq. 18.3 as a weighted orthogonal distance regression problem, in order to handle uncertainties in the data and model spaces. A software package (Zwolak et al. 2005) is used to

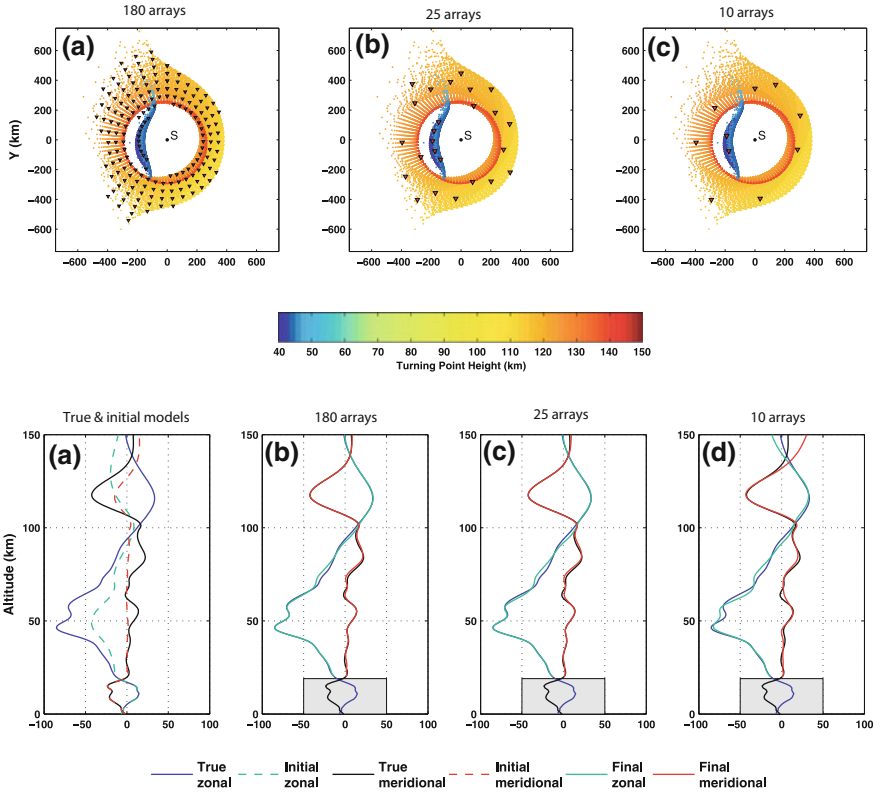

Fig. 18.9 Linearized inversion results obtained by the method of Lalande et al. (2012). Infrasound wavefront parameters are generated using ray theory and the wind profiles (solid lines, lower left frame). A subset of these points is sampled and used to invert for the wind model, using a different initial profile (dashed line, lower left frame). In all cases, the true model is retrieved

solve the regression problem and estimate a number of EOF parameters. The objective function is iteratively approximated within a trust region to find an update to the initial parameter guess. The Jacobian matrix, required to find next iteration, is approximated using finite differences. As with the linearized inversion method by Lalande et al. (2012), the algorithm is sensitive to local minima. The method uses the derivatives around the final solution to compute the 95% confidence intervals.

Arrowsmith et al. (2013) and Blom and Marcillo (2017) have extended the method to estimate stratospheric wind speeds from non-ground truth events using a network of infrasound arrays. In this approach, the celerity of a unique ray path (ducted in the stratosphere) is estimated from measurements made at distances covering a full stratospheric bounce (between 150 and 250 km). The estimated celerity is used to identify perturbations to an initial atmospheric specification that improve agreement between observed and predicted celerities.

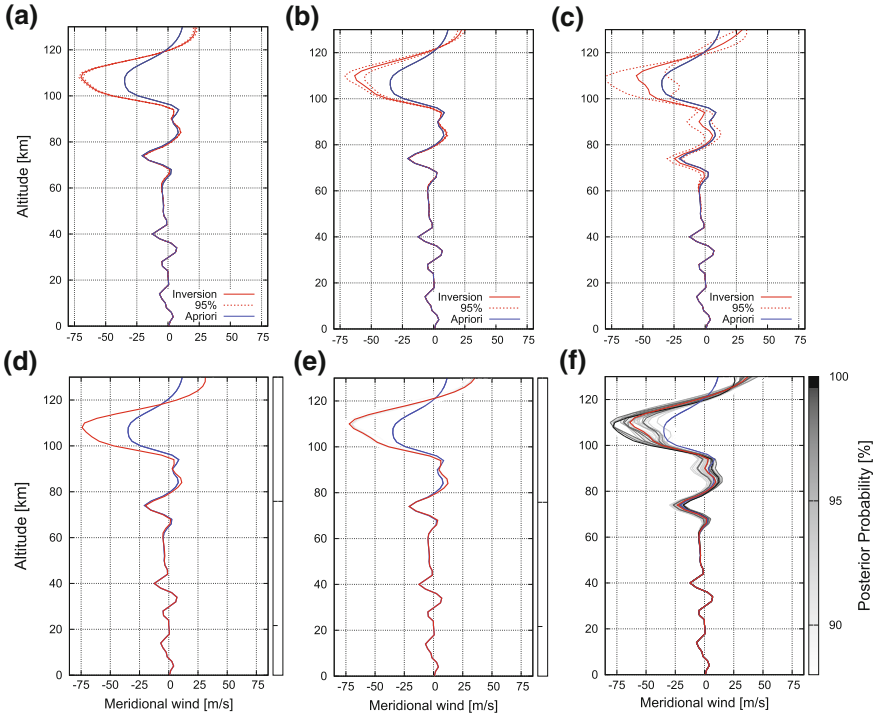

Fig. 18.10 Comparison of the methods described by Drob et al. (2010) and Assink et al. (2013) for a inversion case in which **a**–**d** two, **b**–**e** three and **c**–**f** four EOF parameters are adjusted

Although the search algorithm allows for a quick search and provides uncertainty estimates, it is not clear how well the algorithm can deal with nonlinearities in the objective function. Figure 18.10 shows a comparison between the optimization algorithm and a grid search (see next subsection). Although the methods compare well, more studies are required to see toward which extent such an approach can be used, for example, for cases for which nonlinearities due to interaction between different acoustic ducts becomes significant (Lalande et al. 2012).

18.3.2.3 Direct Search Methods

In some cases, direct search methods are the only option to search the model space for potential solutions due to nonlinearities in the objective functions. Large populations of models can be generated, e.g., using Monte Carlo techniques or grid searches if the model space is not too large (which is the case for specific problems). Generating populations can be computationally demanding, especially when the forward problem is numerically involved or the dimensionality of the model space is large.

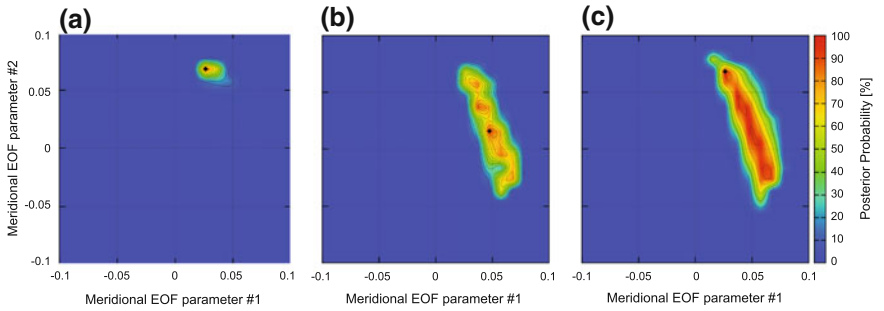

Fig. 18.11 Posterior probability for an inversion using a grid search where respectively **a** two, **b** three and **c** four parameters are varied. The uncertainty in traveltime and trace velocity are 1 s and 5 m s^{-1}, respectively. The addition of parameters to the search broadens the posterior distribution, as expected from the stochastic formulation. Figure adapted from Assink et al. (2013)

The advantage of direct search methods is that uncertainty analyses are easily incorporated. Grid searches in combination with Bayesian statistics have been used for the solution of thermospheric (Assink et al. 2013) and stratospheric (Assink et al. 2014a) inverse problems, allowing for an assessment of the posterior uncertainties. Posterior distributions σ are determined from the apriori model space $\rho(\mathbf{m})$ distribution and the likelihood function L (Tarantola 2005):

$$\sigma(\mathbf{m}|\mathbf{d}) \propto \rho(\mathbf{m})L(\mathbf{m},\mathbf{d}) \tag{18.5}$$

Both the likelihood function L and apriori model space $\rho(\mathbf{m})$ can be represented by a Gaussian probability density function (pdf). $\rho(\mathbf{m})$ expresses the likelihood of a model given apriori values and associated uncertainties, while L expresses how well the observations are predicted:

$$\rho(\mathbf{m}) = e^{-\frac{1}{2}\left[\left(\mathbf{m}(z)-\mathbf{m}_{\text{prior}}(z)\right)^T \mathbb{C}_M{}^{-2}\left(\mathbf{m}(z)-\mathbf{m}_{\text{prior}}(z)\right)\right]} \tag{18.6}$$

$$L(\mathbf{m},\mathbf{d}) = e^{-\frac{1}{2}\left[(\mathbf{G}(\mathbf{m})-\mathbf{d})^T \mathbb{C}_D{}^{-2}(\mathbf{G}(\mathbf{m})-\mathbf{d})\right]} \tag{18.7}$$

Here, the $\mathbb{C}_M$ and $\mathbb{C}_D$ covariance matrices describe uncertainties in model and data space. Typically, uncertainties between observations and model parameters are assumed to be uncorrelated, reducing $\mathbb{C}_M$ and $\mathbb{C}_D$ to diagonal matrices describing variances. When using EOF analysis, β replaces $\mathbf{m}$ in the aforementioned equations.

Figure 18.11 shows the posterior distributions for a grid search using volcanic infrasound data (Assink et al. 2013), where respectively (a) two, (b) three, and (c) four EOF parameters of the meridional wind field are adjusted, while others are kept fixed. It can be seen that the addition of parameters to the search leads to (1) an increase of posterior probability and (2) a broadening of the posterior distribution. This is consistent with the formulation of the posterior model as a linear combination

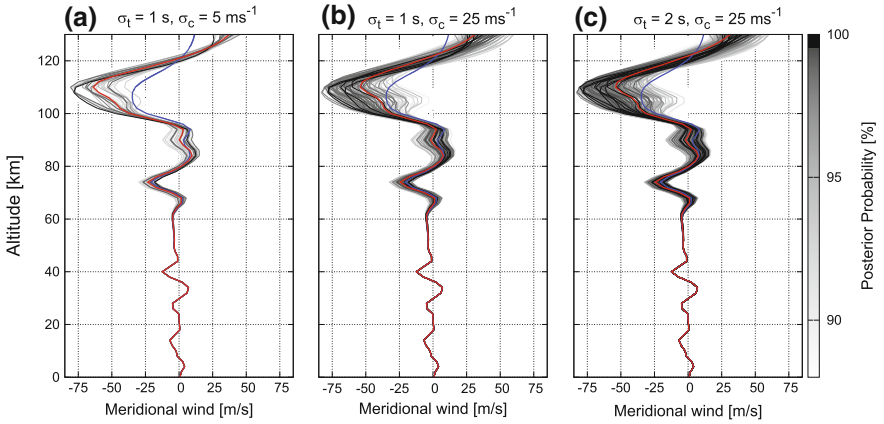

Fig. 18.12 Meridional wind profiles obtained from the posterior model distribution, for different choices of observational uncertainties. The model space is given by a uniform distribution centered within 50 m s^{-1} of the prior model. Figure adapted from Assink et al. (2013)

of stochastic variables. As expected, the posterior distribution also broadens when the observational uncertainty is increased (Fig. 18.12).

Another example of such an Bayesian inversion is presented in Fig. 18.13. The figure shows a comparison of infrasound parameters associated with Mt. Etna (black) with simulations using ECMWF profiles for the year 2008. Differences in observations and predictions of trace velocity (e.g., at the blue arrow) are used as an input for the inversion procedure for effective sound speed profiles (Assink et al. 2014a). An EOF parameterization (Fig. 18.8) is used to parameterize the model space. An example inversion for 2 October 2008 is shown on the right of Fig. 18.13 and suggests that during equinox periods, the effective sound speed profiles are underestimated.

18.4 Toward Assimilation in Numerical Weather Prediction Models

While significant progress has been made in the development of infrasonic remote sensing methods, the approaches are limited to inversions for 1-D atmospheric structure on a local scale. It is also important to realize that the scales of interest of atmospheric variability are different for infrasound monitoring and NWP modeling applications (Le Pichon et al. 2015). Thus, it may be of interest for the infrasound community to estimate upper atmospheric wind and temperature corrections for the precise modeling of infrasound arrivals (e.g., for explosion yield estimation) (Assink et al. 2013; Lonzaga et al. 2015).

However, for the assimilation of infrasound data in NWP models, there is a need to develop techniques on a more global scale. Instead of inverting observations to

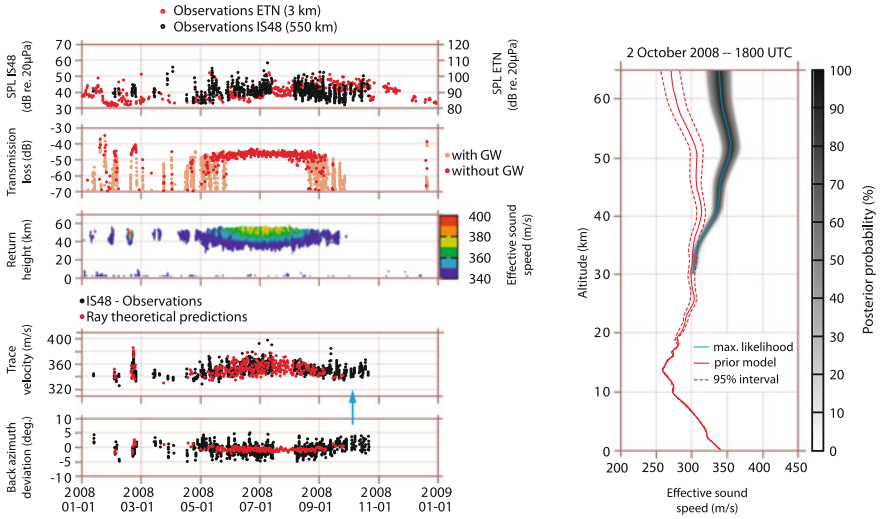

Fig. 18.13 Left: the two lower frames compare the predicted variations (red dots) with the observations (black dots). The middle frame shows the possible return heights of infrasound with the associated effective sound speed values. The two upper frames show the sound pressure levels near the source and receiver and the calculated transmission losses, respectively. The transmission losses are calculated using an ensemble of atmospheric profiles with gravity wave realizations. Right: an example Bayesian inversion of the effective sound velocity profiles for 2 October 2008 (blue arrow, left subfigure). The dotted red lines indicate the estimated 95% uncertainty interval around the apriori model state. The gray area corresponds to the posterior distribution of retrieved effective sound speeds. The maximum likelihood profile is represented by a solid cyan line. Figure adapted from Assink et al. (2014a)

atmospheric properties, a useful approach could be with the forward simulation of infrasound observables from NWP models, to be compared with global infrasound observations. Thus, rather than extracting atmospheric specification at one specific point in time and space with high detail, it might be more suitable to feed the assimilation with path integrated specifications. Such an approach would help to overcome current limitations (e.g., 1-D, uncoupled temperature and wind) and would be in line with existing assimilation strategy (e.g., 4D-Var). Moreover, the approach has already been applied to similar remote sensing techniques such as GPS Radio Occultation for the estimation of temperature. Such an effort should be carried in close collaboration with the NWP community; this has been one of the goals of the Atmospheric dynamics Research InfraStructure in Europe (ARISE) projects (Smets et al. 2014).

Before this effort is realized, infrasound data already represents a valuable resource to evaluate NWP models and help select which forecast members are more likely than others (Figs. 18.14 and 18.15). This shift in focus has lead to research on the evaluation of analyses (Assink et al. 2014a), ensemble members (Smets et al. 2015) as well as forecasts (Smets et al. 2016). In particular evaluations of

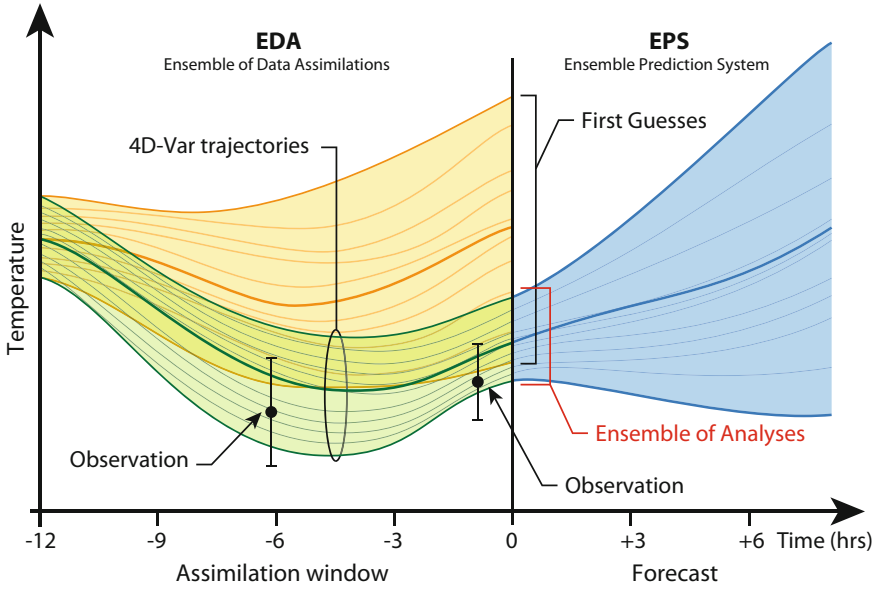

Fig. 18.14 Figure by ECMWF. Schematic overview showing the ensemble of data assimilation and prediction systems, such as used by NWP centers. Infrasound could be used to constrain which members of the ensemble are more likely than others. EDA and EPS are ECMWF products

SSW events, during which significant stratosphere–troposphere coupling may occur (Charlton and Polvani 2007), is of direct interest to the NWP community because the skills of NWP models in the stratosphere are then challenged.

18.5 Interferometric Techniques for Atmospheric Infrasound

In the majority of the studies that have previously been discussed, signals from steady (either transient or quasi-continuous) infrasound sources have been used. Notable examples are anthropogenic (accidental) explosions and volcanoes. Such sources, however, are relatively sparse. Because of its ubiquitous nature, microbaroms are a viable alternative for atmospheric imaging purposes. For example, both major (Evers and Siegmund 2009; Smets and Evers 2014) and minor (Assink et al. 2014b) SSW events have been detected using microbaroms. In addition, advances in microbarom source modeling (e.g., Waxler and Gilbert 2006) may aid such applications.

The ubiquitous nature of the microbaroms fosters the development of infrasonic remote sensing methods that can be applied to such type of coherent noise. For that purpose, so-called interferometric techniques are of particular interest. Applied to acoustic wavefields, interferometry refers to the principle of generating new

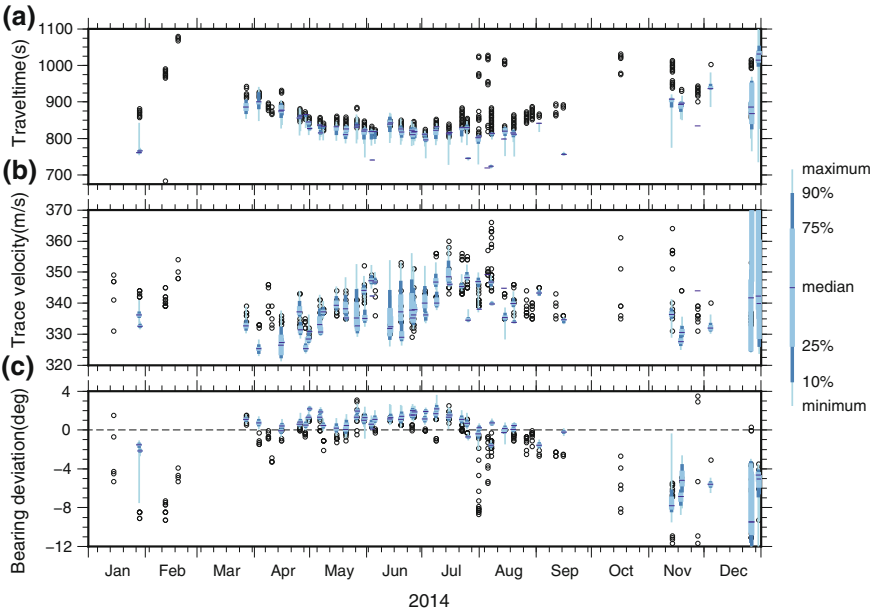

Fig. 18.15 Evaluation of a ensemble of analyses (see Fig. 18.14) using infrasound recordings of mine explosions (black dots). For each simulated event, the percentile distribution (blue) indicates the minimum, 10th centile, 25th centile, median, 75th centile, 90th centile, and the maximum value. Figure adapted from Smets et al. (2015)

acoustic responses from existing wavefields. By cross-correlating pressure fluctuations recorded by a pair of receivers, the medium's Green's function between the locations of those two receivers can be retrieved (e.g., Lobkis and Weaver 2001; Wapenaar and Fokkema 2006). In case of illumination by transient sources, an explicit summation over sources is required. Application to noise sources, however, renders this summation unnecessary. Instead, cross-correlations need to be averaged over a large amount of time (e.g., Godin et al. 2010; Weemstra et al. 2012). As such, the lack of correlation of the noise sources is exploited (Wapenaar and Fokkema 2006; Seats et al. 2012).

The relation between the time-averaged cross-correlation and the Green's function is only exact under specific conditions. The two most notable conditions are (i) a uniform illumination of the medium and (ii) the absence of dissipation (Wapenaar and Fokkema 2006). In practice, the violation of these conditions implies that only an estimate of that Green's function is retrieved (e.g., Weemstra et al. 2015). Nevertheless, as long as sufficient sources are present in the so-called stationary-phase directions (Snieder 2004), the retrieved Green's function estimate is sufficiently accurate to be exploited. Sources need only to be in the Fresnel zone to retrieve the stationary phase. For most interferometric applications, the medium parameters are assumed to be time-invariant. Implicitly, these applications rely on a so-called correlation-type

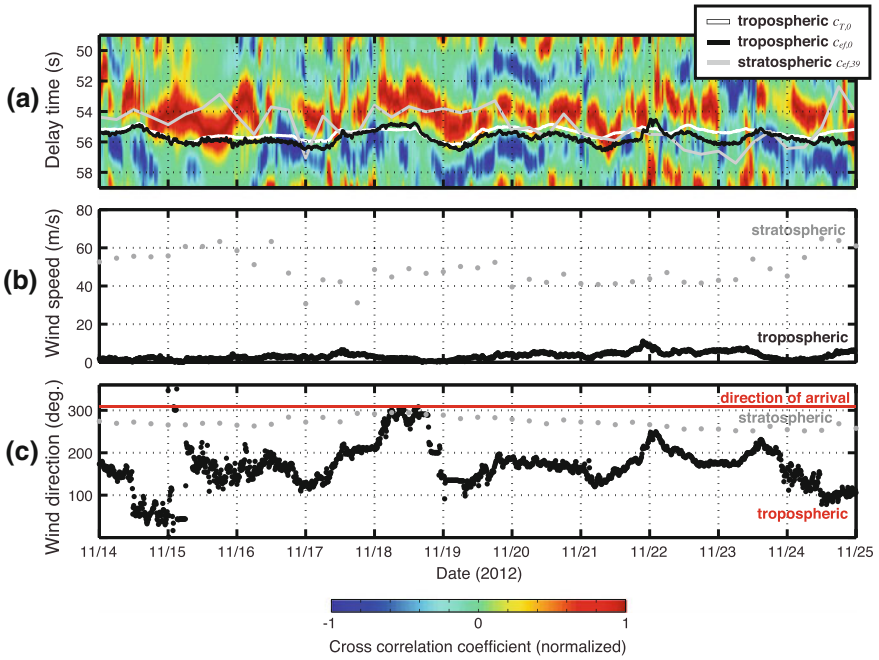

Fig. 18.16 Application of infrasonic interferometry to estimate tropospheric effective sound speed conditions. Figure adapted from Fricke et al. (2014)

reciprocity theorem (Wapenaar and Fokkema 2006). The first successful application of interferometry using microseisms (the seismic counterpart of microbaroms) is due to Shapiro and Campillo (2004). Interferometry has also been applied to other media and/or in other contexts: for example, helioseismology (Duvall et al. 1993), underwater acoustics (Roux and Kuperman 2004; Evers et al. 2017) and ultrasonics (Weaver and Lobkis 2001).

Infrasonic interferometry is based on the theory of nonreciprocal Green's function retrieval (Wapenaar and Fokkema 2006; Godin 2006). Nonreciprocity, due to the anisotropic propagation by wind, is overcome by reversing the horizontal wind for propagation in opposite directions. This holds for a laminar flow with a constant wind velocity. Once the delay time between two stations is found, it can be used to retrieve wind and temperature conditions (e.g., Marcillo and Johnson 2010; Godin 2014). In contrast to seismology, the averaging time is much shorter for infrasonic interferometry as the variability of the medium is on much smaller timescales.

Both Haney (2009) and Fricke et al. (2014) have demonstrated that it is possible to apply interferometry to tropospherically propagating microbarom signals that are in the stationary-phase direction. Thus, it is possible to estimate the changes of the tropospheric sound speed and the wind speed nearly continuously in time (Fig. 18.16). Infrasound produced by wind turbines, which can propagate tens of kilometers in tropospheric ducts is another source of quasi-continuous noise with the potential to be

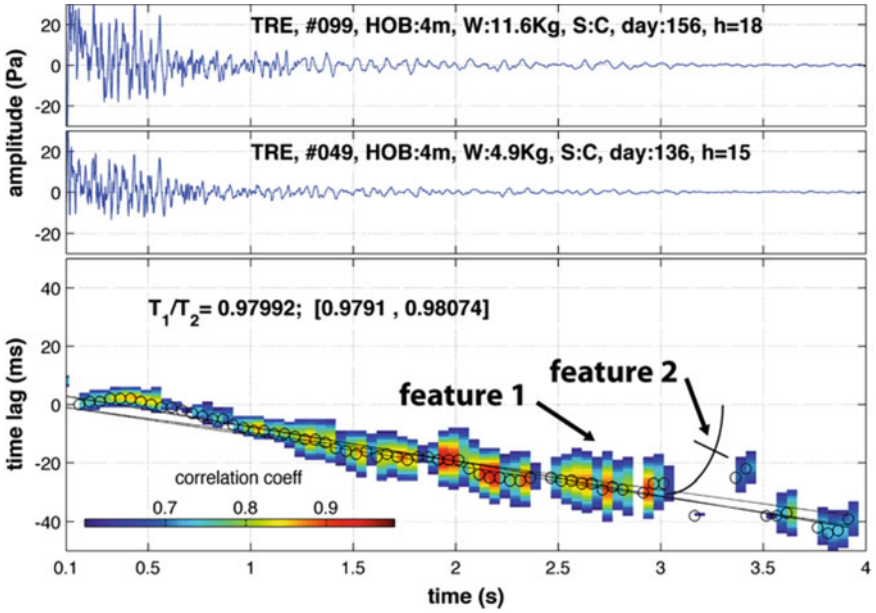

Fig. 18.17 The upper panels show the acoustic coda from two explosions (with different charge sizes) recorded at the same location 20 days apart. The lower panel shows the corresponding cross-correlogram (XC). Feature 2 in the XC is modeled as a variation in bulk air temperature that produces a small change in effective velocity. Adapted from Marcillo et al. (2014)

used for interferometric studies in the lower atmosphere (Marcillo et al. 2015; Pilger and Ceranna 2017). Coda wave interferometry (Snieder 2006) can also be applied to acoustic waveforms from the same source-sensor pair (assuming a discrete repeating source) to estimate changes in atmospheric conditions. Small time delays between similar features in the waveforms (relative to the signals' onset) are extracted and modeled as bulk changes in air temperature (Marcillo et al. 2014). An example of coda wave interferometry is shown in Fig. 18.17.

As such, the technique is useful for the evaluation of weather models near the ground surface, for example in the atmospheric boundary layer. This is of particular interest in regions with a limited number of in situ observations, e.g., over sea and around the equator. Stratospheric propagation between receiver pairs requires longer propagation distances and traveltimes, hence both the required period of constant illumination and the required time length of stationarity of the atmosphere increase. The application of this technique to stratospherically propagating signals therefore remains a challenge for the future.

18.6 Conclusions

The sensitivity of infrasound to atmospheric temperature and wind, the ability to propagate over large horizontal distances through the middle and upper atmosphere, and the presence of a global infrasound network make infrasound an interesting technique for atmospheric remote sensing. Over the recent years, significant progress has been made in the development of infrasonic remote sensing methods for the estimation of 1-D atmospheric structure. The developed methods range from linearized inversions to direct search methods. Current research focuses on the application of methods that sample larger model spaces more efficiently and interferometric techniques for atmospheric infrasound.

For the assimilation of infrasound data in NWP models, there is a need to develop techniques on a more global scale. Instead of inverting observations to atmospheric properties, a useful approach could be with the forward simulation of infrasound observables from NWP models, to be compared with global infrasound observations. Such an approach would be compatible with existing assimilation strategies. Application of this method in the evaluation of NWP weather products (ensembles of analyses, forecasts, climatologies) shows the added value of infrasound, e.g., during SSWs and equinox periods.

Acknowledgements This work was partly performed during the course of the ARISE design study project: part one (2012–2014) funded by European Union FP7 program (grant number 284387) and part two (2015–2017) funded by the European Commission H2020 program (grant number 653980). L.E.'s contribution is funded through a VIDI project from the Dutch Science Foundation (NWO), project number 864.14.005. The authors thank the CTBTO and station operators for the high quality of IMS data and products and would like to acknowledge the Acoustic Surveillance for Hazardous Eruptions (ASHE) project (Garcés et al. 2007).

References

Andrews DG, Holton JR, Leovy CB (1987) Middle atmosphere dynamics, 1st edn. Academic Press

Antier K, Le Pichon A, Vergniolle S, Zielinski C, Lardy M (2007) Multiyear validation of the NRL-G2S wind fields using infrasound from Yasur. J Geophys Res 112(D23110). https://doi.org/10.1029/2007JD008462

Arrowsmith S, Marcillo O, Drob DP (2013) A framework for estimating stratospheric wind speeds from unknown sources and application to the 2010 December 25 bolide. Geophys J Int 195(1). https://doi.org/10.1093/gji/ggt228

Assink JD, Waxler R, Frazier W, Lonzaga J (2013) The estimation of upper atmospheric wind model updates from infrasound data. J Geophys Res: Atmos 118(19):10,707–10,724

Assink JD, Pichon AL, Blanc E, Kallel M, Khemiri L (2014a) Evaluation of wind and temperature profiles from ecmwf analysis on two hemispheres using volcanic infrasound. J Geophys Res: Atmos 119(14):8659–8683

Assink JD, Waxler R, Smets P, Evers L (2014b) Bidirectional infrasonic ducts associated with sudden stratospheric warming events. J Geophys Res: Atmos 119(3):1140–1153

Assink JD, Waxler R, Drob DP (2012) On the sensitivity of infrasonic traveltimes in the equatorial region to the atmospheric tides. J Geophys Res 117. https://doi.org/10.1029/2011JD016107

Assink JD, Waxler R, Velea D (2017) A wide-angle high mach number modal expansion for infrasound propagation. J Acoust Soc Am

Bertin M, Millet C, Bouche D (2014) A low-order reduced model for the long range propagation of infrasounds in the atmosphere. J Acoust Soc Am 136(1):37–52. https://doi.org/10.1121/1.4883388

Blom PS, Marcillo OE (2017) An optimal parametrization framework for infrasonic tomography of the stratospheric winds using non-local sources. Geophys J Int 208(3):1557. https://doi.org/10.1093/gji/ggw449

Brekhovskikh LM, Godin O (1999) Acoustics of layered media II: point sources and bounded beams. Springer, Heidelberg, Germany, p 524

Cansi Y (1995) An automatic seismic event processing for detection and location: the P.M.C.C. method. Geophys Res Lett 22. https://doi.org/10.1029/95GL00468

Charlton AJ, Polvani LM (2007) A new look at stratospheric sudden warmings. Part I: Climatology and modeling benchmarks. J Clim 20:449–469

Charlton-Perez AJ, Baldwin MP, Birner T, Black RX, Butler AH, Calvo N, Davis NA, Gerber EP, Gillett N, Hardiman S, Kim J, Krüger K, Lee YY, Manzini E, McDaniel BA, Polvani L, Reichler T, Shaw TA, Sigmond M, Son SW, Toohey M, Wilcox L, Yoden S, Christiansen B, Lott F, Shindell D, Yukimoto S, Watanabe S (2013) On the lack of stratospheric dynamical variability in low-top versions of the CMIP5 models. J Geophys Res 118:2494–2505. https://doi.org/10.1002/jgrd.50125

Chunchuzov I, Kulichkov S (2019) Internal gravity wave perturbations and their impacts on infrasound propagation in the atmosphere. In: Le Pichon A, Blanc E, Hauchecorne A (eds) Infrasound monitoring for atmospheric studies, 2nd edn. Springer, Dordrecht, pp 551–590

Chunchuzov I, Kulichkov S, Perepelkin V, Popov O, Firstov P, Assink J, Marchetti E (2015) Study of the wind velocity-layered structure in the stratosphere, mesosphere, and lower thermosphere by using infrasound probing of the atmosphere. J Geophys Res: Atmos 120(17):8828–8840

Donn WL, Rind DH (1972) Microbaroms and the temperature and wind of the upper atmosphere. J Atmos Sci 29:156–172

Drob DP, Picone JM, Garcés MA (2003) The global morphology of infrasound propagation. J Geophys Res 108(4680)

Drob DP, Emmert JT, Crowley G, Picone JM, Shepherd GG, Skinner W, Hays P, Niciejewski RJ, Larsen M, She CY, Meriwether JW, Hernandez G, Jarvis MJ, Sipler DP, Tepley CA, O'Brien MS, Bowman JR, Wu Q, Murayama Y, Kawamura S, Reid IM, Vincent RA (2008) An empirical model of the Earth's horizontal wind fields: HWM07. J Geophys Res 113(A12304). https://doi.org/10.1029/2008JA013668

Drob DP, Meier RR, Picone JM, Garcés M (2010) Inversion of infrasound signals for passive atmospheric remote sensing. In: Le Pichon A, Blanc E, Hauchecorne A (eds) Infrasound monitoring for atmospheric studies, chapter 24. Springer, New York, pp 701–732

Drob DP, Broutman D, Hedlin MA, Winslow NW, Gibson RG (2013) A method for specifying atmospheric gravity-wave fields for long-range infrasound propagation calculations. J Geophys Res 118. https://doi.org/10.1029/2012JD018077

Duvall T, Jeffferies S, Harvey J, Pomerantz M (1993) Time-distance helioseismology. Nature 362(6419):430–432

Evers LG, Siegmund P (2009) Infrasonic signature of the 2009 major sudden stratospheric warming. Geophys Res Lett 36:L23808. https://doi.org/10.1029/2009GL041323

Evers LG, Wapenaar K, Heaney KD, Snellen M (2017) Deep ocean sound speed characteristics passively derived from the ambient acoustic noise field. Geophys J Int. https://doi.org/10.1093/gji/ggx061

Fricke JT, Evers LG, Smets PSM, Wapenaar K, Simons DG (2014) Infrasonic interferometry applied to microbaroms observed at the large aperture infrasound array in the netherlands. J Geophys Res 119. https://doi.org/10.1002/2014JD021663

Fujiwhara S (1916) On the abnormal propagation of sound waves in the atmosphere. Monthly Weather Rev 44(8):436–439. https://doi.org/10.1175/1520-0493(1916)44<436:OTAPOS>2.0.CO;2

Garcés M, Fee D, McCormack D, Servranckx R, Bass H, Hetzer C, Hedlin M, Matoza R, Yepes H (2007) Prototype ASHE volcano monitoring system captures the acoustic fingerprint of stratospheric ash injection. Inframatics 3

Garcés MA, Willis M, Hetzer C, Le Pichon A, Drob DP (2004) On using ocean swells for continuous infrasonic measurements of winds and temperature in the lower, middle, and upper atmosphere. Geophys Res Lett 31:l19304. https://doi.org/10.1029/2004GL020696.

Gibbons SJ et al (2015) The European arctic: a laboratory for seismoacoustic studies. Seismol Res Lett 86(3)

Godin OA (2002) An effective quiescent medium for sound propagating through an inhomogeneous, moving fluid. J Acoust Soc Am 112(4):1269–1275

Godin OA (2006) Recovering the acoustic greens function from ambient noise cross correlation in an inhomogeneous moving medium. Phys Rev Lett 97(5):054,301

Godin OA (2014) Dissipation of acoustic-gravity waves: an asymptotic approach. J Acoust Soc Am 136(EL411):411–417. https://doi.org/10.1121/1.4902426

Godin OA, Zabotin NA, Goncharov VV (2010) Ocean tomography with acoustic daylight. Geophys Res Lett 37(13):l13605

Haney MM (2009) Infrasonic ambient noise interferometry from correlations of microbaroms. Geophys Res Lett 36(19):L19808. https://doi.org/10.1029/2009GL040179

Kulichkov S (2002) Nonlinear acoustic phenomena in atmosphere. In: Nonlinear acoustics at the beginning of the 21st century, 16th international symposium on nonlinear acoustics (ISNA Moscow)

Kulichkov S (2010) On the prospects for acoustic sounding of the fine structure of the middle atmosphere. In: Le Pichon A, Blanc E, Hauchecorne A (eds) Infrasound monitoring for atmospheric studies, chapter 16. Springer, New York, USA, pp 511–540

Lalande JM, Sèbe O, Landès M, Blanc-Benon P, Matoza R, Pichon AL, Blanc E (2012) Infrasound data inversion for atmospheric sounding. Geophys J Int 190. https://doi.org/10.1111/j.1365-246X.2012.05518.x

Landès M, Ceranna L, Le Pichon A, Matoza RS (2012) Localization of microbarom sources using the IMS infrasound network. J Geophys Res: Atmos 117(D6):D06102. https://doi.org/10.1029/2011JD016684

Lee C, Smets P, Charlton-Perez A, Evers L, Harrison G, Marlton GJ (2019) The potential impact of upper stratospheric measurements on sub-seasonal forecasts in the extra-tropics. In: Le Pichon A, Blanc E, Hauchecorne A (eds) Infrasound monitoring for atmospheric studies. Springer, pp 889–910

Le Pichon A, Blanc E, Drob D, Lambotte S, Dessa JX, Lardy M, Bani P, Vergniolle S (2005) Infrasound monitoring of volcanoes to probe high-altitude winds. J Geophys Res: Atmos 110:d13106

Le Pichon A, Blanc E, Drob DP (2005) Probing high-altitude winds using infrasound. J Geophys Res 110

Le Pichon A, Assink JD, Heinrich P, Blanc E, Charlton-Perez A, Lee CF, Keckhut P, Hauchecorne A, Rüfenacht R, Kämpfer N, Drob DP, Smets PSM, Evers LG, Ceranna L, Pilger C, Ross O, Claud C (2015) Comparison of co-located independent ground-based middle atmospheric wind and temperature measurements with numerical weather prediction models. J Geophys Res: Atmos 120:8318–8331

Lingevitch J, Collins M, Siegmann W (1999) Parabolic equations for gravity and acousto-gravity waves. J Acoust Soc Am 105(6):3049–3056

Lobkis OI, Weaver RL (2001) On the emergence of the greens function in the correlations of a diffuse field. J Acoust Soc Am 110(6):3011–3017. https://doi.org/10.1121/1.1417528

Lonzaga JB, Waxler R, Assink JD, Talmadge C (2015) Modelling waveforms of infrasound arrivals from impulsive sources using weakly non-linear ray theory. Geophys J Int 200:1347–1361. https://doi.org/10.1093/gji/ggu479

Manson AH, Meek C, Koshyk J, Franke S, Fritts D, Riggin D, Hall C, Hocking W, MacDougall J, Igarashi K, Vincent R (2002) Gravity wave activity and dynamical effects in the middle atmosphere (60–90 km): observations from an MF/MLT radar network, and results from the Canadian Middle Atmosphere Model (CMAM). J Atmos Solar-Terr Phys 64(2):65–90

Marcillo O, Johnson JB (2010) Tracking near-surface atmospheric conditions using an infrasound network. J Acoust Soc Am 128(1):EL14–EL19. https://doi.org/10.1121/1.3442725

Marcillo O, Arrowsmith S, Whitaker R, Morton E, Scott Phillips W (2014) Extracting changes in air temperature using acoustic coda phase delays. J Acoust Soc Am 136(4):EL309–EL314

Marcillo O, Arrowsmith S, Blom P, Jones K (2015) On infrasound generated by wind farms and its propagation in low-altitude tropospheric waveguides. J Geophys Res: Atmos 120(19):9855–9868

Melton BS, Bailey LF (1957) Multiple signal correlators. Geophysics 22(3):565–588

Picone JM, Hedin A, Drob D, Aikin A (2002) NRL MSISE-00 empirical model of the atmosphere: statistical comparisons and scientific issues. J Geophys Res 107. https://doi.org/10.1029/2002JA009430

Pilger C, Ceranna L (2017) The influence of periodic wind turbine noise on infrasound array measurements. J Sound Vib 388:188–200

Randel W, Udelhofen P, Fleming E, Geller M, Gelman M, Hamilton K, Karoly D, Ortland D, Pawson S, Swinbank R, Wu F, Baldwin M, Chanin ML, Keckhut P, Labitzke K, Remsberg E, Simmons A, Wu D (2004) The SPARC intercomparison of middle-atmosphere climatologies. J Clim 17(5):986–1003

Rind DH, Donn WL, Dede E (1973) Upper air wind speeds calculated from observations of natural infrasound. J Atmos Sci 30:1726–1729

Roux P, Kuperman W (2004) Extracting coherent wave fronts from acoustic ambient noise in the ocean. J Acoust Soc Am 116(4):1995–2003

Sambridge M, Mosegaard K (2002) Monte Carlo methods in geophysical inverse problems. Rev Geophys 40(3). https://doi.org/10.1029/2000RG000089

Seats KJ, Lawrence JF, Prieto GA (2012) Improved ambient noise correlation functions using Welchs method. Geophys J Int 188(2):513. https://doi.org/10.1111/j.1365-246X.2011.05263.x

Shapiro NM, Campillo M (2004) Emergence of broadband Rayleigh waves from correlations of the ambient seismic noise. Geophys Res Lett 31(7)

Shaw TA, Shepherd TG (2008) Raising the roof. Nat Geosci 1:12–13. https://doi.org/10.1038/ngeo.2007.53

Smart E, Flinn EA (1971) Fast frequency-wavenumber analysis and Fisher signal detection in real-time infrasonic array data processing. Geophys J R Astron Soc 26:279–284

Smets PSM, Evers LG (2014) The life cycle of a sudden stratospheric warming from infrasonic ambient noise observations. J Geophys Res: Atmos 119(21):12,084–12,099

Smets PSM, Evers LG, Charlon-Perez AJ, Lee CF, Harrison RG (2014) Roadmap on the use of arise data for weather and climate monitoring in Europe. Technical report D5.5, Atmospheric dynamics research InfraStructure in Europe - ARISE - project, FP7 Grant Agreement nr 284387

Smets PSM, Evers LG, Näsholm SP, Gibbons SJ (2015) Probabilistic infrasound propagation using realistic atmospheric perturbations. Geophys Res Lett 42:6510–6517. https://doi.org/10.1002/2015GL064992

Smets P, Assink J, Läslo GE (2019) The study of sudden stratospheric warmings using infrasound. In: Le Pichon A, Blanc E, Hauchecorne (eds) Infrasound monitoring for atmospheric studies, 2nd edn. Springer, Dordrecht, pp 723–755

Smets PSM, Assink J, Le Pichon A, Evers LG (2016) ECMWF SSW forecast evaluation using infrasound. J Geophys Res: Atmos 121(9):4637–4650

Snieder R (2004) Extracting the greens function from the correlation of coda waves: a derivation based on stationary phase. Phys Rev E 69(4):046,610

Snieder R (2006) The theory of coda wave interferometry. Pure Appl Geophys 163(2):455–473

Snieder R, Trampert J (1999) Inverse problems in geophysics. In: Wirgin A (ed) Wavefield inversion. Springer, New York, pp 119–190

Sutherland LC, Bass HE (2004) Atmospheric absorption in the atmosphere up to 160 km. J Acoust Soc Am 115(3):1012–1030
Szuberla C, Olson J (2004) Uncertainties associated with parameter estimation in atmospheric infrasound arrays. J Acoust Soc Am 115(1)
Tarantola A (2005) Inverse problem theory and methods for model parameter estimation. Society for Industrial and Applied Mathematics
Trampert J, Leveque JJ (1990) Simultaneous iterative reconstruction technique: Physical interpretation based on the generalized least squares solution. J Geophys Res: Solid Earth 95(B8):12,553–12,559. https://doi.org/10.1029/JB095iB08p12553
Wapenaar K, Fokkema J (2006) Greens function representations for seismic interferometry. Geophysics 71(4):SI33–SI46
Waxler R, Gilbert K (2006) The radiation of atmospheric microbaroms by ocean waves. J Acoust Soc Am 119(5):2651–2661
Waxler R, Assink J (2019) Propagation modeling through realistic atmosphere and benchmarking. In: Le Pichon A, Blanc E, Hauchecorne (eds) Infrasound monitoring for atmospheric studies, 2nd edn. Springer, Dordrecht, pp 509–549
Waxler R, Assink JD, Velea D (2017) Modal expansions for infrasound propagation and their consequences for ground-to-ground propagation. J Acoust Soc Am
Weaver RL, Lobkis OI (2001) Ultrasonics without a source: thermal fluctuation correlations at MHz frequencies. Phys Rev Lett 87(13):134,301
Weemstra C, Boschi L, Goertz A, Artman B (2012) Seismic attenuation from recordings of ambient noise. Geophysics
Weemstra C, Snieder R, Boschi L (2015) On the estimation of attenuation from the ambient seismic field: inferences from distributions of isotropic point scatterers. Geophys J Int 203(2):1054
Whipple F (1926) Audibility of explosions and the constitution of the upper atmosphere. Nature 118:309–313
Zwolak JW, Boggs P, Watson LT (2005) ODRPACK95; a weighted orthogonal distance regression code with bound constraints. Technical report TR-04-31, Computer Science, Virginia Tech., U.S.A

Part VII
Evaluating and Improving Global Circulation and Climate Models and Weather Forecasts (GCM): Model Bias and Gravity Wave Characterization

Chapter 19
Continuous Middle-Atmospheric Wind Profile Observations by Doppler Microwave Radiometry

Rolf Rüfenacht and Niklaus Kämpfer

Abstract Observations of wind profiles in the upper stratosphere/lower mesosphere are challenging as the established measurement techniques based on in situ methods, radars or airglow spectrometers cannot cover this altitude range. Nevertheless, wind information from these altitudes is important for the assessment of middle-atmospheric dynamics in general and as basis for planetary wave or infrasound propagation estimates. Benefitting from recent developments in spectrometers and low-noise amplifiers, microwave radiometry now offers the opportunity to directly and continuously measure horizontal wind profiles at altitudes between 35 and 70 km. This is achieved by retrieving the wind-induced Doppler shifts from pressure broadened atmospheric emission spectra. The typical measurement uncertainties and vertical resolutions of daily average wind profiles lie between 10–20 m/s and 10–16 km, respectively. In this chapter, comparisons of the measured wind profiles to different ECMWF model versions and MERRA re-analysis data are shown. Moreover, the oscillatory behaviour of ECMWF winds is investigated. It appears that the longer period wave activities agree well with the observations, but that the model shows less variability on timescales shorter than 10 days.

R. Rüfenacht (✉)
Leibniz Institute of Atmospheric Physics, Schlossstrasse 6, 18225 Kühlungsborn, Germany
e-mail: ruefenacht@iap-kborn.de; Rolf.Ruefenacht@meteoswiss.ch

N. Kämpfer
Institute of Applied Physics, University of Bern, Sidlerstrasse 5, 3012 Bern, Switzerland
e-mail: niklaus.kaempfer@iap.unibe.ch

A. Le Pichon et al. (eds.), *Infrasound Monitoring for Atmospheric Studies*,
https://doi.org/10.1007/978-3-319-75140-5_19

19.1 Introduction

Wind measurements in the range between 35 and 70 km altitude are extremely rare. Despite past initiatives targeting at observations from this altitude range by space-borne instruments (Hays et al. 1993; Ortland et al. 1996; Baron et al. 2013), to date the only approach providing direct measurements of zonal and meridional wind profiles on a continuous basis is the recently developed technique of ground-based Doppler microwave radiometry. A novel wind lidar technique (Baumgarten 2010) offers better vertical and temporal resolution, but measurements are impossible under overcast sky and can only be obtained with an operator on site. Therefore, such an instrument is not able of delivering a continuous or near-continuous data series. Microwave wind radiometers on the other hand are only marginally affected by weather conditions and their operation can be highly automated what makes it possible to provide uninterrupted time series of middle-atmospheric zonal and meridional wind on a routine basis.

19.2 The Measurement Technique

Wind radiometers passively observe atmospheric emissions originating from rotational transitions of molecules. As the frequency of the emitted photons is governed by the quantum mechanical selection rules, the emission frequency ν_0 is sharply defined. In the event of a non-zero line-of-sight wind component v_{LOS}, the signal is Doppler shifted in frequency by

$$\delta\nu = \frac{v_{\mathrm{LOS}}}{c} \cdot \nu_0, \tag{19.1}$$

where c denotes the speed of light.

Moreover, the emission process is affected by collisions with other molecules what leads to the effect of pressure broadening of the spectral line. Therefore, the signal on the wings of the emission spectrum, far away from ν_0, predominantly originates from high-pressure environments, whereas the line peak in the vicinity ν_0 is dominated by emissions under low-pressure conditions. As the vertical pressure profile of the atmosphere is accurately known, this effect can be exploited to derive altitude-dependent wind information from spectrally resolved measurements of microwave radiation.

The effect of wind at different altitudes on the atmospheric emission spectra is illustrated in Fig. 19.1. It should, however, be noted that this figure shows the situation for unrealistically high wind speeds. In practice, the challenge lies in determining a tiny Doppler shift in the order of less than 10^{-7} of the observation frequency. The used heterodyne-type receivers thus need to feature a high spectral resolution, high-frequency stability, and low receiver noise.

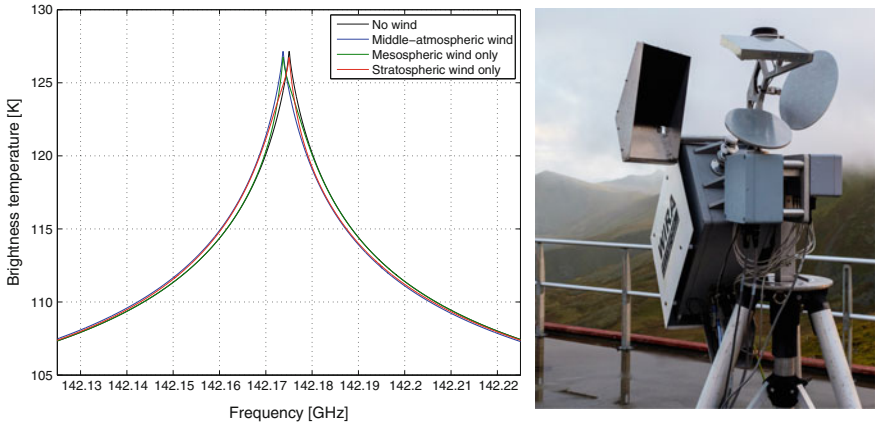

Fig. 19.1 **left:** Illustration of the effect of wind at different altitudes on ozone emission spectra as observable by ground-based radiometers at 142 GHz. For demonstration purposes, a wind speed of 3000 m/s has been chosen for these simulations which is far off any realistic values. The maximum wind speed in the middle atmosphere is generally below 150 m/s. **right:** The wind radiometer WIRA in operation in cloudy conditions

The mentioned frequency requirements can be achieved by the use of state-of-the-art Fourier transform spectrometers and stable local oscillator frequency references produced by actively multiplied synthesiser signals or Gunn oscillators phase locked to an oven-controlled quartz or GPS frequency normal. The receiver signal-to-noise ratio can be highly improved by the integration of high-frequency low-noise amplifiers and sideband filters on the radio frequency (RF) side of the mixer. Owing to recent developments in semiconductor technology, such amplifiers have become available at frequencies suitable for wind radiometry. Lower noise levels could be achieved by using cryogenic receiver electronics. The price for the higher sensitivity would, however, be a loss in autarchy, weathering resistance and transportability of the instrument what might be supportable for laboratory instruments but excludes this option for campaign radiometers. For the determination of the wind profiles from the measured radiation spectra, the atmospheric radiative transfer model is inverted by using the optimal estimation technique (Rodgers 2000). A detailed description of optimal estimation wind profile retrievals from ground-based microwave radiometers including the assessment of measurement uncertainties can be found in Rüfenacht et al. (2014), Rüfenacht and Kämpfer (2017), Rüfenacht et al. (2019).

Worldwide, there are currently three ground-based microwave radiometers capable of wind profile retrievals (Rüfenacht et al. 2012; Hagen 2015; Fernandez et al. 2016). They provide continuous observations of daily average wind profiles between altitudes of 10 and 0.01 hPa (approx. 35–70 km) with typical uncertainties ranging from 10 to 20 m/s and vertical resolutions between 10 and 16 km. A picture of such an instrument is shown in Fig. 19.1.

19.3 Observations of Zonal and Meridional Wind

From the three existing radiometers capable of Doppler wind measurements, the ground-based receiver WIRA (Rüfenacht et al. 2012, 2014) has acquired most observational data. Between 2010 and 2015, it has been measuring at four stations located at high (Sodankylä at 67°22' N, 26°38' E), mid (Bern at 46°57 N, 7°26 E and Observatoire de Haute-Provence at 43°56' N, 5°43' E) and low latitudes (Observatoire du Maïdo, La Réunion at 21°04' S, 55°23' E). Figures 19.2 and 19.3 display the time series of zonal and meridional wind profiles as measured by WIRA during these campaigns. The grey horizontal lines identify the upper and lower limit of the altitude range within which the measurements are judged trustworthy (according to conditions defined in Rüfenacht et al. 2014). Meridional wind measurements are only available since a major instrumental upgrade in autumn 2012. In Figs. 19.2 and 19.3, the most prominent data gaps originate from down periods of the instrument (due to a tropical cyclone necessitating the dismounting of the instrument, a loose connector, etc.). Apart from these few interruptions, the figures illustrate the long-term continuity which can be achieved by wind radiometer observations even under adverse

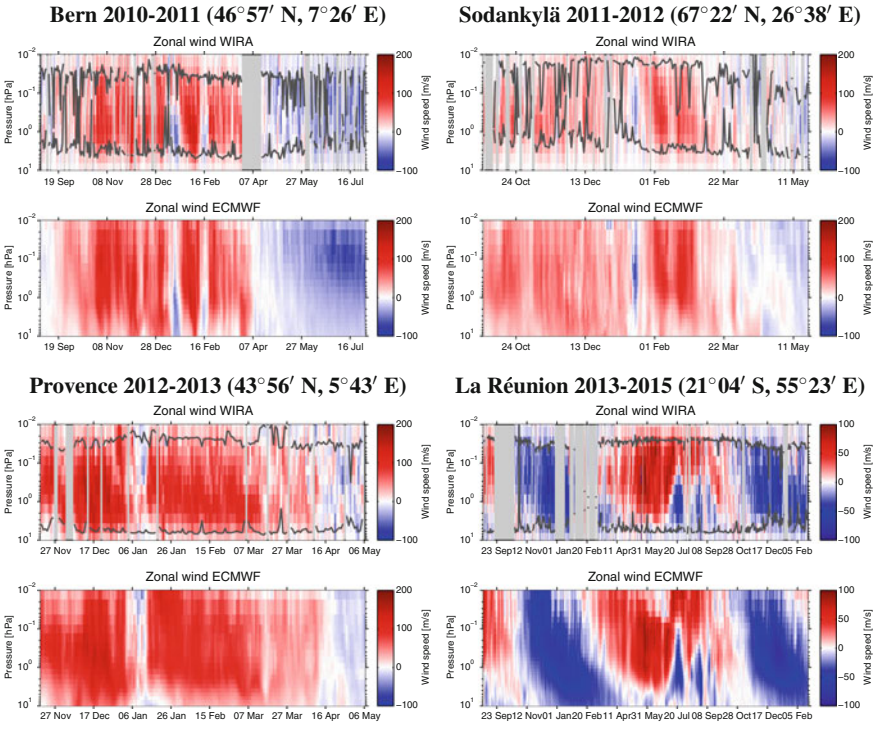

Fig. 19.2 Zonal wind profiles measured by WIRA in comparison with ECMWF operational analysis data

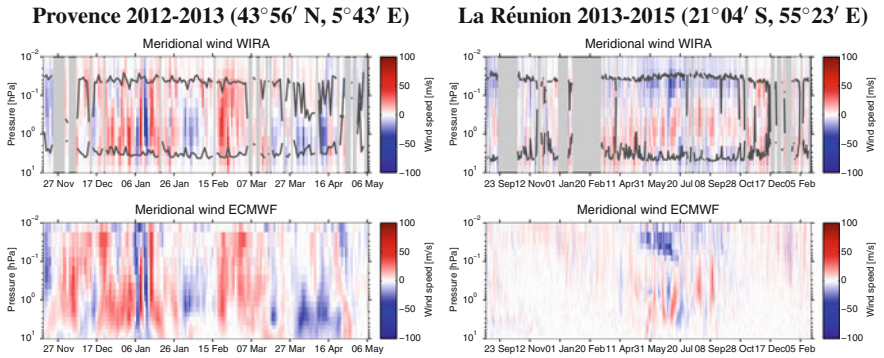

Fig. 19.3 Meridional wind profiles measured by WIRA in comparison with ECMWF operational analysis data

weather conditions. Due to the relatively long wavelength of microwave radiation, measurements remain possible under overcast skies or in the event of frozen precipitation, only particularly strong tropospheric attenuation caused by high liquid water contents in the presence of rain or thick liquid water clouds can temporarily suspend the observations. Moreover, a high degree of automation of microwave radiometers can be achieved.

19.3.1 Comparing Wind Radiometer Observations to General Circulation Models

The continuous nature of the observations and the fact of being unbiased to certain weather patterns make wind radiometers ideal tools for assessing the quality of middle-atmospheric dynamics in global circulation models (GCM). Such assessments are not only of interest in order to uncover possibilities for further model developments. Due to the scarcity of wind measurements in the middle atmosphere, the background wind for calculating the propagation of infrasound or gravity waves is usually taken from some GCMs.

Operational analysis data from the GCM of the European Centre for Medium-Range Weather Forecasts ECMWF (ECMWF 2017) are plotted in the panels below the radiometer observations in Figs. 19.2 and 19.3. They agree well with the observations in the larger structures such as the annual cycle for the mid- and high latitude stations or the mixed influence of the semi-annual oscillation and annual cycle for La Réunion. Even shorter, highly dynamical features such as the wind reversals associated with sudden stratospheric warmings or vortex displacement events are relatively well captured.

For quantitative comparisons between models and radiometer observations, the model data should be convolved with the averaging kernels of the radiometer

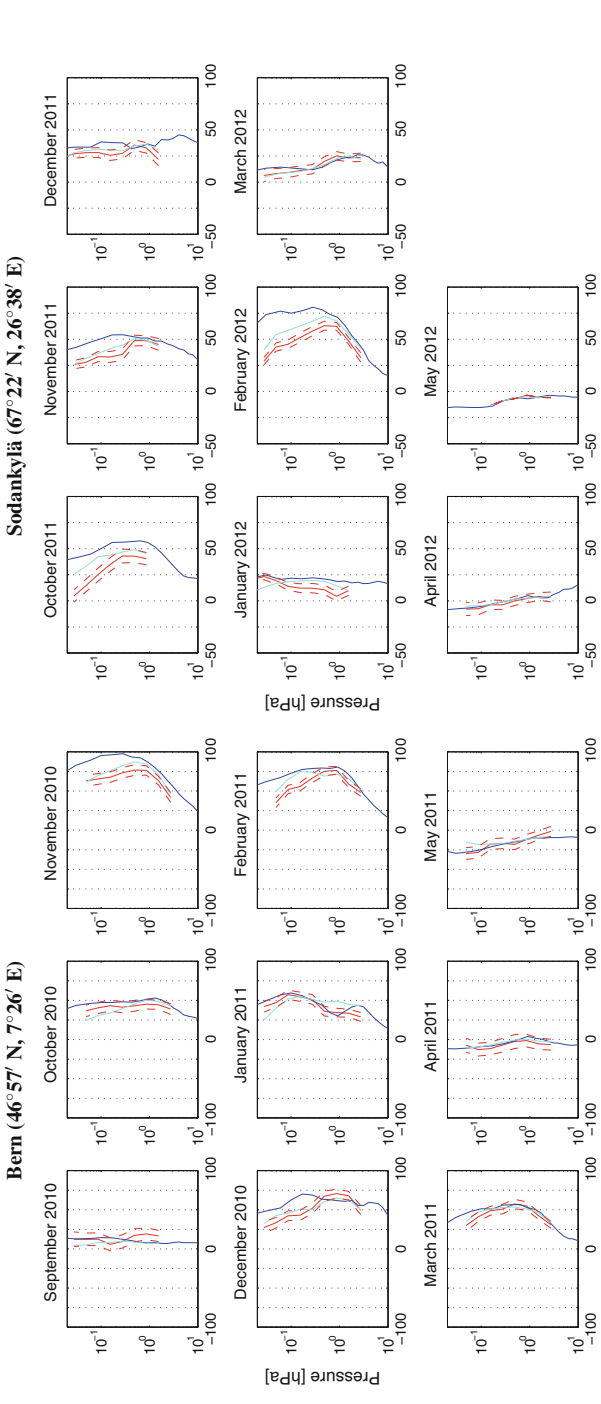

Fig. 19.4 Monthly averaged zonal wind profiles (median) from WIRA along with their random error (red), model data from ECMWF operational analysis (blue) and ECMWF data convolved with WIRA's averaging kernels (cyan). These panels present data from the Bern and Sodankylä campaigns which were obtained with the first operational version of the instrument. The panels in the continuation of the figure on the next page show the observations from the Provence and La Réunion campaigns which were obtained with an upgraded version of the receiver

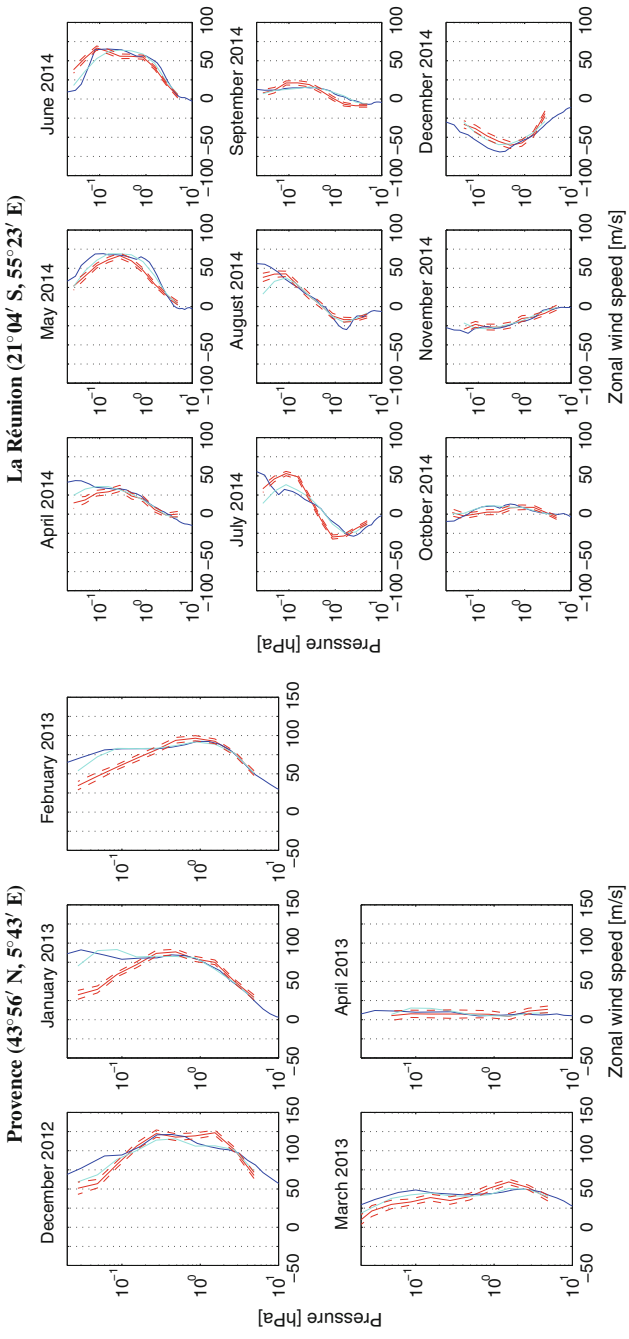

Fig. 19.4 (continued)

measurements (Rodgers 2000), in order to account for the limited altitude resolution of the measurements. Moreover, artificial data gaps have been added to the model data at altitudes and times where WIRA was not able to provide measurements. Model data treated in this way are directly comparable to the observations. Monthly averages of zonal wind from ECMWF and WIRA are compared in Fig. 19.4. Convolved model data and observations generally agree within their errors. Notable exceptions are the higher ECMWF absolute wind speeds at mesospheric altitudes which occur during certain months at mid- and high latitudes. These are especially present in the observations from Provence. This period is investigated in more detail in Fig. 19.5. In addition to the data from ECMWF 37r3 being the observational version by this time, data from ECMWF 38r1 are shown. The major upgrade from ECMWF from 37r3 to 38r1 which comprised among others the increase from 91 to 137 model levels had drastically reduced the mesospheric discrepancy in temperature between model data and lidar observations (Le Pichon et al. 2015). Similarly, for zonal wind, the discrepancy is significantly reduced. However, the winds in the model remain slightly stronger than in the observations. In contrast, the MERRA re-analysis of the GEOS-5 general circulation model (Rienecker et al. 2011) rather indicates lower zonal wind speeds than measured by WIRA. No definite tendency for under or overestimation could be established for the meridional winds.

19.4 Assessment of Oscillation Activity

Waves and oscillations play a fundamental role in the dynamics of the middle atmosphere. Thanks to the continuous nature of the observations by wind radiometry, such periodicities can be assessed. In a study on long-period oscillations in the middle-atmospheric zonal and meridional wind field (Rüfenacht et al. 2016), observations from WIRA have been compared to ECMWF model data. The results are summarised in Figs. 19.6 and 19.7 showing time series of oscillation amplitudes at the stratopause for WIRA and ECMWF. This altitude has been chosen because wind speeds tend to reach their middle-atmospheric maximum at this level and because the average winds of ECMWF and WIRA agree well in this region.

Obviously, observations and model capture the same dominant periodicities. The agreement on the timing of the peaks in oscillation activity at the different periods is excellent. Nevertheless, ECMWF appears to incorporate lower oscillation amplitudes in comparison with WIRA. Moreover, variations at periods shorter than about 10 days are less present in the model data. This fact cannot fully be explained by the presence of measurement noise but might be related to some modelling issues. Similarly, Le Pichon et al. (2015) had reported on the underestimation of the short periodicities in ECMWF's middle-atmospheric temperature field at lidar observation sites in Europe and North America.

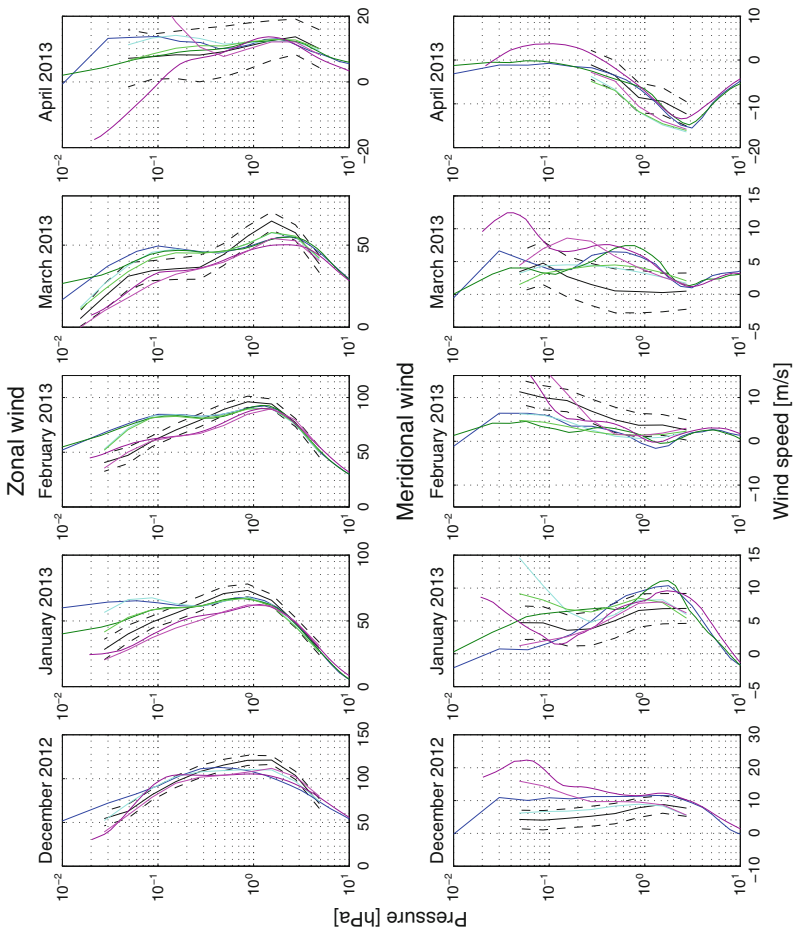

Fig. 19.5 Zonal and meridional monthly average wind profiles for the measurement campaign at Observatoire de Haute-Provence. Observations by WIRA in black (with the corresponding random error represented by dashed lines) compared to model data from ECMWF version 37r3 (blue), ECMWF version 38r1 (green) and MERRA (pink). The lines with darker shading represent the original model data. The brighter lines correspond to the model data convolved with WIRA's averaging kernels and with data gaps introduced for altitudes and times where WIRA has no measurement point

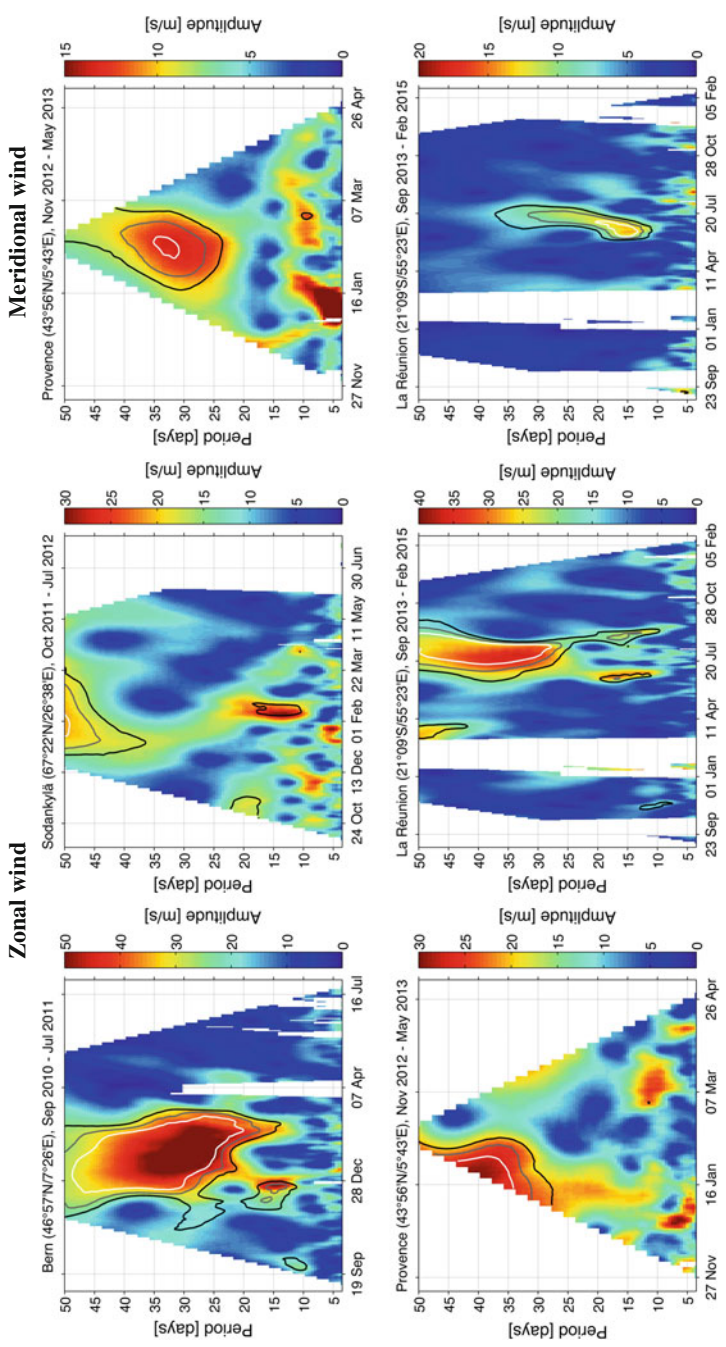

Fig. 19.6 Time series of long-period oscillation activity in zonal and meridional wind at 0.9 hPa measured by WIRA. The black, grey and white contour lines mark the false alarm probabilities of $\alpha = 0.5$, 0.1 and 0.01

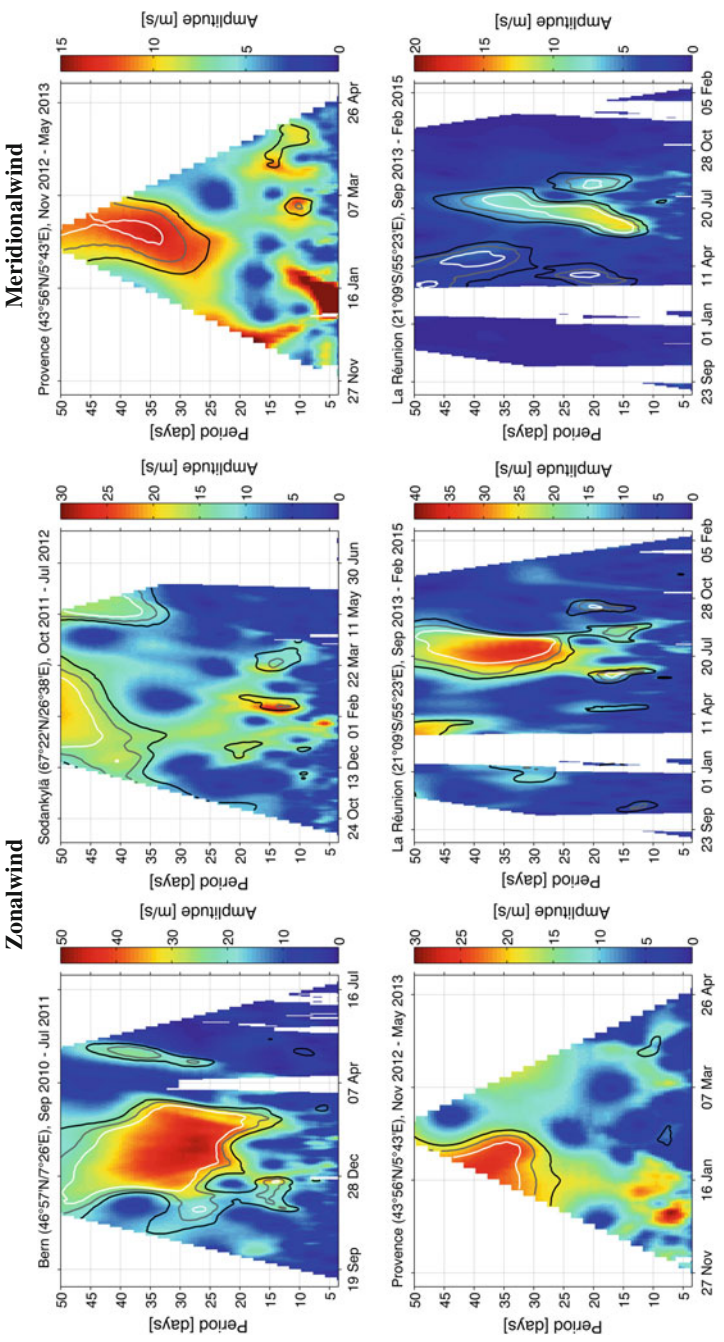

Fig. 19.7 As Fig. 19.6 but for ECMWF profiles convolved with WIRA's averaging kernels and with data gaps introduced where WIRA did not provide reliable measurements

19.5 Conclusions

The novel measurement technique of ground-based Doppler microwave radiometry has proven to be a reliable tool for the assessment of horizontal winds between 35 and 70 km altitude, where observations are extremely rare. Near-continuous time series of observations can be recorded due to the relative transparency of clouds and frozen precipitation to microwave radiation and thanks to the possibility of operating radiometers in a highly automated way. Wind radiometer measurements are valuable for the evaluation of the middle-atmospheric wind field of numerical weather prediction models. Observations from the wind radiometer WIRA have been compared to ECMWF model data showing good agreement in the stratosphere with occasional overestimation of the modelled zonal wind in the mesosphere. The timing of long-period oscillations at stratopause level agrees very well between WIRA and ECMWF but the oscillation amplitudes for ECMWF tend to be lower and less variability at periods shorter than 10 days is present in the model data.

Acknowledgements This research is part of the Atmospheric Dynamics Research Infrastructure in Europe (ARISE) project, funded by the European Union's Seventh Framework Program.

References

Baron P, Murtagh DP, Urban J, Sagawa H, Ochiai S, Kasai Y, Kikuchi K, Khosrawi F, Körnich H, Mizobuchi S, Sagi K, Yasui M (2013) Observation of horizontal winds in the middle-atmosphere between 30° S and 55° N during the northern winter 2009–2010. Atmos Chem Phys 13(12):6049–6064. https://doi.org/10.5194/acp-13-6049-2013

Baumgarten G (2010) Doppler Rayleigh/Mie/Raman lidar for wind and temperature measurements in the middle atmosphere up to 80 km. Atmos Meas Tech 3(6):1509–1518. https://doi.org/10.5194/amt-3-1509-2010

ECMWF (2017) http://www.ecmwf.int/en/forecasts/documentation-and-support/changes-ecmwf-model. Accessed 12 Aug 2017

Fernandez S, Rüfenacht R, Kämpfer N, Portafaix T, Posny F, Payen G (2016) Results from the validation campaign of the ozone radiometer gromos-c at the ndacc station of réunion island. Atmos Chem Phys 16(12):7531–7543. https://doi.org/10.5194/acp-16-7531-2016

Hagen J (2015) Design and characterisation of a compact 142-GHz-radiometer for middle-atmospheric wind measurements. Master's thesis, Faculty of Science, University of Bern, Bern, Switzerland

Hays PB, Abreu VJ, Dobbs ME, Gell DA, Grassl HJ, Skinner WR (1993) The high-resolution doppler imager on the upper Atmosphere research Satellite. J Geophys Res-Atmos 98(D6):10713–10723. https://doi.org/10.1029/93JD00409

Le Pichon A, Assink JD, Heinrich P, Blanc E, Charlton-Perez A, Lee CF, Keckhut P, Hauchecorne A, Rüfenacht R, Kämpfer N, Drob DP, Smets PSM, Evers LG, Ceranna L, Pilger C, Ross O, Claud C (2015) Comparison of co-located independent ground-based middle-atmospheric wind and temperature measurements with numerical weather prediction models. J Geophys Res-Atmos. https://doi.org/10.1002/2015JD023273

Ortland DA, Skinner WR, Hays PB, Burrage MD, Lieberman RS, Marshall AR, Gell DA (1996) Measurements of stratospheric winds by the high resolution doppler imager. J Geophys Res Atmos 101(D6):10351–10363. https://doi.org/10.1029/95JD02142

Rienecker MM, Suarez MJ, Gelaro R, Todling R, Bacmeister J, Liu E, Bosilovich MG, Schubert SD, Takacs L, Kim GK, Bloom S, Chen J, Collins D, Conaty A, da Silva A, Gu W, Joiner J, Koster RD, Lucchesi R, Molod A, Owens T, Pawson S, Pegion P, Redder CR, Reichle R, Robertson FR, Ruddick AG, Sienkiewicz M, Woollen J (2011) MERRA: NASA's Modern-Era retrospective analysis for research and applications. J Clim 24(14):3624–3648. https://doi.org/10.1175/JCLI-D-11-00015.1

Rodgers CD (2000) Inverse methods for atmospheric sounding: theory and practice. In: Series on atmospheric, oceanic and planetary physics, vol 2. World Scientific, Singapore. Reprint 2008

Rüfenacht R, Hocke K, Kämpfer N (2016) First continuous ground-based observations of long period oscillations in the vertically resolved wind field of the stratosphere and mesosphere. Atmos Chem Phys 16(8):4915–4925. https://doi.org/10.5194/acp-16-4915-2016

Rüfenacht R, Kämpfer N, Murk A (2012) First middle-atmospheric zonal wind profile measurements with a new ground-based microwave Doppler-spectro-radiometer. Atmos Meas Tech 5(11):2647–2659. https://doi.org/10.5194/amt-5-2647-2012

Rüfenacht R, Kämpfer N (2017) The importance of signals in the Doppler broadening range for middle-atmospheric microwave wind and ozone radiometry. J Quant Spectrosc Radiat Transfer 199:77–88. https://doi.org/10.1016/j.jqsrt.2017.05.028

Rüfenacht R, Kämpfer N (2019) Continuous middle-atmospheric wind profile observations by doppler microwave radiometry. In: Le Pichon A, Blanc E, Hauchecorne A (eds) Infrasound monitoring for atmospheric studies, 2nd edn. Springer, Dordrecht, pp 635–647

Rüfenacht R, Murk A, Kämpfer N, Eriksson P, Buehler SA (2014) Middle-atmospheric zonal and meridional wind profiles from polar, tropical and midlatitudes with the ground-based microwave Doppler wind radiometer WIRA. Atmos Meas Tech 7(12):4491–4505. https://doi.org/10.5194/amt-7-4491-2014

Chapter 20
Gravity-Wave Detection in the Mesosphere Using Airglow Spectrometers and Meteor Radars

Robert Hibbins, Patrick Espy and Rosmarie de Wit

Abstract The atmospheric winds, density and temperature of the region between 80 and 100 km, known as the mesosphere and lower thermosphere (MLT), are subject to the effects of solar and particle precipitation from above as well as to tidal and gravity-wave forcing from below (Fritts and Alexander 2003). Additionally, the solar heating of ozone and chemical heating due to oxygen recombination chemistry in this region compete with long-term cooling of the upper atmosphere caused by increases in greenhouse gases (Robel and Dickenson 1989; Akmaev et al. 2006; Hervig et al. 2016). However, naturally occurring fluctuations associated with variations in ozone, solar or wave forcing can mask, or even mimic, the evidence of secular change in measurements of the temperature, density and winds of the MLT. Thus, these naturally occurring variations, their mechanisms and their seasonal and solar cycle behaviour must be quantified along with the driving forces associated with small-scale wave activity that governs the general circulation of the upper atmosphere. This is only possible using long-term observations with high time resolution so that the underlying secular trends that may be associated with human activity can be assessed. However, long-term, semi-continuous measurements of MLT parameters such as wind and temperature are difficult to obtain. In this article,

R. Hibbins (✉) · P. Espy (✉)
Department of Physics, Norwegian University of Science and Technology (NTNU), Trondheim, Norway
e-mail: robert.hibbins@ntnu.no

P. Espy
e-mail: patrick.espy@ntnu.no

R. Hibbins · P. Espy
Birkeland Centre for Space Science, Bergen, Norway

R. de Wit
Space Weather Laboratory, NASA Goddard Space Flight Center, Greenbelt, MD, USA

R. de Wit
Zentralanstalt für Meteorologie und Geodynamik (ZAMG), Vienna, Austria

A. Le Pichon et al. (eds.), *Infrasound Monitoring for Atmospheric Studies*,
https://doi.org/10.1007/978-3-319-75140-5_20

we discuss two complementary techniques for monitoring the MLT region with a particular focus on the influence of small-scale gravity-wave processes. In the first section, we discuss the use of meteor radars to quantify gravity-wave momentum flux from observations of the Doppler drift velocities of meteor trails. In the second section, we outline how spectroscopic measurements of the nightglow emission, resulting from the recombination of oxygen atoms produced during the daytime, have evolved into an important tool for gravity-wave studies.

20.1 Meteor Radars

20.1.1 Introduction

Gravity waves are mesoscale waves with horizontal scales between a few km and several thousand km. They are excited by a number of different processes such as atmospheric flow over mountainous terrain, geostrophic adjustment within wind jets or atmospheric convective processes. Gravity waves play an important role in coupling different atmospheric regions both through their ability to transport atmospheric energy and momentum from their source region, and through their role in wave-mean flow interactions (see Fritts and Alexander 2003 for a comprehensive review). As the density of the atmosphere decreases exponentially with altitude, conservation of energy considerations dictate that the wave amplitude must grow with altitude. At some critical altitude, the gravity wave becomes convectively unstable and can deposit momentum to the background flow, thus adding an additional term to the net forcing of the atmosphere (Holton 1983; Fritts 1984).

At high altitudes (in the mesosphere and lower thermosphere) and in particular at high latitudes, the symmetry of the spectrum of upward-propagating gravity waves generated in the lower atmosphere can be skewed by critical level filtering in the background wind field of the stratosphere and lower mesosphere (e.g. Lindzen 1981). For example, in winter when the high latitude stratospheric jets are predominantly eastward, gravity waves with eastward phase speeds will be preferentially filtered as they propagate up from the troposphere. Thus, a net residual westward wave momentum flux will propagate into the MLT region, and when these waves dissipate and deposit their momentum, a net westward forcing will be imparted to the atmosphere. During summer, the opposite situation arises when the net gravity-wave forcing in the MLT is eastward. Here, gravity-wave forcing can become the dominant forcing, responsible for driving the background atmosphere to states far from radiative equilibrium by driving a summer-pole to winter-pole mesospheric circulation (Holton and Alexander 2000). This residual circulation in turn produces upwelling at the summer polar mesopause with corresponding adiabatic cooling and temperatures as low as 130 K, providing the conditions for polar mesospheric clouds to form (Thomas 1991). In the winter polar upper mesosphere, the gravity-wave forcing drives descent and heating of the atmosphere and can lead

to transport of long-lived chemically reactive species from the upper atmosphere down into the winter polar stratosphere (e.g. Funke et al. 2005).

Given the role of gravity waves in driving global circulation, a key parameter in atmospheric models, is the vertical flux of horizontal momentum carried by these waves (designated $u'w'$ and $v'w'$ for the zonal and meridional terms, respectively). This is, in effect, the flux of momentum per unit of atmospheric density carried by the waves. A measurement of how this flux of momentum changes with altitude, weighted by the local density (the density-weighted divergence), can be used to estimate the net force per unit area (pressure) imparted on the atmosphere as the waves break or dissipate their energy (e.g. Reid and Vincent 1987).

Previous efforts to study gravity-wave momentum flux in the MLT region by radar originated with the 'dual-beam' technique of Vincent and Reid (1983). Here, narrow coplanar beam pairs from an MF radar were directed off vertical to measure the perturbation of the background wind at a given altitude due to the presence of a gravity wave passing through the field of view. The principle of the technique is illustrated in Fig. 20.1 taken from de Wit (2015), and based on Vincent and Reid (1983). Here, a single-plane gravity wave with perturbation velocities u' and w' passes through the field of view of the coplanar beams in the same xz plane.

The narrow radar beams are directed at opposite zenith angles (Vincent and Reid 1983). The instantaneous total radial Doppler velocity detected by each radar beam is the vector sum of the projection of both the background wind and the gravity-wave perturbation velocity along the radar's line-of-sight. Assuming that the background wind is uniform throughout the radar field of view, the component of the background wind can be subtracted from each beam. The beam pointing in the positive direction records a residual radial velocity, $v_{rad}(+\theta)$, given by $u' \sin\theta + w' \cos\theta$, whereas the residual radial velocity for the beam pointing in the

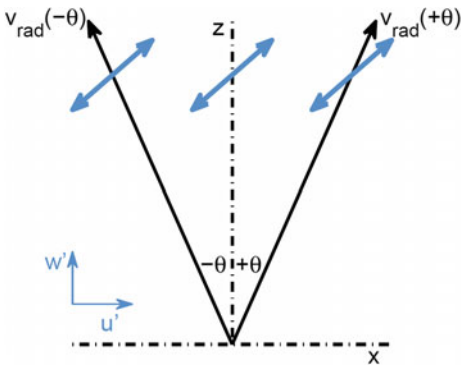

Fig. 20.1 Sketch of two radar beams pointing in the same vertical plane but opposite zenith angles $-\theta$ and $+\theta$ (black solid lines), and a plane gravity wave with its associated perturbation velocity indicated by the thick blue arrows (the gravity-wave phase fronts are aligned with the arrows). This perturbation velocity can be divided up into a horizontal (u') and vertical (w') component. Based on Vincent and Reid (1983)

negative direction, $v_{rad}(-\theta)$, is $-u' \sin\theta + w' \cos\theta$. Using an overbar to denote time averages, the variance in the two beams is given by

$$\overline{v_{rad}^2(+\theta)} = \overline{u'^2} \sin^2\theta + \overline{w'^2} \cos^2\theta + 2\overline{u'w'} \sin\theta \cos\theta$$
$$\overline{v_{rad}^2(-\theta)} = \overline{u'^2} \sin^2\theta + \overline{w'^2} \cos^2\theta - 2\overline{u'w'} \sin\theta \cos\theta$$

and hence,

$$\overline{u'w'} = \frac{\overline{v_{rad}^2(+\theta)} - \overline{v_{rad}^2(-\theta)}}{2 \sin 2\theta}$$

20.1.2 Meteor Radar Observations of Gravity-Wave Momentum Flux

An all-sky interferometric meteor radar measures the position, range and line-of-sight velocity of the ionization trail of a meteor as it ablates in the MLT region (Hocking et al. 2001). In principle, it should be possible to recreate the dual-beam technique using the radial velocities of meteors measured in opposite patches of the sky. In practice, meteor densities are too low and sporadic to fully capture the high-frequency perturbations to the background winds observed with continuous narrow-beam radars (e.g. de Wit et al. 2015a). Instead, a meteor radar presents an all-sky view of meteor trail Doppler velocities in which the location and height of the individual meteor trails can be unambiguously determined. Over a short period of time and a finite altitude range, the individual meteor trail velocities can be combined to determine a mean background horizontal wind, assuming that the background wind is uniform throughout the radar field of view. This 'background' wind can then be subtracted from the individual meteor drift velocities and any perturbations in these residual velocities are assumed to be due to small-scale gravity-wave activity within the radar field of view. Hocking (2005) proposed a generalization of the dual-beam method from which the two horizontal components of the vertical flux of gravity-wave momentum can be derived from the full field of view available from such meteor radar observations. It was demonstrated that over a given altitude range $u'u'$, $v'v'$, $w'w'$, $u'v'$, $u'w'$ and $v'w'$ can be solved simply from a set of six simultaneous equations dependent on the meteor trail position and the perturbation of the Doppler drift velocity of the meteor trail due to gravity waves (see Hocking (2005) for details of the procedure).

In order to fully capture the vertical and horizontal perturbations to the wind field due to gravity waves, meteor detections at small zenith angles are required. A standard meteor radar system with a single isotropic transmitter typically returns the maximum density of meteor detections at zenith angles around 60° or greater. At these angles, the ratio of the relative contribution from the vertical and horizontal velocities to the radial velocity is less than 0.58:1. Thus, routine observations from

standard meteor radar systems are less sensitive to the vertical component of the velocity perturbations due to gravity waves. To overcome this limitation, the Hocking inversion technique is typically only applied to meteors detected at small zenith angles (limiting zenith angles of 45, 50 or 60° have been chosen in the past) which can restrict the number of meteor drift velocities available in the matrix inversion. A modification of the standard meteor radar system, installed by Fritts et al. (2010a, b) in Tierra del Fuego (54°S 68°W), uses a circular array of eight cross-dipole transmitters. The high power signal transmitted from this array is phased to direct most of the transmit power towards zenith angles between 15° and 50° maximizing the number of meteor detections that can be used for momentum flux analysis. Similar systems were installed at King George Island (54°S 68°W) on the Antarctic Peninsula in 2010 (Fritts et al. 2012a) and at Trondheim, Norway (63°N, 10°E) in 2012 (de Wit et al. 2015a). In Fig. 20.2, the beam pattern can clearly be seen in the unambiguous meteor trail detections recorded between 70 and 100 km altitude over a typical day with the Trondheim radar. Around 50% of the meteors detected with this system are from zenith angles less than 45°.

Even with observations that provide high meteor densities at low zenith angles, it is still important to remove a correct background wind from the individual line-of-sight meteor drift velocities before a reliable momentum flux estimate can be made. The importance of this point was highlighted by Andrioli et al. (2013a), especially in relation to momentum flux measurements in regions where large amplitude, relatively low-frequency wind fluctuations such as tides and short-period planetary waves can be present. To illustrate the effect, Fig. 20.3a shows an example of a day of hourly mean zonal wind data recorded between 80 and 100 km over Trondheim with the NTNU SKiYMET meteor radar (filled contours) with

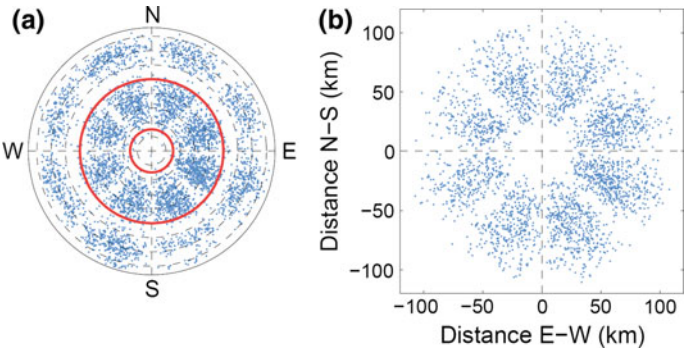

Fig. 20.2 **a** Typical azimuth- and zenith-angle distribution for all unambiguously detected meteors observed between 70 and 100 km over 24 h on 26 November 2013 with the Trondheim meteor radar. Zenith angles from 10° to 80° have been indicated with circular dashed lines in increments of 10°, and the 15° and 50° zenith angles have been highlighted with red lines. **b** As panel (**a**), but shown in km away from the meteor radar in the north–south (vertical) and east–west (horizontal) direction for all meteors between 15° and 50° zenith angles (the region between the red lines in panel **a**)

black circles representing the average time and height of the individual data points typically used in meteor radar data analysis (Hocking et al. 2001). A semidiurnal tide maximizing at around 70 m/s amplitude in the lower thermosphere is clearly visible in the data.

Tidal amplitudes as large as this are not atypical for the MLT in autumn and winter at high latitudes (e.g. Mitchell et al. 2002). One consequence of the large amplitude tides is large wind shears between adjacent time intervals. Figure 20.3b shows the time differential of the winds at each altitude presented in Fig. 20.3a. The temporal wind shear maximizes at over 95 m/s/h around 98 km altitude. de Wit (2015) discusses the effect that this wind shear can have on momentum flux measurements, and in particular the importance of interpolating the component of the background wind in both time and height for each individual meteor drift velocity included in the momentum flux analysis. Simply subtracting a mean component of the measured background wind from all meteor drift velocities recorded during an hour within a finite height bin introduces a large erroneous signal into the momentum flux estimates at times when the magnitude of dU/dt and/or dU/dz is large.

Fritts et al. (2012b) investigated the ability of the Hocking technique to reliably reproduce gravity-wave momentum flux with typical meteor detection rates and

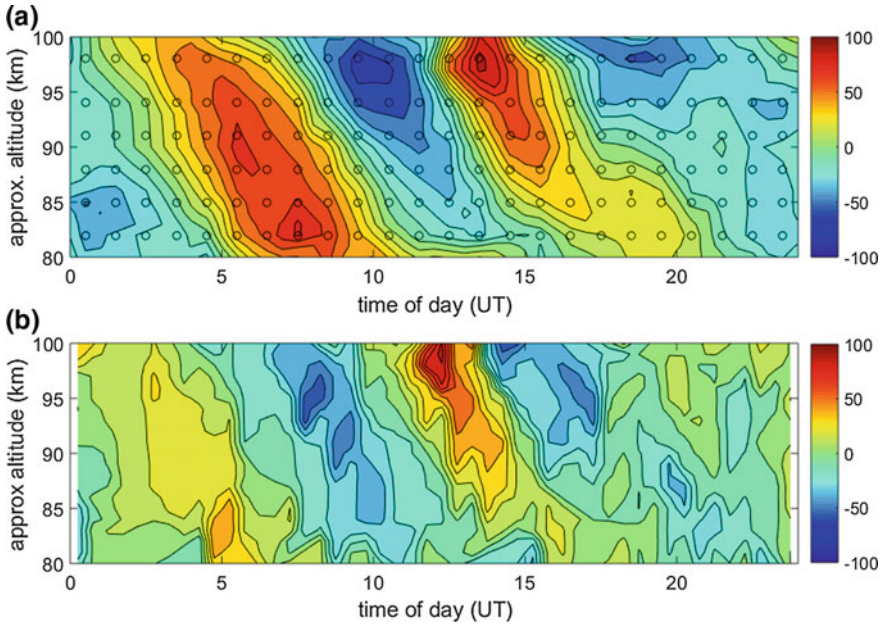

Fig. 20.3 **a** The zonal wind (m/s) recorded over Trondheim on 26 November 2013 (filled contours). The black circles represent the meantime and altitude of the individual time and height bins over which winds are typically averaged. **b** The time differential (dU/dt, m/s/h) of the winds shown in panel (**a**). Over 1 h the wind can change by as much as 95 m/s in a single height bin

beam patterns seen in a number of different meteor-radar transmit-power and antenna configurations. Various test wind fields composed of mean winds, tides and superposed gravity waves with different known amplitudes, scales, periods, propagation directions and momentum fluxes were applied to the meteor detection statistics of each radar. The ability of the Hocking technique to recover the known gravity-wave momentum flux was then assessed. It was concluded that high meteor densities at small zenith angles across all azimuths were essential to adequately resolve the differences in radial velocity variances at opposite azimuths as required by the Hocking technique. High power systems (capable of detecting up to 20,000 meteors per day) and systems with multiple antenna configurations were shown to reproduce the time-averaged wind and gravity-wave momentum flux well when the integration period was long enough to include at least 60,000 usable (small zenith angle) meteors in an individual altitude bin. To put this figure into perspective, the 30 kW Trondheim radar detects between 10 and 20 thousand meteors per day depending on the time of year (maximum in summer, minimum in early winter) with an approximately Gaussian distribution in height, centred close to 90 km with a full width half maximum around 12 km (de Wit et al 2015a).

20.1.3 Some Recent Results

The following section summarizes some recent results using the Hocking technique (and modifications thereof) to determine gravity-wave momentum flux and its divergence using meteor radar observations. It is by no means exhaustive, but more intended to illustrate the range of circumstances where meteor-radar momentum flux measurements have been made.

The Hocking (2005) paper demonstrating the technique showed that the seasonal cycle of two monthly mean data from meteor radars in New Mexico (34°N 107°W) and Resolute Bay (75°N 95°W) produced the theoretically expected seasonal forcing. Momentum fluxes were shown to increase as a function of height in winter and decrease in summer at both sites, indicative of westward forcing of the MLT in winter and eastward forcing in summer. Typical magnitudes of the mean flow acceleration due to gravity-wave momentum flux divergence of up to ±100 m/s/day were measured.

Fritts et al. (2010a) used the Southern Argentina Agile MEteor Radar (SAAMER) on Tierra del Fuego (54°S 68°W) to show that monthly mean zonal winds and gravity-wave momentum fluxes were anti-correlated during Austral spring and summer when no strong local gravity-wave sources were apparent. During winter, when stratospheric variances measured over the Drake Passage ‘hotspot’ (Ern et al. 2004) were elevated, MLT momentum fluxes measured over SAAMER were shown to be strongly influenced by the local gravity-wave sources within this region. de Wit et al. (2016) further used data from this radar to demonstrate a quasi-biennial modulation of gravity-wave momentum flux during the Austral summer that influences the interhemispheric coupling to the northern winter polar

stratosphere (de Wit et al. 2015b; Körnich and Becker 2010 and references therein). At higher southern latitudes, Fritts et al. (2012a) measured monthly mean gravity-wave momentum fluxes with the DrAAMER radar on the Antarctic Peninsula in early winter. Results again appeared to indicate the presence of significant gravity-wave sources at lower altitudes over Drake Passage confirming this as an important source region for the southern hemisphere gravity-wave 'hotspot' (see Fig. 20.4).

de Wit et al. (2014) used data from the Trondheim meteor radar to measure the change in MLT gravity-wave momentum flux over the course of the January 2013 major stratospheric warming for comparison with simulations using the Whole Atmosphere Community Climate (WACCM) model. The model agreed well with the observations and showed a clear shift toward eastward gravity-wave momentum flux and forcing during the stratospheric wind reversal. A westward gravity-wave momentum flux followed this during the subsequent elevated stratopause event. Data from the same radar have also been used to measure the complete seasonal cycle of MLT gravity-wave momentum flux and forcing (de Wit et al. 2015a). During the autumn equinox, it was shown that the net gravity-wave forcing turns from eastwards to westwards (Stray et al. 2014). By considering the average of the maximum and minimum zonal wind in the column below 80 km, it was demonstrated that the asymmetry in the wind field underlying the mesopause region can be

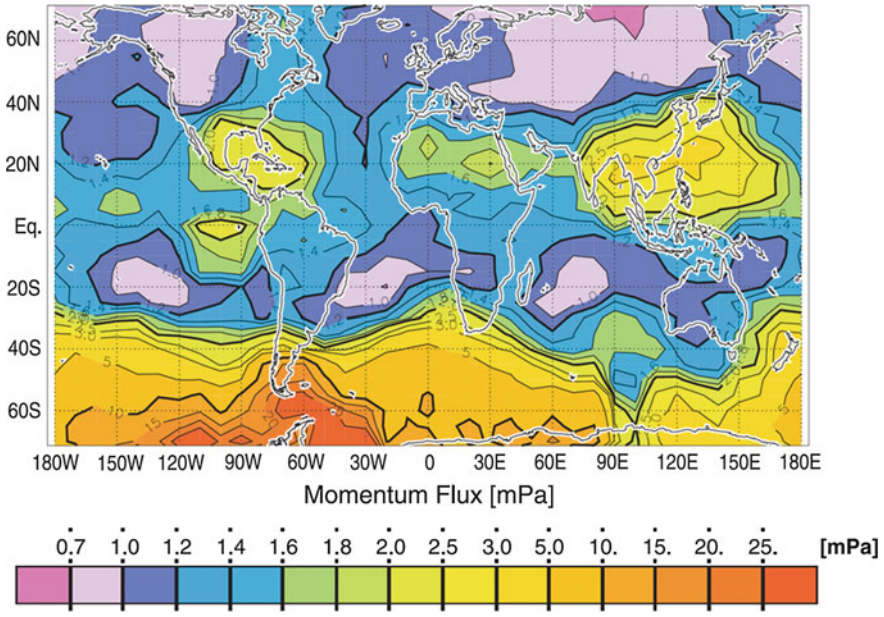

Fig. 20.4 Absolute values of the vertical flux of horizontal momentum due to gravity waves derived from CRISTA-2 satellite data for August 1997 at 25 km altitude showing the 'hotspot' in stratospheric gravity wave activity over Drake Passage. Adapted from Ern et al. (2004)

used as a simple yet quantitative proxy for the seasonal variability of gravity-wave forcing in the mesopause (de Wit et al. 2015a). Figure 20.5, taken from de Wit et al. (2015a), demonstrates this relationship. Panel b (blue line) shows the zonal component of the gravity-wave forcing at 90 km derived from the divergence of the momentum flux that is presented in panel a. Also, panel b (black line) is the average of the maximum and minimum wind measured in the column from 0 to 80 km altitude—a measure of the asymmetry of the underlying wind field that is shown in panel c. A clear anti-correlation ($r = -0.66$) between the two time series is apparent from panel b.

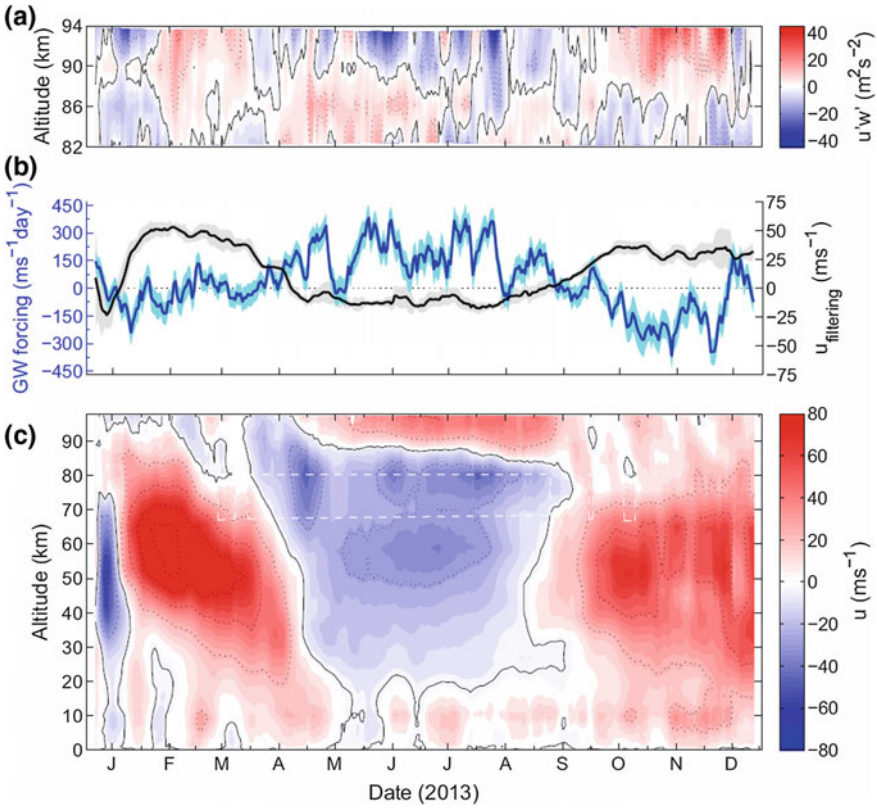

Fig. 20.5 **a** 10-day moving-average zonal gravity-wave momentum flux over Trondheim during 2013. **b** 10-day moving-average gravity-wave forcing (blue, left axis, uncertainty shaded) at ~90 km. The 10-day moving-average net zonal wind between the surface and 80.5 km (black, right axis) is included. **c** 10-day moving-average zonal wind over Trondheim, using meteor radar observations (70–100 km) complemented with UKMO reanalysis results (below ~65 km). Areas inside white dashed line indicate regions during which no meteor radar winds could be derived, and results have been linearly interpolated in height

Placke et al. (2011a) derived wind variances and gravity-wave momentum fluxes in the mesosphere and lower thermosphere using meteor radar wind measurements at Collm, Germany (51°N 13°E). They found a similar anti-correlation between gravity-wave momentum flux and mean winds as observed by Fritts et al. (2010a) indicative of the importance of critical level filtering by the underlying wind field at this site and also at higher latitudes (Placke et al. 2011b).

At low latitudes, Moss et al. (2016) used the Ascension Island meteor radar (8°S 14°W) to investigate the role of gravity-wave momentum flux in forcing the equatorial mesospheric semiannual oscillation. They measured large westward accelerations in the MLT coincident with an unusually large westward phase of the MSAO in 2002. Andrioli et al. (2015) used meteor wind measurements from three southern hemisphere low-latitude sites between 7° and 30° south to estimate gravity-wave momentum fluxes and variances in the MLT region. Analysis of the variability in the zonal component of horizontal momentum flux revealed a 12-month oscillation with maximum positive flux in June over all three latitudes as well as evidence for other intra-annual components contributing to the low-latitude gravity-wave activity. Andrioli et al. (2013b) have also reported diurnal and semidiurnal modulations of gravity-wave activity over a range of latitudes from meteor radar observations.

20.1.4 Summary and Outlook

Application of the Hocking technique, together with subsequent refinements, to meteor radar data has established the seasonal relationship between gravity-wave momentum flux and the underlying wind field over a wide range of latitudes. The role that preferential filtering of upward-propagating gravity waves by the stratospheric winds plays in modulating the vertical flux of horizontal momentum into the MLT and the subsequent forcing of the background wind has been well documented. With new generation meteor radar systems coming on line with high power directional transmitters, the possibility to measure reliable changes in MLT momentum flux and forcing over smaller timescales is becoming a reality. With such data, new studies quantifying the role of tides and planetary waves in modulating the gravity-wave forcing of the MLT will be possible. In addition, the large global variability in gravity-wave activity which has been well documented in the stratosphere and lower mesosphere (e.g. Ern et al. 2004, 2011) has clearly demonstrated the existence of strong localized gravity-wave hotspots. Long-term high-quality new generation meteor radar observations have the potential to determine the role that these hotspots play in driving differential gravity-wave forcing of the MLT.

20.2 Airglow Spectrometers

20.2.1 Oxygen and Hydroxyl Airglow

During the day, solar ultraviolet radiation photolyses O_2 and O_3 and produces a Chapman-like profile of atomic oxygen that peaks near 120 km and cuts off sharply below 90 km. After sunset, this atomic oxygen recombines into ozone as well as excited electronic states of O_2 at the lower altitudes where the collision frequency is higher due to the increased density (Bates 1988). While this secondary ozone maximum in the MLT extends to lower altitudes, the resulting distribution of the O_2-excited electronic states forms an approximately 8-km-thick layer centred near 95 km due to collisional quenching of the excitation at the lower altitudes. As these excited states radiatively relax to the ground state, they produce ultraviolet, visible and near-infrared emissions throughout this region. These emissions, observed from the ground or space, constitute the oxygen night airglow or nightglow (Bates 1992; Murtagh 1995; Bellisario et al. 2014). An example of the O_2 atmospheric band observed in the nightglow from satellites is presented in Fig. 20.6.

The emission structure of the oxygen electronic transitions between individual vibrational states includes transitions from the rotational manifold. In the example of the O_2 atmospheric electronic transition shown in Fig. 20.6, the spectrum of the transition from vibrational level 0 in the upper electronic state to vibrational level 0 of the lower state is comprised of approximately 40 closely spaced rotational lines. These are in two groups known as the R- and P-branches, depending upon whether the rotational angular momentum has changed by ± 1 during the transition. Since the upper states of these dipole forbidden electronic transitions have long lifetimes, collisions with the surrounding atmosphere thermalize the populations of the rotational levels into a Boltzmann distribution before radiating. Using the quantum mechanical transition line strengths, the intensity distribution of the rotational structure of the emission band gives the temperature of the neutral atmosphere

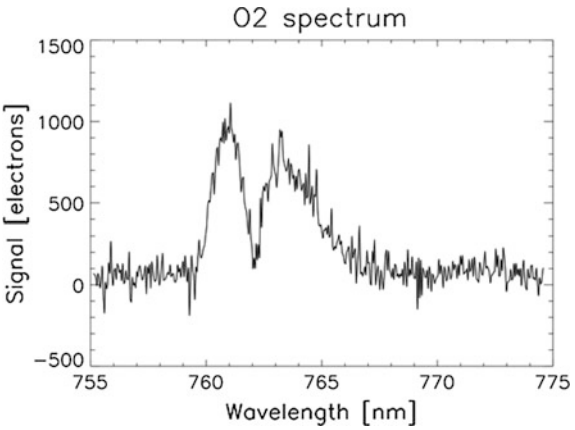

Fig. 20.6 O_2 Atmospheric (0,0) electronic-vibration-rotation band taken from the Global Ozone Monitoring by Occultation of Stars (GOMOS) satellite observing in the limb with a resolving power of ~4000. Adapted from Bellisario et al. (2014)

averaged over the emission region. In this way, spectroscopic observations of the oxygen nightglow can remotely sense the atmospheric temperature near 95 km (Shepherd et al. 1998).

In a similar fashion, the ozone formed by the oxygen recombination at night reacts exothermically with the atomic hydrogen in the MLT to produce the free radical, hydroxyl (OH). Although produced in the ground electronic state, the excess energy of the reaction is captured as internal energy by the OH molecule and results in excitation of high vibrational levels (5–9) as well as rotational excitation (Adler-Golden 1997). Since the atomic hydrogen density falls rapidly below 80 km due to its own recombination, this excited OH forms a narrow, approximately 8-km-thick layer centred at altitudes between 86 and 89 km (Baker and Stair 1988). These high vibrational–rotational levels undergo radiative relaxation, primarily through transitions involving the decrease of two vibrational quanta, and the near to mid-infrared photons emitted constitute the OH Meinel band nightglow emissions (Meinel 1950a, b). Due to the longer radiative lifetimes in the infrared, along with the time spent in the vibrational cascade, the lowest rotational levels of the OH thermalize through repeated collisions with the surrounding gas (Pendelton et al. 1993; Dodd et al. 1994). Thus, the mean atmospheric temperature in the OH emission region may be remotely sensed from ground or space by observing the distribution of the intensity of rotational transitions within an individual vibrational band (Espy and Hammond 1995; von Savigny et al. 2004). An example of an OH Meinel band transition from vibrational level 3 to 1 in the nightglow is shown in Fig. 20.7.

Comparing the spectra from O_2 and OH in Figs. 20.6 and 20.7, taken at similar spectral resolving power, it is clear that the large mass differential in the OH molecule causes the rotational structure of these bands to extend over a large

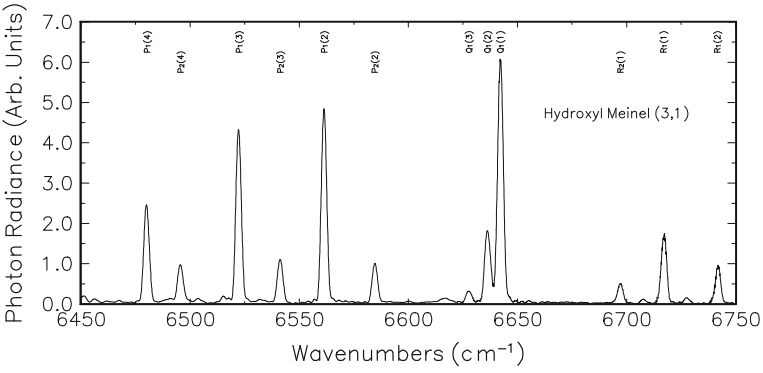

Fig. 20.7 OH Meinel (3,1) vibration–rotation band with rotational lines marked. The spectrum is taken from the ground at a resolving power of ~3000. Adapted from Espy and Hammond (1995)

wavelength range. Thus, the individual rotational lines may be easily resolved in even low-resolution spectra. Due to the ease of observing the individual lines, the OH Meinel nightglow has been extensively used for remote sensing of temperature. Thus, we will focus on the hydroxyl emissions in the following.

The distribution of intensity within the rotational levels of the vibrational band can be approximated by

$$I_{J' \to J''} = N_{v'} \cdot S_{J' \to J''} \cdot \nu^4_{J' \to J''} \cdot e^{-\frac{E_{J'}}{(k_B \cdot T_R)}}$$

Here $N_{v'}$ is the total population of the upper state vibrational level; $E_{J'}$ is the energy of the upper rotational state, J'; $\nu_{J' \to J''}$ is the wavenumber of the transition with the quantum mechanical line strength, $S_{J' \to J''}$; and k_B and T_R are Boltzmann's constant and the temperature characterizing the Boltzmann distribution of population in the rotational levels, respectively. Using laboratory spectroscopic data, the measured intensity of the rotational lines, $I_{J' \to J''}$, normalized by their individual line strengths and wavenumbers, will fall exponentially as a function of upper state energy, $E_{J'}$, with a decay factor proportional to $1/T_R$. Figure 20.8 shows the result of fitting this exponential factor for the OH Meinel (3,1) spectrum presented in Fig. 20.7, and yields a rotational temperature for the band of 161.48 ± 0.08 K. Here, one must bear in mind that this is the statistical uncertainty of the fit and does

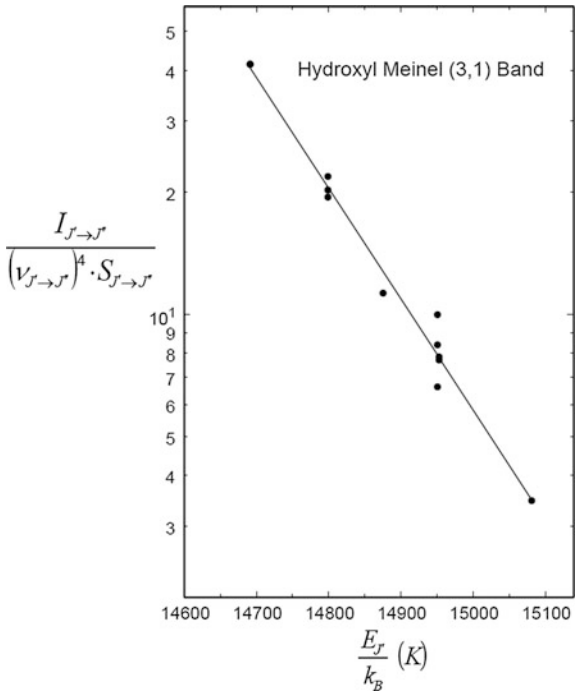

Fig. 20.8 Normalized rotational line intensities as a function of the upper state energy for the hydroxyl Meinel (3,1) vibrational band spectrum shown in Fig. 20.7. Adapted from Espy and Hammond (1995)

not represent the variation of the atmospheric temperature through the ~8-km-thick emission layer of the hydroxyl.

20.2.2 Recent Results

As can be seen from Fig. 20.8, the exponential fit is sensitive to any background that may contaminate the rotational line intensities. Thus, spectra with good signal-to-noise and enough spectral resolution to obtain an estimate of contaminating backgrounds are required. This requirement is particularly difficult to meet if one is to measure perturbations in the OH caused by the passage of short-period ($\geq$5 min) gravity waves through the layer. Although specialty, field-widened instrumentation with cryogenic cooling has been able to observe these high-frequency fluctuations (Taylor et al. 1991), the advent of new infrared detector technology, in particular, the development of low-noise Indium Gallium Arsenide (InGaAs) detectors, has made it possible to observe the brightest hydroxyl emission in the 1000–2000 nm region without cryogenic cooling.

The original single-element InGaAs detectors, using only Peltier coolers, allowed routine OH observations by Fourier Transform Infrared (FTIR) interferometers to characterize the variations of MLT temperatures on timescales from decadal down to the perturbations caused by gravity waves passing through the hydroxyl layer (Won et al. 2001; Espy and Stegman 2002). With the development of InGaAs linear detectors, high signal-to-noise spectra of the hydroxyl with integration times under one minute could be achieved with imaging spectrometers (Schmidt et al. 2013). Using imaging spectrometers with InGaAs linear detectors, Wüst et al. (2016) have been able to observe gravity-wave perturbations in the OH airglow and to quantify the potential energy of these waves. Figure 20.9 shows a typical time series with gravity-wave perturbations, as well as the derived potential energy that compares favourably with that derived using satellite and lidar techniques. Extending this technique further, Pilger et al. (2013) were able to achieve accurate ($\pm$7.5 K) rotational temperatures with 5-s integration times to observe OH airglow perturbations of infrasonic waves with periods on the order of 1 min that were produced by weather disturbances and volcanic eruptions.

InGaAs detectors have now been extended to two-dimensional arrays. Using such an array detector, Pautet et al. (2014) have used narrowband filters to isolate individual OH rotational lines and their backgrounds. By ratioing the background corrected images, they succeeded in constructing maps of the OH airglow temperature that reveal the small-scale perturbations caused by gravity waves moving through the layer. As shown in Fig. 20.10, this allows both the density perturbation (proportional to the total intensity fluctuation) and the temperature perturbation of

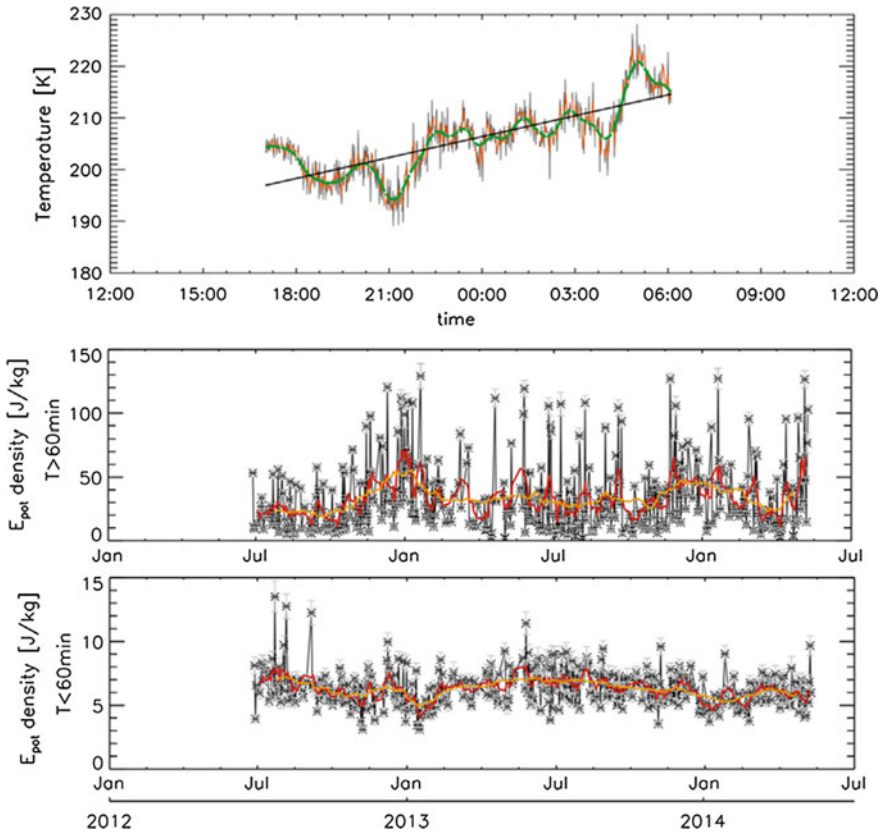

Fig. 20.9 The top panel shows the hydroxyl rotational temperature time series. The orange curve represents a 3-min mean of the original data, while the green curve shows variations greater than 60 min and represents the background for the short-period ($\tau < 60$ min) oscillations. The black curve is the linear trend that represents the background for the long-period ($\tau > 60$ min) oscillations. The lower two panels show the potential energy density calculated from these long (>60 min)- and short (<60 min)-period gravity-wave fluctuations, with the red and orange curves indicating the weekly and monthly smoothed data, respectively. Figure is adapted from Wüst et al. (2016)

the wave to be observed. Moreover, both the wavelength and direction of propagation of the wave may be determined. Using this information, it is possible to examine the details of gravity-wave propagation in the atmosphere and to derive the energy and momentum carried by individual waves into the MLT region. This technique has recently been used in a comprehensive ground and aircraft, multi-instrument campaign to examine the generation and propagation of gravity waves as well as the energy and momentum they carry from the lower atmosphere and deposit in the MLT (Fritts et al. 2016). Using these imaging techniques in conjunction with lidar and radar observations, the momentum forcing of the MLT

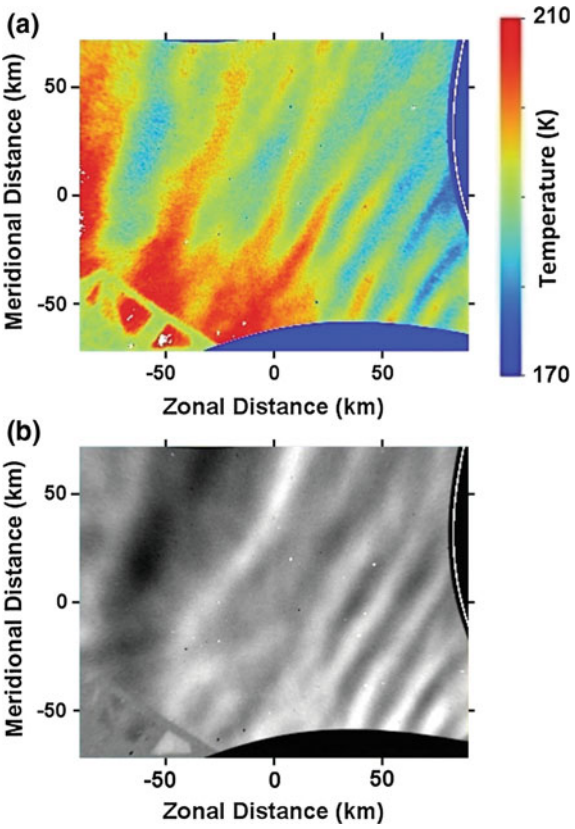

Fig. 20.10 **a** OH (3,1) rotational temperature and **b** intensity showing perturbations created by a small-scale gravity wave propagating through the OH layer. The wave period for this event was ~6.4 min. Figure taken from Pautet et al. (2014)

due to the propagation and secondary production of gravity waves from tropospheric sources could be determined (Fritts et al. 2014; Bossert et al. 2015).

20.2.3 Summary and Outlook

Observations of the nightglow provide a tool for remote sensing of the neutral temperature and density of the MLT, as well as the perturbations caused by the short-scale wave activity that drives the global, upper atmospheric circulation. Advances in infrared detector technology have allowed some of the most intense airglow emissions to be observed without the use of cryogens, enabling routine, high time-resolution observations over extended periods. These observations have established the long-term trends of MLT temperature (Beig et al. 2003) as well as the inter- and intra-seasonal variations (Espy and Stegman 2002). The use of linear detectors with simple, moderate resolution imaging spectrometers has enabled routine airglow observations of the perturbations due to gravity waves with periods

down to 5 min, as well as the observations of infrasonic waves with sub-one-minute periods. These observations have provided long-term data on the energy within the gravity-wave field reaching the MLT. Finally, two-dimensional imaging detectors have made possible observations of the spatial structure of the temperature and density perturbations associated with the passage of these waves through the airglow, and allow the momentum associated with the gravity waves to be quantified. Combining these, we see that airglow observations can characterize the forcing of the MLT on scales from secular trends down to infrasonic periods.

With continued developments in detector technology, and increased production associated with industrial uses, one can foresee the development of low-cost instrumentation for airglow observations. Given the semi-autonomous nature of this instrumentation, existing radar stations could be supplemented with synergistic airglow measurements. These multiple one- and two-dimensional observations of the airglow will allow the quantification of the forcing of the MLT and its latitudinal and longitudinal variations, providing a new understanding of the vertical coupling of energy throughout the atmosphere.

Acknowledgements REH and PJE are funded by the Research Council of Norway/CoE Contract 223252/F50 and through the ARISE2 project which is funded by the European Community's Horizon 2020 programme under grant agreement no. 653980. RJW is supported through the NASA Postdoctoral Program, administered by Universities Space Research Association through a contract with NASA.

References

Adler-Golden S (1997) Kinetic parameters for OH nightglow modeling consistent with recent laboratory measurements. J Geophys Res 102(A9):19969–19976. https://doi.org/10.1029/97JA01622

Akmaev RA, Fomichev VI, Zhu X (2006) Impact of middle-atmospheric composition changes on greenhouse cooling in the upper atmosphere. J Atmos Sol-Terr Phys 68:1879–1889

Andrioli VF, Fritts DC, Batista PP, Clemesha BR (2013a) Improved analysis of all-sky meteor radar measurements of gravity wave variances and momentum fluxes. Ann Geophys 31 (5):889–908. https://doi.org/10.5194/angeo-31-889-2013

Andrioli VF, Fritts DC, Batista PP, Clemesha BR, Janches D (2013b) Diurnal variation in gravity wave activity at low and middle latitudes. Ann Geophys 31:2123–2135. https://doi.org/10.5194/angeo-31-2123-2013

Andrioli VF, Batista PP, Clemesha BR, Schuch NJ, Buriti RA (2015) Multi-year observations of gravity wave momentum fluxes at low and middle latitudes inferred by all-sky meteor radar. Ann Geophys 33:1183–1193. https://doi.org/10.5194/angeo-33-1183-2015

Baker DJ, Stair AT Jr (1988) Rocket measurements of the altitude distributions of the hydroxyl airglow. Phys. Scripta 37:611–622

Bates DR (1988) Excitation and quenching of the oxygen bands in the nightglow. Planet Space Sci 36:875–881

Bates DR (1992) Nightglow emissions from oxygen in the lower thermosphere. Planet Space Sci 40(211–221):1992

Beig G, Keckhut P, Lowe RP, Roble RG, Mlynczak MG, Scheer J, Fomichev VI, Offermann D, French WJR, Shepherd MG, Semenov AI, Remsberg EE, She CY, Lübken FJ, Bremer J,

Clemesha BR, Stegman J, Sigernes F, Fadnavis S (2003) Review of mesospheric temperature trends. Rev Geophys 41:1015–1055

Bellisario C, Keckhut P, Blanot L, Hauchecorne A, Simoneau P (2014) O_2 and OH night airglow emission derived from GOMOS-Envisat instrument. J Atmos Oceanic Technol 31:1301–1311. https://doi.org/10.1175/JTECH-D-13-00135.1

Bossert K, Fritts DC, Pautet P-D, Williams BP, Taylor MJ, Kaifler B, Dörnbrack A, Reid IM, Murphy DJ, Spargo AJ, MacKinnon AD (2015) Momentum flux estimates accompanying multiscale gravity waves over Mount Cook, New Zealand, on 13 July 2014 during the DEEPWAVE campaign. J Geophys Res 120(18):9323–9337

de Wit RJ (2015) Quantifying the influence of the stratosphere on the mesosphere and lower thermosphere. PhD thesis, Norwegian University of Science and Technology

de Wit RJ, Hibbins RE, Espy PJ, Orsolini YJ, Limpasuvan V, Kinnison DE (2014) Observations of gravity wave forcing of the mesopause region during the January 2013 major sudden stratospheric warming. Geophys Res Lett 41(13):4745–4752. https://doi.org/10.1002/2014GL060501

de Wit RJ, Hibbins RE, Espy PJ (2015a) The seasonal cycle of gravity wave momentum flux and forcing in the high latitude northern hemisphere mesopause region. J Atmos Solar Terr Phys 127:21–29. https://doi.org/10.1016/j.jastp.2014.10.002

de Wit RJ, Hibbins RE, Espy PJ, Hennum EA (2015b) Coupling in the middle atmosphere related to the 2013 major sudden stratospheric warming. Ann Geophys 33(3):309–319. https://doi.org/10.5194/angeo-33-309-2015

de Wit RJ, Janches D, Fritts DC, Hibbins RE (2016) QBO modulation of the mesopause gravity wave momentum flux over Tierra del Fuego. Geophys Res Lett 43(8):4049–4055. https://doi.org/10.1002/2016GL068599

Dodd JA, Lipson SJ, Lowell JR, Armstrong PS, Blumberg WAM, Nadile RM, Adler-Golden SM, Marinelli WJ, Holtzclaw KW, Green BD (1994) Analysis of hydroxyl earthlimb airglow emissions: Kinetic model for state-to-state dynamics of OH (v, N). J Geophys Res 99 (D2):3559–3585. https://doi.org/10.1029/93JD03338

Ern M, Preusse P, Alexander MJ, Warner CD (2004) Absolute values of gravity wave momentum flux derived from satellite data. J Geophys Res 109:D20103. https://doi.org/10.1029/2004JD004752

Ern M, Preusse P, Gille JC, Hepplewhite CL, Mlynczak MG, Russell JM III, Riese M (2011) Implications for atmospheric dynamics derived from global observations of gravity wave momentum flux in stratosphere and mesosphere. J Geophys Res 116:D19107. https://doi.org/10.1029/2011JD015821

Espy PJ, Hammond MR (1995) Atmospheric transmission coefficients for hydroxyl rotational lines used in rotational temperature determinations. J Quant Spectrosc Radiat Transf 54:879–889

Espy PJ, Stegman J (2002) Trends and variability of mesospheric temperature at high latitudes. Phys Chem Earth 27:543–553

Fritts DC (1984) Gravity wave saturation in the middle atmosphere: a review of theory and observations. Rev Geophys 22(3):275–308. https://doi.org/10.1029/RG022i003p00275

Fritts D, Alexander M (2003) Gravity wave dynamics and effects in the middle atmosphere. Rev Geophys 41(1). https://doi.org/10.1029/2001rg000106

Fritts DC, Janches D, Hocking WK (2010a) Southern Argentina Agile Meteor Radar: initial assessment of gravity wave momentum fluxes. J Geophys Res 115(D19123). https://doi.org/10.1029/2010jd013891

Fritts DC, Janches D, Iimura H, Hocking WK, Mitchell NJ, Stockwell RG, Fuller B, Vandepeer B, Hormaechea J, Brunini C, Levato H (2010b) Southern Argentina Agile Meteor Radar: system design and initial measurements of large-scale winds and tides. J Geophys Res 115(D18112). https://doi.org/10.1029/2010jd013850

Fritts DC, Janches D, Iimura H, Hocking WK, Bageston JV, Leme NMP (2012a) Drake Antarctic Agile Meteor Radar first results: configuration and comparison of mean and tidal wind and gravity wave momentum flux measurements with Southern Argentina Agile Meteor Radar. J Geophys Res 117. https://doi.org/10.1029/2011jd016651

Fritts DC, Janches D, Hocking WK, Mitchell NJ, Taylor MJ (2012b) Assessment of gravity wave momentum flux measurement capabilities by meteor radars having different transmitter power and antenna configurations. J Geophys Res 117:D10108. https://doi.org/10.1029/2011JD017174

Fritts DC, Pautet P-D, Bossert K, Taylor MJ, Williams BP, Iimura H, Yuan T, Mitchell NJ, Stober G (2014) Quantifying gravity wave momentum fluxes with mesosphere temperature mappers and correlative instrumentation. J Geophys Res Atmos 119:13583–13603. https://doi.org/10.1002/2014JD022150

Fritts DC et al (2016) The Deep Propagating Gravity Wave Experiment (DEEPWAVE): an airborne and ground-based exploration of gravity wave propagation and effects from their sources throughout the lower and middle atmosphere. Bull Am Meteorol Soc 97:425–453. https://doi.org/10.1175/BAMS-D-14-00269.1

Funke B, López-Puertas M, Gil-López S, von Clarmann T, Stiller GP, Fisher H, Kellmann S (2005) Downward transport of upper atmospheric NOx into the polar stratosphere and lower mesosphere during the Antarctic 2003 and Arctic 2002/2003 winters. J Geophys Res 110: D24308. https://doi.org/10.1029/2005JD006463

Hervig ME, Berger U, Siskind DE (2016) Decadal variability in PMCs and implications for changing temperature and water vapor in the upper mesosphere. J Geophys Res Atmos 121:2383–2392. https://doi.org/10.1002/2015JD024439

Hocking WK (2005) A new approach to momentum flux determinations using SKiYMET meteor radars. Ann Geophys 23(7):2433–2439. https://doi.org/10.5194/angeo-23-2433-2005

Hocking WK, Fuller B, Vandepeer B (2001) Real-time determination of meteor-related parameters utilizing modern digital technology. J Atmos Solar-Terr Phys 63:155–169

Holton JR (1983) The influence of gravity wave breaking on the general circulation of the middle atmosphere. J Atmos Sci 40(10):2497–2507. https://doi.org/10.1175/1520-0469(1983)040h2497:TIOGWBi2.0.CO;2

Holton JR, Alexander MJ (2000) The role of waves in the transport circulation of the middle atmosphere. In: Siskind DE, Eckermann SD, Summers ME (eds) Atmospheric science across the stratopause. American Geophysical Union, https://doi.org/10.1029/gm123p0021

Körnich H, Becker E (2010) A simple model for the interhemispheric coupling of the middle atmosphere circulation. Adv Space Res 45(5):661–668. https://doi.org/10.1016/j.asr.2009.11.001

Lindzen RS (1981) Turbulence and stress owing to gravity-wave and tidal breakdown. J Geophys Res 86(NC10):9707–9714. https://doi.org/10.1029/JC086iC10p09707

Meinel AB (1950a) OH emission bands in the spectrum of the night sky-I. Astrophys J 111:555

Meinel AB (1950b) OH emission bands in the spectrum of the night sky-II. Astrophys J 112:120

Mitchell NJ, Pancheva D, Middleton HR, Hagan M (2002) Mean winds and tides in the Arctic mesosphere and lower thermosphere. J Geophys Res 107(A1). https://doi.org/10.1029/2001ja900127

Moss AC, Wright CJ, Davis RN, Mitchell NJ (2016) Gravity-wave momentum fluxes in the mesosphere over Ascension Island (8°S, 14°W) and the anomalous zonal winds of the semi-annual oscillation in 2002. Ann Geophys 34:323–330. https://doi.org/10.5194/angeo-34-323-2016

Murtagh DP (1995) The state of O_2 in the mesopause region. In: Johnson RM, Killeen TL (eds) Energetics, dynamics, and electrodynamics of the mesosphere and lower thermosphere, vol 87. Geophys. Monograph, Publ. AGU, Washington, pp 243–250

Pautet P-D, Taylor MJ, Pendleton WR, Zhao Y, Yuan T, Esplin R, McLain D (2014) Advanced mesospheric temperature mapper for high-latitude airglow studies. Appl Opt 53:5934–5943

Pendleton WR Jr, Espy PJ, Hammond MR (1993) Evidence for non-local-thermodynamic-equilibrium in the OH nightglow. J Geophys Res 98:11567–11579

Pilger C, Schmidt C, Streicher F, Wüst S, Bittner M (2013) Airglow observations of orographic, volcanic and meteorological infrasound signatures. J Atmos Sol-Terr Phys 104:55–66

Placke M, Stober G, Jacobi C (2011a) Gravity wave momentum fluxes in the MLT—Part I: Seasonal variation at Collm (51.3°N, 13.0°E). J Atmos Solar-Terr Phys 73(9):904–910

Placke M, Hoffmann P, Becker E, Jacobi C, Singer W, Rapp M (2011b) Gravity wave momentum fluxes in the MLT—Part II: Meteor radar investigations at high and midlatitudes in comparison with modeling studies. J Atmos Solar-Terr Phys 73(9):911–920. https://doi.org/10.1016/j.jastp.2010.05.007

Reid IM, Vincent RA (1987) Measurements of mesospheric gravity-wave momentum fluxes and mean flow accelerations at Adelaide, Australia. J Atmos Terr Phys 49(5):443–460

Roble RG, Dickinson RE (1989) How will changes in carbon dioxide and methane modify the mean structure of the mesosphere and thermosphere? Geophys Res Lett 16:1441–1444

Schmidt C, Höppner K, Bittner M (2013) A ground-based spectrometer equipped with an InGaAs array for routine observations of OH(3-1) rotational temperatures in the mesopause region. J Atmos Sol-Terr Phys 102:125–139

Shepherd GG, Roble RG, Zhang S-P, McLandress C, Wiens RH (1998) Tidal influence on midlatitude airglow: comparison of satellite and ground-based observations with TIME-GCM predictions. J Geophys Res 103(A7):14741–14751. https://doi.org/10.1029/98JA00884

Stray NH, de Wit RJ, Espy PJ, Hibbins RE (2014) Observational evidence for temporary planetary-wave forcing of the MLT during fall equinox. Geophys Res Lett 41(17):6281–6288. https://doi.org/10.1002/2014GL061119

Taylor MJ, Espy PJ, Baker DJ, Sica RJ, Neal PC, Pendleton WR Jr (1991) Simultaneous temperature, intensity and imaging measurements of gravity waves in the OH nightglow emission. Planet Space Sci 39:1171–1188

Thomas GE (1991) Mesospheric clouds and the physics of the mesopause region. Rev Geophys 29 (4):553–575. https://doi.org/10.1029/91RG01604

Vincent RA, Reid IM (1983) MF Doppler measurements of mesospheric gravity-wave momentum fluxes. J Atmos Sci 40(5):1321–1333. https://doi.org/10.1175/1520-0469(1983)040h1321:HDMOMGi2.0.CO;2

von Savigny C, Eichmann K-U, Llewellyn EJ, Bovensmann H, Burrows JP, Bittner M, Höppner K, Offermann D, Steinbrecht W, Winkler P, Taylor MJ, Cheng Y (2004) First near-global retrieval of OH rotational temperatures from satellite-based Meinel band emission measurements. Geophys Res Lett 31(15):L15111. https://doi.org/10.1029/2004GL020410

Won Y-I, Cho Y-M, Lee BY, Kim J (2001) Studies of gravity waves using Michelson interferometer measurements of OH (3-1) bands. J Astron Space Sci 18(1):21–26

Wüst S, Wendt V, Schmidt C, Lichtenstern S, Bittner M, Yee J-H, Mlynczak MG, Russell JM III (2016) Derivation of gravity wave potential energy density from NDMC measurements. J Atmos Sol-Terr Phys 138–139:32–36

Chapter 21
Detection of Infrasound Signals and Sources Using a Dense Seismic Network

Catherine de Groot-Hedlin and Michael Hedlin

Abstract This new era of massive datasets gives us the opportunity to examine Earth structure and geophysical phenomena in more detail than previously possible. Large datasets hold much promise for transformative research but require new analytical methods that are both efficient and capable of extracting useful information from faint signals immersed in noise. With these needs in mind, we developed the AELUMA (Automated Event Location Using a Mesh of Arrays) method that recasts any dense network of sensors as a distributed mesh of small triangular arrays (triads). Each array provides a local estimate of signal properties. Information from arrays distributed across the footprint of the network is combined to estimate the source origin time and location. The process is repeated without oversight to catalog events that have occurred over a period of time. We have analyzed ground-coupled airwaves recorded on vertical component broadband seismometers of the USArray Transportable Array (TA). We estimate the accuracy of the AELUMA algorithm using ground truth events at the Utah Test and Training Range (UTTR). In a study of 23 surface explosions, the mean AELUMA source location estimate is 8.6 km northwest of the ground truth location. The origin time estimates were late for most events. The mean time misfit is 19 s with a standard deviation of 39 s. We attribute the positive bias in origin time estimates to signal dispersion, as the AELUMA method estimates the time of the signal's peak amplitude, not its onset. A comparison of AELUMA and a reverse time migration method indicates that AELUMA is more sensitive to faint signals from weak events and the event locations are more accurate in space and time. A catalog of acoustic activity from across the continental United States in the band from 0.7 to 4.0 Hz includes 7935 events that were detected by 10 or more triads. Most events were clustered into hotspots and are likely anthropogenic.

C. de Groot-Hedlin (✉) · M. Hedlin (✉)
Laboratory for Atmospheric Acoustics, Institute of Geophysics and Planetary Physics, Scripps Institution of Oceanography, University of California, San Diego, La Jolla, CA 92093-0225, USA
e-mail: chedlin@ucsd.edu

M. Hedlin
e-mail: hedlin@ucsd.edu

A. Le Pichon et al. (eds.), *Infrasound Monitoring for Atmospheric Studies*,
https://doi.org/10.1007/978-3-319-75140-5_21

21.1 Introduction

A new technique to detect geophysical signals within a dense sensor network, called Automated Event Location Using a Mesh of Arrays (AELUMA), was described by de Groot-Hedlin and Hedlin (2015). The AELUMA method relies on partitioning a network of sensors into large ensembles of three-element arrays, enabling the identification of weak sources that generate detectable signals over a subset of the network sensors. The method is not strongly dependent upon the characteristics of the propagation medium and can be applied to identifying a wide range of signal types. For instance, variations of this method have been applied to the detection of gravity waves generated by a severe storm system (de Groot-Hedlin et al. 2013), to seismic source detection, as well as the detection of infrasound sources at USArray pressure sensors (de Groot-Hedlin and Hedlin 2015). In this chapter, it is applied to detecting and cataloging infrasound sources using seismic sensor data. This allows for the identification of repeating sources that can be used to study the temporal variability of the infrasonic wave field (Gibbons et al. 2019).

Infrasonic waves can propagate to ranges up to thousands of kilometers through ducts formed by the stratification of temperatures and winds in Earth's atmosphere (Drob et al. 2003; Evers and Haak 2010, and references therein). Multiple infrasound signals separated by several minutes are sometimes observed at a single source–receiver pair (Hedlin et al. 2010; Fee et al. 2013), each arrival having traveled along a distinct propagation path. Most infrasound signals travel through tropospheric ducts, which result from nocturnal temperature inversions (Fee and Garcés 2007) or the tropospheric wind jet (Fee et al. 2013), or stratospheric ducts, caused by seasonally varying stratospheric winds (Drob et al. 2003). The existence of these temporally and spatially varying ducts often determines whether or not infrasonic signals are recorded at the Earth's surface (e.g., Le Pichon et al. 2009; de Groot-Hedlin et al. 2010, and references therein). Observations of thermospherically ducted energy are comparatively infrequent because infrasound undergoes significant intrinsic attenuation within the rarefied upper atmosphere (Sutherland and Bass 2004). Since acoustic absorption increases with frequency, thermospherically ducted signals are associated only with sources that generate significant low-frequency infrasonic energy (e.g., Garcés et al. 2004; de Groot-Hedlin and Hedlin 2014a, b; Pilger et al. 2015).

Infrasonic waves have been to study energetic sources like meteors and bolides (Revelle et al. 2004; Ishihara et al. 2004; Pilger et al. 2019; Silber and Brown 2019), volcanoes (Delclos et al. 1990; Matoza et al. 2009; Fee and Matoza 2013; Matoza et al. 2019; Marchetti et al. 2019), auroral arcs (Pasko 2012), and tsunami-genic earthquakes (Walker et al. 2013; Le Pichon et al. 2005c). Anthropogenic sources can also be powerful sources of infrasound signals (Campus and Christie 2010), including mining blasts (Hagerty et al. 2002; Gibbons et al. 2019), chemical explosions (Öttemoller and Evers 2008; Ceranna et al. 2009; Vergoz et al. 2019),

and supersonic aircraft including the Concorde (Le Pichon et al. 2002) and the space shuttle Atlantis (de Groot-Hedlin et al. 2008). Infrasound has also proven useful in investigating the nature of the propagation medium—the Earth's atmosphere. A basic formalism for applying passive acoustic remote sensing techniques to infrasound data was presented by Drob et al. (2010). Infrasound recordings have been used to study atmospheric dynamics up to the lower thermosphere (Donn and Rind 1971; Garcés et al. 2004; Le Pichon et al. 2005a, b; Assink et al. 2013, 2019; Chunchuzov et al. 2015; Smets et al. 2016), and to investigate the effects of gravity waves on infrasound signal coda (e.g., Millet et al. 2007; Kulichkov et al. 2010; Green et al. 2011; Hedlin and Drob 2014; Lalande and Waxler 2016; Chunchuzov and Kulichkov 2019).

Infrasound is one of the four primary technologies in monitoring the Comprehensive Nuclear-Test-Ban Treaty (CTBT) (Campus and Christie 2010). Infrasonic waves are continuously recorded at a global network of infrasound sensors deployed as one component of the International Monitoring Systems (IMS) (Christie and Campus 2010), designed to monitor compliance with the CTBT. The network is designed to have a uniform distribution of stations over the globe, at an average interstation spacing of approximately 2000 km. However, due to the sparse station sampling, many infrasound signals detected at this network have an unknown origin (Campus and Christie 2010; Marty 2019). Matoza et al. (2017) and Arrowsmith et al. (2015) developed automated methods of detecting and locating infrasound signals from explosive volcanic events using IMS infrasound network data.

In recent years, infrasound networks with much denser spatial sampling have been deployed, allowing for more detailed studies of infrasound sources and of infrasound propagation characteristics. Data from the Large Aperture Infrasound Array (LAIA) in the Netherlands, which comprises 30 receivers and has an aperture of 100 km, have been used in interferometric studies to estimate the temporal variability of tropospheric wind and sound speeds (Fricke et al. 2014). The USArray Transportable Array (TA) is a semi-permanent network that comprises 400 infrasonic stations installed in a nearly regular east–west/north–south Cartesian grid distributed over a 2,000,000 km^2 area between the Mexican and Canadian borders, with an average interstation spacing of 70 km. The TA gradually moved eastward at an average pace of ~500 km/year through station redeployments. This network has allowed for the detection and identification of much smaller sources than would be observed at much sparser station spacing (Edwards et al. 2014; de Groot-Hedlin and Hedlin 2015).

The infrasonic network is one component of the TA network, which originated as a seismic observatory (Busby et al. 2006) intended for studies of seismic sources and the Earth's interior. The seismic TA network was initially deployed along the west coast in 2004. It was not until mid-2010, when the TA was located in the central United States, that infrasound sensors were installed along with the broadband seismometers at each site, transforming it into a large seismo-acoustic network (Vernon et al. 2012). However, it is well understood that infrasound signals couple to seismic waves at the Earth's surface and are often recorded on seismometers (Arrowsmith et al. 2010). These ground-coupled airwaves arise when

acoustic waves couple to Rayleigh waves at the Earth's surface (Crampin 1966; Edwards et al. 2007). Infrasonic waves recorded at seismic networks have been used to localize infrasound sources (Cochran and Shearer 2006; Fee et al. 2016). Seismic data from the TA have been used for infrasound studies in the western US (de Groot-Hedlin et al. 2008; Hedlin et al. 2010; Walker et al. 2010). Walker et al. (2011) constructed an infrasound event catalog by applying a Reverse Time Migration (RTM) to TA seismic sensor data.

New analytic methods of detecting and locating infrasonic signals hold the promise of providing extensive catalogs of sources that can be used either for basic infrasound research or to understand the background noise that may hamper efforts in monitoring nuclear test ban treaties. Section 21.2 reviews previously published methods of locating infrasound sources using array data. Section 21.3 introduces the TA seismic data used to develop a catalog of infrasound events for the continental United States and describes the ground truth data used to verify the accuracy of the AELUMA algorithm. The AELUMA method and its application to seismic data are described in Sect. 21.4. Section 21.5 presents the view of acoustic sources and noise in the continental US that results from applying AELUMA to 9 years of TA seismic data. Section 21.6 compares the sensitivity of the AELUMA method to previously published results. Conclusions are stated in Sect. 21.7.

21.2 Infrasound Source Location Methods

Infrasound source location estimates are adversely affected by spatial and temporal variations in sound and wind speeds, especially for sparse networks. Evers and Haak (2005) observed that infrasonic waves generated by eruptions of Mt. Etna at infrasonic arrays located in the Netherland and Germany, at ranges over 1000 km, were deflected by stratospheric winds. The resulting deflections in the measured azimuths at these arrays led to an error of nearly 100 km in the apparent source location. Arrowsmith et al. (2015) and Matoza et al. (2017) developed algorithms to detect and catalog event using only data from global the IMS infrasound stations; in both studies, some source locations were mis-estimated by over 100 km. Another drawback of using only the IMS network is that only very energetic sources are detectable at two or more stations. The global IMS infrasound network is designed to reliably detect atmospheric explosions with yields of at least 1 kT (Le Pichon et al. 2009), which may be an unreachable goal with the current sparse IMS infrasound network (Arrowsmith et al. 2015). Additional data from regional networks are often needed to improve source identification (Campus and Christie 2010) and location (Matoza et al. 2017).

Arrowsmith et al. (2008) presented an automated technique for the detection and location of infrasound events using data from two regional infrasound networks: one in Utah that comprised three arrays separated by approximately 80 km, and one in Washington state that included three arrays separated by 200–300 km. Processing was performed separately at each network to produce localized source maps

for each region. In another regional infrasound study, Park et al. (2014) developed an automated method to detect infrasound sources in the western US using data from twelve infrasonic arrays, nine located in Utah and three in Nevada. Data from all twelve of these arrays were combined to develop a catalog characterizing regional infrasound sources in the western US from November 2010 through October 2012. They found 1510 events over this time period and identified many of the same acoustic hotspots found in the Walker et al. (2011) study for the 2007–2008 period. Park and Stump (2015) also observed seasonal variations in infrasound source detections that correlated with seasonal variations in stratospheric winds.

Apart from the TA infrasound network and the LAIA in the Netherlands, dense networks are much more common for seismic sensors than for infrasound sensors. This has led to the development of several independent methods of using ground-coupled airwaves to detect and characterize infrasound events. Before the TA was in place, Cochran and Shearer (2006) used seismic data from over 200 stations in the Southern California Seismic Network to identify infrasound events. They used cross-correlation of signal envelopes to locate 76 previously undetected infrasound sources in 2003. Fee et al. (2016) applied several methods to detect volcanic explosions recorded on volcano-seismic networks in Alaska. For sources that were far from the network, they assumed that infrasonic waves crossing the network were roughly planar and applied an f-k analysis to estimate the phase velocity and the azimuth to source. For source located within the network, they used differential travel times between station pairs found by cross-correlating waveform envelopes to invert for source parameters.

Walker et al. (2011) used an RTM method to detect infrasound sources recorded at TA seismic sensors and construct maps of "acoustic hotspots" in the western US. RTM is a standard geophysical method that relies on the assumption that energy originates at a single point in a medium with known velocities; records are aligned for travel times corresponding to the known velocities and a grid of candidate source locations and stacked. The source location corresponds to the stack with the greatest constructive interference. An advantage of the RTM method is that it is broadly applicable to data from both dense arrays and sparser networks. A drawback is that the stacking velocities must be accurately known. Walker et al. (2011) used a constant stacking velocity and very sparse time sampling rate, thus smoothing the envelopes and limiting the size of the infrasound sources that could be detected. Although the accuracy could be improved with more accurate information about the range- and azimuth-dependent celerity of the medium, this is complicated by the temporally varying nature of wind and sound speeds that govern infrasound velocities.

21.3 Dataset

21.3.1 Ground Truth Sources

Rocket motor fuel blasts conducted at the Utah Test and Training Range (UTTR) offer a natural laboratory for infrasound propagation research. In this study, these sources are used to assess the precision, accuracy, and sensitivity of the AELUMA method and make possible a direct comparison with the RTM method. The UTTR facility, located approximately 130 km west of Salt Lake City, is used for military training and testing, as well as the disposal of explosive ordnance. Each year a number of rocket motors from Trident long-range missiles are destroyed as required by an agreement between the United States and Russia. Because of its location west of Salt Lake City, these detonations occur only during the summer so that stratospheric winds from the east can be relied on to carry much of the acoustic energy away from the city. These sources are very useful for assessing detection/location algorithms given that the sources are large, impulsive, repeating, and have accurately known source locations and detonation times.

The detonations that occurred at UTTR in 2007 and 2008 are listed in Table 21.1. All explosions occurred on a semi-circular pad at 41.13152°N, 112.89577°W, and origin times are reported to the nearest second (personal communication, Relu Burlacu, University of Utah). Explosive yields are reported in pounds and converted to the nearest kg. Table 21.1 summarizes ground truth information on 21 explosions at UTTR in the 2 years (12 in 2007, the remainder in 2008). All explosions except one had a reported explosive yield of approximately 17,500 kg with one considerably smaller (7955 kg) detonation.

21.3.2 Seismic Data

In this study, vertical component broadband seismic data recorded at the USArray Transportable Array from January 1, 2006 through the end of 2014 (Fig. 21.1) are used to detect and catalog infrasound sources. First, data recorded in 2007 and 2008 are used to assess the accuracy and sensitivity of AELUMA, and to directly compare it with the RTM method of Walker et al. (2011). During these years, the bulk of the TA was located downwind of the UTTR facility (Fig. 21.1) and did not yet include infrasonic microphones. At the beginning of the study period, the TA comprised only 311 stations but a full complement of 470 stations was available by the end of 2008. Various networks were incorporated into the TA during this time period (see anf.ucsd.edu).

Table 21.1 UTTR event origin dates/times and explosive yields. The AELUMA results were based on detections in the 0.7–4 Hz band. T_{miss} is AELUMA origin time minus GT origin time (i.e., positive values means AELUMA origin time is late). D_{miss} is the distance between the AELUMA location estimate and the known UTTR source location

Year/day	GT-OT	Expl. Yield	AELUMA-OT	T_{miss}	D_{miss}	# triads
	(UTC)	(kg)	(UTC)	(s)	(km)	
2007135	19:30:48	17634	19:31:30	42	16.79	60
2007155	19:52:21	17597	19:52:40	19	13.31	57
2007162	19:49:24	17688	19:49:20	−4	15.80	93
2007177	19:43:20	17688	19:43:50	30	21.60	91
2007190	21:38:37	17634	21:37:50	−47	9.83	96
2007197	17:33:31	17634	17:35:10	99	34.04	100
2007213	20:01:24	17634	20:01:50	26	22.96	109
2007218	20:33:03	17634	20:33:40	37	19.67	100
2007225	19:38:21	17634	19:39:00	39	21.22	94
2007239	20:43:12	17634	20:44:15	58	8.79	104
2007253	17:33:02	17634	17:33:10	8	3.53	34
2007260	20:21:38	17634	20:22:30	12	6.54	38
2008168	20:32:27	17597	20:32:20	−7	9.42	45
2008175	20:12:14	17143	20:13:00	46	9.84	68
2008189	20:16:23	17688	20:16:30	7	10.51	57
2008197	20:05:46	17688	20:05:50	4	5.74	40
2008203	17:56:39	17688	17:57:00	21	9.43	37
2008212	20:20:24	17688	20:21:50	86	2.08	31
2008217	20:06:29	17688	20:05:50	−39	4.73	27
2008224	19:52:03	7955	19:51:00	−63	14.94	19
2008232	20:49:32	17688	20:50:00	28	12.88	19
2008254	17:02:11	Not known				
2008261	16:54:50	Not known				

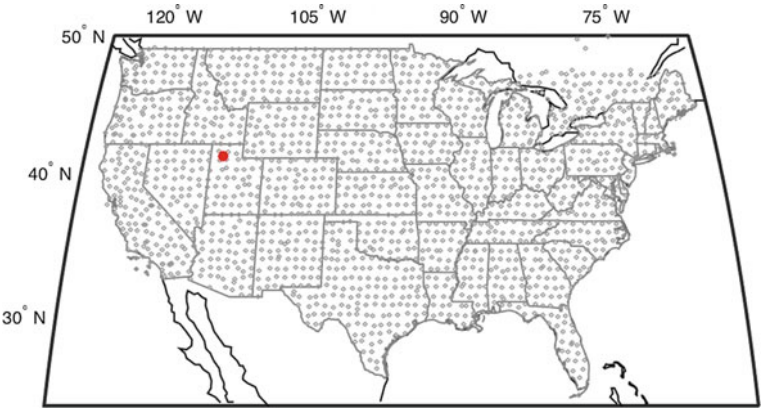

Fig. 21.1 A total of 1,986 broadband seismic stations operated in the TA from 2004 through 2015. At any given time, an average of about 400 stations was running. Explosions at the UTTR facility in Utah were used to assess location accuracy (red dot)

21.4 The AELUMA Source Location Method

An automated method to detect and locate infrasound sources using signals recorded at a dense network of seismic stations is described in this section. This approach builds on the AELUMA algorithm, first described in de Groot-Hedlin and Hedlin (2015), which was applied to data collected by infrasound microphones deployed at USArray Transportable Array (TA) stations in the eastern United States. In this method, a large network of sensors is recast as a mesh of small arrays, each comprising three adjacent stations. Data from each three-element array (or "triad") are processed to detect signals that are consistent with plane wave propagation across the triad. When a coherent signal is detected, its phase velocity and direction of propagation are computed. Results from all triads with signal detections are collectively used to automatically and rapidly provide an accurate estimate of the source's origin time and location.

Because seismometers are, by design, more sensitive to seismic energy than to infrasound signals, the basic AELUMA algorithm described in de Groot-Hedlin and Hedlin (2015) has been altered for use in finding infrasound events using seismic data. The steps for the AELUMA method are described for infrasound signals recorded at TA seismometers on day 218 of 2007. The events on this day include a surface explosion at the UTTR facility with an accurately known source time and location. The AELUMA method is applicable to a wide range of signal types and network configurations. The appendix includes a table with a description of the parameters that are used to tune the algorithm to a particular signal type and array configuration, and the values used for this study.

21.4.1 Computation of Waveform Envelopes

For cases where the interstation spacing is small in comparison to the signal wavelength of interest, waveforms from adjacent stations can be cross-correlated to determine whether they are spatially coherent. This was the case in de Groot-Hedlin et al. (2014) where long-period atmospheric gravity waves generated by a tornadic convective storm system were observed crossing the TA. However, because infrasound signals are coherent over distances of several kilometers at most, much less than the typical TA interstation spacing of 70 km, signal envelopes are computed for each waveform and cross-correlations are performed over the demeaned envelopes at adjacent stations. As noted by Fee et al. (2016), acoustic-to-seismic coupling at the Earth's surface leads to incoherent waveforms, even at more closely spaced stations.

The data are examined one day at a time along with 2 h of the following day in order to capture events that occur at the end of the day. Stations are discarded if

there is a gap of more than 1 s in that time interval. A Hilbert transform is applied to band-passed waveform data to compute the initial envelope. A short-term-average over long-term-average (STA/LTA) filter is applied to the initial envelope to enhance small-scale signals, and the result is decimated to 1 point per second. The envelopes are an approximate measure of the signal-to-noise ratio (SNR) of the arrivals. In this study, the time spans chosen for the STA and LTA filters were 10 s and 600 s, respectively, and the frequency range is from 0.7 to 4 Hz.

Band-passed seismic waveforms and associated envelopes are shown in Fig. 21.2 for a 1-h time span for signals from a rocket motor fuel cylinder blast at the Utah Test and Training Range (UTTR). This surface explosion generated infrasound signals that were recorded over a wide area to the west of the blast, as well as seismic signals detected over a smaller radius near the event. The east–west transect in Fig. 21.2 shows that the amplitudes of the earlier-arriving seismic signals are much higher than for infrasound signals near the source, but they decrease much more rapidly with distance. At least two more seismic signals can be seen in this 1 h time span, a larger one at about 21:10 UT and a smaller one at 21:25 UT; these arrivals are characterized by their much higher velocity than for the infrasound signals.

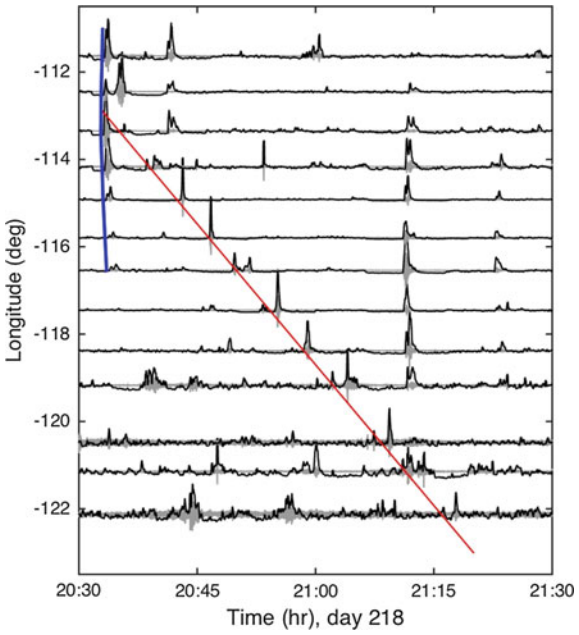

Fig. 21.2 An east–west transect through the TA within a latitude range of 41–41.7°N shows signals from a 17,634 kg surface explosion that occurred at time 20:33:03 UT on day 218, 2007, at UTTR [41.131°N, −112.8965°E.]. The band-passed waveforms are shown in gray, and their envelopes are shown in black. The data and envelopes are scaled such that the maxima are equal for all waveforms. The blue curve shows seismic arrivals from the UTTR blast; the red line indicates infrasound signals. Seismic signals from unrelated events arrive at about 21:10 and 21:25 UT

21.4.2 Network Discretization and Array Analysis at Each Triad

The TA network has a slightly different configuration from day to day due to data availability at individual stations, or as sites are either deployed or removed from the network. For any given day, the network of available stations is discretized into a nonoverlapping mesh of small triangular arrays, each composed of three adjacent stations. Although there are many ways of triangulating any given set of points, the array analysis is ideally performed on triads with equal side lengths. For that reason, a Delaunay triangulation (Lee and Schachter 1980) is used as it avoids triangulations that include triangles with very small interior angles. However, given the configuration of the TA, some highly obtuse triangles remain after the Delaunay triangulation step, so all triads with interior angles greater than 130° or less than 15° are eliminated from further analysis. Triads with arm lengths over 150 km, about twice the average station separation, are also eliminated.

A two-step array analysis is performed at each triad; first signals consistent with the passage of a plane wave across the array are sought and then, once found, the azimuth and phase velocity for each of these signals is computed. To detect coherent signals crossing a triad, the envelope time series are divided into time windows of 10 min duration, with 5 min of overlap. This time window allows for a signal with a phase velocity of 260 m/s to cross a triad having a maximum arm length of 150 km. Time windows with low signal-to-noise (SNR) are discarded if the maximum amplitude for all three envelopes is less than a given cutoff value—a minimum allowable SNR of 2.0 is used here.

Cross-correlations are computed between each of three envelope pairs within the triad for time windows having adequate SNR, yielding the time delay between each sensor pair.

The signal envelopes are coherent if the time delays between station pairs satisfy the criterion

$$T_{ij} + T_{jk} + T_{ki} < t_{cons}, \tag{1}$$

(Cansi 1995) where the stations are denoted i, j, and k; T_{ij} is the delay time from station i to station j; and t_{cons} is a consistency cutoff. Ideally, the time delays sum to zero for a coherent signal but due to noise and signal variability between stations, the consistency requirement must be relaxed. A large consistency cutoff would lead to larger errors in the phase velocity and azimuth estimates. However, at a minimum, the consistency cutoff should be greater than the duration of the STA filter used to compute the envelopes, so the t_{cons} parameter was set to 25 s in this study. Signals detected using this criterion are assumed to be consistent with plane wave propagation across the triad, although nonplanar waves can also satisfy it. A standard tau-p array processing method (e.g., Havskov and Öttemoller 2010) is applied to the station time delays to compute the signal's phase velocity and heading across the triad, for each time window in which the time delays satisfy the consistency

criterion of Eq. 1. The azimuth and phase velocities are used to compute the equivalent beam-formed envelope for a point at the center of the triad, and the peak amplitude of the beam-formed envelope is identified as the arrival time.

This step is demonstrated in Fig. 21.3 for a triad located west of UTTR that registered both seismic and infrasound arrivals from the rocket motor blast. The triad configuration is shown to the left along with a line showing the direction to the known blast location. The 0.7–4 Hz band-passed waveforms for each of the numbered stations are shown in the upper right panel, with the corresponding envelopes. Three nonoverlapping time windows are shown. The small time delays in the first window suggest seismic signal; the larger time delays in the second suggest an infrasound signal. The final time window is discarded from further computation because the envelope maxima do not exceed the SNR cutoff. For the first two windows, the delay times between station pairs are estimated by cross-correlating the demeaned envelopes. Since the time delays satisfy the consistency criterion (Eq. 1), they are input to the tau-p method to find the phase velocity and bearing across the array for each window. These values are used to compute the beam-formed envelopes for a point at the centroid of the triad for each time window, as shown in the lower right panel. The peak amplitudes of each time window give the signal arrival times. As shown, the azimuths of the signals in the first two time windows agree with the ground truth value to within 5°. The phase velocity of the signal in the first time window is approximately 4 km/s, consistent

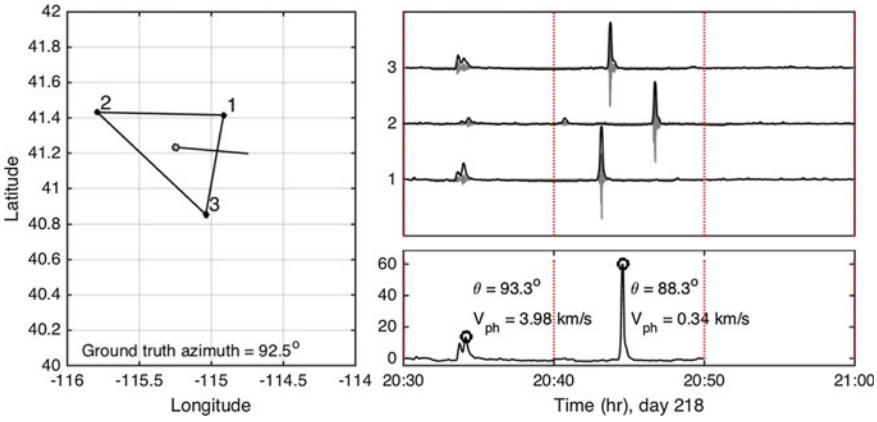

Fig. 21.3 Left: A triad configuration, with numbered stations. A gray circle marks the centroid location, with a line indicating the direction to UTTR. Top right: 0.7–4 Hz band-passed waveforms of the UTTR event and their envelopes. Dotted lines separate three nonoverlapping time windows. A seismic arrival is followed by an infrasound arrival at each station. Time delays were computed for each time window, and an azimuth and phase velocity was computed for each coherent signal. Bottom right: Beam-formed envelopes computed using the estimated azimuth and phase velocity for each time window, for a point corresponding to the center of the triad. Envelopes are computed only for time windows with a coherent arrival. A circle marking the maximum of the beam-formed envelope for each signal gives the estimate of the arrival time at the centroid location

with a shear wave, and the signal in the second time window has a phase velocity of 0.34 km/s, consistent with an infrasound arrival.

This method allows only for the detection of a single signal within a given time window. If both seismic and infrasound signals arrive within the same time window, the estimates of the phase velocity, azimuth, and arrival time will correspond to the one with the larger amplitude. For events that generate both seismic and infrasound energies, seismic signals are preferentially detected near the source where their amplitudes are higher, and infrasound signals are detected at greater ranges. Signals that propagate more slowly than infrasound signals can be eliminated by choosing a window duration that is too short for propagation across the entire triad. However, signals that travel faster than infrasound, like seismic signals, are not eliminated using the tau-p method. Other methods, such as an f-k analysis or correlation procedure (Brown et al. 2002; Gibbons et al. 2015), may be useful for separating multiple signal types that arrive in a single time window.

21.4.3 Assembling Signal Detections into Common Events

Each coherent detection at each triad has an associated phase velocity, azimuth, arrival time, an average cross-correlation computed from the three station pairs, an amplitude given by the peak amplitude of the beam-formed envelope, and a location, given by the centroid of the triad. From 6000 to 10000, unique coherent signals are detected daily over an average of 550 triads, with 287 10-min time windows analyzed at each triad. The use of seismic data to detect infrasound signals leads to the detection of far more coherent signals per day than for barometric data (de Groot-Hedlin and Hedlin 2015), because the data are contaminated with seismic signals.

Figure 21.4a shows all coherent signals with phase velocities from 300 m/s to 9000 m/s that occurred over a 1-h period from 20:30 to 21:30 UT on Julian day 218, 2007. That is, both seismic and infrasound signals are included. Figure 21.4b limits the coherent signal detections to those with phase velocities from 300 to 600 m/s, consistent with infrasound arrivals. Comparing Fig. 21.4a, b, the seismic signals can be distinguished from the infrasound arrivals by their very fast velocities across the array. A total of 883 coherent seismic and infrasound arrivals are shown in Fig. 21.4a, in comparison with only 324 signals consistent with infrasound propagation velocities in Fig. 21.4b; as indicated, many of the signals are seismic signals, which are not of interest to this study. The next step is to assemble the infrasound signal detections into groups, each consistent with a single source. Each group may include many infrasound propagation branches.

The detection of a coherent arrival at a single triad indicates either the passage of a signal across three stations or a chance correlation in a noisy dataset. To reduce the false alarm rate, AELUMA requires a lower threshold of N detections that are consistent with a single infrasound source to form a common event group. The choice of N is somewhat heuristic and depends on the source size of interest;

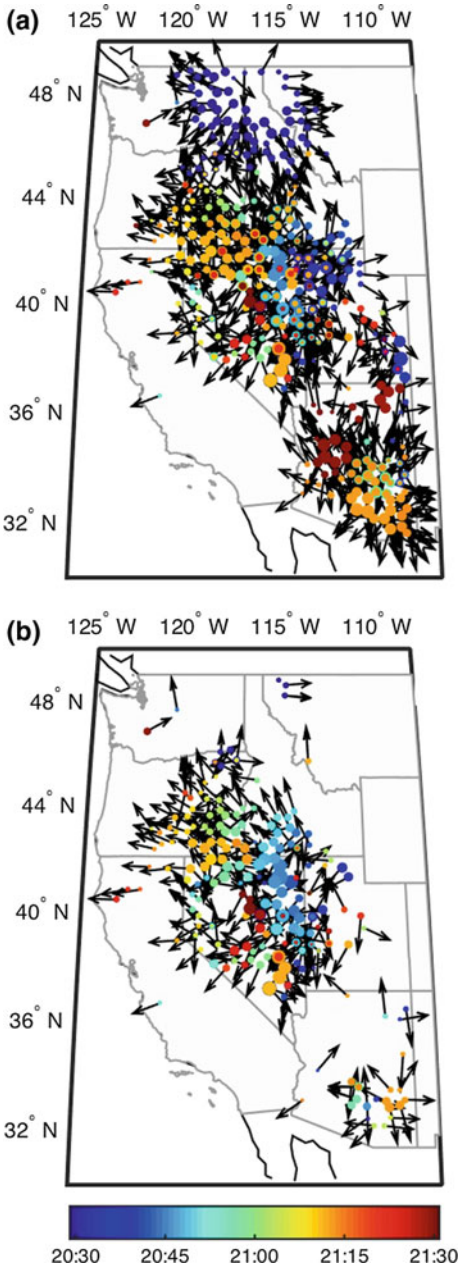

Fig. 21.4 Maps of signal detections in the 0.7–4 Hz band within the time period from 2030 to 2130 UT on day 218, 2007. Events on this day include a rocket motor fuel blast at UTTR at 20:33:03. Arrows show the direction of wave propagation across each triad. The circle size scales with SNR. The color scale shows the detection time on day 218. **a** All coherent signal detections with phase velocities ranging from 300 to 9000 m/s, which includes seismic and infrasound arrivals. **b** All coherent signal detections with phase velocities from 300 to 600 m/s, which eliminates seismic signals

N is set as low as 10 in this study, which limits events to those that were recorded across a region of at least 40,000 km^2. This choice leads to an event catalog that characterizes the acoustics of a region and also provides large infrasound events for further study.

Most signal detections on any given day are ultimately discarded as they are associated either with very small sources or noise. The task of finding sufficiently large infrasound sources for the catalog thus involves finding bundles of N or more detections consistent with a single source. The detection algorithm places a uniform grid of hypothetical source locations across the study area. For each test gridpoint, the distance and azimuth to the triad centroid is computed for all coherent signal detections, and a subset of detections with propagation azimuths consistent with travel from that gridpoint is found. An azimuth is consistent if it fits to within (A + *d*) degrees, where A is set to 10° in this study to accommodate errors in the azimuth estimates and deflections due to wind. The value *d* is the angle subtended by the distance between adjacent grid points, which increases with the coarseness of the search grid and decreases with the distance between the test gridpoint and the center of the triad.

The method of grouping detections into common events is illustrated in Fig. 21.5 for the infrasound detections shown in Fig. 21.4b, i.e., from 20:30 to 21:30 UT on Julian day 218, 2007, which includes signals from UTTR. The grid of test source locations is indicated by the red dots; the green circle indicates the known location of the UTTR blast. Figure 21.5a shows the subset of detections that are consistent with a source about one degree north and two degrees west of the known location; Fig. 21.5b shows those that are consistent with a grid point near the known location. There are no infrasound signal detections within about 100 km from the UTTR source, although faint infrasound signals may be seen in nearby recordings, see Fig. 21.2. Near the source, seismic amplitudes are larger than the infrasound arrivals, and the coherent signals have phase velocities that are consistent with seismic arrivals. As may be expected, far more detections are consistent with a source at the known location. If the subset had fewer than N members, the test point would be inconsistent with a source location and discarded from further computations for that day.

If there is a subset of at least N detections with azimuths that are consistent with the grid point being tested, the travel times are found for each member within the subset, for a set of potential source times t_k. The vector t_k is sampled at a uniform time sampling interval *dt*. The count $n(t_k)$ denotes the number of detections consistent with celerities between 250 and 340 m/s, for each time t_k. This range of celerities allows infrasound phases that travel along different paths through the atmosphere to be counted equally. This step is illustrated in Fig. 21.6. For each time t_k, AELUMA counts the number of detections within the subset between the minimum travel time as a function of range, given by $t_k - dt + R/340$ where R is the range in meters from the grid point to the triad centroids, and maximum travel time, given by $t_k + dt + R/250$. In Fig. 21.6, the maximum and minimum time

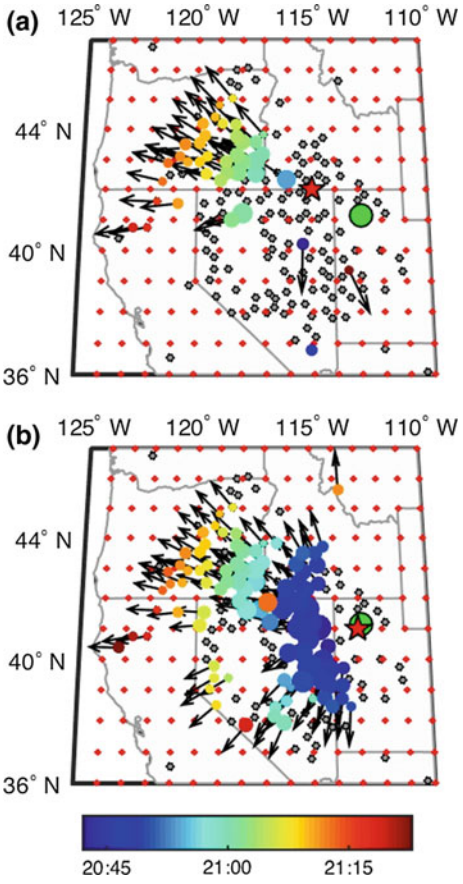

Fig. 21.5 Subsets of the detections shown in Fig. 21.4b, superimposed on a regular grid of test source points, shown by red dots, and the known UTTR source location, shown by green circles. Gray dots indicate the locations of all triad centroids with detections that have an azimuth that is inconsistent with the test gridpoint, marked by the red star. **a** The subset of detections with azimuths consistent with a source points at 42.0°N, −115°W. **b** The subset of detections with azimuths consistent with a source points at 41.0°N, −113°W, near the known source location

limits are shown for the times that yield the highest $n(t_k)$ value for each of the test locations shown in Fig. 21.5. If $n(t_k) < N$ for all potential source times, the grid point is discarded as inconsistent with an infrasound source location. The source time associated with the maximum $n(t_k)$ for the *ij*th grid point is the optimal source time for that gridpoint and is denoted T_{ij}. Figure 21.6b, for detections at a grid point near UTTR, shows that they do not fall along a straight line on a time versus distance plot, suggesting varying propagation paths.

The number of triads with detections that are consistent with an infrasound source at the *ij*th grid point for source time T_{ij} is denoted M_{ij} (T_{ij}). However, this value may be identical at several adjacent points so a penalty, equal to the rms azimuth misfit, is applied at each point to break ties between potential source locations. AELUMA defines a fitness level f_{ij} for each point with a group of at least N signal azimuths consistent with the *ij*th grid point, as

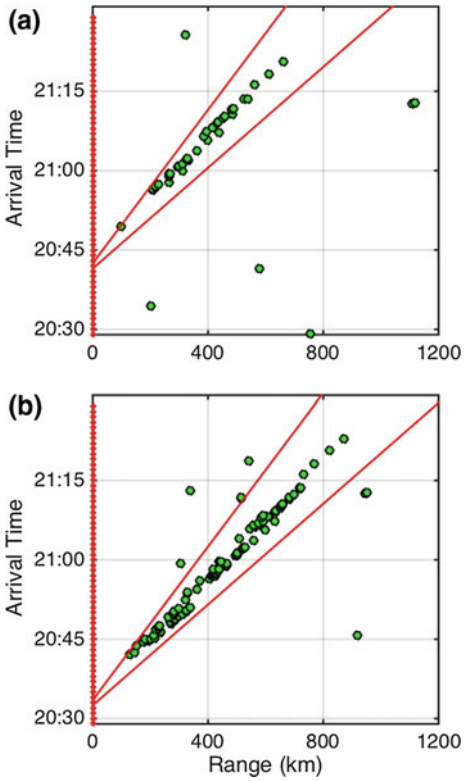

Fig. 21.6 Plots of arrival time versus range for detections with propagation azimuths corresponding to test grid points at **a** 42.0°N, −115°W, and **b** 41.0°N, −113°W, as shown in Fig. 21.5. The red dots at zero range indicate the vector of potential origin times t_k. The red lines bracket the minimum and maximum arrival times for the origin times that yield the highest number of detections within the bracket

$$f_{ij} = M_{ij}(T_{ij}) - \sqrt{\frac{\sum_{k=1}^{M} (\alpha_k - \alpha_{ij})^2}{M_{ij}(T_{ij})}} \tag{2}$$

where the second term is the rms azimuth misfit for triads within that group. The fitness level is zero if there are fewer than N detections with signal azimuths consistent with the point. Figure 21.7 shows a map of fitness levels computed for infrasound signals detected over a 4 h period from 20:00 to 24:00 UT on Julian day 218, 2007. The map suggests that there are at least two potential source locations: a larger one associated with the UTTR event and a smaller one to the south. There may, in fact, be more shots in this time span because events with small spatial separation but at different times overlap in this figure. The gridpoint with the highest fitness level is taken as an approximate source location and the value of T_{ij} at that point is taken as the initial estimate of the source time.

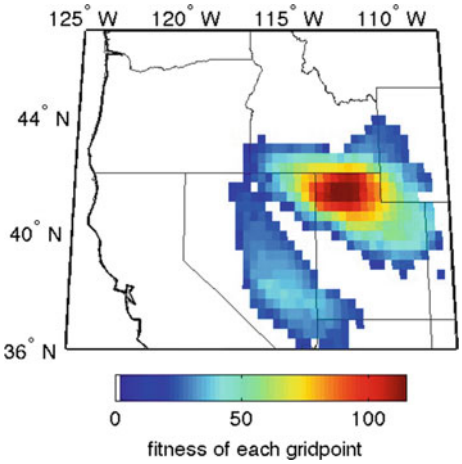

Fig. 21.7 A map of possible source locations for coherent signal detections found from 20:00 to 24:00 UT on Julian day 218, day 2007; this encompasses the 1 h of infrasound detections shown in Fig. 21.4b. The search area is discretized at three samples per degree in latitude and longitude. The fitness level is approximately the number of detections with propagation azimuths and arrival times that correspond to an infrasound source at each grid point. Areas where there are fewer than the minimum allowable detections to define an event group are shown in white

Figures 21.4 through 21.7 illustrate a single iteration of the event identification method. Each iteration identifies a single source time and location, along with its associated coherent detections. Following each iteration, the detections associated with the largest event group are removed from the ensemble and the remaining detections are used to locate another source. When no additional groups of at least N infrasound detections can be identified, the iterations are terminated.

The iterations are performed twice: once over spatially and temporally coarse grids to get rough estimates of the source parameters, and a second time to obtain more refined estimates. In this study, the coarse spatial grid is sampled at three grid points per degree in both latitude and longitude, with the limits of the grid covering the entire region covered by the TA, plus three degrees on each side. A time sampling interval of 60 s over an entire day is used to define the set of potential source times t_k. On the second pass, the grid is discretized into twenty points per degree, over a $3° \times 3°$ grid centered at the rough source location estimates found in the first pass, and a finer time sampling interval of 10 s over an 8 min time span centered at the coarse source time estimate. This has been amended from the initial AELUMA method (de Groot-Hedlin and Hedlin 2015), which sought to find fine-scale estimates of the source parameters by forcing uniform celerities. The revised method allows for a range of infrasound celerities, as in nature.

21.5 Results

21.5.1 Error Analysis Using UTTR Blasts

Events at UTTR are particularly useful for a study of AELUMA's accuracy because their locations are not only accurately recorded but their yields fall in a narrow range. Virtually, all blasts used in this study have explosive yields ranging from 17143 to 17688 kg. Acoustic signals from these large events are commonly recorded by seismometers to a range of 800 km or more (Hedlin and Drob 2014; Chunchuzov et al. 2014).

In this study period, there were 23 blasts at UTTR (12 in 2007 and 11 in 2008). All events occur through the summer season. Estimates of explosive yields for the first 21 blasts are listed in Table 21.1. Of these events, all but one had an explosive yield of over 17000 kg. The TA had moved too far to the east to reliably detect the final two blasts, mainly due to the fact that the summertime zonal winds carry the stratospherically ducted energy to the west of the source. Although some acoustic energy may be tropospherically ducted to the east due to the presence of the tropospheric jet stream, this wind generally decreases in magnitude and is less stable during the summer (Fee et al. 2013), so that TA detections more rare at stations to the east. By the time of the last two detonations, all TA stations located to the west of UTTR had been removed and moved east of the facility.

Table 21.1 also includes the AELUMA estimates of event origin time, misfit in time (in s), and misfit in location (in km). Origin times are typically late (16 of 21 detected events). The mean time misfit is 19 s with a standard deviation of 39 s. The time estimates have a positive bias because AELUMA picks the peak amplitude of the detected signal, not the signal onset, as discussed in de Groot-Hedlin and Hedlin (2015). As discussed by Hedlin and Drob (2014) and others, small-scale atmospheric structure disperses infrasonic signals, causing most of the wave packet to arrive later than the minimum travel time.

In contrast, the RTM method (Walker et al. 2011) located 10 of the 23 events (9 in 2007 and 1 in 2008). On average the RTM origin time estimates were 60 s early, which is within one time sample point, given that the data envelopes were decimated to 1 sample per 100 s. The mean AELUMA location, taken from the population of 21 events detected, was 8.6 km to the northwest of UTTR as shown in Fig. 21.8. This is only slightly greater than the average fine grid spacing of 5 km, and well under the mean TA station spacing (Fig. 21.8). The mean RTM location, taken from a population of 10 detected events, was 19.3 km to the east.

21.5.2 Event Detection in the Western United States

The TA was located in the western United States in 2007 and 2008, which is a very acoustically active part of the country (Walker et al. 2011). Just over 600 stations

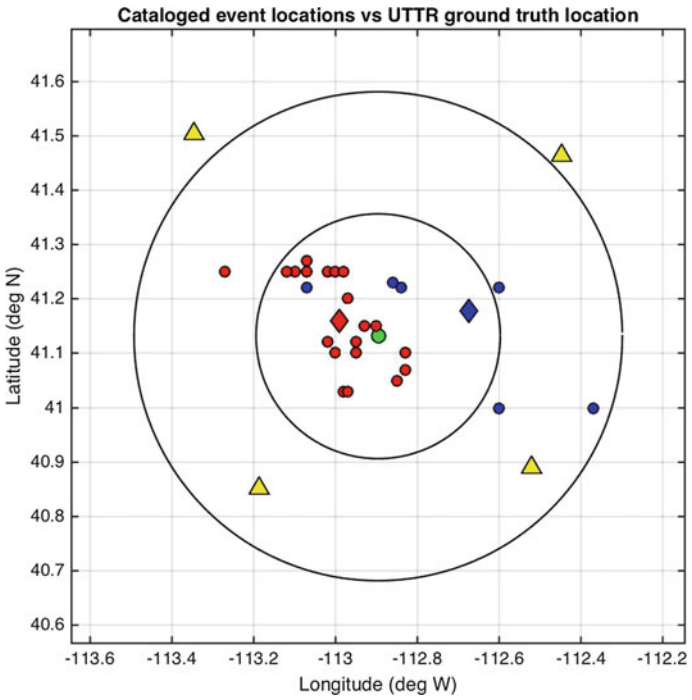

Fig. 21.8 Location estimates of the UTTR events that were detected by the AELUMA method (in red) and RTM (blue) plotted with the known location of the UTTR facility (green). The circles centered on UTTR mark range from the facility in 25 km increments. Mean estimated locations are represented by the diamond-shaped symbols. The four closest TA stations are shown as yellow triangles

operated for part or all of this time and 4966 triads were formed using these stations. An example event that was detected by 38 triads is shown in Fig. 21.9. This event was placed by AELUMA at 40.27°N, 113.02°W, which is about 100 km to the SSW of the UTTR facility. The cause of this event is unknown.

Figure 21.10 shows a histogram of acoustic sources detected by AELUMA in 2007 and 2008 in the western US. This map resembles the one in Walker et al. (2011) that shows significant activity in Nevada, Idaho, NW Utah, and southern California. The AELUMA catalog shows an additional site of activity near Socorro, New Mexico, which is the site of various explosive tests conducted by the Energetic Materials Research and Testing Center, EMRTC, located at 106.96°W 34.04°N, (personal communication, Jeff Johnson). Only sources consistent with detections at a minimum of 20 triads are plotted; smaller events are more poorly located, causing the hotspots to be blurred. Setting the lower threshold to 20 triads leads to 1686 events; at a threshold of 10 triads, 4791 events are found. In contrast, the RTM code found 901 events in this time period.

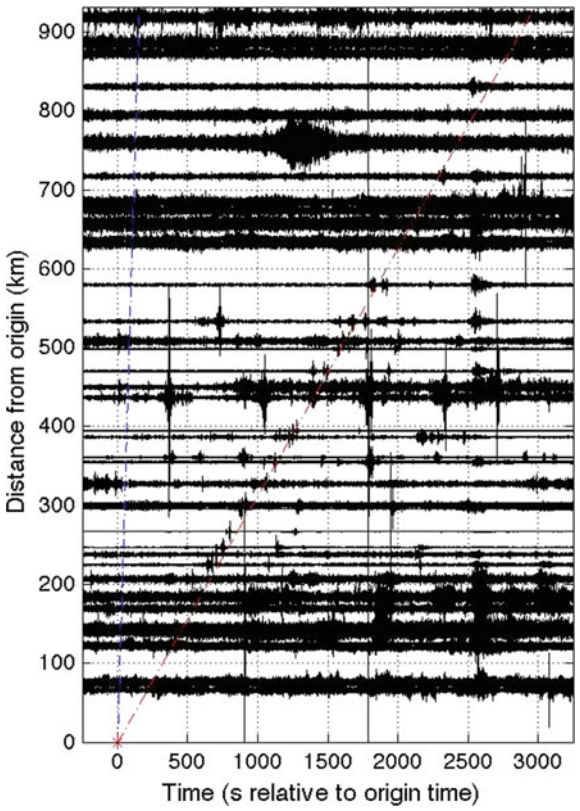

Fig. 21.9 Vertical component broadband seismic recordings of an unidentified event that occurred at 40.27°N, 113.02°W on JD 165, 2007 at 17:12:10 UT. The event was detected by 38 triads. The recordings have been bandpass filtered from 0.7 to 4 Hz and normalized to the same amplitude using data points lying within 250 s of the dashed red line which marks the average celerity of the detected signals

21.5.3 Acoustic Activity as a Function of Time

Seismic data for the entire 9-year time span from January 1, 2006 through December 31, 2014, were analyzed to examine acoustic activity across the entire continental United States. The TA moved eastward at an average rate of about 500 km/year during this time. The effect of this movement is shown in Fig. 21.11, which shows, in the upper panel, the longitude of the detected events as a function of time. In building the national catalog, all sources detected by at least 10 triads are considered. This lower limit is used because far fewer events, only 170, were detected in the east in 2012 through 2014 when the detection threshold was set to 20 triads. Using a threshold of N = 10 for the 9-year time span increased the number of detected events in this time span to 964, although it produces a blurred histogram as discussed in Sect. 21.5.2. In the lower panel of Fig. 21.11, a weekly count of detected events is shown, suggesting much higher acoustic activity in the western United States. The effect of seasonally varying stratospheric zonal winds is seen the lower panel, with increased numbers of detected events during the winter

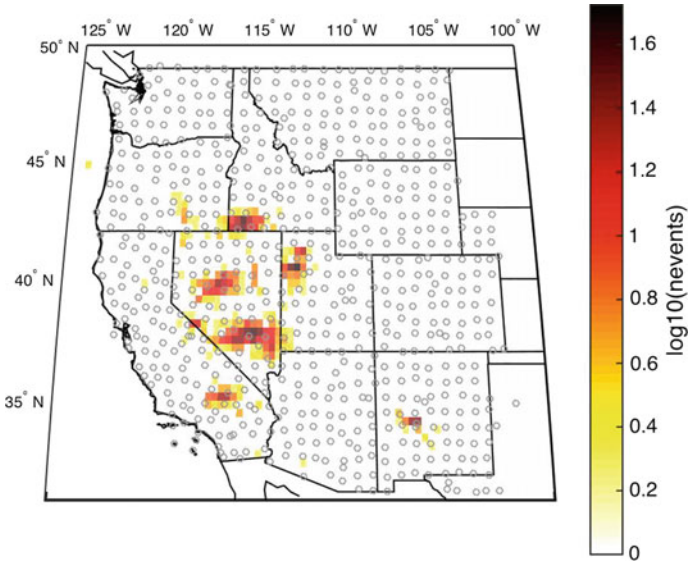

Fig. 21.10 Histogram of 1686 events detected in 2007 and 2008 by at least 20 triads. The catalog finds the same hotspots as detected by RTM and several more, such as the events located just west of Socorro, New Mexico. The histogram shows two sharp peaks in Utah, which are due to events at UTTR and the Dugway proving grounds (northern and southern peaks, respectively). There is considerably more activity in Nevada, with other concentrations of events in southern California, southern Idaho, and south-central Oregon. All stations in the TA that operated for at least of part of the 2 years are plotted

months, especially for the second through fifth years when the TA was fully deployed in the west. The rate at which events are detected surges when zonal winds place the bulk of the TA downwind of the most active source regions. There is relatively little activity detected by the seismometers from early 2011 through early 2013 as the network approached the Atlantic coast. In mid-2013 and 2014, the level of activity increased again in areas just off the Atlantic coast.

Figure 21.12 shows statistics on the time and day of detected events. The upper panel shows that most events occur after 08:00 local time, with the number of acoustic sources decreasing by the local mid-afternoon. The higher number of sources detected in daytime indicates that increased noise levels due to increased surface wind speeds during the day do not hamper the AELUMA algorithm. This is mainly due to the careful choice of frequency band chosen for our analysis; Fee and Garcés (2007) show that noise levels scale with wind speeds at frequencies below 0.3 Hz. The lower panel of Fig. 21.12 shows that the majority of events occurred from Monday through Friday.

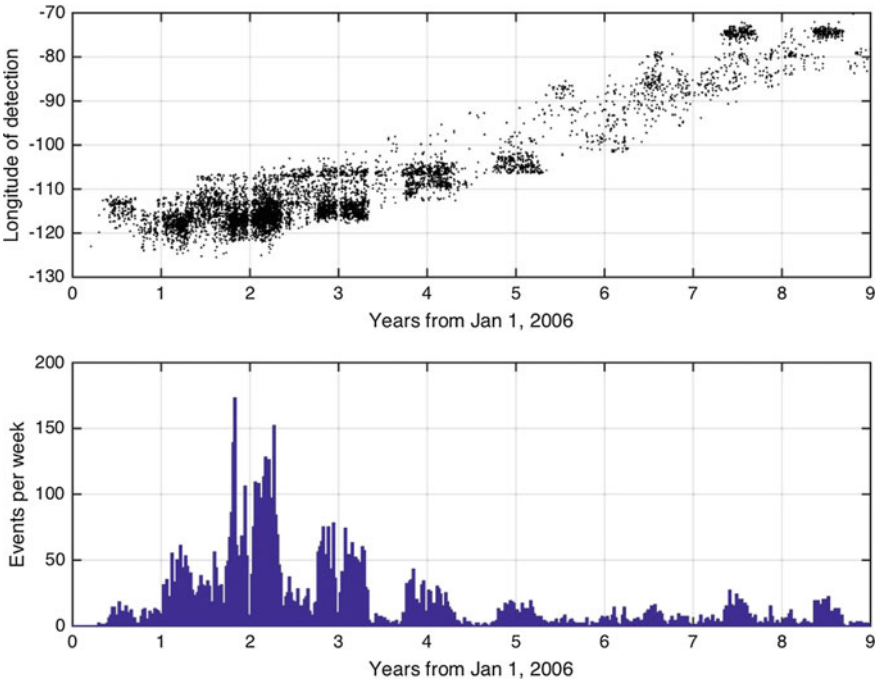

Fig. 21.11 The upper panel shows the longitude of events detected by the AELUMA method as a function of time from January 1, 2006 to December 31, 2014. The lower panel shows the number of events detected each week. The gradual shift to more eastern events is due to the movement of the TA. These results are for the 0.7–4.0 band and include events that were detected by at least 10 triads. In total, 7935 events were found. In comparison, 15430 events were found in the 2–8 Hz band and 1921 events in the 0.5–2.0 Hz band

21.5.4 US National Map of Acoustic Activity

Figure 21.13 shows a map of infrasonic activity across the continental United States for the 9-year time span beginning on January 1, 2006. During this time period, nearly 2,000 TA sites were occupied. This map, derived using a lower threshold of 10 triad detections, reveals new source regions not shown in Fig. 21.10. For example, source regions are observed in south-central New Mexico at the White Sands Missile Range. A concentration of activity in the Powder River Basin in eastern Wyoming due to coal mining is observed. Two areas of activity in Montana have not yet been identified. The hotspot, at 31.26°N, 103.25°W near Pecos, Texas is due to the use of explosives to make industrial diamonds (Paul Golden, SMU personal communication). The application of the AELUMA code to seismic data reveals far fewer acoustic hotspots in the east than were seen in de Groot-Hedlin and Hedlin (2015),

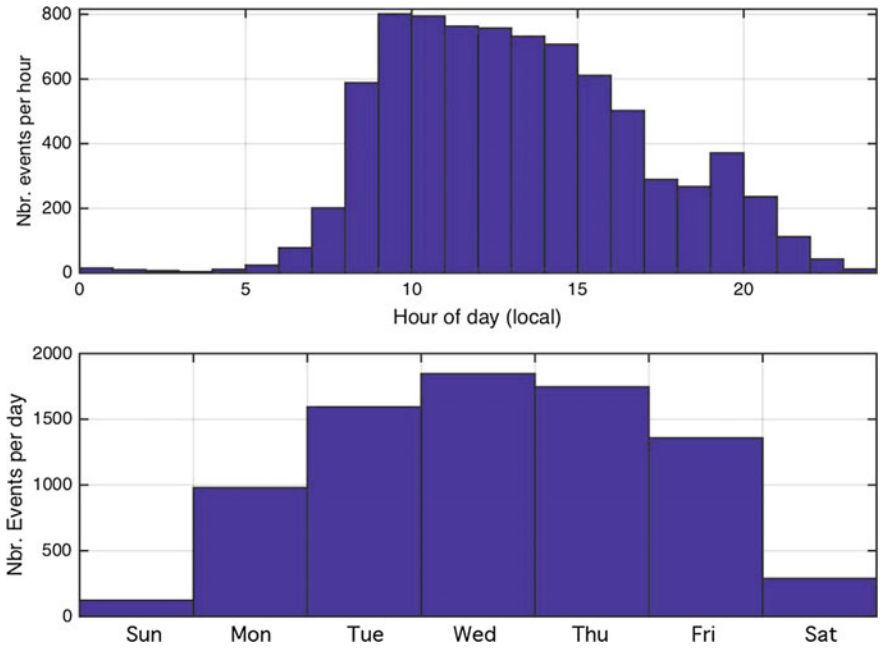

Fig. 21.12 Local time-of-day of detections by the AELUMA method occurrence rate as a function of time from January 1, 2006 to December 31, 2014 are shown in the upper panel. The lower panel shows the number of events detected each day of the week. These results are for event detections in the 0.7–4.0 Hz band and include sources that were detected by at least 10 triads. The distribution of events through the day and week is not uniform and points to anthropogenic activity

which used infrasonic data. The evidence of mining activity, and the intense acoustic activity in the Gulf of Mexico and off the Atlantic coast found in that study, is not seen here.

21.6 Discussion

21.6.1 The Detected Events

The time-of-day and day-of-week statistics clearly show that most infrasonic events that were detected in the western United States in 2007 and 2008 were anthropogenic, as also concluded by Walker et al. (2011). This includes the previously unreported source region located just west of Socorro, New Mexico. Further east, the level of activity detected using seismic data decreases significantly. Nationwide, most source regions are small and become active during normal working hours. Although the acoustic fingerprint of mankind was expected in the data, it is still

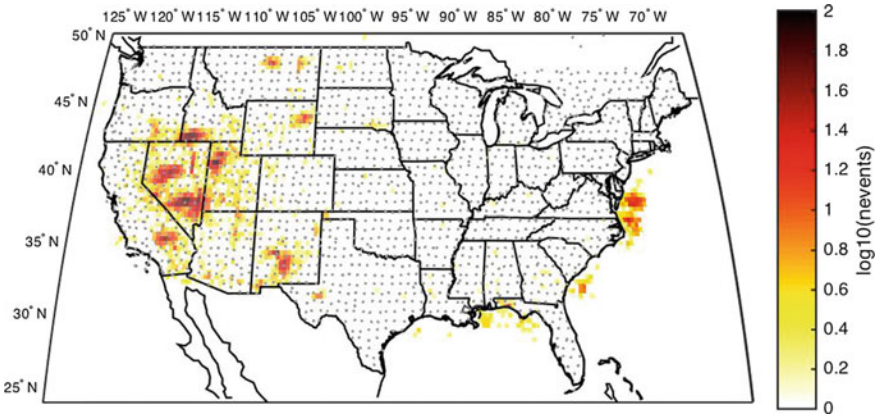

Fig. 21.13 A map of infrasound sources detected using seismic data during the 9-year period beginning on January 1, 2006, in the 0.7–4 Hz band. The lower threshold to define an event is 10 triads here, rather than 20 triads, as shown in Fig. 21.10. This allows smaller events to be seen, but blurs some of the acoustic hotspots observed in Fig. 21.10, because smaller events typically have poorer source location estimates. In total, 7935 events nationally were found in the 0.7–4 Hz band. Over 15000 events were found in the 2–8 Hz band; fewer than 2000 events were found in the 0.5–2 Hz band

surprising that sound waves from the largest of these events can be detected seismically at distances of several 100 to over 1000 km.

21.6.2 Sensitivity of AELUMA and RTM

A disadvantage of the RTM method, as applied by Walker et al. (2011), is that celerity is assumed to be constant across the TA. However, infrasound arrivals fall on distinct time branches (Hedlin et al. 2010) depending on their path through the atmosphere. Arrivals from different infrasonic branches at a given station may be separated by up to a 100 s. In order to ensure that all infrasound branches would stack coherently over ranges of hundreds of km, the RTM implementation of Walker et al. (2011) required that envelopes were severely smoothed, with one point per 100 s, which limited the detections to relatively larger source. By contrast, AELUMA requires only that the phase velocity is uniform over the aperture of any given triad. It allows for a range of celerities over hundreds of km of propagation without requiring that the envelopes be severely smoothed. Furthermore, AELUMA is fully automated and does not require the input of an analyst.

Comparing the number of events in the catalogs produced by AELUMA and RTM, and the relative number of UTTR events detected by the two methods, AELUMA is clearly more sensitive to weak signals from small events. Although the frequency band used in this analysis was slightly lower than the one used by

RTM (0.7–4 Hz vs. 1–5 Hz), it seems unlikely that this would significantly favor one approach over the other. The AELUMA code detected 21 of the 23 detonations that occurred at the UTTR facility in 2007 and 2008, including all 12 events in 2007 and the first 9 events in 2008. The last two events that year (on JD 254 and 261) were not detected because the TA was located mainly east of the UTTR, upwind of the summertime stratospheric winds, and tropospheric ducting was apparently insignificant. Also, the yield of those two final events is unknown. In comparison, the RTM approach (Walker et al. 2011) found only 10 of the events in total: 9 in 2007 (on JD 135, 155, 162, 177, 190, 197, 213, 225, and 239), and 1 in 2008 (on JD 168).

Of the entire population of 7935 events in the national AELUMA catalog in the 0.7–4 Hz band, at most 178 triads were used to define a single source location. More than half the events were detected by 10 to 20 triads. The lower limit of triads used to define a source location in this study is somewhat arbitrary. A threshold of 10 was chosen partly to reduce the computational load but also to reduce the false alarm rate. Location accuracy decreases as the number of triads used in the solution decreases.

21.6.3 Seismic Versus Infrasonic Data

In 2012 through 2014, the TA stations were equipped with both infrasonic and broadband seismic sensors. In a study of the acoustics of the eastern United States, de Groot-Hedlin and Hedlin (2015) used the infrasonic sensors to find considerable activity, both offshore and in mining regions. In this study, this analysis is repeated using vertical component seismic data. Although a careful comparison of the utility of using infrasonic versus seismic data for detecting atmospheric sources is beyond the scope of this paper, there is a significant difference in the size of the two catalogs. Using infrasonic data and a lower threshold of 20 triads to define a source location, 5666 events were found using AELUMA. Using the same parameters for seismic data, only 170 events were found. This large difference is attributable to poor acoustic-to-seismic coupling at the seismic stations in the eastern US. Given that infrasonic data were not available in the western US, it cannot be concluded that the coupling is poorer in the eastern US than the western US. Conversely, it cannot be concluded with certainty that the western US is significantly more acoustically active than the eastern US as it remains possible that the different activity levels (cf. Fig. 21.13) result from differences in acoustic-to-seismic coupling.

21.7 Conclusions

Although infrasonic signals near 1 Hz are uncorrelated between stations that are separated by more than several km, this study confirms that signal envelopes are correlated to distances of at least 70 km. This fact is exploited to develop a new approach to signal detection and event location that, in broad terms, finds and characterizes coherent signals recorded by small three-element arrays within a sensor network, then combines information from many similar arrays distributed across the network to estimate the source time and location corresponding to these coherent detections. The efficacy of migration methods, such as RTM, to detect and locate sources is well known. However, considering the relative performance of AELUMA and RTM (specifically, the number of events detected during 2007 and 2008 and the accuracy of the source estimates), it appears that this use of local wave-field characteristics gives AELUMA a critical advantage.

Our national catalog of infrasonic activity confirms the general features of the western US catalog first identified by Walker et al. (2011). Infrasonic activity is not uniformly distributed but is concentrated in "hotspots". Concentrations of infrasonic sources are detected across the country but are largest in the west. The concentration of sources during the mid-day each week from Monday through Friday indicates that most activity is anthropogenic. Aside from these diurnal and weekly cycles, the seasonal effect of reversing zonal winds is clearly observed. For this reason, we expect that the catalog should provide a wealth of data for tests of atmospheric models as well as studies of the sources themselves.

The source parameters listed in the catalogs developed here and in de Groot-Hedlin and Hedlin (2015) are more accurate for acoustic events that lie within the network, surrounded by stations, than for those on the edge of the network or in the far field. They do not have the precision of ground truth information, as in Gibbons et al. (2019). There is a place for catalogs produced by any method, such as RTM and AELUMA, in nuclear monitoring. As discussed by Walker et al. (2011), an area of ongoing interest in the infrasound community is distinguishing events that are possibly nuclear in origin from the clutter of other anthropogenic and natural events. These catalogs clearly define acoustic hotspots that would likely clutter data recorded by the region's IMS infrasound arrays. Event catalogs have historically been important in geophysical research by providing a starting point for many studies—e.g., studies of fine-scale atmospheric structure using dispersed infrasound signals and fine-scale structure due to gravity waves (e.g., Drob et al. 2013; Hedlin and Walker 2013), and studies of variations of large-scale atmospheric structure using infrasonic wave trains.

Acknowledgements This material is based upon work supported by the National Science Foundation under Grant No. EAR-1358520. We thank Relu Burlacu for providing ground truth information on the explosions at UTTR. This study would not have been possible without the high-quality data from the USArray TA. The TA is part of the Incorporated Research Institutions for Seismology (IRIS) EarthScope program. The authors thank Jelle Assink for a constructive review.

Supporting Information

National event catalogs in three bands (0.5–2.0 Hz, 0.7–4.0 Hz, and 2–8 Hz) computed using seismic data collected from 2006 through 2014. Catalog of events in the eastern United States computed using infrasonic data collected in 2012, 2013, and 2014. The AELUMA code is now available on request through product@iris.washington.edu.

Appendix

The AELUMA method is applicable to a wide range of network configurations and signal types, given that parameters are set correctly for signal type sought and the array configuration. Table 21.2 describes the main parameters needed; values used for this study are listed in the final column. The AELUMA code is available on request through product@iris.washington.edu.

Table 21.2 AELUMA parameters

Parameter	Description	Suggested range	Value
			(this study)
R	Mean interstation distance	Network dependent	70 km
f_{min}–f_{max}	Signal frequency band	Signal dependent	0.7–4 Hz
v_{min}	Minimum phase velocity	Signal dependent	0.25 km/s
v_{max}	Maximum phase velocity	Signal dependent	0.8 km/s
c_{min}	Minimum celerity	Signal dependent	0.25 km/s
c_{max}	Maximum celerity	Signal dependent	0.34 km/s
R_{max}	Maximum triad arm length	(2–3) × R	150 km
t_{STA}	Short-term average smoothing	(2–8)/f_{min}	10 s
t_{LTA}	Long-term average smoothing	(40–80) × t_{STA}	600 s
t_{win}	Time window	max(R_{max}/v_{min}, 15 * t_{STA})	600 s
t_{step}	Time step between windows	$t_{win}/2$	300 s
t_{cons}	Consistency limit (see Eq. 1)	$t_{win}/10 > t_{cons} > t_{STA}$	25 s
φ_{min}	Minimum interior angle for triad	10–20°	15°
φ_{max}	Maximum interior angle for triad	130–150°	130°
N	Minimum #triads to identify a source	10–25	10 and 20
A	Azimuth misfit threshold (see Fig. 21.5)	10–15°	10°
G_{course}	Course spatial grid	R/4–R/2	0.33°
G_{fine}	Fine spatial grid	$G_{course}/10$–$G_{course}/5$	0.05°

The phase and celerity values depend on the signal type sought. For example, for infrasound, the true phase velocities range from about 320 m/s and up, depending on whether the signal propagates horizontally across the triad or has steep incidence from above. The phase velocities are allowed a wide range, to allow for errors in phase velocity and propagation angle across the triad that derives from the imperfect fit to Eq. 1.

References

Arrowsmith SJ, Whitaker R, Taylor SR, Burlacu R, Stump B, Hedlin M, Randall G, Hayward C, ReVelle D (2008) Regional monitoring of infrasound events using multiple arrays: application to Utah and Washington State. Geophys J Int 175:291–300. https://doi.org/10.1111/j.1365-246X.2008.03912.x

Arrowsmith SJ, Johnson JB, Drob DP, Hedlin MAH (2010) The seismoacoustic wavefield: a new paradigm in studying geophysical phenomena. Rev Geophys. 48:RG4003. https://doi.org/10.1029/2010rg000335

Arrowsmith S, Euler G, Marcillo O, Blom P, Whitaker R, Randall G (2015) Development of a robust and automated infrasound event catalogue using the International Monitoring System. Geophys J Int 200:1411–1422. https://doi.org/10.1093/gji/ggu486

Assink J, Smets P, Marcillo O, Weemstra C, Lalande J-M, Waxler R, Evers LG (2019) Advances in infrasonic remote sensing methods. In: Le Pichon A, Blanc E, Hauchecorne A (eds) Infrasound monitoring for atmospheric studies, 2nd edn. Springer, Dordrecht, pp 605–632

Assink JD, Waxler R, Frazier WG, Lonzaga J (2013) The estimation of upper atmospheric wind model updates from infrasound data. J Geophys Res Atmos 118:10707–10724. https://doi.org/10.1002/jgrd.50833

Brown DJ, Katz CN, Le Bras R, Flanagan MP, Wang J, Gault AK (2002) Infrasonic signal detection and source location at the Prototype International Data Centre. Pure Appl Geophys. 159:1081–1125. https://doi.org/10.1007/s00024-002-8674-2

Busby RW, Vernon FL, Newman RL, Astiz L (2006) Earth-Scope's USArray: advancing eastward. EOS, Trans Am Geophys Un 87(52), Fall Meeting, Supplement, Abstract U41B-0820

Cansi Y (1995) An automatic seismic event processing for detection and location: the P.M.C.C. method. Geophys Res Lett 22:1021–1024

Campus P, Christie DR (2010) In: Le Pichon A, Blanc E, Hauchecorne A (eds) Worldwide observations of infrasonic waves. Springer, pp 185–234. https://doi.org/10.1007/978-1-4020-9508-5_6

Ceranna L, Le Pichon A, Green DN, Mialle P (2009) The Buncefield explosion: a benchmark for infrasound analysis across central Europe. Geophys J Int 177(2):491–508. https://doi.org/10.1111/j.1365-246X.2008.03998.x

Christie DR, Campus P (2010) The IMS infrasound network: design and establishment of infrasound stations. In: Le Pichon A, Blanc E, Hauchecorne A (eds) Infrasound monitoring for atmospheric studies. Springer, pp 27–72. https://doi.org/10.1007/978-1-4020-9508-5_2

Chunchuzov I, Kulichkov S (2019) Internal gravity wave perturbations and their impacts on infrasound propagation in the atmosphere. In: Le Pichon A, Blanc E, Hauchecorne A (eds) Infrasound monitoring for atmospheric studies, 2nd edn. Springer, Dordrecht, pp 551–590

Chunchuzov I, Kulichkov S, Popov O, Hedlin M (2014) Modeling propagation of infrasound signals observed by a dense seismic network. J Acoust Soc Am 135(1)

Chunchuzov I, Kulichkov S, Perepelkin V, Popov O, Firstov P, Assink JD, Marchetti E (2015) Study of the wind velocity-layered structure in the stratosphere, mesosphere, and lower thermosphere by using infrasound probing of the atmosphere. J Geophys Res Atmos 120:8828–8840. https://doi.org/10.1002/2015JD023276

Crampin S (1966) Higher-mode seismic surface waves from atmospheric nuclear explosions over Novaya Zemlya. J Geophys Res 71:2951–2958

Cochran ES, Shearer PM (2006) Infrasound events detected with the Southern California Seismic Network. Geophys Res Lett 33:L19803. https://doi.org/10.1029/2006GL026951

de Groot-Hedlin CD, Hedlin MAH, Walker KT, Drob DD, Zumberge MA (2008) Evaluation of infrasound signals from the shuttle Atlantis using a large seismic network. J Acoust Soc Am 124:1442–1451. https://doi.org/10.1121/1.2956475

de Groot-Hedlin CD, Hedlin MAH, Drob D (2010) Atmospheric variability and infrasound monitoring. In: Le Pichon A, Blanc E, Hauchecorne A (eds) Infrasound monitoring for atmospheric studies. Springer, New York, pp 475–507. https://doi.org/10.1007/978-1-4020-9508-5_15

de Groot-Hedlin CD, Hedlin MAH, Walker KT (2013) Detection of gravity waves across the USArray: a case study. Earth Planet Sci Lett. http://dx.doi.org/10.1016/j.epsl.2013.06.042

de Groot-Hedlin CD, Hedlin MAH (2014a) Infrasound detection of the Chelyabinsk meteor at the USArray. Earth Planet Sci Lett 402:337–345

de Groot-Hedlin CD, Hedlin MAH (2014b) Detection of seismic and infrasound sources at the USArray Transportable Array, 2016 AGU meeting

de Groot-Hedlin CD, Hedlin MAH (2015) A method for detecting and locating geophysical events using groups of arrays. Geophys J Int 203:960–971. https://doi.org/10.1093/gji/ggv345

Delclos C, Blanc E, Broche P, Glangeaud F, Lacoume JL (1990) Processing and interpretation of microbarograph signals generated by the explosion of Mount St. Helens. J Geophys Res 95 (D5):5485–5494. https://doi.org/10.1029/JD095iD05p05485

Donn WL, Rind D (1971) Natural infrasound as an atmospheric probe. Geophys J R Astron Soc 26:111–133

Drob DP, Picone JM, Garcés M (2003) Global morphology of infrasound propagation. J Geophys Res Atmos 108(D21):4680. https://doi.org/10.1029/2002JD003307

Drob DP, Broutman D, Hedlin MAH, Winslow NW, Gibson RG (2013) A method for specifying atmospheric gravity-wave fields for long-range infrasound propagation calculations. J Geophys Res. https://doi.org/10.1029/2012JD018077

Drob DP, Meier RR, Picone JM, Garcés MM (2010) Inversion of infrasound signals for passive remote sensing. In: Le Pichon A, Blanc E, Hauchecorne A (eds) Infrasound monitoring for atmospheric studies. Springer, New York, pp 701–731. https://doi.org/10.1007/978-1-4020-9508-5_24

Edwards WN, Eaton DW, McCausland PJ, ReVelle DO, Brown PG (2007) Calibrating infrasonic to seismic coupling using the Stardust sample return capsule shockwave: implications for seismic observations of meteors. J Geophys Res 112(B10306):1–13. https://doi.org/10.1029/2006JB004621

Edwards WN, de Groot-Hedlin CD, Hedlin MAH (2014) Forensic investigation of a probable meteor sighting using USArray acoustic data. Seismol Res Lett 85:1012–1018

Evers LG, Haak HW (2005) The detectability of infrasound in The Netherlands from the Italian volcano Mt. Etna. J Atmos Solar-Terr Phys 67:259–268

Evers LG, Haak HW (2010) The characteristics of infrasound, its propagation and some early history. In: Le Pichon A, Blanc E, Hauchecorne A (eds) Infrasound monitoring for atmospheric studies. Springer, New York, pp 3–27. https://doi.org/10.1007/978-1-4020-9508-5_1

Fee D, Garcés M (2007) Infrasonic tremor in the diffraction zone. Geophys Res Lett 34:L16826. https://doi.org/10.1029/2007GL030616

Fee D, Matoza RS (2013) An overview of volcano infrasound; from Hawaiian to Plinian, local to global. J. Volcanol Geotherm Res 249:123–139. https://doi.org/10.1016/j.jvolgeores.2912.09.002

Fee D, Waxler R, Assink J, Gitterman Y, Given J, Coyne J, Mialle P, Garcés M, Drob D, Kleinert D, Hofstetter R, Granard P (2013) Overview of the 2009 and 2011 Sayarim infrasound calibration experiments. J Geophys Res Atmos 118:6122–6143. https://doi.org/10.1002/jgrd.50398

Fee D, Haney M, Matoza R, Curt Szuberla C, Lyons J, Waythomas C (2016) Seismic envelope-based detection and location of ground-coupled airwaves from Volcanoes in Alaska. Bull Seismol Soc Am. https://doi.org/10.1785/0120150244

Fricke JT, Evers LG, Wapenaar K, Simons DG (2014) Infrasonic interferometry applied to microbaroms observed at the Large Aperture Infrasound Array in the Netherlands. J Geophys Res Atmos 119:9654–9665. https://doi.org/10.1002/2014JD021663

Garcés M, Willis M, Hetzer C, Le Pichon A, Drob D (2004) On using ocean swells for continuous infrasonic measurements of winds and temperature in the lower, middle, and upper atmosphere. Geophys Res Lett 31:L19304. https://doi.org/10.1029/2004GL020696

Green D, Vergoz J, Gibson R, Pichon AL, Ceranna L (2011) Infrasound radiated by the Gerdec and Chelopechene explosions: propagation along unexpected paths. Geophys J Int 185:890–910. https://doi.org/10.1111/j.1365-246X.2011.04975.x

Gibbons SJ, Kværna T, Mykkeltveit S (2015) Could the IMS infrasound stations support a global network of small aperture seismic arrays. Seismol Res Lett 86. https://doi.org/10.1758/0220150068

Gibbons S, Kværna T, Näsholm P (2019) Characterization of the infrasonic wavefield from repeating seismo-acoustic events. In: Le Pichon A, Blanc E, Hauchecorne A (eds) Infrasound monitoring for atmospheric studies, 2nd edn. Springer, Dordrecht, pp 387-407

Hagerty MT, Kim WY, Martysevich P (2002) Infrasound detection of large mining blasts in Kazakstan. Pure Appl Geophys 159(5):1063–1079. https://doi.org/10.1007/s00024-002-8673-3

Havskov J, Öttemoller L (2010) Routine data processing in earthquake seismology. Springer. https://doi.org/10.1007/978-90-481-8697-6_1

Hedlin MAH, Walker K (2013) A study of infrasonic anisotropy and multipathing in the atmosphere using seismic networks. Philos Trans R Soc A 371:20110542. https://doi.org/10.1098/rsta.2011.0542

Hedlin MAH, Drob D, Walker K, de Groot-Hedlin C (2010) A study of acoustic propagation from a large bolide in the atmosphere with a dense seismic network. J Geophys Res 115:B11312. https://doi.org/10.1029/2010JB007669

Hedlin MAH, Drob D (2014) Statistical characterization of atmospheric gravity waves by seismoacoustic observations. J Geophys Res Atmos 119. https://doi.org/10.1002/2013jd021304

Ishihara Y, Furumoto M, Sakai S, Tsukada S (2004) The 2003 Kanto large bolide's trajectory determined from shockwaves recorded by a seismic network and images taken by a video camera. Geophys Res Lett 31:L14702, 0094-8276

Kulichkov SN, Chunchuzov IP, Pupov OI (2010) Simulating the influence of an atmospheric fine inhomogeneous structure on long-range propagation of pulsed acoustic signals. Izv Atmos Ocean Phys 46:60–68. https://doi.org/10.1134/S0001433810010093

Lalande J-M, Waxler R (2016) The interaction between infrasonic waves and gravity wave perturbations: application to observations using UTTR rocket motor fuel elimination events. J Geophys Res Atmos 121:5585–5600. https://doi.org/10.1002/2015JD024527

Lee DT, Schachter BJ (1980) Two algorithms for constructing a Delaunay triangulation. Int J Comput Inf Sci 9:219–242

Le Pichon A, Garcés M, Blanc E, Barthelemy M, Drob DP (2002) Acoustic propagation and atmosphere characteristics derived from infrasonic waves generated by the Concorde. J Acoust Soc Am 111:629–641

Le Pichon A, Blanc E, Drob D (2005a) Probing high-altitude winds using infrasound. J Geophys Res 110. https://doi.org/10.1029/2005JD006020

Le Pichon A, Blanc E, Drob D, Lambotte S, Dessa JX, Lardy M, Bani P, Vergniolle S (2005b) Infrasound monitoring of volcanoes to probe high-altitude winds. J Geophys Res 110. https://doi.org/10.1029/2004JD005587

Le Pichon A, Herry P, Mialle P, Vergoz J, Brachet N, Garcés M, Drob D, Ceranna L (2005c) Infrasound associated with 2004–2005 large Sumatra earthquakes and tsunami. Geophys Res Lett 32:L19802. https://doi.org/10.1029/2005GL023893

Le Pichon A, Vergoz J, Blanc E, Guilbert J, Ceranna L, Evers L, Brachet N (2009) Assessing the performance of the International Monitoring System's infrasound network: geographical coverage and temporal variabilities. J Geophys Res 114:D08112. https://doi.org/10.1029/2008JD010907

Marchetti E, Ripepe M, Campus P, Le Pichon A, Brachet N, Blanc E, Gaillard P, Mialle P, Husson P (2019) Infrasound monitoring of volcanic eruptions and contribution of ARISE to the volcanic ash advisory centers. In: Le Pichon A, Blanc E, Hauchecorne A (eds) Infrasound monitoring for atmospheric studies, 2nd edn. Springer, Dordrecht, pp 1141–1162

Marty J (2019) The IMS infrasound network: current status and technological developments. In: Le Pichon A, Blanc E, Hauchecorne A (eds) Infrasound monitoring for atmospheric studies, 2nd edn. Springer, Dordrecht, pp 3–62

Matoza RS, Garcés MA, Chouet BA, D'Auria L, Hedlin MAH, de Groot-Hedlin C, Waite GP (2009) The source of infrasound associated with long-period events at Mount St. Helens. J Geophys Res 114:B04305. https://doi.org/10.1029/2008JB006128

Matoza R, Green D, Le Pichon A, Shearer PM, Fee D, Mialle P, Ceranna L (2017) Automated detection and cataloging of global explosive volcanism using the International Monitoring System infrasound network. J Geophys Res 122:2946–2971. https://doi.org/10.1002/2016JB013356

Matoza R, Fee D, Green D, Mialle P (2019) Volcano infrasound and the international monitoring system. In: Le Pichon A, Blanc E, Hauchecorne A (eds) Infrasound monitoring for atmospheric studies, 2nd edn. Springer, Dordrecht, pp 1023–1077

Millet C, Robinet J-C, Roblin C (2007) On using computational aeroacoustics for long-range propagation of infrasounds in realistic atmospheres. Geophys Res Lett 34:L14814. https://doi.org/10.1029/2007GL029449

Öttemoller L, Evers LG (2008) Seismo-acoustic analysis of the Buncefield oil depot explosion in the UK, 2005 December 11. Geophys J Int 172:1123–1134

Park J, Arrowsmith SJ, Hayward C, Stump BW, Blom P (2014) Automatic infrasound detection and location of sources in the western United States. J Geophys Res Atmos 119:7773–7798. https://doi.org/10.1002/2013JD021084

Park J, Stump BW (2015) Seasonal variations of infrasound detections and their characteristics in the western US. Geosci J 19:97. https://doi.org/10.1007/s12303-014-0034-6

Pasko VP (2012) Infrasonic waves generated by supersonic auroral arcs. Geophys Res Lett 39:L19105. https://doi.org/10.1029/2012GL053587

Pilger C, Ceranna L, Ross JO, Le Pichon A, Mialle P, Garcés MA (2015) CTBT infrasound network performance to detect the 2013 Russian fireball event. Geophys Res Lett 42:2523–2531. https://doi.org/10.1002/2015GL063482

Pilger C, Ceranna L, Le Pichon A, Brown P (2019) Large meteoroids as global infrasound reference events. In: Le Pichon A, Blanc E, Hauchecorne A (eds) Infrasound monitoring for atmospheric studies, 2nd edn. Springer, Dordrecht, pp 451–470

Revelle DO, Brown PG, Spurny P (2004) Entry dynamics and acoustics/infrasonic/seismic analysis for the Neuschwanstein meteorite fall. Meteorit Planet Sci 39:1605–1626

Silber E, Brown P (2019) Infrasound monitoring as a tool to characterize impacting near-earth objects (NEOs). In: Le Pichon A, Blanc E, Hauchecorne A (eds) Infrasound monitoring for atmospheric studies. 2nd edn. Springer, Dordrecht, pp 939–986

Smets PSM, Assink JD, Le Pichon A, Evers LG (2016) ECMWF SSW forecast evaluation using infrasound. J Geophys Res Atmos 121:4637–4650. https://doi.org/10.1002/2015jd024251

Sutherland LC, Bass HE (2004) Atmospheric absorption in the atmosphere up to 160 km. J Acoust Soc Am 115:1012–1032

Vergoz J, Le Pichon A, Millet C (2019) The antares explosion observed by the USArray: an unprecedented collection of infrasound phases recorded from the same event. In: Le Pichon A,

Blanc E, Hauchecorne A (eds) Infrasound monitoring for atmospheric studies, 2nd edn. Springer, Dordrecht, pp 349–386

Vernon F, Tytell J, Busby B, Eakins J, Hedlin M, Muschinski A, Walker K, Woodward B (2012) Scientific viability of the USArray Transportable Array Network as a real-time weather monitoring platform. In: 92nd American meteorological society annual meeting, American Meteor Society, New Orleans, La. https://ams.confex.com/ams/92Annual/webprogram/Paper200044.html

Walker K, Hedlin MAH, de Groot-Hedlin CD, Vergoz J, Le Pichon A, Drob D (2010) Source location of the 19 February 2008 Oregon bolide using seismic networks and infrasound arrays. J Geophys Res. https://doi.org/10.1029/2010jb007863

Walker KT, Shelby R, Hedlin M, de Groot-Hedlin C, Vernon F (2011) Western U.S. infrasonic catalog: illuminating infrasonic hot spots in the western U.S. with the USArray. J Geophys Res 116:B12305. https://doi.org/10.1029/2011JB008579

Walker KT, Le Pichon A, Kim TS, de Groot-Hedlin C, Che Il-Y, Garcés M (2013) An analysis of ground shaking and transmission loss from infrasound generated by the 2011 Tohoku earthquake. J Geophys Res Atmos 118:12805–12815. https://doi.org/10.1002/2013JD020187

Chapter 22
Calculating Atmospheric Gravity Wave Parameters from Infrasound Measurements

Graeme Marlton, Andrew Charlton-Perez, Giles Harrison and Christopher Lee

Abstract Infrasound arrays are sensitive enough to be able to detect the subtle pressure changes that occur as an overhead atmospheric gravity wave passes. The array can then provide information regarding the back azimuth, amplitude, frequency and pressure perturbation of the gravity wave. It is shown that by combining this data with meteorological data recorded at the array, further gravity wave parameters can be calculated. Some examples of time series analysis are shown for an infrasound station in the Ivory Coast illustrating how seasonal and daily variations in the weather can change the properties of gravity waves being detected. Ultimately, the parameters calculated using this method can be used by the meteorological community to improve the parametrisation of gravity waves in their models and increase understanding of the diurnal and seasonal variability in gravity wave parameters.

22.1 Introduction

Atmospheric gravity waves are generated by atmospheric disturbances and regions of dynamical imbalance in the atmosphere. Common gravity wave sources in the troposphere include rising air from convection, flow over topography and from spontaneous imbalance in the vicinity of jet streams (Knox et al. 2008). The gravity waves propagate outwards from the source transporting momentum as they do so. It has been shown in Blanc et al. (2014) and Lane et al. (2012) that gravity waves and their effects can be experienced at least 100 km away from a known source. Gravity waves can propagate vertically upwards into the stratosphere and mesosphere and also towards the ground (Gill 1982). Gravity waves that propagate towards the ground commonly become trapped or ducted between the Earth's surface and regions of the atmosphere where atmospheric stability or wind speed vary, due to reflection

G. Marlton (✉) · A. Charlton-Perez · G. Harrison · C. Lee
Department of Meteorology, University of Reading, Reading RG6 6BB, UK
e-mail: graeme.marlton@reading.ac.uk

A. Le Pichon et al. (eds.), *Infrasound Monitoring for Atmospheric Studies*,
https://doi.org/10.1007/978-3-319-75140-5_22

(Nappo 2013). These trapped waves cause subtle pressure perturbations to be observed at the surface which can be detected using microbarometers and precision barometers. Extensive work has been undertaken by examining pressure series to identify gravity waves (Gossard and Hooke 1975) generated by many sources including those generated by the adjustment of the atmosphere to sudden changes in solar heating during a solar eclipse (Marty et al. 2013; Aplin and Harrison 2003; Marlton et al. 2016). A single barometer can yield the surface frequency and pressure amplitude of a gravity wave. However, by combining several microbarometers into an array with approximately 1 km spacing between each instrument, some further basic wave parameters can be inferred. These basic parameters are the back azimuth ϕ, which is the compass bearing from which the gravity wave arrived from, and ground-based velocity c, which is the speed at which the gravity wave transits the array (Hauf et al. 1996; Marty et al. 2010; de Groot-Hedlin et al. 2014; Blanc et al. 2014).

From a meteorological prospective, one of the most important gravity wave parameters is the gravity wave momentum flux; this quantity is important as it shows how much of the wave's horizontal momentum is being transported vertically in the atmosphere. It also helps diagnose where the drag from the breaking waves is exerted on the mean flow (Geller et al. 2013). Geller et al. (2013) further explains that only a few methods can be used to estimate gravity wave momentum flux, and of them only a few methods have an extensive temporal and global coverage which are satellite and radiosonde observations. Of these most look at momentum fluxes in the stratosphere (Alexander et al. 2010) where wave breaking and drag can affect the upper level flow. A perfectly ducted gravity wave near the surface will not transfer momentum vertically as the duct boundary reflects the waves back into the duct. However, perfect reflection is rare and thus a portion of the wave is refracted through the upper boundary in a similar fashion to light waves and Snell's law (Nappo 2013). This has implications for understanding momentum budget and constraining gravity wave parameters in global circulation models within the troposphere.

The Comprehensive Nuclear-Test-Ban Treaty Organisation (CTBTO) has commissioned approximately 60 microbarometer arrays, also referred to infrasound stations, across the globe as shown in Fig. 22.1 (Marty 2019). This provides a global network from which basic gravity wave parameters can be derived from and climatological estimates made. Meteorological data is also needed in the form of wind speed and direction to remove the effects of the background flow on the wave and hence enable the calculation of gravity wave parameters such as intrinsic frequency and wave number. Fortunately, all infrasound stations have a meteorological station that can provide this data at each array. Hence, the potential for using a global network of infrasound stations to produce meteorological gravity wave parameters across the globe is now a possibility. In this chapter, a brief introduction into how gravity waves are detected at infrasound stations is given, followed by a method which outlines how the meteorological wave parameters are then calculated. As the majority of stations have been operational for 10 years, it is also possible to look at trends in derived gravity wave parameters over long timescales. An example will be provided showing meteorological gravity wave parameters from 5 years of data at IS17 Ivory Coast.

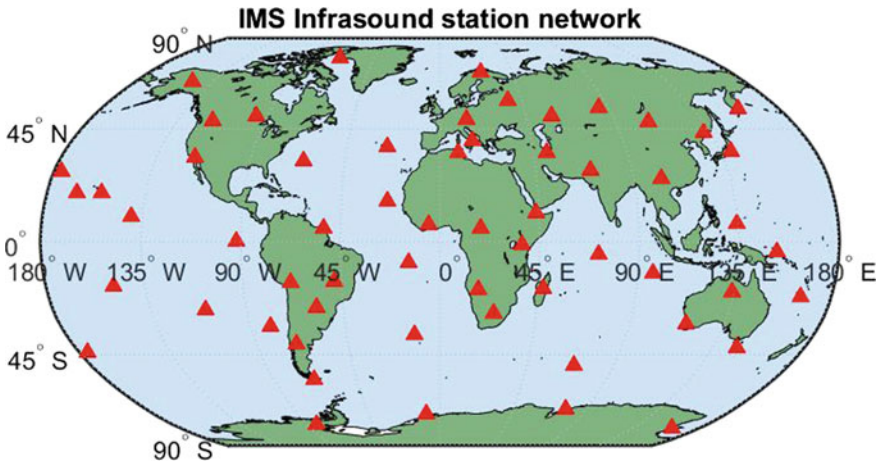

Fig. 22.1 Position of the 59 operational IMS infrasound stations across the globe

Blanc et al. (2014) has undertaken an analysis of the basic gravity wave parameters focussing mainly on gravity wave back azimuth, here a more in-depth analysis of other gravity wave parameters is undertaken. Finally, a short example will be given of how to calculate the momentum flux at the upper boundary of the wave duct.

22.2 Detecting Gravity Waves Using an Infrasound Station

Infrasound stations comprise a network of at least four microbarometers that continuously measure atmospheric pressure fluctuations. The microbarometers are typically arranged in a triangular configuration with the fourth instrument at the centre (Fig. 22.2), the distance between each sensor being approximately 1 km. Other configurations using a larger number of sensors at different spacings have also been used (Evers 2008). The microbarometers measure pressure using an aneroid capsule to give an absolute pressure. Each microbarometer is connected to a network of porous sampling hoses which are designed to reduce wind-generated noise by averaging out pressure fluctuations caused by turbulent eddies. The aneroid capsule and the transducer that measures the pressure fluctuations are buried to reduce the influence of thermal fluctuations on the measurements. Marty et al. (2010) showed that temperature effects are recorded by the microbarometers, but that the signal is at least 25 dB below that of average atmospheric pressure fluctuations in the gravity wave range. It was also found that the self-noise of the sensor was 30 dB below the lowest atmospheric pressure fluctuation detected in their study.

One method to identify gravity waves events across an array of microbarometers is to use a Progressive Multi-Channel Correlation (PMCC) algorithm first described in Cansi (1995). Originally, the method was created to use an array of seismometers

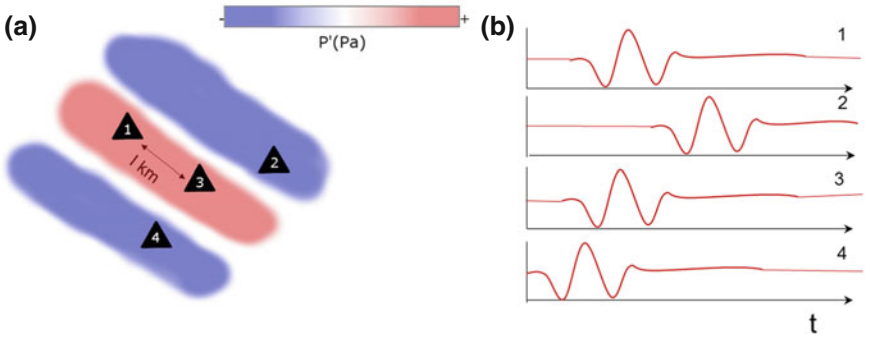

Fig. 22.2 **a** A schematic of a infrasound array as a gravity wave passes over the station. **b** The bandpass-filtered pressure time series at each microbarometer as the wave passes over the array. The amplitude of gravity waves at the surface is typically 2–3 Pa

to infer the frequency, azimuth, amplitude, and phase speed of seismic waves. Work by Le Pichon et al. (2002), Farges et al. (2003), Marty et al. (2013, 2010), Blanc et al. (2014), de Groot-Hedlin et al. (2014), etc. has shown how the same technique can be used to detect atmospheric gravity waves using infrasound microbarometer arrays. An alternate method is to use an approach which uses the Fisher correlation test to infer wave information. A brief description of the two methods will now be given; however, in either case we consider that the gravity wave crossing the array is a planar wave.

22.2.1 Progressive Multi-channel Correlation

The pressure time series from each microbarometer across the array is first bandpass filtered using Chebyshev bandpass filters at 10 logarithmically spaced frequency bands, spanning from 0.0001 to 0.00675 Hz. This frequency range is chosen as it spans the Coriolis parameter f_c, which accounts for the effects of the Earth's rotation on a gravity wave, and the Brunt–Vaisala frequency N, which accounts for the effects of buoyancy on a wave (Fritts and Alexander 2003). The bandpass-filtered pressure time series from each microbarometer is then truncated into smaller time windows. Figure 22.2 shows a schematic of a typical truncated bandpass-filtered pressure time series.

The time-windowed bandpass-filtered pressure series from each sensor is then cross-correlated with the corresponding bandpass-filtered time windows for each other sensor in the array. If the cross-correlation is high and the sum of the time lags between a subset of three microbarometers is close to zero, then a wave has been detected (Hauf et al. 1996). As the precise position of each microbarometer is known, the back azimuth ϕ and phase speed c of the detected wave can be calculated using

$$\phi = atan\left(\frac{S_x}{S_y}\right) \tag{22.1}$$

$$c = \frac{1}{\sqrt{S_x^2 + S_y^2}} \tag{22.2}$$

where S_x and S_y are the slowness vectors of the wave in $m^{-1}s$ calculated in a least squares sense by solving for all time lags and associated their inter-sensor distances using

$$\begin{bmatrix} \Delta x_{12} & \Delta y_{12} \\ \Delta x_{13} & \Delta y_{13} \\ \cdots & \cdots \\ \Delta x_{ij} & \Delta y_{ij} \end{bmatrix} \begin{bmatrix} S_x \\ S_y \end{bmatrix} = \begin{bmatrix} \tau_{12} \\ \tau_{13} \\ \cdots \\ \tau_{ij} \end{bmatrix}. \tag{22.3}$$

Here, τ_{ij} is the time delay along the vector given by Δx_{ij}, Δy_{ij}. The ground frequency Ω in Hz of the gravity wave is found by examining which set of bandpass-filtered pressure series it was observed in. Likewise, the time at which the wave was detected is inferred from the time windows. When all detections are combined, it gives a time–frequency domain of detected gravity waves such as that shown in Fig. 22.3.

Figure 22.3 also shows that some detections are very similar in a time, frequency, back azimuth and wave speed sense. This is due to the same wave being found in neighbouring time and frequency windows. Hence, a clustering method is used to cluster time–frequency windows which are very similar in the t, Ω, ϕ and c domain together as one wave. The raw pressure series data is then bandpass filtered using the frequency range inferred by the cluster and from this Ω is calculated and the size of the peaks is used to give P'.

22.2.2 Fisher Analysis

An alternate method to find a detected gravity wave at an infrasound station is to use a Fisher analysis to find t, Ω, ϕ and c. Described in Melton and Bailey (1957), the Fisher analysis takes any given amount of co-located time series and performs a statistical test to see if they consist of uncorrelated noise. Like its PMCC counterpart, it was first used for seismic detection by Blandford (1974). For this method, (which is thoroughly documented in Evers 2008) beamforming is carried out which effectively defines a wave back azimuth and speed. Truncated pressure time series, from each microbarometer, is then time-shifted appropriately based on the back azimuth and speed selected in the beamforming. If a gravity wave is present at that speed and back azimuth, the sinusoids in each time-shifted pressure series would be correlated. The algorithm scans all azimuths and wave speeds of interest. The best beam is considered the one which exhibits the most significant correlation, and is selected to calculate ϕ and c. By performing this analysis at different frequency windows or

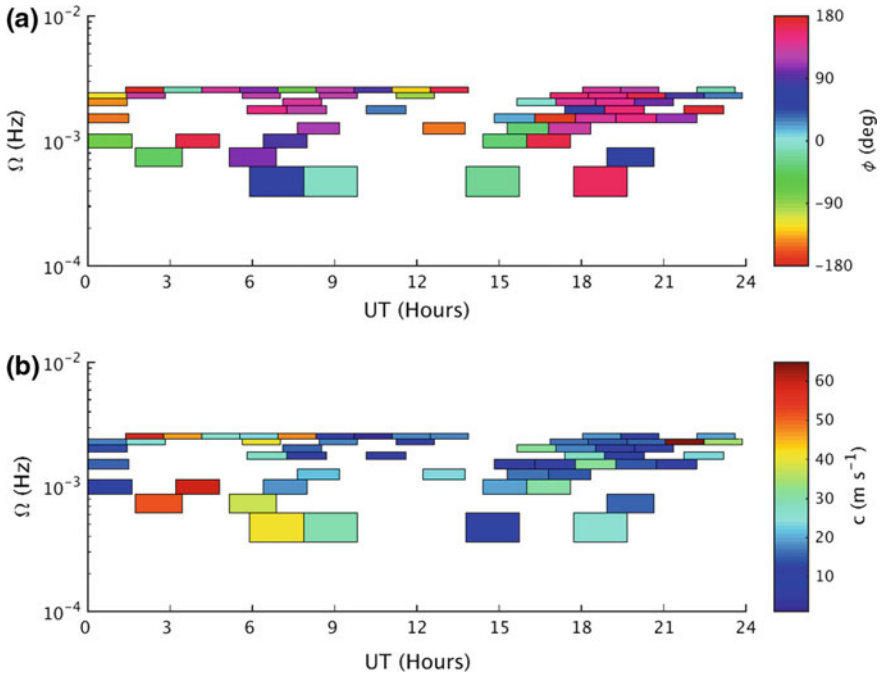

Fig. 22.3 Discrete spectrograms of detected gravity waves on 3 January 2009 at IS17 Ivory Coast. Colour bars refer to **a** the back azimuth and **b** the wave velocity of the gravity wave detections using PMCC

by performing an fourier transform, Ω and the P' can be found by examining the peak amplitudes.

22.3 Calculating Meteorological Gravity Wave Parameters

A list of the gravity wave detections calculated using PMCC or Fisher methods, containing information about the wave detection time, Ω, c, ϕ and P' is provided in the form of a gravity wave bulletin for a given infrasound station. However, as previously discussed, this information is insufficient to calculate parameters such as wave number. In this section, a brief explanation is given as to which parameters are important and how they can be calculated utilising the data from a meteorological station co-located at the infrasound station. The parameters calculated here utilise linear dispersion relationships. This is primarily because most waves which pass arrays are distant from their source and consequently represent a plane wave. Furthermore, unless an infrasound station with a large network of microbarometers is used, it is difficult to calculate curvature of the wavefront. Using a simple linear

dispersion method for monochromatic gravity wave does have some disadvantages, such as when looking at gravity waves with long wavelength or when no account is taken for wave packets of varying wavelength.

22.3.1 Calculating the True Pressure Perturbation P′

The microbarometers used at infrasound stations are primarily designed to measure pressure perturbations in the 0.01–0.4 Hz range (Marty et al. 2010). Gravity waves occur at lower frequencies (10^{-4}–10^{-2} Hz); hence, their signals are attenuated by the instrument. A correction is applied to the wave's pressure amplitude to correct for the attenuation at that frequency. As the response of each microbarometer is different, the specific instrument documentation should be consulted to design a suitable correction.

22.3.2 Intrinsic Wave Speed and Frequency

A gravity wave that is passing a fixed point of measurement through the atmosphere has a ground-based wave speed c which is given by

$$c = c_i + u_p, \tag{22.4}$$

where c_i is the intrinsic speed of the wave, i.e. the speed the wave would propagate at in zero mean background flow. u_p is the projected wind speed along the direction of propagation of the wave and is given by

$$u_p = u \sin(-\phi) + v \cos(-\phi), \tag{22.5}$$

where u and v are the zonal and meridional wind components derived from the anemometer and wind vane installed at the infrasound array. Knowing the intrinsic wave speed is important as it allows the characteristics of the wave in the flow to be isolated. The relationship between ground-based frequency, Ω and the intrinsic frequency, ω is given by

$$\Omega = \omega + \frac{u_p}{\lambda}, \tag{22.6}$$

where λ is the intrinsic wavelength of the wave. As c_i is known, $\lambda = c_i/\omega$ can be substituted into Eq. 22.6 to yield an expression for the intrinsic wave frequency in the form

$$\omega = \frac{\Omega}{\left(\frac{u_p}{c_i} + 1\right)}. \tag{22.7}$$

Knowing the intrinsic wave frequency is important, as it allows other meteorological parameters to be calculated. More importantly, it allows information about whether the gravity wave is being affected more by buoyancy or by the effects of the Earth's rotation. High-frequency waves ($>10^{-2}$ s^{-1}) are more likely affected by buoyancy, whereas low-frequency waves ($<10^{-4}$ s^{-1}) are more likely affected by rotation.

22.3.3 Horizontal and Vertical Wave Numbers

Once the intrinsic frequency of each wave is calculated, it is then possible to calculate the horizontal and vertical wave numbers of the wave. Wave numbers are important as they allow the horizontal and vertical velocity perturbations to be calculated (Gill 1982). The horizontal wave number k_H is given by

$$k_H = \frac{\Omega - \omega}{u_p}, \tag{22.8}$$

which is achieved by substituting $\lambda = 1/k_H$ into Eq. 22.6. The x and y components of the wave number k_H, k and l can then be calculated using

$$k = k_H \sin(-\phi), \tag{22.9}$$

$$l = k_H \cos(-\phi). \tag{22.10}$$

As we are observing ducted waves, the dispersion relations shown in Gill (1982), Fritts and Alexander (2003), etc. cannot be used, so a different relationship must be used to yield the vertical wave number m. Nappo (2013) states that the vertical wave number m can be given by

$$m^2 = k_H^2 * (\frac{N^2}{\Omega^2} - 1), \tag{22.11}$$

where N is the Brunt–Vaisala frequency which has a tropospheric value of 0.01 s^{-1}.

22.3.4 Wave Velocity Perturbations

In order to calculate the momentum fluxes at upper boundary of the wave duct, the amplitudes of the horizontal and vertical velocity perturbations of the trapped wave are needed; these can be calculated using the polarisation relations which are shown in Gill (1982). The horizontal velocity perturbation is given by

$$u' = \frac{P'}{\rho c_i}, \tag{22.12}$$

where ρ is the density of dry air which can be calculated using

$$\rho = \frac{P}{R_d T}, \tag{22.13}$$

where P is the pressure in Pa, R_d is the gas constant of dry air which is 287 J K^{-1} kg^{-1} and T is the dry bulb temperature in K. For these purposes, the mean temperature from the weather station for the duration of the wave is used and the mean pressure can be retrieved from the microbarometer array. The vertical velocity perturbation w can be calculated using

$$w' = \frac{k_H^2 P'}{\omega m \rho}. \tag{22.14}$$

Nappo (2013) showed that by integrating the momentum flux equation

$$F = \rho u' w' \tag{22.15}$$

over the wavelength of the trapped or ducted wave that $F = 0$. In Sect. 22.5, a method for calculating the momentum flux at the top of a ducted layer will be explored, but first more attention will be given to how N and ρ are derived.

22.3.5 Calculating ρ

In the previous section, it was shown that ρ could be calculated using a dry air assumption, however, in reality the atmosphere, especially near the ground is far from dry. The question that should then be asked is: Could the inclusion of moisture cause a significant change in perturbation velocities in Eqs. 22.12 and 22.14? To include moisture in a density calculation, an adjustment is made to Eq. 22.13 so that

$$\rho_v = \frac{P'}{R T_v}, \tag{22.16}$$

where T_v is the virtual temperature, which is similar to sonic temperature (Harrison 2001). T_v is given by

$$T_v = \frac{T}{1 - \frac{e}{P}(1 - \epsilon)}, \tag{22.17}$$

where e is the water vapour pressure and ϵ is the ratio of the dry air gas constant to the gas constant for 1 kg of water vapour which equates to 0.622 (Wallace and Hobbs 2006). The density of saturated air is equal to the density of warmer unsaturated air.

Thus, virtual temperature is the temperature of an air parcel with the same density and pressure as moist air, and hence $T_v > T$. One of the most common meteorological measures of humidity is relative humidity (RH %). e can be calculated from RH using

$$e = \frac{RH}{100} e_s, \tag{22.18}$$

where e_s is the saturation vapour pressure and is a function of T (Ambaum 2010). In order to assess whether the inclusion of moisture would have any effects on the calculation of ρ, a sensitivity test was carried out. For a range of temperatures between −20 and 40 °C, the density, using Eq. 22.16, was calculated and then compared as a percentage of the density calculated for a dry atmosphere using Eq. 22.13.

Figure 22.4 shows clearly that density is affected by moisture content only when temperature >30 °C and relative humidity >60% does the air become significantly less dense. It will likely be important, therefore, to make this correction at many tropical infrasound stations. Further, sensitivity testing is needed, however, to find out if this would have a significant effect on velocity perturbations. The simplest approach is to propagate this reduction as an uncertainty on the quantities calculated in Eqs. 22.12 and 22.14. It was found that for sensitivity tests at IS17, w' was 13% larger and u' was 3% larger when humidity was included in the density equation.

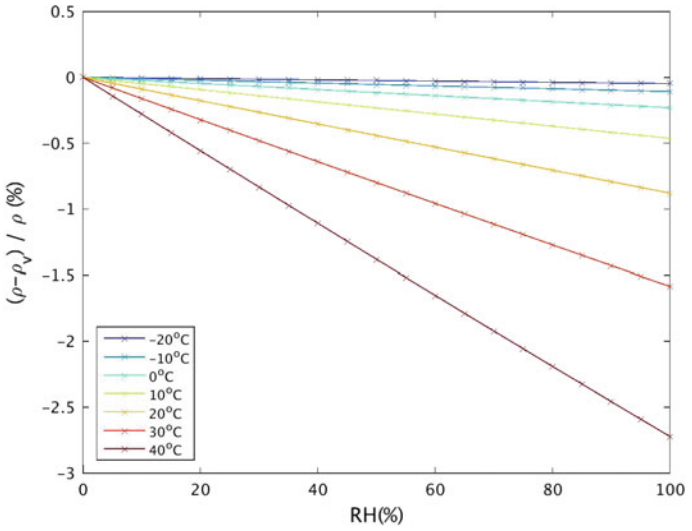

Fig. 22.4 The percentage difference in density calculated using RH plotted, against density calculated for a dry atmosphere for different humidities. Each line colour refers to different temperatures

22.3.6 Calculating the Brunt Vaisala Frequency

In Eq. 22.13, a assumed climatological value of $N = 0.01$ s^{-1} Brunt–Vaisala frequency N is used to infer the vertical wave number m. How good is this assumption? In order to test this, the Brunt–Vaisala frequency was calculated over an infrasound station. The Brunt Vaisala frequency is given by

$$N = \sqrt{\frac{g}{\theta}\frac{\partial \theta}{\partial z}}, \tag{22.19}$$

where g is the acceleration due to gravity and z is the height. θ is the potential temperature given by

$$\theta = T\left(\frac{1000}{P}\right)^{\frac{R}{c_p}}, \tag{22.20}$$

where c_p =1004 J kg^{-1}. As inferred in Eq. 22.19, a vertical profile of θ is needed. The most reliable source of near ground vertical profiles of θ is from radiosondes. Radiosondes are small balloon-borne devices which are able to obtain in situ measurements to construct vertical profiles of temperature pressure and relative humidity as well as wind speeds (Marlton et al. 2015). They can provide the core information for this at up to 1 s intervals giving 5 m vertical resolution, however, not all are archived in this manner. Thus, using data from nearby radiosondes, the Brunt Vaisala frequency in the vicinity of an infrasound station can be estimated.

Figure 22.5 shows N calculated from radiosondes 100 km south of IS17 for 2015; it can be seen that the observed N is higher than the assumed tropospheric value which is depicted by the black dashed line. The higher value of N near the surface also gives some evidence that conditions that allow the ducting of gravity waves are present Nappo (2013). A sensitivity test was carried out to see the difference in vertical wave number and velocity perturbation using the observed values compared to the assumed value of 0.01 s^{-1}. To achieve this, a ΔN of 0.003 was set as being the difference between the observed and climatological value as this represents the largest change from the tropospheric values in Fig. 22.5. ΔN was then propagated through Eqs. 22.11 and 22.14. The error at each stage was calculated as a percentage and was found to be 28% for m which when further propagated gave 21% for w'. Therefore, the use of a climatologically correct value of N is important, not only to calculate the correct wave number but also to ensure that the vertical wavenumber within the duct is calculated correctly. However, in some parts of the globe, radiosonde profiles are sparse meaning a microbarometer array may be 1000s of km away from a radiosonde site. In these cases, a reanalysis dataset may have to be used to estimate the vertical temperature and pressure profiles. Reanalysis datasets are large atmospheric datasets which span the entire height of the atmosphere from the surface to a pressure height of 1 hPa (Kalnay et al. 1996; Dee et al. 2011). They are constructed from a global network of surface, radiosonde and satellite observations which are assimilated to give the best approximation of the state of the atmosphere. This means that the

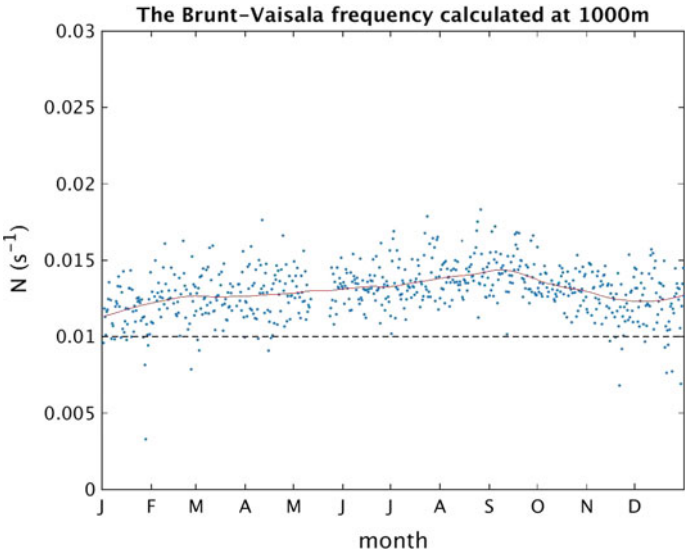

Fig. 22.5 Brunt–Vaisala frequency calculated at 1000 m from radiosonde profiles made at Abidjan, (approximately 100 km south of IS17) Ivory Coast for 2015, the black dashed line is the tropospheric value and the black solid line is a loess fit to the data points

reanalysis can generate an atmospheric profile in a part of the atmosphere where there are no radiosonde observations; however, the result may not be as accurate as that from a radiosonde observation. Although a Reanalysis radiosonde comparison is beyond the scope of this chapter, some preliminary results in Marlton (2016) show that T, Z, u and v compare well when compared to independent radiosondes.

22.4 Example Analysis from the Ivory Coast Infrasound Station

As shown in Fig. 22.1, the CTBTO has installed approximately 60 infrasound stations globally, thus providing an excellent network to make gravity wave measurements. In this section, a preliminary analysis of infrasound data collected at IS17 is undertaken. A study by Blanc et al. (2014) analysed 10 years worth of gravity wave bulletins at IS17 and was able to relate the annual shift in gravity wave back azimuth to convective storms generated at the Intertropical Convergence Zone (ITCZ). However, only the base quantities of ϕ, P', c and Ω were used. Here, the analysis is expanded to examine how other gravity wave parameters vary throughout the year. The period of study is from 2007 to 2011 as this is the time period when both meteorological and infrasound bulletins were available. For this analysis, the gravity wave parameters derived in the previous section will be calculated; for the purposes of these calculations, N will be derived from the loess fit shown in Fig. 22.5. Given that

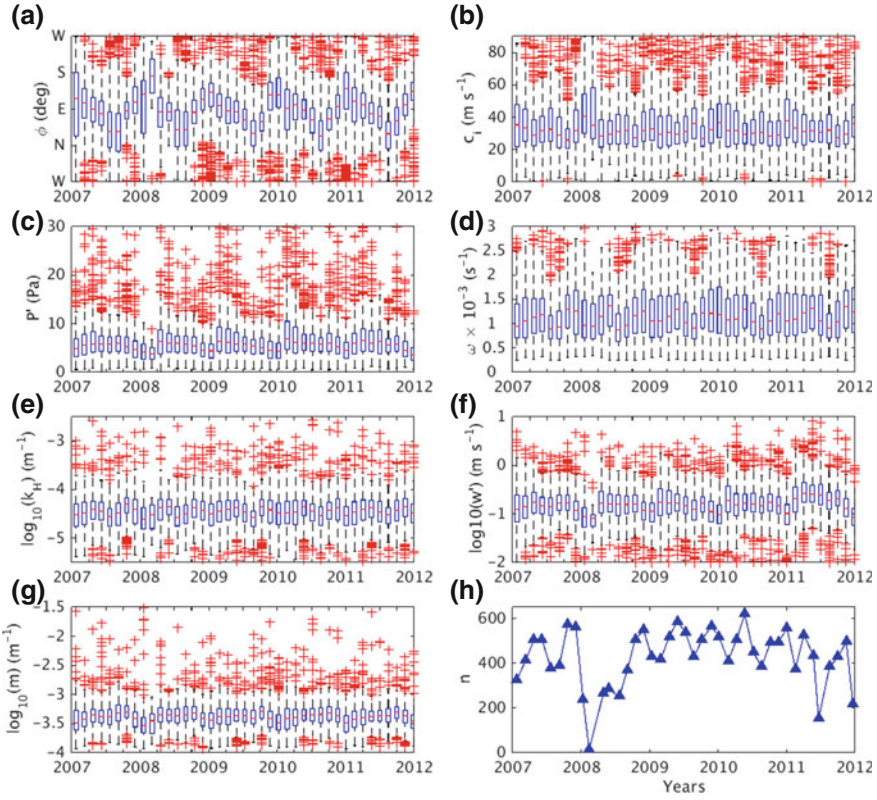

Fig. 22.6 Boxplots of **a** back azimuth ϕ (deg), **b** intrinsic wave speed c_i (m s^{-1}), **c** pressure perturbation P' (Pa), **d** intrinsic frequency (s^{-1}), **e** $\log_{10}$ horizontal wave number k_H (m^{-1}), **f** $\log_{10}$ vertical velocity perturbation w' (m s^{-1}) and **g** $\log_{10}$ vertical wave number m (m^{-1}) binned over 45 day periods. The red line is the median of the quantity, with the blue box representing interquartile range ($q_3 - q_1$) of the quantities. Upper black stems represent the lowest of either the 75th percentile plus one and a half times the interquartile range of the binned data or the maximum value of the binned data. Lower black stems represent the greatest of either the 25th percentile minus one and a half times the interquartile range of the binned data or the minimum value of the binned data. Red crosses show outliers which are data points that fall outside range given by the black stems. **h** shows the number of gravity wave detections n for each 45 day period

the Ivory Coast is situated in the tropics, the relative humidity is included within the density calculations.

Figure 22.6 shows boxplots of the meteorological gravity wave parameters binned over 45 day periods. In panel (a), the annual variation in ϕ which has been shown Blanc et al. (2014) is reproduced. There are also similar observed annual variations in ω, P' and c_i. In P' (panel (c)), it appears that there is a peak during April and May and a minima in December and January. k_H and w' are shown in panels (e) and (f); whilst there are periodicities within the data, an annual periodicity is not immediately clear. m is plotted in panel (g), which also shows an annual periodicity.

Given the different source regions, it is also likely that there are further annual variations in the other quantities. This means that the properties of the gravity waves change throughout the year, which could be due to the fact as they propagate their properties alter. This could mean that gravity waves that have sources close to the infrasound station may have different properties to those where the source is more distant. To further explore the nature of the annual variability in the gravity wave detections, a spectral analysis is needed to find periodic variations. However, the gravity waves presented in the gravity wave bulletin are not evenly spaced in time. A spectral method which can deal with irregularly spaced data is needed. One method is to use the Lomb periodogram which can find periodicities in unevenly sampled data (Lomb 1976).[1] The Lomb periodogram generated for the gravity wave data here is based on a fast Lomb routine as shown in Press (2007), due to the large quantity of ($>10^4$) detections of gravity waves.

Figure 22.7 shows Lomb periodograms for gravity waves detected at IS17 between 2007 and 2012. All quantities with the exception of k_H have an annual periodicity. All parameters, however, do show a peak at 6 months, which implies that the gravity waves detected are modulated by seasonal variation. For azimuth, this seasonal variation is understandable as the inter-tropical convergence zone shifts northward in July and southward in December. For other meteorological quantities, the annual variation could be due to the fact that gravity waves have propagated further and hence their properties may change. Periodicities shorter than 6 months as shown in Fig. 22.7 could be due to the north African monsoon which affects the Ivory Coast between June and September causing a clustering of additional thunderstorms north of the Ivory Coast. Each parameter also has a daily periodicity, which is not surprising as the main source of gravity waves detected at IS17 is those generated by convective updraughts. Daily periodicities within detections could occur as gravity waves from nearby sources have differing properties from those which arrive later from more distant sources.

Figure 22.8 shows the daily distribution of gravity wave detections for the 5-year Ivory Coast dataset. The peak in detections happens at about 18 UTC. This is due to the infrasound station detecting gravity waves from local thunderstorms. In the early hours of the morning, there is a second peak in gravity wave detections which is likely due to far-field gravity waves which were generated at the same time but by a more distant source. By midday, the gravity wave detections fall to a minimum; this is likely due to the lack of convective gravity wave sources as significant heating at the ground has not yet occurred.

[1]The Lomb periodogram was originally used to find periodicities from irregularly sampled astronomical data.

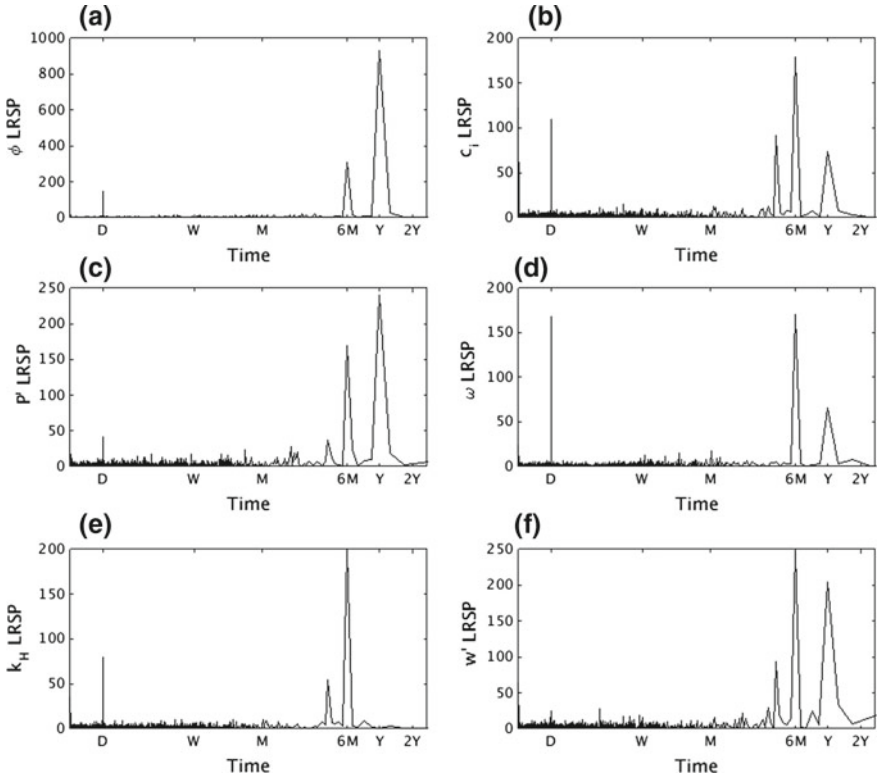

Fig. 22.7 Lomb periodograms showing the Lomb Relative Spectral Power (LRSP) (dimensionless) for **a** back azimuth ϕ (deg), **b** intrinsic wave speed c_i (m s^{-1}), **c** pressure perturbation P' (Pa), **d** intrinsic frequency (s^{-1}), **e** $\log_{10}$ horizontal wave number k_H (m^{-1}), and **f** $\log_{10}$ vertical velocity perturbation w' (m s^{-1}). The horizontal axis mark day (D), week (W), month (M), half-year (6M), year (Y) and biannual (2Y) periodicities

22.5 Calculating the Gravity Wave Momentum Flux at the Upper Duct Boundary

For the modelling of the atmosphere having a knowledge of the gravity wave momentum flux is important, given that a trapped wave can be refracted through the upper boundary, a method to calculate the momentum flux at the upper boundary of the duct is explored. As discussed in Sect. 22.1, a duct can form between the Earth's surface and a region of the atmosphere with a discontinuity in N or U as both cause gravity waves to be reflected towards each other, causing the wave to become trapped. Due to the nature of the Earth's surface, the gravity wave is reflected. However, at the upper boundary, a portion of the wave is refracted out of the duct. An example will be given showing how the gravity wave momentum flux at the top of a simple wave duct can be calculated.

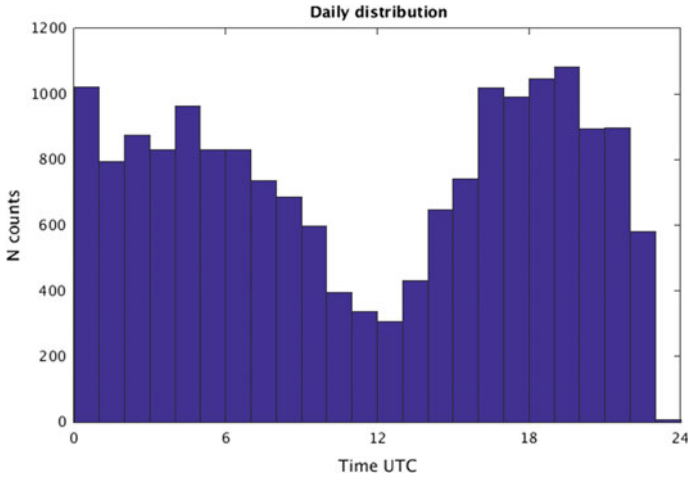

Fig. 22.8 Histogram showing the number of gravity wave detections binned by hour of day, for IS17 between 2007 and 2012

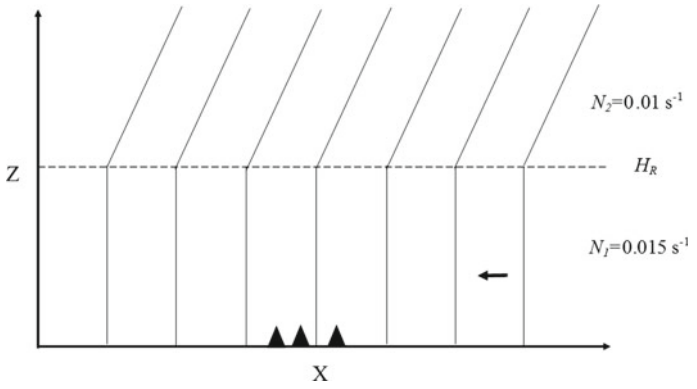

Fig. 22.9 A diagram showing a ducted gravity wave close to the ground, over a distance x and a height z. The thin lines represent the wave crests, the dashed line represents the upper boundary of the wave duct at height H_R, which is formed due to a discontinuity in N. The black triangles represent the infrasound station

Figure 22.9 shows a ducted gravity wave between the Earth's surface and a height H_R which is established by a discontinuity in N. In this example, we will assume N_1, the Brunt–Vaisala frequency near the ground to be 0.015 s^{-1}, which is similar to the value given in Fig. 22.9 and make N_2 above the duct to be 0.01 s^{-1}. In order to work out the momentum flux, the vertical velocity perturbation is needed which can be calculated from Eq. 22.14, but Eq. 22.14 does not account for the motions of both the upward and downward motions of the reflected waves. w' at a point in the wave duct can be given by

$$w' = \frac{k_H^2 P'}{m_1 \omega \rho_0 \left[-\exp(im_1(z - H_R)) + r \exp\left(-im_1(z - H_R)\right)\right] \exp\left(i(k_H x - \omega t)\right)}, \tag{22.21}$$

where z is the height, m_1 is the vertical wave number within the duct, and r is the reflection coefficient (Gill 1982) given by

$$r = \frac{m_1 - m_2}{m_1 + m_2}. \tag{22.22}$$

m_2 is the vertical wave number in the layer above the duct and can be calculated using Eq. 22.11 or by using the dispersion relation if it is known the waves above are not in another duct and follow the behaviour of inertia-gravity waves (Fritts and Alexander 2003). These relations hold beyond the duct as ω and k_H are constant with height above and below the duct boundary (Gill 1982). The reflection coefficient is the ratio between the amplitudes of the upward and downward motions of waves in the wave duct. By evaluating Eq. 22.21 at the surface ($z = 0$) and for $t = 0$ and $X = 0$, w' at the surface can be calculated. Thus, the vertical gravity wave momentum flux density F'_z can be calculated using

$$F'_z = \frac{U m_2 \rho w_0'^2 / 2k_H}{(1 + (m_2/m_1)^2 - 1)\sin^2(m_1 H_R)}, \tag{22.23}$$

given by Gill (1982) where w_0 is the vertical velocity perturbation at the ground. F'_z is related to the vertical momentum flux F by

$$F = \frac{F'_z}{U}. \tag{22.24}$$

For our example calculation, the background values of N will be used from Fig. 22.9 and U is set constant with height at 10 m s^{-1}, and finally $H_R = 1500$ m. The gravity wave momentum flux at the upper boundary for an observed gravity wave with $P' = 4$ Pa, $k_H = 2.4 \times 10^{-4}$ rad m^{-1}, $\omega = 0.0036$ rad s^{-1}, was found to be of the order 10^{-3} kg m^2 s^{-1}. It should be noted that the atmosphere may not be as simple as that shown in Fig. 22.9. For example, a jet may be present which could form a duct (Nappo 2013). Furthermore, a discontinuity in N often causes mountain waves to become trapped against the tropopause (Worthington 1998).

22.6 Conclusions

In this chapter, a method to allow data from an infrasound station to be used to observe gravity waves has been described. A description of how the meteorological gravity wave parameters can be calculated from both a combination of infra-

sound data and meteorological data was shown. The inclusion of the Brunt–Vaisala frequency was important in these calculations, with climatologically correct values from a nearby upper air station giving 20% larger perturbation properties. Inclusion of relative humidity was shown to cause a 3–13% increase in wave perturbation velocities, but only in tropical regions. Examples of time series analysis of the derived parameters were also shown to highlight how daily and annual meteorological variations in a region can affect the gravity waves detected. An example calculation was also shown which demonstrates how the gravity wave momentum flux can be calculated at the top of the wave duct. An extensive analysis is beyond the scope of this chapter; further research should aim at undertaking an in-depth analysis of the gravity wave time series to characterise the gravity wave parameters under different conditions. This can allow modellers to better constrain gravity wave parameters about the waves source in their models. At the time of writing, efforts are being undertaken to bring together gravity wave detections from the whole CTBTO network to begin creating a global dataset of gravity wave parameters that can be used by the meteorological community.

Acknowledgements This research is part of the Atmospheric Dynamics Research Infrastructure in Europe (ARISE) project, funded by the European Union's Seventh Framework Program.

References

Alexander MJ, Geller M, McLandress C, Polavarapu S, Preusse P, Sassi F, Sato K, Eckermann S, Ern M, Hertzog A et al (2010) Recent developments in gravity-wave effects in climate models and the global distribution of gravity-wave momentum flux from observations and models. Q J R Meteorol Soc 136(650):1103–1124

Ambaum MHP (2010) Thermal physics of the atmosphere, vol 1. Wiley

Aplin KL, Harrison RG (2003) Meteorological effects of the eclipse of 11 August 1999 in cloudy and clear conditions. Proc R Soc Lond A: Math Phys Eng Sci 459:353–371

Blanc E, Farges T, Le Pichon A, Heinrich P (2014) Ten year observations of gravity waves from thunderstorms in Western Africa. J Geophys Res: Atmos 119(11):6409–6418

Blandford RR (1974) An automatic event detector at the Tonto Forest seismic observatory. Geophysics 39(5):633–643

Cansi Y (1995) An automatic seismic event processing for detection and location: the PMCC method. Geophys Res Lett 22(9):1021–1024

de Groot-Hedlin CD, Hedlin MAH, Walker KT (2014) Detection of gravity waves across the USArray: a case study. Earth Planet Sci Lett 402:346–352

Dee DP, Uppala SM, Simmons AJ, Berrisford Paul, Poli P, Kobayashi S, Andrae U, Balmaseda MA, Balsamo G, Bauer P et al (2011) The era-interim reanalysis: configuration and performance of the data assimilation system. Q J R Meteorol Soc 137(656):553–597

Evers LG (2008) The inaudible symphony: on the detection and source identification of atmospheric infrasound. PhD thesis, TU Delft, Delft University of Technology

Farges T, Le Pichon A, Blanc E, Perez S, Alcoverro B (2003) Response of the lower atmosphere and the ionosphere to the eclipse of August 11. J Atmos Solar-Terr Phys 65(6):717–726

Fritts DC, Alexander MJ (2003) Gravity wave dynamics and effects in the middle atmosphere. Rev Geophys 41(1)

Geller MA, Alexander MJ, Love PT, Bacmeister J, Ern M, Hertzog A, Manzini E, Preusse P, Sato K, Scaife AA et al (2013) A comparison between gravity wave momentum fluxes in observations and climate models. J Clim 26(17):6383–6405

Gill AE (1982) Atmosphere-ocean dynamics, vol 30. Academic Press

Gossard EE, Hooke WH (1975) Waves in the atmosphere: atmospheric infrasound and gravity waves-their generation and propagation. Atmos Sci 2

Harrison RG (2001) Ultrasonic detection of atmospheric humidity variations. Rev Sci Instrum 72(3):1910–1913

Hauf T, Finke U, Neisser J, Bull G, Stangenberg JG (1996) A ground-based network for atmospheric pressure fluctuations. J Atmos Oceanic Technol 13(5):1001–1023

Kalnay E, Kanamitsu M, Kistler R, Collins W, Deaven D, Gandin L, Iredell M, Saha S, White G, Woollen J et al (1996) The NCEP/NCAR 40-year reanalysis project. Bull Am Meteorol Soc 77(3):437–471

Knox JA, McCann DW, Williams PD (2008) Application of the Lighthill-Ford theory of spontaneous imbalance to clear-air turbulence forecasting. J Atmos Sci 65(10):3292–3304

Lane TP, Sharman RD, Trier SB, Fovell RG, Williams JK (2012) Recent advances in the understanding of near-cloud turbulence. Bull Am Meteorol Soc 93(4):499

Le Pichon A, Garcés M, Blanc E, Barthélémy M, Drob DP (2002) Acoustic propagation and atmosphere characteristics derived from infrasonic waves generated by the Concorde. J Acoust Soc Am 111(1):629–641

Lomb NR (1976) Least-squares frequency analysis of unequally spaced data. Astrophys Space Sci 39(2):447–462

Marlton GJ, Williams PD, Nicoll KA (2016) On the detection and attribution of gravity waves generated by the 20 march 2015 solar eclipse. Philos Trans R Soc Lond A: Math Phys Eng Sci 374(2077). https://doi.org/10.1098/rsta.2015.0222. http://rsta.royalsocietypublishing.org/content/374/2077/20150222. ISSN 1364-503X

Marlton GJ (2016) On the development, characterisation and applications of a balloon-borne atmospheric turbulence sensor. PhD thesis, Department of Meteorology, University of Reading

Marlton GJ, Harrison RG, Nicoll KA, Williams PD (2015) Note: a balloon-borne accelerometer technique for measuring atmospheric turbulence. Rev Sci Instrum 86(1):016109

Marty J (2019) The IMS infrasound network: current status and technological developments. In: Le Pichon A, Blanc E, Hauchecorne A (eds) Infrasound monitoring for atmospheric studies, 2nd edn. Springer, Dordrecht, 3–62

Marty J, Ponceau D, Dalaudier F (2010) Using the international monitoring system infrasound network to study gravity waves. Geophys Res Lett 37(19)

Marty J, Dalaudier F, Ponceau D, Blanc E, Munkhuu U (2013) Surface pressure fluctuations produced by the total solar eclipse of 1 August 2008. J Atmos Sci 70(3):809–823

Melton BS, Bailey LF (1957) Multiple signal correlators. Geophysics 22(3):565–588

Nappo CJ (2013) An introduction to atmospheric gravity waves. Academic Press

Press WH (2007) Numerical recipes 3rd edition: The art of scientific computing. Cambridge University Press

Wallace JM, Hobbs PV (2006) Atmospheric science: an introductory survey. Academic Press

Worthington RM (1998) Tropopausal turbulence caused by the breaking of mountain waves. J Atmos Solar-Terr Phys 60(16):1543–1547

Part VIII
Evaluating and Improving Global Circulation and Climate Models and Weather Forecasts (GCM): Middle Atmospheric Disturbances and Trends

Chapter 23
The Study of Sudden Stratospheric Warmings Using Infrasound

Pieter Smets, Jelle Assink and Läslo Evers

Abstract Infrasound has a long history of monitoring sudden stratospheric warmings. Several pioneering studies have focused on the various effects of a major warming on the propagation of infrasound. A clear transition has been made from observing anomalous signatures towards the use of these signals to study anomalies in upper atmospheric conditions. Typically, the infrasonic signature of a major warming corresponds to summer-like infrasound characteristics observed in mid-winter. More subtle changes occur during a minor warming, recognisable by the presence of a bidirectional stratospheric duct or propagation through a warm stratosphere leading to small shadow zones. A combined analysis of all signal characteristics unravels the general stratospheric structure throughout the life cycle of the warming. A new methodology to evaluate the state of the atmosphere as represented by various weather and climate models is demonstrated. A case study comparing regional volcano infrasound with simulations using various forecast steps indicates significant differences in stratospheric forecast skill, associated with a data assimilation issue during the warming.

P. Smets (✉) · J. Assink · L. Evers
R&D Department of Seismology and Acoustics, Royal Netherlands Meteorological Institute (KNMI), Utrechtseweg 297, 3137 GA De Bilt, The Netherlands
e-mail: smets@knmi.nl; pieter.smets@knmi.nl

P. Smets · L. Evers
Faculty of Civil Engineering and Geosciences, Department of Geoscience and Engineering, Delft University of Technology, Stevinweg 1, 2628 CN Delft, The Netherlands

A. Le Pichon et al. (eds.), *Infrasound Monitoring for Atmospheric Studies*,
https://doi.org/10.1007/978-3-319-75140-5_23

23.1 Introduction

Sudden stratospheric warmings (SSWs) are important features of the winter atmosphere (Charlton and Polvani 2007). During such events, the strongest transient forcing of the stratosphere on the troposphere is observed (Gerber et al. 2009; Tripathi et al. 2014), influencing weather conditions and its predictability in the troposphere (Jung et al. 2010). Consequentially, improving the predictability of stratospheric variability, such as during SSWs, is important to Numerical Weather Prediction (NWP) Lee et al. (2019). Infrasound, part of the Atmospheric Dynamics Research Infrastructure in Europe (ARISE) project (Blanc et al. 2019), has shown its ability in probing the upper atmosphere (e.g. Donn and Rind 1971; Le Pichon et al. 2009), discussed by Assink et al. (2019). Infrasound is low-frequency inaudible sound (<20 Hz), used as a waveform verification technique for the Comprehensive Nuclear-Test-Ban Treaty (CTBT). A key benefit of infrasound is the sensitivity to both temperature and wind in a region where atmospheric observations are scarce. Infrasound has a long history of monitoring sudden stratospheric warmings. Several pioneering studies have focused on the various effects of a major warming on the propagation of infrasound. For that reason, studying SSWs using infrasound is part of the ARISE roadmap demonstrating the use of infrasound data for weather and climate monitoring (Smets et al. 2014). Further ARISE techniques to probe the middle atmosphere (10–100 km) are ground-based lidars, radars, wind radiometers and ionospheric sounders (Blanc et al. 2019 and http://arise-project.eu). This chapter describes how infrasound can provide additional insight into SSW events and how this information can be used in current atmospheric models for evaluation of stratospheric predictability. First, we elucidate the relation between infrasound and sudden stratospheric warmings and why studying these events is important for both weather and climate as well as for infrasound monitoring. Second, an overview of infrasound studies of SSWs is presented, evolving from observing anomalous infrasonic signatures attributed to a warming towards the use of these signals to study anomalies in upper atmospheric conditions. Finally, an outlook is given on the future impact of infrasound on stratospheric predictability.

23.2 Sudden Stratospheric Warmings

Sudden stratospheric warmings (SSWs) are regularly occurring features in winter in the northern hemisphere (Charlton and Polvani 2007) characterised by dramatic changes in the stratospheric wind and temperature. SSWs are the strongest transient manifestation of the stratosphere–troposphere interaction (Charlton and Polvani 2007; Shaw and Shepherd 2008; Gerber et al. 2009).

23.2.1 Principle Mechanism

In the stratosphere, the temperature increases with height to a maximum at the stratopause due to the absorption of solar ultraviolet radiation by ozone (Holton 2004). The unequal solar insolation induces a temperature gradient from warm summer pole to cold winter pole, driving the circumpolar vortex. For this induced geostrophic circulation, the Coriolis force balances the horizontal pressure gradient whereas the thermal-wind balance relates the vertical wind shear to the horizontal temperature gradient (Muench 1965). The seasonal variation in the atmosphere's heat balance changes the direction of the polar vortex, typically around the vernal and autumnal equinoxes. In summer, during polar day, the circumpolar vortex is easterly, characterised by a stable stratospheric wind and temperature structure. In winter, the westerly circumpolar vortex is stronger but unstable.

During polar night, the high-latitude westerly jets provide a waveguide for vertical propagation of quasi-stationary planetary waves, primarily of zonal wave numbers 1 and 2 (Holton 2004). Rossby waves propagate vertically from the troposphere up into the stratosphere and break in the polar vortex, which can trigger an SSW (Matsuno 1971). This planetary wave breaking decelerates the westerly zonal-mean flow, reducing the pole-to-equator mean temperature gradient (Charney and Drazin 1961). The effect increases with height as the vertically propagating Rossby wave amplitude increases because of the reduced air density. Due to the repeated Rossby wave breaking, the stratospheric polar vortex gets highly distorted, breaks down and eventually reverses to an easterly flow. As the zonal-mean flow is to remain geostrophic, air descends adiabatically into the easterly polar vortex which strongly increasing the polar stratospheric temperature. When these stratospheric changes are severe, it is defined as a sudden stratospheric warming. Throughout a major stratospheric warming, two types of vortex disturbances can be denoted: a displacement of the cold vortex away from the pole or a vortex split into two separate daughter vortices (Charlton and Polvani 2007). SSWs occur mainly in the northern hemisphere since the enhanced upward propagation of Rossby waves is primarily induced by continental blocking (Kodera et al. 2013).

Sudden stratospheric warmings can be classified into four characteristic scales; however, various definitions exist for each. The definition according to the World Meteorological Organisation (WMO) and Labitzke and van Loon (1999) is specified by their strength.

Major A latitudinal mean temperature increases poleward of 60° latitude with an associated easterly circulation around 10 hPa accompanied with either a vortex displacement or vortex split. Major warmings occur mostly in January–February.

Minor	Zonal winds in the stratosphere weaken, reversing the temperature gradient between the poles and midlatitudes, but do not lead to a breakdown nor reversing of the polar vortex.
Canadian	An early winter warming with strong non-zonal character solely occurring in the northern hemisphere. The net zonal winds briefly change but are not strong enough to cause a breakdown of the polar vortex.
Final	A major warming which appears at the end of the winter indicating the transition from a cold winter system to a warm high-pressure system due to the change from polar night to polar day.

23.2.2 Importance of Weather and Climate

The importance of the middle atmosphere upon weather and climate has been increasingly appreciated following evidence indicating that processes in the stratosphere couple to the troposphere (Baldwin and Dunkerton 2001; Limpasuvan et al. 2004; Charlton et al. 2004; Shaw and Shepherd 2008). Progress has been made towards a more comprehensive representation of the atmosphere in order to better capture the stratospheric–tropospheric coupling (Randel et al. 2004; Charlton-Perez et al. 2013).

Significant effort has been made by numerical weather prediction (NWP) to better characterise SSWs. Accurate SSW prediction is justified due to its delayed impact on the weather as experienced on the Earth's surface (Sigmond et al. 2013; Tripathi et al. 2015). Recently, a significant update has been made to the numerical scheme in the stratosphere of the Integrated Forecast System (IFS) at the European Centre for Medium-range Weather Forecasts (ECMWF) (Diamantakis 2014), leading to an improved characterisation of SSWs. However, the stratospheric region is notoriously difficult to monitor, discussed elaborately in Chap. 29.

In the past, frequent in situ wind observations were retrieved by rocket sounding (e.g. Seibert 2006). Currently, radiosonde and aircraft are the main sources of information about the upper air wind up to 30 km altitude (WMO 2013). Beyond the middle stratosphere, direct information of wind is lacking. In this region, NWP is limited to observations of the thermal structure by GPS radio occultation and satellite-based sounding (microwave and high-spectral-resolution infrared[1]). From the stratopause upward, no data is assimilated (see Chap. 29). In the past, frequent in situ observations of wind were retrieved by rocket sounding, usually by campaigns (e.g. Seibert 2006), yet these have significantly reduced in the last three decades. Currently, the only upcoming mission designed for global wind-component-profile

[1]Examples of infrared sounder instruments are Atmospheric Infrared Sounder (AIRS), Infrared Atmospheric Sounding Interferometer (IASI) and Crosstrack Infrared Sounder (CrIS).

observations is ESA's ADM—Aeolus Earth observation satellite (e.g. Källén 2008; Straume et al. 2016). Hence, filling the vast gap in the global observing system with new wind observations can have a big impact on weather forecasting. Radiance observations are dominated by Advanced Microwave Sounding Unit type A (AMSU-A), but other[2] microwave sounders are now taking its place.

The quality of both the stratospheric analysis and forecast during a stratospheric warming can be inadequate, as discussed by Diamantakis (2014) and Smets et al. (2016) for the 2013 SSW. AMSU-A is capable of capturing the fast temperature variations related to an SSW. However, due to these very rapid changes, the NWP model first-guess field and assimilated observations can differ significantly at the onset of a warming. Significant discrepancies can result in a possible rejection of all good AMSU-A data, hence affecting the stratospheric predictability. At the European weather centre, improved stratospheric forecast skill during an SSW is obtained by a refined numerical scheme, noticeably increasing in the number of assimilated satellite observations. Further improvements in SSW predictions can be obtained from better resolving the stratosphere (Gerber et al. 2009; Roff et al. 2011) and mesosphere (Coy et al. 2011) together with assimilating data using additional techniques.

23.3 Infrasound and Sudden Stratospheric Warmings

Infrasound has notably progressed in its ability as a remote sensing technique for the upper atmosphere (e.g. Le Pichon et al. 2010). Since the Comprehensive Nuclear-Test-Ban Treaty (CTBT) opened for signing in 1996 (Dahlman et al. 2009), there has been a renaissance in exploiting ground-based infrasound arrays for upper atmospheric remote sensing (e.g. Lalande et al. 2012; Assink et al. 2013; Fricke et al. 2014; Chunchuzov et al. 2015; Assink et al. 2019). Several authors realised the potential of the CTBT International Monitoring System (IMS) infrasound network in global monitoring of natural infrasound for stratospheric variations related to a stratospheric warming (e.g. Le Pichon et al. 2006; Evers and Siegmund 2009; Le Pichon et al. 2009). The latest tendency of infrasound studies touches upon the evaluation of stratospheric conditions, i.e. analyses (Assink et al. 2014a; Le Pichon et al. 2015), ensemble members (Smets et al. 2015) and forecasts (Smets et al. 2016) and the study of SSW events (e.g. Smets and Evers 2014), discussed in Assink et al. (2019).

23.3.1 Sensitivity of Infrasound to SSWs

Infrasound propagation strongly depends on the state of the atmosphere, which may result in either reflection or refraction and attenuation of the signal.

[2]Advanced Technology Microwave Sounder (ATMS) on NOAA's National Polar-orbiting Operational Environmental Satellite System (NPOESS) and the temperature and humidity sounders (MWTS and MWHS) and radiation imager (MWTS) on CMA/NSMC FengYun-3 (FY-3) polar-orbiting meteorological satellite series.

The low-frequency signals propagate efficiently over long distances, since attenuation is in general relatively low. In a horizontally layered atmosphere, infrasound propagation can be approximated to first order by the effective speed of sound $c_{\text{eff}} = c_T + w_a$, a function of the adiabatic speed of sound $c_T \approx 20.04\sqrt{T}\,\text{m s}^{-1}$ for temperature (T) and the horizontal wind in direction of propagation (w_a) (Godin 2002). Refraction of the infrasonic signals is constrained by variations in the speed of sound gradient (Brekhovskikh and Godin 1999), propagating upwards for a decrease in sound speed gradient and downwards for an increase. Since most sources of interest and almost all receivers are ground based, of interest is predominantly ground-to-ground propagation, e.g. ducting is considered between the ground and the top of the waveguide aloft. The refractivity or ducting of the atmosphere can be indicated by the ratio of the effective speed of sound at an altitude with respect to the effective speed of sound at the ground. Signals refract back to the ground when the effective speed of sound ratio is approximately one or larger, indicating an atmospheric waveguide or duct. Infrasound is most sensitive when the vertical velocity component is minimal: at the refracting or return altitude.

In general, three different atmospheric waveguides can be differentiated: signals refracting in either the troposphere, stratosphere or thermosphere. The tropospheric waveguide is mainly bound by wind, i.e. the mid-latitude jet stream around the tropopause (~10 km). The stratospheric waveguide depends on the increase of both wind and temperature, induced by the temperature increase due to the presence of ozone driving the stratospheric polar vortex. Both tropospheric and stratospheric waveguides are predominantly anisotropic due to the strong wind jets. Propagation in directions opposite to the tropospheric and stratospheric wind is possible, but ducting is not. The thermospheric waveguide is dominated by a strong positive temperature gradient above the mesopause, causing more isotropic ducting. However, infrasound from these return altitudes is strongly attenuated (Sutherland and Bass 2004; Assink et al. 2012). During SSWs, the top of the stratospheric waveguide may extend from the lower stratosphere to the lower mesosphere. In addition, an SSW affects the atmospheric waveguide, ranging from minor variations to dramatic changes, detectable in the infrasound observations at the ground (e.g. Donn and Rind 1971; Evers and Siegmund 2009; Hedlin et al. 2010; Assink et al. 2014b).

23.3.2 Importance to Infrasound Monitoring

Improved knowledge and observations of stratospheric warmings are not only of great interest to numerical weather prediction but as well to infrasound monitoring purposes, e.g. CTBT treaty verification.

Capabilities of the CTBT IMS infrasound network considering long-range propagation aspects are determined by the state of the stratosphere. Stratospheric variability, e.g. during equinox periods and stratospheric warmings, strongly influences the detectability of infrasound (Le Pichon et al. 2008, 2010; Tailpied et al. 2016). During

the last decade, the number of studies coming across unexpected atmospheric conditions related to SSWs has increased significantly.

On 19 February 2008, a large bolide was observed by several hundreds of broadband seismic stations in the U.S. Pacific Northwest. Hedlin et al. (2010) found an unexpected predominant easterly propagation direction of the acoustic-to-seismic signals related to a sudden stratospheric warming event. Infrasound propagation simulations using ECMWF and G2S (Ground-to-space[3]) atmospheric conditions were unable to explain the observation. The study of Hedlin et al. (2010) indicates for the first time discrepancies in atmospheric models by infrasound during a stratospheric warming.

In 2009 and 2011, two large-scale infrasound calibration experiments consisting of three explosions were conducted to test the IMS infrasound network of the CTBT and provide ground-truth data for infrasound propagation studies (Fee et al. 2013). For the 2011 experiments, portable infrasound arrays in the source region were deployed to the east of the of the source, aiming to take advantage of the typical winter westerly tropospheric and stratospheric winds. However, prior to the 2011 tests, a minor stratospheric warming occurred (see Sect. 23.4.4) affecting the stratospheric duct. Infrasound propagation and detectability were strongly influenced. The results of the Sayarim experiments, designed to test the IMS, would have been significantly different if the explosions had occurred a week earlier.

The study of De Angelis et al. (2012) demonstrates an automatic infrasound and seismo-acoustic eruption detection algorithm for real-time volcano monitoring operations in remote regions. Acoustic propagation modelling shows how strong tropospheric ducting allows infrasound to travel long distances across the Aleutian Arc. For the stratospheric signals, De Angelis et al. (2012) point out an unusual winter stratospheric jet characterised by easterly winds, identified as a sudden stratospheric warming event in NWP analyses.

More recently, the study of Assink et al. (2016) analysed the atmospheric infrasound of the underground nuclear tests by the Democratic People's Republic of Korea (DPRK) of 12 February 2013 and 6 January 2016. During the 2013 and 2016 tests, the stratospheric waveguide was in a very different state. Clear detections were made in the Russian Federation (IS45) and Japan (IS30) in 2013 at stations from the International Monitoring System. Both tropospheric and stratospheric refractions arrived at the stations. In 2016, only one weak return was potentially observed at IS45 due to the presence of an early stage SSW. Despite the stratospheric variability, the 2016 event could be simulated using the ECMWF HRES (High Resolution) deterministic forecast. Observations and the modelled parameters associate this arrival to both the tropospheric and stratospheric propagation paths.

Therefore, understanding the detectability of infrasound and its dependencies is crucial for successfully applying infrasound as a verification technique.

[3]Whole atmosphere conditions of the U.S. Naval Research Laboratory (NRL) obtained by a combination of various atmospheric products from NOAA and NASA, vertically extended by empirical modelling of the upper atmosphere using HWM/MSIS (Picone et al. 2002; Drob et al. 2015).

23.4 Progression of Infrasound from SSW Monitoring Towards Predictability Evaluation

23.4.1 From the 1970s to 2009

The first infrasound signature of a stratospheric warming goes back to the pioneering studies by both Donn and Rind, intrigued by the ability of natural infrasound to probe the upper atmosphere. Their studies are characterised by the use of ambient noise from interacting ocean waves, microbaroms and microseisms, as a continuously natural mechanism for exploring the atmosphere. Fundamental to their studies of the SSW is the identification of a characteristic diurnal variation in the amplitude of the ambient noise observations. Donn and Rind (1971) relate amplitude changes to the state of the atmosphere, independent of any variation in the source. In winter, high amplitudes with a strong semidiurnal variation are denoted while summer amplitudes are lower with a weak diurnal variation. They associate typical amplitude variations to viscous dissipation associated with reflection height variation, described more thoroughly in Rind and Donn (1975). More important is the link between abnormal microbarom intensities in the early winter of 1967–1968 to variations in the stratosphere, the first infrasonic signature of a stratospheric warming. As the winds turn, around the equinoxes and during SSWs, the amplitude of ambient coherent infrasound noise increases due to the formed stratospheric waveguide between the Atlantic and Palisades.

The stratospheric warming of December 1967 is studied more elaborately in Donn and Rind (1972), including early propagation simulations. In addition to amplitude variations, Rind et al. (1973) made use of microbarom trace velocities for estimating upper air wind speeds. The latter led to the studies of Rind and Donn (1975, 1978), utilising sound intensity variations from infrasound-seismic ambient noise variations as a preliminary atmospheric probe. These studies came to a stop when nuclear tests were diverted to the subsurface under the Limited or Partial Test Ban Treaty. Nevertheless, Donn and Rind paved the path for using natural ambient noise as a comprehensive technique for monitoring several upper atmospheric parameters.

Microbaroms are atmospheric pressure oscillations radiated from non-linear ocean surface wave interaction at double the ocean wave frequency (Gutenberg 1939; Longuet-Higgins 1950; Posmentier 1967). Interacting large regions of high-energetic ocean waves of similar frequency with opposite directions, e.g. ocean swell and marine storms, radiate acoustic energy almost continuously well characterised by a radiation frequency of 0.2 ± 0.1 Hz. Microbaroms dominate the infrasound ambient noise field due to their continuous presence, making them a preferred source for passive atmospheric probing.

Microbarom source modelling can be obtained using a two-fluid model, over air and seawater, and a coupled ocean wave model providing the sea state (Hasselmann 1963; Brekhovskikh et al. 1973). Air–sea coupling is crucial due to the two-way interaction of surface winds and ocean waves (Janssen 2009). The state-of-the-art infrasound microbarom radiation source model, assuming an infinite ocean depth (Waxler and Gilbert 2006), has been validated by Walker (2012) and Stopa et al. (2012), studying ambient swell- and hurricane-induced microbaroms, respectively. The more recent Waxler et al. (2007) microbarom radiation model takes into account the effect of resonance due to bathymetry, affecting the source location, amplitude and frequency.

23.4.2 The 2009 Major SSW: An Infrasonic Game Changer

In January 2009, a major sudden stratospheric warming caused drastic changes in the stratosphere. The midwinter westerly stratospheric vortex quickly displaced and elongated, followed by a full vortex split and an increased amplitude of the zonal wavenumber 2 planetary wave. For several days, two vortices and reversed winds characterise the stratosphere (see Fig. 23.1 and Sect. 23.4.5). By the beginning of February 2009, the stratosphere recovered to its typical midwinter state.

The infrasonic signature of the 2009 SSW is described by Evers and Siegmund (2009), exploiting back azimuths of oceanic noise at the IMS infrasound arrays in the northern hemisphere. For the first time, passive infrasonic observations at the surface provided detailed information on upper atmospheric processes on a global scale. IMS arrays north of 15°N detect a large amount of coherent ambient infrasound noise, as long as the local wind speeds are low. High local wind speed causes coherent wind noise at the instrument which reduces the signal-to-noise ratio and detection capability (Walker and Hedlin 2009). Sensitivity of infrasound arrays to sources located in specific directions is controlled by the atmospheric state, described in Sect. 23.3.1. Therefore, variations in the direction and intensity of the stratospheric polar vortex, such as during an SSW, seriously affect the microbarom's detectability in terms of back azimuth. Figure 23.1 illustrates the stratospheric wind and temperature at 50 km prior to the SSW and during the vortex split. The SSW caused ambient noise observations to arrive from the opposite direction than expected during regular midwinter conditions at multiple infrasound arrays, marked in Fig. 23.1. In normal winter conditions, westerly ambient noise observations are expected, since the stratospheric duct is favourable to downwind conditions. However, throughout the major stratospheric warming, the polar vortex breaks down and reverses which alters the duct from westerly to easterly. This dramatic change is clearly observable in microbarom observations by an altered or (dis)appeared microbarom source region, leading up to the infrasonic signature of an SSW. Evers and Siegmund (2009) indicate clear infrasonic signatures of the stratospheric warming observed in Greenland (IS18), Alaska (IS53), over the western US (IS56) and central Canada (IS10). Even in Kazakhstan

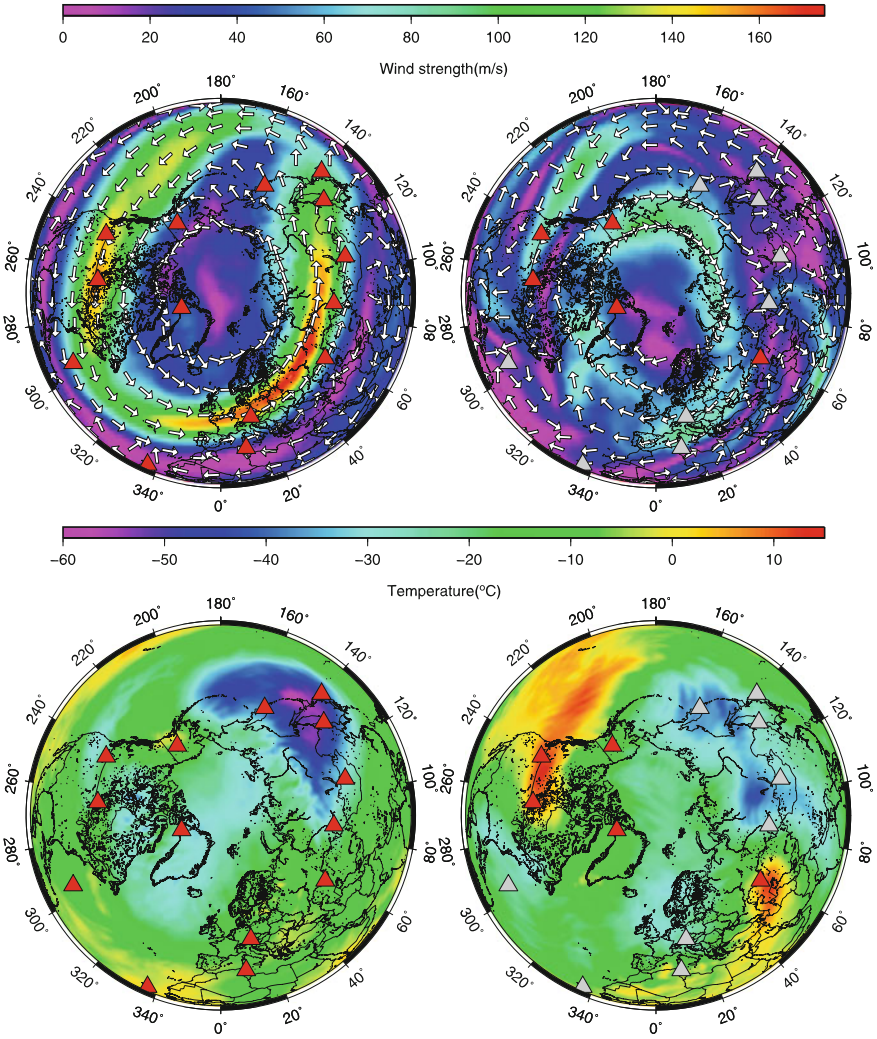

Fig. 23.1 (Top) wind and (Bottom) temperature at 50 km altitude from ECMWF analyses. (left) Valid for 2 January 2009, at 00 UTC, prior to the SSW; (right) values during the vortex split phase of the SSW on 23 January at 00 UTC. The red triangles in the right column indicate arrays which sensed the SSW, the grey triangles represent arrays where no clear signature was found in the observed back azimuths. Figure adapted from Evers and Siegmund (2009)

(IS31), slight changes in the retrieved back azimuths are notable. At the Russian arrays (IS44, IS45 and IS46), no pronounced changes in the observed back azimuths are visible. Similar results are also found for the German (IS26), Japanese (IS30), Mongolian (IS34) and Tunisian (IS48) arrays.

23.4.3 Anomalous Infrasound Propagation in a Warm Stratosphere

So far, less attention has been paid to stratospheric temperature variations than to the wind variations. Evers et al. (2012) studied the temperature effect in the stratosphere on infrasound propagation. A case study of an explosion indicates a significant reduction of the size of the classical stratospheric shadow zone. The reduction corresponds with a lowering of the return height following the stratospheric temperature increase. During the January 2010 SSW, the extent of the classical stratospheric shadow zone (~200 km) reduces by a factor of 2, leading to extremely small shadow zones. When the temperature in the vicinity of the stratopause is higher than the Earth's surface temperature, for example, throughout an SSW, pure temperature gradient-induced refractions can occur.

The occurrence of such conditions is quantified by analysing 10 years of ECMWF analyses, four times per day. The stratospheric shadow zone is simulated by ray theory in a 1-D model in direction of the wind at 50 km. A minimum value in stratospheric shadow is obtained by using the steepest gradient in c_{eff}. Stratospheric returns occurred 62% of the time and mostly in winter (51%). Hardly, any returns are observed around the equinoxes due to the lack of significant downwind component at 50 km altitude. Very small shadow zones of less than 100 km occurred 3% of the time. For 1% of the time, no additional downwind component w_a is necessary to enable refraction back to the Earth's surface, mostly associated with SSWs.

The existence of small shadow zones is confirmed by infrasound from mining blasts in southwestern Siberia, Russia, observed by IMS infrasound array IS46 (Russia). Events are obtained from the Reviewed Event Bulletin (REB) from the International Data Centre (IDC) for verification of the CTBT. Locations are seismically determined using IMS arrays in Russia using at least two arrays. Location errors are of the order of a couple of kilometres. Selected events in this low-seismic area, within the back azimuthal interval between 59.5° and 90.5° of IS46 at a maximum distance of 250 km, most likely correspond to open-pit mining. Stratospheric conditions of wind and temperature correspond to the number of detections at I46RU, see Fig. 23.2, and consequently to the variation in the apparent velocity c_{app} of the events. c_{app} is the horizontal projection of the propagation velocity vector. For a layered medium, apparent velocity is invariant (Pierce 1981). The infrasound signals correspond to stratospheric refractions, indicated by the agreement of the structure of c_{app} to the structure of the stratosphere. This would not have been the case for tropospheric arrivals. During the equinoxes, hardly any detections are made and during winter conditions, summer-like apparent velocities appear which could only be

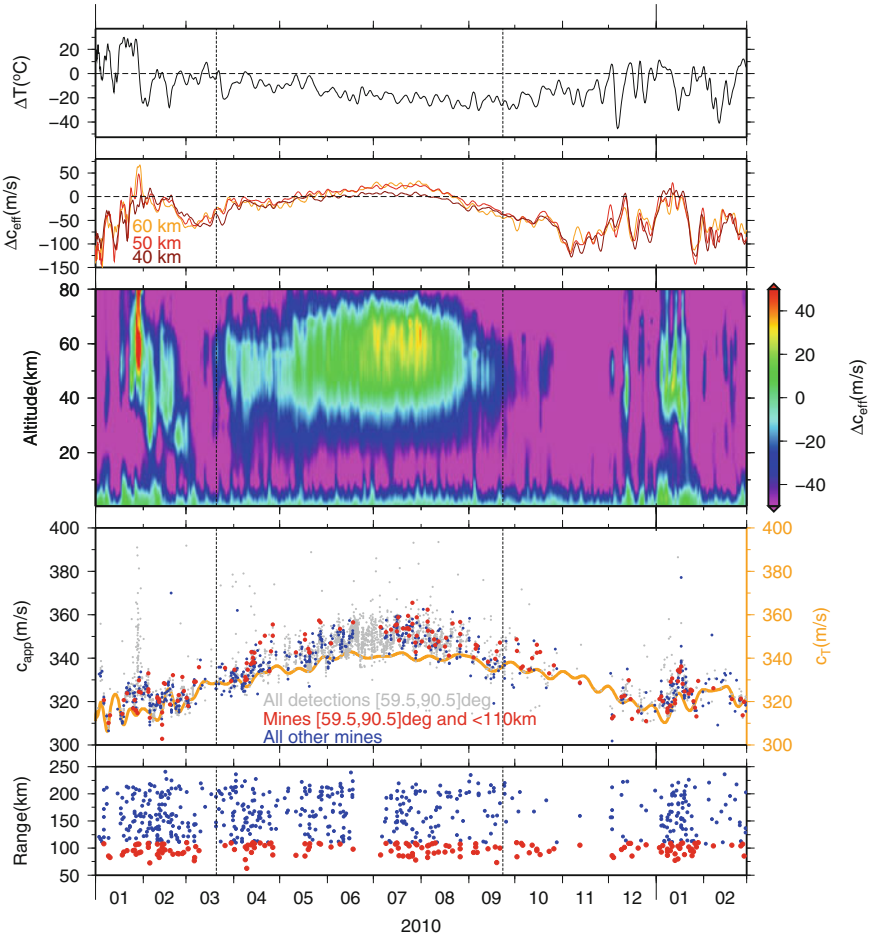

Fig. 23.2 From top to bottom are listed: atmospheric conditions and REB detections at IMS infrasound array IS46 (Russia) from seismic ground-truth locations. Only associated infrasound detections within the back azimuthal interval between 59.5° and 90.5° are used. Vertical dashed lines indicate the vernal and autumnal equinox. (first panel) The temperature difference between 50 km altitude and the surface, ΔT. The c_T, Δc_T and ΔT curves are smoothed with a polynomial fit. (second panel) Cross sections from Δc_{eff} at an altitude of 40, 50 and 60 km. (third panel) The difference between the effective sound speed at a certain altitude and near the surface, colour coded as Δc_{eff}. The latter are derived from ECMWF analyses at 54.0°N, 85.5°E. (fourth panel) The apparent sound speed, c_{app}, of the detections. The red and blue dots are seismic locations from the REB assumed to correlate with mining activity, i.e. blasting. Mines at a distance of less than 110 km are denoted by red dots, all other detections within the back azimuth range are added as grey dots. The surface sound speed c_T is given as orange line and calculated from the temperature. (fifth panel) The distances of the mining activity sources with respect to IS46 as function of time. Figure adapted from Evers et al. (2012)

caused by SSWs. However, it should be noted that more stratospheric arrivals are observed than predicted by the modelling. Fine-scale structure in the wind and temperature caused by internal gravity waves, not resolved by, e.g. the ECMWF models, is responsible for generating additional arrivals in the classical shadow zone, as predicted by ray theory (Kulichkov et al. 2010; Revelle 2010; Chunchuzov et al. 2011).

Some observed c_{app} lay below the c_T curve, which is physically impossible (see Fig. 23.2, fourth panel). The adiabatic speed of sound c_T is the lowest possible propagation velocity. Lower values of c_{app} are in first order attributed to uncertainties in array processing (timing and c_{app}) and the surface temperature estimates and the impact of ignoring wind. The temperature is obtained from NWP specifications and is not an actual measurement at the station. Nevertheless, the general trends of near-surface and stratospheric variations, i.e. summer versus winter characteristics are reflected in the observed c_{app}. Lower surface temperatures and stronger gradients in c_{eff} during winter explain the lower values of c_{app} with respect to summer.

Observations at IS46 deliver the proof for the existence of extremely small shadow zones, less than 100 km in size, for stratospheric arrivals. These results are applicable to a broad latitudinal range defined as the stratospheric surf zone, i.e. 20°N to 60°N where a rather stationary flow of stratospheric air occurs.

23.4.4 Bidirectional Infrasonic Ducts Associated with a Minor SSW

Donn and Rind (1972, Subsection 4.1) and Evers and Siegmund (2009, Subsection 4.2) reported on significant azimuthal reversal due to the reversal of the zonal jet as a result of a major warming event. Nevertheless, Assink et al. (2014b) denoted simultaneous arrivals from two nearly opposite stratospheric ducts during a minor warming. In January 2011, a bidirectional stratospheric duct persisted for 2 weeks in the wake of a minor SSW. This situation occurred just prior to the 2011 Sayarim experiments (Fee et al. 2013), which took place on 24 and 26 January 2011 (see Sect. 23.3.2). The existence of bidirectional ducting during stratospheric warming events has not been considered in the past.

The development of a bidirectional duct has significant effects on infrasound propagation in the middle atmosphere, which is typically expected to be unidirectional. Such ducting significantly improves infrasound detection capability during these periods, since the anisotropy is strongly reduced. In general, the detectability is determined by the source strength, distance to the source, atmospheric wind and temperature, and the ambient noise conditions near the receiving array (Evers and Siegmund 2009).

The existence of the bidirectional duct has been demonstrated at IMS infrasound array IS48 (Tunisia). The bidirectional ducting effect is clearly captured at IS48, due to its favourable location with respect to microbarom sources at both sides of the station. Two microbarom signals, from nearly opposite back azimuth directions, are

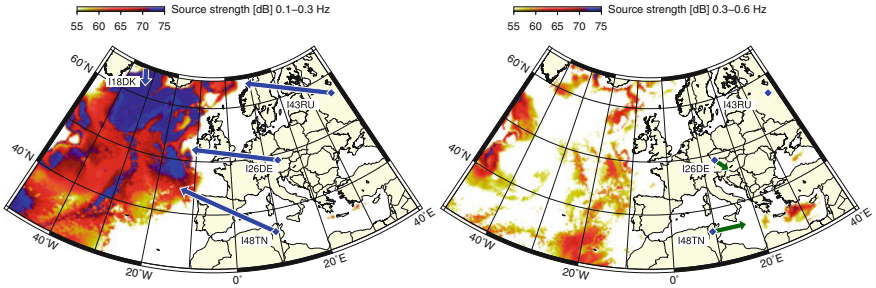

Fig. 23.3 Microbarom source region predictions for two distinct frequency bands, computed using the source model described by Waxler et al. (2007) and ECMWF HRES-WAM two-dimensional ocean wave spectra, for 17 January 2011 00 UTC for the **a** 0.1–0.3 Hz and **b** 0.3–0.6 Hz frequency bands. Blue and green arrows correspond to observed back azimuth directions at IMS infrasound arrays for the specific frequency ranges. Figure adapted from Assink et al. (2014b)

observed in January 2011. A strong and persistent signal from the northwest, with frequencies around 0.2 Hz, is detected with a weaker signal from the east, in the 0.2–0.6 Hz band. The observed microbarom sources, induced by non-linear ocean surface wave interaction, are explained by source modelling (Waxler and Gilbert 2006) based on two-dimensional ocean wave spectra from the ECMWF operational HRES-WAM (High RESolution WAve Model) analysis. Source modelling, see Fig. 23.3, reveals a previously unidentified microbarom source region in the eastern Mediterranean besides the more typical microbarom source region in the Atlantic Ocean. Figure 23.4a shows microbarom source activity in the northern Atlantic and eastern Mediterranean Basins in terms of back azimuth with respect to IS48 as a function of time. The detectability is mostly constrained by the local noise conditions, assuming efficient propagation conditions and a relatively nearby microbarom source. Low wind noise conditions are defined as local winds less than $1\,\mathrm{m\,s^{-1}}$, similar to Le Pichon et al. (2005), shown in Fig. 23.4a (bottom frame). Figure 23.4b shows the ducting conditions throughout the winter of 2010–2011 in direction of the northern Atlantic and Mediterranean in terms of effective sound speed ratio as a function of altitude. Several intervals of bidirectional ducting conditions exist throughout the winter of 2010–2011, indicated in Fig. 23.4 by the dashed rectangles. The most significant interval occurs during January 2011. Note that the eastward duct would have disappeared if a major SSW had occurred. While a continuous, broadband energetic microbarom source is present in the northern Atlantic Basin, the eastern Mediterranean activity is more sporadic and weaker.

The observed directions (Fig. 23.4c) correspond well with the predicted source locations for low wind noise conditions (Fig. 23.4a, bottom frame). While the frequency bands of the two source directions overlap, the Mediterranean signal is coherent up to about 0.6 Hz. This observation is consistent with the predicted sources. Microbarom source predictions indicate that various high-intensity source regions are present in the Atlantic Ocean in the classic microbarom band 0.1–0.3 Hz. At higher frequencies, the Atlantic source regions weaken and source regions appear in

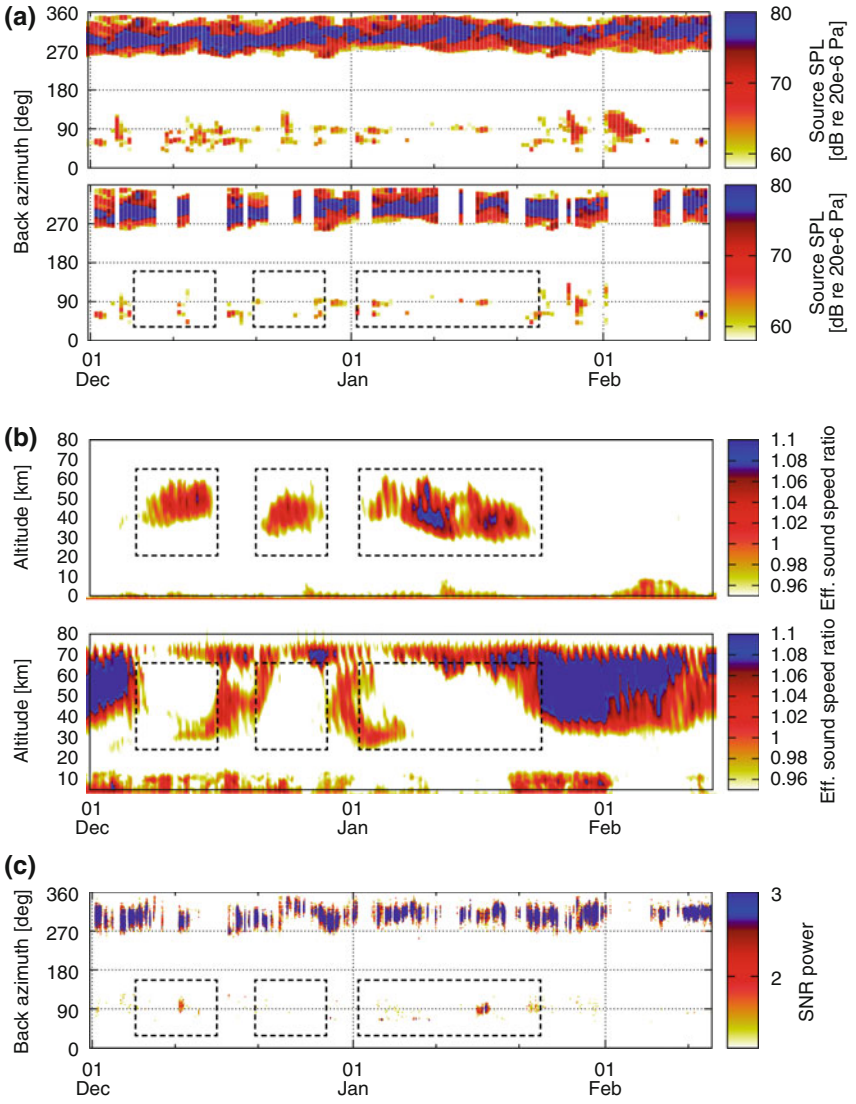

Fig. 23.4 **a** Microbarom source activity in the Atlantic and Mediterranean Basins, modelled using ECMWF HRES-WAM two-dimensional wave spectra and the Waxler and Gilbert (2006) source model. The back azimuths with respect to IS48 (Tunisia) and the source intensity are given as a function of time. While a continuous, broadband of energetic microbarom sources is present in the northwest, the Mediterranean activity is more sporadic. The top frame shows all sources; the bottom frame shows the source activity for which local winds are less than 1 m s^{-1}, leading to low wind noise conditions and increased infrasound detectability. Thus, the remaining microbarom sources are effective sources. **b** Effective sound speed ratio values as a function of altitude and time for (top) westward and (bottom) eastward propagation. **c** Infrasound detections during the winter of 2010–2011. Intervals of bidirectional ducting conditions are indicated with dashed rectangles; the eastward duct nearly always exists. During favourable conditions, microbarom signals from two opposite directions are detected at IS48. Figure adapted from Assink et al. (2014b)

the eastern Mediterranean Sea, in between Crete and Cyprus. As the Mediterranean signal is typically much weaker than the Atlantic signal, such events are predominantly detected when beamforming specifically towards the east.

Signals from both directions are detected when all criteria are fulfilled. During intervals of bidirectional ducting with low local noise conditions and when microbarom sources are sufficiently strong. Around 10 December and 17 January 2011, the most significant eastward detections occur, indicated by the first and third dashed rectangle in Fig. 23.4, respectively. These detections correspond with the onset and offset of bidirectional ducting conditions throughout December 2010 to February 2011. Only very few detections from the east are made during the second anomalous period in December 2010, likely due to the presence of strong local winds that masked the microbarom sources in the eastern Mediterranean (see Fig. 23.4a). Around 17 January, the signal intensity of both signals is about equal.

23.4.5 Life Cycle of a Major SSW

Evers and Siegmund (2009, see Subsection 4.2) obtained the infrasonic signature of a sudden stratospheric warming from the dramatic changes in the back azimuth of the observed ambient noise. The 2009 major SSW is re-exploited to better understand the relation between the variations of the stratospheric polar vortex and the altered microbarom observations. Smets and Evers (2014) incorporate additional signal characteristics to acquire more insight on the variations in stratospheric wind and temperature. In addition, microbarom source modelling and infrasound propagation modelling are applied to provide insight into the sensitivity of the infrasonic signature.

The study of Smets and Evers (2014) focusses on the northerly IMS infrasound arrays IS18 (Greenland) and IS53 (Alaska), since these arrays have the most pronounced and detailed signature (Evers and Siegmund 2009). Figure 23.5 (left) shows the observed microbarom amplitudes and frequencies as a function of back azimuth over time. Note the infrasonic signature during the second half of January 2009. Ambient noise observations at IS53 change from the Pacific Ocean (PO) to the Atlantic Ocean (AO), while the PO microbaroms disappear at IS18 during the SSW. In order to understand the signature of the varying stratospheric vortex in the ambient noise observations, the source variation is isolated by simulating the microbarom sources. Spectral microbarom amplitudes are simulated using the theory of Waxler et al. (2007), including bathymetry resonance effects and two-dimensional ocean wave spectra provided by the ECMWF HRES-WAM-coupled ocean wave model. Microbarom simulations for the AO and PO are shown in Fig. 23.5 (right) projected to the point of view of infrasound arrays IS18 and IS53. Figure 23.5 shows a good first-order agreement between the observations and microbarom predictions in the absence of propagation effects. Microbaroms are continuously active, but varying in amplitude, frequency and location over time. Good resemblance between observations and source simulations indicates the dominance of the source effect. However,

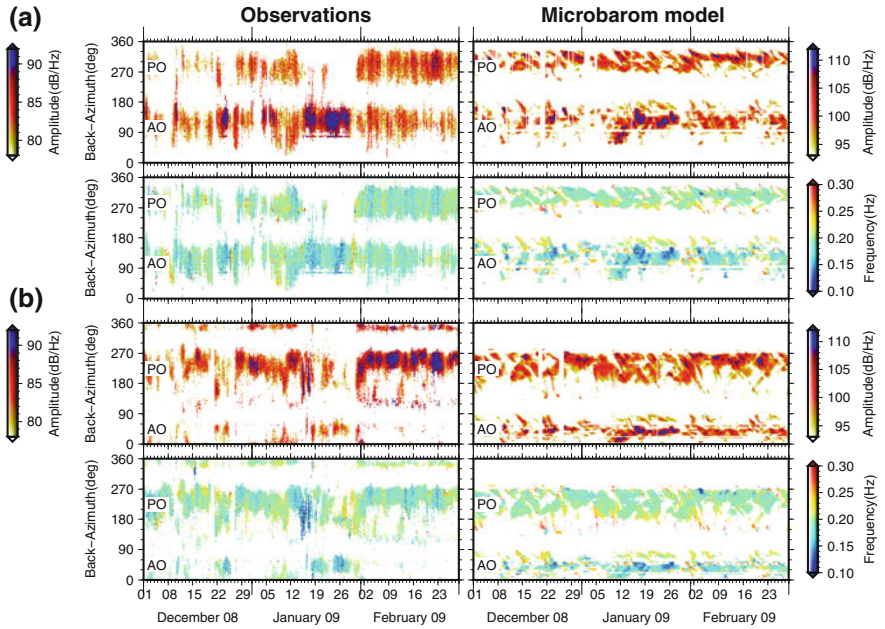

Fig. 23.5 Comparison of the microbarom observations (left) and simulations (right), for **a** IS18 and **b** IS53. Each subfigure shows (top) the peak spectral amplitude with (bottom) the corresponding frequency, for windows of one degree in back azimuth and one hour for the observations and 6 h for the modelled microbaroms. Gaps in the observations, due to high wind noise or data loss, are recreated in the microbarom predictions. Figure adapted from Smets and Evers (2014)

clear propagation effects can be denoted, for example, the SSW signature and the northerly observations at IS18. Note that both observations and simulations indicate different frequencies for the AO and the PO due the distinctive ocean depth.

To fully understand the microbarom observations and the signature of the warming, one should know the atmospheric duct between source and receiver. IS18 simultaneously observes Atlantic and Pacific microbaroms, except during the major SSW. These simultaneous arrivals do not correspond to bidirectional stratospheric ducting, as explained by Assink et al. (2014b, see Subsection 4.4), as this phenomenon only occurs during a minor SSW. The observations imply a stratospheric duct from the Pacific and a thermospheric duct from the direction of the Atlantic during regular midwinter conditions. Since IS18 is relatively close to the AO, approximately 2000 km, thermospheric ducting is feasible. Infrasound is most sensitive to the atmosphere at the return height. Stratospheric returns are distinguished from thermospheric returns by a characteristic (semi)diurnal signature in the observed microbarom amplitudes, without any a priori atmospheric information. The method is based on previous studies of Donn and Rind (1971), Rind et al. (1973), Rind and Donn (1975, 1978), where they characterise variations of stacked microbarom amplitudes per time of day. The preliminary method involves long-period averaging,

using several months of data, losing all small-scale fluctuations of interest. Other studies have identified the typical signature in various detection characteristics, e.g. the number of detections, back azimuth angle, apparent velocity, bandwidth, amplitude and travel time (Le Pichon et al. 2005; Whitaker and Mutschlecner 2008; Green et al. 2012; Assink et al. 2012). However, these studies make use of strong impulsive sources with a well-known position, e.g. volcanoes, which makes it hard to implement the used methodologies on varying ambient noise. In Fig. 23.6, spectral amplitude time of day, $\bar{A}_{tod}$, for half hour, windows are shown in direction of the AO and PO. Throughout the boreal winter, IS18 in AO direction shows a semidiurnal amplitude variation, while the PO amplitudes indicate more of a diurnal pattern. For IS53, a clear diurnal pattern is present. However, the diurnal peak varies over time due to the movement of the source, yielding the stratospheric peak at various longitudes (and thus times).

These findings are verified by simulations, using 3-D reverse ray tracing cast in spherical coordinates and the microbarom source model, with the known implications of a vertically limited atmospheric model up to the mesosphere. Despite these limitations, clear regions of stratospheric propagation can be identified, confirming the amplitude variation method. Thermospheric signals of IS18 towards Atlantic Ocean, with distance of 2000 up to 3500 km (February 2009), can be observed.

Distinguishing stratospheric from thermospheric returns. The stratosphere and thermosphere are exposed differently to solar tidal fluctuations of temperature and wind (Sutherland and Bass 2004). This yields a different signature in the recordings at the surface, which can be used to differentiate the type of atmospheric duct.

Stratospheric returns are characterised by a weak diurnal variation. Water vapour heating in the troposphere primarily excites a diurnal thermotidal oscillation. This remains true until the thermosphere, where viscosity, conductivity and electromagnetic damping may attenuate incoming waves (Lindzen and Chapman 1969).

Thermospheric returns show a strong semidiurnal variation. The high attenuating nature of the thermosphere, due to the low density, causes a strong excitation to the heat generated by the absorption of solar ultraviolet radiation by oxygen around 120 km altitudes, twice a day. This semidiurnal irregular heating results in a variation of the thermospheric return height, due to a severe change in wind strength and attenuation.

The amplitude signature combined with the variation in back azimuth is used to reanalyse the 2009 SSW in detail. The effect of the warming is most pronounced for IS53 as AO microbaroms, see Fig. 23.6d, are only expected in summer or in the case of an SSW. Hemispheric 10 hPa (∼31 km) wind from the ECMWF HRES analysis in Fig. 23.7 show the evolution of the stratospheric polar vortex before, during and after the SSW. This indicates a displaced westerly elongated vortex from 18 to 22 January

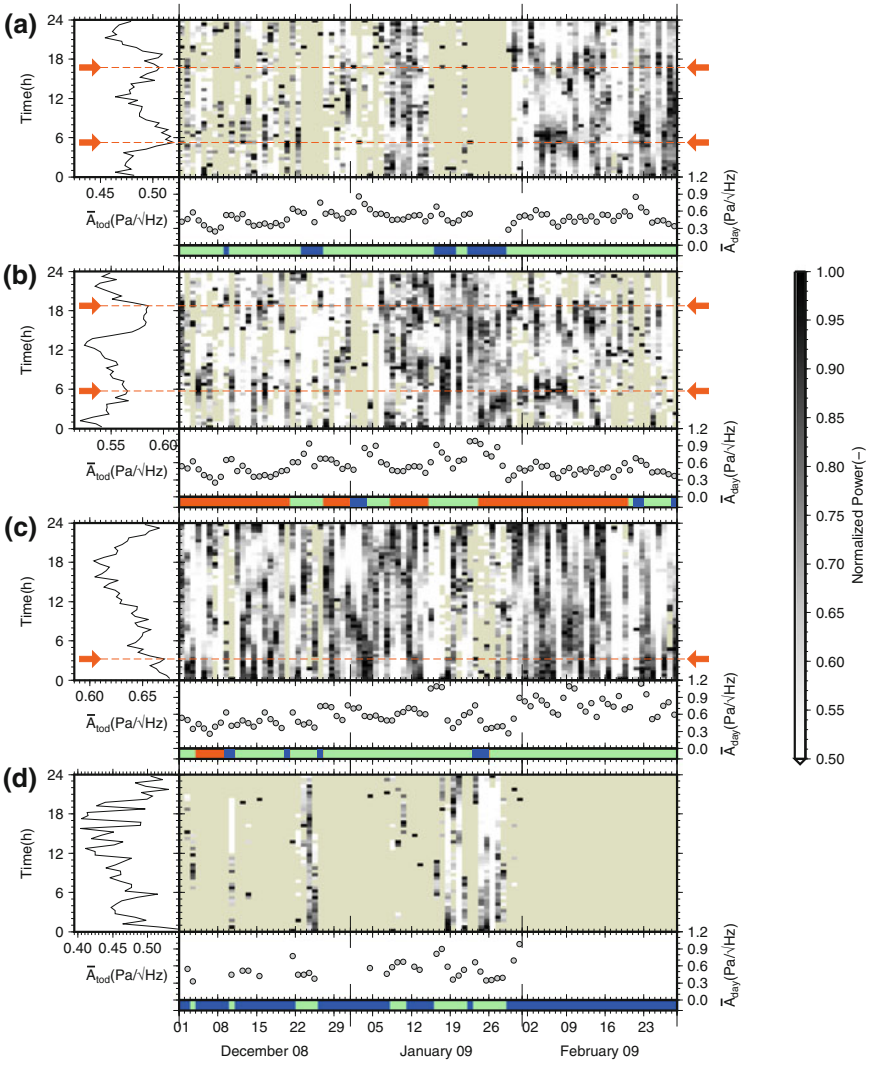

Fig. 23.6 Directional time-averaged spectral amplitude variations. From top to bottom are shown, IS18 in direction of the **a** Pacific Ocean and **b** Atlantic Ocean, IS53 in direction of the **c** Pacific Ocean and **d** Atlantic Ocean. Each subfigure consists of a vertical graph (left) and an image (right) with below one horizontal graph and one colour-coded bar. The vertical graph (left) shows the spectral amplitude averaged per time of day, $\bar{A}_{tod}$, for each half hour. The red arrows and dashed lines indicate the tidal peaks in the mean time of day amplitude, if present. The image (right) shows the half hour averaged spectral power, normalised per day. Each pixel column corresponds with one single day, while each row indicates the time of day. The horizontal graph shows the daily mean spectral amplitude $\bar{A}_{day}$. The colour-coded bar roughly indicates manually picked periods with either no peak (blue), one peak (green) or two peaks (red) per day. Only detections are used with $SNR \geq 1.5$ for IS18 and $SNR \geq 1.3$ for IS53. Figure adapted from Smets and Evers (2014)

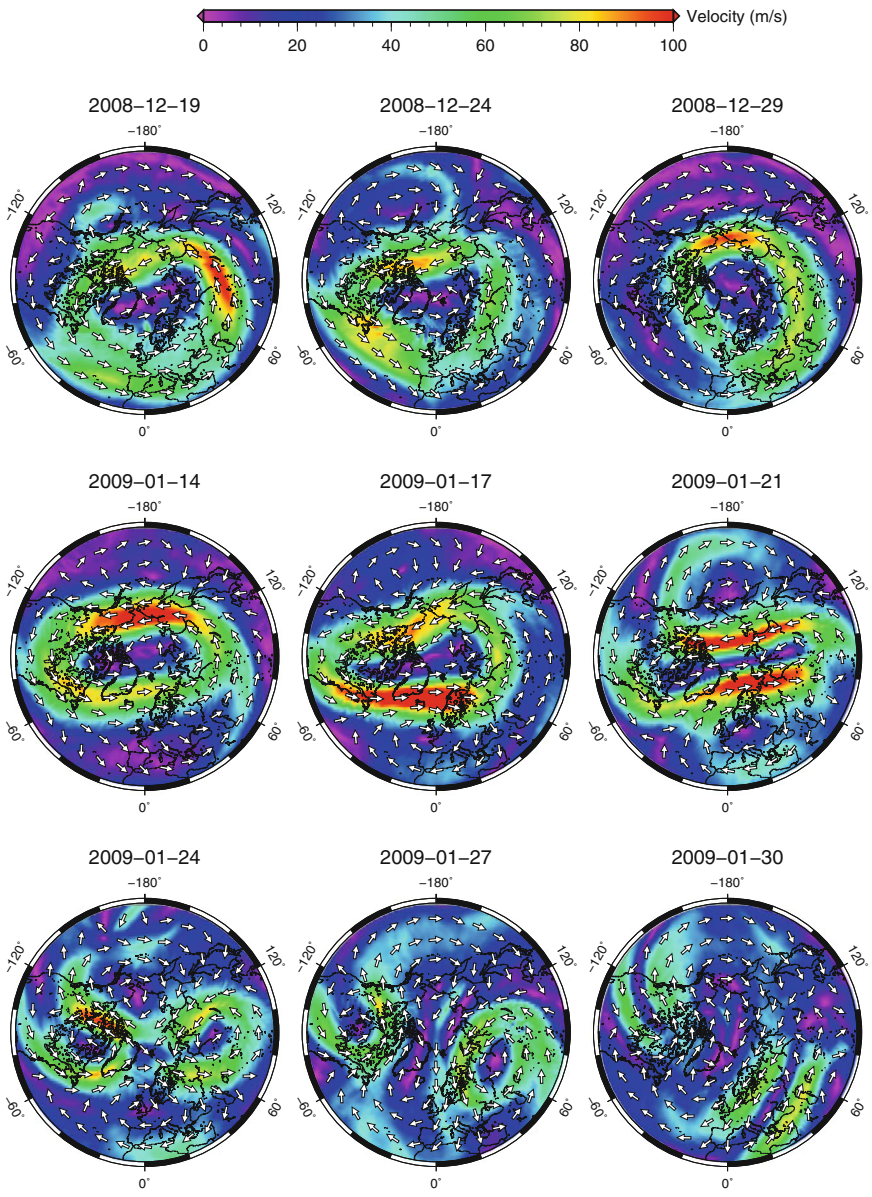

Fig. 23.7 ECMWF HRES analyses for wind velocity and direction at 10 hPa (∼31 km) at midnight. Note the different signatures of the vortex in the lower stratosphere in comparison to Fig. 23.1, showing the wind and temperature in the upper stratosphere. Figure adapted from Smets and Evers (2014)

2009 and a split into two vortices from 24 to 28 January 2009, followed by a recovery on 4 February 2009. The ECMWF analysis indicates first signatures of the warming around 22 December 2008 and 7–8 January 2009. However, infrasound observations reveal more and earlier abrupt changes, increasing in intensity and duration. These preliminary signatures correspond to Rossby wave breaking in the stratospheric polar vortex, disturbing the circumpolar vortex via momentum deposition. Rossby waves, type 2 planetary, have a typical period of 10–16 days, repeatedly disturbing the polar vortex (Holton 2004). A similar pattern can be denoted in Fig. 23.6, occurring on 3 and 10 December 2010. The signature is most clear for IS53 (Fig. 23.6c, d) only observing stratospheric returns. Hence, altering signatures between the frames Fig. 23.6c, d do correspond to severe changes in the stratospheric wind. At the beginning of the winter, the cyclonic circumpolar vortex is strong but highly unstable, being very sensitive to any disturbance. The vortex weakens, resulting in a clear AO stratospheric duct denoted at IS53, from 22 to 25 December, with diurnal peak at approximately 16 h. A stronger, longer lasting disturbance occurs from 17 to 21 January 2009, yielding a displaced and elongated rather unstable cyclonic vortex. For that period, IS53 indicates a stratospheric duct in AO direction with a diurnal maximum at approximately 14 h. Between 23 and 28 January 2009, the cyclonic vortex becomes critically disturbed, breaks down and reverses to an anticyclonic vortex and finally splits into two anticyclonic vortices located above Canada and Russia. Due to these locations, no clear difference in back azimuth is present. However, the change in observed amplitude and phase shift of the (semi)diurnal signature do indicate a stratospheric variation. The anticyclonic vortices dissolve at the end of January 2009 and the stratosphere recovers to its normal winter situation. Because of the weak polar vortex, recovering slowly due to the gradually radiative cooling of the polar cap (Limpasuvan et al. 2005), a stable continuous stratospheric duct in PO direction is present, clearly noticeable in the microbarom observations.

The study of Smets and Evers (2014) shows the ability of observed microbarom amplitudes to provide more details on the life cycle of an SSW. Two most important differences between the infrasound observations and the ECMWF analysis are: (1) A strong AO stratospheric duct is observed from 22 to 25 December 2008 at IS53, likely corresponding to a preliminary vortex disturbance, but missing in the analysis. (2) An earlier recovery of the stratospheric vortex, at 30 January 2009.

23.4.6 SSW Forecast Predictability Evaluation

In the study of Smets et al. (2016), a novel method for the evaluation of middle atmospheric weather forecasts is introduced. For the first time, weather forecasts for different forecast steps are evaluated using infrasound. A year of near-continuous infrasound detections from the Mount Tolbachik volcano is used, observed by IMS infrasound array IS44 on the Kamchatka peninsula in Russian Federation (55.8°N, 160.3°E). Volcanoes represent valuable sources for passive acoustic remote sensing

of the atmosphere, as the source location is fixed and the source is relatively well understood (Fee et al. 2010; Matoza et al. 2011; Marchetti et al. 2013).

IS44 is located at approximately 347 km southwest of Mount Tolbachik, with a true bearing of 28.11° clockwise from north. Typically, IS44 is reached after one stratospheric bounce in summer. Throughout the course of a stratospheric warming, the warm stratosphere induces shallower and shorter stratospheric bounces, making two returns possible. This effect of a warm stratosphere on the propagation of infrasound is explained by Evers and Siegmund (2009, see Subsection 4.2). The relative small acoustic wavelength and near-continuous character of the source lead to high temporal resolution sensitive to small atmospheric changes. This results in clear variations in array characteristics such as back azimuth and apparent velocity (also named trace velocity), shown in Figs. 23.8a and 23.9a, respectively. Figure 23.8a shows the back azimuth deviation, which is the difference between the true bearing and the propagation azimuth needed to arrive at the receiver location. Back azimuth deviation is a good indicator of crosswinds (see Chap. 18). The latitudinal propagation prompts an increased sensitivity to changes in the zonal stratospheric wind, dominating the crosswind conditions. A clear infrasonic signature is denotable, marked by the grey rectangle, inducing summer-like conditions since in winter no stratospheric returns are expected. The continuous high-frequency infrasound observations are interpreted as low stratospheric altitude returns (<40 km return altitude). The increase in trace velocity indicates a stratospheric temperature increase and decreased return height. A strong variation in back azimuth deviation is present, which indicates altering crosswinds from easterly (positive back azimuth deviation) to westerly (negative back azimuth deviation). Therefore, these low stratospheric returns are interpreted to be due to the SSW indicating the assumed warming onset (28 December 2012) and recovery (16 January 2013).

The method of Smets et al. (2016) to evaluate the stratospheric predictability, especially of interest during the SSW, is based on forward modelling the propagation of infrasound from Mount Tolbachik towards IS44. A year of near-continuous infrasound from the volcano Mount Tolbachik is compared with simulations using the high-resolution deterministic forecasts of ECMWF. An in-house developed ray tracing algorithm (cast in spherical coordinates) is used that takes into account the full effect of the 3-D inhomogeneous wind and temperature fields, see, for example, Brekhovskikh and Godin (1999). As such, array characteristics of back azimuth, trace velocity and travel time are simulated for the entire period, every 12 h, using various forecast steps. These wavefront simulations are compared to the array observations for each forecast step. Significant inconsistencies or lack of simulated returns indicates a possible difference between the true state of the atmosphere and the consulted forecast in the vicinity of the return height.

This relative performance is illustrated in Fig. 23.10, presenting a minimal mean difference between the observed and modelled back azimuth. All forecasts are able to reproduce the general SSW characteristics, including the sudden reversal of the back azimuth deviation (Fig. 23.8) as well as the sudden increase in trace velocity (Fig. 23.9). Nevertheless, the performance skill during the SSW is significantly smaller and clearly different for all three forecast steps when compared to the sum-

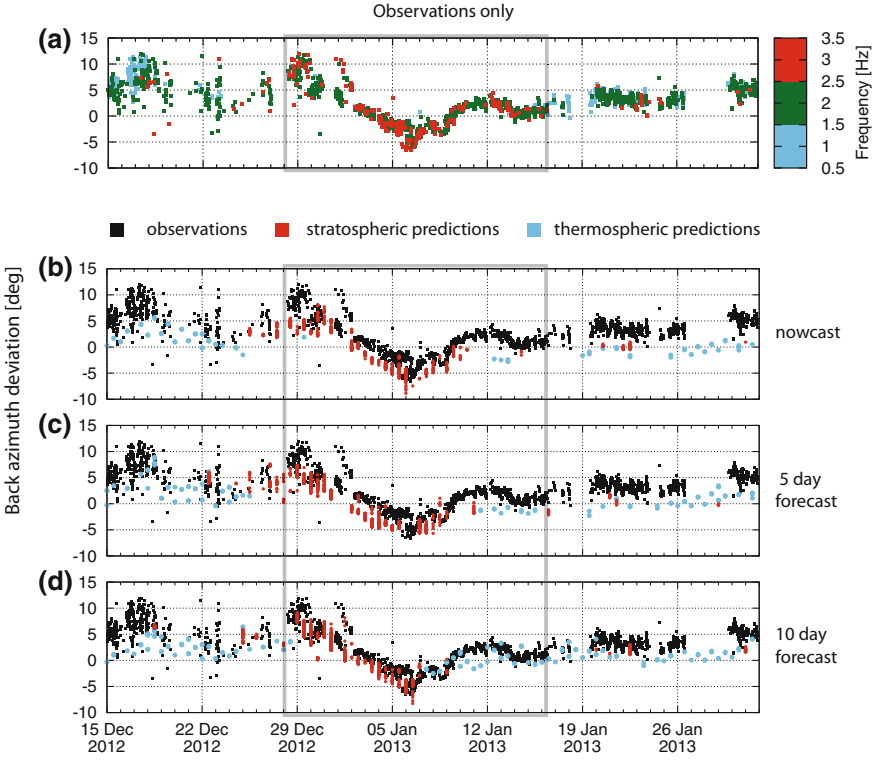

Fig. 23.8 **a** Back azimuth deviation values from Mount Tolbachik infrasound detections, for which trace velocity values are shown in Fig. 23.9a. **b–d** Comparisons between observations (black dots) and 3-D ray tracing results (red dots) as a function of time, using three different ECMWF HRES forecasts: **b** nowcast, **c** 5-day forecast and **d** 10-day forecast. The blue dots correspond to simulated arrivals that have propagated through the mesosphere and lower thermosphere, for which the MSIS and HWM climatologies have been used. The grey rectangle points to the continuous high-frequency infrasound observations interpreted as low stratospheric altitude returns (<40 km return altitude). These low stratospheric returns with sudden reversal in back azimuth are interpreted to be due to the SSW. Figure adapted from Smets et al. (2016)

mer predictions. Minimal back azimuth differences are obtained using the 10-day forecast, while the nowcast yields the highest continuity of the predictions. Poorest performance is by the 5-day forecast. The study of Smets et al. (2016) states four important findings based on the observations at IS44 of Mount Tolbachik, sampling the local stratosphere above.

1. The warming onset (28 December 2012) is well predicted by all three forecasts; both the nowcast and 5-day forecast predict the same warming onset followed twelve hours later by the 10-day forecast, although the 10-day forecast appears to be more accurate in predicting the larger back azimuth deviations and corresponding trace velocities during the first days of the warming. The resemblance

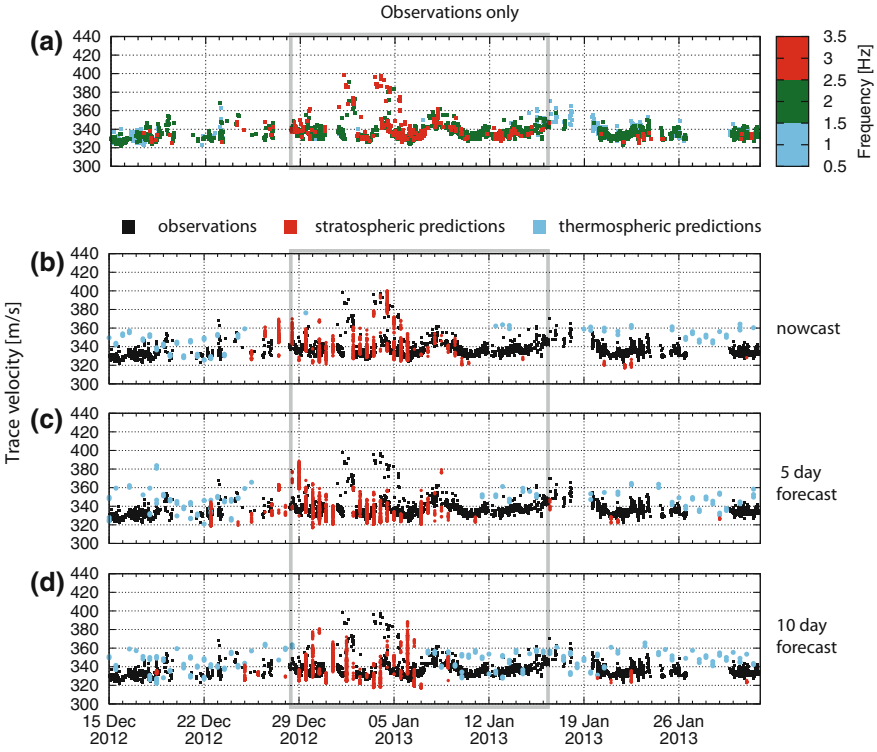

Fig. 23.9 **a** Trace velocity values from Mount Tolbachik infrasound detections. **b–d** Comparisons between observations (black dots) and 3-D ray tracing results (red dots) as a function of time, using three different ECMWF HRES forecasts: **b** nowcast, **c** 5-day forecast and **d** 10-day forecast. The blue dots correspond to simulated arrivals that have propagated through the mesosphere and lower thermosphere, for which the MSIS and HWM climatologies have been used. Figure adapted from Smets et al. (2016)

in timing of the predicted and observed stratospheric returns using the 10-day forecast is better as well.

2. During the vortex displacement phase of the major warming (before 7 January 2013), the 10-day forecast most accurately predicts the varying back azimuth deviation, including a sudden wind direction change around 2 January 2013 with corresponding increase in trace velocity (Fig. 23.9). Note that the difference in back azimuth prediction of both the nowcast and the 10-day forecast is below the array uncertainty. Yet, the large difference of the 5-day forecast when compared to the nowcast and 10-day forecast is remarkable.
3. When the vortex splits (around 7 January 2013), the 10-day forecast no longer predicts stratospheric returns, while the 5-day forecast and nowcast continue, respectively, 2 and 4 days with a quasi-similar back azimuth difference.

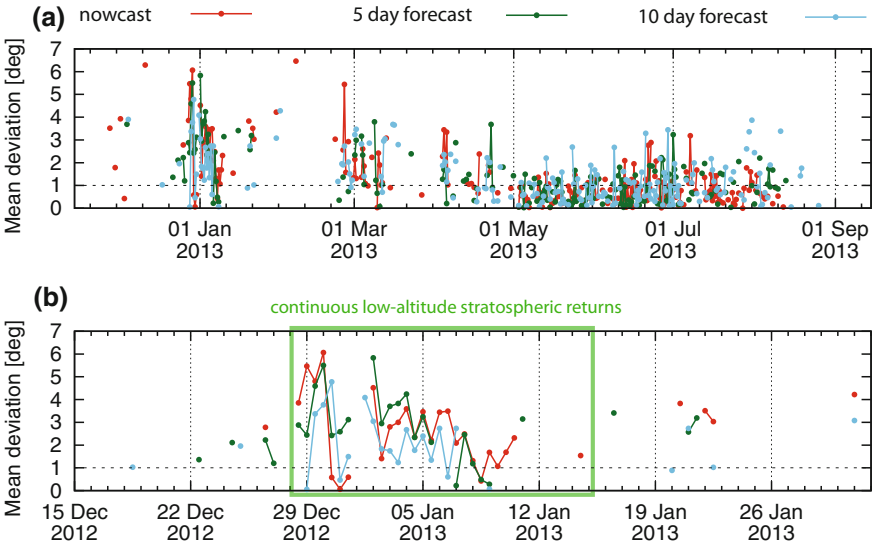

Fig. 23.10 **a** Estimated difference between the observed and predicted back azimuth of all returns over the full-time span of observation. Observations are averaged for 12 h time bins and contain at least six detections. The different colours correspond to the different ECMWF forecasts that are used in the simulations. The lines connecting the dots indicate the continuity of the predictions. The horizontal dashed black line is indicative of the uncertainty of the infrasound array. **b** Similar as (**a**), but focusing on the midwinter with the SSW period (green rectangle). Figure adapted from Smets et al. (2016)

4. All forecasts have difficulties to predict the stratospheric observations up to the expected warming recovery (16 January 2013). Predictions for all forecast steps indicate a too early recovery. The 10-day forecast predicts a difference of about 9 days with respect to the moment that no stratospheric arrivals are expected anymore (8 January 2016). The recovery is best captured by the nowcast model, continuously predicting up to 11 January 2013.

To understand the differences in performance between the forecasts, it is important to establish that the nowcast is most constrained by the data assimilation, whereas the 10-day forecast tends to be quasi-free running, with the 5-day forecast positioned somewhere in between. For a typical forecast, more forecast skill is expected for a shorter forecast step, as it is closer to the data assimilation. This is observed during summer (Fig. 23.10), where the nowcast performs best. Surprisingly, in winter, the 10-day forecast appears to be most accurate at predicting the first phase of the warming. Our interpretation is that the 10-day forecast is able to obtain sufficient information from the small a priori warming signatures with enough time to propagate through the atmosphere, to predict the warming including the sudden recovery around 2 January 2013. Once data has to be assimilated during the warming, the 10-day forecast loses a lot of forecast skill. At this stage, data gets most likely rejected

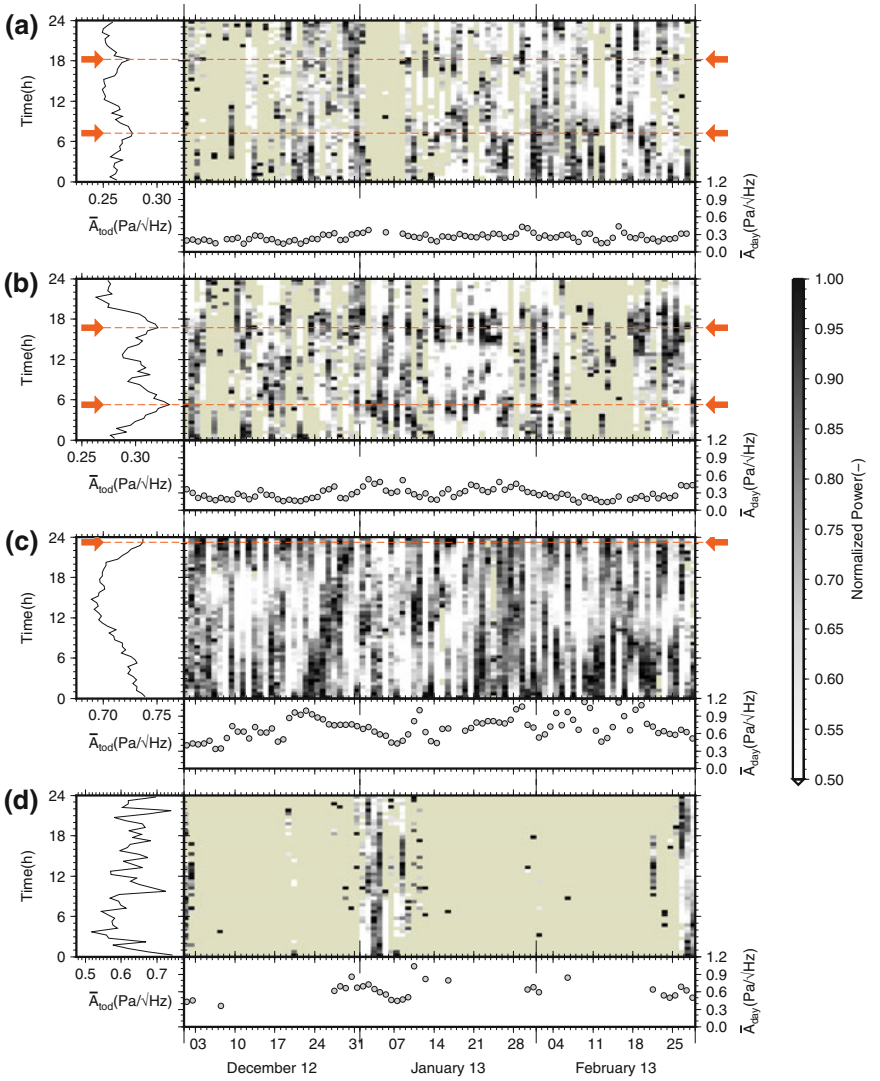

Fig. 23.11 Directional time-averaged spectral amplitude variations for the 2013 winter. From top to bottom are shown, IS18 in direction of the **a** Pacific Ocean and **b** Atlantic Ocean, IS53 in direction of the **c** Pacific Ocean and **d** Atlantic Ocean. Each subfigure consists of a vertical graph (left) and an image (right) with below one horizontal graph and one colour-coded bar. The vertical graph (left) shows the spectral amplitude averaged per time of day for each half hour. The red arrows and dashed lines indicate the tidal peaks in the mean time of day amplitude, if present. The image (right) shows the half hour averaged spectral power, normalised per day. The horizontal graph shows the daily mean spectral amplitude. Only detections are used with SNR $\geq$ 1.5 for IS18 and SNR $\geq$ 1.3 for IS53. Figure adapted from Smets and Evers (2014)

or modified by the data assimilation system leading to inaccurate initialisation as addressed by Diamantakis (2014). The nowcast is affected similarly, but recovers approximately at once with the data assimilation system such that it predicts best the SSW duration and recovery.

Broadening the view on the Arctic stratosphere by incorporating ambient noise observations of IS18 and IS53 as introduced by Smets and Evers (2014, see Subsection 4.5) gives a different perception of the warming offset. Figure 23.11 shows the amplitude variations during the 2013 SSW. Observations at IS44 of Mount Tolbachik sample a regional part of the stratosphere, while the ambient noise crosses thousands of kilometres. This is of importance in probing a hemispheric signature of the stratospheric warming. Figure 23.11 indicates a somewhat later warming onset (1 January 2013). More important is the recovery. Both IS18 and IS53 point to a regular midwinter ducting around 11 January, which agrees with simulations using the nowcast. Note the gap around 7 January in Fig. 23.11d and the diurnal phase shift, indicative of a split of the stratospheric vortex.

23.5 Outlook

Infrasound has a long history in monitoring SSWs. Several pioneering studies have focused on the various effects of a major warming on the propagation of infrasound. A clear transition can be identified from observing anomalous signatures towards the use of these signals to study anomalies in atmospheric conditions. The typical infrasonic signatures of a warming are the odd summer-like conditions in midwinter characterised by a significant change in direction of the observed infrasound (Donn and Rind 1972; Evers and Siegmund 2009), a change in amplitude of the ambient coherent infrasound noise (Rind and Donn 1978) and the existence of small stratospheric shadow zones due to a warm stratosphere (Evers et al. 2012). More subtle changes are found during a minor warming, recognisable by the presence of a bidirectional stratospheric duct (Assink et al. 2014b). The observed reduction in anisotropy is a measure for weakening of the stratospheric vortex during a minor warming. A general view of stratospheric polar vortex during an SSW is obtained by a combined analysis of all signal characteristic to unravel the stratospheric structure during an SSW (Smets and Evers 2014). This method allows the return height to be estimated from the amplitude variations, which provides detailed information on the life cycle of a warming. For the first time, differences between infrasound observations and the best deterministic state of the atmosphere (analysis) related to an SSW are indicated. Comparison of regional volcano infrasound with simulations, using various forecast steps, indicates interesting variations in stratospheric skill (Smets et al. 2016). The onset of the warming is better predicted by the 10-day forecast and duration by the nowcast. However, it is crucial to mention that the combination of infrasound observations and atmospheric models is essential in the study of SSWs.

In a next step, the method of Smets et al. (2016) for the evaluation of middle atmospheric weather forecasts using near-continuous infrasound detections can directly

be applied to similar setups, making use of other IMS or even national infrasound arrays. The demonstrated forecast evaluation method relies on an active volcano. However, the same methodology can be applied to ambient noise, using microbarom source predictions. In addition, source-independent techniques are being developed based on interferometry of the ambient noise field (Fricke et al. 2013, 2014). It is shown that infrasound is capable of providing detailed insight into the state of the atmosphere, of great value during an SSW. Nevertheless, it is essential to evolve towards a global comprehensive signature. Expanding towards ambient noise observations provides the ability to probe larger parts of the stratosphere. This is highly important for NWP, since improved knowledge of the global stratosphere induces a gain in tropospheric forecast skill but only when incorporating global observation (see Chap. 29). Maybe in the future infrasound can supplement the other observations to force the first-guess field more towards the actual state of the rapidly varying atmosphere.

Acknowledgements This work was performed during the course of the ARISE design studio project: part one (2012–2014) funded by European Union FP7 program (grant number 284387) and part two (2015–2017) funded by the European Commission H2020 program (grant number 653980). Läslo Evers' contribution is partly funded through a VIDI project from the Netherlands Organisation for Scientific Research (NWO), project number 864.14.005. CTBTO and station operators are thanked for guaranteeing the high quality of the IMS data and products. Figures in this chapter were made with the generic mapping tools (Wessel and Smith 1991).

References

Assink JD, Waxler R, Drob D (2012) On the sensitivity of infrasonic traveltimes in the equatorial region to the atmospheric tides. J Geophys Res 117:D01,110+. https://doi.org/10.1029/2011JD016107. https://doi.org/10.1029/2011JD016107/abstract

Assink JD, Waxler R, Frazier WG, Lonzaga J (2013) The estimation of upper atmospheric wind model updates from infrasound data. J Geophys Res Atmos 118:10,707–10,724. https://doi.org/10.1002/jgrd.50833

Assink JD, Pichon AL, Blanc E, Kallel M, Khemiri L (2014a) Evaluation of wind and temperature profiles from ECMWF analysis on two hemispheres using volcanic infrasound. J Geophys Res 119(14):8659–8683. https://doi.org/10.1002/2014jd021632

Assink JD, Waxler R, Smets P, Evers LG (2014b) Bidirectional infrasonic ducts associated with sudden stratospheric warming events. J Geophys Res 119:1140–1153. https://doi.org/10.1002/2013jd021062

Assink JD, Averbuch G, Smets PSM, Evers LG (2016) On the infrasound detected from the 2013 and 2016 DPRK's underground nuclear tests. Geophys Res Lett 43:3526–3533. https://doi.org/10.1002/2016gl068497

Assink J, Smets P, Marcillo O, Weemstra C, Lalande J-M, Waxler R, Evers L (2019) Advances in infrasonic remote sensing methods. In: Le Pichon A, Blanc E, Hauchecorne A (eds) Infrasound monitoring for atmospheric studies, 2nd edn. Springer, Dordrecht, pp 605–632

Baldwin MP, Dunkerton TJ (2001) Stratospheric harbingers of anomalous weather regimes. Science 294:581–584. https://doi.org/10.1126/science.1063315

Blanc E, Pol K, Le Pichon A, Hauchecorne A, Keckhut P, Baumgarten G, Hildebrand J, Höffner J, Stober G, Hibbins R, Espy P, Rapp M, Kaifler B, Ceranna L, Hupe P, Hagen J, Rüfenacht R, Kämpfer N, Smets P (2019) Middle atmosphere variability and model uncertainties as investi-

gated in the framework of the ARISE project. In: Le Pichon A, Blanc E, Hauchecorne A (eds) Infrasound monitoring for atmospheric studies, 2nd edn. Springer, Dordrecht, pp 845–887

Brekhovskikh IM, Goncharov VV, Kurtepov VM, Naugol'nykh KA (1973) The radiation of infrasound into the atmosphere by surface waves in the ocean. Atmos Oceanic Phys 9:899–907

Brekhovskikh LM, Godin OA (1999) Acoustics of layered media II: point sources and bounded beams. Springer series on wave phenomena, vol 10, 2nd edn. Springer, Berlin. http://www.worldcat.org/isbn/9783662038895

Charlton AJ, Polvani LM (2007) A new look at stratospheric sudden warmings. Part I: Climatology and modeling benchmarks. J Clim 20:449–469. https://doi.org/10.1175/JCLI3996.1

Charlton AJ, O'neill A, Lahoz WA, Massacand AC (2004) Sensitivity of tropospheric forecasts to stratospheric initial conditions. QJR Meteorol Soc 130(600):1771–1792. https://doi.org/10.1256/qj.03.167

Charlton-Perez AJ, Baldwin MP, Birner T, Black RX, Butler AH, Calvo N, Davis NA, Gerber EP, Gillett N, Hardiman S, Kim J, Krüger K, Lee YY, Manzini E, McDaniel BA, Polvani L, Reichler T, Shaw TA, Sigmond M, Son SW, Toohey M, Wilcox L, Yoden S, Christiansen B, Lott F, Shindell D, Yukimoto S, Watanabe S (2013) On the lack of stratospheric dynamical variability in low-top versions of the CMIP5 models. J Geophys Res Atmos 118:2494–2505. https://doi.org/10.1002/jgrd.50125

Charney JG, Drazin PG (1961) Propagation of planetary-scale disturbances from the lower into the upper atmosphere. J Geophys Res 66:83–109. https://doi.org/10.1029/jz066i001p00083

Chunchuzov I, Kulichkov S, Perepelkin V, Popov O, Firstov P, Assink JD, Marchetti E (2015) Study of the wind velocity-layered structure in the stratosphere, mesosphere, and lower thermosphere by using infrasound probing of the atmosphere. J Geophys Res Atmos 120(17):2015JD023,276–8840. https://doi.org/10.1002/2015jd023276

Chunchuzov IP, Kulichkov SN, Popov OE, Waxler R, Assink J (2011) Infrasound scattering from atmospheric anisotropic inhomogeneities. Izv Atmos Ocean Phys 47:540–557. https://doi.org/10.1134/s0001433811050045

Coy L, Eckermann SD, Hoppel KW, Sassi F (2011) Mesospheric precursors to the major stratospheric sudden warming of 2009: validation and dynamical attribution using a ground-to-edge-of-space data assimilation system. J Adv Model Earth Syst 3(4):M10,002+. https://doi.org/10.1029/2011ms000067

Dahlman O, Mykkeltveit S, Haak H (2009) The treaty, chapter 4. Springer, Netherlands, Dordrecht, pp 83–98. https://doi.org/10.1007/978-1-4020-6885-0_4

De Angelis S, Fee D, Haney M, Schneider D (2012) Detecting hidden volcanic explosions from Mt. Cleveland Volcano, Alaska with infrasound and ground-coupled airwaves. Geophys Res Lett 39:L21,312+. https://doi.org/10.1029/2012gl053635

Diamantakis M (2014) Improving ECMWF forecasts of sudden stratospheric warmings. ECMWF Newslett 141:30–36

Donn WL, Rind D (1971) Natural infrasound as an atmospheric probe. Geophys J R Astron Soc 26:111–133. https://doi.org/10.1111/j.1365-246x.1971.tb03386.x

Donn WL, Rind D (1972) Microbaroms and the temperature and wind of the upper atmosphere. J Atmos Sci 29:156–172. https://doi.org/10.1175/1520-0469(1972)029<0156:mattaw>2.0.co;2

Drob DP, Emmert JT, Meriwether JW, Makela JJ, Doornbos E, Conde M, Hernandez G, Noto J, Zawdie KA, McDonald SE, Huba JD, Klenzing JH (2015) An update to the horizontal wind model (HWM): the quiet time thermosphere. Earth Space Sci 2(7):2014EA000,089+. https://doi.org/10.1002/2014ea000089

Evers LG, Siegmund P (2009) Infrasonic signature of the 2009 major sudden stratospheric warming. Geophys Res Lett 36:L23,808+. https://doi.org/10.1029/2009gl041323

Evers LG, van Geyt ARJ, Smets P, Fricke JT (2012) Anomalous infrasound propagation in a hot stratosphere and the existence of extremely small shadow zones. J Geophys Res 117:D06,120+. https://doi.org/10.1029/2011jd017014

Fee D, Steffke A, Garces M (2010) Characterization of the 2008 Kasatochi and Okmok eruptions using remote infrasound arrays. J Geophys Res 115(D2):D00L10+. https://doi.org/10.1029/2009jd013621

Fee D, Waxler R, Assink J, Gitterman Y, Given J, Coyne J, Mialle P, Garces M, Drob D, Kleinert D, Hofstetter R, Grenard P (2013) Overview of the 2009 and 2011 Sayarim infrasound calibration experiments. J Geophys Res Atmos 118:6122–6143. https://doi.org/10.1002/jgrd.50398

Fricke JT, Allouche NE, Simons DG, Ruigrok EN, Wapenaar K, Evers LG (2013) Infrasonic interferometry of stratospherically refracted microbaroms—a numerical study. J Acoust Soc Am 134:2660–2668. https://doi.org/10.1121/1.4819117

Fricke JT, Evers LG, Smets PSM, Wapenaar K, Simons DG (2014) Infrasonic interferometry applied to microbaroms observed at the large aperture infrasound array in the Netherlands. J Geophys Res 119:9654–9665. https://doi.org/10.1002/2014jd021663

Gerber EP, Orbe C, Polvani LM (2009) Stratospheric influence on the tropospheric circulation revealed by idealized ensemble forecasts. Geophys Res Lett 36:L24,801+. https://doi.org/10.1029/2009gl040913

Godin OA (2002) An effective quiescent medium for sound propagating through an inhomogeneous, moving fluid. J Acoust Soc Am 112(4):1269–1275. https://doi.org/10.1121/1.1504853

Green DN, Matoza RS, Vergoz J, Le Pichon A (2012) Infrasonic propagation from the 2010 Eyjafjallajökull eruption: investigating the influence of stratospheric solar tides. J Geophys Res 117:D21,202+. https://doi.org/10.1029/2012jd017988

Gutenberg B (1939) The velocity of sound waves and the temperature in the stratosphere in southern California. Bull Am Meteorol Soc 20:192–201

Hasselmann K (1963) A statistical analysis of the generation of microseisms. Rev Geophys 1:177–210. https://doi.org/10.1029/rg001i002p00177

Hedlin MAH, Drob D, Walker K, de Groot-Hedlin C (2010) A study of acoustic propagation from a large bolide in the atmosphere with a dense seismic network. J Geophys Res 115:B11,312+. https://doi.org/10.1029/2010jb007669

Holton JR (2004) An introduction to dynamic meteorology, 4th edn. Elsevier Academic Press, Oxford. http://www.worldcat.org/isbn/0123540151

Janssen P (2009) The interaction of ocean waves and wind, 1st edn. Cambridge University Press. http://www.worldcat.org/isbn/0521121043

Jung T, Miller MJ, Palmer TN (2010) Diagnosing the origin of extended-range forecast errors. Mon Wea Rev 138(6):2434–2446. https://doi.org/10.1175/2010mwr3255.1

Källén E (2008) Special issue with manuscripts related to ESA's atmospheric dynamics mission/Aeolus. Tellus A: Dyn Meteorol Oceanogr 60(2):189–190. https://doi.org/10.1111/j.1600-0870.2007.00296.x

Kodera K, Mukougawa H, Fujii A (2013) Influence of the vertical and zonal propagation of stratospheric planetary waves on tropospheric blockings. J Geophys Res 118:8333–8345. https://doi.org/10.1002/jgrd.50650

Kulichkov SN, Chunchuzov IP, Popov OI (2010) Simulating the influence of an atmospheric fine inhomogeneous structure on long-range propagation of pulsed acoustic signals. Izv Atmos Ocean Phys 46:69–77. https://doi.org/10.1134/S0001433810010093

Labitzke KG, van Loon H (1999) The stratosphere. Springer, Berlin, Heidelberg. https://doi.org/10.1007/978-3-642-58541-8

Lalande JM, Sèbe O, Landès M, Blanc-Benon P, Matoza RS, Le Pichon A, Blanc E (2012) Infrasound data inversion for atmospheric sounding. Geophys J Int 190:687–701. https://doi.org/10.1111/j.1365-246x.2012.05518.x

Lee C, Smets P, Charlton-Perez A, Evers L, Harrison G, Marlton G (2019) The potential impact of upper stratospheric measurements on sub-seasonal forecasts in the extra-tropics. In: Le Pichon A, Blanc E, Hauchecorne A (eds) Infrasound monitoring for atmospheric studies, 2nd edn. Springer, Dordrecht, pp 889–910

Le Pichon A, Blanc E, Drob D, Lambotte S, Dessa JX, Lardy M, Bani P, Vergniolle S (2005) Infrasound monitoring of volcanoes to probe high-altitude winds. J Geophys Res 110:D13,106+. https://doi.org/10.1029/2004jd005587

Le Pichon A, Ceranna L, Garcés M, Drob D, Millet C (2006) On using infrasound from interacting ocean swells for global continuous measurements of winds and temperature in the stratosphere. J Geophys Res 111. https://doi.org/10.1029/2005jd006690

Le Pichon A, Vergoz J, Herry P, Ceranna L (2008) Analyzing the detection capability of infrasound arrays in Central Europe. J Geophys Res 113(D12):D12,115+. https://doi.org/10.1029/2007jd009509

Le Pichon A, Vergoz J, Blanc E, Guilbert J, Ceranna L, Evers L, Brachet N (2009) Assessing the performance of the international monitoring system's infrasound network: geographical coverage and temporal variabilities. J Geophys Res 114:D08,112+. https://doi.org/10.1029/2008jd010907

Le Pichon A, Blanc E, Hauchecorne A (eds) (2010) Infrasound monitoring for atmospheric studies, 1st edn. Springer Netherlands, Dordrecht. http://www.worldcat.org/isbn/1402095074

Le Pichon A, Assink JD, Heinrich P, Blanc E, Charlton-Perez A, Lee CF, Keckhut P, Hauchecorne A, Rüfenacht R, Kämpfer N, Drob DP, Smets PSM, Evers LG, Ceranna L, Pilger C, Ross O, Claud C (2015) Comparison of co-located independent ground-based middle atmospheric wind and temperature measurements with numerical weather prediction models. J Geophys Res Atmos 120(16):2015JD023,273–8331. https://doi.org/10.1002/2015jd023273

Limpasuvan V, Thompson DWJ, Hartmann DL (2004) The life cycle of the northern hemisphere sudden stratospheric warmings. J Clim 17:2584–2596. https://doi.org/10.1175/1520-0442(2004)017<2584:TLCOTN>2.0.CO;2

Limpasuvan V, Hartmann DL, Thompson DWJ, Jeev K, Yung YL (2005) Stratosphere-troposphere evolution during polar vortex intensification. J Geophys Res 110. https://doi.org/10.1029/2005jd006302

Lindzen SR, Chapman S (1969) Atmospheric tides. Space Sci Rev 10:3–188. https://doi.org/10.1007/BF00171584

Longuet-Higgins MS (1950) A theory of the origin of microseisms. Philos Trans R Soc A 243:1–35. https://doi.org/10.1098/rsta.1950.0012

Marchetti E, Ripepe M, Delle Donne D, Genco R, Finizola A, Garaebiti E (2013) Blast waves from violent explosive activity at Yasur Volcano, Vanuatu. Geophys Res Lett 40(22):2013GL057,900+. https://doi.org/10.1002/2013gl057900

Matoza RS, Vergoz J, Le Pichon A, Ceranna L, Green DN, Evers LG, Ripepe M, Campus P, Liszka L, Kvaerna T, Kjartansson E, Höskuldsson A (2011) Long-range acoustic observations of the Eyjafjallajökull eruption, Iceland, April–May 2010. Geophys Res Lett 38(6):L06,308+. https://doi.org/10.1029/2011gl047019

Matsuno T (1971) A dynamical model of the stratospheric sudden warming. J Atmos Sci 28:1479–1494. https://doi.org/10.1175/1520-0469(1971)028<1479:admots>2.0.co;2

Muench HS (1965) On the dynamics of the wintertime stratosphere circulation. J Atmos Sci 22:349–360. https://doi.org/10.1175/1520-0469(1965)022<0349:otdotw>2.0.co;2

Picone JM, Hedin AE, Drob DP, Aikin AC (2002) NRLMSISE-00 empirical model of the atmosphere: statistical comparisons and scientific issues. J Geophys Res 107(A12):1468+. https://doi.org/10.1029/2002ja009430

Pierce AD (1981) Acoustics—an introduction to its physical principles and applications. McGraw-Hill series in mechanical engineering. McGraw-Hill, New York. http://www.worldcat.org/isbn/0883186128

Posmentier ES (1967) A theory of microbaroms. Geophys J R Astron Soc 13. https://doi.org/10.1111/j.1365-246x.1967.tb02301.x

Randel W, Udelhofen P, Fleming E, Geller M, Gelman M, Hamilton K, Karoly D, Ortland D, Pawson S, Swinbank R, Wu F, Baldwin M, Chanin ML, Keckhut P, Labitzke K, Remsberg E, Simmons A, Wu D (2004) The SPARC intercomparison of middle-atmosphere climatologies. J Clim 17:986–1003. https://doi.org/10.1175/1520-0442(2004)017<0986:tsiomc>2.0.co;2

Revelle DO (2010) Modified ray-mode (phase) theory: understanding counter-wind propagation effects from atmospheric explosions. J Atmos Sol-Terr Phys 72:241–261. https://doi.org/10.1016/j.jastp.2009.11.017

Rind D, Donn WL (1975) Further use of natural infrasound as a continuous monitor of the upper atmosphere. J Atmos Sci 32:1694–1704. https://doi.org/10.1175/1520-0469(1975)032<1694:fuonia>2.0.co;2

Rind D, Donn WL, Dede E (1973) Upper Air Wind Speeds Calculated from Observations of Natural Infrasound. J Atmos Sci 30:1726–1729. https://doi.org/10.1175/1520-0469(1973)030<1726:uawscf>2.0.co;2

Rind DH, Donn WL (1978) Infrasound observations of variability during stratospheric warmings. J Atmos Sci 35:546–553. https://doi.org/10.1175/1520-0469(1978)035<0546:ioovds>2.0.co;2

Roff G, Thompson DWJ, Hendon H (2011) Does increasing model stratospheric resolution improve extended-range forecast skill? Geophys Res Lett 38(5):L05,809+. https://doi.org/10.1029/2010gl046515

Seibert G (2006) The history of sounding rockets and their contribution to European Space Research. ESA Publications. http://www.worldcat.org/isbn/9290925507

Shaw TA, Shepherd TG (2008) Raising the roof. Nat Geosci 1:12–13. https://doi.org/10.1038/ngeo.2007.53

Sigmond M, Scinocca JF, Kharin VV, Shepherd TG (2013) Enhanced seasonal forecast skill following stratospheric sudden warmings. Nat Geosci 6:98–102. https://doi.org/10.1038/ngeo1698

Smets PSM, Evers LG (2014) The life cycle of a sudden stratospheric warming from infrasonic ambient noise observations. J Geophys Res 119:12,084–12,099. https://doi.org/10.1002/2014jd021905

Smets PSM, Evers LG, Charlton-Perez AJ, Lee CF, Harrison RG (2014) Roadmap on the use of ARISE data for weather and climate monitoring in Europe—D5.5. Technical report, Atmospheric dynamics Research InfraStructure in Europe–ARISE–project, FP7 Grant Agreement nr 284387

Smets PSM, Evers LG, Näsholm SP, Gibbons SJ (2015) Probabilistic infrasound propagation using realistic atmospheric perturbations. Geophys Res Lett 42(15):2015GL064,992–6517. https://doi.org/10.1002/2015gl064992

Smets PSM, Assink JD, Le Pichon A, Evers LG (2016) ECMWF SSW forecast evaluation using infrasound. J Geophys Res Atmos 121(9):2015JD024,251–4650. https://doi.org/10.1002/2015jd024251

Stopa JE, Cheung KF, Garcés MA, Badger N (2012) Atmospheric infrasound from nonlinear wave interactions during Hurricanes Felicia and Neki of 2009. J Geophys Res 117. https://doi.org/10.1029/2012jc008257

Straume AG, Elfving A, Wernham D, Culoma A, Mondin L, de Bruin F, Kanitz T, Schuettemeyer D, Buscaglione F, Dehn A (2016) ESA's Spaceborne Lidar Mission ADM-Aeolus; recent achievements and preparations for launch. EPJ Web Conf 119:01,001+. https://doi.org/10.1051/epjconf/201611901001

Sutherland LC, Bass HE (2004) Atmospheric absorption in the atmosphere up to 160 km. J Acoust Soc Am 115:1012–1032. https://doi.org/10.1121/1.1631937

Tailpied D, Le Pichon A, Marchetti E, Assink J, Vergniolle S (2016) Assessing and optimizing the performance of infrasound networks to monitor volcanic eruptions. Geophys J Int 208(1):437–448. https://doi.org/10.1093/gji/ggw400

Tripathi OP, Baldwin M, Charlton-Perez A, Charron M, Eckermann SD, Gerber E, Harrison RG, Jackson DR, Kim BM, Kuroda Y, Lang A, Mahmood S, Mizuta R, Roff G, Sigmond M, Son SW (2014) The predictability of the extratropical stratosphere on monthly time-scales and its impact on the skill of tropospheric forecasts. QJR Meteorol Soc 141(689). https://doi.org/10.1002/qj.2432

Tripathi OP, Charlton-Perez A, Sigmond M, Vitart F (2015) Enhanced long-range forecast skill in boreal winter following stratospheric strong vortex conditions. Environ Res Lett 10(10):104,007+. https://doi.org/10.1088/1748-9326/10/10/104007

Walker KT (2012) Evaluating the opposing wave interaction hypothesis for the generation of microbaroms in the eastern North Pacific. J Geophys Res 117:C12,016+. https://doi.org/10.1029/2012jc008409

Walker KT, Hedlin MAH (2009) A review of wind-noise reduction methodologies. Infrasound monitoring for atmospheric studies, chapter 5. Springer, Netherlands, Dordrecht, pp 141–182. https://doi.org/10.1007/978-1-4020-9508-5_5

Waxler R, Gilbert KE (2006) The radiation of atmospheric microbaroms by ocean waves. J Acoust Soc Am 119:2651–2664. https://doi.org/10.1121/1.2191607

Waxler R, Gilbert K, Talmadge C, Hetzer C (2007) The effects of the finite depth of the ocean on microbarom signals. In: 8th international conference on theoretical and computational acoustics (ICTCA). European Acoustics Association (EAA), Crete, Greece

Wessel P, Smith WHF (1991) Free software helps map and display data. Eos Trans AGU 72:441–446. https://doi.org/10.1029/90eo00319

Whitaker RW, Mutschlecner JP (2008) A comparison of infrasound signals refracted from stratospheric and thermospheric altitudes. J Geophys Res 113:D08,117+. https://doi.org/10.1029/2007jd008852

WMO (2013) Guide to the global observing system. WMO-No. 488, World Meteorological Organization, Geneva, Switzerland. http://www.worldcat.org/isbn/9789263104885

Chapter 24
Recent Dynamic Studies on the Middle Atmosphere at Mid- and Low-Latitudes Using Rayleigh Lidar and Other Technologies

Alain Hauchecorne, Sergey Khaykin, Philippe Keckhut, Nahoudha Mzé, Guillaume Angot and Chantal Claud

Abstract The vertical structure of the middle atmosphere (stratosphere and mesosphere) is mainly driven by the absorption of solar radiation by ozone, which is maximum at the stratopause defining the limit between the two layers. However, the meridional structure of the temperature field is far from the radiative equilibrium, especially in the upper mesosphere where the coldest temperatures are reached at the summer pole. This structure can be only explained if we consider the vertical and meridional circulation driven by planetary and gravity wave propagation and breaking. Rayleigh lidars providing time-resolved accurate temperature profiles from the middle stratosphere to the top of mesosphere are very efficient tools to study the characteristics of these waves and their impact on the mean temperature and wind fields. Together with other types of instrument setup in the frame of the European Design Study projects ARISE and -ARISE2, Doppler wind lidars, Mesosphere–Stratosphere–Troposphere (MST) and meteor radars, the IMS (International Monitoring System) infrasound network, airglow imagers and ionospheric sounders, they will contribute to a better knowledge and a better representation of middle atmospheric processes in numerical weather prediction and climate models.

A. Hauchecorne (✉) · S. Khaykin · P. Keckhut · N. Mzé · G. Angot
Laboratoire atmosphères, milieux et observations spatiales (LATMOS), UVSQ Université Paris-Saclay, Sorbonne Université, CNRS, Guyancourt, France
e-mail: alain.hauchecorne@latmos.ipsl.fr

C. Claud
Laboratoire de Météorologie Dynamique (LMD) CNRS,
Ecole Polytechnique, Palaiseau, France

A. Le Pichon et al. (eds.), *Infrasound Monitoring for Atmospheric Studies*,
https://doi.org/10.1007/978-3-319-75140-5_24

24.1 Introduction

The middle atmosphere is the region of the atmosphere between about 12 and 90 km above the troposphere where clouds are formed and below the thermosphere strongly controlled by the solar radiation. It is divided into two main layers defined by their vertical gradient of temperature (Fig. 24.1). The stratosphere with a positive temperature gradient extends from 12 to 48 km. This is the region where the ozone layer is formed, protecting us against the harmful UV solar radiation. The mesosphere with a negative temperature gradient is located between 48 and 90 km. This is a region very dynamically active. The vertical structure of the middle atmosphere is mainly driven by the absorption of solar radiation by ozone, which is maximum at the stratopause defining the limit between the two layers. However, the meridional structure of the temperature field is far from the radiative equilibrium, especially in the upper mesosphere where the coldest temperatures are reached at the summer pole with 24 h per day of solar illumination (Fig. 24.2). The meridional–vertical structure of the middle atmospheric temperature field can only be explained if we take into account the dynamics that transports air masses, energy and momentum flux between the different parts of the atmosphere. In the stratosphere, the main meridional–vertical dynamical feature is the Brewer-Dobson circulation (Shepherd 2000) with an ascending branch in the equatorial region, a meridional transport from the equator to the poles and a descending branch in the

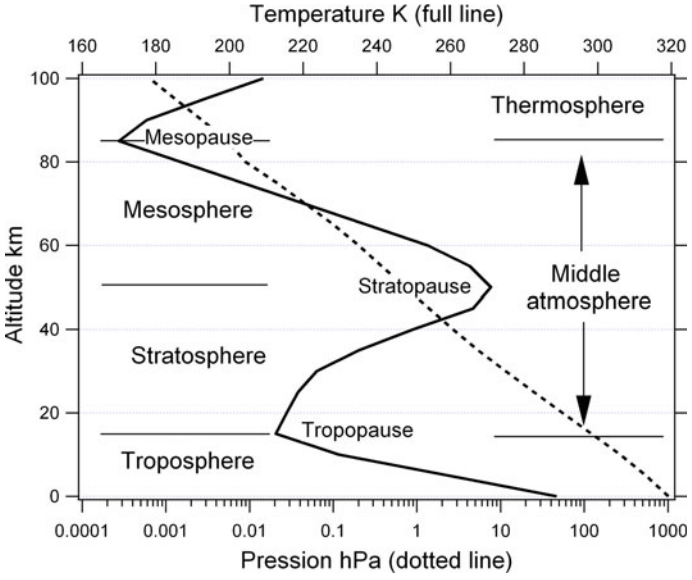

Fig. 24.1 Schematic representation of the vertical profile of atmospheric temperature and pressure showing the separation between different atmospheric layers. The middle atmosphere includes the stratosphere and the mesosphere. From Hauchecorne et al. (2010)

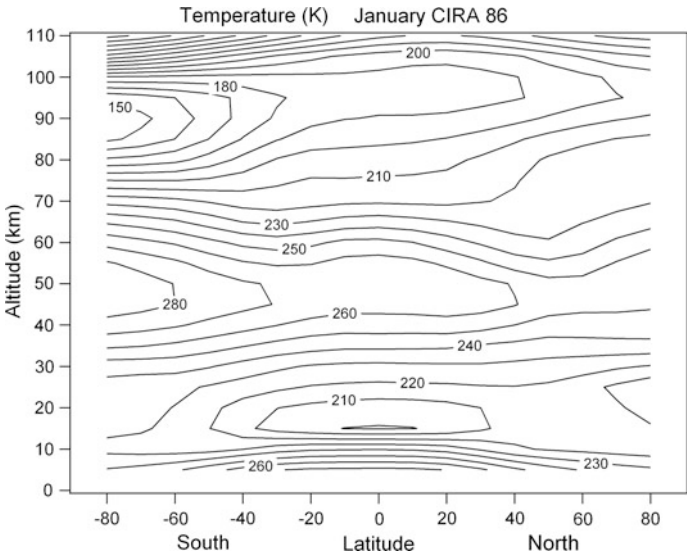

Fig. 24.2 Zonally averaged temperature (K) from the surface to approximately 120 km altitude in January, based on CIRA 86 (Fleming et al. 1988)

polar region. In the mesosphere, the main circulation is from the summer pole to the winter pole, with an ascent (descent) of air and an adiabatic cooling (warming) at the summer (winter) pole. For more explanations, see Hauchecorne et al. (2010).

Atmospheric waves are known to play a major role in the energy and momentum budget of the middle atmosphere, and their influences on the atmospheric structure and circulation have been widely recognized (e.g. Andrews et al. 1987; Fritts and Alexander 2003). Atmospheric waves carry energy and momentum from one region to another. It is crucial to have a good knowledge of the characteristics of atmospheric waves to better understand their role in the middle atmosphere dynamics and thermal structure.

A large spectrum of waves exists in the atmosphere. We consider here two main wave families, the planetary Rossby waves (PWs) and the gravity waves (GWs). They have very different characteristics and origins. PWs owe their existence to the equator to pole gradient of Coriolis force and are produced by the flow over orography and by contrasts in temperature between the land and ocean. Extratropical PWs can only propagate upwards in the middle atmosphere during the period of westerly winds (Charney and Drazin 1961). In summer, easterly winds prevail (Fig. 24.3) and PWs are blocked in the lower stratosphere. In winter, PWs can propagate upwards at middle and high latitudes and can lead to dramatic deviations of the flow from its climatological mean, as for instance during Sudden Stratospheric Warmings (SSWs) (Matsuno 1971; Labitzke 1981; Charlton and Polvani 2007; Butler et al. 2015; Maury et al. 2016). SSWs appear to be a strong issue for the evolution of the stratosphere and induced-tropospheric changes. Not only they affect the polar vortex where the ozone depletion takes place but they

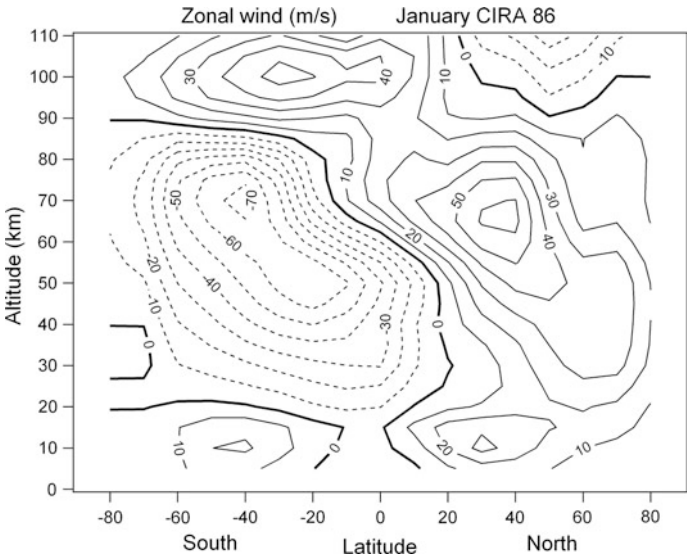

Fig. 24.3 Zonally averaged zonal wind (ms^{-1}) from the surface to 110 km altitude in January, based on CIRA 86 model (Fleming et al. 1988)

have also an impact on weather circulation at ground (Baldwin et al. 2001; Cohen and Jones 2011). PWs are explicitly represented in numerical weather forecast models. However, their representation in the upper stratosphere and mesosphere lacks observations assimilated in the models at these altitudes (Lee et al. 2019).

GWs are generated by the vertical displacement of air masses that creates a restoring gravity force in the opposite direction. The main sources of GWs are the orography, the cloud convection and the geostrophic adjustment of the jet stream. GWs propagate upwards in the stratosphere and the mesosphere depending on the vertical profile of horizontal wind until they break and they transfer their energy and momentum flux to the mean flow (Lindzen et al. 1981). GWs are sub-grid phenomena for most numerical weather forecast and climate models and they cannot be represented explicitly. It is then necessary to parameterize their effect on the general circulation. However, very few data are available to adjust these parameterizations and high-resolution observations of GWs are strongly needed. Mesoscale models like WRF (Weather Research and Forecasting Model) can represent explicitly GWs and then build the bridge between observations and global models.

Time-resolved observations of the temperature profiles in the middle atmosphere are needed to validate the representation of atmospheric waves in the models. The Rayleigh lidar technique is well adapted to fulfil this role. Hauchecorne and Chanin (1980) initiated the measurement of stratospheric and mesospheric temperature using the Rayleigh Lidar technique 30 years ago at Haute-Provence Observatory (OHP). Monochromatic laser pulses are sent vertically into the atmosphere and a temporal analysis of the backscattered light provides information about the vertical

structure and composition of the atmosphere. Above the top of the stratospheric aerosol layer (about 30 km), Mie scattering by aerosols is negligible and the received signal, only due to Rayleigh scattering by air molecules, is directly proportional to the density of the atmosphere. The temperature profile is deduced from the density profile assuming that the density is in hydrostatic equilibrium and obeys the perfect gas law. The top altitude of the profile is limited upwards to 80 to 90 km by the signal-to-noise ratio depending on the power of the lidar system.

Rayleigh lidars, belonging to the Network for the Detection of Atmospheric Composition Changes (NDACC), are well adapted to the study of PWs (Hauchecorne and Chanin 1983, 1988), SSWs (Angot et al. 2012) and GWs (Wilson et al. 1990) in the upper stratosphere and in the mesosphere, as well as their interactions with the mean flow to induce mesospheric temperature inversions (Hauchecorne et al. 1987). The OHP Rayleigh lidar database is the longest temperature series and allowed one of the first detection of the cooling of the upper stratosphere and mesosphere (Hauchecorne et al. 1991; Keckhut et al. 1995; Ramaswamy et al. 2001). Now it is a key instrument to insure inter-satellite adjustment like AMSU series (Keckhut et al. 2015a; Funatsu et al. 2016). One of the most powerful NDACC Rayleigh lidars is located at OHP and is operated in routine typically 4–5 h per night with clear sky since 1979 (Keckhut et al. 1993). These observations allow studying the evolution of density and temperature profiles during the night. Vertical structures in these profiles reveal the presence of GWs that are usually generated in the troposphere and propagate upwards in the stratosphere and in the mesosphere. When they reach critical amplitude, they break and they transfer their momentum flux and energy to the mean flow. Rayleigh lidar observations have been extensively used for the study of gravity waves in the stratosphere and in the mesosphere. Wilson et al. (1990, 1991a, b) analysed the characteristics and built the climatology of gravity waves above OHP. Hauchecorne et al. (1994) established the link between the gravity wave activity and prevailing winds during the DYANA campaign. Following these studies, Rayleigh lidar data have been extensively analysed for GW studies at low-latitude (Chane-Ming et al. 2000; Sivakumar et al. 2006; Li et al. 2010; Mzé et al. 2014), mid-latitudes (Rauthe et al. 2006, 2008; Sica and Argall 2007) and high latitudes (Whiteway et al. 1997; Duck et al. 2001; Yamashita et al. 2009; Alexander et al. 2010). We present in this chapter recent results on atmospheric dynamics obtained from the analysis of Rayleigh lidar data at OHP. In the second section, we present a new climatology of GWs obtained from 16 years of Rayleigh lidar data at OHP. We show also that, in the middle stratosphere, it is possible to obtain consistent results on GWs energy between GPS radio occultation and lidar observations. In the third section, we demonstrate that it is necessary to take into account possible changes in PW activity and SSW occurrence for the evaluation of temperature trends in the middle atmosphere.

24.2 Gravity Waves

24.2.1 Gravity Wave Characterization from NDACC Rayleigh Lidar Data at Haute-Provence Observatory

As presented in the introduction, Rayleigh lidars produce accurate observations with high temporal and vertical resolution, well adapted for studying atmospheric GWs. Rayleigh lidars provide vertical profiles of the total density of the atmosphere from about 30 to 90 km depending on the signal-to-noise ratio, and are powerful tools for studying atmospheric perturbations. Lidar measurements are performed continuously at OHP since late 1979 (in the beginning, the vertical resolution was 0.3 km, and it has been improved to 0.075 km since 1994.

Another powerful Rayleigh lidar has been set up recently at Maido Observatory. This new high-altitude atmospheric Observatory is located in the Western part of Reunion Island (21°S, 55°E) and benefits from very favourable weather conditions for lidar observations. The operations began in 2013 (Keckhut et al. 2015b). Figure 24.4 shows a series of temperature profiles reaching above 80 km in only 15 min of integration, which illustrates the potential of the lidar for GW studies. The propagation of wavy structures due to GWs is clearly visible, especially in the stratosphere. The temperature anomaly (deviation from the nightly mean profile) allows following the downward propagation of long period GWs during the 8 h of observations (Fig. 24.5). This downward propagation of the wave phase is expected for GWs generated in the troposphere, the vertical direction of propagation of the wave phase being in opposite to the direction of propagation of the wave energy (Wilson et al. 1990).

GW activity, in terms of potential energy (E_p), is estimated by analysing raw lidar signals with a variance method at OHP (Hauchecorne et al. 1994; Mzé et al. 2014).

We used the potential energy per unit mass, E_p (in J kg^{-1}), in order to characterize gravity wave activity, given by

$$E_p = \frac{1}{2}\left(\frac{g}{N}\right)^2 V_{atm}$$

where g is the gravitational acceleration ($\sim$ 9.8 m s^{-2}), N the Brunt-Väisälä frequency and V_{atm} the atmospheric variance.

Figure 24.6 displays contour plots of the GW *Ep* climatology in 30–50 km and 50–85 km altitude ranges, as computed from nighttime lidar measurements during 1996–2012. The variance is estimated using a vertical broadband filter centred around 3.5 km in the lower region and 7 km in the upper region to take into account the increase of dominant wavelengths from the stratosphere to the mesosphere. We found an annual cycle with maxima of GW activity occurring in winter and

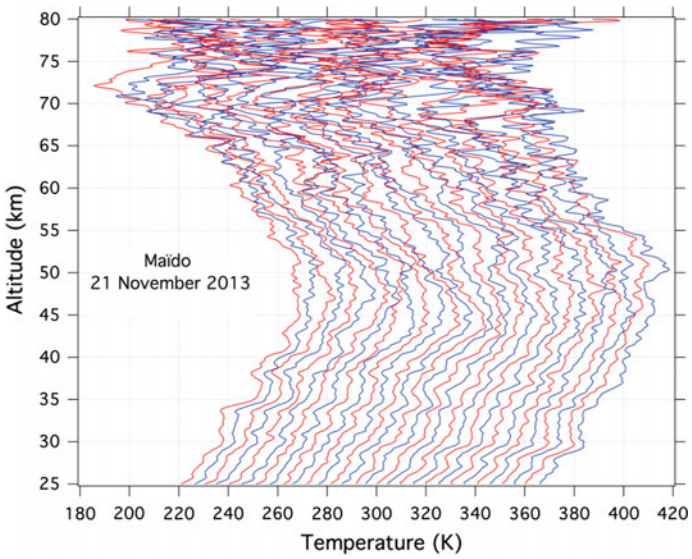

Fig. 24.4 Consecutive lidar temperature profiles at Maïdo Observatory on 21 November 2013. Each profile is integrated during 15 min. A 5 K shift is applied between two consecutive profiles for visibility

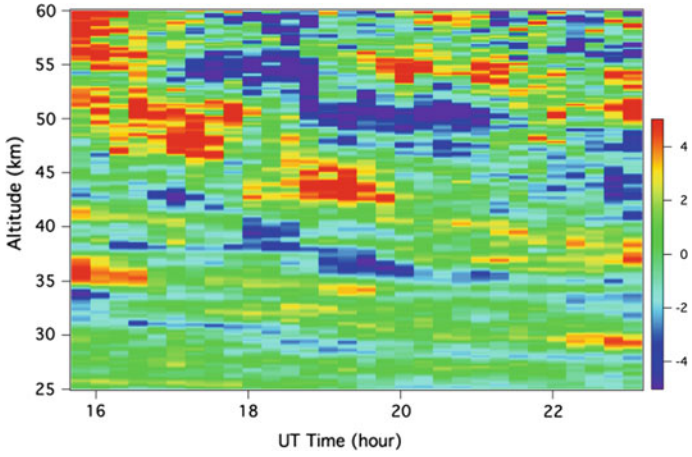

Fig. 24.5 Evolution of the temperature anomaly as seen by the lidar at Maïdo Observatory on 21 November 2013. Units are in K. The time resolution is 15 min

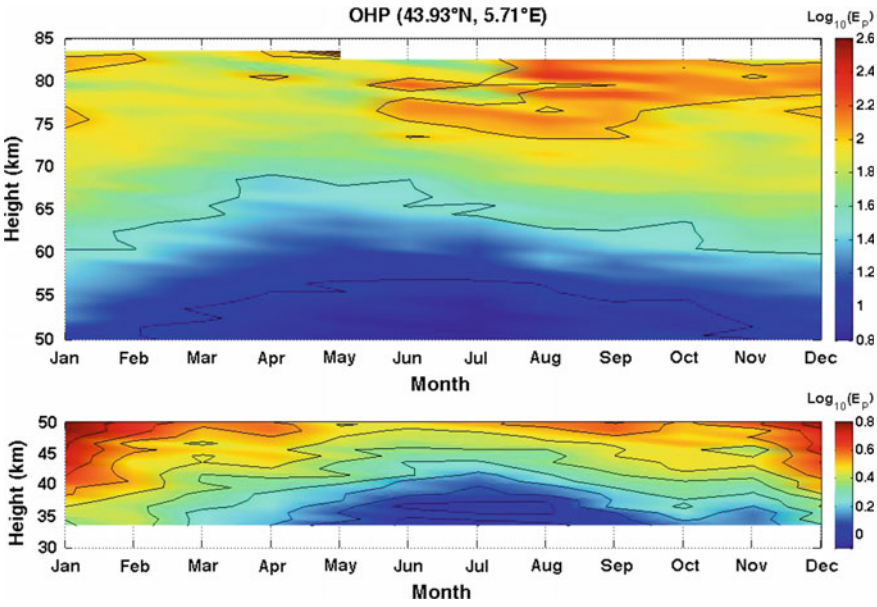

Fig. 24.6 Contour plots of the gravity wave E_p climatology (in J Kg^{-1}) from lidar observations. E_p is coloured in a logarithmic scale (log10) in 30–50 km and 50–85 km altitude ranges. The contours are separated by 0.2 J Kg^{-1}. Adapted from Mzé et al. (2014)

minimum in summer in the upper stratosphere and the lower mesosphere. We also found a semi-annual cycle with a maximum of GW activity occurring in winter and in summer and a minimum during the equinoxes in the upper mesosphere/lower thermosphere. For more information, see Mzé et al. (2014).

Seasonal averages of GW E_p based on lidar observations over the 16-year time period are illustrated in Fig. 24.7. The E_p increases with height but at a lower rate than the growth without dissipation indicated by the dashed black line. In order to better visualize the layers where GWs dissipate, Fig. 24.8 shows the profile of GW potential energy expressed in J m^{-3} instead of J kg^{-1} in the previous figures. With this unit, an upward propagation without dissipation, and with the assumption that the wave frequency is not changing, corresponds to a vertical line. We observe dissipation at all altitudes and seasons except between 55 and 75 km in summer. The two main regions of wave dissipation are in the upper stratosphere between 30 and 50 km and in the upper mesosphere above 70 km in winter and above 75 km in summer.

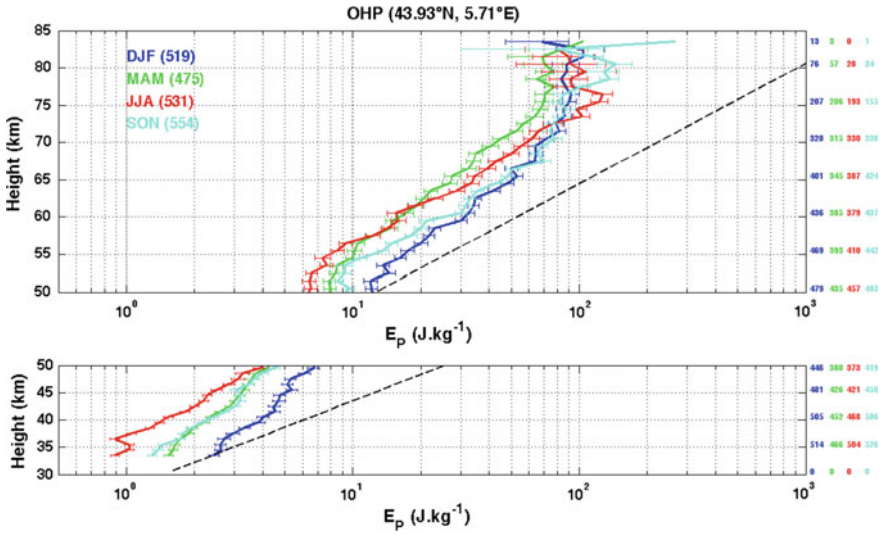

Fig. 24.7 Vertical profiles of E_p per unit mass (in J Kg^{-1}) in the upper stratosphere and the mesosphere averaged over winter (DJF, blue line), spring (MAM, green line), summer (JJA, red line) and autumn (SON, cyan line). The conservative growth curve is also superimposed (black dashed line) with a constant density scale height H ~ 7 km. The numbers on the right part of the figure indicate the number of nights averaged per season for each altitude. Adapted from Mzé et al. (2014)

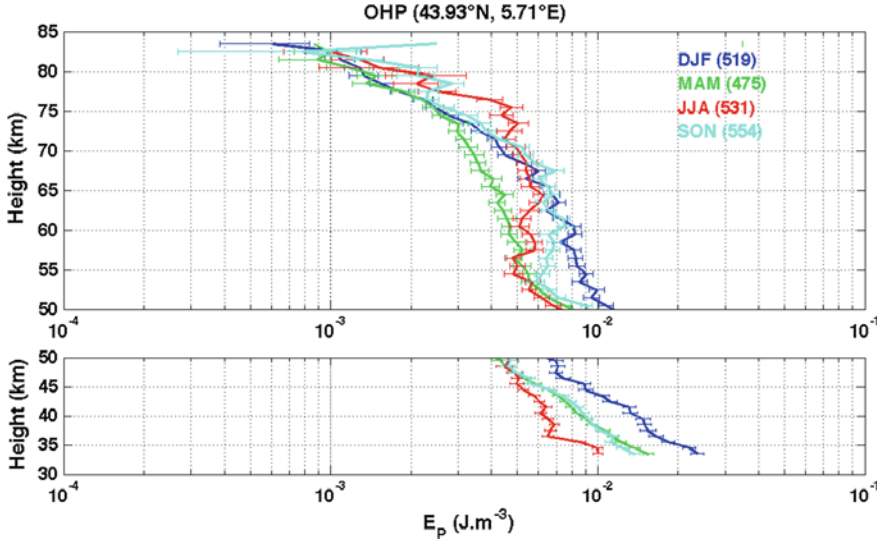

Fig. 24.8 The same as in Fig. 24.7 except for the vertical profiles of potential energy per unit volume (in J m^{-3}). Adapted from Mzé et al. (2014)

24.2.2 *Evaluation of Gravity Wave Potential Energy Combining GPS Radio Occultations and Rayleigh Lidar Data*

Global Positioning System Radio Occultation (GPS-RO) temperature profiling technique, featuring high vertical resolution and global coverage (Kursinsky et al. 1997; Hajj et al. 2002; Wickert et al. 2004), represents a powerful tool for climate and trend studies in the upper troposphere–lower stratosphere (Randel et al. 2009; Steiner et al. 2013) and for studying the sources and climatology of gravity waves (Belloul and Hauchecorne 1997; Faber et al. 2013). Operational since April 2006 until present, COSMIC GPS-RO system, consisting of six low Earth-orbiting micro-satellites, provides 1500–2000 occultations per day with sampling density maximizing at mid-latitudes, about 1–2 profiles per day in a 5° × 5° bin at OHP latitude (Anthes et al. 2008). GPS-RO temperature observations cover the altitude range between about 8 and 35 km, with the highest accuracy (<0.5 K) in the lower stratosphere and a vertical resolution of 0.2–1.4 km.

Figure 24.9 shows a time series of GW potential energy (E_p) retrieved through analysis of temperature perturbations (Khaykin et al. 2015). The potential energy of GW has been evaluated from the fluctuations in vertical temperature profiles using two different techniques, GPS-RO from 10 to 35 km and Rayleigh lidar above 33.5 km. This allows reconstructing the time evolution of GW E_p from the 10 to 50 km (Fig. 24.9). In the overlapping altitude range between 33.5 and 35 km, we observe a good agreement between the two techniques (not shown). The time of enhancement of GW E_p estimated from MERRA meteorological reanalysis (contour lines) is also in good agreement with the observations, but the energy is about 5 times lower in the reanalysis because the model can only capture one part of the

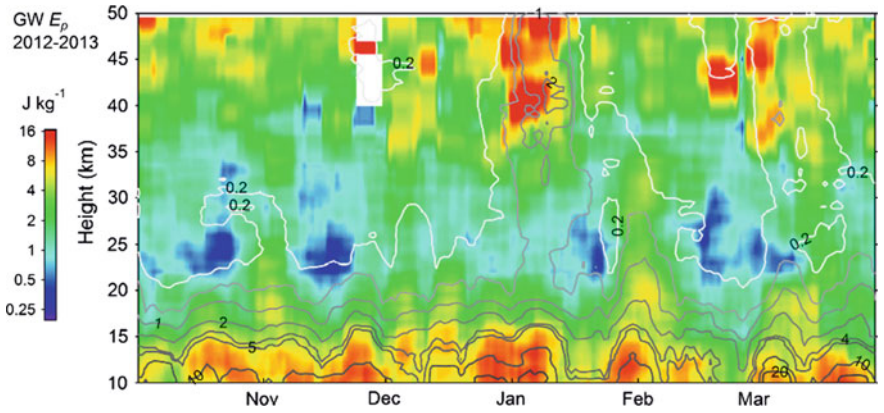

Fig. 24.9 Evolution of GW E_p at OHP from combined GPS-RO and Rayleigh lidar data during winter 2012–2013. Adapted from Khaykin et al. (2015). Contour lines show the GW E_p computed from MERRA meteorological reanalysis

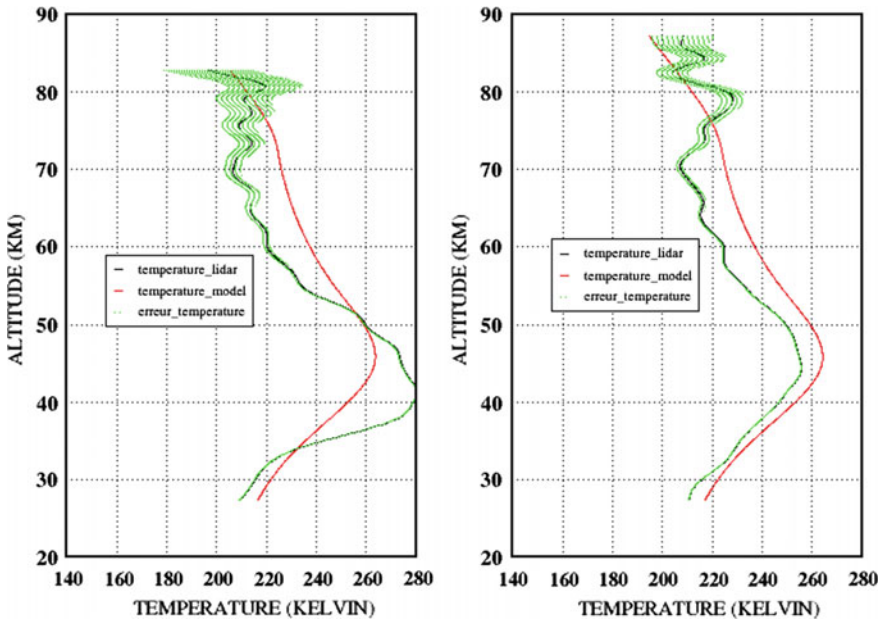

Fig. 24.10 Nightly mean Rayleigh lidar profiles at OHP (left side) on 10 January 2013 during a major stratospheric warming and (right side) 1 week later on 17 January 2013 with a cold middle atmosphere. The green shaded area indicates uncertainty (∓1 sigma) and the black line represents the NRLMSISE-00 empirical model (Picone et al. 2002)

GW spectrum. A strong increase of GW E_p is observed at the beginning of January above 35 km. This enhancement is related to the strong dynamical perturbation due to the occurrence of an SSW (Le Pichon et al. 2015). This event was reflected in the lidar temperature profile on 10 January 2013 (Fig. 24.10 left) with an enhancement and a descent of the stratopause and a strong positive temperature gradient between 35 and 40 km, corresponding to a very stable atmospheric layer favouring the increase of GW amplitude (Hauchecorne et al. 1987).

24.3 Large-Scale Dynamics and Impact on Temperature Climatology and Trend

As mentioned in the introduction, the upward propagation of extratropical PWs is only possible during the period of westerly zonal wind from October to April. These waves create perturbations in the vertical profile of temperature with typical periods ranging from 1 week to 1 month. These perturbations are captured by the OHP Rayleigh lidar during each winter season (Fig. 24.11), allowing studying their characteristics (Hauchecorne et al. 2006). The propagation of PWs depends on the

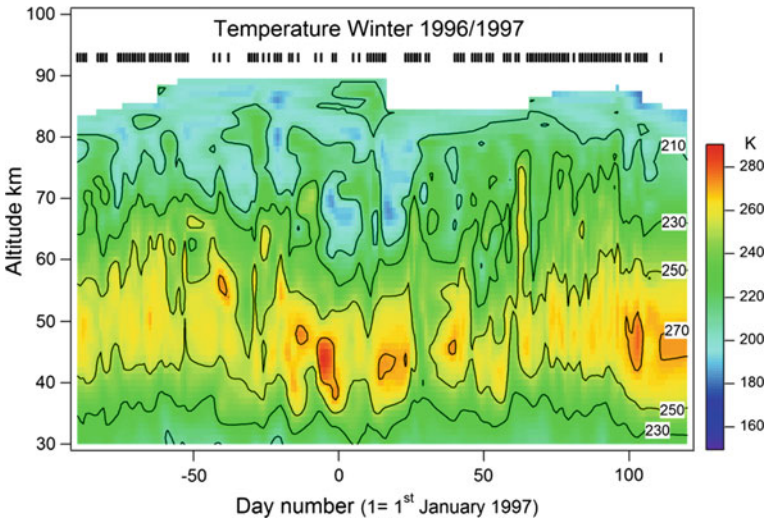

Fig. 24.11 Evolution of the temperature at OHP during winter 1996–1997. Days with measurements are indicated with a vertical bar at the top of the figure. Adapted from Hauchecorne et al. (2006)

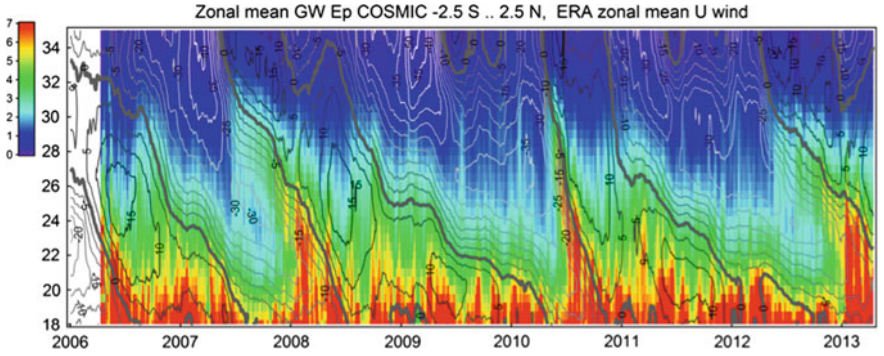

Fig. 24.12 Contour lines represent the time-pressure section of the equatorial zonal wind updated from Naujokat (1986), showing the downward propagation of the QBO zonal wind from 2006 to 2013. Easterly wind contours (negative values) are plotted with grey lines and Westerly winds (positive values) with black lines. Colour filling represents the GW E_p in J kg^{-1} in the latitude band 2.5°S–2.5°N, estimated using GPS-RO data

meridional–vertical structure of zonal wind and temperature fields. It is then sensitive to one of the major dynamical phenomena, the Quasi-Biennial Oscillation (QBO). The QBO is a quasi-periodic oscillation of the equatorial zonal wind with a 28-month average period (Fig. 24.12). The downward propagation of the QBO wind is due to the interaction of the zonal wind with GWs and equatorial PWs propagating in both directions and accelerating the mean flow in their direction of

propagation when they break (see Baldwin et al. 2001 for a review paper on QBO). The interaction between GWs and the QBO zonal wind is illustrated in Fig. 24.12 showing the enhancement of GW E_p in the equatorial band along the zero wind line.

Free planetary Rossby waves have a westward propagation with preferential periods depending on their zonal wave number and their mode (Kasahara 1980). In the Northern winter stratosphere, the two dominant modes are the so-called 16-day wave with zonal number 1 (one maximum and one minimum along a latitude circle) and the 12-day wave with zonal wave number 2. In order to detect the spectral distribution of PWs observed with the OHP lidar, a spectral analysis of temperature anomalies (deviations from the climatology) is performed at all altitudes for all winters from 1982 to 2001. Integrated nightly mean lidar data interpolated in time using cubic spline functions (Hauchecorne et al. 1991) are used. Energy spectra are averaged over winters with QBO West phase and winters with QBO East phase and are represented in Fig. 24.13. The QBO sign is defined according to the zonal wind at 40 hPa in January–February (Table 24.1).

For both QBO phases, we observe two regions of enhanced PW energy, in the upper stratosphere around 40 km and in middle the mesosphere above 65 km. The lower one is clearly associated with PWs and is limited to frequencies lower than 0.1 day^{-1} (periods longer than 10 days). The upper one extends to higher frequencies and has been attributed by Hauchecorne et al. (1991) to a combination of PWs and the effect of GW breaking on the mean temperature. For QBO West (Fig. 24.13, top), two maxima appear at 40 km around 0.050–0.055 day^{-1} (18–20 days) and 0.075 day^{-1} (13 days). These two peaks are tentatively attributed to the two dominant 12-day and 16-day Rossby waves.

The shift towards longer periods compared to theoretical values may be explained by the Doppler shift due to the wave propagation in westerly winds (Hauchecorne et al. 2006). For QBO East, the two peaks are also visible but with a smaller amplitude. This seems to indicate that the propagation of planetary Rossby waves is favoured in the QBO West phase. The interpretation of the results in the mesosphere is more difficult due to a combination of PW and GW effects but the enhanced PW energy around 18–20 days is observed for both QBO phases. The variability of the temperature may also be affected by thermal tides in the mesosphere. However, we do not expect a significant impact on our results because lidar observations are usually made in the first part half of the night with little change in local time.

The temperature of the middle atmospheric temperature is not only driven by radiative processes but also by wave-mean flow interactions, unambiguously noticeable in Northern winter through large events like SSWs. This makes the interpretation of observed trends more complex. Angot et al. (2012) described a new method to separate the contribution of radiative and dynamics processes in observed temperature trends. In this new method, the strong influence of SSWs in temperature trend evaluation is identified and removed to provide a 'background' temperature trend estimate, in better agreement with what is expected from direct radiative effects induced by atmospheric composition changes. The dataset used

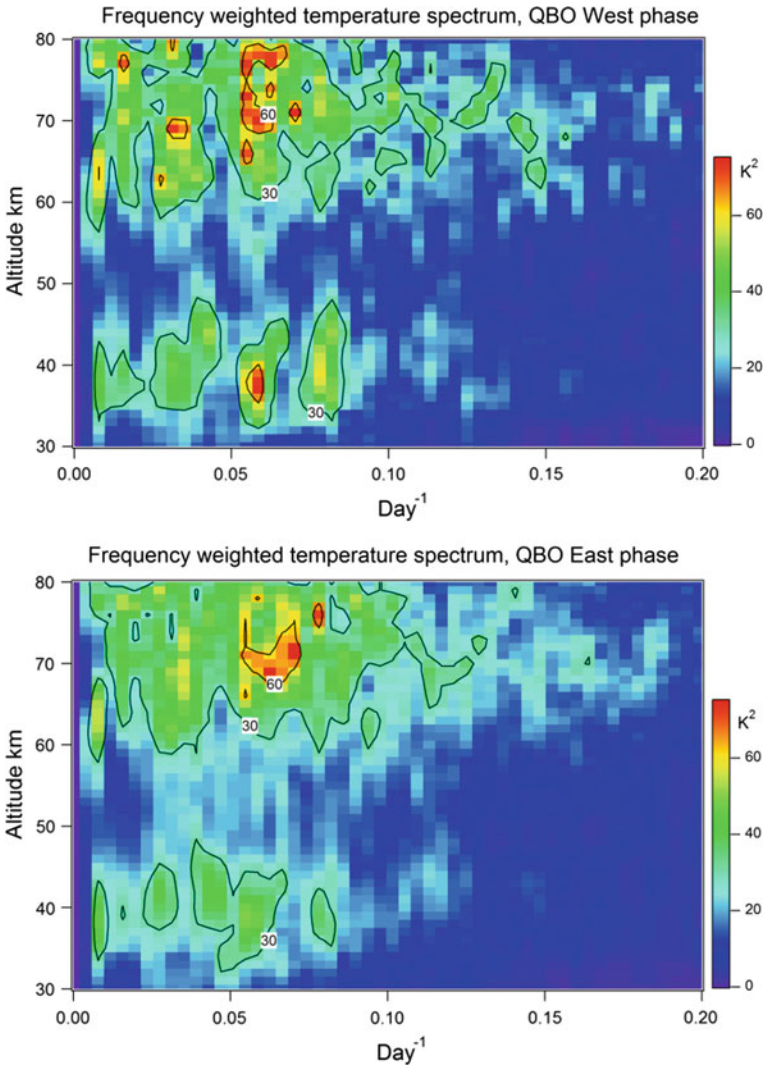

Fig. 24.13 Energy spectrum of temperature perturbations averaged over winters in QBO West phase (top) and in QBO East phase (bottom). The power spectral density is multiplied by the frequency to have a better visualization of energy maxima due to dominant PW modes. Consequently the unit is K^2 $day^{-1}/day^{-1} = K^2$. Adapted from Hauchecorne et al. (2006)

results from OHP Rayleigh lidar measurements from 1979 to 2009 and combined with daily-collocated radiosonde profiles. Figure 24.14 presents the histogram of temperature anomalies (deviations from the seasonal evolution) at 40 km for two half-month periods. In the first half of May (left part), the distribution is narrow and mono-modal, showing no clear effect of the dynamics on the temperature. Conversely, the distribution is much broader and clearly bimodal in the first half of

Table 24.1 Amplitude of equatorial wind in January–February at 40 hPa. QBO data series from Stratospheric Research Group, Freie Universität Berlin, are available at http://www.geo.fu-berlin.de/en/met/ag/strat/produkte/qbo/index.html. Updated from Naujokat (1986)

Year	Wind m/s	QBO sign	Year	Wind m/s	QBO sign
1982	−14	E	1992	−16.5	E
1983	15	W	1993	12.5	W
1984	−8	E	1994	−1.5	E
1985	−12	E	1995	5.5	W
1986	15	W	1996	3.5	W
1987	−9	E	1997	−24	E
1988	9	W	1998	12.5	W
1989	12	W	1999	−14	E
1990	−26	E	2000	12	W
1991	11.5	W	2001	−7	E

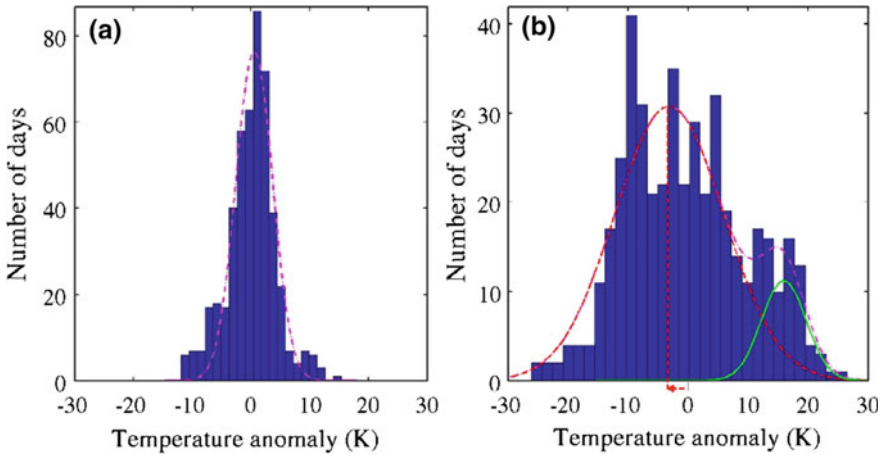

Fig. 24.14 Histogram of temperature anomalies from the seasonal evolution (left) during the second half of May and (right) during the first half of February for the period 1979–2009. The histogram is fitted with a double Gaussian curve to separate the background (red dashed line) and the dynamically perturbed (green solid line) conditions. The red arrows highlight the mean temperature anomaly (−3.2 K) in background conditions. Adapted from Angot et al. (2012)

February, with the larger and colder Gaussian curve attributed to background conditions, weakly affected by PW activity, and the smaller and warmer Gaussian curve attributed to perturbed conditions with enhanced PW activity and occurrence of an SSW.

In winter, Temperature trends are then calculated using the derived background anomalies and compared to the estimation using all data (Fig. 24.15). With this new methodology, the long-term trend during winter showed a larger cooling at all altitudes from 30 and 80 km (−2 K/decade at 40 km) than when all data are used (−0.4 K/decade at 40 km). The cooling of the winter background temperature is

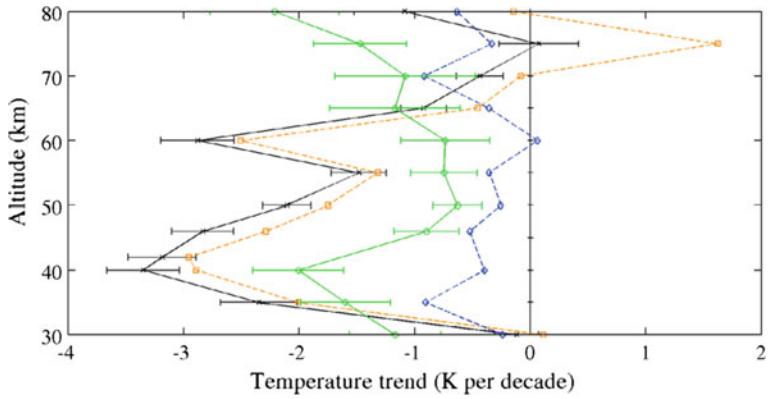

Fig. 24.15 Linear temperature trend during the period 1979–2009 at 40 km using all summer data (orange dashed line and squares), summer background data (black line and crosses), all winter data (blue dashed line and diamonds) and winter background data (green lines and circles). One-sigma uncertainties are indicated for summer and winter background conditions. Adapted from Angot et al. (2012)

then closer to the summer trend estimate, not perturbed by the dynamical activity. Temperature warmings associated with dynamical disturbances like SSWs (not shown) experienced an increase both in their intensity and occurrence that led to partly cancel out the long-term cooling due to radiative processes. A possible explanation of this evolution is the acceleration of the Brewer-Dobson circulation predicted by Chemistry-Climate Models (Butchart 2014). A better characterization of SSW events (Maury et al. 2016) could help to improve our understanding of the role of these events in the long-term evolution of the temperature in the middle atmosphere.

24.4 Conclusion

The middle atmosphere is a region very sensitive not only to changes in the radiative budget of the whole atmosphere but also to its dynamical response to these changes at different space and timescales. The already observed cooling of the middle atmosphere due to the increase of greenhouse gases is expected to continue. However, the rate of cooling will strongly depend on the evolution of complex interactions between dynamical, radiative and photochemical processes. Observations are then highly needed to improve our understanding of the role of the dynamics in the past and future evolution of the middle atmosphere. Rayleigh lidars providing time-resolved accurate temperature profiles from the middle stratosphere to the top of mesosphere are very efficient tools to study the characteristics of GWs and PWs and their impact on the mean temperature field. Together with other types of instrument setup in the frame of the European Design Study projects ARISE and

ARISE2, Doppler wind lidars, Mesosphere–Stratosphere–Troposphere (MST) and meteor radars, the IMS (International Monitoring System) infrasound network, airglow imagers and ionospheric sounders (Blanc et al. 2019), they will contribute to a better knowledge and a better representation of middle atmospheric processes in numerical weather prediction and climate models.

Acknowledgements This work was partly supported by ARISE (FP7) and ARISE2 (H2020), Grant agreement 653980 design study projects, funded by the European Union and by Stradivarius project funded by the Agence Nationale de la Recherche, France.

References

Alexander MJ, Geller M, McLandress C, Polavarapu S, Preusse P, Sassi F, Sato K, Eckermann S, Ern M, Hertzog A, Kawatani YA, Pulido M, Shaw T, Sigmond M, Vincent R, Watanabe S (2010) Recent developments in gravity-wave effects in climate models and the global distribution of gravity-wave momentum flux from observations and models. Q J R Meteorol Soc 136:1103–1124. https://doi.org/10.1002/qj.637

Andrews D, Taylor F, McIntyre M (1987) The influence of atmospheric waves on the general circulation of the middle atmosphere [and discussion]. Philos Trans R Soc Lond Ser A Math Phys Sci 323(1575):693–705. http://www.jstor.org/stable/38143

Angot G, Keckhut P, Hauchecorne A, Claud C (2012) Contribution of stratospheric warmings to temperature trends in the middle atmosphere from the lidar series obtained at Haute-Provence Observatory (44°N). J Geophys Res 117:D21102. https://doi.org/10.1029/2012JD017631

Anthes RA, Bernhardt PA, Chen Y, Cucurull L, Dymond KF, Ector D, Healy SB, Ho SP, Hunt DC, Kuo YH, Liu H, Manning K, McCormick C, Meethan TK, Randel WJ, Rocken C, Schreiner WS, Sokolovskiy SV, Syndergaard S, Thompson DC, Trenberth KE, Wee TK, Yen NL, Zeng Z (2008) The COSMIC/FORMOSAT-3 mission early results. Bull Am Meteorol Soc 89(3): 313–333. https://doi.org/10.1175/bams-89-3-313

Baldwin MP, Gray LJ, Dunkerton TJ, Hamilton K, Haynes PH, Randel WJ, Holton JR, Alexander MJ, Hirota I, Horinouchi T, Jones DBA, Kinnersley JS, Marquardt C, Sato K, Takahashi M (2001) The Quasi-Biennial Oscillation. Rev Geophys 39:179–229

Belloul B, Hauchecorne A (1997) Horizontal homogeneities in occultation methods: the case of atmospheric gravity waves. Radio Sci 32:469–478

Blanc E, Pol K, Le Pichon A, Hauchecorne A, Keckhut P, Baumgarten G, Hildebrand J, Höffner J, Stober G, Hibbins R, Espy P, Rapp M, Kaifler B, Ceranna L, Hupe P, Hagen J, Rüfenacht R, Kämpfer N, Smets P (2019) Middle atmosphere variability and model uncertainties as investigated in the framework of the ARISE project. In: Le Pichon A, Blanc E, Hauchecorne A (eds) Infrasound monitoring for atmospheric studies, 2nd edn. Springer, Dordrecht, pp 845–887

Butchart N (2014) The Brewer-Dobson circulation. Rev Geophys 52:157–184. https://doi.org/10.1002/2013RG000448

Butler AH, Seidel DJ, Hardiman SC, Butchart N, Birner T, Match A (2015) Defining sudden stratospheric warmings. Bull Am Meteorol Soc 96:1913–1928

Chane Ming F, Molinaro F, Leveau J, Keckhut P, Hauchecorne A (2000) Analysis of gravity waves in the tropical middle atmosphere with lidar using wavelet techniques. Ann Geophys 18:485–498

Charlton AJ, Polvani LM (2007) A new look at stratospheric sudden warmings. Part I: Climatology and modeling benchmarks. J Clim 20(3):449–469. https://doi.org/10.1175/JCLI3996.1

Charney JG, Drazin PG (1961) Propagation of planetary scale disturbances from the lower into the upper atmosphere. J Geophys Res 66:83–109

Cohen J, Jones J (2011) Tropospheric precursors and stratospheric warmings. J Clim 24:6562–6572. https://doi.org/10.1175/2011JCLI4160.1

Duck TJ, Whiteway JA, Carswell AI (2001) The gravity wave-arctic stratospheric vortex interaction. J Atmos Sci 58(23):3581–3596. https://doi.org/10.1175/1520-0469(2001)058<3581:tgwasv>2.0.co;2

Faber A, Llamedo P, Schmidt T, de la Torre A, Wickert J (2013) On the determination of gravity wave momentum flux from GPS radio occultation data. Atmos Meas Tech 6:3169–3180. https://doi.org/10.5194/amt-6-3169-2013

Fleming EL, Chandra S, Schoeberl MR, Barnett JJ (1988) Monthly mean global climatology of temperature, wind, geopotential height, and pressure for 0–120 km. NASA Tech Memo 100697

Fritts DC, Alexander MJ (2003) Gravity wave dynamics and effects in the middle atmosphere. Rev Geophys 41:1003. https://doi.org/10.1029/2001RG000106

Funatsu B, Claud C, Keckhu P, Hauchecorne A, Leblanc T (2016) Regional and seasonal stratospheric temperature trends in the last decade (2002–2014) from AMSU observations. J Geophys Res 121(14):8172–8185

Hajj GA, Kursinski ER, Romans LJ, Bertiger WI, Leroy SS (2002) A technical description of atmospheric sounding by GPS occultation. J Atmos Sol-Terr Phys 64:451–469. https://doi.org/10.1016/S1364-6826(01)00114-6

Hauchecorne A, Chanin ML (1980) Density and temperature profiles obtained by lidar between 30 and 70 km. Geophys Res Lett 7:564–568

Hauchecorne A, Chanin ML (1983) Mid-latitude observations of planetary waves in the middle atmosphere during the winter of 1981–1982. J Geophys Res 88:3843–3849

Hauchecorne A, Chanin ML, Wilson R (1987) Mesospheric temperature inversion and gravity wave breaking. Geophys Res Lett 14:933–936

Hauchecorne A, Chanin ML (1988) Planetary waves-mean flow interaction in the middle atmosphere: modelisation and comparison with lidar observations. Ann Geophys 6:409–416

Hauchecorne A, Chanin ML, Keckhut P (1991) Climatology and trends of the middle atmospheric temperature (33–87 km) as seen by Rayleigh lidar above south of France. J Geophys Res 96:15297–15309

Hauchecorne A, Gonzalez N, Souprayen C, Manson AH, Meek CE, Singer W, Fahrytdinova AN, Hoppe UP, Boska J, Lastovicka J, Scheer J, Reisin ER, Graef H (1994) Gravity wave activity and its relation with prevailing winds during DYANA. J Atmos Terr Phys 56:1765–1778

Hauchecorne A, Keckhut P, Chanin ML (2006) Interannual variability and long term changes in planetary wave activity in the middle atmosphere observed by lidar. Atmos Chem Phys Discuss 6:11299–11316. https://doi.org/10.5194/acpd-6-11299-2006

Hauchecorne A, Keckhut P, Chanin ML (2009) Dynamics and transport in the middle atmosphere. Infrasound monitoring for atmospheric studies, Springer, pp 665–683, Earth and Environmental

Hauchecorne A, Bertaux JL, Dalaudier F, Keckhut P, Lemennais P, Bekki S, Marchand M, Lebrun JC, Kyrölä E, Tamminen J, Sofieva V, Fussen D, Vanhellemont F, Fanton d'Andon O, Barrot G, Blanot L, Fehr T, Saavedra de Miguel L (2010) Response of tropical stratospheric O_3, NO_2 and NO_3 to the equatorial Quasi-Biennial Oscillation and to temperature as seen from GOMOS/ENVISAT. Atmos Chem Phys 10:8873–8879

Kasahara A (1980) Effect of zonal flows on the free oscillations of a barotropic atmosphere. J Atmos Sci 37:917–929

Khaykin S, Hauchecorne A, Mze N, Keckhut P (2015) Seasonal variation of gravity wave activity at midlatitudes from 7 years of COSMIC GPS and Rayleigh lidar temperature observations. Geophys Res Lett 42(4):1251–1258

Keckhut P, Hauchecorne A, Chanin ML (1993) A critical review of the data base acquired for the long term surveillance of the middle atmosphere by Rayleigh lidar. J Atmos Ocean Tech 10:850–867

Keckhut P, Hauchecorne A, Chanin ML (1995) Mid-latitude long-term variability of the middle atmosphere: trends, cyclic and episodic changes. J Geophys Res 100:18887–18897

Keckhut P, Courcoux Y, Baray J-L, Porteneuve J, Vérèmes H, Hauchecorne A, Dionisi D, Posny F, Cammas J-P, Payen G, Gabarrot F et al (2015a) Introduction to the Maïdo Lidar Calibration Campaign dedicated to the validation of upper air meteorological parameters. J Appl Remote Sens 9(1):094099. https://doi.org/10.1117/1.JRS.9.094099

Keckhut P, Funatsu BM, Claud C, Hauchecorne A (2015b) Tidal effects on stratospheric temperature series derived from successive advanced microwave sounding units. Q J R Meteorol Soc 141(687):477–483

Kursinski ER, Hajj GA, Schofield JT, Linfield RP, Hardy KR (1997) Observing Earth's atmosphere with radio occultation measurements using the Global Positioning System. J Geophys Res 102:23429–23465. https://doi.org/10.1029/97JD01569

Labitzke K (1981) Stratospheric-mesospheric midwinter disturbances: a summary of observed characteristics. J Geophys Res 86(C10):9665–9678. https://doi.org/10.1029/JC086iC10p09665

Lee C, Smets P, Charlton-Perez A, Evers L, Harrison G, Marlton G (2019) The potential impact of upper stratospheric measurements on sub-seasonal forecasts in the extra-tropics. In: Le Pichon A, Blanc E, Hauchecorne A (eds) Infrasound monitoring for atmospheric studies, 2nd edn. Springer, Dordrecht, pp 889–910

Le Pichon A, Assink JD, Heinrich P, Blanc E, Charlton-Perez AJ, Lee C-F, Keckhut P, Hauchecorne A, Rüfenacht R, Kämpfer N, Drob D et al (2015) Comparison of co-located independent ground-based middle-atmospheric wind and temperature measurements with numerical weather prediction models. J Geophys Res 120 (16):8318–8331. https://doi.org/10.1002/2015jd023273

Li T, Leblanc T, McDermid IS, Wu DL, Dou X, Wang S (2010) Seasonal and interannual variability of gravity wave activity revealed by long-term lidar observations over Mauna Loa Observatory, Hawaii. J Geophys Res 115:D13103. https://doi.org/10.1029/2009JD013586

Lindzen RS (1981) Turbulence and stress owing to gravity wave and tidal breakdown. J Geophys Res 86(C10):9707–9714. https://doi.org/10.1029/JC086iC10p09707

Matsuno T (1971) A dynamical model of the stratospheric sudden warming. J Atmos Sci 28:1479–1494

Maury P, Claud C, Manzini E, Hauchecorne A, Keckhut P (2016) Characteristics of stratospheric warming events during Northern winter. J Geophys Res 121:5368–5380. https://doi.org/10.1002/2015jd024226

Mzé N, Hauchecorne A, Keckhut P, Thétis M (2014) Vertical distribution of gravity wave potential energy from long-term Rayleigh lidar data at a northern middle-latitude site. J Geoph Res: Atmos 119(21):12069–12083. https://doi.org/10.1002/2014jd022035

Naujokat B (1986) An update of the observed quasi-biennial oscillation of the stratospheric winds over the tropics. J Atmos Sci 43:1873–1877

Picone JM, Hedin AE, Drob DP, Aikin AC (2002) NRLMSISE-00 empirical model of the atmosphere: statistical comparisons and scientific issues. J Geophys Res 107(A12):1468. https://doi.org/10.1029/2002JA009430

Ramaswamy V et al (2001) Stratospheric temperature trends: observations and model simulations. Rev Geophys 39(1):71–122. https://doi.org/10.1029/1999RG000065

Randel WJ, Shine KP, Austin J, Barnett J, Claud C, Gillett NP, Keckhut P, Langematz U, Lin R, Long C, Mears C, Miller A, Nash J, Seidel DJ, Thompson DWJ, Wu F, Yoden S (2009) An update of observed stratospheric temperature trends. J Geophys Res 114:D02107. https://doi.org/10.1029/2008JD010421

Rauthe M, Gerding M, Höffner J, Lübken FJ (2006) Lidar temperature measurements of gravity waves over Kühlungsborn (54 N) from 1 to 105 km: A winter-summer comparison. J Geophys Res 111:D24108. https://doi.org/10.1029/2006JD007354

Rauthe M, Gerding M, Lübken FJ (2008) Seasonal changes in gravity wave activity measured by lidars at mid-latitudes. Atmos Chem Phys 8:6775–6787. https://doi.org/10.5194/acp-8-6775-2008

Shepherd TG (2000) The middle atmosphere. J Atmos Sol-Terr Phys 62:1587–1601

Sica RJ, Argall PS (2007) Seasonal and nightly variations of gravity-wave energy density in the middle atmosphere measured by the Purple Crow Lidar. Ann Geophys 25:2139–2145. https://doi.org/10.5194/angeo-25-2139-2007

Sivakumar V, Rao PB, Bencherif H (2006) Lidar observations of middle atmospheric gravity wave activity over a low-latitude site (Gadanki, 13.5°N, 79.2°E). Ann Geophys 24:823–834: https://doi.org/10.5194/angeo-24-823-2006

Steiner AK, Hunt D, Ho SP, Kirchengast G, Mannucci AJ, Scherllin-Pirscher B, Gleisner H, von Engeln A, Schmidt T, Ao C, Leroy SS, Kursinski ER, Foelsche U, Gorbunov M, Heise S, Kuo YH, Lauritsen KB, Marquardt C, Rocken C, Schreiner W, Sokolovskiy S, Syndergaard S, Wickert J (2013) Quantification of structural uncertainty in climate data records from GPS radio occultation. Atmos Chem Phys 13:1469–1484. https://doi.org/10.5194/acp-13-1469-2013

Whiteway JA, Duck TJ, Donovan DP, Bird JC, Pal SR, Carswell AI (1997) Measurements of gravity wave activity within and around the Arctic stratospheric vortex. Geophys Res Lett 24:1387–1390. https://doi.org/10.1029/97GL01322

Wickert J, Schmidt T, Beyerle G, Konig R, Reigber C, Jakowski N (2004) The radio occultation experiment aboard CHAMP: operational data analysis and validation of vertical atmospheric profiles. J Meteorol Soc Jpn 82:381–395. https://doi.org/10.2151/jmsj.2004.381

Wilson R, Hauchecorne A, Chanin ML (1990) Gravity wave spectra in the middle atmosphere as observed by Rayleigh lidar. Geophys Res Lett 17:1585–1588

Wilson R, Chanin ML, Hauchecorne A (1991a) Gravity waves in the middle atmosphere by Rayleigh Lidar, Part. 1: Case studies. J Geophys Res 96:5153–5167

Wilson R, Chanin ML, Hauchecorne A (1991b) Gravity waves in the middle atmosphere by Rayleigh Lidar, Part. 2: Climatology. J Geophys Res 96:5169–5183

Yamashita C, Chu X, Liu HL, Espy PJ, Nott GJ, Huang W (2009) Stratospheric gravity wave characteristics and seasonal variations observed by lidar at the South Pole and Rothera, Antarctica. J Geophys Res 114:D12101. https://doi.org/10.1029/2008JD011472

Chapter 25
Large-Scale and Transient Disturbances and Trends: From the Ground to the Ionosphere

Jan Laštovička and Tereza Šindelářová

Abstract Infrasonic waves excited at surface or in the troposphere propagate to longer distances via reflections from the middle and upper stratosphere or the lower thermosphere. These two atmospheric regions are affected by large-scale and transient disturbances, by long-term changes and trends. A brief review is given with particular emphasis on the stratosphere and lower thermosphere. The impact of such disturbances and long-term trends on the propagation of infrasonic waves is qualitatively estimated. Two dominant disturbances of solar origin, which substantially affect the atmosphere, and particularly the ionosphere, are solar flares and geomagnetic storms. Atmospheric waves, namely gravity waves, planetary waves, and tidal waves, affect both regions of infrasound reflections. The major midwinter stratospheric warming has pronounced effect on the height profile of temperature, thus they are capable to significantly affect propagation of infrasonic waves. There are also sporadic effects like earthquakes, which excite infrasound and gravity waves, but their overall impact on infrasound propagation is small. The impact of atmospheric waves is smaller than that of some sporadic effects like the major stratospheric warmings but atmospheric waves are continuously present in the atmosphere. Both the stratosphere and thermosphere experience also long-term changes and trends, in recent decades of predominantly anthropogenic origin (greenhouse effect, ozone depletion). These long-term changes are small but continuous, so they do not affect behavior of infrasonic waves on short-term scales but might have some effect on long-term scales like changes from decade to decade.

25.1 Introduction

The propagation of infrasound is mainly controlled by temperature and wind fields in the atmosphere; its absorption is also influenced by changes in atmospheric composition. The atmospheric temperature and winds are modified by disturbances

J. Laštovička (✉) · T. Šindelářová
Institute of Atmospheric Physics ASCR, Bocni II, 14131 Prague, Czech Republic
e-mail: jla@ufa.cas.cz

A. Le Pichon et al. (eds.), *Infrasound Monitoring for Atmospheric Studies*,
https://doi.org/10.1007/978-3-319-75140-5_25

of various time- and space scales, of transient as well as of periodic (atmospheric waves) type. Geomagnetic storms and other space weather effects, solar flares, earthquakes, large man-made explosions, bolides, etc. are sources of transient events. Atmospheric waves have periods extending from days to fractions of seconds and include planetary waves, tides, gravity waves, and infrasound. The waves can interact. Andrioli et al. (2013) observed a modulation of gravity waves by tides in the low to middle latitudes. Nonlinear interaction of tides with planetary waves has also been observed (e.g., Pancheva 2001). Upward propagation of atmospheric waves from the lower atmosphere into the middle and upper atmosphere has recently been reviewed by Yiğit and Medvedev (2015). Effects of atmospheric waves on the ionosphere have briefly been reviewed by Laštovička (2006).

Since the infrasonic effects in the stratosphere and troposphere and their ground-based measurements are treated in several chapters of (Blanc et al. 2019; Marchetti et al. 2019; Smets et al. 2019), we shall focus mainly on infrasonic effects in the ionosphere and their measurements by ionospheric Doppler sounders and/or other methods like analysis of GPS observations of the total electron content. The most recent review of infrasonic effects in the ionosphere was done by Krasnov et al. (2006).

Infrasound itself belongs to wave disturbances that are able to modify the conditions for propagation of infrasonic waves as it transfers the energy between atmospheric layers. Hickey et al. (2001) estimated from a numerical model that a 10 s wave may heat the atmosphere at the altitude of 140 km by up to 11 K/day, a 2 min wave can cause heating by up to 43 K/day at 200 km and a maximum heating of 170 K/day induced by a 4 min wave may occur at the altitude of 280 km.

However, infrasound events are mostly transient and spatially limited. Acoustic waves from a spatially limited sources experience geometrical spreading during the upward propagation. The geometric spreading together with small time and space scales of the source results in a limited influence of acoustic waves on the energy budget of the upper atmosphere. Lamb waves that exist near layers of temperature extremes in a non-isothermal atmosphere act as a filter and reduce the acoustic-gravity wave vertical propagation up into the ionosphere (Besalpov and Savina 2015).

The exception are regions exposed to long-lived sources, e.g., ocean swells. The dissipating acoustic waves generated by ocean swells can heat the atmosphere in the altitude range 110–140 km by up to 30 K/day (Rind 1977). The energy input is larger in winter than in summer. Hickey et al. (2001) state that the hotspot observed in ionospheric F-region in the O I 630 nm airglow by Meriwether et al. (1996, 1997) can be a manifestation of heating of the thermosphere by acoustic waves.

Gravity waves (GWs) are a big player in the field of atmospheric structure, dynamics, and coupling between atmospheric layers. GWs influence significantly the mean atmospheric circulation and thermal structure through wave momentum transport, wave filtering, and the body forces arising from wave dissipation and momentum flux divergence. The dissipation altitude of a GW is determined by its intrinsic properties (Vadas and Fritts 2005). The maximum forcing by gravity waves occurs in the middle atmosphere (Fritts and Alexander 2003), in the stratosphere, and particularly in the mesosphere. Vadas and Fritts (2004) emphasize the potential of gravity waves to affect very high atmospheric altitudes as well

because of the relatively large vertical wavelength and the propagation, at least initial, in all directions from the source. Moreover, secondary GWs can be excited during the momentum deposition by GW dissipation in the mesosphere/lower thermosphere region. These secondary GWs can travel to altitudes of 300–500 km before dissipation (Vadas 2007). Gravity waves are also important for the ionosphere, where they are best monitored by ionospheric Doppler sounders, which measure changing Doppler shift of radio waves caused by the passage of GWs (e.g., Chum et al. 2012a).

Tides are excited by absorption of solar radiation in the atmosphere. The basic period is 24 h. Due to nonlinearity of atmospheric dynamics, higher order harmonics are excited. Among them, the semidiurnal (T = 12 h) and terdiurnal (T = 8 h) tides are significant in the middle atmosphere together with the diurnal tide (T = 24 h). Based on the synchronization with the apparent motion of the Sun, migrating and non-migrating tides are distinguished. Migrating tides follow the Sun and move westward, whereas non-migrating tides excited due to inhomogeneities in absorption of solar radiation and nonlinearity of atmospheric motions can move either westward or eastward, depending on the zonal wavenumber and the harmonics (Yiğit and Medvedev 2015). The amplitudes of tidal winds in the mesopause region can be larger than amplitudes of background winds (Laštovička 2006).

Planetary waves are long-period waves (periods about 2–30 days) with planetary spatial scales. The most important planetary waves are those with zonal wave numbers 1 and 2, which among others excite the sudden stratospheric warmings. They are either transient or stationary. Planetary waves mostly affect the stratosphere but they also play a role in the mesosphere and thermosphere/ionosphere. They interact with and modulate the GW and tidal wave flux. Planetary waves were detected also in the ionosphere (Laštovička et al. 2003). In the thermosphere, they cannot propagate directly above 120–150 km due to the atmospheric viscosity; therefore, they propagate indirectly by modulating other agents such as GWs. They can also modulate the background conditions for the propagation of infrasonic waves.

The Earth's atmosphere and ionosphere experience not only disturbances but also long-term changes and trends. In recent decades, particularly trends of anthropogenic origin are becoming to be more and more important. They are caused by two groups of chemical agents. One group is various ozone-depleting substances (ODS) that substantially depleted ozone in the region of its maximum concentration, which is the stratosphere. Fortunately, the Montreal Protocol and its amendments resulted in the slow decrease of the concentration of ODS in the stratosphere since the second half of the 1990s leading to a leveling off of the ozone depletion and finally to partial recovery of ozone. The other group is greenhouse gases, particularly carbon dioxide. They cause the greenhouse warming in the troposphere but the greenhouse cooling in the stratosphere and above including the thermosphere and ionosphere. There are also some natural drivers of long-term changes and trends like long-term change of geomagnetic activity or the secular trend of the Earth's magnetic field. All these changes are capable slowly but permanently change the conditions of infrasound propagation.

Section 25.2 deals with wave-like and transient disturbances, namely disturbances of solar origin (Sect. 25.2.1), disturbances of atmospheric and meteorological origin (Sect. 25.2.2), and disturbances of seismic and other sporadic event origins. Long-term trends are treated in Sect. 25.3 with emphasis on trends in regions of stratospheric and thermospheric infrasound reflections, namely trends in the middle and upper stratosphere (Sect. 25.3.1) and in the lower thermosphere (Sect. 25.3.2). The chapter is closed with Sect. 25.4, Summary.

25.2 Wave-like and Transient Disturbances

There are various spatial and temporal scales of disturbances of different origins in the atmosphere–ionosphere system. The disturbances can either be transient or wave-like, short-term or very long-term like the 11-year solar cycle. Here, we shall deal only with the former (short-term disturbances). Such disturbances may be of solar and/or solar-terrestrial origin like solar flares and geomagnetic storms. They may be also of atmospheric/meteorological origin like typhoons, deep convection in the troposphere penetrating into the lowermost stratosphere, strong cold fronts, high lightning activity storms, or passage of solar terminator in the thermosphere, which excite atmospheric waves. The last general category is disturbances caused by various events, which occur sporadically, like earthquakes and tsunamis, volcanic eruptions, man-made strong explosion, bolides, etc. Disturbances of these three categories are further treated in more detail. Special attention is paid to impact of all these disturbances on excitation and propagation of infrasonic waves. Since the stratospheric and the thermospheric mode governs the infrasound propagation on longer distances, we shall mention preferentially (but not only) effects on the respective parts of the stratosphere (~30–50 km) and lower thermosphere (~100–120 km), where infrasound is reflected back to surface.

25.2.1 Disturbances of Solar Origin

Solar flares, solar eruptive phenomena of a duration of minutes to hours, affect the Earth's system through a large enhancement of the solar X-ray flux, up to a few orders of magnitude for harder X-rays, and through a substantial enhancement of the solar EUV (extreme ultraviolet) flux. Due to their limited penetration depth into the atmosphere, they do not affect the stratosphere directly. In contrast, their impact on the ionosphere is large.

The largest effects of solar flares have been observed in the lower ionosphere (heights of about 60–100 km). They are called sudden ionospheric disturbances (SID). SIDs were relatively recently reviewed by Laštovička (2009). Starting from the bottom of the ionosphere, we observe the sudden decrease of atmospherics (SDA—peaking near 5 kHz) and sudden enhancement of atmospherics (SEA—peaking near 27 kHz) as a consequence of competition between two oppositely acting processes, a decrease of the upper boundary of the Earth–ionosphere

waveguide and an increase of sharpness of this upper boundary. Slightly higher in the ionospheric D layer, a sudden phase anomaly (SPA) in the VLF and low LF radio wave range is observed on signals of large-distance transmitters. This is the most sensitive method of SID detection. The sudden field anomaly (SFA), an indirect method of SPA monitoring, is used for transmitters at frequencies between 100 and 300 kHz. The sudden enhancement of signal (SES) at these frequencies is a less pronounced effect. MF and low HF radio waves experience short-wave fade-outs (SWF) as a consequence of substantially increased absorption of radio waves reflecting usually at heights of about 85–100 km. Figure 25.1 shows an example of a typical SWF event, where a large depletion of the radio signal is well pronounced. The sudden cosmic noise absorption (SCNA) as measured by riometers is also observed in the lower ionosphere. Higher up, in the ionospheric E-region, the effect of flares is relatively small due to the behavior of dominant part of the solar ionizing radiation at these heights. Therefore, flare impact on thermospheric reflections of infrasonic waves is also relatively small. In the ionospheric F-region above about 200 km, the sudden frequency deviation (SFD) and the sudden increase of the total electron content (SITEC) are observed. In the past, when reliable satellite measurements of the solar ionizing radiation were not available, SID was used to estimate the magnitude of X-ray flux enhancement during flares.

Geomagnetic storms are the most important and most powerful space weather feature with impact on the ionosphere. Their effects may last a few days or even slightly longer. Older studies on the effects of geomagnetic storms on the lower and middle atmosphere and lower ionosphere were reviewed by Laštovička (1996), those on effects on the ionosphere and thermosphere by Buonsanto (1999). In the lower ionosphere, the geomagnetic storms act in the high (particularly auroral) and partly middle latitudes; effects of strong storms may be observed down to geomagnetic latitudes of about 35° but the majority of effects do not reach latitudes below 50°. The main agents responsible for mid-latitude effects are precipitating electrons with energies of about 10–300 keV. The effect in the lower ionosphere consists in substantial increase of electron density and, consequently, of radio wave absorption resulting sometimes in the radio wave propagation blackout.

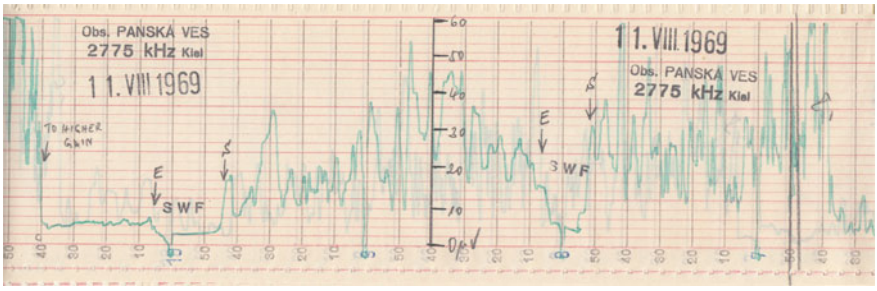

Fig. 25.1 Two SWF events of August 11, 1969 observed at Panska Ves, northern Czechia; copy of record. The first one around 08 UT is weaker, only large depression of signal. The other event around 10 UT was stronger with at least 15 min of total blackout of radio signal

In the F-region and the topside ionosphere, substantial changes in electron density are observed, both positive and negative pending on the phase of the storm, season, latitude, local time, etc. The height of F-region maximum substantially increases. The whole ionosphere from high latitudes to equator is affected. The ionospheric effect is organized in geomagnetic, not geographic coordinates. The ionospheric effects mainly reflect changes in the thermosphere due to prevailingly, even though not only, highly enhanced Joule heating in the dynamo region in the lower thermosphere. At low and equatorial latitudes, the role of penetrating electric fields from high latitudes is important.

Fortunately, the height range of stratospheric infrasonic reflections (~30–50 km) is little affected by geomagnetic storms except for its upper part at auroral latitudes. The heights of thermospheric reflections belong mainly to the ionospheric E-region, which is affected by geomagnetic storms much less than the lower ionosphere and the F-region ionosphere. However, the lower thermosphere heating at high latitudes is capable of affecting to some extent the background thermospheric conditions of infrasound reflections.

Another magnetospheric/extraterrestrial agent, which affects the lower ionosphere and middle atmosphere at high latitudes, is the solar proton events (SPE) in the polar cap and the relativistic electron precipitation (REP) events at auroral and sub-auroral latitudes. The solar proton events cause the polar cap absorption (PCA) events as measured by riometers. They have little influence on thermospheric reflections of infrasound. The energy deposited into the atmosphere is carried mainly by protons with energies of ~3–300 MeV. They can penetrate a bit down into the upper stratosphere. However, during polar night conditions, the extra production of NO_x and its transport down to the upper and (rarely) middle stratosphere can change chemical composition and other properties of the polar cap upper stratosphere for up to a few months, thus modulating conditions for the stratospheric reflection of infrasound in polar cap. Relativistic electrons (energies higher than several keV) enhance electron density in the lower ionosphere as observed by riometers at respective latitudes. To a lower extent, they can also affect background conditions and electrical conductivity in the upper stratosphere. Typical duration of such events is 5–7 days (Baker et al. 1986).

25.2.2 Disturbances of Atmospheric and Meteorological Origin

Various processes occurring throughout the atmosphere generate waves of a wide range of periods. As already mentioned, the influence of infrasonic waves on the middle and upper atmosphere is temporally and spatially limited. Moreover, disturbances of infrasonic origin are treated also in other chapters of this book (Farges et al. 2019). On the other hand, methods of measurements of infrasonic effects are suitable also for studying effects of gravity waves, particularly of short-period gravity waves, but they are usually less efficient for studying effects of longer period waves like tides and planetary waves. Therefore, we further focus mainly on effects of gravity waves (GWs) on the upper atmosphere and ionosphere but effects

of infrasound will be mentioned, as well. Ionospheric effects of planetary, tidal, gravity, and infrasonic waves had briefly been reviewed by Laštovička (2006).

When assessing the influence of gravity waves in the lower and middle atmosphere (at altitudes up to ~110 km), there is an important property of gravity waves to be reminded. Dominant energies and momentum fluxes occur at opposite ends of the frequency spectrum. This implies that gravity waves which are easily observable by various techniques (waves with the largest amplitudes, energy densities, and horizontal scales) do not reach simultaneously the largest energy and momentum fluxes and atmospheric effects (Fritts et al. 2006).

GWs play a very important role in the momentum and energy budget of the mesosphere—lower thermosphere region (MLT) (Laštovička 2006). GWs participate in the reversals of zonal mean jets and in driving the mean meridional transport circulation that leads to warm winter mesopause and cold summer mesopause (Fritts et al. 2006). In summer, the momentum forcing by GW is directed eastward while in winter forcing in the opposite direction (westward) dominates. The driving is larger in the Southern than in the Northern Hemisphere. Gravity waves contribute to driving the mesopause semi-annual oscillation (SAO) and mesopause quasi-biennial oscillation (QBO) (Fritts and Alexander 2003). At high latitudes, GW forcing of the winter mesosphere can have effects down to ~30 km and modify the stratosphere circulation (Fritts and Alexander 2003).

In the stratosphere, GW dissipation and turbulent mixing and transport play a relatively minor role in the impact on the large-scale thermal and constituent structures. Their influence is stronger in the mesosphere and lower thermosphere. GWs are involved in driving the summer hemisphere equator-to-pole meridional transport circulation (Fritts and Alexander 2003). In lower latitudes, GWs are important for driving the eastward part of the stratospheric SAO. The role of GWs in driving QBO is still uncertain as direct estimation based on global observations is missing. Momentum flux spectra observed by satellite instruments HIRDLS and SABER show that GWs with intrinsic phase speeds <30 ms^{-1} (vertical wavelengths <10 km) interact with QBO (Ern et al. 2014). Responses to GWs occur in meridional and vertical circulation and in the mean temperature structure of the polar winter stratosphere (Fritts et al. 2006). Albers and Birner (2014) found support for the assumptions that GWs play an important role in driving the sudden stratospheric warming (SSW) or that GW drag may even trigger an SSW. However, the participation of GWs in triggering and driving SSWs is not fully understood yet. On the contrary, the impact of SSW—namely changes in the mean zonal winds during an SSW—on GWs propagation has been proved. Yiğit and Medvedev (2012) found enhanced propagation of GWs into the thermosphere during SSW. It caused the amplification of the eastward GW momentum deposition in the lower and upper thermosphere which consequently affected zonal mean winds.

Two approaches exist in the modeling of GWs. (1) Full-wave models assume a steady-state spatially uniform source of GWs (e.g., Yeh and Liu 1974; Walterscheid and Hickey 2011). (2) Wave packet approach assumes time-dependent and spatially localized source of GWs (e.g., Vadas 2007; Vadas and Nicholls 2012). When modeling GWs, it is important to consider by which type of source the waves were likely generated. Most of the GWs commonly observed in the thermosphere seem

to be produced from temporally and spatially localized sources, e.g., convection, mountain ranges, and Aurora (Vadas and Nicholls 2012).

Vadas (2007) derived a dispersion relation for gravity waves which includes the damping effects of molecular kinematic viscosity and thermal diffusivity in the thermosphere and is valid before and during dissipation; acoustic waves were neglected. Incorporating this dispersion relation in a ray tracing, Vadas (2007) modeled propagation and dissipation of GWs in the thermosphere under different temperature conditions corresponding to different phases of the solar cycle. Dissipation altitudes, range of vertical wavelength, horizontal distances traveled, and time of propagation before a GW dissipates were estimated for GWs of horizontal wavelength of 10–3200 km and vertical wavelength of 5–400 km. The highest dissipation altitudes are expected at ~400–500 km for GWs of horizontal wavelength of ~400–2000 km and intrinsic periods of ~10–50 min. Only GWs with short intrinsic periods between ~7 min and 300 min can dissipate above 150 km. The dissipation altitude means the altitude of maximum momentum flux of a GW, not the maximum attainable altitude. Vadas and Nicholls (2012) derived the high-frequency, compressible, dissipative dispersion, and polarization relations for linear acoustic-gravity waves and acoustic waves in a single species thermosphere. The authors found that phase shifts and amplitude ratios between the GW components (horizontal and vertical velocity, density, pressure, and temperature disturbances) depend strongly on the vertical wavelength of the GW.

The most efficient sources of GWs in the lower atmosphere are convection, airflow over hilly terrain, and wind shear. Other sources that under certain conditions contribute to GWs generation include weather fronts, adjustment of unbalanced flow, wave–wave interaction, and local body forcing. In the upper atmosphere, GWs can be generated by auroral activity, geomagnetic storms, or passage of the solar terminator and/or of solar eclipse (Fritts and Alexander 2003; Fritts et al. 2006; Boška et al. 2003; Altadill et al. 2004) and by some sporadic sources treated in Sect. 25.2.3, i.e., GWs which are excited also by non-atmospheric/meteorological sources.

The Earth's major atmospheric sources of GWs seem to be zones of deep convection in the tropics (Vadas and Fritts 2004). GWs emitted by deep and narrow sources—which tropical convective plumes can be regarded as—have large vertical scales, high phase speeds, and high vertical group velocities. Such waves can propagate up to and influence the upper atmosphere (Fritts et al. 2006). Convective plumes can be organized into mesoscale convective complexes (MCC). The characteristics of GWs emitted by tropical MCCs depend on the distance between the individual plumes. Coherent plumes separated by less than two plume diameters generate GWs of larger horizontal scales. Plumes distant more than two plume diameters from each other act as independent sources of GWs emitting GWs with characteristics similar to GWs from a single plume (Vadas and Fritts 2004). The convection as a source of gravity waves is modified by wind shear in the troposphere resulting in GWs with tilted phase and direction of propagation (Fritts et al. 2006).

Convection generates gravity waves throughout the full range of phase speeds and wave frequencies, and vertical and horizontal wavelengths (Fritts and Alexander 2003). In real measurements, we often observe one dominant GW structure. On the other hand, the average GW spectra have a joint universal shape;

they differ little in spectrum slope in spite of different localities, seasons, times of the day, etc. Convectively generated gravity waves are of horizontal wavelengths ~10–1000 km and of periods of minutes to tens of hours (Fritts et al. 2006 and references therein). Three mechanisms are thought to participate in the generation of gravity waves by convection. These are (1) the obstacle effect where the wind shear at cloud tops imposes relative motion over convective cells, (2) thermal forcing through latent heat release, and (3) an effect of a mechanical oscillator in which oscillatory convective plumes project those periods onto the gravity waves field (Fritts and Alexander 2003). The three mechanisms operate simultaneously (Sentman et al. 2003).

Vadas and Fritts (2004, 2005, 2006) modeled forcing of the thermosphere by GWs arising from convection. The penetration height of the GWs depends on the phase of the solar cycle. It is larger during solar maximum than during periods of low solar activity. When the small- and medium-scale GWs excited by convection dissipate in the thermosphere, large-scale horizontal body forces arise. The body forcing provides very strong acceleration of ~0.15–0.25 ms^{-2} during solar minimum and of ~0.5–0.75 ms^{-2} during solar maximum. The maximum body forces resulting from dissipation of the GWs occur at ~180–200 km during both solar maximum and minimum.

The horizontal body forces are localized and highly intermittent and might be an important source of horizontal thermospheric winds and of large-scale long-period secondary GWs propagating both upward and downward from the source region in the thermosphere. Deep, rapid instability process can generate GWs of significantly larger time and spatial scales and vertical group velocities than those of the mother GW. These secondary GWs may penetrate and influence much higher altitudes than the primary GW (Fritts et al. 2006).

Mountain waves are generated by air flowing over mountain terrain. The waves may significantly modify local airflow in the troposphere and also the tropospheric jet. Their impact on the middle and upper atmosphere can be considerable as well but it is limited by the required specific conditions in the atmosphere that would enable vertical propagation of the mountain waves. The phase speed of mountain waves is close to zero and therefore the waves can propagate to higher altitudes only in case of sufficient nonzero winds being present throughout the entire atmospheric column (Fritts et al. 2006). The horizontal wavelengths of vertically propagating mountain waves are of the order of tens to hundreds of km. Vertical wavelengths are determined by the local static stability of the atmosphere and by the mean wind in the plane of wave propagation (Fritts and Alexander 2003).

A typical zone for formation of mountain waves is the Andes in South America. Waves generated by airflow over the high central Andes ridge and over Patagonian peaks in the southern Andes (1) were absorbed by a critical level in the stratosphere at altitude of ~15–20 km to the northeast from their origin site in the Central Andes and Patagonia; (2) broke down in the stratosphere and lower mesosphere (altitudes of ~50–60 km) directly above Patagonia; and (3) propagated to the southeast, entered polar vortex jet in the stratosphere and eventually broke in the lower mesosphere above the vortex jet core at altitude of ~55 km with momentum deposition in the stratosphere and mesosphere near 60°S (Jiang et al. 2013).

Figure 25.2 shows the main hotspots of stratospheric gravity wave activity based on satellite observations (Hoffmann et al. 2013). Stratospheric hotspots of GWs occur over the Andes, at the southern tip of Greenland, in the region of the Pamir Mountains, the Altai Mountains and Lake Baikal, the Rocky Mountains, over Antarctic Peninsula, South Georgia and Kerguelen Islands and over Paleozoic mountains in Western Europe and Scandinavia, the Ural, the Alps, the Carpathian Mountains, and the Balkans (Hoffmann et al. 2013). Some of these hotspots are quasi-permanent features, particularly the strongest one in the area of the Andes/Patagonia–Antarctic Peninsula, as it is as strong also in equinoctial periods and it is less pronounced only in austral summer. Others, like the large hotspot over the central United States, are only seasonal feature; it exists only in boreal summer.

Wind shear is believed to contribute significantly to the middle atmosphere momentum budget. The waves are radiated mainly near the tropopause and higher and in the vicinity of jet streams. Gravity waves are generated due to the instability of the shear layer. The instability can be excited by nonlinear collapse of Kelvin–Helmholtz billows in the shear layer. There are also observations suggesting that certain linear modes of shear instability can be excited. However, compared to convection and orography, wind shear as a source of gravity waves is relatively poorly understood (Fritts and Alexander 2003; Fritts et al. 2006). Pramitha et al. (2015) reported observations of high-frequency high-phase-speed GWs in the

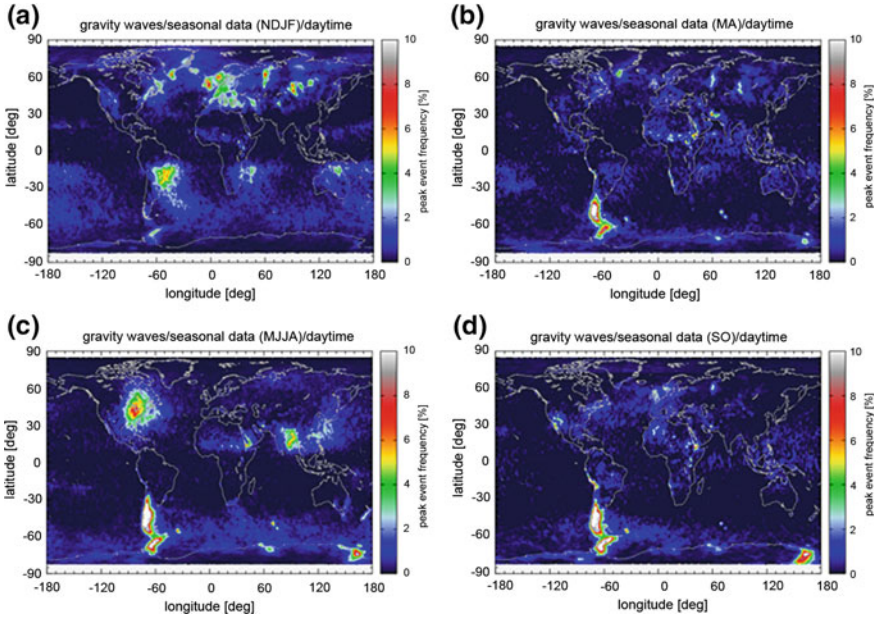

Fig. 25.2 Hotspots of stratospheric gravity waves at daytime, based on satellite observations (AIRS) over 2003–2011. The maps combine data for **a** November to February, **b** March and April, **c** May to August, and **d** September and October. After Hoffmann et al. (2013)

mesospheric airglow over India and came to a conclusion that the waves were generated by strong vertical shear in the horizontal winds (~9 ms^{-1} km^{-1}) in the upper troposphere at altitudes of 10–12 km.

Radiation of GWs of a wide range of spatial and time scales may accompany adjustment processes of unbalanced flow. Large-scale adjustment processes generate inertia–gravity waves with large horizontal and small vertical scales and frequencies near the inertia frequency. The time and spatial scales of waves radiated from smaller scale adjustment processes depend on the geometry and timescale of the event and are therefore highly variable (Fritts et al. 2006).

The mechanism of gravity waves excitation during the frontogenesis is similar to that of the jet stream adjustment. Moreover, associated convection and instability dynamics may in addition excite gravity waves at higher ends of frequency and wave number spectra (Fritts et al. 2006). In mid-latitudes, cold fronts are considered the most efficient meteorological source of GWs (Laštovička 2006). Šauli and Boška (2001) described increased wave activity in the ionosphere during the passage of weather fronts over the Czech Republic. The observed GWs were of periods of 50–100 min and propagated upward.

Nonlinear wave–wave interactions occur throughout the atmosphere and play an important role in energy exchange, amplitude constraints, and spectral evolution of GWs. The interaction rate increases with increasing wave amplitude. GW spectral energy transfers result in generation of waves of larger as well as smaller scales (Fritts and Alexander 2003).

Tropical cyclones, tornadoes, convective storms, cyclones, weather fronts, mesoscale convective complexes, and airflow over mountainous terrain are considered the most efficient meteorological sources of infrasonic waves (Laštovička 2006). Observations of infrasound in the upper atmosphere were reviewed by Blanc (1985) and Krasnov et al. (2006).

The occurrence of infrasound at ionospheric heights during convective storms was broadly studied in North America, particularly in the 1960 and 1970s. Observations of infrasonic waves of periods between 1 and 5 min in the ionosphere during nearby tropospheric convective storms were repeatedly reported (Georges 1967; Baker and Davies 1969; Georges 1973; Prasad et al. 1975). The wave spectrum may vary from event to event or even during one convective storm (Georges 1973; Prasad et al. 1975). Prasad et al. (1975) found different spectral contents in different geographical locations; in Oklahoma, the spectral peak was stable at 4–5 min period, whereas it varied in Florida. It is accepted that a convective storm system generates a broad spectrum of acoustic waves. The relatively narrow period band observed at ionospheric heights is caused by atmospheric filtering (Georges 1967). Acoustic cutoff prevents waves at the end of long-period range of the acoustic spectrum from reaching the ionosphere; crucial is the minimum cutoff period which normally occurs at the temperature minimum at the mesopause. Waves in the short-period band are damped by absorption. Ionospheric effects are usually observed when a convective storm is active within the radius of up to 300 km from an ionospheric observation point (Georges 1973; Prasad et al. 1975). Ionospheric infrasound of periods of 3–5 min was also observed in Central

Europe during severe convective storms in summer that were passing over the region of ionospheric sounding (Šindelářová et al. 2009).

Pilger et al. (2013a) observed infrasound (and short-period GWs) signatures in OH airglow in the southern Germany and in the north of Norway. Spectral intensities of wave signatures in the period band of 2.5 and 10 min were estimated. Many of the signals had dominant periods near the atmospheric resonant modes, namely the spectral peaks at 190, 270, and 300 s. The most likely sources of these resonance frequencies are severe weather and convective storms. The increased occurrence of the signals was found in winter months (including late autumn and early spring)—in the season of increased severe weather activity. Infrasound signatures in OH airglow were observed over Palma de Mallorca. A Mediterranean tropical storm and frontal passage over the observational site were identified as sources of the 3–5 min signals in the respective events (Pilger et al. 2013b).

As already mentioned, the influence of infrasonic waves on the middle and upper atmosphere is temporally and spatially limited.

One more factor of atmospheric origin, which affects the state of the atmosphere–ionosphere system and the propagation of infrasound, is major midwinter stratospheric warmings, when the temperature in the middle stratosphere at high latitudes increases by several tens of degrees K and circulation substantially changes. It affects not only the lower and middle atmosphere but also the thermosphere and the lower ionosphere as well as the F-region ionosphere. In the F-region ionosphere, the effect consists predominantly in strengthening of the westward propagation semidiurnal tide with zonal wave number 1, which results in increasing TEC in the morning and early afternoon and decreasing TEC in the late afternoon. The effect is developed best in low latitudes due to their high sensitivity to the vertical **ExB** drift (e.g., Azeem et al. 2015). Similar effects have also been observed in the thermosphere. The effect in the lower ionosphere is different; it consists in some increase of electron density and radio wave absorption at middle and high latitudes in accord with reversal of zonal wind near 90 km altitude.

The major midwinter stratospheric warming has very pronounced effect on the height profile of temperature: huge warming in the stratosphere, substantial cooling in the mesosphere, and remarkable warming in the lower thermosphere. Since the index of refraction of infrasonic waves is a sensitive function of temperature, stratospheric warmings are capable to substantially affect both the infrasonic waves reflected from the middle–upper stratosphere and from the lower thermosphere (e.g., Smets and Evers 2014).

25.2.3 Disturbances of Seismic and Other Event Origin

In this category, the most interesting are ionospheric disturbances caused by earthquakes, as they are both co-seismic and pre-seismic, the latter having potential to be used in future complex systems for earthquake predictions. These changes are either electron density changes of wavy character (infrasonic and gravity waves) or

anomalous values of the total electron content (TEC) and of the maximum electron concentration in the ionosphere, as well as changes in electron density profile. Here, we shall deal only with changes of wavy nature. The infrasonic oscillations in the ionosphere attributable to earthquakes may be expected to be caused only by stronger earthquakes. Weaker earthquakes excite weaker infrasound but, particularly, infrasound very predominantly at too high frequencies to be able to penetrate to ionospheric heights well above 100 km; therefore, this infrasound is recorded only by ground-based microbarometers (Laštovička et al. 2010).

We shall illustrate ionospheric wavy effects of large earthquakes on example of the very strong Tohoku 2011 M9.0 earthquake in Japan. During the Tohoku earthquake, the Japanese GEONET system of the GPS/TEC monitoring recorded concentric waves in the ionosphere excited by this earthquake as shown in Fig. 25.3. The ionospheric "epicenter", which was displaced from the seismic epicenter by about 170 km, was roughly consistent with the position of the estimated center of tsunami source (Tsugawa et al. 2012). The Czech ionospheric Doppler sounder recorded infrasonic signal of this earthquake over a distance of about 9,000 km from the epicenter (Chum et al. 2012b). The cross-correlation coefficients between ionospheric and local ground (seismic) measurements were higher than 0.9 (up to 0.98). The observed time delay of ~9 min between the record of seismic wave packets on the ground and ionospheric response at a height of about 210 km corresponded well with the calculated time for infrasound propagation. The individual wave packets were related to all different types of seismic waves, starting from P-waves even at a distance of ~9,000 km from epicenter. The majority of previous reports of similar measurements at comparable distances from epicenter reported only ionospheric response to seismic Rayleigh waves, exceptionally to S waves but never to P-waves. Various Doppler and GPS/TEC observations allowed Hao et al. (2012) to report the seismic Rayleigh wave-induced ionospheric infrasound from the direct arrival of Rayleigh waves, from arrival from

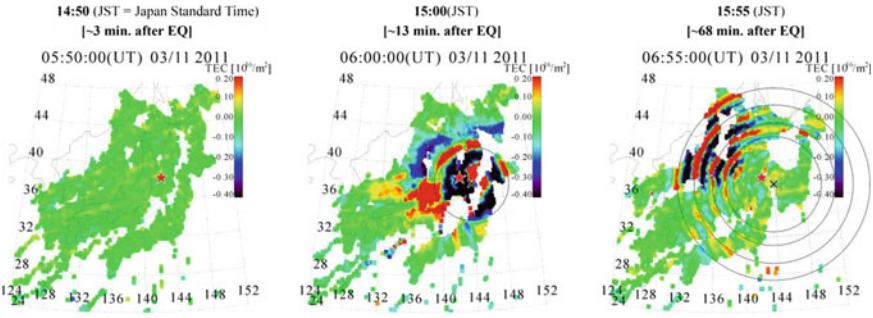

Fig. 25.3 Two-dimensional maps of TEC variation derived using the data of GEONET network. The TEC data are detrended values derived by subtracting 10-minute running average of the data. The star and cross marks represent epicenter and ionospheric epicenter, respectively. Gray circles represent concentric circles with the ionospheric epicenter. Courtesy by Tsugawa et al. (2012). The animation of TEC maps is available on http://www.seg.nict.go.jp/2011TohokuEarthquake

the other side along the great circle, and from the direction from epicenter but after one complete circle around the Earth. Altogether three types of waves were observed in the vicinity of epicenter: quick blast wave (shock-acoustic wave), slower infrasound, and relatively slow gravity waves. The Japanese TEC GEONET network observations made possible to distinguish in the ionosphere three different groups of wave propagation velocities of about 3400, 1000, and 200–300 m/s, which correspond to propagation of seismic Rayleigh waves, acoustic waves (infrasound), and gravity waves, respectively (Galvan et al. 2012). The infrasound in the ionosphere excited via impact on the ionospheric dynamo was observed as the teleseismic magnetic effects in the period range 2.1–3.3 min by magnetometers in East Asia after the Tohoku 2011 earthquake (Hao et al. 2013). Ionospheric measurements even made it possible to get information about the seismic fault slip during the Tohoku earthquake (Astafyeva et al. 2011).

Strong earthquakes with foci beneath ocean floor excite infrasound and particularly short-period gravity waves related to tsunamis which are observable in the ionosphere. These gravity waves can be discriminated from direct earthquake excited gravity waves (Occhipinti et al. 2013). Monitoring of such waves could in future serve as a part of tsunami warning system. The observations of airglow at Maui/Hawaii detected the Tohoku tsunami-excited atmospheric waves about one hour before arrival of the tsunami itself to Maui, which illustrates some warning capacity of upper atmospheric airglow monitoring (Makela et al. 2011). The question remains open whether both ground-based and ionospheric monitoring of infrasound and short-period gravity waves can reveal precursory information on coming earthquake; no deep study in this direction has been realized.

Another interesting type of events is effects excited by bolides and meteoroids. The recent Chelyabinsk meteoroid excited infrasonic waves of periods 3–4 min and gravity waves in two ranges, ~10–15 min and ~70–135 min according to various ionospheric observations (Chernogor 2015). Also, underground nuclear explosions are capable to excite infrasound. Such infrasonic waves have been observed in the ionosphere, for example, after the 2009 North Korean underground nuclear explosions as reported by Zhang and Tang (2015). A worldwide network of microbarometer arrays is used by the international treaty on the ban of underground nuclear explosions (CTBT) as one of the tools for monitoring. Also, big industrial explosions excite infrasound observed not only by ground-based microbarometers (e.g., Ceranna et al. 2009) but also by ionospheric Doppler sounders (Krasnov et al. 2003).

25.3 Long-Term Trends

The 0.6 °C increase in global surface air temperature during the twentieth century (e.g., IPCC 2007) has been attributed predominantly to the increasing atmospheric concentration of greenhouse gases. The greenhouse gas increase has an opposite, cooling effect in the middle and upper atmosphere beginning from the stratosphere. There are also other drivers of long-term trends: aerosols and volcanic eruptions

(troposphere and stratosphere), solar and geomagnetic activity (whole atmosphere and ionosphere), changes in atmospheric wave forcing and dynamics (whole atmosphere), ozone depletion (stratosphere to lower thermosphere), stratospheric water vapor content (stratosphere to lower thermosphere), and secular trend of the Earth's magnetic field (ionosphere and thermosphere). The long-term trends in the troposphere have regularly been summarized and broadly discussed in detail by reports of the Intergovernmental Panel for Climatic Change (IPCC—reports IPCC 2007, 2013). After remarkable increase of global surface temperature in the last decades of the twentieth century, the increase almost stopped with the beginning of the twenty-first century. A role in this temperature "hiatus" is played by the Southern Ocean, which cools on the surface but rapidly warms at depth. However, 2014 was globally the warmest year on record and 2015 seems to be even warmer, so maybe the hiatus is coming to its end. Long-term trends at higher levels in the mesosphere, thermosphere, and ionosphere have recently been reviewed by Laštovička et al. (2012).

Figure 25.4 shows the global pattern of long-term trends in terms of atmospheric temperature and ionospheric electron density. In temperature, the trend consists in greenhouse heating in the troposphere, some cooling in the stratosphere, larger cooling in the mesosphere, no change in the mesopause region, and a cooling well in the thermosphere deduced from ion temperature and neutral density observations. In electron density, which represents the ionosphere, the trend consists in some lowering of the lower ionosphere (below ~100 km) and the E-layer and F2 layer, mainly as a consequence of thermal shrinking of the atmosphere. The descent of the ionosphere is accompanied by some increase of the maximum electron density of E-layer and F1 layer, and a slight decrease of the maximum electron density of F2-layer (e.g., Laštovička et al. 2012). All these changes together form a self-consistent scenario of long-term trends in the atmosphere and ionosphere system. Figure 25.4 reflects situation prior to the turnaround of ozone trends in the mid- to late-1990. After this turnaround, trends of stratospheric, mesospheric, and mesopause region temperatures to some extent changed (see Sects. 25.3.1 and 25.3.2).

Trends in the troposphere and at surface are very important for our life but until now they are small in magnitude, so their impact on propagation of infrasound is negligible. On the other hand, they can change intensity and distribution of infrasound sources in the troposphere. For example, a relatively small increase of temperature should result in remarkable increase of lightning activity due to the associated increase of convection.

Since the stratospheric and the thermospheric mode govern the infrasound propagation on longer distances, we shall deal preferentially with trends in the respective parts of the stratosphere (~30–50 km) and lower thermosphere (~100–120 km), where infrasound is reflected back to surface. Trends in the stratosphere and mesosphere are also treated but from partly a different point of view. Two most important parameters for infrasound propagation are temperature and wind, some role is also played by atmospheric composition which influences absorption; therefore, we shall focus mainly on trends in temperature and wind, even though

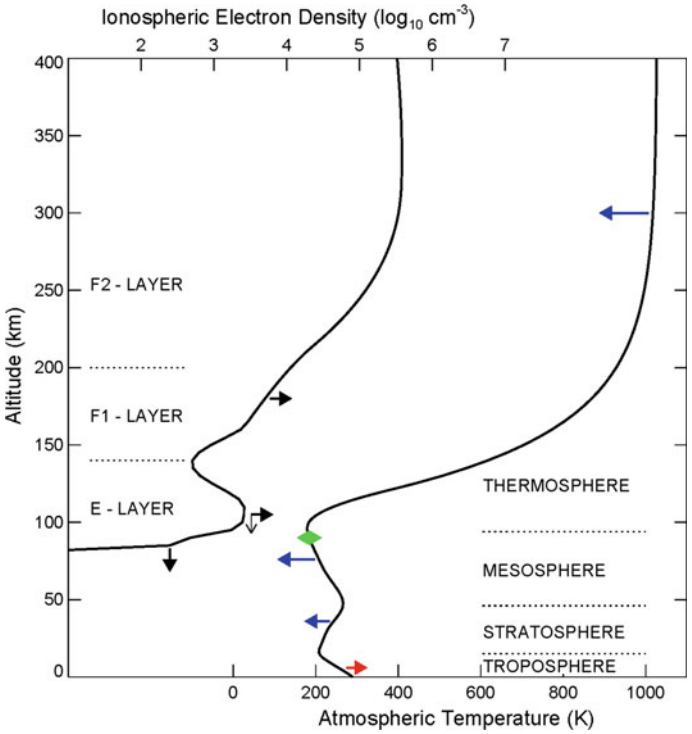

Fig. 25.4 Global pattern of trends in temperature and electron density as a function of height. After Laštovička et al. (2008)

trends in some other parameters will also be mentioned. A lower temperature means slower but stronger vertical propagation of infrasound. Wind results in a filtering of arrival azimuths as it is treated in more details in other chapters of this book (Waxler and Assink 2019; Assink et al. 2019).

25.3.1 Trends in the Middle and Upper Stratosphere

The two main drivers of temperature trends are two anthropogenic sources, the increasing concentration of greenhouse gases, mainly CO_2, and the time development of ozone depletion. Their interplay is responsible for temperature trends and their changes. In general, cooling has been observed in the whole middle and upper stratosphere, but this cooling has not been stable.

Global temperature trends can directly be obtained from satellite observations only. However, satellite observations suffer from the aging of the instruments, which introduces artificial trends requiring corrections and re-calibrations. As a consequence, the temperature measurements by satellites used to exist in several

versions from the first to the most recent one, which includes all corrections and re-calibrations. The temperature series from measurements of SSU (Stratospheric Sounding Unit) onboard NOAA satellites was re-calibrated and used for establishing trends by Zou et al. (2014). They reported for the period 1979–2006 the global temperature trends of -0.69 ± 0.18 K/decade for the middle stratosphere and -0.77 ± 0.15 K/decade for the upper stratosphere. These trends are relatively weak as they include the period after the mid-1990s when stratospheric temperature trend substantially weakened or leveled off due to ozone recovery. Huang et al. (2014) analyzed SABER/TIMED measurements over 2002–2012 for latitudinal range 48°N–48°S. They found positive trends in low latitudes and negative trends in extratropics in the middle stratosphere and rather weak negative trends in the upper stratosphere. Simmons et al. (2014) analyzed stratospheric temperature trends over 1979–2012 based on the ERA-Interim reanalysis. They found relatively strong cooling in the upper stratosphere, which is in agreement with model simulations. In the middle stratosphere, the agreement between various reanalyses is less good than below and above; middle stratospheric cooling is somewhat uncertain. The net cooling for ERA-Interim from 1979 to 2009 is around 3 K at 5 hPa and 4.5 K at 1 hPa, which means a trend of about −1.0 K/decade and −1.5 K/decade, respectively. At low latitudes, both lidar (Gadanki, Reunion, and São José dos Campos) and satellite data (HALOE and SABER) show a cooling trend at about 0.5–0.7 K/decade between 40 and 55 km (Kishore et al. 2014), which is in reasonable agreement with other results. Angot et al. (2012) studied temperature trends at heights 30–80 km above Haute Provence Observatory (OHP, France, 44°N). The trends became stronger (more negative) after eliminating disturbed stratospheric warming days. Ren and Yang (2012) show that models are capable of qualitatively reproducing the climatology of the stratosphere and capture the general features of its long-term changes during 1950–2000, including the global stratospheric cooling and the strengthening of the westerly polar jet. Li et al. (2011) analyzed long-term data series of three lidars at Mauna Loa (MLO, 19.5°N), Table Mountain Facility (TMF, 34.4°N), and Observatoire de Haute Provence (OHP, 43.9°N). A stratospheric cooling trend of 2–3 K/decade was found for both TMF and OHP, and a trend of -0.5 ± 0.5 K/decade was found at MLO. The lidar trends agree well with earlier rocketsonde and satellite trends in the stratosphere. The cooling trend in the upper stratosphere at OHP during 1981–1994 (similar to 2–3 K/decade) was much larger than that during 1995–2009 (0.8 K/decade), coincident with the slightly increasing upper stratospheric ozone density after the mid-1990s. Randel (2010) summarized older results and investigated trends in global stratospheric temperature based on radiosonde observations since the 1960s and satellite measurements since 1979. New radiosonde-based data sets were available that included adjustments for instrumental inhomogeneities, and these data showed good agreement with satellite measurements in the lower stratosphere. The stratosphere exhibited long-term cooling with magnitudes similar to −0.5 K/decade in the lower stratosphere to similar to −1.2 K/decade in the upper stratosphere.

Trends in winds in the middle and upper stratosphere have been studied separately for the zonal and meridional components but rather rarely for the meridional

component except for the Brewer-Dobson circulation. As for the zonal wind, Jadin (1997) analyzed variations in stratospheric zonal wind and angular momentum of the Earth's atmosphere are analyzed on the basis of the data of the US National Meteorological Center for 1979–1992. A rapid transition of stratospheric circulation to a new regime in the summer of 1980 was revealed, not a smooth trend. Strong easterly anomalies in the global stratospheric angular momentum in the period from 1979 to the beginning of 1980, a sharp transition to westerly anomalies in the second half of 1980, and the subsequent long-term downward trend in 1980–1992 are due to the corresponding changes in zonal wind in the tropical and subtropical lower stratosphere. Another perturbation was due to the Mount Pinatubo volcanic eruption. Hood et al. (1999) statistically analyzed trends of National Centers for Environmental Prediction (NCEP) gradient zonal winds for February and March. They demonstrated that the zonal mean meridional wind shear for these months in the mid-latitude lower stratosphere had tended to become more anticyclonic with time over the period from 1979 to 1998. Such a tendency favors the increased occurrence at these latitudes of anticyclonic, poleward, Rossby wave breaking events that transport low potential vorticity (PV), ozone-poor air from the subtropical upper troposphere to the mid-latitude lower stratosphere while favoring the decreased occurrence of equatorward breaking, and cyclonic events. Analyses of NCEP-derived PV on the 330 K isentropic surface showed that zonal mean PV values at mid-latitudes in February and March have decreased with time, consistent with the expected trends in Rossby wave breaking behavior. Monier and Weare (2011) used ERA-40 and NCEP-2 reanalyses. They outlined the considerable contribution of unresolved waves, deduced to be gravity waves, to the forcing of the zonal mean flow. A trend analysis, from 1980 to 2001, shows that the onset and breakdown of the Northern Hemisphere (NH) stratospheric polar night jet has a tendency to occur later in the season in the more recent years. This temporal shift follows long-term changes in planetary wave activity that is mainly due to synoptic waves, with a lag of one month.

The meridional wind is generally substantially weaker than the zonal wind but it plays a role in the Brewer-Dobson (B-D) circulation, which is vital for stratospheric ozone. Its upper branch is located in the middle and upper stratosphere. Many model studies reveal an acceleration of the B-D circulation due to the increasing greenhouse gas concentration (see review by Butchart 2014). Age of air data does not confirm the simple positive trend in B-D circulation. Fortunately, Ploeger et al. (2015) largely explained the difference by finding the effect of mixing on the age of air. But they also found significant difference between trends over 1990–2013 and 2002–2012. Osso et al. (2015) analyzed MSU and SSU satellite observations of stratospheric temperatures over 1979–2013 and they derived from these measurement trends in the B-D circulation, which were found to be weak and insignificant. Remsberg (2015) used satellite measurements of methane by HALOE over 1992–2005 as a diagnostic tracer of changes in the B-D circulation. He found acceleration of B-D circulation in the middle stratosphere over this period. Monier and Weare (2011) identified a long-term weakening in the B-D circulation in the polar region

in the NH winter and early spring based on data of reanalyses ERA-40 and NCEP-2 over 1980–2001.

Kozubek et al. (2015) investigated behavior of meridional circulation at 10 hPa, 20–60°N, based on three different reanalyses. They found for winter (January), northern higher middle, and high latitudes the existence of two cores of substantially stronger meridional wind. Further investigations reveal existence of these cores, shown in Fig. 25.5, not only for 10 hPa (middle stratosphere) but also for 1 hPa (upper stratosphere) and 0.1 hPa (lower mesosphere—less developed). These cores exist only in the winter half of the year northward of 40–50°N; they represent response of wind to the blocking Aleutian pressure high. These cores also affect substantially trends in meridional winds. Kozubek et al. (2015) found sufficiently strong and statistically significant trends (mostly at the 99% level) of meridional wind at 10 hPa, 50–60°N, only in longitudinal sectors with cores, not in sectors without cores where trends were much weaker and statistically significant at the 90% level only or totally insignificant. Moreover, the significant trends in "core" sectors changed in the mid-1990 from ∼−4.5 m/s per decade in 1970–1995 to ∼+7 m/s per decade in 1996–2012 in line with turnaround of ozone trends at northern middle latitudes (Harris et al. 2008) and with the trend difference found by Ploeger et al. (2015). Thus, trends in meridional wind experience substantial

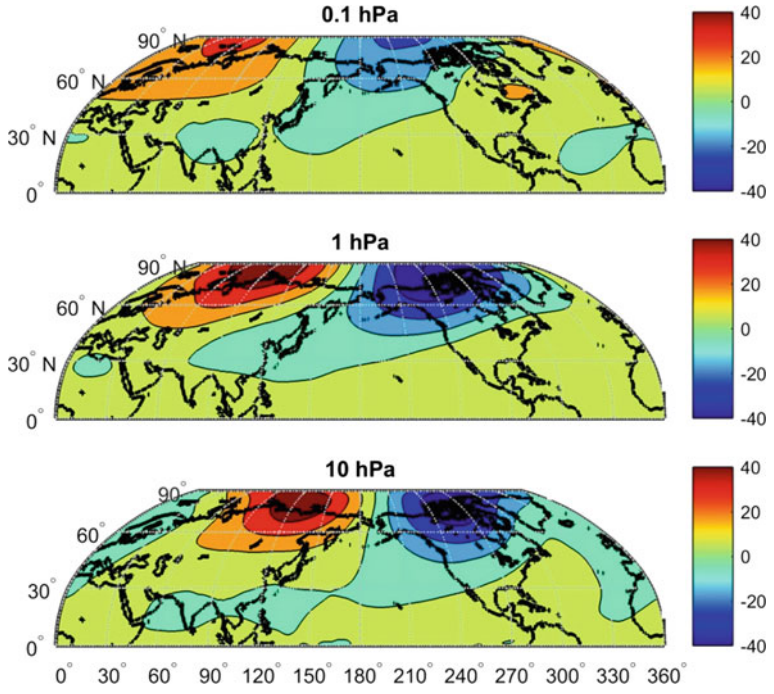

Fig. 25.5 The climatology of meridional wind (scale in m/s) for January at 0.1 hPa (upper panel), 1 hPa (middle panel), and 10 hPa (lower panel), 1979–2012

longitudinal difference and trend reversal, the latter in line with turnaround of ozone trends. This may in principle also explain the weak, insignificant trends in B-D circulation found by Osso et al. (2015) over 1979–2013, as Kozubek et al. (2015) 10 hPa trends provide for 1970–2012 zero overall trend for January even in cores with high partial trends, and an acceleration of the B-D circulation in the middle stratosphere over 1992–2005 found by Remsberg (2015), as the period 1992–2005 belongs by its predominant part into the period of the middle stratospheric meridional wind acceleration found by Kozubek et al. (2015).

Summing up, we may say that in the middle and upper stratosphere there is a trend of cooling, stronger in the upper stratosphere, even though individual results somewhat differ quantitatively. This cooling substantially weakened or leveled off after the change of ozone trends in the mid-1990s. Trends in winds provide a less consistent pattern. They also changed near the mid-1990s. They seem to depend not only on latitude but also on longitude/region. From the point of view of infrasound propagation, both temperature and wind speed trends are relatively weak, so they can play a role when comparing present-day propagation conditions with propagation conditions several decades ago but on short-term scale including timescale of years they are unimportant for the infrasound propagation conditions.

In the following, trends are briefly described in two important stratospheric compounds, ozone and water vapor.

A very important component in the stratosphere is ozone. The anthropogenic depletion of ozone concentration and its development belongs to crucial processes in the stratosphere. The first paper on observations of the Antarctic springtime ozone hole was published in 1985 with detection of the ozone hole since 1979–1980. Soon, in 1987, the Montreal Protocol was signed and in the following years several amendments were added to protect ozone layer from the ozone-depleting compounds (ODS), which produce Cl (dominates in ozone depleting) and Br. These international agreements resulted in a slow recovery of ODS and ozone toward initial values. The Cl source compounds in the troposphere peaked in 1993–1994, and the equivalent effective stratospheric chlorine (EESC) peaked in the stratosphere in 1997; EESC was reduced by 10–15% by 2012. The stratospheric ozone concentration has been decreasing at least since about 1979, with a leveling off and turnaround of the trend in 1995–1997 at northern middle latitudes according to the results of European project CANDIDOZ (Harris et al. 2008). If we focus only on middle and upper stratosphere (~30–50 km) and global satellite measurements, the results are as follows. Merged SAGE II and Odin-ORISIS record reveals negative trends of 5–10%/decade for 1984–1997 and positive trends 3–8%/decade for 1998–2013 (Bourassa et al. 2014). SABER/TIMED data over 2002–2012 at 48°N–48°S provide a complex altitudinal–latitudinal structure of trends with basically negative trends at low latitudes and positive trends at middle latitudes (Huang et al. 2014). Mixed SAGE II and GOMOS data over 1984–2011, 60°N–60°S, analyzed using the DLM model show mostly the pattern decay–recovery with turning point 1997–2001 with a few exceptions; a continuous decay in 50–60°S and the third type of pattern, decay–recovery–decay with the second turning point in 2007 at 40–60°N in the 35–45 km altitude bin (Laine et al. 2014). As for the Antarctic ozone hole,

classical methods have been unable to detect a statistically significant recovery of ozone due to its large year-to-year variability. Therefore. Várai et al. (2015) used another approach. They calculated the difference between total ozone at 59.5 and 79.5°S, and they found in the mid-1990s a robust trend reversal in the occurrence frequency of extremely low values at 79.5°S relative to 59.5°S values. Summarizing we may say that, except for polar regions, the ozone concentration in the middle and upper stratosphere was decreasing until the mid- to late-1990s, when the trend reversed to some increase. This change of ozone trend reflected in various parameters in the stratosphere, mesosphere, and lower thermosphere (e.g., Laštovička et al. 2012).

The story of ozone hole until now represents an example of successful fight of humans against global environmental risk. The Montreal Protocol with amendments does not limit very short living halogens (lifetime shorter than 6 months—their atmospheric concentration relatively quickly increases) and N_2O. Their ability to reduce ozone is substantially less than that of classical ODS like freons; therefore, they were not considered in the past, but the development of their atmospheric concentration and impact on ozone layer will have to be monitored, as their relative role in ozone layer development is increasing.

Some role in long-term trends in the stratosphere is played also by water vapor, another greenhouse gas, even though its mixing ratio is substantially lower than in the troposphere. The positive trend in the lower stratospheric water vapor mixing ratio revealed by Boulder regular frost point hygrometer balloon-borne measurements had been considered for a long time to be stable and globally representative. However, HALOE, POAM, and balloon measurements have shown a considerable decrease in the lower stratospheric water vapor following a sudden drop in 2000, which coincided with anomalous cooling of the tropical tropopause; then, the stratospheric water vapor recovered but another even stronger drop of lower stratospheric water vapor occurred in 2011–2012 (Urban et al. 2014). Thus, contrary to the twentieth century, the twenty-first-century data do not show a trend in stratospheric water vapor due to sudden drops. Moreover, Hegglin et al. (2014) used the global merged water vapor record and showed the Boulder record to be non-representative for global water vapor trend due to geographic reasons. They found globally no significant trend at 100 hPa level, a negative trend higher in the lower and middle stratosphere (50 and 30 hPa), and a positive trend in the upper stratosphere (their Tab. 1 allows estimate trend changeover to be near 10 hPa). The origins of such a behavior of stratospheric water vapor trends are changes in the stratospheric entry from below, in methane concentration, and in circulation.

25.3.2 Long-Term Trends in the Lower Thermosphere

No continuous direct measurements of neutral temperature at heights of about 100–120 km, which would allow to determine the temperature trends, are available. Even no series of measurements of a suitable proxy like ion temperatures (available

higher) is available at these heights. Just below, at heights 85–100 km, satellite observations by instrument SABER at satellite TIMED are available since 2002. Huang et al. (2014) analyzed SABER data over 2002–2012 at latitudes 48°N–48°S. They found negative trends at 85–100 km, typically near −2 K/decade but latitude dependent.

Longer data series are available predominantly from airglow observations at mesopause heights, e.g., OH* emissions centered near 87 km. Beig (2011) reviewed mesopause temperature trends and found no statistically significant trends before the mid-1990s (1995–1997) and negative trends in more recent years. This turnaround of temperature trends coincides with turnaround of trends in stratospheric ozone, which is likely the cause of change of trends in the mesopause region temperature (Laštovička 2013).

The most recent model calculations provide some information also on temperature trends at respective heights. Solomon et al. (2015) used the 3-D version of model TIME-GCM and simulated temperature trends from 1996 to 2008 with the observed increase of CO_2 but other variables fixed for two levels of solar activity. Trends of temperature at 100–120 km in fixed altitude coordinates are nearly zero for the solar cycle minimum and slightly positive for the solar cycle maximum. However, this trend includes both temperature trend and impact of thermal shrinking. At fixed altitudes, thermal shrinking moves in warmer air parcels from above; this effect overcompensates cooling itself under solar maximum conditions due to the steep vertical gradient of temperature. If the trends are presented in fixed pressure coordinates, the temperature trends are negative. Also, temperature trends at heights 85–100 km are negative (independent of coordinates used due to a small vertical temperature gradient), which is in qualitative agreement with the above-reported observations.

The situation with long-term trends in winds is even worse than with trends in temperature. There is no information available on trends in winds at heights of 100–120 km, neither from direct wind observations, nor from proxies. There is only trend information from data of a few ground-based stations with long data series of measurements centered at heights of about 90 km. Trends at different stations reveal some similarities but also many differences. Trends of zonal wind at different stations agree better than trends of meridional wind. Trends are not stable, sometimes they change (even as to sign), and they seem to be regionally different. However, it seems that due to changes in trends the overall effect on winds over several decades is relatively small. Similar conclusion is likely valid also for trends in atmospheric wave activity—planetary waves, tides, and gravity waves, even though results of various authors are to some extent contradictory (Laštovička et al. 2012).

The only quantities where we have enough observational information for estimating global trends are two ionospheric parameters from the worldwide network of ionosondes: the critical frequency of the E-region (foE), which is a measure of the maximum electron density, and the height of the E-region maximum (hmE). These two variables are from heights around 110 km. Based on data from this network, Bremer (2008) found the average trend of foE to be $+0.013 \pm 0.005$

MHz/decade. Most individual stations displayed positive trends but the number of stations displaying negative trends is non-negligible. Trends slightly weaken with increasing latitude; their longitudinal dependence seems to be affected, if not determined, by longitudinal dependence of total (stratospheric) ozone. The global trend in hmE is negative, -0.29 ± 0.20 km/decade, as expected consequence of mesospheric cooling and, thus, of thermal shrinking. However, there is rather large scatter of trends obtained from data of individual stations. This all makes this trend rather insignificant and/or questionable, mainly due to data problems. First, historical hmE data have coarse height resolution of 5 km. To reach 5 km decrease of hmE, the average trend should continue for 170 years. Second, evidently, there are specific data problems at some stations.

Summarizing, it can be concluded that, despite very limited observational information, there are probably some long-term trends at heights of 100–120 km (proved for the E-region ionosphere) but they are probably rather weak and until now have not produced significant changes in propagation of infrasound.

Infrasonic signals from some sources (strong meteorological disturbances, strong earthquakes, etc.) penetrate to much higher altitudes, to the ionospheric F layer, where they are observed by the ionospheric Doppler sounders. At these altitudes, the trends in both the neutral thermosphere (neutral density and temperature) and the ionosphere (foF2, hmF2, maybe total electron content TEC) are substantially stronger than those at altitudes of 100–120 km (Laštovička et al. 2012) but the overall role of infrasound at these altitudes is rather unimportant.

25.4 Summary

A brief review is given of the state-of-the-art knowledge on large-scale and transient disturbances and long-term trends with particular emphasis on the middle and upper stratosphere and the lower thermosphere, two regions where the infrasound launched at surface or in the troposphere is reflected.

Two dominant disturbances of solar origin, which substantially affect the atmosphere and particularly the ionosphere, are solar flares and geomagnetic storms. Fortunately, flares affect both regions of infrasound reflection rather little and the geomagnetic storm effect on them is essentially limited to high latitudes.

Atmospheric waves, namely gravity waves, planetary waves, and tidal waves, affect both regions of infrasound reflections. Their effects could be quite substantial but the quantitative knowledge of these effects is still limited. The major midwinter stratospheric warming has very pronounced effect on the height profile of temperature. Since the index of refraction of infrasonic waves is a sensitive function of temperature, stratospheric warmings are capable to strongly affect both the infrasonic waves reflected from the middle–upper stratosphere and from the lower thermosphere.

There are also sporadic effects like earthquakes, which excite infrasound and gravity waves, but their overall impact on infrasound propagation is small.

Both the stratosphere and thermosphere experience also long-term changes and trends, in recent decades of predominantly anthropogenic origin (greenhouse effect, ozone depletion). These long-term changes are small but continuous, so they do not affect behavior of infrasonic waves on short-term scales but might have some effect on long-term scales like changes from decade to decade.

Acknowledgements Support by the Grant Agency of the Czech Republic via Grants 15-03909S and 13-09778P is acknowledged and the European Commission's project ARISE2 (Grant Agreement 653980).

References

Albers JR, Birner T (2014) Vortex preconditioning due to planetary and gravity waves prior to sudden stratospheric warmings. J Atmos Sci 71:4028–4054. https://doi.org/10.1175/JAS-D-14-0026.1

Altadill D, Apostolov EM, Boska J, Lastovicka J, Sauli P (2004) Planetary and gravity wave signatures in the F region ionosphere with impact to radio propagation predictions and variability. Annals Geophys 47:1109–1119

Andrioli VF, Fritts DC, Batista PP, Clemensha BR, Janches D (2013) Diurnal variation in gravity wave activity at low and middle latitudes. Ann Geophys 31:2123–2135. https://doi.org/10.5194/angeo-31-2123-2013

Angot G, Keckhut P, Hauchecorne A, Claud C (2012) Contribution of stratospheric warmings to temperature trends in the middle atmosphere from the lidar series obtained at Haute-Provence Observatory (44°N). J Geophys Res 117:D21102. https://doi.org/10.1029/2012JD017631

Assink J, Smets P, Marcillo O, Weemstra C, Lalande J-M, Waxler R, Evers L (2019) Advances in infrasonic remote sensing methods. In: Le Pichon A, Blanc E, Hauchecorne A (eds) Infrasound monitoring for atmospheric studies, 2nd edn. Springer, Dordrecht, pp 605–632

Astafyeva E, Lognonne P, Rolland L (2011) First ionospheric images of the seismic fault slip on the example of the Tohoku-oki earthquake. Geophys Res Lett 38:L22104. https://doi.org/10.1029/2011GL049623

Azeem I, Crowley G, Honniball C (2015) Global ionospheric response to the 2009 sudden stratospheric warming event using ionospheric data assimilation four-dimensional (IDA4D) algorithm. J Geophys Res Space Phys 120:4009–4019. https://doi.org/10.1002/2015JA020993

Baker DM, Davies K (1969) F2-region acoustic waves from severe weather. J Atmos Sol-Terr Phys 31:1345–1352

Baker DN, Blake JD, Klebesadel WR, Higbie PR (1986) Highly relativistic electrons in the Earth's outer magnetosphere, 1, lifetimes and temporal history 1979–1984. J Geophys Res 91:4265–4273

Beig G (2011) Long-term trends in the temperature of the mesosphere/lower thermosphere region: 1. Anthropogenic influences. J Geophys Res 116:A00H11. https://doi.org/10.1029/2011ja016646

Besalpov PA, Savina ON (2015) Exponential and local Lamb waves in the nonisothermal atmosphere as an obstacle to the acoustic-gravity disturbance propagation up to the ionosphere. J Atmos Sol-Ter Phys 123:137–143. https://doi.org/10.1016/j.jastp.2015.01.002

Blanc E (1985) Observations in the upper atmosphere of infrasonic waves from natural or artificial sources: a summary. Ann Geophys 3:673–688

Blanc E, Pol K, Le Pichon A, Hauchecorne A, Keckhut P, Baumgarten G, Hildebrand J, Höffner J, Stober G, Hibbins R, Espy P, Rapp M, Kaifler B, Ceranna L, Hupe P, Hagen J, Rüfenacht R, Kämpfer N, Smets P (2019) Middle atmosphere variability and model uncertainties as investigated in the framework of the ARISE project. In: Le Pichon A, Blanc E, Hauchecorne A (eds) Infrasound monitoring for atmospheric studies, 2nd edn. Springer, Dordrecht, pp 845–887

Boska J, Sauli P, Altadill D, Sole G, Alberca LF (2003) Diurnal variation of the gravity wave activity at midlatitudes of the ionospheric F region. Stud Geoph Geod 47:579–586

Bourassa AE, Degenstein DA, Randel WJ, Zawodny JM, Kyrölä E, McLinden CA, Sioris CE, Roth CZ (2014) Trends in stratospheric ozone derived from merged SAGE II and Odin-ORISIS satellite observations. Atmos Chem Phys 14:6983–6994. http://www.atmos-chem-phys.net/14/6983/2014/

Bremer J (2008) Long-term trends in the ionospheric E and F1 regions. Ann Geophys 26:1189–1197

Buonsanto MJ (1999) Ionospheric storms—a review. Space Sci Rev 88:563–601. https://doi.org/10.1023/A:1005107532631

Butchart N (2014) The Brewer-Dobson circulation. Rev Geophys 52:157–184. https://doi.org/10.1002/2013RG000448

Ceranna L, Le Pichon A, Green DN, Mialle P (2009) The Buncefield explosion: a benchmark for infrasound analysis across Central Europe. Geophys J Int 177:491–508. https://doi.org/10.1111/j.1365-246x.2008.03998.x

Chernogor LF (2015) Ionospheric effects oif the Chelyabinsk meteoroid. Geomagn Aeron 55:353–368

Chum J, Athieno R, Baše J, Burešová D, Hruška F, Laštovička J, McKinnell LA, Šindelářová T (2012a) Statistical investigation of horizontal propagation of gravity waves in the ionosphere over Europe and South Africa. J Geophys Res Space Phys 117. https://doi.org/10.1029/2011ja017161

Chum J, Hruska F, Zednik J, Lastovicka J (2012b) Ionospheric disturbances (infrasound waves) over the Czech Republic excited by the 2011 Tohoku earthquake. J Geophys Res 117:A08319. https://doi.org/10.1029/2012JA017767

Ern M, Ploeger F, Preusse P, Gille JC, Gray LJ, Kalisch S, Mlynczak MG, Russell JM, Riese M (2014) Interaction of gravity waves with QBO: a satellite perspective. J Geophys Res Atmos 119:2329–2355. https://doi.org/10.1002/2013JD020731

Farges T, Coulouvrat F, Gallin LJ, Marchiano R (2019) Infrasound for detection, localization, and geometrical reconstruction of lightning flashes. In: Le Pichon A, Blanc E, Hauchecorne A (eds) Infrasound monitoring for atmospheric studies, 2nd edn. Springer, Dordrecht, pp 911–938

Fritts DC, Alexander MJ (2003) Gravity wave dynamics and effects in the middle atmosphere. Rev Geophys 41(1):1003. https://doi.org/10.1029/2001RG000106

Fritts DC, Vadas SL, Wan K, Werne JA (2006) Mean and variable forcing of the middle atmosphere by gravity waves. J Atmos Sol-Terr Phys 68:247–265. https://doi.org/10.1016/j.jastp.2005.04.010

Galvan DA, Komjathy A, Hickey MP, Stephens P, Snively J, Song YT, Butala MD, Mannucci AJ (2012) Ionospheric signatures of Tohoku-Oki tsunami of March 11, 2011: model comparisons near the epicenter. Radio Sci 47:RS4003. https://doi.org/10.1029/2012rs.005023

Georges TM (1967) ESSA Technical report IER 57-ITSA 54. Ionospheric effects of atmospheric waves. Institute for Telecomunication Sciences and Aeronomy, Boulder, 341 pp

Georges TM (1973) Infrasound from convective storms: examining the evidence. Rev Geophys Space Phys 11:571–594

Hao YQ, Xiao Z, Zhang DH (2012) Multi-instrument observation on co-seismic ionospheric effects after great Tohoku earthquake. J Geophys Res 117:A02305. https://doi.org/10.1029/2011JA017036

Hao YQ, Xiao Z, Zhang DH (2013) Teleseismic magnetic effects (TMDs) of 2011 Tohoku earthquake. J Geophys Res Space Phys 118:3914–3923. https://doi.org/10.1002/jgra.50326

Harris NRP et al (2008) Ozone trends at northern mid- and high latitudes—a European perspective. Ann Geophys 26:1207–1220. https://doi.org/10.5194/angeo-26-1207-2008

Hegglin M, Plummer DA, Shepherd TG, Scinocca JF, Anderson J, Froidevaux L, Funke B, Hurst D, Rozanov A, Urban J, von Clarman T, Walker KA, Wang HJ, Tegtmeier S, Weigel K (2014) Vertical structure of stratospheric water vapour trends derived from merged satellite data. Nat Geosci 7:768–776

Hickey MP, Schubert G, Walterscheid RL (2001) Acoustic wave heating of the thermosphere. J Geophys Res Space Phys 106(A10):21453–21548

Hoffmann L, Xue X, Alexander MJ (2013) A global view of stratospheric gravity wvae hotspots located with Atmospheric Infrared Sounder observations. J Geophys Res Atmos 118:416–434. https://doi.org/10.1029/2012JD018658

Hood L, Rossi S, Beulen M (1999) Trends in lower stratospheric zonal winds, Rossby wave breaking behavior, and column ozone at northern midlatitudes. J Geophys Res Atmos 104 (D20):24321–24339

Huang FT, Mayr HG, Russell III JM, Mlynczak MG (2014) Ozone and temperature decadal trends in the stratosphere, mesosphere and lower thermosphere, based on measurements from SABER on TIMED. Ann Geophys 32:935–949. www.ann-geophys.net/32/935/2014/

IPCC (Intergovernmental Panel on Climate Change) (2007) In: Solomon S et al (eds) Climate change 2007: the physical science basis. Cambridge Univ. Press, Cambridge

IPCC (Intergovernmental Panel on Climate Change) (2013) In: Stocker TF et al (eds) Climate change 2013: the physical science basis. Cambridge Univ. Press, Cambridge

Jadin EA (1997) Diagnosis of long-term changes in stratospheric dynamics. Izv FIZ Atmos Ocean 33:787–794

Jiang Q, Doyle JD, Reinecke A, Smith RB, Eckermann SD (2013) A modeling study of stratospheric waves over the Southern Andes and Drake Passage. J Atmos Sci 70:1668–1689. https://doi.org/10.1175/JAS-D-12-0180.1

Kishore P, Venkat Ratnam M, Velicogna I, Sivakumar V, Bencherif H, Clemesha BR, Simonich DM, Batista PP, Beig G (2014) Long-term trends observed in the middle atmosphere temperatures using ground based LIDARs and satellite borne measurements. Ann Geophys 32:301–317. www.ann-geophys.net/32/301/2014/

Kozubek M, Križan P, Laštovička J (2015) Northern hemisphere stratospheric winds in higher midlatitudes: longitudinal distribution and long-term trends. Atmos Chem Phys 15:2203–2213. http://www.atmos-chem-phys.net/15/2203/2015/

Krasnov VM, Drobzheva Ya V, Laštovička J (2006) Recent advances and difficulties of infrasonic wave investigation in the ionosphere. Surv Geophys 27:169–209

Krasnov VM, Drobzheva Ya V, Venart JES, Laštovička J (2003) A re-analysis of the atmospheric and ionospheric effects of the Flixborough explosion. J Atmos Sol-Terr Phys 65:1205–1212

Laine M, Latva-Pukkila N, Kyrölä E (2014) Analysing time-varying trends in stratospheric ozone time series using the state space approach. Atmos Chem Phys 14:9707–9725. http://www.atmos-chem-phys.net/14/9707/2014/

Laštovička J (1996) Effects of geomagnetic storms in the lower ionosphere, middle atmosphere and troposphere. J Atmos Terr Phys 58:831–843

Laštovička J (2006) Forcing of the ionosphere by waves from below. J Atmos Sol-Terr Phys 68:479–497. https://doi.org/10.1016/j.jastp.2005.01.018

Laštovička J (2009) Lower ionosphere response to external forcing. Adv Space Res 43:1–14

Laštovička J (2013) Trends in the upper atmosphere and ionosphere: recent progress. J Geophys Res Space Phys 118:3924–3935. https://doi.org/10.1002/jgra.50341

Laštovička J, Akmaev RA, Beig G, Bremer J, Emmert JT, Jacobi C, Jarvis MJ, Nedoluha G, Portnyagin YI, Ulich T (2008) Emerging pattern of global change in the upper atmosphere and ionosphere. Ann Geophys 26:1255–1268. www.ann-geophys.net/26/1255/2008/

Laštovička J, Baše J, Hruška F, Chum J, Šindelářová T, Horálek J, Zedník J, Krasnov V (2010) Simultaneous infrasonic, seismic, magnetic and ionospheric observations in an earthquake epicenter. J Atmos Sol-Terr Phys 72:1231–1240. https://doi.org/10.1016/j.jastp.2010.08.005

Laštovička J, Šauli P, Križan P, Novotná D (2003) Persistence of the planetary wave type oscillations in foF2 over Europe. Ann Geophys 21:1543–1552

Laštovička J, Solomon SC, Qian L (2012) Trends in the neutral and ionized upper atmosphere. Space Sci Rev 168:113–145. https://doi.org/10.1007/s11214-011-9799-3

Li T, Leblanc T, McDermid IS, Keckhut P, Hauchecorne A, Dou XK (2011) Middle atmosphere temperature trend and solar cycle revealed by long-term Rayleigh lidar observations. J Geophys Res Atmos 116:D00P05. https://doi.org/10.1029/2010jd01527

Makela JJ, Lognonne P, Hebert H, Gehrels T, Rolland L, Aligeyer S, Kherani A, Occhipinti G, Astafyeva E, Coisson P, Loevenbruck A, Clevede E, Kelley MC, Lamouroux J (2011) Imaging

and modeling the ionospheric airglow response over Hawaii to the tsunami generate dby the Tohoku earthquake of 11 March 2011. Geophys Res Lett 38:L00G02. https://doi.org/10.1029/2011gl047860

Marchetti E, Ripepe M, Campus P, Le Pichon A, Brachet N, Blanc E, Gaillard P, Mialle P, Husson P (2019) Infrasound monitoring of volcanic eruptions and contribution of ARISE to the volcanic ash advisory centers. In: Le Pichon A, Blanc E, Hauchecorne A (eds) Infrasound monitoring for atmospheric studies, 2nd edn. Springer, Dordrecht, pp 1141–1162

Meriwether JW, Mirick JL, Biondi MA, Herraro FA, Fesen CG (1996) Evidence for orographic wave heating in the equatorial thermosphere at solar maximum. Geophys Res Lett 23:2177–2180

Meriwether JW, Biondi MA, Herraro FA, Fesen CG, Hallenback DC (1997) Optical interferometric studies of the nighttime equatorial thermosphere; enahanced temperatures and zonal wind gradients. J Geophys Res 102:20041–20058

Monier E, Weare BC (2011) Climatology and trends in the forcing of the stratospheric zonal-mean flow. Atmos Chem Phys 11:12751–12771

Occhipinti G, Rolland L, Lognonne P, Watada S (2013) From Sumatra 2004 to Tohoko-Oki 2011: the systematic GPS detection of the ionospheric signatures induced by tsunamigenic earthquakes. J Geophys Res Space Phys 118:3626–3636. https://doi.org/10.1002/jgra.50322

Osso A, Sola Y, Rosenlof K, Hassler B, Bech J, Lorente J (2015) How robust are trends in the Brewer-Dobson circulation derived from observed stratospheric temperatures? J Clim 28:3024–3039. https://doi.org/10.1175/JCLI-D-14-00295.1

Pancheva D (2001) Non-linear interaction of tides and planetary waves in the mesosphere and lower thermosphere: observations over Europe. Phys Chem Earth Part C 26:411–418

Pilger C, Schmidt C, Bittner M (2013a) Statistical analysis of infrasound signatures in aiglow observations: indications for acoustic resonance. J Atmos Sol-Terr Phys 93:70–79. https://doi.org/10.1016/j.jastp.2012.11.011

Pilger C, Schmidt C, Streicher F, Wust S, Bittner M (2013b) Airglow observations of orographic, volcanic and meteorological infrasound signatures. J Atmos Sol-Terr Phys 104:55–66. https://doi.org/10.1016/j.jastp.2013.08.008

Ploeger F, Abalos M, Birner T, Konopka P, Legras B, Muller R, Riese M (2015) Quantifying the effects of mixing and residual circulation on trends of stratospheric mean age of air. Geophys Res Lett 42:2047–2054. https://doi.org/10.1002/2014GL062927

Pramitha M, Venkat Ratnam M, Taori A, Krishna Murthy BV, Pallamraju D, Vijaya S, Rao B (2015) Evidence for tropospheric wind shear excitation of high-phase-speed gravity waves reaching the mesosphere using the ray tracing technique. Atmos Chem Phys 15:2709–2721. https://doi.org/10.5194/acp-15-2709-2015

Prasad SS, Schneck LJ, Davies K (1975) Ionospheric disturbances by severe tropospheric weather storms. J Atmos Terr Phys 37:1357–1363

Randel WJ (2010) Variability and trends in stratospheric temperature and water vapor. In: Polvani LM, Sobel AH, Waugh DW (eds) Stratosphere: dynamics, transport and chemistry, geophysical monograph series, vol 190, pp 123–135. https://doi.org/10.1029/2009gm000870

Remsberg E (2015) Methane as a diagnostic tracer of changes in the Brewer-Dobson circulation of the stratosphere. Atmos Chem Phys 15:3739–3754. http://www.atmos-chem-phys.net/15/3739/2015/

Ren RC, Yang Y (2012) Changes in winter stratospheric circulation in CMIP5 scenarios simulated by the climate system model FGOALS-s2. Adv Atmos Sci 29:1374–1389. https://doi.org/10.1007/s00376-012-1184-y

Rind D (1977) Heating of lower thermosphere by dissipation of acoustic waves. J Atmos Sol-Terr Phys 39:445–456

Šauli P, Boska J (2001) Tropospheric events and possible related gravity wave activity effects on the ionosphere. J Atmos Sol Terr Phys 63:945–950

Sentman DD, Wescott EM, Picard RH, Winick JR, Stenbaek-Nielsen HC, Dewan EM, Moudry DR, Sao Sabbas FT, Heavner MJ, Morrill J (2003) Simultaneous observations of mesospheric gravity waves and sprites generated by a Midwestern thunderstorm. J Atmos Sol-Terr Phys 65:537–550. https://doi.org/10.1016/S1364-6826(02)00328-0

Simmons AJ, Poli P, Dee DP, Berrisford P, Hersbach H, Kobayashi S, Peubey C (2014) Estimating low-frequency variability and trends in atmospheric temperature using ERA-Interim. Q J R Meteorol Soc 140:329–353. https://doi.org/10.1002/qj.2317

Šindelářová T, Buresova D, Chum J, Hruska F (2009) Doppler observations of infrasonic waves of meteorological origin at ionospheric heights. Adv Space Res 43:1644–1651. https://doi.org/10.1016/j.asr.2008.08.022

Smets PSM, Evers LG (2014) The life cycle of a sudden stratospheric warming from infrasonic ambient noise observations. J Geophys Res Atmos 119:12084–12099. https://doi.org/10.1002/2014JD021905

Smets P, Assink J, Evers L (2019) The study of sudden stratospheric warmings using infrasound. In: Le Pichon A, Blanc E, Hauchecorne A (eds) Infrasound monitoring for atmospheric studies, 2nd edn. Springer, Dordrecht, pp 605–632

Solomon SC, Qian L, Roble RG (2015) New 3-D simulations of climate change in the thermosphere. J Geophys Res Space Phys 120:2183–2193. https://doi.org/10.1002/2014JA020886

Tsugawa T, Saito A, Otsuka Y, Nishioka M, Maruyama T, Kato H, Nagatsuma T, Murata KT (2012) Concentric waves observed in the ionosphere after the 2011 Tohoku earthquake. CAWSES-II TG4 Newsletter 8:2–4

Urban J, Lossow S, Stiller G, Read W (2014) Another drop in water vapor, EOS. Trans AGU 95 (27):245–246. https://doi.org/10.1002/2014EO27

Vadas SL, Fritts DC (2004) Thermospheric responses to gravity waves arising from mesoscale convective complexes. J Atmos Sol-Ter Phys 66:781–804. https://doi.org/10.1016/j.jastp.2004.01.25

Vadas SL, Fritts DC (2005) Thermospheric responses to gravity waves: Influences of increasing viscosity and thermal diffusivity. J Geophys Res 110:D15103. https://doi.org/10.1029/2004JD005574

Vadas SL, Fritts DC (2006) Influence of solar variability on gravity wave structure and dissipation in the thermosphere from tropospheric convection, J Geophys Res 111:A10S12. https://doi.org/10.1029/2005ja011510

Vadas SL (2007) Horizontal and vertical propagation and dissipation of gravity waves in the thermosphere from lower atmospheric and thermospheric sources. J Geophys Res 112:A06305. https://doi.org/10.1029/2006JA011845

Vadas SL, Nicholls MJ (2012) The phases and amplitudes of gravity waves propagating and dissipating in the thermosphere: theory. J Geophys Res 117:A05322. https://doi.org/10.1029/2011JA017426

Várai A, Homonnai V, Jánosi IM, Müller R (2015) Early signatures of ozone trend reversal over the Antarctic. Earth's Future 3:95–109. https://doi.org/10.1002/2014EF000270

Walterscheid RL, Hickey MP (2011) Group velocity and energy flux in the thermosphere: limits on the validity of group velocity in a viscous atmosphere. J Geophys Res 116:D12101. https://doi.org/10.1029/2010JD014987

Waxler R, Assink J (2019) Propagation modeling through realistic atmosphere and benchmarking. In: Le Pichon A, Blanc E, Hauchecorne A (eds) Infrasound monitoring for atmospheric studies, 2nd edn. Springer, Dordrecht, pp 509–549

Yeh KC, Liu CH (1974) Acoustic-gravity waves in the upper atmosphere. Rev Geophys 12:193–216. https://doi.org/10.1029/RG012i002p00193

Yiğit E, Medvedev AS (2012) Gravity waves in the thermosphere during a sudden stratospheric warming. Geophys Res Lett 39:L21101. https://doi.org/10.1029/2012GL053812

Yiğit E, Medvedev AS (2015) Internal wave coupling processes in Earth's atmosphere. Adv Space Res 55:983–1003. https://doi.org/10.1016/j.asr.2014.11.020

Zhang X, Tang L (2015) Traveling ionospheric disturbances triggered by the 2009 North Korean underground nuclear explosion. Ann Geophys 33:137–142. https://doi.org/10.5194/angeo-33-137-2015

Zou C-Z, Qian H, Wang W et al (2014) Recalibration and merging of SSU observations for stratospheric temperature trend studies. J Geophys Res Atmos 119:13180–13205. https://doi.org/10.1002/2014JD021603

Chapter 26
Temperature Trends Observed in the Middle Atmosphere and Future Directions

Philippe Keckhut, Chantal Claud, Beatriz Funatsu, Alain Hauchecorne, Pauline Maury, Sergey Khaykin, Alexis Le Pichon and Wolfgang Steinbrecht

Abstract Temperature trends in the middle atmosphere were derived from several temperature datasets including radiosondes, rocketsondes, lidars, and from successive radiometers onboard satellites like the Stratospheric Sounder Unit (SSU) and the Advanced Microwave Sounding Unit (AMSU). All exhibits limitation for deriving accurate trends, while none of them were set up for climate issues. While ground-based suffer discontinuities, satellite measurements have atmospheric tides interferences depending on their orbits and sometimes drifting. For the future, ground-based continuity will be improved concerning their quality check for climate issues and need to continue at some reference locations and operational meteorological radiometers will be onboard satellite having stable orbits. GPS occultation technique will offer a much better coverage of the lower stratosphere with fewer risks of bias compared to in situ sensors. Meteorological analyses will require improved models of the mesospheric dynamical processes including gravity waves. In this regard, assimilated wind information will be highly strategic.

P. Keckhut (✉) · A. Hauchecorne · P. Maury · S. Khaykin
Laboratoire Atmosphères Milieux et Observations Spatiales/IPSL, CNRS, UMR 8190, UVSQ, UPMC, Guyancourt, France
e-mail: keckhut@latmos.ipsl.fr

C. Claud
Laboratoire de Météorologie Dynamique (LMD) CNRS, Ecole Polytechnique, Palaiseau, France

B. Funatsu
CNRS, Université de Nantes, UMR 6554 LETG, Nantes, France

A. Le Pichon
CEA, DAM, DIF, F-91297 Arpajon, France

W. Steinbrecht
Meteorologisches Observatorium, Deutscher Wetterdienst, Hohenpeißenberg, Germany

A. Le Pichon et al. (eds.), *Infrasound Monitoring for Atmospheric Studies*,
https://doi.org/10.1007/978-3-319-75140-5_26

26.1 Introduction

Associated with the global surface warming due to greenhouse gases, a long-term cooling of the middle atmosphere (around 10–90 km) is expected. Early numerical simulations have shown that this cooling is one order of magnitude larger than the warming at surface and can be detected. Then, this signal is considered as a fingerprint of the climate changes induced by greenhouse gases increases (Ramanathan et al. 1987). The main issue to access the temperature changes of the vertical profile on a decadal scale is the availability of long series of observations in the upper atmosphere. Those observations, not initiated for climate change issues, are indeed highly inhomogeneous in time, in space, and in quality exhibiting drifts, and abrupt changes that are not favorable for global trend detection and quantification. The second issue in the stratosphere (10–50 km) concerns the other sources of inter-annual variability such as solar variability, major volcanic eruptions (providing aerosols in the stratosphere for month/years), and stratospheric ozone changes that are also induced by increasing anthropic activities. However, the time evolution as well as the vertical behavior is key parameters to separate and quantify the different forcings, either natural or anthropic. So the evolution of the 3D thermal structure of our atmosphere appears as an important information required to understand climate changes (Santer et al. 1996) and then is an essential input for conducting the analyses of the inter-governmental panel on climate change (IPCC 1996). However, the first significant investigations were only initiated in the frame of the ozone assessment conducted by the World Meteorological Organization (WMO 1990). These assessments are also conducted within the World Climate Research Program, the SPARC (Stratospheric Processes And their Role in Climate) project that has led several temperature trend reviews (Ramaswamy et al. 2001; Randel et al. 2009), while the mesosphere has been also specifically studied (Beig et al. 2003). With careful inspection of existing datasets, bias and drifts have been corrected and temperature trend estimates were retrieved and the cooling detected; however, the quantification and the vertical description for the whole middle atmosphere and all latitudes remains an issue. Important collective efforts in the future will be required to extend ad hoc datasets and complementary information to better understand upper atmospheric changes under both natural and anthropic origins.

Here, a review of analyses performed in the last decades is presented for the stratosphere (Sect. 26.2) and for the mesosphere (Sect. 26.3) that are covered by different observational techniques. Then, the contribution of numerical models and meteorological analyses and their comparisons with direct observations is presented in Sect. 26.4. Finally, future potential directions are proposed in Sect. 26.5.

26.2 Data Series Available

The first studies were based first on historic balloon and rocketsondes and second using satellite measurements performed by NOAA since 1979 and the lidar sounding conducted within the Network for the Detection of Stratospheric Changes (NDSC) that was renamed NDACC (Network for the Detection of Atmospheric Composition Changes) when observations were extended to the upper troposphere.

26.2.1 Radiosondes

These data developed for meteorological needs in the 1940s and established as a growing global network during the geophysical year in 1956 were the first natural data source for climate research for the upper air domain. The basic concept consists in measuring the temperature with a thermistor coupled with a radio emitter onboard a balloon going up from the ground to an altitude of 10–40 km according to the balloon-type and meteorological conditions. While the first temperature trend estimates were performed with the data from this worldwide network and a strong international coordination insured by WMO, the main limitations came from the time discontinuity at different sites due to sensor changes (Gaffen 1994) Especially above 30 km, the accuracy of the temperature measurements is very limited, although the different national manufactures have improved their sensors significantly over the last decades. Considerable efforts, mainly by the NOAA, have been performed to document such inhomogeneities and many attempts to correct or use a selection of specific stations have been performed, leading to several subsets that complicate to draw firm conclusions as the spatial representativeness is different and reduced. Note that even with all available stations, land/sea distribution of balloon sites induces a strong spatial bias. To avoid such effect, the Berlin group made global daily contour maps from individual radiosonde profiles to provide regular temperature grid on the Northern Hemisphere (Labitzke and van Loon 1995).

26.2.2 Rocketsondes

In the frame of the space conquest, an intensive program of systematic upper atmospheric sounding with rocket launches has been conducted by US, Soviets, and Japan from 1960s up to mid-1990s. However, the cost and alternative emerging techniques like lidars from the ground and satellite measurements have probably led to stop these long-term data series (Finger et al. 1993). Temperature measurements from meteorological rockets were performed from the apogee (80–100 km). These measurements were performed using small rocket (around 2 m), from a payload

equipped with a thermistor falling from the rocket apogee under a parachute or using a falling sphere that allows to deduce density profiles from their trajectory recorded by a ground-based radar (Schmidlin 1991). These datasets provided the first data series covering the altitude range from 25 to 75 km over 2–3 decades over around 13 sites. Large corrections (Lübken et al. 1994) need to be applied (aerothermic, aerodynamic) and an accuracy of around 1 K is achieved. However, changes of sensor and time of measurements need to be taken into account for accurate trend estimates.

26.2.3 Lidar

A more recent technique based on the vertical emission of a laser pulse allows to collect backscattering light by molecules and deduce air density from 30 to around 80 km height (Hauchecorne et Chanin 1980). This technique allows temperature retrieval with an accuracy of less than 1 K below 70 km. Systematic measurements have been performed since 1979 at Observatory of Haute-Provence (OHP) and more recently from several other sites within the Network of the Detection of Atmospheric Composition Changes) since 1991 (Kurylo et Salomon 1990). The main bias is found for the highest altitudes and around 30 km. Only five sites provide regular data series over more than a decade. These series have revealed before 1995 a cooling that was somehow similar to the rockets.

26.2.4 Satellite Data

If numerous techniques have been developed from space for temperature measurements in the middle atmosphere, only two series in space have been developed through successive launches of the same instruments on different platforms. Others are research instruments that insure measurement over several years except few of them that reach nearly a decade. The first one is based on the thermal infrared radiance measurements (Nash et Forester 1986) and the second one corresponds to the microwave bands (Spencer et Christy 1993). A temperature monitoring was possible, thanks to the succession of NOAA satellites and nowadays continues under the coordination of all space agency through the sentinel strategy (Aschbacher 2008).

The Stratospheric Sounder Unit (SSU), with several radiometers measuring the CO2 radiance, allows the retrieval of mean temperature of thick layers (10–15 km) up to the lower mesosphere since 1979 up to 2006. One specific problem with SSU was that CO2, which changed over this period of time, was supposed to be monitored and these problems needed to be solved (Shine et al. 2008).

Since 1998, the AMSU (Advanced Microwave Sounding Unit) has progressively replaced SSU and provides temperature measurements over thinner bands in

the middle atmosphere with 6 out of 12 radiometers in the oxygen band 50–58 GHz. AMSU instrument on NOAA satellites 15, 16, 17, 18, and 19, respectively, launched in 1998, 2000, 2002, 2005, and 2009, with different lifetimes. Note that temperature provided by AMSU on NOAA-16, that is the longest series (some channels of NOAA15 have experienced problems), is in good agreement with OHP lidar (Funatsu et al. 2008). AQUA and METOP platforms have also onboard AMSU instruments with a more stable orbit that avoids tidal interferences.

One of the main difficulties with SSU and AMSU series is their cross-compatibility and their ability to insure a sufficient time continuity to derive accurate temperature trends. NOAA used the temperature series obtained from US rocket sites (Finger et al. 1993). However, orbit drifts have induced large drift of the time of measurements that have induced temperature drifts and discontinuities between instruments onboard different satellites (Keckhut et al. 2001). Adjustments using zonal mean temperature (Nash and Forester 1986) had partially canceled out such discontinuities as shown when data were compared with the OHP lidar (Keckhut et al. 2011). The continuation of the series was performed by two groups that finally agree (Seidel et al. 2016). Recent platforms having stable orbits and carrying AMSU do not face these problems associated with atmospheric tides.

Other space observations were available through research experiments despite they were not longer than a decade; the NASA/UARS mission (Upper atmosphere Research Satellite) has provided the most complete data on middle atmosphere energy inputs, winds, and chemical composition ever gathered from 1991 to 2005; more recently, Envisat (ENVIronment SATellite) launched in 2002 by ESA with 10 instruments aboard dedicated to the middle atmosphere aboard running up to 2012 for some of them, is the largest civilian Earth observation mission, the NASA/AURA mission launched in 2004 provides long series of temperature observations using the Microwave Limb Sounder, and finally the SABER (Sounding of the atmosphere using Broadband Emission Radiometry) launched in 2001 is one of the four instruments on NASA's TIMED (Thermosphere Ionosphere Mesosphere Energetics Dynamics) satellite. The primary goal of the SABER experiment is to provide the data needed to advance our understanding of the fundamental processes governing the energetics, chemistry, dynamics, and transport in the mesosphere and lower thermosphere.

26.3 Temperature Trends in the Stratosphere

During the first temperature trend assessment (Ramaswamy et al. 2001), ground-based measurements were largely used. Balloon series since the Geophysical year (1956) exhibit regular measurements over large geographical coverage (except sea), but they suffer from discontinuities and manufacturer differences from one country to another and the individual quality on a long-term was then uncertain in many sites. NOAA and many other group filter and correct these series. Then, cooling amplitude retrieved from these different subsets either geographical

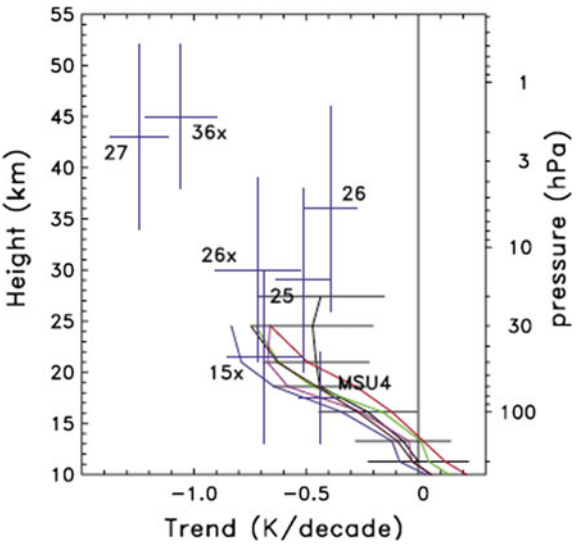

Fig. 26.1 Vertical profiles of temperature trends over the period 1979–2005, deduced from radiosondes and SSU channels (Randel et al. 2009)

or subject to quality check slightly differ but show all a cooling increase with altitude with larger uncertainties over tropics and at high latitudes (Fig. 26.1).

Rocketsondes and lidars, even if located at a limited number of sites, also clearly identify a cooling of 1 K/decade in the upper stratosphere when averaged (Fig. 26.2). The initial dataset composed by the successive SSU present large discontinuities (Wild et al. 1995; Keckhut et al. 2001), while the zonal mean temperature derived by the so-called "Nash method" reveal much better agreement with individual ground-based sites (Keckhut et al. 2011) as shown in Fig. 26.2. The Chemistry-Climate Model Validation project (CCMVal), which includes numerical models with a good representation of the stratosphere and an interactive chemistry (Eyring et al. 2006, 2007), also revealed an overall good agreement with observations. However, the temperature plateau observed in 1995 as well as the simultaneous shift between the SSU and AMSU series lead to reinvestigate individual series revealing some uncertainty in the observation series mainly when individual sites are evaluated.

The next temperature trend assessments had a strong focus on SSU data series (Randell et al. 2009) and two groups insure independent re-analyses of the SSU analyses, calibration, and adjustments that lead first to large differences on trends (larger than provided by models); after a fruitful collaboration between both teams, they converged to a similar combination of the successive SSU measurements (Wang and Zhou 2013; Seidel et al. 2016) and trend estimates. The SSU series show that after 1995, the previously observed cooling stopped. It is not clear if this relative slowdown of the trends is due to real climate changes, related to the combination of other forcings like volcanoes, solar activity, or to internal dynamic fluctuations, while SSU series were stopped. This slowdown was also observed on global surface temperature (Trenberth and Fasullo 2013) and was also clearly

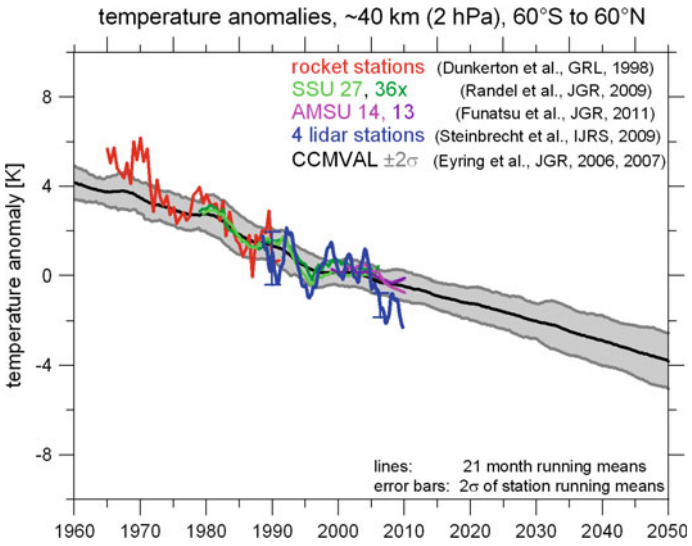

Fig. 26.2 Temperature evolution in the mid–upper stratosphere deduced by US rockesondes (Dunkerton et al. 1998), SSU (Randel et al. 2009) and AMSU (Funatsu et al. 2011) channels, lidar stations (Steinbrecht et al. 2009) and CCMVAL models (Eyring et al. 2006, 2007) (@ W Steinbrecht)

reported by all lidars (Steinbrecht et al. 2009; Keckhut et al. 2011) and also can be noted on CCMVal models (Fig. 26.2).

The AMSU series insure the continuity of the SSU series with different vertical weighting functions. Similar to SSU, the NOAA satellites with the longest lifetime have drifting orbit and so their time of measurements for a given location changes. The comparison of NOAA 15 and 16 confirms that the amplitude of the difference can be due to the combined effects of atmospheric tides and orbit drifts (Keckhut et al. 2015) and can be somehow corrected. After tidal adjustment, a cooling can be derived from this decadal series. However, tide corrections are complex as tides exhibit seasonal changes and include non-migrating components that are difficult to quantify. Some platforms exhibit stable orbit and can be used to derive temperature trends (Funatsu et al. 2016) and confirm that cooling continue after the slowdown with a similar amplitude (je dirais plutot reduced que similar).

Comparisons of lidar series with corresponding SSU channels (Fig. 26.3) also show large differences (Keckhut et al. 2011) that were not obviously due to any instrumental origins. The analyses of AMSU observations show that large uncertainties can be associated with time and space sampling (Funatsu et al. 2011) for ground-based measurements. Analyses of AMSU series show that a factor of 2 can be found between zonal means decadal trends and regional estimates and between daily measurement and less frequent time sampling. The differences between two lidar series obtained in two different alpine sites were investigated using AMSU series extracted above both sites (Funatsu et al. 2011). This study seems to indicate that

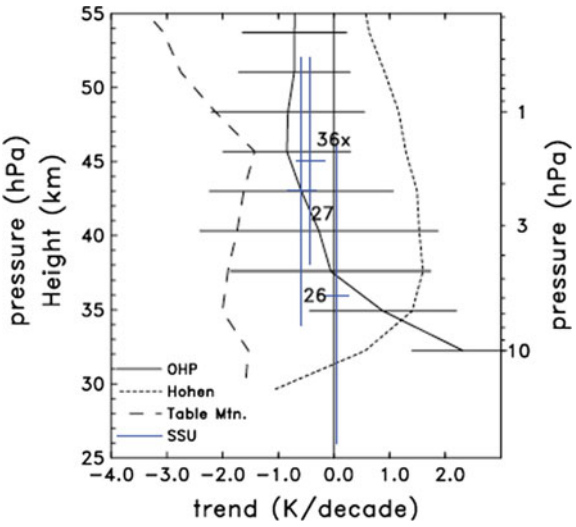

Fig. 26.3 Vertical temperature trends deduced over the period 1988–2005 from lidar and SSU (Randel et al. 2009)

these disparities could be representative of atmospheric variability. For example, the stratospheric temperature at Hohenpeissenberg (Germany) is systematically colder in winter and warmer in summer than at Observatory of Haute-Provence (France). Because temperature gradients are strong and highly variable particularly in wintertime due to the wobbling of the polar vortex, even a distance of hundreds of km can induce systematic differences. Different sampling is a considerable issue during winter in the northern hemisphere due to the occurrence of sudden stratospheric warmings that can induce temperature changes of several tens of Kelvin during typically a week (Hauchecorne et al. 2019; Smets et al. 2019). The new trend analysis of OHP lidar data, based on temperature distributions, shows that the frequent occurrence of stratospheric warming (Maury et al. 2016) has a large impact on trend estimates, and taking into account such effect reveals larger radiative trends (Angot et al. 2012), indicating that there is a strong dynamical feedback.

Recent lidar series also confirm that trends over the last decade are similar to the previous estimates derived from rocketsondes series (Fig. 26.4) and OHP lidar starting in 1979. However, temperature trends derived with AMSU on the same period are smaller at all sites (Funatsu et al. 2016) around 32 and 36 km. When lidar and AMSU series were compared on a daily basis, smaller variability is also observed from space, maybe due to the larger vertical sampling (Funatsu et al. 2008).

The new NOAA STAR version of SSU series from 1979 to 2006 (Zou et al. 2014) was extended to 2015 using MLS (AURA), SABER (TIMED), and AMSU (NOAA) series using a set of empirically weighting functions and the overlap periods of several years (McLandress et al. 2015; Randel et al. 2016), while the recent temperature series exhibit much better vertical resolution. Linear trends calculated from the entire 1979–2015 period show good agreement among the

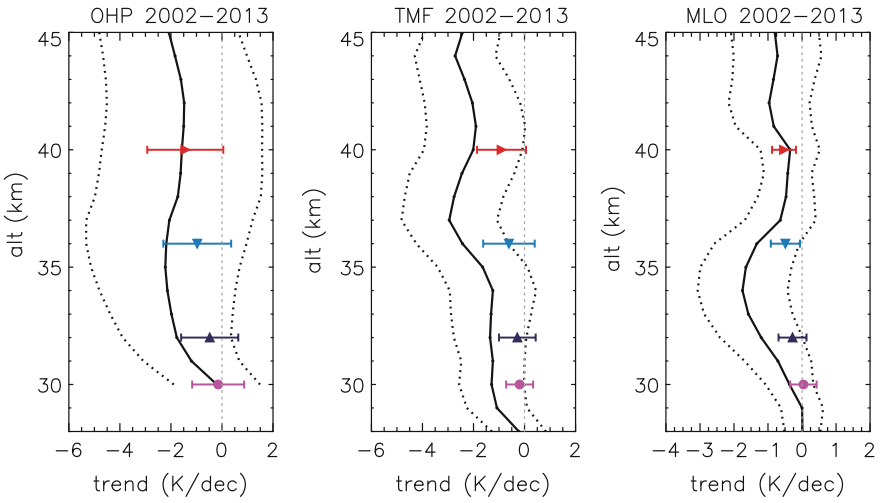

Fig. 26.4 Temperature trends derived from three lidar sites and extrapolated AMSU series (NOAA 18) from Funatsu et al. (2016)

different datasets with slightly larger cooling for the combination of SSU and AMSU, but all confirm the global cooling of the middle and upper stratosphere (−0.5 to −0.6 K/decade), with a slight increase in trends with altitude. As observed with lidar (Funatsu et al. 2016), trends for 1979–2015 are somewhat smaller than the trends over 1980–2012 reported in McLandress et al. (2015), due to the temperature plateau between 1995 and 2005. The cause of the asymmetric cooling pattern in the middle–upper stratosphere observed between the two hemispheres with SSU-AMSU merged dataset could confirm the role of stratospheric warmings (Randel et al. 2016).

26.4 Temperature Trends in the Mesosphere and Above

A large set of temperature data series in the mesosphere is provided by rocketsondes operated since the 1960s up to the end of the 1980s. The longest US data series were obtained mainly in tropical and subtropical zones, except for a few sites at mid-latitudes such as Wallops Island. The former USSR provides a smaller network. Nevertheless, the long Russian data series can be found at high, mid-, and low latitudes. A long dataset is also available from a site operated by Japan, at Ryori site (39°N). Trends have been derived by several groups (Beig et al. 2003); however, all these sites have known instrumental evolution and variations in time of measurements. All these discontinuities have been taken into account in a similar

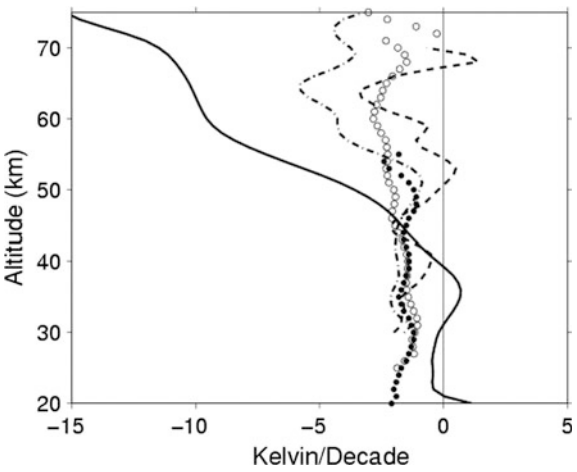

Fig. 26.5 Summer temperature trend profiles from 20 to 75 km at Volgograd (solid line), Wallops Islands (dashed line), OHP (dash-dotted line), Ryori (..), and US low latitude rocketsondes (oo) from Kubicki et al. (2006)

trend re-analyses (Keckhut et al. 1999; Keckhut and Kodera 1999; Kubicki et al. 2006). For summer months, trends are quite similar (Fig. 26.5) and compare well with OHP Rayleigh lidar (Keckhut et al. 1995) with a maximum around 65 km of 3–4 K/decade, decreasing toward the mesopause. However, the Volgograd trend estimates were reduced in such analyses but remained twice the others. The HALOE experiment aboard UARS has provided atmospheric temperature profiles from about 35–86 km for a decade since October 1991 using the solar occultation technique. Despite the fact it has covered only a decade, Remsberg et al. (2002), using a multi-regression analysis, found a significant long-term cooling trend of 1.0–1.6 K per decade at 1 hPa in the tropics.

Temperature can also be deduced from the hydroxyl airglow emissions at around 87 km with different sites coordinated within the Network for the Detection of Mesospheric Changes. Sigernes et al. (2003) conclude that there has been no significant trend during the past 20 years in the above time series, and many other studies reach similar conclusions (Beig et al. 2003; Offermann et al. 2010). Measurements at high and polar latitudes exhibit larger variability, and therefore the detection of trends in this time series remains challenging. Such finding is in agreement with Na lidar series at Colorado (She et al. 1995) showing a temperature trend changing from 5 K/decade at 87 km to −5 K/decade at 101 km, with the trend changing sign at 92 km.

Temperature changes have also been reported above the mesosphere from trends of thermospheric neutral density estimated from satellite drag data (Quian et al. 2011) as well as the turnaround observed at the end of 1990s.

26.5 Temperature Trends on Models and Meteorological Re-Analyses

Middle atmosphere trends have been well established using numerical Chemistry-Climate Models and reproduce similarly the vertical shape of both the warming in the troposphere and the cooling above (Austin et al. 2009). On average, the value of the mean trends of all models is in good agreement with observations (Fig. 26.6), with differences up to 50% among the models. However, they differ much more at high latitudes where the dynamical feedback is more important with large differences between trend estimates at mid-latitudes over Northern hemisphere. Over polar regions, differences are larger with even disagreements about the sign of the trends. At mid- and high latitudes, trends are highly dependent on the seasons and annual mean trend estimates should be avoided for trend inter-comparisons and attribution. One main difference between the different models concerns the occurrence of sudden stratospheric warming (Charlton et al. 2007) that are represented differently from one model to another.

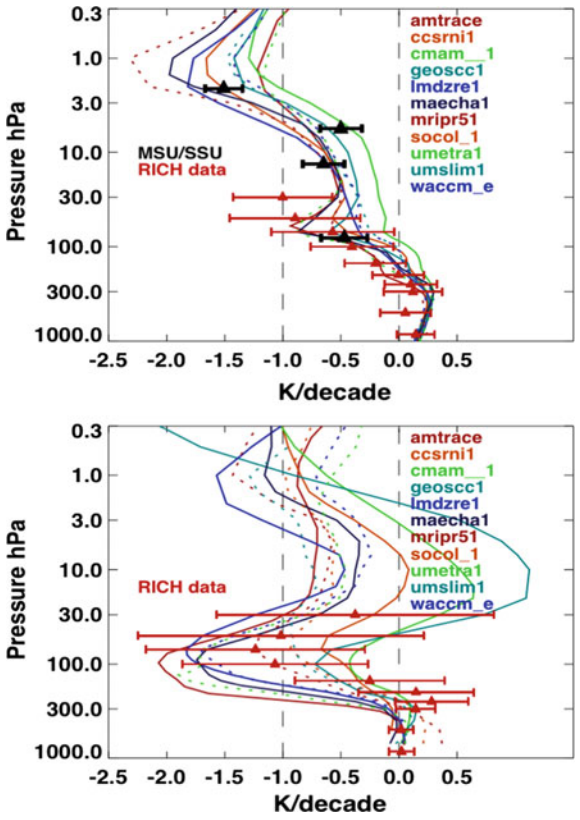

Fig. 26.6 Annual trends (K/decade) on the band between 70°N and 70°S (top) and between 67°N and 90°N (bottom) from several Chemistry-Climate Models compared together in the frame of the CCMVal (Austin et al. 2009) and with the RICH radiosonde dataset. The covered period corresponds to the SSU operation from 1980 to 1999

Meteorological analyses could be a good tool for inter-annual studies and trend estimates since they include different datasets linked with physical equations that should insure spatial and long-term coherency. However, limitations come from the evolution of the observing system and of assimilation methods Haimberger et al. (2012) compared to time series and linear trends of ERA_I temperatures with both MSU records and the profile information provided by radiosondes and found surprisingly a good agreement. However, differences appear in the vicinity of the tropical tropopause probably due to substantial amounts of assimilated warm-biased aircraft data. In the lower stratosphere, all re-analyses, while all constrained by the assimilated radiance data, infrared as well as microwave, exhibit similar cooling (Simmons et al. 2014).

In the middle stratosphere, the different re-analyses show larger differences, due to the different treatments of the change from SSU to AMSU-A. Some meteorological analyses reach the mesosphere, and present large differences with Lidar series (Steinbrecht et al. 2009; Le Pichon et al. 2015) due to the lack of assimilated data in this altitude domain and some deficiencies about gravity waves parametrization and impact of the top sponge layer. As the ARISE, meteorological temperature analyses are very close lidar measurements as well as anomaly correlation up to 35 km and above analyses do not track the observations at all.

While the numerical chemistry-transport models are excellent tools to understand climate changes, the stratospheric dynamics shows large variability when models and observations are compared on a monthly/yearly basis (Simmons et al. 2014). In the upper atmosphere, it is always difficult to figure out the individual contributions of the changes of the dynamical forcing from the troposphere and surface to the specific mesospheric dynamics induced by planetary waves as well as gravity waves and tides (Fig. 26.7).

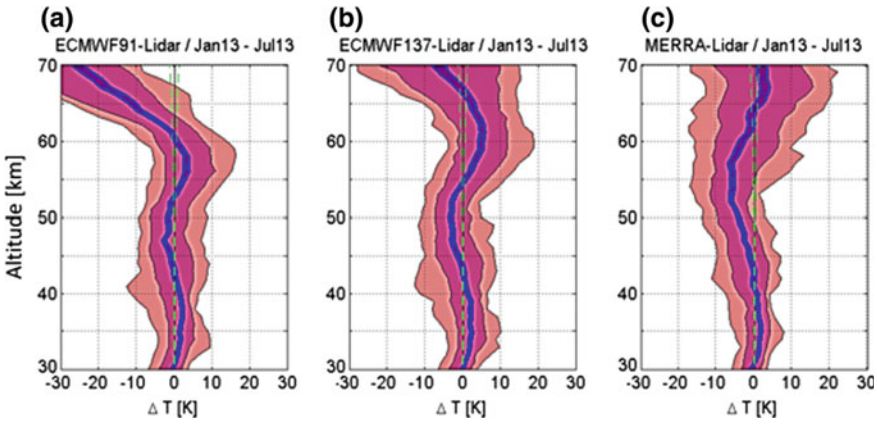

Fig. 26.7 Difference between L91 (**a**), L137 (**b**), and MERRA (**c**) temperature products at 0 h UTC and nightly averaged lidar measurements at Observatory of Haute-Provence versus altitude. Blue lines: standard error of the mean. Green dashed lines: instrumental error bars. Purple and pink regions: 66% and 95% confidence intervals of the differences (Le Pichon et al. 2015)

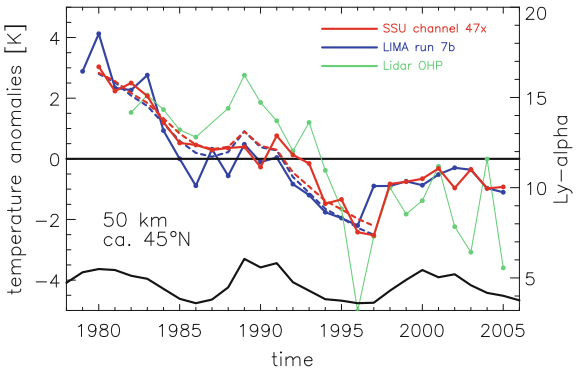

Fig. 26.8 Time series of summer temperature anomalies from the OHP lidar (green) and the LIMA model (blue line) extract above the OHP sites (44°N, 6°E) at 50 km compared with the zonal mean temperature from SSU 47x channel (from Berger and Lübken 2011)

An alternative approach to account more realistic lower atmospheric conditions consists of force models by meteorological analyses in the troposphere and lower stratosphere where re-analyses are quite accurate. A good example is given by the LIMA model (Leibniz- Institute Middle atmosphere) that includes forcing of greenhouse gases and solar activity, interactive ozone chemistry, microphysics, gravity waves, and effects from nonlocal thermodynamic equilibrium. As reported in Fig. 26.8, the model reproduces the large cooling (3–4 K) observed by satellite and lidar series from 1980 to 1995 and changes of radio wave reflection heights and also the trend reduction after 1997 (Berger and Lübken 2011).

26.6 Conclusions and Future Directions

Temperature trend estimates all reveal a cooling in the middle atmosphere with inter-annual variability associated with solar and volcanic forcings. However, individual data series inter-comparisons reveal large differences that are too large to be used to validate numerical simulations. In the stratosphere, operational meteorological satellites present limitations due to orbit changes and sensor evolutions that complicate the time adjustment. Radiosonde network exhibits some inhomogeneities (in time and space) and non-global coverage and we can expect for cost reasons this situation to even in the future. In the mesosphere, the situation is worse while satellite experiments are research oriented with extension shorter than a decade and exhibiting different methods and vertical resolutions. Temperature monitoring in the middle atmosphere is yet required as a complementary information for climate changes, for change associated with ozone recovery, for unpredicted volcanic and solar effects or any other dynamical changes (Newman et al. 2016).

In the future, more long independent series will be required to cross-check temperature evolution and better evaluate bias. In the middle atmosphere,

measurements should remain on a fixed orbit to avoid interferences with atmospheric tides that are difficult to evaluate due to non-migrating component and nonstationary effect (Morel et al. 2004).

In the lower stratosphere, GPS will provide data that can insure a good continuity a global coverage and could be assimilated as soon as the satellite constellation is maintained. Figure 26.9 shows that series are now long enough to start such investigations and compare with operational microwave series. In the stratosphere, AMSU and SSU need to be merged (McLandress et al. 2015; Randel et al. 2016; Zou and Qian 2016). However, ground-based lidar will be useful to check for the adjustment quality during the transition period. Also, addition global observation as IASI series (Hoffman et al. 2014) will be an alternative source of temperature data over at least 40 years that offer independent trend estimates. In the mesosphere, temperature measurements can be deduced from the molecular scattering (Shepherd et al. 2002) from several instruments and hence provide a relatively homogeneous long-term series that can be also merged and used for decadal monitoring.

Homogeneous long-term ground-based measurements, even if local, could be really a good complementary source of data to insure the continuity in case of nonoverlapping of the series from space. Despite the number of radiosonde sites decreases, the increase of their quality check allows a reduced series with a better accuracy for climate issues that can serve as reference. These international initiatives that appear within GRUAN (Siedel et al. 2008) or SHADOZ (Thompson et al. 2003) networks need to be supported on a long-term basis. For the upper atmosphere, temperature lidar series need to continue to exhibit similar reference series up to the mesosphere (Keckhut et al. 2011; Kurylo and Solomon 1990). Finally, for the mesopause region, airglow temperature measurements can complement such references (Bittner et al. 2002; Offermann et al. 2010).

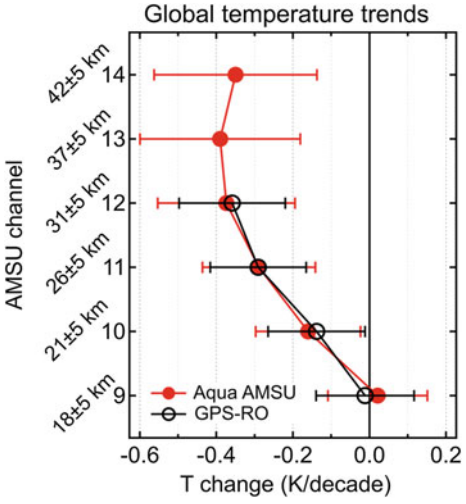

Fig. 26.9 Global temperature trends derived from AMSU series (Funatsu et al. 2016) and GPS cosmic data over the same period and with AMSU vertical weighting function (Khaykin et al. 2017)

Most probably that assimilated wind information using routinely the existing operational infrasound data (Blanc et al. 2016) and global additional temperature datasets as described above will largely improve re-analyses in this domain and will allow to derive accurate trends. Several well-located wind ground-based series using lidar (Chanin et al. 1989) or microwave spectrometers (Rüfenacht et al. 2014) will be quite useful for checking re-analysis outputs.

Temperature changes induce indirect changes through the dynamic processes at different scales. Then, trend investigations on zonal and annual estimates need to be avoided for attribution purposes. Trend analyses can also be performed on temperature distribution, allowing to separate temperatures anomalies due to sudden stratospheric warmings and to direct radiative effects (Angot et al. 2012). It is also interesting to understand the feedback of the dynamic induced by radiative forcing (Cnossen et al. 2011) while not only major sudden stratospheric warming has an impact on trends and their occurrence may change in terms of frequency, timing, type, or amplitude (Maury et al. 2016). Gravity wave activity may also change under mean conditions and could be modified on regional scale as some data analyses have already suggested these possibilities using GPS (Khaykin et al. 2015), lidar (Mze et al. 2014), airglow temperature observations (Offermann et al. 2010), or MF radar wind series (Hoffmann et al. 2011). Such results will need to be consolidated with longer series.

Acknowledgements FP7-ARISE, H2020-ARISE 2, (Grant Agreement 653980) STTA/SPARC/WCRP.

References

Angot G, Keckhut P, Hauchecorne A, Claud C (2012) Contribution of stratospheric warmings on temperature trends in the middle atmosphere as revealed by the lidar series obtained at observatory of Haute-Provence (44°N). J Geophys Res 117. https://doi.org/10.1029/2012jd017631

Aschbacher J (2008) Les "Sentinelles" spatiales, de nouveaux outils au service d'une amélioration des politiques européennes en matière d'environnement et de sécurité, communiqué de presse de l'ESA du 28 février 2008. (http://www.esa.int)

Austin J, Wilson RJ, Akiyoshi H, Bekki S, Butchart N, Claud C, Fomichev VI, Forster P, Garcia RR, Gillett NP, Keckhut P, Langematz U, Manzini E, Nagashima T, Randel WJ, Rozanov E, Shibata K, Shine KP, Struthers H, Thompson DWJ, Wu F, Yoden S (2009) Coupled chemistry climate model simulations of stratospheric temperatures and their trends for the recent past. Geophys Res Lett 36:L13809. https://doi.org/10.1029/2009GL038462

Beig G et al (2003) Review of mesospheric temperature trends. Rev Geophys 41. https://doi.org/10.1029/2002rg000121

Berger U, Lübken F-J (2011), Mesospheric temperature trends at mid-latitudes in summer. Geophys Res Lett 38:L22804. https://doi.org/10.1029/2011GL049528

Blanc E, Ceranna L, Hauchecorne A, Charlton Perez A, Marchetti E, Evers L, Kvaerna T, Lastovicka J, Eliasson L, Crosby N, Blanc Benon P, Le Pichon A, Brachet N, Pilger C, Keckhut P, Assink J, Smets P, Lee C, Kero J, Sindelarova T, Kämpfer N, Rüfenacht R, Farges T, Millet C, Näsholm P, Gibbons S, Espy P, Hibbins R, Heinrich P, Ripepe M, Khaykin S, Mze N, Chum J (2016) Recent progress in understanding middle atmospheric dynamics as part of the arise project. Submitt Sur Geophys

Bittner M, Offermann D, Graef H-H, Donner M, Hamilton K (2002) An 18-year time series of OH rotational temperatures and middle atmosphere decadal variations. J.Atmos Sol Terr Phys 64:1147–1166

Chanin ML, Garnier A, Hauchecorne A, Porteneuve J (1989) A Doppler Lidar for measuring winds in the middle atmosphere. Geophys Res Lett 16:1273–1276

Charlton AJ, Polvani LM, Perlwitz J, Sassi F, Manzini E, Shibata K, Pawson S, Nielsen JE, Rind D (2007) A new look at stratospheric sudden warmings. Part II: evaluation of numerical model simulations. J Clim 20(3):470–488. https://doi.org/10.1175/JCLI3994.1

Cnossen I, Lu H, Bell CJ, Gray LJ, Joshi MM (2011) Solar signal propagation: the role of gravity waves and stratospheric sudden warmings. J Geophys Res 116:D02118. https://doi.org/10.1029/2010JD014535

Dunkerton TJ, Delisi DP, Baldwin MP (1998) Middle atmosphere cooling trend in historical rocketsonde data. Geophys Res Lett 25:3371–3374

Eyring V et al (2006) Assessment of temperature, trace species and ozone in chemistry-climate simulations of the recent past. J Geophys Res 111:D22308. https://doi.org/10.1029/2006JD007327

Eyring V et al (2007) Multimodel projections of stratospheric ozone in the 21st century. J Geophys Res 112:D16303. https://doi.org/10.1029/2006JD008332

Finger FG, Gelman ME, Wild JD, Chanin ML, Hauchecorne A, Miller AJ (1993) Evaluation of NMC upper-stratospheric temperature analyses using rocket-sonde and lidar data. Bull Am Meteorol Soc 74:789–799

Funatsu BM, Claud C, Keckhut P, Hauchecorne A (2008) Cross-validation of AMSU and lidar for long-term upper-stratospheric temperature monitoring. J Geophys Res 113:D23108. https://doi.org/10.1029/2008JD010743

Funatsu BM, Claud C, Keckhut P, Steinbrecht W, Hauchecorne A (2011) Investigations of stratospheric temperature regional variability with lidar and advanced microwave sounding unit. J Geophys Res 116:D08106. https://doi.org/10.1029/2010JD014974

Funatsu BM, Claud C, Keckhut P, Hauchecorne A, Leblanc T (2016) Regional and seasonal stratospheric temperature trends in the last decade (2002–2014) from AMSU observations. Geophys Res Lett Am Geophys Union 121(14):8172–8185. <https://doi.org/10.1002/2015jd024305>

Gaffen DJ (1994) Temporal inhomogeinities in radiosonde temperature records. J Geophys Res 99:3667–3676. https://doi.org/10.1029/93JD03179

Haimberger L, Tavolato C, Sperka S (2012) Homogenization of the global radiosonde temperature dataset through combined comparison with reanalysis background series and neighboring stations. J Clim 25:8108–8131. https://doi.org/10.1175/JCLI-D-11-00668.1

Hoffmann P, Rapp M, Singer W, Keuer D (2011) Trends of mesospheric gravity waves at northern middle latitudes during summer. J Geophys Res 116(D00P08). https://doi.org/10.1029/2011jd015717

Hoffmann L, Alexander MJ, Clerbaux C, Grimsdell AW, Meyer CI, Rößler T, Tournier B (2014) Intercomparison of stratospheric gravity wave observations with AIRS and IASI. Atmos Meas Tech 7: 4517–4537. https://doi.org/10.5194/amt-7-4517-2014

Hauchecorne A, Chanin M-L (1980) Density and temperature profiles obtained by lidar between 35 and 70 km. Geophys Res Lett 7:565–568. https://doi.org/10.1029/GL007i008p00565

Hauchecorne A, Khaykin S, Keckhut P, Mzé N, Angot G, Claud C (2019) Recent dynamic studies on the middle atmosphere at mid- and low-latitudes sing rayleigh lidar and other technologies. In: Le Pichon A, Blanc E, Hauchecorne A (eds) Infrasound monitoring for atmospheric studies, 2nd edn. Springer, Dordrecht, pp 757–776

Keckhut P, Hauchecorne A, Chanin ML (1995) Mid-latitude long-term variability of the middle atmosphere trends, and cyclic and episodic changes. J Geophys Res 100:18.887–18.897

Keckhut P, Schmidlin FJ, Hauchecorne A, Chanin ML (1999) Stratospheric and mesospheric cooling trend estimates from us rocketsondes at low latitude stations (8°S-34°N), taking into account instrumental changes and natural variability. J Atmos Sol Terr Phys 61:447–459

Keckhut P, Kodera K (1999) Long-term changes of the upper stratosphere as seen by rocketsondes at Ryori, (39°N, 141°E). Ann Geophys 17:1210–1217

Keckhut P, Wild J, Gelman M, Miller AJ, Hauchecorne A (2001) Investigations on long-term temperature changes in the upper stratosphere using lidar data and NCEP analyses. J Geophys Res 106:7937–7944

Keckhut P, Randel WJ, Claud C, Leblanc T, Steinbrecht W, Funatsu BM, Bencherif H, McDermid IS, Hauchecorne A, Long C, Lin R, Baumgarten G (2011) An evaluation of uncertainties in monitoring middle atmosphere temperatures with the lidar network in support of space observations. J Atmos Solar-Terr Phys 73(5–6):627–642. https://doi.org/10.1016/j.jastp.2011.01.003

Keckhut P, Funatsu BM, Claud C, Hauchecorne A (2015) Tidal effects on stratospheric temperature series derived from successive advanced microwave sounding units. Q J R Meteorol Soc 141:477–483. https://doi.org/10.1002/qj.2368

Khaykin S, Hauchecorne A, Mzé N, Keckhut P (2015) Seasonal variation of gravity wave activity at mid-latitudes from 7 years of cosmic GPS and Rayleigh lidar temperature observations. Geophys Res Lett 42(4):1251–1258. https://doi.org/10.1002/2014gl062891/hal-01109116

Khaykin SM, Funatsu BM, Hauchecorne A, Godin-Beekmann S, Claud C, Keckhut P, Pazmino A, Gleisner H, Nielsen JK, Syndergaard S, Lauritsen KB (2017) Post-millennium changes in stratospheric temperature consistently resolved by GPS radio occultation and AMSU observations, Geophys Res Lett, Am Geophys Union 44(14):7510–7518. https://doi.org/10.1002/2017GL074353

Kubicki A, Keckhut P, Chanin M-L, Hauchecorne A, Lysenko E, Golitsyn G-S (2006) Temperature trends in the middle atmosphere of the mid-latitude as seen by historical russian rocket launches part 1: Volgograd (48,68°N, 44,35°E). J Atmos Sol Terr Phys 68:1075–1086. https://doi.org/10.1016/j.jastp.2006.02.001

Kurylo MJ, Solomon S (1990) Network for the detection of stratospheric change. NASA Rep, Code EEU

Labitzke K, von Loon H (1995) A note on the distribution of trends below 10 hPa : The extratropical Northern Hemisphere. J Meteorol Soc Jpn 73:883–889

Le Pichon A, Blanc E, Drob D (2015a) Probing high-altitude winds using infrasound. J Geophys Res 110:D20104. https://doi.org/10.1029/2005JD006020

Le Pichon A, Assink JD, Heinrich P, Blanc E, Charlton-Perez A, Lee CF, Keckhut P, Hauchecorne A, Rüfenacht R, Kämpfer N, Drob DP, Smets PSM, Evers LG, Ceranna L, Pilger C, Ross O, Claud C (2015b) Comparison of co-located independent ground-based middle-atmospheric wind and temperature measurements with numerical weather prediction models. J Geophys Res Atmos Am Geophys Union (AGU) 120(16):8318–8331. https://doi.org/10.1002/2015jd023273

Lübken F-J et al (1994) Intercomparison of density and temperature profiles obtained by lidar ionization gauges, falling spheres, datasondes and radiosondes during the DYANA campaign. J Atmos Terr Phys 56:1969–1984

Maury P, Claud C, Manzini E, Hauchecorne A, Keckhut P (2016) Characteristics of stratospheric warming events during northern winter. J Geophys Res Atmos. https://doi.org/10.1002/2015jd024226

McLandress C, Shepherd TG, Jonsson AI, von Clarmann T, Funke B (2015) A method for merging nadir-sounding climate records, with an application to the global-mean stratospheric temperature data sets from SSU and AMSU. Atmos Chem Phys Disc 15:10085–10122. https://doi.org/10.5194/acpd-15-10085-626

Morel B, Keckhut P, Bencherif H, Hauchecorne A, Megie G, Baldy S (2004) Investigation of the tidal variations in a 3-d dynamics-chemistry-transport model of the middle atmosphere. J Atmos Sol Terr Phys 66:251–265

Mzé N, Hauchecorne A, Keckhut P, Thétis M (2014) Vertical distribution of gravity wave potential energy from long-term Rayleigh lidar data at a northern middle-latitude site. J Geoph Res Atmos 119(21):12069–12083. https://doi.org/10.1002/2014jd022035

Nash J, Forrester GF (1986) Long-term monitoring of stratospheric temperature trends using radiance measurements obtained by the TIROS-N series of NOAA spacecraft. Adv Space Res 6:37–44

Newman PA et al (2016) The anomalous change in the QBO in 2015–2016. Geophys Res Lett. https://doi.org/10.1002/2016GL070373

Offermann D, Hoffmann P, Knieling P, Koppmann R, Oberheide J, Steinbrecht W (2010) Long-term trends and solar cycle variations of mesospheric temperature and dynamics. J Geophys Res 115:D18127. https://doi.org/10.1029/2009JD013363

Quian L, Lastovicka J, Roble RG, Solomon SC (2011) Progress in observations and simulations of global change in the upper atmosphere. J Geophys Ress 116:1–16. https://doi.org/10.1029/2010JA016317

Ramanathan V, Callis L, Cess R, Hansen J, Isaksen I, Kuhn W, Lacis A, Luther F, Mahlmanl J, Reck E, Schlesinger M (1987) Climate-chemical interactions and effects of changing atmospheric trace gases. Rev Geophys 7:1441–1482

Ramaswamy V, Chanin ML, Angell J, Barnett J, Gaffen D, Gelman M, Keckhut P, Kolshelkov Y, Labitzke K, Lin J-JR, O'Neill A, Nash J, Randel W, Rood R, Shine K, Shiotani M, Swinbank R (2001) Stratospheric temperature trends: observations and model simulations. Rev Geophys 39:71–122

Randel WJ, Shine K, Austin J, Barnett J, Claud C, Gillett NP, Keckhut P, Langematz U, Lin R, Long G, Mears C, Miller A, Nash J, Seidel DJ, Thompson DWJ, Wu F, Yoden S (2009) 2009: An updated of observed stratospheric temperature trends. J Geophys Res 114:D02107. https://doi.org/10.1029/2008JD010421

Randel W, Smith A, Wu F, Zou C, Qian H (2016) Stratospheric temperature trends over 1979–2015 derived from combined SSU, MLS and SABER satellite observations. J Clim (in press). https://doi.org/10.1175/jcli-d-15-0629.1

Remsberg EE, Deaver LE, Wells JG, Lingenfelser G, Bhatt PP, Gordley LL, Thompson R, McHugh M, Russell III JM, Keckhut P, Schmidlin FJ (2002) An assessment of the quality of HALOE temperature profiles in the Mesosphere with Rayleigh Backscatter Lidar and inflatable falling sphere measurements. J Geophys Res 107(D19). https://doi.org/10.1029/2001jD001521

Rüfenacht R, Murk A, Kämpfer N, Eriksson P, Buehler SA (2014) Middle-atmospheric zonal and meridional wind profiles from polar, tropical and mid-latitudes with the ground-based microwave Doppler wind radiometer WIRA. Atmos Meas Tech 7:4491–4505. https://doi.org/10.5194/amt-7-4491-2014

Santer BD et al (1996) A search for human influences on the thermal structure of the atmosphere. Nature 382:39–46

Shepherd MG, Espy PJ, She CY, Hocking W, Keckhut P, Gavrilyeva G, Shepherd GG, Naujokat B (2002) springtime transition in upper mesospheric temperature in the northern hemisphere. J Atmos Sol Terr Phys 64:1183–1199

Schmidlin FJ (1991) Rocket techniques used to measure the middle atmosphere. In Goldberg A (ed) Handbook of map 19:1–28

Seidel DJ et al (2008) Reference upper-air observations for climate: rationale, progress, and plans. Bull Am Meteorol Soc 1. https://doi.org/10.1175/2008bams2540.1

Seidel DJ, Li J, Mears C, Moradi I, Nash J, Randel WJ, Saunders R, Thompson DWJ (2016) C-Z. Zou, Stratospheric temperature changes during the satellite era. J Geophys Res 121:664–681

She CY, Yu JR, Krueger DA, Roble R, Keckhut P, Hauchecorne A, Chanin ML (1995) vertical structure of mid-latitude temperature from stratosphere to mesopause (30-105 km). Geophys Res Let 22:377–380

Shine KP, Barnett JJ, Randel WJ (2008) Temperature trends derived from Stratospheric Sounding Unit radiances: the effect of increasing CO2 on the weighting function. Geophys Res Lett 35: L02710. https://doi.org/10.1029/2007GL032218

Sigernes F, Shumilov N, Deehr CS, Nielsen KP, Svenøe T, Havnes O (2003) Hydroxyl rotational temperature record from the auroral station in Adventdalen, Svalbard (78 N, 15 E). J Geophys Res 108(A9):1342. https://doi.org/10.1029/2001JA009023

Simmons AJ, Poli P, Dee DP, Berrisford P, Hersbach H, Kobayashi S, Peubey C (2014) Estimating low-frequency variability and trends in atmospheric temperature using ERA-Interim. Q J R Meteorol Soc 140:329–353. https://doi.org/10.1002/qj.2317

Smets P, Assink J, Evers L (2019) The study of sudden stratospheric warmings using infrasound. In: Le Pichon A, Blanc E, Hauchecorne A (eds) Infrasound monitoring for atmospheric studies, 2nd edn. Springer, Dordrecht, pp 723–755

Spencer RW, Christy JR (1993) Precision lower stratospheric temperature monitoring with the MSU technique: validation and results, 1979–1991. J Clim 6:1191–1204

Steinbrecht W, Claude H, Schonenborn F, McDermid IS, Leblanc T, Godin-Beekmann S, Keckhut P, Hauchecorne A, Van Gijsel JAE, Swart DPJ, Bodeker G, Parrish A, Boyd I, Kampfer N, Hocke C, Stolarski RS, Frith SM, Thomason LW, Remsberg EE, Von Savigny C, Rozanov A, Burrows JP (2009) Ozone and temperature trends in the upper stratosphere at five stations of the network for the dectection of atmospheric composition change. Int J Remote Sens 30:3875–3886

Trenberth K, Fasullo JT (2013) An apparent hiatus in global warming? Earth Future 1:19–32. https://doi.org/10.1002/2013EF000165

Thompson AM et al (2003) Southern hemisphere additional ozonesondes (SHADOZ) 1998–2000 tropical ozone climatology: 1. Comparison with Total Ozone Mapping Spectrometer (TOMS) and ground-based measurements. J Geophys Res 108(D2):8238. https://doi.org/10.1029/2001JD000967

Wang L, Zou C-Z (2013) Inter-comparison of SSU temperature data records with Lidar, GPS RO, and MLS Observations. https://doi.org/10.1002/jgrd.50162

Wild JD, Gelman ME, Miller AJ, Chanin ML, Hauchecorne A, Keckhut P, Farley R, Dao PD, Gobbi GP, Adriani A, Coneduti F, McDermid IS, McGee TJ, Fishbein EF (1995) Comparison of stratospheric temperature from several lidars using NMC and MLS data as transfer reference. J Geophys Res 100:11.105–11.111

World Meteorological Organisation (1990) Scientific assessment of stratospheric ozone: 1989, Global Ozone Res. Monit. Proj., Geneva

Zou C-Z, Qian H, Wang W, Wang L, Long C (2014) Recalibration and merging of SSU observations for stratospheric temperature trend studies. J Geophys Res Atmos 119:13180–13205. https://doi.org/10.1002/2014JD021603

Zou C-Z, Qian H (2016) Stratospheric temperature climate record from merged SSU and AMSU-A observations. J Atmos Ocean Tech (submitted)

Part IX
Evaluating and Improving Global Circulation and Climate Models and Weather Forecasts (GCM): Improving Stratospheric Variability in Numerical Weather Prediction Model (NWP) and Expected Improvements in Weather Forecasts

Chapter 27
Non-orographic Gravity Waves: Representation in Climate Models and Effects on Infrasound

David Cugnet, Alvaro de la Camara, François Lott, Christophe Millet and Bruno Ribstein

Abstract Long-range infrasound propagation is controlled by atmospheric waveguides that extend up to the mesosphere and lower thermosphere and whose efficiency is affected by gravity waves (GWs). These GWs are not explicitly represented in the global models often used to calculate infrasound propagation because their spatial scales are well below the models' resolution. These unresolved GWs also transport momentum and control in good part the large-scale circulation in the middle atmosphere. These two issues make that the GWs need to be parameterized to improve the datasets used to calculate infrasound propagation as well as in the atmospheric general circulation model (AGCMs) that are used to make weather forecasts and climate predictions. These two issues gain in being treated in conjunction. From this, improved infrasound calculations could be made by using a realistic amount of GWs. In return, using infrasound records could help specifying important characteristics of the GWs that are parameterized in the climate models. The paper presents a research framework developed to address these issues. It first presents a non-orographic GWs parameterization used and tested in a well-established AGCM, emphasizing the most recent developments, like the introduction of stochastic techniques and a better specification of the GWs sources. The significance of GWs on the global climate is then illustrated by making sensitivity tests where the frontal and convective GWs parameters are moderately changed. These changes impact the structure of the jets in the midlatitude stratosphere and the intensity of the sudden

D. Cugnet · F. Lott (✉)
LMD, PSL Research University, Ecole Normale Supérieure, Paris, France
e-mail: flott@lmd.ens.fr

A. de la Camara
Dpto. Fisica de la Tierra y Astrofisica, Univ. Complutense de Madrid, Madrid, Spain

C. Millet (✉) · B. Ribstein
CEA, DAM, DIF, F-91297 Arpajon, France
e-mail: christophe.millet@cea.fr

B. Ribstein
CMLA, ENS Cachan, CNRS, Université Paris-Saclay, 94235 Cachan, France

A. Le Pichon et al. (eds.), *Infrasound Monitoring for Atmospheric Studies*,
https://doi.org/10.1007/978-3-319-75140-5_27

stratospheric warmings. The paper also presents a method to calculate long-range infrasound propagation, and to incorporate the contribution of the GWs that are parameterized in the AGCM. We then show that the changes in GW parameters tested in the model also impact infrasound propagation. This makes infrasound detection a potential tool to tune GWs parameterization in large-scale models.

27.1 Introduction

The parameterization of gravity waves in climate models is critical for the proper representation of the circulations of both the troposphere and the middle atmosphere in atmospheric general circulation models (AGCMs). The orographic gravity waves significance is described in the previous issue of this series (Lott and Millet 2009), whereas it is well established that the non-orographic GWs are responsible for the reversal of the meridional temperature gradient at the mesopause (Holton 1982) and that they are a substantially driving the quasi-biennial oscillation (QBO) in the equatorial lower stratosphere (Lindzen and Tsay 1975).

In order to parameterize the non-orographic GWs, some schemes like (Alexander and Dunkerton 1999) bin the spectral domain with a large number of monochromatic waves, an approach where the GWs sources can be easily introduced (Beres et al. 2005), but that can be very expensive. Today, to circumvent this difficulty, the spectral domain is sampled by stochastic methods (Eckermann 2011; Lott et al. 2012; Lott and Guez 2013; de la Camara and Lott 2015), an approach that is further justified by the fact that (i) the mesoscale dynamics producing the GWs is chaotic and (ii) the spread of the ensemble climate predictions need to be increased by stochastic forcings (Palmer 2012).

It is now generally recognized that long-range infrasound propagation is controlled by the stratospheric and mesospheric wind and temperature vertical profiles (Rind 1978; Gossard and Hooke 1975). During the past 10 years, extensive simulations were carried out (Kulichkov et al. 2010; Chunchuzov et al. 2011; Hedlin et al. 2012; Bertin et al. 2014; Chunchuzov and Kulichkov 2019, among others) confirming that these profiles yield distinct infrasound ducts, which make that a sound emitted at a given source can have several distinct arrivals. In infrasound propagation modeling, the wind and temperature profiles are usually obtained by blending results of weather prediction centers (e.g., ECMWF) with semi-empirical models of winds and temperature for altitude around 90 km and above (upper mesosphere–lower thermosphere Drob et al. 2008; Picone et al. 2002). Nevertheless, these datasets only capture variations along quite large horizontal and vertical scales (the so-called "resolved scales"), and using these data, there are systematic misfits between predicted and observed infrasound amplitudes and waveform. One reason can be that when the acoustic ducts are borderline, in the sense that small disturbances can create or destroy a duct, the signal propagation becomes very sensitive to wind fluctuations (e.g., Bertin et al. 2014; Dergham and Millet 2013), which produces highly dispersed signals. In the middle atmosphere, the origin of these fluctuations is likely to be due

to GWs, and recent works (e.g., Lalande and Waxler 2016; Hedlin and Drob 2014; Drob et al. 2013) show that their main effect is to spread the incoming infrasound signal. Without accounting for GWs, the duration of stratospheric signals is often underestimated, by a factor of 5–10. In such cases also, deterministic modeling fails in predicting the waveforms and a statistical analysis of sound propagation appears necessary to estimate the uncertainties. A problem with these studies is that in the middle atmosphere, the amplitude and characteristic of the GWs are still not well known. In this context, we propose to test GWs field which is consistent with those reducing systematic biases in AGCMs. To specify large-scale winds that are consistent with in situ infrasound observations, we will nevertheless follow (de la Camara et al. 2014) and run the scheme offline using the large-scale winds provided by the ECMWF ERAI analysis up to the mesosphere and by an empirical model above.

The purpose of the present paper is to present the research framework we have recently built to improve infrasound calculations and gravity wave parameterizations. To that end, Sect. 27.2 presents the non-orographic gravity wave scheme recently introduced in the stratospheric version of the LMDz climate model and its impact. To illustrate the significance of the parameterized waves, we will make changes in the parameterization setup and discuss their impacts. In Sect. 27.3, we briefly expose one of the techniques we use to evaluate infrasound propagation from a given source to a given receiver, and take the example of the Hukkakero ammunition destruction done on August 18, 2016, at 12:30 p.m. We then expose how gravity waves fields can be included and show results for the two setups of the GWs parameterization we use.

27.2 Formalism

The stochastic method introduced in Eckermann (2011), Lott et al. (2012) to represent GWs consists in representing the subgrid-scale GWs field by a stochastic Fourier series

$$w' = \sum_{n=1}^{n=\infty} C_n \hat{w}_n(z) e^{z/2H} e^{i(\vec{k}_n \cdot \vec{x} - \omega_n t)}, \tag{27.1}$$

where w' is the vertical velocity, z is the vertical log-pressure coordinate, $H = 7\,\mathrm{km}$ a vertical scale characteristic of the middle atmosphere temperatures, $\hat{w}_n(z)$ is the complex vertical structure of a given harmonic, $\vec{k}$ is its horizontal wavenumber, ω its absolute frequency, and $\vec{x}$ and t being horizontal position and time, respectively. In (27.1), the parameter C_n measures the amplitude of a given harmonic to represent the total wave field (for instance at a given place inside the model gridbox), it is often referred to as an intermittency coefficient, and its statistical interpretation makes that it satisfies

$$\sum_{1}^{\infty} C_n^2 = 1. \tag{27.2}$$

On top of this statistical decomposition, $\vec{k}_n$ and ω_n are also chosen randomly within bounds covering the space and timescales we believe the model does not solve well. To describe vertical propagation, we derive from (27.1) an EP flux due to the waves

$$\vec{F}^z = \rho_0(z)\overline{\vec{u}'w'} = \sum_{n=1}^{n=\infty} C_n^2 \vec{F}_n^z \text{ where } \vec{F}_n^z = \rho_r \Re\left\{\frac{\vec{\hat{u}}_n \hat{w}_n^*}{2}\right\}, \tag{27.3}$$

where $\vec{F}_n(z)$ is the EP flux carried by each wave, $\rho_0(z) = \rho_r e^{-z/H}$ being a characteristic density vertical profile ρ_r being constant. We then make a WKB evaluation of each harmonics introducing a diffusivity $\nu(z) = \mu/\rho_0(z)$, and limiting each wave amplitude to its statically marginal stability limit. From such consideration and from the Eliassen–Palm theorem, telling that the EP flux is constant for steady linear wave in the absence of dissipation, we construct the vertical profile of $\overline{F}_n^z$ following the iterative rule from one model level (z) to the next above $(z + \delta z)$:

$$\begin{aligned}\vec{F}_n^z(z+\delta z) = {} & \frac{\vec{k}_n \Omega}{|\vec{k}_n||\Omega|}\Theta\left(\Omega(z+\delta z)\Omega(z)\right) \\ & \text{Min}\left\{|\overline{F}_n^z(z)|e^{-2\frac{\mu N^3|\vec{k}_n|^3}{\rho_0\Omega^4}\delta z}, \rho_r S_c^2 \frac{|\Omega|^3 k^{*2}}{N|\vec{k}_n|^4}\right\},\end{aligned} \tag{27.4}$$

where the first fraction guarantees that the EP flux is in the direction of the phase speed, the second term with Heaviside function $\Theta(z)$ handles critical levels, e.g., places where the intrinsic frequency $\Omega = \omega_n - \vec{k}_n \cdot \vec{U}$ changes sign ($\vec{U}$ being the background wind), the first term in the parenthesis expresses the decay of the EP flux due to diffusion, and the last term is the saturated EP flux. Still in (27.4) N is the buoyancy frequency, whereas k^* is the minimum GW wavelength parameterized and S_c is a tunable parameter that controls the wavebreaking.

To relate the gravity waves to their non-orographic sources, e.g., convections and fronts, we then follow (Lott and Guez 2013; de la Camara and Lott 2015) and represent the subgrid-scale precipitation and vorticity by stochastic series,

$$P' = \sum_{n=1}^{\infty} C_n P_n e^{i(\vec{k}_n \cdot \vec{x} - \omega_n t)}, \quad q' = \sum_{n=1}^{\infty} C_n q_n e^{i(\vec{k}_n \cdot \vec{x} - \omega_n t)}. \tag{27.5}$$

In Lott and Guez (2013), the precipitation is translated into a heating over a characteristic depth Δz and integrated into a forced Taylor–Goldstein equation solved via a Green function method. It yields a "launched" momentum flux,

$$|\overline{F}^z| = G_0 \rho_r \left(\frac{RL_c}{\rho_r H c_p} \right)^2 \frac{|k|^2 e^{-\frac{N^2 |\vec{k}|^2 \Delta z_1^2}{\Omega^2}}}{N|\Omega|^3} P^2, \tag{27.6}$$

where we have assumed that the amplitude of the stochastic projection of subgrid-scale precipitation onto the nth harmonics is equal to the gridscale precipitation P: $|\hat{P}_n| = P$. In (27.6), the n-indices are dropped for conciseness, R is the dry air gas constant, L_c is the latent heat of condensation, Δz_1 scales the depth of convection, and G_0 is a tunable constant of order 1.

In de la Camara and Lott (2015), the frontal waves are parameterized by realizing that within fronts, relative vorticity anomalies q' are always substantial, and by using closed formula for spontaneous GWs emission from PV anomalies derived in Lott et al. (2010), Lott et al. (2012), e.g., by writing,

$$|\overline{F}^z| = G_1 \frac{\Delta z_2}{4f} \int_0^\infty \rho(z') N(z') Q^2 e^{-\pi \frac{N}{U_z}} dz', \tag{27.7}$$

where Q is the gridscale PV, Δz_2 is a tuneable depth for the PV anomalies, it is near the gridscale depth δz, f is the Coriolis parameter, U_z is the wind shear, and G_1 is a tuneable parameter, again of order 1.

27.3 Test in LMDz

27.3.1 Experimental Setup

The LMDz version used here is one of the configurations designed for the preparation of the sixth coupled model intercomparison project (CMIP6), an evolution of its CMIP5 version presented in Hourdin et al. (2013). For the middle atmosphere, important differences nevertheless need to be detailed. First, the model now has 80 levels, with a top at 1 Pa and a resolution in the lower stratosphere of $\delta z \approx 1$ km near $z = 20$ km, increasing smoothly to reach $\delta z \approx 1.4$ km near $z = 40$ km; then, the resolution increases more rapidly and it equals $\delta z \approx 6$ km at the top and there are only 13 levels in the mesosphere ($50 < z < 80$ km). Second, the model has ozone specifications that are derived from observational data, rather than from the LMDz-Reprobus model as in CMIP5. The ozone data used being defined only below 1 hPa, we make the O_3 mixing ratio above decreasing rapidly as a function of pressure by using the relation

$$\chi_{O_3}(P < 1\,\text{hPa}) = \chi_{0_3}(1\,\text{hPa}) \sqrt{\frac{P}{P(1\,\text{hPa})}}, \tag{27.8}$$

which reproduces qualitatively the decay with altitude of the daily ozone in the mesosphere used in Hourdin et al. (2013).

Concerning the parameterization of the non-orographic gravity waves, we choose the wavenumber of the waves randomly using a uniform distribution between $10^{-3} > k > k^* = 2 \times 10^{-5}$. Their intrinsic phase speed is also chosen randomly using a Gaussian distribution with standard deviation $U^* = 50$ m/s for the convective waves and $U^* = 30$ m/s for the frontal waves. Concerning the non-dimensional parameters, we take $G_0 = 0.23$ for the convective waves and $G_1 = 4$ for the frontal waves. Also, the launching altitudes is around $z_l = 500$ m for the frontal waves and $z_l = 5$ km for the convective ones. Finally, we take for the saturation parameter $S_c = 0.6$ and for the diffusion $\nu = 1$. For completeness, the subgrid-scale orography parameter values are quite different from those given in Lott and Millet (2009), see their Eqs. 23.1–23.6: we now take $H_{NC} = 1$, $C_d = 0.5$, $G = 0.1$, $\beta = 0.1$, $Ri_c = 1$, and $C_l = 0.5$. Here, H_{NC} represents the critical value of the non-dimensional mountain height above which the low-level flow is blocked, C_d the drag coefficient applied to the blocked flow, G the gravity wave drag coefficient, β the fraction of the gravity wave drag that propagates freely in and aloft the free troposphere, Ri_c the critical Richardson number controlling orographic gravity waves breaking, and C_l the mountain lift coefficient introduced in Lott (1999).

The results presented in this paper are from a 15-year experiment where sea surface temperature, sea ice, and ozone are imposed from climatologies constructed with 1979–2008 data. To illustrate how the GWs impact the simulated climate in the middle atmosphere, we also show an experiment with slower frontal waves, $U^* = 10$ m/s. In this configuration, the drags stay reasonable in the middle atmosphere if we take a slightly smaller $G_1 = 2$ and a much larger $S_c = 6.7$. In this setup, the frontal wave drag is slightly smaller than in the first experiment. Conversely, we also increase the convective wave drag constant to $G_0 = 0.6$ in order to increase the convective wave drag.

27.3.2 Midlatitude Climatologies and Sudden Stratospheric Warmings

The zonal mean zonal winds for January, April, August, and October are shown in the four panels in Fig. 27.1a. It shows that the stratospheric winds in the winter midlatitudes are oriented eastward and exhibit well-defined jets with maxima centered near 60°N in the NH and 60°S in the SH. These are the so-called polar night jets and their maximum value is about right in the NH midlatitude. Still during solstices, the winds are essentially westward in the summer hemisphere, with well-defined maxima in the subtropical regions above the stratopause. In the mesosphere, the winds decay in amplitude as a function of altitude, also consistent with observations, and we know that these decays are only realistic if we have the right amount of gravity wave drag (see Lott and Millet 2009). During equinoxes, the polar jets are eastward

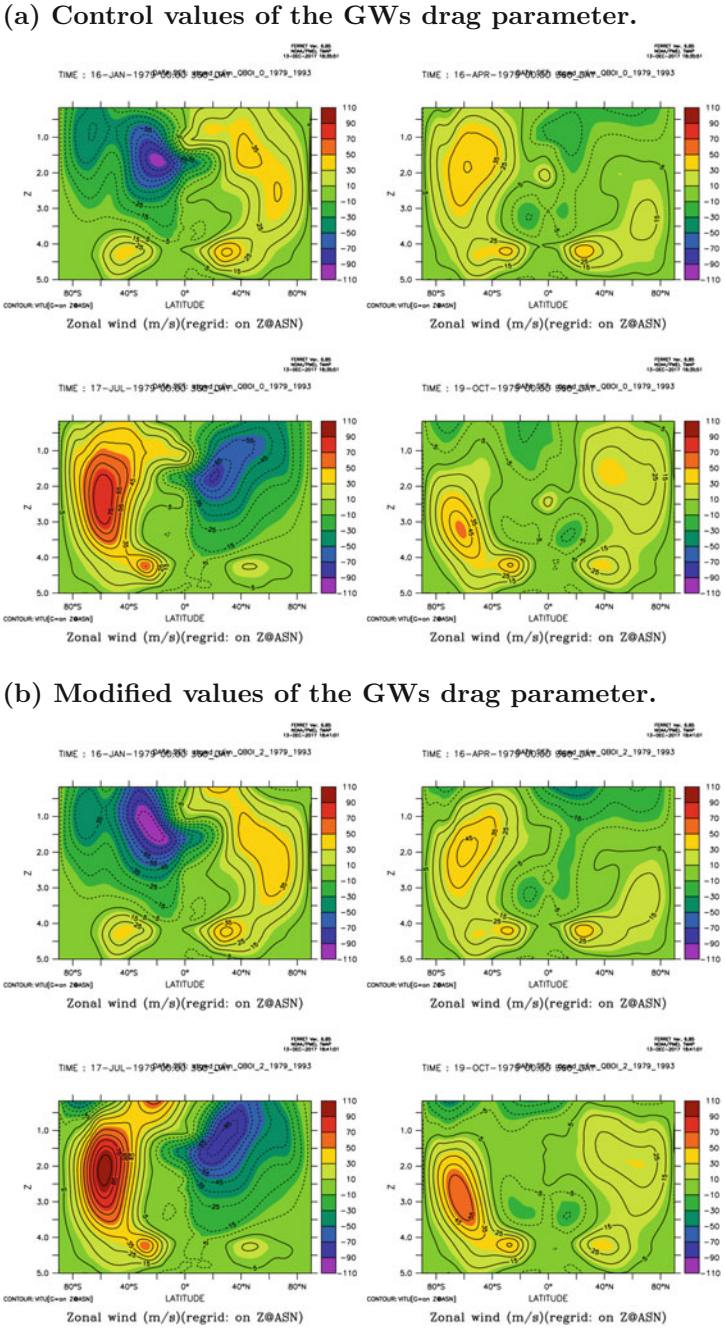

Fig. 27.1 Climatology of the zonal wind in the control and experiments with changed GWs drag parameter

in both hemispheres, with amplitudes substantially smaller than the polar night jet during the solstices. In autumn, these easterlies indicate the building up of the winter polar night characterizing the polar vortices, whereas in spring they are associated to their breakdown. The fact that the GW drag controls the amplitude of these jets is clearly illustrated in Fig. 27.1b, which shows that the maximum jet amplitudes are everywhere larger when the launched frontal GW drags are reduced.

To characterize the variability of the polar night jets, Fig. 27.2a presents the evolution of the 30 hPa zonal mean zonal wind at 60° South and North of the 10 hPa zonal mean polar temperature at 10 hPa. This diagnostics usually characterizes the onset of the so-called sudden stratospheric warmings (SSWs), corresponding to years with polar vortex breakdown, e.g., a time when the polar jet ceases and even reverses (Fig. 27.2a) and when the winter temperature can be 90 K above its climatological value, e.g., larger than its summer mean. Again, the model winter warmings are quite realistic in the NH, where they are much more pronounced than in the SH. This is of course consistent with observations: SSWs are first related to the breaking of planetary-scale Rossby waves; these are much smaller in the SH because there the land–sea contrasts are much less pronounced than in the NH.

The gravity waves also affect the SSW, to a certain extent, and this is partly because they affect the zonal mean flow which controls the index of refraction of the Rossby waves. To illustrate this point, Fig. 27.2b presents the diagnostics of SSWs with reduced frontal GWs. In them, we see that the maximum winds attained in winter are almost 10 m/s larger than with larger frontal GW drag. The minimum polar temperatures are also typically 10 K smaller. The amplitude of the variabilities is also increased accordingly by almost the same amount (i.e., 10 K). As a "rule of thumb", we could say that the winter variability, from minimum to maximum, goes from the average winter minimum to the averaged summer maximum. As GW drag increases the former, it increases within the same amount the variability.

27.3.3 Tropics and the Quasi-biennial Oscillation

In the absence of GWs drag the LMDz model, like any other model, fails in producing a QBO. This is related to the observational fact that the large-scale equatorial waves alone are not large enough to force the QBO: it is generally admitted that they contribute one-half only, the second being the GWs. Therefore, we have tuned the convective GWs scheme in order that the model produces a QBO, and the results are shown in Fig. 27.3a. In it, we see that the equatorial winds at the equator alternate positive and negative phases, within a cycle that has an irregular period of almost 26 months. This is a little faster than the observed QBO (e.g., 27–28 months) but the difference can easily be corrected by slightly decreasing the GWs amplitude. Apart from this difference, the model QBO presents the characteristic features of this oscillation, like a descending phase, a relation with the annual cycle at its top near 1 hPa. To illustrate again that the oscillation is very sensitive to the GW drag, Fig. 27.3b shows the zonal mean wind at the equator when the launched convective GWs stress

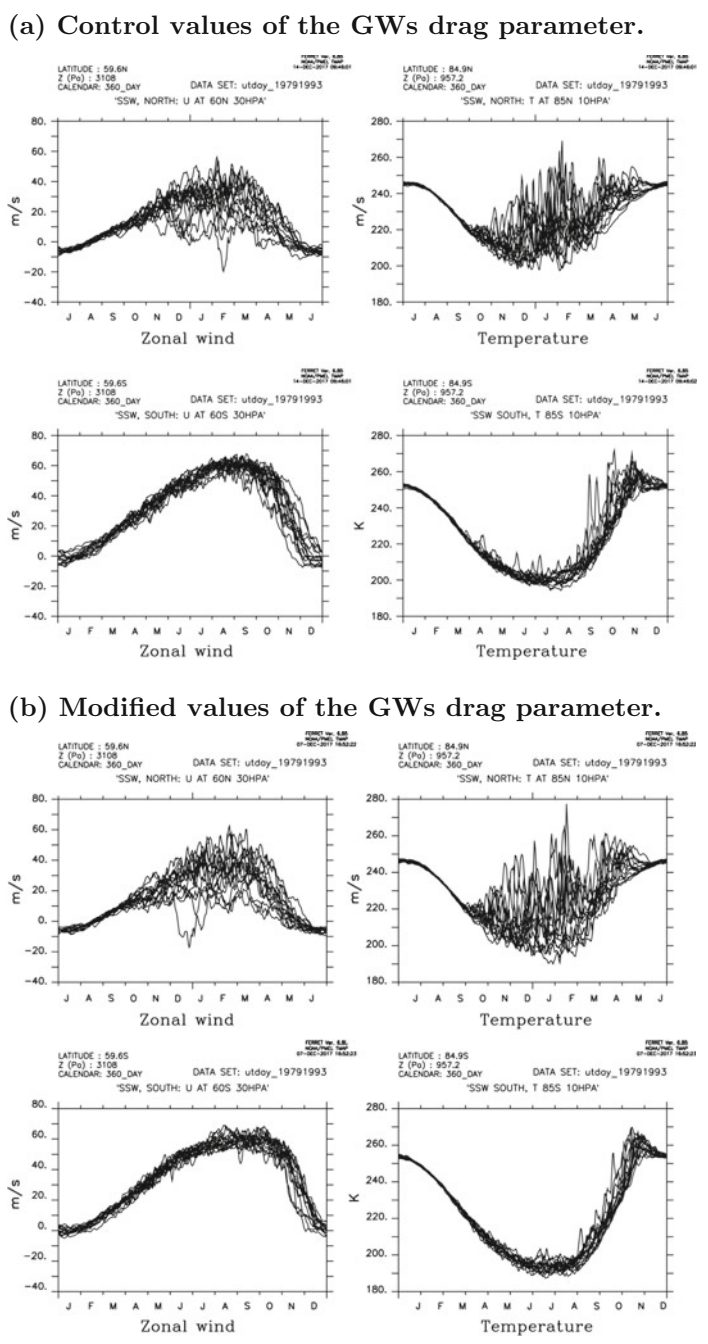

Fig. 27.2 Zonal mean zonal wind at 30 hPa (upper left: 60°N, upper right: 60°S), and polar temperature at 10 hPa (upper right: 85°N, lower right 85°S)

(a) Control values of the GWs drag parameter.

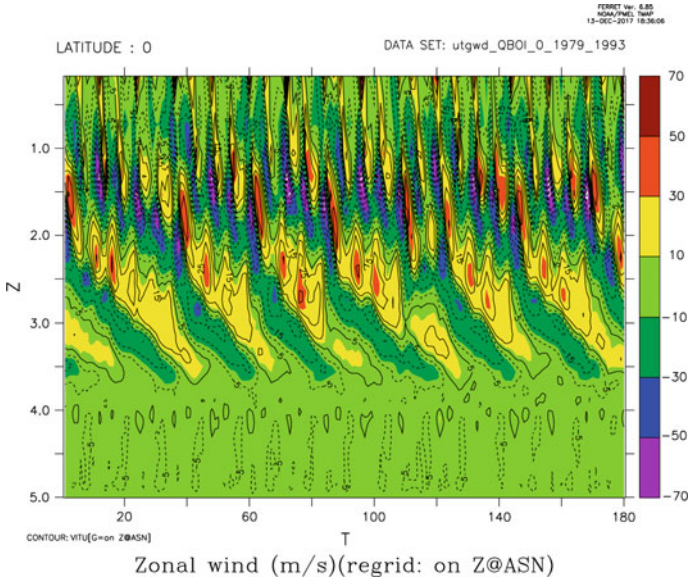

(b) Modified values of the GWs drag parameter.

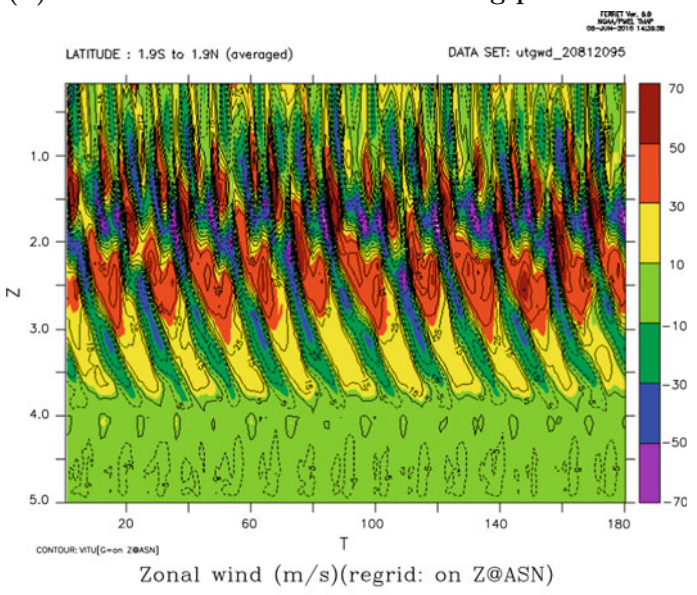

Fig. 27.3 Zonal mean zonal wind at equator

is increased. In this case, the periods of the oscillation fall to 16 months, and the amplitude of the oscillation in the low stratosphere is also substantially increased.

27.4 Impact of GWs on Infrasound Propagation

27.4.1 Formalism

The classical approach in infrasound propagation modeling consists in solving the wave equation, often in cylindrical coordinates (r, θ, z), where r and z are the distances from the source and altitude, respectively. While the nature of the source significantly influences the pressure field, a simpler and common way to account for the source is to introduce driving forces on the right-hand side of the wave equation. Hence, using the form of a Dirac delta function $\delta(z - z_0)\delta(r)s(t)$, where $s(t)$ is the source function, the pressure fluctuation reads as

$$p(z, r, t) = \frac{1}{2\pi} \int_{-\infty}^{+\infty} \tilde{s}(\omega)\tilde{p}(z; r, \omega)e^{-i\omega t} \mathrm{d}\omega, \tag{27.9}$$

where $\tilde{s}$ is the Fourier transform of the source. The solution of the homogeneous wave equation is then a solution of the inhomogeneous equation except at height z_0 where the field variables are not generally continuous.

The solution in normal modes (Jensen et al. 1994) of the wave equation can be attacked as two quite distinct problems: (1) finding the eigenpairs in a horizontally homogeneous atmosphere of arbitrary temperature and wind distribution in the vertical direction and (2) synthesis of the waveform at a given range r and time t resulting from a specified source. While the general solution of such problems leads to the so-called leaky modes, open modes (Budden 1961), these modes are usually neglected for infrasound application. Hence, in the normal mode approximation, one seeks the total pressure fluctuation as a sum of M modal contributions:

$$\tilde{p}(r, z; \omega) \approx \sum_{m=1}^{M(\omega)} \frac{\phi_m(0, \omega)\phi_m(z; \omega)}{\sqrt{k_m(\omega)}} e^{ik_m r}, \tag{27.10}$$

where ϕ_m and k_m satisfy the Helmholtz equation

$$\frac{\partial^2 \phi_m}{\partial z^2} + \left[\frac{\omega^2}{c(z)^2} - k_m^2\right] \phi_m = 0, \tag{27.11}$$

where $c(z)$ is the effective sound speed. Here, we use the effective sound speed approximation (Godin 2002), in which the component of the horizontal wind speed

in the direction of propagation is added to the thermodynamic sound speed,

$$c(z) = \sqrt{\gamma RT(z)} + \frac{\vec{k} \cdot \vec{u}(z)}{|\vec{k}|}, \tag{27.12}$$

where the index m on the wavevector is dropped because only the projection on the direction of sound propagation matters: $c(z)$ is not a function of m.

At $z = 0$, we use a Neumann boundary condition and the eigenfunction ϕ_m in (27.10) is suitably normalized (Jensen et al. 1994). Finally, the signal is obtained by applying the inverse Fourier transform (27.9), where the integration is performed along a path lying along the real axis. In order to avoid singularities and spurious noncausal effects, the frequency parameter ω is treated as a complex variable $\omega = \omega_r + i\omega_i$ (Bertin et al. 2014), with a small positive imaginary part $\omega_i \ll 1$ and thus, the eigenvalues $k_m(\omega)$ are also complex.

Using the normal mode approach to compute the acoustic pressure field, the impact of GWs is evaluated as follows. First, the large-scale vertical profiles of temperature and winds are extracted from ECMWF products, typically up to 70 km. The profiles are matched with the empirical models HWM07 (Drob et al. 2008) and MSIS-90 (Mass Spectrometer and Incoherent Radar Model) through interpolation functions. These two empirical models provide a statistical representation of the mesosphere and thermosphere. The resulting profiles allow computing both the effective sound speed $c(z)$, through the effective sound speed approximation, and the GW field. Second, the offline version of the GW model is used to estimate the impact of GWs onto the vertical profiles. Since the scheme described in Sect. 27.2 only predicts fluxes $\vec{F}_n^z$ for randomly chosen wavevectors $\vec{k}_n$ and frequencies ω_n, it is necessary to rederive the GW fields by applying local polarization relations and a WKB formalism, yielding

$$(\vec{u}', T') = \Re\left\{ \sum_{n=1}^{N} C_n(\hat{\vec{u}}_n, T_n) e^{z/2H}, e^{i(\vec{k}_n \cdot \vec{x}) - \omega_n t)} \right\}, \tag{27.13}$$

where

$$(\hat{\vec{u}}_n, T_n) = \Re\left\{ \left(\frac{N}{\Omega_n} \frac{\vec{k}_n}{|\vec{k}_n|}, -i\frac{N^2 H}{R\Omega_n} \right) \hat{w}_n \right\}, \tag{27.14}$$

and where the vertical profiles of vertical velocity,

$$\hat{w}_n = \sqrt{\frac{2\|\vec{F}_n^z \Omega_n\|}{\rho_r N}} \exp\left(-i \int_0^z \frac{N\|\vec{k}_n\|}{\Omega_n} dz' + i\chi_n \right), \tag{27.15}$$

where χ_n is a phase that can be chosen randomly. Then, to evaluate wave fields that are consistent with the parameterization presented in Sect. 27.2, we proceed stochas-

tically and first compute $n = 100$ realizations of vertical profiles choosing $\vec{k}_n$ and ω_n randomly. From this large number of realizations, we reconstruct an ensemble of GW fields picking the intermittent factors C_n randomly as well, but conserving the normalization condition (27.2).

27.4.2 A Case Study

We generally refer to the low-frequency band of the acoustic spectrum ($2\pi N < \omega < 2\pi$) as infrasound. Man-made sources in this band are limited to large explosions and to sonic booms generated by rockets and aircrafts. Extensive investigations of such sources have been carried out by numerous authors and examples of infrasonic pressure signatures can be found in the literature. For illustration purpose, we consider sound propagation of regional distances and model the source function in (27.9) by

$$s(t) = \cos\left(2\pi f_c t\right) \frac{1 - \cos(\pi f_c t)}{2}, \tag{27.16}$$

where $0 < t < 1/f_c$, and $s(t) = 0$ otherwise.

Figure 27.4 shows the vertical profiles of effective sound speed as obtained by adding GWs onto the atmospheric specification provided by ECMWF (analysis, 137 levels). Due to large-scale winds, the effective sound speed presents two relative maxima, at the surface and near the stratopause (around 50 km), and two relative minima, at the tropopause and the mesopause. These relative extrema define two regions, often called tropospheric and stratospheric ducts, in which $\omega^2/c^2 - k^2$ can be positive and bounded by regions where it can be negative. The efficiency of the stratospheric duct is controlled by the ability of the mesopause to reflect infrasound or, in terms of normal modes, to trigger a large number of normal modes. When including GWs disturbances, an ensemble of effective celerities is produced, replacing T and $\vec{u}$ in Eq. (27.12) by $T + T'$ and $\vec{u} + \vec{u}'$, respectively. Figure 27.4c and 27.4a shows the standard deviations (gray lines) of the resulting profiles predicted by the non-orographic gravity wave parameterization, as obtained with the two sets of GWs parameters used in Fig. 27.1a and 27.1b, respectively. As pointed out in Sect. 27.2 and noticed by numerous authors (e.g., Lalande and Waxler 2016; Drob et al. 2013), the GW field produces substantial variations in the effective sound speed all the way through the middle atmosphere. Whereas the first setup of the parameterization induces substantial variations at the mesopause level, the fluctuations obtained with the second setup are more important in the stratosphere and lower mesosphere.

Results of infrasound propagation simulations obtained with the source function defined by (27.16) are given in Fig. 27.5 in the form of space-time diagrams. The normalized Hilbert transform of signals is indicated in colors. The most obvious interpretation of signals in Fig. 27.5 is that each succeeding arrival is "reflected" from higher in the atmosphere so that its path is longer than preceding arrivals. Figure 27.6a shows a typical signal, recorded at the I37NO IMS station in

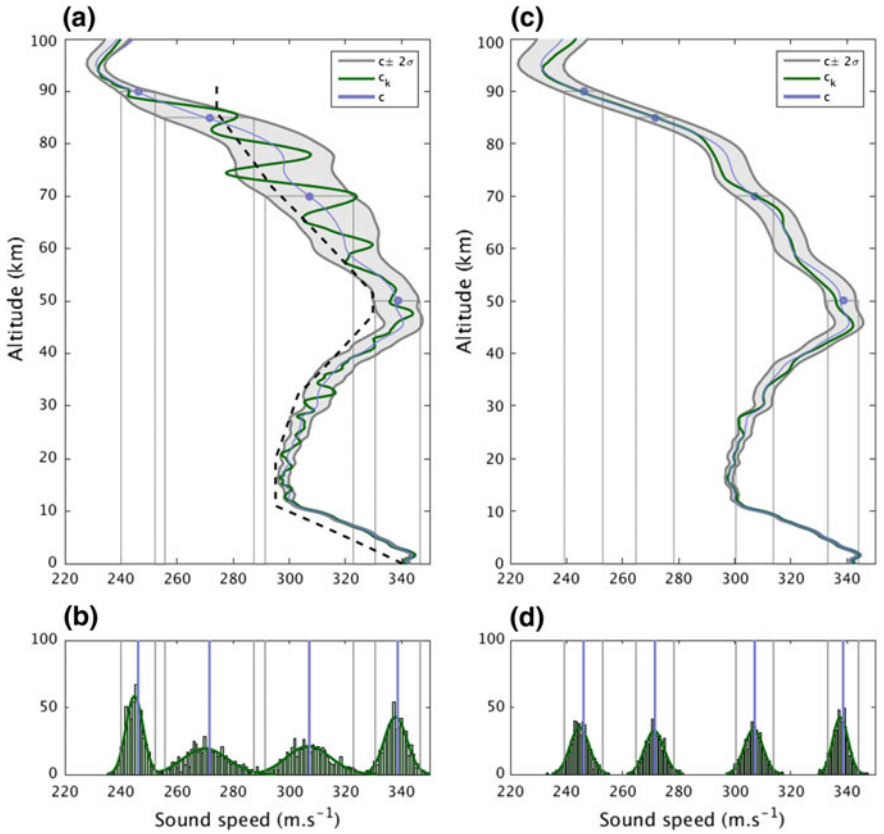

Fig. 27.4 **a**, **c** Profiles of effective sound speed at I37NO on August 16, 2016 (12:30 p.m.) and associated probability density functions **b**, **d** for fixed altitudes of 50, 70, 85, and 90 km. The dashed black line gives the profile as obtained from the US76 empirical model. The envelope delimited by gray lines represents the standard deviation $c \pm 2\sigma$ obtained for an ensemble of 500 profiles evaluated stochastically using the setup of Fig. 27.1 (**c**, **d**) and from a parameterization with reduced phase speed waves (**a**, **b**). The original reference profile is indicated by $c(z)$ (which is also the mean profile) and a particular realization $c_k(z)$ is given by the green line

northern Norway on August 18, 2016 and particular realizations of numerically obtained signals. In this case, the source is known to be associated with a near-surface explosion (with a yield of approximately 20–30 t) at the Hukkakero military range in Finland (Gibbons et al. 2015), located 320 km away from I37NO. Such event occurs on consecutive days in August and September and provides a useful dataset for the study of infrasound propagation.

The signal in Fig. 27.6a shows a function of the retarded time $t - r/c_0$ where $c_0 = 356\ \mathrm{m\,s^{-1}}$. The first striking result is that the sound signal arrives for positive retarded time, witnessing that it is dominated by signals that have traveled substantially in the upper atmosphere. The first arrival time is due to the tropospheric duct,

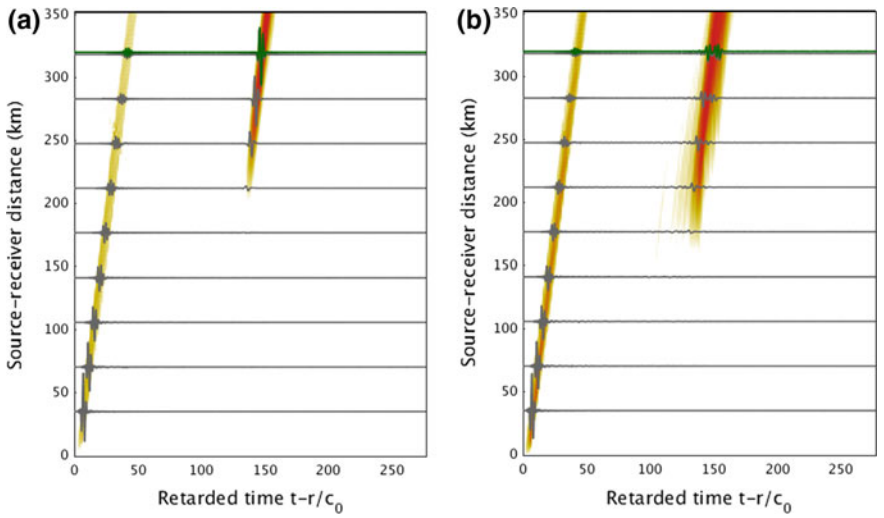

Fig. 27.5 Space-time diagrams showing infrasound signals (green lines) propagating through a particular realization of the perturbed atmospheric specification. The standard deviation of the normalized Hilbert transform of signals is given by colors for an ensemble of 100 vertical profiles. **a** Results obtained using the setup of Fig. 27.1; **b** results obtained from a parameterization with reduced phase speed waves. The source frequency is $f_c = 0.35$ Hz

and we see that it is quite small in amplitude, whereas the second one is much more substantial and due to the stratospheric duct. The next three panels below show the signals calculated via the normal mode and for a source of the form given by (27.16) with $f_c = 0.35$ Hz. The second panel from the top gives the infrasound prediction without GWs. It shows that the model predicts well the time of arrival and the duration of the tropospheric response but largely underestimates the amplitude of the stratospheric arrival. In the presence of GWs, the separation between the tropospheric and stratospheric ducts can be much more permeable, allowing a fraction of the signal to travel easier through the stratospheric duct. This is clearly shown in the next two panels where the green curve shows that in the presence of GWs field a stronger second arrival is predicted. Interestingly, it is when the GWs phase speed is smaller in the bottom panel that the stratospheric arrivals duration is larger. It is interesting to recall that in this configuration the GWs modify more the celerity maxima at the stratopause according to the left panel in Fig. 27.4 than the effective celerity minima at the mesopause (right panel in Fig. 27.4). Finally, it is important to notice that the increase of the stratospheric arrival when there are more GWs in the stratosphere than in the mesosphere is not the result of one particular GW field. The gray-shaded curves show the standard deviation of the signals out of 100 GWs fields built stochastically, and confirm that our infrasound prediction clearly improves when the GWs are more confined to the stratosphere.

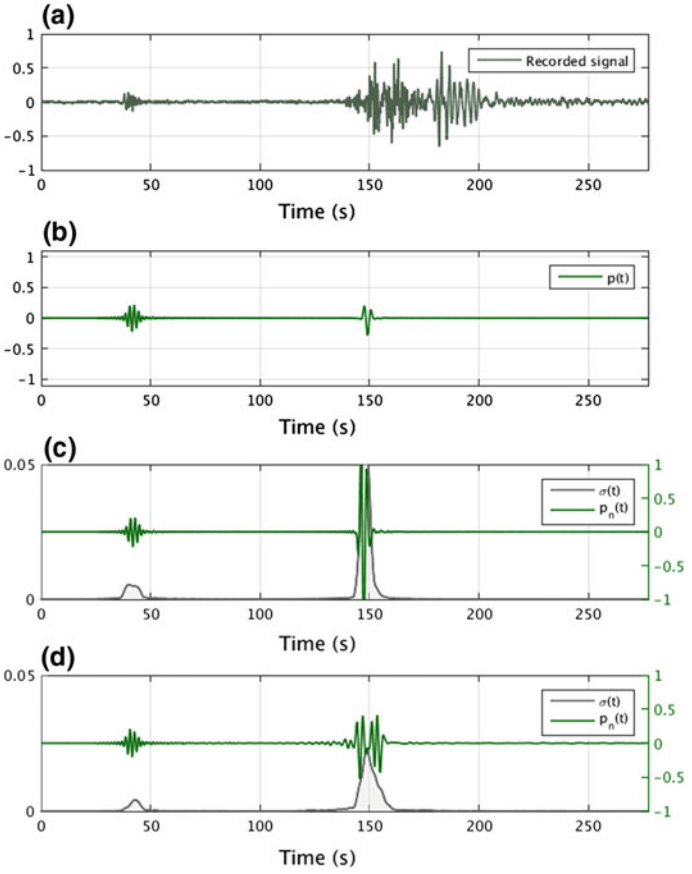

Fig. 27.6 Recorded signal at I37NO (**a**) and numerically obtained signals using the 137-level ECMWF profile (**b**) and by adding gravity waves. **a** Particular signal obtained using the setup of Fig. 27.1 and **b** from a parameterization with reduced phase speed waves. Results are obtained for a source function defined by Eq. (27.16) with $f_c = 0.35$ Hz. The standard deviation σ is plotted in solid gray line as a function of time and normalized by the maximum amplitude of each realization

27.5 Perspective

While long-range infrasound propagation modeling is a useful tool in geophysics and nuclear treaty verification, the inherent unpredictability of subgrid-scale atmosphere dynamics results in a poorly constrained propagation medium. The general approach in the infrasound research community is to superimpose a single ad hoc "frozen" disturbance onto the atmospheric specification, obtained through spectral models and to propagate infrasound in the resulting medium. Such an approach, however, fails in representing the impact of small-scale dynamics which is intrinsically statistical and indeed, direct observations in the lower stratosphere show that the gravity wave

field is very intermittent, and often dominated by well-defined large-amplitude and low-probability wave packets.

In this paper, we propose another approach, in which the GW field is described by a stochastic field obtained with a multiwave stochastic parameterization of GWs currently in use in an AGCM. The propagation of infrasound can be obtained at a rather low numerical cost with low-order reduced models (Bertin et al. 2014). Such an approach illustrates how two disciplines can benefit from a mutual interaction. Gravity wave fields can be adapted from the climate models and superimposed onto atmospheric specifications in order to improve infrasound predictions. In turn, the infrasound calculations can be used together with observations to constrain the GW parameterizations. In this paper, we only give preliminary results and show that a state-of-the-art GW scheme can yield some improvement in infrasound prediction, provided that the phase speed of GWs is much smaller than that currently in use in AGCMs. As pointed out in this paper, the duration of signals remains smaller than that observed. On the other hand, to improve GWs parameterization, one should understand which physical processes could place more low-phase speed GWs in the stratosphere To improve infrasound models, one direction could be to consider coupling between modes, especially when GWs fields vary in the horizontal and vertical directions.

Acknowledgements This work was supported by the European Commission's project ARISE2 (Grant Agreement 653980), the ANR/JPI-Climate/Belmont Forum project GOTHAM (ANR-15-JCLI-0004-01), and the Commissariat à l'Énergie Atomique et aux Énergies Alternatives (CEA).

References

Alexander MJ, Dunkerton TJ (1999) A spectral parameterization of mean-flow forcing due to breaking gravity waves. J Atmos Sci 56(24):4167–4182

Beres JH, Garcia RR, Boville BA, Sassi F (2005) Implementation of a gravity wave source spectrum parameterization dependent on the properties of convection in the whole atmosphere community climate model (waccm). J Geophys Res 110(10):1–13

Bertin M, Millet C, Bouche D (2014) A low-order reduced model for the long range propagation of infrasounds in the atmosphere. J Acoust Soc Am 136(1):37–52

Budden KF (1961) The wave-guide mode theory of wave propagation. Logos Press and Elek Book

Chunchuzov I, Kulichkov S (2019) Internal gravity wave perturbations and their impacts on infrasound propagation in the atmosphere. In: Le Pichon A, Blanc E, Hauchecorne A (eds) Infrasound monitoring for atmospheric studies. 2nd edn. Springer, Dordrecht pp 551–590

Chunchuzov IP, Kulichkov SN, Popov OE, Waxler R, Assink J (2011) Infrasound scattering from atmospheric anisotropic inhomogeneities. Izv Atmos Ocean Phys 47(5):540–557

de la Camara A, Lott F (2015) A parameterization of gravity waves emitted by fronts and jets. Geophys Res Lett 42:2071–2078

de la Camara A, Lott F, Hertzog H (2014) Intermittency in a stochastic parameterization of non-orographic gravity waves. J Geophys Res Atmos 119:11905–11919

Dergham G, Millet C (2013) Range-dependent propagation modeling of infrasound in complex atmospheres. AIAA Paper 2013-3209

Drob DP et al (2008) An empirical model of the Earth's horizontal wind fields: HWM07. J Geophys Res: Space Phys 113:2156–2202

Drob DP, Broutman D, Hedlin MA, Winslow NW, Gibson RG (2013) A method for specifying atmospheric gravity wavefields for long-range infrasound propagation calculations. J Geophys Res 118(10):3933–3943

Eckermann SD (2011) Explicitly stochastic parameterization of nonorographic gravity wave drag. J Atmos Sci 68(8):1749–1765

Gibbons SJ et al (2015) The European Arctic: a laboratory for seismoacoustic studies. Seismmol Res Lett 86(3):917–928

Godin OA (2002) An effective quiescent medium for sound propagating through an inhomogeneous moving fluid. J Acoust Soc Am 112:1269–1275

Gossard EE, Hooke WH (1975) Waves in the atmosphere. Elsevier Scientific Publishing Company, Amsterdam

Hedlin MA, de Groot-Hedlin CD, Drob D (2012) A study of infrasound propagation using dense seismic network recordings of surface explosions. Bull Seismol Soc Am 102:1927–1937

Hedlin MAH, Drob DP (2014) Statistical characterization of atmospheric gravity waves by seismoacoustic observations. J Geophys Res: Atmos 119(9):5345–5363

Holton JR (1982) The role of gravity wave induced drag and diffusion in the momentum budget of the mesosphere. J Atmos Sci 39:791–799

Hourdin F et al (2013) Impact of the lmdz atmospheric grid configuration on the climate and sensitivity of the ipsl-cm5a coupled model. Clim Dyn 40:2167–2192

Jensen FB, Kuperman WA, Porter MB, Schmidt H (1994) Computational ocean acoustics. American Institute of Physics

Kulichkov SN, Chunchuzov IP, Popov OI (2010) Simulating the influence of an atmospheric fine inhomogeneous structure on long-range propagation of pulsed acoustic signals. Izv Atmos Ocean Phys 46(1):60–68

Lalande J-M, Waxler R (2016) The interaction between infrasonic waves and gravity wave perturbations: application to observations using UTTR rocket motor fuel elimination events. J Geophys Res: Atmos 121(10):5585–5600

Lindzen RS, Tsay CY (1975) Wave structure of the tropical stratosphere over the Marshall Island area during 1 April–1 July 1958. J Atmos Sci 32(10):2008–2021

Lott F (1999) Alleviation of stationary biases in a GCM through a mountain drag parameterization scheme and a simple representation of mountain lift forces. Monthly Weather Rev 127(5):788–801

Lott F, Guez L (2013) A stochastic parameterization of the gravity waves due to convection and its impact on the equatorial stratosphere. J Geophys Res 118(16)

Lott F, Millet C (2009) The representation of gravity waves in atmospheric general circulation models (GCMs). Springer Netherlands, pp 685-699

Lott F, Plougonven R, Vanneste J (2010) Gravity waves generated by potential vorticity anomalies. J Atmos Sci 67:157–170

Lott F, Guez L, Maury P (2012a) A stochastic parameterization of non-orographic gravity waves: formalism and impact on the equatorial stratosphere. Geophys Res Lett 39(6)

Lott F, Plougonven R, Vanneste J (2012b) Gravity waves generated by sheared three-dimensional potential vorticity anomalies. J Atmos Sci 69(7):2134–2151

Palmer TN (2012) Towards the probabilistic earth-system simulator: a vision for the future of climate and weather prediction. Q J R Meteorol Soc 138:841–861

Picone JM, Hedlin A, Drob D, Aikin A (2002) NRL MSISE-00 empirical model of the atmosphere: statistical comparisons and scientific issues. J Geophys Res 107. https://doi.org/10.1029/2002JA009430

Rind DH (1978) Investigation of the lower thermosphere results of ten years of continuous observations with natural infrasound. J Atmos Solar-Terr Phys 40:1199–1209

Chapter 28
Middle Atmosphere Variability and Model Uncertainties as Investigated in the Framework of the ARISE Project

Elisabeth Blanc, Katy Pol, Alexis Le Pichon, Alain Hauchecorne, Philippe Keckhut, Gerd Baumgarten, Jens Hildebrand, Josef Höffner, Gunter Stober, Robert Hibbins, Patrick Espy, Markus Rapp, Bernd Kaifler, Lars Ceranna, Patrick Hupe, Jonas Hagen, Rolf Rüfenacht, Niklaus Kämpfer and Pieter Smets

Abstract The middle atmosphere (from about 10–110 km altitude) is a highly variable environment at seasonal and sub-seasonal timescales. This variability influences the general atmospheric circulation through the propagation and breaking of planetary and gravity waves. Multi-instrument observations, performed in the framework of the ARISE (Atmospheric Dynamics Research InfraStructure in Europe) project, are used to quantify uncertainties in Numerical Weather Prediction (NWP) models such as the one of the European Centre for Medium-Range Weather

E. Blanc (✉) · K. Pol · A. Le Pichon
CEA, DAM, DIF, F-91297 Arpajon, France
e-mail: elisabeth.blanc@cea.fr

A. Hauchecorne · P. Keckhut
LATMOS-IPSL, Guyancourt, France

G. Baumgarten · J. Hildebrand · J. Höffner · G. Stober
Leibniz-Institute of Atmospheric Physics, Rostock University, Kühlungsborn, Germany

R. Hibbins · P. Espy
Norwegian University of Science and Technology, Trondheim, Norway

M. Rapp · B. Kaifler
DLR, German Aerospace Center, Oberpfaffenhofen, Germany

L. Ceranna · P. Hupe
Federal Institute for Geosciences and Natural Resources, Hannover, Germany

J. Hagen · R. Rüfenacht · N. Kämpfer
Institute of Applied Physics, University of Bern, Bern, Switzerland

P. Smets
Department of Seismology and Acoustics, KNMI, De Bilt, Netherlands

P. Smets
Department of Geoscience and Engineering, Delft University of Technology, Delft, Netherlands

A. Le Pichon et al. (eds.), *Infrasound Monitoring for Atmospheric Studies*,
https://doi.org/10.1007/978-3-319-75140-5_28

Forecasts (ECMWF). We show the potential of routine and measurement campaigns to monitor the evolution of the middle atmosphere and demonstrate the limitations of NWP models to properly depict small-scale atmospheric disturbances. Continuous lidar and radar measurements conducted over several days at ALOMAR provide a unique high-resolution full description of solar tides and small-scale structures. Nightly averaged lidar profiles routinely performed in fair weather conditions at the Observatoire Haute-Provence (OHP) and Maïdo observatory (Reunion Island) provide a year-to-year evolution of stratosphere and mesosphere temperature profiles. Routine meteor radar observations depict the evolution of wind profiles and solar tides in the mesosphere and lower thermosphere. With the recent development of the portable Compact Rayleigh Autonomous Lidar (CORAL) which automatically measures temperature profiles at high temporal resolution, the possibility of combining different instruments at different places is now offered, promising the expansion of multi-instrument stations in the near future. Through a better description of infrasound propagation in the middle atmosphere and stratosphere–troposphere couplings, these new middle atmosphere datasets are relevant for infrasound monitoring operations, as well as for weather forecasting and other civil applications.

28.1 Introduction

The Middle Atmosphere (MA)—located between the tropopause at 10–15 km and the turbopause at 100–110 km—is a highly variable region, marked by the intensive activity of gravity (GW) and planetary waves (PW), tides, or by the occurrence of other large-scale disturbances such as Sudden Stratospheric Warming (SSW) events. While this variability is known to influence the MA mean circulation and its tropospheric counterpart (Baldwin and Dunkerton 2001; Shaw and Sheperd 2008a), its integration into weather and climate models is rudimentary because most models do not assimilate any data above 60 km where temperature and wind observations are sparse.

During the 70s, the possibility of using infrasound measurements from regional to global networks to depict MA variability was suggested by pioneer infrasound observations (Donn and Rind 1971; Rind and Donn 1975). Propagating in the waveguide between ground and regions of increasing temperatures (mainly in the stratosphere and lower thermosphere) in the direction of prevailing winds (Delclos et al. 1990; Bedard and Georges 2000; Le Pichon et al. 2006), infrasound signals indeed integrate the effects of MA disturbances along their path. These can then be derived from the analysis of infrasound parameters such as back azimuth, elevation angle, and amplitude (Rind and Donn 1975). While atmospheric variations are the main source of uncertainties in operational monitoring, Rind et al. (1973) and Rind and Donn (1975) first proposed to use infrasound from well-identified repetitive sources to remotely determine upper atmosphere wind speeds. This challenging

objective needed high-performance observations, which were only achieved years later with the development of atmospheric monitoring systems.

The infrasound technology is one of the technologies selected for the verification of the Comprehensive Nuclear-Test-Ban Treaty (CTBT) in the 90s. To determine the network specifications of the infrasound International Monitoring System (IMS) (Conference on disarmament 1995), computations of detection capability were performed, including the MA variability. Empirical attenuation laws roughly integrated the seasonal effects of the stratospheric wind provided by climatological models (Whitaker 1995), while the background infrasound noise was deduced from surface wind estimation at the detection stations (Clauter and Blanford 1998; Blanc and Plantet 1998).

With advances in meteorological modeling, new computations of infrasound network detection capability were performed in the 2000s. The infrasound noise—highly variable in space and time depending on the ground surface wind (Alcoverro and Le Pichon 2005; Bowman et al. 2005)—was better integrated. The MA variability as prescribed by the HWM-93 and ECMWF models (Drob et al. 2008) was also included in the computations. Despite such variable detection performances, it was demonstrated and further confirmed by a probabilistic approach (Green and Bowers 2010) that explosions equivalent to 500 t of TNT can be detected by at least two stations at any time of the year (Le Pichon et al. 2009). A frequency-dependent semiempirical attenuation relation derived from massive numerical propagation computations was used to quantify the spatial and temporal variability at higher time and space resolution (Le Pichon et al. 2012).

Backed by this progress, infrasound observations of repetitive and well-identified sources have eventually been used to validate the computations under different atmospheric conditions. The deviation of back azimuth produced by the seasonal inversion of the stratospheric wind was quantified for the first time in 2002, using the infrasound signal of the Concorde aircraft, detected every day in France in the 90s (Le Pichon et al. 2002). This azimuth deviation can be corrected at a first order using ray tracing simulations. However, quasi-continuous observations of the Lopevi volcano eruptions (New Caledonia) showed residual azimuth changes of several degrees even after correction, which were attributed to uncertainties in the representation of the ECMWF zonal wind model. A method was then proposed to retrieve winds in the upper stratosphere and mesosphere using such observations (Le Pichon et al. 2005). Likewise, Antier et al. (2007) extracted planetary wave features from the same dataset (2007). Since then, different methods for inversion exercises have emerged (Assink et al. 2019). Analyzing the ambient noise produced by ocean swells permanently recorded worldwide opens doors for further investigations (Le Pichon et al. 2006; Smets and Evers 2014).

Other comparisons over several years between quasi-permanent infrasound detections from the Etna volcano in Tunisia and simulations have also showed large differences, especially in the equinox period, arising from the lack of representation of gravity waves in the ECMWF model (Blanc et al. 2017). In parallel, infrasound observations in the lower frequency range have been used to provide a unique description of the mountain wave activity (Hupe et al. 2017a), stratospheric

warming events (Smets et al. 2016), and tropical GW in relation to the Intertropical Convergence Zone of the Winds (Blanc et al. 2014), demonstrating the interest of ARISE data for a better representation of GW and other MA disturbances in atmospheric models in the near future.

First lidar investigations begun in the 70s, following advances in laser technologies which enabled vertical profiling of many atmospheric components and parameters. All lidars are sensitive to molecular scattering and allow one to derive temperature profiles extending to high altitudes with sufficient photon counts and in the absence of other scattering mechanisms (Hauchecorne and Chanin 1980). The long-term and high vertical resolution capabilities allow lidars to make significant contributions to atmospheric dynamic studies. Gravity and planetary wave investigations (Wilson et al. 1991; Hauchecorne and Chanin 1983) and long-term cooling detection (Hauchecorne et al. 1991) were initiated with the first decade of continuous measurements performed at Observatory of Haute-Provence. Those measurements became more mature and more sites use this technique following the construction in 1991 of the Network for Detection of Stratospheric Changes (NDSC) to address the issue of ozone loss and the NASA Upper Atmosphere Research Satellite validation (Kurylo and Salomon 1990). Later, more sophisticated methods were developed to extend downward (below 30 km) and above the mesopause, the temperature profiles using Raman and resonance techniques of metallic species by different groups. Also, the double-edge technique has demonstrated the lidar capability to measure wind (Chanin et al. 1989). With the additional climate issues, the NDSC was relabeled as Network for the Detection of Atmospheric Composition Changes (NDACC).

In the 2010s, many studies demonstrated the benefits of different technologies in addition to infrasound and lidars, in order to better understand the MA variability and quantify model uncertainties (Le Pichon et al. 2010). This challenging objective was the main motivation for the ARISE project (Blanc et al. 2018). This project combines different observation networks, such as the IMS infrasound network developed for the CTBT verification, the complementary European infrasound network, complemented by the Network for the Detection of Atmospheric Composition Changes (NDACC) lidar network, multi-instrument observatories in tropics, middle latitude and polar regions and satellites. The measurement campaign performed at the Haute-Provence Observatory in 2013 and 2014 showed systematic differences between modeled and observed temperature and wind fields, with a maximum deviation between 40 and 60 km altitude. The mean standard deviation exceeds 5 K and 20 m/s in temperature and zonal wind speed respectively, while the 95% confidence intervals reach 30 K and 40 m/s. The largest deviations were observed in winter when the variability from large-scale planetary waves dominates the general circulation (Le Pichon et al. 2015).

The objective of this paper is to describe progress in the determination of the atmospheric variability and quantification of model uncertainties performed in the framework of the ARISE project (Blanc et al. 2018). The paper is organized as follows: the next session describes the origins of the atmospheric variability and its

representation in models, Sect. 28.3 provides examples of systematic MA observations performed within the ARISE instrumental network to quantify model uncertainties, and Sect. 28.4.1 shows impacts of these uncertainties on infrasound simulations. MA routine observations are improved but are still well short of providing a full understanding of the MA variability and model uncertainties. Section 28.5 presents new experimental possibilities, especially facilitated by the recent development of high-resolution portable lidars, and discusses associated perspectives.

28.2 Atmospheric Variability and Representation in Models

28.2.1 Origin of the Atmospheric Variability

The general circulation of the atmosphere is the result of the uneven seasonal and latitudinal distribution of radiative energy over a tilted, rotating Earth. At smaller spatiotemporal scales, however, this mean circulation is continuously disrupted by dynamical phenomena resulting from large- and small-scale wave motions that arise due to land/sea contrasts, jet stream instabilities, frontal systems, orography, and convection, among others. Between 0 and ~10–15 km, in the atmospheric layer known as the troposphere, one can regularly experience such atmospheric variations, from seasonal monsoon effects to daily weather variations and intensive and short-living phenomena like cyclones and thunderstorms. In contrast, the MA is characterized by variability essentially caused by the upward propagation and breaking of different waves, generated in the troposphere and forcing the MA via energy and momentum inputs accompanying wave dissipation (see Fig. 28.1 for a summary of the different waves measured in the framework of ARISE). Since the pioneering studies of Baldwin and Dunkerton (2001), there has been an increasing interest in the MA variability, for its influence on the current and future tropospheric weather and climate (e.g., Shaw and Shepherd 2008a; Manzini et al. 2014).

The MA is notably composed of the stable stratified stratosphere between 10 and 50 km, characterized by a positive gradient of temperature due to the ozone layer, and the mesosphere between 50 and 90 km—characterized by a negative temperature gradient and consequently a weaker vertical stability. This specific thermal structure of the MA cannot only be explained by the absorption of solar radiation by the ozone layer. It also relies on the associated global-scale mean meridional and vertical circulation, from low to high latitudes known as the Brewer–Dobson circulation (Shepherd 2000) in the lower stratosphere, and from the summer to the winter hemisphere in the upper stratosphere and mesosphere. However, to maintain this so-called diabatic circulation, the role of atmospheric waves is crucial (Lindzen 1981; Holton 1982) and the study of propagating waves becomes essential to understand and properly simulate the MA mean circulation and its associated

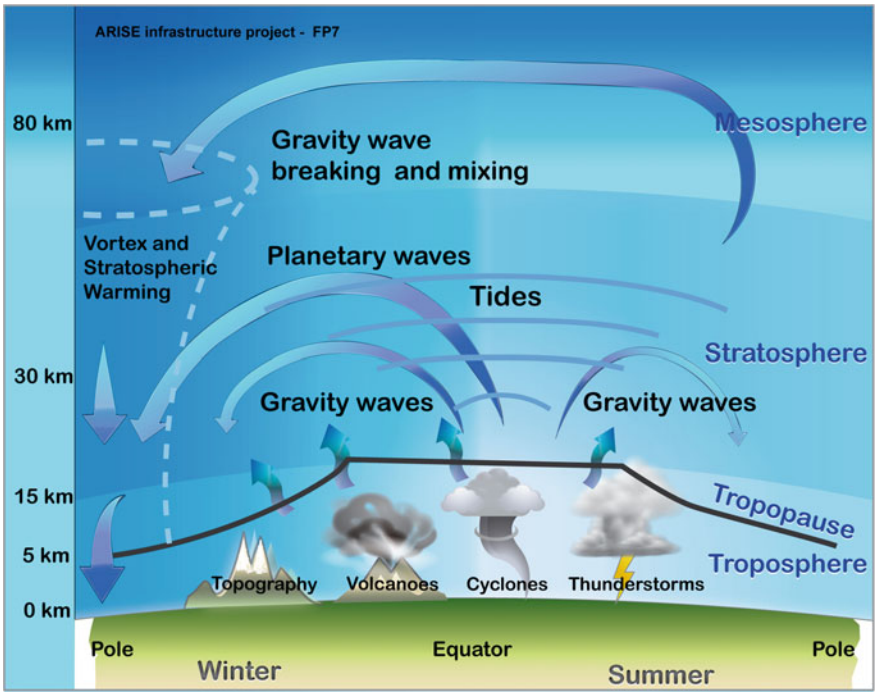

Fig. 28.1 Schematic diagram of the atmospheric dynamic processes encountered in the Earth's atmosphere. Planetary and gravity waves contribute to the middle atmospheric transport illustrated by arrows

variability. This is especially true when considering the connection with the thermosphere, whose heterogeneous composition—which strongly interacts with the magnetic field—make the model investigations even more complex.

Rossby Planetary Waves

MA dynamics are highly diverse and differ from tropical to extratropical regions (see Hauchecorne 2010 for a more detailed description). Main types of waves interacting with the middle atmospheric circulation include extratropical Rossby planetary waves (PW) and internal gravity waves (GW) (Fig. 28.1). PWs have their origins in the Coriolis forces forming a meridional gradient of potential vorticity (McIntyre 1992). Characterized by relatively slow phase and westward propagation relative to the mean flow (Charney and Drazin 1961), PWs are blocked by easterly stratospheric winds in summer and consequently, mainly active in wintertime, in presence of the westerly stratospheric flow. Due to the exponential decrease of the atmospheric density with height, their relative amplitude increases until reaching a critical value, where PWs break and interact with the zonal flow. With characteristic timescales of 5–20 days, PWs with the largest horizontal wavelengths propagate up to the middle stratosphere and mesosphere, while the shortest ones dissipate in the

lower atmosphere (Salby 1984). They play a major role in the stratospheric dynamics, causing large variability in wintertime temperature and wind profiles for instance, and especially in the evolution of the winter polar vortex (see Sudden Stratospheric Events in the following section). PWs are quite easily detectable by different kinds of instruments, from satellites (Hirooka 2000) to radio soundings (Hirota and Hirooka 1984). A Rayleigh lidar like the one operating at OHP (see Sect. 28.4.2), which is routinely used to measure 3–4 mean nightly temperature profiles per week, can easily provide a good survey of the winter evolution of PW in the MA, with clear alternation between cold and warm perturbations throughout the PW phase (Hauchecorne et al. 1987).

Internal Gravity Waves

Most important waves for MA dynamics are internal GWs, originating from buoyancy forces in a vertically stable stratified atmosphere caused by different tropospheric sources: flow over topography, convective and frontal activities (Bretherton and Smolarkiewicz 1989; Shutts and Gray 1994), wind shear instabilities (Lalas and Einaudi 1976; Lott et al. 2010), non-modal growth (Bakas and Ioannou 2007), and geostrophic adjustment. Through their breaking in the upper atmosphere and interactions with other dynamical processes (e.g., Lindzen 1981; Fritts 1984; Medvedev and Klaasen 2000; Fritts and Alexander 2003), GWs are known for influencing, driving, and modifying the observed MA circulation (Holton 1983; Holton et al. 1995; Shaw and Sheperd 2008b, Kulichkov 2010). GWs are selectively filtered by the mean and large-scale wind at all levels, leading to a prevalence of propagation directions opposite to the mean winds in the stratosphere and lower mesosphere (toward west in winter, east in summer). Due to their relatively small vertical scales (a few tenths of km to several km) and short periods (few minutes to few or several 10's of hours), GWs are difficult to be observed from space. Ground-based remote sensing instruments such as Rayleigh temperature lidars (Wilson et al. 1991), Mesosphere–Stratosphere–Troposphere (MST) radars (Venkat Ratnam et al. 2008), or infrasound technology (Blanc et al. 2010) are then very valuable to improve the knowledge of GW characteristics.

Tides

Besides PW and GW effects, the MA also experiences temperature and wind oscillations caused by the diurnal absorption of solar radiation by ozone in the stratosphere (and by water vapor in the troposphere). Logically known as thermal tides, periods of observed variations vary from 24 h to associated harmonics (semidiurnal and terdiurnal tides, with periods 12 and 8 h, respectively, and up to 6 h). Despite weak observed effects in the tropospheric and stratospheric source regions, upward propagating tides grow in amplitude as the atmospheric density decreases, until their dissipation in the upper mesosphere/lower thermosphere (and at even much higher latitudes in some cases). Therefore, they are observed by MF radars between 70 and 100 km altitude in horizontal wind components (Kishore et al. 2002) and by lidars, in temperature and wind profiles of the upper stratosphere and mesosphere (e.g., Keckhut et al. 1996). Recently, an infrasound-based study

has also highlighted tide-associated infrasound signals as detected by the stations of the global IMS network (Hupe et al. 2016, 2017b).

Sudden Stratospheric Warmings

One of the most remarkable phenomena of the MA variability is the occurrence of Sudden Stratospheric Warmings (SSWs) in wintertime. Directly caused by the breaking of PW in the stratosphere and consequent nonlinear interactions with the zonal flow (Charney and Drazin 1961; Matsuno 1971; Hauchecorne and Chanin 1983), SSW can be characterized by polar stratospheric temperatures increasing by ~40–60 K in 1 week at 30 km altitude (Labitzke 1977). Such increases in temperature are associated with PW EP flux divergence at polar latitudes, leading to either weakening or reversal of the wintertime westerly stratospheric winds at 60°N and a vortex displacement or split for the most severe cases, depending on the PW zonal wave number (Andrews et al. 1987; Mathias et al. 2013; Butler et al. 2015). SSW have major impacts on the Northern Hemisphere wintertime surface climate (extreme cold air outbreaks over North America and Eurasia or warming over Greenland, (Thompson et al. 2002)) or on meteorological conditions in general (e.g., on polar tropospheric clouds, Kohma and Sato 2014, or on equatorial tropospheric convective activity, Kodera 2006), that can last up to 30 days (Baldwin and Dunkerton 2001; Polvani and Waugh 2004; Gerber et al. 2009). They also play a major role in the Arctic and Antarctic ozone variability (Schoeberl and Hartmann 1991). Many studies to date have focused on reversal cases known as major SSW, due to their strong influences on lower tropospheric dynamics (Gerber et al. 2009; Charlton and Polvani 2007; Cohen and Jones 2011). However, other cases are also suggested to have a tropospheric counterpart (Limpasuvan et al. 2004; Maury et al. 2016). SSW preferentially occur in the Northern Hemisphere (Schoeberl 1978) (with one case occurring in the Southern Hemisphere in 2002, Baldwin 2003) but not every winter. Impacting temperature and wind profiles, they can be detected in a broad altitude range using temperature and wind lidars (Baumgarten 2010; Angot et al. 2012) and ionospheric radars (Goncharenko et al. 2013). Because of changes in conducting wind direction, SSW also implies source changes in infrasound detections; the infrasound technology can thus also be used to characterize SSW responses at lower altitudes (Smets and Evers 2014; Le Pichon et al. 2015).

Infrasound Waves

Infrasound waves could impact the atmosphere and contribute to the MA variability. Because of their large attenuation when the altitude increases, their influence is expected to be small for most infrasound sources at frequencies of several Hz (Pilger and Bittner 2009). At lower frequencies, infrasound sources like ocean swells affect quasi continuously large ocean surfaces (Landes et al. 2014) and could produce significant heating in the 110–140 km altitude range as early suggested by Rind (1977) and Hickey et al. (2001). However, observations are still missing to quantify this effect.

28.2.2 Representation of the Atmospheric Variability in Models

The previously described complex wave-driven dynamical system and its associated large-scale disturbances are only poorly represented in weather and climate models. As shown by Charlton-Perez et al. (2013), only about half of the climate models used for the most recent Coupled Model Intercomparison Project (CMIPS5) extend above the stratopause around 1 hPa. Such differences in model vertical extension have been shown to yield significant biases in the Numerical Weather Prediction model (NWP) performances for simulations of the stratospheric climate, its variability and the coupling with the troposphere (Manzini et al. 2014). One reason for this lack of representation of MA in NWP models is the limited observations covering this region of the atmosphere. Moreover, the representation of wave dynamics is unequal, due to very poor NWP representation of the important smaller scale GWs.

As fully described by Lee et al. (2019), a diversity of observation techniques (radiosondes, satellite remote sounding from nadir, zenith and limb directions, tropospheric wind profilers, mesosphere radars, and lidars) is used to study the state of the atmosphere. However, only a small fraction is assimilated into NWP models. This is the case for radiosondes, which have provided historical datasets from the early 1900s and are—even today—often used as reference observations. Satellite remote soundings are systematically assimilated by NWP as the only technique that can provide global coverage of the atmosphere from a single platform, yet associated with low temporal resolution and biases which need to be corrected. To complete the list, lower stratosphere wind observations from MST radars are also occasionally assimilated by a few NWP models. As a result, NWP are generally observed to suffer from a lack of stratospheric and mesospheric wind and temperature measurements. Since lidar observations are not assimilated, the data gap between 40 and 70 km is particularly stark.

In addition to a lack of assimilable data, the capacity of models to properly simulate the MA dynamics is also restricted by inadequate representation of characteristic features of the MA variability. If the simulation of PWs (Pendlebury et al. 2008) and atmospheric tides (e.g., Lindzen 1966; Chapman and Lindzen 1970; Forbes 1982, 1995) is globally satisfying, this is neither the case for GWs nor for the prediction of SSW occurrence. The theory of GWs is in principle well established (Fritts and Alexander 2003). But their assimilation into NWP models is made complicated by the diversity and complexity of sources and processes at their origin and especially by the inability of current NWP models to resolve the most important smaller scales (Alexander et al. 2010; Lott and Guez 2013). That is why the simulation of GWs remains the prime challenge for NWP models, which—for now—only incorporate coarse parametrization of GW effects, mostly based on the associated linear theory (Jones et al. 1997). At present, both ECMWF and UK Met Office models, for instance, are equipped with an associated GW source model. However, they can only resolve horizontal wavelengths of more than ~100

and ~4–6 km vertical resolution, in the case of ECMWF (Wu and Eckermann 2008). For both models, GW parametrization improvements would be really useful and additional GW assimilations of great help (Marlton et al. 2019).

The most remarkable limitation of the current NWP models concerns the prediction of SSW. Charlton-Perez et al. in 2013 highlighted that the main difference between models of the CMIP5 consortium was the possibility or not to correctly predict the realistic frequency of SSW events and associated tropospheric counterparts, depending on the model internal representation of MA variability. However, the decadal variability of such events remained generally poorly reproduced, even by models extending up to 1 hPa and beyond. In the present edition, Lee et al. (2019) have performed idealized simulations with the MetOffice HadGEM2 model, which was artificially forced with given stratospheric changes to simulate the same SSW. They thus demonstrate that an improved knowledge of the MA state in the vicinity of an SSW does improve at the same time the forecast of associated tropospheric climate features of the most northern areas of the Northern Hemisphere.

Those two studies thus confirm the expected high benefit of concentrating future efforts in better integrating GWs in NWP models, as well as assimilating upper atmosphere observational datasets. This is especially true in the context of ongoing climate change, which will probably impact the generation and propagation of atmospheric waves, and the frequency of climate-related extreme events.

28.3 Intercomparisons of Observations and Models: Toward a Systematic Quantification of Uncertainties

As previously mentioned, measurements commonly assimilated into NWP models are radio soundings and satellite-based radiances that often include a significant contribution from the upper stratosphere and lower mesosphere but are mainly reliable in the troposphere and lower stratosphere (Hoppel et al. 2013). Ground-based radars and lidars are well adapted to observations in the MA. However, they are mostly used for research applications rather than in operational measurement modes. Following numerous previous studies (e.g., Le Pichon et al. 2015; Pawson et al. 2000 and Randel et al. 2004 for the assessment of MA climate model performance conducted within the GCM-Reality Intercomparison Project for Stratospheric Processes and their Role in Climate), this chapter presents ongoing efforts performed in the framework of ARISE to systematically compare the obtained measurements to model estimates. The aim is to highlight and quantify persisting mismatches, as well as to demonstrate the relevance of such new MA datasets for future assimilations in the NWP model.

Four different model-data comparisons are presented. They have been obtained from measurements conducted at four different stations of the ARISE network: the ALOMAR, Trondheim, OHP, and GERES stations (Fig. 28.2). Models used for the comparisons include ECMWF products for temperature and zonal wind profiles in

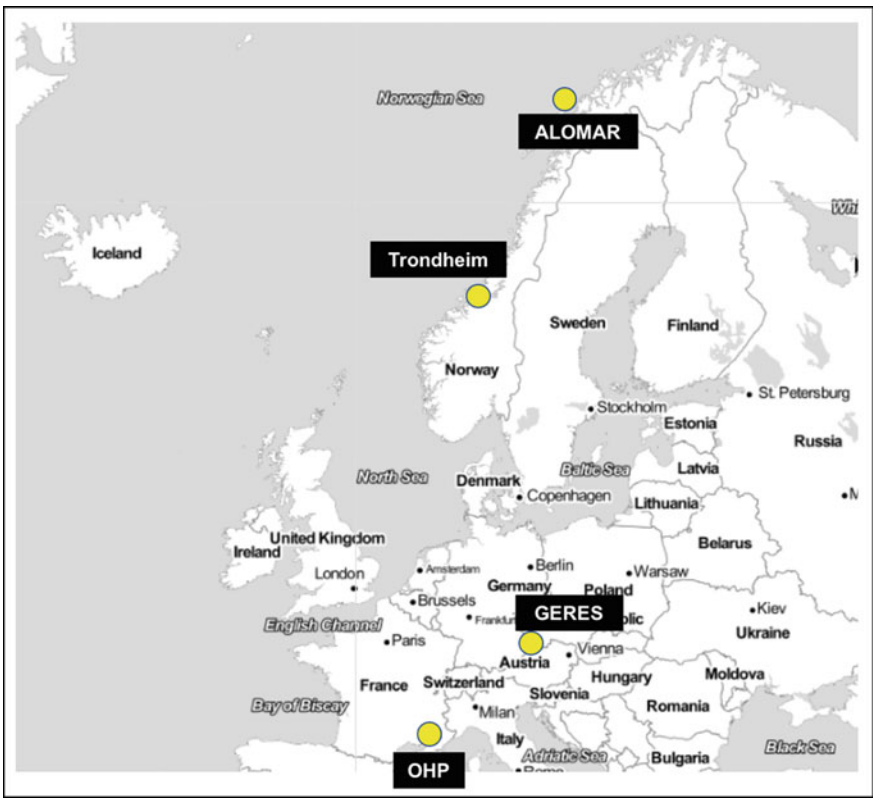

Fig. 28.2 Location of the four different stations of the ARISE network used to perform the presented observational measurements in the middle atmosphere

the 0–80 km altitude range and the quiet time HWM-07 climatological model (Drob et al. 2008) for zonal wind estimates in the 80–100 km interval. The benefits of using infrasound as a monitoring technology to improve our current knowledge of the MA dynamics are also illustrated in this chapter.

28.3.1 High-Resolution Observations at ALOMAR, Norway

The ALOMAR (Arctic Lidar Observatory for Middle Atmosphere Research) station is located in Northern Norway (69.3°N, 16.0°E) and hosts a number of remote sensing instruments. While most lidar instruments are located in the observatory building on top of a 379 m high mountain, the radar instruments are located near sea level. An experiment campaign was performed using the Rayleigh/Mie/Raman (RMR) and the iron lidars to obtain temperature and wind profiles from the

stratosphere to the lower thermosphere, under clear sky conditions during day and night. In addition, the MAARSY MST radar system provides continuous wind observations from the troposphere to the lower stratosphere, as well as in the upper mesosphere. The Andenes meteor radar provides continuous mesospheric wind profiles. The combination of these different techniques thus provides—under clear weather conditions when all instruments are operating—continuous wind speed and temperature profiles from the lower stratosphere up to the mesopause. In the future, the operation of the instruments will be automated, providing data on an even more regular basis.

Instrument description

The Andenes meteor radar is located approximately 2 km southeast of the observatory and measures wind in the mesopause region. The system transmits with a peak power of 30 kW at a frequency of 32.55 MHz and detects more than 10000 specular meteor trails per day. More details can be found in (Hocking et al. 2001). The meteor radar-derived winds presented in this study are processed with a temporal resolution of 1 h by moving a 1 h window. The vertical resolution of 1 km was obtained using a 3 km oversampling window centered at each height. The 3D winds (zonal, meridional, and vertical) are obtained by fitting each radial velocity measurement weighted by its statistical uncertainty. The algorithm includes a regularization scheme to get a smooth solution in space (vertical) and time. Additionally, we assume the vertical wind to be very small, which is justified considering the large measurement volume of about 450 km in diameter of the meteor radar. This procedure leads to statistical uncertainties in the horizontal wind components in the order of 1–5 m/s. The larger uncertainties usually occur at the upper and lower boundaries of the meteor layer, due to the smaller number of meteor detections.

The mobile Iron (Fe) resonance fluorescence lidar is located on the roof of the observatory and uses a two-wavelength (386, 772 nm) alexandrite laser, one at the Doppler-broadened iron resonance line and the other one at twice the frequency of the iron resonance (Höffner and Lautenbach 2009). The system has full daylight capabilities and hence is suitable for performing continuous temperature observations in the Mesosphere and Lower Thermosphere (MLT) region, under clear weather conditions. A more detailed description of the lidar results are found in Lübken et al. (2015) and Kaifler et al. (2015).

The RMR lidar is a twin lidar with two identical transmitting lasers and receiving telescopes, as well as one detection system. It has been measuring temperatures and aerosols in the middle atmosphere on a routine basis since 1997 (von Zahn et al. 2000; Schöch et al. 2008), and wind speeds since 2009, using the Doppler Rayleigh Iodine Spectrometer (DoRIS) (Baumgarten 2010). Detailed descriptions and validation of results for the altitude range from 30 to 85 km are found in Hildebrand et al. (2012), and Lübken et al. (2016). Basically, the temperature and wind retrieval relies on hydrostatic integration of the relative air density altitude profile (e.g., Hauchecorne and Chanin 1980) by measuring the Doppler shift of the backscattered light using iodine absorption spectroscopy. The system is capable to measure winds

and temperatures even during daytime, which are mandatory in order to observe and analyze long-period GWs, as well as background thermal and dynamical structure (Baumgarten et al. 2015).

Results

For the first time, these observations were analyzed and interpreted jointly, yielding unique whole-atmosphere observations of temperatures and wind. Figure 28.3 shows the thermal and dynamical structure above ALOMAR from the combined observations of lidar and radar. In the period between January 19, 2015, and January 24, 2015, clear weather conditions persisted for nearly 118 h and allowed to perform continuous lidar observations. While the RMR lidar allows one to calculate temperature and wind in the stratosphere and mesosphere, the Fe lidar and the

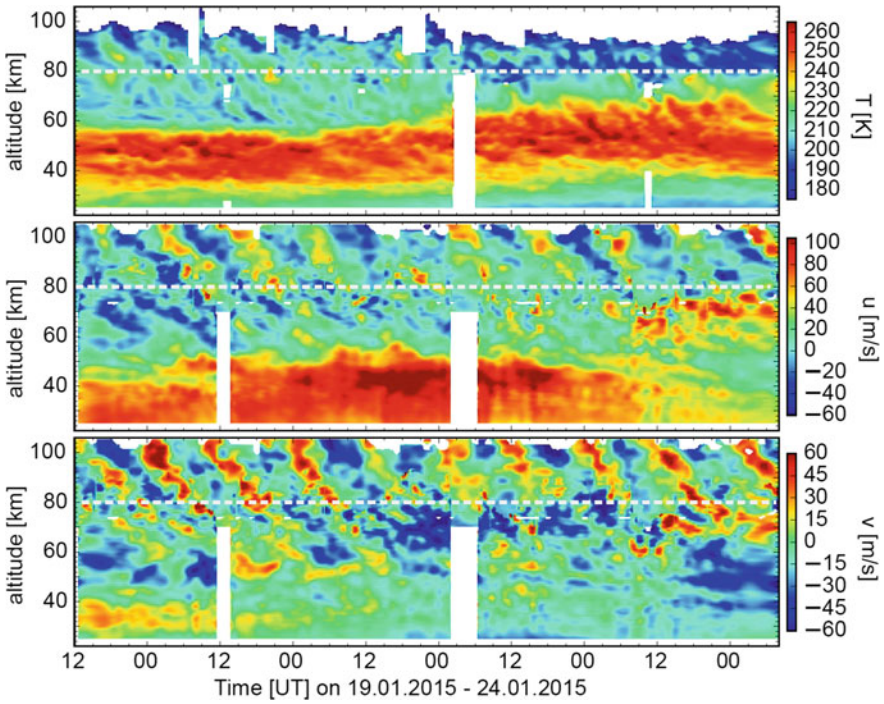

Fig. 28.3 Lidar and radar observations at ALOMAR spanning about 100 h of continuous observations of temperature (top panel), zonal (middle panel), and meridional wind (lower panel). Measurements below about 80 km altitude (horizontal dashed line) were performed by the RMR lidar. Temperature and wind measurements above about 80 km altitude were performed with the Fe lidar and the meteor radar, respectively. White areas denote times/altitudes without measurements

Meteor radar allow one to extend the observations to higher altitudes. The observations show variations of temperature and winds due to GWs, solar tides and planetary waves. GWs are present through the whole measurement period and altitude range and can be identified as short scale fluctuations forming a quasi-continuous noise. Tides are especially prominent in the MLT region above 80 km and can be seen in wind component variations. Planetary waves are responsible for the change in stratopause altitude throughout the measurements, but also for the observed variations of horizontal winds in the stratosphere.

Observations are compared to the temperatures and winds calculated by the Integrated Forecast System (IFS) of the ECMWF cycle Cy40r1. We extracted data with a horizontal resolution T1279 at the location of the observations (69.28°N, 16.01°E) with a temporal resolution of 1 h. Profiles between midnight and noon were taken from the model run initialized at 00 UTC; profiles between noon and midnight were taken from the 12 UTC run. Figure 28.4 displays the ECMWF data in the same altitude and time range as for observations in Fig. 28.3. We do notice remarkable agreements but also large differences, especially in the GW-induced structures. For example, the increase in the stratopause altitude is partially captured; the same observation applies to the increase/decrease in zonal wind. But GW and tidal signatures highlighted by the observations are not reproduced in the ECMWF

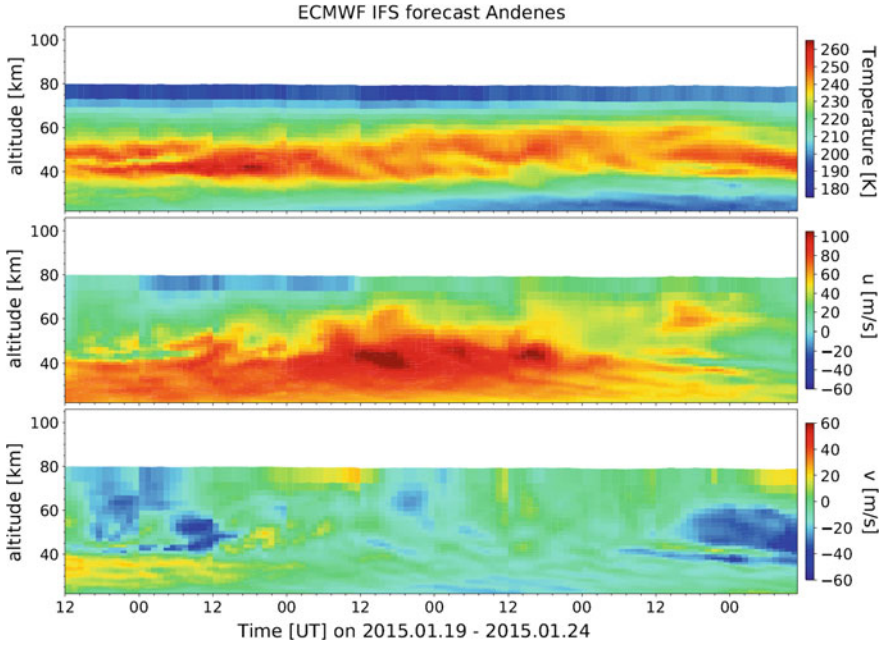

Fig. 28.4 ECMWF IFS forecast data extracted for ALOMAR with a temporal resolution of 1 h. The data were extracted on model levels. We use the same axis scaling as for the observations; top panel: temperature, middle panel: zonal wind, and lower panel: meridional wind. White areas denote times/altitudes without data

estimates, neither in temperature nor in winds. Yet, the ECMWF data noticeably reproduce a long period of wave activity—between January 23 and 24—around 40 km altitude (e.g., meridional wind), whose pattern is comparable to the observational one. Detailed comparisons of the wave activity under January conditions observed by lidar and ECMWF are presented in Hildebrand et al. (2017). They show that the GW amplitudes in temperature and wind fluctuations are underestimated in ECMWF by more than a factor of 3 above 50 km.

28.3.2 Meteor Radars: Routine Wind Observations at Trondheim, Norway

The Trondheim meteor radar is an all-sky SKiYMET system (Hocking et al. 2001) located at 63.5°N, 10.5°E. The radar consists of a transmitter array of 8 three-element Yagi antennas in a circular orientation and a cross receiver of 5 three-element antennas. The transmitter array provides a peak power of 30 kW at 34.21 MHz with a pulse repetition frequency of 925 Hz and a pulse width of 2 km. During standard operations, most of the power is directed into eight beams at 45° azimuth increments, with peak power at around 35° off-zenith. The radar records meteor trail Doppler drift velocities, within the meteor ablation region around 70–100 km; the majority of meteor trails detected by this system come from between 15° and 50° zenith angles. Peak count rates are observed around 90 km. On average, the radar detects between 10 and 20 thousand meteors per day—depending on the time of year (maximum in summer, minimum in winter)—with an approximately Gaussian distribution in height with a full-width half-maximum of around 12 km. The radar has been operating nearly continuously since September 2012. Further details on the technical specifications of the radar and the meteor statistics observed from Trondheim can be found in de Wit et al. (2014, 2015).

Over a short period of time and within a small altitude range, it is assumed that the background wind is uniform throughout the radar field of view, and hence, the individual meteor trail velocities can be combined to determine a mean background horizontal wind. In this instance, hourly mean horizontal winds are determined in six altitude intervals centered around 82, 85, 88, 91, 94, and 98 km, by performing a least-square fit to the measured meteor trail radial velocities, provided that at least seven unambiguous meteors are detected within a given altitude interval (Hocking et al. 2001). Thereafter, moving averages of the background wind and periodic components were created by performing a least-squares fit over a time period of 4 days (time-stepped by 1 day) to the zonal and meridional components of the horizontal hourly mean winds derived from each altitude bin. Oscillations with periods of 48, 24, 12, and 8 h (representing perturbations to the wind field due to the 2-day planetary wave and principle solar tides) are fitted together with an offset corresponding to the 4-day moving-average horizontal background wind. Fits were

only attempted when at least half of the hourly mean wind data were present in the 4-day time interval, and these spanned at least 16 different hours.

An example of the data recorded by the radar is presented in Fig. 28.5 (top), which shows the 4-day running mean zonal wind recorded during 2016. During the summer months, a strong positive zonal wind shear is observed in the MLT region, as the stratospheric and lower mesospheric westward flow is dragged eastward by gravity wave breaking (Fritts and Alexander 2003; de Wit et al. 2015). The altitude of the zero wind line is seen to descend within the field of view of the radar over the course of the summer. Outside the summer months, the wind field is much more variable as planetary waves are able to propagate up into the MLT, through the underlying eastward winds (Charney and Drazin 1961). Wintertime winds are highly variable and the unusual high latitude strong eastward MLT wind conditions during January 2016 (as discussed by Stober et al. 2017) are clearly visible over Trondheim, together with the influence of the sudden stratospheric warming in early March 2016 (Manney and Lawrence 2016). For comparison, Fig. 28.5 (bottom) shows the quiet time HWM-07 climatological model (Drob et al. 2008) zonal winds for Trondheim's latitude and longitude treated in exactly the same way as the radar winds. The model reproduces the wind shear seen during the summer months, although the altitude of the zero zonal wind line is not well reproduced. In spring and autumn, the model tends to overestimate the observed zonal winds; the strong low-frequency (>4 days) variability seen in the zonal winds during wintertime is not captured.

In addition to this low-frequency variability, any instantaneous measurement of the MLT winds can also be strongly influenced by perturbations due to relatively

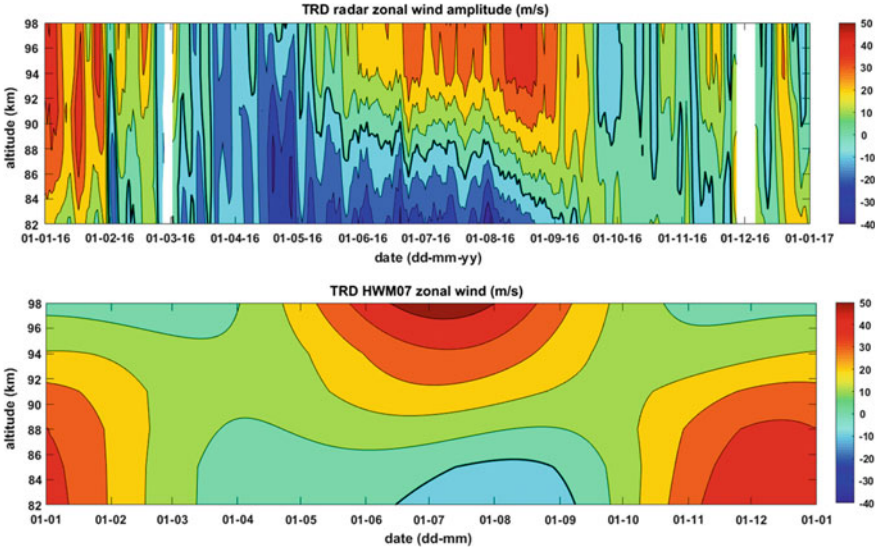

Fig. 28.5 (Top) Trondheim meteor radar 4-day running mean zonal wind (82–98 km) during 2016. (Bottom) 4-day running mean zonal wind derived from the quiet time HWM07 model at 63.5°N, 10°E. Contours are at 10 m/s intervals and missing data are shown in white

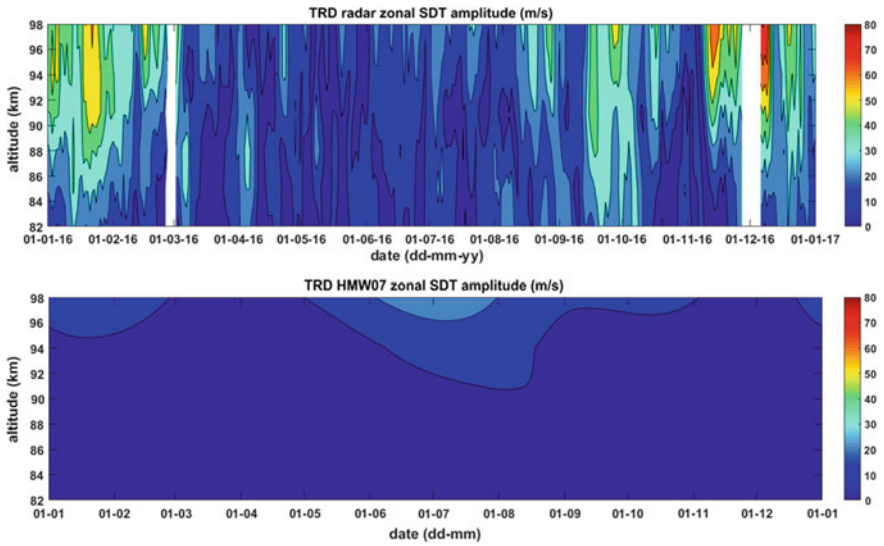

Fig. 28.6 (Top) Amplitude of the 4-day running mean semidiurnal tide derived from the Trondheim meteor radar hourly zonal wind (82–98 km) during 2016. (Bottom) 4-day running mean semidiurnal tide derived from the quiet time HWM07 model hourly zonal winds at 63.5°N, 10.5°E. Contours are at 10 m/s intervals and missing data are shown in white

high-frequency tides and GWs. In particular, the semidiurnal tide can reach large amplitudes during the autumn and winter months at mid to high latitudes in the Northern Hemisphere (e.g., Mitchell et al. 2002), and its intensity can be highly variable. To illustrate this, Fig. 28.6 (top) shows the variation in the amplitude of the 12 h component of the zonal wind perturbation (representing the vector sum of all the individual components of the semidiurnal tide observed over Trondheim) over the course of 2016. By way of comparison, the amplitude of the 12 h wave derived in the same way from the hourly quiet time HWM-07 model zonal wind is reproduced in Fig. 28.6 (bottom). Clearly, the variability and magnitude of the observed tides are not well captured in the climatological model. Neither is the seasonality of the tide. The pronounced autumn and winter maxima, seen in these data and by other authors (e.g., Mitchell et al. 2002; Portnyagin et al. 2004; Sandford et al. 2010), are not well reproduced in the HWM-07 model.

28.3.3 Passive Microwave Wind Radiometers: Continuous Wind Observation Campaigns

Passive microwave wind radiometers observe emission lines from molecular rotational transitions with a high spectral resolution. The measurement principle is based on the classical Doppler shift of the observed emission line, due to the

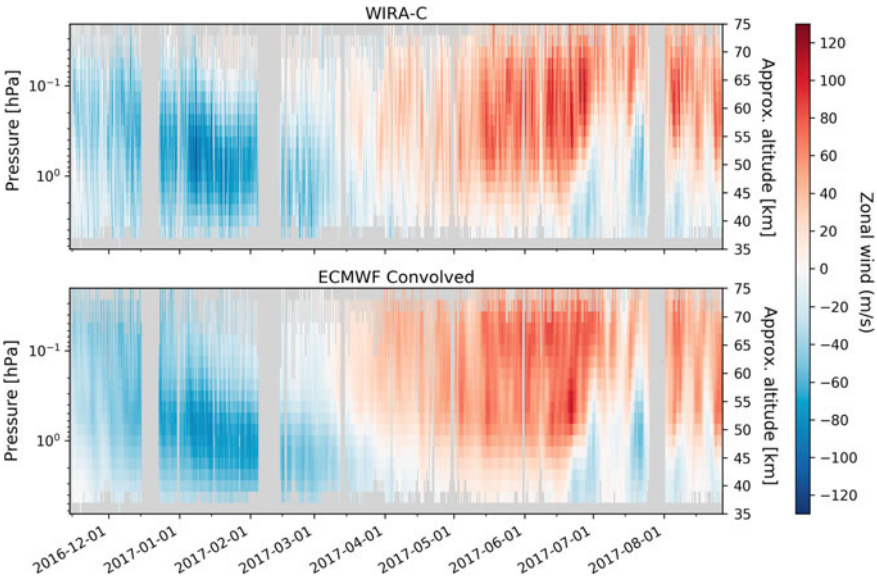

Fig. 28.7 Time series of WIRA-C measurements of zonal wind speeds (top) at altitudes between 35 and 75 km, from November 2016 to end of August 2017 and corresponding ECMWF model data (bottom). The gaps in the data are due to power cuts and the presence of a tropical cyclone. The model data is convolved with the averaging kernels of the retrieval to have the same resolution in space and time for both datasets. Invalid measurements are grayed out in both panels

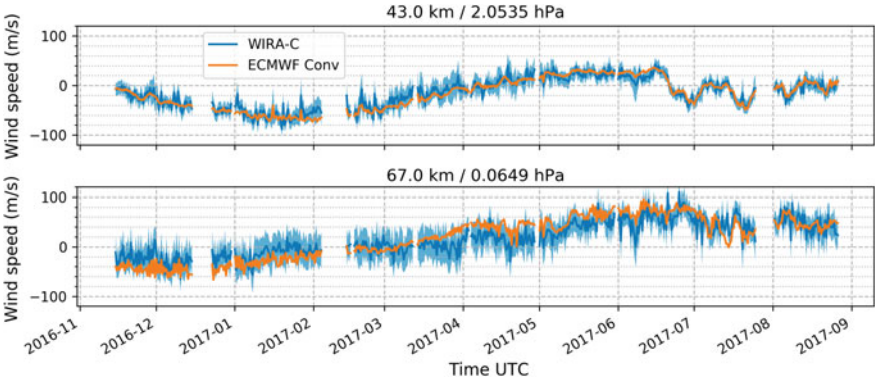

Fig. 28.8 Two different pressure levels of the WIRA-C time series from the Maïdo observatory (21°S) at 43 and 67 km altitude. The model data is convolved with the averaging kernels of the retrieval to have the same resolution in space and time for both datasets

movement of emitting molecules with the air flow. According to the pressure broadening effect, the line width depends on altitude; it is thus possible to directly retrieve altitude resolved wind profiles from the measured spectra by inverting an atmospheric radiative transfer model.

The key strength of microwave wind radiometers is the continuous measurement of wind speeds between 35 and 70 km altitude. They can measure during day and nighttime, independent of clouds and work autonomously as they do not need any manual calibration. Currently, two instruments are operational, namely, WIRA (WInd RAdiometer) and WIRA-C (WInd RAdiometer for Campaigns). Both instruments observe the emission line of ozone at 142 GHz with a single-sideband heterodyne receiver and a radiometric noise temperature as low as 800 K and 500 K, respectively. A digital FFT spectrometer provides the high spectral resolution of 12.2 kHz over a bandwidth of 120 MHz. The current setup can provide wind observations with time resolution of 12 h and altitude resolution of 10–16 km; associated uncertainty is approximately 15 m/s for the altitude range from 35 to 70 km (Rüfenacht et al. 2014). The WIRA instrument has been used in several campaigns in Bern (47°N), OHP (44°N), at the Maïdo observatory at La Reunion island (21°S) and at ALOMAR (67°N) from 2012 until now (Rüfenacht et al. 2014; Rüfenacht and Kämpfer 2018). The WIRA-C (WInd RAdiometer for Campaigns) instrument is highly compact and portable and has been operating at the Maïdo observatory since 2016. Both instruments have delivered continuous measurements of middle atmospheric wind speeds during their respective campaigns.

Figure 28.7 presents the continuous measurement of zonal wind speeds from the WIRA-C campaign at the Maïdo observatory between November 2016 and September 2017. Corresponding data from the ECMWF operational model is given for comparison. Figure 28.8 presents two horizontal slices of the same data at 45 and 65 km altitude. WIRA-C measurements and ECMWF data are consistent at the lower level except for short-term variations that are not resolved by the model. At the upper level, the differences are more substantial and indicate the presence of a bias. Moreover, the WIRA-C records more variability than the ECMWF model can predict, as expected since the model levels above 70 km are artificially stabilized.

28.3.4 Lidar Temperatures: Routine Observations at OHP, France

At the Haute-Provence observatory—hereafter OHP (43.9°N, 5.7°E), an RMR lidar, which is part of the NDAAC (http://www.ndsc.ncep.noaa.gov/), has been routinely operating in clear sky conditions since 1979. It is based on the Rayleigh backscattering of a laser beam in the absence of aerosols, which is further used to infer the atmospheric density and temperature vertical profiles (Hauchecorne and Chanin 1980). The current system setup features vertical resolution of 0.075 km and temporal resolution better than 3 min, with a sub-Kelvin accuracy up to 70 km (Keckhut et al. 1993). Density fluctuations are retrieved from raw lidar signals using a variance method (Hauchecorne et al. 1994; Mzé et al. 2014). The method is based on the computation of the signal fluctuations over short temporal and vertical

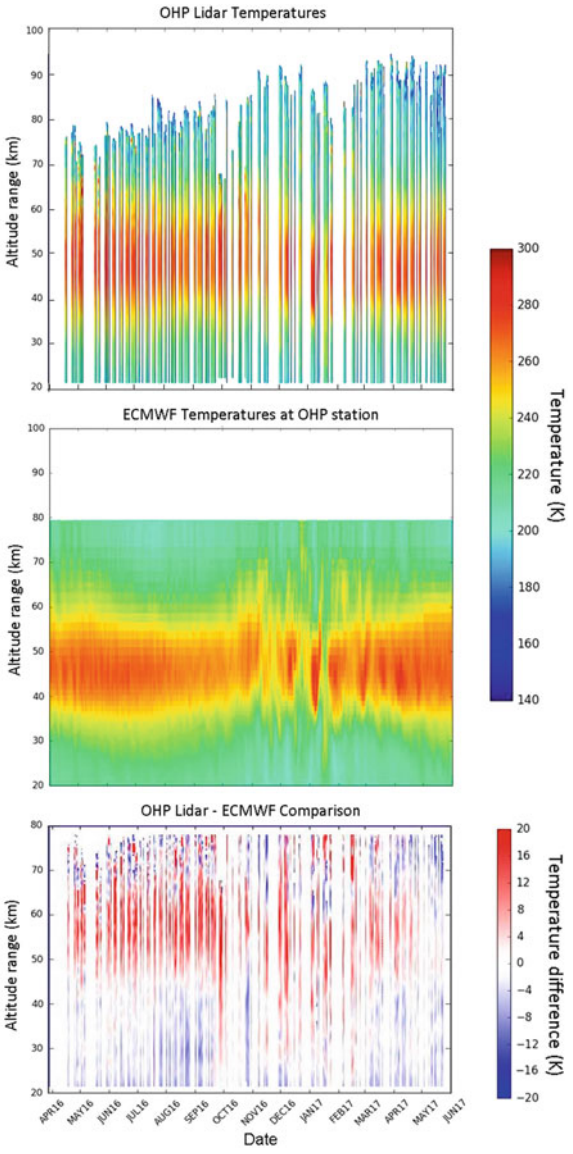

Fig. 28.9 (Top) Vertical temperature profiles as derived from OHP lidar measurements between January 2016 and May 2017. Missing data are shown in white. (Middle) Corresponding temperature estimates from ECMWF HRES analysis and 00 h UTC runs. (Bottom) Resulting differences between observed temperature values and modeled ones

intervals, followed by summation of the squares of these fluctuations over a large number of elementary intervals (here $\Delta T = 26$ min and $\Delta Z = 1.125$ km, respectively). The observed variance of the lidar signal is then defined as the sum of atmospheric and instrumental variances. The latter is estimated assuming a statistical Poisson noise, for the photon counting signal.

Here are presented the nighttime measurements obtained between April 2016 and May 2017 (Fig. 28.9). The system is operated 3–4 times a week—according to

sky conditions—and allow one mean profile per night (average performed over measurements typically obtained between 20:00 and 01:00 UTC), in the ~30–90 km altitude range (Keckhut et al. 1993). Data are compared to the operational ECMWF high-resolution (HRES) atmospheric model analysis, equipped with the IFS cycle 38r2 (experimental version 62). The vertical resolution of the model is composed of 137 levels, up to 0.01 hPa. Presented ECMWF temperature profiles correspond to the 00:00 UTC run of the model and have been extracted in order to match the location of OHP.

At the OHP latitude, the temporal evolution of MA temperatures is under the influence of Rossby PWs in winter and controlled by internal GWs in summer. As shown in Fig. 28.9, a general pattern stands out from the model-data comparison: the ECMWF analysis tends to underestimate both the temperature values and the vertical extension of the maximum temperature layer in the upper stratosphere and lower mesosphere. Differences are particularly marked in the 45–70 km altitude range (mismatches above 70 km height are not discussed, since the upper pressure levels of the ECMWF model are artificially forced for model stability reasons). The model overall better estimates spring and summer temperature values, with good agreements especially shown in July 2016 and from late February 2017 to June 2017. In 2016, the observed temperature differences until June 2016 may be due to a persisting influence of the preceding SSW of March 2016, which is expectedly poorly resolved by the ECMWF model (see Sect. 28.2.2). Likewise, the intensive variability observed in temperatures from September 2016 to January 2017 between altitudes from ~40 (and punctually below) to ~65 km is hardly captured by the model. This particular period is further explored in Sect. 28.4.5.

28.3.5 Lidar Temperatures: New Measurements from the Portable Lidar CORAL at GERES, Germany

As part of the ARISE project, the development of a portable lidar named CORAL has been initiated for the specific investigation of MA disturbances such as GWs between 25 and 85 km altitude with high temporal and vertical resolution (5 min by 1 km vertical). The innovative aspect of this instrument lies in the design of a fully autonomous system. For example, the system is equipped with cloud cameras, in situ weather measurements, and weather forecasts which allow the incorporated software to automatically start the lidar up, when the sky conditions are ideal. Conversely, the lidar stops in presence of clouds or when the sun rises. This high level of automation is unique in mesospheric lidar systems. It allows for an unprecedented increase in observation hours, as the run-time of the lidar is not limited anymore to the working time of an operator. This technique is well adapted to provide information about the vertical state of the atmosphere, which are relevant for the infrasound operational system to improve the infrasound propagation simulations. This technique could also be used to extend the present lidar system for other applications such as weather forecasting.

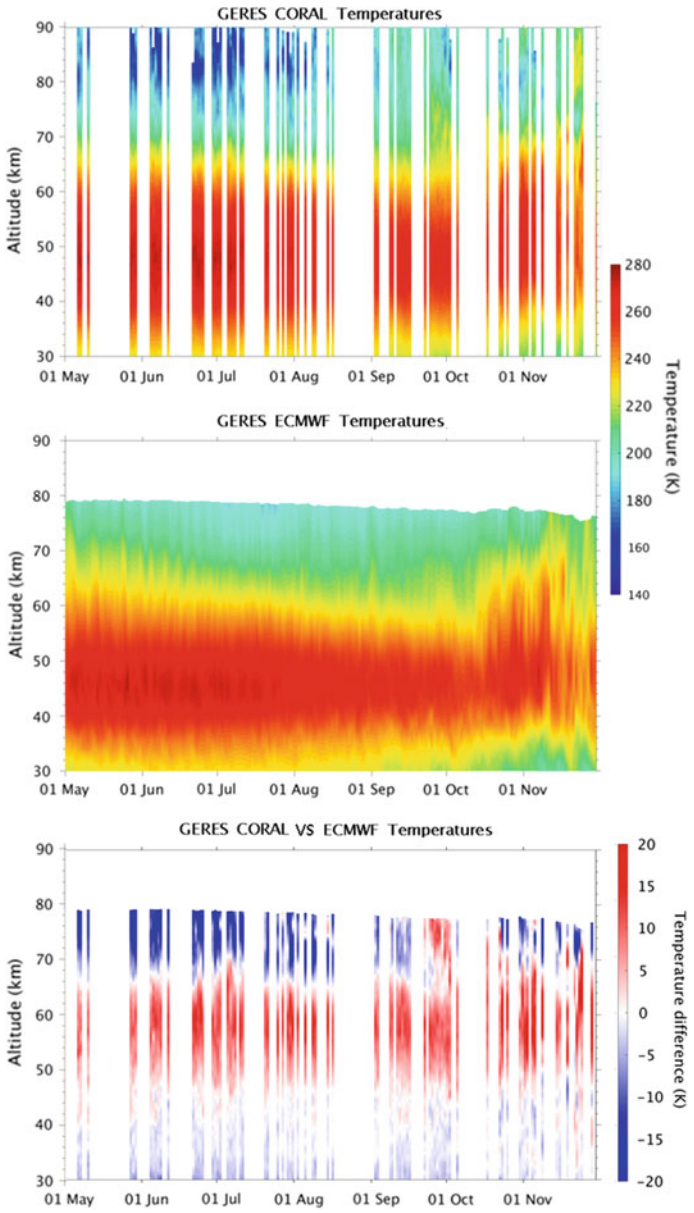

Fig. 28.10 (Top) Vertical temperature profiles as measured by the new portable autonomous lidar located at GERES in Germany, during the year 2016. Results are here presented for a 7-month campaign from May to November 2016. Missing data are shown in white. (Middle) Corresponding temperature estimates from ECMWF HRES analysis at 00:00 UTC (Bottom) Differences between observations and ECMWF model outputs

The prototype instrument had first been tested in 2016 at the German Experimental Seismic System (GERES) in Germany, co-located with the German IS26 infrasound station (48.85°N, 13.71°E). Figure 28.10 presents the results over a 7-month period, from May to November 2016. As an example for this new system high capacity of measurements, during the night of the 31st of October 2016, the period of measurements extended from 16:45 UTC on the 30th to 05:05 UTC on the 31st. With a time resolution of ∼15 min, 148 temperature profiles were retrieved this night.

As for the OHP measurements (see Sect. 28.4.3 for details), CORAL data are compared to the outputs of the ECMWF HRES operational analysis. The same mismatches between model outputs and data are here again evidenced, as regards noticeable differences in estimates of highest temperature values reached in the 45–65 km interval. Likewise, the extent of the maximal temperature region encompassing the upper stratosphere and the lower mesosphere is underestimated by the model. Detailed quantitative comparisons are described in the following section.

28.3.6 Comparison Between Lidar CORAL and OHP Observations

To better assess the differences previously observed at OHP and GERES between lidar observations and ECMWF-derived temperatures, we compare here the vertical profiles for the measurement period between September and October 2016, common to the two sites (Fig. 28.11) (this is an arbitrary choice to better visualize the differences between data and model temperature estimates observed at OHP at this time in Fig. 28.9). The performance of the model is assessed on both temporal and spatial scales. On a temporal basis, daily and monthly performances are considered. Because the highest layers are not resolved by the model, the altitude range for comparison is restricted to the 20–70 km interval.

Over the studied period, we first notice the remarkable variability affecting the mesospheric region (here from ∼45 to 70 km) as recorded by lidar observations at this time. This variability is more apparent at OHP than at GERES. This difference can be explained by the larger number of observation hours per night of the CORAL lidar at GERES which influence the GW representation in nightly means. Therefore, the nightly mean temperature profiles are smaller for GERES compared to OHP.

It is highly probable, that the overall observed ECMWF model underperformance in reproducing OHP vertical thermal atmospheric state is explained by intense gravity wave activity, not resolved by the model. On a monthly basis, the observed temperatures are higher than ECMWF temperatures between 45 and 65 km. The difference can reach values of 15 K in both September and October

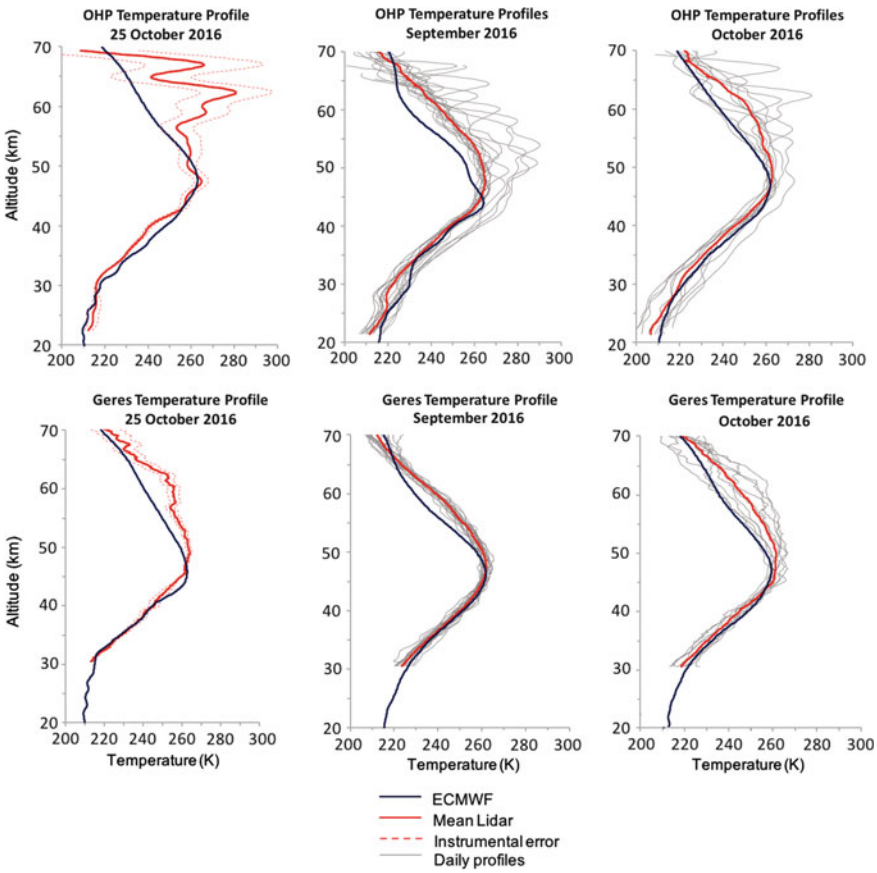

Fig. 28.11 (Top panel) Results for temperature lidar measurements conducted at OHP, France. Left: daily mean temperature profile for the 25th of October 2016 (red) and associated instrumental errors (dashed red), compared to the ECMWF profile for the same day at 00UTC (blue); middle: averaged temperature profile for September 2016 and associated nightly mean profiles used for the calculation period (gray, 18 days of measurements); they are compared to the averaged ECMWF profile of the model outputs for the measurement days at 00UTC; right: same as before for October 2016 (10 days of measurements). (Low panel) Same results for the CORAL measurements at GERES, Germany. Monthly mean profiles are obtained, respectively, from 18 days of measurements in September and 9 days of measurements in October

at ~60 km. The temperature differences are even more impressive on a daily basis, with a recorded maximal deviation of 45 K on the 25th of October at ~62 km, where the usually decreasing mesospheric temperature profile reverses.

Albeit less pronounced, the same bias toward lower temperatures is observed at GERES in October, with a maximal 11 K temperature difference recorded between monthly mean profiles at ~57 km. This difference reaches 16 K on the 25th of October at ~60 km. Interestingly, even under relatively more stable conditions as

the ones prevailing in September 2016 at GERES, the same systematic bias (up to 10 K) is noticed between model estimates and lidar temperatures observations in the lower mesosphere. It is maximum at ~58 km.

It has, however, to be noticed that the overall performance of the ECMWF model in the stratosphere (within the 20–45 km interval) is rather good, with coherent profiles—especially at GERES—on both monthly and daily bases. At OHP, the stratospheric temperature estimates are overall satisfying, with the exception nevertheless of the 25–35 km interval on the September 2016 ECMWF mean profile, which shows temperatures overestimated by up to 7 K. Such differences may once again be attributed to the intensive gravity wave activity between 55 and 70 km which may indicate unrepresented dynamics at underlying layers.

This comparison supports earlier findings focusing on OHP temperature and wind observations (Le Pichon et al. 2015), which evidenced systematic temperature biases of 5 K in average and up to 30 K (respectively, of 20 m/s and up to 40 m/s for wind estimates) between 2013 and 2014. Present observations show that biases in the 45–65 km altitude range can be repeatable in time and extend to regional areas, and cannot only be restricted to conditions of GW activity, which are expectedly (see Sect. 28.2.2) not resolved by models.

28.3.7 Determination of Uncertainties Using Infrasound Technology

The IMS infrasound system (Marty 2019) provides ground pressure variations spanning a broad frequency range at global scale. It uses microbarometers as infrasound sensors designed to combine good sensitivity (1 mPa) and large dynamic range (80 dB, 24 bits), in order to detect remote source signals. They are equipped with acoustic filtering systems to reduce noise from local wind turbulence (Walker and Hedlin 2010). The microbarometers are configured in arrays of 4–9 sensors with 1–3 km aperture geometry to form sensitive acoustic antennas, which further provide wave azimuth and phase velocity. Data processing algorithms such as the Progressive Multichannel Correlation method (PMCC) detect coherent waves within noncoherent noise and characterize low-amplitude pressure signals in real time (Cansi 1995). Different coherent wave systems can hence be differentiated according to their time–frequency signature and azimuth.

Through the study of well-identified infrasound sources such as explosions (Kulichkov 2010; Chunchuzov et al. 2013) or quasi-continuous volcano eruptions (Le Pichon et al. 2005b), it has been showed that small-scale structures of temperature and wind affecting infrasound propagation in the MA can be extracted from ground recorded infrasound signals. This has motivated the development of atmospheric infrasound remote sensing methods (e.g., Drob et al. 2010; Lalande et al. 2012; Landès et al. 2014; Assink et al. 2019) to study MA variability. In particular, Assink et al. (2014a)—using Etna volcano signals detected in Tunisia—have provided

evidence that ECMWF model wind speeds were underestimated in summer and overestimated in winter, with differences estimated up to 20 m/s. Infrasound inversions start to be considered as a useful technology for MA studies (Newnham et al. 2016).

During SSW, changes in stratospheric winds and temperature substantially alter the propagation of infrasound (Evers and Siegmund 2009; Assink et al. 2014b; Smets et al. 2019), from small bearing variations to no longer detected signals in a specific direction. A global SSW signature can be obtained from the infrasonic ambient noise generated by ocean surface wave interactions in the microbarom domain (e.g., Evers and Siegmund 2009; Smets and Evers 2014), using CTBT infrasound stations spread over the globe. However, such sources vary in time and space. Volcanoes—which are isolated and well-understood sources—can alternatively be used to test the benefit of infrasound technology to assess the stratospheric predictability (Fee et al. 2010; Matoza et al. 2011; Marchetti et al. 2013).

Focusing on one year of near-continuous infrasound detections from Mount Tolbachik observed by the IMS infrasound station IS44 on the Kamchatka peninsula in Russian Federation (55.8°N, 160.3°E), Smets et al. (2016) have thus assessed the reliability of ECMWF forecast. IS44 is located at approximately 347 km southwest of Mount Tolbachik, with a true bearing of 28° clockwise from north. Figure 28.12 shows a comparison between the observed signals and the wave-front simulations by three-dimensional ray tracing using various forecast steps of the ECMWF high-resolution deterministic forecast. The back azimuth

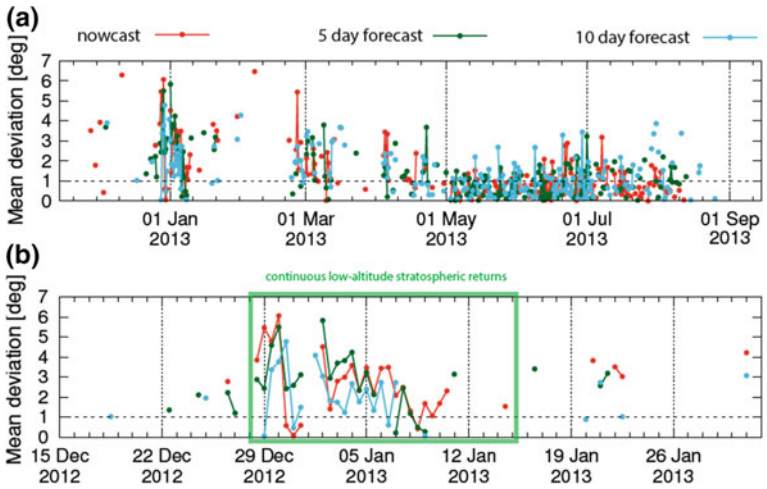

Fig. 28.12 **a** Estimated difference between the observed and predicted back azimuth of all returns over the full time span of observation. Data are averaged on 12 h time bins and contain at least six detections. The different colors correspond to the different ECMWF forecasts that are used in the simulations. The lines connecting the dots indicate the continuity of the predictions. The horizontal dashed black line indicates the uncertainty of the infrasound data. **b** Similar to top panel, but focusing on the midwinter period with the SSW period highlighted by the green rectangle (from Smets et al. 2016)

seasonal deviations represent the seasonal inversion of the stratospheric winds. During the SSW, the stratospheric wind reverses producing summer detection conditions in winter. Significant differences of several degrees are observed between simulations and detections during and after the SSW event, thus providing further evidence of SSW-related uncertainties in simulations. Significant inconsistencies or absence of simulated returns suggests a possible difference in the vicinity of the return height between the true state of the atmosphere and the forecast. In summer, nearly all mean deviations for all forecasts fall within the array uncertainty.

The largest bearing deviations are thus observed at the SSW onset and offset, with best predictions by the 10-day forecast and nowcast; significant deviations are also recorded during the equinox period. The middle atmospheric forecast skill drop —here highlighted by the use of infrasound—was previously related to data assimilation issues (Diamantakis 2014).

28.3.8 Gravity Wave Routine Observations from Infrasound Technology

The capability of the IMS infrasound arrays to accurately measure pressure fluctuations in the GW band—extending from a few minutes to 24 h—was demonstrated by Marty et al. (2010). The routinely processed infrasound frequency range extends from 0.01 to 5 Hz. But, signals at lower frequencies can also be measured, including signals from solar tides which can be used as a calibration source for the operational system, for instance. The GW spectra measured at ten IMS stations present striking similarities, despite the broad station geographical distribution (Marty et al. 2010); examples of observations have been presented by Blanc et al. (2014).

In spite of their short spatiotemporal scales, GWs have important global-scale effects, as they drive the global summer-to-winter pole circulation in addition to PW action (see Sect. 28.2). The GW parameterization moreover suffers from a lack of observational constraints. This is, for instance, the case for the link between the generation of GWs by tropical convection and regular oscillations of stratospheric and mesospheric winds such as the Quasi-Biannual Oscillation (Hauchecorne et al. 2010). Although well established in theory and represented in some models, this link only benefits from limited observational constraint. Conversely, most small-scale GWs are not resolved by typical climate models and only partially resolved by weather forecasting models (see Sects. 28.3.1 and 28.4.1, Lee et al. 2019).

In the framework of the ARISE project, it is proposed to complement lidar and radar data by using the IMS infrasound network data, to achieve a better representation of GWs from ground level. Figure 28.13 presents an example of infrasound detections recorded at the IS33 IMS station in Madagascar related to the regional GW activity. A characteristic seasonal variation is well identified. The GW origin is mainly related to convection and mountain waves.

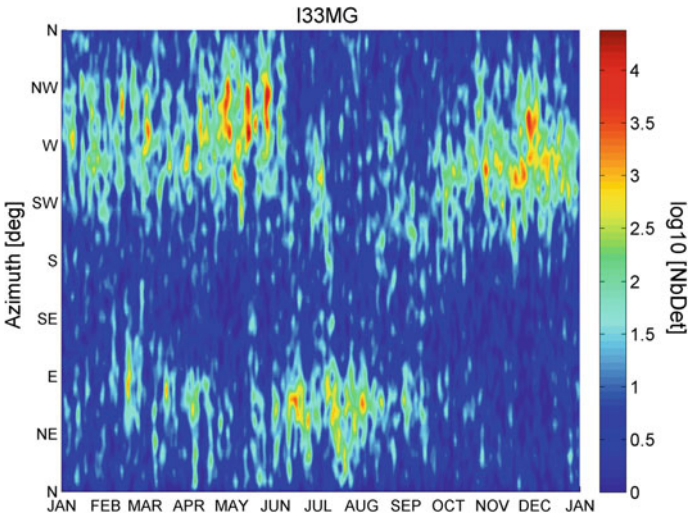

Fig. 28.13 Example of GWs observed at the IS33 infrasound station in Madagascar

In the equatorial region, the IMS IS33 station located in the Ivory Coast has been recording for 10 years the GW produced by deep convection. With maxima reached in April and October, such GW activity has been demonstrated to dominate other possible wave sources (Blanc et al. 2014) and propagate upward into the stratosphere and mesosphere. As for others, equatorial GWs are subjected to the MA wind filtering effect: in the downwind direction, waves break and no longer penetrate the upper stratosphere; in the opposite direction, they penetrate the MA up to the MLT, until reaching the threshold value beyond which wave saturation occurs (Costantino et al. 2015).

On a global scale, the IMS network can either be used to observe stationary mountain acoustic waves. By crossing azimuth, orographic waves can indeed be accurately located over associated originating mountain areas (Wilson et al. 2010; Hupe et al. 2017a) and could be used to study the evolution through time of such activity.

28.4 Impacts of Atmospheric Variability on Infrasound Monitoring

The results presented in Chap. 3 motivated the development of routine observations to provide new datasets relevant for NWP models (Sigmond et al. 2013; Charlton-Perez et al. 2013) and infrasound monitoring (Bertin et al. 2014). Impacts in weather forecasting are developed by Lee et al. (2019). This chapter illustrates impacts on infrasound monitoring and discusses related perspectives.

28.4.1 MA Uncertainties in Infrasound Simulations

The MA variability strongly impacts the infrasound propagation. The uncertainties in NWP models at small timescales mainly originate from the poor representation of GWs and other large-scale disturbances (see Sects. 28.2, 28.3.1 and 28.3.2). Such inhomogeneities induce partial reflection (scattering) of infrasound at the origin of anomalies in the infrasound propagation (Kulichkov 2010; Kulichkov et al. 2010) and unexpected infrasound signatures (Kulichkov and Bush 2001; Gainville et al. 2010).

In order to better interpret infrasound propagation in the MA, an initiative within the ARISE project has been developed to combine different atmospheric sounding techniques in the same location. First attempted at the Maïdo Observatory in La Reunion Island, a wind lidar has been operating in routine mode twice a week together with a temperature lidar; those two lidar instruments have been associated to a co-located infrasound array to further explore atmospheric remote sensing methods. In that part of the world, infrasound coherent energy is almost continuously

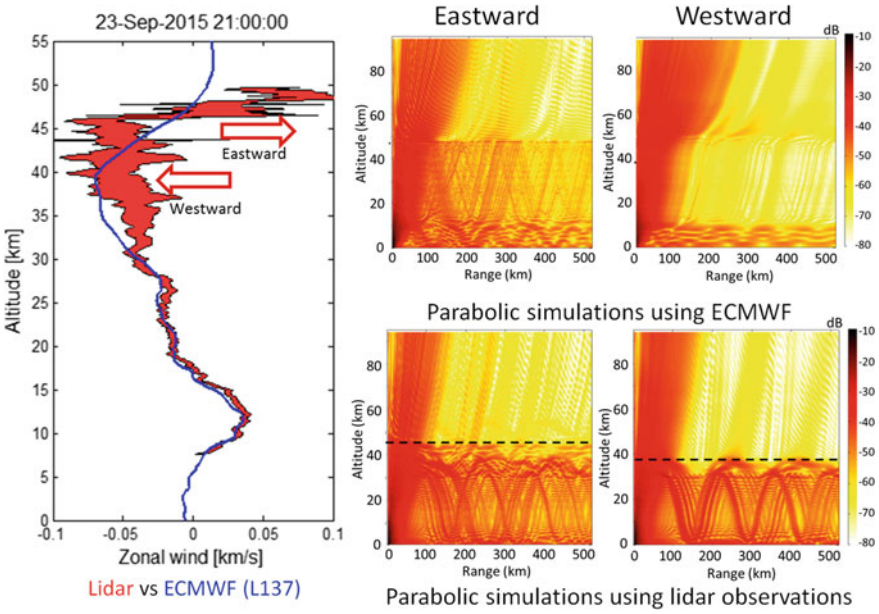

Fig. 28.14 (Left) Comparisons between wind lidar measurements at the Maïdo observatory (instrumental error bars in red) and ECMWF (L137, in blue) on September 25, 2013. (Right) simulations of the infrasound propagation at 0.3 Hz (attenuation in dB with a reference distance of 1 km to the source) with the ECMWF profile (top) and the lidar profile (bottom). A double infrasound ducting is explained by the double jet observed in the wind profile, which is not represented by the ECMWF model

dominated by microbarom signals resulting from the nonlinear interaction of large swell systems, which circulate along the Antarctic Circumpolar Current.

In late September 2015, the vertical profile of zonal wind observed by the Maïdo wind lidar (Fig. 28.14, left) showed at the same time an eastward jet around 40 km and a westward jet around 50 km. This structure produced a double atmospheric duct allowing microbaroms signals to propagate toward both west and east direction (Le Pichon et al. 2016). As expected, the propagation simulation performed using the lidar profile reliably reproduces the observed double infrasound stratospheric duct, unlike the simulation performed with the ECMWF profile (in blue) which only predicts eastward propagation (Fig. 28.14, right). This particular situation has thus provided one with a prime illustration of the potential benefit for infrasound propagation simulations of co-locating instruments, in order to locally supplant model outputs and thus limit propagation uncertainties related to current model inaccuracies.

28.4.2 Uncertainties in Detection Capability

The detection capability of infrasound networks needs to be determined in any atmospheric conditions. Here again, the challenge of the recent years has been to better integrate the atmospheric variability in computations and determine model uncertainties.

The numerical modeling technique is based on a frequency-dependent attenuation relation and time-varying station noise, to further assess, quantify, and optimize the performance of any arbitrary infrasound network (Le Pichon et al. 2012). The model includes a description of the spatiotemporal variability of the MA and a first-order uncertainty of the effective sound speed (sound speed plus along path wind) which controls the infrasound propagation. It incorporates a perturbation term representative of GW in the effective sound speed profile (Le Pichon et al. 2012). Following the ARISE observations (Le Pichon et al. 2015), the perturbation term is estimated to be 5 percent of the effective sound speed (about 15 m/s). The parabolic equation method is used to represent diffraction and scattering due to GW structures. This is one of the most effective techniques to realistically propagate the acoustic energy over various distances in a stratified atmosphere (Gainville et al. 2010). The detection capability maps were computed using a deterministic approach for the IMS infrasound network in Europe completed by the European infrasound network (Tailpied et al. 2016); Fig. 28.15 illustrates their seasonal variations. In January, the eastward stratospheric wind favors propagation of signals originating from westerly direction. Sources located west of the station are thus detected within thresholds of ~10 Pa. Differently in July, because of changes in the stratospheric wind direction, signals from easterly directions are predicted.

The detection capability is higher in January and July when the zonal stratospheric winds are strongest, compared to equinox when winds reduce and reverse.

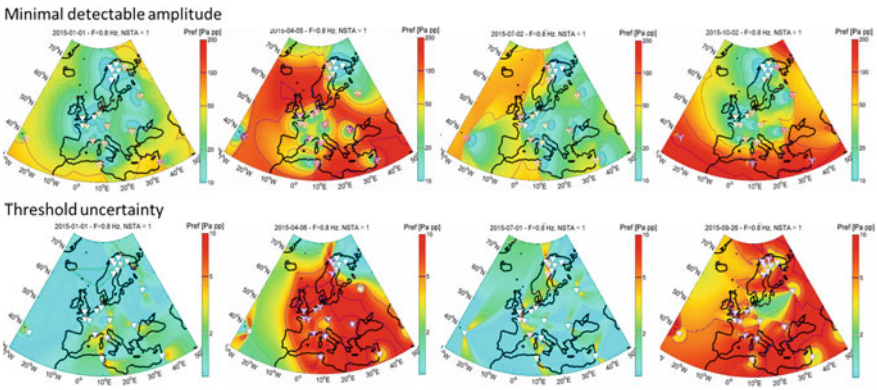

Fig. 28.15 Comparison of the smallest detectable source amplitude at 0.8 Hz considering one-station coverage. The color codes the minimum detectable source amplitude at a reference distance of 1 km from the source (in Pa peak-to-peak) (top) and the threshold uncertainty (bottom). White and gray triangles indicate IMS and national arrays, respectively. The four columns from left to right correspond to January, April, July, and October

Differently, the location capability deteriorates in the presence of high stratospheric winds, since the detecting stations only cover a small azimuthal segment, making cross bearing difficult (Le Pichon et al. 2009).

Calibrations of the infrasound simulations for operational purposes generally use explosive sources (Ceranna et al. 2009; Green et al. 2010; Fee et al. 2013; Gibbons et al. 2015). However, quasi-continuous sources such as volcanoes are needed for routine calibrations in any atmospheric conditions.

The present model has been validated using infrasound signals from Mt. Etna recorded in Tunisia and from Mt. Yasur recorded in New Caledonia. A good agreement is found when wind perturbations were added to reproduce GW inhomogeneities, especially during the equinoxes when the differences between NWP models and observations are currently identified. However, these perturbations should be strengthened during other periods of the years in order to better explain the still significant amount of uncovered predictions (Tailpied et al. 2016).

Detection capability simulations are useful to assess the performance of existing networks and predict the best locations for the installation of additional arrays. Additionally, such calculations are also crucial for providing in near real time a realistic confidence level to volcanic eruption detections, in order to mitigate the risk of aircrafts encountering volcanic ash (see Volcano Parametrization System presented, Marchetti et al. 2019). This technology is particularly relevant for remote volcano monitoring especially when near-field observations are not available. Accurate detection capability estimates at any time of the year are essential to predict the effects of the atmospheric variability and determine the uncertainties due to the presence of GW fluctuations.

28.5 Perspectives

The multi-instrument data presented in Sect. 28.3 are currently recorded in few ARISE reference stations where routine observation modes are operated. Through different possible operational applications such as medium-range weather forecasting (Tripathi et al. 2014), infrasound monitoring for the CTBT verification (Le Pichon et al. 2015) and remote volcano monitoring for civil aviation (Marchetti et al. 2019), we have demonstrated the manifest interest of generalizing such developments to a larger scale.

A first perspective to the present ARISE initiatives would thus consist in extending those routine modes to other stations, including the NDACC lidar stations. The instruments able to provide routine MA observations of the wind and temperature variability are still limited and prototypes are in development. The CORAL (see Sect. 28.3.5) portable lidar automatically measures atmospheric temperature profiles with high temporal and vertical resolutions. The observation campaign performed in 2016 at GERES in Germany, fully demonstrated its reliability and potential, in particular in depicting small-scale temperature structures unresolved by current ECMWF model configurations.

If the measured temperature fluctuations can be associated to fluctuations in wind profiles in case of GW activity, the same does not apply for PW or other disturbances, for which temperatures and winds still need to be measured simultaneously to properly depict their impacts on the MA structure. The parallel development of a portable wind lidar would thus be highly beneficial, especially while searching for model uncertainty reduction. Additionally, as regards Sect. 28.4.1 and the foreseen possibility to co-locate such portable systems with infrasound stations, portable wind lidars would be of great help to improve propagation simulations.

Second, the IMS infrasound stations could provide unique high-quality GW parameters at global scale. While IMS GW data are currently not processed because of frequency range restricted to operational uses only, their analysis for selected stations are underway for ARISE purposes. A highly significant perspective would thus be to assimilate such data in NWP models; a first test phase using European and African infrasound data is expected in the framework of the ARISE project. The state-of-the-art models of infrasound detection capability (see Sect. 28.4.6) integrate fluctuations representing GW of 5% of the effective sound speed which showed a general good agreement with observations. However, difficulties to fully represent the atmospheric variability would need future developments with better representation of GW and variability. Instead of fixing a constant value of perturbations in effective sound speeds, future studies could integrate realistic uncertainties that are dependent on the time and space. Also, only the deterministic ECMWF model is used. There is an ensemble of models that could equally well be used (Smets et al. 2015).

Other prototypes in development include the WIRA microwave wind radiometers (Rüfenacht et al. 2014), which provide—in complement to lidar data—continuous

long-term MA wind profiles (background) regardless of light and meteorological conditions. This system is passive, compact, and portable. Its resolution in time and altitude is limited compared to other technologies as lidars; however, it provides continuous background wind measurement which could be relevant for some applications when other instruments are not in operation. Airglow cameras alternatively provide mesospheric GW images and temperature fluctuations.

28.6 Summary and Conclusion

Improving the representation of the MA variability is challenging, given that instruments capable of providing high time resolution routine observations—especially between 40 and 70 km altitude—are rare (see Sect. 28.2 and Lee et al. 2019). This study demonstrated the potential of associating complementary instruments at reference and international network stations, summarized in Table 28.1, to describe MA disturbances in broad timescales and assess model uncertainties.

The combination of RMR and Fe lidars, MST, and meteor radar at the ALOMAR observatory has provided unique high-resolution continuous observations over 5 days of the MA wind and temperature profiles detailing the evolution of MA structures. New routine observations by meteor radars and lidars have been developed in other observatories. The Trondheim meteor radar provides seasonal and sub-seasonal evolution of the mean zonal wind. Wintertime winds are particularly variable and unusual structures are observed during sudden stratospheric warming events. Rayleigh lidars are operated in routine observation modes at OHP and at Reunion Island, providing three or four nightly averaged profiles per week, depending on meteorological conditions. Regular wind lidar observations are now additionally performed at both observatories. New operational modes are developed to increase the time resolution during observation campaigns. Such modes could be in future developed in other NDACC lidar stations.

Overall, the observed small-scale fluctuations either in temperature or wind profiles are not represented by the ECMWF model. Such structures are difficult to represent because of their small scale and transient nature. This is the case for GW and tide structures observed at ALOMAR, as well as for SSW-related fluctuations in wind profiles recorded at Trondheim. The full representation of the MA variability is essential for improving our knowledge of GW, tides, and other MA disturbances. In the future, automation in the operation of the instruments will provide data on a more regular basis.

The IMS infrasound network provides continuous infrasound data at global scale. Infrasound MA remote sensing is performed in few stations, observing quasi-continuously well-identified sources such as volcanoes. The Etna volcano eruptions recorded in Tunisia and Mt. Yasur recorded in New Caledonia are currently used for long-term validations and ECMWF evaluation. In complement, the

Table 28.1 Comparison between ARISE facilities

Observation stations	Instrument	Measured parameters	Altitude range	Resolution in altitude and time	Observation periods	Comments/Applications
ALOMAR reference station	RMR lidar	Temperature and zonal, meridional wind	30–85 km	1 km, 1 h	Day and night, campaigns	Full high resolution profiles for case studies and model validations (GW, tides) Polar regions
	Meteor radar	Zonal wind	80–100 km			
	Fe lidar	Temperature	80–95km			
OHP and Maïdo reference stations	RMR lidar	Temperature and zonal wind	25–90 km (temperature)	1 km, 1 h	Night-time, during campaigns	High resolution profiles for case studies and model validations (GW) Mid latitude and tropics
			5–50 km (wind)			
NDACC network	RMR lidars	Temperature	25–90 km	One mean profile per night	Night-time, 3 days per week, operational	Stratospheric climatology, SSW, trends
CTBT IMS Infrasound network	infrasound mini arrays	Gravity waves	Ground based observations	Less than 1 min	Continuously	Extreme event monitoring GW climatology at global scale
Selected infrasound station	Infrasound mini array	Effective sound speed	30–90 km	1 km, 1 h	Repetitive infrasound sources needed	Stratospheric climatology, SSW
Trondheim station	Meteor radar	Horizontal wind	80–100 km	3 km, 1 h	Routine observations	Mesospheric climatology (GW, tides) and case studies
Prototypes/ campaigns	WIRA (campaigns in the reference stations)	Zonal, meridional wind	30–75 km	Typically 10–12km, 6–12 h	Quasi continuously; tests during campaigns	Wind background; continuity in observations in complement to lidars
	CORAL lidar (IMS I26 station, Argentina)	Temperature	30–78 km	1 km, 5 min	Night-time; tests during campaigns	Mobile automatic high resolution lidar; infrasound-lidar synergy

low-frequency GW data recorded by most of the IMS sensors are relevant for atmospheric studies and assimilation in models.

However, despite those technical and scientific advances, tools providing a description of the MA variability are still sparse, and new prototypes are developed to provide complementary observations. The presented new portable autonomous CORAL lidar installed at the IS26 IMS German station provided high-quality routine observations of small timescale disturbances such as GWs. Observed lidar temperatures exceeded ECMWF ones by values up to 15 K between 45 and 65 km. Comparable differences have been observed at OHP between Rayleigh lidar and ECMWF outputs, thus highlighting regional trends. Such observations are relevant for climate and weather models. The synergy between infrasound and lidar observations also relies on lidar real-time measurements, which can be used to reduce uncertainties in infrasound simulations and source characterization. In parallel, a portable wind lidar could be developed to complete the observations.

The evaluation of NWP models and the perspectives of uncertainty reduction are essential for many applications related to the knowledge of atmospheric disturbances, from medium-range weather forecasting to climate modeling. Beyond such applications, the routine and global use of infrasound for civil applications also present a strong potential in improving technical and scientific infrasound methods related to operational monitoring.

Acknowledgements This work was partly performed during the course of the ARISE design study project, funded by the European Community's Horizon 2020 program under grant agreement 653980. We thank Gerard Rambolamanana and the team of the Institut and Geophysics Observatory of Antananarivo (Madagascar). The Madagascar infrasound results would not have been possible without their involvement. We thank M Gausa and JP Camas from Alomar and Maïdo observatories and D. Fritts for relevant comments on this paper.

References

Alcoverro B, Le Pichon A (2005) Design and optimization of a noise reduction system for infrasonic measurements using elements with low acoustic impedance. J Acoust Soc Am 117:1717–1727

Alexander MJ, Geller M, McLandress C, Polavarapu S, Preusse P, Sassi F, Sato K, Eckermann S, Ern M, Hertzog A, Kawatani YA, Pulido M, Shaw T, Sigmond M, Vincent R, Watanabe S (2010) Recent developments in gravity-wave effects in climate models and the global distribution of gravity-wave momentum flux from observations and models. QJR Meteorol Soc 136:1103–1124. https://doi.org/10.1002/qj.637

Andrews DG, Holton JR, Leovy CB (1987) Middle atmosphere dynamics. Academic Press, New York, Harcourt Brace Jovanovich

Angot G, Keckhut P, Hauchecorne A, Claud C (2012) Contribution of stratospheric warmings to temperature trends in the middle atmosphere from the lidar series obtained at Haute Provence Observatory (44°N). J Geophys Res 117

Antier K, Le Pichon A, Vergniolle S, Zielinski C, Lardy M (2007) Multiyear validation of the NRL-G2S wind fields using infrasound from Yasur. J Geophys Res 112:D23110. https://doi.org/10.1029/2007JD008462

Assink JD, Le Pichon A, Blanc E, Kallel M, Khemiri L (2014a) Evaluation of wind and temperature profiles from ECMWF analysis on two hemispheres using volcanic infrasound. J Geophys Res 119. https://doi.org/10.1002/2014jd021632

Assink JD, Waxler P, Smets PSM, Evers LG (2014b) Bidirectional infrasonic ducts associated with sudden stratospheric warming events. J Geophys Res 119. https://doi.org/10.1002/2013jd021062

Assink J, Smets P, Marcillo O, Weemstra C, Lalande J-M, Waxler R, Evers L (2019) Advances in infrasonic remote sensing methods. In: Le Pichon A, Blanc E, Hauchecorne A (eds) Infrasound monitoring for atmospheric studies, 2nd edn. Springer, Dordrecht, pp 605–632

Bakas NA, Ioannou PJ (2007) Momentum and energy transport by gravity waves in stochastically driven stratified flows. Part I: radiation of gravity waves from a shear layer. J Atmos Sci 64 (5):1509–1529

Baldwin M (2003) Major stratospheric warming in the Southern Hemisphere in 2002: Dynamical aspects of the ozone hole split. SPARC newsletter 20:24–26

Baldwin MP, Dunkerton TJ (2001) Stratospheric harbingers of anomalous weather regimes. Science 294:581–584. https://doi.org/10.1126/science.1063315

Baumgarten G (2010) Doppler Rayleigh/Mie/Raman lidar for wind and temperature measurements in the middle atmosphere up to 80 km. Atmos Meas Tech 3:1509–1518. https://doi.org/10.5194/amt-3-1509-2010

Baumgarten G, Fiedler J, Hildebrand J, Lübken FJ (2015) Inertia gravity wave in the stratosphere and mesosphere observed by Doppler wind and temperature lidar. Geophys Res Lett 42:10929–10936. https://doi.org/10.1002/2015GL066991

Bedard AJ Jr, Georges TM (2000) Atmospheric infrasound. Phys Today 32–37 (2000)

Bertin M, Millet C, Bouche D (2014) A low-order reduced model for the long range propagation of infrasounds in the atmosphere. J Acoust Soc Am 136:37. https://doi.org/10.1121/1.4883388

Blanc E, Plantet JL (1998) Detection capability of the IMS infrasound network: a more realistic approach. Infrasound workshop for CTBT monitoring, comprehensive Nuclear-Test-Ban treaty organization, Bruyères-le-Châtel, France, 21–24 July 1998

Blanc E, Le Pichon A., Ceranna L, Farges T, Marty J, Herry P (2010) Global scale monitoring of acoustic and gravity waves for the study of the atmospheric dynamics. In: Le Pichon A., Blanc E., Hauchecorne A. (eds) Infrasound monitoring for atmospheric studies. Chapter 21. Springer, Dordrecht, pp 647–664

Blanc E, Farges T, Le Pichon A, Heinrich P (2014) Ten year observations of gravity waves from thunderstorms in Western Africa. J Geophys Res 119(11):6409–6418. https://doi.org/10.1002/2013JD020499

Blanc E, Ceranna L, Hauchecorn A, Charlton Perez A, Marchetti E, Evers L, Kvaerna T, Lastovicka J, Eliasson L, Crosby N, Blanc Benon P, Le Pichon A, Brachet N, Pilger C, Keckhut P. Assink J, Smets P, Lee C, Kero J, Sindelarova T, Kämpfer N, Rüfenacht R, Farges T, Millet C, Näsholm P, Gibbons S, Espy P, Hibbins R, Heinrich P, Ripepe M, Khaykin S, Mze N, Chum J (2018) Toward an improved representation of the middle atmospheric dynamics thanks to the ARISE project. Surv Geophy 39(2):171–225. https://doi.org/10.1007/s10712-017-9444-0

Bowman JR, Baker GE, Bahavar M (2005) Ambient infrasound noise. Geophys Res Lett 32: L09803. https://doi.org/10.1029/2005GL022486

Bretherton CS, Smolarkiewicz PK (1989) Gravity waves, compensating subsidence and detrainment around cumulus clouds. J Atmos Sci 46(6):740–759

Butler A, Seidel D, Hardiman S, Butchart N, Birner T, Match A (2015) Defining sudden stratospheric warmings. Bull Am Meteorol Soc 96:1913–1928. https://doi.org/10.1175/BAMS-D-13-00173.1

Cansi Y (1995) An automatic seismic event processing for detection and location: The PMCC method. Geophys Res Lett 22(9):1021–1024

Ceranna L, Le Pichon A, Green DN, Mialle P (2009) The Buncefield explosion: a benchmark for infrasound analysis across Central Europe. Geophys J Int 177:491–508. https://doi.org/10.1111/j.1365-246X.2008.03998.x

Chanin ML, Garnier A, Hauchecorne A, Porteneuve J (1989) A Doppler lidar for measuring winds in the middle atmosphere. Geophy Res Let 16(11):1273

Chapman S, Lindzen RS (1970) Atmospheric tides: thermal and gravitational, Gordon and Breach, New York, 200 pp

Charlton AJ, Polvani LM (2007) A new look at stratospheric sudden warmings. Part I: climatology and modeling benchmarks. J Clim 20:449–469

Charlton-Perez AJ, Baldwin MP, Birner T, Black RX, Butler AH, Calvo N, Davis NA, Gerber EP, Gillett N, Hardiman S, Kim J, Krüger K, Lee Y, Manzini E, McDaniel BA, Polvani L, Reichler T, Shaw TA, Sigmond M, Son S, Toohey M, Wilcox L, Yoden S, Christiansen B, Lott F, Shindell D, Yukimoto S, Watanabe S (2013) On the lack of stratospheric dynamical variability in low-top versions of the CMIP5 models. J Geophys Res 118(6):2494–2505. https://doi.org/10.1002/jgrd.50125

Charney JG, Drazin PG (1961) Propagation of planetary-scale disturbances from the lower into the upper atmosphere. J Geophys Res 66(1):83–109. https://doi.org/10.1029/JZ066i001p00083

Chunchuzov IP, Kulichkov SN, Firstov PP (2013) On acoustic N-wave reflections from atmospheric layered inhomogeneities. Izv Atmos Ocean Phys 49(3):285–297

Clauter D, Blandford R (1998) Capability modeling of the proposed international system 60-station infrasonic network. In: Proceedings of the infrasound workshop for CTBT monitoring, Los Alamos National Laboratory report LA-UR-98-56

Cohen J, Jones J (2011) Tropospheric precursors and stratospheric warmings. J Clim 24:6562–6572. https://doi.org/10.1175/2011JCLI4160.1

Conference on disarmament (1995) Report of the expert group to the Ad Hoc committee on a nuclear test ban, The international monitoring system, CD/NTB/WP.283, 20 Dec 1995

Costantino L, Heinrich P, Mze N, Hauchecorne A (2015) A convective gravity wave propagation and breaking in the stratosphere, comparison between WRF model simulations and LIDAR data. Ann Geophys 33:1155–1171. www.ann-geophys.net/33/1155/2015/, https://doi.org/10.5194/angeo-33-1155-2015e

Delclos C, Blanc E, Broche P, Glangeaud F, Lacoume JL (1990) Processing and interpretation of microbarograph signals generated by the explosion of Mount St. Helens. J Geophys Res 95 (D5):5485–5494

de Wit RJ, Hibbins RE, Espy PJ, Orsolini YJ, Limpasuvan V, Kinnison DE (2014) Observations of gravity wave forcing of the mesopause region during the January 2013 major sudden stratospheric warming. Geophys Res Lett 41(13):4745–4752. https://doi.org/10.1002/2014GL060501

de Wit RJ, Hibbins RE, Espy PJ (2015) The seasonal cycle of gravity wave momentum flux and forcing in the high latitude northern hemisphere mesopause region. J Atmos Solar Terr Phys 127:21–29. https://doi.org/10.1016/j.jastp.2014.10.002

Diamantakis M (2014) Improving ECMWF forecasts of sudden stratospheric warmings. ECMWF Newsletter 141:30–36

Donn WL, Rind D (1971) Natural infrasound as an atmospheric probe. Geophys J R Astron Soc 26:111–133

Drob DP et al (2008) An empirical model of the Earth's horizontal wind fields: HWM07. J Geophys Res 113:A12304. https://doi.org/10.1029/2008JA013668

Drob DP, Meier RR, Picone JM, Garcés M (2010) Inversion of infrasound signals for passive atmospheric remote sensing. In: Le Pichon A, Blanc E, Hauchecorne A (eds) Infrasound monitoring for atmospheric studies, chapter 24. Springer, Dordrecht, pp 701–732

Evers LG, Siegmund P (2009) Infrasonic signature of the 2009 major sudden stratospheric warming. Geophys Res Lett. https://doi.org/10.1029/2009GL041323

Fee D, Waxler R, Assink J, Gitterman Y, Given J, Coyne J, Mialle P, Garces M, Drob D, Kleiner D, Hofstetter R, Grenard P (2013) Overview of the 2009 and 2011 Sayarim infrasound calibration experiments. J Geophys Res 118:6122–6143. https://doi.org/10.1002/jgrd.50398

Forbes JM (1982) Atmospheric tides: 1. Model description and results for the solar diurnal component. J Geophys Res 87(A7):5222–5240

Forbes JM (1995) Tidal and planetary waves. The upper mesosphere and lower thermosphere: a review of experiment and theory. In: Modeling the Ionosphere-Thermosphere, Geophysical Monograph Series, vol 87. AGU, Washington DC, pp 67–87

Fritts DC (1984) Shear excitation of atmospheric gravity waves. Part II: Nonlinear radiation from a free shear laye. J Atmos Sci 41(4):524–537

Fritts DC, Alexander MJ (2003) Gravity wave dynamics and effects in the middle atmosphere. Rev Geophys 41(1):1003. https://doi.org/10.1029/2001rg000106

Gainville O, Blanc-Benon P, Blanc E, Roche R, Millet C, Le Piver F, Despres B, Piserchia PF (2010) Misty picture: a unique experiment for the interpretation of the infrasound propagation from large explosive sources. In: Le Pichon A, Blanc E, Hauchecorne A (eds) Infrasound monitoring for atmospheric studies, chapter 18. Springer, Dordrecht, pp 569–592

Gerber EP, Orbe C, Polvani LM (2009) Stratospheric influence on the tropospheric circulation revealed by idealized ensemble forecasts. Geophys Res Lett 36:L24801. https://doi.org/10.1029/2009GL040913

Gibbons SJ, Asming V, Eliasson L, Fedorov A, Fyen J, Kero J, Koslovskaya E, Kvaerna T, Liszka L, Näsholm SP, Raita T, Roth M, Tiira T, Vinogradov Y (2015) The European Arctic: A laboratory for seismoacoustic studies. Seismol Res Lett 86(3). https://doi.org/10.1785/0220140230

Goncharenko L, Chau JL, Condor P, Coster A, Benkevitch L (2013) Ionospheric effects of sudden stratospheric warming during moderate to high solar activity: case study of January 2013. Geophys Res Lett 40(19):4982–4986

Green DN, Bowers D (2010) Estimating the detection capability of the International Monitoring System infrasound network. J Geophys Res 115:D18116. https://doi.org/10.1029/2010JD014017

Green DN, Le Pichon A, Ceranna L, Evers L (2010) Ground truth events: assessing the capability of infrasound networks using high resolution data analyses. In: Le Pichon A, Blanc E, Hauchecorne A (eds) Infrasound monitoring for atmospheric studies. Springer, Dordrecht

Hauchecorne A, Chanin ML (1980) Density and temperature profiles obtained by lidar between 35 and 70 km. Geophys Res Lett 7:565–568. https://doi.org/10.1029/GL007i008p00565

Hauchecorne A, Chanin ML (1983) Mid-latitude Lidar observations of planetary waves in the middle atmosphere during the winter of 1981–1982. J Geophys Res 88(C6):3843–3849

Hauchecorne A, Chanin ML, Wilson R (1987) Mesospheric temperature inversion and gravity wave breaking. Geophys Res Lett 14(9):933–936

Hauchecorne A, Chanin ML, Keckhut P (1991) Climatology and trends of the middle atmospheric temperature (33–87 km) as seen by Rayleigh lidar over the south of France, J Geophys Res 96:15.297–15.309

Hauchecorne A, Gonzalez N, Souprayen C, Manson AH, Meek CE, SingerW Scheer J (1994) Gravity-wave activity and its relation with prevailing winds during DYANA. J Atmos Terr Phys 56(13–14):1765–1778

Hauchecorne A, Keckhut P, Chanin ML (2010) Dynamics and transport in the middle atmosphere using remote sensing techniques from ground and space. In: Le Pichon A, Blanc E,. Hauchecorne A (eds) Infrasound monitoring for atmospheric studies, chapter 22. Springer, Dordrecht, pp 665–683

Hickey MP, Schubert G, Walterscheid RL (2001) Acoustic wave heating of the thermosphere. J Geophys Res 106(A10):21543–21548

Hildebrand J, Baumgarten G, Fiedler J, Lübken FJ (2017) Winds and temperatures of the Arctic middle atmosphere during January measured by Doppler lidar. Atmos Chem Phys Discuss. https://doi.org/10.5194/acp-2017-167

Hildebrand J, Baumgarten G, Fiedler J, Hoppe UP, Kaifler B, Lübken FJ, Williams BP (2012) Combined wind measurements by two different lidar instruments in the Arctic middle atmosphere. Atmos Meas Tech 5:2433–2445. https://doi.org/10.5194/amt-5-2433-2012

Hirooka T (2000) Normal mode Rossby waves as revealed by UARS/ISAMS observations. J Atmos Sci 57(9):1277–1285

HirotaI, Hirooka T (1984) Normal mode Rossby waves observed in the upper stratosphere. Part I: First symmetric modes of zonal wavenumbers 1 and 2. J Atmos Sci 41:8, 1253–1267

Hocking WK, Fuller B, Vandepeer B (2001) Real-time determination of meteor—related parameters utilizing modern digital technology. J Atmos Solar Terr Phys 63(2–3):155–169. https://doi.org/10.1016/S1364-6826(00)00138-3

Höffner J, Lautenbach J (2009) Daylight measurements of mesopause temperature and vertical wind with the mobile scanning iron lidar. Opt Lett 34:1351–1353. https://doi.org/10.1364/OL.34.001351

Holton JR (1982) The role of gravity wave induced drag and diffusion in the momentum budget of the mesosphere. J Atmos Sci 39(4):791–799

Holton JR (1983) The influence of gravity wave breaking on the general circulation of the middle atmosphere. J Atmos Sci 40:2497–2507

Holton JR, Haynes PH, McIntyre ME, Douglass AR, Rood RB, Pfister L (1995) Stratosphere-troposphere exchange. Rev Geophys 33(4):403–439

Hoppel KW, Eckermann SD, Coy L, Nedoluha GE, Allen DR, Swadley SD, Baker NL (2013) Evaluation of SSMIS upper atmosphere sounding channels for high-altitude data assimilation. Mon Weather Rev 141:3314–3330. https://doi.org/10.1175/mwr-d-13-00003.1

Hupe P, Ceranna L, Pilger C (2016) Data mining on long-term barometric data within the ARISE2 project. In: 18th EGU general assembly, EGU2016, proceedings from the conference held 17–22 Apr 2016 in Vienna, Austria, p 3004

Hupe P, Ceranna L, Pilger C, Le Pichon A (2017a) Using the IMS infrasound network for the identification of mountain-associated waves and gravity waves hotspots. In: 19th EGU general assembly, EGU2017, proceedings from the conference held 23–28 Apr 2017 in Vienna, Austria, p 13671

Hupe P, Pilger C, Ceranna L (2017b) Using barometric time series of the ims infrasound network for a global analysis of thermally induced atmospheric tides. J Atmos Sci (submitted)

Jones PW, Hamilton K, Wilson RJ (1997) A very high resolution general circulation model simulation of the global circulation in austral winter. J Atmos Sci 54(8):1107–1116

Kaifler B, Lübken FJ, Höffner J, Morris RJ, Viehl TP (2015) Lidar observations of gravity wave activity in the middle atmosphere over Davis (69°S, 78°E), Antarctica. J Geophys Res 4506–4521. https://doi.org/10.1002/2014jd022879

Keckhut P, Hauchecorne A, Chanin ML (1993) A critical review of the database acquired for the long-term surveillance of the middle atmosphere by the French Rayleigh lidars. J Atmos Ocean tech 10(6):850–867

Keckhut P, Gelman ME, Wild JD, Tissot F, Miller AJ, Hauchecorne A, Taylor FW (1996) Semidiurnal and diurnal temperature tides (30–55 km): climatology and effect on UARS-LIDAR data comparisons. J Geophys Res, 101:D6, 10299–10310

Kishore P, Namboothiri SP, Igarashi K, Murayama Y, Watkins BJ (2002) MF radar observations of mean winds and tides over Poker Flat, Alaska (65.1 N, 147.5 W). Ann Geophys 20:5, 679–690

Kodera K (2006) Influence of stratospheric sudden warmings on the equatorial troposphere. Geophys Res Lett 33:L06804. https://doi.org/10.1029/2005GL024510

Kohma M, Sato K (2014) Variability of upper tropospheric clouds in the polar region during stratospheric sudden warmings. J Geophys Res Atmos 119:10100–10113. https://doi.org/10.1002/2014JD021746

Kulichkov SN, Bush GA (2001) Rapid variations in infrasonic signals at long distances from one-type explosions. Izv Atmos Ocean Phys 37(3):306–313

Kulichkov S (2010) On the prospect for acoustic sounding of the fine structure of the middle-atmosphere. In: Le Pichon A, Blanc E, Hauchecorne A (eds) Infrasound monitoring for atmospheric studies, chapter 16. Springer, Dordrecht, pp 511–540

Kulichkov SN, Chunchuzov IP, Popov OI (2010) simulating the influence of an atmospheric fine inhomogeneous structure on long-range propagation of pulsed acoustic signals. Izv.Atmos Oceanic Phys 46(1):60–68

Kurylo MJ, Solomon S (1990) Network for the detection of stratospheric change: a status and implementation report. NASA upper atmosphere research program and NOAA climate and global change program (NASA), Washington DC

Labitzke K (1977) Interannual variability of the winter stratosphere in the Northern Hemisphere. Mon Weather Rev 105:762–770

Lalande JM, Sèbe O, Landès M, Blanc-Benon P, Matoza R, Le Pichon A, Blanc E (2012) Infrasound data inversion for atmospheric sounding. Geophys J Int 190:687–701. https://doi.org/10.1111/j.1365-246X.2012.05518.x

Lalas DP, Einaudi F (1976) On the characteristics of gravity waves generated by atmospheric shear layers. J Atmos Sci 33(7):1248–1259

Landes M, Le Pichon A, Shapiro NM, Hillers G, Campillo M (2014) Explaining global patterns of microbarom observations with wave action models. Geophys J Int 199:1328–1337. https://doi.org/10.1093/gji/ggu324

Lee C, Smets P, Charlton-Perez A, Evers L, Harrison G, Marlton G (2019) The potential impact of upper stratospheric measurements on sub-seasonal forecasts in the extra-tropics. In: Le Pichon A, Blanc E, Hauchecorne A (eds) Infrasound monitoring for atmospheric studies, 2nd edn. Springer, Dordrecht, pp 889–910

Le Pichon A, Garcés M, Blanc E, Barthélémy M, Drob D (2002) Acoustic propagation and atmosphere characteristics derived from infrasonic waves generated by the Concorde. J Acoust Soc Am 111(1):629–641

Le Pichon A, Blanc E, Drob D (2005) Probing high-altitude winds using infrasound. J Geophys Res 110:D20104. https://doi.org/10.1029/2005JD006020

Le Pichon A, Ceranna L, Garcés M, Drob D, Millet C (2006) On using infrasound from interacting ocean swells for global continuous measurements of winds and temperature in the stratosphere. J Geophys Res 111:D11106. https://doi.org/10.1029/2005JD006690

Le Pichon A, Vergoz J, Blanc E, Guilbert J, Ceranna L, Evers L, Brachet N (2009) Assessing the performance of the International Monitoring System's infrasound network: geographical coverage and temporal variabilities. J Geophys Res 114:D08112. https://doi.org/10.1029/2008JD010907

Le Pichon A, Blanc E, Hauchecorne A (2010) Infrasound monitoring for atmospheric studies. Springer, Dortrecht. ISBN: 978-1-4020-9507-8

Le Pichon A, Ceranna L, Vergoz J (2012) Incorporating numerical modeling into estimates of the detection capability of the IMS infrasound network. J Geophys Res 117:D05121. https://doi.org/10.1029/2011JD016670

Le Pichon A, Assink JD, Heinrich P, Blanc E, Charlton-Perez A, Lee CF, Keckhut P, Hauchecorne A, Rüfenacht R, Kämpfer N, Drob DP, Smets PSM, Evers LG, Ceranna L, Pilger C, Ross O, Claud C (2015) Comparison of co-located independent ground-based middle atmospheric wind and temperature measurements with numerical weather prediction models. J Geophys Res 120. https://doi.org/10.1002/.2015jd023273

Le Pichon A, Hauchecorne A, Keckhut P, Khaykin S, Camas JP, Payen G, Kämpfer N, Rüfenacht R, Ceranna L (2016) Monitoring middle-atmospheric dynamics using independent ground-based wind and temperature measurements at Reunion Island. Geophys Res Abst 18, EGU2016-18553

Limpasuvan V, Thompson DWJ, Hartmann DL (2004) The life-cycle of the Northern Hemisphere sudden stratospheric warmings. J Clim 17:2584–2596

Lindzen RS (1966) On the theory of the diurnal tide. Mon Wea Rev 94(5):295–301

Lindzen RS (1981) Turbulence and stress owing to gravity wave and tidal breakdown. J Geophys Res, 86:C10, 9707–9714

Lott F, Plougonven R, Vanneste J (2010) Gravity waves generated by sheared potential vorticity anomalies. J Atmos Sci 67:1, 157-–70

Lott F, Guez L (2013) A stochastic parameterization of the gravity waves due to convection and impact on the equatorial stratosphere. J Geophys Res 118(16):8897–8909. https://doi.org/10.1002/jgrd.50705

Lübken FJ, Höffner J, Viehl TP, Becker E, Latteck R, Kaifler B, Murphy DJ, Morris RJ (2015) Winter/summer transition in the Antarctic mesopause region. J Geophys Res 120:12394–12409. https://doi.org/10.1002/2015JD023928

Lübken FJ, Baumgarten G, Hildebrand J, Schmidlin FJ (2016) Simultaneous and co-located wind measurements in the middle atmosphere by lidar and rocket-borne techniques. Atmos Meas Tech 9, 3911–3919. https://doi.org/10.5194/amt-9-3911-2016, http://www.atmos-meas-tech.net/9/3911/2016/

Manney GL, Lawrence ZD (2016) The major stratospheric final warming in 2016: dispersal of vortex air and termination of Arctic chemical ozone loss. Atmos Chem Phys 16:15371–15396. https://doi.org/10.5194/acp-16-15371-2016

Manzini E, Karpechko AY, Anstey J, Baldwin MP, Black RX, Cagnazzo C, Calvo N, Charlton-Perez A, Christiansen B, Davini P, Gerber E (2014) Northern winter climate change: assessment of uncertainty in CMIP5 projections related to stratosphere-troposphere coupling. J Geophys Res 119(13):7979–7998

Marchetti E, Ripepe M, Delle Donne D, Genco R, Finizola A, Garaebiti E (2013) Blast waves from violent explosive activity at Yasur Volcano, Vanuatu. Geophys Res Lett 40:5838–5843. https://doi.org/10.1002/2013GL057900

Marchetti E, Ripepe M, Campus P, Le Pichon A, Brachet N, Blanc E, Gaillard P, Mialle P, Husson P (2019) Infrasound monitoring of volcanic eruptions and contribution of ARISE to the volcanic ash advisory centers. In: Le Pichon A, Blanc E, Hauchecorne A (eds) Infrasound monitoring for atmospheric studies, 2nd edn. Springer, Dordrecht, pp 1141–1162

Marlton G, Charlton-Perez A, Harrison G, Lee C (2019) Calculating atmospheric gravity waves parameters from infrasound measurements. In: Le Pichon A, Blanc E, Hauchecorne A (eds) Infrasound monitoring for atmospheric studies, 2nd edn. Springer, Dordrecht, pp 701–719

Marty J (2019) The IMS infrasound network: current status and technological developments. In: Le Pichon A, Blanc E, Hauchecorne A (eds) Infrasound monitoring for atmospheric studies, 2nd edn. Springer, Dordrecht, pp 3–62

Matthias V, Hoffmann P, Manson A, Meek C, Stober G, Brown P, Rapp M (2013) The impact of planetary waves on the latitudinal displacement of sudden stratospheric warmings. Ann Geophys 31:1397–1415. https://doi.org/10.5194/angeo-31-1397-2013

Matoza RS, Le Pichon A, Vergoz J, Herry P, Lalande JM, Lee H, Che IY, Rybin A (2011) Infrasonic observations of the June 2009 Sarychev Peak eruption, Kuril Islands: implications for infrasonic monitoring of remote explosive volcanism. J Volcanol Geotherm Res. https://doi.org/10.1016/j.jvolgeores.2010.11.022

Matsuno T (1971) A dynamical model of the stratospheric sudden warming. J Atmos Sci 28 (8):1479–1494

Maury P, Claud C, Manzini E, Hauchecorne A, Keckhut P (2016) Charcateristics of stratospheric warming events during Northern winter. J Geophys Res 121:5368–5380. https://doi.org/10.1002/2015JD024226

McIntyre ME (1992) Atmospheric dynamics: some fundamentals, with observational implications. In: The use of EOS for studies of atmospheric physics, pp 313–386

Medvedev AS, Klaassen GP (2000) Parameterization of gravity wave momentum deposition based on nonlinear wave interactions: basic formulation and sensitivity tests. J Atmos Solar Terr Phys 62(11):1015–1033

Newnham DA, Ford JP, Moffat-Griffin T, Pumphrey HC (2016) Simulation study for measurement of horizontal wind profiles in the polar stratosphere and mesosphere using ground-based observations of ozone and carbon monoxide lines in the 230–250 GHz region. Atmos Meas Tech 9:3309–3323. www.atmos-meas-tech.net/9/3309/2016/, https://doi.org/10.5194/amt-9-3309-2016

Mitchell NJ, Pancheva D, Middleton HR, Hagan M (2002) Mean winds and tides in the Arctic mesosphere and lower thermosphere. J Geophys Res 107:A1. https://doi.org/10.1029/2001JA900127

Mzé N, Hauchecorne A, Keckhut P, Thétis M (2014) Vertical distribution of gravity wave potential energy from long-term Rayleigh lidar data at a northern middle latitude site. J Geophys Res 119(21)

Pawson S, Kodera K, Hamilton K, Shepherd TG, Beagley SR, Boville BA, Langematz U (2000) The GCM–reality intercomparison project for SPARC (GRIPS): scientific issues and initial results. Bull Am Meteorol Soc 81:4, 781–796

Pendlebury D, Shepherd TG, Pritchard M, McLandress C (2008) Normal mode Rossby waves and their effects on chemical composition in the late summer stratosphere. Atmos Chem Phys 8 (7):1925–1935

Pilger C, Bittner M (2009) Infrasound from tropospheric sources: impact on mesopause temperature? J Atmos Solar Terr Phys 71(8–9):816–822. https://doi.org/10.1016/j.jastp.2009.03.008

Polvani LM, Waugh DW (2004) Upward wave activity flux as precursor to extreme stratospheric events and subsequent weather regimes. J Clim 17:3548–3554

Portnyagin YI et al (2004) Monthly mean climatology of the prevailing winds and tides in the Arctic mesosphere/lower thermosphere. Ann Geophys 22:3395–3410

Randel WJ, Wu F, Oltmans SJ, Rosenlof K, Nedoluha GE (2004) Interannual changes of stratospheric water vapor and correlations with tropical tropopause temperatures. J Atmos Sci 61(17):2133–2148

Rind D, Donn WL, Dede E (1973) Upper air wind speeds calculated from observations of natural infrasound. J Atmos Sci 30:1726–1729

Rind D, Donn WL (1975) Further use of natural infrasound as a continuous monitor of the upper atmosphere. J Atmos Sci 32:1694–1704

Rind D (1977) Heating of the lower thermosphere by the dissipation of acoustic waves. J Atmos Terr Phys 39(4):445–456

Rüfenacht R, Murk A, Kämpfer N, Eriksson P, Buehler SA (2014) Middle-atmospheric zonal and meridional wind profiles from polar, tropical and mid-latitudes with the ground-based microwave Doppler wind radiometer WIRA. Atmos Meas Tech 7:4491–4505. https://doi.org/10.5194/amt-7-4491-2014

Rüfenacht R, Kämpfer N (2019) Continuous middle-atmospheric wind profile observations by Doppler microwave radiometry. In: Le Pichon A, Blanc E, Hauchecorne A (eds) Infrasound monitoring for atmospheric studies, 2nd edn. Springer, Dordrecht, pp 635–647

Salby ML (1984) Survey of planetary-scale traveling waves: the state of theory and observations. Rev Geophys 22(2):209–236

Sandford DJ, Beldon CL, Hibbins RE, Mitchell NJ (2010) Dynamics of the Antarctic and Arctic mesosphere and lower thermosphere—part 1: mean winds. Atmos Chem Phys 10:10273–10289

Schöch A, Baumgarten G, Fiedler J (2008) Polar middle atmosphere temperature climatology from Rayleigh lidar measurements at ALOMAR (69°N). Ann Geophys 26:1681–1698

Schoeberl MR (1978) Stratospheric warmings: observations and theory. Rev Geophys 16 (4):521–538

Schoeberl MR, Hartmann DL (1991) The dynamics of the stratospheric polar vortex and its relation to springtime ozone depletions. Science 251:46–52. https://doi.org/10.1126/science.251.4989.46

Shaw TA, Shepherd TG (2008a) Atmospheric science: raising the roof. Nat Geosci 1(1):12–13

Shaw TA, Shepherd TG (2008b) Wave-activity conservation laws for the three-dimensional anelastic and Boussinesq equations with a horizontally homogeneous background flow. J Fluid Mech 594:493–506

Shepherd TG (2000) The middle atmosphere. J Atmos Solar Terr Phys 62(17):1587–1601

Shutts GJ, Gray MEB (1994) A numerical modelling study of the geostrophic adjustment process following deep convection. QJR Meteorol Soc 120(519):1145–1178

Sigmond M, Scinocca JF, Kharin VV, Shepherd TG (2013) Enhanced seasonal forecast skill following stratospheric sudden warmings. Nature Geosci 6:98–102. https://doi.org/10.1038/ngeo1698

Smets PSM, Evers LG (2014) The life cycle of a sudden stratospheric warming from infrasonic ambient noise observations. J Geophys Res 119:12084–12099. https://doi.org/10.1002/2014JD021905

Smets PSM, Assink JD, Le Pichon A, Evers LG (2016) ECMWF SSW forecast evaluation using infrasound. J Geophys Res 121:4637–4650. https://doi.org/10.1002/2015JD024251

Smets SM, Assink J, Evers L (2019) The study of sudden stratospheric warmingsusing infrasound. In: Le Pichon A, Blanc E, Hauchecorne A (eds) Infrasound monitoring for atmospheric studies, 2nd edn. Springer, Dordrecht, pp 723–755

Stober G, Matthias V, Jacobi C, Wilhelm S, Höffner J, Chau JL (2017) Exceptionally strong summer-like zonal wind reversal in the upper mesosphere during winter 2015/16. Ann Geophys 35:711–720. https://doi.org/10.5194/angeo-35-711-2017

Tailpied D, Le Pichon A, Marchetti E, Assink S Vergniolle (2016) Assessing and optimizing the performance of infrasound networks to monitor volcanic eruptions. Geophys J Int 208(1):437–448. https://doi.org/10.1093/gji/ggw400

Thompson DWJ, Baldwin MP, Wallace JM (2002) Stratospheric connection to Northern Hemisphere wintertime weather: implications for prediction. J Clim 15:1421–1428

Tripathi OP, Baldwin M, Charlton-Perez AJ, Charron M, Eckermann SD, Gerber E, Harrison RG, Jackson DR, Kim BM, Kuroda Y, Lang A, Mahmood S, Mizuta R, Roff G, Sigmond M, Son SW (2014) Review: the predictability of the extra-tropical Stratosphere on monthly timescales and its impact on the skill of tropospheric forecasts. Q J R Meteoro Soc. ISSN 1477-870X. https://doi.org/10.1002/qj.2432

Venkat Ratnam M, Narendra Babu A, Jagannadha Rao VVM, Vijaya Bhaskar Rao S, Narayana Rao D (2008) MST radar and radiosonde observations of inertial gravity wave climatology over tropical stations: source mechanisms. J Geophys Res 113:D7

von Zahn U, von Cossart G, Fiedler J, Fricke KH, Nelke G, Baumgarten G, Rees D, Hauchecorne A, Adolfsen K (2000) The ALOMAR Rayleigh/Mie/Raman lidar: objectives, configuration, and performance. Ann Geophys 18:815–833

Walker KT, Hedlin MA (2010) A Review of Wind-Noise Reduction Methodologies. In: Le Pichon A, Blanc E, Hauchecorne A (eds) Infrasound monitoring for atmospheric studies. Springer, Dordrecht

Whitaker RW (1995) Infrasonic monitoring. In: Proceedings of the 17th annual seismic research symposium, Scottsdale, Arizona. Phillips Lab, Hanscom AFB, Mass, pp 997–1000

Williams BP, Fritts DC, She CY, Goldberg RA (2006) Gravity wave propagation through a large semidiurnal tide and instabilities in the mesosphere and lower thermosphere during the winter 2003 MaCWAVE rocket campaign. Ann Geophys 24(4):1199–1208

Wilson CR, Szuberla CA, Olson JV (2010) High-latitude observations of infrasound from Alaska and Antarctica: mountains Associated Waves and Geomagnetic/Auroral infrasonic signals. In: Le Pichon A, Blanc E, Hauchecorne A (eds) Infrasound monitoring for atmospheric studies, chapter. Springer, pp 415–451. ISBN:978-1-4020-9507-8

Wilson R, Chanin ML, Hauchecorne A (1991) Gravity waves in the middle atmosphere observed by Rayleigh lidar: 1, case studies. J Geophys Res 96(D3):5153–5167

Wu DL, Eckermann SD (2008) Global gravity wave variances from Aura MLS: characteristics and interpretation. J Atmos Sci 65(12):3695–3718

Chapter 29
The Potential Impact of Upper Stratospheric Measurements on Sub-seasonal Forecasts in the Extra-Tropics

Christopher Lee, Pieter Smets, Andrew Charlton-Perez, Läslo Evers, Giles Harrison and Graeme Marlton

Abstract This chapter examines the potential improvements in tropospheric weather forecasts that might arise from an enhanced representation of the upper stratospheric state. First, the chapter reviews current operational practice regarding observation of the atmosphere and the relative paucity of observations in the altitude range 40–70 km. Then, we describe some idealised model calculations to quantify the potential gain in skill available from improved monitoring in this region. The idealised model experiments use a relaxation technique with the Hadley Centre General Environment Model, to assess the potential gain in skill from observations both of the whole stratosphere and the upper stratosphere. At weather forecasting timescales (up to forecast day 30), better knowledge of the stratosphere, close to the onset of a sudden stratospheric warming, improves forecasts of the tropospheric northern annular mode. Whole-stratosphere information significantly improved average surface temperature anomalies over northern North America, whilst upper stratosphere information improved anomalies over Central Siberia. These results suggest any new observational technique which can contribute to monitoring of the 40–70 km region would likely benefit tropospheric forecast skill during wintertime.

C. Lee · A. Charlton-Perez (✉) · G. Harrison · G. Marlton
Department of Meteorology, University of Reading, Reading, UK
e-mail: a.j.charlton-perez@reading.ac.uk

P. Smets · L. Evers
Seismology Division, Royal Netherlands Meteorological Institute, Wilhelminalaan 10, 3732 GK De Bilt, The Netherlands

P. Smets · L. Evers
Faculty of Civil Engineering and Geosciences, Department of Geoscience and Engineering, Delft University of Technology, Stevinweg 1, 2628 CN Delft, The Netherlands

A. Le Pichon et al. (eds.), *Infrasound Monitoring for Atmospheric Studies*,
https://doi.org/10.1007/978-3-319-75140-5_29

29.1 Introduction

Variability in the extra-tropical stratosphere is known to influence tropospheric weather conditions and their predictability in numerical models. The origins of this predictability were reviewed by Tripathi et al. (2014) and have been demonstrated to have an impact on tropospheric forecast skill on the timescales of routine weather forecasting by, for example, Jung et al. (2010). Our ability to exploit this predictability is limited both by the availability of routine stratospheric observations and uncertainties in the mechanism for stratosphere–troposphere coupling and its representation in numerical models. Additional stratospheric observations could be provided by a suite of novel observation techniques (for example, those studied by the Atmospheric Dynamics Research Infrastructure in Europe—ARISE—project Blanc et al. 2019). Before investing in new operational monitoring networks and the data assimilation methods needed to incorporate new observations into Numerical Weather Prediction (NWP) suites, it is necessary to assess the potential benefit of the new technique to fill current or future gaps in the observing system and its potential impact on forecast skill. This chapter attempts to take the first step towards assessing the benefit of the ARISE measurement network. First, we review the current observing system and identify the gap that exists in the region 40–70 km. Second, we perform idealised experiments to quantify the potential value of new observations in this region for NWP. An idealised approach to estimating the value of additional stratospheric observations is adopted because, at this early stage, their operational characteristics (e.g. sampling frequency, deployment locations and accuracy) are unknown and performing an experiment in which pseudo-observations were assimilated into a full NWP system would be premature.

29.2 Atmospheric Measurements Used for Numerical Weather Prediction in the Stratosphere

A broad diversity of observational techniques are used to capture the state of the atmosphere. Only a limited number offer observation of the upper stratosphere, and above (<100 hPa). In this section, the following instruments, commonly assimilated in NWP models or used for middle atmosphere research, are briefly described:

- Radiosondes;
- Remote sounding: nadir, zenith and limb;
- Stratospheric wind profilers;
- Mesosphere radars;
- Atmospheric lidar.

Following the overview of their operation, an indication of the vertical range that the observation types cover is given in Fig. 29.1.

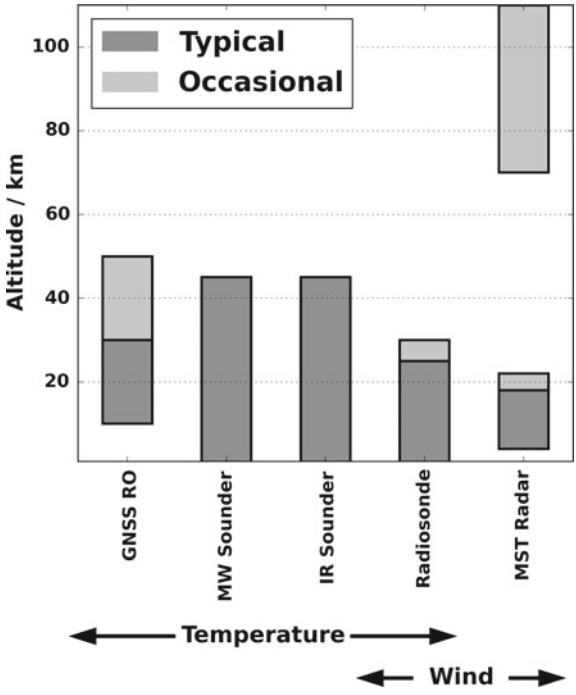

Fig. 29.1 Typical and occasional altitude ranges for the reviewed instruments. Note that wind profiling radars, both stratospheric and mesospheric, and lidar are not commonly assimilated by NWP models and so are not included in this figure

29.2.1 Radiosondes

Balloons have been used to carry instrumentation to measure the vertical profile of the atmosphere since the late eighteenth century. One of the first of these flights was a manned flight made by J. A. C. Charles, whom ascended above 2000 m using a hydrogen-filled balloon to record an air temperature of −5 °C on 1 December 1783 (Pfotzer 1972). During the next 100 years, these pioneers yearned for more observations from greater altitudes. Because of increased costs and safety limitations to such ascents, unmanned flights began to be made (Hoinka 1997). These unmanned balloon flights recorded observations using a meteograph, an instrument which recorded: pressure, temperature and humidity on to a clockwork drum, allowing the recovery of data for analysis (Renard 1903). Following developments in radio and electronics during the 1920s, Robert Bureau replaced the clockwork system with an electronic system which relayed the meteorological information over a radio link to a ground station. He made the first flight on 7 January 1929, and soon coined the phrase 'radiosonde'. Within the next decade, companies[1] across the globe began mass-producing radiosondes for meteorological organisations. Since then, radiosondes have been developed to utilise the current technologies of the age. A standard

[1]One such individual was Professor Vilho Vaisala. The company which still bears his name began commercial production of radiosondes in 1936.

radiosonde can measure temperature T, relative humidity RH, pressure P, height Z, and u and v wind components derived from its position up to heights of 40 km.

The radiosonde package is suspended 20–30 m below a balloon on a string tether. A standard radiosonde, such as the Vaisala RS92, make measurements of T, RH, P, u and v once a second which, given a typical ascent speed of 5 m/s this means the radiosonde, can produce atmospheric profiles with 5 m resolution. Temperature measurements are made using capacitive thermometers or platinum resistance thermometers; the typical uncertainty on a radiosonde temperature sensor is 0.2–0.3 K below 100 hPa and 0.4–0.5 K above 100 hPa. Pressure measurements are typically made using an aneroid capsule which has an accuracy of 0.3 hPa which becomes less sensitive in the upper stratosphere due to the logarithmic nature of the pressure profile. Relative humidity measurements are made using capacitance- based hygrometers which have an uncertainty of 5%. Wind velocity and direction are obtained by tracking the radiosonde in flight using GPS or a radio direction finding antenna. GPS measurements of the wind components are accurate to about 0.15 m/s. The meteorological and tracking instruments are powered by battery which also powers a VHF radio transmitter which relays all the sensor data to a ground station in real time. Traditionally, radiosondes use thermodynamic variables to determine the geopotential height of the balloon from pressure and temperature. However, some of the latest radiosondes have scrapped the pressure sensors and solely rely on GPS to infer its height and from that, pressure.

Radiosondes are launched with a nominal frequency of 12 h from more than 500 locations across the globe. This builds the longest temporal and spatial dataset of the higher atmosphere (Jeannet et al. 2008). The earlier radiosondes only reached heights of 16 km, and furthermore the radiosonde instrumentation may not have been as accurate as modern day technologies. This was highlighted by Luers et al. (1998) who also discussed the variability between manufacturers' radiosondes. With many different radiosondes used over many years, the Global Climate Observing System (GCOS) Reference Upper-Air Network (GRUAN) only use manufacturer radiosondes which have been independently verified to strict specifications as documented in GCOS-134, 2009 to build an accurate network of upper air observations. Modern radiosondes often reach 30 or even 10 hPa and so provide significant amounts of stratospheric data.

Climatologies of gravity wave parameters in the lower and mid-stratosphere have also been derived from radiosonde observations (Wang et al. 2009; Zink and Vincent 2001). Gravity waves can also be detected in ascent speed profiles (Marlton et al. 2016). No extra equipment on the radiosonde is required to make observations of gravity waves; however, there are some quantities that do require modification to the radiosonde. For many years, manufacturers have made provision for the addition of an ozone sensor that can be connected to the radiosonde. Using this inbuilt provision, Harrison et al. (2012) has developed an inexpensive data acquisition system that allows the incorporation of additional instruments with standard packages; for example, improved resolution of cloud-to-air transitions can be achieved using radiometers (Nicoll and Harrison 2012) and turbulence detection can be achieved

with accelerometers (Marlton et al. 2015). The scientific community has also developed balloon-borne instruments for measuring aerosol optical depth, light scattering and absorption, carbon dioxide and methane concentrations (Gcos-134 2009), atmospheric charge, and electric fields.

Related in situ measurements have in the past been provided by rocketsondes (although their use has declined significantly since the 1970s), from dropsondes released from aircraft during measurement campaigns and from Aircraft Meteorological Data Relay (AMDAR) on commercial aircraft (although note this information is restricted to flight level—around 10 km).

29.2.2 Remote Sensing

Remote sensing is the process of deriving information temperature, and atmospheric constituents such as humidity or ozone, from radiative signals (Okamoto 2008). Remote sensing can be both passive (observing radiation already present in the Earth system) or active (using radiation artificially generated by the observing system).

29.2.2.1 Nadir Profiling

A detailed review of nadir sounding can be found in Rees (2012); in this section, we briefly review the techniques used to produce the measurements widely used to constrain the stratosphere in NWP. Passive sounding captures the upward radiation from the surface and from the atmosphere at a number of different wavelengths close to a broad absorption line. In general terms, observations made closer to an absorption line are more sensitive to atmospheric properties higher in the atmosphere since the optical thickness is also greater near the centre of the absorption line. Since each observation is sensitive to temperature at a range of different altitudes, a weighting function is introduced which describes the contribution of different altitudes to the received signal. Temperature profiles can be derived by inversion, but data assimilation for NWP typically uses the observed radiance (by transforming the model state to the same variable using an observation operator).

Nadir sounding for numerical weather prediction uses both infrared (IR) and microwave (MW) channels. With six operational satellite platforms, the MW AMSU-A instruments on board the NOAA polar orbiting and European Metop satellites series are the flagship for NWP data assimilation, having delivered global temperature records for more than a decade (Kidwell et al. 2009). AMSU, a 20-channel microwave sounder comprises three separate instruments: AMSU-A1 and AMSU-A2, which have the 15 lower frequency channels (23.8–89.0 GHz) primarily for temperature sounding (surface to 2 hPa or 43 km); and AMSU-B which has five higher frequency channels (89–190 GHz) primarily for humidity sounding (surface to 200 hPa or 12 km). Other operational MW sounders include the Advanced Technology Microwave Sounder (ATMS) on the NPP satellite and the Microwave

Humidity Sounder 2 (MWHS-2) on the Feng-Yun series of satellites. In the IR, the Atmospheric Infrared Sounder (AIRS) on the Aqua satellite, the two Infrared Atmospheric Sounding Interferometer (IASI) instruments on the Metop satellites and the Cross-track Infrared Sounder (CrIS) on the NPP satellite are all used for NWP. Detailed information about the data available from different satellites can be found using the WMO OSCAR/Space Tool (https://www.wmo-sat.info/oscar/spacecapabilities).

Horizontal resolution is characterised by the sensor field-of-view (FOV), the channel frequency and the viewing angle. Temporal resolution depends on the orbit of the satellite, the maximum off-nadir looking angle and the number of satellites. For AMSU, flown by the NOAA KLM spacecrafts, the temporal resolution using 1 satellite varies from 90 min at the poles up to 6 days at the equator. The temporal resolution is improved by using multiple satellites. Using six satellites (as assimilated for example by ECMWF), the global coverage from equator to 60° varies between 76 and 84%.

A major problem with nadir sounders is bias correction. Since most AMSU channels have a beam position-dependent bias, it is crucial to remove the biases when using AMSU and similar satellites for NWP. Typically, limb-sounding data (for example, GNSS-RO) is used for this purpose, but for channels which sense the upper stratosphere and no GNSS-RO data is available bias correction is a significant issue.

29.2.2.2 Limb Sounding

Limb sounding is quite similar to nadir sounding, except that the satellite measures only the limb of the atmosphere. Limb sounders do not point towards the Earth's surface, but look at the atmosphere from the side, measuring the attenuation of, for example, solar radiation (passive) or radio waves (active). Limb-sounding radiometers measure in some channels whose characteristics are comparable to those used in nadir sounding and also use radio frequencies (for example, from GNSS signals in the COSMIC constellation) (Okamoto 2008).

Vertical information is extracted using a progressive scan of many paths, resulting in a much finer vertical resolution (0.5–2 km), but poorer horizontal resolution (>100 km), compared to nadir sounding. Limb sounding is also not influenced by surface interactions. Examples of limb-sounding sensors are ENVISAT/MIPAS, Aura/MLS and GNSS Radio Occultation (RO). For NWP, GNSS-RO is most widely used. The accuracy of GNSS-RO derived temperature depends on precise orbit determination and the thermal noise of the receiver, along with other atmospheric sources of error. GNSS-RO temperature data is globally measured with an accuracy of around 1 K from the lower troposphere to 40 km (Kuo et al. 2005). The vertical resolution of the processed data is high, 0.5 km in the troposphere up to 1.5 km in the stratosphere (Steiner et al. 2007) and with a horizontal resolution of 100–300 km.

29.2.3 Wind Profiling Radars in the Stratosphere

Radar wind profilers exploit Bragg scatter (scattering from slight changes in atmospheric refractive index) to infer wind velocities. Echoes from a moving scatterer are Doppler shifted by an amount proportional to their speed, so a spectrum of atmospheric motions can be constructed from the echo frequencies observed by the radar. Different radars have been designed to concentrate on different regions of the atmosphere. Mesosphere, stratosphere and troposphere (MST) radars operate at 40 MHz, which gives a measurement ceiling of 20 km. The radar antenna comprises many (typically hundreds) of individual antennae. The signals from each of the antennae constructively and destructively interfere to create the radar beam. Altering the phase of the signal, transmitted at different regions of the array, alters the beam pointing direction, allowing a 3D wind vector to be derived over the station.

Most MST radars can achieve a vertical resolution of 150–300 m; temporal resolutions vary, but typically fall between 2 and 5 min for routine measurements (e.g. Lee et al. 2014). Temporal resolution is determined by the number of radar beams. MST radar data is assimilated into some models (for example, the UK Met Office assimilates winds from the Capel Dewi MST radar up to 15 km, as well as measurements from the Canadian Q-NET instruments). A clear limitation, though, is the ceiling of the instruments. Echo power is proportional to the square of the range to the target; doubling a radar's transmitting power only increases altitude coverage by a few kilometres at lower stratospheric heights. There are very few MST radars worldwide and so their contribution to NWP is small on the global scale.

29.2.4 Mesosphere Radars

29.2.4.1 MST Radars

There is a large gap between the MST observation ceiling in the stratosphere, and the lowest measurement made in the mesosphere. From approximately 70 km, electron densities can be large enough to generate radio refractive index changes observable by radar. The process governing enhancements in radar detectable electron density is a subject of much debate; many days can pass without the detection of any mesospheric echoes, and winds can only be derived where such echoes exist. Nevertheless, where echoes do occur, the multi-beam approach used in the stratosphere and troposphere can be used to infer wind velocities. Echo layers are more common and widespread in summer (Polar Mesosphere Summer Echoes—PMSE), though winter echoes (PMWE) have been routinely observed (Latteck and Stelnikova 2015). MST observations of the mesosphere are largely restricted to altitudes between 70 and 110 km (Hocking 2011).

29.2.4.2 MF Radars

Medium Frequency (MF) radars also exploit scattering from radio refractive index fluctuations in the upper mesosphere. Unlike MST radars though, they examine the correlation of echoes received on several groups of antennae to infer wind velocities (the spaced antenna technique—Doviak et al. 1996). An MF radar's observing altitudes are limited by the same electron density effects that constrain MST radar observations in the mesosphere. Nevertheless, they routinely provide wind velocities between 80 and 100 km, with most instruments providing coverage down to 70 km.

29.2.4.3 Meteor Radars

Meteor radars use interferometry techniques (similar to the spaced antenna method) to measure the ionisation trails left by meteors. Those trails are advected by the background wind, and so can be used to quantify wind speed and direction. Meteor radars typically measure between 80 and 100 km; outside that range, there are typically too few meteors to obtain reliable measurements (Day and Mitchell 2010).

29.2.5 Atmospheric Lidar

Lidar operates on the same principle as radar, using light rather than radio signals to exploit different scattering mechanisms of gases and aerosols. Of particular interest to stratospheric and mesospheric dynamics are lidar temperature observations, typically exploiting Rayleigh and/or Raman scatter: Rayleigh scatter (an elastic scattering process) can be used to infer temperatures where aerosol concentrations are negligible (typically above 30 km). Raman scatter is an inelastic process that alters the energy state of the scattering molecules. The lidar pulse stimulates rotational energy levels of oxygen and nitrogen. The strength of the resulting backscatter varies with temperature, with strengthening scatter from some modes and weakening from others. Comparing scattering intensities from modes with opposing tendencies gives a measure of temperature that is independent of illuminating signal strength (i.e. independent of atmospheric attenuation along the signal path).

Typically, the lidar techniques listed here are restricted to nighttime observations, but some high-power systems can operate in daylight (Keckhut et al. 2019). Rayleigh temperature measurements reach from around 30 km to the mesopause, but can be extended to lower altitudes with additional observations. A summary of lidar temperature uncertainties can be found in Keckhut et al. (2004) and are typically of the order of 1 K.

29.2.6 Summary

Of the measurement types mentioned above, only a subset is typically assimilated by operational NWP systems. A summary of the sampling range for typically assimilated measurement types is presented in Fig. 29.1, with MST radar data only

assimilated in some systems and the top of the radiosonde range only available for some soundings. Aircraft AMDAR data are widely used but are concentrated at flight level (around 10 km).

Figure 29.1 highlights the lack of stratospheric wind measurements, and higher stratospheric and mesospheric temperature observations. Since lidar observations are not assimilated by NWP models, the data gap between 50 and 70 km is particularly stark. Radiosondes' temperature biases (<1 K) have remained relatively constant over the last 20 years. The accuracy and bias of geopotential height and pressure have improved significantly since the introduction of GNSS. Radiosondes are assumed to have well-identified biases that can be easily removed. They are therefore often used as a reference for other observation systems. Even though nadir-sounding measurements are affected by significant biases, they are instrumental for NWP where efficient bias correction methodologies have been developed during the last 10 years. To reduce these bias, a small set (a few hundred points distributed around the globe) of anchor points is used, comprising mainly measurements from radiosondes (in the troposphere) and GNSS-RO (in the stratosphere up to 35 km). Mesosphere–stratosphere–troposphere radars are able to observe winds from ground to the lower stratosphere, and occasionally in the mesosphere. MST, MF and meteor radars are, at present, the only instruments capable of observing mesospheric winds. Currently, only tropospheric and some lower stratospheric winds from MST radars are assimilated in some NWP models. Atmospheric lidars are capable of providing fine detail temperature observations of the stratosphere and (lower) mesosphere, typically operating only at night. Lidar data is not yet assimilated by NWP models. Any additional opportunity to increase observational coverage in the middle and upper stratosphere would be welcome. In the context of this book, a number of ARISE measurement techniques, particularly infrasound inversion, have the potential to fill this observational gap. In the remainder of the chapter, we present the results of a series of experiments which are designed to attempt to quantify the extent and location of potential gains in predictability which might result from additional observational capability in this region of the upper stratosphere.

29.3 Potential Predictability Experiments

The remainder of this chapter will describe the results of idealised experiments designed to quantify the importance of measurements in the middle and upper stratospheres for tropospheric forecasts. We focus on forecasts of Sudden Stratospheric Warming (SSW) events, since SSWs are known to influence surface weather conditions for several months after their onset (e.g. Thompson et al. 2002; Sigmond et al. 2013). They are characterised by a breakdown of the stratospheric polar vortex. Over a period of several weeks, these anomalous flows, which exhibit a pattern similar to the negative phase of the Northern Annular Mode (NAM), can propagate to the surface. They are associated with surface temperatures anomalies of −1 to −2 K in Northern Europe and eastern North America (Thompson and Wallace 2001;

Thompson et al. 2002). Experiments with NWP models have shown a shift in the tropospheric jet and extra-tropical cyclone tracks, to lower latitudes, after SSWs. Such shifts are associated with enhanced South Atlantic, and reduced North Atlantic, precipitation; along with an increased frequency of severe storms in the UK and Southern Europe (Baldwin and Dunkerton 2001; Gerber et al. 2009; Garfinkel et al. 2013; Sigmond et al. 2013). A recent study which compared the forecast of the 2013 SSW event between different NWP systems (Tripathi et al. 2016) showed there can be significant differences in the skill of the forecasts of SSW events, which may be partly dependent on the data assimilation scheme and observations used by each modelling centre.

29.3.1 Methodology and Model

In the experiments reported, we have used relaxation experiments to identify the response of troposphere to changes in the stratospheric state. This approach allows multiple forecasts of the same SSW to be run, with small changes made to the stratospheric state. Any differences in the forecasts are directly attributable to the stratospheric changes.

The model used in the experiment is the Met Office HadGEM2 (Hadley centre General Environment Model version 2) high-top version (N96, L60), extending to 0.01 hPa (approximately 85 km), with a slab ocean, and run at a temporal resolution of 20 min. The SSWs studied in the experiment are generated from an unconstrained 50-year-long model run. SSWs were identified using the method of Charlton and Polvani (2007), where the SSW onset is defined as the date where the daily ZMZW at 10 hPa and 60°N becomes negative. Subsequent transitions to negative ZMZW in the following 30 days are regarded as the same event. 15 SSW cases were selected from the long model run for further study. To avoid final warmings, and those associated with a weak vortex at the beginning of winter, only SSWs with onset dates lying between December and February were chosen. A five-member ensemble forecast was generated for each case, initialised 6–10 days before the SSW onset, with ensemble members produced by perturbing the initial conditions at all levels. To generate the ensemble, perturbations were made to the vorticity field, at wavenumbers 4–10. Rather than add or subtract vorticity as has been done in some studies, e.g. Gerber et al. (2009), Simpson et al. (2011), we re-distribute vorticity by randomly shifting the phase of each wave; this preserves the spectral power at a given wavenumber. For a given wavenumber and ensemble member, the phase shift is the same at each model level. Examination of the corresponding ensemble spread indicated that they were comparable to those of forecasts produced by the ECMWF, and so are representative of typical weather forecast behaviour.

To quantify how an improved knowledge of the stratosphere would enhance tropospheric forecast skill, the ensembles were re-run (from the same perturbed initial conditions) with stratosphere wind velocities relaxed back to those from the unperturbed model run (hereafter referred to as the truth run). We follow the approach used

in previous studies, such as Jung et al. (2010); Hitchcock and Simpson (2014) and nudge at every time step (i.e. every 20 min). In our experiment, we use the nudging method of Telford et al. (2008), adding an additional non-physical relaxation term to the model equations for the wind components. For example, the zonal component (u) is relaxed towards the velocities of the truth run as shown in Eq. 29.1:

$$\Delta u = F_{mt}(u) + (G\Delta t)(u_T - u). \tag{29.1}$$

Here, Δu indicates the change of the zonal wind from timestep to timestep, and F_{mt} represents zonal wind tendencies due to other processes. G is an arbitrary relaxation parameter which we set to the same value as used in Telford et al. (2008), $\frac{1}{6}\,\mathrm{h}^{-1}$. This is a relatively rigid constraint on the stratosphere, which means that it evolves very similar to the truth run without causing model instability. Consequently, these experiments identify the upper limits of forecast improvement arising from additional stratospheric information. Even if stratospheric observations could generate a perfect representation of stratosphere in operational weather forecasts, this state would not persist throughout the model run. This approach helps to identify the regions of the stratosphere where such information is likely to be particularly valuable. Relaxation is performed above 100 hPa and above 40 km in separate experiments, to estimate the potential impacts of improved knowledge of the whole stratosphere, and upper stratosphere only, respectively. At the bottom of the relaxation region, λ is tapered from 1 to zero over three model levels. The impact of the relaxation experiments on tropospheric forecast skill is quantified over three regions in the Northern Hemisphere, using the Correlation Skill Score (CSS, Eq. 29.2).

$$CSS = \frac{\overline{(f-c)(T-c)}}{\sqrt{\overline{(f-c)^2}\;\overline{(T-c)^2}}}. \tag{29.2}$$

The CSS compares the forecast (f) with the truth state in this controlled environment (T), with respect to the climatology (c). (Note that the observations in our experiments are represented by the truth run.) In this study, the climatology is taken from the long 50-year run, and the forecast is the ensemble mean for relaxed or unrelaxed stratosphere runs, depending on the type of forecast being analysed. The CSS is evaluated for 10-day forecast intervals, and over the following three regions (where stratospheric impacts are known to be important from previous studies): Eastern Canada, 45°–70°N, 100°–60°W; Western Europe, 45°–70°N, 12°W–35°E; and Northern Russia, 50°–70°N, 30°–130°E. Significance levels are calculated by bootstrapping, using random sampling with replacement of ensemble means from the 15 cases. The Northern Annular Mode (NAM) index is calculated using zonal mean zonal winds, following the method of Gerber et al. (2009). We use the NAM index as a standard measure of the variability of the jet in both the stratosphere and troposphere. The Empirical Orthogonal Function (EOF), onto which the winds are projected, is calculated from the 50-year climate run.

29.3.2 Results and Discussion

First, we examine the nature of the truth states, generated by the climate run of the model, to assess their similarity to the observed behaviour of the stratosphere, and associated tropospheric phenomena. Charlton-Perez et al. (2013) compared the frequency of observed SSWs (a mean frequency of 6.2 per decade) with those generated in various CMIP5 (Coupled Model Intercomparison Project 5) models. The high-top HadGEM2 CC (Carbon Cycle) model used in the comparison generated an average of 8.0 SSWs per decade. However, the HadGEM2 model used in this comparison does not include the carbon cycle component and generates SSWs at a frequency of 6.8 per decade. This is well within the confidence intervals of observed SSWs.

Second, we examine the tropospheric impact of SSWs, in the model, at timescales out to 60 days. The focus of this experiment is on shorter forecasts (out to 30 days); however, these longer runs allow us to make an initial comparison to previous studies. Figure 29.2 shows the surface temperature, pressure, precipitation and 500 hPa geopotential height anomalies between 15–60 days after SSW onset. Warm and cold surface temperature anomalies (Fig. 29.2a) over eastern North America and Northern Europe, respectively, are consistent with the negative phase of the NAM and the temperature signatures shown by Sigmond et al. (2013). The authors presented surface temperature maps from re-analysis of the Canadian Middle Atmosphere Model (CMAM). Their results showed that the surface temperature anomalies peaked between Greenland and Eastern Canada, at around 1.4–1.8 °C, similar to the values shown in Fig. 29.2a. Temperature anomalies over Western Canada are also consistent between the two studies, peaking at around 1.4 °C. Over Northern Russia, CMAM forecast runs presented by Sigmond et al. (2013) produce large temperature anomalies associated with SSW events and this is replicated in our model runs, with temperature anomalies peaking at <−2.2 °C. Our model results show a slight overestimation of surface temperature anomalies over Central Europe (of around 0.4 °C), but warmer anomalies over Eastern Europe are captured in our results. Sigmond et al. (2013) also examined precipitation signals following SSWs and found a shift in North Atlantic precipitation, consistent with an equator-ward shift in storm tracks. That feature is replicated in our results (Fig. 29.2b). Though the anomalies observed in the two studies are comparable, Sigmond et al. (2013) showed that there can be considerable differences between modelled and observed precipitation anomalies, suggesting that the precipitation signal associated with SSWs is weaker than that of surface temperature. Surface pressure and geopotential height anomalies (Fig. 29.2c, d) exhibit similar patterns to surface temperature, with positive and negative values over North America and Northern Europe.

The correlation between surface pressure, surface temperature and 500 hPa geopotential height anomalies is indicative of the downward propagation of the SSW signals. This propagation, from the upper stratosphere into the troposphere, is evident, at sub-seasonal timescales, in the NAM index. Figure 29.3a–d shows the NAM calculated for the different relaxed and control model runs. On average, the control runs underestimate the negative NAM index of the stratosphere seen in the truth

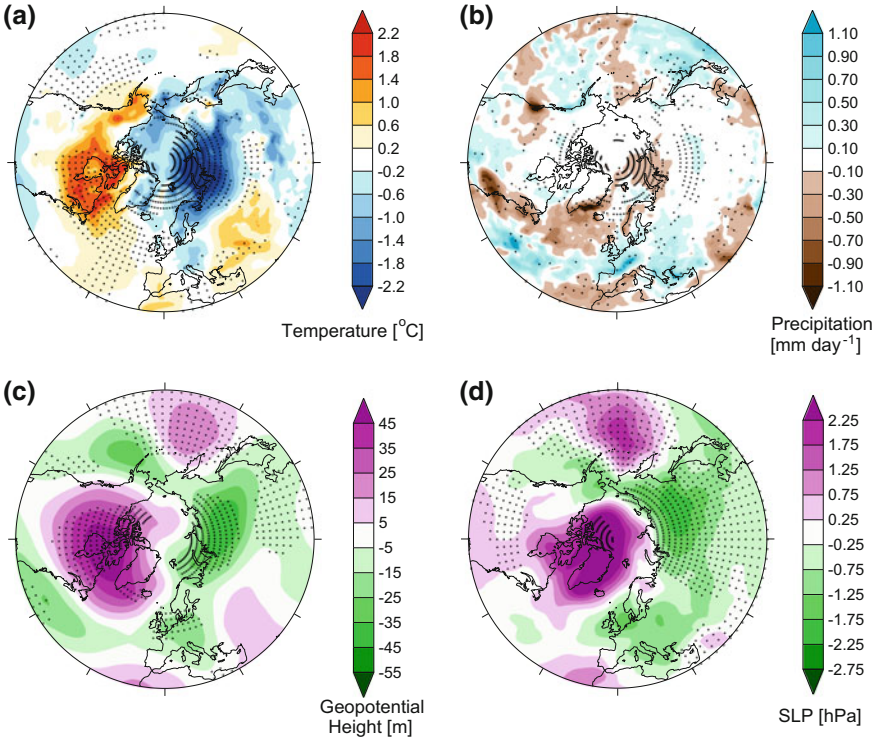

Fig. 29.2 Average anomalies of **a** surface temperature, **b** precipitation, **c** 500 hPa geopotential height and **d** sea level pressure, 15–60 days after the onset of 15 SSWs in a 50-year unconstrained climate run of the HadGEM2 unified model. Stippling indicates regions where the anomalies are significant at the 95% level

runs (Panel e), though the difference is largely insignificant. This underestimation is slightly reduced, in the first 15 days of the forecast, when relaxation of the upper stratosphere is used (Panel g). In the lower troposphere, after 25 days, there are significant differences between the NAM indices of the control and truth runs. The truth runs return to an approximately neutral NAM index after 25 days; but this is not captured by the control, which remains significantly negative. This underestimation is reduced with either relaxation of the whole or upper stratosphere, such that it becomes insignificant at most times and altitudes.

The negative NAM index in the stratosphere and upper troposphere, in the last 10 days of the forecasts, is associated with positive geopotential height anomalies over the pole, corresponding to the absence of the polar vortex (Fig. 29.4a, which shows geopotential heights at 100 hPa). Positive anomalies are also observed at 500 hPa at the same time (Fig. 29.4e), with a large negative anomaly over North Western Europe, which extends towards polar latitudes. The corresponding control runs fail to capture this structure at 500 hPa (Fig. 29.4f); instead, the positive anomaly

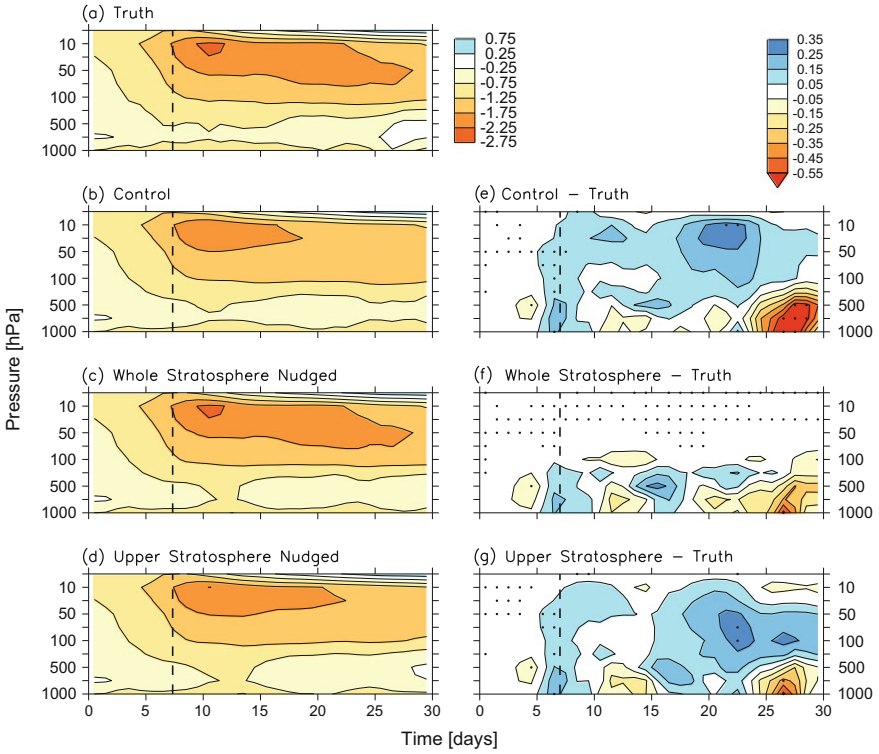

Fig. 29.3 NAM index averaged over 15 SSW cases for **a** truth run, **b** the control forecast ensemble mean, **c** forecasts with whole-stratosphere relaxation, **d** forecasts with upper stratosphere relaxation, **e** control NAM index minus truth NAM index, **f** whole-stratosphere relaxation minus truth and **g** upper stratosphere relaxation minus truth. The vertical dashed line indicates the average SSW onset date. Stippling indicates a statistically significantly difference at the 95% confidence level, calculated with bootstrapping, in figures **e**–**g**

extends into the Arctic Ocean, and the negative anomaly over Western Europe is too weak. There is also a large negative anomaly over the coast of eastern North America. These anomalies contribute to the persistence of the negative NAM signal shown in Fig. 29.3. Relaxing the whole or upper stratosphere reduces these anomalies (Fig. 29.4g, h), consistent with the more neutral NAM indices for these runs, shown in Fig. 29.3. The impact of stratospheric relaxation at the surface is illustrated by the CSS of surface temperature (Fig. 29.5). Over both eastern North America and Western Europe, relaxation of the whole stratosphere improves the surface temperature CSS. These differences are not significant, compared to either the control or upper stratosphere relaxation runs; however, there is a significant improvement in the local temperatures over eastern North America, in the whole-stratosphere relaxed runs (Fig. 29.4k).

The most significant improvement in surface temperature CSS is seen over Northern Russia, for the upper stratosphere relaxed runs (Fig. 29.5). Over much of this region, the control forecast predicts surface temperatures that are too cold (Fig.

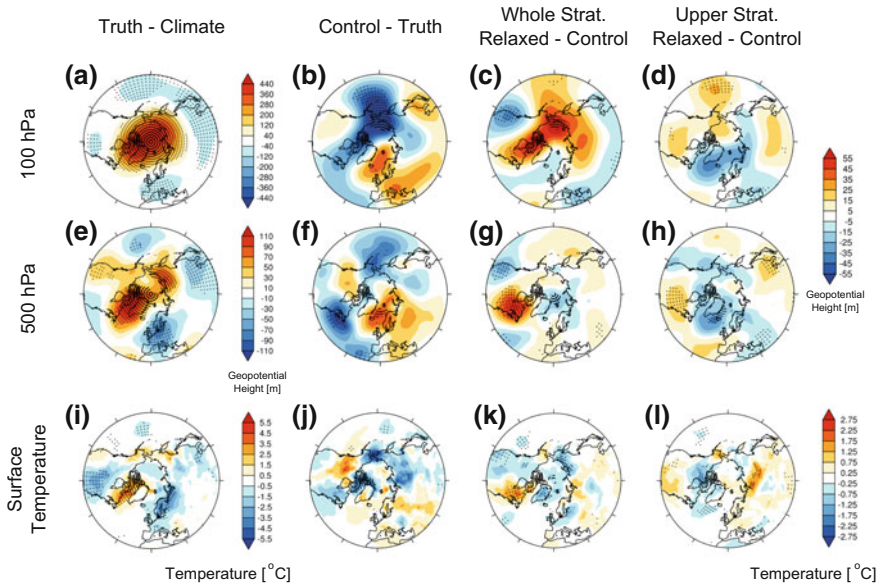

Fig. 29.4 Geopotential height and surface temperature anomalies, averaged over 15 SSW cases and forecast days 21–30. The top two rows (panels **a–d** and **e–h** correspond to 100, and 500 hPa geopotential height anomalies, respectively. The bottom row shows surface temperature anomalies. The columns correspond to anomalies of (i) the truth runs with respect to the climate; (ii) the control runs with respect to the truth; (iii) the whole-stratosphere relaxed forecasts and (iv) the upper stratosphere relaxed forecasts, with respect to the control runs

29.4j); however, this anomaly is corrected, over Central Siberia, in the upper stratosphere relaxed runs (Fig. 29.4l), contributing to the improvement in CSS. The origin of this improvement is not clear; however, it strongly influences the CSS calculations. We have varied the area over which the Northern Russia CSS is evaluated (not shown), and where the evaluation area encompasses the Central Siberian region, the upper stratosphere relaxation experiments consistently return a larger CSS than the other forecasts. It is important to remember that the forecasts used here are shorter than those used in similar studies. This is particularly important in the context of the surface temperature patterns over Northern Russia: the typical SSW-related surface temperature anomalies are not as prominent at day 30 as they are at day 60 of the truth run (compare Figs. 29.2a and 29.4i; note that Fig. 29.2a uses a finer temperature resolution, for consistency with Sigmond et al. 2013). Over Northwestern Russia, the 21–30-day surface temperatures do not exhibit the cold anomalies seen between 15 and 60 days, suggesting that this feature appears later in the truth runs. However, the cold anomalies do begin to appear in control runs, so upper stratosphere relaxation has moved the forecast away from this familiar pattern, towards the truth.

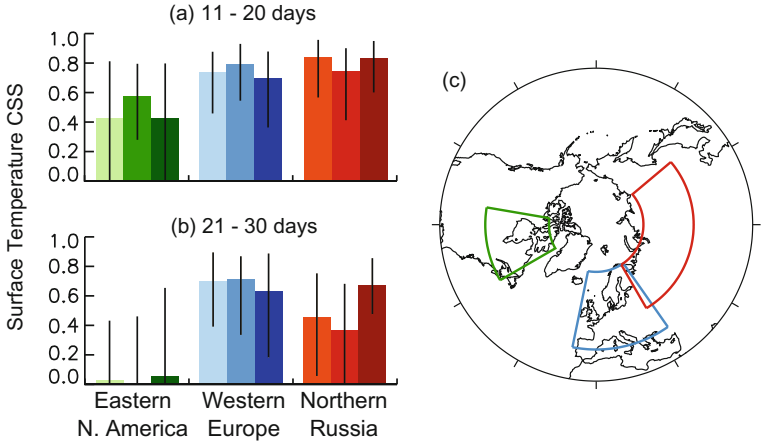

Fig. 29.5 CSS of surface temperature averaged over **a** days 11–20 and **b** 21–30; for eastern North America, Western Europe and Northern Russia. The three boxes for each region give the CSS for (i) the control (light boxes), (ii) whole-stratosphere relaxed and (iii) upper stratosphere relaxed (dark boxes) forecasts, from left to right. Black lines give the 95% confidence intervals, calculated with bootstrapping. The three analysis regions are highlighted in (**c**)

29.4 Conclusions

This chapter has shown that improved characterisation of the stratosphere in the region where stratospheric observations are sparse can improve tropospheric forecast skill at the timescales of routine weather forecasting. The relaxation experiments presented here have focused on forecasts initialised close to SSWs, when there is known to be a correlation with surface weather patterns at sub-seasonal timescales (e.g. Sigmond et al. 2013). In this study, we have examined shorter, 30-day, forecasts, where the average surface temperature anomalies that follow SSWs (warmer and cooler temperatures in eastern North America, and Northern Europe, respectively) are apparent, but not fully established.

The impacts of additional information in the whole stratosphere and the upper stratosphere only (above 40 km) have been examined separately. In both cases, the additional information improved the forecast of the tropospheric NAM, capturing a return to a near-neutral NAM index, 25 days into the forecast (15 days after SSW onset). Additional information in the whole stratosphere significantly improved the forecasting of local surface temperatures in eastern North America, over forecast days 21–30. Relaxation of the upper stratosphere improved surface temperature forecasts over Central Siberia, over the same period.

A perfect model approach has been used in these experiments, so the results presented here represent the upper limit of improvements that might be expected from more comprehensive measurements of the stratosphere. Nevertheless, the relative paucity of routine observations in the upper stratosphere means that additional mea-

surements in this region could make a significant contribution to the improvement of tropospheric forecasts. As noted in Blanc et al. (2019), ARISE measurements are one potential way to improve routine monitoring in the region between 40 and 70 km, but much more work needs to be done to understand the reliability and error characteristics of such measurements before more detailed experiments which assess the direct benefit for NWP could be conducted.

Acknowledgements This work made use of the facilities of HECToR, the UK's former national high-performance computing service. Access was provided by the Natural Environment Research Council's High Performance Computing Facility. This research is part of the Atmospheric Dynamics Research Infrastructure in Europe (ARISE) project, funded by the European Union's Seventh Framework Program. We would like to thank Kirsty Hanley, Grenville Lister, Scott Osprey, Paul Telford and Peter Watson, for their help setting up the experiments discussed here.

References

Baldwin MP, Dunkerton TJ (2001) Stratospheric harbingers of anomalous weather regimes. Science 294(5542):581–584

Blanc E, Pol K, Le Pichon A, Hauchecorne A, Keckhut P, Baumgarten G, Hildebrand J, Höffner J, Stober G, Hibbins R, Espy P, Rapp M, Kaifler B, Ceranna L, Hupe P, Hagen J, Rüfenacht R, Kämpfer N, Smets P (2019) Middle atmosphere variability and model uncertainties as investigated in the framework of the ARISE project, In: Le Pichon A, Blanc E, Hauchecorne A (eds) Infrasound monitoring for atmospheric studies, 2nd edn. Springer, Dordrecht, pp 845–887

Charlton-Perez AJ et al (2013) On the lack of stratospheric dynamical variability in low-top versions of the CMIP5 models. J Res Geophys. https://doi.org/10.1002/jgrd.50125

Charlton AJ, Polvani LM (2007) A new look at stratospheric sudden warmings. Part I: Climatology and modeling benchmarks. J Clim 20(3):449–469

Day KA, Mitchell NJ (2010) The 16-day wave in the arctic and antarctic mesosphere and lower thermosphere. Atmos Chem Phys 10(3):1461–1472

Doviak RJ, Lataitis RJ, Holloway CL (1996) Cross correlations and cross spectra for spaced antenna wind profilers. 1. Theorecal analysis. Radio Sci 31(1):157–180

Garfinkel CI, Waugh DW, Gerber EP (2013) The effect of tropospheric jet latitude on coupling between the stratospheric polar vortex and the troposphere. J Clim 26(6):2077–2095

Gcos-134 (2009) Implementation plan for the global climate observing system reference upper air network 2009–2013. Technical report, World Meteorological Organization, WMO/TD No. 1506, Geneva, Switzerland

Gerber EP, Orbe C, Polvani LM (2009) Stratospheric influence on the tropospheric circulation revealed by idealized ensemble forecasts. Geophys Res Lett 36

Harrison RG, Nicoll KA, Lomas AG (2012) Note: programmable data acquisition system for research measurements from meteorological radiosondes. Rev Sci Instrum 83(3):036106

Hitchcock P, Simpson IR (2014) The downward influence of stratospheric sudden warmings. J Sci Atmos. https://doi.org/10.1175/JAS-D-14-0012.1

Hocking WK (2011) A review of mesosphere-stratosphere-troposphere (MST) radar developments and studies, circa 1997–2008. J Atmos Solar-Terr Phys 73:848882

Hoinka KP (1997) The tropopause: discovery, definition and demarcation. Meteorologische Zeitschrift 6(6):281–303

Jeannet P, Bower C, Calpini B (2008) Global criteria for tracing the improvements of radiosondes over the last decades. Technical report, World Meteorological Organization, Instruments and Observing Methods Report No. 95, WMO/TD-No. 1433

Jung T, Miller MJ, Palmer TN (2010) Diagnosing the origin of extended-range forecast errors. Monthly Weather Rev 138(6):2434–2446

Keckhut P, McDermid S, Swart D, McGee T, Godin-Beekmann S, Adriani A, Barnes J, Baray JL, Bencherif H, Claude H, di Sarra AG, Fiocco G, Hansen G, Hauchecorne A, Leblanc T, Lee CH, Pal S, Megie G, Nakane H, Neuber R, Steinbrecht W, Thayer J (2004) Review of ozone and temperature lidar validations performed within the framework of the network for the detection of stratospheric change. J Environ Monit 6(9):721–733

Keckhut P, Claud C, Funatsu B, Hauchecorne A, Maury P, Khaykin S, Le Pichon A, Steinbrecht W (2019) Temperature trends observed in the middle atmosphere and future directions. In: Le Pichon A, Blanc E, Hauchecorne A (eds) Infrasound monitoring for atmospheric studies, 2nd edn. Springer, Dordrecht pp 805–823

Kidwell KB, Goodrum G, Winston W (2009) NOAA KLM user's guide, with NOAA-N, -N′ supplement. Technical report, National Environmental Satellite, Data, and Information Services, Silver Spring, MD

Kuo YH, Schreiner WS, Wang J, Rossiter DL, Zhang Y (2005) Comparison of GPS radio occultation soundings with radiosondes. Geophys Res Lett 32(5):L05817+

Latteck R, Strelnikova I (2015) Extended observation of polar mesosphere winter echoes over Andya (69°N) using MAARSY. J Geophys Res 120:8216–8226. https://doi.org/10.1002/2015JD023291

Lee CF, Vaughan G, Hooper DA (2014) Evaluation of wind profiles from the NERC MST radar, Aberystwyth, UK. Atmos Meas Tech 7:3113–3126

Luers JK, Eskridge RE (1998) Use of radiosonde temperature data in climate studies. J Clim 11(5):1002–1019

Marlton GJ, Harrison RG, Nicoll KA, Williams PD (2015) Note: a balloon-borne accelerometer technique for measuring atmospheric turbulence. Rev Sci Instrum 86(1):016109

Marlton GJ, Williams PD, Nicoll KA (2016) On the detection and attribution of gravity waves generated by the 20 March 2015 solar eclipse. Philos Trans R Soc A 374:20150222

Nicoll KA, Harrison RG (2012) Balloon-borne disposable radiometer for cloud detection. Rev Sci Instrum 83(2):025111

Okamoto K (2008) L5 satellite remote sensing by temperature and humidity sounders. Satellite remote sensing of atmospheric constituents. In The Eighteenth IHP Training Course, Nagoya, Japan

Pfotzer G (1972) History of the use of balloons in scientific experiments. Space Sci Rev 13:199–242

Rees WG (2012) Physical principles of remote sensing. Cambridge University Press, p 426. ISBN 9781283818063

Renard C (1903) On the use of sounding balloons for meteorological observations at great heights. Monthly Weather Rev 31:570–571

Sigmond M, Scinocca JF, Kharin VV, Shepherd TG (2013) Enhanced seasonal forecast skill following stratospheric sudden warmings. Nat Geosci 6(2):98–102

Simpson IR, Hitchcock P, Shepherd TG, Scinocca JF (2011) Stratospheric variability and tropospheric annular-mode timescales. Geophys Res Lett 38(20)

Steiner AK, Kirchengast G, Borsche M, Foelsche U, Schoengassner T (2007) A multi-year comparison of lower stratospheric temperatures from CHAMP radio occultation data with MSU/AMSU records. J Geophys Res 112(D22):D22110+

Telford PJ, Braesicke P, Morgenstern O, Pyle JA (2008) Technical note: description and assessment of a nudged version of the new dynamics unified model. Atmos Chem Phys 8(6):1701–1712

Thompson DWJ, Baldwin MP, Wallace JM (2002) Stratospheric connection to Northern Hemisphere wintertime weather: implications for prediction. J Clim 15(12):1421–1428

Thompson DWJ, Wallace JM (2001) Regional climate impacts of the Northern Hemisphere annular mode. Science 293(85):85–89

Tripathi OP, Baldwin M, Charlton-Perez A, Charron M, Eckermann SD, Gerber E, Harrison RG, Jackson DR, Kim B-M, Kuroda Y, Lang A, Mahmood S, Mizuta R, Roff G, Sigmond M, Son S-W (2014) The predictability of the extratropical stratosphere on monthly time-scales and its impact on the skill of tropospheric forecasts. Q J R Meteorol Soc

Tripathi OP, Baldwin M, Charlton-Perez A, Charron M, Cheung JCH, Eckermann SD, Gerber E, Jackson DR, Kuroda Y, Lang A, Mclay J, Mizuta R, Reynolds C, Roff G, Sigmond M, Son S-W, Stockdale T (2016) Examining the predictability of the stratospheric sudden warming of January 2013 using multiple NWP systems. Monthly Weather Rev 144(5):1935–1960. https://doi.org/10.1175/MWR-D-15-0010.1

Wang J, Bian J, Brown WO, Cole H, Grubisic V, Young K (2009) Vertical air motion from T-REX radiosonde and dropsonde data. J Atmos Oceanic Technol 26(5):928–942

Zink F, Vincent RA (2001) Wavelet analysis of stratosphere gravity wave packets over Macquarie Island 1. Wave parameters. J Geophys Res 106(D10):10275–10288

Part X
Benefits for Monitoring Natural Hazards: Extreme Atmospheric Events

Chapter 30
Infrasound for Detection, Localization, and Geometrical Reconstruction of Lightning Flashes

Thomas Farges, François Coulouvrat, Louis-Jonardan Gallin and Régis Marchiano

Abstract In the context of the infrasound network of the International Monitoring System of CTBT, infrasounds and low- frequency sounds are reviewed as a method to characterize lightning flashes in a complementary way to electromagnetic observations. The physics of lightning discharges is briefly recalled, in relation with thunder characteristics and mechanisms of generation. The possibilities and limitations of following storms at various distances by means of remote acoustic detection of lightning flashes is discussed. Influence of distance, wind and ambient noise is examined. The three-dimensional reconstruction of lightning flashes is illustrated by several examples from a recent 2012 observation campaign in the French Mediterranean region. Comparison with outputs from a high-resolution electromagnetic lightning mapping array delineates the performances of acoustical reconstruction of individual lightning flashes for both intra-cloud or cloud-to-ground discharges. Analysis of a significant number of discharges allows to perform a statistical comparison of the two approaches. Special attention is brought to the lower parts of cloud-to-ground discharges. Opportunities for further investigations are finally outlined.

T. Farges (✉) · L.-J. Gallin
CEA, DAM, DIF, F-91297 Arpajon, France
e-mail: thomas.farges@cea.fr

L.-J. Gallin
e-mail: louis.gallin@univ-pau.fr

F. Coulouvrat · R. Marchiano
Sorbonne Universités, UPMC Univ Paris, CNRS, UMR 7190,
Institut Jean Le Rond d'Alembert, 75005 Paris, France
e-mail: francois.coulouvrat@upmc.fr

R. Marchiano
e-mail: regis.marchiano@upmc.fr

A. Le Pichon et al. (eds.), *Infrasound Monitoring for Atmospheric Studies*,
https://doi.org/10.1007/978-3-319-75140-5_30

30.1 Introduction

From a historical point of view, thunderstorm activity over different geographical regions was evaluated through an empirical index named "keraunic level". The keraunic level at a given place is defined as the number of days per year during which thunder has been heard there at least once. Thus, the first estimations of a given place's exposure to storms were based on thunder hearing by humans (World Meteorological Organization 1956).

Most studies about thunder were performed from 1960 to 1985 (Rakov and Uman 2003). They mainly concerned the audible part of thunder, though some works also investigated the infrasound domain. The lightning location systems based on electromagnetic measurements were not available at that time. So one-to-one comparison between electromagnetic and acoustic measurements was then not possible. Nearly all theoretical studies on generation mechanisms were developed in that period of time to explain the spectrum of the acoustic wave (Few 1995).

The first characterizations of the geometry of lightning channels were performed during the 1970s–1980s relying on acoustic measurements. Few (1970) succeeded in reconstructing the geometry of several flashes. He showed that a flash has a considerable horizontal extension (of several tens of kilometers) inside the thunderclouds. Few and Teer (1974) found a good agreement between the acoustic reconstructions and the pictures they obtained from photographic surveys, when the discharge is visible, being outside the storm cloud. Moreover, acoustic reconstruction showed that the Cloud-to-Ground (CG) channel is still present inside the cloud but is invisible for optical devices. MacGorman et al. (1981) showed 3D maps of acoustic activity from thunder and analyzed the statistical distribution of altitudes of the reconstructed sources inside thunderclouds. Acoustic method results (e.g., Arechiga et al. 2011) can nowadays be compared to reconstructed geometries of discharges provided by high-resolution electromagnetic detection networks such as a lightning mapping array (see Sect. 30.2.2) thanks to their development in the 1980s–1990s.

The development of the International Monitoring System (IMS) infrasound network dedicated to the verification of the Comprehensive Nuclear Test-Ban-Treaty (CTBT) and, simultaneously, the deployment of global, continental, or regional lightning location networks motivate new scientific investigations about thunder. The IMS network will consist of 60 infrasound stations distributed uniformly over the surface of the globe (Campus and Christie 2010). Today, 80% of this network is operational (Marty 2019). The IMS network is unique by its global and homogeneous coverage as well as its data quality. Infrasound stations are very sensitive acoustic antenna including at least 4 microbarometers at distances from one another in the range of 1–3 km. These arrays are able to detect and characterize low-amplitude coherent infrasound signals within the background noise, including natural or man-made atmospheric sources, such as exploding meteoroids, volcanic eruptions, hurricanes, earthquakes, and ocean swell (Le Pichon et al. 2013; Matoza et al. 2013; Drob 2019).

Since 2000, some studies have been realized to better understand the impact of lightning flashes for the IMS because some of these stations are located in places where the lightning activity is high, such as in Africa or South America (see Fig. 30.1).

Large thunderstorm systems are able to produce high-energy transient events as Transient Luminous Events (TLE) which were discovered in the 90s. TLEs occur above thunderstorm from 20 to 100 km altitude (Pasko et al. 2012). Sprites, which are streamer-type air discharges, appear at mesospheric altitudes and are triggered by lightning discharges (with positive polarity). They last a few milliseconds and are usually composed of a cluster of vertical columns typically characterized by diameters ranging from a few tens to a few hundreds of meters. Sprites can also emit infrasound. Their observation shows that the infrasonic signal presents a chirp shape in their spectrogram (Farges et al. 2005; Farges and Blanc 2010). Theoretical studies show that this shape is due to propagation effect (de Larquier and Pasko 2010). The source of these infrasound waves is the heating inside the sprite streamer. Recent studies show that only the stronger sprites are able to produce infrasound da Silva and Pasko (2014). We do not go further on this subject in this chapter, because the signal characteristics and the production mechanisms are quite different from lightning.

We detail briefly in the Sect. 30.2 the lightning discharges and the thunder characteristics. In the Sect. 30.3, we show how lightning flashes are detected by infrasound

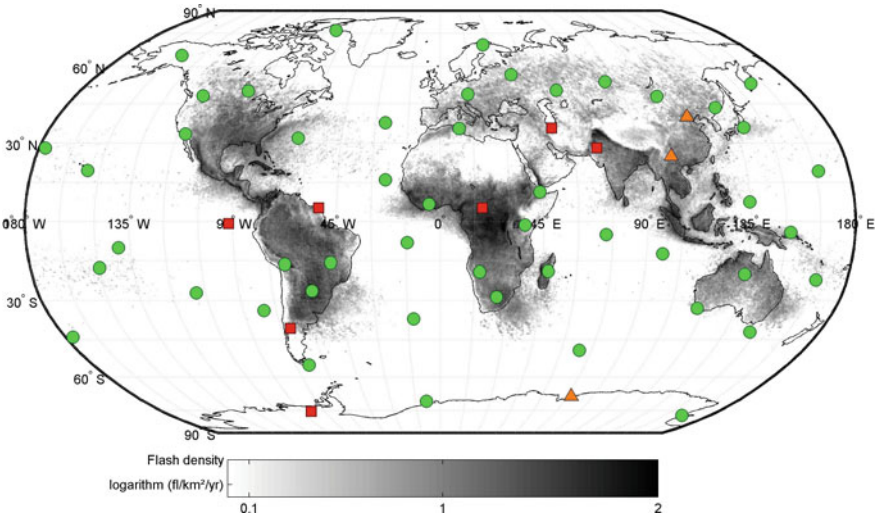

Fig. 30.1 Location of the 60 infrasound stations of the IMS of the CTBT (diamond) compared to the annual flash density measured by lightning imaging sensor instrument (using the gridded lightning climatology dataset by Cecil et al. 2014). The color and the of the type of marker correspond to the status of the station in 2016: green circle stands for certified, orange triangle for installed or under construction, and red square for planned

networks. In the Sect. 30.4, we show recent results of 3D geometrical reconstruction of lightning flashes using acoustic waves and compare them to the reconstruction obtained with electromagnetic measurements.

30.2 Lightning Discharges and Thunder

Lightning discharges appear in cumulonimbus clouds in order to neutralize the charges, which are generated inside these very large clouds. The purpose of this section is to give general information about lightning flashes (their different categories and the different phases constituting a flash), their electromagnetic radiation and their use to locate them, and finally the characteristics of the thunder—the acoustic byproduct of lightning flashes—and the different physical mechanisms explaining it. Readers who want to have more information could read, for instance, the review works of Rakov and Uman (2003) or of Betz et al. (2009).

30.2.1 Lightning Discharges

Schematically, the charges in cumulonimbus are organized vertically in a tripole structure (cf. Fig. 30.2):

- at the bottom, a thin positively charged layer,
- at the middle, a negatively charged pocket,
- and at the top, a positively charged pocket.

Different kinds of discharges can occur inside a thundercloud. They are classified into two main categories (e.g., Cummins and Murphy 2009) as follows:

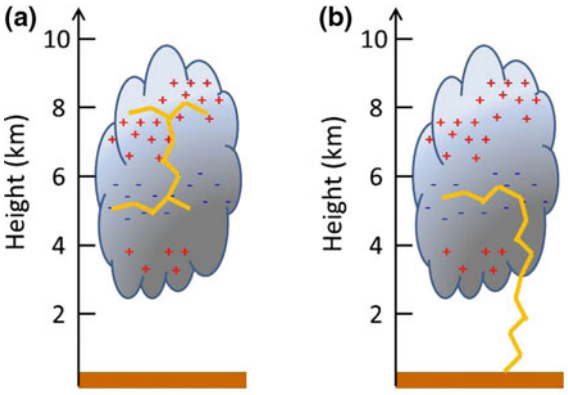

Fig. 30.2 Sketch of the tripole structure of a cumulonimbus cloud (the blue "−" indicates the negative charges while the red "+" the positive charges) and of the two main categories of discharges: intra-cloud (**a**) or cloud-to-ground (**b**)

- those which develop and propagate within the cloud or from one cloud to another; they are named respectively Intra-Cloud (IC) discharges or Cloud-to-Cloud (CC) discharges;
- and those which develop within the cloud but propagate outside it and reach the ground; they are called Cloud-to-Ground (CG) discharges.

ICs and CCs represent typically 75% of all the discharges while CGs only 25% (Rakov and Uman 2003).

A lightning flash is composed of several phases (cf. Fig. 30.3). The first step is the inception, also called *Preliminary Breakdown*; its generation is still in debate. *Stepped leaders* propagate from the inception point inside the cloud. They are electric discharges which are able to propagate in the air thanks to the large electric field localized at their head and making an ionized channel. The leaders propagate step-by-step. In case of CGs, they go toward the ground. The median length of a step is 30 m and its direction is random. This induces the observed tortuosity of a lightning flash. After about 20 ms of propagation, the stepped leaders are close enough to the ground. Another discharge, of opposite polarity, then emerges from the ground and connects to the stepped leader. This is the *attachment process*. In a few microseconds, the most powerful part of the flash happens; it is the *Return Stroke* (RS). A very-high electric current flows from the ground to the cloud to neutralize the charged pocket from where the stepped leaders are coming from. In order to complete this neutralization, the discharge propagates, mainly horizontally, in the pocket (*J- and K-processes*). The neutralization by only one single return stroke is often not complete. Several subsequent return strokes, preceded by *dart leaders*, are usually necessary to fully neutralize the cloud.

Table 30.1 gives typical values for parameters describing the return strokes and the lightning flashes.

In most of the cases (90% of CGs), the stepped leaders are coming from the negatively charged pocket, as shown in Fig. 30.3; they are called negative cloud-to-ground lightning flash (−CG). There are some differences between −CGs and +CGs. For

Table 30.1 Numerical data for cloud-to-ground lightning flash (from Ogawa 1995)

Parameter	Minimum	Typical	Maximum
Return stroke			
Peak current (kA)	1	30	250
Temperature (K)	0.8×10^4	2×10^4	3.6×10^4
Channel length (km)	2	5	14
Lightning flash			
Number of strokes per flash	1	3	26
Time interval between strokes (ms)	3	40	380
Time duration (s)	0.01	0.3	2
Charge transferred (C)	1	20	400

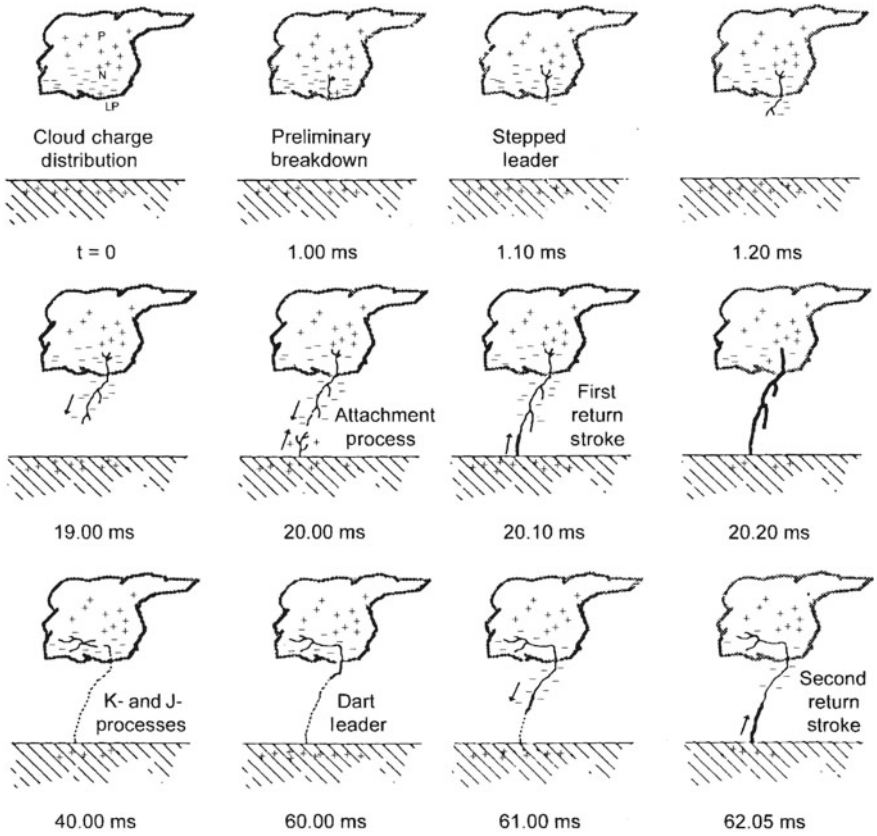

Fig. 30.3 A drawing showing the different steps comprising a negative cloud-to-ground (−CG) lightning flash. "LP" means "lower positive". From Rakov and Uman (2003)

instance, the −CGs typically consist of 3–5 return strokes while the +CGs contain only one return stroke. Furthermore, the transferred charge of a −CG is typically of 20 C while it is much larger for +CGs. Finally, +CGs present less tortuosity than −CGs.

The currents flowing in the lightning channel induce various optical, radio-electromagnetic, and acoustic radiations. A lightning flash could be considered as a dipole antenna. The current inside the channel produces an electromagnetic field which is usually recorded in order to detect and localize the flashes, as discussed below. The current flow, inside a 5 cm diameter channel, causes the heating and the ionization of the air inside. The temperature could rise up to 5,000 K for the leaders and from 10,000 to 30,000 K for the return strokes. This heating induces optical emissions which can be analyzed by a spectrometer. The temperature can be precisely measured by the identification of specific atomic or molecular lines inside the light spectrum. Unfortunately, this kind of diagnostic is possible only for the bottom

part of the flash, where the channel is below the cloud, that is for altitudes below 2 or 3 km. Inside the cloud, the light is scattered, or even fully damped. With the increase of the temperature up to 30,000 K in only a few microseconds, the pressure inside the channel exceeds 1×10^6 Pa, that is 10 times the atmospheric pressure. It produces an acoustic shock wave which propagates outwards; this is the thunder. We describe, in the Sect. 30.2.3, the characteristics of thunder and its generation mechanism.

30.2.2 Electromagnetic Radiation and Lightning Location

A lightning flash radiates broadband radio-electromagnetic signals (Fig. 30.4). Due to the length of the different lightning processes, the signal due to the return stroke has its main frequency around 5–10 kHz (Very Low Frequency—VLF—band) while stepped leaders radiate mainly at higher frequencies (>1 MHz). At the same time, it is well known that VLF waves propagate inside the Earth–ionosphere waveguide over several thousands of kilometers while HF-VHF (High and Very-High Frequency—HF and VHF—and bands) signals can propagate only over a few hundreds of kilometers.

Therefore, the Lightning Location System (LLS) coverage and its detection capacity depend strongly on the bandwidth of the used sensors.

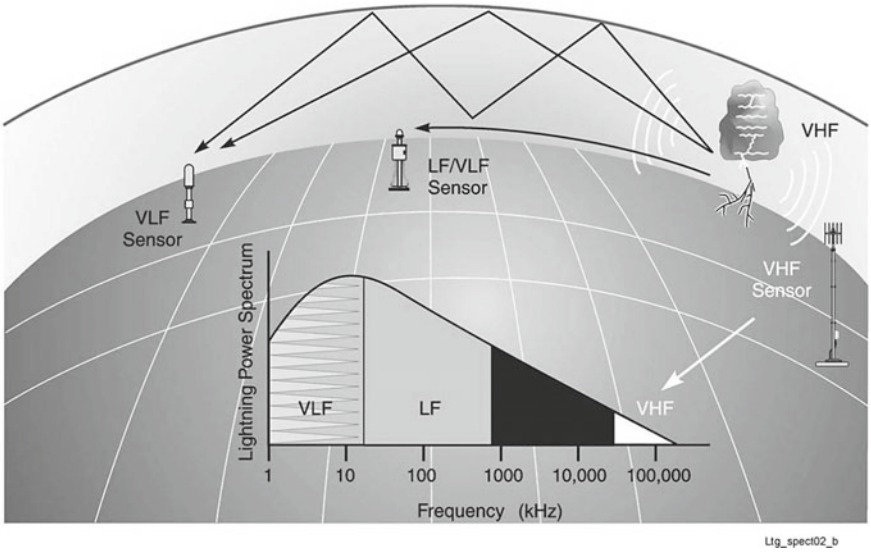

Fig. 30.4 Different localization techniques depending on the lightning spectrum in the radio wave bands. A waveguide is formed between ground and the ionosphere. The ionosphere is the ionized part of the atmosphere from 60 to 1000 km altitude. The VLF waves reflect at about 80 km. From Cummins and Murphy (2009)

- With 50–60 VLF sensors well distributed all around the world, as the World Wide Lightning Location network (WWLLN, www.wwlln.net), it is possible to monitor the lightning activity at a global scale, but it is not easy to get the peak current and its polarity neither to sort out the flashes as CGs or ICs.
- With regional networks, such as the NLDN (National Lightning Detection Network) in the USA or EUCLID (EUropean Cooperation for LIghtning Detection) in Europe, made of hundreds of stations measuring the VLF/LF signals it is possible to get the precise date (a few microseconds) and location of lightning (a few hundreds of meters) along with its peak current and polarity, and also to differentiate CGs from long length vertical ICs.
- Lastly, the local networks, as the LMA (Lightning Mapping Array (Rison et al. 1999)) using about ten stations measuring VHF signals within a 300-km radius. For nearby lightning, such network provides high-resolution description of the discharges' stages. These local networks measure the short-length discharges inside the cloud and the stepped leaders. It is then possible to give the 3D geometry of the source with a precision of tens of meters and a time resolution of tens of nanoseconds (Thomas et al. 2004). An LMA measures mainly the IC activity, and is, therefore, very complimentary to regional networks.

30.2.3 Thunder: Characteristics and Generation Mechanisms

30.2.3.1 Thunder Characteristics

Rakov and Uman (2003) review thunder studies. We sum up here the main characteristics of this phenomenon. Thunder is audible at distances less than 25 km from lightning flashes (Fleagle 1949). The pressure wave is generally composed of several pulses each lasting from 0.2 to 2 s with a gap of 1–3 s between them (see Figs. 30.5 and 30.6). The duration of a single thunder event is from 10 s to 1 min. This duration is due to the vertical and horizontal extent of the source. The amplitude ranges from 0.1 to 10 Pa. As mentioned in the introduction, the listening capability of the thunder was used in the middle of the twentieth century to evaluate the thunderstorm activity through the "keraunic level". This measure is then very local and subject to propagation effects resulting from wind or topography.

The first acoustic records of thunders and of their associated spectral contents date back to years 1960–1970. Holmes et al. (1971) investigated spectra associated to thunder waveforms recorded for several CGs and ICs (see Fig. 30.7). They pointed out that the spectral content varies during the signal, with an audible frequency content from 50 to 200 Hz being recorded first. It is then followed by pulses of frequencies below 20 Hz. Balachandran (1979) noted the existence of very low-frequency waveforms (infrasound), with small acoustic amplitudes. Electromagnetic lightning

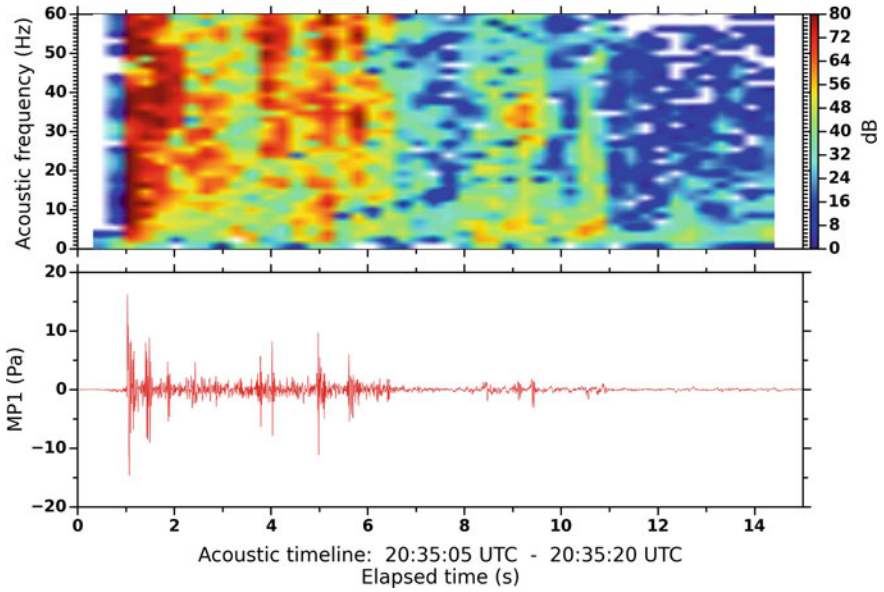

Fig. 30.5 Spectrogram and signal of an acoustic wave induced by a CG flash which occurred on 10/26/2012 at 20:35:00.08 UT at 2.2 km from microphone. Adapted from Gallin et al. (2016)

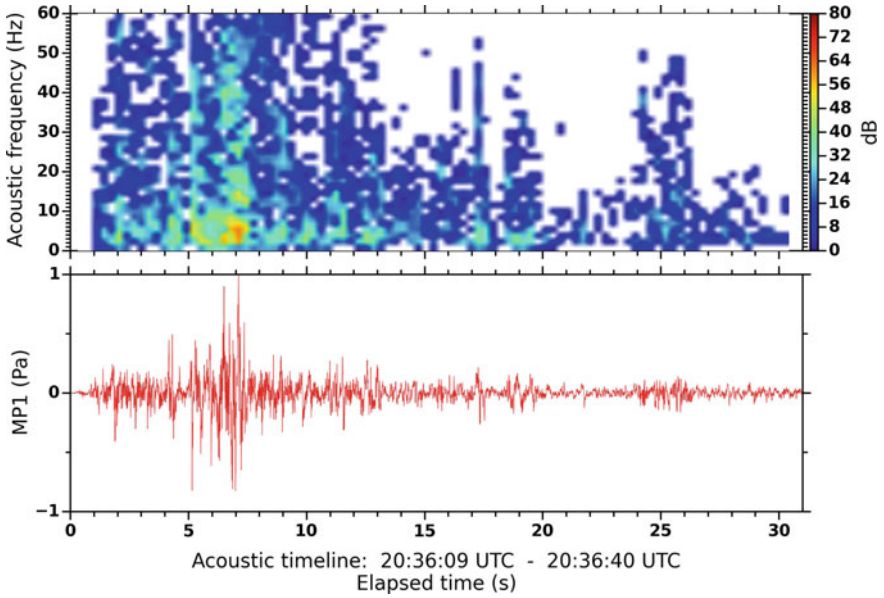

Fig. 30.6 Spectrogram and signal of an acoustic wave induced by an IC flash which occurred on 10/26/2012 at 20:35:58.86 UT at 5.7 km from microphone. Adapted from Gallin et al. (2016)

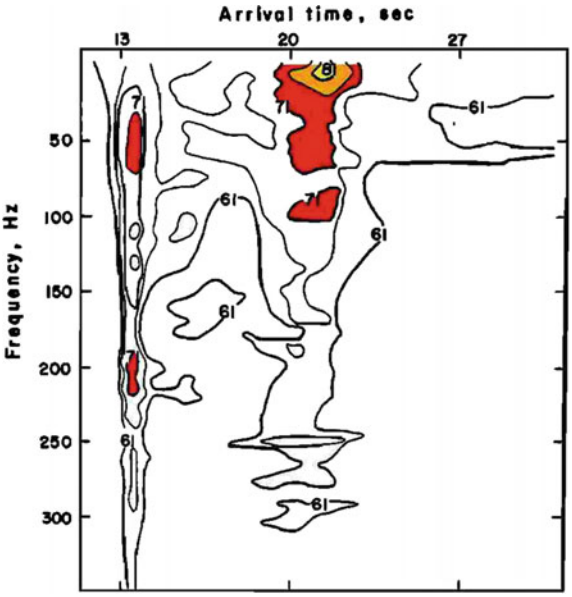

Fig. 30.7 Power spectrum as a function of thunder arrival time calculated for windows of 1 s duration and displayed as power contours in dB above standard level of 10^{-12} J m^{-2} s^{-1} Hz^{-1}. Adapted from Holmes et al. (1971)

detection tools being not available at that time, comparative studies of lightning properties and their acoustic characteristics could not be realized.

30.2.3.2 Thunder Generation Mechanisms

Few (1995) reviews the two main mechanisms explaining the generation of acoustic waves by lightning flash. Audible thunder is due to acoustic radiation from heated channels while infrasonic thunder could be due to conversion of the thundercloud electrostatic field to sound.

Radiation from Hot Channels

Few (1995) underlines the main difficulties to explain individual thunder measurements:

- the acoustic signal is the superposition of a lot of shock waves which are emitted by the leaders and the return stokes of a lightning flash,
- this signal is the convolution of these shock waves with the geometry of the flash, including the tortuosity,
- each lightning channel is unique and cannot be repeated; a large number of highly variable parameters are then necessary to calculate the acoustic wave,
- it is very difficult to obtain quantitative values of these parameters (describing the flash), and also of the very local meteorology (temperature and wind speed with high spatial and temporal resolution), while other sources can moreover perturb the measurements.

However, after Jones et al. (1968), Few (1969) developed a model which can explain the acoustic waves produced by lightning. He introduced the *relaxation radius* defined as the radius of the volume that can be generated if all the explosion energy is used in performing a thermodynamic work on the surrounding atmosphere, assumed at constant pressure P_0. For a cylindrical geometry of the source, the relaxation radius is

$$R_c = \left(\frac{E_l}{\pi \times P_0} \right)^{1/2} \tag{30.1}$$

where E_l is the energy per unit length of the cylindrical shock wave. Brode (1956) showed that the shock wave goes from the strong shock region to the weak shock region, when the distance to the source is larger than R_c. Few (1969) deduced from this that, provided observation is performed at distances larger than R_c, the cylindrical source associated to an elementary part of the tortuous discharge could be replaced by a unique spherical source. Thus, a whole discharge can be represented as a small number of spherical sources, which justifies the name of "string of pearls model". Therefore, thunder is expected to behave more as a spherical source than as a cylindrical one. Using this model, Few calculated the spectrum of an acoustic wave due to lightning flash. He found an empirical relation giving the maximum frequency of the spectrum as follows:

$$f_m = 0.63 \times c_0 \times \left(\frac{P_0}{E_l} \right)^{1/2}, \tag{30.2}$$

where c_0 is the speed of sound. This relation is similar to the one found for sparks produced in the laboratory. Note that the full spectrum cannot be obtained with these simplifications. For a reasonable energy per unit length of 10^6 J/m, a maximum frequency of 68 Hz is found. Depasse (1994) showed that for triggered lightning this relation is valid but the whole signal has to be taken into account and not some shorter parts. This relation cannot explain the generation of infrasound because it would require energy hundred times greater (Rakov and Uman 2003).

This model justifies why we can consider in the next section that the acoustic wave sources are co-located with the lightning discharges.

Electrostatic Mechanism

Wilson (1920) suggested that *the pressure within a charged cloud—like that within a charged soap bubble must be less than the pressure outside. [] It is evident, however, that the sudden contraction of a large volume of air must furnish a by no means a negligible contribution to the thunder which follows the discharge*. Dessler (1973), using this idea, explained how an electrostatic field produces an atmospheric pressure expansion inside the charged region of the cloud which is canceled when a lightning discharge occurs. He modeled the charged thundercloud as a horizontal disk. Dessler gave a formula linking the pressure wave amplitude ΔP to the neutralized thundercloud charge ΔQ and the horizontal size of the slab, r:

$$\Delta P = \frac{\Delta Q^2}{8 \times \pi^2 \times \varepsilon_0 \times r^4}, \tag{30.3}$$

and the dominant frequency, f, to the thickness of the charge slab, d, and the sound speed, c: $f = c/d$. With these formula and typical charged thundercloud values, we find that the pressure wave amplitude is from 0.05 to 5 Pa. ΔP is quite sensitive to changes in r. The dominant frequency is from 0.2 to 2 Hz, inside the infrasound frequency range.

Few (1985) improved Dessler's model, adding a preliminary heating, to explain why overpressure is measured at first (Balachandran 1979). Differently, Pasko (2009) shows that the growth of charge density in the thundercloud before the lightning discharge is able to create a pressure reduction in the thundercloud, which produces this first compression wave when the return stroke occurs.

A horizontal disk-shaped model of the charge slab leads to a radiation strongly oriented in the vertical direction Dessler (1973). The only location where it is possible to measure such infrasound is then just below the thundercloud. Moreover, in these models, the acoustic source is then located only in the cloud and not, for instance, in the lightning channel.

30.3 Acoustic Detection of Lightning Flashes

With the simultaneous development of the LLS and the new infrasound stations since about 25 years, comparative studies have been carried out. An infrasound station is here defined as a set of several sensors (greater or equal to 4), whose measurements are cross-correlated to detect any coherent signal and to associate to these detected waves some characteristics such as their azimuth, their trace velocity or their amplitude.

30.3.1 Azimuth Versus Time Correlation

Assink et al. (2008) studied infrasound measurements in the Netherlands when thunderstorms occurred within 50 km of two microbarometer stations. The recorded waveforms looked like a series of several explosive pulses. The azimuth of the coherent signals (events) is very similar to one of the lightning flashes taking into account the time of propagation.

Farges and Blanc (2010) measured two thunderstorms in 2005 with one station composed of four microbarometers organized in a 1 km side triangle with one sensor at its barycenter. Figure 30.8 shows the results for the September 5, 2005 thunderstorm from 18 to 24 UT. The thunderstorm arrived from Southwest at 19 UT; it was 300 km away. It moved towards the station and arrived just over it at 23:30 UT.

Different events occurred during this thunderstorm. The numbered boxes in the Fig. 30.8 correspond to the enumerated list below.

1. Acoustic detections are associated with signals coming from the Atlantic (Box 1 in Fig. 30.8c). These detections are in azimuths 270°–315°, which corresponds to west to northwest directions.
2. Between 19:30 and 20:30 UT, the storm is far from the station (between 150 and 250 km, Fig. 30.8b), in the azimuth range 210°–260° (Fig. 30.8c) by comparison to the acoustic station). Acoustic detections are associated with infrasound of thunder: the colored dots and black dots are superimposed in Box 2 graph (Fig. 30.8c).
3. Between 20:45 and 22:00 UT, the storm is between 100 and 200 km away from the acoustic station. A shadow zone is present and no infrasound detection is associated with lightning detections. Indeed in Box 3 (Fig. 30.8c), no black dot can be associated to any colored dots.
4. The storm moves closer to the station (between 22 and 23 UT), it is within 100 km, now out of the shadow zone. Infrasound detections are again associated with lightning detections (Box 4 in Fig. 30.8c).
5. The wind increases sharply (Box 5 in Fig. 30.8a) at 23:20 UT and the acoustic detectability stops (Box 5 in Fig. 30.8c). There is no infrasound detection associated with electromagnetic lightning detections even though CGs are close to the station (within 25 km).
6. The wind drops and infrasound again become detectable (Boxes 6 in Fig. 30.8a, c).

Using a network of 4 microphones (frequency range 1–40 Hz) organized in a 50 m side triangle located in south of France (so- called MPA, or MicroPhones Array), near the airfield of Uzès (Gard), Gallin et al. (2016) showed it is possible to follow similarly a thunderstorm over a 70 km range. Figure 30.9 shows several synthetic views of electromagnetic detections (from an LMA and from the EUCLID network) superimposed to acoustic detections for different time windows of 10 min duration during the storm. The active cells passed above MPA, moving from southwest toward northeast.

A cell was present in the northeast azimuth from MPA, at about 25 km in horizontal distance (Fig. 30.9a): acoustic detections are correctly associated to it. Then, this cell moved away in the same direction (Fig. 30.9b, c) but it was not detected acoustically anymore. In Fig. 30.9c, the effect of masking by acoustic sources very close from MPA explains this fact. However, this interpretation does not hold for the case presented in Fig. 30.9b. On the contrary, a distant cell (between 50 and 75 km from MPA, Fig. 30.9d), which appeared in the southeast of MPA at the end of the storm (around 21:30 UTC), was clearly acoustically detected (Fig. 30.9d). With such a small array, it is also possible to calculate the elevation angle of the sound wave when the thunderstorm is within 25 km. This last property is used in Sect. 30.4 to rebuild in 3D the geometry of the sound sources.

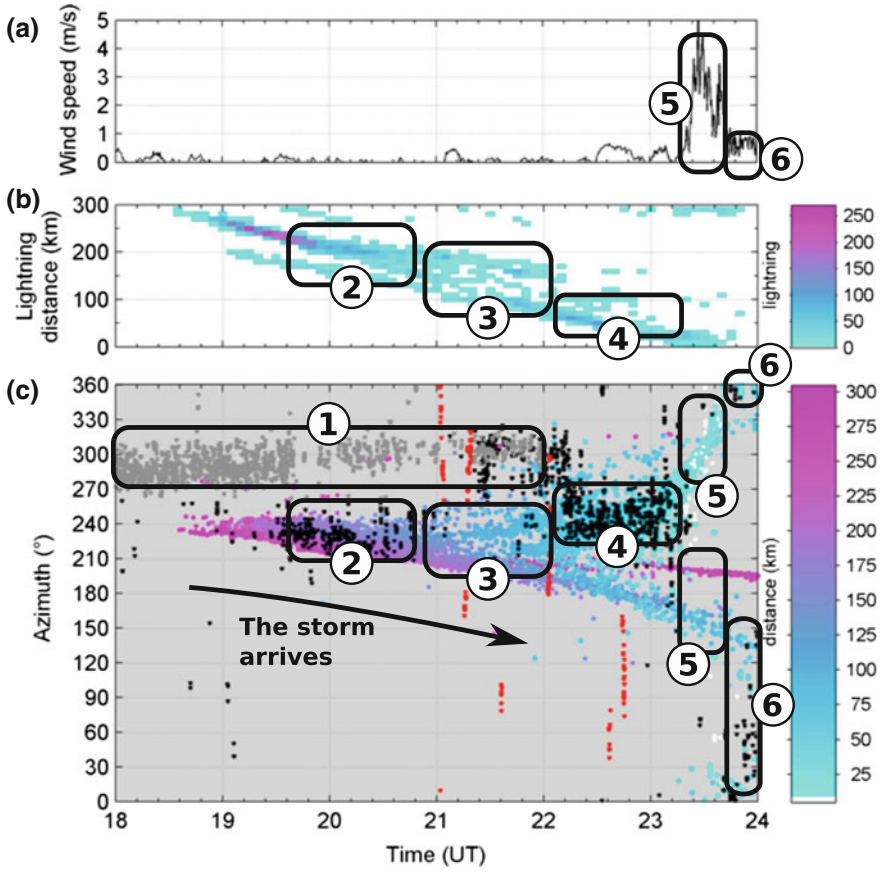

Fig. 30.8 Thunderstorm of September 5, 2005 in the southwest of France. **a** Wind speed measured at the station at 2 m height. **b** lightning distance from the station. The color codes the number of lightning per 5 min and intervals of 10 km. **c** comparison of lightning azimuth (colored dots, where the color indicates the lightning distance) with infrasound azimuths: gray (microbarom), black (lightning), and red (long duration events) dots. Adapted from Farges and Blanc (2010)

30.3.2 Amplitude Variation

Farges and Blanc (2010) correlated on a one-to-one basis 88 acoustic detections with CGs. An inverse of the distance curve fits relatively well with data. Events are sorted out in three peak current ranges. They infer that there is no clear link between CG peak current and infrasound amplitude, especially for discharges close to the station (within 10 km).

After one-to-one correlation, Assink et al. (2008) also associated 84 infrasound events to a CG. After normalizing the infrasound amplitude to the CG strength (taking into account the CG peak current and its duration), they show that this normalized

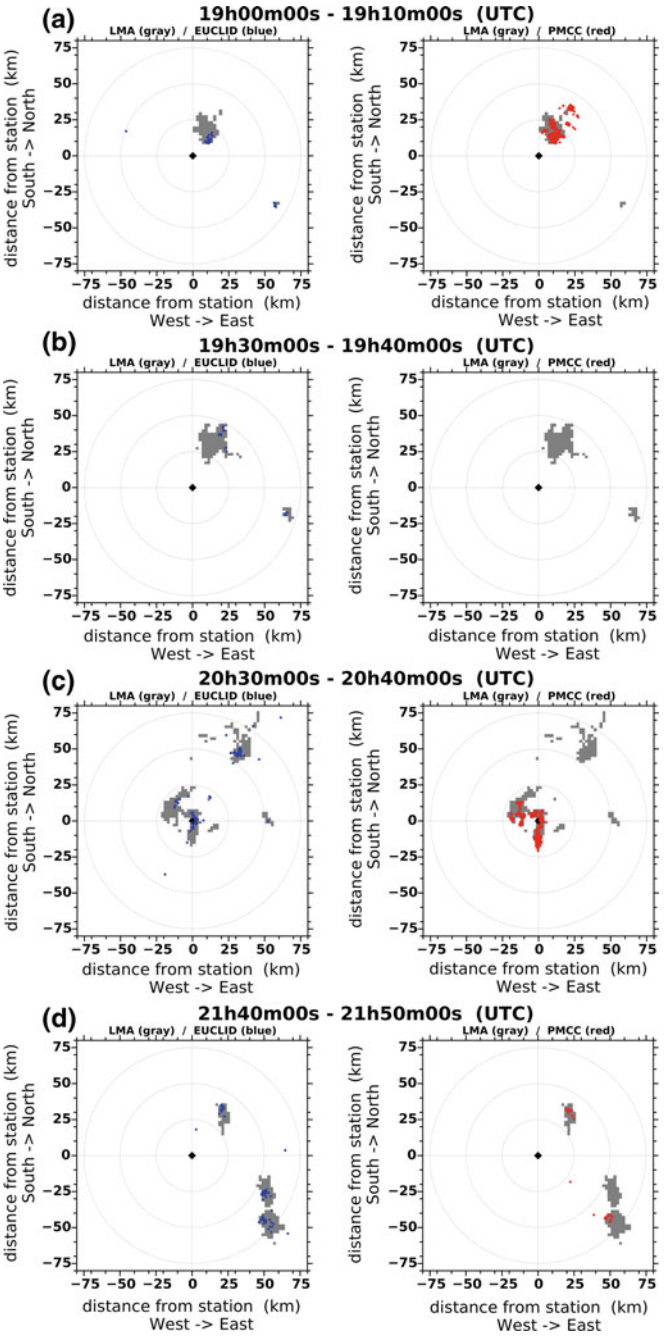

Fig. 30.9 Six windows of 10 min duration during the thunderstorm from 18 to 22 UTC, on October 26, 2012: map of the LMA detections (gray dots) superimposed to EUCLID observations (blue dots, left subplots) and to the reconstructed acoustic detections (red dots, right subplots). From Gallin et al. (2016)

sound energy varies with distance in a similar way as the sound signal resulting from a vertical 4 km long line source in tropospheric conditions.

More recently, Farges et al. (2016) showed, using 10 years of data recorded in Ivory Coast, that the infrasound amplitude due to thunder varies with a distance to power relation of −2/3 within 70 km.

These results show that the amplitude variation with the distance, and the relation between the acoustic amplitude and some lightning characteristics (such as the peak current, the duration, or the neutralized charge) are not yet fully understood and need further studies.

30.3.3 Contribution of Lightning Flashes to the Local Ambient Noise

Farges and Blanc (2010) calculated the contribution of a thunderstorm to the local ambient noise in the frequency range 0.01–10 Hz. When the thunderstorm approaches the station, the background level increases and reaches its maximum when the storm is just above the station. It is mainly the sum of signals from multiple distant lightning flashes. This background level masks the acoustic signal produced by a single lightning flash and makes it hardly detectable (as shown in Fig. 30.9d). Nevertheless, in a short time window (a few minutes), the flash which is the closest to the infrasound station, can be detected. The other flashes, which occurred far away, only increase the background noise. Hence, infrasound station measurements cannot be used to quantitatively evaluate the flash density during a thunderstorm.

30.4 3D Acoustical Reconstruction of Lightning Flashes

30.4.1 Methodology and Assumptions

Using the already described MPA, Gallin et al. (2016) could reconstruct several individual acoustical flashes during the same thunderstorm of October 26, 2012 (Fig. 30.9). They compared them to electromagnetic reconstruction using a LMA deployed in Europe, over a square of 100 km side length, in the frame of the HyMeX 2012 campaign Defer et al. (2015). It was a network of 12 antennas operating in the very-high-frequency range (60–66 MHz) able to localize sources with an error of 30 m vertically, and 10 m horizontally Defer et al. (2015). The October 26th storm was chosen precisely because the lightning rate was not too high. Acoustic signals are typically 1 min long, due to the considerable spatial extension of one flash, approximately 20 km horizontally and 5–8 km vertically. The farthest sources contribute to the tail of the signal.

The detection time of the first electromagnetic event is chosen as the time origin of the flash, flash duration being negligible compared to acoustic propagation times. The processing of trace velocity allows to reconstruct the elevation angle knowing

the local temperature and, therefore, the speed of sound. Assuming a rectilinear propagation as if the atmosphere was homogeneous, it is then possible to localize in 3D the position of each coherent sound source detected in the signal. Detection of coherent signals was achieved by means of the automatic Progressive Multichannel Cross-Correlation (PMCC) algorithm (Cansi 1995; Cansi and Le Pichon 2009; Brachet et al. 2010) analyzing coherency over sliding time windows and by frequency bands. This analysis gives the azimuth angle and the trace velocity for each coherent wave propagating over the acoustic array.

The assumption of rectilinear propagation is questionable and has been compared with curvilinear propagation using ray tracing based on meteorological data (temperature, pressure, wind) provided by Météo France through AROME-WMED, a local weather forecast model for West Mediterranean region (horizontal resolution: 2.5 km, temporal resolution: 1 h) (Fourrié et al. 2015). Comparison between reconstructions based on either ray tracing or rectilinear propagation shows no benefit due to many artifacts associated to ray tracing, especially a large proportion of distant sound sources (in the range 10–30 km) erroneously located very near the ground. This is explained by the existence of a small acoustic waveguide below 2 km altitude for which approximations of ray tracing are not satisfying in the considered frequency range Gallin et al. (2014). Moreover, many small size spatial and temporal wind structures occurring during a thunderstorm Thobois and Soderholm (2015) cannot be resolved by AROME-WMED but could be expected to strongly influence sound propagation.

30.4.2 Reconstruction of Individual Flashes

Reconstruction of the individual flash that occurred at 20:35:00 UT (Fig. 30.5) is presented in Figs. 30.10 and 30.11. Figure 30.10 shows the recorded time signal at the central microphone and the corresponding reconstructed altitudes of the acoustic sources compared to the similar LMA electromagnetic reconstructions. Obviously the first, most intense part of the signal (first 10 s, up to 15 Pa), comes from near above the ground and increases in altitude up to about 5 km. The second part of the signal is of much lower amplitude but is nevertheless detectable and coherent. Source altitude is more or less constant around 4–5 km. In both cases, altitude reconstruction is in good agreement with EM detections. Figure 30.11 displays the 3D reconstruction. The first part of the acoustic signal is clearly associated to the CG return stroke, whose tilted path is well reconstructed from a low altitude of 500 m up to 5 km into the cloud. The acoustic ground localization of this return stroke is in excellent agreement with the EUCLID one, at about 2 km from the acoustic station. Note that LMA does not reconstruct the return stroke below 2 km. Also noticeable is the large infrasound content of the return stroke signal that has a relatively uniform energy distribution over the considered 1–40 Hz frequency range (Gallin et al. 2016). The horizontal intra-cloud layer at about 2 km altitude could not be acoustically reconstructed, as it has been masked by the more intense acoustic signal emanating from

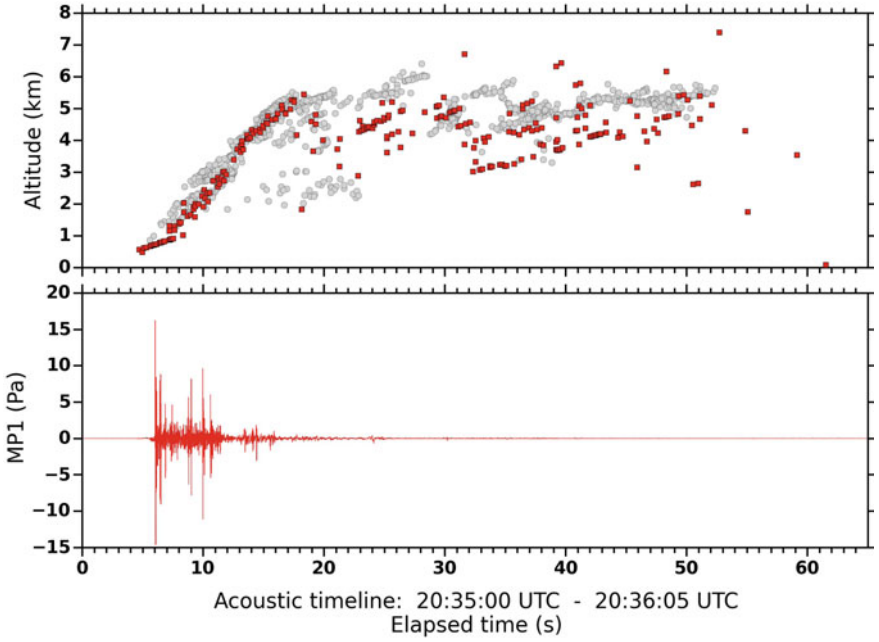

Fig. 30.10 Acoustic reconstruction of the flash occurred on October 26, 2012 at 20:35:00 UT. Gray dots: LMA detections, red squares: reconstructed acoustic detections. (top) Altitude of LMA and MPA detections versus time. (bottom) Corresponding thunder pressure signature recorded by central microphone versus time. Adapted from Gallin et al. (2016)

the return stroke and arriving at the same time. On the contrary, the horizontal layer at about 4–5 km is well localized by the acoustic method provided it is sufficient distant so as not to be masked by the return stroke signal. In particular, the part extending southward over a distance up to 20 km includes a large number of acoustically detected sources.

Figures 30.12 and 30.13 show the analysis of a second flash, occurring just after the previous one at 20:35:58 UT (Fig. 30.6). According to LMA analysis, it is a regular bilevel normal polarity IC flash with two vertical channels. These ones are acoustically well reconstructed with a large number of points, Fig. 30.13. The two horizontal layers have also been detected, but with less points. The microphone array cannot detect sound sources in both levels at the same time, so that acoustic detections alternate between the upper and lower flash layers, see Fig. 30.12, around respectively 8 km and 4 km. Quite distant coherent sources are detected despite the very low recorded pressure level at the end of the time signal. The burst in the signal from 10 to 12 s corresponds to the positive IC observed by EUCLID. It is acoustically one order of magnitude less intense than the return stroke signal of the previous flash. Its frequency spectrum has a peak in the infrasound range below 10 Hz.

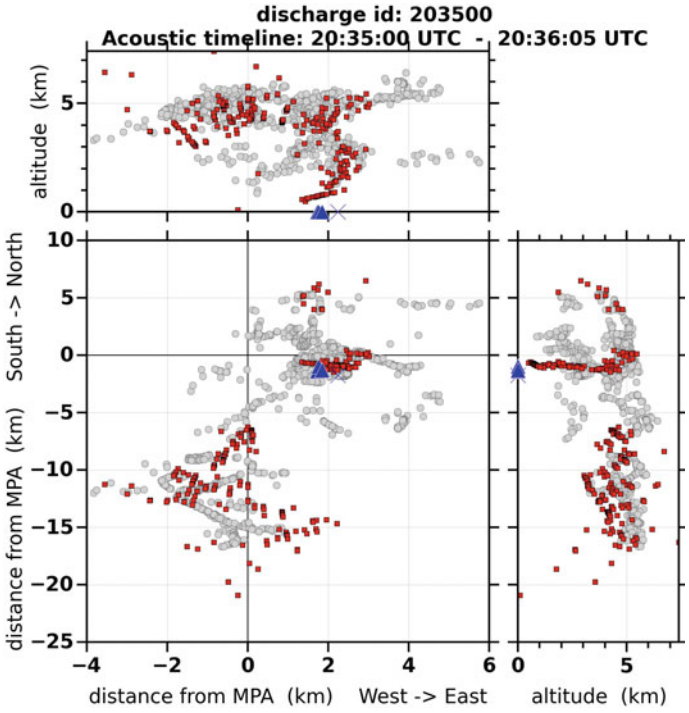

Fig. 30.11 Acoustic reconstruction of the flash occurred on October 26th 2012 at 20:35:00 UT. Gray dots: LMA detections, red squares: reconstructed acoustic detections, and blue symbols: EUCLID strokes from raw detections. (top) Locations of LMA detections, EUCLID observations, and reconstructed MPA detections in longitude–altitude plane. (bottom left) In longitude–latitude plane (MPA is at the origin). (bottom right) In altitude–latitude plane. Adapted from Gallin et al. (2016)

30.4.3 Lower Parts of CG Flashes

The ability of acoustical source detection at low altitude below 2 km is not specific to the particular flash analyzed previously. Figure 30.14 zooms on the lower part (below 5 km) of the acoustical reconstruction of 2 different flashes (20:35:00 UT and 20:49:00) compared to EUCLID and LMA detections. For the 20:35:00 flash, the acoustic method was clearly able to reconstruct the part of the return stroke below 1 km, unambiguously associated to EUCLID detections, while LMA points at such low altitude are scarce and diffuse. For the 20:49:00 flash, acoustic detections are separated in two groups, each one associated to one EUCLID negative CG. Figure 30.15 presents a global statistic for the altitudes below 2 km, for 50 reconstructed lightning flashes presenting at least one ground connection. The ratio of detection between LMA and acoustics is about 3.5. The detection capabilities of the LMA decrease exponentially near the ground with less than 2% detections below

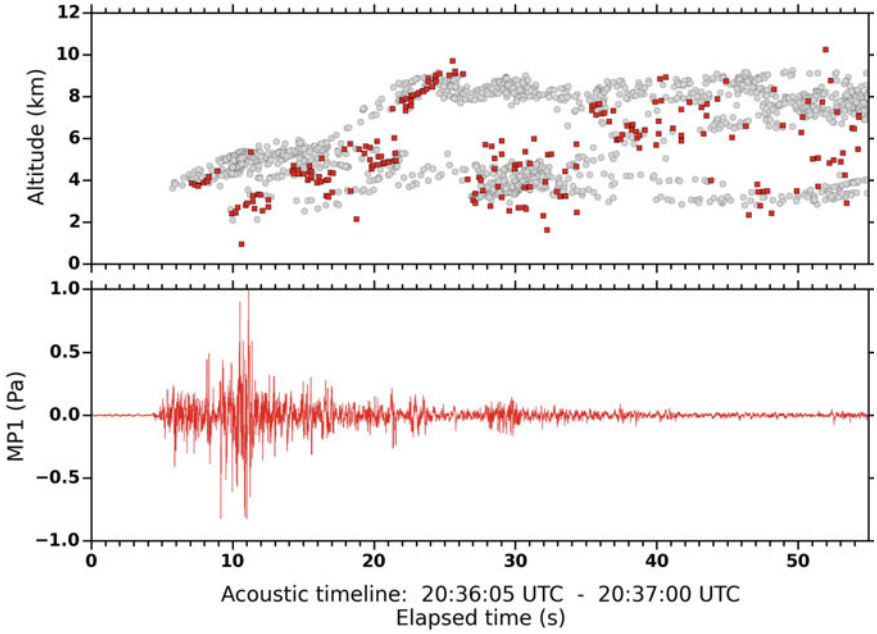

Fig. 30.12 Acoustic reconstruction of the flash occurred on October 26, 2012 at 20:35:58 UT. Same legend as in Fig. 30.10. Adapted from Gallin et al. (2016)

1 km height, while acoustic detection capability decreases approximately linearly near the ground. This outlines the efficiency of the acoustic method to reconstruct lower parts of nearby CGs.

30.4.4 Acoustics Versus Electromagnetism: Statistical Comparisons

During the 26th October storm, 56 flashes were acoustically recorded, 50 of them associated to an EUCLID observation with ground connection (CGs). These 56 flashes lead to a total of 69,606 LMA reconstructions and 10,243 acoustic reconstructions. These numbers are sufficiently large to allow for a significant statistical analysis now detailed. Let us recall that additional distant flashes could be detected by LMA but not by MPA. Figure 30.16 compares the histograms of azimuth (top line) and horizontal distance (bottom line) resulting from LMA (left column) and MPA (right column) reconstructions of the 56 acoustically detected flashes. The shape of LMA and MPA azimuth distributions are very similar, with approximately equal populations for the populations of bins. All the azimuths were scanned by the flashes. They are correctly calculated by PMCC using the MPA signals. This outlines the fact that the efficiency of the acoustic method was uniformly distributed over the direc-

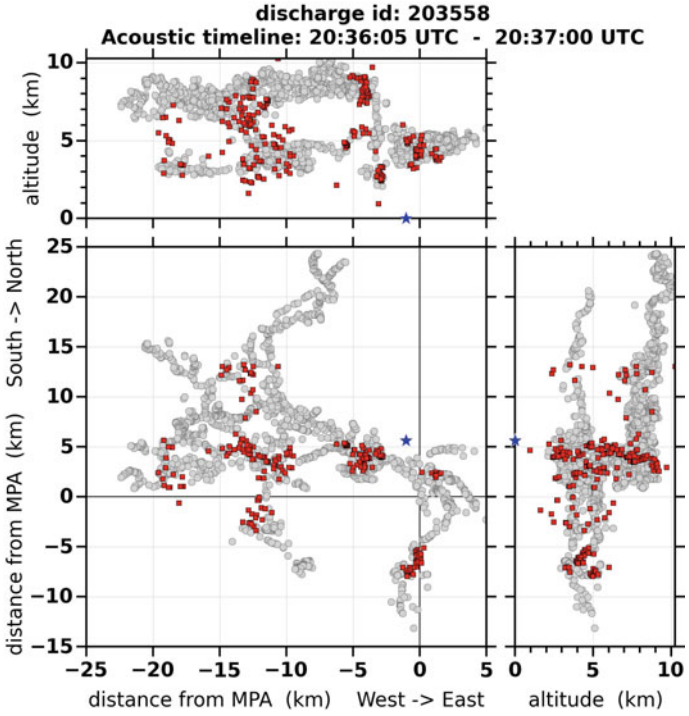

Fig. 30.13 Acoustic reconstruction of the flash occurred on October 26, 2012 at 20:35:58 UTC. Same legend as in Fig. 30.11. Adapted from Gallin et al. (2016)

tions and in particular, is not too sensitive to wind shear. Nevertheless, the slightly more increased MPA distribution around azimuth 270° comes from the fact there was no distant electrical activity at more than 25 km from the MPA in the westward direction as can be seen on Fig. 30.9. This tends to increase the relative weight of this direction in the MPA distribution as acoustical detection is more efficient near field than far field. For the same reason, MPA detections in the southeast azimuth around 135° are underestimated because activity in this direction was quite remote. This difference in efficiency range is outlined by the second row, where one can see that 97% of the acoustical detections are distant from less than 25 km from the MPA. A few flashes, less than 1% could be detected in the range 60–80 km, most of them in the southeastern direction between 21:40 and 21:50 (Fig. 30.9). This indicates that distant acoustic detections at more than 25 km (for the present MPA) are likely to be very sensitive to local and instantaneous meteorological conditions. Though relatively infrequent, remote detections are nevertheless possible in case of favorable meteorological conditions like formation of waveguides near the ground. This has already been outlined by Farges and Blanc (2010). However such detections may be erroneously associated to other sources than lightning flashes. Within the CTBT context, a clear understanding of the influence of local meteorological conditions on

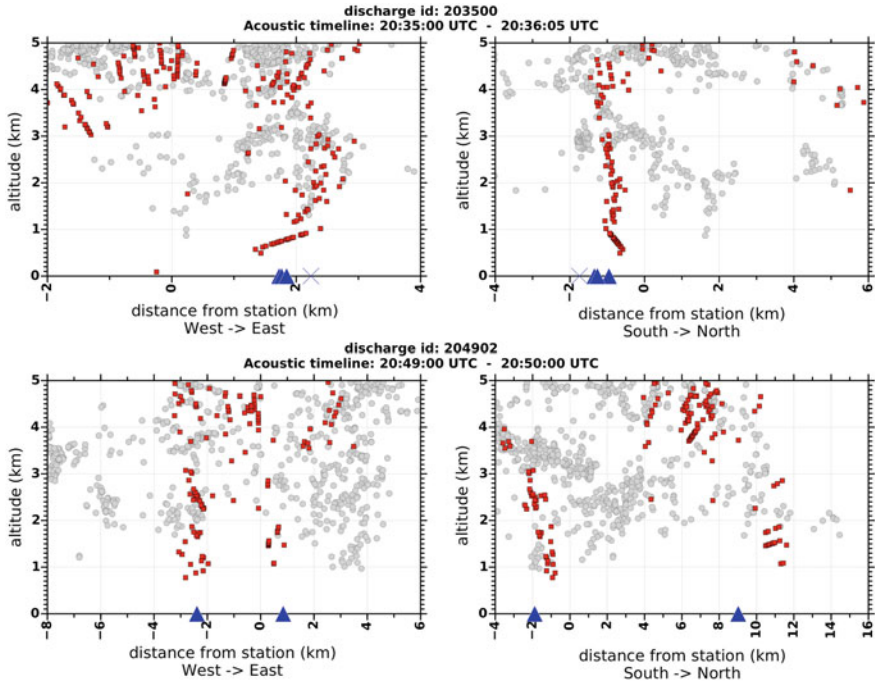

Fig. 30.14 Comparison of the detection capabilities of the LMA (gray points) and the reconstructed acoustic sources (red squares) for lower altitudes (under 5 km height). The blue symbols are the EUCLID observations. CGs which occurred at 20:35:00 UT (top) and 20:49:02 UT (bottom). The MPA is at the origin. Left column: projections in the west to east direction. Right column: projections in the south to north direction. Adapted from Gallin et al. (2016)

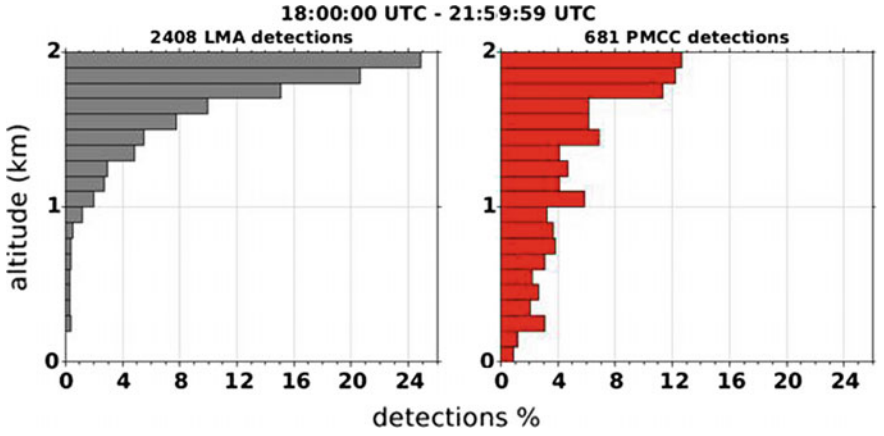

Fig. 30.15 Among the 56 flashes which were detected both by the LMA and the acoustic network, 50 of them present at least one EUCLID observation with connection to the ground. (left) Distribution between 0 and 2 km in altitude of the LMA detections associated to these 50 CGs. (right) Altitudes of the reconstructed acoustic detections for these same 50 CGs. From Gallin et al. (2016)

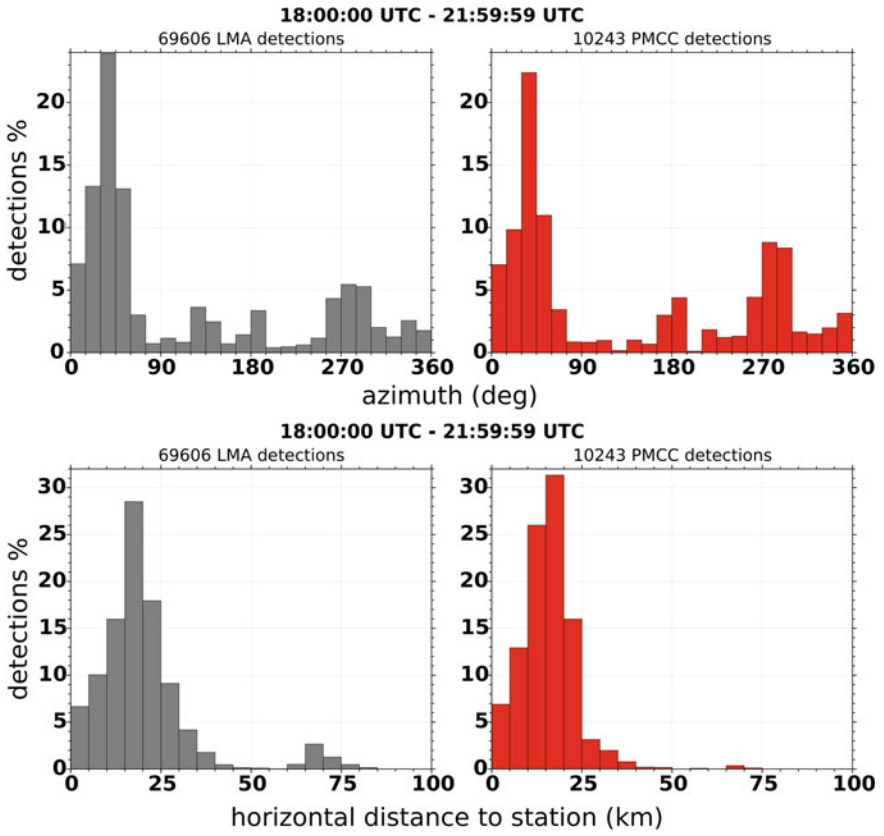

Fig. 30.16 Global statistics for the 56 flashes which were detected by the acoustic method from 18 to 22 UT, on October 26th 2012. (Top) Distribution of azimuths around the MPA (Bottom) Distribution of horizontal distances from the MPA. LMA (gray, left) and MPA (red, right) detections. Adapted from Gallin et al. (2016)

infrasonic remote detections of lightning flashes, and an efficient way of identifying signals from lightning flashes, therefore turns out to be of main interest and would deserve further investigations.

This trend is consolidated by compared histograms of LMA versus MPA altitude reconstruction shown on Fig. 30.17. They are presented by distance ranges from MPA: 0–10 km (top line), 10–20 km (middle line) and 20–30 km (bottom line). The corresponding number of EM or acoustic reconstructions is indicated for each case over the graph. In the nearby range 0–10 km, the two histograms, though not strictly identical, present very similar shapes. In particular, for both methods, the two layers of discharges peaking around 4 km and 9 km respectively, are perfectly identified. To be noticed is however that many more detections are achieved in the lower layer than in the upper one. No sources above 11 km are detected. The main difference

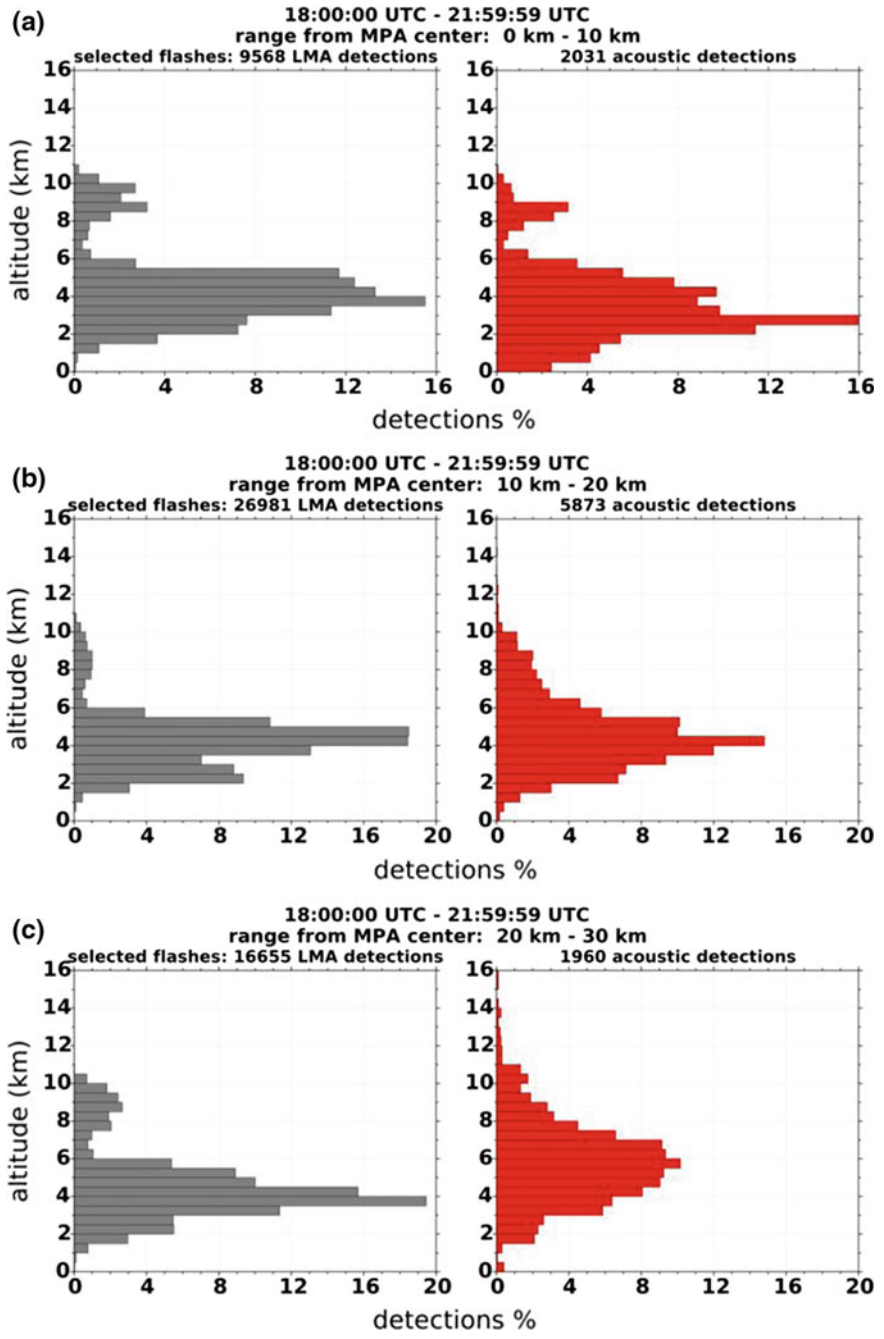

Fig. 30.17 Global statistics from 18 to 22 UT, on October 26th 2012. Altitude of detections for different ranges of horizontal distance from MPA center. Gray/left: LMA detections for the 56 selected flashes. Red/right: corresponding reconstructed acoustic detections. **a** Range 0–10 km. **b** Range 10–20 km. **c** Range 20–30 km. From Gallin et al. (2016)

emanates from the lowest altitudes, for which MPA is comparatively more efficient, especially for return stroke detection near the ground.

Beyond 10 km, the two layers are still present, as observable from LMA detections. However, acoustical altitude reconstruction looses its precision, the distribution gets blurred and more widespread, so that the top layer peak is masked. Nevertheless, the first layer peak is still clearly observable at the correct altitude (4–5 km) in the 10–20 km range. For the largest considered range 20–30 km, the performances of altitude reconstruction by means of acoustics degrade, with a general trend of overestimating altitudes, with a peak located at 6 km instead of 4 km and some sources localized above 11 km.

30.5 Conclusions

The use of infrasound and low-frequency sound for detecting, localizing and reconstructing lightning flashes has been reviewed and analyzed. Especially, very recent results from a 2-month observation campaign carried out in Southern France in fall 2012 provide a statistical overview by systematic comparison between electromagnetic and acoustic detections. These ones emanate from a relatively small size (50 m) triangular array of 4 microphones in the frequency range 1–40 Hz. Data have been only partially exploited, only a single day of moderate storm activity (October 26, 2012) was extensively analyzed. Nevertheless, the number of events is sufficiently large for statistical significance. Thunder detection can be performed up to 250 km by larger stations (typically 1 km side triangles) but is very sensitive to wind conditions, detection capabilities falling out in case of shadow zone or intense local wind. For a smaller microphone array, a few detections up to 75 km could be achieved, but the array was most efficient in detecting events at less than 25 km. Within this distance range, azimuthal detection turned out to be quite uniform. Individual flash reconstruction compares very favorably to LMA ones both for CGs and ICs flashes. Vertical parts of the flash, such as return strokes, are especially well reconstructed and can be clearly identified to low-frequency ground EM detections such as EUCLID ones. Horizontal discharge layers can also be satisfactorily reconstructed but can be masked by more intense sources. Altitude reconstruction is more range dependent and compares very well to EM reconstruction up to 10 km, with the two discharge layers being unambiguously identified and localized.

Moreover, acoustics appears to be a privileged way to explore return strokes near the ground, below 2 km, where a LMA looses its efficiency. On the contrary, acoustic altitude reconstruction progressively degrades beyond 10 km. One of the main reasons may be the influence of local meteorological wind conditions. However, a ray tracing approach based on local up-to-date weather predictions turn out insufficient to improve localization. More advanced propagation methods, and more detailed atmospherical data describing very local wind structures in time and space, would probably be necessary to overcome these limitations and would deserve further studies. Another promising approach would be to further investigate the physical

characteristics of the recorded signals, such as its frequency content, number and duration of bursts, or amplitude. Association to nearby reconstruction, and especially to return strokes near the ground, would provide new insights in the sound and infrasound characterization of lightning flashes.

The 3D reconstruction of the acoustic sources shows they are mainly organized around the lightning channel as proposed by the radiation from hot channel model while the electrostatic mechanism only locates the acoustic source inside the thundercloud. Nevertheless, future studies about the source mechanism for infrasound from lightning are still necessary.

Farges et al. (2016) analyzed 10 years of infrasonic measurements in Ivory Coast and compared them with WWLLN measurements. The lightning activity in this part of the world is much more important than in France: it is possible to measure strong thunderstorms near the station every 3 days where only a few are observable in the South of France for 2 or 3 months. The weakness of the Ivory Coast IMS station's noise makes it possible to detect infrasound linked to storm activity up to 500 km from the station. Adding a small microphone network near this station or another in the equatorial area would allow to investigate the three-dimensional structure of lightning discharges that can reach almost 18 km of altitude. Finally, future geostationary weather satellites (GOES-R/GLM and MTG/LI) will allow to monitor storm activity in two major sectors (respectively Americas and Europe/Africa) and will help to study the presence of lightning infrasound signals in the IMS measurements.

Two European space-borne missions dedicated to the study of TLEs and Terrestrial Gamma-ray Flashes are soon to be launched: ASIM, developed by ESA, will be on board the International Space Station (https://directory.eoportal.org/web/eoportal/satellite-missions/i/iss-asim), and TARANIS, which is a microsatellite of CNES (taranis.cnes.fr). Most of TLEs occur in the equatorial and tropical regions but very few observatories are located there. Searching sprite occurrences in infrasound CTBTO IMS stations located in these regions (Ivory Coast station, for instance) is the only way to validate the observation of sprites detected by the dedicated instruments on board these two space missions.

Acknowledgements The SOP1 was funded by grants MISTRALS/HYMEX and ANR-11-BS56-0005 IODA-MED. The authors acknowledge Meteo-France and the HyMeX program for supplying the data, sponsored by grants MISTRALS/HyMeX and ANR-11-BS56-0005 IODA-MED project. Present results have been obtained within the frame of the LETMA (Laboratoire ETudes et Modélisation Acoustique), Contractual Research Laboratory between CEA, CNRS, Ecole Centrale Lyon, C-Innov, and Université Pierre et Marie Curie.

References

Arechiga RO, Johnson JB, Edens HE, Thomas RJ, Rison W (2011) Acoustic localization of triggered lightning. J Geophys Res 116(D09103):1–11

Assink JD, Evers LG, Holleman I, Paulssen H (2008) Characterization of infrasound from lightning. Geophys Res Lett 35(L15802):1–5

Balachandran NK (1979) Infrasonic signals from thunder. J Geophys Res 84:1735–1745
Betz HD, Schumann U, Laroche P (2009) Lightning: principles, instruments and applications. Springer, Netherlands
Brachet N, Brown D, Le Bras R, Cansi Y, Mialle P, Coyne J (2010) Monitoring the Earths atmosphere with the global IMS infrasound network. In: Le Pichon A, Blanc E, Hauchecorne A (eds) Infrasound monitoring for atmospheric studies, pp 77–118. Springer editions
Brode HL (1956) The blast wave in air resulting from a high temperature, high pressure sphere of air. Rand Corp. Res. Mem. RM-1825-AEC
Cansi Y (1995) An automatic seismic event processing for detection and location: the P.M.C.C. method. Geophys Res Lett 22:1021–1024
Cansi Y, Le Pichon A (2009) Infrasound event detection using the progressive multi-channel correlation algorithm. In: Havelock D, Kuwano S, Vorländer M (eds) Handbook of signal processing in acoustics. Springer, New York, pp 1425–1435
Campus P, Christie DR (2010) Worldwide observations of infrasonic waves. In: Le Pichon A, Blanc E, Hauchecorne A (eds) Infrasound monitoring for atmospheric studies, pp 29–75. Springer editions
Cecil DJ, Buechler DE, Blakeslee RJ (2014) Gridded lightning climatology from TRMM-LIS and OTD: dataset description. Atmos Res 135–136:404–414. https://doi.org/10.1016/j.atmosres.2012.06.028
Cummins KL, Murphy MJ (2009) An overview of lightning locating systems: history, techniques, and data uses, with an in-depth look at the U.S. NLDN. IEEE Trans Electromagn Compat 51:499–518
da Silva CL, Pasko VP (2014) Infrasonic acoustic waves generated by fast air heating in sprite cores. Geophys Res Lett 41:17891795. https://doi.org/10.1002/2013GL059164
Defer E, Pinty JP, Coquillat S, Martin J-M, Prieur S, Soula S, Richard E, Rison W, Krehbiel P, Thomas R, Rodeheffer D, Vergeiner C, Malaterre F, Pedeboy S, Schulz W, Farges T, Gallin L-J, Ortéga P, Ribaud J-F, Anderson G, Betz HD, Meneux B, Kotroni V, Lagouvardos K, Roos S, Ducrocq V, Roussot O, Labatut L, Molinié G (2015) An overview of the lightning and atmospheric electricity observations collected in southern France during the HYdrological cycle in Mediterranean EXperiment (HyMeX), Special Observation Period 1. Atmos Meas Tech 8:649–669
de Larquier S, Pasko VP (2010) Mechanism of invertedchirp infrasonic radiation from sprites. Geophys Res Lett 37:L24803. https://doi.org/10.1029/2010GL045304
Depasse P (1994) Lightning acoustic signature. J Geophys Res 99:25933–25940
Dessler AJ (1973) Infrasonic thunder. J Geophys Res 78:1889–1896
Drob D (2019) Meteorology, climatology, and upper atmospheric composition for infrasound propagation modeling. In: Le Pichon A, Blanc E, Hauchecorne A (eds) Infrasound monitoring for atmospheric studies, 2nd edn. Springer, Dordrecht, pp 485–508
Farges T, Blanc E, Le Pichon A, Neubert T, Allin TH (2005) Identification of infrasound produced by sprites during the Sprite, (2003) campaign. Geophys Res Lett 32:L01813. https://doi.org/10.1029/2004GL021212
Farges T, Blanc E (2010) Characteristics of infrasound from lightning and sprites near thunderstorm areas. J Geophys Res 115:A00E31, 1–17, https://doi.org/10.1029/2009JA014700
Farges T, Le Pichon A, Ceranna L, Diawara A (2016) Infrasound from lightning measured in Ivory Coast from 2004 to 2014. Geophys Res Abs 18:EGU2016-4519
Few AA (1969) Power spectrum of thunder. J Geophys Res 74:6926–6934
Few AA (1970) Lightning channel reconstruction from thunder measurements. J Geophys Res 75:7517–7523
Few AA (1985) The production of lightning-associated infrasonic acoustic sources in thunderclouds. J Geophys Res 90:6175–6180
Few AA (1995) Acoustic radiations from lightning. In: Volland H (ed) Handbook of atmospheric electrodynamics, vol 2. CRC Press, pp 1–31

Few AA, Teer TL (1974) The accuracy of acoustic reconstructions of lightning channels. J Geophys Res 79:5007–5011

Fleagle RG (1949) The audibility of thunder. J Acoust Soc Am 21:411–412

Fourrié N, Bresson E, Nuret M, Jany C, Brousseau P, Doerenbecher A, Nuissier O, Sevault E, Kreitz M, Bénichou H, Amodeï M, Pouponneau F (2015) AROME-WMED: a real-time mesoscale model designed for the HyMeX special observation periods. Geosci Model Dev Discuss 8:18011856

Gallin L-J, Rénier M, Gaudard E, Farges T, Marchiano R, Coulouvrat F (2014) One-way approximation for the simulation of weak shock wave propagation in atmospheric flows. J Acoust Soc Am 135:2559–2570. http://dx.doi.org/10.1121/1.4869685

Gallin L-J, Farges T, Marchiano R, Coulouvrat F, Defer E, Rison W, Schulz W, Nuret M (2016) Statistical analysis of storm electrical discharges reconstituted from a lightning mapping system, a lightning location system, and an acoustic array. J Geophys Res 121;3929-3953. https://doi.org/10.1002/2015JD023745

Holmes CR, Brook M, Krehbiel P, McCrory R (1971) On the power spectrum and mechanism of thunder. J Geophys Res 76:2106–2115

Jones DL, Goyer GG, Plooster MN (1968) Shock wave from a lightning discharge. J Geophys Res 73:3121–3127

Le Pichon A, Ceranna L, Pilger C, Mialle P, Brown D, Herry P, Brachet N (2013) The 2013 Russian fireball largest ever detected by CTBTO infrasound sensors. Geophys Res Lett 40:3732–3737. https://doi.org/10.1002/grl.50619

MacGorman DR, Few AA, Teer TL (1981) Layered lightning activity. J Geophys Res 86:9900–9910

Marty J (2019) The IMS infrasound network: current status and technological developments. In: Le Pichon A, Blanc E, Hauchecorne A (eds) Infrasound monitoring for atmospheric studies, 2nd edn. Springer, Dordrecht, pp 3–62

Matoza RS, Landès M, Le Pichon A, Ceranna L, Brown D (2013) Coherent ambient infrasound recorded by the international monitoring system. Geophys Res Lett 40:429-433. https://doi.org/10.1029/2012GL054329

Ogawa T (1995) Lightning currents. In: Volland H (ed) Handbook of atmospheric electrodynamics, vol 1, pp 95–136. CRC Press

Pasko VP (2009) Mechanism of lightning-associated infrasonic pulses from thunderclouds. J Geophys Res 114(D08205):1–10

Pasko VP, Yair Y, Kuo C-L (2012) Lightning related transient luminous events at high altitude in the Earth's atmosphere: phenomenology. Mech Effects Space Sci Rev 168:475516. https://doi.org/10.1007/s11214-011-9813-9

Rakov VA, Uman MA (2003) Lightning: physics and effects. Cambridge University Press

Rison W, Thomas RJ, Krehbiel PR, Hamlin T, Harlin J (1999) A GPS-based three-dimensional lightning mapping system: initial observations in central New Mexico. Geophys Res Lett 26:3573–3576

Thobois L, Soderholm J (2015) Nowcasting severe storms—observing clear air close proximity environment of severe storms. Meteorological Technology International, UKIP Media & Events Ltd., Dorking, U.K., pp 132-135

Thomas RJ, Krehbiel PR, Rison W, Hunyady SJ, Winn WP, Hamlin T, Harlin J (2004) Accuracy of the lightning mapping array. J Geophys Res 109(D14207):1–34

Wilson CTR (1920) Investigation on lightning discharges and on the electric field of thunderstorms. Philos Trans R Soc Ser A 221:73–115

World Meteorological Organization (1956) World distribution of thunderstorm days. Secretariat of the World Meteorological Organization, Publ. 21, TP 6 and Suppl

Chapter 31
Infrasound Monitoring as a Tool to Characterize Impacting Near-Earth Objects (NEOs)

Elizabeth Silber and Peter Brown

Abstract Infrasound, the low-frequency sound lying below the human hearing range, has the capability to propagate over very long distances in the atmosphere due to its low attenuation. Thus, infrasound can serve as a tool for monitoring explosive sources, including extraterrestrial bodies impacting the Earth's atmosphere. This chapter describes the theoretical background on meteor physics and bolide infrasound, as well as applications of infrasound in Near-Earth Objects (NEOs) monitoring and characterization. In addition to presenting a comprehensive list of empirical relations to estimate bolide energy release, this chapter summarizes recent case studies where infrasound served as an instrumental tool in characterizing the source.

31.1 Introduction

The Earth is continuously bombarded by extraterrestrial material, ranging from dust-sized grains (Campbell-Brown and Koschny 2004; Briani et al. 2007) to large impactors 100s of metres in diameter (Ceplecha et al. 1998). Albeit rarely occurring, the latter group, as inferred from geological records, has the potential of ending human civilization as we know it, causing biological mass extinctions (O'Keefe and Ahrens 1982) and climate perturbations (Toon et al. 1997). Aside from terrestrial large-scale impacts, there is a significant danger from the class of objects that produce strong shock waves during their terminal flight stage through the lower atmosphere as demonstrated by the recent Chelyabinsk event. The Chelyabinsk bolide, the largest airburst on the Earth since the great Siberian bolide

E. Silber (✉)
Department of Earth, Environmental and Planetary Sciences, Brown University, Providence, RI, USA
e-mail: esilber@uwo.ca

P. Brown
Department of Physics and Astronomy, University of Western Ontario, London, ON N6A 3K7, Canada

A. Le Pichon et al. (eds.), *Infrasound Monitoring for Atmospheric Studies*,
https://doi.org/10.1007/978-3-319-75140-5_31

in 1908 (Brown et al. 2013; Popova et al. 2013), attests to the reality of the unpredictable nature and destructive power of cosmic impacts. In light of the Chelyabinsk bolide, as well as several other notable global events which will be described further in this chapter (see Sect. 31.6, and Pilger et al. 2019), now, more than ever, there is a need for better constraining the shock production mechanisms, as well as quantifying the potential impact hazard threat from Near-Earth Objects (NEOs).

There is an ongoing campaign to identify and catalogue as many potentially hazardous NEOs as possible, and devise possible mitigation measures. NEOs are any small solar system objects which have perihelion less than 1.3 Astronomical Unit (AU). They are the subset of asteroids and comets which may over long periods be perturbed into Earth-intersecting orbits and become Potentially Hazardous Objects (PHOs). PHOs are objects which have orbits which intersect the Earth's orbit at some point with a minimum distance of 0.05 AU and are larger than ~150 m; these objects are large enough to cause regional damage/devastation and have orbits which could be perturbed to actual cause Earth impact in of order a century or less (Bowell and Muinonen 1994). However, this is a very complicated and lengthy task, hampered by inherent limitations such as the lack of capabilities to efficiently detect very faint objects, and the deficiency in our knowledge of the detailed characteristics (e.g. composition, structural integrity, etc.) of the NEOs, especially when it comes to the population of small objects (Jedicke et al. 2015).

The majority of our present knowledge about physical characteristics of NEOs comes from studying those that enter the Earth's atmosphere. To better understand and characterize impacting NEOs, various technologies are being used, from ground-based (visual, radar, infrasound and seismic) to satellite observations. One of these technologies is infrasound monitoring, a passive, low maintenance and fairly inexpensive technology, which allows for global detection of explosive sources in the atmosphere, and by extension bolides, as well as quantifying and constraining source parameters, such as energy deposition, timing and geolocation. In recent years, infrasound has become an increasingly common technique used in bolide detection and characterization (Ens et al. 2012; Marty 2019).

This chapter is organized as follows: This section (Sect. 31.1) provides a brief primer on meteor and shock physics. The basics of theoretical framework relevant to meteor infrasound are given in Sect. 31.2. Sections 31.3 and 31.4 discuss impact effects of the NEOs and energy estimates from infrasonic observations of NEOs, respectively. Section 31.5 provides an overview of the characteristics of NEOs. Applications of infrasound monitoring are given in Sect. 31.6. Finally, in Sect. 31.7, the future and upcoming early-warning systems being developed for NEO impacts and the future role of the IMS infrasound monitoring system in characterizing these NEO impacts are examined.

31.1.1 Meteor Physics: The Basics

When a meteoroid, which is usually a fragment of a comet or an asteroid, enters the Earth's atmosphere at hypersonic velocities (11.2–72.3 km/s), it sputters, ablates and almost always fragments as a result of frictional heating induced by hypervelocity collisions with the ambient atmosphere. The resulting ionization and luminous phenomena are collectively called a meteor, or colloquially "a shooting star". Depending on the meteoroid's size, velocity, density and composition, some fraction of the mass might survive its passage through the atmosphere, and land on the surface of the Earth as a meteorite (Wetherill and ReVelle 1981). Very bright meteors, exceeding the brightness of Venus (stellar magnitude−4), are typically referred to as fireballs or bolides (Ceplecha et al. 1998), whereas larger, more deeply penetrating meteoroids may be associated with shock waves which ultimately decay into low-frequency acoustic waves (infrasound). Bolides brighter than magnitude−17 are termed superbolides (Ceplecha et al. 1998). Meteors might produce audible phenomena on the ground; these are either instantaneously arriving electrophonic sounds, believed to be associated with electromagnetic emissions at audio frequencies (e.g. Wylie 1932; Keay 1980; Bronshten 1983; Keay and Ceplecha 1994), and/or delayed sound in the form of a sonic boom, similar to that of aircraft moving faster than the local speed of sound and producing a 'sonic' boom (Ceplecha et al. 1998).

As a meteoroid enters the rarefied atmosphere, it begins to heat up due to high-energy collisions with atmospheric molecules. The heating of the meteoroid is a function of the overall size and velocity of the impacting body, and it generally begins in the ionospheric F-region (~150 km). There are some exceptions, such as the very high-speed Leonid meteor shower, whose particles start to heat up and subsequently produce luminosity at altitudes as high as 200 km (Popova et al. 2001).

There are three ablation flow regimes: the free molecular flow, transitional flow regime and continuum flow. The meteoroid is said to be ablating in the free molecular flow regime when the mean free path of atmospheric molecules at a particular height is significantly larger than the radius of the meteoroid (Campbell-Brown and Koschny 2004). Here, the Knudsen number (Kn) (the ratio of the molecular mean free path to the particle radius) is larger than 10 (Popova 2005). The flow regime is termed continuum if the meteoroid radius is much larger than the mean free path of the ambient atmosphere, and the $Kn < 0.01$ (Ceplecha et al. 2000; Popova et al. 2001; Campbell-Brown and Koschny 2004). For intermediate Knudsen numbers, there is a transitional flow regime. Meteoroids capable of producing fireballs (cm-sized and larger) move in the continuum flow regime below 90 km (Popova 2005).

In continuum flow, a hydrodynamic layer forms in the front of the meteoroid and attenuates the rate of ablation (Öpik 1958) by shielding the meteoroid surface from direct impacts with air molecules. The meteoroid type and composition play a significant role in ablation, as more volatile compounds ablate first at higher

altitudes, while Ca, Al and Ti ablate last at lower heights (Vondrak et al. 2008), a process defined as differential ablation. The term ablation here refers to the removal of the material from the meteoroid surface. This usually occurs as evaporation or melting after some critical temperature, generally above 1800 K, has been reached (Marsh et al. 2013). It may also include the removal of material in the form of melted droplets or through solid particle fragmentation. Meteoroid ablation reveals the physical and chemical properties of the ablating meteoroid through observation of its mass deposition, energy release and resulting emission spectrum (Borovička 1993; Trigo-Rodriguez et al. 2003).

The kinetic energy of the incident meteoroid colliding with the atmosphere is several orders of magnitude larger than the energy required to completely vaporize the meteoroid (Zinn et al. 2004). Early studies suggested that the kinetic energy of the meteoroid is partitioned such that only 0.1% goes towards ionization, 1% towards light and the rest towards heating the surrounding atmosphere (Romig 1965). More recently, however, lab measurements and modelling of meteoroid ablation indicate that the percentage of energy distributed in the production of light for fireballs may be somewhat larger (of order a few percents (Ceplecha and ReVelle 2005; Weryk and Brown 2013).

Here, the discussion is limited to single body ablation and discrete, gross fragmentation (Ceplecha et al. 1993). Consider a meteoroid with mass (m), velocity (v), of a spherical shape with projected cross-sectional surface area (S) and having a drag coefficient (Γ) (defined as the fraction of momentum transferred to the meteoroid from the oncoming air molecules). Conceptually, a single spherical body with the projected surface area (S) enters the atmosphere (for the purpose of calculations assumed to be hydrostatic and isothermal) with hypersonic velocity and sweeps through a volume of air in a time increment (dt), transferring kinetic energy from the meteoroid to the atmosphere. Hypersonic velocity refers to the aerodynamic flow where the Mach number, or the ratio between the speed of an object (meteoroid) and the local atmospheric speed of sound, is greater than 5 (Anderson 2006). For a spherical meteoroid with radius r, the parameter $S = \pi r^2$ can be related to the meteoroid mass m = 4/3 $\pi \rho_m r^3$, where ρ_m is the density of the meteoroid. Equating the radii in the aforementioned equations, one can solve for S. Generalizing the solution for any shape, it can be shown that

$$S = A_s \left(\frac{m}{\rho_m} \right)^{2/3} \tag{31.1}$$

where A_s is the dimensionless shape factor for a specific body shape. For the sphere, A_s is 1.209, and for a cube moving face on to the flow it is 1.0, while for a hemisphere it is 1.92 (McKinley 1961). Because of rotation, irregularly shaped bodies will have their shape factor approaching the value of the spherical shape, a commonly used assumption.

The parcel of air swept up by the body as it moves through the atmosphere is a cylinder with volume $Svdt$. The mass of the parcel in terms of the atmospheric density (ρ_a) is $dm_a = \rho_a Svdt$. Substituting for S from Eq. (31.1), it is possible to write the expression for the rate of changing air mass (m_a) encountered by the meteoroid (McKinley 1961) as

$$dm_a = \rho_a \left(\frac{m}{\rho_m}\right)^{2/3} A_s v dt \tag{31.2}$$

Now, this parcel of air with a height specific mass density will transfer momentum as a result of impacts with the meteoroid, resulting in a rate of change of momentum of the meteoroid of

$$\frac{d(mv)}{dt} = v\frac{dm}{dt} + m\frac{dv}{dt} \tag{31.3}$$

In this volume, the air particles will gain momentum per unit time:

$$\Gamma \frac{dm_a}{dt} v = \Gamma A_s \left(\frac{m}{\rho_m}\right)^{\frac{2}{3}} \rho_a v^2 \tag{31.4}$$

The term vdm/dt in Eq. (31.3) is negligible for small meteoroids ($m \gg dm$) and is therefore ignored. Equating the loss of momentum per second of the meteoroid (mdv/dt) with the momentum gained by the air particles leads to the drag equation:

$$\frac{dv}{dt} = -\frac{\Gamma A_s \rho_a v^2}{m^{1/3} \rho_m^{2/3}} \tag{31.5}$$

where the presence of the negative sign indicates deceleration. The rate of mass loss, which is proportional to the kinetic energy of the hypersonic airflow impinging on the meteoroid, can be written in terms of the differential mass equation (McKinley 1961), also known as the mass-loss equation (Ceplecha et al. 1998):

$$\frac{dm}{dt} = -\frac{\Lambda A_s \rho_a v^3 m^{2/3}}{2\xi \rho_m^{2/3}} \tag{31.6}$$

Here, ξ is the heat of ablation of the meteoroid material (or energy required to ablate a unit mass of the meteoroid, with dimensions: L^2, T^{-2}) and Λ is the heat transfer coefficient, which is a measure of efficiency of the collision process in converting kinetic energy into heat (McKinley 1961).

It is possible to relate the visual meteor luminosity, expressed as the absolute visual magnitude M_v, to the luminous power I (in watts), which is a portion of the total radiation in the visual bandpass (400–700 nm) having a peak sensitivity at about 560 nm. The absolute visual magnitude of a meteor is defined as the

magnitude it would have if the meteor was placed in the zenith at a height of 100 km (McKinley 1961). The expression for M_v has been given by Öpik (1958) as

$$M_v = 6.8 - 2.5 log_{10} I \tag{31.7}$$

This relation was derived from early theoretical considerations and suggests that a zero magnitude meteor radiates visible light at a rate of 525 W (Öpik 1958). This luminous power depends on the spectral energy distribution of the meteor, which is dominated by line emission at smaller sizes (e.g. Ceplecha et al. 1998). For meteoroids which have a sufficient size and velocity to produce luminous phenomena, it is assumed that the light production in a specific bandpass (e.g. panchromatic passband, appropriate to photographic film on which the earliest meteor measurements were made) is proportional to the rate of change of the particle's kinetic energy, and correspondingly proportional to the meteoroid mass-loss rate.The expression of luminous power is given as

$$I = -\tau_I \frac{dE_k}{dt} = -\tau_I \left(\frac{v^2}{2} \frac{dm}{dt} + mv \frac{dv}{dt} \right) \tag{31.8}$$

where the term I can be more precisely defined as the power radiated in the specific instrument passband. The symbol τ_I represents the dimensionless luminous efficiency factor (Öpik 1958; Weryk and Brown 2013) which may or may not have a velocity dependence, and E_k is the kinetic energy of the meteoroid. The term $mv(dv/dt)$ is generally ignored for meteoroids with velocities exceeding 16 km/s as deceleration is negligible at higher speeds (Ceplecha et al. 1998). Under the assumption that meteor light production is related to the mass loss, the initial mass of the meteoroid can be estimated from the observed luminosity by integrating Eq. (31.8) over the length of the entire light curve. Mass estimated in this way is termed photometric mass. The lowermost size limit of the meteoroids capable of producing a sufficiently strong shock wave and subsequently an infrasonic signature at the ground is not well constrained, but is approximately in the cm-size range.

31.1.2 Infrasound: A Brief Primer and Application to Bolides

Sound audible to humans lies within the frequency range between approximately 20 and 20 kHz. The frequencies lower than about 20 Hz are called infrasound. The speed of sound (c) in the atmosphere is given by

$$c = \sqrt{\gamma RT} \tag{31.9}$$

where γ is the ratio of the specific heat of air at constant pressure to that at constant volume, R is the specific gas constant and T is the temperature. The speed of sound in air at 20 °C and 1 atmosphere is 343 m/s. This was first correctly determined in the 1630s by the French mathematician and philosopher Marin Mersenne (Mersenne 1636; Krehl 2009). The limiting frequency for infrasound on the lower end of the spectrum is the Brunt–Väisälä frequency (~0.003 Hz in the lower atmosphere), or natural oscillation frequency of the atmosphere. As the frequency decreases, the wavelength becomes progressively longer, until it reaches the point where the gravitational restoring force becomes significant.

The thermal structure of the atmosphere, driven by the absorption of the incoming and re-radiated solar energy, plays a major role in long-range acoustic propagation. The temperature profile of the atmosphere is not 'stationary', but a complex function of solar radiation and how that radiation is absorbed by various molecular species in the atmosphere. In the troposphere, the temperature decreases with altitude until a local minimum is reached at the tropopause, the boundary layer located approximately 7–10 km in altitude depending on season and latitude (Beer 1974). The temperature increases up to the stratopause, where it starts to decrease again to a minimum at the mesopause (80–85 km). In the thermosphere, temperature increases up to the altitude of 200 km and then remains constant since the thermal conductivity of the gas is sufficiently high to absorb energy and rapidly transport it downwards (Willmore 1970; Beer 1974).

In considering acoustic propagation in the atmosphere, the speed of sound may be significantly affected by winds, especially if the channel propagation extends to the upper regions of the atmosphere, which is typical for infrasound. Therefore, the effective speed of sound (c_{eff}) is given by sum of the adiabatic sound speed and the dot product between the ray normal $(\hat{n})$ and the wind vector $(\vec{u})$: $c_{eff} = c + \hat{n} \cdot \vec{u} \Rightarrow \sqrt{\gamma RT} + \hat{n} \cdot \vec{u}$.

Daily and seasonal variations in the atmospheric temperature and wind will modify the effective speed of sound (Donn and Rind 1971; Rind and Donn 1975). Atmospheric waveguides (or ducts) are formed by temperature and wind variations in different atmospheric layers (Tolstoy 1973; Georges and Beasley 1977; Drob et al. 2003; Kulichkov 2010). Consequently, infrasonic rays emanating from a source may become trapped in several atmospheric waveguides (ducts), which can lead to two or more infrasonic phases being recorded at the receiver. 'Zones of silence' or 'shadow zones' are the regions where geometrical ray theory predicts that no infrasound energy should reach the receiver. A number of studies, both historical (e.g. Evers and Haak 2010) and recent, confirm that infrasound signals (sometimes called anomalous signals) can still be recorded in these zones as a result of scattering and diffraction effects not taken into account in geometrical ray theory (McKisic 1997; Golden et al. 2007; Herrin et al. 2007; Green et al. 2011).

As infrasonic waves propagate outward from the source, they also undergo attenuation. Attenuation of sound in the atmosphere occurs due to spreading and

absorption losses (Evans et al. 1972). Spreading losses can be uniform (e.g. spherical spreading and inverse square law) and non-uniform (reflection by finite boundaries, refraction, diffraction or scattering) (Evans et al. 1972). Atmospheric absorption occurs due to molecular relaxation (vibration and rotation) and classical (molecular diffusion, heat conduction and internal friction) effects (Evans et al. 1972; Sutherland and Bass 2004). These effects combined are a function of the square of the wave frequency (f), such that attenuation is proportional to f^2 (Bass 1972). Therefore, infrasonic waves, particularly those with f<1 Hz, are capable of propagating over very long distances with negligible attenuation, making them an excellent tool for studying distant explosive sources in the atmosphere.

There are many sources of infrasound (Fig. 31.1), both natural and anthropogenic. Among natural sources of infrasound are meteors. However, meteor infrasound can fall within typical signal periods associated with other sources, such as microbaroms, volcanoes or severe weather, impeding the identification process.

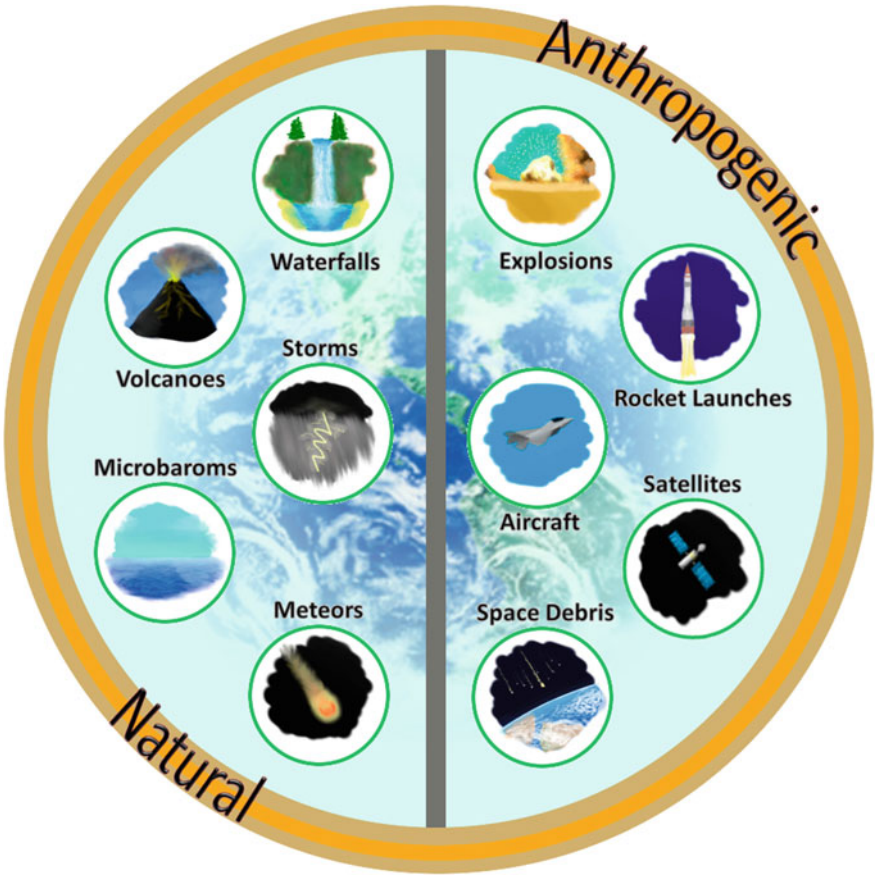

Fig. 31.1 Sources of infrasound

Interpreting infrasound source characteristics may be further complicated by the complex dynamics of the atmosphere which modifies infrasound signals sometimes producing irreversible modifications to the signal as it travels between the source and the receiver. Often, as a consequence, it is not possible to determine the nature of the source without ground truth information or further observational data from other techniques. Dynamic changes of the atmosphere, which occur on a scale shorter than the infrasound wave propagation time, need to be adequately quantified in order to extract information about the source (e.g. de Groot-Hedlin 2010; Norris et al. 2010).

The first documented infrasound recording from an extraterrestrial body was not captured until the early twentieth century. In the morning hours of June 30, 1908, an extraterrestrial body entered the Earth's atmosphere and exploded approximately 5–10 km above the ground (Chyba et al. 1993) near the Podkamennaya Tunguska River (now Krasnoyarsk Krai) in Siberia, Russia, generating an intense blast wave which flattened much of the surrounding forest (Whipple 1930; Krinov 1966). It is estimated that this event released between 10 MT (Hunt et al. 1960) and 20 MT (Chyba et al. 1993) of energy (high explosive equivalent; 1 MT = 4.185×10^{15} J). However, the origin, size and composition of the impactor (Chyba et al. 1993), remains unclear. The blast wave generated by this event was so intense that it generated low-frequency acoustic waves recorded by microbarographs around the world. Coincidentally, the microbarograph was invented only 5 years earlier, in 1903, by Shaw and Dines (1905). The recordings of the Tunguska event presented in Whipple (1930) represent some of the earliest published microbarograph records.

After the Tunguska explosion and until the onset of the Cold War, infrasound received very little attention. After World War II, infrasound became a key technology for source identification and geolocation from explosive sources in the atmosphere, particularly nuclear explosions. The United States Air Force Technical Applications Centre (AFTAC) deployed a number of infrasound arrays worldwide, with sensor separations (6–12 km) optimized to detect large explosions (Cook and Bedard 1972; ReVelle 1997; Silber et al. 2009).

As the source yield was a key physical parameter of interest for all types of atmospheric explosions, much effort focused on how best to estimate this value. A number of approaches to estimate the explosive source yield from infrasound measurements were developed, all of them empirical. These include the Lamb wave approach (Pierce and Posey 1971; Pierce and Kinney 1976), which utilizes the vertically evanescent, horizontally propagating surface waves; the period at maximum amplitude approach, which relates the period at maximum amplitude from stratospheric phases to the source energy (ReVelle 1997) and other amplitude-based scaling relations (e.g. Posey and Pierce 1971). The summary of attenuation relations, concurrently developed by Soviet and American scientists to estimate nuclear explosion yield is given by Stevens et al. (2002). Some of these empirical relations were applied to bolides in order to estimate their energy (ReVelle 1997; Silber et al.

2009; Ens et al. 2012). Section 31.4.2 of this chapter includes a summary of important yield relations for estimating energy release by bolides.

One by-product of the early global monitoring effort for nuclear explosions was detection of atmospheric explosions producing infrasound from other sources. Shoemaker and Lowery (1967) recognized that some of the signals recorded by the AFTAC network between 1960 and 1974, although belonging to seemingly energetic sources, were not associated with nuclear explosions, but were from large bolides. If not for infrasound monitoring, these bolides would otherwise have gone undetected. This historical large bolide data set provides invaluable information on the influx of NEOs (ReVelle 1997; Silber et al. 2009), especially since global monitoring and recording of bolides only effectively commenced during the twentieth century. However, with advent of satellite monitoring in the 1960 and 1970s, infrasound became less attractive as a monitoring technology and entered a 'dark age', becoming nearly forgotten.

The recent renaissance in infrasound studies is due to the Comprehensive Nuclear Test Ban Treaty (CTBT) which was opened for signature at the United Nations in on September 24, 1996. The CTBT Organization, stationed in Vienna, Austria, has implemented an International Monitoring Network (IMS), consisting of four monitoring technologies (radionuclide, seismic, hydroacoustic and infrasound), with stations distributed around the globe. With the implementation of the IMS network, infrasound has experienced revitalization. The infrasound component of the IMS consists of 60 arrays, most of which are certified and operational. While the arrays developed during the Cold War were optimized for monitoring large explosions, the IMS network is set up to reliably detect and geolocate a 1 kt of TNT equivalent (1 kt = $4.184 \cdot 10^{12}$ J) nuclear explosion anywhere on the globe (Christie and Campus 2010).

In its most basic form, the infrasound from meteors is generated by the shock produced by the hypersonic passage of a meteoroid and so we begin with some basics of shock wave physics and then apply this to the specific case of meteor infrasound.

31.1.3 Shockwave Physics: An Overview

Shock waves can be generated in all four states of matter. Győzy Zemplén provided an operational definition of a shock in 1905: '*A shock wave is a surface of discontinuity propagating in a gas at which density and velocity experience abrupt changes. One can imagine two types of shock waves: (positive) compression shocks which propagate into the direction where the density of the gas is a minimum, and (negative) rarefaction waves which propagate into the direction of maximum density*' (Krehl 2001). The intensity of a shock wave can be divided into two categories: the weak shock regime (waves of small, but finite pressure amplitude) and the strong shock regime (waves of large pressure amplitude) (Krehl 2009 and references therein). These are defined in terms of shock strength ($\zeta = p/p_0$), or the pressure ratio across the shock front. In the strong shock regime ($\zeta \gg 1$), shocks

propagate supersonically displaying highly non-linear effects, while in the weak shock regime, $\zeta \sim 1$ (or barely exceeds 1), shocks move at nearly the speed of sound (Sakurai 1964; Krehl 2009; Needham 2010). It is in the weak shock regime that the signal can be treated as nearly linear (Sakurai 1964). It is also convenient to define the strength of a shock wave with the Mach number (M), a dimensionless quantity which represents the ratio between the shock (or an object's) velocity (v) and the velocity (ambient speed of sound or v_a) with which a weak acoustic disturbance would travel in the undisturbed fluid (e.g. Hayes and Probstein 1959; ReVelle 1974; Emanuel 2000):

$$M = \frac{v}{v_a} \tag{31.10}$$

The pressure–time behaviour of an initially small disturbance may grow in non-linear acoustics into a significant distortion over many thousands of wavelengths due to a number of cumulative, long duration evolutionary processes (Krehl 2009). In shock wave physics, the waveform is confined to a single pulse (Sakurai 1964), which at some distance from the source take on the ubiquitous N-wave behaviour (DuMond et al. 1946) associated with sonic booms. Landau (1945) showed that cylindrical and spherical N-waves should decay more rapidly than predicted by geometrical spreading and elongate as they travel away from the source. The second-order weak non-linear effects are the cause of the wave elongation (or increase in the wave period) and enhanced decay (Wright 1983; Maglieri and Plotkin 1991). The same result was independently obtained by DuMond et al. (1946), albeit by a different method. DuMond et al. (1946) also attached the term N-wave to the resultant waveform as the pressure–time signature resembles the capital letter 'N' (Fig. 31.2a).

While the term shock wave is used in a more general context, a blast wave (Fig. 31.2b) is a shock wave in the air, such that it is accompanied by both significant overpressure and at large amplitudes a strong wind (indicating a high dynamic pressure) as felt by an observer. Blast waves always propagate at supersonic velocity and at sufficiently large distances from the source approach spherical geometry (Kinney and Graham 1985; Krehl 2009). Blast waves are characterized by a steep pressure rise time or shock intensity (or peak overpressure) and have a finite duration (usually defined as the length of the positive phase). The air blast produces an impulse per unit area resulting from its overpressure (Kinney and Graham 1985), and if the blast wave is sufficiently strong, the air behind it may be accelerated to high velocities, creating a strong wind which in turn creates a dynamic pressure on objects in its path producing destructive effects collectively termed blast damage (Kinney and Graham 1985; Krehl 2009). Energetic bolide events are capable of producing significant blast damage on the ground, as demonstrated by the recent bolide over Chelyabinsk (Brown et al. 2013; Popova et al. 2013) where damage was produced due to overpressure, but not high dynamic pressure. At larger distances away from the source, however, the blast wave undergoes distortion and may propagate along multiple paths resulting in a more complicated waveform.

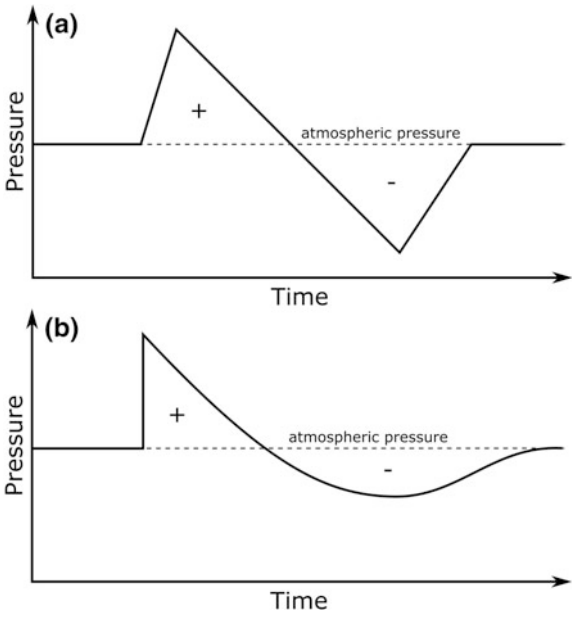

Fig. 31.2 Shock wave pressure versus time representing **a** an N-wave and **b** a typical blast wave signature

The complex mathematical problem of wave propagation non-linearity was resolved using the similarity principle (Sedov 1946; Taylor 1950), in which the number of independent variables is decreased, such that a set of fundamental partial differential equations is reduced to ordinary differential equations, while retaining the essential nature of the non-linear behaviour (Sakurai 1964; Sachdev 2004). The problem of shock waves and the infrasound produced by meteors has been studied over the past several decades; however, compared to other problems of shock dynamics, not as extensively. Generally, an object moving at supersonic/hypersonic speeds will generate a conical bow shock, where the Mach angle (η) is defined as $\eta = \sin^{-1}(1/M)$. Here, M is the Mach number.

Meteoroids propagate through the Earth's atmosphere at high Mach numbers; from ~35 up to 270 (e.g. Boyd 1998) thereby producing a very narrow Mach cone ($\eta < 1.7°$), which can be approximated as a cylinder. This has led to the concept of a meteor shock being equivalent to an instantaneous cylindrical line source charge (Tsikulin 1970; ReVelle 1976). We now extend our discussion to bolide infrasound.

31.2 Bolide Infrasound

Infrasonic waves detected at the ground offer valuable information and an insight into the shock wave phenomena generated by meteors. In particular, infrasound from meteors offers another independent means of determining the energy deposition by a meteoroid during ablation and thus provides an independent estimate of

mass/energy to calibrate mass from optical/radar techniques. However, non-linear influences, attenuation, dispersion and other often irreversible propagation effects pose a great challenge when attempting to determine the source parameters such as the meteoroid's mass, energy deposition and source height. Without ground truth information (eyewitness reports, other instruments, etc.), infrasound records alone are often not sufficient in determining whether infrasound is generated ballistically (cylindrical line source) or from fragmentation (quasi-spherical source).

In the early 1950s, Whitham (1952) developed the F-function, a novel approach in treating the flow pattern of shock signatures generated by supersonic projectiles, now widely used in supersonics and classical sonic boom theory (e.g. Maglieri and Plotkin 1991). It was realized early on that the F-function offers excellent correlation between experiment and theory for low Mach numbers (up to $M = \sim 3$), but was not as successful at hypersonic speeds (e.g. Carlson and Maglieri 1972; Plotkin 1989). The Whitham F-function theory has been recently applied to meteor shocks (Haynes and Millet 2013), but detailed observational validation for meteor infrasound has not yet been obtained.

31.2.1 A Review of ReVelle's Meteor Weak Shock Theory

Following early works on cylindrical line source related to exploding wires (Sakurai 1964; Plooster 1970), lightning phenomena (Jones et al. 1968; Few 1969) and subsequently meteors (Tsikulin 1970; ReVelle 1974, 1976) developed an analytical blast wave model for meteors following the non-linear disturbance initiated by an equivalent explosive line source. Here, we update and revise the discussion of this topic presented in Edwards (2010).

Physically, as a meteoroid penetrates deeper into the denser regions of the atmosphere, stagnation pressure builds up as air molecules pile-up in front of the body. If this stagnation pressure exceeds the internal strength of the meteoroid, gross fragmentation (or multiple fragmentation events) may occur, resulting in more complicated blast wave geometry, voiding the applicability of the pure cylindrical blast wave theory. For the cylindrical blast wave analogy to hypersonic flow to be valid (Pan and Sotomayer 1972), certain conditions, in addition to $M \gg 1$, must be satisfied.

First, the energy release must be instantaneous, which is a good approximation for meteoroids which must encounter the Earth with $v > 11$ km/s. Second, the cylindrical line source approximation is only valid if $v \gg c_s$ and v is constant (Tsikulin 1970). Additionally, the Mach angle still has to be very small many meteoroid diameters behind the body. Therefore, if there is significant deceleration ($v < 0.95 v_{entry}$) and strong ablation, the above criteria for the conditions necessary for the similarity principle in the cylindrical blast wave theory are not met (Bronshten 1964; ReVelle 1974, 1976). In this model, the line source is also considered to be in the free field, independent of any reflections due to finite boundaries, such as topographical features (ReVelle 1974).

The coordinate system to describe the motion and trajectory of the meteoroid, as originally developed by ReVelle (1974, 1976), is shown in Fig. 31.3a. The plane of meteoroid entry is referred to as the plane of entry. In this coordinate system, the variables are as follows:

φ = azimuth angle of the meteoroid heading.
φ' = azimuth angle of a given infrasonic ray outside the entry plane.
$\Delta\varphi = |\varphi - \varphi'|$ = infrasound ray deviation from the plane of entry ($\Delta\varphi = 0$ in the plane of entry, $\Delta\varphi = \pi/2$ out of the entry plane, i.e. purely horizontal).
θ = entry elevation angle from the horizontal ($\theta = \pi/2$ is vertical entry).
ε = nadir angle of the infrasonic ray with respect to the local vertical, $\varepsilon \geq \theta$ ($\varepsilon = 0$ is vertically downward, $\varepsilon = \theta$ in the plane of entry), always viewed in a plane perpendicular to the plane of entry. ReVelle (1974) originally defined ε as the zenith angle pointing downward.
x = the distance between the point along the trail and the observer in units of blast radii ($x = R/R_0$).

Azimuth angles, as viewed from the top looking downward, are measured clockwise from North. Other treatments (Edwards 2010) have not always correctly and consistently defined these quantities relative to the original definitions given in ReVelle (1974).

The relationship between the nadir angle (ε), entry elevation angle (θ) and ray deviation angle ($\Delta\varphi$) is

$$\varepsilon = tan^{-1}\left[\left(1 - \frac{2\Delta\phi}{\pi}\right)cot\,\theta\right]^{-1} \tag{31.11}$$

where $\varepsilon \neq 0; \theta \neq \frac{\pi}{2}; \varepsilon \geq \theta$ and $\Delta\phi = \frac{\pi}{2}(1 - tan\,\theta\,cot\,\varepsilon)$.

In this model, only those rays which propagate downward and are direct arrivals are considered. The requirement of direct arrival effectively limits the source–observer distance to be less than 300 km, as returns from longer ranges experience stratospheric ducting. Only part of the shock generated along the trajectory will reach the observer; however, for certain propagation conditions, no paths at all may be available between the source and the receiver. A typical ground footprint of the boom corridor is shown in Fig. 31.4. Hence, meteors which produce infrasound may go undetected at any given receiver due to such geometrical effects.

Once formed, the shock wave generated by a meteoroid is highly non-linear, propagating outward at supersonic speed and losing energy to the ambient air as the blast wave propagates. The relaxation (or blast) radius R_0 is the radius of the volume of a 'channel' that would be generated if all the explosion energy was used in performing work (pV) on the surrounding atmosphere, at ambient pressure (e.g. Tsikulin 1970):

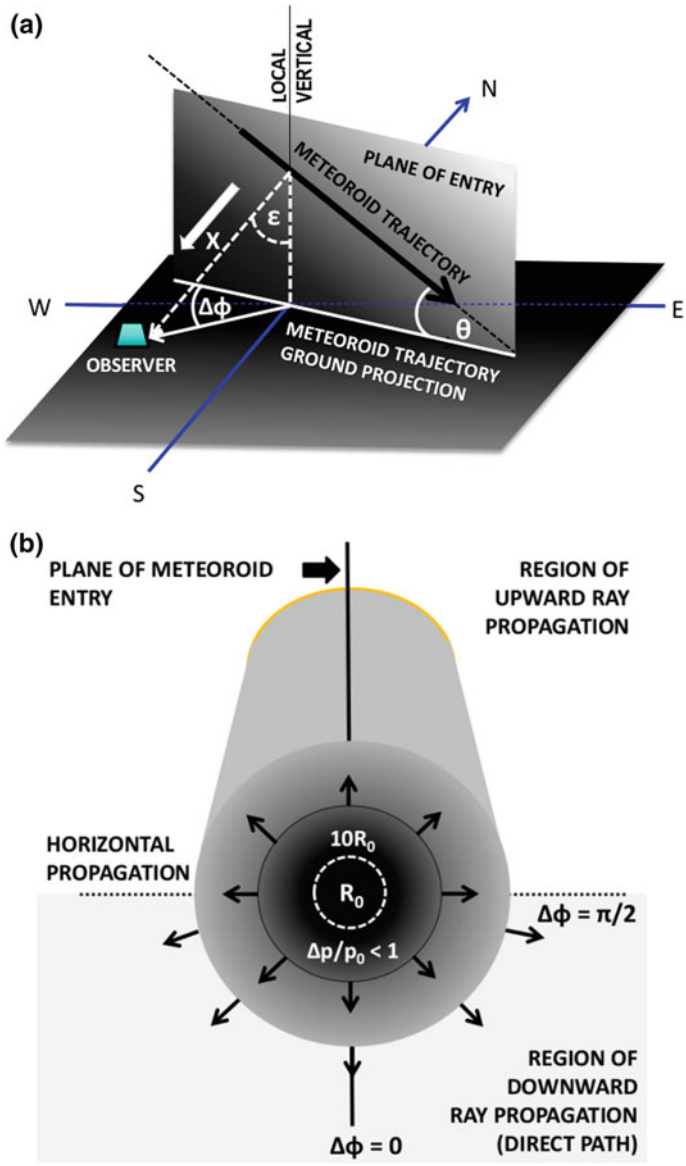

Fig. 31.3 The coordinate system as originally defined by ReVelle (1974, 1976). **a** The side view of the meteor path and **b** the cross-sectional view of the shock cavity with the meteoroid moving out of the plane of the page in the coordinate system used for modelling meteor infrasound as originally defined by ReVelle (1974) where the colouring refers to the overpressure as a function of radial distance from the meteoroid path—black and dark grey being higher than light grey. After Silber et al. (2015)

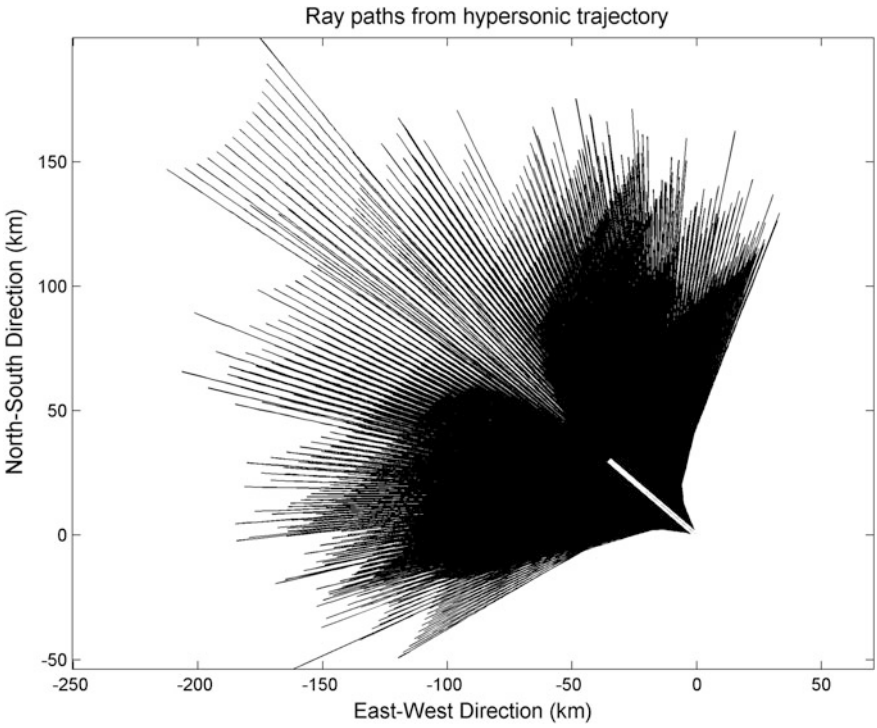

Fig. 31.4 The top-down view of the meteoroid hypersonic boom corridor. This particular figure represents the theoretical corridor for the meteorite dropping Grimsby fireball, which occurred on 25 September 2009 over Grimsby, Ontario in Canada (Brown et al. 2011). The white line represents the meteoroid trajectory, with southeast heading (towards bottom right corner). If the receiver is located outside of the hypersonic boom corridor range, infrasound signal may go undetected. Further considerations for detection are the noise levels at the receiver, in addition to the frequency content and atmospheric attenuation during propagation

$$R_0 = \left(\frac{E_0}{p_0}\right)^{1/2} \tag{31.12}$$

Here, E_0 is the amount of energy deposited by the meteoroid per unit length, and p_0 is the ambient hydrostatic atmospheric pressure (Sakurai 1964; ReVelle 1974). Physically, this corresponds to roughly the radius at which the overpressure matches the ambient atmospheric pressure. The blast radius, however, is expressed in a slightly different way by various authors, as shown in Table 31.1.

For the special case of a non-fragmenting, single body meteoroid, the energy can also be written in terms of the drag force as (ReVelle 1974):

Table 31.1 Examples of expressions for R_0 as defined by various authors. All of these are fundamentally the same except the proportionality constant, leading to a maximum difference of a factor of 3.53 (ReVelle 1974)

Blast radius definition	Author
$R_0 = \left(\frac{E_0}{\pi p_0}\right)^{1/2}$	Few (1969)
$R_0 = \left(\frac{E_0}{\gamma b p_0}\right)^{1/2}$	Jones et al. (1968) Plooster (1970) b = 3.94 and γ = 1.4
$R_0 = \left(\frac{E_0}{2\pi p_0}\right)^{1/2}$	Sakurai (1964)
$R_0 = \left(\frac{E_0}{p_0}\right)^{1/2}$	Tsikulin (1970) *standard definition*
$R_0 = \left(\frac{2E_0}{p_0}\right)^{1/2}$	Tsikulin (1970) *modified definition*

$$E_0 = \frac{1}{2}\rho_0 v^2 C_D S \tag{31.13}$$

where C_D is the wave drag coefficient and S is meteoroid cross-sectional area. Since the blast radius is directly related to the drag force in the non-fragmenting case, it can also be expressed as a function of Mach number and the meteoroid diameter (d_m):

$$R_0 \simeq M d_m \tag{31.14}$$

From the cylindrical blast wave similarity solution, the scaled distance (x) from the trajectory is given by $x = R/R_0$, where R is the actual radius of the shock front at a given time.

While the similarity solutions to the equations of hydrodynamics are applicable within the strong shock region, they are not valid for $x < \sim 0.05$, mainly due to severe non-linear non-equilibrium processes, voiding the assumption of local thermodynamic equilibrium, and thus the existence of a classical equation of state. For $x > 0.05$, the size of the meteoroid no longer has a significant effect on blast wave propagation (Tsikulin 1970; ReVelle 1974). Once the wave reaches the state of weak non-linearity (where the pressure at the shock front $p_s \sim p_0$), using the Hugoniot relation between the overpressure (p/p_0) and the shock front Mach number (M_a) (Lin 1954): $\frac{p}{p_0} = \left(\frac{2\gamma}{\gamma+1}\right) M_a^2$, the shock front velocity approaches the local adiabatic velocity of sound ($M_a \to 1$). When $\Delta p/p_0 \lesssim 1$ (at $x \gtrsim 1$), weak shock propagation takes place and geometric acoustics becomes valid (Jones et al. 1968; ReVelle 1974). Moreover, beyond $x = 1$, steady-state theory is applicable (Groves 1963). The linear sound theory is derived under the assumption that

$$\frac{\Delta p}{p_0} \to 0 \quad \text{and} \quad \frac{p_s}{p_0} \to 1 \tag{31.15}$$

In the strong shock regime, where $p_s/p_0 > 10$, the relationship between the shock front pressure and the ambient atmospheric pressure is given by (Jones et al. 1968):

$$\frac{p}{p_0} = \frac{\gamma}{2(\gamma+1)}\frac{1}{x^2} \tag{31.16}$$

It should be noted that the main difference in the terms p_s/p_0 and p/p_0 is simply the convention of writing and describing the strong shock regime ($p_s \gg p_0$) and the weak shock regime ($p_s \leq p_0$), respectively. As the shock propagates outward, it will reach the point where the strong shock similarity principle is no longer valid. Following Jones et al. (1968):

$$\underset{x\to 0}{f(x)} = \frac{2(\gamma+1)}{\gamma}\frac{\Delta p}{p_0} \to x^{-2} \tag{31.17}$$

and

$$\underset{x\to \infty}{f(x)} = \left(\frac{3}{8}\right)^{-3/5}\left\{\left[1+\left(\frac{8}{3}\right)^{8/5}x^2\right]^{3/8}-1\right\}^{-1} \to x^{-3/4} \tag{31.18}$$

In the limit as $x \to 0$ (Eq. 31.17), where $p/p_0 > 10$, attenuation is quite rapid (x^{-2}), transitioning to $x^{-3/4}$ as $x \to \infty$, where $p/p_0 < 0.04$ (or $M = 1.017$) (Jones et al. 1968). Both Landau (1945) and DuMond et al. (1946) note that the shock strength decay in the axisymmetric case clearly follows $x^{-3/4}$. Due to elevated temperature and forward velocity of the positive-pressure pulse, the wave steepens (Landau 1945), becoming a shock resembling the well-known N-wave pressure signature in the far field (Fig. 31.2a). The function *f(x)* can be slightly modified using constants Y_C and Y_D from the work of Plooster (1968). Y_C is Plooster's adjustable parameter (ReVelle 1976) which defines the region where the non-linear to weak shock transition occurs, while Y_D describes the efficiency with which cylindrical blast waves are generated as compared to the results of an asymptotic strong shock as numerically determined by Lin (Lin 1954). The variables Y_C and Y_D are the same as the variables C and δ, respectively, in Plooster (1970) and ReVelle (1974, 1976); however, they are renamed here to avoid confusion with other unrelated variables used in this chapter. A high value of Y_D implies that the rate of internal energy dissipation is low, thereby leaving more energy available for driving the leading shock (Plooster 1968). Table 31.2 includes all values for Y_C and Y_D found for a variety of initial conditions (Plooster 1968). For now, we set, $Y_C = Y_D = 1$.

Taking advantage of both Eqs. (31.17) and (31.18), and using results from experiments (Jones et al. 1968; Tsikulin 1970), the overpressure (for $x \geq 0.05$) can now be expressed as

Table 31.2 A summary of initial conditions, Y_C and Y_D as found by Plooster (1968). The values for low-density gas were not established (Plooster 1968). The last column represents the values of p_z extrapolated to $x = 10$. It should be remarked that the published value of 0.563 $p(z)$ in ReVelle (1976) refers to the p_z at $x = 1$

Initial conditions		Y_C	Y_D	Non-linear to weak shock transition	p_z at $x = 10$
Line source	Constant density Ideal gas	0.7	1	<7	0.0805 $p(z)$
Isothermal cylinder	Constant density Real gas	0.7	0.66	<7	0.0680 $p(z)$
Isothermal cylinder	High density gas Ideal gas	0.95	1.61	>2	0.0736 $p(z)$
Isothermal cylinder	Best fit to experimental data	0.95	2.62	≥3	0.0906 $p(z)$
Isothermal cylinder	Low-density gas Ideal gas	No determination made		–	–
Lightning[a]	–	1	1	10	0.0575 $p(z)$

[a]The value of p_z as determined by Jones et al. (1968) is included for the sake of completeness

$$\frac{\Delta p}{p_0} = \frac{2(\gamma+1)}{\gamma}\left(\frac{3}{8}\right)^{-\frac{3}{5}}\left\{\left[1+\left(\frac{8}{3}\right)^{\frac{8}{5}}x^2\right]^{\frac{3}{8}}-1\right\}^{-1} \tag{31.19}$$

The limits within which this expression is applicable are $0.04 \leq p/p_0 \leq 10$ (Jones et al. 1968). [Note that this was erroneously stated in Edwards (2010) as $p/p_0 \geq 10$]. The above expression can also be written as

$$\frac{\Delta p}{p_0} \cong \frac{2\gamma}{\gamma+1}\left[\frac{0.4503}{\left(1+4.803x^2\right)^{3/8}-1}\right] \tag{31.20}$$

This implies that $\Delta p \cong 0.0575 p_0$ at $x = 10$. The assumption in the expressions above (Eqs. 31.19 and 31.20) is that the ambient air density is uniform, which, in reality, is not completely true for the atmosphere proximal to the meteoroid in flight. The shock wave, as it travels from high altitudes down to the observer, encounters ambient pressures from lower to higher values over many scale heights. Therefore, a correction term will need to be applied at a later point to account for variations in the atmospheric pressure between the source and the observer.

After the shock wave has travelled the distance of approximately $10R_0$, where the disturbance is still relatively strong, but remains in the weak shock regime, its fundamental period (τ_0) can be related to the blast radius via:

$$\tau_0 = \frac{2.81\,R_0}{c_a} \tag{31.21}$$

where c_a is the local ambient thermodynamic speed of sound. The factor 2.81 at $x = 10$ was determined experimentally (Few 1969) and numerically (Plooster 1968). The fundamental frequency (f_0) is then simply $1/\tau_0$. The frequency of the wave at maximum amplitude of the pressure pulse as recorded by the receiver is referred to as the 'dominant' frequency (ReVelle 1974). The choice of $10R_0$ is somewhat arbitrary but it had arisen from the notion that non-linear propagation effects may still be important at some distance from the origin (e.g. Yuldashev et al. 2010). It is also common usage to begin model calculations at $10R_0$ ($x = 10$) under the assumption that the shock is clearly no longer in the strong shock regime.

From these relations, it should be clear that large meteoroids produce large blast radii, long fundamental periods and small fundamental frequencies. As a result, given favourable infrasonic ray propagation paths, they are more likely to produce infrasound detectable at the ground. As previously described, due to non-linear effects, this fundamental period will lengthen as the shock propagates outward, eventually forming into an N-wave after it has travelled a certain distance from the source, as predicted by sonic boom theory (Landau 1945; DuMond et al. 1946; Carlson and Maglieri 1972; Maglieri and Plotkin 1991).

For sufficiently large R and assuming weakly non-linear propagation, the line source wave period (τ) for ($x \geq 10$) is predicted to increase with range as

$$\tau(x) = 0.562\,\tau_0\,x^{1/4} \tag{31.22}$$

The above will be valid as long as the wave remains in the weak shock regime. Far from the source, the shape of the wave at any point will mainly depend on the two competing processes acting on the propagating wave—dispersion, which reduces the overpressure and 'stretches' the period; and steepening, which is the cumulative effect of small disturbances, increasing the overpressure (ReVelle 1974).

There are two primary sets of expressions which are used to estimate the predicted infrasound amplitude and period at the ground. One set of expressions deals with the wave propagation in the weak shock regime, while the other one describes the wave propagation in the linear regime (Table 31.3).

In addition to the damping coefficients, additional correction terms are required to account for linear propagation, non-uniform refracting path and density variations along the propagation path. These are as follows:

(i) The asymptotic form of the wave overpressure decay in the linear propagation regime is $x^{-1/2}$ (Officer 1958) as opposed to $x^{-3/4}$ in the weak shock regime.
(ii) A correction term (Table 31.4) for amplitude used to account for differences between the actual refractive path to that of a straight-line path between the source and the receiver (Pierce and Thomas 1969).
(iii) An atmospheric density correction term (Pierce and Thomas 1969; ReVelle 1974) (Table 31.4), which serves to correct the amplitude for the differences between the source altitude to the receiver altitude.

The predicted signal period, amplitude and overpressure ratio as a function of altitude are shown in Fig. 31.5 for an example event. The precise transition, or the distortion distance, between the weak shock and linear regime is rather ambiguous.

Table 31.3 The summary of expressions to describe the predicted infrasound period and amplitude as per ReVelle (1976), updated to reflect the propagation in a non-isothermal atmosphere (Edwards 2010; Silber 2014; Silber et al. 2015)

Regime	Period	Amplitude
Weak shock	$\tau(x) = 0.562\,\tau_0\,x^{1/4}$	$\Delta p_{z\to obs} = (f(x)\ D_{ws}(z)\ N^*(z)\ Z^*(z))\ p_0$
Linear	constant	$\Delta p_{z\to obs} = \left[\Delta p_{z\to t} D_l(z) \frac{N^*(z)_{z\to obs} Z^*(z)_{z\to obs}}{N^*(z)_{z\to t} Z^*(z)_{z\to t}} \left(\frac{x_{z\to t}}{x_{z\to obs}}\right)^{1/2}\right] p_0$
N^a and Z^a—the correction factors (Table 31.4)		
D_{ws}, D_l—the weak shock and the linear damping coefficients[a]		
p_0—ambient atmospheric pressure		
p_z, p_{obs}—atmospheric pressure as measured at given altitude and at observer, respectively, z—altitude		
z_{obs}, z_t—altitude as measured at observer and transition, respectively		

[a]For the complete treatment for non-isothermal atmosphere, see Edwards (2010), Silber (2014) and Silber et al. (2015)

Table 31.4 A summary of correction terms employed in the weak shock approach

Term	Expression	Description of variables
(ii)	$N^*(z) = \left(\frac{\rho(z)}{\rho_z}\right)^{\frac{1}{2}} \frac{c(z)}{\overline{c_z}} N_c$	$c(z)$—sound speed $\rho(z)$—atmospheric density as a function of altitude H—atmospheric scale height $\overline{c_z}$—average speed of sound between the source and the receiver ρ_z—atmospheric density N_c—non-linear propagation correction term, assumed to be unity (Cotten and Don 1971; ReVelle 1974) between the source and the receiver z_{obs}—altitude (0 if at the ground) at the receiver z_z—altitude at the source
	$\overline{c_z} = \frac{\int_{z_{obs}}^{z_z} c(z)\,dz}{z_z - z_{obs}}$ $N_c < 1 + \frac{z_z}{12H}$ $N_c < \begin{cases} 2.1\ (< \sim 100\,\text{km}) \\ 1.55\ (< 50\,\text{km}) \end{cases} \approx 1$	
(iii)	$Z^*(z) = \frac{\rho_z}{\rho(z)} \left(\frac{c_z}{c(z)}\right)^2$	

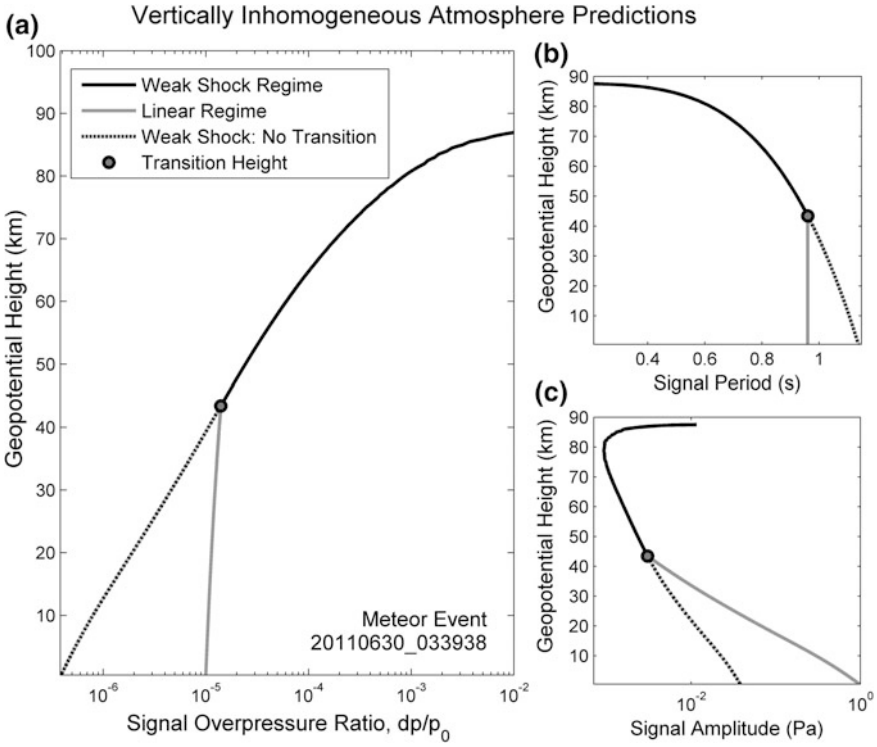

Fig. 31.5 The change in signal **a** overpressure ratio (dp/p_0), **b** period and **c** amplitude as a function of height from source to receiver in a fully realistic atmosphere (with winds and true temperature variations with height) according to the ReVelle (1974) weak shock model. The example shown here represents one of the meteor events analysed by Silber and Brown (2014)

As per Sakurai (1964), the transition takes place when $p/p_0 = 10^{-6}$, while Morse and Ingard (1968) calculated the distortion distance (d_s) to the 'shocked' state as

$$d_s = \frac{c\tau}{5.38\,\frac{\Delta p}{p_0}} \tag{31.23}$$

ReVelle (1974) adopted Towne's definition for the distortion distance (d'), which is defined as the distance at which the acoustic period decays by 10%:

$$d' = \frac{\lambda}{20(\gamma+1)\,\frac{\Delta\rho}{\rho_0}} = \frac{c\tau}{34.3\,\frac{\Delta p}{p_0}} \tag{31.24}$$

Thus, from (31.23) and (31.24) it follows that $d_s = 6.38d$ and $d > d_a$, where d_a is the remaining propagation distance of the disturbance before it reaches the observer.

As mentioned in the earlier sections of this chapter, the ReVelle (1974, 1976) model is applicable only to direct arrivals. Therefore, infrasound producing meteoritic events recorded at large distances are not suitable for validating the weak shock model. Due to inherent lack of statistically meaningful sample of well-documented and characterized fireballs, the testing and validation of the weak shock model did not take place until four decades after it was first developed (Silber et al. 2015).

Note that the foregoing analytic approach provides a simple and mathematically trackable framework for computing expected signal periods and amplitudes from meteor shocks as observed at the ground. A potentially higher fidelity approach to the problem using computational fluid dynamics which follows the weak shock numerically using computational fluid dynamics (CFD) solvers from the source to the ground has recently been presented by several groups (Henneton et al. 2015; Aftosmis et al. 2016).

31.2.2 The ReVelle Weak Shock Model: Validation Study

Groundwork

The importance of observing bright fireballs simultaneously with multiple technologies and instruments is multifold. For example, it is not possible to infer detailed fireball characteristics, such as entry velocity or orbit, with infrasound alone. Additionally, to validate and improve infrasound propagation models and theoretical treatments, it is necessary to measure meteor trajectories. The overview of the early attempts to observe bright fireballs simultaneously with optical, radar and infrasound instruments (McIntosh et al. 1976; Kraemer 1977) is well described in Edwards (2010). Notably, only two possible meteors were detected infrasonically over a period of 5 years during the late 1970s and early 1980s (Kraemer 1977) as part of a campaign of infrasound measurements run in concert with the Prairie Network of fireball cameras in the US (McCrosky and Boeschenstein 1968) and the Meteorite Observation and Recovery Project (MORP) in Canada (Halliday et al. 1978).

It was not until the inception of the IMS network in the late 1990s that infrasound observations of bolides started to become common (ReVelle and Whitaker 1999; Evers and Haak 2003). In most cases, however, meteors producing infrasound signatures did not have well-constrained ground truth information (ie. measured meteor velocity vectors), making validation of the ReVelle (1976) analytic theory nearly impossible. Additionally, the scarcity of meteor events at any given geographical location, insensitivity of older instruments and lack of computer algorithms for sensitive detection of weak signals along with poor constraints of the type of shock (cylindrical vs. spherical) further complicated early attempts to validate the weak shock model.

With the emergence of several regional meteor networks, including the Southern Ontario Meteor Network (SOMN) in Canada (Brown et al. 2007; Weryk et al. 2008; Brown et al. 2010), a handful of well-documented meteor events having infrasound records have become available. The SOMN network uses all-sky cameras and infrasound technologies to monitor, detect and measure the trajectory of bright regional meteor events (centimetre size meteoroids). Shortly after the infrasound array went online in 2006, it became apparent that it would be possible to simultaneously optically observe one meteor a month and identify its associated infrasound signal. The early pilot study (Edwards et al. 2008) analysed 12 such bright meteor events.

During the period between 2006 and 2011, ~7000 meteors (including many fireballs) were detected optically by the SOMN. In total, over 70 were also positively identified as sources of direct infrasound. Silber and Brown (2014) (SB14) and Silber et al. (2015), carried out a large, two-phase study, with the primary aim to test, validate and update the weak shock model. The scope of the study also extended to the comprehensive analyses of the meteor signal phenomenology, infrasound signal taxonomy as it pertains to meteors, the nature of the shock production and detailed characterization of the source function. The detailed overview of the study can be found in SB14. Here, we note the key findings only.

In phase one of SB14, infrasound signals from 71 simultaneously detected bright optical meteors were examined to investigate the phenomenology and characteristics of meteor near-field infrasound (<300 km) and shock production. A small number of bright fireballs produced two or even three distinct signals. Recall that the ReVelle (1974, 1976) theory assumes the source is a cylindrical line source; therefore, in order to test and validate the model, it is imperative to positively identify the characteristics of the source function. This involves knowledge of the mode of shock production (spherical vs. cylindrical geometry), the shock source height, meteoroid entry velocity and entry angle, as well as the infrasound ray launch angle from the meteoroid heading. The ray launch angle is the angle between the meteoroid trajectory and an infrasonic ray with respect to the trajectory in 3D space, independent on any geometrical planes. Note that the ray launch angle definition described here and ReVelle's definition of the infrasound ray deviation from the plane of entry ($d\varphi$) (Fig. 31.3a) refer to the same ray, but from different geometrical perspectives. Therefore, for simplicity and consistency, throughout this chapter, the term ray deviation always implies $d\varphi$ or ReVelle's definition

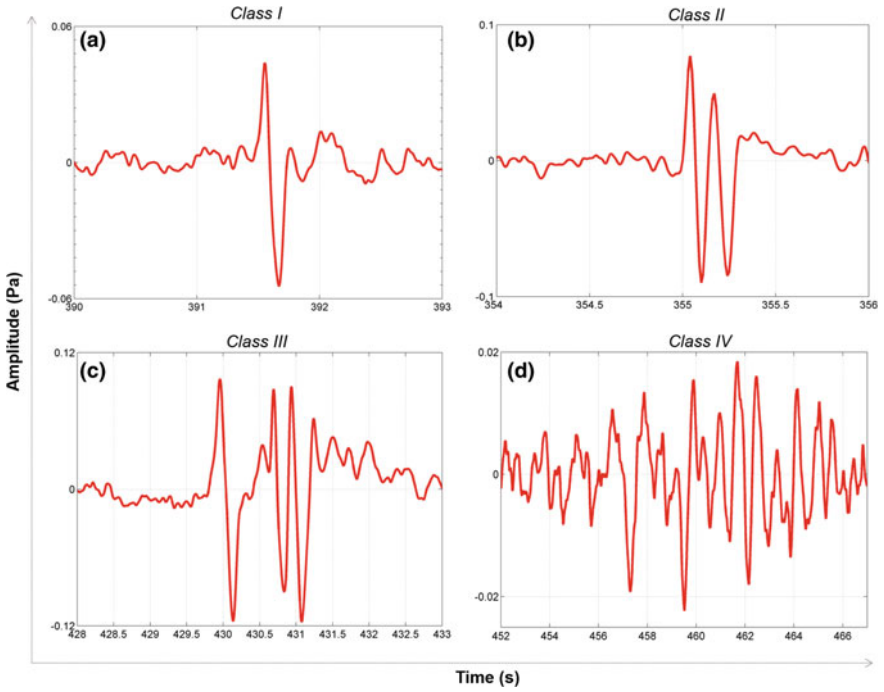

Fig. 31.6 Examples of each meteor infrasound taxonomic class as proposed by Silber and Brown (2014). The meteor infrasound classes are based upon the apparent shape of the pressure versus time record. **a** Class I is characterized by a single complete cycle, with the peak-to-peak (P2P) amplitude well above background noise (any other peak which is < ½ P2P of the main cycle is not counted). **b** Class II and **c** Class III signals exhibit two and three prominent and complete cycles similar in size, respectively. **d** Class IV, has four or more cycles all within ½ P2P amplitude of the dominant cycle. After Silber and Brown (2014)

(Fig. 31.3a). In the ballistic regime, the ray launch angle is expected to be within 90° ± 25° from the meteoroid's velocity vector (e.g. Brown et al. 2007).

The infrasound signal alone is not sufficient to discriminate the mode of shock production (SB14). The new signal phenomenology and taxonomic classification scheme for meteor generated infrasound suggest that both spherical and cylindrical shocks can produce very different pressure–time signals at the ground (Fig. 31.6). Well-constrained optical observations can provide necessary trajectory parameters, such as the meteoroid entry velocity and angle, the trajectory in 3D space (begin and end height) and timing. However, the major unknowns that still need to be resolved are the shock source height, ray launch angle and the nature of the shock production.

Ray tracing is a useful approach to simulate ray propagation from the meteoroid's path to the receiver. SB14 showed that even at short ranges (<300 km), the implementation of small-scale atmospheric perturbations in the winds due to gravity waves (Gardner et al. 1993; Peitgen and Saupe 1998) resulted in infrasound propagation paths which were not present when only averaged atmospheric profiles

were used in the model. Having the information about the propagation path, the next step is to determine the most probable point along the meteor trail where the infrasound signal is generated (for more details and the algorithm, see SB14). Once the propagation path and shock source height are known, it is straightforward to obtain the ray launch angle from the associated geometry.

SB14 found that all events with large ray launch angles (>117°) from the trajectory heading were most likely generated by a spherical shock as evidenced by a correlation with point-like flares in the meteor light curves (from video data), while infrasound produced by the meteors with ray launch angles $\leq 117°$ were a mix of cylindrical line source and a spherical shock. The latter is consistent with the findings of Brown et al. (2007), who suggested that the ballistic regime falls within $90° \pm 25°$.

Zinn et al. (2004) showed that the region of maximum luminosity is also where energy deposition peaks and hence is normally the point where the blast radius is the largest. This would also be the location where the refractive effects (i.e. gradient in local sound speed produced by the shock) are the largest. Nonetheless, point source shocks are still present in the ballistic region, based on the occurrence of flares along the trail. This suggests that it is not only essential to investigate the type of signal but also to understand the geometry of each event to uniquely associate it with a meteor infrasound signal and a particular source shock type. SB14 found that there is strong directional anisotropy in acoustic emission from meteors, which tend to be dominated by the cylindrical line source geometry, even in the presence of fragmentation.

ReVelle's Weak Shock Model: Improvements and Validation

Phase two of the meteor infrasound study involved the validation of the ReVelle weak shock model (Silber et al. 2015). The weak shock model behaviour was examined in a sensitivity analysis to estimate the effects of (i) winds, (ii) perturbed wind fields due to gravity waves, (iii) Doppler shift and (iv) Sutherland and Bass (2004) absorption coefficients. The overall effect of these factors on the estimated initial value of the blast radius was found to be relatively small (~10%) for regional meteor events.

The first step was to implement a bottom-up modelling approach, which uses the observed infrasound signal period and amplitude together with the weak shock model to predict the blast radius (R_0) at the shock source altitude. This could then be compared to the measurements of the same meteor using optical instruments which provide brightness as a function of height, a direct proxy for energy deposition. It was found that the period-based blast radius computed by the ReVelle model produced values close to that found from the optical values, assuming luminous efficiencies followed the expression given in Ceplecha and ReVelle (2005). However, the amplitude-based blast radius predictions exhibited a large systematic deviation in both the linear and weak shock regimes compared to the optically determined values of energy deposition, as well as large deviations when compared to the period-based blast radius. The amplitude-based R_0 was severely underestimated in the linear regime and overestimated in the weak shock regime. For a visual comparison, the predicted weak shock and linear amplitude and period

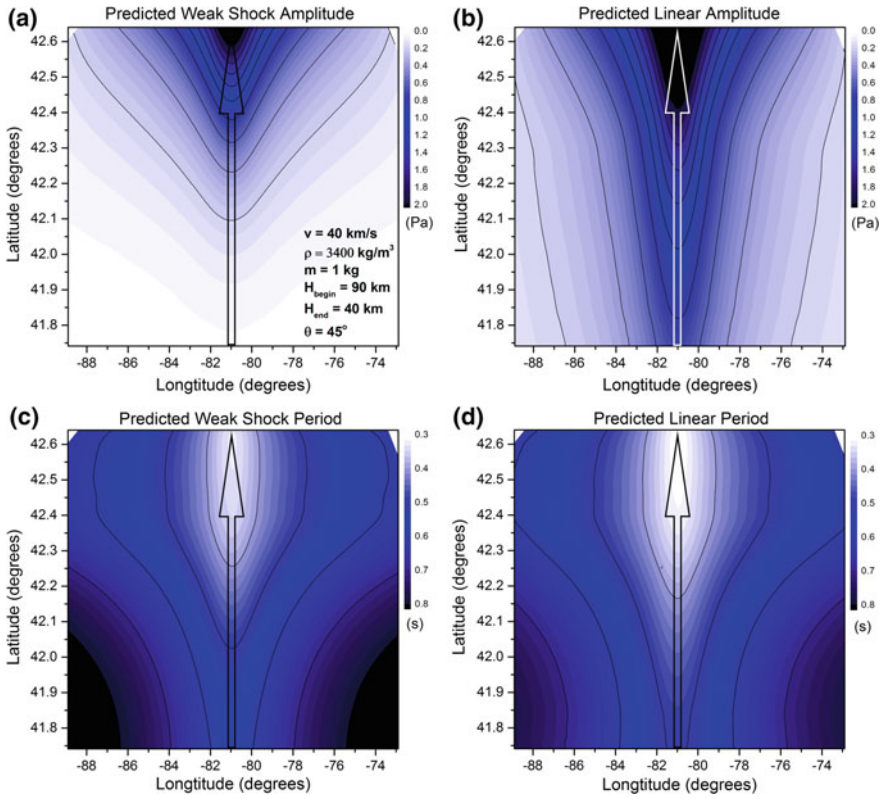

Fig. 31.7 An example of the predicted ground-level amplitude and period of a meteoroid shock using the ReVelle (1974) theoretical model. The meteor in this example is moving northward with an entry angle of 45 degrees from the horizontal. The top two panels show the predicted **a** weak shock and **b** linear amplitude. The bottom two panels show the predicted **c** weak shock and **d** linear period. The amplitude in the linear regime has a larger magnitude than that in the weak shock regime, while the opposite is true for the signal period. The synthetic meteor parameters are shown in the lower right of plot (**a**). After Silber et al. (2015)

are shown for a synthetic meteor propagating in a realistic windy atmosphere. The meteoroid ablation starts at an altitude of 90 km and ends at 40 km (Fig. 31.7).

Silber et al. (2015) isolated one possible cause of the discrepancy in amplitude-based R_0 estimates, namely, to the adoption of Towne's (1967) definition for the distortion distance, used by ReVelle (1974). Assuming this arbitrary definition is not correct, it was empirically determined that a modified distortion distance for the data set of <6% explained the linear amplitude observations, contrary to the proposed value of 10% (Towne 1967). A 'best fit' linear regime R_0 which simultaneously matched both amplitude and period within their measurement uncertainties was established using this modified distortion distance. The fragmentation model of meteoroid ablation was applied (Ceplecha and ReVelle 2005) mainly constrained by photometric data as measured from video observations of

meteor events to calculate independently the blast radius using the fundamental definition for R_0 in terms of energy deposition per unit path length. This blast radius was used as an input for top-down modelling to determine the predicted signal amplitude and period in both the weak shock and linear regimes. Silber et al. (2015) found good agreement with the observed period, while the linear amplitude using the nominal distortion distance of 10% was again underestimated. However, the predicted values of the period and amplitude agree when the modified distortion distance (<6%), as obtained from the best fit R_0, was used. Silber et al. (2015) also derived new empirical relations that link the observed dominant signal period (τ) to the meteoroid blast radius:

$$R_0 = 15.4231\,\tau - 0.5294 \text{ (for observed signals } \tau \leq 0.7\text{s) and}$$
$$R_0 = 29.14597\,\tau - 11.5811 \text{ (for observed signals } \tau > 0.7\text{s).}$$

In principle, the blast radius will depend on the total energy of the event and its height, but the above relations are population averages of the meteors detected by the SOMN. The dominant signal period is proportional to the blast radius, and therefore energy deposition by a meteoroid (mass and velocity) and the shock altitude. Therefore, the dominant signal period is more robust than signal amplitude when estimating meteoroid energy deposition, since it is less susceptible to adverse propagation effects in the atmosphere (ReVelle 1974; Edwards et al. 2008; Ens et al. 2012).

31.3 Impact Effects of NEOs

Here, we examine the effects of NEO impacts on the atmosphere and at the ground with emphasis on the Chelyabinsk event.

A detailed discussion about the Chelyabinsk fireball is given by Pilger et al. (2019). We focus the discussion on the shockwave and other destructive effects of a Chelyabinsk class of potentially hazardous NEOs. The emphasis on the Chelyabinsk bolide is used to illustrate the newly established paradigm regarding the NEO risk assessment and quantification (Boslough et al. 2015). Brown et al. (2013) and Popova et al. (2013) independently determined the explosive yield of this remarkable event at 500–600 kt TNT and size of about 20 m with an entry speed of 19 km/s. The detailed fragmentation behaviour (Borovička et al. 2013) and energy deposition/light curve for Chelyabinsk have also been measured, making it an ideal calibration event for modelling studies.

An airburst with the energy of the Chelyabinsk bolide is expected only once in several decades (Boslough et al. 2015) and such an airburst proximal to an urban centre where air blast damage could occur is a once per several millennia occurrence. The Chelyabinsk fireball was the largest recorded atmospheric explosion to date by the CTBTO IMS network of infrasonic stations (Pilger et al. 2015). The event was also recorded by the 400-station US Transportable array deployed in the continental United States and Alaska (de Groot-Hedlin and Hedlin 2014).

The ground hazard related to events of the Chelyabinsk class (sub-megaton yields) of NEOs is primarily air blast. For such small events, some potential hazard due to ground impact of meteorites exists, but the primary mode of damage will result from the different types of shockwaves (with cylindrical or quasi-spherical sources due to terminal fragmentation) discussed in previous sections. The key factor in determining air blast damage is the airburst height, often taken to mean the height at which the main surviving body has its speed reduced to half its initial value (Shuvalov et al. 2016a). The airburst height is determined by the fragmentation behaviour of the meteoroid; the more extensive and earlier the fragmentation, the higher the airburst height and the smaller the air blast damage at the ground (Shuvalov et al. 2015). In general, Chelyabinsk-class NEOs ($D < 20$ m) are expected to have airburst heights above 15 km and more typically above 20 km except for very strong objects (Shuvalov et al. 2016a).

For NEO impactor sizes of many tens of metres to 100 m, most of the energy is deposited within 1–2 atmospheric scale heights of the ground and the air blast is strong enough to cause structural failure and local fires due to large thermal loading from the shock radiation (Collins et al. 2005). These impactors are closer in character to the Tunguska event of 1908.

The magnitude of the air blast damage might be expected to be slightly greater if the object enters the atmosphere at a steeper angle, mainly due to the lower penetration height of the airburst. However, for the shallow (18°) entry angle of Chelyabinsk where the air blast was dominated by the cylindrical shock, simulations of steeper entry suggest only moderate (factor of two or less) increases in the ground-level overpressure for near vertical incidence (Mathias et al. 2015; Shuvalov et al. 2016b), so steeper entry alone does not seem to be a strong factor in ground damage. Clearly very shallow entry angles (<10 degrees) will result in less damage as airbursts will be at much higher altitudes.

The energy, and consequently the destructive potential of the large fireball induced shockwaves, is a direct function of the pressure jump at the shock wave front during its formation, duration of the compression and rarefaction stages and the gas velocity behind the shock front (Shuvalov et al. 2016a).

In addition to the destructive effects of bolide generated shockwaves from Tunguska class and larger impacts on the ground such as tsunamis, radiation ignition and crater production (Collins et al. 2005), the formation of high altitude plumes has the potential of endangering satellites in low-Earth orbit (Boslough et al. 2015). Boslough and Crawford (2008) showed that Tunguska-class airbursts may be more destructive in part because of downward transport of energy and forward momentum of the large ablated mass which continues along the impact trajectory even after most of the solid body is vaporized. This implies that smaller objects, penetrating to within 1–2 scale heights of the ground, have much greater destructive potential than predicted by the classical pancake-model of airbursts (e.g. Chyba et al. 1993).

In the following sections, we review the source energy estimates from infrasound observations of bolides, most of which are necessarily empirical as the detailed physics per event is largely unknown. We also summarize the population of the Near-Earth Objects (NEOs) and how infrasound monitoring can be used to

infer the characteristics and energy deposition by NEOs, thus providing invaluable information that sometimes cannot be obtained by any other means (e.g. Silber et al. 2011; Chesley 2015).

31.4 Energy Estimates Using Infrasonic Observations of NEOs

As discussed in Sect. 31.1.2, the US AFTAC developed empirical range independent period–yield relations to gauge the yield of atmospheric nuclear explosions. These relations were later modified to be utilized for estimating energy produced by bolides (ReVelle 1997; Ceplecha et al. 1998). The only modification in the AFTAC relation for yield was removal of the radiation term, as a much greater fraction of the bolide energy is available for shock production than is the case for nuclear explosions where close to half the total energy is lost to radiation (Glasstone and Dolan 1977). Another set of empirical relations relate the signal amplitude and propagation distance to energy (amplitude–range relations); however, these are not as robust as the period–yield relations due to inherent sensitivity of signal amplitude to propagation effects (particularly winds). Ens et al. (2012) provide a detailed discussion and analysis of energy estimates of bolides from infrasound which we summarize below.

31.4.1 Meteor Infrasound Signal Propagation, Detection and Interpretation Considerations

While the dominant infrasound signal period is a robust measure of the meteor source energy (ReVelle 1974; Edwards et al. 2008; Ens et al. 2012; Silber et al. 2015), it is often found that the dominant periods of bolide infrasound signals detected at different stations exhibit variations in their duration, even though these are related to the same event (Silber et al. 2009; Silber et al. 2011; Ens et al. 2012).

The difference in dominant periods is generally attributed to the dispersion effects with range and the fact that the signal might be coming from different parts of the trajectory (ReVelle 1974; Silber et al. 2009; Silber et al. 2011) and therefore different heights. It may also be due to differences in the signal to noise ratio at different stations. As described in the preceding sections, the dominant signal period is a proxy for the size of the blast radius and is representative of the energy deposition (ReVelle 1974, 1976) at a point from which the signal emanates. Any given station might ‘see’ the signal(s) coming from a distinct portion of the trail.

For example, Fig. 31.4 demonstrates that the receiver will record signals from different parts of the trail depending on its geographical location with respect to the bolide trajectory.

The study of regional fireballs (Edwards et al. 2008; Brown et al. 2011; Silber and Brown 2014) showed that multiple infrasound signals can indeed originate from a single meteor event. Silber and Brown (2014) found that there are two possible scenarios: first, airwaves can originate from different portions of the trail, such as the case of the well-documented Grimsby meteorite (Brown et al. 2011); and in second, more rare scenario, the airwave originating at a single point might undergo slightly different paths due to atmospheric conditions (see Sect. 31.1.2).

In terms of the size of the blast radius, there are two main considerations. First, the simple drag force relation tells us that the blast cavity will not retain the same size as the bolide descends deeper into the atmosphere. Second, the blast cavity will depend on the mode of shock production. This means that a spherical shock (e.g. gross fragmentation or significant ablation along a short segment of the trail) will produce predominantly larger blast radius, compared to a cylindrical line source. Each fragment that breaks off and remains in the proximity of the main fragment will make its own contribution to the overall blast radius. In general, we expect fragmentation to artificially increase the apparent blast radius and result in over-prediction for meteoroid mass.

Nevertheless, the period–yield relations are commonly used because no other knowledge about the source (e.g. height, distance) or atmospheric conditions is required to estimate the kinetic energy deposition. Numerous studies have shown that the averaged signal period across all detecting stations is a robust means of estimating the total energy released by a bolide (e.g. Silber et al. 2011; Ens et al. 2012; Brown et al. 2013). At large ranges, the cylindrical blast geometry becomes increasing spherical, suggesting the greater applicability of long-range empirical blast relations derived from man-made atmospheric explosions.

Silber et al. (2011) used the Indonesian bolide (Pilger et al. 2019) as a case study to investigate if it is possible to determine the most likely source height and estimate energy. This particular bolide showed large variation in the recorded infrasound signal periods and at the time of the study, there was no ground truth other than infrasound records. They implemented and combined ray tracing (Norris and Gibson 2001) and the weak shock model (ReVelle 1974, 1976), as well as the numerical entry model (ReVelle 2001), which includes full meteoroid ablation and fragmentation in a realistic atmosphere. Silber et al. (2011) concluded that the signals with the shortest period likely came from higher altitudes (30–50 km), while the signal with the longest was most likely generated by the terminal airburst at an altitude of 20 km. The bolide and fireball data released by JPL/NASA 3 years later confirmed the height of the peak brightness at 19 km, as recorded by US Government sensors (see Sect. 31.6.1).

31.4.2 Empirical Energy Relations

There are a number of empirical yield relations that were developed from nuclear and chemical explosions that are commonly applied to bolides. A major drawback is that most of the explosions used to construct these relations were made near ground level, whereas bolide energy release is much higher in the atmosphere. Nevertheless, the amplitude–yield relations can often provide correct values within an order of magnitude. These amplitude–range relations are summarized in Table 31.5.

Ens et al. (2012) examined a large data set of global bolide events simultaneously detected by the IMS infrasound network and by US Government (USG) sensors. The latter observations provide geographical location and energy, which were used to refine and update the empirical yield estimate relations for bolides. The data set of 71 distinct events produced 143 infrasound signals recorded by the IMS network stations around the globe. In their study, Ens et al. (2012) concluded that events generating energies >20 kt should be detected globally, while 1 kt bolides have a detection distance threshold of about 7000 km. Their revised and updated period–yield relationship (Table 31.6) is strikingly similar to the AFTAC period–yield relationship derived from nuclear tests (ReVelle 1997), also shown in the table. Based on the statistical analysis of the entire data set, Ens et al. (2012) also derived an empirical maximum detection range and frequency cut-off (Table 31.6). For completeness, we also include the empirical amplitude–range relations that include the wind correction factor in Table 31.7 (Reed 1972; Mutschlecner et al. 1999; Edwards 2007; Ens et al. 2012).

Table 31.5 Empirical estimates of yield using infrasound amplitude measurements associated with nuclear explosions. Here, E is the source yield in kt of equivalent TNT. A^* represents the signal amplitude in Pa (A_p) or the wind-corrected amplitude in microbars (A_w). R^* denotes the range from the source to receiver in either km (R) or degrees (Δ). The last relation (Mutschlecner and Whitaker 2010) was developed using known explosion yields of ammonium nitrate fuel oil (ANFO). A_a, B_a and C_a are the constants in the amplitude–range relations

$\log E = A_a \log A^* + B_a \log (R^*) - C_a$					
A_a	B_a	C_a	A^*	R^*	Reference
1.00	0.50	1.54	A_p	$R \sin \Delta$	Pierce and Posey (1971)
2.00	2.94	1.84	A_p	Δ	Clauter and Blandford (1998)
1.47	2.00	4.96	A_p	R	Whitaker (1995)
3.03	3.03	9.09	A_p	R	Russian-crosswind, Stevens et al. (2002)
3.03	3.03	10.00	A_p	R	Russian-downwind, Stevens et al. (2002)
2.00	3.52	10.62	A_p	R	Blanc et al. (1997)
1.49	2.00	4.18	A_w	R	Mutschlecner and Whittaker (2010)

Table 31.6 A summary of period–yield relations from ReVelle (1997) and Ens et al. (2012). A_p and B_p are the constants in the period–yield relations. Here, E is the source energy in kt, R is the distance from the source to receiver in km, τ is the dominant signal period in seconds, F_U and F_L are the observed upper and lower signal frequencies in Hz, respectively for the ensemble of events in Ens et al. (2012). Note that energy in Ens et al. (2012) is in tons of TNT equivalent (not kt, as in other relations)

$\log E/2 = A_p \log \tau - B_p$			
A_p	B_p		Reference
3.34	2.58	$E/2 \leq 100$ kT	ReVelle (1997)
4.14	3.61	$E/2 \geq 40$ kT	ReVelle (1997)
$\log E = A_p \log \tau - B_p$			
A_p	B_p		Reference/notes
3.75	0.50	Entire data set	Ens et al. (2012)
3.28	0.71	Averaged multi-station events	Ens et al. (2012)
$\log R = 2.80 + 0.33 \log E$			The maximum range R an event of energy E is observed
$F_U = 0.51 + 20.9 \exp(-R/1883)$			Maximum upper frequency content of a signal at R
$F_L = 0.06 + 102 \exp(-R/678)$			Maximum lower frequency cut-off of a signal at R

Table 31.7 The amplitude–range relation. Here, kt R is the range in km, A_{P2P} is the peak-to-peak signal amplitude, a and b are regression coefficients, k is empirical correction constant and v_w is the average wind velocity component along the great circle propagation path between the source and the receiver. E is energy in tons of TNT equivalent, not kt, as in other relations. However, the energy ranges where these relations are valid, are expressed in kt

$\log A_{P2P} = a + b \log R + c \log E - kv_w$					
a	b	c	k		Reference
3.36 ± 0.60	−1.74 ± 0.24	–	−0.0177	$E < 3.5$ kt	Edwards (2007)
2.58 ± 0.41	−1.35 ± 0.18	–	−0.0018	$E > 7$ kt	Edwards (2007)
4.33 ± 0.78	−1.00 ± 0.13	−0.43 ± 0.07	−0.0084 ± 0.0014	$E < 3.5$ kt all ranges	Ens et al. (2012)
11.35 ± 3.30	−1.20 ± 0.35	0.77 ± 0.97	0.0013 ± 0.0040	$E > 7$ kt all ranges	Ens et al. (2012)
4.71 ± 0.73	−1.08 ± 0.12	−0.46 ± 0.05	−0.0068 ± 0.0014	All energies, all ranges	Ens et al. (2012)
5.30 ± 1.18	−1.20 ± 0.19	−1.20 ± 0.19	−0.0084 ± 0.0018	Within 300 km, all ranges	Ens et al. (2012)
–	–	−0.46 ± 0.05	–	–	Mutschlecner et al. (1999)
–	−1.28	−0.43	–	–	Reed (1972)

31.5 NEOs: Characteristics of the Impacting Population

31.5.1 NEO Flux and Hazard

The flux and physical characteristics of NEOs impacting the Earth is an ongoing topic of interest. The earliest risk assessment was done by Chapman and Morrison (1994), who determined that the largest asteroids (>1 km in diameter), despite being only a small fraction of the total NEO population, pose the greatest impact threat. This was because impacts at these sizes (and larger) are at the threshold where human civilization itself would be at risk. While these largest and most destructive impacts have the lowest probability of occurrence, they continue to dominate the long-term hazard from impacts (Boslough et al. 2015) despite the fact that more than 90% of all 1 km asteroids are now catalogued. Data constraining the physical characteristics and flux of NEOs includes observations of fresh craters on Mars and Moon (Nemtchinov et al. 1998; Ortiz et al. 2002; Buratti and Johnson 2003; Malin et al. 2006) and telescopic surveys (Morrison 1992; Werner et al. 2004; Harris and D'Abramo 2015; Wright et al. 2010). In particular, numerous telescopic search programmes, such as the Panoramic Survey Telescope and Rapid Response System (Pan-STARRS) and the Catalina Sky Survey (Harris et al. 2015), have increasingly focused on detection of small (<1 km) NEOs in the last few years. In addition, bolide measurements (Brown et al. 2013) provide a direct estimate of the contemporary impact rate at ~10 m and smaller sizes. However, the temporal record of actual (small) NEOs observed to impact the Earth is relatively short, spanning only several decades.

Despite advances in telescopic surveys, many near Earth asteroids remain undiscovered, particularly in the sub-kilometre size range. More generally, there remains large uncertainty in the size of the population in some size regimes. For example, at Chelyabinsk sizes (20–50 m) there remains up to an order of magnitude variance in published population estimates (e.g. Harris and D'Abramo (2015) versus Tricarico 2016). The NEO population and impact rate have been modified and updated over the last few decades reflecting new models and data sets. The Spaceguard Survey, mandated by the US Congress in 1998, was designed to find >90% of NEOs >1 km in size and has since accomplished that task, albeit with a slight delay (Morrison 1992; Harris et al. 2008). Based upon 8 years of US Government sensor observations of 300 meteoroids, Brown et al. (2002) derived the cumulative number of impacts per year (N) as a function of energy (E) as $N = 3.7E^{-0.9}$, where energy is in units of kt. Silber et al. (2009) derived the flux rates using records of infrasound observations of large bolides by AFTAC during the 14 year period in the 1960s and the early 1970s. Their flux rate was predominantly higher than that derived by Brown et al. (2002). Utilizing a much longer time period, Brown et al. (2013) recently revised the flux rates at larger meteoroid sizes (>6 m) to arrive to higher flux rates ($N = (3.31 \pm 0.11)E^{-(0.68\pm0.06)}$), which are consistent with those found by Silber et al. (2009) ($N = 4.5E^{-0.6}$).

Boslough et al. (2015) published updated population and risk assessment for NEOs, which suggests that the rate of decameter-sized impacts is several times greater than previously thought. According to Boslough et al. (2015), NEOs in the size range of tens of metres are too abundant and too small to be appropriately counted via optical means, but too scarce for statistically meaningful bolide counting. Consequently, the uncertainty of the impact rate at these sizes remains high, despite the fact that they are a significant fraction of the residual impact risk from undetected NEOs.

The IMS network enables continuous monitoring and characterization of bolide events over areas where other observational methodologies are limited. Both seismic and infrasound observations are invaluable tools, and as such might be utilized in refining the flux rates in the future. In particular, well-established bolide influx rates at metre-sizes from US Government sensor data (Brown et al. 2013) may provide a baseline rate to estimate the sensitivity of the IMS network through direct comparison with raw IMS bolide detection rates. The main limitation, however, is the non-unique infrasound waveforms from bolides. In general, infrasound-only bolide detections can only be identified statistically, through isolation of non-repeating events in isolated areas (e.g. over the oceans) where large atmospheric explosions are generally unlikely.

31.5.2 Characteristics of NEOs

Better constraints on the strength and composition of NEOs are important for assessing their potential of penetrating deep into the atmosphere and the likelihood of ground damage. Even if the bulk of an object itself does not reach the ground, an atmospheric airburst may deposit sufficient energy deep in the atmosphere to cause a strong air blast as exemplified by the spectacular events over Tunguska in 1908 and more recently, Chelyabinsk in 2013. Depending on the entry angle of a bolide, as well as its size, velocity, density and composition, the resulting shock wave reaching the ground may be strong enough to cause ground damage, though the exact energy deposition height limits remain unclear (Shuvalov et al. 2015; Aftosims et al. 2016). The strength and fragmentation behaviour also affect the height at which energy is deposited and the efficiency of infrasonic production, with acoustic efficiency generally increasing at lower heights (ReVelle 2005).

At the high end of the strength spectrum are monolithic, generally large bulk density asteroids, usually composed of iron. While larger meteoroids of iron composition are very rare (3–5% of all observed falls), they are frequently found associated with smaller impact craters (Shuvalov et al. 2016a). This is because for metre-sized iron impactors, the column of atmosphere encountered during atmospheric passage is smaller than the mass of the original meteoroid and hence, in the absence of fragmentation, the object reaches the ground with much of its original speed. A notable example of such impact is the Sikhote-Alin iron meteorite shower, which fell on the Sikhote-Alin Mountains in southeastern Russia on 12 February

1947 during daytime. The meteoroid experienced several gross fragmentation episodes (at altitudes of 58, 34, 16 and 6 km) during its descent through the atmosphere (Nemtchinov and Popova 1997) and showered the surface with thousands of fragments, the largest of which impacted at several km/s (Svettsov 1998). The fireball was accompanied by loud detonations, producing many small impact craters, the largest being 27 m in diameter (Krinov 1963; Murdin 2000).

At the opposite end of the spectrum are weak rubble-pile objects (see Richardson et al. 2002 for a description of the expected continuum in strength/structure of NEOs), including rare metre-sized cometary objects (Brown et al. 2016). Most of these objects break up at high altitude and only small fragments survive as meteorites to the ground. However, these objects can produce an airburst and if they penetrate sufficiently deep could cause ground damage. The Tunguska event, which flattened 2000 km^2 of forest, was produced by an impactor 30–50 m in diameter which fragmented several atmospheric scale heights above the ground (e.g. Hills and Goda 1998), though it was not necessarily unusually weak for a stony object. For comparison, an iron asteroid of similar size would impact the ground with all its energy and produce a crater ~1 km in diameter, similar in scale to the Barringer Crater in Arizona (Barringer 1928; Shoemaker 1959; Bjork 1961; Kring 2007).

In their recent study, Brown et al. (2016) analysed the orbits and ablation characteristics of 59 metre-scale impacting NEOs (with median impact energy of 0.4 kt). They found that the majority of the impactors are of asteroidal origin and most originate in the inner asteroid belt. This is contrary to earlier work which suggested that metre to tens of metre-sized NEOs impacting the Earth's atmosphere are of cometary origin (Ceplecha 1994). The impact velocity distribution of the metre-sized NEOs is shifted towards lower values consistent with their asteroidal origins and models of NEO delivery to Earth which predict mean impact speeds of ~20 km/s (Chesley and Spahr 2004). They also noted that the peak energy deposition (presumed to be coincident with the altitude of peak brightness) fell between 20 and 40 km altitude. This provides a good height range for the expected source altitudes for large bolide infrasound production.

While physical characteristics of most of NEOs, as determined from their reflectance spectra in space, are consistent with linkage to stony/chondritic meteorites (Binzel et al. 2015), the overall strength of these bodies determined by their height of fragmentation (0.1–1 MPa; Popova et al. 2011) is on the lower end of the laboratory measurements of meteorite compressive strengths (Petrovic 2001). Our modern picture of NEOs is weak agglomerations of chondritic-like boulders and dust riddled with cracks due to repeated collisions in space that fragment under low aerodynamic ram pressures high in the atmosphere and experience significant mass loss in the form of dust (e.g. Borovička et al. 2013; Popova et al. 2013). Chelyabinsk, for example, underwent maximum catastrophic fragmentation at an altitude of about 30 km, by which time about 95% of the initial mass ablated and transformed mainly into dust and a small fraction of meteorites (Borovička et al. 2013, 2015).

Generally, due to heavy attenuation, infrasound generated by meteors at high altitudes (>90 km) is extremely rare (McIntosh et al. 1976; ReVelle and Whitaker 1999). Deep penetrating fireballs and bolides are much more likely to produce infrasound detectable at the ground. While infrasound from high altitude rocket tests was reported by Cotten and Donn (1971), such observations for meteors were largely absent until nearly a decade ago. Unambiguous infrasound signals from high altitude and high-velocity meteors were first documented by Brown et al. (2007) in relation to four fireballs, three of which were associated with major meteor showers (Leonids and Perseids). Recently, Silber and Brown (2014) found that nearly 10% of the centimetre-sized meteoroid population they observed via infrasound generated shocks at altitudes of ~100 km, indicating that infrasound originating at such altitudes may be more common than previously thought. In their infrasound analyses of regional centimetre-sized fireballs, a lower bound of 1% of all optically detected regional centimetre-sized meteors have associated airwaves detectable at the ground.

31.6 Applications of Infrasound Monitoring

31.6.1 NASA Fireball and Bolide Database

The JPL/NASA Near-Earth Object Program was established with the aim to '*co-ordinate NASA-sponsored efforts to detect, track and characterize potentially hazardous asteroids and comets that could approach the Earth*' (http://www.neo.jpl.nasa.gov/faq/). One of the reporting aspects of this programme is the summary of bolides observed by the US Government (USG) sensors. Currently, the USG sensor database includes over 340 detected events from 1988 until the present (2017). While data are not reported in real time, recent bolide events are occasionally posted within a day or less of having occurred. For each reported fireball, the list features the following information: date, time, geographic location, altitude at peak brightness, pre-impact velocity components (in a geocentric Earth-fixed reference frame), the total radiated energy and the total impact energy (http://www.neo.jpl.nasa.gov/fireball/). This database is a valuable resource for it can be used as a cue to search for possible infrasound signals from large bolides.

31.6.2 Current IMS NEO Detection Efficiency

There is an ongoing effort to improve the identification of valid signals and optimize the detection threshold for the IMS (Mialle et al. 2019; Le Pichon et al. 2019). Detections automatically registered by the IMS are included in the daily Standard Event List (SEL) of the International Data Centre (IDC) of the CTBTO. If these detections are reviewed and updated, the events built upon the association and

localization of infrasonic wave arrivals are subsequently included in the Reviewed Event Bulletin (REB).

The 2014 AA NEO impact (discussed in more detail in Sect. 31.6.3) was one of the events that were registered and identified automatically by the IMS as part of SEL level 3 and subsequently revised to include an additional station (IS51) and a more constrained solution as part of REB. The main reason for not initially including the third station in SEL was the fact that the signal was very weak and required manual verification (Chesley et al. 2015; Farnocchia et al. 2016).

Brown et al. (2014) carried out a survey to determine how well REB captures the bolide events detected by the IMS network during the first 7 months of the calendar year 2014. This time segment was chosen as US Government bolides had been fully reported in this interval at the time of the study. A total of 16 bolides were reported in this interval (http://neo.jpl.nasa.gov/fireballs/) having energies above 0.1 kt. From this early analysis, Brown et al. (2014) determined that the IMS system was able to identify approximately 25% of fireballs with $E > 0.1$ kt (TNT equivalent) energy. Fully 75% of these events were detectable on at least one IMS station. The apparently large difference in automated vs. manual detection rate stems from the way the signal arrivals are being screened and identified as viable events (arrival-quality probability, probability detection tests used by the IMS) and the need for more than one infrasound station for automated detection. Only 25% of these events went completely undetected. Interestingly, among this undetectable population was a 1.3 kt bolide off the coast of Ecuador on March 18, 2014. This shows that kiloton-class atmospheric detonations remain undetectable to the IMS at certain locations and times of the year, a result predicted earlier in modelling of the IMS efficiency (Green and Bowers 2010).

31.6.3 Case Studies

Table 31.8 lists several notable recent NEO impacts for which the infrasound observations were instrumental in characterization of the source. A brief overview of these events is presented below.

Table 31.8 The list of recent notable NEO impacts where the associated bolide was detected by the IMS infrasound network. Detected a priori indicates the discovery of the NEO by telescopic surveys in the hours or day before impact

Event date	Location	Number of detecting IMS stations	Yield (kT TNT equivalent)	Notable characteristics
15 Sep 2007	Carancas, Peru	2	0.002–0.003	Formed a crater
7 Oct 2008	Nubian Desert, Sudan	1	1.6	Detected a priori
2 Jan 2014	The Atlantic Ocean	3	0.4–0.7	Detected a priori

Near noon local time on 15 September 2007, a crater-forming meteorite fall occurred in the Carancas area, Peru. The meteoroid entered at the velocity of ~12 km/s, slowing down to 1.5–4 km/s before impacting the surface and producing the 13.5 m diameter crater (Brown et al. 2008; Tancredi et al. 2009). The event, observed by a number of witnesses, was accompanied by a dust cloud, bright light and loud detonations. Coincidentally, infrasound signals were picked up by the two closest infrasound stations (IS08 and IS41) of the IMS network (Brown et al. 2008), and several seismic stations (Le Pichon et al. 2008). Conditions for forming an impact crater were favourable in two respects: first, the high altitude of the impact site contributed to a higher impact speed than it would have been at the sea level. Second, the stony impactor was coherent and high strength; therefore, very little in-atmosphere fragmentation occurred. The energy released by the creation of the impact crater was estimated at ~2–3 tonnes of TNT equivalent. This event has often served as a means for improving and validating hypersonic entry and long-range atmospheric propagation numerical models (e.g. Millet and Haynes 2010; Haynes and Millet 2013; Henneton et al. 2015), though the trajectory remains only crudely estimated and the speed was not measured.

To date, only two successful cases exist of telescopic NEO surveys detecting a small object prior to impact (Chelsey et al. 2015). Such exoatmospheric detections are of great scientific value as they permit linkage of telescopically derived properties for an NEO (e.g. spectral reflectance characteristics, spin rate, size) with bolide properties (fragmentation, light and shock production) and may result in meteorite recovery.

The first and most studied documented case of a small asteroid detected prior to the impact was 2008 TC_3. It was discovered via ground-based telescopes as a part of Catalina Sky Survey (Kowalski et al. 2008) only 19 h before entering the Earth's atmosphere on 7 October 2008, and falling above the Nubian Desert in Northern Sudan (Jenniskens et al. 2009). The coordinated campaign before and after the impact using visual, infrared and infrasound observations resulted in accurate prediction of the fall location and excellent characterization of the event as a whole, including the impactor taxonomic type and pre-impact tumbling rate (Borovička 2008; Jenniskens et al. 2009; Harris 2008; Scheirich et al. 2010; Kozubal et al. 2011). Additionally, a collection of hundreds of meteorites (Shaddad et al. 2010; Jenniskens and Shaddad 2010) completed this first-ever 'reverse' asteroid sample return mission.

Almost 5 years after detecting the 2008 TC_3 impact, on 1 January 2014, the telescopic observations as a part of the Catalina Sky Survey (Kowalski et al. 2014) once again led to the discovery of a small asteroid, approximately 2–4 m in diameter, bound for the Earth. By the time the asteroid, designated 2014 AA, was recognized as an impactor, it had already collided with the Earth (Chesley et al. 2015; Farnocchia et al. 2016). Another complication was the fact that the impact occurred over the Atlantic Ocean, meaning there were no witnesses or methods of meaningful observations. However, this is exactly where infrasonic observations of meteoritic events play an instrumental role. The analysis of an airwave detected by three stations (IS51, IS08 and IS09) of the IMS infrasound network produced an

approximate geolocation (Chesley et al. 2015), thereby providing a key constraint needed to compute the likely pre-impact orbit for 2014 AA (Farnocchia et al. 2016).

31.7 Early-Warning System and the Future Role of the IMS Network in Global Bolide Detections

Based on the rate of re-detections, the estimated number of NEOs with diameters of 10, 30 and 50 m is approximately 100 million, 3 million and 500,000, respectively (Harris et al. 2015). The corresponding average interval between impacts is roughly once per decade, once per century and once per millennium. The NASA Near-Earth Object Science Definition Team report and the George E. Brown, Jr. Near-Earth Object Survey Act (law passed by the U.S. Congress in 2005) call for finding 90% of all NEOs with diameters >140 m by 2020. As a result, ground-based NEO surveys have proliferated and the rate of NEO discoveries continues to rise.

Unique among currently funded surveys is The Asteroid Terrestrial-impact Last Alert System (ATLAS). This survey is designed as an early-warning system consisting of two observatories located approximately 100 km apart, with the primary goal of detecting small NEOs just prior to an impact and provide advance warning for potentially hazardous NEOs (Tonry 2011). As designed, the system is predicted to provide one day's warning for a 30 kt impact, a week warning for a 5 MT impact (50 m diameter) and three weeks for a 100 MT (150 m diameter) impact. The instruments scan the visible sky two or more times a night and look for moving objects by comparing the data between the successive scans. One of the observatories (Haleakala, Hawaii) is fully operational, with the second (Mauna Loa, Hawaii) expected to come online in late 2016. The plans include up to eight small observatories (Harris et al. 2015). As of March 2016, ATLAS has already discovered seven NEOs that now have official designations with the Minor Planet Center, with diameters ranging from 30 m up to 650 m (http://blog.fallingstar.com/).

Another ground-based initiative, currently under development in El Peñón, Chile, is the Large Synoptic Survey Telescope (LSST). LSST is an observatory featuring a wide field of view (9.6°) design and the world's largest digital camera (3.2 gigapixels), with the aim to perform a dynamic survey of the universe over the period of 10 years (Tyson 2002; Ivezic et al. 2008). It is expected to come online in 2022, with the capability to image the entire visible sky every few nights and map out objects far (e.g. stars and galaxies) and near (asteroids).

As ATLAS and LSST begin discovering NEOs just prior to impact on a regular basis, the IMS infrasound network will provide key ground-based confirmation of the impact and ancillary data, notably total yield. This is particularly significant as most impacts will occur over the ocean where no other instruments are likely to record the bolide.

References

Aftosmis MJ, Nemec M, Mathias D, Berger M (2016) Numerical simulation of bolide entry with ground footprint prediction. In: 54th AIAA Aerospace sciences meeting. American Institute of Aeronautics and Astronautics, Reston, VA, pp 1–18. https://doi.org/10.2514/6.2016-0998

Anderson J (2006) Hypersonic and high-temperature gas dynamics, 2nd Ed. AIAA Education Series

Barringer DM Jr (1928) A new meteor crater. In: Proceedings of the academy of natural sciences of Philadelphia, 307–311

Bass HE (1972) Atmospheric absorption of sound: analytical expressions. J Acoust Soc Am 52:821–825

Beer T (1974) Atmospheric waves. Halsted Press, Adam Hilger, Ltd, New York, London, 315 pp

Binzel RP, Reddy V, Dunn T (2015) The Near-Earth object population: connections to Comets, Main-Belt Asteroids, and Meteorites. In: Michel P et al. (ed), Asteroids IV. University of Arizona Press, pp 243–256. https://doi.org/10.2458/azu_uapress_9780816532131-ch013

Bjork RL (1961) Analysis of the formation of Meteor Crater, Arizona: a preliminary report. J Geophys Res 66(10):3379–3387

Blanc E, Perez S, Issartel JP, Millies-Lacroix JC (1997) Detection of nuclear explosions in the atmosphere. Chocs 23–34

Borovička (2008) Event reported on IAU circular 8994, central bureau of astronomical telegrams. Smithsonian Astrophysical Observatory, Cambridge, MA, 8 Oct 2008

Borovička J (1993) A fireball spectrum analysis. Astron Astrophys 279:627–645

Borovička J, Spurný P, Brown P (2015) Small near-Earth asteroids as a source of meteorites. Asteroids IV, 257

Borovička J, Spurný P, Brown P, Wiegert P, Kalenda P, Clark D, Shrbený L (2013) The trajectory, structure and origin of the Chelyabinsk asteroidal impactor. Nature 503(7475):235–237

Boslough MBE, Crawford DA (2008) Low-altitude airbursts and the impact threat. Int J Impact Eng 35(12):1441–1448

Boslough M, Brown P, Harris A (2015) Updated population and risk assessment for airbursts from near-Earth objects (NEOs). In: 2015 IEEE aerospace conference. IEEE, pp 1–12

Bowell E, Muinonen K (1994) Earth-crossing asteroids and comets: groundbased search strategies. In: T Gehrels (ed) Hazards due to Comets and Asteroids, pp 149–197

Boyd ID (1998) Computation of atmospheric entry flow about a Leonid meteoroid. Earth Moon Planet 82:93–108. https://doi.org/10.1023/A:1017042404484

Briani G, Pupillo G, Aiello S, Pace E, Shore S, Passaro A (2007) Study of the interaction of micrometeoroids with Earth's atmosphere. Memorie della Societa Astronomica Italiana Supplementi 11:89

Bronshten VA (1964) Problems of the movements of large meteoric bodies in the atmosphere. National Aeronautics and Space Administration, TT-F-247

Bronshten VA (1983) Physics of Meteoric Phenomena. 372 pp. D. Reidel, Dordrecht, Netherlands

Brown PG, Assink JD, Astiz L, Blaauw R, Boslough MB, Borovička J, 26 co-authors (2013) A 500-kiloton airburst over Chelyabinsk and an enhanced hazard from small impactors. Nature 503:238–241. https://doi.org/10.1038/nature12741

Brown PG, Dube K, Silber E (2014) Detecting NEO impacts using the international monitoring system. In AAS/Division for planetary sciences meeting abstracts, vol 46

Brown PG, Spalding RE, ReVelle DO, Tagliaferri E, Worden SP (2002) The flux of small near-Earth objects colliding with the Earth. Nature 420:294–296. https://doi.org/10.1038/nature01238

Brown P, McCausland PJA, Fries M, Silber E, Edwards WN, Wong DK, Weryk RJ, Fries J, Krzeminski Z (2011) The fall of the Grimsby meteorite—I: fireball dynamics and orbit from radar, video, and infrasound records. Meteor Planet Sci 46(3):339–363

Brown P, ReVelle DO, Silber EA, Edwards WN, Arrowsmith S, Jackson LE, Tancredi G, Eaton D (2008) Analysis of a crater-forming meteorite impact in Peru. J Geophys Res Planets 113(E9)

Brown P, Weryk RJ, Kohut S, Edwards WN, Krzeminski Z (2010) Development of an all-sky video meteor network in Southern Ontario, Canada the ASGARD system. WGN J Int Meteor Organ 38:25–30

Brown P, Wiegert P, Clark D, Tagliaferri E (2016) Orbital and physical characteristics of meter-scale impactors from airburst observations. Icarus 266:96–111

Brown PG, Edwards WN, ReVelle DO, Spurny P (2007) Acoustic analysis of shock production by very high-altitude meteors—I: infrasonic observations, dynamics and luminosity. J Atmos Solar Terr Phys 69:600–620. https://doi.org/10.1016/j.jastp.2006.10.011

Buratti BJ, Johnson LL (2003) Identification of the lunar flash of 1953 with a fresh crater on the Moon's surface. Icarus 161(1):192–197

Campbell-Brown MD, Koschny D (2004) Model of the ablation of faint meteors. Astron Astrophys-Berl Then Les Ulis 418(2):751–758

Carlson HW, Maglieri DJ (1972) Review of sonic-boom generation theory and prediction methods. J Acoust Soc Am 51:675

Ceplecha Z (1994) Impacts of meteoroids larger than 1 m into the Earth's Atmosphere. Astron Astrophys 286:967–970

Ceplecha Z, Revelle DO (2005) Fragmentation model of meteoroid motion, mass loss, and radiation in the atmosphere. Meteor Planet Sci 40(1):35–54. https://doi.org/10.1111/j.1945-5100.2005.tb00363.x

Ceplecha Z, Borovička J, Elford WG, ReVelle DO, Hawkes RL, Porubčan V, Šimek M (1998) Meteor phenomena and bodies. Space Sci Rev 84(3–4):327–471

Ceplecha Z, Borovička J, Spurný P (2000) Dynamical behavior of meteoroids in the atmosphere derived from very precise photographic records. Astron Astrophys 357:1115–1122

Ceplecha Z, Spurny P, Borovička J, Keclikova J (1993) Atmospheric fragmentation of meteoriods. Astron Astrophys 279:615–626

Chapman CR, Morrison D (1994) Impacts on the Earth by asteroids and comets: assessing the hazard. Nature 367(6458):33–40

Chesley SR, Farnocchia D, Brown PG, Chodas PW (2015) Orbit estimation for late warning asteroid impacts: The case of 2014 AA. In: Aerospace conference, 2015 IEEE. IEEE, pp 1–8

Chesley SR, Spahr TB (2004) Earth-impactors: Orbital characteristics and warning times. In: Belton MJS, Morgan TH, Samarashinha NH, Yeomans DK (eds) Mitigation of hazardous Comets and Asteroids. Cambridge University Press, Cambridge, pp 22–37

Christie DR, Campus P (2010) The IMS infrasound network: design and establishment of infrasound stations. In: Le Pichon A, Blanc E, Hauchecorne A (eds) Infrasound monitoring for atmospheric studies. Springer, New York, pp 29–75. https://doi.org/10.1007/978-1-4020-9508-5_2

Chyba CF, Thomas PJ, Zahnle KJ (1993) The 1908 Tunguska explosion: atmospheric disruption of a stony asteroid. Nature 361(6407):40–44

Clauter DA, Blandford RR (1998) Capability modeling of the proposed international monitoring system 60-station infrasonic network. Technical report LAUR-98-56. Los Alamos National Labs, Los Alamos, New Mexico

Collins GS, Melosh HJ, Marcus RA (2005) Earth impact effects program: a web-based computer program for calculating the regional environmental consequences of a meteoroid impact on Earth. Meteor Planet Sci 40(6):817–840

Cook RK, Bedard AJ Jr (1972) On the measurement of Infrasound Q. J R Astron Soc 67:5–11

Cotten D, Donn WL (1971) Sound from Apollo rockets in space. Science 171(3971):565–567

de Groot-Hedlin CD, Hedlin MA, Drob DP (2010) Atmospheric variability and infrasound monitoring. In: Infrasound monitoring for atmospheric studies. Springer, Netherlands, pp 475–507

de Groot-Hedlin C, Hedlin M (2014) USArray recordings of infrasound generated by the Chelyabinsk Meteor and other, smaller bolides. In: EGU general assembly conference abstracts, vol 16, p 8823

Donn WL, Rind D (1971) Natural infrasound as an atmospheric probe. Geophys J R Astron Soc 26 (1–4):111–133

Drob DP, Picone JM, Garcés M (2003) Global morphology of infrasound propagation. J Geophys Res Atmos (1984–2012), 108(D21)
DuMond JW, Cohen ER, Panofsky WKH, Deeds E (1946) A determination of the wave forms and laws of propagation and dissipation of ballistic shock waves. J Acoust Soc Am 18:97
Edwards WN (2007) Meteoroid kinetic energy estimation using infrasonic and seismic observations of meteor generated sound. PhD. Thesis, University of Western Ontario, Department of Earth Sciences
Edwards WN, Brown PG, Weryk RJ, ReVelle DO (2008) Infrasonic observations of meteoroids: preliminary results from a coordinated optical-radar-infrasound observing campaign. Earth, Moon, and Planets 102(1–4):221–229. https://doi.org/10.1007/s11038-007-9154-6
Edwards WN (2010) Meteor generated infrasound: theory and observation. Infrasound monitoring for atmospheric studies. Springer, Netherlands, pp 361–414. https://doi.org/10.1007/978-1-4020-9508-5_12
Emanuel G (2000) Theory of shock waves, in handbook of shock waves. In: Ben-Dor G, Igra O, Elperin T (eds) Three volume set. Academic Press
Ens TA, Brown PG, Edwards WN, Silber EA (2012) Infrasound production by bolides: A global statistical study. J Atmos Solar Terr Phys 80:208–229. https://doi.org/10.1016/j.jastp.2012.01.018
Evans LB, Bass HE, Sutherland LC (1972) Atmospheric absorption of sound: theoretical predictions. J Acoust Soc Am 51:1565
Evers LG, Haak HW (2003) Tracing a meteoric trajectory with infrasound. Geophy Res Lett 30 (24):1–4
Evers LG, Haak HW (2010) The characteristics of infrasound, its propagation and some early history. Infrasound monitoring for atmospheric studies. Springer, Netherlands, pp 3–27
Farnocchia D, Chesley SR, Brown PG, Chodas PW (2016) The trajectory and atmospheric impact of asteroid 2014 AA. Icarus 274:327–333
Few AA (1969) Power spectrum of thunder. J Geophys Res 74:6926–6934. https://doi.org/10.1029/JC074i028p06926
Gardner CS, Hostetler CA, Franke SJ (1993) Gravity wave models for the horizontal wave number spectra of atmospheric velocity and density fluctuations. J Geophys Res 98(D1):1035–1049
Georges TM, Beasley WH (1977) Refraction of infrasound by upper-atmospheric winds. J Acoust Soc Am 61:28
Glasstone S, Dolan PJ (1977) The Effects of Nuclear Weapons. United States Department of Defense and Department of Energy, Washington, DC, USA
Golden P, Herrin ET, Negraru PT (2007) Infrasound in the zone of silence. In: Proceedings of the European geophysical union, Vienna, Apr 2007
Green DN, Bowers D (2010) Estimating the detection capability of the International Monitoring System infrasound network. J Geophys Res: Atmos 115(D18)
Green DN, Vergoz J, Gibson R, Le Pichon A, Ceranna L (2011) Infrasound radiated by the Gerdec and Chelopechene explosions: propagation along unexpected paths. Geophys J Int 185(2):890–910
Groves GV (1963) Initial expansion to ambient pressure of chemical explosive releases in the upper atmosphere. J Geophys Res 68(10):3033–3047
Halliday I, Blackwell AT, Griffin A (1978) The Innisfree meteorite and the Canadian camera network. R Astron Soc Can J 72:15–39. http://adsabs.harvard.edu/full/1978JRASC..72…15H
Harris A (2008) What spaceguard did. Nature 453(7199):1178–1179
Harris AW, Boslough M, Chapman CR, Drube L, Michel P (2015) Asteroid impacts and modern civilization: can we prevent a catastrophe?. Asteroids IV 835–854
Harris AW, D'Abramo G (2015) The population of near-Earth asteroids. Icarus 257:302–312
Hayes W, Probstein RF (1959) Hypersonic flow theory, vol 5. Elsevier
Haynes CP, Millet C (2013) A sensitivity analysis of meteoric infrasound. J Geophys Res Planets 118(10):2073–2082. https://doi.org/10.1002/jgre.20116
Henneton M, Gainville O, Coulouvrat F (2015) Numerical simulation of sonic boom from hypersonic meteoroids. AIAA J 53(9):2560–2570. https://doi.org/10.2514/1.J053421

Herrin ET, Golden PW, Negraru PT, McKenna MH (2007) Infrasound in the zone of silence, proceedings of the 29th monitoring research review: ground-based nuclear explosion monitoring technologies. Denver, CO, pp 25–27, Sep 2007
Hills JG, Goda MP (1998) Damage from the impacts of small asteroids. Planet Space Science 46 (2–3):219–229
Hunt JN, Palmer R, Penney W (1960) Atmospheric waves caused by large explosions. Philos Trans R Soc Lond A 252(1011):275–315
Ivezic Z, Tyson JA, Abel B, Acosta E, Allsman R, AlSayyad Y, Anderson SF et al (2008) LSST: from science drivers to reference design and anticipated data products. arXiv:0805.2366
Jedicke R, Granvik M, Micheli M, Ryan E, Spahr T, Yeomans DK (2015) Surveys, astrometric follow-up and population statistics. In: Michel P et al (ed) Asteroids IV. University of Arizona Press, pp 795–813. https://doi.org/10.2458/azu_uapress_9780816532131-ch040
Jenniskens P et al (2009) The impact and recovery of asteroid 2008 TC3. Nature 458(7237):485–488
Jenniskens P, Shaddad MH (2010) 2008 TC3: the small asteroid with an impact. Meteor Planet Sci 45(10–11):1553–1556
Jones DL, Goyer GG, Plooster MN (1968) Shock wave from a lightning discharge. J Geophys Res 73:3121–3127
Keay CS (1980) Anomalous sounds from the entry of meteor fireballs. Science 210(4465):11–15
Keay CSL, Ceplecha Z (1994) Rate of observation of electrophonic meteor fireballs. J Geophys Res Planets (1991–2012), 99(E6):13163–13165
Kinney GF, Graham KJ (1985) Explosive shocks in air, vol 282. Springer, Berlin, New York, p 1
Kowalski RA et al (2008) Minor Planet Electron Circ 2008-T50
Kowalski RA et al (2014) Minor Planet Electron Circ 2014-A02
Kozubal MJ, Gasdia FW, Dantowitz RF, Scheirich P, Harris AW (2011) Photometric observations of Earth-impacting asteroid 2008 TC3. Meteor Planet Sci 46(4):534–542
Kraemer DR (1977) Infrasound from accurately measured meteor trails, PhD thesis Michigan Univ, Ann Arbor, MI, USA
Krehl P (2001) History of shock waves. In: Ben-Dor G et al (ed) Handbook of shock waves, vol 1. Academic Press, New York, pp 1–142
Krehl PO (2009) History of shock waves, explosions and impact: a chronological and biographical reference. Springer
Kring DA (2007) Guidebook to the geology of barringer meteorite crater, arizona (aka Meteor Crater). Lunar and Planetary Institute, Houston
Krinov EL (1963) The Tunguska and Sikhote-Alin meteorites. Moon Meteor Comets 1:208
Krinov EL (1966) Giant meteorites. Translated from the Russian by JS Romankiewicz. Translation edited by MM Beynon, 1. Oxford, New York, Pergamon Press [1966][1st English ed]
Kulichkov S (2010) On the prospects for acoustic sounding of the fine structure of the middle atmosphere. Infrasound monitoring for atmospheric studies. Springer, Netherlands, pp 511–540
Landau LD (1945) On shock waves at a large distance from the place of their origin. Sov J Phys 9:496
Le Pichon A, Ceranna L, Vergoz J, Tailpied D (2019) Modeling the detection capability of the global IMS infrasound network. In: Le Pichon A, Blanc E, Hauchecorne A (eds) Infrasound monitoring for atmospheric studies, 2nd edn. Springer, Dordrecht, pp 593–604
Le Pichon A, Antier K, Cansi Y, Hernandez B, Minaya E, Burgoa B, Drob D, Evers LG, Vaubaillon J (2008) Evidence for a meteoritic origin of the September 15, 2007, Carancas crater. Meteor Planet Sc 43(11):1797–1809
Lin SC (1954) Cylindrical shock waves produced by instantaneous energy release. J Appl Phys 25:54–57. https://doi.org/10.1063/1.1721520
Maglieri DJ, Plotkin KJ (1991) Sonic boom. In Aeroacoustics of flight vehicles: theory and practice. Volume 1: noise sources, vol 1, pp 519–561

Malin MC, Edgett KS, Posiolova LV, McColley SM, Dobrea EZN (2006) Present-day impact cratering rate and contemporary gully activity on Mars. Science 314(5805):1573–1577
Marsh DR, Janches D, Feng W, Plane J (2013) A global model of meteoric sodium. J Geophys Res Atmos 118(19):11–442
Marty J (2019) The IMS infrasound network: currentstatus and technological developments. In: Le Pichon A, Blanc E, Hauchecorne A (eds) Infrasound monitoring for atmospheric studies, 2nd edn. Springer, Dordrecht, pp 3–62
Mathias DL, Robertson DK, Aftosmis MJ (2015) Sensitivity of ground damage predictions to meteoroid breakup modeling assumptions, IAA-PDC-15-05-04. In: 4th IAA planetary defense conference—PDC 2015, 13–17 Apr 2015, Frascati, Roma, Italy
McCrosky RE, Boeschenstein H (1965) The prairie meteorite network. Smithsonian Astrophysical Observatory special report 173:1–26
McIntosh BA, Watson MD, ReVelle DO (1976) Infrasound from a radar-observed meteor. Can J Phys 54(6):655–662
McKinley DWR (1961) Meteor science and engineering. McGraw-Hill Inc., New York, NY
McKisic JM (1997) Infrasound and the infrasonic monitoring of atmospheric nuclear explosions: a literature review. Final report PL-TR-97-2123. Department of Energy and Phillips Laboratory, National Technical Information Service, p 310
Mersenne M (1636) Harmonie universelle; translate Chapman R: (1957). The books on instruments. Nijhoff, The Hague
Mialle P, Brown D, Arora N, colleagues from IDC (2019) Advances in operational processing at the international data centre. In: Le Pichon A, Blanc E, Hauchecorne A (eds) Infrasound monitoring for atmospheric studies, 2nd edn. Springer, Dordrecht, pp 209–248
Millet C, Haynes CP (2010) Stochastic model approach of meteor-generated infrasound. AIAA Paper, 7999
Morrison D (1992) The spaceguard survey: report of the NASA international Near-Earth-Object detection workshop
Morse PM, Ingard KU (1968) Theoretical acoustics. McGraw-Hill, New York
Murdin P (2000) Sikhote Alin Meteorite. Encycl Astron Astrophys 1:5379
Mutschlecner JP, Whitaker RW (2010) Some atmospheric effects on infrasound signal amplitudes. Infrasound monitoring for atmospheric studies. Springer, Netherlands, pp 455–474
Mutschlecner JP, Whitaker R, Auer LH (1999) An empirical study of infrasonic propagation. Technical report LA-13620-MS. Los Alamos National Lab, Los Alamos, NM
Needham CE (2010) Blast waves, shock wave and high pressure phenomena. Springer, pp 339
Nemtchinov IV, Popova OP (1997) An analysis of the 1947 Sikhote-Alin event and a comparison with the phenomenon of February 1, 1994. Sol Syst Res 31:408
Nemtchinov IV, Shuvalov VV, Artem'eva NA, Ivanov BA, Kosarev IB, Trubetskaya IA (1998) Light flashes caused by meteoroid impacts on the lunar surface. Sol Syst Res 32:99
Norris D, Gibson R (2001) InfraMAP propagation modeling enhancements and the study of recent bolide events. In: 23rd Seismic research review: worldwide monitoring of nuclear explosions. Jackson Hole, Wyoming
Norris D, Gibson R, Bongiovanni K (2010) Numerical methods to model infrasonic propagation through realistic specifications of the atmosphere. Infrasound monitoring for atmospheric studies. Springer, Netherlands, pp 541–573
O'Keefe JD, Ahrens TJ (1982) Impact mechanics of the Cretaceous-Tertiary extinction bolide. Nature 298(5870):123–127
Öpik EJ (1958) Physics of meteor flight in the atmosphere. Interscience Publishers, New York 1958:1
Ortiz JL, Quesada JA, Aceituno J, Aceituno FJ, Rubio LB (2002) Observation and interpretation of Leonid impact flashes on the Moon in 2001. Astrophys J 576(1):567
Pan YS, Sotomayer WA (1972) Sonic boom of hypersonic vehicles. AIAA J 10:550–551
Peitgen H, Saupe D (eds) (1998) The science of fractal images. Springer
Petrovic JJ (2001) Mechanical properties of meteorites. J Mater Sci 36:1579–1583

Pierce AD, Kinney WA (1976) Computational techniques for the study of infrasound propagation in the atmosphere. Georgia institute of technology Atlanta school of mechanical engineering
Pierce AD, Posey JW (1971) Theory of the excitation and propagation of Lamb's atmospheric edge mode from nuclear explosions. Geophys J Roy Astron Soc 26(1–4):341–368
Pierce AD, Thomas C (1969) Atmospheric correction factor for sonic-boom pressure amplitudes. J Acoust Soc Am 46:1366–1380
Pilger C, Cerana L, Le Pichon A, Borwn P (2019) Large meteoroids as global infrasound reference events. In: Le Pichon A, Blanc E, Hauchecorne A (eds) Infrasound monitoring for atmospheric studies, 2nd edn. Springer, Dordrecht, pp 451–470
Pilger C, Ceranna L, Ross JO, Le Pichon A, Mialle P, Garcés MA (2015) CTBT infrasound network performance to detect the 2013 Russian fireball event. Geophys Res Lett 42(7):2523–2531
Plooster MN (1968) Shock Waves from Line Sources, National Center for Atmospheric Research, Report TN, pp 1–93
Plooster MN (1970) Shock waves from line sources, numerical solutions and experimental measurements. Phys Fluids 13:2665. https://doi.org/10.1063/1.1692848
Plotkin, K. (1989) Review of sonic boom theory. In: AAIA 12th aeronautics conference, 10–12 Apr 1989, San Antonio, TX, USA
Popova O (2005) Meteoroid ablation models. Earth Moon Planet 95(1–4):303–319
Popova O, Borovička J, Hartmann WK, Spurný P, Gnos E, Nemtchinov I, Trigo-Rodríguez JM (2011) Very low strengths of interplanetary meteoroids and small asteroids. Meteorit Planet Sci 46(10):1525–1550
Popova OP, Jenniskens P, Emel'yanenko V, Kartashova A, Biryukov E, Khaibrakhmanov S et al (2013) Chelyabinsk airburst, damage assessment, meteorite recovery, and characterization. Science 342(6162):1069–1073. https://doi.org/10.1126/science.1242642
Popova OP, Sidneva SN, Strelkov AS, Shuvalov VV (2001) Formation of disturbed area around fast meteor body. In: Meteoroids 2001 conference, vol 495, pp 237–245
Reed JW (1972) Airblast overpressure decay at long ranges. J Geophys Res 77:1623–1629
ReVelle DO (1974) Acoustics of meteors-effects of the atmospheric temperature and wind structure on the sounds produced by meteors. PhD thesis Michigan Univ, Ann Arbor MI, USA
ReVelle DO (1997) Historical detection of atmospheric impacts by large bolides using acoustic-gravity waves. Ann N Y Acad Sci 822(1):284–302
ReVelle DO (1976) On meteor-generated infrasound. J Geophys Res 81(7):1217–1230
ReVelle DO (2001) Theoretical leonid modelling. Barbara Warmbein (ed) Proceedings of the Meteoroids 2001 Conference, 6–10 August 2001, Kiruna, Sweden. ESA SP-495. Noordwijk, ESA Publications Division, ISBN 92-9092-805-0, 2001, pp 149–154
ReVelle DO (2005) Recent advances in bolide entry modeling: a bolide potpourri. Earth, Moon, and Planets 95(1–4):441–476
ReVelle DO, Whitaker RW (1999) Infrasonic detection of a Leonid bolide: 1998 November 17. Meteor Planet Sci 34(6):995–1005
Richardson DC, Leinhardt ZM, Melosh HJ, Bottke WF Jr, Asphaug E (2002) Gravitational aggregates: evidence and evolution. Asteroids III 1:501–515
Rind D, Donn WL (1975) Further use of natural infrasound as a continuous monitor of the upper atmosphere. J Atmos Sci 32:1694–1704
Romig MF (1965) Physics of meteor entry. AIAA J 3(3):385–394
Sachdev PL (2004) Shock waves & explosions. CRC Press
Sakurai A (1964) Blast wave theory, report no. MRC-TSR-497, Wisconsin Univ-Madison Mathematics Research Center, USA
Scheirich P et al (2010) The shape and rotation of asteroid 2008 TC3. Meteor Planet Sci 45(10–11):1804–1811
Sedov LI (1946) Propagation of intense blast waves. Prikl Mat Mekh 10:241–250

Shaddad MH et al (2010) The recovery of asteroid 2008 TC3. Meteor Planet Sci 45(10–11):1557–1589
Shaw WN, Dines WH (1905) The study of the minor fluctuations of atmospheric pressure. Q J R Meteorol Soc 31(133):39–52
Shoemaker EM (1959) Impact mechanics at Meteor crater, Arizona (No 59–108). US Geological Survey
Shoemaker EM, Lowery CJ (1967) Airwaves associated with large fireballs and the frequency distribution of energy of meteoroids. Meteoritics 3:123–124
Shuvalov VV, Popova OP, Svettsov VV, Kovalev RM, Lipnitsky YM, Meshcheryakov SA A global approach to Near-Earth object impact threat mitigation, contract # FP7-SPACE-2011-282703
Shuvalov VV, Popova OP, Svettsov VV, Kovalev RM, Lipnitsky YM, Meshcheryakov SA (2012) NEO shield: a global approach to Near-Earth object impact threat mitigation: atmospheric trajectory analysis and ground-damage limitation
Shuvalov VV, Popova OP, Svettsov VV, Trubetskaya IA, Glazachev DO (2016a) Determination of the height of the "meteoric explosion". Sol Syst Res 50(1):1–12
Shuvalov V, Svetsov V, Popova OP, Glazachev D (2016b) Numerical model of the Chelyabinsk meteoroid as a strengthless object. Meteoroids 2016
Silber EA (2014) Observational and theoretical investigation of cylindrical line source blast theory using meteors, Electronic Thesis and Dissertation Repository. Paper 2112. http://www.ir.lib.uwo.ca/etd/2112
Silber EA, Brown PG (2014) Optical observations of meteors generating infrasound—I: acoustic signal identification and phenomenology. J Atmos Sol Terr Phys 119:116–128
Silber EA, Brown PG, Krzeminski Z (2015) Optical observations of meteors generating infrasound: weak shock theory and validation. J Geophys Res Planets 120(3):413–428
Silber EA, Le Pichon A, Brown P (2011) Infrasonic detection of a near-earth object impact over Indonesia on 8 October, 2009. Geophys Res Lett 38:L12201
Silber EA, ReVelle DO, Brown PG, Edwards WN (2009) An estimate of the terrestrial influx of large meteoroids from infrasonic measurements. J Geophys Res Planets (1991–2012), 114(E8)
Stevens JL, Divnov II, Adams DA, Murphy JR, Bourchik VN (2002) Constraints on infrasound scaling and attenuation relations from Soviet explosion data. Pure appl Geophys 159(5):1045–1062
Sutherland LC, Bass HE (2004) Atmospheric absorption in the atmosphere up to 160 km. J Acoust Soc Am 115:1012. https://doi.org/10.1121/1.1631937
Svettsov VV (1998) Enigmas of the Sikhote Alin crater field. Sol Syst Res 32:67
Tancredi G, Ishitsuka J, Schultz PH, Harris RS, Brown P, Revelle DO, Antier K, Pichon AL, Rosales D, Vidal E, Varela ME (2009) A meteorite crater on Earth formed on September 15, 2007: the carancas hypervelocity impact. Meteor Planet Sci 44(12):1967–1984
Taylor G (1950) The formation of a blast wave by a very intense explosion. I. Theoretical discussion. Proc R Soc Lond A 201(1065):159–174
Tolstoy I (1973) Wave propagation. McGraw-Hill, New York, NY, USA, p 466
Tonry JL (2011) An early warning system for asteroid impact. Publ Astron Soc Pac 123(899):58
Toon OB, Zahnle K, Morrison D, Turco RP, Covey C (1997) Environmental perturbations caused by the impacts of asteroids and Comets. Ann N Y Acad Sci 822 (1 near-earth ob):401. https://doi.org/10.1111/j.1749-6632.1997.tb48357.x
Towne DH (1967) Wave phenomena. Addison-Wesley Publications, Reading, MA, USA
Tricarico P (2016) The near-Earth asteroids population from two decades of observations. arXiv:1604.06328
Trigo-Rodriguez JM, Llorca J, Borovička J, Fabregat J (2003) Chemical abundances determined from meteor spectra: I Ratios of the main chemical elements. Meteor Planet Sci 38(8):1283–1294

Tsikulin MA (1970) Shock waves during the movement of large meteorites in the atmosphere, Report no NIC-Trans-3148, Naval Intelligence Command Alexandria, VA Translation Div, USA

Tyson JA (2002) Large synoptic survey telescope: overview. In: Astronomical telescopes and instrumentation. International Society for Optics and Photonics, pp 10–20

Vondrak T, Plane JMC, Broadley S, Janches D (2008) A chemical model of meteoric ablation. Atmos Chem Phys 8(23):7015–7031

Werner MW, Roellig TL, Low FJ, Rieke GH, Rieke M, Hoffmann WF, Young E, Houck JR, Brandl B, Fazio GG, Hora JL (2004) The spitzer space telescope mission. Astrophys J Suppl Ser 154(1):1

Weryk RJ, Brown PG (2013) Simultaneous radar and video meteors-II: Photometry and ionisation. Planet Space Sci

Weryk RJ, Brown PG, Domokos A, Edwards WN, Krzeminski Z, Nudds SH, Welch DL (2008) The Southern Ontario all-sky meteor camera network. Earth Moon Planet 102(1–4):241–246

Wetherill GW, ReVelle DO (1981) Which fireballs are meteorites? A study of the prairie network photographic meteor data. Icarus 48(2):308–328

Whipple FJW (1930) The great siberian meteor, and the waves, seismic and aerial, which it produces

Whitham GB (1952) The flow pattern of a supersonic projectile. Commun Pure Appl Math 5 (3):301–348

Willmore AP (1970) Electron and ion temperatures in the ionosphere. Space Sci Rev 11(5):607–670

Wright EL, Eisenhardt PR, Mainzer AK, Ressler ME, Cutri RM, Jarrett T, Kirkpatrick JD, Padgett D, McMillan RS, Skrutskie M, Stanford SA (2010) The wide-field infrared survey explorer (WISE): mission description and initial on-orbit performance. Astron J 140(6):1868

Wright WM (1983) Propagation in air of N waves produced by sparks. J Acoust Soc Am 73:1948

Wylie CC (1932) Sounds from meteors. Popular Astron 40:289

Yuldashev P, Ollivier S, Averiyanov M, Sapozhnikov O, Khokhlova V, Blanc-Benon P (2010) Nonlinear propagation of spark-generated N-waves in air: modeling and measurements using acoustical and optical methods. J Acoust Soc Am 128:3321

Zinn J, Judd ODP, ReVelle DO (2004) Leonid meteor ablation, energy exchange, and trail morphology. Adv Space Res 33(9):1466–1474

Part XI
Benefits for Monitoring Natural Hazards: Infrasound Monitoring of On-going Volcanic Eruptions

Chapter 32
Local Volcano Infrasound Monitoring

Jeffrey Johnson

Abstract Infrasound monitoring is employed to enhance understanding of eruption dynamics and to track eruptive activity over time. Local infrasound, where sensors are positioned near to and/or on the flanks of volcanoes, implies that sound transmission from vent to receiver is approximately line-of-sight. Typical assumptions are that pressure decays as the inverse of distance and that attenuation and dispersion effects are minimal. Locally recorded signals thus represent relatively undistorted source time motions and can be used to effectively characterize volcanic activity. Local monitoring can entail a spectrum of installation topologies including single isolated sensors on a volcano, networks of sensors, a single array, or networks of sensor arrays. Stations may be installed as standalone or in telemetered configurations depending upon available resources and research objectives, which may range from simple explosion counting to degassing detection, mapping of vents, or identification of moving sources. Some of these objectives are only possible using arrays. Quantifying volcano infrasound, in terms of both spectral shape, power, and signal envelope, is relatively straightforward using data recorded at local distances. Despite inter-network variability, influenced by potential source directivity, propagation effects, and/or site response, the local infrasound records permit good estimation of total acoustic energy, identification of dominant spectral tones, and signal morphology. These parameters may be robustly compared at a volcano over time and/or compared to other volcanoes. Ultimately, infrasound analysis permits remote surveillance of activity occurring at the vent (or on the slopes) of a volcano that may otherwise be difficult to observe.

J. Johnson (✉)
Department of Geosciences, Boise State University, Boise, ID 83725, USA
e-mail: jeffreybjohnson@boisestate.edu

A. Le Pichon et al. (eds.), *Infrasound Monitoring for Atmospheric Studies*,
https://doi.org/10.1007/978-3-319-75140-5_32

32.1 Introduction

Volcano infrasound overviews have been published in the form of book chapters and review papers in the last few years. Johnson and Ripepe (2011) provided a summary of volcano infrasound literature and summarized general capabilities of volcano infrasound surveillance. Fee and Matoza (2013) concentrated their review article on regional and global eruption detection capabilities and discussed a diversity of eruption types observed using infrasound monitoring. Both Arrowsmith et al. (2010) and McNutt et al. (2015) discussed the monitoring of volcanoes using integrated seismic and infrasound techniques. This book includes five chapters focused principally on volcano infrasound study including regional and global monitoring of volcanoes using the International Monitoring System network (Matoza et al. 2019), infrasound monitoring for civil authorities (Ripepe and Marchetti 2019), and the relations between ash eruption detection and infrasound monitoring (Taisne et al. 2019; Marchetti et al. 2019).

This chapter focuses on *local* (or proximal) monitoring of infrasound produced by volcanic phenomena. Local monitoring should be considered as complementary to more remote infrasound monitoring as each has its own distinct benefits. In brief, local monitoring has the advantage that recorded signal is more representative of source processes because effects of long-distance atmospheric transmission, including multi-pathing, geometric focusing (or de-focusing), and intrinsic attenuation, are minimal. Targeted local study of a volcano using sensors positioned near to, and/or on, the flanks of the volcano provides enhanced capability to identify minor activity and to locate and track sources with precision. Data from local deployments facilitate the detection and study of very small signal transients and low-amplitude tremor, which may not be energetic enough to propagate to distant recording sites. Conversely, regional, or global infrasound data are used to identify activity over a wide geographic domain (or arc) and can be very effective at tracking activity at volcanoes, which are either remote, too expensive to monitor locally, and/or where activity is not anticipated (e.g., Matoza et al. 2010; Dabrowa et al. 2011).

This chapter is divided into three principal sections focused on: infrasound source detection and localization (Sect. 32.2), propagation effects (Sect. 32.3), and techniques to quantify infrasound (Sect. 32.4). Example data and analyses are presented from three volcanoes, Sakurajima (Japan), Stromboli (Italy), and Villarrica (Chile), which are *open-vent* systems. Open-vent activity implies degassing, lava effusion, and/or explosions, which tend to generate prodigious sound in the infrasound band centered around ~1 Hz (e.g., Johnson et al. 2003). The case studies introduced here showcase a range of deployment topologies and a spectrum of volcanic activities, from violent Vulcanian explosions at Sakurajima, to frequent smaller scale Strombolian activity, to continuous degassing from a roiling lava lake at Villarrica (Table 32.1). The examples are chosen to illustrate routine processing that can be implemented to study eruptive processes, identify surface activity, and help understand the influence of local propagation effects.

Table 32.1 The three volcanoes featured in this chapter. All data were collected using infraBSU broadband pressure sensors, similar to infraNMT sensors (Marcillo et al. 2012), which possess a flat calibrated response above 0.05 Hz. Photos of these volcanoes and sensor deployment maps are given in Fig. 32.1

Volcano	Activity	Data presented	Analysis
Sakurajima (Japan)	Episodic vulcanian-style explosions, ash and gas venting from a single active crater	Continuous recordings made in July 2013 from an array located 4.1 km from the active vent	Two and three-element arrays are used to detect explosions and subtle vent-sourced infrasound associated with degassing
Stromboli (Italy)	Strombolian-style activity and continuous degassing from multiple vents	Continuous recordings from June 2016 from a two-station network including an integrated array and a single sensor	Precise vent localization is performed for a complex source region, containing multiple active vents
Villarrica (Chile)	Lava lake degassing	Long-duration (5 month) recordings in 2015 from a ten-station distributed network of arrays and short (week-long) recording from 2016 using a single near-source and three distant arrays	Moving sources are located and atmospheric and topographic effects are assessed

32.2 Identifying and Locating Volcanic Activity with Infrasound

Volcano seismic signals are produced from sources located both internal to a volcano and from sources occurring at a volcano's surface. Volcano infrasound, on the other hand, is generated principally by surface events, including explosions, vent degassing, ash-venting, rapid distension of solid material at the vent, and gravity-driven flow phenomena. Although intense volcano explosions can often be observed with seismic networks, which respond to ground-coupled airwaves (e.g., Fee et al. 2016; Johnson and Malone 2007), the detection and localization of smaller surface events is most effectively accomplished with dedicated infrasound instrumentation. Local infrasound study, involving arrays and/or networks of sensors, is ideally suited for detection of open-vent degassing, precision location of surface activity, and detection and tracking of moving flows. This section focuses on these applications using case studies from Sakurajima, Stromboli, and Villarrica.

32.2.1 Detection of Local Volcano Infrasound (Example: Sakurajima)

Detection of volcano infrasound, including those signals associated with both large explosions and from lower energy, open-vent degassing, is most effectively conducted using arrays of two or more sensors. Infrasound arrays are generally defined

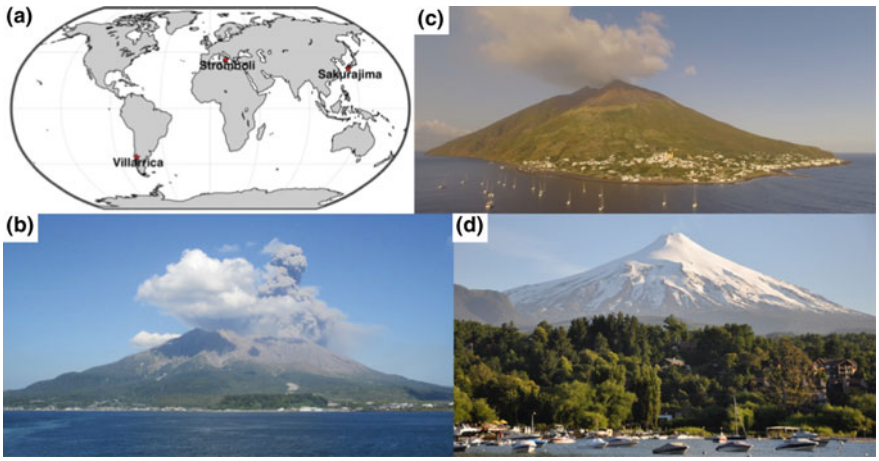

Fig. 32.1 **a** Locator map of featured volcano field sites. **b**, **c**, **d** Photos of Sakurajima, Stromboli, and Villarrica from ~4 km, ~7 km, and ~17 km respectively. Detailed volcano maps with deployment details are provided in Figs. 32.2, 32.6, and 32.9

as three or more pressure sensors distributed in a configuration whose aperture is far smaller than the propagation distance between the source and the array. The size of an infrasound array may be hundreds to thousands of meters and is generally tuned to the expected wavelength of the incident infrasound. For volcano studies in which sensors are located on the slopes of a restless volcano (e.g., Sakurajima; Fig. 32.2) sensors are often spaced with only a few tens of meters of separation because (1) a primary objective is simply to determine whether and when an active vent is producing infrasound and (2) smaller sized arrays are simpler to install and maintain. Observatories, for instance, are interested in determining when degassing is ongoing, comparing surface activity to other observables (such as seismic data), and/or counting explosions. For situations where vent location is well known, the expected lag times for infrasound crossing an array's elements can be estimated. Expected lag times are calculated from array elements' relative positions $\overrightarrow{\Delta d}_{ij}$ and expected propagation direction defined by the *slowness* vector, whose amplitude is the reciprocal of sound speed, $|\vec{s}| = 1/c$. Generally, sound speed varies less than ~5% for a broad range of ambient temperatures, i.e., $c = 332$ m/s at 0° and 349 m/s at 30 °C. For a plane wave traveling in the direction of the slowness vector (e.g., Fig. 32.2b) the time lag between channel i and j will be

$$\Delta t_{ij} = \frac{\hat{s} \cdot \Delta \vec{d}_{ij}}{c}$$

Detections are made when correlated energy crosses the array elements with lag times that are anticipated for a volcano's vent position.

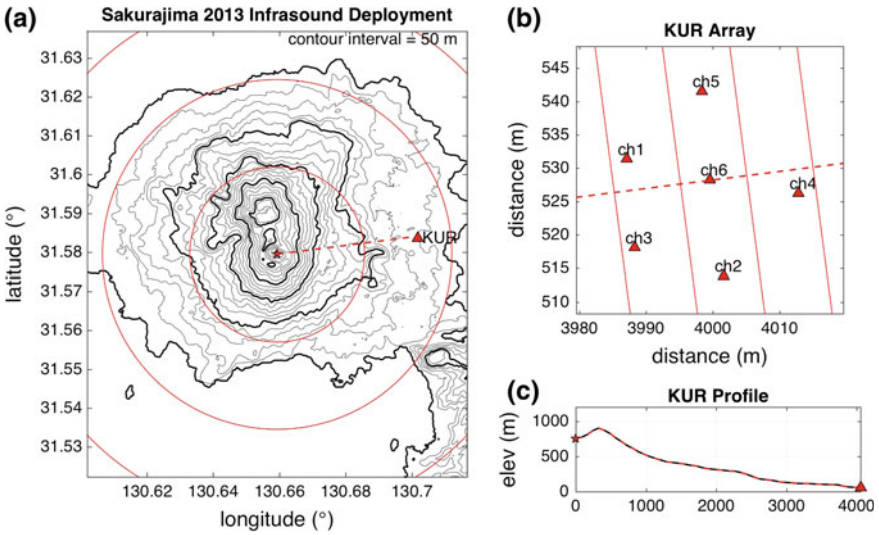

Fig. 32.2 **a** Map of 2013 infrasound deployment at Sakurajima (Japan) showing **b** detail of the Kurokami (KUR) array site and **c** topographic profile between Showa vent and KUR array. Horizontal distances are indicated as 2.5, 5.0, and 7.5 km circles in (**a**). Wavefronts in **b** are drawn 10 m apart and perpendicular to a slowness vector $\vec{s}$ corresponding to vent-sourced infrasound. Data from channels 1, 2, and 3 are analyzed for signal detection

Volcano source detection using a single sensor has limited utility because volcano signal is often visually or spectrally indistinguishable from noise. Although some explosion signals may be identifiable based upon a characteristic appearance, e.g., an impulsive, high-amplitude, short-duration bipolar pulse (Fig. 32.3c), the identification of many volcano infrasound signals is ambiguous based solely on waveform shape. Low-amplitude explosion pulses can be obscured in noise and sustained infrasound *tremor*, which may appear similar to wind-induced noise. Time series data from a single channel of infrasound, and its spectrograms, highlight the complexity in differentiating signal from noise. Figure 32.3 shows a 6-hour record acquired 4.1 km from Sakurajima's intermittently open vent. Featured data have been digitally filtered between 0.25 and 20 Hz and correspond to small pyroclastic-laden explosions, alternating with sustained gas and ash emissions, and periods of time when the vent appears to be temporarily sealed.

The Sakurajima infrasound record in Fig. 32.3 shows fluctuating levels of tremor punctuated by a few short-duration, relatively high-amplitude pulses. Detailed examination of the pulses (e.g., at 0.82 h) reveals bipolar explosion-type waveforms, consisting of an initial impulsive, high-amplitude compression followed by rarefaction (Fig. 32.3c). Although this type of signal is easily recognizable as a volcanic explosion, other time periods correspond to less obvious signal. For example, the low-amplitude ($\sim 10^{-1}$ Pa) sustained signal centered at 0.84 h (Fig. 32.3b) might be mistaken for wind noise. Spectral analysis of this tremor is

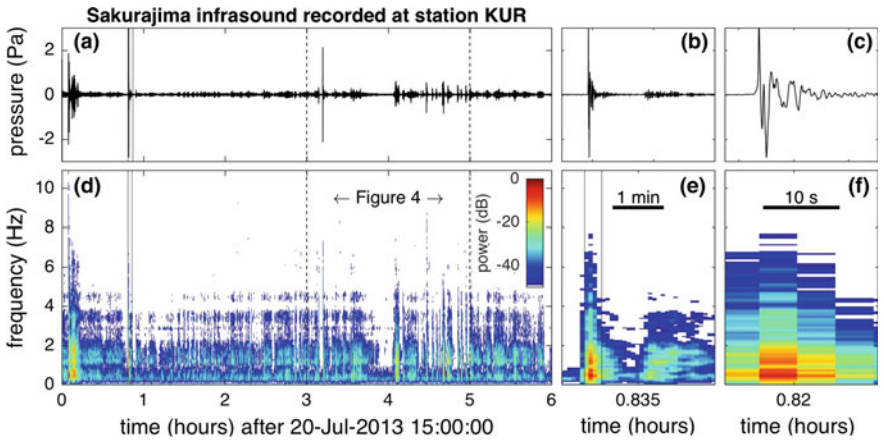

Fig. 32.3 **a** 6-h record **b** 3-min detail, and **c** 20-s detail of 0.25–20 Hz infrasound recorded 4.1 km from the active crater. **d**, **e**, **f** Spectrograms are calculated for 10-s windows with 5-s overlap. The indicated time period between hours 3 and 5 is analyzed in Fig. 32.4

insufficient to definitively distinguish whether it is signal or noise as wind is often prevalent in volcanic environments and typically possesses a broad spectrum that overlaps with (1–10 Hz) volcano infrasound.

Array deployments are practical to distinguish infrasound signal from noise and as few as two sensors separated by just a few meters may be sufficient to differentiate volcano signal from other pressure disturbances. An efficient technique to identify vent-sourced infrasound is to construct a *correlogram*, which is a graphical representation of normalized cross-correlation functions calculated for a sliding time window (e.g., Fig. 32.4b, d, f). The number of inter-array cross-correlation pairs is given as $n(n-1)/2$ for an n channel array. A correlogram quickly illustrates two primary attributes: (1) whether energy crossing the array is correlated, and (2) whether the delay in cross-correlation lag time is consistent with a source originating from a known volcanic source.

Using the array geometry of Fig. 32.2b, expected inter-array lag times for Sakurajima's Showa Crater may be computed as $\Delta t_{21} = 0.03\,\text{s}, \Delta t_{32} = -0.03\,\text{s}$, and $\Delta t_{13} = 0.00\,\text{s}$. These values can be compared against measured cross-correlation time lags, which are derived from peak values of the cross-correlation functions, $\Delta\tau_{ij}(t) = \arg max\left(p_i(t) \star p_j(t)\right)$. Potential volcano sources are indicated when expected phase delays and calculated lag times are equivalent, such that the root-mean-squared (RMS) time residual is small for all pairs of stations, e.g.,

$$\sqrt{\frac{\sum_{i}^{n}\sum_{j}^{n}\left(\Delta t_{ij} - \Delta\tau_{ij}(t)\right)^2}{n(n-1)/2}} \quad \text{for } j > \text{i}$$

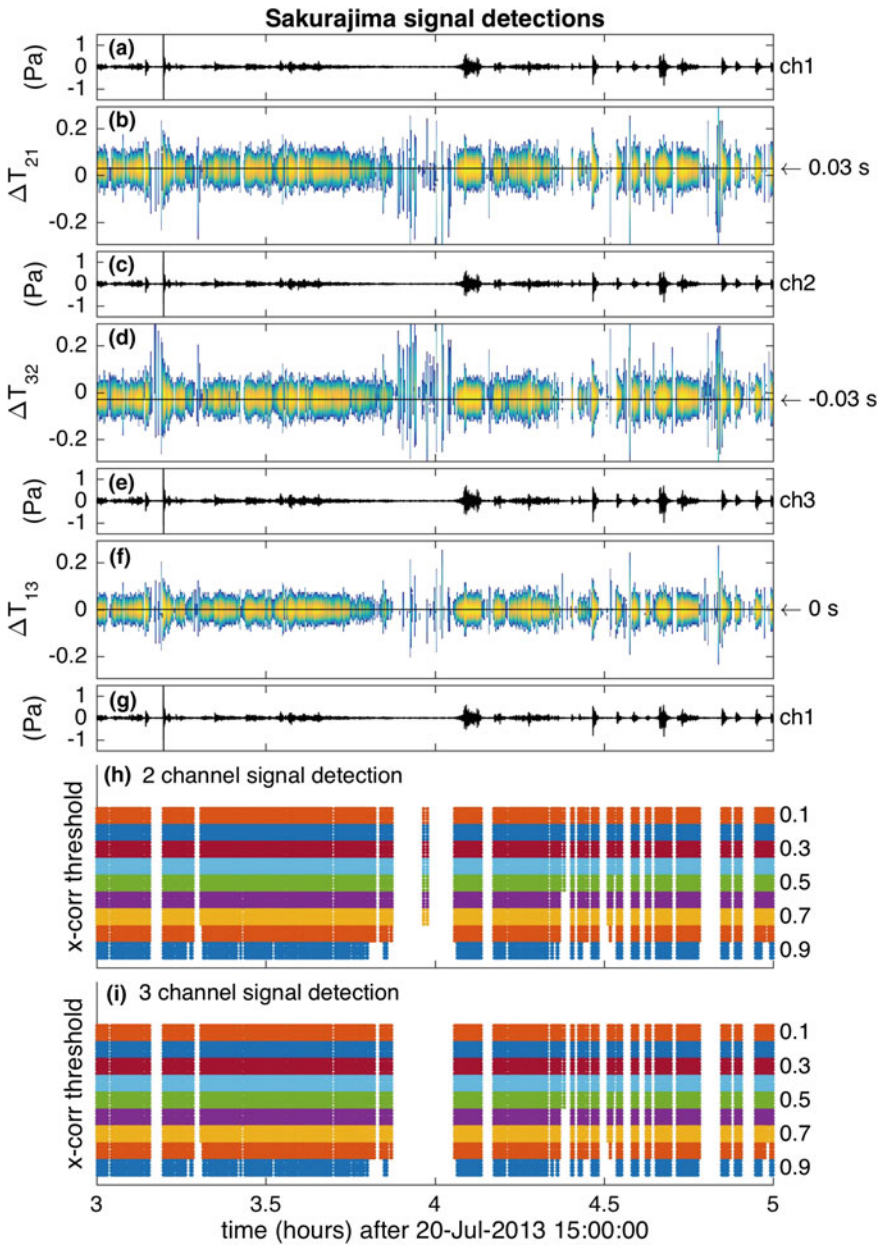

Fig. 32.4 **a**, **c**, **e**, **g** 2-h of infrasound data corresponding to three channels of Sakurajima infrasound. **b**, **d**, **f** Time-varying cross-correlation calculations are computed for these three station pairs using 10-s sliding windows with 5-s overlap. **h**, **i** Volcanic source detections are summarized using single-pair and three-pair consistency verification and for a range of minimum cross-correlation coefficients

For basic volcano monitoring purposes two channels of array data can often be adequate to indicate when infrasound is originating from the direction of the vent. Although beam-stacking from a "two-sensor array" will give two distinct signal back azimuths, it is often enough for one of these back azimuths to be consistent with the known location of a volcano vent. In two-channel array analysis, the minimum criteria for identification of volcano activity is that $\Delta t_{ij} \cong \Delta \tau_{ij}$. In the Sakurajima example of Fig. 32.4h channels 2 and 3 are separated by $\sim 10^1$ m ($\sim$0.03 s) and are used to suggest that the vent region is often producing infrasound. An additional criterion might be that the recordings at both channels are similar in shape, which can be quantified by the normalized cross-correlation peak amplitudes for p_i and p_j. Using a strict cross-correlation threshold of 0.9 the two KUR sensors detect correlated signal 50% of the time. Loosening the normalized correlation threshold criteria to 0.5 and then 0.1, which is reasonable for noise-contaminated recordings, increases detections slightly to 64% and 65% respectively.

Similar results are obtained using three channels, and three-channel pairs, of an array (Fig. 32.4i). Detections during the same 2-h period are 49, 63, and 63% respectively for cross-correlation thresholds of 0.9, 0.5, and 0.1. In this three channel calculation the volcano source detection is defined as the time window when the three station pairs exhibit expected lag times, i.e., $\Delta t_{12} \cong \Delta \tau_{12}, \Delta t_{23} \cong \Delta \tau_{23}, \text{and} \Delta t_{31} \cong \Delta \tau_{31}$. Although it can be argued that more sensors provide important redundancy, the observation that both two-channel and three-channel analyses often yield similar detection totals suggests that two-channel infrasound arrays can be adequate and practical when resources are limited. For example, two-channel detections are summarized in Fig. 32.5 during a 4-day period at Sakurajima and for two different cross-correlation thresholds. Periods when vent-sourced infrasound is absent are clearly indicated by gaps in the detection panels.

Infrasound detection gaps, such as between hour 18.90 and 19.05 on July 20 (Fig. 32.4h, i), can be explained by: (1) high levels of ambient noise, (2) the absence of vent-sourced infrasound, or (3) missed detections due to obfuscating sound arriving from non-vent directions. Although detection of non-vent infrasound may explain some of the periods when Sakurajima signal goes undetected (Yokoo et al. 2014), in most cases the gaps in signal detection coincide with observations that vent activity (degassing) has stopped. Episodic behavior is typical for many open-vent volcanoes, which fluctuate between short-lived violent explosions, semi-continuous ash-venting and degassing, and periods of sealed vent. The periods shown in Figs. 32.4 and 32.5 correspond to alternating intervals of open and closed vents. The observation of closed vents just prior to high-amplitude infrasound explosions supports a hypothesis of intermittent sealing and pressure accumulation preceding many explosions (Garces et al. 1999).

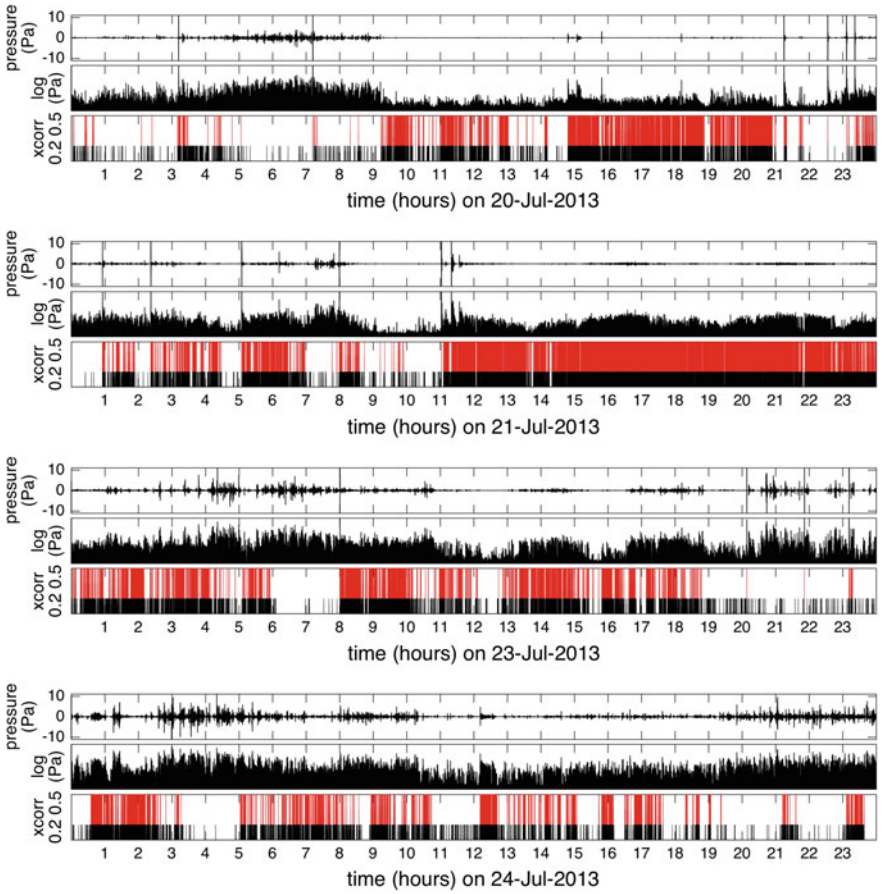

Fig. 32.5 Four days of volcano infrasound signal (top/middle panels) and detections using only two channels of data from the KUR array at Sakurajima. Data are plotted in Pa (top panel) and in absolute log of Pa (middle panel). Red bars indicate inter-channel normalized correlation greater than 0.5 for 10 s overlapping windows and black bars indicate correlation greater than 0.2

32.2.2 Source Localization (Example: Stromboli)

In many situations the location of a volcanic vent is not known precisely and their position(s) can be ephemeral. Network-based techniques for locating volcano infrasound sources including grid searches (McKee et al. 2014; Cannata et al. 2009; Jones et al. 2008; Rowell et al. 2014), inverse location techniques (Rowell et al. 2014), and time-reverse modeling (Kim and Lees 2014) have proven effective for identifying an active vent or crater. Arrays of closely spaced sensors may also be used to identify the back azimuth direction to a volcano vent and have sometimes been used to identify unanticipated volcano sources, such as from lava tube

skylights (Garces et al. 2003). In other cases, such as at Stromboli (Italy), volcanoes may be comprised of multiple closely spaced active vents, and source differentiation has been accomplished using both array and network topologies (Ripepe and Marchetti 2002; Johnson 2005).

Stromboli is a well-studied open-vent volcano featuring regular explosions as well as puffing (gas emissions) from multiple vents distributed within several active near-summit craters. These features span a roughly 200-m terrace, whose morphology varies and evolves over year-long time scales. In the Stromboli study by Johnson (2005) a three-element microphone network at the summit recorded volcano signal, which exhibited variable phase lags across its ~150 m aperture. Cross-correlation analysis was used to quantify delay times for two station pairs, while cross-correlation of the third pair was used to validate "consistency" in which $|\Delta\tau_{12} + \Delta\tau_{23} + \Delta\tau_{31}| \cong 0$. Consistency criterion provides important confirmation that cross-correlation lag times are robust for station triads and may be applied to arrays with three or more sensors (e.g., Cansi 1995). Ripepe and Marchetti (2002) have used arrays at Stromboli to beam stack and identify source back azimuth to illuminate a directional beam where sources of both quasi-continuous (puffing) and discrete (explosion) sources originate. Such infrasound surveillance has been used as a long-term hazard monitoring tool at Stromboli where source locations and infrasound character can be relayed to observatories in near real-time (Ripepe et al. 2007).

Array and network source localization capabilities are illustrated in data from a simple, short-term deployment at Stromboli in May, 2016 (Fig. 32.6). In this experiment a three-element ~30-m array (station NEC) and single-element microphone (station SWC) were situated about 500 m apart on nearly opposite sides of the active crater terrace in order to record the broad spectrum of signals produced by Stromboli. Although its geometry had not been optimized to locate sources, it proved capable for mapping more than four distinct source regions repeatedly active each hour.

Locations of Stromboli sources were determined by comparing both inter-station (within an array) and intra-station time lags and comparing these with expected time lags for sources confined to the surface of Stromboli's summit terrace as defined by

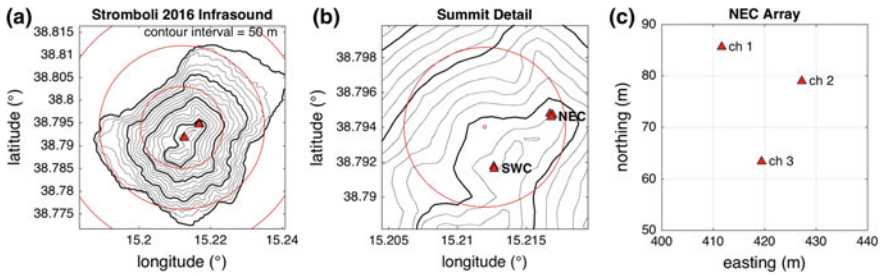

Fig. 32.6 Maps of **a** Stromboli Island, **b** summit area detail, and **c** zoomed-in map of NEC array. Red concentric circles are 1000 m in **a** and 500 m in (**b**)

the ASTER Global Digital Elevation Map (30 m resolution). For each candidate summit terrace location (x_0, y_0, z_0) travel times were estimated as slant distances to the various microphone positions (x_i, y_i, z_i) using a reasonable sound speed of $c = 330$ m/s where

$$t_i = \sqrt{(x_i - x_0)^2 + (y_i - y_0)^2 + (z_i - z_0)^2}/c.$$

Anticipated time delay between sound arriving at any two sensors in the network is then $\Delta t_{ij} = t_j - t_i$ and can be compared with the cross-correlation delay $\Delta\tau_{ij}$ derived from cross-correlation functions for a specific time window. Differences between grid search (synthetic) times and cross-correlation lag times are quantified as *source time residuals* and indicate locales where sources are most probable (Fig. 32.7).

When intra-station data correlation is good a network can provide important constraints on possible infrasound source locations. Source time residuals for the two-station Stromboli network is calculated as $\varepsilon_{N2} = \sqrt{(\Delta t_{01} - \Delta\tau_{01})^2}$ where the subscript 0 indicates the data from the SWC microphone and 1 indicates channel 1 from the NEC array. Candidate sources, where ε_{N2} is minimized, are defined by a paraboloid that intersects the surface of the DEM in a sweeping curve. The lowest residual values mapped in Fig. 32.7d correspond to two different explosion events. Locations of the curved regions are distinct for the two events because cross-correlation lag delays are different. For both events, the 10 ms contour is as narrow as 3 m and corresponds to data cross-correlation error of one sample using a typical 100 Hz sample rate.

For an array of three sensors, such as at NEC, source timing residuals can be quantified as follows:

$$\varepsilon_{A3} = \sqrt{(\Delta t_{12} - \Delta\tau_{12})^2 + (\Delta t_{23} - \Delta\tau_{23})^2 + (\Delta t_{31} - \Delta\tau_{31})^2}.$$

In this case, the timing residual appears as a conical beam that intersects topography and points toward the source (Fig. 32.7e). For the Stromboli ~30 m array the cone's apex angle for 10 ms is about 20°, but improves to ~4° for 2 ms residuals. The aperture of a back azimuth beam is tighter for larger array configurations and for greater precision in cross-correlation time lag resolution. Timing precision may be improved with higher frequency sounds sampled with faster sample rates, however low sample-rate infrasound data may be digitally interpolated to gain time resolution and improve source localization (e.g., Johnson and Ronan 2015; Nakata and Snieder 2011). Compared to the network source location uncertainty the spatial source uncertainty of the array is relatively large. Its value is that cross-correlation between array channels is generally high such that arrays are capable of detecting small amplitude signal.

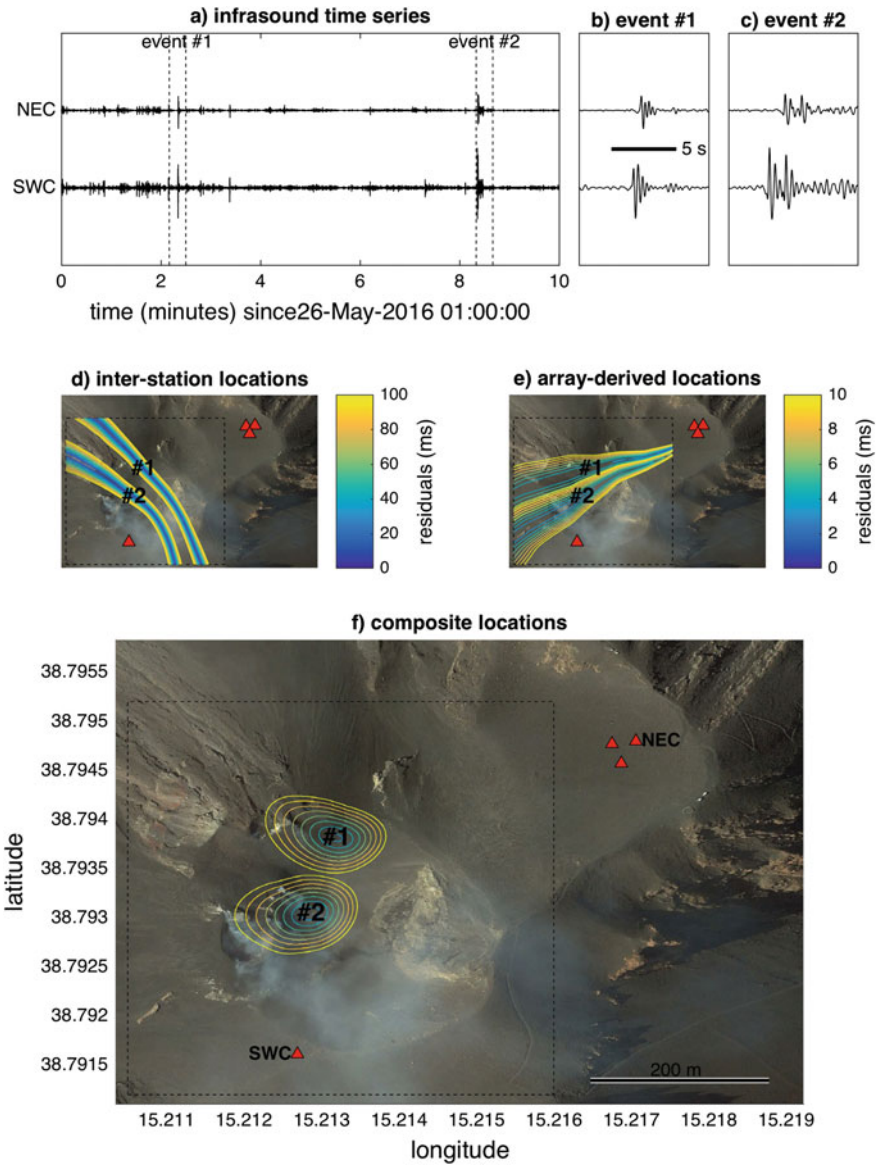

Fig. 32.7 **a** 10-min signals recorded at SWC and NEC (channel 1), and **b**, **c** detail of two distinct explosion events. **d** Source time residual contours ε_{N2} using one channel from each station in the network, and **e** source time residual contours ε_{A3} using the three channels in the NEC array. **f** Composite residuals for the two events using a relative weighting ε_{A3}: $\varepsilon_{N2} = 20{:}1$

The maps of Fig. 32.7d, e may be combined to yield a composite source time residual map, which constrains the source to a single global minimum or source position (Fig. 32.7f). The intersection of composite network and array locations is quantified as $\varepsilon_C = \sqrt{(a\varepsilon_{N2})^2 + (b\varepsilon_{A3})^2}$, where a and b are *weighting constants*. For the deployment geometry at Stromboli the values of a to b are chosen to normalize the ranges of the two independent time residuals. Figure 32.7f shows source locations plotted with a ratio of $b/a = 20$. In this case the array weighting constant is significantly larger than the network constant because the relatively small array dimension leads to large azimuthal uncertainty. Because weighting constants are arbitrary spatial source location errors can not be directly read from the maps.

Figure 32.8 summarizes detections and locations for a 2-hour sequence of Stromboli signals recorded with the four-element, two-station hybrid network.

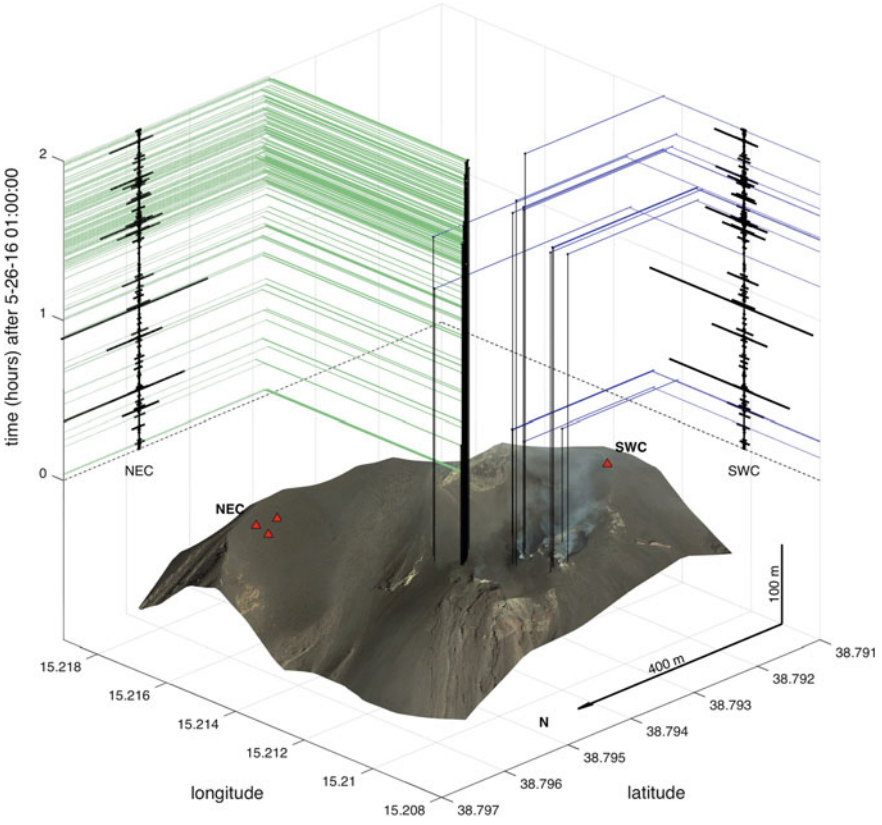

Fig. 32.8 Summit terrace perspective view of 2015 Google Earth imagery draped over an ASTER Global Digital Elevation Map. Infrasound sources are mapped using combined records from the NEC array and SWC sensor during a 2-h period. Infrasound signals from NEC channel #1 and SWC are indicated along vertical axes. Green lines point to sources originating from a frequently exploding and puffing vent, while blue lines indicate several other vents that were active during this period. The first 10 min of the infrasound records correspond to data featured in Fig. 32.7

Locations are indicated graphically as a function of time and include about ten explosions emanating from at least three active vents (blue) in addition to a persistently active source region (green) near the NEC array. It should be noted that sources located in May 2016 correspond to a vent distribution, which was slightly different from the 2015 crater terrace imagery shown in Fig. 32.8.

32.2.3 Localization of Moving Sources (Example: Villarrica)

Identification and tracking of volcanic moving sources, such as pyroclastic flows, rock falls, and lahars, may require infrasound arrays (or multiple arrays) that are strategically located near candidate flow paths. Previous studies have demonstrated the effectiveness of infrasound surveillance to detect and track volcanic flow phenomena, such as lahars (Johnson and Palma 2015), small rockfalls (Johnson and Ronan 2015), or pyroclastic flows (Delle Donne et al. 2014). Because moving sources typically radiate relatively low intensity, higher frequency sound than explosion infrasound, flow signals might not be well registered across all stations in a distributed local network. As an example, the entire network of ten infrasound arrays at Volcan Villarrica (Chile) detected a paroxysmal eruption occurring on March 3, 2015, but only the station VIH (Fig. 32.9) clearly recorded a 3-hour-long lahar that was triggered by the eruption (Johnson and Palma 2015). This array was used to track rapidly moving infrasound sources propagating more than 10 km from the vent in about 5 min. The moving sources were located by mapping lowest source timing residuals within a flow path drainage during successive 10-s analysis windows.

The VIH station was the only array to clearly detect the largest lahar on March 3, however other arrays detected mud flows caused by the same eruption and probably confined to more local drainages. The correlograms from the array at VIC, for example, show signal originating from the summit, but with occasional sound originating from a few other back azimuths. For instance, signal beginning at 6:25 AM in Fig. 32.10 has peak correlation lag times that deviate from the lag times associated with summit infrasound. Gliding lag times, as seen in the correlograms, are indicators of a moving source. In the case of the data shown in Fig. 32.10, these changing lag times were most pronounced when signal was filtered above 10 Hz, which effectively attenuated the low-frequency infrasound produced at Villarrica's summit.

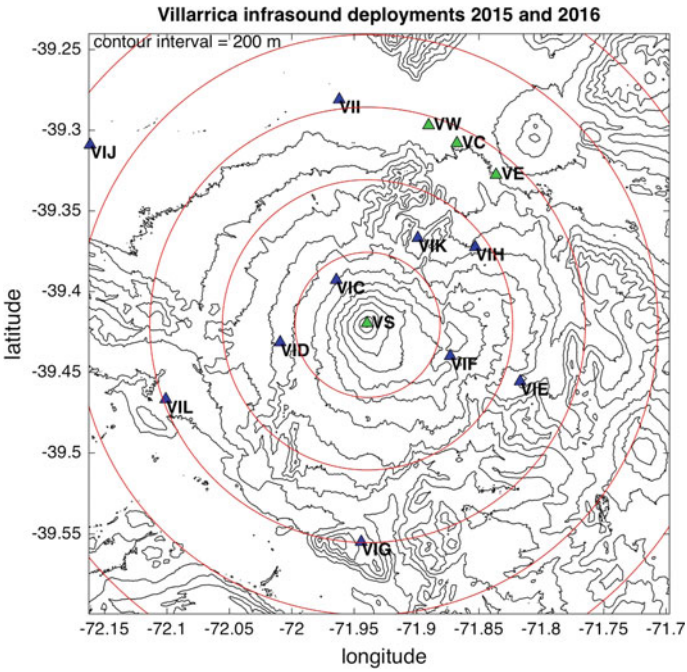

Fig. 32.9 (blue triangles) Ten-station network of infrasound arrays at Volcan Villarrica deployed between January and June 2015 and (green triangles) four-station deployment for a shorter experiment in November 2016. Red concentric circles indicate 5 km radii relative to the summit

Changing lag times are attributed to sound, which crosses a 2-D array with a time-varying slowness vector. For phase delays measured across a three-element array the infrasound slowness vector can be uniquely determined as

$$\vec{s} = \Delta D^{-1} \Delta \mathrm{T},$$

where ΔD^{-1} is the inverse matrix of position vectors Δd_{ij} for $n = 3$ array elements and Δ T is the timing vector comprised of cross-correlation lag times $\Delta\tau_{12}$, $\Delta\tau_{23}$, and $\Delta\tau_{31}$. For a three-element array with consistent timing Δ T can be uniquely defined by two components. Larger arrays with a greater number of intra-channel lag time data can use the generalized inverse as described in Arechiga et al. (2011) to solve for $\vec{s}$.

The slowness vector for a particular time window is converted to back azimuth using $\theta = \tan^{-1}\left(s_x/s_y\right)$ and these directions may be plotted as a time series (Fig. 32.10h). In the Villarrica example the back azimuths initially point to the summit, but show deflections at 06:12-06:16 and 06:26-06:39 as incident energy arrives from SE to N bearings. These directions correspond to a drainage that was

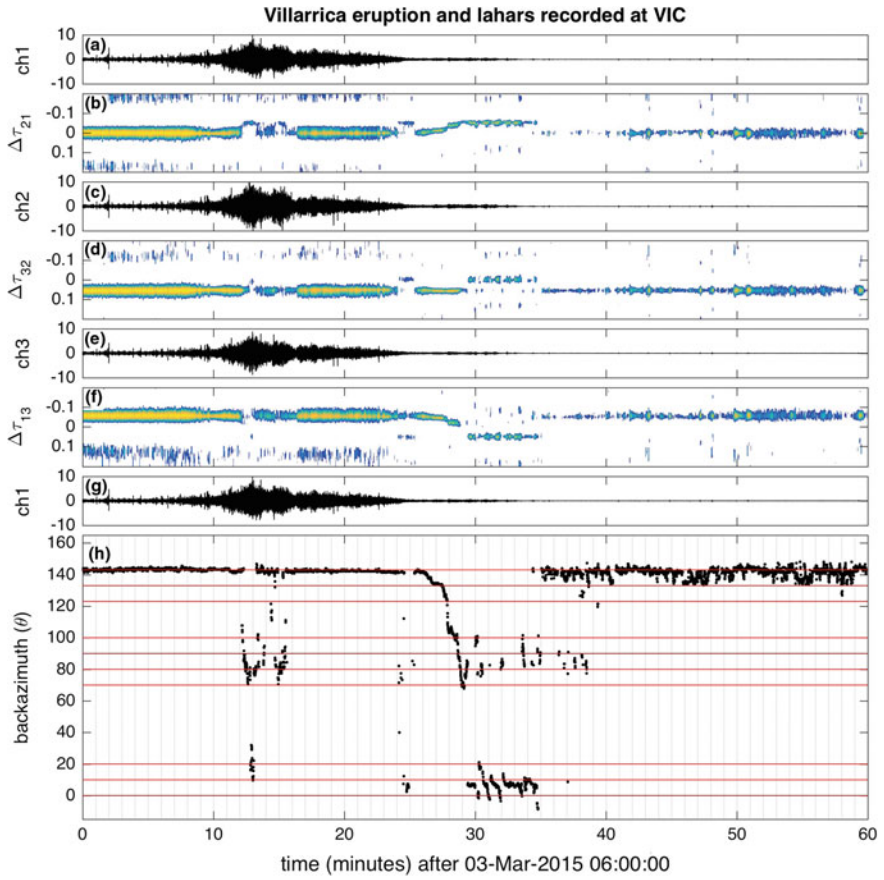

Fig. 32.10 **a**, **c**, **e**, **g** Hour-long infrasound data (in Pa) recorded at VIC channels 1, 2, and 3 and filtered between 10 Hz and Nyquist (~50 Hz). **b**, **d**, **f** Correlograms showing the evolution in lag time (in s) of maximally correlated signals between channels 1, 2, and 3. Cross-correlation functions are computed for moving 10 s windows with 5 s overlap and maximum lag delays of 0.2 s. **h** Array-computed back azimuths changing over time. Select back azimuths that are indicated by horizontal blue lines are shown in the Fig. 32.11 map

known to convey several small lahars on the night of March 3rd, 2015. Between 06:30 and 06:35, for example, the back azimuth data indicate a sequence of minute-long pulses sweeping along ~20° and coinciding with known lahar flow paths that were 3 km from the array. Other infrasound was detected with back azimuths ranging from 70–100°, but their origin is more ambiguous; these directions could either correspond to the larger more distant lahar reported in Johnson and Palma (2015) (Fig. 32.11; dashed lines), or to smaller flows occurring in more proximal drainages (Fig. 32.11; solid lines).

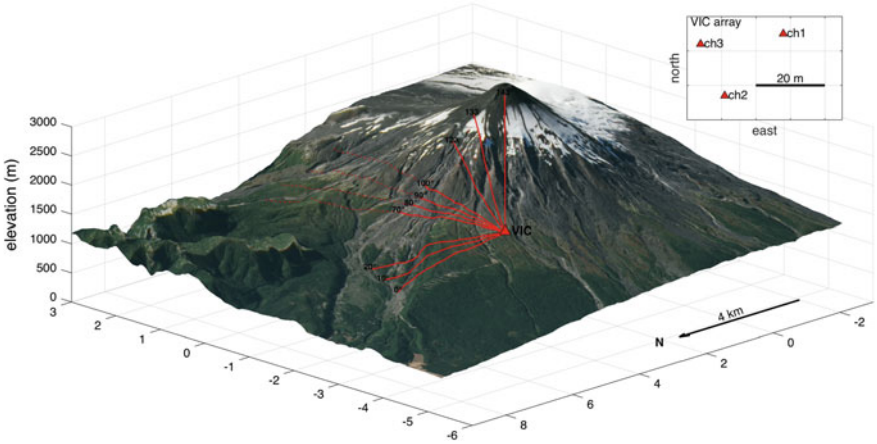

Fig. 32.11 Perspective map of Villarrica showing VIC and select back azimuth directions indicated in Fig. 32.10. Length of solid lines coincides with hypothesized summit and proximal lahar sources. Dashed lines indicate potential lahar sources occurring at distances more than 5 km away and mapped in Johnson and Palma (2015). Image data is from EO-1 ALI courtesy of the NASA EO-1 team and U.S. Geological Survey. Inset map shows arrangement of the VIC array

32.3 Variability of Local Infrasound Measurements Across a Network

Radiation of sound from a volcano point source into a non-attenuating, homogeneous, non-moving atmosphere will result in a sound field with pressure amplitude that is inversely proportional to propagation distance. This approximation breaks down when geometric spreading of acoustic energy departs from spherical, such as is the case when acoustic energy propagates through a stratified atmosphere and/or when surface topography intervenes between source and receiver. In Sects. 32.3.1 and 32.3.2 data from Villarrica are used to quantify both time-varying (e.g., weather) and static (e.g., topographic diffraction) transmission effects. Villarrica serves as a unique test bed for infrasound propagation studies because its infrasound is radiated nearly continuously as an intense, low-frequency (0.7–1.2 Hz) monotone. Its consistency has been attributed to an efficient and stable resonance within a long-lived, steep-walled crater approximately 10^2 m deep (Ripepe et al. 2010; Goto and Johnson 2011; Richardson et al. 2014; Johnson et al. 2018).

32.3.1 Infrasound Statistics from a Local Network

An infrasound network deployed at Volcan Villarrica (Chile) during 5 months in 2015 was designed to quantify the time-dependent variability of infrasound

recorded at stations distributed around the volcano at a range of distances (4 km to 23 km). The experiment expanded upon the scope of observations conducted in 2011 when infrasound was analyzed from two stations deployed during a week-long project (Johnson et al. 2012). In that study the infrasound intensity ~8 km north of the summit was compared with the infrasound intensity recorded near the source at the volcano's summit. At the distant station deviation from *1/r* pressure decay ranged from −9 to +2 dB where −9 dB was observed during a period of strong northerly winds that were opposed to the vent-receiver direction. Another similar set of observations, comparing near-vent and distant (25 km) infrasound, was made for more than 100 explosions at Mount Erebus (Antarctica) (Dabrowa et al. 2014). The near-source/far-source pressure amplitude ratios were found to vary by more than two orders of magnitude (> 40 dB) and this range of ratios was attributed to variations in atmospheric conditions.

In 2015 a 10-station network of ~30-m aperture infrasound arrays was deployed around Villarrica and also at the summit (Fig. 32.8). Although the summit station was destroyed during the paroxysmal eruption of March 3, the remaining network ran with a high degree of continuity between early January and June. To facilitate analysis of the large dataset beam stacks were synthesized from each of the three-channel arrays assuming vent-sourced signal. Data were then filtered between 0.5 and 20 Hz and analyzed in hour-long blocks.

Network data were compared to VIC, which was both the closest surviving array and the most continuously operating station. Power ratios relative to VIC are defined as *power residuals*, which are calculated as the ratios of the hourly power of each station's beam stack to VIC's beam stack power. Spherical spreading and zero attenuation are assumed such that power decay should be $1/r^2$. The power residual (in dB) of station i relative to station j is then

$$P_{ij} = 10\ log\ 10\left(\frac{\int p_i^2 \frac{r_i^2}{r_j^2}}{\int p_j^2}\right).$$

Here p is band-filtered beam-stacked excess pressure at reference station j and network station i, and r is the slant straight-line distance between volcano summit and each station. Power residuals are calculated as a function of time for windowed beam stacks (p_i *and* p_j) of arbitrary time duration. A power residual value of 0 dB corresponds to the expectation for a monopole radiating into a non-attenuating homogeneous space.

Travel time residuals are also quantified and correspond to adjusted time shifts for the maximum cross-correlated lag times between station i and station j. For time-windowed beam stacks p_i *and* p_j the residual time lag is calculated as

$$\Delta\tau_{ij} = \underset{\Delta t}{\arg\max} \left(p_i(\Delta t + r_i/c) \star p_j\left(r_j/c\right)\right)$$

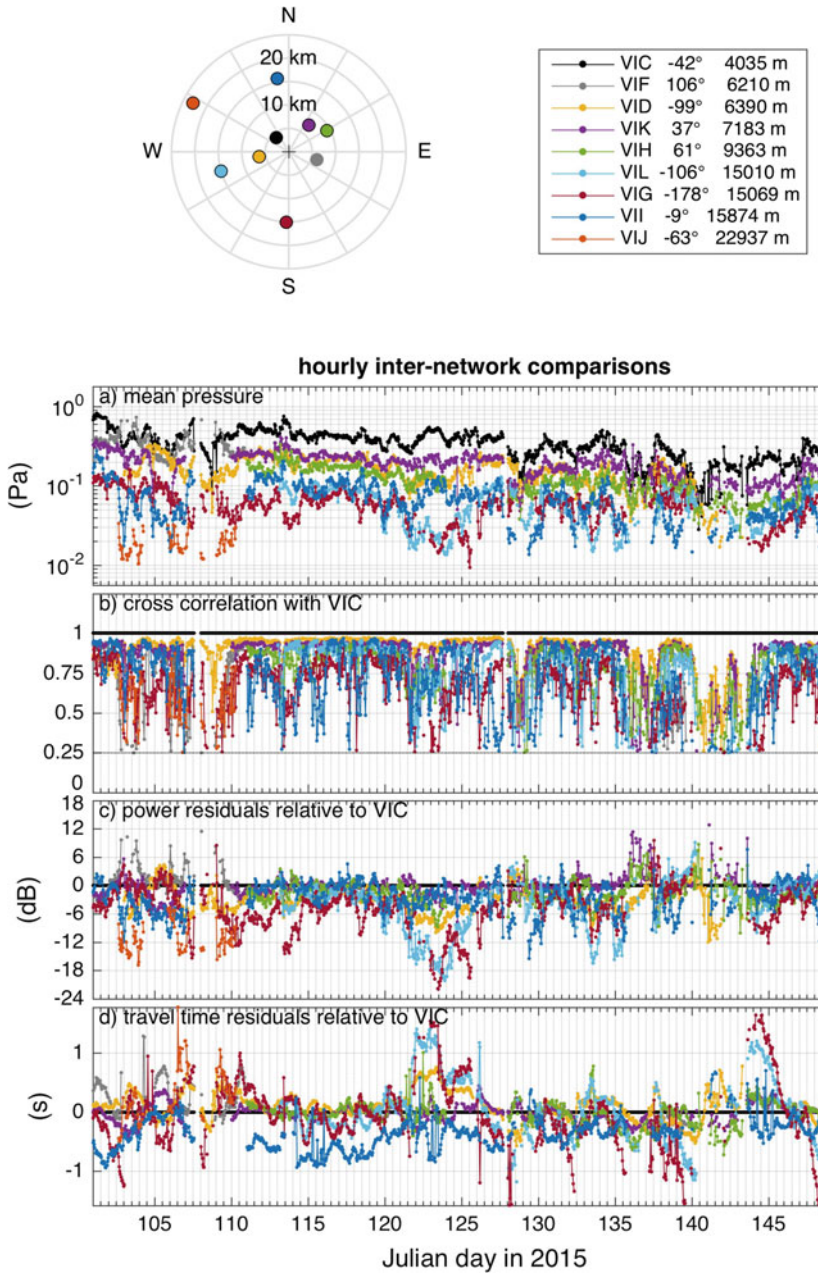
N
20 km
10 km
W
E
S
VIC -42° 4035 m
VIF 106° 6210 m
VID -99° 6390 m
VIK 37° 7183 m
VIH 61° 9363 m
VIL -106° 15010 m
VIG -178° 15069 m
VII -9° 15874 m
VIJ -63° 22937 m
hourly inter-network comparisons
a) mean pressure
(Pa)
b) cross correlation with VIC
c) power residuals relative to VIC
(dB)
d) travel time residuals relative to VIC
(s)
Julian day in 2015

◀**Fig. 32.12** 55-day time series at Villarrica highlighting the variability in network infrasound signals relative to station VIC. Compass plot shows station locations (azimuth and slant distance) relative to the summit. All data were processed in hour-long intervals and filtered in the 0.5–20 Hz band. Data with normalized cross-correlations less than 0.25 are not displayed. **a** Mean absolute beam-stacked acoustic pressures, **b** hourly calculated cross-correlation values, **c** power residuals, and **d** travel time residuals as described in the text

Values of Δt, which are positive imply that sound arrivals are delayed at station i relative to station j. For the experiment at Villarrica the sound speed c was fixed at 334 m/s (3 °C) as it gave rise to the smallest mean travel time residual for the entire network.

The chronologies of Fig. 32.12 show hour-long power residuals and travel time residuals computed in April and May at Villarrica during a period when volcanic activity was relative stable (i.e., consisting of typical open-vent degassing from the lava lake). Data are only shown for those hour-long windows where normalized cross-correlation between network station i and *VIC* exceeded a threshold value of 0.25. Defining a cross-correlation minimum helps to guarantee that power ratios are not significantly affected by high levels of non-volcanic signal or, alternatively, wind noise. Mean hourly absolute pressures are also calculated and hint at a gradual decline in amplitude over the 55-day interval (Fig. 32.12a).

Departure from $1/r$ amplitude-distance (or $1/r^2$ power-distance) decay is suggestive of non-isotropic atmospheric structure that refracts sound either favorably, or unfavorably, to a particular station. Variations in travel time residuals likely indicate the presence of winds, which can increase effective sound speed in one direction and diminish it in an opposing direction (e.g., Garces et al. 1998). Winds that are counter to propagation direction may also affect power residuals by focusing sound preferentially toward the ground (in the case of high altitude along-wind propagation) or upwards (for opposing winds) (Johnson et al. 2012).

Johnson et al. (2012) used 2011 data from Villarrica to show that opposing winds, which tend to increase with elevation, will diminish both the expected intensity of sound received at a station and also retard its arrival. Correlation between these two parameters is demonstrated empirically in the scatter plots of Fig. 32.13, where travel time residuals are compared to power residuals for nine stations in the network. In particular, the stations VIL and VIG, which are located opposite from the control station VIC, appear to record diminished sound power during times when their propagation speed is retarded.

While short-term, hour-to-day fluctuations in both parameters may be attributable to changing weather (wind and/or temperatures), mean values of the power residual seem to negatively correlate with increasing source-receiver distances (Fig. 32.13). For example, stations VIL, VIG, VII, and VIJ possess median power residuals, which are −4, −5, −3, and −12 dB lower than expected for a homogenous, non-attenuating atmosphere. Significantly, their entire interquartile power residual distribution is below 0 dB.

Observation of a greater than $1/r^2$ power decay can be attributed to: (1) intrinsic attenuation, (2) preferential source radiation directionality, (3) geometric focusing

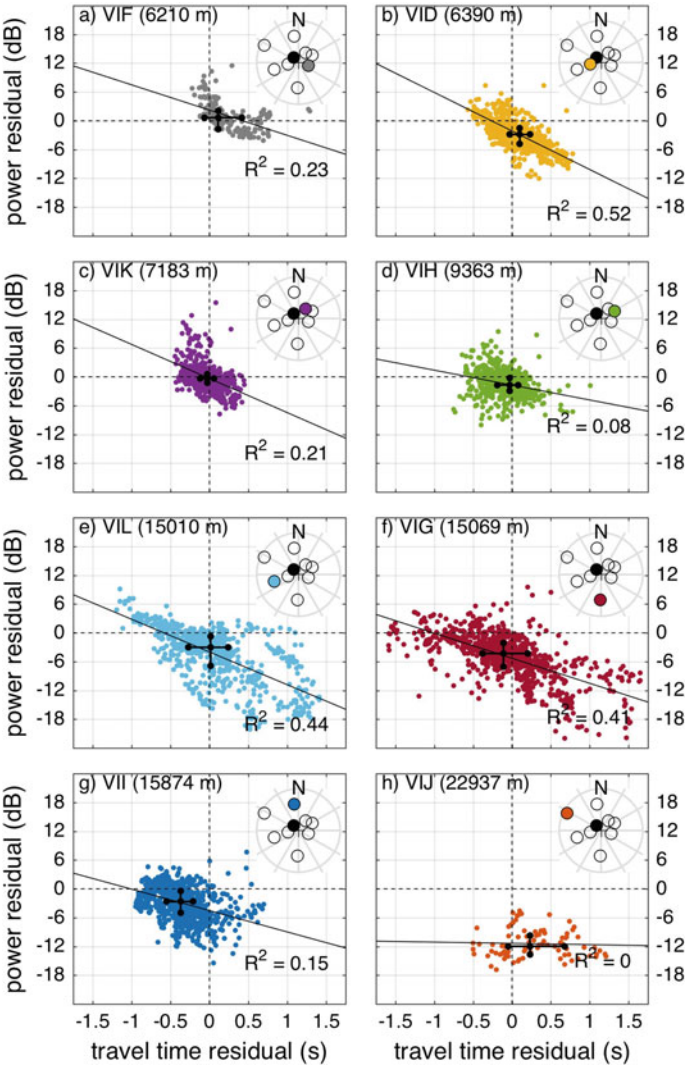

Fig. 32.13 **a**–**h** Scatter plots comparing travel time residuals and power residuals for eight network stations compared with VIC. Data are the same as shown in Fig. 32.12 and correspond to one-hour windows. Panels are arranged in order of increasing propagation distance. Compass plot insets show the relative location of featured stations (colored) and VIC (black-filled circle). Black crosses indicate median and interquartile values for the two parameters. Linear regressions and r-squared values are indicated

of sound, and/or (4) site response and intervening propagation effects. Of these four mechanisms, intrinsic infrasound attenuation is least probable for the surveyed distances. Absorption coefficients for 10 Hz infrasound are on the order of 10^{-2} dB/km in non-dry air and will be even lower for the ~1 Hz sound dominant at

Villarrica (Bass et al. 1995). As such, intrinsic attenuation does not adequately explain observations of a median 0.2–0.3 dB/km decrease at stations VIL, VIG, and VII (Fig. 32.13).

Source directionality might influence sound propagation patterns either due to inherent source radiation asymmetry and/or near-source structure, which can focus or impede sound propagated in certain directions. Asymmetry in infrasound radiation is discussed for volcanic jets (Matoza et al. 2013), and/or for volcano acoustic sources with postulated dipoles or quadrupoles components (Woulff and McGetchin 1976). Non-isotropic radiation may also comprise a component of the acoustic wavefield for some explosions, which erupt non-symmetrically (e.g., Johnson et al. 2008; Kim et al. 2012). In such cases the sound radiates most intensely in preferred directions and its radiation pattern can depend upon the source's frequency content.

Distributed sources that are non-compact in nature can also radiate sounds, which are variable and dependent upon source geometry that may constructively or destructively interfere as postulated at Volcan Santiaguito (Guatemala) for a large 200-m vent region (Johnson and Lees 2010). Finally, crater morphology may influence sound radiation patterns. Lower-than-predicted acoustic intensities have been attributed to non-volumetric source terms (e.g., Kim et al. 2012), as well as crater rim topography, which diffracts acoustic waves (Kim and Lees 2011). An approximate 10° northerly tilt of the crater rim at Villarrica may potentially contribute to the relatively diminished average sound levels observed at VIG, which is situated to the south of the crater.

Another plausible explanation for sound intensity decay at distant stations is due to expected upward sound refraction, which occurs in normally stratified atmospheres, where temperatures decrease on the order of 3–10° C/km (Stull 2000). The influence of upward refraction increases with distance and eventually results in a shadow zone where no ground returns are observed. Time-varying distance to shadow zone may explain observations from station VIJ (23 km from the source), which is the station least well correlated with VIC. When correlated, it possesses a median residual power −12 dB lower than for a homogeneous atmosphere. This distance may sporadically lie within a shadow zone, which was shown in Fee and Garces (2007) to vary diurnally and to approach to within 12.5 km for the infrasound produced by Kilauea Volcano. Such observations, including those made by Dabrowa et al. (2014), intimate that ~20 km may lie beyond the limits of reliable, and thus comprehensive, local volcano monitoring.

32.3.2 Propagation, Topographic Obstructions, and Spectral Response

The impact of topographical diffraction on infrasound spectral content was explored using data collected during a week-long project conducted in November 2016.

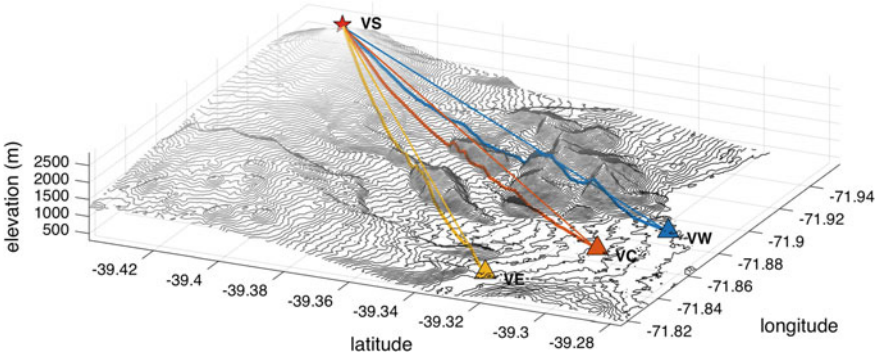

Fig. 32.14 Location of stations VW, VC, and VE with respect to Villarrica's summit infrasound station, VS. Line-of-sight and vertical projection of line-of-sight on to topography are shown

The short experiment consisted of the deployment of four arrays including a station just inside the rim at Villarrica's summit (VS) and three distant stations (VW, VC, and VE) situated at similar NNE azimuths (16, 25, and 39°) and at comparable distances (14.9, 14.4, and 13.8 km) relative to the summit (Fig. 32.9). Each of the distant stations consisted of a two-microphone array that were used to discriminate between noise and signal originating from the volcano. Only data with high inter-array cross-correlation values were analyzed in the frequency domain. Of the three distant stations only VC was situated with unimpeded line-of-sight to the summit. The other two sites (VW and VE) were deployed at locations, which were slightly and significantly obstructed by topographic barriers (Fig. 32.14).

Two channels of the array data are overlain in Fig. 32.15 to demonstrate how intra-array similarity contrasts with inter-station variability (across the network). Inter-array differences are hardly discernible in the time domain and become only slightly evident in the frequency spectra, whose amplitudes have been scaled to account for source–receiver distances. Notably, the spectra of VW and VE indicate somewhat diminished signal amplitudes compared to both stations VS and VC. Station VC, which is not hidden in the lee of intervening topography, has the least modified spectral content of all the stations relative to the summit. Spectral content that deviates across the network suggests an influence due to path-dependent effects. For example, station VW, whose view of Villarrica's summit is most obstructed, has the greatest deficit of spectral power at 1.25 Hz.

The observation that frequency content at all three distant stations is relatively lower than at the summit suggests that either distance or attenuation, due to topographic barriers, is capable of exerting influences on critical-band volcano infrasound. Such observations imply that care must be taken to differentiate source spectrum from propagation and/or site response effects. Importantly, volcano infrasound waveform modeling and quantitative comparison of locally recorded infrasound from different volcanoes (discussed in the next section) should be done with an understanding of the potential influence of path effects.

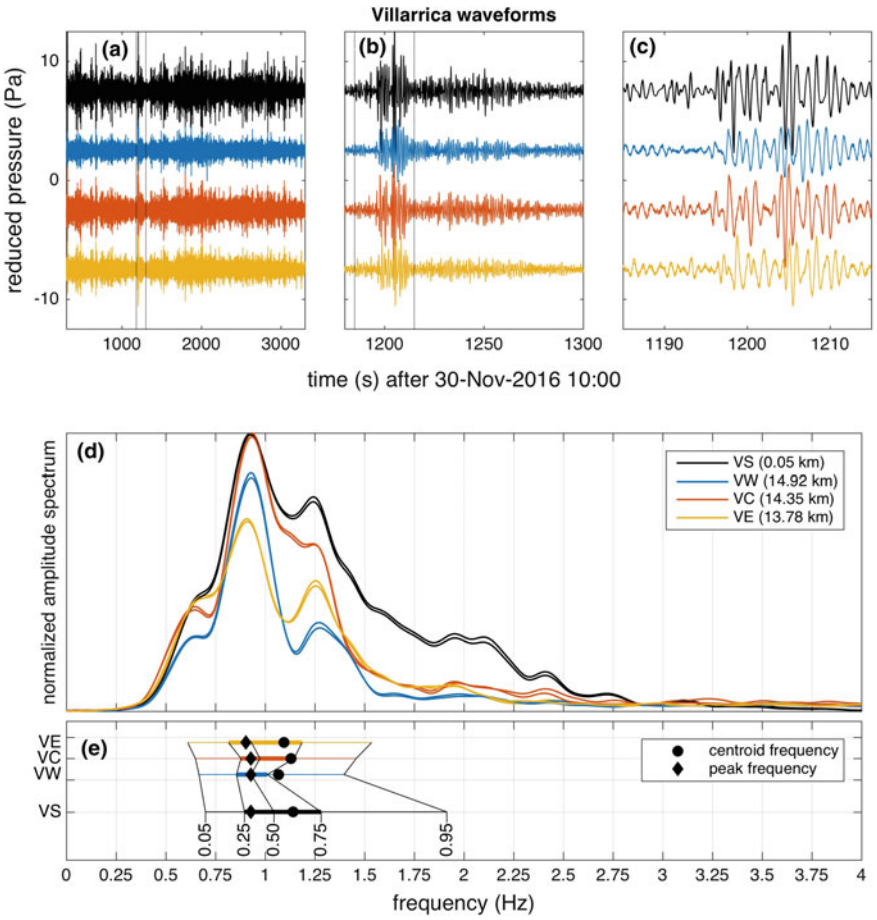

Fig. 32.15 **a**–**c** Example waveforms filtered between 0.5 and 20 Hz shown for hour-long, 120-s long, and 30-s windows. Pressure has been reduced (or scaled) to a common distances of 1 km assuming a 1/r amplitude decay. Time series data from two sensors are plotted for each array. **d** Amplitude spectra correspond to 120-s of data (panel b) smoothed using Welch's method and 10 s overlapping windows. **e** Peak, centroid, and vigintile, quartile, and median quantile frequencies are indicated for each of the spectra according to frequency quantification methods described in Sect. 32.4

32.4 Quantification of Locally Recorded Volcano Infrasound

Quantitative characterization of volcano infrasound is important for comparison of signals recorded at a single volcano, in order to elucidate changing activity, and for inter-comparison of infrasound signal recorded at a variety of volcanoes. Infrasound intensity (or power), spectral content, and signal envelope may be jointly combined

to characterize the style and vigor of a volcanic eruption, open-vent degassing activity, or surface flow phenomena. This section summarizes some useful techniques for measuring the energetics, amplitude, shape, and spectra of infrasound signal using three-hour time series examples from the previously featured volcanoes.

32.4.1 Infrasound Signal Display

Infrasound signals are usually displayed as time series. Fundamental differences in infrasound signal types are immediately evident in digital *helicorder-style* graphs (Fig. 32.16). Such records are especially useful for viewing long-term time series, however infrasound signal can often span many orders of magnitude so that viewing of both smallest and largest transients is difficult in a single figure.

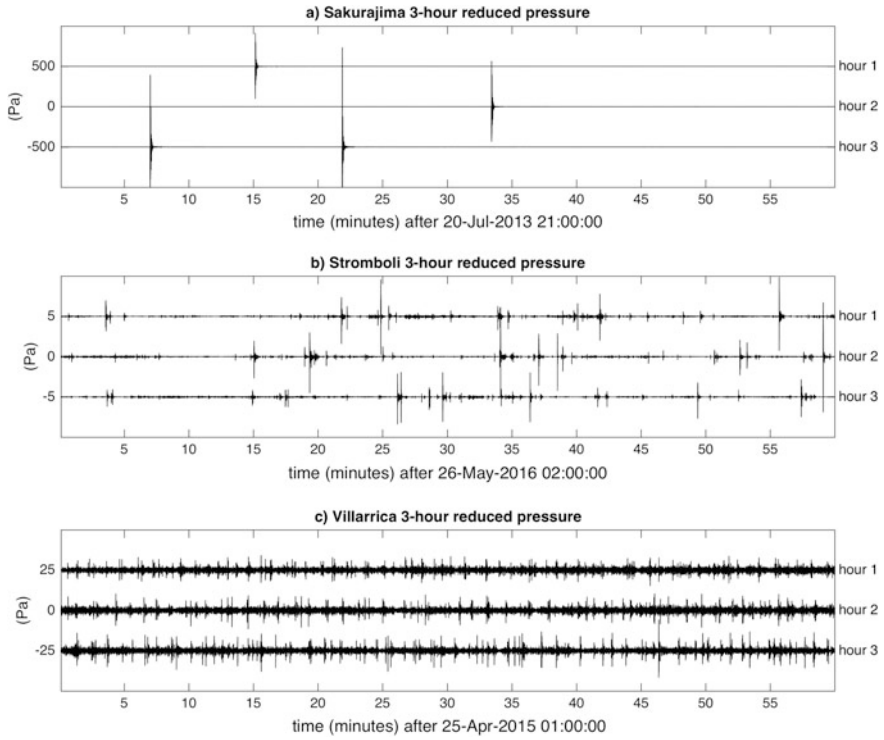

Fig. 32.16 Three-hour time series showing a single channel of beam-stacked infrasound recorded at **a** Sakurajima's KUR array, **b** Stromboli's NEC array, and **c** Villarrica's VIC array. Filtered (0.5–20 Hz) signal is displayed as reduced pressure scaled to a common distance of 1 km. Logarithmic displays of these pressure data are shown in Fig. 32.17 and summary metrics are quantified in Figs. 32.18, 32.19, and 32.20

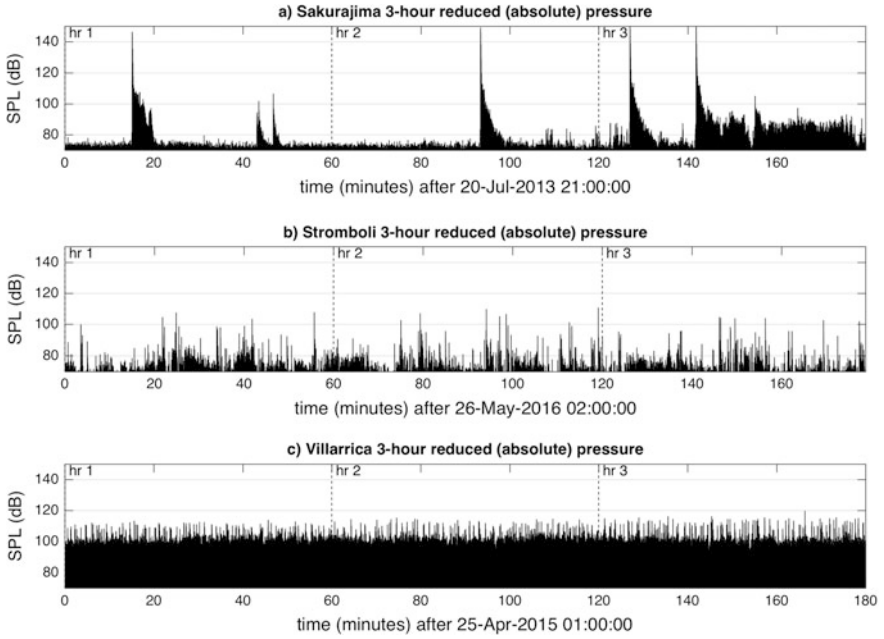

Fig. 32.17 Log absolute amplitude of reduced pressures displayed relative to a fixed pressure level of 2×10^{-5} Pa

An alternative means of viewing the (often) significant dynamic range of volcano infrasound is to display absolute signal amplitudes with a logarithmic ordinate (Fig. 32.17). In the case of the Sakurajima time series more than 80 dB of signal dynamic range is indicated. In the case of Villarrica, the variance in amplitude is much smaller reflecting the more stationary nature of its source.

32.4.2 Reduced and Mean Absolute Pressures

As in volcano seismology, where signals are quantified by their reduced displacement (Aki and Koyanagi 1981), local volcano infrasound may be conveniently scaled to a *reduced pressure* (e.g., Johnson et al. 2004). Assuming both seismic body wave displacement and infrasound pressure amplitudes fall off as *1/r* then their reduced values can be scaled to a common distance. For a reference distance of 1 km the reduced pressure is

$$p_{1km} = p \frac{r}{1000\,\mathrm{m}},$$

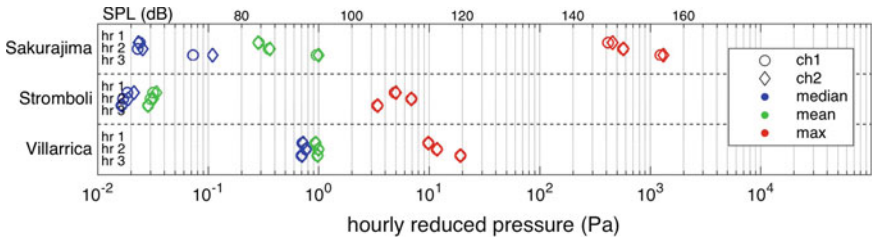

Fig. 32.18 Three volcanoes quantified hourly in terms of their maximum reduced pressure, mean reduced pressure, and median reduced pressure. Pressure data are reduced to 1 km and are shown for two channels from a single array at each volcano. Equivalent SPLs are indicated at top of graph

where r is the slant propagation distance in meters from source to recording site. A one-kilometer scaling distance is commonly used (e.g., Johnson et al. 2004), and is useful for a couple of reasons. First, for many volcanoes it often yields convenient values ranging from a few to a few thousand Pa. And second, one kilometer lies beyond the elastic radius for all but the most intense volcanic explosions. For example, Sakurajima explosions can produce infrasound pulses with particularly high-amplitude compressions (~1000 Pa at 1 km; Fig. 32.18), which may propagate nonlinearly closer to the source.

Mean and median absolute pressures give a sense for the average and most common pressure levels respectively over a specified period of time. Mean absolute pressure is analogous to another commonly used seismic metric, the Real-time Seismic Amplitude Measurement (RSAM), which traditionally is calculated for 10-min intervals and gives an efficient indication of changes that may occur during periods of volcanic unrest (Endo and Murray 1991). The interval used to calculate mean-reduced infrasound amplitudes is arbitrary, but for long time series is often set to one hour (e.g., Figs. 32.12a, 32.18). Changes in mean absolute reduced pressure may be particularly informative for assessing systematic changes in a volcano's comportment, such as the degree to which it is degassing or exploding. For example, the months-long mean pressure trend in Fig. 32.12a may correspond to a gradually diminishing level of lava lake outgassing. Median absolute pressure is similar to mean absolute pressure, but effectively removes amplitude outliers. Median pressures are nearly always lower than mean pressure because one or more high-amplitude (explosion) pulses tend to positively skew the distribution of pressures.

For purely illustrative purposes volcano excess pressure amplitudes are sometimes converted to equivalent sound pressure levels (SPL) (Figs. 32.16, 32.17). SPL is a logarithmic scale referenced to the threshold of human sound perception in the audio band at 1000 Hz, such that $SPL = 20\log\left(p_{rms}/2\times10^{-5}Pa\right)$, where root-mean-squared pressure p_{rms} is equal to $\sqrt{2}/2$ of a sinusoidal pressure wave amplitude. Although auditory perception of infrasound has limited sense it is illuminating to compute SPL to demonstrate: (1) the impressive dynamic range of volcano signals, and (2) the extreme intensity of some volcanic explosions.

For example, Sakurjima's largest explosion would register as an impressive ~160 dB SPL if measured 1 km from the vent (Figs. 32.17, 32.18).

32.4.3 *Infrasound Power*

Instantaneous acoustic intensity radiated by a simple acoustic source and recorded by a calibrated microphone is the product of the sound wave pressure and its particle velocity. Averaged over a finite period of time it is proportional to the mean squared excess pressure and has units of W/m^2.

$$I = \frac{1}{T}\int_0^T p(t)v(t)dt = \frac{\overline{p}^2}{\rho c}.$$

Here ρ and c are the atmosphere's density and sound speed respectively. For standard atmospheres at 0 and 3000 m altitude air densities range from 1.225 to 0.909 kg/m^3 and sounds speeds from 340 to 329 m/s. Their product, or impedance, varies by a factor of 1.4 over this altitude range.

Infrasound recordings provide point measurements of sound intensity that can be integrated to yield an estimated acoustic power output of a volcano. In the case of spherical sound waves confined to a volume with solid angle Ω the total *infrasound power* is estimated by

$$P = \Omega r^2 \mathrm{I} = \Omega r^2 \frac{\overline{p}^2}{\rho c},$$

where solid angles range from 2π for radiation into a half space to 3π for a source radiated from the top of a volcanic cone with slopes of 30°. Acoustic power calculated from the three featured volcanoes shows a wide spectrum of emitted power ranging from 10^1 W to 10^9 W averaged over 10 s intervals (Fig. 32.19).

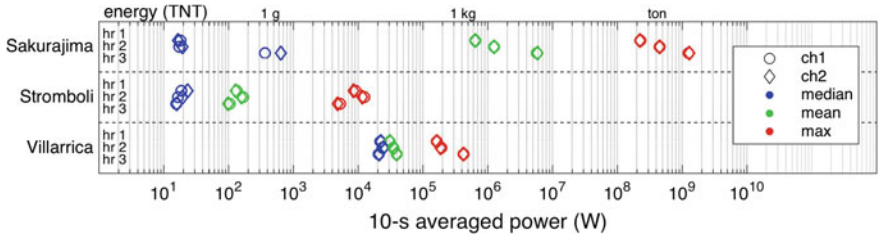

Fig. 32.19 Three volcanoes quantified hourly in terms of their 10-s averaged maximum power, 10-s mean power values, and 10-s median power values. Data are shown for two channels from a single array at each volcano. Equivalent 10-s energy release is shown at top of the graph in terms of mass of TNT explosive, where 1 kg TNT = 4.184 MJ

Maximum or peak power is quantified as the largest value within each hour-long period, while mean and median powers are calculated from the hourly distributions of 10-s powers. The fact that Villarrica's maximum and mean power vary by only one order of magnitude points to relatively minor variations in its tremor amplitude.

Spherical sound radiation may be an appropriate assumption for some types of volcano infrasound, such as discrete explosions radiating sound to local distances in a homogenous non-moving atmosphere, but the assumption leads to less accurate estimates in cases where sound radiation is directional or the atmosphere has complicated structure (refer to discussion in Sect. 32.3.1). Ideally, power estimates can be made by incorporating sound intensity measurements across a network at various distances and elevation angles as suggested by Matoza et al. (2013).

Even in cases where a simple volcano acoustic source is appropriate, the power data collected across a volcano network will likely deviate from the expected $1/r^2$ fall off due to propagation effects. The scatter plots in Fig. 32.13, for example, show that 6 dB of power reduction are common for stations ~15 km from the volcano. Using data from a station at this distance would lead to underestimation of total acoustic power radiation by a factor of four. Despite uncertainties involved in infrasound power estimation using a single (local) station, quantification of acoustic power is still quite useful for characterizing volcanic events, because their acoustic emissions can span many orders of magnitude.

32.4.4 Frequency Characterization

The power spectral content $P(f)$ of volcano infrasound can be quantified in a number of useful ways. Identification of a peak frequency,

$$f_p = \underset{f}{\arg max}\, P(f),$$

is meaningful in cases where a single tone dominates, such as for Villarrica (e.g., Goto and Johnson 2011; Johnson et al. 2018), and also for harmonic tremors, such as at Arenal (Hagerty et al. 2000) and Sangay and Karymsky, Russia (Johnson and Lees 2000), where a fundamental frequency can be identified and may change (or glide) over time. In many other cases, however, a single peak frequency is not well defined and a more useful metric for characterizing dominant spectral energy may be the center-of-mass of the power spectrum (Fig. 32.15e). For a frequency domain ranging from f_1 to f_2 the *centroid frequency*, or alternatively mean/center frequency (Barnes 1993), is defined as

$$f_c = \frac{\int_{f_1}^{f_2} fP(f)df}{\int_{f_1}^{f_2} P(f)df}.$$

Spectral content may also be quantified by *quantile frequencies* f_q associated with cumulative percentile power (Fig. 32.15e). For example, the frequency associated with the first quartile of a power spectrum would be

$$f_{q25} = \arg_{f_q} \frac{\int_{f_1}^{f_q} P(f)df}{\int_{f_1}^{f_2} P(f)df} = 0.25$$

and the interquartile frequency range $f_{q75} - f_{q25}$ provides a fundamental measure of the peakedness of the frequency spectrum.

Integration limits, f_1 and f_2, will influence the evaluation of both centroid and quantile frequencies. When calculating frequency metrics care must be taken to appropriately band-limit the recordings, or set the integration limits, so that only volcano signal is considered. A reasonable approach is to discard spectral power that falls below a noise threshold. It is then necessary to specify the integration limits used in spectral characterization. For instance, in Fig. 32.15e the centroid, vigintile, quantile, and median frequencies are calculated for integration limits between 0.5 and 20 Hz.

Volcano infrasound spectral comparison is shown for the three featured volcanoes (Fig. 32.20). During 3 hours of activity spectral envelopes are relatively consistent for each volcano and provide a volcano-specific "voiceprint". For example, Sakurajima exhibits two distinct frequency peaks separated by a

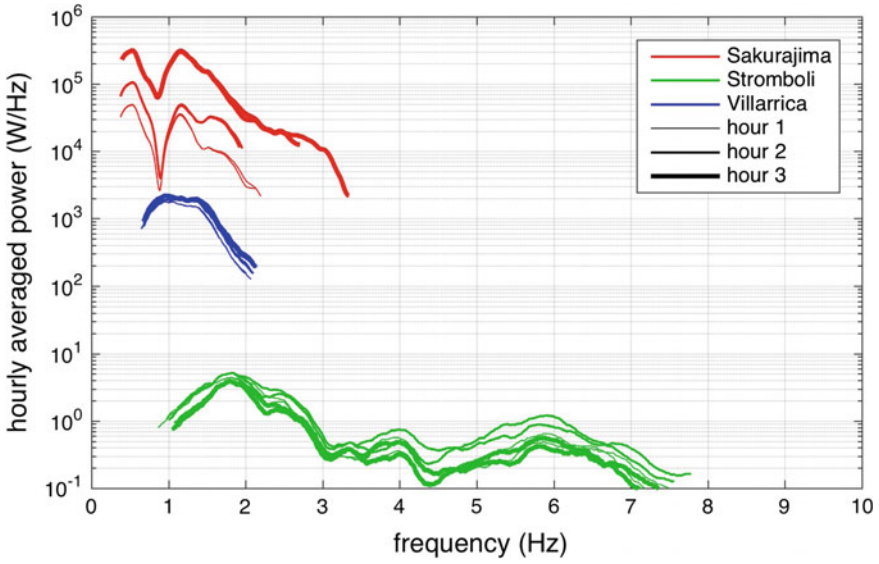

Fig. 32.20 Power spectral density calculated for 3 h of data from the three volcanoes featured in Fig. 32.16. Data are shown for two channels within each array and for $P(f)$ where $f_{q05} < f < f_{q95}$ and f1 = 0.5 and f2 = 20 Hz

pronounced trough in spectral energy. Villarrica has lower spectral energy density than Sakurajima with 90% of its energy is confined to a narrow 1.5 Hz band. Stromboli infrasound radiation is far less energetic than the other two volcanoes and it is spread more evenly across the 1–7 Hz band. Although much of the spectral shape can be attributable to source mechanics, it is critical to recall that propagation influences may also play a significant role in modulating spectral content (Sect. 32.3.2).

32.5 Conclusions

Infrasound has become an established component of the volcano monitoring toolbox and complements seismic, geodetic, thermal, and gas monitoring for both scientific study and permanent volcano surveillance. Infrasound monitoring local to a volcano implies sensors deployed in a region surrounding a volcano where acoustic transmission reaches the receiver without refracting into the stratosphere. Although more work needs to be done to delineate the time-varying extent of what is meant by "local" empirical studies suggest that shadow zones are common at 20 km and that refraction can often significantly attenuate infrasound at distances greater than ~10 km. Topographic barriers between volcano sources and receivers also affect recorded infrasound signal including its amplitude and spectral content. Consideration of these effects is important when quantifying radiated acoustic energy, source spectral content, source timing, and performing waveform analysis.

Data collected 10 km or less from a source and absent intervening topographic can elucidate surface volcanic phenomena including vent activity and gravity-driven mass movement. Infrasound, and its attendant short wavelengths (compared to seismic), permit precise location of surface sources and their positions over time. Both back azimuth and grid-search source location strategies are effective and their implementation depends upon the geometry of the local infrasound network, which can range from single sensors to distributed networks of sensors to networks of arrays. Topologies of volcano infrasound installations will always be variable and depend upon field site accessibility and the resources available to the volcano observatory or scientific team. In general, arrays of closely spaced sensors are optimal. Even an "array" of two sensors permits critical distinction between volcano signal, infrasound produced by non-volcanic sources, and non-acoustic noise such as wind.

Acknowledgements Data presented here were collected with support from the National Science Foundation (NSF) EAR grant 1151662 and the Fulbright Scholar's Program. Appreciation is extended to Dr. Matthew Haney, who provided insightful and helpful review of the chapter.

References

Aki K, Koyanagi R (1981) Deep volcanic tremor and magma ascent mechanism under Kilauea Hawaii. J Geophys Res 86(B8):7095–7110

Arechiga R, Johnson JB, Edens H, Thomas RJ, Rison W (2011) Acoustic localization of triggered lightning. J Geophys Res 116(D09103). https://doi.org/10.1029/2010JD015248

Arrowsmith SJ, Johnson JB, Drob DP, Hedlin MAH (2010) The seismo-acoustic wavefield: a new paradigm in studying geophysical phenomena. Rev Geophys 48, RG4003. http://doi.org/10.1029/2010RG000335

Barnes AE (1993) Instantaneous spectral bandwidth and dominant frequency with applications to seismic reflection data. Geophys 58(3):419–428. https://doi.org/10.1190/1.1443425

Bass HE, Sutherland LC, Zuckerwar AJ, Blackstock DT, Hester DM (1995) Atmospheric absorption of sound: further developments. J Acoust Soc Am 97(1):680–683. https://doi.org/10.1121/1.412989

Cannata A, Montalto P, Privitera E, Russo G, Gresta S (2009) Characterization and location of infrasonic sources in active volcanos: Mt. Etna, Septermber-November 2007. J Geophys Res 114(B8):1–15. https://doi.org/10.1029/2008JB006007

Cansi (1995) An automatic seismic event processing for detection and location; the P.M.C.C. method. Geophys Res Lett 22(9):1021–1024

Dabrowa AL, Green DN, Rust AC, Phillips JC (2011) A global study of volcanic infrasound characteristics and the potential for long-range monitoring. Earth Planet Sci Lett 310:369–379. https://doi.org/10.1016/j.epsl.2011.08.027

Dabrowa AL, Green DN, Johnson JB, Phillips JC, Rust AC (2014) Comparing near-regional and local measurements of infrasound from Mount Erebus, Antarctica: implications for monitoring. J Volcanol Geoth Res 288:46–61. https://doi.org/10.1016/j.jvolgeores.2014.10.001

Delle Donne D, Ripepe M, De Angelis S, Cole PD, Lacanna G, Poggi P, Stewart R (2014) Chapter 9 thermal, acoustic and seismic signals from pyroclastic density currents and vulcanian explosions at Soufriere Hills Volcano, Montserrat Geol Soc Lond Mem 39:169–178. http://doi.org/10.1144/M39.9

Endo ET, Murray T (1991) Real-time seismic amplitude measurement (RSAM): a volcano monitoring and prediction tool. Bull Volcan 53(7):533–545. https://doi.org/10.1007/BF00298154

Fee D, Garces M (2007) Infrasonic tremor in the diffraction zone. Geophys Res Lett 34(16). http://doi.org/10.1029/2007gl030616

Fee D, Matoza RS (2013) An overview of volcano infrasound: from hawaiian to plinian, local to global. J Volc Geotherm Res 249:123–139. https://doi.org/10.1016/j.jvolgeores.2012.09.002

Fee D, Haney M, Matoza R, Szuberla C, Lyons J, Waythomas C (2016) Seismic Envelope-Based Detection and Location of Ground-Coupled Airwaves from Volcanoes in Alaska. Bull Seismol Soc Am 106(3):1024–1035.https://doi.org/10.1785/0120150244

Garces MA, Hansen RA, Lindquist K (1998) Traveltimes for infrasonic waves propagating in a stratified atmosphere. Geophys J Int 135(1):255–263. https://doi.org/10.1046/j.1365-246X.1998.00618.x

Garcés M (2003) Infrasonic tremor observed at Kīlauea Volcano Hawai'i. Geophys Res Lett 30(20):1–4. https://doi.org/10.1029/2003GL018038

Garcés M, Iguchi M, Ishihara K, Morrissey M, Sudo Y, Tsutsui T (1999) Infrasonic precursors to a Vulcanian Eruption at Sakurajima Volcano Japan. Geophys Res Lett 26(16):2537. https://doi.org/10.1029/1998GL005327

Goto A, Johnson JB (2011) Monotonic infrasound and helmholtz resonance at volcan villarrica (Chile). Geophys Res Lett 38(L06301). http://doi.org/10.1029/2011GL046858

Hagerty MT, Protti M, Schwartz SY, Garces MA (2000) Analysis of seismic and acoustic observations at arenal volcano, costa rica, 1995–1997. J Volc Geotherm Res 101(1–2):27–65. https://doi.org/10.1016/S0377-0273(00)00162-1

Johnson JB (2005) Source location variability and volcanic vent mapping with a small-aperture infrasound array at stromboli Volcano Italy. Bull Volcan 67:1–14

Johnson JB, Anderson J, Marcillo O, Arrowsmith S (2012) Probing local wind and temperature structure using infrasound from volcan villarrica (Chile). J Geophys Res 117(D17). http://doi.org/10.1029/2012JD017694

Johnson JB, Aster RC, Kyle PR (2004) Volcanic eruptions observed with infrasound. Geophys Res Lett 31(14). http://doi.org/10.1029/2004gl020020

Johnson JB, Aster RC, Ruiz MC, Malone SD, McChesney PJ, Lees JM, Kyle PR (2003) Interpretation and utility of infrasonic records from erupting volcanoes. J Volc Geotherm Res 121(1–2):15–63

Johnson JB, Lees JM (2000) Plugs and chugs—seismic and acoustic observations of degassing explosions at Karymsky, Russia and Sangay. Ecuador J Volc Geotherm Res 101(1–2):67–82

Johnson JB, Lees JM (2010) Sound produced by the rapidly inflating Santiaguito lava dome Guatemala. Geophys Res Lett 37(22):1–6. https://doi.org/10.1029/2010GL045217

Johnson JB, Malone SD (2007) Ground-coupled acoustic airwaves from Mount St. Helens provide constraints on the May 18, 1980 eruption. Earth Planet Sci Lett 258(1–2):16–31. https://doi.org/10.1016/j.epsl.2007.03.001

Johnson JB, Palma JL (2015) Lahar infrasound associated with volcán villarrica's 3 March 2015 eruption. Geophys Res Lett 42(15):6324–6331. https://doi.org/10.1002/2015GL065024

Johnson JB, Ronan TJ (2015) Infrasound from volcanic rockfalls. J Geophys Res Solid Earth 120 (12):8223–8239. https://doi.org/10.1002/2015JB012436

Johnson JB, Ripepe M (2011) Volcano infrasound: a review. J Volcanol Geoth Res 206(3–4):61–69. https://doi.org/10.1016/j.jvolgeores.2011.06.006

Johnson J, Aster R, Jones KR, Kyle P, McIntosh B (2008) Acoustic source characterization of impulsive strombolian eruptions from the Mount Erebus lava lake. J Volcanol Geoth Res 177 (3):673–686. https://doi.org/10.1016/j.jvolgeores.2008.06.028

Jones K, Johnson JB, Aster R, Kyle P, McIntosh W (2008) Infrasonic tracking of large bubble bursts and ash venting at Erebus volcano, Antarctica. J Volc Geotherm. Res 177:661–672. https://doi.org/10.1016/j.jvolgeores.2008.02.001

Johnson JB, Watson LM, Palma JL, Dunham EM, Anderson JF (2018) Forecasting the Eruption of an Open-Vent Volcano Using Resonant Infrasound Tones. Geophys Res Lett 45(5):2213–2220. https://doi.org/10.1002/2017GL076506

Kim K, Lees JM (2014) Local volcano infrasound and source localization investigated by 3D simulation. Seismol Res Lett

Kim K, Lees JM, Ruiz M (2012) Acoustic multipole source model for volcanic explosions and inversion for source parameters. Geophys J Int 191(3):1192–1204. https://doi.org/10.1111/j.1365-246X.2012.05696.x

Kim K, Lees JM (2011) Finite-difference time-domain modeling of transient infrasonic wavefields excited by volcanic explosions. Geophys Res Lett 38(6):2–6. https://doi.org/10.1029/2010GL046615

Marcillo O, Johnson JB, Hart D (2012) Implementation, characterization, and evaluation of an inexpensive low-power low-noise infrasound sensor based on a micromachined differential pressure transducer and a mechanical filter. J Atmospheric Ocean Technol 29(9):1275–1284. https://doi.org/10.1175/JTECH-D-11-00101.1

Marchetti E, Ripepe M, Campus P, Le Pichon A, Brachet N, Blanc E, Gaillard P, Mialle P, Husson P (2019) Infrasound monitoring of volcanic eruptions and contribution of ARISE to the volcanic ash advisory centers. In: Le Pichon A, Blanc E, Hauchecorne A (eds) Infrasound monitoring for atmospheric studies, 2nd edn. Springer, Dordrecht, pp 1141–1162

Matoza RS, Fee D, Neilsen TB, Gee KL, Ogden DE (2013) Aeroacoustics of volcanic jets: acoustic power estimation and jet velocity dependence. J Geophys Res 118(12):6269–6284. https://doi.org/10.1002/2013JB010303

Matoza R, Fee D, Green D, Mialle P (2019) Volcano infrasound and the international monitoring system. In: Le Pichon A, Blanc E, Hauchecorne A (eds) Infrasound monitoring for atmospheric studies, 2nd edn. Springer, Dordrecht, pp 1023–1077

Matoza R, Le Pichon A, Vergoz J, Herry P, Lalande J-M, Lee H, Rybin A (2010). Infrasonic observations of the June 2009 sarychev peak eruption, Kuril Islands: implications for infrasonic monitoring of explosive volcanism. J Volc Geotherm Res 200:35–48. http://doi.org/101016/j.volgeores.2010.11.022

McKee K, Fee D, Rowell C, Yokoo A (2014) Network-based evaluation of the infrasonic source location at Sakurajima volcano, Japan. Seismol Res Lett 85(6):1200–1211. http://doi.org/10.1785/0220140119

McNutt SR, Thompson G, Johnson JB, De Angelis S, Fee D (2015) Seismic and infrasonic monitoring. In: Encyclopedia of volcanoes, 2nd ed. Academic Press, pp 1071–1099. http://doi.org/10.1016/B978-0-12-385938-9.00063-8

Nakata N, Snieder R (2011) Near - surface weakening in Japan after the 2011 Tohoku - Oki earthquake, 38(July):1–5. https://doi.org/10.1029/2011GL048800

Richardson JP, Waite GP, Palma JL (2014) Varying seismic-acoustic properties of the fluctuating lava lake at Villarrica volcano. Chile. J. Geophys. Res. 119:5560–5573. https://doi.org/10.1002/2014JB011002

Ripepe M, Marchetti E (2002) Array tracking of infrasonic sources at Stromboli volcano. Geophys Res Lett 29:331–334

Ripepe M, Marchetti E (2019) Infrasound monitoring of volcano-related hazards for civil protection. In: Le Pichon A, Blanc E, Hauchecorne A (eds) Infrasound monitoring for atmospheric studies, 2nd edn. Springer, Dordrecht, pp 1107–1140

Ripepe M, Marchetti E, Bonadonna C, Harris AJL, Pioli L, Uliveri G (2010) Monochromatic infrasonic tremor driven by persistent degassing and convection at villarrica volcano, chile. Geophys Res Lett 37(L15303). http://doi.org/10.1029/2010GL043516

Ripepe M, Marchetti E, Ulivieri G (2007) Infrasonic monitoring at Stromboli volcano during the 2003 effusive eruption: Insights on the explosive and degassing process of an open conduit system. J Geophys Res-Solid Earth 112. http://doi.org/10.1029/2006jb004613

Rowell CR, Fee D, Szuberla CAL, Arnoult K, Matoza RS, Firstov PP, Makhmudov E (2014) Three-dimensional volcano-acoustic source localization at Karymsky. J Volcanol Geoth Res 283:101–115.https://doi.org/10.1016/j.jvolgeores.2014.06.015

Stull RB (2000) Meteorology for scientists and engineers, 2nd edn. Brooks/Cole, Pacific Grove, CA

Taisne B, Perttu A, Tailpied D, Caudron C, Simonini L (2019) Atmospheric controls on ground- and space-based remote detection of volcanic ash injection into the atmosphere, and link to early warning systems for aviation hazard mitigation. In: Le Pichon A, Blanc E, Hauchecorne A (eds) Infrasound monitoring for atmospheric studies, 2nd edn. Springer, Dordrecht, pp 1079–1105

Woulff G, McGetchin TR (1976) Acoustic noise from volcanos—theory and experiment. Geophys J Roy Astron Soc 45(3):601–616. https://doi.org/10.1111/j.1365-246X.1976.tb06913

Yokoo A, Suzuki YJ, Iguchi M (2014) Dual infrasound sources from a Vulcanian eruption of Sakurajima volcano inferred from cross-array observation. Seismol Res Lett 85(6):1212–1222. https://doi.org/10.1785/0220140047

Chapter 33
Volcano Infrasound and the International Monitoring System

Robin Matoza, David Fee, David Green and Pierrick Mialle

Abstract Volcanoes generate a wide variety of low-frequency (~0.01–20 Hz) acoustic signals, and infrasound technology is part of an expanding suite of geophysical tools available to characterize, understand, and monitor volcanic processes. We review recent advances in the field of volcano acoustics with an emphasis on scientific and potential civil application gains from the International Monitoring System (IMS) infrasound network. Energetic infrasound from explosive volcanism can propagate hundreds to thousands of kilometers in atmospheric waveguides and large explosive eruptions (which represent significant societal and economic hazards) are routinely recorded by the IMS infrasound network. Significant progress in understanding volcano infrasound has been made through dedicated local deployments (within <15 km of the source) in tandem with other observation systems. This research has identified diverse source mechanisms of volcanically generated infrasound, and elucidated the influence of near-source topography and local atmospheric conditions on acoustic propagation and recordings. Similarly, advances are being achieved in inferring volcanic source processes from signals recorded at the longer ranges typically associated with IMS detections. However, practical challenges remain in the optimization of remote volcano infrasound signal detection, discrimination, association, and location. Many of these challenges are the result of strong signal variability associated with long-range

R. Matoza (✉)
Department of Earth Science and Earth Research Institute,
University of California, Santa Barbara, CA, USA
e-mail: matoza@geol.ucsb.edu

D. Fee
Wilson Alaska Technical Center and Alaska Volcano Observatory,
Geophysical Institute, University of Alaska Fairbanks, Fairbanks, AK, USA

D. Green
AWE Blacknest, Brimpton, UK

P. Mialle
CTBTO, Vienna, Austria

A. Le Pichon et al. (eds.), *Infrasound Monitoring for Atmospheric Studies*,
https://doi.org/10.1007/978-3-319-75140-5_33

acoustic propagation through the temporally and spatially varying atmosphere. We review the state of knowledge on infrasound generation by explosive volcanism, and assess progress toward the development of infrasonic eruption early warning and notification systems at regional and global scales.

33.1 Volcano Acoustics in Context

Infrasound technology adds to a growing suite of geophysical tools available to characterize, understand, and monitor volcanic processes. A better understanding of volcanic eruption processes helps to mitigate the associated societal and economic hazards, which have the potential to affect more people as global population density and air traffic increase (e.g., Casadevall et al. 1994; Chester et al. 2000; Annen and Wagner 2003).

Volcanic eruptions are spectacular manifestations of the dynamic nature of our planet. As a consequence of plate tectonics and mantle convection, melt formed at depth migrates to the surface through a complicated network of cracks, fissures, and conduits to form surface volcanism. On longer timescales, magma migration and storage may be expressed in ground deformation recorded with strain- and tilt-meters, Global Positioning System receivers, and satellite radar interferometry (e.g., Dzurisin 2006; Segall 2010). Volcano seismology and volcano acoustics are two

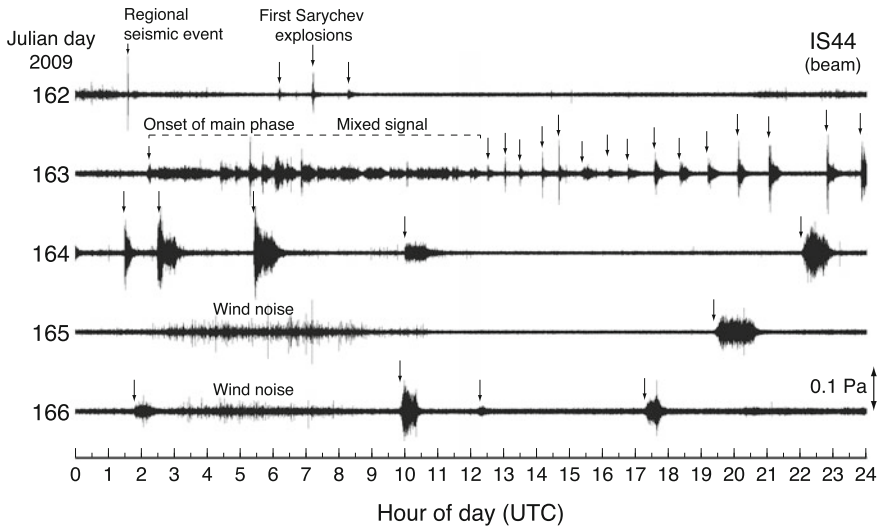

Fig. 33.1 Infrasonic waveforms recorded at IS44 (Kamchatka) for the June 2009 eruption of Sarychev Peak, Kuriles (5 days: 11–15 June 2009, or Julian days 162–166 2009). Each waveform shows one full day of data. Infrasound array data have been beamformed (waveforms aligned and stacked for azimuth of Sarychev Peak and acoustic velocity) using a time-delay beamformer and filtered 0.5–5 Hz. (Figure reproduced from Matoza et al. 2011a)

complementary methods for understanding more rapid phenomena associated with fluid storage, transport, and eruption from the subsurface to the atmosphere. Recording signals in the same frequency range (hundreds of seconds to tens of Hz), seismic and acoustic data together represent a more complete recording of the elastic wavefield radiated by volcanoes. Seismic waves are produced by subsurface magmatic, hydrothermal, and faulting processes occurring within and around volcanoes from mantle depths to the surface (e.g., Chouet and Matoza 2013). Acoustic waves are produced by shallow subsurface and subaerial processes, including explosive eruptions, shallow degassing, surface flow, and mass wasting. Seismic and acoustic signals have been observed for decades at some persistently erupting volcanoes, with temporal evolution in these signals containing rich information on

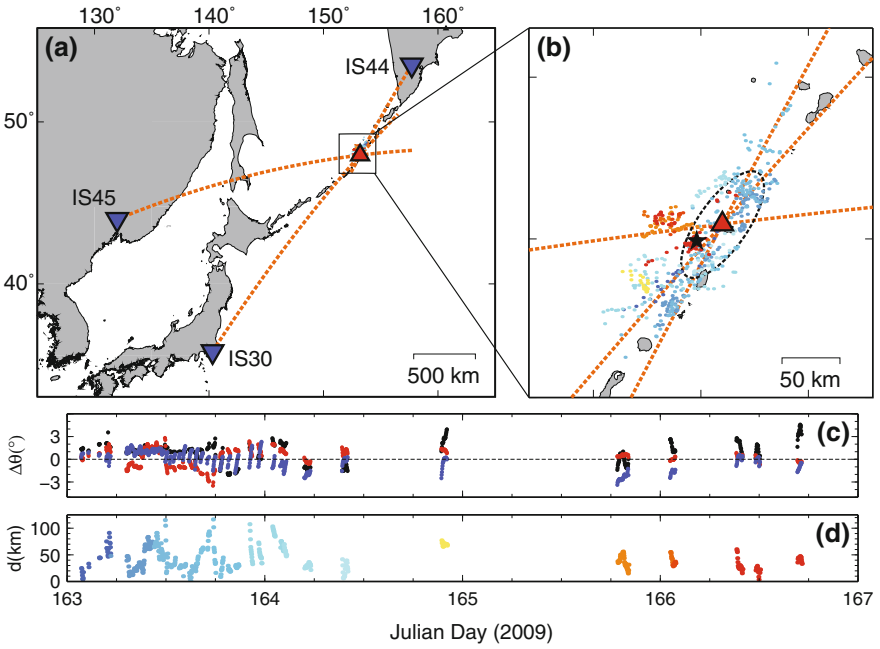

Fig. 33.2 Infrasonic source location for the June 2009 eruption of Sarychev Peak (large red triangle) via back azimuth cross-bearings using the closest three IMS arrays: IS44, IS45, and IS30 (inverted blue triangles). Seven arrays (not shown) recorded infrasound from this event out to 6,400 km from the source. **a**, **b** Source location is performed on a running median of the observed signals and a back azimuth correction is applied using 3D ray-tracing and ECMWF, HWM07, and MSIS90 atmospheric specifications (Matoza et al. 2011a). The source location solutions (dots) are colored as a function of time corresponding to (**d**). The mean source centroid is shown as a black star. Dashed ellipse shows 90% confidence for source location assuming azimuth errors normally distributed around true with a standard deviation of 3°. Dashed lines are the true great-circle path azimuths from each station to Sarychev Peak. **c** Running median signal azimuth deviation at the three stations (black: IS44, red: IS45, blue: IS30). Times are corrected for a constant celerity of 0.33 km/s. **d** Source location error: distance [km] between true Sarychev Peak location and the obtained infrasonic source locations. (Figure modified from Matoza et al. 2011a)

the multi-year eruption dynamics (e.g., Ripepe et al. 2007; Iguchi 2013; Matoza et al. 2013a).

Explosive eruptions are seismo-acoustic phenomena, generating large-amplitude acoustic waves as well as seismic waves. Precursory and co-eruptive seismicity includes individual volcano-tectonic (VT) earthquakes, long-period (LP) (0.5–5 Hz) events, and various types of volcanic tremor (Chouet and Matoza 2013). The typical seismic expression of a sustained explosive eruption, a broadband signal (~0.1–20 Hz) known as *eruption tremor* (McNutt 2000; McNutt and Nishimura 2008), usually has a limited propagation distance. The maximum observation range for eruption tremor is typically a few tens of kilometers, or up to a few hundred kilometers for larger eruptions (e.g., Prejean and Brodsky 2011). In contrast, similar-sized explosive eruptions produce powerful broadband (~0.01–20 Hz) infrasound signals (Fig. 33.1) that can be ducted efficiently over long ranges (thousands of kilometers) in atmospheric waveguides. These infrasound signals are now routinely detected on sparse ground-based infrasound networks such as the International Monitoring System (IMS) (e.g., Fee et al. 2010a, b; Matoza et al. 2011a, b; Dabrowa et al. 2011; Green et al. 2012; Fee et al. 2013a, b). In remote volcanic regions, infrasound is sometimes the only ground-based technology to record an explosive eruption and can therefore provide vital information to complement satellite data and constrain ash-release parameters for aviation safety (Figs. 33.2 and 33.3; e.g., Matoza et al. 2011a). At seismically instrumented

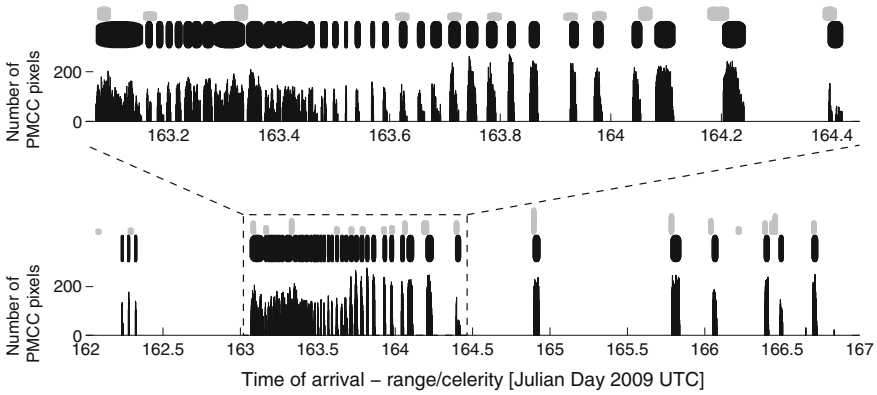

Fig. 33.3 Chronology of coherent infrasonic signal at IS44 from the June 2009 eruption of Sarychev Peak compared to the eruption chronology inferred from satellite data by the Sakhalin Volcanic Eruptions Response Team (SVERT). Lower plot: number of Progressive Multi-Channel Correlation (PMCC) (Cansi 1995) detections per minute at IS44 originating from the direction of Sarychev Peak. Time of arrivals are corrected back to an inferred origin time at Sarychev assuming a celerity of 0.33 km/s. Black horizontal bars above plot represent beginning and end times of coherent signal packets. Gray bars represent explosion onset times ±15 min inferred from satellite data by SVERT. Vertical extent of each gray bar is scaled relative to the maximum plume altitude inferred by SVERT. Upper plot: an expanded view of lower plot between Julian days 163–164.5 2009. (Figure reproduced from Matoza et al. 2011a)

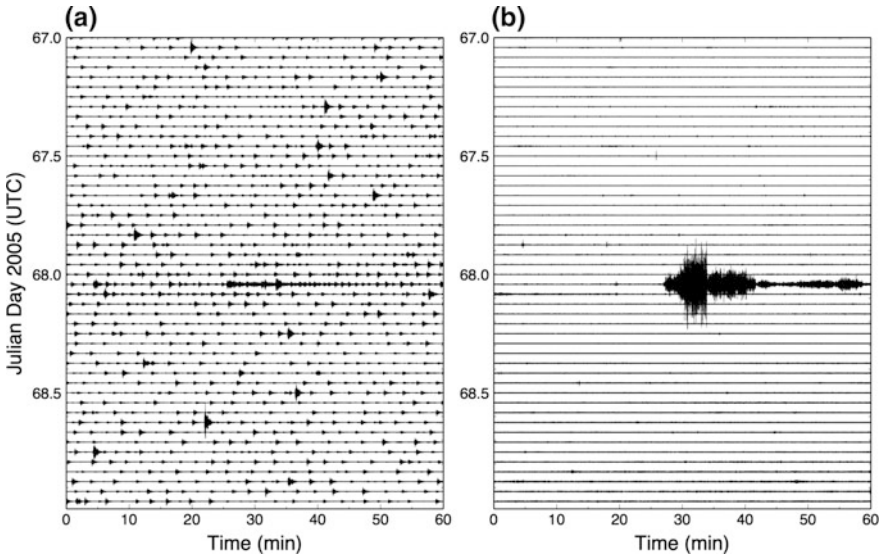

Fig. 33.4 **a** Seismic vertical component velocity and **b** infrasonic pressure recordings of the 8 March 2005 phreatic (steam-driven) explosion of Mount St. Helens, Washington, USA. The broadband seismometer was collocated with the central element of a 4-element infrasound array CDWR in a quiet forest site ~13.4 km from the source (Matoza et al. 2007). In each case, we show data from ±1 day spanning the event at 9 March 2005 ~01:26:17 UTC (day 68). The seismic tremor accompanying the phreatic explosion has a similar amplitude to seismicity before and after. A large unambiguous infrasound signal delineates the explosive eruption timing (Matoza et al. 2007)

volcanoes, infrasound data reduce ambiguity in explosion detection by clearly delineating the timing and duration of explosive eruption (Fig. 33.4); this is particularly useful when the volcano is visually obscured by cloud cover (Matoza et al. 2007). Because infrasound is radiated directly from explosive eruption processes in the atmosphere, the signals contain important constraints for physical volcanology (e.g., Cerminara et al. 2016), including estimates of the time-history of volume flux and potentially mass flux (e.g., Johnson et al. 2008a; Kim et al. 2015).

Several review papers and book chapters already exist, offering various perspectives on the field of volcano infrasound (e.g., Johnson and Ripepe 2011; Garces et al. 2013; Fee and Matoza 2013; McNutt et al. 2015). The present chapter reviews the history, development, and recent advances in the field of volcano acoustics with an emphasis on science and potential civil application gains from the IMS network.

33.2 History of Volcano Infrasound

Volcanoes generate a wide variety of acoustic signals within the infrasonic frequency band (~0.01–20 Hz) and explosive volcanic eruptions are among the most powerful sources of infrasound observed on Earth. More generally, volcano infrasound is part of a broad spectrum of atmospheric waves produced by volcanic activity that includes gravity waves, acoustic-gravity waves, infrasound, and audible acoustic signals (Gossard and Hooke 1975).

33.2.1 Barograph Studies and Infrasound Microphone Arrays (<1 Hz)

In 1883, over 50 weather barometers around the world recorded long-period pressure disturbances from the cataclysmic, Volcanic Explosivity Index[1] (VEI) 6, August 27 eruption of Krakatau Volcano, Indonesia (Fig. 33.5) (Scott 1884; Strachey 1884, 1888; Verbeek 1884). A Royal Society of London report compiled the barometric observations and reports of sounds heard (Strachey 1888). Cannon-like sounds were audible as far away as ~5,000 km. This phenomenon of long-distance audible sound from Krakatau is now explained by nonlinear wave steepening and reshocking rather than unattenuated audible frequencies from near the source (Lonzaga et al. 2015). The long-period pressure wave, recorded as barometric pulses, propagated as many as seven times around the globe (Strachey 1888). It took roughly 1.5 days to make each complete lap, with an average propagation speed of 300–325 m/s; the dominant periods at long range were ~100–200 min (Fig. 33.5) (Gabrielson 2010). These remarkable observations stimulated the development of theory to explain these acoustic-gravity waves, to understand the effects of gravity, buoyancy, and atmospheric structure on the acoustic propagation from such an immense source (e.g., LeConte 1884; Lamb 1911; Taylor 1929, 1936; Pekeris 1939; Pierce 1963; Press and Harkrider 1962, 1966; Harkrider 1964; Harkrider and Press 1967; see Gabrielson 2010 for a review).

In a pioneering study of earthquakes and airborne explosions ("detonations") at Mount Asama, Japan, Omori (1912) used seismometers and barometers to discriminate between seismic signals associated with explosions and non-explosion earthquakes. Many of the explosion events were audible in settlements at distances of ~200–300 km (Fig. 33.6), and some were powerful enough to knock out doors and windows. Omori used this information to map the sound propagation and acoustic shadow zones, and considered the effects of wind and topography on the

[1]VEI is a semi-quantitative measure of the magnitude or size of explosive eruptions based on factors such as the erupted ejecta volume, column height, and explosive eruption duration (Newhall and Self 1962). The VEI estimates given throughout the text are from the Smithsonian database of Siebert and Simkin (2002).

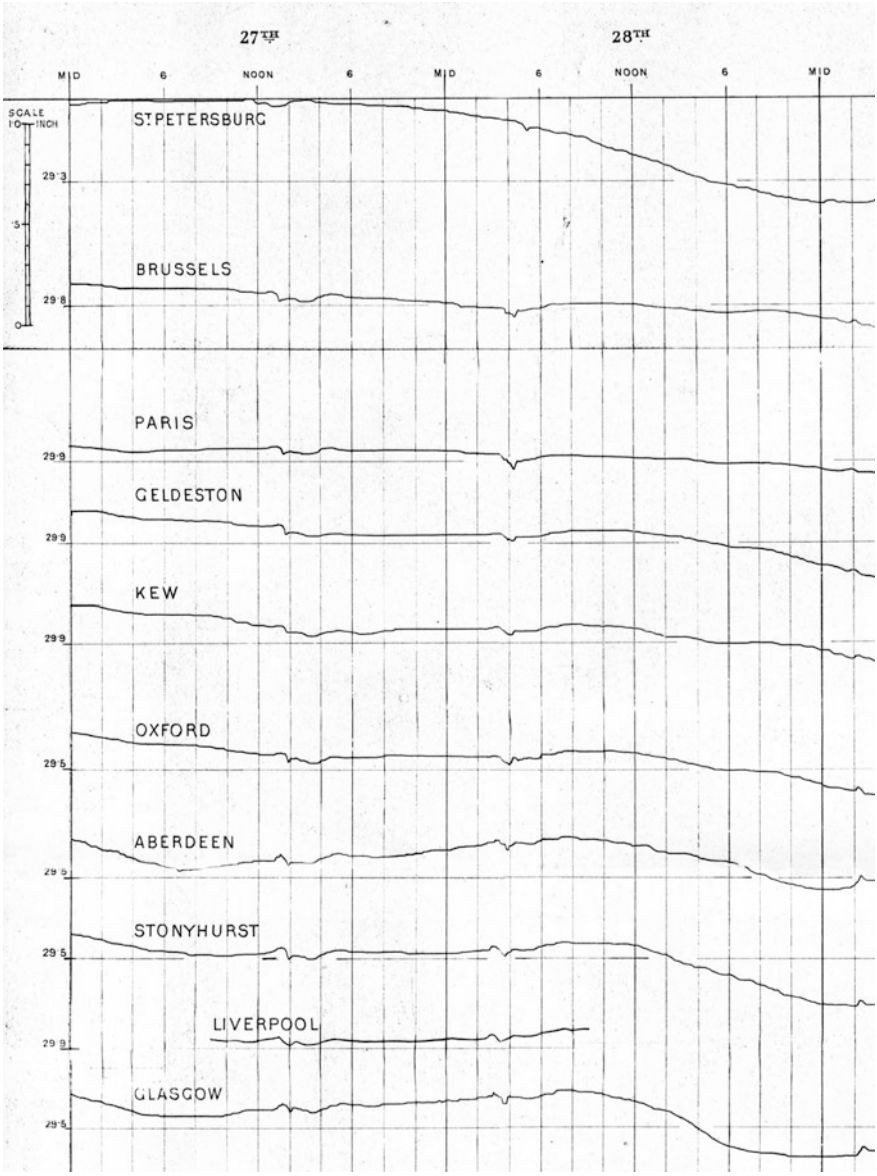

Fig. 33.5 Barograms from the 27 August 1883 eruption of Krakatau showing the first two wave passages. The traces are shown on a common scale and times are in UTC. The horizontal divisions are 2 h and 1 inch of mercury is ~3,386 Pa. (Figure reproduced and modified from Scott 1884)

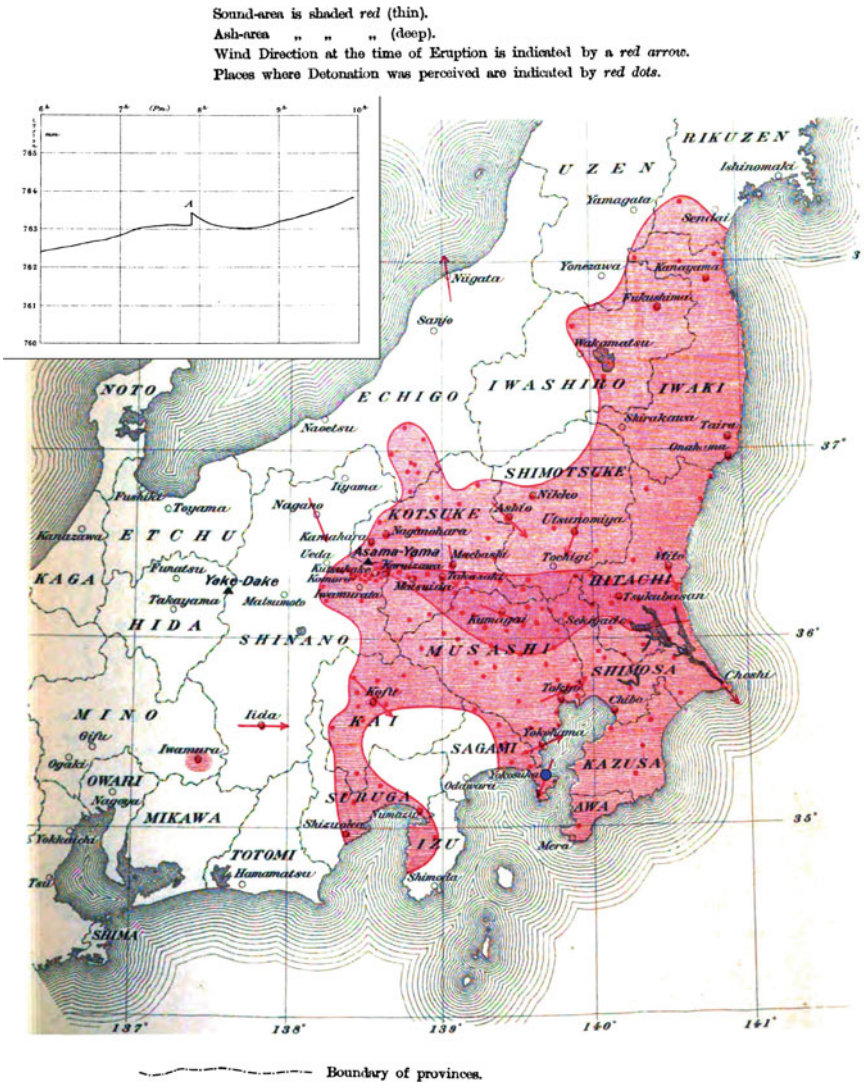

Fig. 33.6 Zone of audibility of "detonation" sound from a 7 December 1909 explosion of Asamayama, Japan (Omori 1912). The light red region is the audibility region, while the dark red region is the ash fallout region. Inset shows barogram at the Meteorological Observatory of Yokosuka (blue circle in map) for the same eruption (*A* marks signal onset). (Figures reproduced and modified from Omori 1912)

acoustic signals (Fig. 33.6). It is noteworthy that this classic early paper in volcano seismology gave equal emphasis to seismic and acoustic wavefields.

The use of weather barometers and infrasonic microphone arrays to study low-frequency (<1 Hz) atmospheric pressure waves from volcanic explosions at regional to global ranges (tens to thousands of kilometers) continued throughout the

twentieth century, e.g., Mount Pelee, Martinique 1902 (Tempest and Flett 1903); Bezymianny, Russia 1956 (Gorshkov 1960); Mount St. Helens, USA 1980 (Reed 1987; Delclos et al. 1990); El Chichon, Mexico 1982 (Mauk 1983); Mount Tokachi, Japan 1988; Sakurajima, Japan 1989; Mount Pinatubo, Philippines 1991; and Ruapehu, New Zealand 1995 (Morrissey and Chouet 1997). Goerke et al. (1965), Wilson et al. (1966), and Wilson and Forbes (1969) provided some of the first infrasonic microphone array observations of volcanoes in the low infrasound band (0.01–0.1 Hz). The 1963 eruption of Mount Agung, Bali was recorded 14,700 km away in Boulder, Colorado (Goerke et al. 1965); and the 1967 eruptions of Redoubt and Trident Volcanoes, Alaska, were recorded in Fairbanks, Alaska (Wilson et al. 1966; Wilson and Forbes 1969). The main emphasis of these studies was the atmospheric propagation of the signals.

The 18 May 1980 VEI 5 eruption of Mount St. Helens was particularly well recorded and studied. Similar to the work by Omori (1912) (Fig. 33.6), audibility zones were mapped by Fairfield (1980) as far as 700 km from the source. Weather barograph stations across the Pacific Northwest (out to ~400 km) recorded the event (Bannister 1984; Reed 1987). Pressure waves were recorded worldwide over 7,000 km from the source on microbarograph and infrasonic microphone arrays, and have been modeled as a combination of Lamb and acoustic-gravity modes (Bolt and Tanimoto 1981; Donn and Balachandran 1981; Bath 1982; Liu et al. 1982; Delclos et al. 1990). Using pressure-distance empirical scaling relations (Glasstone 1977), Reed (1987) estimated the equivalent nuclear yield of the main blast at a few megatons. Barograph signals with period ~300 s and observed peaks in seismic Rayleigh wave spectra were attributed to atmospheric oscillations (gravity mode and acoustic normal modes) excited by the eruption (Kanamori et al. 1994; Watada and Kanamori 2010). Infrasound air–ground-coupled waves were also recorded across a seismic network in Washington State (Johnson and Malone 2007).

Infrasonic microphone arrays were installed at Kariya, Japan (Tahira 1982) and Windless Bight, Antarctica, 26 km from Mount Erebus (Dibble et al. 1984). Although limited to the band 0.1–1 Hz, the Kariya array routinely detected explosions from Sakurajima Volcano at a range of 710 km and also recorded the 1991 Pinatubo, Philippines eruption at a range of 2,770 km. These data were used to infer the eruptive time-history when visual or instrumental observations close to the volcano were impossible (Tahira et al. 1996).

33.2.2 Audible Sound Microphone Recordings (>20 Hz)

Frank Perret made probably the first recordings of audible sounds (>20 Hz) from volcanoes using moving-coil microphones at Vesuvius Volcano, Italy in 1906, eventually recording signals at Etna and Stromboli Volcanoes, Italy; Kilauea Volcano, Hawaii; Sakurajima Volcano, Japan; Mt. Pelee Volcano, Martinique; and Soufriere Hills Volcano, Montserrat (Perret 1950). The NHK Broadcasting Bureau of Japan apparently made the first tape recordings of volcanic sounds (Snodgrass and

Richards 1956). In 1952, a program of volcanic acoustics was initiated by James Snodgrass at the Scripps Institution of Oceanography, leading to a decade's worth of underwater and airborne acoustic recordings of volcanic sounds (Richards 1963). The paper by Richards (1963) summarizes the observations, relating the various sounds to different idealized styles of volcanic activity; however, the sonobuoy-based recording systems had a poor frequency response below 50 Hz. A pioneering study of acoustic signals (>20 Hz) by Woulff and McGetchin (1976) represents the first attempt at a quantitative link between acoustic radiation and fluid mechanics at volcanoes using equivalent source theory (Sect. 33.6.1). Naturally, audible sound from volcanoes is readily recordable close to the source (e.g., Lorenz et al. 2015).

33.2.3 Volcano Infrasound (0.01–20 Hz)

As with volcano seismology, the long-period (LP) band (0.5–5 Hz) tends to be an especially rich band for volcano-acoustic sources. Progress in the field of volcano acoustics was therefore modest until microphones targeting these frequencies were deployed near active volcanoes. *Near-infrasound* (1–20 Hz) from volcanoes is documented from the 1980s (e.g., Dibble et al. 1984; Firstov and Kravchenko 1996). Iguchi and Ishihara (1990) and Yamasato (1997) installed infrasonic microphones at distances of 2–5 km from Sakurajima, Suwanosejima, and Unzen Volcanoes in Japan, recording numerous explosions, pyroclastic flows (Yamasato 1997), harmonic infrasonic tremor (Sakai et al. 1996), and impulsive signals associated with LP events (Iguchi and Ishihara 1990; Yamasato 1998). Acoustic studies began at Stromboli Volcano in the early 1990s (Braun and Ripepe 1993; Vergniolle and Brandeis 1994; Buckingham and Garces 1996). Since then, it has become increasingly clear that a great variety of volcanic processes produce a diverse spectrum of infrasound across the 0.01–20 Hz frequency range (e.g., Fee and Matoza 2013).

33.2.4 The IMS Infrasound Network

In 1996 the Comprehensive Nuclear-Test-Ban Treaty (CTBT) was opened for signature. The treaty called for a verification regime to be established, of which the IMS is one element. The IMS infrasound network (Fig. 33.7) is designed to detect atmospheric explosions anywhere on the planet, with early studies citing a nominal threshold yield equivalent to 1 kiloton of TNT (Christie and Campus 2010). However, simulations show that long-range stratospheric ducting of infrasound significantly enhances the detection capability, with explosions of a couple hundred tons TNT equivalent being detectable globally at two or more stations on the complete network (Le Pichon et al. 2009; Green and Bowers 2010). Data holdings from the IMS infrasound network go back to about 2001 and as of 2015 the IMS has 49 certified stations out of a planned total of 60. Each infrasound station

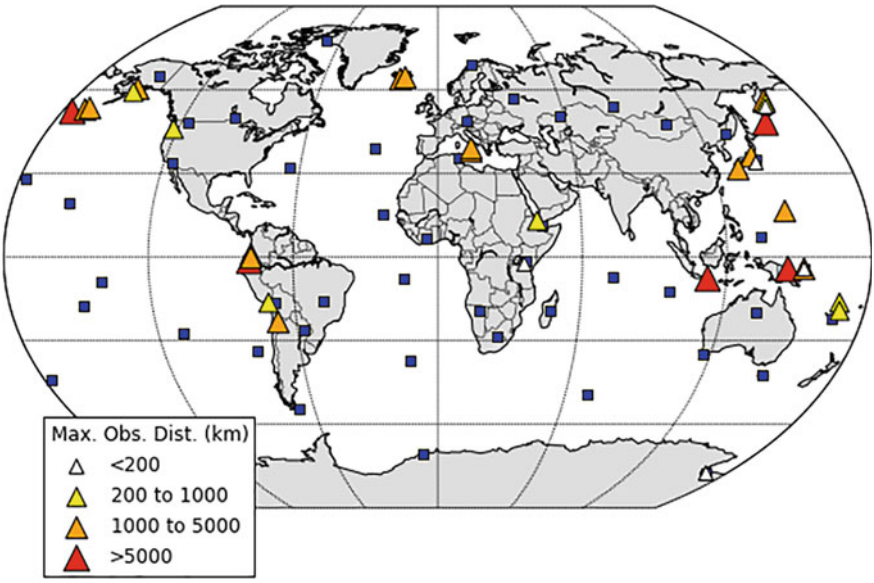

Fig. 33.7 The IMS infrasound array network as of 2015 (blue squares), and 43 volcanoes for which infrasound signals have been reported at an IMS station in the peer-reviewed literature (triangles). The color of the triangle refers to the furthest signal detection distance for all reported eruptions at the volcano. Multiple explosive events have been recorded from many of these volcanoes since the inception of the IMS. (Figure adapted and updated from Dabrowa et al. 2011)

consists of an array of at least four infrasonic sensors sampling atmospheric pressure at 20 Hz with a flat response compliant with IMS minimum requirements from 0.02 to 4 Hz and a sensitivity of about 0.1 mPa per count. The average station spacing for the complete network will be about 2,000 km (Christie and Campus 2010). The construction of the IMS has led to rapid advances in infrasound technology, and improved our ability to use infrasound to understand and monitor volcanic processes (Fig. 33.7). Two of the next stations planned for construction are: IS01 (Bariloche, west of Argentina close to the Andes) and IS20 (Galapagos, Ecuador) that will extend and improve IMS capabilities to monitor volcanic eruptions in the Latin America region.

33.3 Volcano-Acoustic Observation Systems

Volcanic infrasound sensor acquisition geometries include networks of individual infrasound sensors (e.g., Braun and Ripepe 1993; Garces et al. 1999; Hagerty et al. 2000; Johnson 2003; Moran et al. 2008; Lees et al. 2008; Cannata et al. 2009; Fee et al. 2014) and infrasound arrays, including networks of infrasound arrays such as the IMS infrasound network (e.g., Ripepe and Marchetti 2002; Guilbert et al. 2005;

Matoza et al. 2007; Taisne et al. 2019; Garces et al. 2008; Matoza et al. 2011b; De Angelis et al. 2012; Taisne et al. 2012, 2019; Tailpied et al. 2013). Where extensive infrasound sensor observations are limited, infrasound waves may still be tracked using collocated seismic and infrasonic sensor pairs (e.g., Ichihara et al. 2012; Matoza and Fee 2014; Nishida and Ichihara 2016) or solely using air–ground-coupled waves on seismic networks (e.g., Cochran and Shearer 2006; Johnson and Malone 2007; Fee et al. 2016). Networks of single infrasound sensors are often adequate for local deployments (nominally defined as <15 km from the source; Fee and Matoza 2013) around volcanoes that produce high-amplitude transient signals (e.g., volcanic "explosions"), whose relative arrival times can be tracked across the network (e.g., Johnson 2003; Fee et al. 2014). However, low-amplitude transients (e.g., Matoza et al. 2009a) or tremor signals (e.g., associated with sustained degassing or lahars) may require infrasound arrays for unambiguous detection and discrimination from background noise even at local distances (Garces et al. 2003; Matoza et al. 2007; Fee and Garces 2007; Matoza et al. 2010; Johnson and Palma 2015). Local deployments are also still subject to time-varying atmospheric propagation effects (Sect. 33.7), for which arrays provide useful additional information. At regional distances (nominally 15–250 km) and global distances (>250 km), infrasound arrays provide significant advantages for the detection and identification of remote volcanic infrasound signals within incoherent wind noise (Walker and Hedlin 2010) and coherent infrasonic clutter (Matoza et al. 2013c). Nevertheless, significant advances are being made toward using networks of single infrasound sensors or networks of seismic and infrasonic sensor pairs to identify remote volcanic infrasound at regional to global distances (e.g., Ichihara et al. 2012; Matoza and Fee 2014; Nishida and Ichihara 2016).

33.3.1 Remote Volcanic Signal Discrimination Using Arrays

Since the IMS infrasound network consists of a network of infrasound arrays, here we discuss some practical considerations for the use of IMS-style infrasound arrays for the detection of remote explosive volcanism. An example of long-range infrasonic array observations of explosive volcanism is shown in Fig. 33.8, which shows the detection of the 2010 eruption of Eyjafjallajökull, Iceland at station BKNI, UK. An initial burst of infrasound from this event was recorded from 14 to 15 April 2010, with the major long-duration infrasound recorded from April 18 to May 20, 2010 (Matoza et al. 2011b). The 2010 eruption of Eyjafjallajökull was recorded by 14 infrasound arrays at ranges between 1,745 and 3,666 km, indicating that infrasound from modest-size eruptions can propagate for thousands of kilometers in atmospheric waveguides. BKNI (4-element array) was the closest remote infrasound array to Eyjafjallajökull (range 1,745 km) considered by Matoza et al. (2011b). As shown in Fig. 33.8a, the volcano falls at a similar back azimuth to the microbarom source region at this time of year (Landès et al. 2012; see also the work

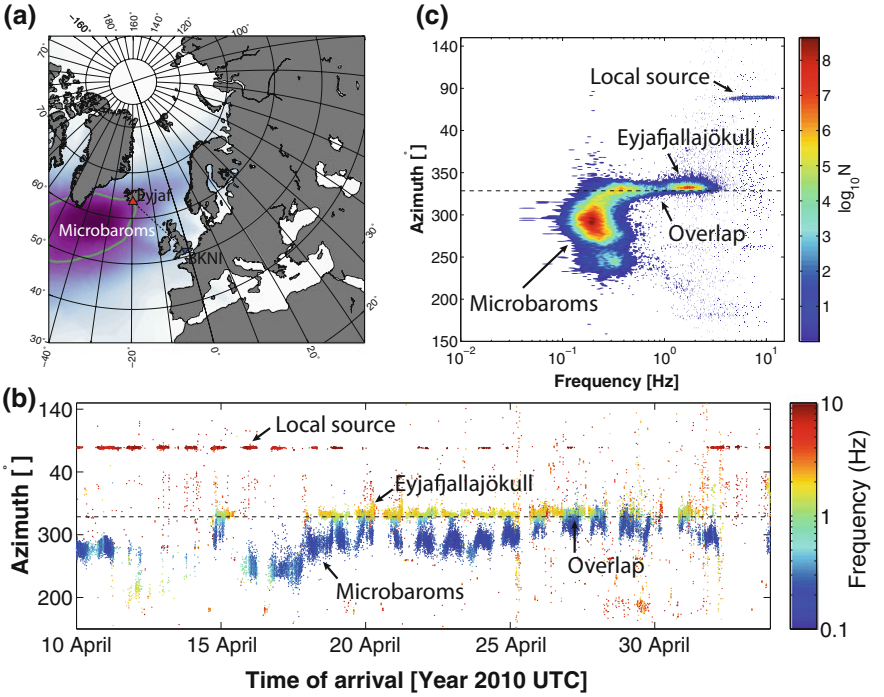

Fig. 33.8 Remote infrasonic array observations of the 2010 eruption of Eyjafjallajökull at station BKNI (Blacknest, UK; range 1,745 km, 4-element infrasound array). **a** Station BKNI (blue inverted triangle) and Eyjafjallajökull (red triangle) are shown in relation to the inferred source distribution of oceanic microbaroms in April from Landès et al. (2012). Purple grid values represent high probability of microbarom sources; the grid represents a multi-year average for 2006–2010 for the calendar month of April. **b** Log-scale PMCC processing results for the eruption onset (Matoza et al. 2011b). PMCC pixels are plotted by back azimuth and color-scaled by frequency content; the dashed line is the true back azimuth to Eyjafjallajökull (see a). An initial burst of infrasonic detections from Eyjafjallajökull (yellow dots) begins on April 14–15, is followed by repose from 15–17 April, and the onset of the main phase occurs on 18 April 2010. A higher frequency local source (red dots) and lower frequency microbarom source (dark blue dots) are also recorded by the array. **c** Frequency-azimuth space density plot of the data shown in (**b**), with the color scale representing the number of points (*N*)

by Evers and Haak 2001); the microbarom back azimuth is variable for this spatially extensive source. At times (e.g., April 15–20, 2010), the azimuths are distinct enough to allow for separation of microbarom and volcanic sources (Fig. 33.8b); however, later in the sequence the back azimuth values overlap and the microbarom interferes with the volcanic signal (Fig. 33.8b). Figure 33.8b, c reveal that each source usually occupies a distinct area of frequency-azimuth space, but occasional overlap in mean frequency and azimuth require more advanced signal detection and discrimination procedures. The example shown in Fig. 33.8 highlights how an infrasound array helps to discriminate volcanic signals of interest (in comparison to a remote single infrasonic sensor).

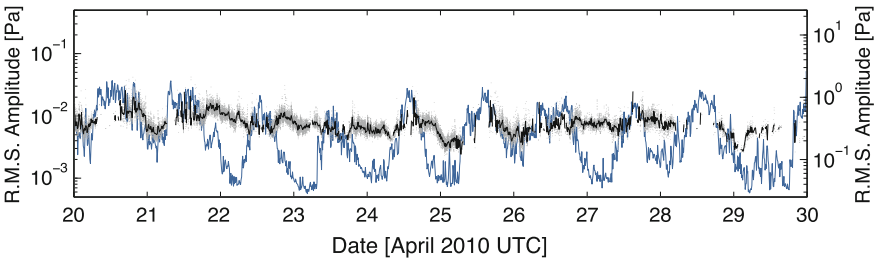

Fig. 33.9 Signal and noise amplitude variations at array BKNI, UK. PMCC detection root-mean-square (RMS) amplitudes (gray dots, left- hand scale) and their 10-minute median values (black line, left-hand scale) indicate coherent acoustic detections associated with Eyjafjallajökull. This is compared to RMS amplitude at one element in the 0.01–0.5 Hz band (blue line, right-hand scale). (Figure reproduced from Matoza et al. 2011b)

An additional feature of the BKNI recordings of the 2010 Eyjafjallajökull eruption is the diurnal variation in received signal characteristics (Fig. 33.8b), which were investigated in detail by Green et al. (2012). This is illustrated in Fig. 33.9, which shows the diurnal variability of signal reception compared to root-mean-square (RMS) amplitude at low frequencies (0.01–0.5 Hz), a useful proxy for wind noise (Fee and Garces 2007). Such observations are important for the remote identification of volcanic infrasound and again are facilitated by the use of arrays rather than single infrasound sensors.

33.3.2 Source-Receiver Network Geometry

Figure 33.10 shows the location of IMS infrasound array IS44 in relation to potentially active volcanoes in Kamchatka, Russia (Siebert and Simkin 2002-). Although IS44 provided high signal-to-noise ratio infrasound recordings of the June 2009 eruption of Sarychev Peak in the Kuriles (Figs. 33.1, 33.2 and 33.3) and seems to provide numerous observations of infrasound from different volcanoes in Kamchatka spanning multiple years (Fig. 33.10c), discrimination of the volcanic signals and their attribution to a particular volcano is complicated for the Kamchatka region. The complication is the location of multiple potentially active volcanoes lying along similar back azimuth trajectories from IS44 (Fig. 33.10b). Additional regional infrasound array or network deployments in the region would greatly facilitate the detection and discrimination of volcanic sources in Kamchatka.

Global acoustic detection and association capabilities are controlled by the overall network density, as well as the locations and noise levels of critical stations in volcanic regions. We anticipate significant improvements in global detectability of volcanic infrasound in the future as the IMS infrasound network achieves planned 59-station global coverage (Fig. 33.11). Figure 33.11 shows the computed great-circle distances from each potentially active volcano identified in the

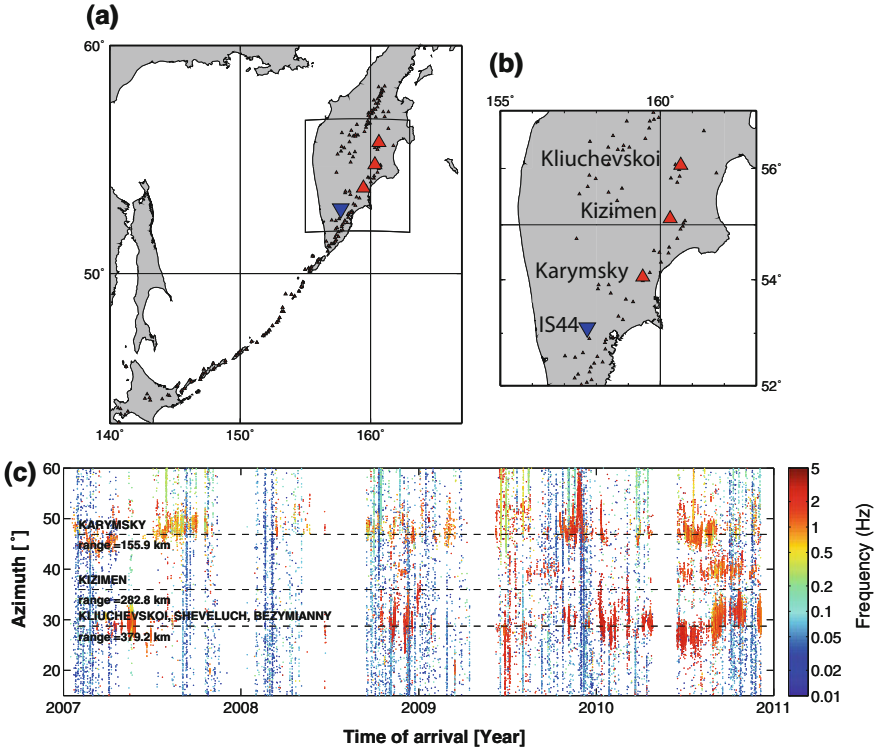

Fig. 33.10 IS44 2007–2010 PMCC results (Matoza et al. 2013) compared to locations of potentially active volcanoes in the Kamchatka and Kuriles regions (red triangles, Siebert and Simkin 2002). **a** and **b** Map of the region with the most active volcanoes labeled. **c** PMCC pixels plotted as a function of time and back azimuth and colored by frequency. Signals with mean frequencies >0.5 Hz (orange and red colors) in (**c**) are possible volcanic signals. Multiple potentially active volcanoes fall along a similar back azimuth trajectory from IS44, complicating the unique attribution of infrasound to a volcanic source given the available network geometry

Smithsonian Global Volcanism Program (GVP) database to the nearest two or three IMS stations, and serves as a first-order proxy for infrasonic network detection capability of global volcanism. Figure 33.11 gives a preliminary view of how volcanic eruption detectability will improve by completing the IMS network and also reveals the volcanic regions (e.g., the Caribbean, Southeast Asia, Aleutians) that would most benefit from additional regional infrasound arrays. Additional infrasound arrays deployed in regions with dense volcanism (e.g., Guilbert et al. 2005; Matoza et al. 2007; Garces et al. 2008; Matoza et al. 2011b; De Angelis et al. 2012; Taisne et al. 2012; Tailpied et al. 2013) will lead to significant improvements by augmenting the network density and decreasing the acoustic source power of explosive eruption detectable with a globally integrated network (Le Pichon et al. 2009; Green and Bowers 2010). In addition to infrasound propagation effects, noise levels experienced by key stations in volcanic regions play an important role in

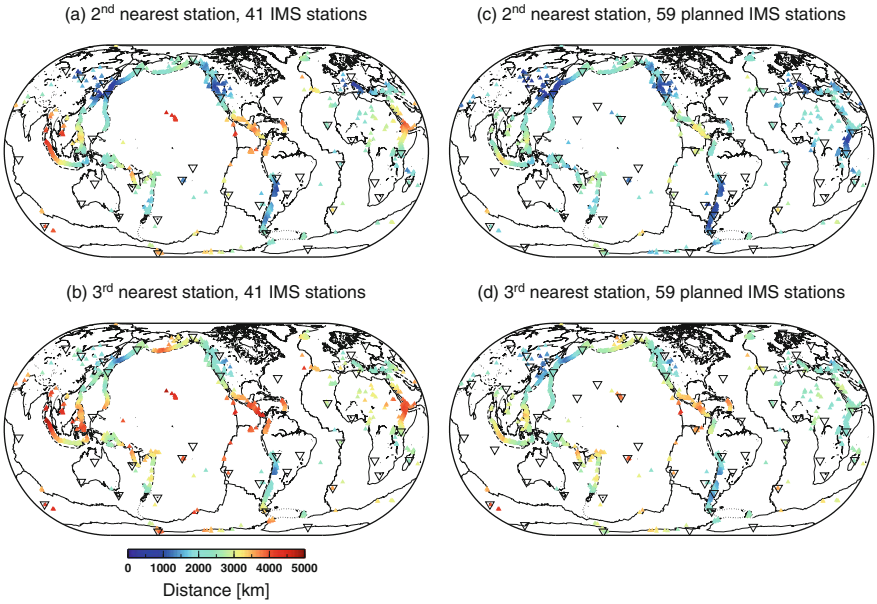

Fig. 33.11 The IMS network and potentially active volcanoes. The distance from each potentially active volcano in the Smithsonian GVP database of Siebert and Simkin (2002-) (inverted triangles with color scale corresponding to distance) are shown with respect to the nearest 2 or 3 IMS stations (open inverted triangles) given (a, b) the 41-station network configuration available from 2005–2010 and (c, d) the planned 59-station IMS network (location of 60th station IS28 is to be determined). The color scale is the same in each case. (Figure reproduced from Matoza et al. 2017)

controlling volcanic signal detection. This is especially the case for island stations, where noise levels are often high and variable; e.g., IS06, Cocos Islands is critical for observing Indonesian volcanoes.

33.4 Diversity of Volcanic Processes and Infrasound

Volcanic processes produce a great diversity of infrasound source mechanisms and signals. The duration of volcanic infrasound waveforms can range from short-duration events lasting ~1 s, to sustained tremor signals lasting months to years. Amplitudes span a wide dynamic range, from small signals approaching the noise level of infrasound sensors [mPa] to larger explosions producing nonlinear shock waves with overpressures exceeding atmospheric pressure ($>10^5$ Pa). Topography and volcanic crater morphology modify the signals and create additional variety (Sect. 33.7). Despite source process diversity and waveform complexity, wavefield modeling and inversion techniques have been used to infer eruption source parameters and processes (e.g., Matoza et al. 2009a; Kim et al. 2015). In this section, we briefly describe the diversity of observed infrasound

signals and highlight imaging and modeling techniques that have been used to characterize and understand volcano infrasound sources. We focus on more recent work in this section; the reader is referred to Johnson and Ripepe (2011) and Fee and Matoza (2013) for more in-depth treatments of these topics.

33.4.1 Low-Viscosity Magmas

Low-viscosity (e.g., basaltic) magmas characteristically exhibit long-lived effusive eruptions punctuated by short explosive bursts, along with occasional gas-rich lava fountaining episodes. Effusive eruptions and roiling lava lakes have been observed to produce near-continuous broadband and/or harmonic infrasound. Kilauea Volcano is a well-studied example with prodigious broadband and harmonic infrasonic tremor and occasional short-duration explosions (e.g., Fee et al. 2010b; Matoza et al. 2010). As another example, lava fountaining from Mount Etna produces high-amplitude, sustained tremor with occasional repeating explosions (e.g., Cannata et al. 2009; Ulivieri et al. 2013).

Of interest for the acoustics of low-viscosity systems is the potential for coupling of the sound field from a magma column into the atmosphere. Buckingham and Garcés (1996), Garcés (2000) and Garcés and McNutt (1997) developed a canonical model, deriving an analytic solution for the airborne Green's function from a resonant magma conduit. To couple the sound field from the magma column to the atmosphere, a near-surface bubbly mixture with high void fraction would lower the impedance contrast between the magma and atmosphere aiding signal transmission (Garcés and McNutt, 1997; Garcés et al. 1998), but may also result in strong attenuation of acoustic waves, hindering transmission (Marchetti et al. 2004). Matoza et al. (2010) proposed that the low-frequency anomalous transparency theory of Godin (2006, 2007) allows infrasound to propagate from a subsurface basaltic magma column into the atmosphere, without requiring a near-surface foam layer.

Cavities and gas-filled conduits above degassing magma bodies also appear to substantially shape the infrasonic signature. The ~200 m cavity above the Halema`uma`u lava lake at Kilauea, Hawaii was modeled as a Helmholtz resonator, producing sustained ~0.5 Hz tremor and explosion pulses (Fig. 33.12) (Fee et al. 2010c), while sustained harmonic tremor from vigorous degassing at the Pu`u O`o cone was attributed to flow-induced oscillations through the shallow cavity structure (Matoza et al. 2010). Similar processes have been invoked at other volcanoes; for example, Villarica, Chile may also generate continuous infrasound through Helmholtz resonance (Goto and Johnson 2011), resonance of a Bessel horn (Richardson et al. 2014), or flow instabilities within the upper conduit (Ripepe et al. 2010b).

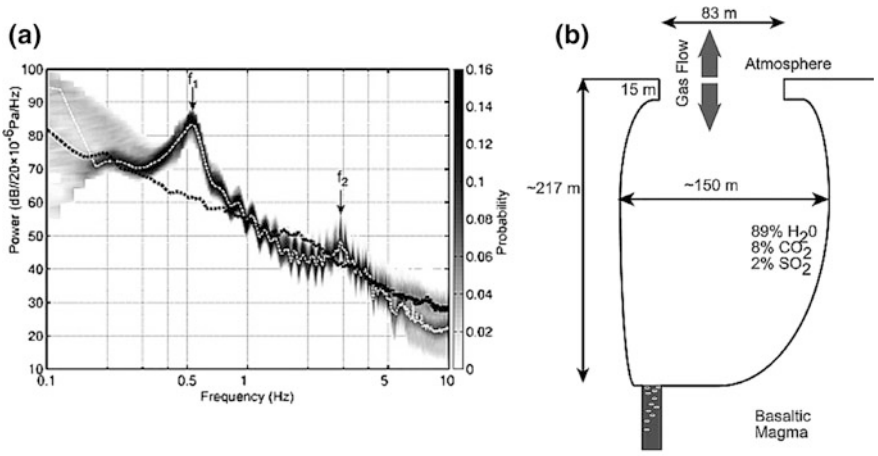

Fig. 33.12 Observed infrasound and its interpretation at Halema`uma`u, Kilauea Volcano (Fee et al. 2010c). **a** Probability density function of the PSD. The dotted white line displays the peak probability, with a dominant peak around 0.55 Hz (f_1) and a secondary peak at $\sim$3 Hz (f_2). The dotted black line represents background noise level. **b** Cartoon of Halema'uma'u cavity, assuming Helmholtz resonance and eigenfunction analysis of a rectangular cavity. The vertical dimension is well constrained from lidar. Comparison of the observed spectra with theoretical modeling suggests that the width of the cavity is variable. (Figures reproduced from Fee et al. 2010c)

33.4.2 Strombolian Eruptions

Strombolian explosions generate short-duration infrasonic signals related to the gas overpressure and gas volume released. Explosions from the archetypical Stromboli Volcano, Aeolian Islands have been studied in particular detail (e.g., Ripepe et al. 2007). The acoustics of Strombolian activity have also been captured at Yasur, Vanuatu (Marchetti et al. 2013), and Mount Erebus (phonolite lava lake "Ray Lake"), Antarctica (Johnson et al. 2008a). Waveforms from Strombolian explosions are characterized by an initial compressional onset followed by a rarefaction, with extended coda reverberation in some cases (e.g., Firstov and Kravchenko 1996; Ripepe et al. 1996; Johnson 2003; Ripepe and Marchetti 2002; Ripepe et al. 2007; Johnson et al. 2008a; Jones et al. 2008). Explosions at Stromboli are understood to result from the coalescence of bubbles in a foam at depth in the conduit, the rise of this gas as a slug flow, and the subsequent bursting of this slug at the magma surface (Harris and Ripepe 2007). Braun and Ripepe (1993) and Ripepe et al. (1996) deployed the first infrasonic microphones at Stromboli, determining that bursting of the large gas bubbles at the surface of the magma column was responsible for simultaneous seismic and acoustic signals. Vergniolle and Brandeis (1994) and Vergniolle et al. (1996) proposed that oscillation of the bubble immediately prior to bursting and kinematic waves on the magma surface after the burst were the significant acoustic sources rather than the bubble burst itself.

Doppler radar observations of Strombolian explosions at Mount Erebus indicate that the bubble does not vibrate prior to bursting (Gerst et al. 2008, 2013). Prior to bursting, a volumetric expansion of the bubble membrane is observed, but the membrane rips before equilibrium pressure is reached (Gerst et al. 2008). Radar, visual, and infrasound data indicate that directivity during bubble rupture can be manifest in the acoustic radiation pattern (Gerst et al. 2008; Johnson et al. 2008a).

33.4.3 Silicic Systems

More viscous magmas are able to build up higher pressures within the conduit and form pressurized solid lava plugs or domes. The destruction of these plugs or domes commonly generates large, ash-rich explosions with sizeable ash plumes and ballistics. The acoustic signals from these eruptions are generally longer in duration, lower frequency, higher amplitude, and more complex than Strombolian explosions (Sect. 33.5.1) (e.g., Ripepe et al. 2010a; Fee et al. 2013b; Yokoo et al. 2013). Exotic infrasound signals are often generated in such systems, perhaps via gas escape through narrowing channels (Fig. 33.13) (Lees et al. 2004).

Hydrothermal and magmatic-hydrothermal interaction processes are also capable of infrasonic signal generation. Infrasonic pulses associated with long-period (LP) seismic events during the 2004–2008 eruption of the stratovolcano Mount St. Helens were attributed by Matoza et al. (2009a) to the repeated rapid pressure loss from a hydrothermal crack by venting into a shallow layer of loosely consolidated, highly permeable material. In this model, heating by magmatic activity causes pressure to rise, periodically reaching the pressure threshold for rupture of a valve sealing the crack. Sudden opening of the valve generates the broadband infrasonic signal and simultaneously triggers the collapse of the crack, initiating resonance of the remaining fluid leading to the seismic LP waveform. Johnson et al. (2008b) used visual, seismic, and geodetic data at Santiaguito Volcano, Guatemala to relate LP events to rapid uplift of a lava dome. The partial collapse of dacitic lava domes (Green and Neuberg 2005; Moran et al. 2008) and explosive blowout of gas-charged blocks impacting the ground (Oshima and Maekawa 2001) generate infrasound, while collapse may depressurize the magmatic system, leading to large explosive eruptions (e.g., Fee et al. 2013b).

Fast-moving, hazardous pyroclastic flows composed of ash and gas have been located and tracked using arrival times and Doppler shift on microphone networks or infrasound arrays (Sect. 33.6.4) (Yamasato 1997; Ripepe et al. 2009; Ripepe et al. 2010a). Lahars, or volcanic mudflows, can also generate infrasound; Johnson and Palma (2015) detected and tracked a large lahar from the 2015 eruption of Villarica Volcano, Chile using a nearby infrasound array. Silicic systems and magmatic-hydrothermal interactions also generate explosive volcanism, which is addressed in Sects. 33.5 and 33.6.

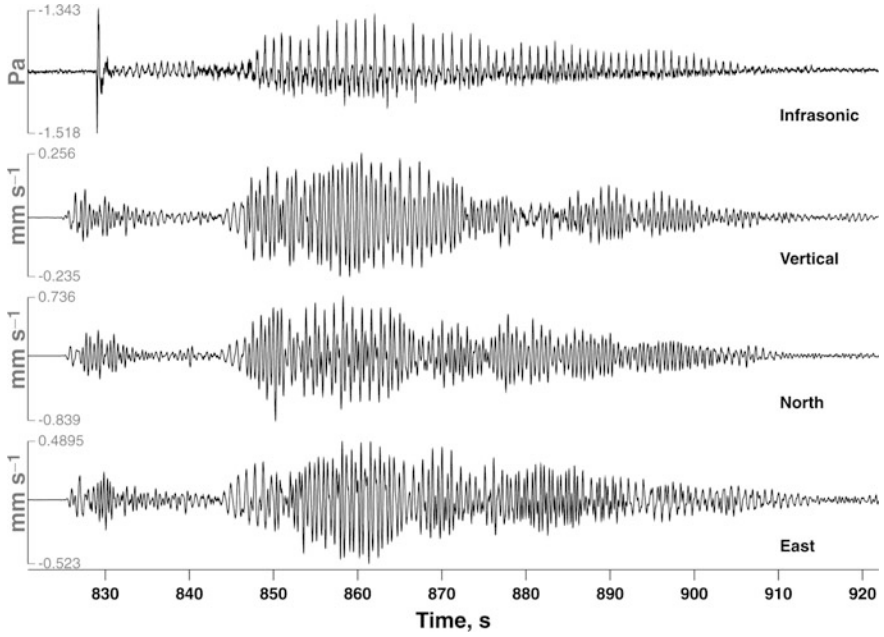

Fig. 33.13 Explosion followed by a sequence of continuous chugging (periodic tremor) at Karymsky Volcano, Kamchatka, Russia (Lees et al. 2004). The top trace is from an infrasonic microphone and the lower three traces are vertical, north, and east seismograms, respectively. (Figure reproduced from Lees et al. 2004)

33.4.4 Imaging Volcano-Infrasonic Sources

Volcano-acoustic studies have an advantage over volcano-seismic studies, in that the source processes are often amenable to direct observation. Visual, infrared (IR), and ultraviolet (UV) imaging synchronized with acoustic instrumentation has enabled a deeper understanding of volcano infrasound sources. High-speed visual (e.g., Yokoo et al. 2009; Genco et al. 2014) and infrared (e.g., Delle Donne and Ripepe 2012) video has been employed to image supersonic shock waves emanating from explosions and reconstruct the resultant acoustic waves. Differencing of images from sustained volcanic jets has revealed repeated shock waves emanating from the edges of the jet (Taddeucci et al. 2014). Imagery provides an independent estimate of the volume flux to constrain acoustic source models. Infrasound-derived gas volumes have been compared to constraints from video (Johnson et al. 2008a; Johnson and Miller 2014), IR (De Angelis et al. 2016), and UV (Dalton et al. 2010; Delle Donne et al. 2016) imagery.

Qualitatively, imagery also helps us to compare eruption styles and eruption parameters derived from infrasonic measurements. Lopez et al. (2013) used visual and infrared imagery, along with infrasound and gas measurements, to identify four

unique eruption styles at Karymsky Volcano, Kamchatka. Combined imagery and acoustic data are also comparable with laboratory and numerical experimental results.

33.4.5 *Experimental Studies of Volcanic Infrasound*

Analog laboratory, theoretical, and computational models have been used to investigate volcano-infrasound signal generation. In particular, the rise and burst of gas slugs and the associated infrasound signals have been investigated. Lane et al. (2013) performed analog experiments and used dimensional analysis to compare the rise and burst of laboratory gas slugs with observed infrasound signals from Strombolian explosions. They found a good qualitative agreement between simulated and observed waveforms, as well as a quantitative correlation between the independently derived gas slug length, mass, and overpressure. Vidal et al. (2010) showed how in laboratory studies, and potentially volcanoes, the complex and unpredictable nature of the slug rupture at the surface may lead to unpredictable source estimates using infrasound.

Explosions within the conduit or shallow subsurface can produce sizeable infrasound signals involving a more complex source process. Analog experiments of explosions underwater and in the shallow subsurface have been performed to investigate acoustic signal generation. Ichihara et al. (2009) analyzed a series of explosions within a lake to better understand the resultant acoustic waves and how they relate to the scaled depth, underwater pressure wave, and motion of the water surface. These observations were then compared to linear acoustic theory, with the observations showing lower amplitudes and higher frequencies than predicted by the theory. Bowman et al. (2014) examined acoustic signals from small subsurface explosions at different burial depths at an outdoor test facility. They observed a sequential three-stage sequence of sound generation due to ground deformation, gas release, and spall slap. These stages are observed from both non-volcanic and volcanic buried explosions (e.g., lava domes and plugs).

Analog modeling of acoustic signals has also been performed to investigate tremor and volcanic explosions in higher viscosity magmas. Lyons et al. (2013) performed flow-driven experiments in which harmonic signals were input into a viscoelastic fluid to simulate volcano-seismic and acoustic tremor. They found that acoustic tremor was produced only when a high fluid stiffness was achieved, allowing a stable pathway for the signals to propagate. This may explain why harmonic infrasonic tremor is only occasionally recorded during periods of harmonic seismic tremor.

33.5 Infrasound from Explosive Volcanism

Explosive eruption processes generate the most energetic infrasound signals associated with volcanoes, and are of most relevance for long-range detection with the IMS. Explosive volcanic eruptions are of immediate interest for their associated societal and economic hazards. Explosive volcanic eruptions are also large, naturally occurring, infrasonic sources, which may be used to validate and improve methods for infrasound propagation modeling, signal detection, discrimination, association, and source location to help improve operational IMS capabilities.

33.5.1 Explosive Volcanism Infrasound Signal Types

Infrasound signals from explosive eruptions capture the rich variety of physical explosion mechanisms (Fig. 33.14). Conceptual understanding of acoustic signals from explosive eruptions has tended to focus on two end-member signal durations: (1) discrete explosion waves with relatively simple waveforms lasting from several to tens of seconds (e.g., Firstov and Kravchenko 1996; Ripepe and Marchetti 2002; Johnson 2003; Marchetti et al. 2009, 2013), and (2) sustained, broadband, infrasonic tremor signals lasting from minutes to hours (e.g., Vergniolle and Caplan-Auerbach 2006; Matoza et al. 2009b; Fee et al. 2010a; Caplan-Auerbach et al. 2010). Commonly, the signals (1) are simply called "explosions" in the volcano acoustics literature and they have been modeled, using linear equivalent source theory (Sect. 33.6.1), as acoustic monopoles, i.e., sources represented as time-varying mass fluxes (e.g., Woulff and McGetchin 1976; Firstov and Kravchenko 1996; Johnson 2003; Delle Donne and Ripepe 2012). However, it is recognized that in many cases these "explosion" waves have nonlinear characteristics (Sect. 33.6.2) (Yokoo and Ishihara 2007; Marchetti et al. 2013; Garces et al. 2013), and nonlinear effects will increase with increasing overpressure release rate and supersonic ejection velocities (Needham 2010). Sustained, broadband infrasonic tremor signals (2) from more sustained eruptions (often described as "Vulcanian," "sub-Plinian," and "Plinian") resemble an infrasonic form of the jet noise produced by smaller scale man-made jets (Matoza et al. 2009b; Fee et al. 2010a, 2013a; Matoza et al. 2013b). Here, for simplicity, we refer to this signal type as *volcanic jet noise* (Sect. 33.6.3).

Observed explosive eruption signals often represent intermediate cases between idealized explosion or blast waves (1) and volcanic jet noise (2), and result from explosive processes that are not adequately described by the type eruption styles (e.g., "Strombolian," "Vulcanian," or "sub-Plinian"). Such complex waveform types appear to be a characteristic feature and behavior of intermediate-composition (andesitic) low-level explosive volcanism. For example, explosions at Sakurajima (Fig. 33.14) are described in papers by Ishihara (1985), Yokoo et al. (2013), and Fee et al. (2014); they are characterized by the rapid explosion of a magma plug and

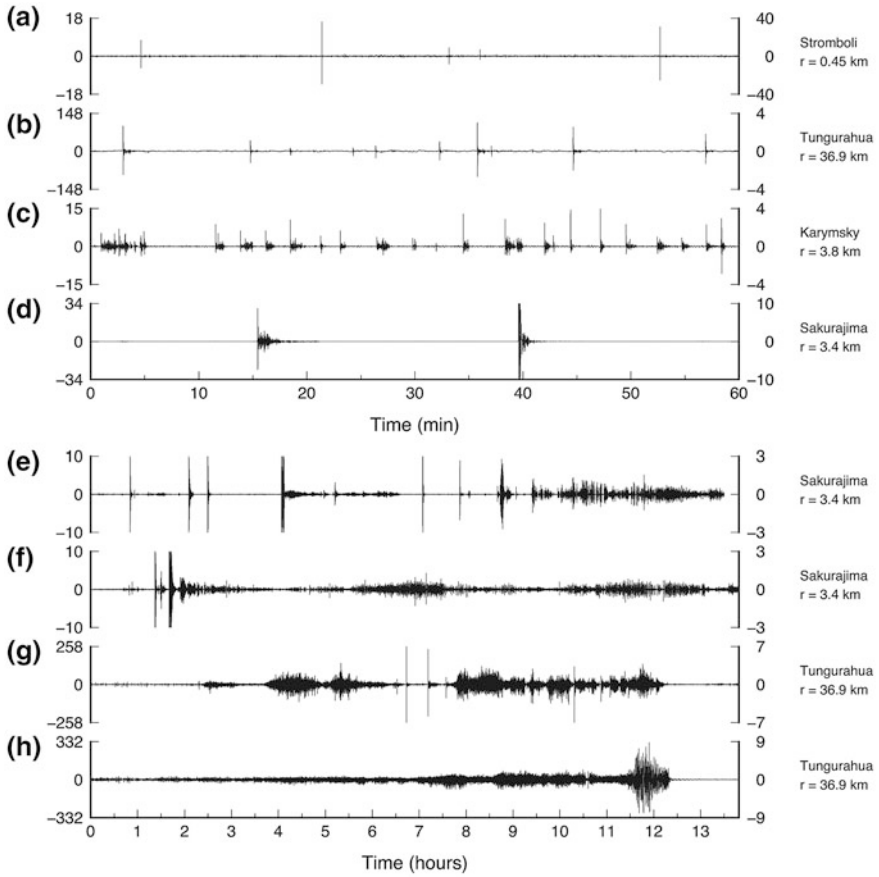

Fig. 33.14 Example infrasonic pressure waveforms associated with different explosive eruptive styles at different volcanoes. The top four traces (a-d) are of 1-hour duration, while the lower four traces (e-h) are of 13.8-hour duration. The right-hand labels indicate the volcano and recording distance (range) r [km]. In each case, the right-hand y-axis is the observed acoustic pressure amplitude at that range, while the left-hand y-axis is the amplitude corrected to a reference distance of 1 km from the source by assuming $1/r$ geometrical spreading for approximate comparison. **a** Typical Strombolian explosions from Stromboli Volcano, Italy (Ripepe and Marchetti 2002). **b** More energetic but still considered "Strombolian" explosions from Tungurahua, Ecuador, with codas containing harmonic tremor (Fee et al. 2010b). **c** Complex explosion waveforms from Karymsky, Kamchatka, with an initial sharp compressional onset followed by short-duration jetting (Lopez et al. 2013) or "blow-off" (Firstov et al. 2013). **d** Complex Vulcanian explosion waveforms at Sakurajima, Japan, similar to those at Karymsky but with longer inter-event times and different amplitudes and coda durations. **e** Complex explosion sequence at Sakurajima, including a mix of discrete explosions, volcanic jet noise, and signals of intermediate type. **f** A different Sakurajima example, more akin to volcanic jet noise but with discrete explosions or shocks interspersed. **g** sub-Plinian eruption from Tungurahua, Ecuador, consisting of multiple sustained sequences of volcanic jet noise interspersed with discrete explosions (Matoza et al. 2009b; Fee et al. 2010b). **h** sub-Plinian to Plinian eruption at Tungurahua: a sustained volcanic jet noise signal with more gradually evolving signal properties. Note: Figs. 33.14d, e, and f have been "clipped" to emphasize lower amplitude explosion codas and jetting; the peak onset compression amplitudes greatly exceed those shown on this plot. (Figure reproduced from Fee and Matoza 2013 and Matoza et al. 2014)

consist of strong acoustic waves, ejection of volcanic bombs, and high ash contents. Similar volcanic explosion complexity has been reported elsewhere, where it has been described variously as (a) "small, ballistic and ash-laden eruptive events," e.g., at Karymsky (e.g., Johnson 2007); (b) "low-intensity explosions" and "weak Vulcanian," e.g., at Santiaguito and Fuego (Guatemala), Villarrica (Chile), and Stromboli (Italy) (e.g., Sahetapy-Engel et al. 2008; Marchetti et al. 2009; Johnson et al. 2008b); or (c) "ash explosion," e.g., at Karymsky (e.g., Lopez et al. 2013; Firstov et al. 2013). Figure 33.14 illustrates selected examples of Sakurajima infrasound data compared to data from other explosive volcanic eruptions (Fee and Matoza 2013; Matoza et al. 2014). Many of the Sakurajima signals resemble "typical" explosion (1) waveforms (Fig. 33.14d–f), but with complex onsets and long-duration codas (tens to hundreds of seconds). Other, more sustained Sakurajima signals are qualitatively closer in character to volcanic jet noise (2, Fig. 33.14e, f), but are not simply a sustained, smoothly time-varying signal; the signals tend to stop and start erratically. In some cases, a sustained jet-noise-like signal is initiated by a more impulsive explosion, while in other cases the sustained signal begins with an emergent onset.

Tephra-rich and gas-rich (tephra poor) explosions have been found to produce quite similar basic waveform metrics (e.g., Fee et al. 2010b; Lopez et al. 2013; Matoza et al. 2014), which would make it challenging to automatically determine ash content based on simple metrics extracted from sparse long-range infrasound data. However, with more local volcano monitoring and dedicated field studies, it may be possible to identify unique waveform properties associated with ash-rich or ash-poor eruptions (e.g., Ripepe and Marchetti 2002; Lopez et al. 2013). Detailed field studies and infrasound waveform modeling, combined with laboratory and numerical studies, may provide eruption velocity source-time functions for this class of low-intensity explosive eruptions, constraining the dynamics of plume ascent and ash dispersal from unsteady eruptions and helping to mitigate societal and economic volcanic hazards.

33.5.2 Infrasound and Satellite-Derived Explosion Chronologies

Explosion chronologies determined from remote infrasound data (e.g., Figure 33.3) provide an independent constraint on eruption chronologies compiled using satellite data (Fee et al. 2010a, b; Matoza et al. 2011a). Comparisons of the two chronologies are relatively straightforward when explosions occur isolated in time. However, comparisons between the two chronologies require a higher level of interpretation when the infrasound detections occur continuously or with short

inter-event times (e.g., between Julian day 163 and 164.5 on Fig. 33.3). Satellite-derived explosion onset times for the June 2009 eruption of Sarychev Peak in Fig. 33.3 were estimated from the time when a dense ash cloud is first visible in satellite data (TERRA, NOAA, MTSAT) above the meteorological cloud layer. However, continuous ash and gas-steam emissions were also observed in satellite data during the eruption, e.g., between Julian day 163 and 164.5. Closely spaced explosions may feed a single sustained eruption column (e.g., Sparks et al. 1997). In addition, pyroclastic flows can generate infrasound (Sect. 33.6.4) (e.g., Yamasato 1997; Ripepe et al. 2009) and not all explosions that generate infrasound produce ash (e.g., Ripepe and Marchetti 2002; Garces et al. 2008; Fee et al. 2010b; Lopez et al. 2013). Therefore, we do not necessarily expect a one-to-one correlation between infrasound signal detections and visual satellite observation of plumes. Furthermore, low-amplitude source activity may not register on remote infrasound stations and weak explosions reaching only low altitudes are more easily obscured in satellite data by cloud cover. Nevertheless, remote infrasound signal detections provide a continuous, high-temporal-resolution chronology of the volcanic source that may be compared with satellite data (Fig. 33.3).

33.5.3 Scaling Between Plume Height and Infrasound

Infrasonic signals have been compared both qualitatively and quantitatively with ash plume height. Johnson et al. (2005) reported a poor correlation between the seismo-acoustic energy release and plume height from small, transient eruptions at Tungurahua Volcano, Ecuador. They concluded that the seismo-acoustic energy partitioning from small eruptions is complex. Fee et al. (2010a) compared acoustic power estimates with ash plume height for a variety of eruption styles at Tungurahua. They found a positive correlation between ash plume height and acoustic power for large, sustained sub-Plinian and Plinian eruptions. Lower frequency infrasound also correlated well with ash plume height from the Plinian eruptions of Kasatochi and Okmok Volcanoes, Alaska (Fee et al. 2010b). Dabrowa et al. (2011) took a comprehensive look at volcanic eruptions recorded on the IMS network, systematically comparing acoustic signal metrics with available ash plume height data. In summary, and similar to other studies of large eruptions, they found that: (1) the distance at which infrasound was recorded increases with ash plume height, (2) the lowest detected infrasonic frequency decreases with increasing plume height, and (3) the total acoustic energy and distance-corrected amplitude increase as a function of plume height.

Numerous authors have built upon the formulation of Lighthill (1978) and Woulff and McGetchin (1976), relating the acoustic source type (monopole, dipole, or quadrupole) and acoustic power to the volcanic jet velocity, and then extrapolating to estimate the plume height (Caplan-Auerbach et al. 2010; Ripepe et al. 2013). However, Matoza et al. (2013b) highlights how the original formulations of

Lighthill (1978) and Woulff and McGetchin (1976) are unlikely to be appropriate for volcanic jet flows, and that estimates of acoustic power at volcanoes are likely incorrect due to undersampling of the directional acoustic wavefield using a standard ground-based monitoring network. A quantitative acoustic source model relating the acoustic wavefield to gas exit velocity and potentially mass flux is needed in order to infer volcanic plume height using infrasound.

33.6 A Closer Look at Explosive Eruption Infrasound

One of the goals of infrasonic volcanic monitoring is to better characterize volcanic eruptions by providing relationships between measured pressure time-series and eruption flow parameters (e.g., Garces et al. 2013 *and references therein*). In order to achieve this, models of acoustic generation (and propagation) are required.

33.6.1 Linear Acoustic Equivalent Sources

The pioneering study by Woulff and McGetchin (1976) introduced the idea of using radiated acoustic power and frequency content to infer gas exit velocity for eruptions involving vigorous release of volcanic gases. This represents a first attempt at a quantitative framework relating volcanic fluid mechanics and acoustic wave generation. Woulff and McGetchin (1976) measured sound-pressure level near volcanic fumaroles. They then used sound-pressure level to estimate the overall sound power level by assuming an acoustic source radiating sound equally in all directions (i.e., no source directionality, spherically symmetric source). Finally, they used results from the classical aeroacoustics literature (Lighthill 1962, 1963; Curle 1955) to relate the total acoustic power to the gas exit velocity for assumed equivalent *monopole*, *dipole*, and *quadrupole* sources. Although Woulff and McGetchin (1976) only considered acoustic signals >20 Hz, recent infrasound studies have built extensively upon their formulation (e.g., Vergniolle et al. 1996, Vergniolle and Caplan-Auerbach 2006; Caplan-Auerbach et al. 2010; Ripepe et al. 2013; Lamb et al. 2015).

The *monopole* is the most elementary linear equivalent source and radiates sound equally in all directions (also called a *simple source* or *point source*). For the monopole, acoustic pressure is related to the rate of change of the rate of mass outflow at the source. The first few seconds of an impulsive volcanic explosion, which involves a rapid acceleration of the atmosphere, are sometimes reasonably well approximated by a monopole (Woulff and McGetchin 1976; Johnson 2003); however, this approximation breaks down as the source amplitude and eruption velocity increase (Sect. 33.6.2). Higher order equivalent sources (dipoles and quadrupoles) can be mathematically constructed from combinations of monopoles (e.g., Morse and Ingard 1968; Lighthill 1962, 1978; Pierce 1989). Woulff and

McGetchin (1976) suggested that such higher order sources might adequately represent fluid-solid interactions (dipole) and aerodynamic sound (quadrupole).

Explosive eruption source mechanisms are likely more complicated than a simple monopole, dipole, or quadrupole assumption. In a reexamination of the approach by Woulff and McGetchin (1976) in the context of the current understanding of jet noise, Matoza et al. (2013b) concluded that the formulation of Woulff and McGetchin (1976) can lead to large errors when inferring eruption parameters from acoustic data and thus requires modification. Quantitative integration of field, numerical, and laboratory studies within a modern aeroacoustics framework will lead to a more accurate relationship between volcanic infrasound and eruption parameters.

33.6.2 Nonlinear Effects

Linear acoustic theory (Sect. 33.6.1) provides a useful starting point for utilizing pressure time-series recordings to estimate eruption parameters. However, it is recognized that supersonic flow at a volcanic vent or a rapid explosive decompression of a pressurized magma-gas mixture can lead to the generation of shock waves, or finite-amplitude acoustic waves, that exhibit nonlinear propagation effects (e.g., Morrissey and Chouet 1997; Johnson 2003; Fee et al. 2013a; Marchetti et al. 2013).

Linear acoustic waves satisfy the small-signal approximation, where pressure fluctuations in the wave are significantly smaller than the product of ambient density and the square of the small-signal sound speed (which for air is comparable to the static pressure, e.g., Blackstock 2000). When this approximation is violated, finite-amplitude effects occur. These effects result in the high-amplitude, higher temperature compressions propagating faster than the small-signal sound speed, progressively leading to a steeper wave onset as the wave develops (see Atchley 2005, for an informative primer).

Explosions generate a high-amplitude positive overpressure phase. In the case of chemical explosions, this is a consequence of the rapid expansion of the gases produced; in a volcanic eruption, it is a combination of rapid mass injection into the atmosphere and the resulting expansion of the gas phase. The nonlinear propagation of this high-amplitude positive pressure perturbation leads to the formation of a waveform often described as a blast wave: a short-duration high-amplitude positive overpressure with a steep onset (the shock front) followed by a quasi-exponential decay and a lower amplitude longer rarefaction phase (e.g., Kinney and Graham 1985). The blast wave elongates during the nonlinear propagation phase (Fig. 33.15) and undergoes faster pressure amplitude decay at short propagation distances when compared to acoustic waves, leading to a relatively rapid transition from nonlinear to approximately linear acoustic propagation.

Volcanic explosions often generate pressure waveforms with the general form of a blast wave (Fig. 33.16). For large Vulcanian explosions, the transition from

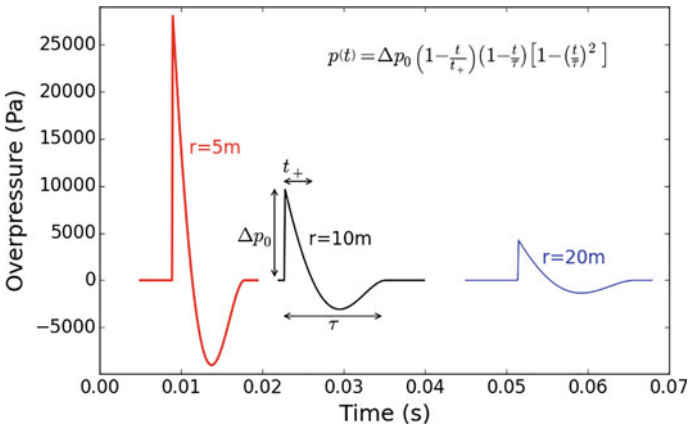

Fig. 33.15 Modeled blast waveforms. The distances correspond to 5 m (red line), 10 m, (black line) and 20 m (blue line) from a 1 kg chemical (TNT) detonation scaled using the Kinney and Graham (1985) reference explosion values for positive overpressure Δp_0 and positive phase duration t_+. The pressure time-series $p(t)$ is calculated using the modified Friedlander equation proposed by Reed (1977), which is given at the top of the figure

nonlinear to approximately linear propagation is expected to occur at several hundred meters from the vent (Medici et al. 2014). Using models that do not account for the initial nonlinear propagation can lead to underestimation of source power (as recognized by, e.g., Caplan-Auerbach et al. 2010; Kim and Rodgers 2016).

Marchetti et al. (2013) noted the similarity between the waveform shape of infrasonic transients recorded at Yasur volcano, Vanuatu, and blast waves recorded from chemical explosions. However, care must be taken to appropriately scale both time and amplitude when comparing with blast waveforms from chemical detonations, as the general waveform shape is characteristic of any nonlinear acoustic propagation from a transient event (Kinney and Graham 1985). In the volcanic case, the positive overpressure phase duration is significantly longer than for blast waves generated by chemical explosives. In Fig. 33.17 a waveform recorded at Sakurajima is compared to an appropriately scaled chemical blast waveform generated using the modified Friedlander function of Reed (1977). This empirically derived blast waveform shape (see Fig. 33.15) was scaled such that the peak overpressure matches the Sakurajima time-series at the recording distance of 3.4 km. It is clear that in the volcanic case the positive pressure pulse is longer for the given peak pressure. Indeed, to match the positive phase duration (~0.7 s for the Sakurajima case, Fig. 33.17), an equivalent surface chemical explosion is required to have a yield of approximately 2,500 tons of TNT. The overpressure expected for a chemical detonation with this pulse length at 3.4 km distance would be on the order

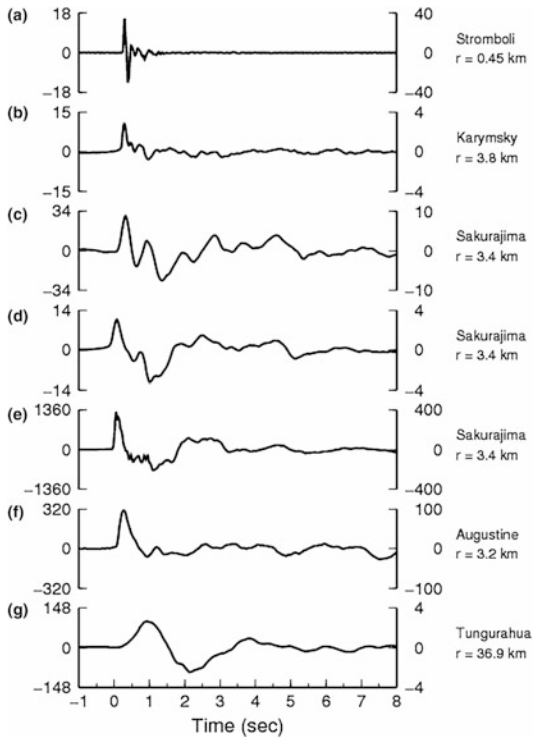

Fig. 33.16 Examples of the onset of transient infrasonic pressure waveforms from different explosive eruption styles at different volcanoes. The right-hand *y*-axis values are the observed pressure amplitude at the station [Pa]. The left-hand *y*-axis values are the amplitudes corrected to a reference distance of 1 km from the source assuming an approximate 1/*r* geometrical spreading for relative comparison. Adapted from Fee and Matoza 2013 and Matoza et al. (2014)

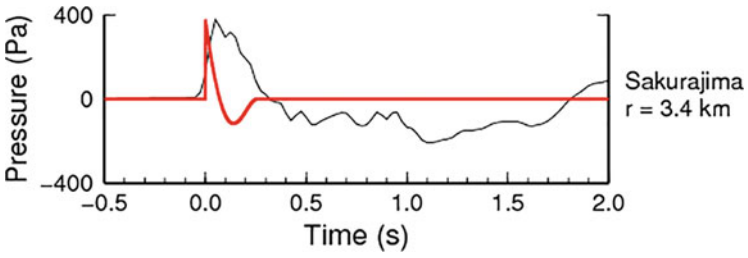

Fig. 33.17 A comparison of a signal recorded at 3.4 km from an explosion at Sakurajima (black line) and the Reed (1977) blast waveform (red line) with peak amplitude matched to the volcanic signal. The positive phase duration of the blast waveform consistent with the peak amplitude was determined using the Kinney and Graham (1985) chemical explosion scaling laws

of 4,300 Pa (i.e., over an order of magnitude higher than observed, Fig. 33.17). As a data example of a chemical explosion of this magnitude, the study by Gainville et al. (2010) describes pressure recordings from a comparable explosion (3,840 tons of TNT equivalent exploded at the surface, equivalent to a 7.6 kt free air explosion). The pulse duration observed by Gainville et al. (2010) was 0.855 s at 7.26 km from the blast, which matches well with the Kinney and Graham (1985) scaling laws. Modeling of volcanic explosions suggests that the longer positive phase duration (e.g., Fig. 33.17) may be a consequence of shock generation within a particle-rich magma–gas mixture in which the small-signal sound speed is slower than that in the atmosphere (Morrissey and Chouet 1997). Near-source topography may also significantly affect the waveform (Sect. 33.7).

Methods to interpret infrasonic recordings using knowledge of near-source nonlinear propagation are starting to be developed (e.g., Medici et al. 2014; Genco et al. 2014). Because infrasonic recordings are most likely to be made in the linear acoustic regime, models are required to relate these measurements to the source that generated the shock waves (as is done in explosion forensics, e.g., Ford et al. 2014; Kim and Rodgers 2016). In order to develop models for volcanic nonlinear acoustic sources, estimation of shock velocities at near-vent locations using visual methods are especially important (e.g., Yokoo and Ishihara 2007; Genco et al. 2014).

Many large eruptions are recorded at global distances from the volcano (e.g., Dabrowa et al. 2011), but interpretation of signal features recorded at these ranges in terms of nonlinear source processes is not trivial. Infrasound propagating within global waveguides reach stratospheric and possibly thermospheric altitudes (50–110 km), where low-density atmosphere is encountered resulting in large-amplitude increases of the acoustic wave. These amplitude increases can be large enough to initiate nonlinear wave propagation (e.g., Lonzaga et al. 2015). Such a mechanism was proposed to explain audible returns at distances of between 100 and 800 km from the 1980 Mount St. Helens eruption (Reed 1987) (see Sect. 33.2.1).

33.6.3 Volcanic Jet Noise

The lowermost section of a sustained sub-Plinian or Plinian volcanic eruption column represents a momentum-driven, turbulent, free-shear jet flow. Recent work has suggested that eruptions involving volcanic jet flows generate a low-frequency (infrasonic) form of the aeroacoustic jet noise produced by smaller scale man-made jets (Matoza et al. 2009b; Fee et al. 2010a, b, 2013a; Taddeucci et al. 2014). Jet noise is the noise generated by a turbulent jet flow itself. Man-made jet noise has

been extensively studied for noise and vibration control purposes (e.g., Tam 1998). Jet noise has been characterized in laboratory and field aeroacoustics studies by considering how acoustic signal properties vary as a function of angle to the jet axis and jet operating parameters such as the jet velocity, diameter, temperature, density, and nozzle geometry. In current jet noise studies, the idea of jet noise as composed of equivalent sources of monopoles, dipoles, and quadrupoles (Sect. 33.6.1) has largely been abandoned (Tam 1998; Tam et al. 2008; Viswanathan 2009). Also of note is that jet noise is highly directional, i.e., jets do not radiate sound equally in all directions.

Although the spectral shapes of observed infrasonic signals are in approximate agreement with those scaled from man-made jets (Matoza et al. 2009b), the observed volcanic signals have additional complexities not present in the pure-air laboratory data. These features may result from multiphase flow containing solid particles and liquid droplets, very high temperatures, and complex crater morphology. Recently, volcanic jet noise has begun to be investigated computationally (Fig. 33.18) (e.g., Taddeucci et al. 2014; Brogi et al. 2015; Cerminara et al. 2016). Taddeucci et al. (2014) combined high-speed imaging with infrasound and seismic observations of jet noise from Strombolian explosions together with numerical simulations. They conclude that both microphone measurements and wave imaging reveal the presence of high-frequency, likely shock-related, jet noise, which they contend to be in agreement with supersonic velocities of pyroclasts measured in some Strombolian explosions (Taddeucci et al. 2012). For more detail about volcanic jet noise, the reader is referred to the paper by Matoza et al. (2013b).

33.6.4 Infrasound from Pyroclastic Flows

Hot, dense, flows of particles and gas, referred to as pyroclastic flows or pyroclastic density currents (PDCs), represent a significant hazard to local populations. These flows have also been found to produce notable infrasound signals (Yamasato 1997; Oshima and Maekawa 2001; Ripepe et al. 2010a, b; Delle Donne et al. 2014). Yamasato (1997) tracked PDCs with seismic and acoustic sensors at Mount Unzen, Japan. At Soufrière Hills Volcano, Montserrat, Ripepe et al. (2010a) characterized, tracked, and estimated velocities of a PDC using a local infrasound array. Delle Donne et al. (2014) built upon this work by integrating thermal and seismic data to further constrain the PDC movement and evolution. Future work relating PDCs and infrasound to understand the acoustic source process has the potential to help mitigate this dangerous volcanic hazard.

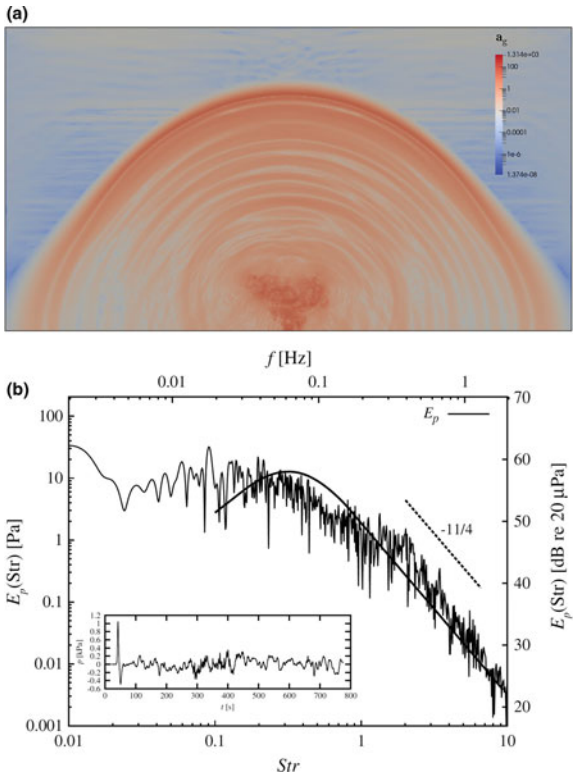

Fig. 33.18 Numerical simulation of infrasound from a volcanic jet (Cerminara et al. 2016). Simulation snapshot showing infrasonic signal generated by turbulent eddies. Infrasound is visualized using the magnitude of the acceleration field with a logarithmic color scale [m/s^2], 120 s after the eruption onset. **b** Infrasonic spectrum of the pressure fluctuations as measured from a probe placed at the ground level 15 km from the vent center. The frequency is expressed in both dimensional (f) and non-dimensional ($Str = fD/U$) forms. The empirically derived large-scale turbulence similarity spectrum is shown by the bold solid line (see Tam 1998). (Figure reproduced from Cerminara et al. 2016)

33.7 Topographic and Near-Source Effects

Before volcanic source parameters can be estimated from infrasound recordings, any acoustic propagation effects between the source and receiver have to be accounted for. Near-source topographic effects may also become convolved with the volcanic source function, complicating the interpretation of long-range

(e.g., IMS) recordings. Characterizing propagation effects in volcanic environments is challenging; modifications to the Green's function (compared to a source within a homogeneous atmospheric halfspace) arise from interactions of the infrasonic wavefield with both along-path topography and meteorologically generated refractive index variations. For example, diffraction and reflection from prominent along-path topographic features, including near-vent structure, results in anisotropic acoustic amplitudes across local infrasound recording networks (e.g., Matoza et al. 2009a; Kim and Lees 2011; Lacanna and Ripepe 2013; Kim and Lees 2014; Kim et al. 2015). In addition, mesoscale meteorological changes can generate significant acoustic ducting variations (e.g., Drob et al. 2010), with infrasonic signal amplitudes varying by over an order of magnitude across periods of a few days (e.g., Fee and Garces 2007; Matoza et al. 2009a; Johnson et al. 2012; Dabrowa et al. 2014; Lacanna et al. 2014).

Prominent topography in volcanic environments (e.g., vents, craters, domes, and ridges) makes it difficult to find non-obstructed propagation paths between a volcanic infrasound source and a local receiver. Acoustic propagation across such topography causes diffraction and reflection resulting in waveform distortion and amplitude variation compared to the wavefield generated by a compact source within a homogeneous halfspace. These effects are described mathematically by a modified Green's function connecting source and receiver, and have been modeled using numerical methods.

Matoza et al. (2009a) simulated the full seismo-acoustic wavefield from a shallow-buried explosive source at Mount St. Helens using a finite-difference method, and showed that the strong crater topography generates an asymmetry in infrasound waveforms radiated in different directions. At Stromboli, time-independent amplitude reductions of up to 11 dB (a factor of 3.5) compared to hemispherical acoustic spreading are observed, over path lengths of several hundred meters (Lacanna and Ripepe 2013). Finite-difference acoustic modeling using rigid topography (no seismic wavefield) indicates that the source of the amplitude reductions is primarily along-path topographic diffraction and reflections.

Kim and Lees (2014) investigated topographically generated waveform distortion at Sakurajima Volcano, Japan, with source-to-receiver path lengths between 2 and 7 kilometers. They observed amplitude reductions at most stations (of up to 8 dB compared to hemispherical spreading), but also observed a repeatable amplitude increase (~2 dB) at one station. Finite-difference time-domain (FDTD) modeling, accounting for 3D effects, successfully simulated both the amplitude reductions and increases (Fig. 33.19). These studies indicate that the superposition of along-path acoustic diffraction and reflection effects, especially those generated close to the active vent, need to be understood in order to interpret absolute infrasonic amplitudes.

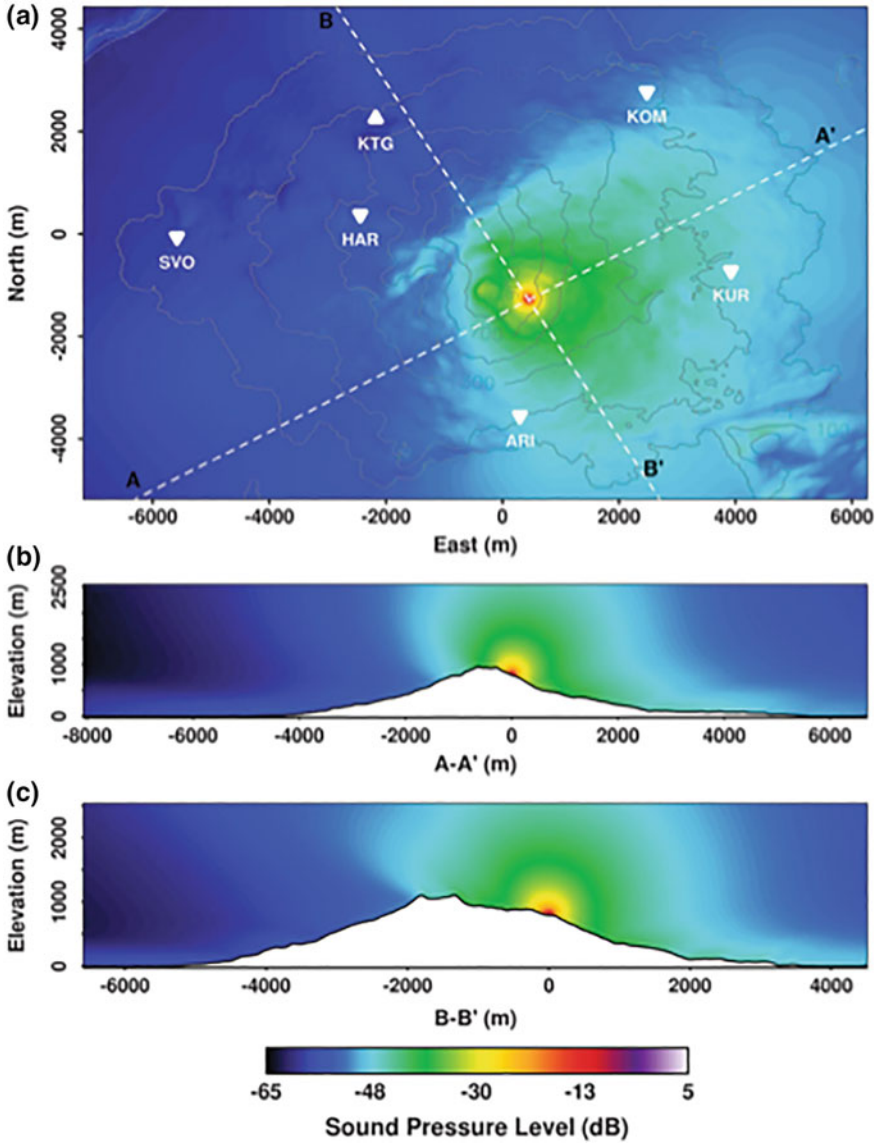

Fig. 33.19 An example of asymmetric sound pressures levels (SPL) due to the influence of along-path topography at Sakurajima Volcano (Kim and Lees 2014). The SPL is relative to the pressure 10 m from the source and is computed using a 3D FDTD simulation. (Figure reproduced from Kim and Lees 2014)

Topographically generated waveform distortion can also have a large effect on the estimation of explosive source parameters that are of potential use to the volcano monitoring community, such as volume flux. Kim et al. (2015) compare volume flux inversions using both (1) the standard approximation of the acoustic pressure being only a function of source strength and source-to-receiver distance, and (2) a full 3D numerical calculation of the Green's function using FDTD and a high resolution digital elevation model. Their results indicate that if 3D structure is neglected along a relatively unobstructed source-to-receiver path at Sakurajima, the total volume flux for a typical explosive event is underestimated by ~50%.

Although topography dominates short path (<5 km) amplitude reductions at volcanoes with relatively simple sources (e.g., Stromboli, Lacanna and Ripepe 2013), at volcanic dome complexes the acoustic wavefield may be a superposition of spatially separated sources. This is a potential additional source of anisotropic acoustic radiation (e.g., Jones and Johnson 2011). This adds extra complexity when interpreting infrasonic waveforms at some silicic volcanoes.

In addition to generating amplitude variations, topographic obstacles can generate waveform time delays. Kim and Lees (2014) show that for stations with prominent along-path topographic blockages at Sakurajima, time delays of greater than 0.5 s are observed over distances of ~4.5 km compared to those expected for a single-velocity, no-topography model. These delays can be predicted using 3D FDTD simulations with accurate volcanic topography models. This allowed Kim and Lees (2014) to locate a series of ten typical explosions at Sakurajima within a tight cluster (<100 m radius) at the base of the active crater, consistent with thermal infrared source vent locations. In a similar manner, Rowell et al. (2014) illustrate the difficulties in resolving the altitude of high-frequency jetting sources when time delays generated by topography are not accounted for.

Over propagation paths of several kilometers, atmospheric rather than topographic controls begin to dominate the variations in observed infrasonic signal characteristics. When considering infrasound propagation, the most significant of these effects are (1) refraction from vertical gradients in temperature and wind (e.g., Reynolds 1878), and (2) scattering from turbulence (e.g., Ostashev 1997). Sound absorption at low frequencies (<10 Hz) is negligible along short path lengths (<20 km) and little energy is lost to the ground such that surface impedance effects can be neglected (e.g., Piercy et al. 1977; Sutherland and Bass 2004). To first order, infrasonic propagation is controlled by temperature and wind gradients, while turbulence may result in additional fluctuations in signal amplitude and phase.

Infrasonic propagation from volcanic vents to local stations at distances less than 20 km is confined to the atmospheric boundary layer, where temperature and wind variations can result in variable acoustic ducting and can lead to significant waveform distortion. For example, Matoza et al. (2009a) observed rapid evolution of infrasonic waveforms recorded 13.4 km from the source at Mount St. Helens (as quantified by the cross-correlation coefficient). This evolution was attributed to changes in microscale and mesoscale meteorology (i.e., propagation conditions)

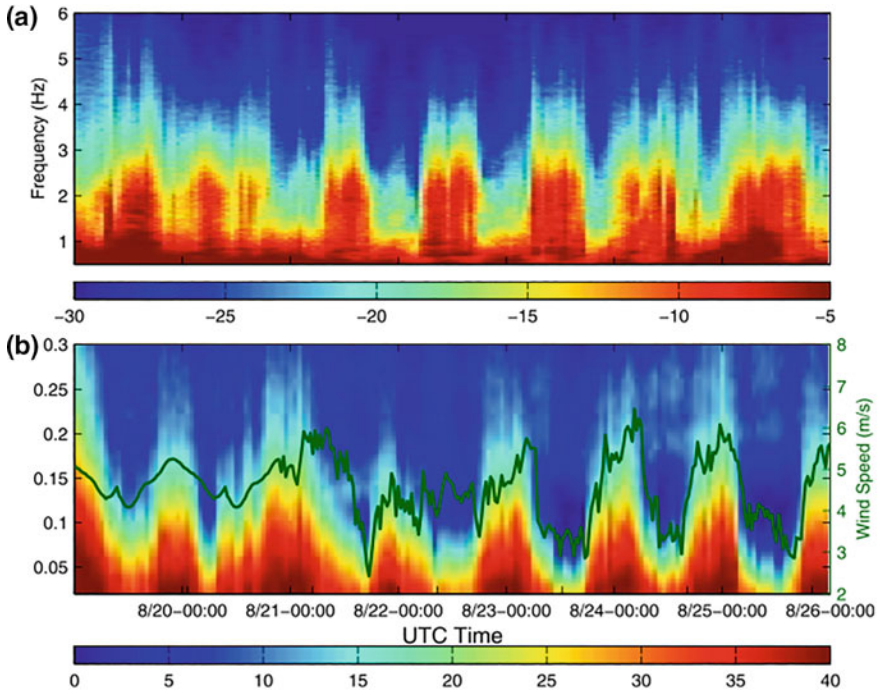

Fig. 33.20 Beamed spectrograms between **a** 0.5 and 6 Hz and **b** 0.02 and 0.3 Hz for infrasound signals at an array ~12.5 km from an active vent at Kilauea, Hawaii (Fee and Garces 2007). Spectral amplitudes are given in dB re 1 Pa. Panel **b** indicates the wind speed recorded at a nearby tower as a green line, showing that low-frequency acoustic power is indicative of increased wind speeds. The volcanic signal is observed between 1 and 3 Hz in (**a**) and indicates that favorable propagation conditions occur during low-wind, stable nocturnal conditions. (Figure reproduced from Fee and Garces 2007)

rather than source location or source-time function (as is often the case when analyzing seismic signals).

Variable acoustic ducting results in large variations in signal amplitudes between source/receiver pairs. Unfavorable propagation conditions, where acoustic energy undergoes strong upward refraction into the upper atmosphere, can lead to non-detection of signals at stations located several to tens of kilometers from the vent. Fee and Garces (2007) observed an order-of-magnitude diurnal variation in infrasonic tremor signal power at 12.5 km from the active vent at Kilauea, most likely generated by the formation and dissipation of an acoustic waveguide within the stable nocturnal atmospheric boundary layer (Fig. 33.20). Over a longer time period of 2 weeks, Dabrowa et al. (2014) observed over an order-of-magnitude variation in signal amplitude decay across a 25 km propagation path at Mount Erebus, which was well-correlated with mesoscale variations in lower atmospheric wind and temperature gradients recorded by local radiosondes. During periods of increased negative sound speed gradients with altitude, increased upward refraction

of infrasonic energy leads to lower recorded amplitude levels at 25 km from the vent. Such studies show that time- and location-specific meteorological data is required in order to be able to successfully interpret changes in infrasonic amplitudes at these ranges. One method of estimating near-volcano meteorological conditions is to use collected infrasound data. If the microbarograph network density is sufficient, and there is an almost continuous volcanic infrasound signal, estimates of the near-surface sound speed gradients and wind vector may be estimated from inter-station phase delays (Marcillo and Johnson 2010) and acoustic power fluctuations (Johnson et al. 2012).

33.8 Regional-Global Infrasound Propagation

Due to efficient low-frequency acoustic energy propagation within the atmosphere, eruptions at over 40 volcanoes have been recorded across the IMS global infrasound network over the past 15 years (see Fig. 33.7 and e.g., Le Pichon et al. 2005; Dabrowa et al. 2011). The more intense eruptions have been recorded on multiple arrays out to distances of several thousands of kilometers (e.g., Fee et al. 2010a; Matoza et al. 2011a; Fee et al. 2013a).

Regional and global infrasound recordings have helped constrain chronologies for eruptive sequences in situations where there are no local ground-based recording instruments (e.g., Matoza et al. 2011a), where only part of the eruptive sequence is subaerial (e.g., Green et al. 2013), and where local instruments have been destroyed by the onset of an intense eruption (e.g., Caudron et al. 2015). The continuous nature of infrasound recordings is also important; for the 2009 Sarychev Peak, Kuriles, eruption Matoza et al. (2011a) used a 5-day long infrasound time-series to corroborate, and improve upon, a satellite imagery based chronology that had a lower temporal resolution.

Propagation of infrasound out to thousands of kilometers from the source occurs because the acoustic waves are channeled within ducts between the ground and the upper atmosphere (e.g., Georges and Beasley 1977). Unlike local infrasonic recordings where the sound has propagated exclusively through the lower troposphere, regional and global infrasound will have propagated up into the stratosphere, mesosphere, or lower thermosphere before being refracted back to Earth's surface. This refraction is the result of refractive index increases generated by a combination of increased temperature and/or along-path wind speed. Drob et al. (2010a) provide an overview of the major propagation ducts: the stratospheric duct where acoustic energy reaches a maximum altitude of between 35 and 55 km, and the thermospheric duct where infrasound returns to the ground surface from altitudes of between 90 and 120 km. The majority of long-range infrasound propagates within the stratospheric duct, because thermospheric paths suffer from significantly

higher acoustic attenuation (Sutherland and Bass 2004). Propagation within the stratospheric duct is highly anisotropic; the winds associated with the stratospheric polar vortex assist in channeling energy propagating in a downwind direction, while refracting acoustic energy up into the thermosphere along upwind paths (e.g., Le Pichon et al. 2012). As infrasonic energy passes through layers with rapidly varying windspeeds in the stratosphere, the waves undergo multi-pathing and scattering (Kulichkov 2004), such that the recorded wavefield at long-range is comprised of a superposition of multi-pathed wavefronts (Green 2015).

Given the complexities of long-range infrasound propagation within the atmosphere, and the impact this has upon the radiated wavefield, identifying eruption characteristics from acoustic recordings at long distance is challenging. Despite this, progress has been made in identifying volcanic source characteristics using long-range infrasound recordings. Regional infrasound studies have shown that as eruptive intensity increases, with the consequence of higher altitude plume generation, the dominant infrasonic signal frequency decreases (often to below 0.1 Hz) resulting in wider signal bandwidths and greater radiated acoustic power (e.g., Garces et al. 2008; Fee et al. 2010b). Similar relationships are observed at global distances; for infrasound recordings made across the IMS from over 65 volcanic eruptions, events with higher altitude plumes generated lower detectable signal frequencies (Dabrowa et al. 2011). Acoustic source characteristics are sometimes identifiable at long range, especially if the propagation path is relatively simple. For example, Fee et al. (2013b) observe infrasound at 260 km from the intense 2011 eruption of Nabro Volcano, Eritrea, consistent with energy propagation up to the lower thermosphere, where it is refracted back to the station. The signal exhibits positively skewed infrasonic waveforms, which the authors interpret as similar to "crackle," a phenomenon that is indicative of supersonic jet noise.

Uncertainties in the source to receiver propagation path result in uncertainties in both source location and origin time. For both the Sarychev Peak and Eyjafjallajökull eruptions, source location estimates using back azimuth intersection of long-range infrasound recordings have mean centroids that can be several tens of kilometers away from the volcanic source (Matoza et al. 2011a, b). For some phases of the 2008 Kasatochi, Alaska, eruption Fee et al. (2010a) identify discrepancies of ~15 min between origin times derived using either infrasonic or seismic data; they interpret these differences as being due to possible mis-identification of the atmospheric duct through which the infrasound propagated.

As many volcanoes are sources of strong and persistent infrasound, volcano infrasound has been extensively used for remote sensing of the upper atmosphere. The long duration (weeks, months, years) of volcanic infrasound activity has allowed (1) the identification of periodic fluctuations in infrasonic signal characteristics, (2) infrasound signals to be used to validate meteorological and climatological specifications, and (3) estimation of updates to upper atmosphere meteorological specifications (i.e., wind vectors) by minimizing the difference between observed and predicted signal characteristics.

Semi-diurnal fluctuations in regional volcanic infrasound amplitudes (Le Pichon et al. 2005), trace velocities (Matoza et al. 2011a) and travel-times (Assink et al. 2012) have been shown to correlate well with expected tidal fluctuations in the turning height of thermospheric infrasonic propagation paths. Likewise, diurnal fluctuations in signal amplitude and trace velocity over a 10-day period at approximately 2000 km from Eyjafjallajökull were generated by solar tidal fluctuations in windspeeds that modulated the strength of the stratospheric acoustic duct (Green et al. 2012). By using volcanoes with known, fixed locations these studies have allowed higher fidelity comparisons with numerical propagation predictions compared to earlier studies that used microbarom and rocket-generated infrasound to identify tidal signatures (e.g., Donn and Rind 1971; Donn et al. 1975).

Infrasound recordings of continuously erupting explosive volcanoes provide an opportunity to compare observed signal characteristics with those predicted using numerical models and state-of-the-art atmospheric specifications. Studies of one year of explosions from Yasur Volcano, Vanuatu led Le Pichon et al. (2005) to conclude that current meteorological specifications are inadequate for accurately predicting observed thermospheric arrival azimuthal deviations of up to 10°. Specifically, these authors showed that mesospheric zonal winds are underestimated in the models by between 20 and 50 m/s. In contrast, Antier et al. (2007) studied stratospheric arrivals from Yasur over a 3-year period and showed that the meteorological profiles at altitudes below 55 km are accurate enough to account for the observed values and variations in travel-time, trace velocity and back azimuth during the Austral summer months. Le Pichon et al. (2010) extended this study and showed that state-of-the-art meteorological specifications are excellent at predicting back azimuth variations over timescales of between a few days and a few months. For more than 90% of the time, the error between observed and predicted back azimuths is less than 0.5° for this particular summertime stratospheric propagation path. At other times of year, the meteorological specifications are less capable of predicting observed infrasound characteristics; using data from Etna, Assink et al. (2014) showed that trace-velocity observations at times of atmospheric transition (e.g., the equinoxes) can only be modeled by increasing the effective sound speed at the stratopause by up to 10% of the original atmospheric specification value.

Inversion techniques that use infrasound observations to improve high-altitude meteorological profiles have been proposed (Drob et al. 2010b; Lalande et al. 2012), and well-characterized ground-truth signals, such as those collected from volcanoes, allow such inversions to be undertaken in practice. Assink et al. (2013) showed that although variations in observed thermospheric arrival travel-times from eruptions of Tungurahua, Ecuador, correlate with the phase of the thermospheric semi-diurnal tides, the travel-time observations do not match those predicted by numerical modeling. The predicted travel-time discrepancies result in predicted

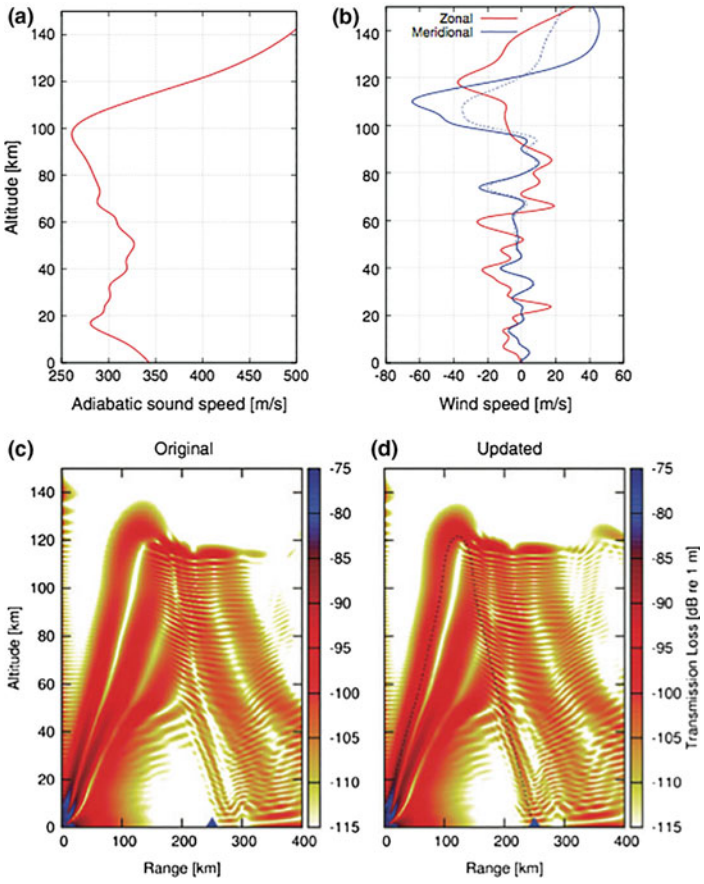

Fig. 33.21 An example, from Assink et al. (2013), of undertaking a wind-speed parameter update (solid lines, panel b) from an original meteorological specification (dashed lines, panel b) in order to explain the occurrence and arrival times of thermospheric arrivals at the LITE array 250 km from Tungurahua, Ecuador (blue triangle, panels c and d). The original specifications predict that the station is at the edge of the thermospheric shadow zone, while the updated specification indicates that a thermospheric arrival turning at an altitude of approximately 120 km is received at the station. (Figure adapted and updated from Assink et al. 2013)

celerities almost 10% lower than observed. Therefore Assink et al. (2013) employed an inversion procedure to identify the best-fitting low-order (four-parameter) wind model in the upper mesosphere and lower thermosphere using the recorded regional thermospheric phases from individual explosions (Fig. 33.21). The results indicate that such an approach provides a physically realistic updated atmospheric profile.

This updated profile was used to correctly predict the nonlinear distortion of the waveform along the path, providing confidence that the inversion method improved the prediction of the true thermospheric propagation path.

These studies highlight that volcano infrasound has the potential to contribute to upper atmospheric remote sensing efforts. Encouragingly, Assink et al. (2014) showed that the amplitudes of the required updates to the windspeeds are consistent with those predicted from other measurements (e.g., lidar).

33.9 Acoustic Early Warning Systems for Explosive Volcanic Eruptions

Infrasound can provide detailed constraints on the timing, duration, and relative vigor of local and remote explosive volcanism (Sects. 33.5, 33.6) and has been used in prototype eruption early warning systems (e.g., Kamo et al. 1994; Garces et al. 2008; Ripepe et al. 2009; Fee et al. 2010a; Matoza et al. 2011a; De Angelis et al. 2012; Fee and Matoza 2013; Marchetti et al. 2019; Ripepe and Marchetti 2019). A global infrasonic *Volcanic Information System* (or VIS) is currently being developed in support of the Volcanic Ash Advisory Centers (VAACs) designated by the International Civil Aviation Organization (ICAO) (Mialle et al. 2015). The VAACs are specialized operational centers responsible for producing and disseminating information on volcanic ash clouds that may endanger aviation, as defined by the International Airways Volcano Watch (IAVW) (Tupper et al. 2007). As such, the VAACs explore opportunities for enhancing their operational capabilities.

The first proposal for an acoustic early warning system for explosive eruptions of which we are aware was that of Kamo et al. (1994), who noted that the Kariya array, 710 km from Sakurajima (see Sect. 33.2.1), was capable of detecting infrasound from volcanoes thousands of kilometers distant (e.g., the 1991 eruption of Pinatubo, Philippines). Kamo et al. (1994) concluded that "this capability forms the basis of a proposal for a worldwide network of air-wave sensors to monitor volcanic explosions," proposing the PEGASAS-VE early warning system consisting of a set of infrasonic microphone arrays with 500–1,000 km spacing. Kamo et al. (1994) proposed that PEGASAS-VE "would be a very effective means of enhancing aviation safety and would be similar to the tsunami warning system, which is in worldwide operation." PEGASAS-VE was not constructed, but the IMS infrasound network was initiated after the CTBT was opened for signature in 1996. The proposed 500-km spacing of PEGASAS-VE was chosen to provide timely warnings within 30 min. For reference, the average station spacing for the complete IMS infrasound network will be about 2,000 km (Christie and Campus 2010).

The Acoustic Surveillance for Hazardous Eruptions (ASHE) project was initiated after the third international workshop on volcanic ash and aviation safety in Toulouse (2003), in which ICAO requested that State Signatories of the CTBT

investigate the use of the IMS for eruption warnings. During this project, two infrasound arrays were deployed near Mount St. Helens (Matoza et al. 2007), and two in Ecuador (Garces et al. 2008; Fee et al. 2010b). The initial goal of the ASHE project was to determine the feasibility of detecting significant atmospheric ash emissions acoustically and rapidly notifying civil defense authorities (ideally, within 5 min).

The ASHE proof-of-concept project demonstrated that acoustic array monitoring of large volcanic eruptions at regional distances is not only viable, but also sufficiently mature to transition into operational volcano monitoring. The ASHE experiment in Ecuador developed an operational monitoring tool for the highly active Tungurahua Volcano using an infrasound array ~37 km away. Fee et al. (2010b) describe how multiple eruptions and a variety of eruption styles were used as case studies to construct the system. Sustained, low-frequency infrasound was found to correspond with hazardous ash plumes (Sect. 33.5.3), while short-duration explosions were found to be primarily gas-rich and/or produce low-level ash plumes. A sub-Plinian eruption on February 6, 2008 was subsequently detected by the ASHE system ~6 min after the eruption onset and a notification to civil aviation authorities was distributed. Changes in the eruption intensity and the eruption cessation were also detected and additional notifications were disseminated. This project demonstrated that acoustic early warning of hazardous eruptions is indeed feasible, even at regional distances (tens of km).

The combination of numerous active volcanoes and its stark remoteness makes Alaska (AK) a prime target for volcano infrasound monitoring. After extensive research showing that significant infrasound is produced from eruptions in Alaska (e.g., Wilson and Forbes 1969; Vergniolle and Caplan-Auerbach 2006; Fee et al. 2010b, 2013b), as well as demonstrating its utility in eruption monitoring, the Alaska Volcano Observatory (AVO) began using infrasound operationally in the early 2010s. De Angelis et al. (2012) describe how both a remote infrasound array and ground-coupled airwaves (GCA) recorded on seismometers from a nearby seismic network were used to detect explosions from the remote Cleveland Volcano, AK. These methods, even with the infrasound array at nearly 1,000 km range, were able to detect numerous eruptions from Cleveland Volcano that were previously going undetected using satellite remote sensing. GCA methods have also been helpful in detecting and characterizing activity at the difficult-to-monitor, but often-active Pavlof Volcano, AK (Waythomas et al. 2014, Fee et al. 2016). Currently, numerous infrasound array and GCA algorithms are running to detect explosive activity from volcanoes in Alaska and produce email and SMS alerts, and the technology is being implemented further with more stations and detection algorithms.

While the utility of infrasound technology for monitoring large explosive eruptions has been demonstrated for specific case studies or regions (e.g., the current operational system in Alaska), the transition to a global approach remains a challenge. Building upon research programs and moving toward achieving an operational VIS, the Comprehensive Nuclear-Test-Ban Treaty Organization

(CTBTO) is coordinating a two-way approach in order to set up the framework agreement for creating the VIS and its technical implementation.

The international framework agreement is being discussed between the CTBTO, ICAO, and the World Meteorological Organization (WMO). ICAO collaborates closely with the WMO on aviation safety issues associated with hazardous weather. Both organizations coordinate activities and generate VAAC advisories on the detection of volcanic ash clouds and their transport and dispersion in the atmosphere because of their potential impact on aviation (e.g., Casadevall et al. 1994). In parallel, the International Data Center (IDC) of the CTBTO informed the Air Navigation Bureau of ICAO that it was working on a "significant eruption" notification system within the ARISE (Atmospheric dynamics Research InfraStructure in Europe) project together with VAAC Toulouse. This project is mandated by IAVW to work on the link between infrasound technology and VAAC activities. The cooperation between the international organizations is further strengthened by a 2011 agreement between the CTBTO and WMO that permits the sharing of data for development activities that are of substantial interest to both parties.

The VIS technical implementation has now been initiated utilizing synergy between the CTBTO, ARISE, and VAAC Toulouse. The IMS infrasound network allows for global remote monitoring of volcanic activity, which permits notifying the international civil aviation community regarding significant volcanic eruptions in near-real time using IDC automatic processing results. The CTBTO provides an operational, robust, and sustainable environment with high-quality infrasound data and derived products, being reinforced by ARISE-advanced products that provide valuable parametric inputs on the atmosphere dynamics that drives the infrasound wave propagation. The combined results are to serve as quality indicators increasing the VAACs confidence when receiving VIS messages.

The first version of the VIS is a two-step process, similar to the IDC automatic processing. First, at the station level, the VIS searches the matching IDC infrasound detections within a database of known volcanoes using simple criteria on detection time of arrival, back azimuth and central frequency for ranges up to 4,000 km and combines it with atmospheric ducting propagation metrics based on the effective sound speed ratio (Le Pichon et al. 2012). Subsequently, the VIS is consolidated at the network level by associating detections from various stations and aggregating detection parameters into eruptive sequences, rather than overloading the VAAC with redundant messages from an ongoing eruption.

This proposed approach is undergoing testing with the VAAC Toulouse using the CTBTO vDEC (virtual Data Exploitation Centre: https://www.ctbto.org/specials/vdec/) platform to demonstrate the usefulness of infrasonic data to the IAVW. While the disseminated information initially focuses on straightforward criteria, it is envisioned to be an iterative process that will later be enriched with advanced research parameters from ARISE and from the international volcano-acoustic scientific community. For example, the multi-year eruptive sequences at Mount Etna, Sicily have been tracked using IMS data from IS48 in Tunisia based on a propagation probability criterion which combines an empirical attenuation relation (Le Pichon et al. 2012) and atmospheric uncertainty estimation

(Tailpied et al. 2013). This example from Mount Etna shows how additional data and parameters are expected to help further enhance and validate the VIS performance.

The initial system serves as a demonstration of the utility of the VIS prior to its possible extension to other VAACs. Looking ahead, support from the volcano-infrasound community is critical in order to lower the volcanic detection threshold and reduce the latency of the VIS. The addition of regional and local infrasound data from volcanic areas and the refinement of the system criteria with state-of-the-art results from the scientific community will help with VIS sustainability.

In line with the goal of the global VIS, Matoza et al. (2017) developed a new alternative algorithm for searching systematically through multi-year data from the IMS infrasound network to identify explosive volcanic eruption signals originating anywhere on Earth. Detecting, quantifying, and cataloging the global occurrence of explosive volcanism helps toward several goals in Earth sciences and has direct applications in volcanic hazard mitigation for both regional (e.g., Alaska) and global (e.g., VIS) systems. The new algorithm by Matoza et al. (2017) combines infrasound signal association across multiple stations with source location using a brute-force, grid-search, cross-bearings approach. The algorithm corrects for a background prior rate of coherent unwanted infrasound signals (clutter) in a global grid, without needing to screen array processing detection lists from individual stations prior to association. This algorithm was developed using case studies of explosive eruptions: 2008 Kasatochi, AK; 2009 Sarychev Peak, Kuriles; and 2010 Eyjafjallajökull, Iceland. They applied the method to global IMS data from 2005–2010 to construct a preliminary acoustic catalog that emphasizes sustained explosive volcanic activity. This work represents a step toward the goal of integrating IMS infrasound data products into global volcanic eruption early warning, parameter estimation, and notification systems.

33.10 Conclusions

Infrasound monitoring is becoming an established geophysical technique for capturing local and remote explosive volcanism, and for understanding the dynamics of shallow degassing and eruption columns. Infrasound signals are recorded from a broad spectrum of volcanic processes ranging from effusive to explosive eruptions. Explosive eruptions produce powerful broadband (~0.01–20 Hz) infrasound signals that can be ducted efficiently over long ranges (thousands of kilometers) in atmospheric waveguides. Although not designed for the purpose, the construction of the IMS is providing an unprecedented opportunity to study and monitor Earth's explosively erupting volcanoes using a global network of ground-based acoustic sensors. The utility of the IMS network for detecting, locating, and providing detailed chronologies of remote explosive volcanism is well established. The

initiation of the global Volcanic Information System (VIS) provides a formal context for research on the improved use of infrasound data for estimating parameters of remote explosive volcanism using the global IMS network. Major research goals in-line with this objective include: (1) continued development of quantitative source models linking acoustic signal generation to eruption parameters, (2) improved propagation modeling of infrasound from sustained broadband sources in a time-varying atmosphere at multiple scales, and (3) the development of robust detection algorithms for identifying and locating volcanic eruption signals in the presence of wind noise and multiple interfering coherent ambient sources. We anticipate significant improvements in the global detectability of volcanic infrasound using the IMS network in the future as the IMS infrasound network achieves planned 59-station global coverage. Additional infrasound arrays or network deployments in volcanically active regions will lead to substantial improvements by augmenting the network density and decreasing the acoustic source power of explosive eruptions detectable with a globally integrated network.

Acknowledgements This work was partially supported by NSF grants EAR-1546139 and EAR-1614855.

References

Annen C, Wagner JJ (2003) The impact of volcanic eruptions during the 1990s. Nat. Hazards Rev 4(4):169–175. https://doi.org/10.1061/(asce)1527-6988(2003)4:4(169

Antier K, Le Pichon A, Vergniolle S, Zielinski C, Lardy M (2007) Multiyear validation of the NRL-G2S wind fields using infrasound from Yasur. J Geophys Res 112:D23110. https://doi.org/10.1029/2007JD008462

Assink JD, Waxler R, Drob D (2012) On the sensitivity of infrasonic traveltimes in the equatorial region to theatmospheric tides. J Geophys Res Atmospheres 117.D01110. https://doi.org/10.1029/2011JD016107

Assink JD, Waxler R, Frazier WG, Lonzaga J (2013) The estimation of upper atmospheric wind model updates from infrasound data. J Geophys Res 118:1–18. https://doi.org/10.1002/jgrd.50833

Assink JD, Le Pichon A, Blanc E, Kallel M, Khemiri L (2014) Evaluation of wind and temperature profiles from ECMWF analysis on two hemispheres using volcanic infrasound. J Geophys Res 119. https://doi.org/10.1002/2014jd021632

Atchley AA (2005) Not your ordinary sound experience: a nonlinear-acoustics primer. Acoust Today 1(1):19–24

Banister JR (1984) Pressure wave generated by the Mount St. Helens eruption. J Geophys Res Atmospheres 89(D3):4895–4904

Båth M (1982) Atmospheric waves from Mount St. Helens. EOS Trans AGU 63(11):193–193

Blackstock DT (2000) Fundamentals of physical acoustics. Wiley-Interscience

Bolt BA, Tanimoto T (1981) Atmospheric oscillations after the May 18, 1980 eruption of Mount St. Helens EOS Trans AGU. 62(23):529–530

Bowman DC, Taddeucci J, Kim K, Anderson JF, Lees JM, Graettinger AH, Sonder I, Valentine GA (2014) The acoustic signatures of ground acceleration, gas expansion, and spall fallback in experimental volcanic explosions. Geophys Res Lett 41(6):1916–1922. https://doi.org/10.1002/2014GL05932

Braun T, Ripepe M (1993) Interaction of seismic and air waves as recorded at Stromboli volcano. Geophys Res Lett 20:65–68

Brogi F, Malaspinas O, Bonadonna C, Chopard B, Ripepe M (2015) Towards a numerical description of volcano aeroacoustic source processes using Lattice Boltzmann strategies. EOS Trans AGU Fall Meet Suppl Abstract S53D-04

Buckingham MJ, Garcés MA (1996) Canonical model of volcano acoustics. J Geophys Res Solid Earth 101(B4):8129–8151

Cansi Y (1995) An automatic seismic event processing for detection and location: the PMCC method. Geophys Res Lett 22(9):1021–1024

Cannata A, Montalto P, Privitera E, Russo G, Gresta S (2009) Tracking eruptive phenomena by infrasound: May 13, 2008 eruption at Mt. Etna. Geophys Res Lett 36:L05304. https://doi.org/10.1029/2008gl036738

Caplan-Auerbach J, Bellesiles A, Fernandes JK (2010) Estimates of eruption velocity and plume height from infrasonic recordings of the 2006 eruption of Augustine Volcano, Alaska. J Volcanol Geoth Res 189(1):12–18

Casadevall TJ (ed) (1994) Volcanic ash and aviation safety: proceedings of the first international symposium on volcanic ash and aviation safety. US Geolo Sur Bull 2047

Caudron C, Taisne B, Garces M, Le Pichon A, Mialle P (2015) On the use of remote infrasound and seismic stations to constrain the eruptive sequence and intensity for the 2014 Kelud eruption. Geophys Res Lett 42. https://doi.org/10.1002/2015gl064885

Cerminara M, Ongaro TE, Neri A (2016) Large Eddy Simulation of gas–particle kinematic decoupling and turbulent entrainment in volcanic plumes. J Volcanol Geotherm Res 326:143–171. https://doi.org/10.1016/j.jvolgeores.2016.06.018

Chester DK, Degg M, Duncan AM, Guest JE (2000) The increasing exposure of cities to the effects of volcanic eruptions: a global survey. Environ Hazards 2(3):89–103. https://doi.org/10.1016/S1464-2867(01)00004-3

Christie D, Campus P (2010) The IMS infrasound network: design and establishment of infrasound stations. In: Pichon AL, Blanc E, Hauchecorne A (eds) Infrasound monitoring for atmospheric studies. chap. 2. Springer, Netherlands, pp 29–75

Cochran E, Shearer P (2006) Infrasound events detected with the Southern California seismic network. Geophys Res Lett 33(19)

Chouet BA, Matoza RS (2013) A multi-decadal view of seismic methods for detecting precursors of magma movement and eruption. J Volcanol Geotherm Res 252:108–175. https://doi.org/10.1016/j.jvolgeores.2012.11.013

Curle N (1955) The influence of solid boundaries upon aerodynamic sound. Proc R Soc London Ser A 231(1187):505–514

Dabrowa AL, Green DN, Rust AC, Phillips JC (2011) A global study of volcanic infrasound characteristics and the potential for long-range monitoring. Earth Planet Sci Lett 310:369–379. https://doi.org/10.1016/j.epsl.2011.08.027

Dabrowa AL, Green DN, Johnson JB, Phillips JC, Rust AC (2014) Comparing near-regional and local measurements of infrasound from Mount Erebus, Antarctica: implications for monitoring. J Volcanol Geotherm Res 288:46–61. https://doi.org/10.1016/j.volgeores.2014.10.001

Dalton MP, Waite GP, Watson IM, Nadeau PA (2010) Multiparameter quantification of gas release during weak Strombolian eruptions at Pacaya Volcano, Guatemala. Geophys Res Lett 37:L09303. https://doi.org/10.1029/2010gl042617

De Angelis S, Fee D, Haney M, Schneider D (2012) Detecting hidden volcanic explosions from Mt. Cleveland Volcano, Alaska with infrasound and ground-coupled airwaves. Geophys Res Lett 39:L21312. https://doi.org/10.1029/2012GL053635

De Angelis S, Lamb O, Lamur A, Hornby A, Aulock F, Chigna G, Lavallée Y, Rietbrock A (2016) Characterization of moderate ash-and-gas explosions at Santiaguito volcano, Guatemala, from infrasound waveform inversion and thermal infrared measurements. Geophys Res Lett 43 (12):6220–6227

Delclos C, Blanc E, Broche P, Glangeaud F, Lacoume JL (1990) Processing and interpretation of microbarograph signals generated by the explosion of Mount St. Helens. J Geophys Res Atmos 95(D5):5485–5494

Delle Donne D, Ripepe M, De Angelis S, Cole PD, Lacanna G, Poggi P, Stewart R (2014) Chapter 9 Thermal, acoustic and seismic signals from pyroclastic density currents and Vulcanian explosions at Soufrière Hills Volcano, Montserrat. Geolo Soc Lon Mem 39(1):169–178

Delle Donne D, Ripepe M (2012) High-frame rate thermal imagery of Strombolian explosions: implications for explosive and infrasonic source dynamics. J Geophys Res Solid Earth (1978–2012):117(B9)

Delle Donne D, Ripepe M, Lacanna G, Tamburello G, Bitetto M, Aiuppa A (2016) Gas mass derived by infrasound and UV cameras: implications for mass flow rate. J Volcanol Geoth Res 325:169–178

Dibble RR, Kienle J, Kyle PR, Shibuya K (1984) Geophysical studies of Erebus Volcano, Antarctica, from 1974 December to 1982 January. NZ J Geol Geophys 27(4):425–455

Donn WL, Rind D (1971) Natural Infrasound as an Atmospheric Probe. Geophys J R Astr Soc 26:111–133

Donn WL, Balachandran NK, Rind D (1975) Tidal wind control of long-range rocket infrasound. J Geophys Res 80(12):1662–1664

Donn WL, Balachandran NK (1981) Mount St. Helens eruption of 18 May 1980: air waves and explosive yield. Science 213(4507):539–541

Drob DP, Garces M, Hedlin M, Brachet N (2010a) The temporal morphology of infrasound propagation. Pure Appl Geophys 167:437–453. https://doi.org/10.1007/s00024-010-0080-6

Drob DP, Meier RR, Picone JM, Garces MM (2010b) Inversion of infrasound signals for passive atmospheric remote sensing. In: infrasound Monitoring for Atmospheric Studies, pp 701–731. https://doi.org/10.1007/978-1-4020-9508-5_24

Dzurisin D (2006) Volcano deformation: new geodetic monitoring techniques. Springer-Verlag, Berlin Heidelberg

Evers LG, Haak HW (2001) Listening to sounds from an exploding meteor and oceanic waves. Geophys Res Lett 28(1):41–44

Fairfield C (1980) OMSI sound project: the acoustic effects of the Mount St. Helens eruption on May 18 1980. Oregon Geol 42(12):200–202

Fee D, Garces M (2007) Infrasonic tremor in the diffraction zone. Geophys Res Lett 34:L16826. https://doi.org/10.1029/2007GL030616

Fee D, Steffke A, Garces, M (2010a) Characterization of the 2008 Kasatochi and Okmok eruptions using remote infrasound arrays. J Geophys Res Atmos 115(D2). https://doi.org/10.1029/2009jd013621

Fee D, Garces M, Steffke A (2010a) Infrasound from Tungurahua Volcano 2006–2008: Strombolian to Plinian eruptive activity. J Volcanol Geotherm Res 193:67–81. https://doi.org/10.1016/j.jvolgeores.2010.03.006

Fee D, Garces M, Patrick M, Chouet B, Dawson P, Swanson D (2010b) Infrasonic harmonic tremor and degassing bursts from Halema'uma'u Crater, Kilauea Volcano, Hawaii. J Geophys Res 115:B11316. https://doi.org/10.1029/2010JB007642

Fee D, Matoza RS (2013) An overview of volcano infrasound: from hawaiian to plinian, local to global. J Volcanol Geotherm Res 249:123–139. https://doi.org/10.1016/j.jvolgeores.2012.09.002

Fee D, Matoza RS, Gee KL, Neilsen TB, Ogden DE (2013a) Infrasonic crackle and supersonic jet noise from the eruption of Nabro Volcano, Eritrea. Geophys Res Lett 40:1–5. https://doi.org/10.1002/grl.5082

Fee D, McNutt SR, Lopez TM, Arnoult KM, Szuberla CAL, Olson JV (2013b) Combining local and remote infrasound recordings from the 2009 Redoubt Volcano eruption. J Volcanol Geotherm Res 259:100–114

Fee D, Yokoo A, Johnson JB (2014) Introduction to an open community infrasound dataset from the actively erupting Sakurajima Volcano, Japan. Seismol Res Lett 85(6):1151–1162

Fee D, Haney M, Matoza R, Szuberla C, Lyons J, Waythomas C (2016), Seismic envelope-based detection and location of ground-coupled airwaves from volcanoes in Alaska. Bull Seismol Soc Am 106:3. https://doi.org/10.1785/0120150244

Firstov PP, Kravchenko NM (1996) Estimation of the amount of explosive gas released in volcanic eruptions using air waves. Volcanol Seismol 17:547–560

Firstov PP, Fee D, Makhmudov ER (2013) The explosive activity of Karymskii Volcano, Kamchatka: Acoustic andseismic observations. J Volcanol Seismol 7(4):252–264

Ford SR, Rodgers AJ, Xu H, Templeton DC, Harben P, Foxall W, Reinke RE (2014) Partitioning of seismoacoustic energy and estimation of yield and height-of-burst/depth-of-burial for near-surface explosions. Bull Seismol Soc Am 104(2):608–623

Gabrielson T (2010) Krakatoa and the Royal Society: the Krakatoa explosion of 1883. Acoust Today 6(2):14–19

Gainville O, Blanc-Benon P, Blanc E, Roche R, Millet C, Le Piver F, Despres B, Piserchia, PF (2010) Misty picture: a unique experiment for the interpretation of the infrasound propagation from large explosive sources. In: infrasound monitoring for atmospheric studies, Springer Netherland, pp 575–598

Garces MA, McNutt SR (1997) Theory of the airborne sound field generated in a resonant magma conduit. J Volcanol Geotherm Res 78:155–178

Garces MA, Hagerty MT, Schwartz SY (1998) Magma acoustics and time-varying melt properties at Arenal Volcano, Costa Rica. Geophys Res Lett 25:2293–2296

Garces M, Iguchi M, Ishihara K, Morrissey M, Sudo Y, Tsutsui T (1999) Infrasonic precursors to a Vulcanian eruption at Sakurajima Volcano, Japan. Geophys Res Lett 26:2537–2540

Garces MA (2000) Theory of acoustic propagation in a multi-phase stratified liquid flowing within an elastic-walled conduit of varying cross-sectional area. J Volcanol. Geotherm. Res 101(1):1–17

Garcés M, Harris A, Hetzer C, Johnson J, Rowland S, Marchetti E, Okubo P (2003) Infrasonic tremor observed at Kīlauea Volcano, Hawai'i. Geophys Res Lett 30(20)

Garces M et al (2008) Capturing the acoustic fingerprint of stratospheric ash injection. EOS Trans AGU 89(40):377

Garces MA, Fee D, Matoza R (2013) Volcano acoustics, chapter 16. In: Fagents SA, Gregg TKP, Lopes RMC (eds) Modeling volcanic processes: the physics and mathematics of volcanism. Cambridge University Press

Genco R, Ripepe M, Marchetti E, Bonadonna C, Biass S (2014) Acoustic wavefield and Mach wave radiation of flashing arcs in strombolian explosion measured by image luminance. Geophys Res Lett 41(20):7135–7142

Georges TM, Beasley WH (1977) Refraction of infrasound by upper-atmospheric winds. J Acoust Soc Am 61(1):28–34

Gerst A, Hort M, Kyle PR, Vöge M (2008) 4D velocity of Strombolian eruptions and man-made explosions derived from multiple Doppler radar instruments. J Volcanol Geoth Res 177 (3):648–660

Gerst A, Hort M, Aster RC, Johnson JB, Kyle PR (2013) The first second of volcanic eruptions from the Erebus volcano lava lake, Antarctica—energies, pressures, seismology, and infrasound. J Geophys Res Solid Earth 118(7):3318–3340

Glasstone S (ed) (1977) The effects of nuclear weapons, *US Department of Defense*

Godin OA (2006) Anomalous transparency of water-air interface for low-frequency sound. Phys Rev Lett 97:164301. https://doi.org/10.1103/PhysRevLett.97.164301

Godin OA (2007) Transmission of low-frequency sound through the water-to-air interface. Acoust Phys 53(3):305–312. https://doi.org/10.1134/S1063771007030074

Goerke VH, Young JM, Cook RK (1965) Infrasonic observations of the May 16, 1963, volcanic explosion on the Island of Bali. J Geophys Res 70(24):6017–6022

Gorshkov GS (1960) Determination of the explosion energy in some volcanoes according to barograms. Bull Volcanol 23:141–144

Gossard EE and Hooke WH (1975) Waves in the atmosphere: atmospheric infrasound and gravity waves: their generation and propagation. Elsevier, Amsterdam

Goto A, and Johnson JB (2011) Monotonic infrasound and Helmholtz resonance at Volcan Villarrica (Chile). Geophys Res Lett 38. https://doi.org/10.1029/2011gl046858
Green DN, Neuberg J (2005) Seismic and infrasonic signals associated with an unusual collapse event at the Soufrière Hills volcano, Montserrat. Geophys Res Lett 32(7)
Green DN, Bowers D (2010) Estimating the detection capability of the International Monitoring System infrasound network. J Geophys Res 115:D18116. https://doi.org/10.1029/2010JD014017
Green DN, Matoza RS, Vergoz J, Le Pichon A (2012) Infrasonic propagation from the 2010 Eyjafjallajökull eruption: investigating the influence of stratospheric solar tides. J Geophys Res 117:D21202. https://doi.org/10.1029/2012JD017988
Green DN, Evers LG, Fee D, Matoza RS, Snellen M, Smets P, Simons D (2013) Hydroacoustic, infrasonic and seismic monitoring of the submarine eruptive activity and sub-aerial plume generation at South Sarigan, May 2010. J Volcanol Geotherm. Res 257:31–43. https://doi.org/10.1016/j.jvolgeores.2013.03.006
Green DN (2015) The spatial coherence structure of infrasonic waves: analysis of data from International Monitoring System arrays. Geophys J Int 201(1):377–389. https://doi.org/10.1093/gji/ggu495
Guilbert J, Harjadi P, Purbawinata M, Jammes S, Le Pichon A, Feignier B (2005) Monitoring of Indonesian volcanoes with infrasound: preliminary results. In: Infrasound technology workshop, Tahiti
Hagerty MT, Schwartz SY, Garces MA, Protti M (2000) Analysis of seismic and acoustic observations at Arenal Volcano, Costa Rica, 1995-1997. J Volcanol Geotherm Res 101:27–65
Harkrider DG (1964) Theoretical and observed acoustic-gravity waves from explosive sources in the atmosphere. J Geophys Res 69(24):5295–5321
Harkrider D, Press F (1967) The Krakatoa air-sea waves: an example of pulse propagation in coupled systems. Geophys J Int 13(1–3):149–159
Harris A, Ripepe M (2007) Synergy of multiple geophysical approaches to unravel explosive eruption conduit and source dynamics–A case study from Stromboli. Chemie der Erde-Geochemistry 67(1):1–35
Ichihara M, Ripepe M, Goto A, Oshima H, Aoyama H, Iguchi M, Tanaka K, Taniguchi H (2009) Airwaves generated by an underwater explosion: implications for volcanic infrasound. J Geophys Res-Solid Earth 114:B03210. https://doi.org/10.1029/2008jb005792
Ichihara M, Takeo M, Yokoo A, Oikawa J, Ohminato T (2012) Monitoring volcanic activity using correlation patterns between infrasound and ground motion. Geophys Res Lett 39:L04304. https://doi.org/10.1029/2011GL050542
Iguchi M (2013) Magma movement from the deep to shallow Sakurajima Volcano as revealed by geophysical observations. Bull Volcanol Soc Japan 58(1):1–18
Iguchi M, Ishihara K (1990) Comparison of earthquakes and airshocks accompanied with explosive eruptions at Sakurajima and Suwanosejima volcanoes (in Japanese). Annu Disas Prev Res Inst Kyoto Univ 33B–1:1–11
Ishihara K (1985) Dynamical analysis of volcanic explosion. J Geodyn 3:327–349. https://doi.org/10.1016/0264-3707(85)90041-9
Johnson JB (2003) Generation and propagation of infrasonic airwaves from volcanic explosions. J Volcanol Geoth Res 121(1):1–14
Johnson JB (2007) On the relation between infrasound, seismicity, and small pyroclastic explosions at KarymskyVolcano. J Geophys Res Solid Earth 112:B08203. https://doi.org/10.1029/2006JB004654
Johnson JB, Ruiz MC, Lees JM, Ramon P (2005) Poor scaling between elastic energy release and eruption intensity at Tungurahua Volcano, Ecuador. Geophys Res Lett 32(15)
Johnson JB, Malone SD (2007) Ground-coupled acoustic airwaves from Mount St. Helens provide constraints on the May 18, 1980 eruption. Earth Planet Sci Lett 258 (1–2):16–31
Johnson J, Aster R, Jones KR, Kyle P, McIntosh B (2008a) Acoustic source characterization of impulsive Strombolian eruptions from the Mount Erebus lava lake. J Volcanol Geoth Res 177 (3):673–686. https://doi.org/10.1016/j.jvolgeores.2008.06.028

Johnson JB, Lees JM, Gerst A, Sahagian D, Varley N (2008b) Long-period earthquakes and co-eruptive dome inflation seen with particle image velocimetry. Nature 456(7220):377–381
Johnson JB, Ripepe M (2011) Volcano infrasound: a review. J Volcanol Geotherm Res 206(3):61–69
Johnson JB, Anderson J, Marcillo O, Arrowsmith S (2012) Probing local wind and temperature structure using infrasound from Volcan Villarrica (Chile). J Geophys Res 117:D17107. https://doi.org/10.1029/2012JD017694
Johnson JB, Miller AJ (2014) Application of the monopole source to quantify explosive flux during vulcanian explosions at Sakurajima Volcano (Japan). Seismol Res Lett 85(6):1163–1176
Johnson JB, Palma JL (2015) Lahar infrasound associated with Volcán Villarrica's 3 March 2015 eruption. Geophys Res Lett 42(15):6324–6331
Jones KR, Johnson JB, Aster R, Kyle PR, McIntosh WC (2008) Infrasonic tracking of large bubble bursts and ash venting at Erebus volcano, Antarctica. J Volcanol Geoth Res 177(3):661–672
Jones KR, Johnson JB (2011) Mapping complex vent eruptive activity at Santiaguito, Guatemala using network infrasound semblance. J Volcanol Geotherm Res 199:15–24. https://doi.org/10.1016/j.volgeores.2010.08.006
Kamo K, Ishihara K, Tahira M (1994) Infrasonic and seismic detection of explosive eruptions at Sakurajima volcano, Japan, and the PEGASAS-VE early-warning system. In: Proceedings of the first international symposium on volcanic ash and aviation safety, U.S. Geological Survey Bulletin 2047, pp 357–365
Kanamori H, Mori J, Harkrider DG (1994) Excitation of atmospheric oscillations by volcanic eruptions. J Geophys Res 99(B11):21947–21961
Kim K, Lees JM (2011) Finite-difference time-domain modeling of transient infrasonic wavefields excited by volcanic explosions. Geophys Res Lett 38:L06804. https://doi.org/10.1029/2010GL046615
Kim K, Lees JM (2014) Local volcano infrasound and source localization investigated by 3D simulation. Seismol Res Lett 85(6):1177–1186. https://doi.org/10.1785/0220140029
Kim K, Fee D, Yokoo A, Lees JM (2015) Acoustic source inversion to estimate volume flux from volcanic explosions. Geophys Res Lett 42:5243–5249. https://doi.org/10.1002/2015GL064466
Kim K, Rodgers A (2016) Waveform inversion of acoustic waves for explosion yield estimation. Geophys Res Lett 43(13):6883–6890
Kinney GF, Graham KJ (1985) Explosive shocks in air. Springer Science & Business Media
Kulichkov SN (2004) Long-range propagation and scattering of low-frequency sound pulses in the middle atmosphere. Meteorol Atmos Phys 85:47–60. https://doi.org/10.1007/s00703-003-0033-z
Lacanna G, Ripepe M (2013) Influence of near-source volcano topography on the acoustic wavefield and implication for source modeling. J Volcanol Geotherm Res 250:9–18. https://doi.org/10.1016/j.volgeores.2012.10.005
Lacanna G, Ichihara M, Iwakuni M, Takeo M, Iguchi M, Ripepe M (2014) Influence of atmospheric structure and topography on infrasonic wave propagation. J Geophys Res 119:2988–3005. https://doi.org/10.1002/2013JB010827
Lalande J-M, Sebe O, Landes M, Blanc-Benon P, Matoza RS, Le Pichon A, Blanc E (2012) Infrasound data inversion for atmospheric sounding. Geophys J Int 190:687–701
Lamb H (1911) On atmospheric oscillations. Proc R Soc Lond Ser A 84(574):551–572
Lamb OD, De Angelis S, Lavallée Y (2015) Using infrasound to constrain ash plume rise. J Appl Volcanol 4(1):1
Landès M, Ceranna L, Le Pichon A, Matoza RS (2012) Localization of microbarom sources using the IMS infrasound network. J Geophys Res 117:D06102. https://doi.org/10.1029/2011JD016684
Lane SJ, James MR, Corder SB (2013) Volcano infrasonic signals and magma degassing: first-order experimental insights and application to Stromboli. Earth Planet Sci Lett 377–378:169–179. https://doi.org/10.1016/j.epsl.2013.06.048
LeConte J (1884) Atmospheric waves from Krakatoa. Science 3(71):701–702

Lees JM, Gordeev EI, Ripepe M (2004) Explosions and periodic tremor at Karymsky volcano, Kamchatka, Russia. Geophys J Int 158(3):1151–1167

Lees JM, Johnson JB, Ruiz M, Troncoso L, Welsh M (2008) Reventador Volcano 2005: eruptive activity inferred from seismo-acoustic observation. J Volcanol Geoth Res 176(1):179–190

Le Pichon A, Blanc E, Drob D, Lambotte S, Dessa JX, Lardy M, Bani P, Vergniolle S (2005) Infrasound monitoring of volcanoes to probe high-altitude winds. J Geophys Res 110:D13106. https://doi.org/10.1029/2004JD005587

Le Pichon A, Vergoz J, Blanc E, Guilbert J, Ceranna L, Evers L, Brachet N (2009) Assessing the performance of the International Monitoring System infrasound network: geographical coverage and temporal variabilities. J Geophys Res 114:D08112. https://doi.org/10.1029/2008JD010907

Le Pichon A, Vergoz J, Cansi Y, Ceranna L, Drob D (2010) Contribution of infrasound monitoring for atmospheric remote sensing. In: infrasound monitoring for atmospheric studies, p 629–646. https://doi.org/10.1007/978-1-4020-9508-5_20

Le Pichon A, Ceranna L, Vergoz J (2012) Incorporating numerical modeling into estimates of the detection capability of the IMS infrasound network. J Geophys Res 117:D05121. https://doi.org/10.1029/2011JD016670

Lighthill MJ (1962) The Bakerian Lecture, 1961: sound generated aerodynamically. Proc R Soc Lon Ser A 267(1329):147–182

Lighthill MJ (1963) Jet noise. AIAA J. 1(7):1507–1517

Lighthill MJ (1978) Waves in fluids. Cambridge University Press

Liu CH, Klostermeyer J, Yeh KC, Jones TB, Robinson T, Holt O et al (1982) Global dynamic responses of the atmosphere to the eruption of Mount St. Helens on May 18, 1980. J Geophys Res Sp Phys 87(A8):6281–6290

Lonzaga JB, Waxler RM, Assink JD, Talmadge CL (2015) Modelling waveforms of infrasound arrivals from impulsive sources using weakly non-linear ray theory. Geophys J Int 200:1347–1361

Lopez T, Fee D, Prata F, Dehn J (2013) Characterization and interpretation of volcanic activity at Karymsky Volcano, Kamchatka, Russia, using observations of infrasound, volcanic emissions, and thermal imagery. Geochem Geophys Geosyst 14(12):5106–5127. https://doi.org/10.1002/2013GC004817

Lorenz RD, Turtle EP, Howell R, Radebaugh J, Lopes RM (2015) The roar of Yasur: Handheld audio recorder monitoring of Vanuatu volcanic vent activity, *J*. Geotherm Res, Volcanol in press

Lyons JJ, Ichihara M, Kurokawa A, Lees JM (2013) Switching between seismic and seismo-acoustic harmonic tremor simulated in the laboratory: insights into the role of open degassing channels and magma viscosity. J Geophys Res Solid Earth 118(1):277–289

Marchetti E, Ichihara M, Ripepe M (2004) Propagation of acoustic waves in a viscoelastic two-phase system: influence of gas bubble concentration. J Volcanol Geotherm Res 137(1–3):93–108. https://doi.org/10.1016/j.jvolgeores.2004.05.002

Marchetti E, Ripepe M, Harris AJL, Delle Donne D (2009) Tracing the differences between Vulcanian and Strombolian explosions using infrasonic and thermal radiation energy. Earth Planet Sci Lett 279(3):273–281

Marchetti E, Ripepe M, Delle Donne D, Genco R, Finizola A, Garaebiti E (2013) Blast waves from violent explosive activity at Yasur Volcano, Vanuatu. Geophys Res Lett 40(22):5838–5843

Marchetti E, Ripepe M, Campus P, Le Pichon A, Brachet N, Blanc E, Gaillard P, Mialle P, Husson P (2019) Infrasound monitoring of volcanic eruptions and contribution of ARISE to the volcanic ash advisory centers. In: Le Pichon A, Blanc E, Hauchecorne A (eds) Infrasound monitoring for atmospheric studies, 2nd edn. Springer, Dordrecht, pp 1141–1162

Marcillo O, Johnson JB (2010) Tracking near-surface atmospheric conditions using an infrasound network. J Acoust Soc Am 128:EL14–19, https://doi.org/10.1121/1.3442725

Matoza RS, Hedlin MSH, Garces MA (2007) An infrasound array study of Mount St. Helens. J Volcanol Geotherm. Res. 160:249–262. https://doi.org/10.1016/j.jvolgeores.2006.10.006

Matoza RS, Garces MA, Chouet BA, D'Auria L, Hedlin MAH, de Groot-Hedlin C, Waite GP (2009a) The source of infrasound associated with long-period events at Mount St. Helens. J Geophys Res 114:B04305. https://doi.org/10.1029/2008jb006128

Matoza RS, Fee D, Garces MA, Seiner JM, Ramon PA, Hedlin MAH (2009b) Infrasonic jet noise from volcanic eruptions. Geophys Res Lett 36:L08303. https://doi.org/10.1029/2008GL036486

Matoza RS, Fee D, Garces M (2010) Infrasonic tremor wavefield of the Pu'u O'o crater complex and lava tube system, Hawaii, in April 2007. J Geophys Res 115:B12312. https://doi.org/10.1029/2009JB007192

Matoza RS, Le Pichon A, Vergoz J, Herry P, Lalande J, Lee H, Che I, Rybin A (2011a) Infrasonic observations of the June 2009 Sarychev Peak eruption, Kuril Islands: implications for infrasonic monitoring of remote explosive volcanism. J Volcanol Geotherm Res 200:35–48. https://doi.org/10.1016/j.jvolgeores.2010.11.022

Matoza RS, Vergoz J, Le Pichon A, Ceranna L, Green DN, Evers LG, Ripepe M, Campus P, Liszka L, Kvaerna T, Kjartansson E, Hoskuldsson A (2011b) Long-range acoustic observations of the Eyjafjallajökull eruption, Iceland, April-May 2010. Geophys Res Lett 38:L06308. https://doi.org/10.1029/2011GL047019

Matoza RS, Shearer PM, Lin G, Wolfe CJ, Okubo PG (2013a) Systematic relocation of seismicity on Hawaii Island from 1992 to 2009 using waveform cross correlation and cluster analysis. J Geophys Res Solid Earth 118(5):2275–2288

Matoza RS, Fee D, Neilsen TB, Gee KL, Ogden DE (2013b) Aeroacoustics of volcanic jets: acoustic power estimation and jet velocity dependence. J Geophys Res Solid Earth 118:6269–6284. https://doi.org/10.1002/2013JB010303

Matoza RS, Landès M, Le Pichon A, Ceranna L, Brown D (2013c) Coherent ambient infrasound recorded by the International Monitoring System. Geophys Res Lett 40. https://doi.org/10.1029/2012gl054329

Matoza RS, Fee D (2014) Infrasonic component of volcano-seismic eruption tremor. Geophys Res Lett 41:2014GL059301. https://doi.org/10.1002/2014gl059301

Matoza RS, Fee D, Lopez TM (2014) Acoustic characterization of explosion complexity at Sakurajima, Karymsky, and Tungurahua Volcanoes. Seismol Res Lett 85(6):1187–1199. https://doi.org/10.1785/0220140110

Matoza RS, Green DN, Le Pichon A, Shearer PM, Fee D, Mialle P, Ceranna L (2017) Automated detection and cataloging of global explosive volcanism using the International Monitoring System infrasound network. J Geophys Res Solid Earth 122:2946–2971. https://doi.org/10.1002/2016JB013356

Mauk FJ (1983) Utilization of seismically recorded infrasonic-acoustic signals to monitor volcanic explosions: the El Chichon Sequence 1982–A case study. J Geophys Res Solid Earth 88 (B12):10385–10401

Mialle P et al (2015) Towards a volcanic notification system with infrasound data: use of infrasound data in support of the VAACs in the framework of ARISE project. In: World meteorological organization 7th international workshop on volcanic ash (IWVA/7), Anchorage, Alaska

McNutt SR (2000) Seismic monitoring. In: Sigurdsson H (ed) Encyclopedia of volcanoes. Academic Press, San Diego, Calif

McNutt SR, Nishimura T (2008) Volcanic tremor during eruptions: temporal characteristics, scaling and constraints on conduit size and processes. J Volcanol Geotherm Res 178:10–18. https://doi.org/10.1016/j.jvolgeores.2008.03.010

McNutt SR, Thompson G, Johnson J, De Angelis S, Fee D (2015) Seismic and infrasonic monitoring, Chapter 63. In: Sigurdsson H, Houghton B, McNutt S, Rymer H (eds) The Encyclopedia of Volcanoes, Second Edition. Academic Press, J. Stix, pp 1071–1099

Medici EF, Allen JS, Waite GP (2014) Modeling shock waves generated by explosive volcanic eruptions. Geophys Res Lett 41(2):414–421

Moran SC, Matoza RS, Garces MA, Hedlin MAH, Bowers D, Scott WE, Sherrod DR, Vallance JW (2008) Seismic and acoustic recordings of an unusually large rockfall at Mount St. Helens, Washington. Geophys Res Lett 35(19). https://doi.org/10.1029/2008gl035176
Morrissey MM, Chouet BA (1997) Burst conditions of explosive volcanic eruptions recorded on microbarographs. Science 275(5304):1290–1293
Morse PM, Ingard KU (1968) Theoretical acoustics. McGraw-Hill, Princeton, NJ
Needham CE (2010) Blast wave propagation. Springer, Berlin, Germany, pp 87–99
Newhall CG, Self S (1982) The volcanic explosivity index (VEI): an estimate of explosive magnitude of historical volcanism. J Geophys Res 87:1231–1238
Nishida K, Ichihara M (2016) Real-time infrasonic monitoring of the eruption at a remote island volcano using seismoacoustic cross correlation. Geophys J Int 204(2):748–752
Omori F (1912) The eruptions and earthquakes of the Asama-Yama. Bull Imp Earthq Inv Commitee 6(1)
Oshima H, Maekawa T (2001) Excitation process of infrasonic waves associated with Merapi-type pyroclastic flow as revealed by a new recording system. Geophys Res Lett 28(6):1099–1102
Ostashev VE (1997) Acoustics in moving inhomogeneous media. E & FN Spon, London
Pekeris CL (1939) The propagation of a pulse in the atmosphere. Proc R Soc LonSer A 171 (947):434–449
Perret FA (1950) Volcanological Observations. Carnegie Institution Of Washington Publication
Pierce AD (1963) Propagation of acoustic-gravity waves from a small source above the ground in an isothermal atmosphere. J Acoust Soc Am 35(11):1798–1807
Pierce AD (1989) Acoustics: an introduction to its physical principals and applications. Acoustical Society of America, Melville, N. Y.
Piercy JE, Embleton TFW, Sutherland LC (1977) Review of noise propagation in the atmosphere. J Acoust Soc Am 61(6):1403–1418
Prejean SG, Brodsky EE (2011) Volcanic plume height measured by seismic waves based on a mechanical model. J Geophys Res 116:B01306. https://doi.org/10.1029/2010JB007620
Press F, Harkrider D (1962) Propagation of acoustic-gravity waves in the atmosphere. J Geophys Res 67(10):3889–3908
Press F, Harkrider D (1966) Air-sea waves from the explosion of Krakatoa. Science 154 (3754):1325–1327
Reed JW (1977) Atmospheric attenuation of explosion waves. J Acoust Soc Am 61(1):39–47
Reed JW (1987) Air-pressure waves from Mount St. Helens Eruptions. J Geophys Res Atmos 92 (D10):11979–11992, https://doi.org/10.1029/jd092id10p11979
Reynolds JWS (1878) The theory of sound, vol II. The Macmillan Company
Richards AF (1963) Volcanic sounds, investigation and analysis. J Geophys Res Solid Earth 68:919–928
Richardson JP, Waite GP, Palma JL (2014) Varying seismic-acoustic properties of the fluctuating lava lake at Villarrica volcano, Chile. J Geophys Res Solid Earth 119(7):5560–5573
Ripepe M, Poggi P, Braun T, Gordeev E (1996) Infrasonic waves and volcanic tremor at Stromboli. Geophys Res Lett 23(2):181–184
Ripepe M, Marchetti E (2002) Array tracking of infrasonic sources at Stromboli volcano. Geophys Res Lett 29(22)
Ripepe M, Marchetti E (2019) Infrasound monitoring of volcano-related hazards for civil protection. In: Le Pichon A, Blanc E, Hauchecorne A (eds) Infrasound monitoring for atmospheric studies, 2nd edn. Springer, Dordrecht, pp 1107–1140
Ripepe M, Marchetti E, Ulivieri G (2007) Infrasonic monitoring at Stromboli volcano during the 2003. J Geophys Res Solid Earth 112:B09207. https://doi.org/10.1029/2006JB004613
Ripepe M, De Angelis S, Lacanna G, Poggi P, Williams C, Marchetti E, Donne DD, Ulivieri G. Tracking pyroclastic flows at Soufrière Hills Volcano (2009) Eos. Trans Am GeophysChile 90 (27):229–30
Ripepe M, De Angelis S, Lacanna G, Voight B (2010a) Observation of infrasonic and gravity waves at Soufrière Hills Volcano, Montserrat. Geophys Res Lett. 37(L00E14). https://doi.org/10.1029/2010gl042557

Ripepe M, Marchetti E, Bonadonna C, Harris AJL, Pioli L, Ulivieri G (2010b) Monochromatic infrasonic tremor driven by persistent degassing and convection at Villarrica Volcano, Chile. Geophys Res Lett 37:L15303. https://doi.org/10.1029/2010gl043516

Ripepe M, Bonadonna C, Folch A, Delle Donne D, Lacanna G, Marchetti E, Höskuldsson A (2013) Ash-plume dynamics and eruption source parameters by infrasound and thermal imagery: the 2010 Eyjafjallajökull eruption. Earth Planet Sci Lett 366:112–121

Rowell CR, Fee D, Szuberla CAL, Arnoult K, Matoza RS, Firstov PP, Kim K, Makhmudov E (2014) Three-dimensional volcano-acoustic source localization at Karymsky Volcano, Kamtchatka, Russia. J Volcanol Geotherm Res 283:101–115. https://doi.org/10.1016/j.volgeores.2014.06.015

Sahetapy-Engel ST, Harris AJ, Marchetti E (2008) Thermal, seismic and infrasound observations of persistent explosive activity and conduit dynamics at Santiaguito lava dome, Guatemala. J Volcanol Geoth Res 173(1):1–14

Sakai T, Yamasato H, Uhira K (1996) Infrasound accompanying C-type tremor at Sakurajima volcano. Bull Volcano Soc Jpn 41:181–185 (in Japanese)

Scott RH (1884) Note on a series of barometrical disturbances which passed over Europe between the 27th and the 31st of August, 1883. Proc R Soc Lon 36:139–143

Segall P (2010) Earthquake and volcano deformation. Princeton University Press, New Jersey

Siebert L, Simkin T (2002-) Volcanoes of the world: an illustrated catalog of Holocene volcanoes and their eruptions, Smithsonian Institution, Global Volcanism Program digital information series, GVP-3

Snodgrass JM, Richards AF (1956) Observations of underwater volcanic acoustics at Barcena volcano, San Benedicto Island, Mexico, and in Shelikof Strait, Alaska. Trans Am Geophys Union 37:97–104

Sparks, RSJ, Burski MI, Carey SN, Gilbert JS, Glaze LS, Sigurdsson H, Woods AW (1997) Volcanic plumes. Wiley-Blackwell

Strachey RH (1884) Note on the foregoing paper. Proc R Soc Lond 36:143–151

Strachey RH (1888) On the air waves and sounds caused by the eruption of Krakatoa in August 1883. In: Symons GJ (ed) The eruption of Krakatoa and subsequent phenomena, Report of the Krakatoa Committee of the Royal Society, Trübner and Co, Ludgate Hill

Sutherland LC, Bass HE (2004) Atmospheric absorption in the atmosphere up to 160 km. J Acoust Soc Am 115(3):1012–1032. https://doi.org/10.1121/1.1631937

Taddeucci J, Scarlato P, Capponi A, Del Bello E, Cimarelli C, Palladino DM, Kueppers U (2012) High-speed imaging of Strombolian explosions: the ejection velocity of pyroclasts. Geophys Res Lett 39:L02301. https://doi.org/10.1029/2011GL050404

Taddeucci J, Sesterhenn J, Scarlato P, Stampka K, Del Bello E, Pena Fernandez JJ, Gaudin D (2014) High-speed imaging, acoustic features, and aeroacoustic computations of jet noise from Strombolian (and Vulcanian) explosions. Geophys Res Lett 41(9):2014GL059925. https://doi.org/10.1002/2014gl059925

Tahira M (1982) A study of the infrasonic wave in the atmosphere: (II) infrasonic waves generated by the explosions of the volcano Sakurajima. J Meteorol Soc Jpn 60(3):896–907

Tahira M, Nomura M, Sawada Y, Kamo K (1996) Infrasonic and acoustic-gravity waves generated by the Mount Pinatubo eruption of June 15, 1991. In: Newhall C, Punongbayan R (eds) Fire and mud: eruptions and lahars of mount Pinatubo, Philippines. University of Washington Press, Seattle and London

Tailpied D, Le Pichon A, Marchetti E, Ripepe M, Kallel M, Ceranna L, Brachet N (2013) Remote infrasound monitoring of Mount Etna: observed and predicted network detection capability. InfraMatics 2(1). https://doi.org/10.4236/inframatics.2013.21001

Taisne B, Whelley P, Le Pichon A, Newhall C (2012) On the use of an infrasonic array at Singapore for volcanoes monitoring, EGU General Assembly

Taisne B, Perttu A, Tailpied D, Caudron C, Simonini L (2019) Atmospheric controls on ground- and space-based remote detection of volcanic ash injection into the atmosphere, and link to early warning systems for aviation hazard mitigation. In: Le Pichon A, Blanc E,

Hauchecorne A (eds) Infrasound monitoring for atmospheric studies, 2nd edn. Springer, Dordrecht, pp 1079–1105
Tam CKW (1998) Jet noise: since 1952. Theor Comput Fluid Dyn 10:393–405
Tam CKW, Viswanathan K, Ahuja KK, Panda J (2008) The sources of jet noise: experimental evidence. J Fluid Mech 615:253–292
Taylor GI (1929) Waves and tides in the atmosphere. Proc R Soc Lond Ser A, 126(800):169–183
Taylor GI (1936) The oscillations of the atmosphere. Proc R Soc Lond Ser A, 156(888):318–326
Tempest A, Flett JS (1903) Report on the Eruptions of the Soufriere, in St. Vincent, in 1902, and on a Visit to Montagne Pelee, in Martinique - Part I. Philos Trans R Soc Lond Ser A 200: 353–553
Tupper A, Itikarai I, Richards M, Prata F, Carn S, Rosenfeld D (2007) Facing the challenges of the international airways volcano watch: the 2004/05 eruptions of Manam, Papua New Guinea. Weather Forecast 22(1):175–191
Ulivieri G, Ripepe M, Marchetti E (2013) Infrasound reveals transition to oscillatory discharge regime during lava fountaining: implication for early warning. Geophys Res Lett 40(12): 3008–3013
Verbeek (1884) The Krakatoa eruption. Nature 30(757):10–15
Vergniolle S, Brandeis G (1994) Origin of the sound generated by strombolian explosions. Geophys Res Lett 21:1959–1962
Vergniolle S, Brandeis G, Mareschal JC (1996) Strombolian explosions: 2. Eruption dynamics determined from acoustic measurements. J Geophys Res Solid Earth 101(B9):20449–20466
Vergniolle S, Caplan-Auerbach J (2006) Basaltic thermals and subplinian plumes: constraints from acoustic measurements at Shishaldin volcano, Alaska. Bull Volcanol 68(7–8):611–630
Vidal V, Ripepe M, Divoux T, Legrand D, Géminard JC, Melo F (2010) Dynamics of soap bubble bursting and its implications to volcano acoustics. Geophys Res Lett 37(7)
Viswanathan K (2009) Mechanisms of jet noise generation: classical theories and recent developments. Int J Aeroacoust 8(4):355–408
Walker KT, Hedlin MAH (2010) A review of wind-noise reduction methodologies. In: Pichon AL, Blanc E, Hauchecorne A (eds) Infrasound monitoring for atmospheric studies, chap. 5, Springer, Netherlands, pp 141–182
Watada S, Kanamori H (2010) Acoustic resonant oscillations between the atmosphere and the solid earth during the 1991 Mt. Pinatubo eruption. J Geophys Res Solid Earth 115:B12319. https://doi.org/10.1029/2010JB007747
Waythomas CF, Haney MM, Fee D, Schneider DJ, Wech A (2014) The 2013 eruption of Pavlof Volcano, Alaska: a spatter eruption at an ice-and snow-clad volcano. Bull Volcanol 76(10): 1–12
Wilson CR, Forbes RB (1969) Infrasonic waves from Alaskan volcanic eruptions. J Geophys Res 74:4511–4522
Wilson CR, Nichparenko S, Forbes RB (1966) Evidence of two sound channels in the polar atmosphere from infrasonic observations of the eruption of an Alaskan volcano. Nature 211:163–165
Woulff G, McGetchin TR (1976) Acoustic noise from volcanoes: theory and experiment. Geophys J R Astr Soc 45:601–616
Yamasato H (1997) Quantitative analysis of pyroclastic flows using infrasonic and seismic data at Unzen volcano, Japan. J Phys Earth 45(6):397–416
Yamasato H (1998) Nature of infrasonic pulse accompanying low frequency earthquake at Unzen Volcano, Japan. Bull Volcanol Soc Jpn 43:1–13
Yokoo A, Ishihara K (2007) Analysis of pressure waves observed in Sakurajima eruption movies. Earth Planet Sp 59(3):177–181
Yokoo A, Tameguri T (2007) Iguchi M (2009) Swelling of a lava plug associated with a Vulcanian eruption at Sakurajima Volcano, Japan, as revealed by infrasound record: case study of the eruption on January 2. Bull Volc 71(6):619–630. https://doi.org/10.1007/s00445-008-0247-5
Yokoo A, Iguchi M, Tameguri T, Yamamoto K (2013) Processes prior to outbursts of vulcanian eruption at Showa crater of Sakurajima volcano. Bull Volcanol Soc Jpn 58:163–181

Chapter 34
Atmospheric Controls on Ground- and Space-Based Remote Detection of Volcanic Ash Injection into the Atmosphere, and Link to Early Warning Systems for Aviation Hazard Mitigation

Benoit Taisne, Anna Perttu, Dorianne Tailpied, Corentin Caudron and Luca Simonini

Abstract Violent volcanic eruptions, common especially in Southeast Asia, pose an ongoing serious threat to aviation and local communities. However, the physical conditions at the eruptive vent are difficult to estimate. In order to tackle this problem, satellite imagery and infrasound can rapidly provide information about strong eruptions of volcanoes not closely monitored by on-site instruments. For example, the recent infrasonic array at Singapore, installed to support the coverage of the International Monitoring System, allows identification of nearby erupting volcanoes based on the characteristics of the recorded signal. But, due to its location close to the equator, seasonal changes in the wind velocity structure of the atmosphere strongly affect its potential to detect small volcanic eruptions at certain azimuths. To overcome this limit, infrasound could be augmented with satellite

B. Taisne (✉) · A. Perttu · D. Tailpied
Earth Observatory of Singapore, Singapore, Singapore
e-mail: BTaisne@ntu.edu.sg

B. Taisne
Asian School of the Environment, Nanyang Technological University, Singapore, Singapore

C. Caudron
Laboratoire de Volcanologie, G-Time, Département de Géosciences, Environnement et Société, Université Libre de Bruxelles, Brussels, Belgium

L. Simonini
Thales Alenia Space, Cannes, France

L. Simonini
Thales Solution Asia, Thales Research and Technology, Singapore, Singapore

A. Le Pichon et al. (eds.), *Infrasound Monitoring for Atmospheric Studies*,
https://doi.org/10.1007/978-3-319-75140-5_34

data. Yet, with the high average cloud cover in Southeast Asia, there are also challenges to identify weak volcanic plumes using satellite-based monitoring techniques. In this chapter, we aim to examine the relative strengths and weaknesses of the two technologies to better understand the possibility to improve overall detection capability by combining infrasound with satellite imagery.

34.1 Introduction

On August 26, 1883, meteorologists across Europe observed an anomaly in the atmospheric pressure measurements. The anomaly was in fact generated by an explosive eruption of Krakatau volcano in Indonesia, more than 11,000 km away. That was the first remote detection of a volcanic eruption via atmospheric disturbance. The eruption was so energetic that its sound traveled four times around the globe, each time producing a measurable air-pressure anomaly observed on the barometers (Scott 1883). Also, the eruption was audible up to 5,000 km away.

If a similar eruption occurred today, in the context of ever-growing demand for air traffic and increasing numbers of commercial flights, the amount of ash in the atmosphere would seriously disrupt air traffic. In Southeast Asia, air travel would stall for weeks to months, while in neighboring regions planes would likely have to be rerouted. In fact, even a moderate-sized event like the 2010 eruption of Eyjafjallajökull in Iceland can cost the airline industry billions of dollars and affect the global Gross World Product (Lechner et al. 2017).

The vulnerability of air traffic to volcanic eruptions brings with it the need to improve early detection of volcanic ash so that planes can be rerouted to safer paths. To this end, the International Civil Aviation Organization (ICAO), in cooperation with numerous countries and several organizations, set up nine Volcanic Ash Advisory Centres (VAACs) in 2002 as part of the International Airways Volcanic Watch (IAVW). Each VAAC covers a geographic area in which it monitors and forecasts ash movement through atmospheric dispersion models based on all available information from observatories, pilot reports, and measurements from the ground, aircraft, and space instruments. The timeliness of these forecasts, provided to civil aviation authorities, is vital since the majority of encounters between aircraft and volcanic ash have occurred within 24 h and 1,000 km of the eruption (Lechner et al. 2017).

Having accurate and timely information depends on monitoring instruments. While today's technologies will record an eruption similar to Krakatau's with continuous and high-quality data all around the globe, such a major event will likely destroy or damage all near-field instruments. In this context, the need for remote monitoring techniques is all the more urgent as it can provide valuable information. But we need to be aware of their limits. For example, space observations, which often provide the earliest remote detection of volcanic eruptions, depend on atmospheric conditions, with cloud coverage reducing the chances of observing an ash cloud. infrasound propagation mainly depends on atmospheric conditions at the

source, along the path, and at the receiver, with seasonal winds affecting the detection capability.

In this chapter, we consider early warning capabilities of remote monitoring. First, we describe satellites and infrasound as remote monitoring techniques. We then focus on their efficiency in Southeast Asia due to the region's large number of volcanoes and increased air traffic. Finally, we compare the strengths and weaknesses of satellites and infrasound for real-time monitoring of volcanoes.

34.2 Remote Monitoring Techniques

34.2.1 Satellite

Satellites are valuable remote observation tools for near-real-time monitoring thanks to their range of spatial and temporal resolutions in visible, ultraviolet (UV), and infrared (IR) wavelengths. Satellites have proven to be efficient since the 1980s in tracking drifting volcanic clouds (Hanstrum and Watson 1983; Sawada 1987; Prata 1989), yet, to date, no satellite has been specifically designed for volcano monitoring. Instead, several algorithms have been developed to analyze available data, acquired for other purposes, to detect the presence of ash and volcanic gases into the atmosphere.

Volcanic ash is detected (e.g., by the VAAC) via thermal IR imagers (e.g., MODIS, AVHRR, GOES, SEVIRI) and so-called reverse absorption methods (Prata 1989; Tupper et al. 2004). The latter exploit the difference in absorption channels between water and ice clouds (wavelet of 12 μm), and ash clouds (wavelet of 10 μm) (Clarisse et al. 2010). False detections, however, occur if absorbing aerosols other than ash are present (e.g., desert dust; Brenot et al. 2014). Also, a number of limitations exist, such as when water and ice clouds mask volcanic ash (Pavolonis et al. 2006). The detection of volcanic ash in the atmosphere is critical but unfortunately far from straightforward (Brenot et al. 2014). Thus, volcanic ash has also been detected via proxies, such as gases. Among the dominant gases emitted by volcanoes, only sulfur dioxide (SO_2) can be easily tracked due to its low background concentrations in the atmosphere and the accessibility of absorption bands for remote sensing in the UV, IR, and microwave spectral regions (Carn et al. 2016). SO_2 was first detected via UV measurements after the 1982 El Chichón eruption in Mexico (Krueger 1983). Since then, SO_2 emissions have been detected and quantified for every volcanic eruption with a plume height of at least 10 km. It has also become the most frequently measured volcanic gas in terms of satellite remote sensing, with up to 18 SO_2 observations potentially available per day (Carn et al. 2016).

There have been advances during the last decade in the availability of altitude information for SO_2 (Carn et al. 2016). Due to the frequency and redundancy of measurements from multiple techniques some altitude information is nearly always

available for detected plumes (Carn et al. 2016). While SO_2 is often a good proxy for volcanic ash plumes (Thomas and Prata 2011), not all eruptions are accompanied by a detectable amount of SO_2. For a complete presentation of the pros and cons of each satellite, the reader is referred to the review by Carn et al. (2016).

SO_2 emissions and ash are tracked in real time through several systems based on various algorithms. One of these automated global systems is the Support to Aviation Control Service (SACS). The SACS jointly detects SO_2 and ash using multiple satellite instruments operating in the UV and visible wavelengths for daylight hours only, and IR wavelengths for both day and night (Brenot et al. 2014). On the one hand, the SACS determines the Absorption Aerosol Index (AAI) through UV wavelengths detections; the presence of ash can be the dominant part in AAI, but the index is not purely selective for ash since desert dust and biomass-burning aerosols are also detected. AAI can be used over ocean, land, and cloud-covered areas, but it is sensitive to calibration issues. On the other hand, the SACS usually retrieves ash from thermal IR sensors on a three-step procedure (Brenot et al. 2014). First, the algorithm calculates the relative distance between the measured spectra and fixed ash spectral signatures; then it finds the subset of observations which are almost certainly ash; and finally it considers the spatial context for promoting ash candidates to low and medium-confidence detections in the neighborhood of high-confidence detections (see Clarisse et al. 2013, for more details). The procedure therefore provides different levels of confidence (Brenot et al. 2014). In the SACS scheme, the combined detection of both elevated aerosol and SO_2 is highly selective for the volcanic plume, but often miss the low-concentration ash plumes. SACS monitors any location in the world within a 24 h interval. However, a lower sampling rate is observed for lowlatitude regions due to overlapping orbits for higher latitudes.

The NOAA/CIMSS Volcanic Cloud Monitoring system is another fully automated global system (https://volcano.ssec.wisc.edu). It uses infrared imagery from geostationary and low-earth orbit satellites to retrieve ash and dust properties. Depending on the satellite and the region of interest, data latency ranges from 2.5 to 30 min (weather satellite Himawari-8) to more than 4 h (MODIS). Ash clouds are first detected using a multi-spectral approach depending on the sensors available (Pavolonis et al. 2006). The height, mass loading, and effective radii can be estimated and included within alert reports, only in the case when a collection of pixels that has the spectral signature of ash or dust have been identified (Pavolonis et al. 2015a, b). This approach minimizes false alarms without affecting the probability of detection (Pavolonis et al. 2015b). Even then, detection sensitivity can still be impaired, for example, in the tropics, because of the high water vapor may mask the negative brightness temperature differences (Pavolonis et al. 2006).

Another algorithm designed to track ash clouds from volcanoes is called RST (ASH), which stands for Robust Satellite Techniques (Pergola et al. 2016). RST (ASH) determines if a pixel deviates from a background state, using different spectral bands. It has been applied to the satellites NOAA-AVHRR and EOS-MODIS. It has also been tested with the MTSAT fleet, which includes geostationary satellites that cover East Asia and the Western Pacific, with a temporal

resolution of 1 h, and a pixel size of 1 km^2 in the visible band, and 4 km^2 in the infrared band. This method can produce results in the form of ash cloud maps a few minutes after acquisition. These maps are generated using the IR records for background reference fields and from there the temporal mean and standard deviation are calculated for each pixel using multi-year time series. However, this method can miss ash detections, or fail when a low contrast between the volcanic cloud and the background exists (e.g., meteorological clouds are masking the plume; the plume is of short duration when compared to the temporal resolution of the satellite; the plume contains a high percentage of water vapor; or ash is coated with ice while entering the ice-level). False detections have occurred, for example, due to dust from the Sahara which exhibited similar spectral signature to ash.

In addition to the above methods using IR, visible and UV bands, Lidar can also be used to detect the presence of ash and aerosols. Launched in 2006, the Cloud-Aerosol Lidar and Infrared Pathfinder Satellite Observations (CALIPSO) satellite is able to determine, in a narrow swath, the altitude of aerosols and clouds in a quantitative manner. Even if this satellite has poor temporal resolution and cannot be relied on for the early detection of volcanic plumes (Carn et al. 2016), results from CALIPSO have been used as a ground-truth constraint for ash dispersal modeling (e.g. 2014 Kelud eruption, Kristiansen et al. 2015).

34.2.2 Infrasound

34.2.2.1 Infrasound Background

After the Krakatau eruption was recorded by barometers, the next documented work on volcano acoustics was the 1906 eruption of Mt Vesuvius (Woulff and McGetchin 1976). Then, in the 1920s, the first known recordings of volcanic sounds were made on wax phonograph cylinder, and the first tape recordings of volcanic sounds were made by the NHK broadcasting Bureau of Japan in 1950 (Snodgrass and Richards 1956). The first known work using microbarographs to estimate energy from volcanic eruptions was completed in the 1960s (Gorshkov 1960). Since Krakatau's 1883 eruption, instruments measuring and recording atmospheric pressure disturbances have evolved tremendously, from the barographs that recorded the one-minute period signal from Krakatau to today's microbarometers, which can record a range from 0.001 to 50 Hz. Along with the broadening of frequency range, the sensitivity has also improved, allowing detection of smaller amplitude volcanic events.

The improved frequency range and sensitivity allows us to record a variety of volcanic sources, which produce a wide spectrum of infrasonic signatures ranging in frequency from 0.002 Hz up into the audible range (20–20,000 Hz), and can be over 100 Pa at close range and in the tens of Pa at ranges of 1,000 km (Campus and Christie 2010). These signals can be generated from effusive activity like lava lakes (e.g., Jones et al. 2008; Bouche et al. 2010; Fee et al. 2010a; Goto and Johnson

2011), lava flows and tube systems (Matoza et al. 2010), fissure eruptions (Fee et al. 2011; Thelen and Cooper 2015), from moderate explosive activity like pyroclastic flows (Ripepe et al. 2009), or from other associated volcanic processes like lahars (Johnson and Palma 2015). Moderate to large explosive activities, which inject ash into the atmosphere, produce wide range of frequencies due to their eruption dynamics, including the amount of material ejected into the atmosphere through time (Wouff and McGetchin 1976), and changes of vent geometry with time (Fee et al. 2017). Today volcanic infrasound is becoming an accepted and a commonly used tool for volcano monitoring especially in remote areas with sparse local networks like the Aleutians (e.g., De Angelis et al. 2012).

Infrasound stations for volcano monitoring are deployed either as single sensors within around 10 km of the volcano (e.g., Augustine and Redoubt), as distributed sensors around a volcano (e.g., Sakurajima and Santiaguito), or arrays of various designs (e.g., Kilauea and Cleveland). On the one hand, local infrasound recorded from single sensors can be used to count explosions (Peterson et al. 2006; De Angelis et al. 2012), calculate a plume height using waveform data (Caplan-Auerbach et al. 2010), assess the path and furthest reach of pyroclastic flows (e.g., Ripepe et al. 2009), or track lahars (e.g., Johnson and Palma 2015), and signals at distributed sensors can be inverted for source parameters (Kim et al. 2015; De Angelis et al. 2016). On the other hand, array data can be used at a greater distance to identify and characterize volcanic signals. Waveform data from arrays of sensors are generally either used as a beamform, or with array processing. Moreover, in regions where ground-based observations are sparse or unavailable, infrasound has proven a valuable asset (Dabrowa et al. 2011; Matoza et al. 2011a, b; Fee and Matoza 2013; Caudron et al. 2015).

In this chapter, we focus mostly on volcanic eruptions remotely recorded by infrasound arrays. For stations located on or very close to specific volcanoes, the majority of the signals are assumed to be from volcanic activities. However, in the case of regional and global range stations, detections cannot be automatically assumed to be of volcanic origin, and more subtle analysis is needed (e.g., array processing and/or machine learning). The major worldwide distributed network of infrasound arrays is the International Monitoring System, IMS, established to ensure compliance with the Comprehensive Nuclear Test-ban Treaty, CTBT. While the purpose of deploying these arrays is for the monitoring of clandestine atmospheric nuclear tests, the arrays have proven extremely valuable to the field of volcano infrasound (Johnson 2019; Ripepe and Marchetti 2019; Matoza et al. 2019; Le pichon et al. 2019). At the time of writing, the IMS consists of 49 certified infrasound stations, 3 under construction, and 8 additional stations planned, reaching a total of 60 stations distributed around the globe (Marty et al. 2019).

The two main array processing methods are frequency-wavenumber analysis (Costley et al. 2013) and Progressive Multi-Channel Correlation, PMCC (Cansi 1995), that we exclusively use for all array processing. PMCC estimates wavefront parameters (e.g., back-azimuth, trace velocity and root-mean-square amplitude) of coherent plane waves for a given time window using correlation time delays between successive array element triplets. This method, widely used within the

infrasound community, allows detected signals to be grouped based on their similarities into families, which can then be used to distinguish volcanic activity from other infrasound sources like, for example: bolides (Caudron et al. 2016), typhoons and storms (Hetzer et al. 2008), surf (Garces et al. 2003, 2006; Le Pichon et al. 2004; Arrowsmith and Hedlin 2005), anthropogenic sources (Le Pichon et al. 2002), or Mountain Associated Waves (Le Pichon et al. 2005a).

Neural networking is a type of machine learning that can also be used to identify signals of specific types, such as volcanic activities (Cannata et al. 2011; Ham et al. 2012) or snow avalanches (Thüring et al. 2015). For example, Ham et al. (2012) trained a neural network using a dataset of remote eruptions with plumes over 10 km recorded on the IMS network. This trained network was then used on a different dataset that included a variety of infrasound sources, and was able to discriminate the volcanic events from all the other sources.

In terms of aviation safety, information about ash injection into the atmosphere is of paramount importance. The long-term goal is to retrieve plume parameters from infrasound recordings at any distance, so that they can then be input into ash dispersal models (Kim et al. 2015). Already, the coupling of infrasound with plume dynamic models enables us to successfully reproduce observed column heights using near-field recordings (Vergniolle and Caplan-Auerbach 2006; Caplan-Auerbach et al. 2010; Ripepe et al. 2013; Lamb et al. 2015). In the case of remote volcanic regions, the aim is to retrieve the same information but from remote infrasound recordings. To achieve the goals, regardless of the method used to classify an event, the event has to be detected. First, we need to be aware of the different parameters affecting detection capabilities of an infrasound network, and assess if a potential signal can be detected above the noise level, given the network configuration, distance from the source and atmospheric conditions (Pilger et al. 2015).

34.2.2.2 Infrasound Detection Capability, Propagation, and Atmospheric Controls

Our capabilities to detect volcanic activity are intimately linked to infrasonic noise as well as the propagation conditions between the source and the receiver. The first source of noise for a station is due to local wind conditions that can prevent a station from detecting small amplitude events. Another common noise source is a signal from the microbarom considered as noise. The microbarom is an atmospheric infrasonic wave generated by a complex nonlinear interaction between the atmosphere and the ocean (Garces et al. 2010). It is a continuous source of infrasound, globally recorded with a frequency content between 0.2 and 0.3 Hz, and often used to test the noise level at a station. The fact that microbaroms can be recorded at one station signifies that the station is sensitive enough to record infrasound in the frequency of volcanic eruptions. However, while the strength and location of microbaroms depends on the season (they are stronger during tropical monsoons, cyclones, El Niño, etc.), they continuously produce infrasound in the same

frequency range as volcanic eruptions, thus interfering with the detection of events of interest.

In order to limit this interference, the signals arriving at a given infrasound array can be separated and sorted, using array processing, by back-azimuth and other distinguishing characteristics. One can also use WaveWatch3 (Stoppa et al. 2012; Garces et al. 2013) to model the location of the microbarom and disregard signals coming from this direction. Furthermore, stations could be added around a region that is more likely to be affected by the microbarom to help discriminate different signal sources. Nevertheless, in case of low amplitude events, no workaround may be completely effective and the event might be missed.

Apart from the noise at the station, our capabilities to detect volcanic activity are also limited by infrasound propagation conditions, since the main characteristics of the signal, such as energy, can strongly and quickly dissipate by the time the signal reaches distant infrasound stations. Increasing distances will likely make unambiguous detection of low-intensity signals such as pyroclastic flows, lava fountains or degassing impossible. Only the most energetic phase of an eruption will potentially be recorded. For example, Dabrowa et al. (2011) used infrasound data from the IMS to study 110 individual explosive events, producing plumes 6 km or higher, from 39 globally distributed volcanoes. While the characteristics of the signals did not clearly correlate with column heights, each eruption was detected by all stations located within a 1,600 km radius.

Atmospheric influences on infrasound propagation are, principally, the wind along the path and a frequency-dependent attenuation due to absorption. This absorption is especially strong for high frequencies, and in the thermosphere above 100-km altitude (Bass 1995). In addition, topography can influence the wavefield and also block the high frequency component of the signal (Kim and Lees 2011). Therefore, the less-attenuated lower frequency signals from erupting volcanoes are more likely to be recorded at thousands of kilometers. The attenuation and loss of the higher frequency content in the signal presents a challenge for detailed source inversions as well as for the detection of less energetic volcanic activity besides large explosions, sustained plumes, and large landslides. But in specific atmospheric conditions (De Groot-Hedlin et al. 2010; Mutschlener and Whitaker 2010) that usually occur downwind, an effective waveguide can form in which infrasound can travel long distances, with low attenuation across the whole frequency spectrum (Sutherland and Bass 2004). For example, signals from Yasur volcano will be recorded all the way up to 4 Hz, during favorable downwind conditions, at a range of 400 km by the IMS network (Antier et al. 2007).

Infrasound propagation consists of multiple reflections between the atmospheric layers. At greater distance, the vertical gradients of the effective sound speed profile can result in the ducting, or channeling, of infrasound in waveguides between the ground and the lower, middle, or upper atmosphere, allowing the energy to propagate (Hedlin et al. 2012). The effective sound speed profile is defined by combining the wind speed and the sound speed vectors. The profile varies both spatially and temporally. It is influenced by wind seasonality in the stratosphere, especially during the equinoxes, which may or may not favor the formation of waveguides and

thus control the detection capability of stations. Generally, detection upwind is more challenging and is a reminder that the monitoring efficiency of an infrasound array needs to take into account variable atmospheric conditions (Tailpied et al. 2013, 2016). In the past, in order to estimate the capability of an infrasound network, empirical scaling, and attenuations relations were developed to relate the amplitude of infrasound signals to the explosion yield and source to receiver distance, based on theoretical infrasound modeling and on recordings of atmospheric nuclear and chemical explosions. One of the most famous formulas was the one introduced by Whitaker (1995), used in two different approaches. The probabilistic approach consists of defining the minimum energy for a source (anywhere on Earth) that has a 90% likelihood of being detected by at least two stations of the IMS (Clauter and Blandford 1997; Green and Bowers 2010). The deterministic approach defines a specific threshold of detection (anywhere on Earth) based on the performance of the IMS (Le Pichon et al. 2009b). Since 1995, Whitaker's relationship has been updated to include a corrective term that counts for stratospheric wind speeds at a 50 km altitude, averaged along the propagation path between the source and the receiver (Whitaker 2003). The new formula was further improved to explicitly include the dominant frequency of the infrasound signal as a parameter (Green and Bowers 2010).

Recently, Le Pichon et al. (2012) developed a new method to assess the detection capability of an infrasound network. Unlike previous studies, the method has enhanced spatial and temporal resolution, and is not based on empirical yield-scaling relationships derived from remote observations. Rather, it is derived from range-independent parabolic equation simulations. It is a frequency-dependent modeling technique based on an attenuation relationship, using realistic atmospheric specifications and source effects.

For the application to remote monitoring, range-dependent atmospheric variability has been integrated into the Le Pichon et al. (2012)'s method (de Groot Hedlin and Hedlin 2014; Tailpied et al. 2016). Instead of considering constant atmospheric conditions along the propagation path, the longitudinal variations of the wind and temperature profiles are integrated. Such method is of paramount interest as it has the potential to give near-real-time realistic measurements of the network performance. It can be used to provide reliable information of the eruptive sequence at active volcanoes for local to long-range infrasound observations (Tailpied et al. 2016).

This method was used with 10 years of reanalyzed weather data, and the minimum acoustic pressure, needed for an explosion to be detected by at least one station in Southeast Asia, has been computed for both for the IMS network only and with the addition of Singapore's station, SING (Fig. 34.1a). In the latter case, the minimum acoustic pressure needed to be detected is three times smaller in Sumatra (Zone V) 40% of the time (Fig. 34.1b, e). Even though this effect is seasonal, by the addition of a station in the region, the minimum acoustic pressure in Sumatra required to be detected by at least one station decreases significantly, which is especially important for smaller eruptions.

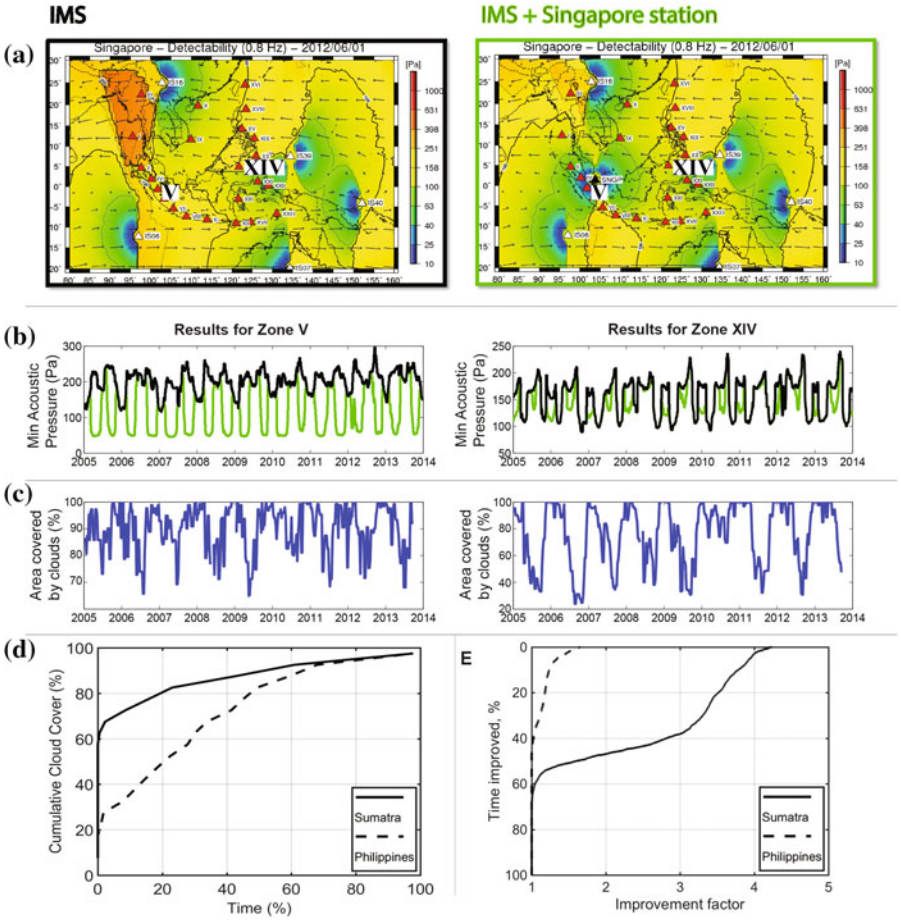

34.3 Application to Southeast Asia

34.3.1 Why Southeast Asia?

It is worth noting that 70% of the global volcanic threat is in Southeast Asia (Brown et al. 2015), with Indonesian volcanoes alone accounting for nearly 40% of all recorded global volcanic fatalities (Auker et al. 2015). The Global Volcanism Program, GVP, database (Siebert and Simkin 2002) lists 287 volcanoes active in the Holocene in Southeast Asia, including volcanoes in Indonesia, Philippines, and Melanesia (Fig. 34.2). Yet, even this number of active volcanoes may significantly underestimate the threat. A recent study, Whelley et al. (2015), has re-examined the number of active or potentially active volcanoes in the region, arriving at 749. After calculating eruption probability in terms of the Volcanic Explosivity Index, VEI, (Newhall and Self 1982), they have found that in Southeast Asia, in any given ten

◀**Fig. 34.1** **Panel a** Minimum detectable acoustic pressure, in Pa, needed for an event to be detected by at least one station from the IMS network (black frame, on the left) or by the IMS + SING network (green frame, on the right). Computed using Le Pichon et al. (2012)'s attenuation formula, using reanalysis atmospheric conditions of the 1st of June 2012, a source frequency of 0.8 Hz and realistic station noise. Red triangles represent the volcanic zones defined by Whelley et al. (2015); white triangles highlight the IMS stations; and the black triangle is the SING station. The wind direction and strength, at 50 km elevation, is represented by the arrows. **Panel b** Minimum detectable acoustic pressure, in Pa, needed to be recorded by at least one station for Sumatra (Zone V, on the left) and Philippines (Zone XIV, on the right), for the regional IMS network only (black curve) and completed by the SING station (green curve). The minimum detectable amplitude is computed the same way as for panel A, from 2005 until 2014. **Panel c** Percent cloud cover for Sumatra (Zones V, on the left) and Philippines (Zone XIV, on the right). Weekly percentage of an area covered by clouds, extracted from MODIS, smoothed using a 4 weeks sliding median filter. Note that a bias might be due to the fact that for one location the measurements are taken at identical local time, therefor missing diurnal variability in cloud cover. **Panel d** Cumulative cloud cover percent for Sumatra (Zone V, solid line), and Philippines (Zone XIV, dashed line), Derived from panel C. For Sumatra cloud cover is up to 90%, 50% of the time, and for the Philippines cloud cover is up to 82 percent, 50% of the time. **Panel e** Improvement factor of the minimum detectable amplitude for the regional network with the addition of the SING station for Sumatra (Zone V, solid line), and the Philippines (Zone XIV, dashed line). This was calculated using the time series in panel B. There is a factor of 3 improvement for Sumatra 40% of the time, meaning that there is a factor of 3 decrease in the minimum acoustic pressure for a signal to be recorded on at least one station. For the Philippines there is a factor of 1.2 improvement 20% of the time

years' span, the likelihood of a VEI-4 event or greater (i.e., the approximate size of the 2010 Eyjafjallajökull eruption with a plume of at least 10 km altitude) is 100%, and the probability of a VEI-5 or greater event (i.e., ash reaching the altitude of at least 25 km) is 63%. In addition to the high probability of significant eruptions in Southeast Asia, the hazard is compounded by the boom in air traffic in the region. From 1998 to 2013, the seat capacity nearly tripled (Bowen 2016), and a further triple expansion is projected by the 2030s (Aneeka and Zhong 2016). In Singapore alone, 58.7 million passengers transited through Changi airport in 2016. While there have fortunately been no fatal incidents involving aircraft and volcanic ash, several such encounters resulted in the loss of power to one or more engines (Guffanti et al. 2010; Lechner et al. 2017): the risk thus continues to be significant.

34.3.2 Satellite Results

Southeast Asian volcanoes are monitored for the aviation industry by the Darwin Volcanic Ash Advisory Centre (VAAC). VAACs uses a combination of satellite monitoring, reports from volcano observatories and local agencies, and pilot reports. The majority of satellites that cover the region are sun-synchronous and meteorological. There are at least three geostationary satellites that can be used to monitor the region for volcanic activity. One of these geostationary satellites is Himawari 8, launched in 2014, that acquires fresh images of the full field of view

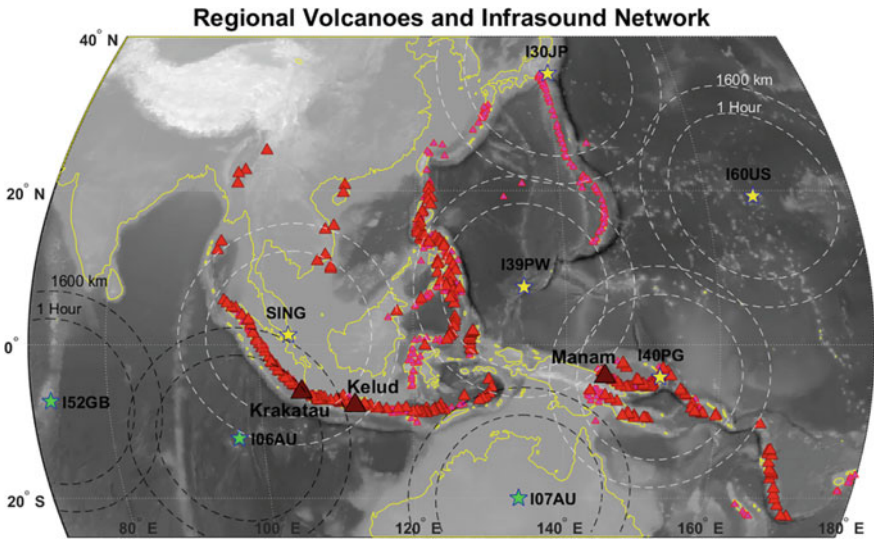

Fig. 34.2 Map of the Southeast Asia region, plotted with volcanoes and infrasound stations. Both the volcanoes from the Whelley et al. (2015) and Global Volcanism Program (GVP) are plotted. The Whelley et al. (2015) database volcanoes are plotted as smaller magenta triangles and GVP volcanoes are plotted slightly larger and in red. The volcanoes from Whelley et al. (2015) that were used in the probability calculations do not include the volcanoes in melanesia, mariana and southern Japanese islands. The GVP volcanoes plotted are the ones used for the calculations in this text. Additionally volcanoes that have been mentioned in the text are highlighted and labeled (Krakatau, Kelut, and Manam). The regional infrasound network is also plotted. Stations with publically available data are plotted as green stars, and stations that do not have public data are plotted as yellow stars. Around each station is plotted the 1 h travel time circle based on a 0.34 km/s sound speed, and the 1600 km distance as mentioned in the text. For volcanoes within the 1600-km circle, all major eruptions are expected to be recorded

every 10 min and Japan every 2.5 min. This new generation of high temporal resolution opens new avenues for ash plume detection based on growth rate (fast growth rate for volcanic plumes versus lower growth rate for meteorological clouds). Still, issues with the detectability of volcanic ash remain, primarily due to cloud cover and icing level. Failures to detect ash generally arise due to a low contrast between the cloud and the background, when there is a cloud masking the plume, when plume duration is short compared to the temporal resolution of the satellite, or when the plume contains a high percentage of water vapor. The cloud cover is a persistent issue throughout the year in the region (Fig. 34.1c, d). Therefore, apart from big eruptions such as the February 2014 eruption of Kelud, most of the more moderate eruptions may not be captured using satellite remote sensing techniques. In Fig. 34.1c, d, cloud cover fractions were calculated from 2005 to 2015 using a four points sliding median filter calculated per week from MODIS data for Southeast Asia, for several defined regions. Over Sumatra the cloud cover is up to 90%, 50% of the time (Fig. 34.1d) with the lowest cloud cover for this region being slightly above 40% during one single week in 2009. In high

latitude "dry" atmosphere conditions, the majority of the water vapor within the plume derives from magmatic water. However, in "wet" equatorial/tropical atmosphere, there is significant entrainment of water vapor into the plume, increasing the amount of ice which can lead to masking of the plume (Tupper et al. 2009).

34.3.3 Infrasound Results

Southeast Asia is home to only four infrasound stations of the International Monitoring System, IMS: I06AU, Cocos Island, Australia; I07AU, Warramunga, Australia; I39PW, Palau and I40PG, Papua New Guinea. In order to assess how effectively these stations monitor regional volcanoes with infrasound, the GVP dataset of volcanoes was examined with two thresholds in mind (Fig. 34.2). The first threshold was the one-hour travel time based on a sound velocity of 340 m/s. The second threshold was the 1,600 km threshold, within which all significant eruptions are expected to be recorded (after Dabrowa et al. 2011). Using these thresholds, 118 volcanoes of the 287 lie within one-hour travel time of the four IMS stations, and this represents about 40% of GVP volcanoes in the region. Additionally, 179 volcanoes are encompassed within the 1,600-km threshold of at least one station, representing 60% of GVP volcanoes in the region. These numbers are a minimum assuming the worst case scenario, where only one station is able to record the eruption. A new research monitoring station, SING, independent of the IMS, was added to the network in July 2015, in Singapore. This new station has increased the number of remotely monitored volcanoes, to 163 volcanoes within one-hour travel time of at least one of the five stations and 210 volcanoes located within 1,600 km of one of the stations. However, this capability to monitor assumes a 100% up-time for all the five stations in the region (IMS + SING). Figure 34.3 illustrates the cumulative number of volcanoes by distance to the closest station, and the effect of each station being down in the network with the one hour and 1,600 km thresholds highlighted. If the closest station to a volcano is down (e.g., maintenance, failure in data transmission), the number of volcanoes within 1,600 km and one-hour travel time will drop depending on which station is affected. For example, the loss of I40PG or I39PW will result in the loss of all of the Papua New Guinea and Melanesia volcanoes or the Philippines, giving the most dramatic change in coverage. Figure 34.3 also illustrates the statistics for the requirement of two stations recording the event, by plotting the cumulative number of volcanoes by distance to the second closest station. In a context of detecting and locating volcanic eruptions, two-station coverage is the baseline condition to form an event in the infrasound community. Only 7% of the volcanoes can be recorded by at least two stations within one hour, and 18% of the volcanoes are within 1,600 km of the second closest station. However, it is also important to note that distance between the station and volcanoes is not the only parameter to take into account when assessing the detection capability of the network.

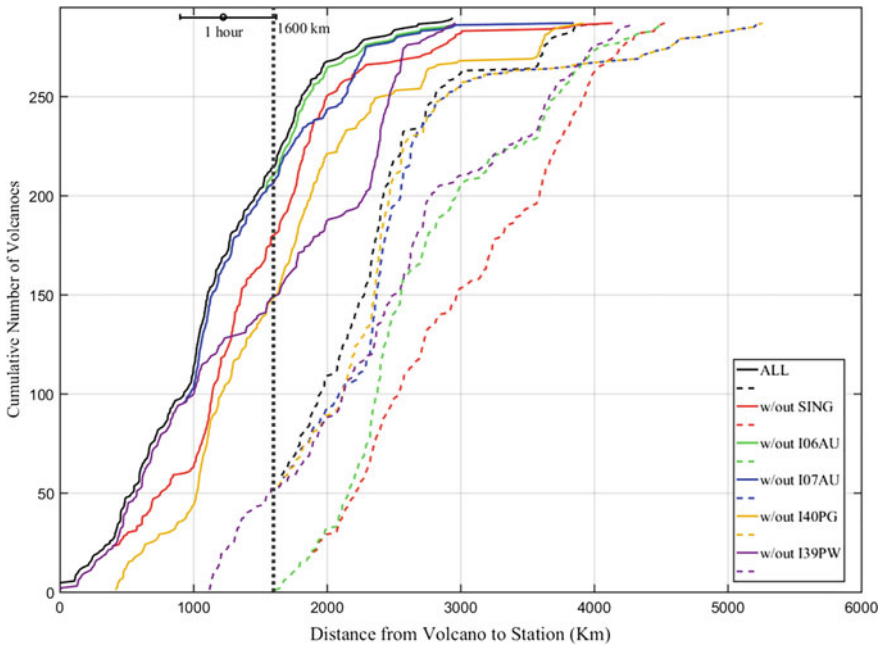

Fig. 34.3 Cumulative number of volcanoes, from GVP database, as a function of distance from the closest station (solid line) and second closest (dashed line). Also plotted along the top is the range for volcanoes within 1 h travel time (dotted line 0.34 km/s) with error bar for 0.25–0.45 km/s celerity range. The black curves represent the cumulative number of volcanoes by distance from the closest station using all the stations in the region (I06AU, I07AU, I40PG, I39PW and SING). The solid curves are the same calculation done to visualize the effect of losing one station out of the five regional stations. There is no change when you lose I06AU IMS station (green line) for the closest volcano due to the fact that the closest volcanoes to I06AU are actually closer to SING. The second closest station calculations are also plotted due to the importance of having more than one array detecting an event for association. The largest impact for the requirement of the second closest station is the I06AU and SING stations due to their proximity to the volcanoes in Sumatra and Java (Fig. 34.2)

One of the major noise source for the SING station is the microbarom generated by the Indian Ocean, the South China Sea or the Pacific. Signals from the Indian Ocean microbarom could prevent the station from picking up small-scale eruptions occurring in parts of Sumatra and Java as it covers the same range of frequency, and there would be no separation in azimuth with array processing using the PMCC algorithm (Cansi 1995). Figure 34.4 illustrates the microbarom array processing results plotted as a rose diagram for 10 days of data. In order to further understand seasonal patterns, 12 months of continuous recorded data from the SING station were processed and filtered into the microbarom range of 0.2–0.3 Hz (Fig. 34.5). The percentage of time a specific back azimuth is affected by the microbarom, was calculated and plotted by month, and for the entire year in Fig. 34.5 (some of the most active volcanoes in the region are plotted for reference). The results show a

clear bimodal distribution with microbarom signals coming from the southwest and northeast, with the intensity of each source varying throughout the year. For example, there is significant microbarom activity in the direction of Marapi (the closest volcano to Singapore) for the majority of the year, except during the southwest monsoon season (June through October).

Due to the compounded issues of a large number of active and potentially active volcanoes, a high eruption probability, challenges in relying on satellite detection, and dense air traffic, Southeast Asia faces unique challenges that will require continued innovation in early warning technologies.

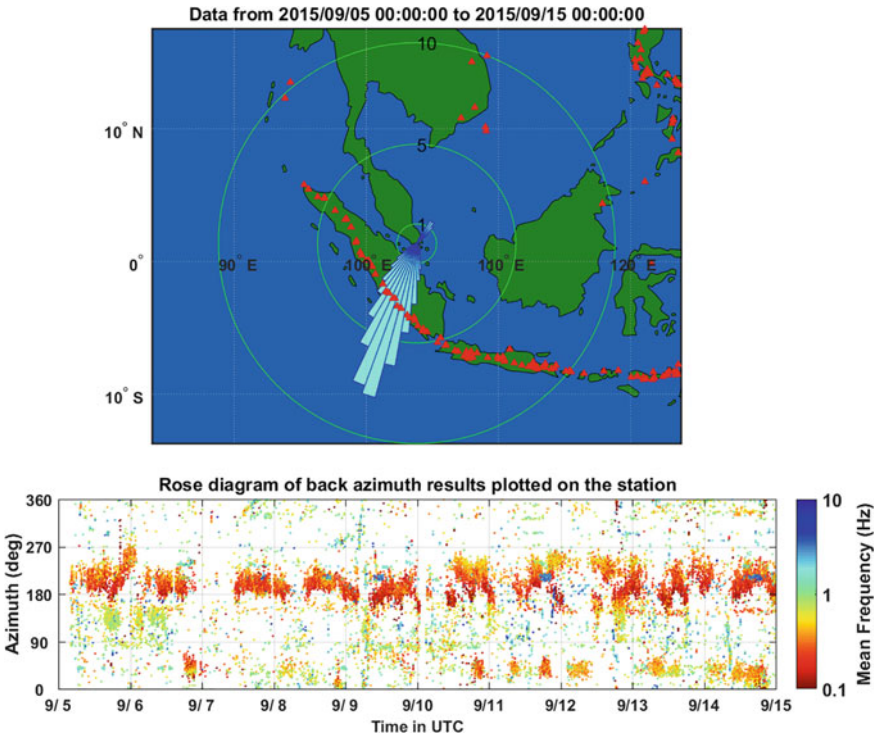

Fig. 34.4 Example of 10 days of data from the Singapore station. Array processing was completed with PMCC. Coherent signals arrival calculated using PMCC detections with frequency between 0.15 and 0.4 Hz were extracted from the dataset (plotted in the lower panel). The percent of time there was a coherent detection was calculated in 5° azimuth bins, plotted as a rose diagram, and is interpreted as being due to the microbarom. For this time period the microbarom is coming from a direction that would affect the detection of signal coming from volcanoes in Sumatra. Bottom panel shows the full PMCC dataset for the ten days by back azimuth and colored by frequency

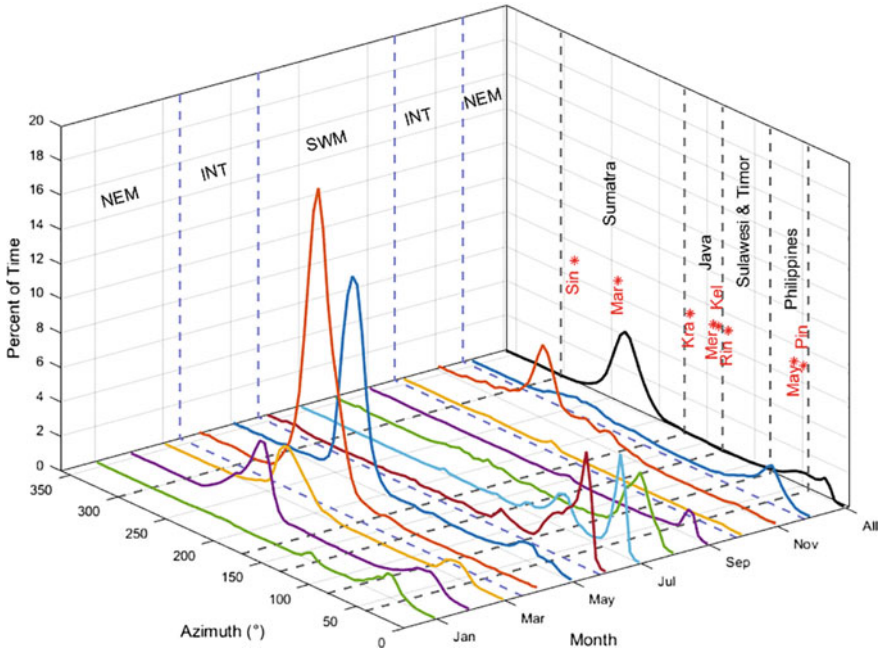

Fig. 34.5 Seasonal impairment in Singapore station's detection capability for a given azimuth due to microbarom. Coherent signal, ranging from 0.15 to 0.4 Hz to capture the range of microbarom frequencies, was extracted between October 2015 and October 2016. For each month, and the whole year, the percentage of time microbarom impairs detection is plotted in 5° azimuth bins. Note that two dominant azimuths correspond to storms in the Indian Ocean (from 200° to 300°) and in the Western Pacific (from 0° to 90°), impairing SING detection capability for events occurring in Sumatra and the Philippines, respectively. For reference, volcanoes are plotted at their respective azimuth from Singapore: Sinabung (Sin), Marapi (Mar), Krakatoa (Kra), Merapi (Mer), Kelud (Kel), Rinjani (Rin), Mayon (May) and Pinatubo (Pin). In addition the dominant weather patterns for Singapore have also been plotted the Northeast Monsoon (NEM) lasting from December to mid March, the Southwest Monsoon (SWM) from June through September, and the two intermonsoon periods (INT)

34.4 Discussion

The two methods of remote monitoring of volcanic activity described in the previous sections should be seen as complementary, as each technique can compensate for some of the limitations of the other. Among the most obvious limitations of satellite-based detection algorithms are that they cannot unambiguously detect volcanic activity during cloudy conditions (Webley and Mastin 2009), they may inaccurately constrain eruption onsets and duration (weak or dilute plume, poor temporal resolution or plume itself hiding the source), and their plume height estimates can suffer from large uncertainties.

These limitations can be overcome by infrasound monitoring, even in an area with a persistent cloud cover like Southeast Asia (Fig. 34.1c). For example, the January 27, 2005 eruption of Manam was not detected for 14 h, not only because the eruption occurred at night, but also due to failure of local communication and cloud coverage (Tupper et al. 2007). At that time, eight of the IMS infrasound stations, including the I33MG located 10,675 km away in Madagascar, did record the event (Brachet et al. 2010). Today, the eruption would also be recorded by the recently installed I40PG in Papua New Guinea only ~800 km from Manam volcano, prompting a more detailed examination of the satellite data (Matoza et al. 2011a). More recently, the 2014 eruption of Kelud injected a plume of ash into the atmosphere to a height of 26 km and destroyed local instruments. Both space (Kristiansen et al. 2015) and ground-based (Caudron et al. 2015) observations were available. The two studies demonstrate that infrasound and satellite data could be used independently to infer the temporal evolution of the eruption dynamic at the source. In the case of Caudron et al. (2015), the dynamic was inferred from the data themselves, and a 2-hour-long phase of intense injection was detected, but without more refined details on the temporal variation of the injection itself. In the case of Kristiansen et al. (2015), the dynamic was inferred from inverse modeling of the satellite observations to retrieve best input parameters for ash dispersal model, leading to a discontinuous injection at the source lasting for 7 h, with temporal resolution of 30 min. The way forward would be to combine the two approaches, with infrasound giving an a priori on the timing of the injection, while satellite observations would be used to constrain the results of the inversion leading to more robust results.

Another case of potentially successful complementary use concerns the detection of explosive eruptions. Infrasound signals can identify the injection of ash and gas into the atmosphere, which can then be tracked by satellites. For example, whereas remote seismic stations did not record the 2009 eruption of Sarychev Peak, it was detected by the IMS infrasound network as well as satellites. At that time, the eruption chronology inferred from infrasound data had an even higher temporal resolution than that obtained with satellite data alone (Matoza et al. 2011a).

Although both satellite and infrasound data have proven useful for volcano monitoring, both techniques have their limitations (Steffke et al. 2010). For example, a maximum plume height can be dependent on the moisture content in the atmosphere: A "wet" atmosphere favoring thermal convection will lead to a taller (up to 9 km difference), but more dilute, plume (Tupper et al. 2009). This is especially important for low intensity eruptions in the tropics that might produce taller and more diffuse plumes. Thinner plumes are more difficult to detect with satellite and smaller amplitude eruptions can be harder to detect with infrasound. It is also good to keep in mind that not all explosions that generate infrasound will necessarily inject ash in the atmosphere (e.g., Garces et al. 2008; Fee et al. 2010c), and that plumes from weak explosions reaching less than ~3 km in altitude may also be invisible in satellite data (Matoza et al. 2011a).

Despite the limitations, combining infrasound and satellite data into automated eruption detection systems has clearly demonstrated potential for more reliable monitoring of remote volcanic regions. The next major step towards mitigating eruption disasters and preventing the impact of ash clouds on aviation is making remote monitoring operational, rather than relying on research studies conducted after the eruptions. As of now, the Alaska Volcano Observatory (AVO) is one of the only observatories to use satellite and infrasound data operationally. Two other experiments are in their prototype stage: ASHE Asia following the American ASHE (Acoustic Surveillance for Hazardous Eruptions) project (Garcés et al. 2007) and the European project ARISE (Le Pichon et al. 2019).

Wider operational use of infrasound monitoring is predicated on addressing complexities related to infrasound propagation in the atmosphere. Experiments with well-calibrated sources have shown that the comparison between observations and simulations may diverge due to the lack of accuracy of atmospheric data (Antier et al. 2007; Cerrana et al. 2009; Assink et al. 2014b). In fact, the atmospheric specifications that are required in the modeling of infrasound propagation are affected by stochastic uncertainties related to the pseudorandom characteristics of atmospheric properties, and by systematic errors of both the measurements and the numerical methods used (Kalnay et al. 1990; Hogan and Rosmond 1991; Courtier et al. 1998; Le Pichon et al. 2015; Smets et al. 2015). Therefore, from the monitoring perspective, considering these uncertainties from propagation and atmospheric models is crucial to understand the reliability of the results (Le Pichon et al. 2005b; Assink et al. 2014a).

The previously mentioned simulation tool already provides valuable results, as it integrates realistic atmospheric specifications along the propagation path (Fig. 34.1a, b). The aim will then be to retrieve the order of magnitude of the acoustic amplitude with the associated uncertainties. Such information could be translated into eruptive intensity using models, such as Woulff and McGetchin (1976)'s, based on the acoustic power and the ejection velocity of the volcanic gases. In this context, beyond a simple detection and timing of an eruption, infrasound has the potential to provide essential timely information about an ongoing eruption dynamics that could be combined with realistic plume modeling to help constrain plume height, which is of great interest to the VAACs. However, we need to be aware that there are still improvements to be made in the current process of plume calculations. For example, studies have shown that it would be preferable to use acoustic intensity rather than acoustic power (Matoza et al. 2013). Moreover, Woulff and McGetchin (1976)'s widely used model presents limitations. Indeed, many effects are neglected such as local persistent atmospheric conditions, or geometry and topography of the vent (Matoza et al. 2009; Lacanna and Ripepe 2012; Dabrowa et al. 2014; Lacanna 2014; Kim et al. 2015). The model also assumes a linear theory of sound to explain the different mechanisms of explosive activity (Lighthill 1954, 1978). But, in a limited number of cases, when the expulsion of eruptive gases reaches supersonic velocities, a shock wave is observed (Morrissey and Mastin 2000) and the nonlinear dynamics of this phenomenon is therefore not taken into account (Garcés et al. 2013; Marchetti et al. 2013).

These limitations are pressing as they often cause an underestimate of gas volume, and thus of plume height. Nevertheless, beyond these complexities related to both propagation and calculation of source parameters, the attenuation simulation tool that are currently used still remain a good source of information to approximate the eruption dynamics.

Another important parameter to consider when designing and optimizing an operational monitoring network is infrasound travel time. The speed of sound is generally around 340 m/s, much slower than seismic waves and modern means of communication. Using the previously mentioned simulation tool, we are currently able to identify areas where better coverage is required (Tailpied 2016). For example, in Southeast Asia, adding the SING station improves the detection capability of the network in the region, as the new network (IMS + SING) covers more than half of the active or potentially active volcanoes within one-hour travel time to the closest station (Figs. 34.1a and 34.3). The exact number of volcanoes covered will vary due to changes in actual sound speed (this range is represented in Fig. 34.3 with an error bar) and seasonality of the detection capability. While the addition of the SING station does improve the overall minimum detection threshold for the regional network (Fig. 34.1e), this effect is seasonal (Fig. 34.1b), due to the change in direction of atmospheric winds.

Adding more stations to improve coverage is not always possible for financial or field constraints. Following the work of Dabrowa et al. (2011) and Matoza et al. (2011a, b, 2013, 2017), historical analysis of volcanic infrasound data provides a basis for useful reference signals to assess and improve the capabilities of detection, localization, and characterization of sources of interest using a ground-truthed dataset. For example, Matoza et al. (2019) have improved on existing methods in order to automatically identify volcanic eruption signals among the IMS infrasound data. This work represents a step toward the goal of integrating IMS infrasound data products into global volcanic eruption early warning and notification systems (Marchetti et al. 2019). In addition, today, numerous affordable infrasound instruments are coming to the market, manufactured by universities or private companies. These allow for a more cost-effective way of supplementing the observations of the IMS network (Fee et al. 2010b; Assink et al. 2014a).

Also, there has been work to take advantage of the ubiquity of mobile phones (e.g. cosmos reentry, Schnurr et al. 2016). In seismology, built-in accelerometers in phones have already been used to pinpoint the epicenter of an earthquake (Kong et al. 2016). In volcanology, social media were used for the quick estimate of the isopack following the February 2014 eruption of Mount Kelud, Indonesia (Pyle et al. 2014). The authors, working from their office in the UK, mined the feeds from social media, searching for different keywords such as "#Kelut" and "#Kelud", which, combined with metadata such as location and time, allowed them to roughly estimate the extent of the fallout. Now, phones are being used for infrasound studies as well, with the release of a smartphone application (infrasound Recorder by Redvox, Inc.) specifically designed for the recording of infrasound via mobile device sensors, or external microphone. This kind of experiment has the potential to significantly increase the density of infrasound measurements, thus aiding not only

in remote monitoring of volcanic activity, but ground-truthing of propagation and attenuation models.

34.5 Conclusions

Since Krakatau's 1883 eruption, methods for remotely monitoring volcanoes have progressed tremendously. For example, infrasound, with its long-range propagation, has demonstrated its operational potential not only to detect, locate and identify an eruption, but also to provide eruption parameters like start time, duration, and increasingly more accurate values of acoustic power at the source that could be linked to the mass flux. If VAACs received such information shortly after an eruption, they could run ash dispersion models whose results could then lead to the issuance of advisories.

As of today, the operational use of infrasound is still constrained by the number of monitoring stations and their distance from erupting volcanoes. The larger the distance, the more challenging timely detection becomes, not only due to the traveling speed of sound, but also due to atmospheric conditions. Strong seasonality and semi-permanent cloud cover may mean that while major events will be detected in real time, moderate to small events will be identified only during postprocessing. With the current relative location of infrasound stations with respect to specific volcanoes, explosive volcanic event identification from one station, combined with the geographical location of the volcanoes, would be sufficient to pinpoint the most likely source of an eruption. It would allow a timely issuance of a preliminary alert that would then be refined as more information is collected through infrasound, satellite or reports of direct observations. With the increasing numbers of infrasound stations worldwide, the number of volcanoes that can be monitored remotely by more than one station and in a timely manner is also increasing, while the size of eruptions that can be detected is decreasing, the source being closer to the station.

In the near future, multi-stream data assimilation will gain from new instruments being deployed on the ground, new satellites, macro, micro and nano being launched regularly from private and public sectors, including universities, as well as the increasing number of people using social media platforms to report observations. All these information sources will provide an overwhelming amount of data. The challenge will be to extract the most relevant details, and make them available to operational agencies.

Acknowledgements This work comprises Earth Observatory of Singapore contribution no. 155. This research is supported by the National Research Foundation Singapore and the Singapore Ministry of Education under the Research Centres of Excellence initiative. The authors would like to thanks Pavel Adamek for his comments and suggestions that greatly improved the flow of this chapter.

References

Aneeka S, Zhong ZW (2016) NO_x and CO_2 emissions from current air traffic in ASEAN region and benefits of free route airspace implementation. J Appl Phys Sci 2(2). https://doi.org/10.20474/japs2.2.1

Antier K, Le Pichon A, Vergniolle S, Zielinski C, Lardy M (2007) Multiyear validation of the NRL-G2S wind fields using infrasound from Yasur. J Geophys Res Atmos 112(D23). https://doi.org/10.1029/2007jd008462

Arrowsmith SJ, Hedlin MAH (2005) Observations of infrasound from surf in southern California. Geophys Res Lett 32(9). https://doi.org/10.1029/2005gl022761

Assink J, Waxler R, Smets P, Evers L (2014a) Bidirectional infrasonic ducts associated with sudden stratospheric warming events. J Geophys Res Atmos 119:1140–1153. https://doi.org/10.1002/2013JD021062

Assink J, Le Pichon A, Blanc E, Kallel M, Khemiri L (2014b) Evaluation of wind and temperature profiles from ECMWF analysis on two hemispheres using volcanic infrasound. J Geophys Res Atmos 119:8659–8683. https://doi.org/10.1002/2014JD021632

Auker M, Sparks RSJ, Jenkins S, Aspinall W, Brown SK, Deligne NI, Jolly G, Loughlin SC, Marzocchi W, Newhall CG, Palma JL (2015) Development of a new global volcanic hazard index (VHI). Global volcanic hazards and risk. Cambridge. ISBN: 9781107111752

Bass H (1995) Atmospheric absorption of sound: further developments. J Acoust Soc Am 97(1): 680–683. https://doi.org/10.1121/1.412989

Bouche E, Vergniolle S, Staudcher T, Nercessian A, Delmont J-C, Frogneux M, Cartault F, Le Pichon A (2010) The role of large bubbles detected from acoustic measurements on the dynamics of Erta 'Ale lava lake (Ethiopia). Earth Planet Sci Lett 295(1–2). https://doi.org/10.1016/j.epsl.2010.03.020

Bowen Jr, JT (2016) Now everyone can fly? Scheduled airline services to secondary cities in Southeast Asia. J Air Transp Manag 53. https://doi.org/10.1016/j.jairtraman.2016.01.007

Brachet N, Brown D, Le Bras R, Mialle P, Coyne J (2010) Monitoring the earth's atmosphere with the global ims infrasound network. Infrasound monitoring for atmospheric studies. Springer. ISBN: 9781402095078

Brenot H, Theys N, Clarisse L, Van Geffen J, Van Gent J, Van Roozendael M, Van der AR, Hurtmans D, Coheur P-F, Clerbaux C, Valks P, Hedelt P, Prata F, Rasson O, Sievers K, Zehner C (2014) Support to aviation control service (SACS): an online service for near real-time satellite monitoring of volcanic plumes. Nat Hazards Earth Syst Sci 14(5). https://doi.org/10.5194/nhess-14-1099-2014

Brown S, Sparks R, Jenkins S (2015) Global distribution of volcanic threat. Global volcanic hazards and risk. Cambridge: Cambridge University Press. ISBN: 9781107111752

Campus P, Christie DR (2010) Worldwide observations of infrasonic waves. Infrasound monitoring for atmospheric studies. Springer. ISBN: 9781402095078

Cansi Y (1995) An automatic seismic event processing for detection and location: the P.M.C.C. method. Geophys Res Lett 22(9). https://doi.org/10.1029/95gl00468

Caplan-Auerbach J, Bellesiles AK, Fernandes JJ (2010) Estimates of eruption velocity and plume height from infrasonic recordings of the 2006 eruption of Augustine Volcano, Alaska. J Volcanol Geoth Res 189(1–2). https://doi.org/10.1016/j.jvolgeores.2009.10.002

Cannata A, Montalto P, Aliotta M, Cassisi C, Pulvirenti E, Patane D (2011) Clustering and classification of infrasonic events at Mount Etna using pattern recognition techniques. Geophys J Int 185(1). https://doi.org/10.1111/j.1365-246x.2011.04951.x

Carn SA, Clarisse L, Prata AJ (2016) Multi-decadal satellite measurements of global volcanic degassing. J Volcanol Geoth Res 311. https://doi.org/10.1016/j.jvolgeores.2016.01.002

Caudron C, Taisne B, Garces MA, Le Pichon A, Mialle P (2015) On the use of remote infrasound and seismic stations to constrain the eruptive sequence and intensity for the 2014 Kelud eruption. Geophys Res Lett 42(16). https://doi.org/10.1002/2015gl064885

Caudron C, Taisne B, Perttu A, Garces M, Silber EA, Mialle P (2016) Infrasound and seismic detections associated with the 7 September 2015 Bangkok fireball. Geosci Lett 26. https://doi.org/10.1186/s40562-016-0058-z

Ceranna L, Le Pichon A, Green D, Mialle P (2009) The Buncefield explosion: a benchmark for infrasound analysis across Central Europe. Geophys J Int 177(2):491–508. https://doi.org/10.1111/j.1365-246X.2008.03998.x

Clarisse L, Prata F, Lacour JL, Hurtmans D, Clerbaux C, Coheur PF (2010) A correlation method for volcanic ash detection using hyperspectral infrared measurements. Geophys Res Lett 37 (19). https://doi.org/10.1029/2010gl044828

Clarisse L, Coheur PF, Prata F, Hadji-Lazaro J, Hurtmans D, Clerbaux C (2013) A unified approach to infrared aerosol remote sensing and type specification. Atmos Chem Phys 13 (4):2195. https://doi.org/10.5194/acp-13-2195-2013

Clauter D, Blandford R (1997) Capability modelling of the proposed international monitoring system 60-station infrasonic network, paper presented at infrasound workshop for CTBT Monitoring. Los Alamos Natl Lab, Santa Fe, N.M

Costley R, Frazier W, Dillion K, Picucci J, Williams J, McKenna M (2013) Frequency-wavenumber processing for infrasound distributed arrays. J Acoust Soc Am 134(EL307). https://doi.org/10.1121/1.4818940

Courtier P, Andersson E, Heckley W, Vasiljevic D, Hamrud M, Hollingsworth A, Rabier F, Fisher M, Pailleux J (1998) The ECMWF implementation of three- dimensional variational assimilation (3D-Var). I: formulation. J R Meteorol Soc 124(550):1783–1807. https://doi.org/10.1002/qj.49712455002

Dabrowa AL, Green DN, Rust AC, Phillips JC (2011) A global study of volcanic infrasound characteristics and the potential for long-range monitoring. Earth Plane Sci Lett 310(3–4). https://doi.org/10.1016/j.epsl.2011.08.027

Dabrowa A, Green D, Johnson J, Phillips J, Rust A (2014) Comparing near-regional and local measurements of infrasound from Mount Erebus, Antarctica: implications for monitoring. J Volcanol Geoth Res 288:46–61. https://doi.org/10.1016/j.jvolgeores.2014.10.001

De Angelis S, Fee D, Haney M, Schneider D (2012) Detecting hidden volcanic explosions from Mt. Cleveland Volcano, Alaska with infrasound and ground-coupled airwaves. Geophys Res Lett 39(21). https://doi.org/10.1029/2012gl053635

De Angelis S, Lamb OD, Lamur A, Hornby AJ, von Aulock FW, Chigna G, Lavallée Y, Rietbrock A (2016) Characterization of moderate ash-and-gas explosions at Santiaguito volcano, Guatemala, from infrasound waveform inversion and thermal infrared measurements. Geophys Res Lett 43(12). https://doi.org/10.1002/2016gl069098

De Groot-Hedlin CD, Hedlin MAH, Drob DP (2010) Atmospheric variability and infrasound monitoring. Infrasound monitoring for atmospheric studies. Springer. ISBN: 9781402095078

De Groot-Hedlin CD, Hedlin MAH (2014) Infrasound detection of the Chelyabinsk meteor at the USArray. Earth Planet Sci Lett 402:337–345. https://doi.org/10.1016/j.epsl.2014.01.031

Fee D, Garces M, Patrick M, Chuet B, Dawson P (2010a) Infrasonic harmonic tremor and degassing bursts from Haema'uma'u Crater, Kilauea Volcano, Hawaii. J Geophys Res 115. https://doi.org/10.1029/2010jb007642

Fee D, Garcés M, Steffke A (2010b) Infrasound from Tungurahua Volcano 2006–2008: Strombolian to Plinian eruptive activity. J Volcanol Geoth Res 193(1–2):67–81. https://doi.org/10.1016/j.jvolgeores.2010.03.006

Fee D, Steffke A, Garcés M (2010c) Characterization of the 2008 Kasatochi and Okmok eruptions using remote infrasound arrays. J Geophys Res 115 (D00L10). https://doi.org/10.1029/2009jd013621

Fee D, Garces A, Orr T, Poland M (2011) Infrasound from the 2007 fissure eruptions of Kilauea Volcano. Hawaii Geophys Res Lett 38. https://doi.org/10.1029/2010gl046422

Fee D, Matoza R (2013) An overview of volcano infrasound: from hawaiian to plinian, local to global. J Volcanol Geoth Res 249:123–139. https://doi.org/10.1016/j.jvolgeores.2012.09.002

Fee D, Haney MM, Matoza RS, Van Eaton AR, Cervelli P, Schneider DJ, Iezzi AM (2017) Volcanic tremor and plume height hysteresis from Pavlof Volcano, Alaska. Science 355(6320). https://doi.org/10.1126/science.aah6108

Garces M, Hetzer C, Merrifield M, Willis M, Aucan J (2003) Observations of surf infrasound in Hawai'i. Geophys Res Lett 30(24). https://doi.org/10.1029/2003gl018614

Garces M, Aucan J, Fee D, Caron P, Merrifield M, Gibson R, Bhattacharyya J, Shah S (2006) Infrasound from large surf. Geophys Res Lett 33(5). https://doi.org/10.1029/2005gl025085

Garcés M, McCormack D, Servranckx R, Bass H, Hedlin M, Yepes H (2007) Acoustic surveillance for hazardous eruptions (ASHE): preliminary results from a pilot infrasound experiment. In: Proceedings of the fourth international workshop on volcanic ash (VAWS/4). World Meteorol Organ, Rotorua, NZ

Garcés M, Fee D, Steffke A, McCormack D, Servranckx R, Bass H, Hetzer C, Hedlin MAH, Matoza RS, Yepes H, Ramon P (2008) Capturing the acoustic fingerprint of stratospheric ash injection. EOS Trans Am Geophys Union 89(40):377–378. https://doi.org/10.1029/2008EO400001

Garces MA, Willis M, Le Pichon A (2010) Infrasonic observations of open ocean swells in the Pacific: deciphering the song of the sea. Infrasound monitoring for atmospheric studies. Springer, pp 185–234. ISBN: 9781402095078

Garcés MA, Stopa JE, Cheung KF, Williams B, Le Pichon A (2013) Global infrasound from nonlinear ocean wave interactions, CTBT Science and Technology 2013. Austria, Vienna

Gorshkov GS (1960) Determination of the explosion energy in some volcanoes according to barographs. Bull Volcanol 23(1). https://doi.org/10.1007/bf02596639

Goto A, Johnson JB (2011) Monotonic infrasound and Helmholtz resonance at Volcan Villarrica (Chile) Geophys Res Lett 38. https://doi.org/10.1029/2011gl046858

Green D, Bowers D (2010) Estimating the detection capability of the International Monitoring System infrasound network. J Geophys Res 115(D18116). https://doi.org/10.1029/2010jd014017

Guffanti M, Thomas JC, Budding K (2010) Encounters of aircraft with volcanic ash clouds: a compilation of known incidents, 1953–2009. U.S. Geol Surv Data Ser 545, ver. 1.0

Ham FM, Iyengar I, Hambebo BM, Garces MA, Deaton J, Perttu A, Williams B (2012) A neurocomputing approach for monitoring plinian volcanic eruptions using infrasound. Procedia Comput Sci 13. https://doi.org/10.1016/j.procs.2012.09.109

Hanstrum BN, Watson AS (1983) A case study of two eruptions of Mount Galunggung and an investigation of volcanic eruption cloud characteristics using remote sensing techniques. Aust Meteorol Mag 31(3)

Hedlin MAH, Walker K, Drob DP, De Groot-Hedlin CD (2012) Infrasound: connecting solid earth, oceans, and atmosphere. Annu Rev Earth Planet Sci 40:327–354. https://doi.org/10.1146/annurev-earth-042711-105508

Hetzer CH, Waxler R, Gilbert KE, Talmadge CL, Bass HE (2008) Infrasound from hurricanes: dependence on the ambient ocean surface wave field. Geophys Res Lett 35(14). https://doi.org/10.1029/2008gl034614

Hogan T, Rosmond T (1991) The description of the navy operational global atmospheric prediction system's spectral forecast model. Monthly Weather Revis 119:1786–1815

Johnson JB, Palma JL (2015) Lahar infrasound associated with Volcán Villarrica's 3 March 2015 eruption. Geophys Res Lett 42(15). https://doi.org/10.1002/2015gl065024

Johnson J (2019) Local volcano infrasound monitoring. In: Le Pichon A, Blanc E, Hauchecorne A (eds) Infrasound monitoring for atmospheric studies, 2nd edn. Springer, Dordrecht, pp 989–1022

Jones KR, Johnson JB, Aster R, Kyle PR, McIntosh WC (2008) Infrasonic tracking of large bubble bursts and ash venting at Erebus Volcano, Antarctica. J Volcanol Geoth Res 177(3). https://doi.org/10.1016/j.jvolgeores.2008.02.001

Kalnay E, Kanamitsu M, Baker W (1990) Global numerical weather prediction at the National Meteorological Center. Am Meteorol Soc 71(10). https://doi.org/10.1175/1520-0477(1990)071<1410:gnwpat>2.0.co;2

Kim K, Lees JM (2011) Finite-difference time-domain modeling of transient infrasonic wavefields excited by volcanic explosions. Geophys Res Lett 38(6). https://doi.org/10.1029/2010gl046615
Kim K, Fee D, Yokoo A, Lees JM (2015) Acoustic source inversion to estimate volume flux from volcanic explosions. Geophys Res Lett 42(13). https://doi.org/10.1002/2015gl064466
Kong Q, Allen RM, Schreier L, Kwon YW (2016) MyShake: a smartphone seismic network for earthquake early warning and beyond. Science Adv 2(2):e1501055. https://doi.org/10.1126/sciadv.1501055
Kristiansen N, Prata P, Stohl A, Carn S (2015) Stratospheric volcanic ash emissions from the 13 February 2014 Kelut eruption. Geophys Res Lett 42:588–596. https://doi.org/10.1002/2014GL062307
Krueger AJ (1983) Sighting of El Chichon sulfur dioxide clouds with the Nimbus 7 total ozone mapping spectrometer. Science 220(4604). https://doi.org/10.1126/science.220.4604.1377
Lacanna G, Ripepe M (2012) Influence of near-source volcano topography on the acoustic wavefield and implication for source modeling. J Volcanol Geoth Res 250:9–18. https://doi.org/10.1016/j.jvolgeores.2012.10.005
Lacanna G, Ichihara M, Iwakuni M, Takeo M, Iguchi M, Ripepe M (2014) Influence of atmospheric structure and topography on infrasonic wave propagation. J Geophys Res Solid Earth 119:2988–3005. https://doi.org/10.1002/2013JB010827
Lamb OD, De Angelis S, Lavallée Y (2015) Using infrasound to constrain ash plume rise. J Appl Volcanol 4(1). https://doi.org/10.1186/s13617-015-0038-6
Lechner P, Tupper A, Guffanti M, Loughlin S, Casadevall T (2017) Volcanic ash and aviation—the challenges of real-time, global communication of a natural hazard. Advances in volcanology. Springer. https://doi.org/10.1007/11157_2016_49
Le Pichon A, Garces M, Blanc E, Barthelemy M, Drob DP (2002) Acoustic propagation and atmosphere characteristics derived from infrasonic waves generated by the Concorde. J Acoust Soc Am 111(1). https://doi.org/10.1121/1.1404434
Le Pichon A, Maurer V, Raymond D, Hyvernaud O (2004) Infrasound from ocean waves observed in Tahiti. Geophys Res Lett 31(19). https://doi.org/10.1029/2004gl020676
Le Pichon A, Herry P, Mialle P, Vergoz J, Brachet N, Garces M, Drob DP, Ceranna L (2005a) Infrasound associated with 2004–2005 large Sumatra earthquakes and tsunami. Geophys Res Lett 32(19). https://doi.org/10.1029/2005gl023893
Le Pichon A, Blanc E, Drob D, Lambotte S, Dessa J, lardy M, Bani P, Vergniolle S (2005b) Infrasound monitoring of volcanoes to probe high-altitude winds. J Geophys Res 110 (D13106). https://doi.org/10.1029/2004jd005587
Le Pichon A., Ceranna L., Vergoz J., D. Tailpied D. (2009a), Modeling the detection capability of the global IMS infrasound network. In: Le Pichon A, Blanc E, Hauchecorne A (eds) Infrasound Monitoring for Atmospheric Studies. Springer, pp 593-603
Le Pichon A, Vergoz J, Blanc E, Guilbert J, Ceranna L, Evers L, Brachet N (2009b) Assessing the performance of the International Monitoring System infrasound network: geographical coverage and temporal variabilities. J Geophys Res 114(D08112). https://doi.org/10.1029/2008jd010907
Le Pichon A, Ceranna L, Vergoz J (2012) Incorporating numerical modeling into estimates of the detection capability of the IMS infrasound network. J Geophys Res 117(D05121). https://doi.org/10.1029/2011jd016670
Le Pichon A, Assink J, Heinrich P, Blanc E, Charlton-Perez A, Lee C, Keckhut P, Hauchecorne A, Rüfenacht R, Kämpfer N, Drob DP, Smets PSM, Evers LG, Ceranna L, Pilger D, Ross O, Claud C (2015) Comparison of co-located independent ground-based middle atmospheric wind and temperature measurements with numerical weather prediction models. J Geophys Res Atmos 120:8318–8331. https://doi.org/10.1002/2015JD023273
Le Pichon A, Ceranna L, Vergoz J, Tailpied D (2019) Modeling the detection capability of the global IMS infrasound network. In: Le Pichon A, Blanc E, Hauchecorne A (eds) Infrasound monitoring for atmospheric studies, 2nd edn. Springer, Dordrecht, pp 593–604
Lighthill M (1954) On sound generated aerodynamically. II. Turbulence as a source of sound. Proc R Soc Lond Ser A Math Phys Sci 222:1–32. https://doi.org/10.1098/rspa.1954.0049

Lighthill M (1978) Acoustic streaming. J Sound Vib 61(3):391–418. https://doi.org/10.1016/0022-460X(78)90388-7

Marchetti E, Ripepe M, Delle Donne D, Genco R, Finizola A, Garaebiti E (2013) Blast waves from violent explosive activity at Yasur Volcano, Vanuatu. Geophys Res Lett 40:5838–5843. https://doi.org/10.1002/2013GL057900

Marchetti E, Ripepe M, Campus P, Le Pichon A, Brachet N, Blanc E, Gaillard P, Mialle P, Husson P (2019) Infrasound monitoring of volcanic eruptions and contribution of ARISE to the volcanic ash advisory centers. In: Le Pichon A, Blanc E, Hauchecorne A (eds) Infrasound monitoring for atmospheric studies, 2nd edn. Springer, Dordrecht, pp 1141–1162

Marty J (2019) The IMS infrasound network: current status and technological developments. In: Le Pichon A, Blanc E, Hauchecorne A (eds) Infrasound monitoring for atmospheric studies, 2nd edn. Springer, Dordrecht, pp 3–62

Matoza R, Fee D, Garcés M, Seiner J, Ramón P, Hedlin M (2009) Infrasonic jet noise from volcanic eruptions. Geophys Res Lett 36(L08303). https://doi.org/10.1029/2008gl036486

Matoza RS, Fee D, Garces MA (2010) Infrasonic tremor wavefield of the Pu'u O'o crater complex and lava tube system, Hawaii, in April 2007. J Geophys Res 115. https://doi.org/10.1029/2009jb007192

Matoza R, Le Pichon A, Vergoz J, Herry P, Lalande J, Lee HI, Che IY, Rybin A (2011a) Infrasonic observations of the June 2009 Sarychev Peak eruption, Kuril Islands: implications for infrasonic monitoring of remote explosive volcanism. J Volcanol Geoth Res 200(1–2):35–48. https://doi.org/10.1016/j.jvolgeores.2010.11.022

Matoza R, Vergoz J, Le Pichon A, Ceranna L, Green D, Evers L, Ripepe M, Campus P, Liszka L, Kvaerna T, Kjartansson E, Höskuldsson A (2011b) Long-range acoustic observations of the Eyjafjallajokull eruption, Iceland, April-May 2010. Geophy Res Lett 38(L06308). https://doi.org/10.1029/2011GL047019

Matoza RS, Landès M, Le Pichon A, Ceranna L, Brown D (2013) Coherent ambient infrasound recorded by the International Monitoring System. Geophys Res Lett 40:429–433. https://doi.org/10.1029/2012GL054329

Matoza RS, Green DN, Le Pichon A, Shearer PM, Fee D, Mialle P, Ceranna L (2017) Automated detection and cataloging of global explosive volcanism using the international monitoring system infrasound network. J Geophys Res Solid Earth 122:2946–2971. https://doi.org/10.1002/2016JB013356

Matoza R, Fee D, Green D, Mialle P (2019) Volcano infrasoundand the international monitoring system. In: Le Pichon A, Blanc E, Hauchecorne A (eds) Infrasound monitoring for atmospheric studies, 2nd edn. Springer, Dordrecht, pp 1023–1077

Morrissey M, Mastin L (2000) Vulcanian eruptions. Encyclopedia of volcanoes. Elsevier. ISBN: 978-0-12-385938-9

Mutschlecner J, Whitaker R (2010) Some atmospheric effects on infrasound signal amplitudes. Infrasound monitoring for atmospheric studies. Springer. ISBN: 9781402095078

Newhall CG, Self S (1982) The volcanic explosivity index (VEI) an estimate of explosive magnitude for historical volcanism. J Geophys Res 87(C2). https://doi.org/10.1029/jc087ic02p01231

Pavolonis MJ, Feltz WF, Heidinger AK, Gallina GM (2006) A daytime complement to the reverse absorption technique for improved automated detection of volcanic ash. J Atmos Oceanic Technol 23(11). https://doi.org/10.1175/jtech1926.1

Pavolonis MJ, Sieglaff J, Cintineo J (2015a) Spectrally enhanced cloud objects—a generalized framework for automated detection of volcanic ash and dust clouds using passive satellite measurements: 1. Multispectral analysis. J Geophys Res Atmos 120(15). https://doi.org/10.1002/2014jd022968

Pavolonis MJ, Sieglaff J, Cintineo J (2015b) Spectrally enhanced cloud objects—a generalized framework for automated detection of volcanic ash and dust clouds using passive satellite measurements: 2. Cloud object analysis and global application. J Geophys Res Atmos 120(15). https://doi.org/10.1002/2014jd022969

Pergola N, Coviello I, Filizzola C, Lacava T, Marchese F, Paciello R, Tramutoli V (2016) A review of RSTVOLC, an original algorithm for automatic detection and near-real-time monitoring of volcanic hotspots from space. Geol Soc, London, Special Publications 426 (1):55–72. https://doi.org/10.1144/SP426.1

Petersen T, De Angelis S, Tygat G, McNutt SR (2006) Local infrasound observations of large ash explosions at Augustine Volcano, Alaska, during January 11–28, 2006. Geophys Res Lett 33 (12). https://doi.org/10.1029/2006gl026491

Pilger C, Ceranna L, Ross J, Le Pichon A, Mialle P, Garcés MA (2015) CTBT infrasound network performance to detect the 2013 Russian fireball event. Geophys Res Lett 42(2523–2531). https://doi.org/10.1002/2015gl063482

Prata AJ (1989) Observations of volcanic ash clouds in the 10–12 μm window using AVHRR/2 data. Int J Remote Sens 10 (4-5). https://doi.org/10.1080/01431168908903916

Pyle D (2014) Oxford University's Earth Sciences Class of 2015, Ash fallout from the 2014 Kelut eruption: a preliminary analysis

Ripepe M, de Angelis S, Lacanna G, Poggi P, Williams C, Marchetti E, Delle Donne D, Ulivieri G (2009) Tracking pyroclastic flows at Soufriere Hills Volcano. EOS Trans Am Geophys Union 90(27). https://doi.org/10.1029/2009eo270001

Ripepe M, Bonadonna C, Folch A, Delle Donne D, Lacanna G, Marchetti E, Höskuldsson A (2013) Ash-plume dynamics and eruption source parameters by infrasound and thermal imagery: the 2010 Eyjafjallajökull eruption. Earth Planet Sci Lett 366:112–121. https://doi.org/10.1016/j.epsl.2013.02.005

Ripepe M, Marchetti E (2019) Infrasound monitoring of volcano-related hazards for civil protection. In: Le Pichon A, Blanc E, Hauchecorne A (eds) Infrasound monitoring for atmospheric studies, 2nd edn. Springer, Dordrecht, pp 1107–1140

Sawada Y (1987) Study on analysis of volcanic eruptions based on eruption cloud image data obtained by the Geostationary Meteorological Satellite (GMS), Technological Report of Meteorological Research Institute, Tsukuba, Japan, vol 22, pp 335

Schnurr J, Garces MA, Christie A (2016) Cosmos supersonic reentry analysis: a case study using traditional and mobile infrasound arrays. J Acoust Soc Am 140(4):2996–2996. https://doi.org/10.1121/1.4969282

Scott RH (1883) Note on a series of barometrical disturbances which passed over Europe between the 27th and the 31st of August, 1883. Proc R Soc Lond 36:139–143

Siebert L, Simkin T (2002) Volcanoes of the world: an illustrated catalog of holocene volcanoes and their eruptions, Smithsonian institution. Global volcanism program digital information series, GVP-3. http://www.volcano.si.edu/world/

Smets P, Evers L, Näsholm S, Gibbons S (2015) Probabilistic infrasound propagation using realistic atmospheric perturbations. Geophys Res Lett 42:6510–6517. https://doi.org/10.1002/2015GL064992

Snodgrass JM, Richards AF (1956) Observations of underwater volcanic acoustics at Bárena Volcano, San Benedicto Island, Mexico, and in Shelikof Strait, Alaska. EOS Trans Am Geophys Union 37(1). https://doi.org/10.1029/tr037i001p00097

Steffke A, Fee D, Garcés M, Harris A (2010) Eruption chronologies, plume heights and eruption styles at Tungurahua Volcano: integrating remote sensing techniques and infrasound. J Volcanol Geoth Res 193(3–4):143–160. https://doi.org/10.1016/j.jvolgeores.2010.03.004

Stoppa JE, Cheung KF, Garces MA, Badger N (2012) Atmospheric infrasound from nonlinear wave interactions during Hurricanes Felicia and Neki of 2009. J Geophys Res 117. https://doi.org/10.1029/2012jc008257

Sutherland L, Bass H (2004) Atmospheric absorption in the atmosphere up to 160 km. J Acoust Soc Am 115(3):1012–1032. https://doi.org/10.1121/1.1631937

Tailpied D, Le Pichon A, Marchetti E, Ripepe M, Kallel M, Ceranna L, Brachet N (2013) Remote infrasound monitoring of Mount Etna: observed and predicted network detection capability. InfraMatics 2(1). https://doi.org/10.4236/inframatics.2013.21001

Tailpied D, Le Pichon A, Marchetti E, Assink J, Vergniolle S (2016) Assessing and optimizing the performance of infrasound networks to monitor volcanic eruptions. Geophys J Int 249–269. https://doi.org/10.1093/gji/ggw400

Tailpied D (2016) Assessing and optimizing infrasound networks to monitor volcanic eruptions, in France. PhD thesis, IPGP, Paris, pp 276

Thelen WA, Cooper J (2015) An analysis of three new infrasound arrays around Kīlauea Volcano, U.S. geological survey open-file report 2014–1253. https://doi.org/10.3133/ofr20141253

Thomas HE, Prata AJ (2011) Sulphur dioxide as a volcanic ash proxy during the April-May 2010 eruption of Eyjafjallajokull Volcano, Iceland. Atmos Chem Phys 11(14):6871. https://doi.org/10.5194/acp-11-6871-2011

Thüring T, Schoch M, van Herwijnen A, Schweizer J (2015) Robust snow avalanche detection using supervised machine learning with infrasonic sensor arrays. Cold Reg Sci Technol 111:60–66. https://doi.org/10.1016/j.coldregions.2014.12.014

Tupper A, Carn S, Davey J, Kamada Y, Potts R, Prata F, Tokuno M (2004) An evaluation of volcanic cloud detection techniques during recent significant eruptions in the western 'Ring of Fire'. Remote Sens Environ 91(1):27–46. https://doi.org/10.1016/j.rse.2004.02.004

Tupper A, Itikarai I, Richards M, Prata F, Carn S, Rosenfeld D (2007) Facing the challenges of the international airways volcano watch: the 2004/05 eruptions of Manam, Papua New Guinea. Weather Forecast 22. https://doi.org/10.1175/waf974.1

Tupper A, Textor C, Herzog M, Graf H, Richards MS (2009) Tall clouds from small eruptions: the sensitivity of eruption height and fine ash content to tropospheric instability. Nat Hazards 51:375–401. https://doi.org/10.1007/s11069-009-9433-9

Vergniolle S, Caplan-Auerbach J (2006) Basaltic thermals and subplinian plumes: constraints from acoustic measurements at Shishaldin volcano, Alaska. Bull Volcanol 68(7). https://doi.org/10.1007/s00445-005-0035-4

Webley P, Mastin L (2009) Improved prediction and tracking of volcanic ash clouds. J Volcanol Geoth Res 186(1–2):1–9. https://doi.org/10.1016/j.jvolgeores.2008.10.022

Whelley P, Newhall C, Bradley K (2015) The frequency of explosive volcanic eruptions in Southeast Asia. Bull Volcanol 77(1). https://doi.org/10.1007/s00445-014-0893-8

Whitaker R (1995) Infrasonic monitoring. In: Proceedings of the 17th annual seismic research symposium, Scottsdale, Arizona, Phillips Lab., Hanscom AFB, Mass, pp 997–1000

Whitaker R, Sandoval T, Mutschlecner J (2003) Recent infrasound analysis, paper presented at 25th annual seismic research symposium. Tucson, Arizona

Woulff G, McGetchin TR (1976) Acoustic noise from volcanoes: theory and experiment. Geophys J Int 45(3). https://doi.org/10.1111/j.1365-246x.1976.tb06913.x

Chapter 35
Infrasound Monitoring of Volcano-Related Hazards for Civil Protection

Maurizio Ripepe and Emanuele Marchetti

Abstract In the last 20 years, infrasound has increased significantly the potentials of volcano monitoring, with direct impact on risk evaluation for civil protection. Automatic systems based on infrasound are nowadays used operationally, and future improvements will reinforce this technique especially when integrated with other ground-based or satellite observations. We show how by using dedicated array processing, infrasound can be used to detect and notify, automatically and in real time, the onset of explosive eruptions and the run-out of density currents based on the apparent velocity, propagation back-azimuth, and frequency change. Such procedures have been tested and tuned for several years and are currently being applied to early warning of explosive eruption at Etna volcano and to avalanche analysis and risk forecasting in several sites in Europe.

35.1 Introduction

Volcanic eruptions can have one of the largest impacts on society among all the natural risks (Self 2006). According to the different levels of volcanic activity, the risk related to volcanoes can be different involving different problems for our society. Effusive eruptions spreading lava flows over areas up to hundreds of square km are able to completely destroy local settlements and infrastructures but the risk of losing lives is small. On the other side, volcanic explosive eruptions can inject in the atmosphere millions of cubic meters of ash, gases, and debris: their dispersal has impacted in several instances life on Earth.

Ash injection in the atmosphere can severely affect air traffic. The experience of the societal impact of the 2010 eruptions of Eyjafjallajökull, Iceland, rated with Volcanic Explosivity Index (VEI) relatively small (VEI 3 to 4), highlighted the

M. Ripepe (✉) · E. Marchetti
Department of Earth Sciences, University of Firenze, Florence, Italy
e-mail: maurizio.ripepe@unifi.it

M. Ripepe · E. Marchetti
Dipartimento Scienze Della Terra, Universita' Di Firenze, Florence, Italy

A. Le Pichon et al. (eds.), *Infrasound Monitoring for Atmospheric Studies*,
https://doi.org/10.1007/978-3-319-75140-5_35

fragility of the society and infrastructures, in particular when such type of events strike highly populated areas as Europe. The analysis of the effects of such relatively small eruption leads civil aviation authority to ask for a prompt notification of volcanic eruption and a robust quantitative estimation of plume evolution and ash concentration in the atmosphere (e.g., Bonadonna et al. 2012).

Moreover, ahead of the massive atmospheric ash injection, large volcanic plumes can collapse driving pyroclastic density currents (PDCs) down the volcano's flanks. These are among the most hazardous volcanic processes, able to produce total destruction and death at several kilometers around the volcanic edifice (e.g., Cole et al. 2015).

PDCs are also generated by lava dome eruptions that are formed by silica-rich lava that is too viscous to flow and, instead, builds up over the point of extrusion. The hazards from lava dome eruptions are well known owing to unpredictable transitions from the slow extrusion of viscous lava to vigorous explosions, and to the propensity of lava domes to suddenly collapse, spawning devastating PDCs down the flanks of volcanic edifices (Sparks and Young 2002). As a lava dome grows, parts of it may collapse because of gravitational instability or as the result of gas explosions within the dome itself, thus forming PDCs. The ability to detect and track the propagation of these fast-moving density currents is of utmost importance in understanding the evolution of lava dome eruptions and mitigating related hazards.

It is clear how the response of civil protection and decision-making agencies is strongly dependent on the knowledge of ongoing processes at an eruptive volcano and for this reason monitoring networks, techniques, and procedures have been exponentially improving in the last few decades.

Classical monitoring techniques such as geochemistry, seismology, and ground deformation are, however, strongly space-dependent, and require instruments to be deployed on and around the volcanic edifice. Moreover, out of 1500 volcanoes known on Earth that were active during the last 10.000 years (www.volcano.si.edu), only a small percentage of them is really well instrumented, and few percents are poorly instrumented while the majority of them is not instrumented at all (Pallister and McNutt 2015).

Since the first measurement with analogue micro-barometer of acoustic-gravity waves triggered by the 1883 Krakatau eruption (Simkin and Fiske 1983), infrasound observations of volcanic eruptions were limited for many decades to few examples of large eruptions obtained with micro-barometers (Richards 1963) or seismic networks at very large distances from the source (e.g., Reed 1987). Only in the late 1990s, infrasound studies moved to higher frequencies, and local observations became progressively more common and started to have a direct impact on the understanding and modeling of explosive source dynamics (e.g., Dibble et al. 1984; Braun and Ripepe 1993; Vergniolle and Brandeis 1994; Buckingham and Garcés 1996).

Infrasound (i.e., low frequency <20 Hz sound) started to be adopted for monitoring active volcanoes very recently (since 1990) but has been increasing rapidly in the last decades (Johnson and Ripepe 2011). Infrasound clearly detects explosive eruptive processes and thanks to the good efficiency of infrasound propagation in the atmosphere, it is now opening new perspective in volcano monitoring.

Since then, the improvement of instruments and array techniques allowed to collecting high-quality infrasound data leading to refined source locations able to discriminate activity at multiple vents only tens of meters apart from each other (e.g., Ripepe and Marchetti 2002) and Doppler frequency shift of infrasound signals related to pyroclastic flows (e.g., Yamasato 1998; Ripepe et al. 2009). These features have been making infrasound observations on volcanoes more common, and infrasound monitoring is now widely applied on many active volcanoes in the world (e.g., Johnson and Ripepe 2011; Fee and Matoza 2013 for a review).

At the meantime, the development and deployment of the International Monitoring System (IMS) infrasound network of the Comprehensive Nuclear Test Ban Treaty Organization (CTBTO) provided evidence on the possibility to detect volcanic eruptions of various energy at large source-to-receiver distances (e.g., Campus and Christie 2010; Dabrowa et al. 2011). The utility of the global IMS infrasound network for remote monitoring of volcanoes has been demonstrated by providing high temporal resolution information of ongoing activity at remote volcanoes (e.g., Matoza et al. 2011a) and global coverage for volcanic eruptions of various sizes (Dabrowa et al. 2011). Nevertheless, the possibility of using IMS network operationally for civil protection purposes and its ability to infer quantitative information on the source term is still to be investigated.

We present an overview of how infrasound monitoring is used on active volcanoes, focusing specifically on requirements for civil protection, and we discuss possible future improvements and perspectives.

35.2 Civil Protection Response to Volcano-Related Hazard

An eruptive volcano can pose a serious threat to people and infrastructures according to the energy and the type of the event. An eruption can produce various phenomena spanning from lava flows, in case of effusive eruptions, to pyroclastic density currents and atmospheric ash injections. These events can differ significantly from each other in terms of precursors, event duration, and extent of affected areas, thus leading eventually to various expected scenarios and responses of civil protection agencies.

For this reason, multiple techniques are usually applied to volcano monitoring (e.g., Pallister and McNutt 2015), mainly looking for precursors (e.g., geodesy,

geochemistry, and seismology) and with the aim of predicting event, possibly their size, or for tracking in real time the evolution of ongoing phenomena (e.g., seismology, thermometry, and infrasound). Being infrasound produced by explosive gas expansion and/or by the rapid movement of large volumes in the atmosphere, infrasound monitoring is not only limited to explosive eruptions but it can be used to track also density current such as pyroclastic flows, lahars, and debris flows, with important applications for civil protection.

At the regional scale, the large amount of hot gas and ash released into the atmosphere can pose a serious risk to human health (Baxter and Horwell 2015) and aviation (O'Regan,2011) also at several thousands of kilometers from the volcanic source. In this case, once a volcano has erupted, the forecast of plume evolution is performed operationally by running dispersion models by the nine Volcanic Ash Advisory Centers (VAACs) established worldwide in mid-1990s as an integral component of the International Civil Aviation Organization (ICAO) International Airways Volcano Watch (IAVW). Satellite images and additional geophysical information (e.g., lidars, ceilometers) on the volcanic plume extent are used operationally for model validation that strongly depends on input parameters such as mass eruption rate (MER) and onset time, which are often unknown.

Infrasound is among the most promising techniques for improving future monitoring of volcanic eruptions at global scale (see Marchetti et al. 2019). This relies on the good efficiency of infrasound propagation, which allows monitoring eruptive volcanoes even at large source-to-receiver distances, and to the high reliability and efficiency of local volcano monitoring. Some examples of the benefits of infrasound for monitoring volcanoes are provided below and operational applications are discussed.

35.3 Infrasound Monitoring of Active Volcanoes

Infrasound recorded for explosive eruptions can span 3 orders of magnitude, both in terms of excess pressure and frequency content (Fig. 35.1). A general increase in excess pressure and a decrease in frequency content are observed for increasing explosivity. Small-scale, mild Strombolian explosions, ejecting scoria and ash up to heights of tens/hundreds of meters above the vent, are typically associated to relatively high frequency (>1 Hz) and low amplitude (tens of Pa) infrasound transients (e.g., Ripepe and Marchetti 2002; Johnson and Ripepe 2011). Whereas, vulcanian explosions, driving discrete thermals up to a height of several km, are, instead, typically generating higher amplitude (hundreds of Pa) and lower frequency (<1 Hz) (e.g., Ripepe et al. 2010; Fee and Matoza 2013). Larger events, such as sub-Plinian and Plinian eruptions, feeding eruptive column up to >10 km of altitude, are generally associated to even lower frequencies around 0.2 Hz (Matoza et al. 2009; Fee and Matoza 2013).

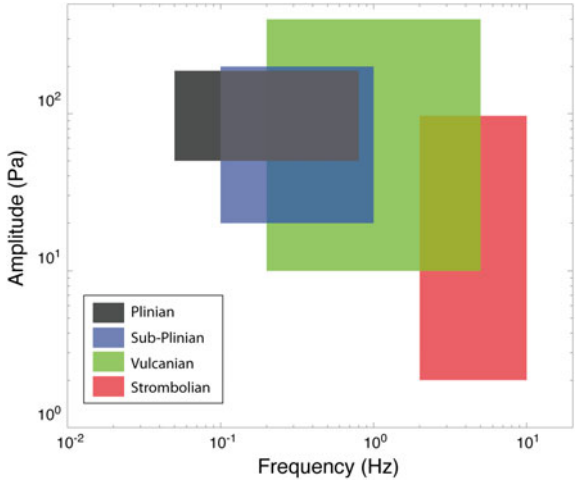

Fig. 35.1 Spectral content and amplitude variability of different kinds of volcanic activity

The sudden ejection of large quantity of ash can perturb the equilibrium of the whole atmosphere triggering oscillations well below the frequencies of acoustic waves, down to much longer periods typical of gravity waves. Acoustic-gravity waves with frequencies ranging between 0.9 and 3.3 MHz have been recorded by seismometers and micro-barometers at large distances (>800 km) during Plinian eruptions, including Mount St. Helens in 1980 (Donn and Balachandran 1981; Mikumo and Bolt 1985), El Chichon in 1982 (Mauk 1983), and Mount Pinatubo in 1991 (Tahira et al. 1991). These oscillations can be modeled as the response of the atmosphere to either mass or energy injection during the eruption (Mikumo and Bolt 1985; Kanamori et al. 1994; Bains and Sacks 2013), and it can be used to estimate the mass eruption rate of the event (Ripepe et al. 2016).

At close range (<10 km), the reduced atmospheric attenuation allows inferring source dynamics from infrasonic waveforms (e.g., Vergniolle and Brandeis 1994) and precise (<100 m) source location (e.g., Ripepe and Marchetti 2002). Moreover, the low absorption of the atmosphere makes infrasound propagation at long range (3000–5000 km) very efficient and allows the monitoring of remote volcanic eruptions by infrasound where local geophysical observations are missing (e.g., Fee and Matoza 2013; Matoza et al. 2019). Moreover, in favorable propagation conditions, even long-range infrasound can provide useful information to monitor ongoing volcanic processes (Dabrowa et al. 2011).

In this chapter, we briefly recall the state of the art of local infrasound monitoring of volcanoes (see Johnson 2019) and further highlight and discuss the most recent results of volcano monitoring for civil protection.

35.3.1 Local Infrasound Monitoring of Volcanoes

The use of infrasound as a monitoring system for explosive volcanoes at short distance from the source is relatively new. Many studies have demonstrated the advantage of combining seismic and infrasound observations to interpret the signals associated with volcanic activity (Dibble et al. 1984; Firstov and Storcheus 1987; Okada et al. 1990; Iguchi and Ishihara 1990; Braun and Ripepe 1993, among the others). Infrasonic waves have also been used to derive the energy of the Bezymianny explosive volcanic eruption already in the '60 (Gorshkov 1959) and the analysis of the infrasonic signals detected by the CTBTO IMS stations reveals a gross correlation between the pressure amplitude and the intensity of the volcanic eruptions (Dabrowa et al. 2011).

At close range (<10 km), infrasound signal is considered free from propagation effects, and its waveform and frequency content have been extensively used to model the possible source mechanisms of volcanic explosions (e.g., Johnson and Ripepe 2011 for a review). Most of the studies on acoustic source dynamics assume the linear theory of sound to model the source of volcanic sound using the monopole, dipole, or quadrupole approximation (Woulff and McGetchin 1976; Matoza et al. 2013). The source mechanism of volcanic explosions is thus analyzed by using both direct and inverse modeling, suggesting a variable combination of monopole and dipole source mechanisms (Johnson et al. 2011; Kim et al. 2012; De Angelis et al. 2012). However, the limited number of stations and inhomogeneous coverage of the infrasonic radiation pattern generally results in a low resolution of the source mechanisms. Besides, experiments focused on modeling the propagation of acoustic waves have demonstrated that topography and local atmosphere have a large effect on the propagation also near the source (<2 km) strongly contaminating the acoustic waveform (Lacanna and Ripepe 2012; Lacanna et al. 2014). Topography and local atmospheric conditions should not be neglected when inversion models are used to constrain the volcano acoustic source (Lacanna and Ripepe 2012).

For this reasons, infrasonic experiments aimed at solving the explosive source process are often combined with additional geophysical observations, which help constraining source parameters (e.g., Ripepe et al. 2001, 2013; Delle Donne and Ripepe 2012). Integration of infrasound with thermal and high-speed cameras have allowed to define that small explosive activity such as Strombolian can be represented by a monopole source embedded in the magmatic conduit (Delle Donne and Ripepe 2012). Whereas exit velocity of ash-rich eruptions (Ripepe et al. 2013) or plume height (Lamb et al. 2015) are consistent with the assumption of the dipole source approximation (Vergniolle and Caplan-Auerbach 2006).

For sustained long-lasting eruptive phases, typically observed during sub-Plinian or Plinian eruptions, recorded infrasound appears consistent with large-scale turbulence of jet noise (e.g., Matoza et al. 2009; Fee et al. 2010) with the relative

acoustic power being a function of the variations in velocity and volume flux of the ejecting gas–ash mixture.

However, some volcanic explosions are produced by the violent expansion of the magmatic gas, which easily reaches supersonic velocity (Nairn 1976). In this case, the linear approximation is not valid and infrasound might result from non-linear attenuation of blast waves even for small explosions (VEI < 2) (e.g., Marchetti et al. 2013; Medici et al. 2014).

In spite of the difficulties in constraining the dynamics of the volcano acoustic source, the accuracy in the location of the infrasound provides an extremely important information to the monitoring systems. Volcanoes with multiple vents, or craters, like Stromboli, Etna, or Kilauea, can show a different activity at the different vents even if they are located at a close distance to each other. This is reflecting a complex explosive dynamics possibly related to the geometry of the shallow magmatic feeding system. The accurate vent-by-vent geophysical analysis becomes then critical to understand the source dynamics helping to infer the possible eruptive scenarios (Valade et al. 2016).

On Etna volcano, infrasound recorded by a small aperture array (Marchetti et al. 2009) showed a systematic switch of activity between two active craters, which occurs more often and with infrasonic amplitude of explosions increasing over time by approaching the eruption onset (Fig. 35.2). This behavior is reflecting a partitioning in the path of the gas flux suggesting a branched dynamics controlled by changes in the magma/gas flux rate (Fig. 35.2).

The link between infrasound and gas flux seems also evident during lava fountaining activity at Mt. Etna. Here, infrasound is characterized by the shift of the spectrum toward lower frequencies when infrasonic amplitude increases while approaching the lava fountaining (Fig. 35.3). This peculiar behavior of the infrasonic wavefield seems reflecting the transition from a slug to churn flow regime as

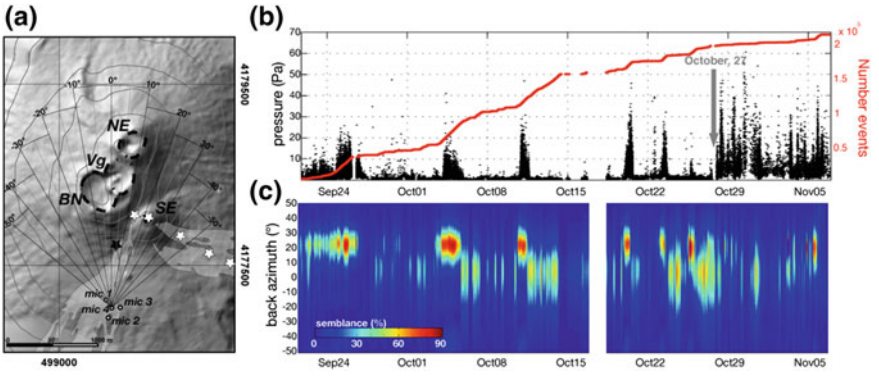

Fig. 35.2 Small aperture array analysis of explosive and degassing activity at Etna volcano (**a**). The switching of activity and the difference of infrasonic amplitude (**b**, **c**) are pointing to a gas flux-controlled dynamics within a branched shallow feeding system (from Marchetti et al. 2009)

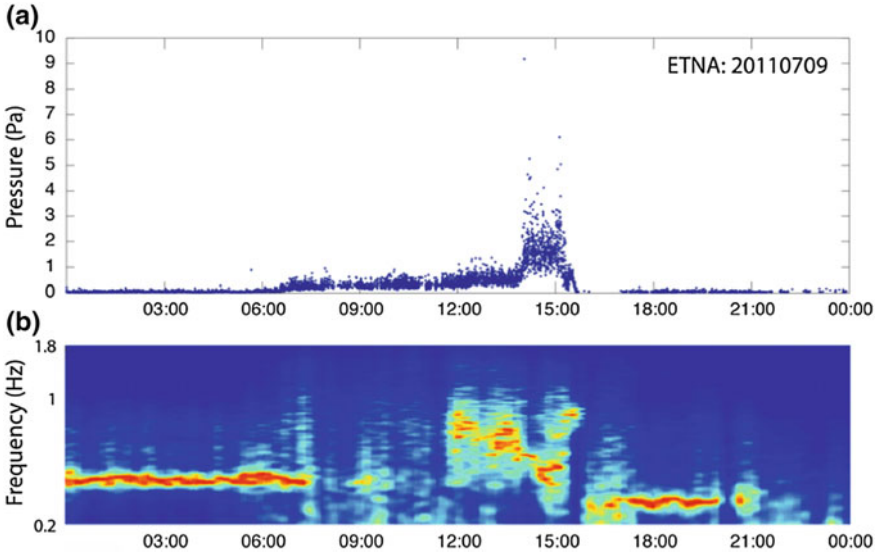

Fig. 35.3 Infrasound pressure amplitude recorded at a distance of 5.5 km from the source (**a**) and frequency content (**b**) of lava fountain activity at Etna volcano. The frequency content shifts to lower values during the ash plume emission between 14:00 and 15:00 UTC. Afterwards, volcanic activity stops and the signal is dominated by microbarom

response to a rapid increase of the gas/magma flow driving the eruptive event (Ulivieri et al. 2013).

The use of infrasound arrays rather than single sensors allows also to identify and locate nonexplosive moving sources like pyroclastic density currents (PDCs) (e.g., Ripepe et al. 2010; Delle Donne et al. 2015), debris flow (Kogelnig et al. 2014) or snow avalanches (Ulivieri et al. 2011; Marchetti et al. 2015). Here, infrasound radiated from the gravitational mass flow is recorded by the array with a variable back-azimuth and decreasing apparent velocity, which reproduces the run-out path of the flow. Given the large variety of seismic signals associated to the ongoing volcanic activity, it is difficult to interpret the relationship of simple seismic observations with PDC dynamics (Cole et al. 2015). This makes infrasound the most promising monitoring system to detect PDCs from distances of several kilometers from the volcano.

The ability to provide a precise source location and important insights on the eruptive source mechanisms makes infrasound a method more frequently used to monitor active volcanoes.

35.3.2 Infrasound Array Processing

An infrasound array consists in the deployment of multiple sensors in a geometrical configuration, which is used as an antenna. The number of elements is variable from

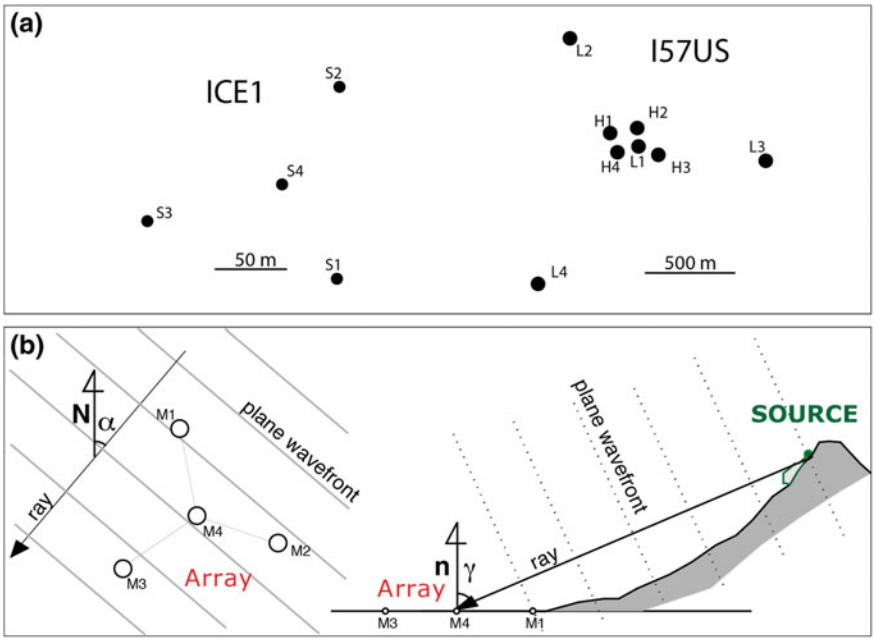

Fig. 35.4 Geometry of infrasound arrays **a** ICE1 is a small aperture array operated in Iceland by UNIFI and IMO for volcano monitoring. IS57US is an infrasound array of the IMS network of the CTBTO in California. **b** Sketch of infrasound array geometry and corresponding wave parameters: notation of back-azimuth (α) and takeoff angle (γ) is the same as in the text

a minimum of 3 up to >8 elements, where the larger number of sensors deployed is providing the best azimuthal resolution and the best signal-to-noise ratio. Similarly, the dimension of an infrasound array, measured as the maximum distance between two array elements (aperture), can vary significantly, spanning from ~100 m, commonly adopted for local monitoring of sources close (<100 km) to the array, up to 1–2 km, typical for arrays with a larger number of elements and deployed for long-range observations of infrasonic sources (Fig. 35.4a).

Arrays are preferred to single sensor for their ability to investigate the infrasonic ray parameters (back-azimuth and apparent velocity) regardless the position of the infrasonic source. Besides, arrays instead of a single sensor have the advantage of being able to increase the signal-to-noise ratio, which allows improving the automatic signal detectability within the noise. Limitations of array detection techniques are, in fact, related to the signal-to-noise ratio, which depends on the local noise, strength of the source, number of array elements as well as propagation effects from the source to the receiver.

Array signal processing is based on the assumption that a signal is coherent at different sensors, while noise does not show any correlation. Infrasound detection is defined when, in a given time window, coherent signal is recorded across the array, which translates in the multichannel semblance exceeding a fixed threshold.

Thus, an infrasonic transient will consist of multiple detections, as a function of event duration and process windowing.

The time shifts dt_{ij} between a signal recorded at different couples of sensors (i, j) are used to derive the infrasonic ray path of a plane wavefield propagating across the array. This is fully described in terms of back-azimuth (α) and apparent velocity (c_a). Back-azimuth identifies the direction from where the signal is coming from (Fig. 35.4b) with azimuthal resolution being strongly related to the array aperture and frequency content of infrasonic signal. The apparent velocity is the velocity measured for a signal propagating within the plane defined by the elements of the array (Fig. 35.4b) and is directly related to the inclination of the incident angle, which reflects the elevation of the infrasonic source:

$$c_a = \frac{c}{\sin(\gamma)}, \tag{1}$$

where γ is the infrasonic takeoff angle, defined as the angle between the infrasonic ray and the normal vector to the surface represented by the array plane ($\hat{n}$), while c is the sound propagation velocity at local atmospheric conditions. It is clear from Eq. 1 that the apparent velocity for a direct arrival depends on the elevation of the source. In the case of a source located right above the array the incident angle would be zero ($\gamma = 0$) and apparent velocity would be infinite ($c_a = \infty$) consistent with a signal being recorded simultaneously at all the elements of the array.

35.4 Infrasound Monitoring for Civil Defence

Ash-rich volcanic explosive eruptions can have a variable duration, spanning from few minutes for Vulcanian explosions driving single thermals (Clark et al. 2015), up to hours for sub-Plinian and Plinian eruptions (Cioni et al. 2015) able to drive sustained ash plumes. Therefore, the prompt report on the occurrence of volcanic activity and its evolution is critical for the correct assessment of ash dispersal in the atmosphere as well as on the ground (e.g., Bonadonna et al. 2012). In case of PDCs, the timing is even more crucial, and it requires for automatic delivery of the alert to be useful for civil defence operational procedure.

Infrasound is the most clear evidence of the direct coupling between the volcanic process and the atmosphere, and it can be directly related to the explosive eruptions and PDCs. Unlike seismic signals, acoustic source is easy to locate, and this offers a simple way to filter out all the signals coming from a direction different than the volcano. Besides, acoustic waves do not rely on good visibility as in case of thermal cameras and this makes infrasound one of the best instrument to detect activity on a volcano.

For these reasons, infrasound monitoring can be used to deliver automatic early-warning messages to infrastructures in charge of triggering civil defense operational procedures.

35.4.1 Alert for Pyroclastic Density Currents

Pyroclastic density currents (PDCs) can be generated by several volcanic activities such as the collapse of the eruptive column, the collapse of the extruding lava dome, or the lateral blast of the volcanic flank. PDCs are fast-moving density currents consisting of a mixture of hot pyroclastic material, with grain size spanning from ash to boulders, and gases. Because of the high velocity (~30–70 m/s) and high temperature (>800 °C), PDC effects are highly devastating able to completely destroy land and infrastructures. Generally, PDCs have a run-out distance of <20 km, but larger events traveling up to >100 km have been recorded historically. The 1883 Krakatoa eruption produced a PDC that traveled >40 km over seas and caused fatalities in the nearby islands (Carey et al. 1996). The devastating impact and the poor predictability of the processes make PDC responsible for most of the casualties during volcanic eruptions in recent times (Cole et al. 2015).

Hazard management of PDCs is mostly based on mapping and modeling the run-out, in order to predict the area possibly affected by the flow deposit. The propagation of dense PDC is strongly related to topography. In case of dilute PDCs, commonly referred to as pyroclastic surges, propagation is irrespective of topography and thus making hazard assessment of PDCs extremely challenging.

Therefore, during a volcanic crisis, the ability to detect and track the propagation of these fast-moving density currents is of utmost importance in understanding the evolution of eruptions and mitigating related hazards.

35.4.1.1 Automatic Detection of PDCs

Methods for the location of PDCs, based on seismic amplitudes, have been proposed in the past (e.g., Jolly et al. 2002) and have proved to be quite effective for the characterization of large collapse events. However, these techniques require dense seismic networks and optimal azimuthal coverage. The use of seismic amplitudes requires an understanding of local site effects and frequency-dependent attenuation, thus introducing another layer of complexity. Finally, these methods are not designed for unsupervised application in real time; events classification and location require visual inspection of the seismograms and manual tuning of a seismic analyst.

The moving front of the PDCs is an excellent source of infrasound (Yamasato 1998), which can be easily detected using array technology (Ripepe et al. 2009). Infrasonic array can be used to track the direction and the speed of the PDCs in real time providing important information for a prompt and reliable hazard assessment. A permanent infrasonic array installed on Montserrat (WI) to monitor the activity of Soufrière Hills volcano (SHV) has proved the efficiency of this technique. In spite of the severe weather conditions, the acoustic record maintain high signal-to-noise ratio and coherence among the array (Fig. 35.5) during the time of the most intense

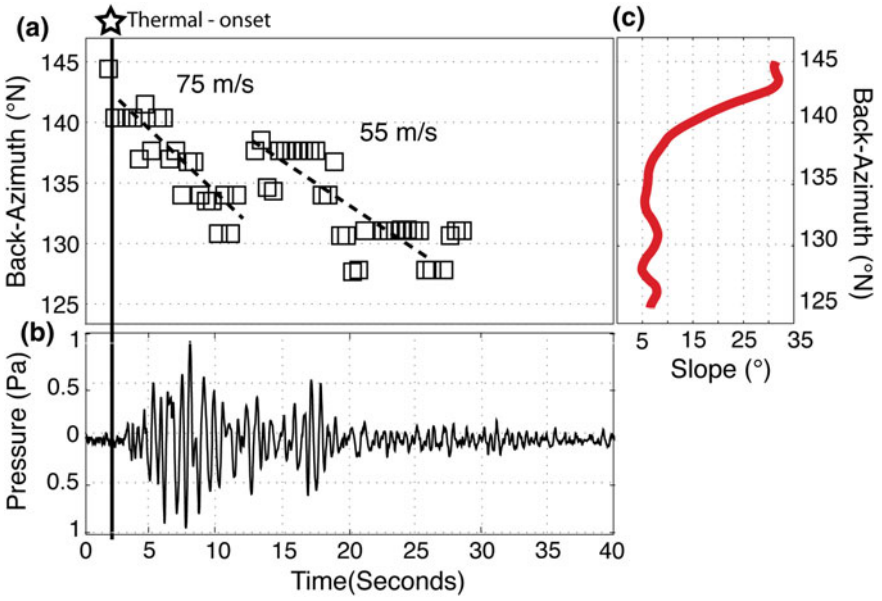

Fig. 35.5 Infrasound record of a PDC at Soufrière Hills volcano, Montserrat (from Delle Donne et al. 2015)

and vigorous phase of the PDC. Infrasound detected by the array shows several changes in the back-azimuth reflecting the moving front of the flow (Fig. 35.5a).

By projecting infrasonic back-azimuth on a DEM topographic map (Fig. 35.5c), the angular variation can be converted in a minimum linear distance covered by the PDC giving a minimum speed of 30 m/s (108 km/h). Infrasound shows also how migration of the propagation back-azimuth from the dome toward SSE can repeat in time indicating the pulsating nature of the flow (Fig. 35.5a). The mean velocity of the flow's propagation front calculated using this infrasonic technique varied between 30 and 75 m/s, in good agreement with theoretical modeling of non-explosive gravitational pyroclastic flows at SHV (Wadge et al. 1998; Hooper and Mattioli 2001).

Infrasound array techniques can be combined with thermal imagery back-projected onto a DEM, allowing location of the thermal anomaly related to the PDC onto a 3D topography increasing our ability to detect and evaluate, with unprecedented resolution, the propagation of PDCs (Fig. 35.5). From a monitoring point of view, infrasound is improving our ability to visualize the flow run-out in real time, even in poor visibility or at night, thus strongly contributing to the monitoring of this highly dangerous volcanic activity, and giving the possibility to issue Early-Warning messages in real time.

This detection technique has been tuned for snow avalanches (Ulivieri et al. 2011; Marchetti et al. 2015) that share many similarities with PDCs and can be

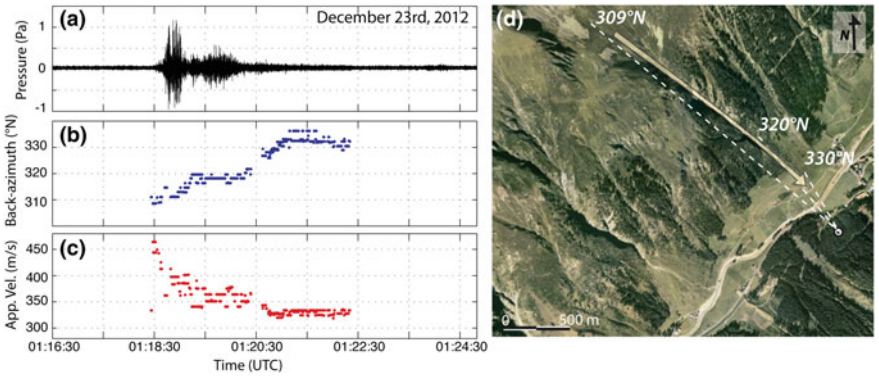

Fig. 35.6 Infrasonic record (**a**), back-azimuth (**b**), and apparent velocity (**c**) for a snow avalanche that occurred on Dec. 23, 2012, nearby Ischgl, Austria (**d**), and was recorded by a small aperture infrasound array. The avalanche path is marked with the yellow arrow in (**d**) while the array is marked with the white triangle

therefore exported to the volcanic environment. Small- to medium-size snow avalanches generate, in fact, an emergent, long-lasting (~20 s) infrasonic signal with amplitudes ranging from 0.1 to <10 Pa, depending on the avalanche size, and characterized by a low-frequency content (~3 Hz) very similar to the one associated to PDC. In the case of density currents, the flow driven by gravity is moving downhill, and the source will change position while elevation is decreasing. This will be marked by a progressive increase of the incident angle resulting into a negative gradient of the apparent velocity (Fig. 35.6).

Video recording of controlled avalanches shows how the avalanche path perfectly matches the infrasonic back-azimuth with an accuracy of ~1° (Ulivieri et al. 2011).

Therefore, density currents can be automatically identified following criteria related to the variation of back-azimuth, decrease in apparent velocity, infrasonic signal amplitude, and duration (Marchetti et al. 2015). Using these four criteria, it is possible to automatically identify avalanches out of thousands of detections (Fig. 35.7) in real time. Direct field observations allowed to validate the efficiency of this automatic system to locate and identify infrasound generated by density currents.

Even if a single array does not provide a precise source location, but simply the propagation direction and the change in apparent velocity, infrasound represents a very efficient monitoring system to detect density current, thus indicating potential sectors where avalanches might have occurred or where to focus further controls. Besides, as for the PDCs at Montserrat, the migration of infrasonic back-azimuth projected on the topography provides an estimate of the instantaneous velocity of

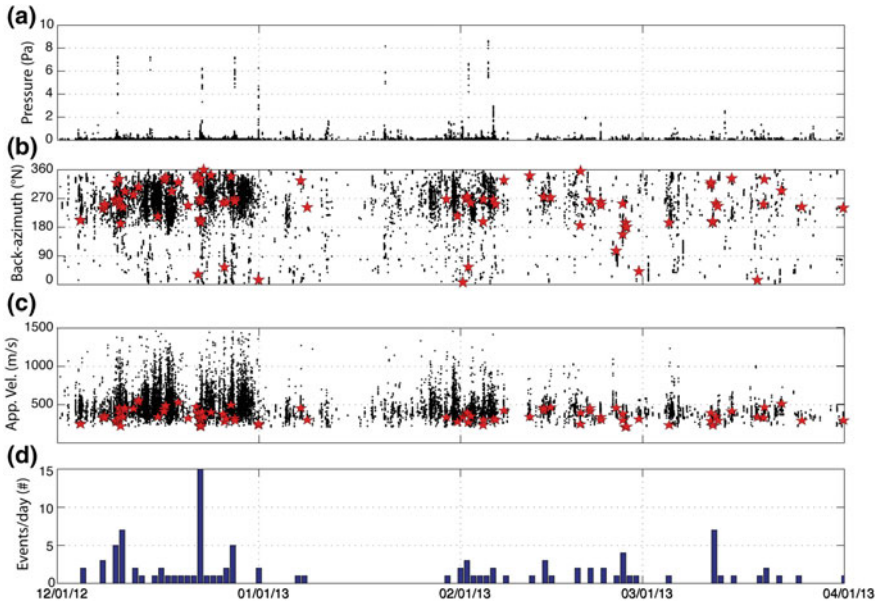

Fig. 35.7 Results of infrasound array processing for the period of analysis (Dec 2012-March 2013) nearby the town of Iscghl (Austria) showing amplitude (**a**), back-azimuth (**b**) and apparent velocity (**c**) of 31770 infrasonic detections (black dots). 103 avalanche are identified automatically from the whole data-set and are highlighted with red stars in (**b**) and (**c**). The number of avalanches per day is shown in (**d**)

the moving front (Fig. 35.8). This procedure was successfully tested at Ischgl (Switzerland) against data collected by a Doppler radar operating nearby the array (Marchetti et al. 2015).

35.4.1.2 Operational Warning Center

Permanent infrasonic monitoring in the Italian Alps integrated with field observation in the last ~10 years indicates that this array analysis allows a robust, real-time, remote detection, and location of snow avalanches activity occurring at a distance of 3–4 km around the array. This represents the key information for a proper validation of avalanche forecast models and risk management. Since then, automatic detection of density currents based on infrasound wave parameters (back-azimuth and apparent velocity) (Marchetti et al. 2015) is now operationally adopted for snow avalanche monitoring, and more than 10 systems are currently active in Europe.

Once an event is detected, an automatic notification is delivered within a maximum latency of 2 min, by sms and e-mail, and it provides operational support to the daily avalanche forecasting, in Italy, Swiss, Norway, and Canada.

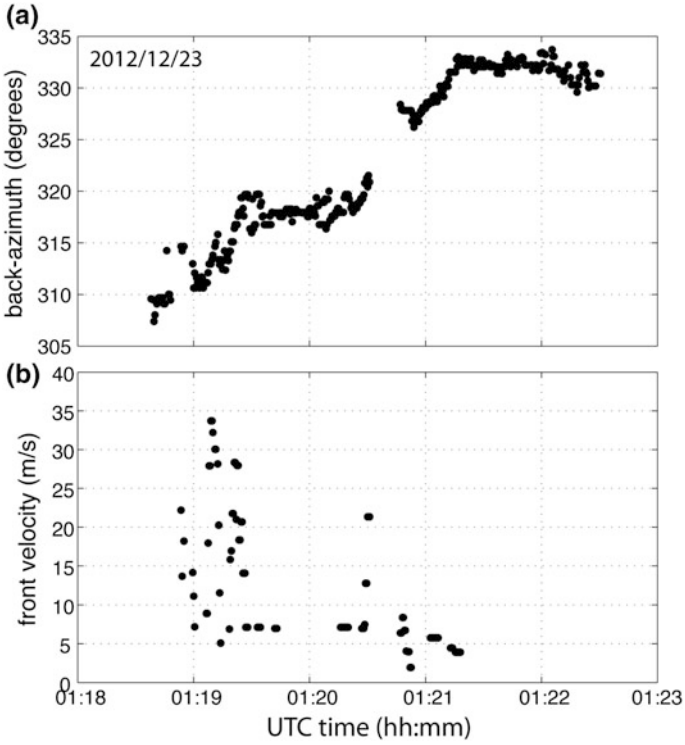

Fig. 35.8 Back-azimuth variation (**a**) detected by the array and derived instantaneous velocity of the front (**b**) for the event shown in Fig. 35.6

The same procedure can be easily applied to PDCs, with a strong improvement of the existing monitoring systems and direct benefit to hazard assessments. The possibility to know also in case of poor visibility if a PDC has occurred, the direction of the run-out as well as its propagation velocity, is indeed of crucial importance to increase preparedness to the hazard and improve time of reactions for emergency plans.

35.4.2 Early Warning for Explosive Eruption

Despite infrasound monitoring and research on active volcanoes has been increasing exponentially in the last few years, its operational use for civil protection purposes is still limited. The first attempt of using operationally infrasound array monitoring was the Acoustic Surveillance for Hazardous Eruptions (ASHE) project (McCormack et al. 2006; Garces et al. 2008), which was a science and technology

experiment that aimed to test the practical utility of infrasound as a detection tool of volcanic activity at regional scale and the feasibility of using infrasound for operational notification of ongoing activity to the VAACs. The project successfully delivered automatic notifications to the VAACs in 2008.

Operational infrasound monitoring of volcanic activity for civil protection purposes is currently performed on Etna volcano, Italy, where two small aperture infrasound arrays (ETN, MVT) are deployed and operating at a source-to-receiver distance of 5.5 and 7 km, respectively (Marchetti et al. 2009; Ulivieri et al. 2013) (Fig. 35.9). Data is broadcasted on the web and processed in real time by the University of Firenze (Italy) for the assessment of the ongoing volcanic activity for the Italian Civil Protection agency.

Etna is one of the most active volcanoes in the world and current activity is typically effusive, with explosive episodes and lava fountaining. Typically, lava fountains (LF) at Etna last between tens of minutes to few hours and are characterized by a sustained lava column of up to 2000 m above the summit craters. These explosive events are feeding ash plume reaching 15–17 km altitude (e.g., Vulpiani et al. 2016), which is then dispersed hundreds of km away from the volcano.

Nearby Etna volcano, explosive episodes can cause the closure of the three airports, thus affecting local and international air traffic, as well as the main railways and freeways in the area. More than 50 LF episodes occurred since January 2011, without being preceded by any clear precursors. Previous attempts of early-warning systems based on seismic tremor were not completely successfully (Alparone et al. 2007).

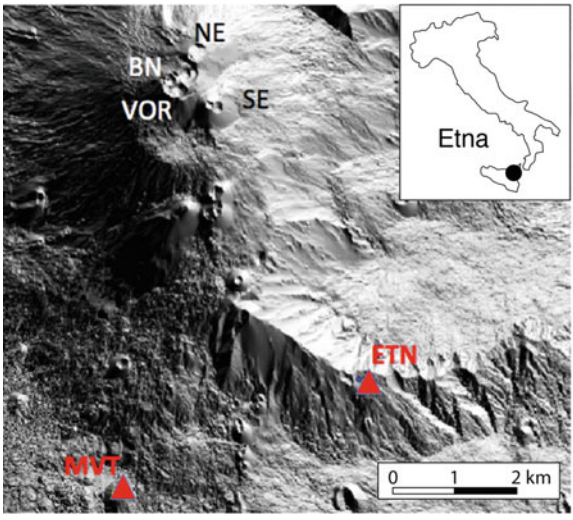

Fig. 35.9 Position of the permanent arrays (ETN and MVT) on Etna volcano. The insert is showing the position of Etna in Southern Italy

35.4.2.1 Acoustic Observations of Explosive Eruptions at Etna Volcano

Observations of explosive eruptions (LF) from Etna volcano showed how the eruptive episodes are commonly marked by a smooth increase in both seismic and acoustic amplitude preceding the onset of the LF (Fig. 35.10). However, while seismic and infrasound share the common amplitude envelope, they show remarkable differences in the time series, with infrasound marked by repetitive pressure transients or sustained low-frequency oscillation while seismic tremor appears to change mostly in amplitude but keeps a stable spectral content (Fig. 35.11). Infrasound array processing, based on multichannel semblance analysis, is particularly efficient to identify and describe this kind of behavior, when processing window is properly selected (see Sect. 3.2).

Based on the amplitude variation, number of infrasound detections, and shift of the frequency content, explosive LF episodes can be divided into two main phases, the precursory Strombolian phase (PH_s) and the paroxysmal phase (PH_f) when the proper LF ash-rich column occurs (Fig. 35.12). Each phase is associated with a different infrasonic signature reflecting a change in eruptive style (Ulivieri et al. 2013).

The initial Strombolian phase (PH_s) is dominated by intermittent, medium to high (1–5 Pa) amplitude, infrasonic pulses with a duration of about 0.8 s and a frequency content of 0.6 Hz, repeating regularly with a constant time delay of about 2 s (Figs. 35.12 and 35.13a).

The second phase (PH_f) is dominated by higher amplitude (3–10 Pa), lower frequency (0.45 Hz) oscillations (Figs. 35.12 and 35.13b) punctuated with few, large amplitude, impulsive transients. This results in continuous infrasound

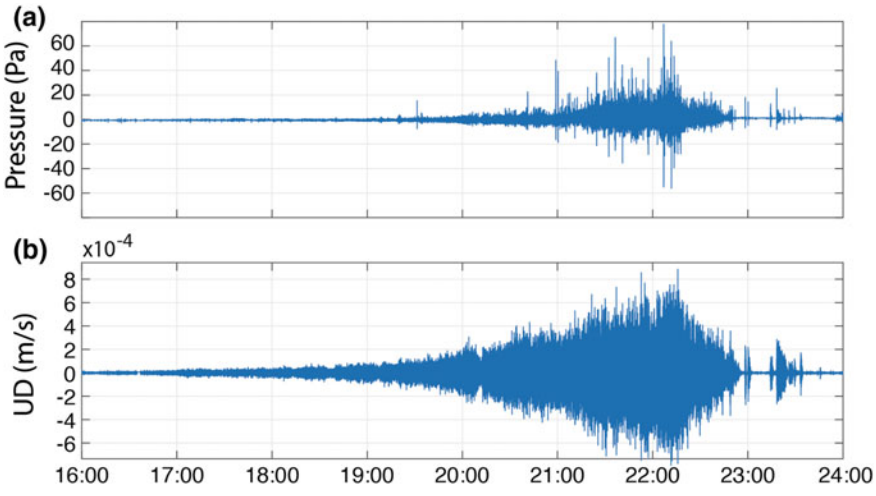

Fig. 35.10 **a** Infrasound and **b** Seismic record of the 2 December 2013 lava fountain event recorded at ETN array, at a source-to-receiver distance of 5.5 km

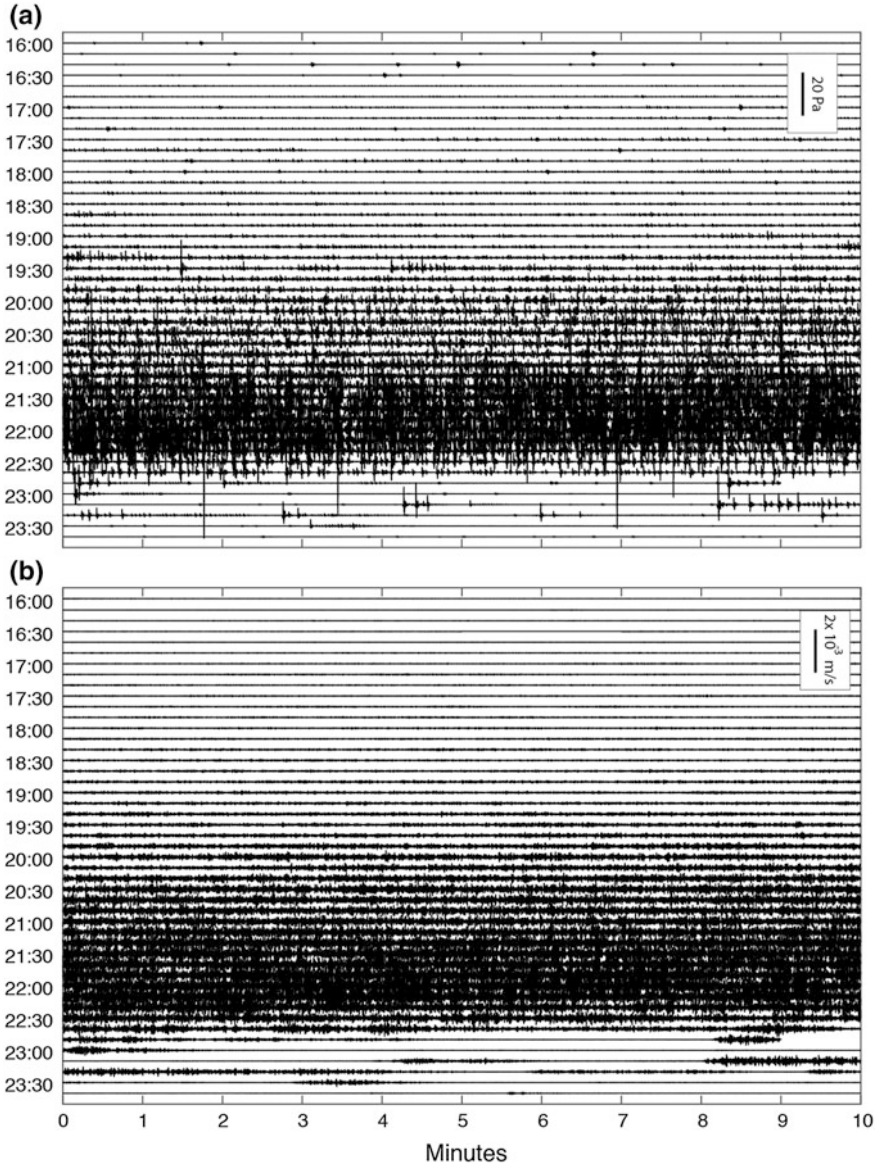

Fig. 35.11 8-h-long sample of infrasound (**a**) and seismic (**b**) data recorded at ETN (@5.5 km from the source) during the Dec. 2, 2013, LF at Etna Volcano. Each line is showing 10 min of data

detections at the array, which during this phase reach the rate of 60 events/min (Fig. 35.12c). This transition is clearly reflected by a spectral shift toward a lower frequency content (Fig. 35.12b) and has been interpreted in terms of a transition of the two-phase flow dynamics within the magmatic conduit, from slug flow (PH_s),

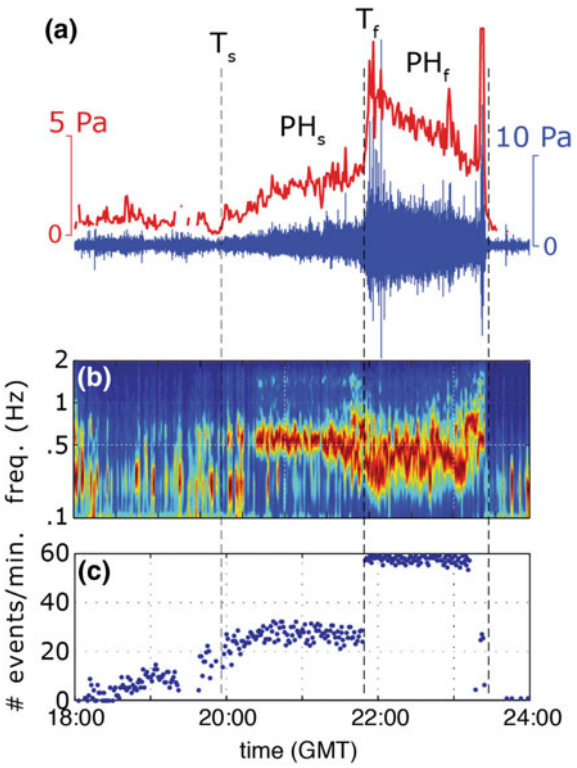

Fig. 35.12 January, 12, 2011, LF event at Etna volcano and recorded at ETN infrasound array at a source-to-receiver distance of 5.5 km: **a** Infrasonic excess pressure; **b** normalised infrasonic spectrogram, **c** number of detected infrasound events/min. Vertical dashed lines separated the three distinct phases (redrawn from Ulivieri et al. 2013)

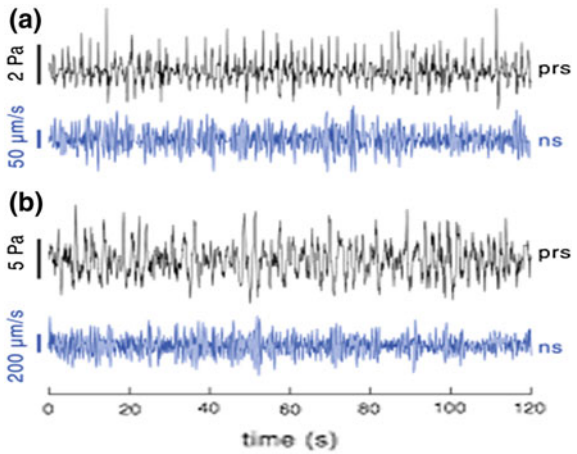

Fig. 35.13 **a** infrasonic signal (black line) recorded during the Strombolian phase (PH_S) shows a series of acoustic transients repeating every ~2 s, which are not evident in the seismic signal (blue line). **b** Infrasound wavefield (black line) becomes almost monochromatic during the lava fountain (PHF), whereas seismic tremor (blue line) shows higher amplitude but keeps the same wavefield features (from Ulivieri et al. 2013)

driving intermittent explosions, to churn flow, driving the sustained column (PH_f) marked by the continuous infrasound oscillation (Ulivieri et al. 2013). Eventually, activity drops rapidly and gets back to background signal.

35.4.2.2 Infrasound-Based Early-Warning System of LF at Etna Volcano

The persistence of this LF dynamics and the ability of infrasound to detect in real time each distinctive eruptive phase has been used as the base for an early-warning system of large explosive episodes at Etna volcano. The early warning (EW) is based on the infrasonic parameter (IP) which is defined as the product between the mean infrasonic amplitude and number of detections per minute (Fig. 35.14) which have the back-azimuth and apparent velocity compatible with the position of the summit craters (Ulivieri et al. 2013).

The IP is strongly related to the rate of the infrasonic activity, and it increases with the number and amplitude of the detections. When detection of infrasonic transients reaches a maximum of 60 events/minute, the IP is totally controlled by the infrasonic pressure (Fig. 35.14). The IP is thus reflecting the eruptive style observed during the different phases (PH_s, PH_f) of the explosive episodes (Fig. 35.12), and it is used to identify their onsets. Based on array data recorded during a period of more than 5 years (2008–2013), which includes 39 episodes of lava fountains, threshold values of IP = 60 and IP = 120 have been chosen to define the onset of the precursory phase (PH_s) and of the fountaining phase (PH_f), respectively (Ulivieri et al. 2013).

Early-warning procedure wants the first notification (EW1) to be delivered if the IP exceeds the first threshold (IP > 60) for more than 5 min. This first notification corresponds to the onset of the strong Strombolian phase (PH_s, Ts in Fig. 35.12)

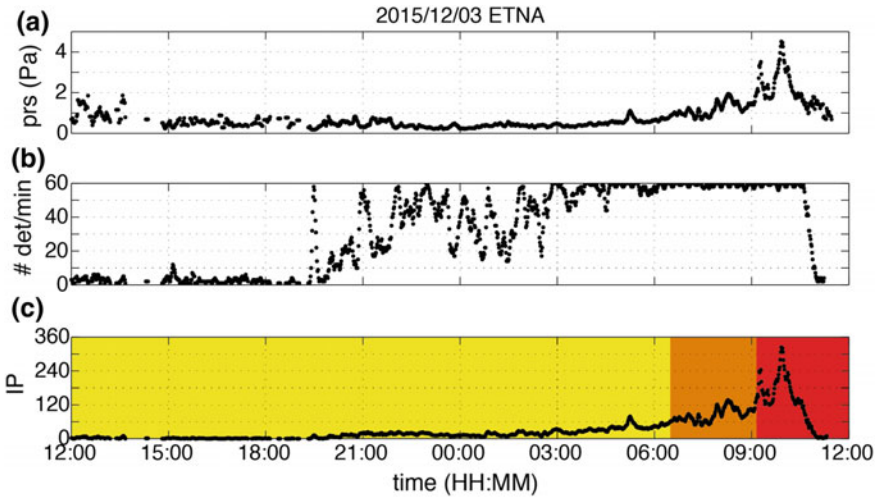

Fig. 35.14 Infrasound excess pressure (**a**), number of detections/minute (**b**) and infrasound parameter (**c**) for a 24-h-long period between Dec. 3- and Dec. 4, 2015, when a lava fountain occurred in the early morning. The IP is color-coded according to threshold values of 60 (orange) and 120 (red) corresponding to EW1 and EW2 respectively

preceding the onset of the lava fountain and it corresponds to a pre-warning phase. The second notification (EW2) is delivered when the IP exceeds the threshold, IP > 120, for more than 5 min, and it marks the onset of the lava fountain explosive episode (PH_f, Tf in Fig. 35.12). To avoid multiple EW messages due to possible fluctuation of the parameter IP, the early-warning system has an hysteresis, and the end of the eruptive phase is thus defined only when the parameter IP < 8 for 24 h. In this case, the third notification message (EW0) is automatically delivered to declare the end of the explosive episode.

Considering the 54 events recorded between January 2011 and May 2016, the IP exceeded the thresholds 51 times which correspond to 94.3% of positive alerts. In the same 6 years long period, the EW system delivered only 6 false positive alerts (8.9%), and 3 false negative (5.5%) due mostly to the strong (>30 kn) wind. The time difference between the EW1 and EW2 messages corresponds to the pre-warning time (Fig. 35.12), and it ranges between 3 min and 26 h, with a mean value of 76 min (Fig. 35.15). This means that the infrasonic-based early-warning system operative at Etna volcano is able to automatically deliver a pre-alert message (EW1) of large explosive eruption more than 1 h before the ash-rich LF plume is erupted and with a 94.3% of success. The IP parameters are issued in real time automatically every minute, and considering the ~5.5 km travel time distance has a latency of <120 s.

35.4.2.3 Operational Communication Workflow

Since 2015, infrasonic early warning at Etna volcano is part of the operational procedure of the Italian Civil Defense and is used to provide alert levels to Regional Civil Protection Agency in Sicily, which manages regional hazards, like moderate (M < 5) earthquakes and explosive volcanic eruptions. As the final part of this chain, the majors of single municipalities are the ultimate responsible for local civil protection actions and are in charge of activating emergency plans (Fig. 35.16).

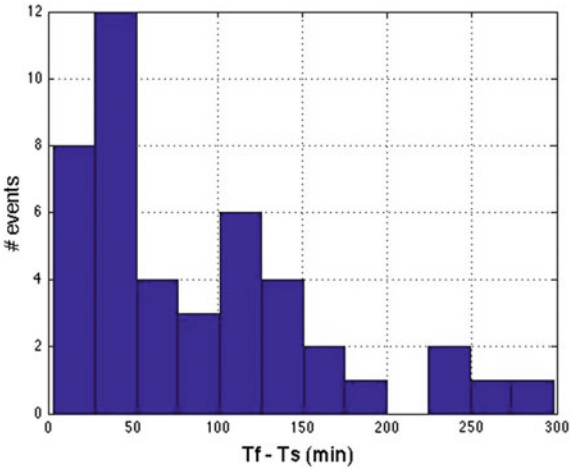

Fig. 35.15 Time duration of the PH_s phase (T_f - T_s), which corresponds to the pre-warning EW1 phase

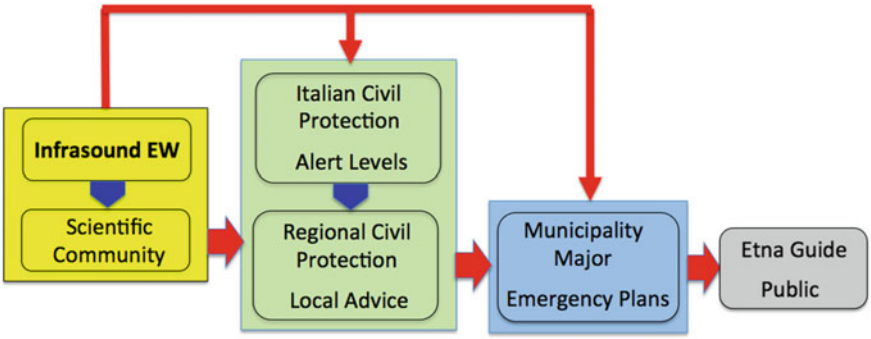

Fig. 35.16 Communication workflow of Civil Protection actions related to volcanic hazard and infrasound-based automatic notification system (EW) of explosive eruptions at Etna volcano

In this working flow, the scientific community interacts with the Civil Protection at various levels, providing services, information, and scientific advices required for defining alert levels and emergency plans. This is usually a medium-term approach, and the alert levels are changed according to significant variations in the observed parameters.

In this framework, after almost 6 years of data calibration, in 2013 the Department of Italian Civil Defense started to officially evaluate the efficiency of the infrasonic early-warning system as a possible automatic operational procedure. Real-time information of infrasound activity in terms of recorded pressure, coherence, and back-azimuth are automatically and in real time delivered to the Operational Centers of Civil Defense via a dedicated website (Fig. 35.17). In 2015, the volcano infrasound early-warning (EW) system became operative and included in the civil defense communication workflow between the Italian Civil Defense headquarters in Rome, the Regional Agency in Sicily and the several Municipalities present around Etna volcano (Fig. 35.16). The system is enabled to send e-mails and sms text messages automatically to key users included into Civil Defense communication workflow (Fig. 35.16).

Explosive eruptions (LF) at Etna volcano evolve rapidly, strongly limiting the possibility to promptly activate emergency plans, like the closure of the airports and freeways or the access to the summit area. Therefore, despite the infrasound-based early-warning system allows a pre-alert of ~1 h before the event occurrence, the standard communication workflow was modified to deliver the notification simultaneously to civil protection and municipalities (Fig. 35.16). Such a procedure, which is currently operational, is allowing a prompt reaction of the people directly working in the field (majors, municipalities, guides) and allows anticipating significantly the activation of emergency plans. On May 18, 2016, the EW1 sms message delivered by the automatic system has allowed the Italian Civil Defense to issue a pre-alert of explosive eruption almost 14 h before the lava fountaining (Fig. 35.18).

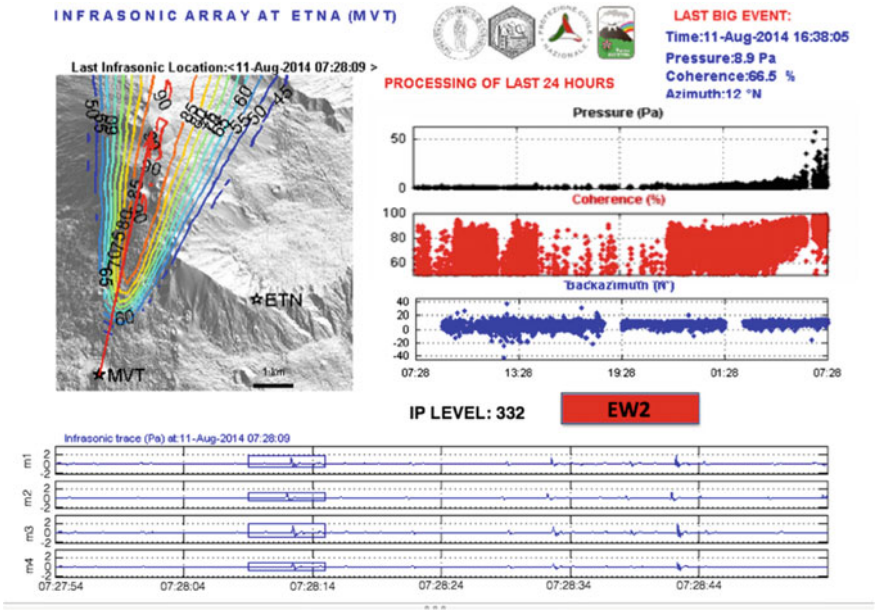

Fig. 35.17 Snapshot of the website for real-time infrasound array monitoring of Mount Etna operated by UNIFI for the Italian Civil Protection (http://lgs.geo.unifi.it), which shows the alert level (Red—Ongoing Lava Fountain), real time data and time history of infrasound detections

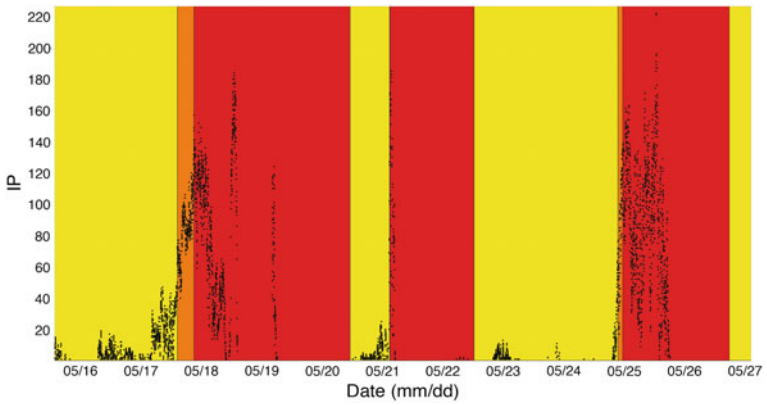

Fig. 35.18 Infrasound Parameter (IP, black dots) and EW levels during the May 2016 eruptive phase of Etna volcano. The pre-warning EW1 was issued ~14 h before the explosive eruption

35.4.3 Eruption Source Parameters from Infrasound

Whenever a volcanic eruption occurs, models of ash dispersion in the atmosphere are run by the VAACs and require information on the volcanic source term, such as the location of the eruption, the origin time, duration of eruption, the mass eruption rate (MER), and the total grain size distribution (TGSD) of erupted material, to be included as input parameter.

While the location, the onset, and the duration of the eruption can be derived by different sources and it can be available in near-real time also in case of unmonitored remote volcanoes by using infrasound (see Marchetti et al. 2019), the MER and the TGSD are never available in real time. Grain size distribution and amount of deposits are mapped only once the eruption is over, and this approach makes impossible to use reliable information during operational ash-cloud forecasting. The TGSD and MER are then of primary interest to model ash dispersion in the atmosphere as they are directly controlling the prediction of ash concentration in the plume.

The approach commonly used by VAACs is to derive the MER from plume height (H, in km) following empirical relationships based on field observations (Sparks et al. 1997; Mastin et al. 2009)

$$H = 2Q^{0.241}, \tag{2}$$

where Q is the volumetric flow rate (in m^3/s) of erupted magma. This empirical relationship is derived from eruptions regardless the eruption dynamics, magma composition, and temperature, which results in a large scatter in the data. The maximum scatter is around plume heights of 10–15 km, and it can vary by a factor of 4. It is clear that such uncertainty derived from the evaluation of the MER from plume height directly affects the final reliability of operational ash-cloud forecasting. Moreover, information on plume height is not always available, and this calls for a more robust strategy possibly based on remote parameters.

The discharge of material ejected into the atmosphere during a volcanic eruptive column is transferring a large momentum on the ground. Physics of the eruptive column can be then represented by a counter single vertical force acting downward on the Earth, which is balancing the momentum generated by the vertical force of the eruption as the material is ejected from the vent (Kanamori and Given 1982). This model can be used to explain the origin of the seismic signal associated to eruptive column, and it can be used to estimate mass ejection rate of material discharged into the atmosphere (Prejean and Brodsky 2011). This explains the correlation, which sometimes is observed between seismic tremor and the plume height or with the volcanic explosivity index (McNutt 2004). However, a clear relationship is still missing (Nishimura and McNutt 2008), and the correlation between seismic tremor and plume height is not always satisfied.

The same eruptive process is an efficient source of infrasound, and unlike seismic tremor, whose source mechanisms can be both related to superficial or deep magma dynamics, infrasound is directly related to the fragmentation process and/or

to the plume dynamics thus reflecting only the injection of volcanic material into the atmosphere. Besides, infrasound observations of high-energy eruptions show a link between acoustic power and plume height, such as for Plinian eruptions at Tungurahua volcano in Ecuador (Fee et al. 2010). This link can reflect the relationship between the exit velocity of volcanic plumes and acoustic pressure (see Delle Donne and Ripepe 2013; Johnson and Ripepe 2011 for a review). Several attempts have been made to calculate MER and plume height from acoustic pressure (Caplan-Auerbach et al. 2010; Ripepe et al. 2013; Lamb et al. 2015), but only in few cases, independent observations of the eruptive column have been used to constrain the acoustic modeling.

The 2010 Eyjafjallajokull eruption is one of the best analyzed and monitored ash plume eruptions, which has provided high-quality data to test models. Also if the eruption itself was small (VEI = 4), it was a powerful source of infrasound, which was recorded at thousands of kilometers from the vent (Matoza et al. 2011b). Infrasound was also recorded with an array at short source-to-receiver distances (~8 km) (Ripepe et al. 2013), and data analysis was compared to thermal cameras, plume height derived by radar, and atmospheric profile above the vent. Thermal infrared imagery, co-located with the array, provided an independent measurement of the plume exit velocity, which is used to constrain the dipolar nature of the acoustic source. Assuming the acoustic linear theory (Lighthill 1978), infrasonic excess pressure (P) was thus converted in velocity (u) of the expanding magma surface considering a dipolar source mechanism:

$$u = 2.154\left(\frac{rcP}{\rho_{air}R}\right)^{1/3}, \tag{3}$$

where r is the source-to-receiver distance, c is the speed of sound, ρ_{air} is the air density, and R is the conduit radius measured a posteriori by satellite images at the end of the eruption.

This acoustic-derived velocity can eventually be converted into MER:

$$Q(t) = \pi\rho_p R^2 u_p(t) \tag{4}$$

assuming that the plume exit velocity (u_p) is equivalent to the acoustic velocity ($u_p = u$) of the expanding surface. With this assumption, it is possible to derive instantaneous and continuous measurements of MER from acoustic observations (Fig. 35.19). The acoustic-derived MER was validated by using independent measurements of plume heights provided by the Icelandic Meteorological Office (IMO) radar. MER derived by infrasound was eventually converted into plume height using a 1D radially averaged buoyant plume theory (BPT) model and considering a reconstructed total grain size distribution. Given the hourly value of acoustic-derived source velocity and MER (Eq. 4), a BPT model accounting for plume bent over in a crosswind (Bursik 2001; Carazzo et al. 2006, 2008) was used to estimate the evolution of the column height. Ambient conditions, necessary to

solve the BPT equations, were supplied interpolating wind field and temperature profiles from the European Centre for Medium-Range Weather Forecasts (ECMWF) reanalysis ERA-Interim data archive. Plume height derived from infrasound (Fig. 35.20) shows a good match with radar measurements, which was observed to rise up to 6–8 km between May 13 and 18, when the wind was lowest, while decreases down to 4–5 km in case of high winds.

This result is suggesting that infrasound can contribute significantly to the understanding of the plume dynamics and allows real-time determination of eruption source parameters. At the same time, the misfit between MER and measured plume height (Fig. 35.19) recalls how atmospheric conditions are of primary importance not only for infrasound propagation but also to derive the volcanic source parameter.

Similar approach has been successfully applied to calculate the MER of two explosive eruptions occurred at Mt. Redoubt in 2009. Also in this case, the velocity derived by infrasound has been constrained using the Doppler radar and is consistent with a dipolar source giving an acoustic-derived MER, which is compatible with the observed plume height (Lamb et al. 2015).

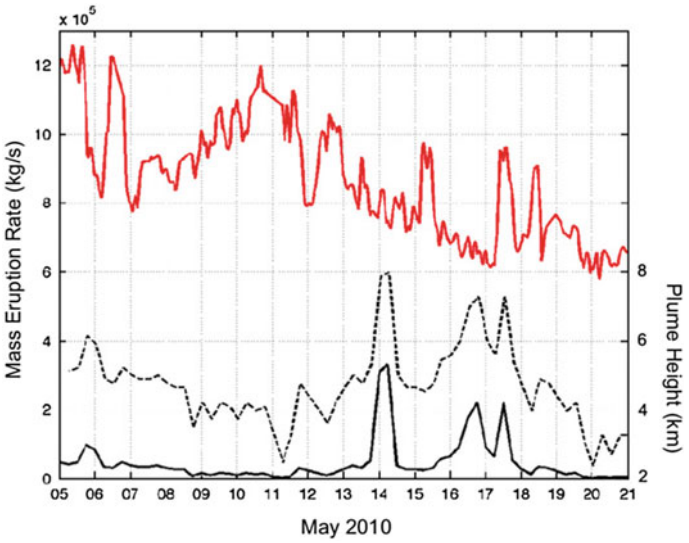

Fig. 35.19 MER calculated from infrasound measurements (red line) and assuming a vent radius of 25 m. Plume height measured by the IMO radar (black line) and derived MER (dashed black line) with the empirical equation proposed by Mastin et al. (2009)

35.4.3.1 Integrated Microwave and Infrasound Studies

Eruption source parameters derived by infrasound can be also constrained by independent measurements using X-band and/or C-band radar deployed in the proximity of the volcanic vent. Microwave weather (MW) radars, being able to penetrate to some extent the optically thick plume, have shown great potentials in evaluating real-time grain size distribution and amount of erupted material (Marzano et al. 2013; Vulpiani et al. 2016), and thus proved to be fundamental instruments to derive eruptive source parameters and for a quantitative estimation of ash (Fig. 35.21).

An algorithm, called volcanic ash radar retrieval (VARR), has been developed in the recent years using radar systems operating at S-, C-, and X-bands at single and dual polarization. This algorithm can provide probability of ash eruption in percent, but one key issue, which is still open, is its extension to the automatic detection of the ash plume onset as early-warning system for volcanic hazard prediction.

Very low reflectivity correlated to small plume can be responsible for missed detection, whereas, false detection could instead occur when rain clouds, developing close to the volcano vent, are confused with ash plumes. In this context, infrasound can be used to trigger automatic procedure of radar analysis, increasing the potentiality for an operational eruption onset early-warning system by combining the two ground-based measurements together.

The integration between MW radar and infrasound is becoming reality at Mt. Etna where the X-band radar system (working at 9.4 GHz) permanently positioned at the Catania airport (Sicily, Italy), at approximately 32 km far away from the Mt. Etna crater is integrated with the real-time automatic early-warning system issued by the infrasonic arrays located at <6 km from the craters. The Catania MW radar covers an area within a circle of 160 km radius every 10 min (Montopoli et al. 2014).

In the case of the November 23, 2013, LF event, the MW radar-based maximum plume height above the vent was about 11.2 km (7.9 km above the vent), and it was reached almost 17 min. after the maximum acoustic pressure (Fig. 35.22). If we assume that acoustic pressure is related to exit velocity, the amplitude of the infrasound detected by the array should represent the evolution of the plume injection rate with time. In this case, time shift between the MW radar and infrasound can be explained as the time necessary for the plume to reach its maximum height, and therefore, it is related to the plume rising velocity. While infrasound is peaking the increase of pressure at the vent, the radar is detecting the MW maximum values above the vent. From the time delay between the plume height measured by the radar and the infrasonic pressure from infrasonic array (Fig. 35.22), it is possible to estimate that the average uprising velocity of the erupted mixture, that is, the vertical component, is about 7.7 m/s, whereas the horizontal component due to the wind is about 11.7 m/s. These estimates seem to be consistent with a buoyancy-driven ascent for volcanic plumes (Sparks et al. 1997) confirming that the integration of radar and infrasound is an ideal ingredient for an automatic ash

eruption onset early warning within a supersite integrated system. Moreover, this may provide also an estimate of the mean buoyant plume velocity field, which is a key factor to predict ash plume dispersion and to mitigate the risk for aviation.

35.5 Conclusions

Infrasound has increased significantly the potentials of volcano monitoring both at local and regional scale, with direct impact on civil protection. Automatic systems based on infrasound are used operationally already and future improvements will reinforce this technique especially when integrated with other ground-based or satellite observations. We showed how infrasound can be used to detect and notify, automatically and in real time, the occurrence of density currents which can be tracked with a dedicated array processing (Fig. 35.7). early warning of density current has been tested and tuned for several years and is currently being adopted for avalanche analysis and risk forecasting in several sites in Europe.

Infrasound-based early-warning system of large ash-rich explosive eruption (LF) on Etna volcano is operational since 2015 delivering automatic notification of ongoing activity to local authorities, which allows a prompt application of emergency plans (Fig. 35.16). The system is based on waveform characteristics, is highly reliable (96% of success), and could be exported and applied elsewhere in the world, where a similar explosive behavior is observed.

More critical is at the moment the possibility to evaluate mass eruption rate (MER) and the plume height in real time from infrasound records, but we show how infrasound can trigger other instruments such as microwave radar able to provide critical inputs for plume evolution modeling and ash forecasting (Figs. 35.20 and 35.22).

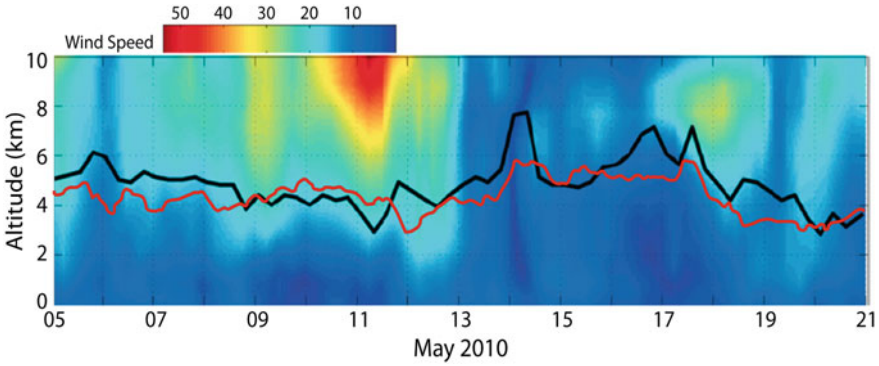

Fig. 35.20 Vertical wind speed profile at the volcano vent for the period May 5–21, 2010, retrieved from ECMWF ERA-Interim re-analysis. Plume height (black line) detected by the weather radar in Keflavik (at 155 km from the volcano) seems to reflect the wind profile reaching the maximum height when wind decreases below 10 m/s. Plume height (red line) modeling the mass eruption rate (MER) derived from infrasound observations by using the radially averaged buoyant plume theory (BPT) equations (redrawn after Ripepe et al. 2013)

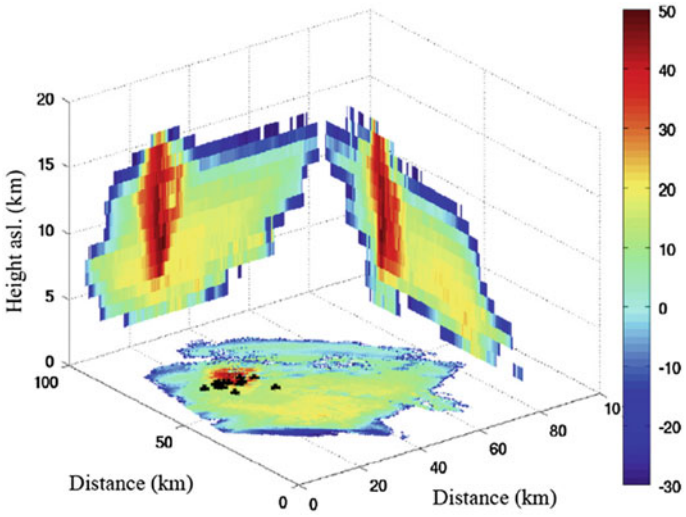

Fig. 35.21 X-band radar observation of the May, 22, 2011, Grimsvotn eruption, in Iceland (from Marzano et al. 2013) collected at a source to receiver distance of ~70 km

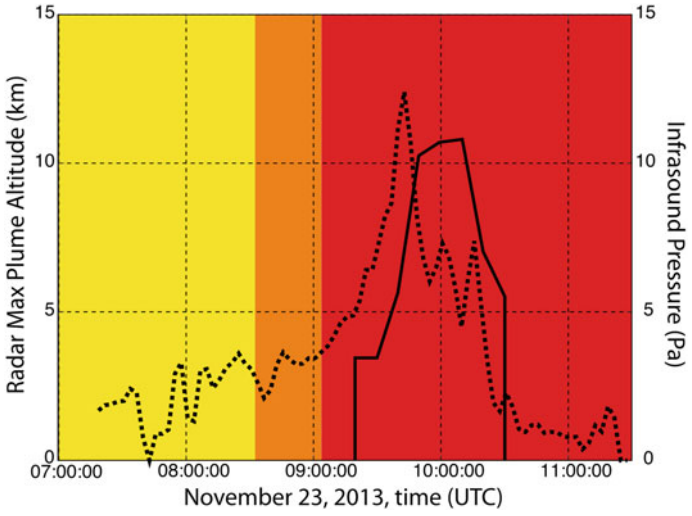

Fig. 35.22 Temporal sequence (black line) of estimated PAE, sampled every 10 min as extracted by VAD from X-band radar data, on November 23, 2013, during the Mt. Etna eruption. Instantaneous mean pressure from IS array (dotted line), sampled every 5 s and temporally averaged with 5-min window, is also shown. The automatic system operating on Etna volcano notified EW1 (orange) at 08:32 UTC and EW2 (red) at 09:04 UTC, approximately 10-20 min before the ash was eventually detected with the radar

Infrasound can propagate large distances (>1000 s km) in atmospheric waveguides, allowing volcano monitoring also at regional scale (see Matoza et al. 2019; Marchetti et al. 2019). whereas shorter time latency can be obtained by adding additional stations. This is particularly critical in specific regions of the world like Southeast Asia, where station coverage is minimal, or Kamchatka, where several active volcanoes have the same back-azimuth toward the existing arrays, thus limiting the efficiency of infrasound to detect activity at a given volcano. Nevertheless, infrasound represents today the only possible ground-based system able to be used operationally for the monitoring of active volcanoes at large scales thus possibly covering also non-instrumented volcanoes worldwide.

Infrasound monitoring of eruptive volcanoes for atmospheric ash injection is of central interest for several research projects currently being developed (e.g., ARISE, ASHE-Asia). In particular, the H2020 ARISE project, which is aimed at building a European Research Infrastructure for Atmospheric Dynamics, is already providing a prototype notification of volcanic eruptions based in infrasound record of IMS and regional infrasound arrays (see Marchetti et al. 2019). By combining IMS and regional arrays, ARISE aims to improve network efficiency and flexibility of the infrasound monitoring network in particular areas of the world but still relying on the sustainability and longevity of the CTBT—IMS network.

Acknowledgements The research leading to these results was performed within the ARISE2 project (www.arise-project.eu) and received funding from the H2020 program under grant agreement 653980.

References

Alparone A, Andronico D, Sgroi T, Ferrari F, Lodato L, Reitano D (2007) Alert system to mitigate tephra fallout hazards at Mt. Etna Volcano, Italy. Nat Hazards 43:333–350. https://doi.org/10.1007/s11069-007-9120-7

Baines PG, Sacks S (2013) Atmospheric internal waves generated by explosive volcanic eruptions In: Wadge G, Voight B (eds) The Eruption of Soufriere Hills Volcano, Montserrat from 2000 to 2010, vol 39. Geological Society, London

Baxter PJ, Horwell KJ (2015) Impacts of eruptions on human health In: The encyclopedia of volcanoes, 2nd edn, pp 1035–1047. https://doi.org/10.1016/b978-0-12-385938-9.00060-2

Bonadonna C, Folch A, Loughlin S, Puempel H (2012) Future developments in modeling and monitoring of volcanic ash clouds: outcomes from the first IAVCEI-WMO workshop on ash dispersal forcast and civil aviation. Bull Volcanol 74(1):1–10. https://doi.org/10.1007/s00445-011-0508-6

Braun T, Ripepe M (1993) Interaction of seismic and air waves recorded at Stromboli volcano. Geophys Res Lett 20. https://doi.org/10.1029/92gl02543

Buckingham M, Garcés M (1996) Canonical model of volcano acoustics. J Geophys Res 101:B4. https://doi.org/10.1029/95JB01680

Bursik M (2001) Effects of wind on the rise height of volcanic plumes. Geophys Res Lett 28 (18):3621–3624

Campus P, Christie DR (2010) Worldwide observations of infrasonic waves. In: Le Pichon A , Balc E, Hauchecorne A (eds) Infrasound monitoring for atmospheric studies. Springer, pp 185–234

Caplan-Auerbach J, Bellesiles A, Fernandez JK (2010) Estimates of eruption velocity and plume height from infrasonic recordings of the 2006 eruption of Augustine volcano, Alaska. J Volcanol Geoth Res 189:12–18. https://doi.org/10.1016/j.jvolgeores.2009.10.002

Carazzo G, Kaminski E, Tait S (2006) The route to self-similarity in turbulent jets and plumes. J Fluid Mech 547:137–148

Carazzo G, Kaminski E, Tait S (2008) On the rise of turbulent plumes: quantitative effects of variable entrainment for submarine hydrothermal vents, terrestrial and extra terrestrial explosive volcanism. J Geophys Res 113:B09201. https://doi.org/10.1029/2007JB005458

Carey S, Sigurdsson H, Mandeville C, Bronto S (1996) Pyroclastic flows and surges over water: an example from the 1883 Krakatau eruption. Bull Volcanol 57:493. https://doi.org/10.1007/bf00304435

Cioni R, Pistolesi M, Rosi M (2015) Plinian and Subplinian eruptions. In: The encyclopedia of volcanoes, 2nd edn, pp 519–536. https://doi.org/10.1016/b978-0-12-385938-9.00029-8

Clarke A, Esposti Ongaro T, Belousov A (2015) Vulcanian eruptions. In: The encyclopedia of volcanoes, 2nd edn, pp 505–518. https://doi.org/10.1016/b978-0-12-385938-9.00028-6

Cole PD, Neri A, Baxter PJ (2015) Hazards from pyroclastic density currents. In: The encyclopedia of volcanoes, 2nd edn, pp 943–956. https://doi.org/10.1016/b978-0-12-385938-9.00054-7

Dabrowa AL, Green DN, Rust AC, Phillips JC (2011) A global study of volcanic infrasound characteristics and the potential for long-range monitoring. Earth Planet Sci Lett 310:369–379

De Angelis S, Fee D, Haney M, Schneider D (2012) Detecting hidden volcanic explosions from Mt. Cleveland Volcano, Alaska with infrasound and ground-coupled airwaves. Geophys Res Lett 39:L21312. https://doi.org/10.1029/2012GL053635

Delle Donne D, Ripepe M (2012) High-frame rate thermal imagery of Strombolian explosions: implications for explosive and infrasonic source dynamics. J Geophys Res 117:B09206. https://doi.org/10.1029/2011JB008987

Delle Donne D, Ripepe M, De Angelis S, Cole PD, Lacanna G, Poggi P, Stewart R (2015) Thermal, acoustic and seismic signals from pyroclastic density currents and Vulcanian explosions at Soufrière Hills Volcano, Montserrat. In: Wadge G, Robertson REA, Voight B (eds) The eruption of Soufrière Hills Volcano, Montserrat from 2000 to 2010, vol 39. Geological Society of London, London, Memoirs, 2014, pp 169–178

Dibble RR, Kienle J, Kyle PR, Shibuya K (1984) Geophysical studies of Erebus volcano, Antarctica, from 1974 December to 1982 January. NZ J Geol Geophys 27(4):425–455

Donn WL, Balachandran NK (1981) Mount St. Helens eruption of 18 May 1980: air waves and explosive yield. Science 213:539–541. https://doi.org/10.1126/science.213.4507.539

Fee D, Garcés M, Steffke A (2010) Infrasound from Tungurahua Volcano 2006–2008: Strombolian to Plinian eruptive activity. J Volcanol Geoth Res 193:67–81. https://doi.org/10.1016/j.jvolgeores.2010.03.006

Fee D, Matoza RS (2013) An overview of volcano infrasound: from hawaiian to plinian, local to global. J Volcanol Geotherm Res 249:123–139. https://doi.org/10.1016/j.jvolgeores.2012.09.002

Firstov PP, Storcheus AV (1987) Acoustic signals that accompanied the March–June 1983 eruption at Klyuchevskoy Volcano. Volcanol Seismol 5:66–80

Garces M, Fee D, Steffke A, McCormack DP, Servranckx R, Bass H, Hetzer C, Hedlin M-, Matoza RS, Yepez H, Ramon P (2008) Capturing the acoustic fingerprint of stratospheric ash injection. EOS Trans Am Geophys Union 89(40):377–378

Gorshkov GS (1959) Gigantic eruption of the Volcano Bezymianny. Bull. Volcan 20:77–109

Hooper DM, Mattioli GS (2001) Kinematic modeling of pyroclastic flows produced by gravitational dome collapse at Soufriere Hills Volcano, Montserrat. Nat Hazards 23:65. https://doi.org/10.1023/A:1008130605558

Iguchi M, Ishihara K (1990) Comparison of earthquakes and airshocks accompanied with explosive eruptions at Sakurajima and Sawunosejima volcanoes. Ann Disaster Prev Res Inst Kyoto Univ 33(B-1):1–12

Johnson JB, Aster R, Jone R, Kyle P, McIntosh B (2011) Acoustic source characterization of impulsive Strombolian eruptions from the Mount Erebus lava lake. J Volcanol Geoth Res 177. https://doi.org/10.1016/j.jvolgeores.2008.06.028

Johnson J (2019) Local volcano infrasound monitoring. In: Le Pichon A, Blanc E, Hauchecorne A (eds) Infrasound monitoring for atmospheric studies, 2nd edn. Springer, Dordrecht, pp 989–1022

Johnson JB, Ripepe M (2011) Volcano Infrasound: a review. J Volcanol Geoth Res 206:61–69. https://doi.org/10.1016/j.jvolgeore.2011.06.006

Jolly AD, Thompson G, Norton GE (2002) Locating pyroclastic flows on Soufrière Hills volcano, Montserrat, West Indies, using amplitude signals from high dynamic range instruments. J Volcan Geoth Res 118:299–317

Kanamori H, Given JW (1982) Analysis of long-period seismic waves excited by the May 18, 1980, eruption of Mount St. Helens—a terrestrial monopole? J Geophys Res 87:5422–5432. https://doi.org/10.1029/JB087iB07p05422

Kanamori H, Mori J, Harkrider DG (1994) Excitation of atmospheric oscillations by volcanic eruptions. J Geophys Res 99:21947–21961. https://doi.org/10.1029/94JB01475

Kim K, Lees JM, Ruiz M (2012) Acoustic multipole source model for volcanic explosions and inversion for source parameters. Geophys J Int 191:1192–1204. https://doi.org/10.1111/j.1365-246X.2012.05696.x

Kogelnig A, Hubl J, Surinach E, Vilajosana I, McArdell BW (2014) Infrasound produced by debris flows: propagation and frequency content evolution. Nat Hazard 70:1713–1733. https://doi.org/10.1007/s11069-011-9741-8

Lacanna G, Ichihara M, Iwakuni M, Takeo M, Iguchi M, Ripepe M (2014) Influence of atmospheric structure and topography on infrasonic wave propagation. J Geophys Res. Solid Earth 119:2988–3005. https://doi.org/10.1002/2013JB010827

Lacanna G, Ripepe M (2012) Influence of near-source volcano topography on the acoustic wavefield and implication for source modeling. J Volcanol Geoth Res 250:9–18. https://doi.org/10.1016/j.jvolgeores.2012.10.005

Lamb OD, De Angelis S, Lavallem Y (2015) Using infrasound to constrain ash plume rise. J Appl Volcanol 4:20. https://doi.org/10.1186/s13617-015-0038-6

Lighthill J (1978) Waves in fluids. Cambridge University Press, Cambridge, London, New York, Melbourne

Marchetti E, Ripepe M, Delle Donne D, Genco R, Finizola A, Garaebiti E (2013) Blast waves from violent explosive activity at Yasur volcano. Vanuatu Geophys Res Lett 40(1–6):5838–5843. https://doi.org/10.1002/2013GL057900

Marchetti E, Ripepe M, Ulivieri G, Caffo S, Privitera E (2009) Infrasonic evidences for branched conduit dynamics at Mt. Etna volcano, Italy. Geoph Res Lett 36:L19308. https://doi.org/10.1029/2009gl040070

Marchetti E, Ripepe M, Ulivieri G, Kogelnig A (2015). Infrasound array criteria for automatic detection and front velocity estimation of snow avalanches: towards a real-time early-warning system. Nat Hazards Earth Syst Sci 15: 2545–2555. ISSN: 1561-8633. https://doi.org/10.5194/nhess-15-2545-2015

Marchetti E, Ripepe M, Campus P, Le Pichon A, Brachet N, Blanc E, Gaillard P, Mialle P, Husson P (2019) Infrasound monitoring of volcanic eruptions and contribution of ARISE to the volcanic ash advisory centers. In: Le Pichon A, Blanc E, Hauchecorne A (eds) Infrasound monitoring for atmospheric studies, 2nd edn. Springer, Dordrecht, pp 1141–1162

Marzano FS, Picciotti E, Montopoli M, Vulpiani G (2013) Inside volcanic clouds: remote sensing of ash plumes using microwave weather radars. Bull Am Meteorol Soc 94(10)

Mastin LG et al (2009) A multidisciplinary effort to assign realistic source parameters to models of volcanic ash-cloud transport and dispersion during eruptions. J Volcanol Geoth Res. https://doi.org/10.1016/j.jvolgeores.2009.01.008

Matoza RS, Fee D, Garcés MA, Seiner JM, Ramón PA, Hedlin MAH (2009) Infrasonic jet noise from volcanic eruptions. Geophys Res Lett 36. ISSN: 0094–8276. https://doi.org/10.1029/2008gl036486

Matoza RS, Fee D, Neilsen TB, Gee KL, Ogden DE (2013) Aeroacoustics of volcanic jets: Acoustic power estimation and jet velocity dependence. J Geophys Res Solid Earth 118:6269–6284. https://doi.org/10.1002/2013JB010303

Matoza R, Fee D, Green D, Mialle P (2019) Volcano infrasound and the international monitoring system. In: Le Pichon A, Blanc E, Hauchecorne A (eds) Infrasound monitoring for atmospheric studies, 2nd edn. Springer, Dordrecht, pp 1023–1077

Matoza RS, Le Pichon A, Vergoz J, Herry P, Lalande JM, Lee H, Che IY, Rybin A (2011a) Infrasonic observations of the June 2009 Sarychev Peak eruption, Kuril Islands: implications for infrasonic monitoring of remote explosive volcanism. J Volcanol Geotherm Res. https://doi.org/10.1016/j.jvolgeores.2010.11.022

Matoza RS, Vergoz J et al (2011b) Long-range acoustic observations of the Eyjafjallajokull eruption, Iceland, April-May 2010. Geophys Res Lett 38:L06308. https://doi.org/10.1029/2011GL047019

Mauk FJ (1983) Utilization of seismically recorded infrasonic and acoustic signals to monitor volcanic explosions: the El Chichon Sequence 1982—a case study. J Geophys Res 88:10385–10401. https://doi.org/10.1029/JB088iB12p10385

McNutt SR (1994) Volcanic tremor amplitude correlated with eruption explosivity and its potential use in determining ash hazard to aviation. In: Proceedings of the 1st international symposium on volcanic ash and aviation safety, vol 2047. US Geological Survey Bulletin, pp 377–385

McCormack D, Bass H, Garcés MA, Hedlin M, Yepez H (2006) Acoustic Sourveillance for Hazardous Eruptions (ASHE): a proof-of-concept experiment for operational near-real-time infrasonic remote sensing. Cities of volcanoes, Quito, January, p 2006

Medici EF, Allen JS, Waite GP (2014) Modeling shock waves generated by explosive volcanic eruptions. Geophys Res Lett 41:414–421. https://doi.org/10.1002/2013GL058340

Mikumo T, Bolt BA (1985) Excitation mechanism of atmospheric pressure waves from the 1980 Mount St Helens eruption. Geophys J Int 81:445–461

Montopoli M, Vulpiani G, Cimini D, Picciotti E, Marzano FS (2014) Interpretation of observed microwave signatures from ground dual polarization radar and space multi frequency radiometer for the 2011 Grímsvötn volcanic eruption. Atmos Meas Tech 7:537–552

Nairn IA (1976) Atmospheric shock waves and condensation clouds from Ngauruhoe explosive eruptions. Nature 259:190–192. https://doi.org/10.1038/259190a0

Nishimura T, McNutt SR (2008) volcanic tremor during eruptions: temporal characteristics, scaling and estimates of vent radius. J Volcanol Geotherm 178:10–18

Okada H, Nishimura Y, Miyamachi H, Mori H, Ishihara K (1990) Geophysical significance of the 1988–1989 explosive eruptions of Mt. Tokachi, Hokkaido, Japan. Bull Volcanol Soc Jpn Ser 2 35(2):175–203

O'Regan M (2011) On the edge of chaos: European aviation and disrupted mobilities. Mobilities 6 (1):21–30

Pallister J, McNutt S (2015) synthesis of volcano monitoring. In: The encyclopedia of volcanoes, 2nd edn, pp 1151–1171. https://doi.org/10.1016/b978-0-12-385938-9.00066-3

Prejean SG, Brodsky EE (2011) Volcanic plume height measured by seismic waves based on a mechanical model. J Geophys Res 116:B01306. https://doi.org/10.1029/2010JB007620

Reed JW.(1987) Air pressure waves from Mount St. Helens eruptions. J Geophys Res 92 (D10):11979–11992

Richards AF (1963) Volcanic sounds: investigation and analysis. J Geophys Res 68(3):919–928

Ripepe M, Barfucci G, De Angelis S, Delle Donne D, Lacanna G, Marchetti E (2016) Modeling volcanic eruption parameters by near-source internal gravity waves, Scientific reports, SREP-16–15817B

Ripepe M, Bonadonna C, Folch A, Delle Donne D, Lacanna G, Marchetti E, Höskuldsson A (2013) Ash-Plume Dynamics and Eruption Source Parameters by infrasound and thermal Imagery: the 2010 Eyjafjallajökull Eruption. Earth Planet Sci Lett 366:112–121. https://doi.org/10.1017/j.epsl.2013.02.005

Ripepe M, Ciliberto S, Della Schiava M (2001) Time constraints for modeling source dynamics of volcanic explosions at Stromboli. J Geophys Res 106(B5):8713–8727. https://doi.org/10.1029/2000JB900374

Ripepe M, De Angelis S, Lacanna G, Poggi P, Williams C, Marchetti E, Delle Donne D, Ulivieri G (2009) Tracking pyroclastic flows at Soufriere Hills Volcano. Eos Trans Am Geophys Union 90(27):229–230. https://doi.org/10.1029/2009eo270001

Ripepe M, De Angelis S, Lacanna G, Voight B (2010) Observation of infrasonic and gravity waves at Soufrière Hills Volcano, Montserrat. Geophys Res Lett 37(L00E14):1–5

Ripepe M, Marchetti E (2002) Array tracking of infrasonic sources at Stromboli volcano. Geophys Res Lett 29(22):2076. https://doi.org/10.1029/2002GL015452

Self S (2006) The effects and consequences of very large explosive volcanic eruptions. Phil Trans R Soc A 364:2073–2097. https://doi.org/10.1098/rsta.2006.1814

Simkin T, Fiske RS (1983) Krakatau 1883—The volcanic eruption and its effects. Smithsonian Institute Press, Washington D.C., p 464

Sparks RSJ, Bursik MI, Carey SN, Gilbert JS, Glaze LS, Sigurdsson H, Woods A (1997) Volcanic plumes. Wiley, Chirchester, UK, 574 p

Sparks RSJ, Young RS (2002) The eruption of Soufrière Hills Volcano, Montserrat (1995–1999): overview of scientific results. Geolog Soc Lond Momoires 21:45–69. https://doi.org/10.1144/gslmem.2002.02.1.01.03

Tahira M, Nomura M, Sawada Y, Kamo K (1996), Infrasonic and acoustic-gravity waves generated by the Mount Pinatubo eruption of June 15, 1991, In Newhall CG, Punongbayan RS (eds) Fire and Mud: Eruptions and Lahars of Mount Pinatubo, Philippines, University of Washington Press, Seattle, pp 601–614

Ulivieri G, Marchetti E, Ripepe M, Chiambretti I, De Rosa G, Segor V (2011) Monitoring snow avalanches in Northwestern Italian Alps using an infrasound array. Cold Reg Sci Technol 69:177–183. ISSN: 0165-232X. https://doi.org/10.1016/j.coldregions.2011.09.006

Ulivieri G, Ripepe M, Marchetti E (2013) Infrasound reveals transition to oscillatory discharge regime during lava fountaining: Implication for early warning. Geophys Res Let 40:3008–3013. ISSN: 0094-8276. https://doi.org/10.1002/grl.50592

Vergniolle S, Brandeis G (1994) Origin of the sound generated by Strombolian explosions. Geophys Res Lett 21(18). https://doi.org/10.1029/94gl01286

Vergniolle S, Caplan-Auerbach J (2006) Basaltic thermals and Subplinian plumes: Constraints from acoustic measurements at Shishaldin volcano, Alaska. Bull Volcanol 68(7–8):611–630. https://doi.org/10.1007/s00445-005-0035-4

Vulpiani G, Ripepe M, Valade S (2016) Mass discharge rate retrieval combining weather radar and thermal camera observations (2016). J Geophys Res 121(8):5679–5695. https://doi.org/10.1002/2016JB013191

Wadge G, Jackson P, Bower SM, Woods AW, Calder E (1998) Computer simulations of pyroclastic flows from dome collapse. Geophys Res Lett 25:3677–3680

Woulff G, McGetchin TR (1976) Acoustic noise from volcanoes: theory and experiments. Geophys J R Astron Soc 45:601–616

Yamasato H (1998) Quantitative analysis of pyroclastic flows using infrasonic and seismic data at Unzen volcano, Japan. J Phys Earth 45(6):397–416

Chapter 36
Infrasound Monitoring of Volcanic Eruptions and Contribution of ARISE to the Volcanic Ash Advisory Centers

Emanuele Marchetti, Maurizio Ripepe, Paola Campus, Alexis Le Pichon, Nicolas Brachet, Elisabeth Blanc, Pierre Gaillard, Pierrick Mialle, Philippe Husson and Thibault Arnal

Abstract In the current society, volcanic eruptions can have a great impact due to the escalation in communications and transport starting from 1950. With the advent of civil aviation and the exponential growth in the air traffic, the problem of a volcanic ash encounter has become an issue of paramount importance, which needs to be addressed in real time. This chapter describes the status of the art in volcano monitoring using infrasound technology at global, regional and local scale, the contribution of the ARISE project to volcano monitoring and to Volcanic Ash Advisory Centers (VAACs), and highlights the need for an integration of the CTBT IMS infrasound network with local and regional infrasound arrays capable of providing a timely early warning to VAACs.

36.1 Volcanic Eruptions and Civil Aviation

Volcanic eruptions have heavily impacted human lives and goods for thousands of years. The deadliest documented (and mostly recent) explosive volcanic eruptions, such as Thera ($\sim$1610 BC, Greece), Vesuvius (79 AD, Italy), Laki (1783, Iceland), Mt. Unzen (1792, Japan), Mt. Tambora (1815, Indonesia), Mt. Galunggung (1882, Indonesia), Mt. Krakatoa (1883, Indonesia), Mt. Pelee (1902, West Indies),

E. Marchetti (✉) · M. Ripepe · P. Campus
Department of Earth Sciences, University of Firenze,
via G. La Pira, 4, 50121 Florence, Italy
e-mail: emanuele.marchetti@unifi.it

A. Le Pichon · N. Brachet · E. Blanc · P. Gaillard · T. Arnal
CEA, DAM, DIF, F-91297 Arpajon, France

P. Mialle
CTBTO, IDC, Vienna International Center, 1400 Vienna, Austria

P. Husson
Meteo France, VAAC Toulouse, 42 Av. Coriolis, Cedex 1, 31057 Toulouse, France

A. Le Pichon et al. (eds.), *Infrasound Monitoring for Atmospheric Studies*,
https://doi.org/10.1007/978-3-319-75140-5_36

Mt. Kelut (1919, Indonesia) and Nevado del Ruiz (1985, Colombia) claimed a high toll of human lives: some of them had also long-range effects, which impacted communities for long periods.

To quantify the scale of an explosive volcanic eruption has been a matter of debate for several years: the most commonly adopted measure is the Volcanic Explosivity Index (VEI), combining, in a logarithmic scale, the estimate of the volume of pyroclastic material ejected by the volcano, the height of the plume and the duration of the volcanic eruption (Newhall and Self 1982).

The long-range damaging effects of ash clouds injected in the atmosphere are linked to the relation between the size of an eruption measured through the VEI and the approximate height of the plume associated to the eruption. Volcanic eruptions with low VEI values (1–2) are typically associated to plume heights spanning from hundreds of metres to, approximately, 5 km. Plumes reaching up to 15 and 25 km altitude are associated with VEI indexes 3 and 4, respectively. Larger eruptions (VEI 5–8) are associated to plume heights greater than 25 km (Newhall and Self 1982).

The advent of civil aviation, after the Second World War, has increased nearly exponentially in a few decades communications and exchanges of goods worldwide by evolving our society. This led inevitably to a progressively increased probability of having one or more flights intercepting ash clouds generated by ongoing volcanic eruptions. Over the recent decades, civil aviation has come in several instances very close to disasters caused by volcanic eruptions, since, when entering the aircraft's engines, volcanic ash impacts their normal functioning and, in the most serious cases, blocks them.

The primary mechanism for engine failure is the melting and re-solidification of volcanic ash within the jet turbine, being the melting temperature of silicate ash lower than the operating temperature of modern engines: the volcanic ash melts in the hotter sections of the engine to solidify again in the cooler section, causing ignition flameout and engine shutdown. Damages have been reported not only for short duration flight within thick ash clouds (with ash concentrations bigger than 2 g/m^3) but also for prolonged exposures to dilute ash (Casadevall 1994; Cosher and Dunn 2016).

A compilation of encounters of aircrafts with volcanic ash clouds in the period 1953–2009 (Guffanti et al. 2010) has highlighted that there have been 94 incidents confirmed as ash encounters: in 79 cases, various degrees of airframe or engine damage have been observed. Among the damaging encounters, 26 involved significant to very severe damage to engines and/or airframes and 9 were associated to engine shutdown during flight. Since 1976, there have been, on average, two reports per year of damaging encounters: most of the damaging encounters occurred within 24 h from the onset of the ash plume generation or at distances less than 1,000 km from the volcanic source.

Being more frequent than large-scale eruptions and capable of generating ash plumes reaching the cruise altitude of commercial aircrafts (most commercial aircraft travel at heights between Flight Levels FL 200 and FL 350), moderate-size

eruptions (VEI 3) have been, however, identified as responsible for nearly half of the damaging encounters.

This was evident during the eruption of the Icelandic volcano Eyjafjallajökull, with a VEI estimated between 3 and 4, that generated an ash plume with a height of approximately 9 km, and which created the highest level of air travel disruption in Europe since the Second World War for about 1 week. As discussed at the Atlantic Conference on Eyjafjallajökull and Aviation (Keflavik Airport, Iceland, 15–16 September 2010), large economic loss derived from the closure of most European airports, but the rapid decision of grounding flights in the European airspace prevented civil aviation disasters, thus saving thousands of human lives.

Considering the current number of active volcanoes in areas densely utilized by commercial flights (Indonesia, Papua New Guinea, Japan, Kamchatka Peninsula (Russian Federation), Aleutian Islands and Washington State (USA), Central America, South America, Iceland and Southern Europe) it is clear that flights are basically constantly subject to the big threat of a volcanic eruption.

As a consequence, the International Civil Aviation Organization (ICAO) recognized the critical importance of avoiding or, at least, limiting the exposure of flights to ash clouds and established in 1990 the Volcanic Ash Advisory Centers (VAACs) as part of the International Airways Volcano Watch (IAVW), a global system for monitoring, forecast of volcanic ash cloud motion and dispersion, and information issuance to aviation users. First steered by the ICAO Volcanic Ash Warnings Study Group (VAWSG) then by the International Airways Volcano Watch Operations Group (IAVWOPSG), the IAVW has now been managed since 2015 by the expert Working Groups of the ICAO MET Panel. The mission of each VAAC is to liaise between meteorologists, volcanologists and the aviation community, gather all the available information from volcano observatories, satellite images and pilot reports and issue warnings to users (pilots, MET Watch Offices, Area Control Centers, Aviation Flow Traffic Management, Airlines, Airport managers, etc.) to mitigate effects on flights over airspace subject to risks of volcanic eruptions (Evans 1991).

The information gathered by each VAAC is disseminated to other adjacent VAACs, in order to assure continuity to the issuance of warnings. There are currently nine fully operational VAACs: Anchorage (USA), Buenos Aires (Argentina), Darwin (Australia), London (United Kingdom), Montreal (Canada), Tokyo (Japan), Toulouse (France), Washington (USA) and Wellington (New Zealand). The individual VAACs are run as part of the national weather forecasting organizations of the country where they are hosted (Fig. 36.1).

Monitoring in support to VAAC's analysis includes satellite (geostationary and polar orbiting) imagery in the visible and infrared frequency band; data from different meteorological satellites (e.g. LIDAR backscattering); ground-based radars, ceilometers LIDAR and Sun photometers. The observations are complemented by VAACs with the computation of dispersion models aiming at forecasting the ash plume's trajectory.

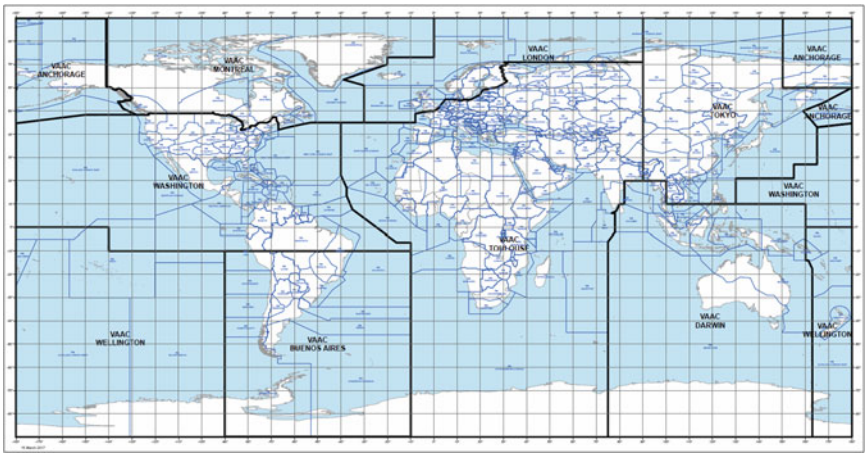

Fig. 36.1 Current (April 2017) map of areas of responsibility of the nine Volcanic Ash Advisory Centers (VAACs) distributed worldwide (from www.icao.int)

Because of their fundamental role in safety risk mitigation for civil aviation, VAACs need to continuously improve the accuracy of their observations, using the most advanced and innovative techniques available for volcano monitoring.

Another source of information comes from the States Volcano Observatories designated by the Regional Air Navigation Plans. Timely provided information on the eruption onset, location and possibly the mass of material erupted, or plume height is critical for the quality and realism of modelling of plume extension and ash dispersal forecasts. Unfortunately, these parameters are not always available as volcano monitoring performed by volcano observatories is highly inhomogeneous, and most of the active volcanoes worldwide are still unmonitored.

This has become a problem of global interest after the 2010 eruption of Eyjafjallajökull (Iceland), when ash plume of this small (VEI4) eruption caused extensive disruption of air traffic worldwide. This eruption has highlighted how exposed air traffic is to volcanic eruption and how vulnerable our economy is to volcanic ash. This leads the ICAO EUR/NAT regional VA Contingency Plan to formulate a new policy: airlines with recognized safety risk assessment procedures are allowed to fly through ash-contaminated airspace under certain conditions. Such a new ash mitigation plan based on ash concentration thresholds strongly depends on timely and proper information on the volcanic source term as input parameters for the models (Bonadonna et al. 2012).

In the last two decades, infrasound technology has gained new popularity thanks to the establishment of the infrasound monitoring on several volcano observatories on the globe and the development of the International Monitoring System (IMS) of the Comprehensive Nuclear-Test-Ban Treaty Organization (CTBTO). Volcanic infrasound originates primarily from the atmospheric perturbation caused by the explosive ejection of tephra, ash and gases from the crater and surrounding vents of

the volcano. Since most of the energy released by a volcano is injected directly into the atmosphere, infrasound observations contain more comprehensive information on the volcanic source than other technologies.

Infrasound can thus play a key role in supporting an enhanced warning system for aviation (e.g. Chen and Christie 1995; McCormac et al. 2006; Ulivieri et al. 2013) and under certain conditions infrasound can provide enhanced information capable of complying with the strict VAAC time requirements for the issuance of early warnings to civil aviation. For this purpose, infrasound is extremely promising because of the presence, in addition to experimental infrasound monitoring systems deployed on several volcanoes, of the globally distributed IMS network of 60 arrays.

36.2 Volcano Infrasound Monitoring at the Global Scale

The IMS infrasound network was designed in 1996 at the Conference on Disarmament in Geneva: after a careful evaluation of a large number of possible network configurations, the final distribution of infrasound stations (designed as arrays) has been selected as uniform as possible over the surface of the globe. The final 60-station configuration represents the most cost-effective network design capable of guaranteeing two-station detection of infrasonic waves generated by a 1-kt explosion (Dahlman et al. 2011). The size of an eruption can range, in terms of equivalent yield, from less than 1 kiloton (1kt) for small eruptions (normally associated to VEI < 2), to 100 megaton (100) MT for powerful eruptions like those of Krakatoa in 1883 (Symons 1888) and Mount St. Helens in 1980 (Donn and Balachandran 1981). The detection capability of the IMS network, once completed, should, therefore, be sufficient to detect with high confidence, eruptions with equivalent yield of 1 kt or higher located at any point on the globe (Christie and Campus 2010). At the end of 2016, the IMS infrasound network has reached more than 80% of its stations certified (Marty et al. 2019).

The performance of the infrasound network is governed by the spacing between the stations, the level of background noise at each station, the efficiency of the wind noise reducing systems installed at each station's array element, the number of array elements forming the station, the sensitivity of the infrasound sensors at all frequencies of interest, the global pattern of the upper atmospheric winds, the uptime of the stations in the network and the performance of the automatic signal detection algorithms routinely used to analyse incoming data from the global network (Christie and Campus 2010).

The average spacing between two nearest-neighbouring stations in the network is 1920 km in the Northern Hemisphere and 2027 km in the southern hemisphere. Clearly, the vast open ocean areas in the Southern Hemisphere are more challenging for monitoring than the land areas in the Northern Hemisphere: in some cases, the nearest-neighbouring distance in the vast open ocean regions exceeds 3000 km.

Stations surrounding these open ocean regions need, therefore, to have good detection capability for explosions that occur at distances of at least 3000 km.

Despite the unevenly distributed station distance between the two Hemispheres, and the large seasonal changes in the atmospheric circulation, two independent studies (Le Pichon et al. 2009; Green and Bowers 2010) have confirmed that, once completed and fully operational, the IMS infrasound network will be capable of detecting explosions down to 1 kt (4.2×10^{12} J) with high confidence all around the world and at every time of the year. The 2014 eruption of Kelut volcano, in Indonesia, produced infrasound that was recorded up to 11,000 km away from the source (Caudron et al. 2015).

Many studies have demonstrated the efficiency of IMS infrasound stations to detect remote volcanic eruptions (e.g. Campus 2006; Dabrowa et al. 2011; Matoza et al. 2011; Fee et al. 2013; Matoza et al. 2017, 2019) but also for the identification of distinct volcanic eruptions occurring simultaneously and with little back azimuth variation in the source-to-station path (Campus and Christie 2010). Besides, during the last decade pilot experiments demonstrated how acoustic remote sensing may complement seismic observations and satellite remote sensing to improve continuous monitoring of potential eruption hazard in South America (Garcés et al. 2008; IAVWOPSG/6-WP/16, 25/7/2011, Dakar, Senegal) and in Italy (Ulivieri et al. 2013).

The great potential of the IMS infrasound network in volcano monitoring, as well as in the refinement of atmospheric profiles has prompted since several years the opportunity of a cooperation with the VAACs to develop an enhanced early-warning system incorporating detections and locations coming from infrasound data (Chen and Christie 1995). After signing a cooperation agreement in 2003 with the World Meteorological Organization (WMO), the CTBTO entered in 2007 into a collaborative project with the Toulouse VAAC Centre (France). The exploratory phase of the project focused on the observation of selected volcanoes in the European and African regions through the CTBT IMS infrasound network and complemented the retrieved information with forward atmospheric transport model calculations to track the ash plume movements (Chen et al. 2008, IAVWOGPS 2008). More details on this initiative will be described in Sect. 36.4 of this chapter.

An example of the great potential of volcanic eruptions by the CTBT IMS Network has been shown by Campus et al. (2005) for the eruption of Manam volcano. Located on a small populated island about 13 km north of Papua New Guinea, Manam produced one of the largest volcanic eruptions in recent years on 27th January 2005: the eruption has been associated to a VEI 4 (Vernier et al. 2011). Infrasonic waves from Manam eruption were observed globally at a large number of IMS infrasound monitoring stations, as depicted in Fig. 36.2.

Table 36.1 provides the list of the IMS stations detecting the signal from Manam, their distance from the source (up to >13,000 km) and some indication about the characteristics of the detected signals. Detected amplitudes ranged between a few Pascal and tenths of Pascal.

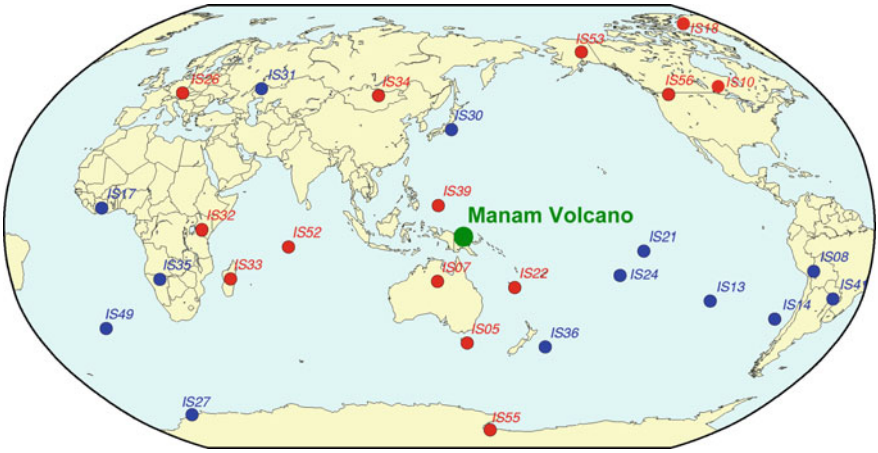

Fig. 36.2 Location of Manam volcano and the CTBT IMS stations operating in 2005. Infrasound from Manam eruption was recorded at 14 IMS arrays (red circle) while it was not detected at 13 stations (blue circles) (Campus et al. 2005)

Table 36.1 Manam eruption on 27th January 2005: list of the IMS stations which detected the eruption, their distance from the source and some indication about the quality of the detected infrasound signals (from Campus et al. 2005)

Station	Distance (km)	Frequency (Hz)	Comment
IS39 Palau	1738	0.4–2.0 0.03–0.1	Good high-frequency signal
ISO7 Warramunga	2103	0.4–2.0 0.01–0.1	High signal-to-noise ratios
IS22 New Caledonia	3086	0.05–0.1	Dominated by long-period signals
IS05 Hobart	4261	0.01–0.1	Long-period signals only. High signal-to-noise ratio
IS34 Mongolia	6874	0.05–0.1	Relatively poor detection
IS52 Diego Garcia	8040	0.05–0.1	Signal obscured by noise. Long-period signal
IS55 Windless Bight	8286	0.03–0.1	Good long-period signal
IS53 Fairbanks	9358	0.03–0.1	Good long-period signal
IS33 Madagascar	10683	0.008–0.1	Good long-period signal
IS56 Newport	10927	0.05–0.1	Good long-period signal
IS18 Qaanaaq	11604	0.05–0.1	Marginal detection
IS32 Kenya	12032	0.03–0.1	Weak, but clear detection
IS10 Lac du Bonnet	12383	0.05–0.1	Very weak signal?—marginal
IS26 Freyung	13257	0.05–0.1	Weak, but clear detection

36.3 The ARISE Project and Infrasound Notification of Volcanic Eruptions

The efficiency of infrasound monitoring is strongly controlled by the atmosphere, which affects infrasound propagation. Whether a signal will be recorded at a given array, depends on the atmospheric vertical temperature and wind profile, which changes dramatically with time. For this reason, long-range infrasound detections are not necessarily reflecting the volcanic source term, and thus reliable infrasound observation of volcanic eruptions is generally range limited. The context described in the first two sections has generated an increasing interest towards the development of collaborative studies and applications to better refine the atmospheric profiles and improve weather forecasts for the benefit of society.

In 2012, a new initiative, the Atmospheric dynamics Research Infrastructure in Europe (ARISE), was funded in the framework of the FP7 European Commission (EC) Program as a Design Study project, aiming at better refining the atmospheric profiles and improve weather forecasts for the benefit of Society (www.arise-project.eu). ARISE aims at establishing a unique atmospheric research and data platform in Europe, combining theoretical modelling with multiple technologies (infrasound, lidar, airglow, radars, microwave radiometry, ionospheric and satellites observations) to improve our understanding of the dynamics of the middle and upper atmosphere.

The ARISE2 project, newly funded under the Horizon 2020 EC Programme (2015–2018), includes 24 Institutes and Universities, belonging to 10 European Member States (France, Germany, United Kingdom, Italy, the Netherlands, Czech Republic, Romania, Ireland and Sweden), 4 Associated Countries (Israel, Switzerland, Norway and Iceland), 1 International Organization (EMSC) and 3 African Countries (Madagascar, Tunisia and Ivory Coast). ARISE2 is more oriented towards optimizing the infrastructure, providing easy-to-use services and open data products to a large community. The coverage of this infrastructure is spanning from Europe to outlying regions, including polar and equatorial regions.

ARISE brings together expertise in atmospheric dynamics, infrasound propagation and volcanology, and aims at improving the efficiency of infrasound monitoring for the detection and notification of volcanic eruptions in Europe. Due to its multidisciplinary nature and to the large spectrum of technologies used to achieve its targets, ARISE is providing an unprecedented system to support the monitoring of natural hazards, in particular of extreme weather events and volcanic eruptions, thus providing a new tool in support to civil aviation.

For this reason, one of the pillars of ARISE in Europe is the monitoring of volcanic eruptions through the combined use of the global IMS, regional and local infrasound networks and stations. Local infrasound observations are investigated to infer volcanic source parameters such as the plume height or mass eruption rate (see Ripepe and Marchetti 2019, for a review). Moreover, local, regional and global records are compared to analyse the potential of long-range observations to reliably reconstruct the pressure time history at the source (Sect. 36.4). This suggests how

combining volcano monitoring and atmospheric dynamics models will allow progress in the detection and notification of volcanic eruptions worldwide and offer new capability to the VAACs to facilitate their daily operations.

36.4 The ARISE Project and the CTBT IMS Network: The Volcanic Information System (VIS)

Infrasound revealed to be extremely efficient both in providing real-time reliable source term parameters from local (tens of km) observations, necessary for improved modelling ash dispersal in the atmosphere and also in monitoring activity from long-range (thousands of km) observations of unmonitored volcanoes. A proper modelling of the ash plume dispersion in the atmosphere is strongly controlled by source term information that is often missing (Bonadonna et al. 2012). Dedicated analyses of remote infrasound signals can cover this gap, providing continuous time information on the source terms. In this regard, it was shown that the eruption chronology can be reconstructed from infrasound signals recorded hundreds of kilometres away from the source with greater temporal resolution compared with the explosion origin times inferred by satellite data alone (Matoza et al. 2011). Other studies further evaluated the potential of the remote infrasound measurements to provide a first-order estimate of the source amplitude (Tailpied et al. 2016).

Eruptions are either effusive or explosive in their behaviour, the largest eruptions being sometimes accompanied by significant release of ash in the upper atmosphere. Studies are ongoing to determine the type of eruption class, its intensity and estimate ash height from the characteristics of the detected infrasound signals and the maximum range for observing these signals. To assess the monitoring capabilities of remote infrasound receivers, it is necessary to predict the signal amplitude at any location, and further evaluate whether the signal is confidently detectable above the noise level at the receivers. Today, numerical modelling techniques provide a basis to better understand the role of different factors describing the source and the atmosphere that affect propagation predictions.

The concept of a Volcanic Information System (VIS) has been proposed in cooperation with CTBTO and the Toulouse VAAC. VIS takes its origins from the WMO-CTBTO cooperation agreement described in Sect. 36.2 (IAVWOGPS, 2008; IAVWOGPS, 2011). This system, applied to the detections of the IMS infrasound network produced by the International Data Center (CTBT-IDC, Vienna), includes long-range propagation effects. A numerical modelling technique based on a frequency-dependent attenuation relation was developed to assess the detection capability of any network to monitor explosive sources. It accounts for near-real time, middle atmospheric specifications as provided by ECMWF's (European Centre for Medium-Range Weather Forecasts, http://www.ecmwf.int/) operational

high spatial resolution forecasts (HRES) between 30 and 60 km (Le Pichon et al. 2012).

Well-monitored volcanoes offer a unique opportunity to validate the proposed approach. In Europe, quasi-permanent infrasound signals from Mt. Etna recorded in near and far field were used to develop a prototype version of the VIS which will contribute to the planned notification system of ongoing volcanic eruption to the VAACs (Mialle et al. 2015).

Figure 36.3 shows an example of attenuation map for infrasound signals produced by the eruptions of the Calbuco volcano in southern Chile in 2015. This volcano had not shown any signs of activity for more than 43 years and entered into eruption ejecting a thick plume of ash to an altitude of almost 20 km on 22nd and 23rd April 2015 (VEI 4) (Van Eaton et al. 2016). Simulations explain to a first order the detection capability of the IMS network with a maximum attenuation of ~70 dB allowing signals to be detected above the background noise. Incorporated into the VIS, these simulations provide an estimate of the confidence level of the detections likely associated with the eruption.

As observations in numerical weather prediction (NWP) models are often limited to the low atmosphere due to the lack of operational atmospheric soundings in the middle atmosphere (~30–90 km altitude), realistic wind speed uncertainties in the stratopause region (40–50 km altitude) (Le Pichon et al. 2015) are now incorporated in the VIS to provide a confidence level of the notification (Tailpied et al. 2016).

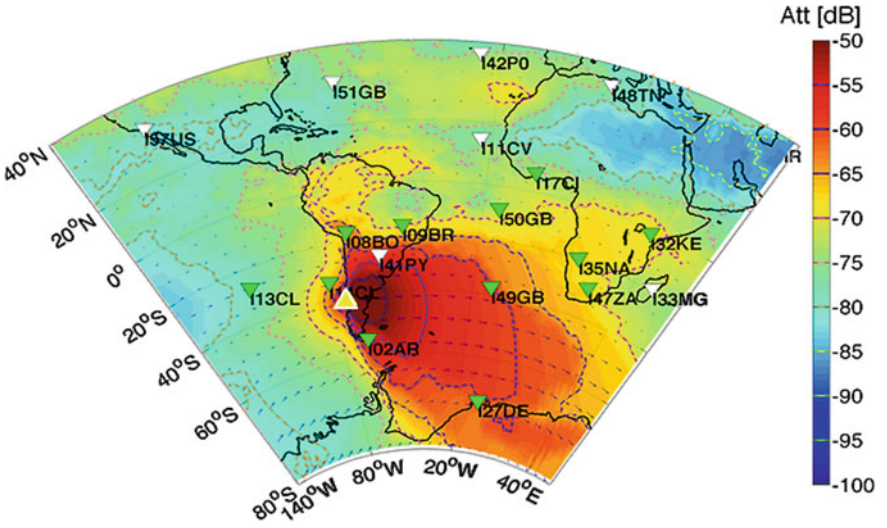

Fig. 36.3 Attenuation map for infrasound signals produced by the eruptions of Calbuco volcano on 22nd and 23rd April 2015. The colour-coded attenuation (in dB) is calculated with respect to a reference distance of 1 km to the source. Simulations are carried out at a frequency of 0.5 Hz and account for range-dependent along-path profiles (ECMWF HRES model). Arrows indicate the ECMWF stratospheric wind field averaged between 40 and 60 km altitudes

In a further stage, following earlier work of Dabrowa et al. (2011), advanced signal parameters characterizing the intensity of the eruptions (VEI) and the amount of ash injected into the atmosphere, as well as ash height, will be explored. Such studies are strongly encouraged by several VAACs including Toulouse and IAVWOPSG. On the one hand, they will help the scientific community to better understand the specificity of individual active volcanoes, on the other hand, they will contribute to volcano warning systems in Europe and worldwide.

The global pattern of the upper atmospheric winds and the performance of the automatic signal detection algorithms routinely used to analyse incoming data play a key role in the detection capability of an infrasound array. The atmospheric vertical profile, which undergoes dramatic seasonal changes, is strongly affecting infrasound propagation causing, in certain period of the year, at least partial loss of information on the volcanic source (Le Pichon et al. 2012). Near-field records of volcanic activity, although still affected by local wind noise and topography (Lacanna et al. 2014), do not suffer from the high spatio-temporal variability of middle atmospheric conditions along the propagation paths. For this reason, complementing the IMS network with additional local infrasound arrays will significantly enhance the network detection capability while increasing the confidence levels of the VIS notifications in specific geographical areas currently suffering from limited coverage.

36.5 ARISE Contribution to Volcano Monitoring with Local and Regional Infrasound Arrays

Based on the Treaty, the IMS infrasound arrays are built at locations with the lowest possible background noise in order to improve signal detection. The proper choice of the installation site, combined with specifically designed wind noise reducing systems and high sensitive microbarometers, ensures the capability of IMS infrasound arrays of detecting signals as low as 1 mPa around 1 Hz (Ponceau and Bosca 2010).

Although very few IMS stations are located in proximity of active volcanoes, the network density results into a median distance from any given volcano and the nearest IMS infrasound array of 980 km (with a standard deviation, std, of 820 km): this results in a mean source-to-station travel time of the infrasonic waves of approximately 55 min (Fig. 36.4). The effect of propagation for such distances might be significant, resulting in a drastic modification of the infrasonic waveform from what is recorded nearby the source. Such an effect is more critical in certain areas of the globe, like Southeast Asia, or Central America, where minimum distances exceed 2000 km.

The global coverage of active volcanoes with IMS arrays will improve slightly in the near future when the IMS network will be completed, with 60 stations

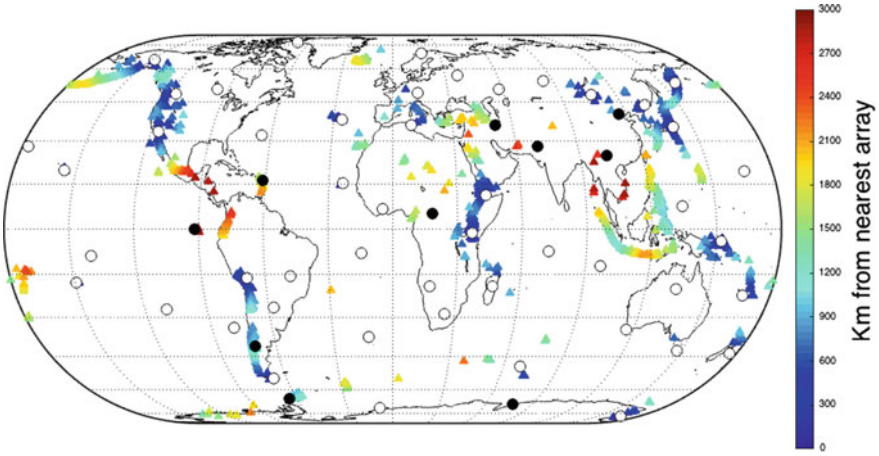

Fig. 36.4 The IMS infrasound network: white circles (49) correspond to certified stations as of December 2016. Black circles (10) correspond to stations not yet installed. Triangles correspond to volcanoes active during the last 10,000 years (GVP, http://volcano.si.edu). The volcanoes are colour-coded according to the distance from the closest certified IMS infrasound array

sending real-time data to International Data Center (CTBT-IDC, Vienna). The expected distance from active volcanoes to the nearest infrasound array will be smaller (median = 840 km, std = 590 km) still resulting into a mean travel time to the closest IMS array of 46 min.

Although the IMS network provides high-quality data at a global scale, additional infrasound arrays might improve significantly the capability of the global network to detect, identify and characterize a volcanic eruption based on waveform characteristics, disturbed by propagation effects at large source-to-receiver distances, by reducing latency between event occurrence and signal detection.

To enhance the IMS infrasound network performance through the use of refined atmospheric models, confidence levels associated to the automatic detections of eruptions and the integration of information deriving from non-IMS stations deployed in the vicinity of active volcanoes are explored. In this context, the establishment of additional infrasound arrays, located at short or regional distances from the most active volcanoes and less biased by the source-to-station propagation effects, might dramatically improve the performance of the IMS infrasound network and provide the key contribution for the issuance of early warnings for the VAACs.

Starting from 2000 onwards, several small aperture (<150 m) 4-element infrasonic arrays have been installed permanently in the vicinity (<20 km from the vents), of active volcanoes for enhanced volcano monitoring (e.g. Ripepe and Marchetti 2002; Garcés et al. 2003; Ripepe et al. 2009): these installations have significantly contributed to acquire a major insight on volcanic sources, pyroclastic flows, explosive dynamics and eruption source parameters.

36.5.1 Infrasound Notification of Explosive Eruptions at Mt. Etna

Mount Etna volcano, in Southern Italy, is a stratovolcano of basaltic composition that showed, in its eruptive history, activity spanning from lava flows to Plinian eruptions. Current activity is typically effusive, with explosive eruptions (called lava fountaining, LF), typically considered as VEI2 events, able to eject large ash volumes in the atmosphere up to 15 km as during the December 2015 eruptive episode. With three airports located within 100 km from the vent, such an activity can affect local air traffic as well as flights from Europe to Africa, within the area of surveillance of the Toulouse VAAC.

The most serious ash encounter occurred in 2000, when an Airbus A320 with 137 passengers on board had the cockpit window damaged by volcanic tephra shortly after taking off at Catania airport (located about 30 km south of the volcano): the Airbus was forced to immediately return to Catania airport and to perform an emergency landing. Significant volcanic activity at Etna restarted since 12th January 2011 and is still ongoing, with more than 50 episodes recorded since the onset of this new phase (Ulivieri et al. 2013).

Lava Fountains at Etna volcano show a peculiar infrasound signature, characterized by a clear increase in the number and amplitude of discrete transients which approaching the eruption can occur at the rate of 1 transient per second, eventually merging together in an oscillatory signal during the most violent eruptive phase (Ulivieri et al. 2013).

This peculiar and persistent characteristic has been used to realize an automatic early-warning system totally based on the infrasonic record. Infrasound is recorded by two small aperture (<150 m) arrays operated by University of Florence (UNIFI) and deployed at local distance from the volcano (about 5 km from the vents). The early-warning system is based on the amplitude and persistency of infrasonic signal radiated by the volcanic eruption through an infrasound parameter (IP), which results from the product between the number of infrasound detection in a given time window and their mean amplitude (Ripepe and Marchetti 2019). Since 2011, the early-warning system provided successfully automatic notification for 94.3% of the eruptive episodes with only six of false alerts and three episodes not detected for high wind noise. The pre-alert phase was issued $\sim$76 min before the occurrence of the eruptive eruption. The early-warning system is currently part of the operational alert procedure of the Italian Civil Protection and is now providing real-time data to the ARISE data portal (see Ripepe and Marchetti 2019).

The early-warning system at Etna is providing the benchmark for the development of an automatic real-time notification procedure of volcanic eruption at regional scale. Depending on propagation conditions, infrasound generated by the eruptions at Etna can be recorded at large source-to-receiver distances. The correlation with near-field records demonstrates how efficient is the stratospheric ducting to preserve waveforms at regional distances (Fig. 36.5).

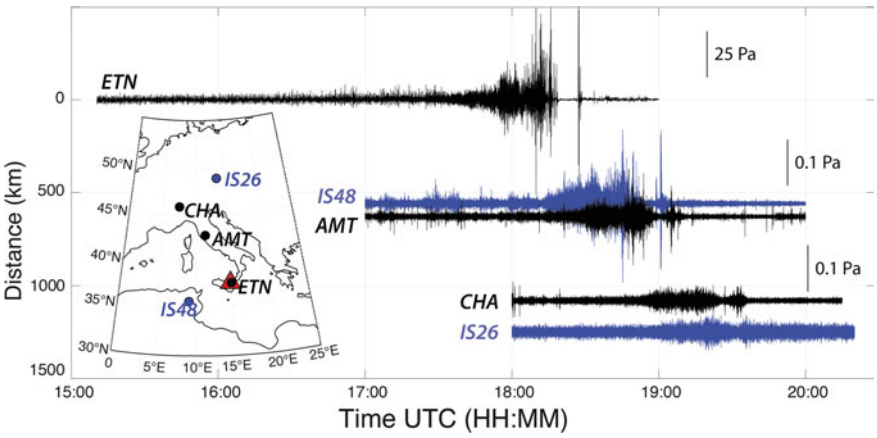

Fig. 36.5 Infrasound records of a lava fountain (LF) at Etna volcano recorded on 16th March 2013 at IMS infrasound arrays (IS48 and IS26, blue) and UNIFI arrays (ETN, AMT and CHA) at source-to-receiver distances spanning between 5 and 1240 km. The inset is showing the position of the different arrays (circles) with respect to Etna volcano (red triangle)

In the framework of ARISE, UNIFI installed in 2012 a 4-element array (AMT) at Mt. Amiata (Tuscany, Italy): the array, located in a dense forest, is distant about 500 and 600 km from Stromboli and Etna volcanoes, respectively. With an aperture of 1.6 km, compatible with the aperture of CTBT IMS infrasound arrays, AMT provides a valuable opportunity of comparing the information on the volcanic source retrieved in near field and at regional distances.

Etna volcano had a significant lava fountain activity in 2013: the LFs have been recorded in multiple instances by the three UNIFI arrays ETN, AMT (at 630 km) and CHA (at 1080 km), as well as by the IMS infrasound stations IS26 (at 1240 km) and IS48 (at 560 km). Infrasonic waveform characteristics are preserved up to about 500–600 km (arrays ETN, AMT and IS48), while signal-to-noise ratio becomes smaller at larger distances (arrays CHA and IS26). We thus tested the reliability of delivering eruption notification using arrays at regional scale by applying to the AMT (at 630 km) and IS48 (at 560 km) arrays the same processing algorithm used at ETN (see Ripepe and Marchetti, this issue).

Figure 36.5 highlights the detections and waveforms characteristics of a lava fountain (LF) episode at Etna volcano recorded on 16th March 2013.

In general, the maximum excess pressure is always recorded immediately after the onset of the lava fountain event (identified by the black vertical bar in Fig. 36.6), although increased explosive activity is recorded much earlier: this pattern allows the issuance of a pre-alert as soon as infrasound parameter (IP) exceeds a fixed threshold (identified by the horizontal orange dashed line in Fig. 36.6).

By applying the same rationale at AMT and IS48 data, which showed features in the waveforms very similar to ETN, it has been observed that both at AMT and at

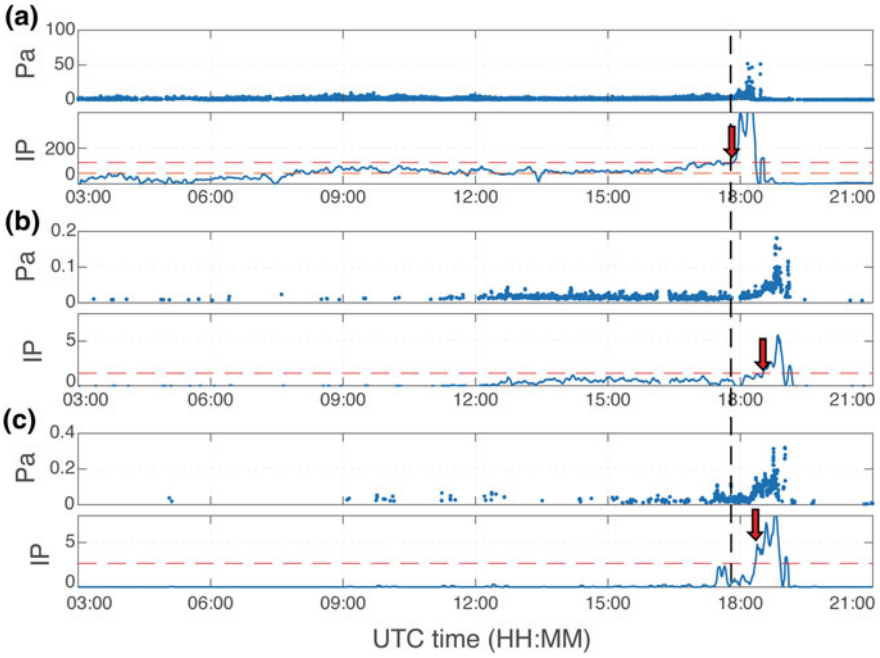

Fig. 36.6 Excess pressure (Pa) and infrasound parameter (IP) for the infrasound detections at the ETN (**a**), AMT (**b**) and IS48 (**c**) infrasound arrays for the Etna lava fountain of 16th March 2013. The event onset at 17:50 UTC is marked with the vertical black dashed line, while the red arrows mark the time when the infrasound is exceeding the fixed thresholds at the different arrays (red dashed lines), and the signal is clearly detected (17:50 UTC at ETN, 18:21 UTC at IS48 and 18:29 UTC at AMT)

IS48 the peak pressure has been recorded after the eruption onset at Etna volcano, as a consequence of the source-to-station travel time and resulting in a latency of ∼31 min for IS48 and ∼35 min for AMT array. Yet, the increase in the infrasound amplitude for the precursory explosive activity at the source has been recorded both at IS48 and at AMT. Both at IS48 and at AMT, the calculated IP has shown a strong consistency with the trend resulting from local observations at ETN and has clearly marked the onset of the precursory phase. In this specific case, the IP increase has allowed to predict the eruptive onset from a few hours with infrasound data recorded at the local ETN array, while the paroxysmal phase is clearly recorded also at distal arrays. This example shows how waveform characterization, when preserved at regional distances, can be used for robust identification of the onset of volcano eruptions and the issuance of early warnings.

We thus expand this analysis to 22 lava fountains occurred at Etna volcano in 2013 to verify how robust the long-range notification system could be. Applying the threshold value of 1 as for Fig. 36.6 to all infrasound data recorded at AMT array for the whole 2013 and with a back azimuth consistent with Etna volcano, 8 out of 22 lava fountains from Etna are clearly detected (Fig. 36.7) while no other

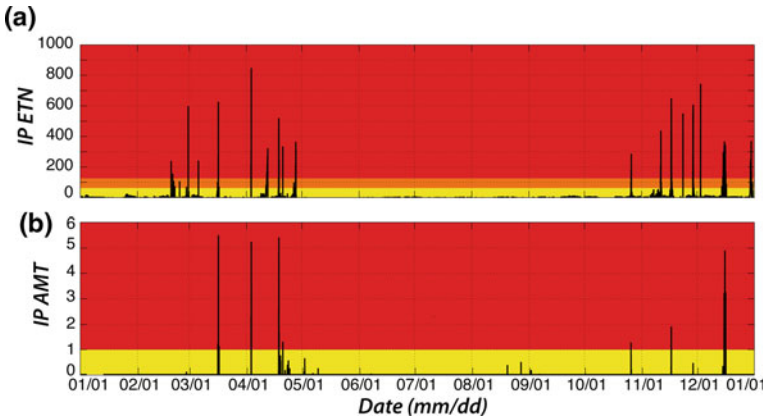

Fig. 36.7 Comparison of early warning for all lava fountains at Etna volcano during 2013 (vertical blue lines) based on infrasound recorded at the local (ETN) and regional (AMT) array. Of the 22 events occurred in 2013, eight events were clearly detected at 630 km distance from the source

signals exceeded such threshold, thus producing any false alerts. Four events could not be detected because the AMT array was not working at that time and 10 had a small amplitude. This suggests how ~43% of the lava fountains (8 out of 18) that did occur at Etna volcano in 2013 would have been picked clearly at AMT array with no false alerts.

The analysis of infrasound detections at AMT array, located at a source-to-receiver distance of 630 km from Etna volcano, clearly shows how infrasound radiated from volcanic eruptions can be recorded efficiently even at regional distances and thus used for event detection and notification. A delay time is obviously to be expected, related to propagation time of atmospheric sound, but still notification of ongoing activity would be valuable for VAACs especially for the many active volcanoes worldwide that are still lacking geophysical monitoring systems.

36.5.2 The Challenge of Latency Reduction for Volcanic Early Warnings: Calbuco Eruption, IMS Detections and Enhanced Local Monitoring

After more than 40 years of quiescence, the stratovolcano Calbuco (Los Lagos Region, South Chile) erupted on 22nd April 2015 at 2105UT (Global Volcanism Program 2015; Romero et al. 2016). The eruption, classified as VEI4 and lasting for about 90 min, generated an ash column spreading to an altitude of more than 15 km. The ash column collapse generated pyroclastic flows travelling up to 7 km

distance. A second significant eruption of longer duration started at about 0400UTC on 23rd April 2015, and injected a new energy pulse in the atmosphere.

The eruption has been recorded by several IMS infrasound arrays, located not only in South America but also at larger distances as well as by permanent small aperture array for volcano monitoring (Figs. 36.3 and 36.8). The vertical wind profiles affecting long-range propagation joint to local wind conditions made the source-to-station propagation more favourable towards north-east, resulting in a partial loss of information on the source at the closest IMS infrasound array (IS14, Juan Fernandez, Chile), located about 1000 km north-west of Calbuco. The second IMS infrasound array closest to Calbuco, IS02, Ushuaia, Argentina (some 1500 km far from the volcano) has recorded very clearly the two eruptions, on April 22nd and April 23rd. Clear detections of both eruptions have been recorded as well at IS08 (La Paz, Bolivia), located at about 2800 km from Calbuco, and IS09 (Brasilia, Brazil), distant about 3700 km from the volcano. Calbuco has been detected at more than 11,000 km also by the IMS infrasound station IS32 (Nairobi, Kenya). Figure 36.8 shows the IMS infrasound stations traces IS02, IS08 and IS09 associated to the two eruptive episodes of Calbuco and provides the back azimuths retrieved using the progressive multichannel correlation (PMCC) analysis (Cansi 1995; Cansi and Le Pichon 2008): the back azimuths of the two eruptions are fully consistent with the source location.

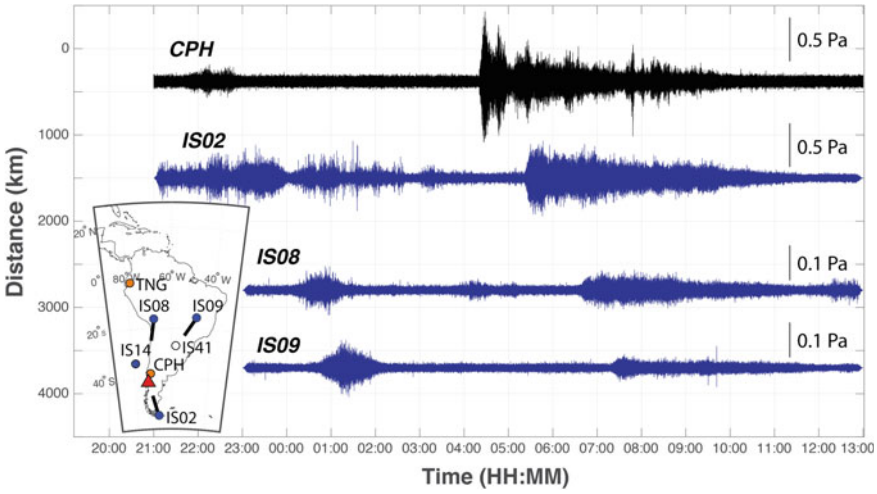

Fig. 36.8 Infrasound by the two eruptions of Calbuco volcano (22nd and 23rd April 2015) as recorded by the CPH infrasound array operated in Argentina by UNIFI and by the IMS infrasound stations IS02 (Argentina), IS08 (Bolivia) and IS09 (Brazil). The inset is showing the position of Calbuco volcano, Chile (red triangle), IMS arrays (blue circles) and retrieved back azimuths (black lines) and permanent arrays for volcano monitoring operated by UNIFI (orange circles), Copahue (CPH) and Tungurahua (TNG). IMS array IS41 (white circle), located in Paraguay at a source-to-receiver distance of 2000 km from Calbuco, was not operational at the time of the event

These results confirm the great potential of the CTBT IMS infrasound network for volcano monitoring. However, even considering the detection at the closest operational IMS infrasound station, the source-to-station travel time has trespassed the ideal latency threshold (of a few minutes), which would provide to the VAACs valuable information to issue a timely early warning to civil aviation.

During Calbuco eruption, UNIFI has operated a small aperture array at approximately 380 km from the volcano: the array was deployed in Argentina, nearby Copahue volcano (CPH in Fig. 36.8): the source-to-station travel time has been in this case about 20 min. Thanks to the reduced distance from the source, in the UNIFI waveform are visible the fine details of the eruptive process (e.g. onset time and source time function).

Latency reduction and finer characterization of the source time function are critical aspects for civil protection purposes and for the issuance of timely and reliable early warnings to civil aviation. Located at a distance from Calbuco smaller than the nearest operational IMS infrasound station, the UNIFI array has played a key role to dramatically reduce the latency for the issuance of an early warning through the relevant VAAC (Buenos Aires, Argentina) and support the modelling of ash plume dispersal.

The results of Fig. 36.8, joint to the current status of the operational IMS infrasound stations, clearly demonstrate the importance of integrating the existing network of IMS infrasound stations with additional arrays capable of reducing the source-to-station distance to a level compatible with the VAAC requirements for the timely issuance of early warnings to civil aviation.

36.6 Discussion: Strengths, Weaknesses, Opportunities and Threats of an Integrated Infrasound Network

The results of Sect. 36.4 show how long-range propagation effects accounting for near-real-time middle atmospheric specifications must be considered to obtain a reliable pressure time history at the source and a confidence level of the detection. While the former is required to infer possible constraints on the volcanic source parameters, the latter is of great use to provide to the VAACs an estimate of the reliability of the information. Although the IMS network is capable of detecting a volcanic eruption at long range, for early-warning purposes, measurements from additional local infrasound arrays would be required in most of cases. Here, the role of the ARISE project is crucial for generating a synergy between the CTBT IMS infrasound network and other existing infrasound arrays located in the vicinity of volcanic sources.

The realization of an integrated monitoring platform capable of joining detections coming from infrasound arrays located in near field or at regional distances and from the global IMS infrasound network will allow an enhanced volcano

monitoring sensitivity for the benefit of VAACs, in particular in specific geographical areas currently suffering from limited coverage.

The integration phase will be delicate, having to assess the level of compatibility of the results acquired through the CTBT IMS infrasound network and the non-IMS infrasound arrays. Different instrumental responses, data acquisition systems, array design, wind noise reducing systems and other data acquisition aspects not necessarily compliant with the minimum requirements for CTBT IMS infrasound stations should be considered.

To assure an enhanced volcano monitoring in support to VAACs, non-IMS arrays should also comply with the stringent data availability requirements for IMS infrasound stations: a set of basic and common requirements for the maintenance of such arrays might be, therefore, envisaged.

The integration process under a common platform of IMS and non-IMS infrasound monitoring stations will certainly offer the opportunity of studying in more detail the source, as well as the source-to-station and propagation effects in near field and far field. Due to its complexity, the integration phase might require a considerable amount of time, which might delay its key contribution to VAACs. Intermediate stages towards a full integration are envisaged in order to facilitate the swift establishment of a long-term and stable cooperation with VAACs.

Acknowledgements The research leading to these results was performed within the ARISE2 project (http://arise-project.eu/) and received funding from the H2020 programme under grant agreement 653980.

References

Bonadonna C, Folch A, Loughlin S, Puempel H (2012) Future developments in modeling and monitoring of volcanic ash clouds: outcomes from the first IAVCEI-WMO workshop on ash dispersal forecast and civil aviation. Bull Volcanol 74(1):1–10. https://doi.org/10.1007/s00445-011-0508-6

Campus P, Christie DR, Brown D (2005) Detection of infrasound from the eruption of Manam volcano on January 27, 2005. In: Proceedings of the 2005 infrasound technology workshop, Tahiti, 28 Nov–2 Dec 2005

Campus P (2006) Monitoring volcanic eruptions with the IMS infrasound network. Inframatics 15:6–12

Campus P, Christie DR (2010) The IMS infrasound network: worldwide observations of infrasonic waves. Infrasound monitoring for atmospheric studies. Springer Geosciences, p 745. ISBN: 978-1-4020-9507-8

Cansi Y (1995) An automatic seismic event processing for detection and location: the P.M.C.C. Method. Geophys Res Lett 22:1021–1024. https://doi.org/10.1029/95GL00468

Cansi Y, Le Pichon A (2008) Infrasound event detection using the progressive multi-channel correlation algorithm. Handbook of signal processing in acoustics, chapter 77. Springer, New York, pp 1423–1434. ISBN: 978-0-387-77698-9

Casadevall TJ (1994) The 1989–1990 eruption of Redoubt volcano, Alaska: impacts on aircraft operations. J Volcanol Geoth Res 62(1):301–316

Caudron C, Taisne B, Garcés M, Alexis LP, Mialle P (2015) On the use of remote infrasound and seismic stations to constrain the eruptive sequence and intensity for the 2014 Kelud eruption. Geophys Res Lett 42:6614–6621. https://doi.org/10.1002/2015GL064885

Chen P, Christie DR (1995) Infrasonic detection of volcanic explosions by the International Monitoring System: implications for aviation safety. In: 2nd meeting international civil aviation volcanic ash warning study group, 2 Nov 1995, Montreal, Canada

Chen P, Wotawa G, Becker A (2008) The importance of atmospheric transport modelling: over ten years of cooperation between the World Meteorological Organization and the CTBTO, CTBTO Spectrum, p 11

Christie DR, Campus P (2010) The IMS infrasound network: design and establishment of infrasound stations. Infrasound monitoring for atmospheric studies. Springer Geosciences, p 745. ISBN: 978-1-4020-9507-8

Cosher CR, Dunn MG (2016) Comparison of the sensitivity to foreign particle ingestion of the GE-F101 and P/W-F100 engines to modern aircraft. J Eng Gas Turbines Power 138 (12):121201, Paper No: GTP-16-1251. https://doi.org/10.1115/1.4034021

Dabrowa AL, Green DN, Rust AC, Phillips JC (2011) A global study of volcanic infrasound characteristics and the potential for long-range monitoring. Earth Planet Sci Lett 310:369–379

Dahlman O, Mackby J, Mykkeltveit S, Haak H (2011) Detect and deter: can countries verify the nuclear test ban?. Springer

Donn WL, Balachandran NK (1981) Mount St. Helens eruption of 18 May 1980: air waves and explosive yield. Science 213:539–541

Evans JE (1991) Development of a real-time ATC volcanic ash advisory system based on the future aviation weather system. In Proceedings of the first international symposium on volcanic ash and aviation safety. US geological survey bulletin 2047

Fee D, McNutt SR, Lopez T, Arnoult KM, Szuberla CAL, Olson JV (2013) Combining local and remote infrasound recordings from the 2009 redoubt volcano eruption. J Volcanol Geoth Res 259:100–114. https://doi.org/10.1016/j.jvolgeores.2011.09.012

Garcés M, Harris A, Hetzer C, Johnson J, Rowland S, Marchetti E, Okubo P (2003) Infrasonic tremor observed at Kilauea Volcano, Hawaii. Geophys Res Lett 30:20. https://doi.org/10.1029/2003GL018038

Garcés M, Fee D, Steffke A, McCormack DP, Servranckx R, Bass H, Hetzer C, Hedlin M, Matoza RS, Yepez H, Ramon P (2008) Capturing the acoustic fingerprint of stratospheric ash injection. EOS Trans Am Geophys Union 89(40):377–378

Global Volcanism Program (2015) Report on Calbuco (Chile). Venzke E (ed) Bulletin of the global volcanism network, vol 40, p 6, Smithsonian Institution

Green DN, Bowers D (2010) Estimating the detection capability of the International Monitoring System infrasound network. J Geophys Res 115:D18. https://doi.org/10.1029/2010JD014017

Guffanti M, Casadevall TJ, Budding K (2010) Encounters of aircraft with volcanic ash clouds; a compilation of known incidents, 1953–2009. U.S. geological survey data series 545, Ver. 1.0, p 12, plus 4 appendixes including the compilation database. http://pubs.usgs.gov/ds/545

IAVWOPSG: International Airways Volcano Watch Operations Group (2008) Volcano infrasound project between Toulouse VAAC and CTBTO, IAVWOPSG. In: Fourth meeting, /4-IP/8, 2/9/2008, 15–19 Sept 2008, Paris, France

IAVWOPSG: International Airways Volcano Watch Operations Group (2011) Report on IAVWOPSG/5 conclusion 5/14—use of infrasound data in support of the VAACs, IAVWOPSG. In: Sixth meeting, /6-WP/16, 25/7/11, 15–23 Sept 2011, Dakar, Senegal

ICAO: International Civil Aviation Organization (2007) Annex 3 to the convention on international civil aviation. Meteorological service for international air navigation, 16th edn. http://www.wmo.int/pages/prog/www/ISS/Meetings/CT-MTDCF-ET-DRC_Geneva2008/Annex3_16ed.pdf

Lacanna G, Ichihara M, Iwakuni M, Takeo M, Iguchi M, Ripepe M (2014) Influence of atmospheric structure and topography on infrasonic wave propagation. J Geophys Res Solid Earth 119:2988–3005. https://doi.org/10.1002/2013JB010827

Le Pichon A, Vergoz J, Blanc E, Guilbert J, Ceranna L, Evers LG, Brachet N (2009) Assessing the performance of the International Monitoring System infrasound network: geographical coverage and temporal variabilities. J Geophys Res 114:D08112. https://doi.org/10.1029/2008JD010907

Le Pichon A, Ceranna L, Vergoz J (2012) Incorporating numerical modelling into estimates of the detection capability of the IMS infrasound network. J Geophys Res. https://doi.org/10.1029/2011jd0166702009

Le Pichon A, Assink JD, Heinrich P, Blanc E, Charlton-Perez A, Lee CF, Keckhut P, Hauchecorne A, Rüfenacht R, Kämpfer N, Drob DP, Smets PSM, Evers LG, Ceranna L, Pilger C, Ross O, Claud C (2015) Comparison of co-located independent ground-based middle-atmospheric wind and temperature measurements with Numerical Weather Prediction models. J Geophys Res 120. https://doi.org/10.1002/2015jd023273

Marty J (2019) The IMS infrasound network: current status and technological developments. In: Le Pichon A, Blanc E, Hauchecorne A (eds) Infrasound monitoring for atmospheric studies, 2nd edn. Springer, Dordrecht, pp 3–62

Matoza RS, Vergoz J, Le Pichon A, Ceranna L, Green DN, Evers LG, Ripepe M, Campus P, Liszka L, Kvaerna T, Kjartansson E, Höskuldsson Á (2011) Long-range acoustic observations of the Eyjafjallajkull eruption, Iceland, April–May 2010 Geophys Res Lett 38 (6)

Matoza RS, Green DN, Le Pichon A, Shearer PM, Fee D, Mialle P, Ceranna L (2017) Automated detection and cataloging of global explosive volcanism using the International Monitoring System infrasound network. J Geophys Res Solid Earth 122. https://doi.org/10.1002/2016jb013356

Matoza R, Fee D, Green D, Mialle P (2019) Volcano infrasound and the international monitoring system. In: Le Pichon A, Blanc E, Hauchecorne A (eds) Infrasound monitoring for atmospheric studies, 2nd edn. Springer, Dordrecht, pp 1023–1077

McCormack D, Bass H, Garcés MA, Hedlin M, Yepez H (2006) Acoustic Surveillance for Hazardous Eruptions (ASHE): a proof-of-concept experiment for operational near-real-time infrasonic remote sensing. Cities of Volcanoes, Quito, p 2006

Mialle P, Brachet N, Gaillard P, Le Pichon A, Blanc E, Tailpied D, Marchetti E, Ripepe M, Husson P, Ceranna L, Khemiri L, Friha N (2015) Towards a volcanic notification system with infrasound data in support of the VAACs in the framework of ARISE project. In: Science and Technology Conference, Vienna, Austria, 22–26 June 2015

Newhall CG, Self S (1982) The volcanic explosivity index (VEI): an estimate of explosive magnitude for historical volcanism. J Geophys Res 87:1231–1238. https://doi.org/10.1029/JC087iC02p01231

Ponceau D, Bosca L (2010) Low-noise broadband microbarometers. Infrasound monitoring for atmospheric studies. Springer Geosciences, p 745. ISBN: 978-1-4020-9507-8

Ripepe M, De Angelis S, Lacanna G, Poggi P, Williams C, Marchetti E, Donne DD, Ulivieri G (2009) Tracking pyroclastic flows at Soufrière Hills Volcano. EOS Trans AGU 90(27):229–230. https://doi.org/10.1029/2009EO270001

Ripepe M, Marchetti E (2002) Array tracking of infrasonic sources at Stromboli volcano. Geophys Res Lett 29(22):2076. https://doi.org/10.1029/2002GL015452

Ripepe M, Marchetti E (2019) Infrasound monitoring of volcano-related hazards for civil protection. In: Le Pichon A, Blanc E, Hauchecorne A (eds) Infrasound monitoring for atmospheric studies, 2nd edn. Springer, Dordrecht, pp 1107–1140

Romero JE, Morgavi D, Arzilli F, Dagad R, Casellie A, Reckziegele F, Viramonte J, Díaz-Alvarado J, Polacci M, Burton M, Perugini D (2016) Eruption dynamics of the 22–23 April 2015 Calbuco Volcano (Southern Chile): analyses of tephra fall deposits. J Volcanol Geoth Res 317:15–29. https://doi.org/10.1016/j.jvolgeores.2016.02.027

Symons GJ (ed) (1888) The eruption of Krakatoa and subsequent phenomena. Harrison & Sons, London

Tailpied D, Le Pichon A, Marchetti E, Assink J (2016) Assessing and optimizing the performance and infrasound monitoring network. Geophys J Int 208. https://doi.org/10.1093/gji/ggw400

Ulivieri G, Ripepe M, Marchetti E (2013) Infrasound reveals transition to oscillatory gas flow regime during lava fountaining: implication for early-warning. Geophys Res Lett 40(12):3008–3013. https://doi.org/10.1002/grl.50592

Van Eaton AR, Amigo Á, Bertin D, Mastin LG, Giacosa RE, González J, Valderrama O, Fontijn K, Behnke SA (2016) Volcanic lightning and plume behavior reveal evolving hazards during the April 2015 eruption of Calbuco volcano, Chile. Geophys Res Lett 43:3563–3571. https://doi.org/10.1002/2016gl068076

Vernier J-P et al (2011) Major influence of tropical volcanic eruptions on the stratospheric aerosol layer during the last decade. Geophys Res Lett 38:L12807. https://doi.org/10.1029/2011GL047563

Index

A. Le Pichon et al. (eds.), *Infrasound Monitoring for Atmospheric Studies*,
https://doi.org/10.1007/978-3-319-75140-5